Lecture Notes on Multidisciplinary Industrial Engineering
Series Editor: J. Paulo Davim

M. S. Shunmugam
M. Kanthababu *Editors*

Advances in Micro and Nano Manufacturing and Surface Engineering

Proceedings of AIMTDR 2018

Springer

Lecture Notes on Multidisciplinary Industrial Engineering

Series Editor

J. Paulo Davim, Department of Mechanical Engineering, University of Aveiro, Aveiro, Portugal

"Lecture Notes on Multidisciplinary Industrial Engineering" publishes special volumes of conferences, workshops and symposia in interdisciplinary topics of interest. Disciplines such as materials science, nanosciences, sustainability science, management sciences, computational sciences, mechanical engineering, industrial engineering, manufacturing, mechatronics, electrical engineering, environmental and civil engineering, chemical engineering, systems engineering and biomedical engineering are covered. Selected and peer-reviewed papers from events in these fields can be considered for publication in this series.

More information about this series at http://www.springer.com/series/15734

M. S. Shunmugam · M. Kanthababu
Editors

Advances in Micro and Nano Manufacturing and Surface Engineering

Proceedings of AIMTDR 2018

Springer

Editors
M. S. Shunmugam
Manufacturing Engineering Section
Department of Mechanical Engineering
Indian Institute of Technology Madras
Chennai, Tamil Nadu, India

M. Kanthababu
Department of Manufacturing Engineering
College of Engineering, Guindy
Anna University
Chennai, Tamil Nadu, India

ISSN 2522-5022 ISSN 2522-5030 (electronic)
Lecture Notes on Multidisciplinary Industrial Engineering
ISBN 978-981-32-9424-0 ISBN 978-981-32-9425-7 (eBook)
https://doi.org/10.1007/978-981-32-9425-7

This Springer imprint is published by the registered company Springer Nature Singapore Pte Ltd.
The registered company address is: 152 Beach Road, #21-01/04 Gateway East, Singapore 189721, Singapore

AIMTDR 2018 Conference's Core Organizing Committee

Patrons

Dr. M. K. Surappa, Vice Chancellor, Anna University
Dr. J. Kumar, Registrar, Anna University

President (NAC-AIMTDR)

Mr. P. Kaniappan, Managing Director, WABCO India Ltd.

Vice-President (NAC-AIMTDR)

Dr. Uday Shanker Dixit, Professor, IIT Guwahati, India

Co-patrons

Dr. A. Rajadurai, Dean, MIT Campus, Anna University
Dr. T. V. Geetha, Dean, CEG Campus, Anna University
Dr. L. Karunamoorthy, Chairman, Faculty of Mechanical Engineering, Anna University
Dr. S. Rajendra Boopathy, Head, Department of Mechanical Engineering, Anna University

Chairman

Dr. S. Gowri, Honorary Professor, Department of Manufacturing Engineering, Anna University

Co-chairman

Dr. P. Hariharan, Professor, Department of Manufacturing Engineering, Anna University

Organizing Secretary

Dr. M. Kanthababu, Professor and Head, Department of Manufacturing Engineering, Anna University

Joint Organizing Secretaries

Dr. M. Pradeep Kumar, Professor, Department of Mechanical Engineering, Anna University
Dr. A. Siddharthan, Associate Professor, Department of Production Technology, Anna University

International Scientific Committee

Prof. Abhijit Chandra, Iowa State University, USA
Prof. Ajay P. Malshe, University of Arkansas, USA
Prof. Andrew Y. C. Nee, NUS, Singapore
Prof. Chandrasekar S., Purdue University, USA
Prof. Dean T. A., University of Birmingham, UK
Prof. Hong Hocheng, National Tsing Hui University, Taiwan
Prof. John Sutherland, Purdue University, USA
Prof. Kamlakar P. Rajurkar, University of Nebraska, USA
Prof. Kornel Ehmann, Northwestern University, USA
Prof. Liao Y. S., National Taiwan University, Taiwan
Prof. McGeough J. A., University of Edinburgh, UK
Prof. Mustafizur Rahman, NUS, Singapore

Prof. Philip Koshy, McMaster University, Canada
Prof. Rakesh Nagi, University of Buffalo, USA
Prof. Shiv Gopal Kapoor, University of Illinois, USA
Prof. Srihari Krishnasami, Binghamton University, USA
Prof. Tae Jo Ko, Yeungnam University, South Korea
Prof. Tugrul Ozel, State University of New Jersey, USA

National Advisory Committee

Prof. Ahuja B. B., Government College of Engineering Pune
Prof. Amitabha Ghosh, BESU
Prof. Bijoy Bhattacharyya, Jadavpur University, Kolkata
Prof. Biswanath Doloi, Jadavpur University, Kolkata
Prof. Chattopadhyay A. K., IIT Kharagpur
Prof. Deshmukh S. G., IIT Gwalior
Shri. Dhand N. K., MD, Ace Micromatic, Bangalore
Prof. Dixit U. S., IIT Guwahati, Guwahati
Prof. Jain P. K., IIT Roorkee, Roorkee
Prof. Jain V. K., IIT Kanpur
Prof. Jose Mathew, NIT Calicut
Shri. Lakshminarayan M., WABCO India Pvt. Ltd.
Prof. Lal G. K., IIT Kanpur
Prof. Mehta N. K., IIT Roorkee
Prof. Mohanram P. V., PSG Institute of Technology and Applied Research
Shri. Mohanram P., IMTMA, Bangalore
Dr. Mukherjee T., Tata Steel Ltd., Jamshedpur
Shri. Muralidharan P., Lucas TVS Ltd., Vellore
Prof. Narayanan S., VIT University, Vellore
Mr. Niraj Sinha, Scientist 'G', PSA, GOI
Prof. Pande S. S., IIT Bombay, Mumbai
Dr. Prasad Raju D. R., MVGREC
Prof. Radhakrishnan P., PSG Institute of Advanced Studies, Coimbatore
Prof. Radhakrishnan V., IIST, Trivandrum
Prof. Ramaswamy N., IIT Bombay (Former)
Prof. Ramesh Babu N., IIT Madras
Shri. Rangachar C. P., Yuken India Ltd., Bangalore
Prof. Rao P. V., IIT Delhi
Dr. Santhosh Kumar, IIT BHU
Dr. Sathyan B. R., CMTI, Bangalore
Prof. Satyanarayan B., Andhra University (Former)
Prof. Selvaraj T., NIT Trichy
Prof. Shan H. S., IIT Roorkee (Former)
Prof. Shunmugam M. S., IIT Madras

Shri. Shirgurkar S. G., Ace Designers Ltd., Bangalore
Dr. Sumantran V., Celeris Technologies
Dr. Suri V. K., BARC, Mumbai
Shri. Venu Gopalan P., DRDL Hyderabad
Prof. Vinod Yadav, Motilal Nehru National Institute of Technology, Allahabad

Foreword

It gives us immense pleasure to present the Advances in Manufacturing Technology and Design—Proceedings of All India Manufacturing Technology, Design and Research (AIMTDR) Conference 2018.

We would like to express our deep gratitude to all the members of Organizing Committee of AIMTDR 2018 Conference and also to authors, reviewers, sponsors, volunteers, etc., for their wholehearted support and active participation. Our special thanks to Mr. P. Kaniappan, Managing Director, WABCO India Ltd., Chennai, who kindly agreed to act as President of National Advisory Committee (NAC) of the AIMTDR 2018 Conference. We also express our sincere thanks to Chairman Dr. S. Gowri, Honorary Professor, and Co-chairman Dr. P. Hariharan, Professor, Department of Manufacturing Engineering, Anna University, Chennai, for their wholehearted support. We would like to express our sincere thanks to Research Scholars Mr. K. R. Sunilkumar, Mr. U. Goutham, Mr. V. Mohankumar and Mr. R. Prabhu and also UG/PG students of the Department of Manufacturing Engineering, Anna University, for their contributions in the preparation of this volume.

High-quality papers have been selected after peer review by technical experts. We hope you find the papers included in the Proceedings of AIMTDR 2018 Conference are interesting and thought-provoking.

We also like to express our gratitude for the support provided by WABCO India Ltd., Chennai; Kistler Instruments India Pvt. Ltd., Chennai; AMETEK Instruments India Pvt. Ltd., Bengaluru; Central Manufacturing Technology Institute, Government of India, Bengaluru; Defence Research and Development Organisation, Government of India, New Delhi; and Ceeyes Engineering Industries Pvt. Ltd., Trichy.

Finally, we would like to express our gratitude to the National Advisory Committee (NAC) members of AIMTDR 2018 Conference for providing the necessary guidance and support.

Guwahati, India

Uday Shanker Dixit
Vice-President
National Advisory Committee
AIMTDR

Preface

All India Manufacturing Technology, Design and Research (AIMTDR) Conference is considered globally as one of the most prestigious conferences held once in two years. It was started in 1967 at national level at Jadavpur University, Kolkata, India, and achieved the international status in the year 2006. It was organized by various prestigious institutions such as Jadavpur University, IIT Bombay, IIT Madras, CMTI Bangalore, PSG iTech, IIT Kanpur, CMERI, IIT Delhi, NIT Warangal, IIT Kharagpur, BITS Ranchi, VIT Vellore, IIT Roorkee, Andhra University, IIT Guwahati and College of Engineering Pune.

The recent edition of the AIMTDR Conference, 7th International and 28th All India Manufacturing Technology, Design and Research (AIMTDR) Conference 2018, was jointly organized by the Departments of Manufacturing Engineering, Mechanical Engineering and Production Technology during 13–15 December 2018 at College of Engineering Guindy, Anna University, Chennai, India, with the theme 'Make in India – Global Vision'. A major focus was given on recent developments and innovations in the field of manufacturing technology and design through keynote lectures. About 550 participants registered for the conference. During the conference, researchers from academia and industries presented their findings and exchanged ideas related to manufacturing technology and design.

Of the 750 papers received initially, 330 papers were finally selected after rigorous review process for publication. Selected papers from the conference are being published by Springer in the series Lecture Notes on Multidisciplinary Industrial Engineering in five volumes, namely **Volume 1**—Additive Manufacturing and Joining, **Volume 2**—Forming, Machining and Automation, **Volume 3**—Unconventional Machining and Composites, **Volume 4**—Micro and Nano Manufacturing and Surface Engineering and **Volume 5**—Simulation and Product Design and Development.

Chennai, India
December 2018

M. S. Shunmugam
M. Kanthababu

Contents

About the Editors

M. S. Shunmugam is a Professor (Emeritus) in the Manufacturing Engineering Section in the Department of Mechanical Engineering, Indian Institute of Technology (IIT) Madras. After receiving his PhD in Mechanical Engineering from IIT Madras in 1976, he has worked in IIT Bombay (from 1977 to 1980) and in IIT Madras from 1980 onwards. He was a visiting faculty member at Michigan Technological University during 1989-1991 and was a member in the board of governors of IIT Madras during 2012-2013. Dr. Shunmugam's research interests include metrology, machine tools, manufacturing, gears, micro-machining and computer applications in manufacturing. He has published about 130 peer-reviewed international journal papers, 15 peer-reviewed national journal papers, 75 international conferences and about 80 national conferences.

M. Kanthababu is a Professor in the Department of Manufacturing Engineering in Anna University, Chennai, India and the Director of the Centre for Intellectual Property Right and Trade Marks in Anna University. He has completed his MS in Mechanical engineering and PhD in Advanced Manufacturing Technology from IIT Madras. Prof. Kanthababu's research interests include manufacturing technology, composite materials and machining, and automation in manufacturing. He has published more than 30 peer reviewed international journal papers and 2 books, and holds one patent.

Part I
Micro and Nano Manufacturing

Chapter 1
Fabrication and Experimental Investigation of Micro-fluidic Channel-Based Mixing System Using Micro-electric Discharge Machining

Mamilla Ravi Sankar, Abhishek Sharma, Nuthi Dinesh Kumar, Siddharth Vikram, Mamidi Siva Kumar, Alokesh Pramanik and Kishor Kumar Gajrani

Abstract Electric discharge machining (EDM) is an advanced machining process, which harnesses the energy of series of electrical sparks for material removal from the workpiece. EDM is not only limited to machining of mechanical components but also finds its applications in aerospace, biomedical and other fields. Owing to the miniaturization of components, the fabrication at micro level paved the way for the development of micro-EDM (μ-EDM) process. In this study, the principle of μ-EDM has been used for machining open micro-channels for the efficient mixing of different fluids using micro-fluidic system. Micro-fluidic channels are fabricated using a stainless steel tool and the effect of peak current, pulse-on time and spark time has been investigated. Channel width, channel depth and its surface roughness are the

M. R. Sankar (✉) · S. Vikram · K. K. Gajrani
Department of Mechanical Engineering, Indian Institute of Technology Guwahati, Guwahati, Assam, India
e-mail: evmrs@iitg.ac.in

M. R. Sankar
Department of Mechanical Engineering, Indian Institute of Technology Tirupati, Tirupati, Andhra Pradesh, India

A. Sharma
Department of Precision and Microsystem Engineering, Delft University of Technology, Delft, The Netherlands

N. D. Kumar
Department of Production Engineering, National Institute of Technology Tiruchirappalli, Tiruchirappalli, Tamil Nadu, India

M. S. Kumar
University of Illinois at Chicago, College of Medicine, Rockford, USA

A. Pramanik
Department of Mechanical Engineering, Curtin University, Perth, Australia

K. K. Gajrani
Department of Mechanical Engineering, Indian Institute of Technology Bombay, Powai, Mumbai 400076, India

M. S. Shunmugam and M. Kanthababu (eds.), *Advances in Micro and Nano Manufacturing and Surface Engineering*, Lecture Notes on Multidisciplinary Industrial Engineering,
https://doi.org/10.1007/978-981-32-9425-7_1

response parameters. Input parameters are identified for minimum surface roughness of micro-fluidic channels to provide efficient mixing while achieving desired mixing time and homogeneity.

Keywords Micro-EDM · Micro-fluidic channels · Channel width · Channel depth · Surface roughness

1.1 Introduction

Micro-channel is defined as a channel having a dimension in the range of 1–500 μm. It is widely used in biological and chemical industries in order to analyse the biological structure and chemicals reagents [1–4]. Owing to their application, they are also known as "lab-on-chip" devices. The working of veins and arteries allowing for movement of blood through them can be considered as an example of micro-fluidic channels. Bioreactors are also considered as one of the applications of micro-channel that has been used for growth of bacteria and their analysis, as well as for examination [5]. Another important application of micro-channel is its utilization for heat exchange reactions due to the advantage provided by its high surface area to volume ratio. The major benefit provided is the increase in sensitivity and resolution of analysis of material along with the minimum amount of material wastage and reduced experimental cost [6]. They also find their application in micro-electromechanical systems (MEMS) as well as semiconductor industries [7–10]. Micro-channels also find their utility in devices like pipes and mixers along with some other components like pumps and valves [11–15]. They are also known as micro-reactors as they provide low volume for testing of some hazardous as well as expensive materials. Currently, they are mostly used in micro-jet printers, CD drives, hard disk devices and some other electronic devices.

There are various methods that are used for the fabrication of micro-channels, including conventional methods, like embossing, micro-cutters, moulding, and some advanced fabrication techniques, like photolithography, laser beam machining, ultrasonic machining, micro-electrical discharge machining (μEDM), and so on. [16–21]. Among all, the method of die sinking EDM is considered as an economic technique for the fabrication of micro-channels due to low setup cost as well as ease of machining. Also, the method helps in generating a replica of the tool onto the workpiece, especially in the cases where the workpiece material is harder than that of the tool material [22]. Another benefit of using this method is the fabrication of intricate and complex shapes along with close tolerance on the workpiece.

The major disadvantage associated with the usage of EDM is its limited application to conducting material only due to which non-conducting materials cannot be machined by this method. The principle of this process is that it utilizes a series of electric discharge that takes place between the tool and the workpiece in the presence of a dielectric medium. Tool movement is controlled using a servo control mechanism for maintaining a gap between the workpiece and the tool, which is of the order

of 25–50 μm [23]. These electric discharges are of pulsed mode types consisting of an ON and OFF time, which can be varied by changing the duty cycle and pulse-on time. The dielectric present between the tool and the workpiece gets ionized due to the applied voltage, which provides necessary medium for the spark to occur. As the material removal in this unconventional machining process mainly occurs because of erosion, a small amount is also attributed to cavitation. This process not only affects the workpiece but also affects the tool while the machining is carried away. According to Mohri et al., the precipitation of carbon due to dielectric breakdown onto the electrode surface and its inability to reach the difficult areas caused an increase in tool wear [24].

In the present work, die sinking μ-EDM method is used to fabricate open micro-fluidic channels. The effect of peak current, pulse-on time and spark time on the width, depth and surface roughness of micro-channels is investigated. These are affected by various factors, such as the electrode material used and the different process parameters. Optical microscope and non-contact surface profilometer is used for investigating the surface morphology of micro-fluidic channel.

1.2 Experimentation

1.2.1 Design of Experiments

The experiments to be performed are planned and designed in such a way that useful inferences are easily determined by performing a minimum number of experiments using the design of experiments. The methodology used is central composite rotatable design (CCRD), which helps in determining the number of experiments to be performed as:

$$\text{Number of experiments} = 2^{k} + 2k + \text{central run} \tag{1.1}$$

where k is the number of input parameters chosen which are three: peak current (I), pulse-on time (P) and spark time (S). Therefore, the total number of experiments required to be performed is calculated as per Eq. (1.1):

$$\text{Number of experiments} = 2^{3} + (2 * 3) + 6 = 20 \tag{1.2}$$

Six central runs were selected in order to reduce the error and to easily evaluate the repeatability. Based on the preliminary examination, the value of peak current (I) is varied in the range of 2–10 A, while the values of pulse-on time (P) and spark time (S) are varied in the range of 18–28 and 1–5 μs, respectively. The coded as well as the original values of the input parameters as per CCRD are listed in Table 1.1. All the experiments are repeated thrice and the average values are reported. The influences of these parameters on the output responses are also evaluated.

Table 1.1 Coded and original values of input parameters as per the central composite rotatable design

Coded value	−1.414	−1.000	0.00	1.000	1.414
Peak current (A)	2	3.171	6	8.828	10
Pulse on time (μs)	18	19.464	23	26.536	28
Spark time (μs)	1	1.585	3	4.415	5

1.2.2 Experimental Setup

An EDM machine (Make: Sparkonix®) is used to fabricate a Y-shaped micro-fluidic system. Figure 1.1a illustrates the overview of experimental setup. The desired width of micro-channel is in microns. Therefore, 0.1 mm thick tool was used for fabrication of micro-channel. However, it cannot be directly mounted on EDM machine. Hence, a separate tool-holding device was fabricated to hold the tool. The holding device or the fixture should be fabricated in such a way that when this thin-walled tool is subjected to flowing dielectric, the tool holder must hold the grip of the tool firmly so that the tool is able to bear the force exerted by the shocks as well as sparks generating simultaneously during the machining operation. The tool edge has to be perfectly straight in such a way that it is parallel to the plane of the workpiece. As the stray

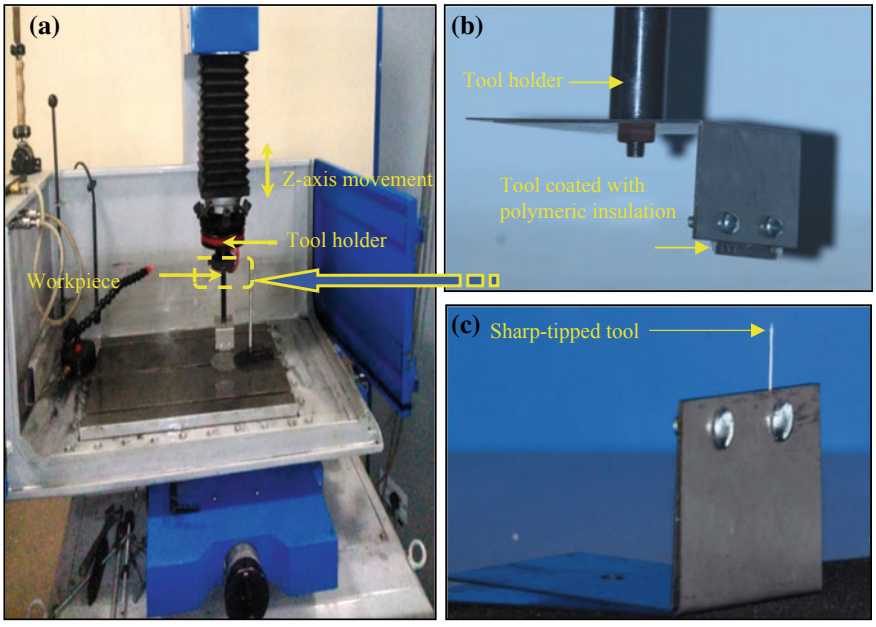

Fig. 1.1 **a** Overview of experimental setup, **b** tool holding assembly with polymeric insulated tool for micro-channels, and **c** sharp-tipped tool for fabrication of micro-holes

Table 1.2 Materials and equipments

Workpiece	Stainless steel 316 L (thickness = 0.6 mm)
Tool	Stainless steel (13% Cr, 0.6% C)
Equipment	Sparkonix-S35 EDM machine
Surface analyser	Taylor Hobson surface profilometer
Optical microscope	Zeiss, AxioCam MRc

currents generated during machining operation results in an increment in channel width and subsequently poor finishing at the channel boundary, they were minimized using a polymeric insulation on the side of tool cutting edge. Polymeric insulation-coated stainless steel tool is used for fabrication of micro-fluidic channel. Figure 1.1b, c illustrates the tool holding assembly for fabrication of micro-channels and micro-holes, respectively. Stainless steel material is chosen as workpiece material. Table 1.2 illustrates the tool and workpiece materials as well as equipment used for this study.

1.2.3 Fabrication of Micro-fluidic Channel

Micro-fluidic channels of different channel width, channel depth and having varying surface roughness are fabricated by varying the input parameters such as peak current (I), spark time (S) and pulse-on time (P). These input parameters were kept low in order to have a good surface finish and lesser channel width. The peak current was varied from 2 to 10 A, the spark time from 1 to 5 μs and pulse-on time from 18 to 28 μs. The low pulse-on time facilitates proper flushing of the eroded debris. Each of the above parameters was varied in discrete steps. I represents current in Ampere, P is pulse-on time (μS), S denotes spark time (μS), C_w represents channel width (μm), C_d denotes channel depth (μm) and R_a is surface roughness of channel (μm).

A total of 20 experiments with different input parameters keeping a constant duration of 150 s were conducted. The channel width, channel depth and channel surface roughness were measured using the non-contact surface profilometer and optical microscope. The input parameters and corresponding responses are illustrated in Table 1.3. Fig. 1.2a illustrates the fabricated micro-fluidic channels and Fig. 1.2b shows the fabrication of micro-channels. From the experiment conducted, it was found that at 8 A peak current, 20 μs pulse-on time and 2.0 μs spark time, the average value of channel surface roughness (R_a) was found to be the lowest among others (2.9 μm). For the same parameter, the channel width and depth were 170 and 38.2 μm, respectively.

These values of input parameters were then selected for the fabrication of a Y-shaped micro-fluidic system. At the starting point of micro-channels, a micro-hole is also fabricated. Micro-holes at the outer end of each micro-channel are used to deliver the fluid into the channel. Two different fluids are delivered from each of the two limbs of the Y-shape channel system and the mixture was collected through the

Table 1.3 Input parameters and corresponding responses

Channel no.	I	P	S	C_w	C_d	R_a
1	6	23	3	152	25.10	4.23
2	6	23	5	136	22.00	4.49
3	10	23	3	171	45.30	4.88
4	8	26	4	165	37.40	4.92
5	6	23	3	152	25.10	4.23
6	6	23	3	152	25.10	4.23
7	4	26	2	140	13.10	3.87
8	8	20	2	170	38.20	2.90
9	6	23	3	152	25.10	4.23
10	4	20	2	138	24.10	3.18
11	4	26	4	134	25.05	2.81
12	6	23	1	150	25.80	2.38
13	6	23	3	152	23.40	4.23
14	6	18	3	160	31.00	2.51
15	8	20	4	172	35.90	4.47
16	6	28	3	166	32.00	4.72
17	8	26	2	199	41.60	3.60
18	6	23	3	152	25.10	4.23
19	4	20	4	99.10	16.90	2.01
20	2	23	3	56.70	10.90	2.00

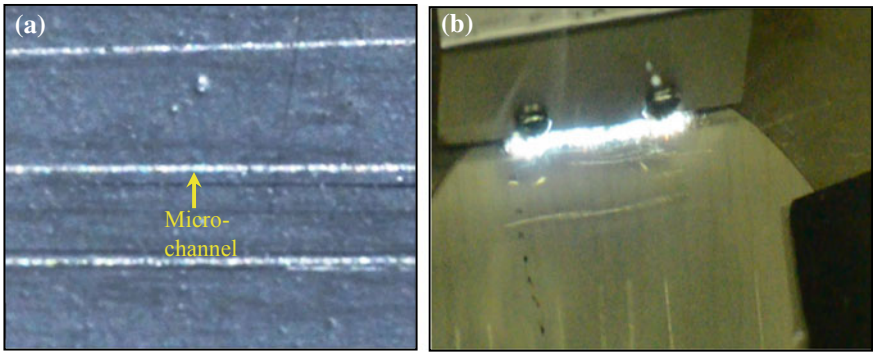

Fig. 1.2 **a** Fabricated micro-channels and, b sparks produced during micro-channel machining

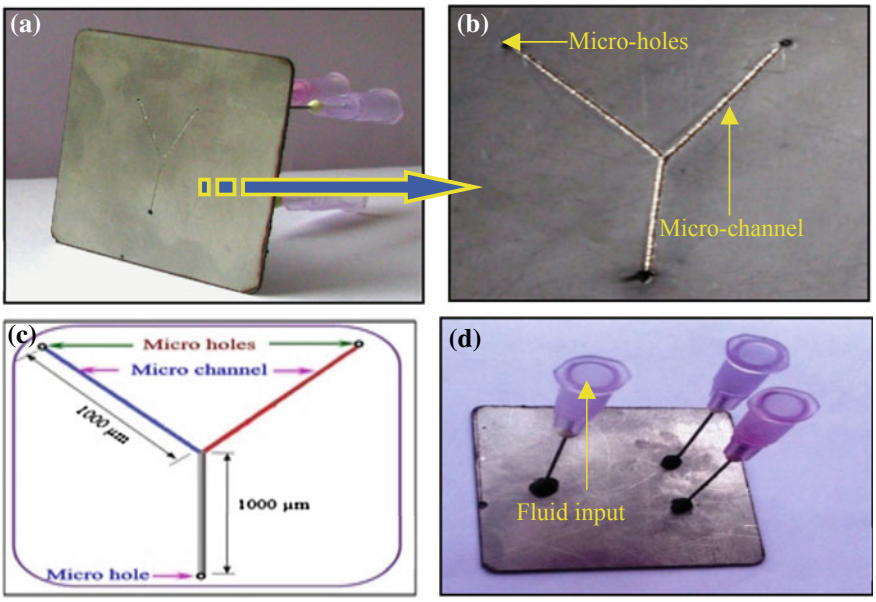

Fig. 1.3 **a** Setup for fluid delivery into the micro-fluidic channels, **b** Y-shaped micro-fluidic system for micro-mixing, **c** schematic flow of fluids in micro-fluidic system and **d** rear side of the setup

third outlet limb. This system is used as a prototype to show a typical application of micro-fluidic channels fabricated through die sinking EDM. After the fabrication of this Y-shaped channel, the feasibility of this channel for the efficient mixing of the fluids were analysed. Two different coloured fluids were injected using syringes through two upper limbs. The necessary turbulence needed for the efficient and proper mixing of these fluids was provided by the surface roughness of the channel. This roughness has to be optimized depending upon the nature of fluids to be mixed, for example, specific gravity and miscibility. The setup for liquids flow through the micro-channels is shown in Fig. 1.3.

1.3 Results and Discussion

The width and depth of micro-fluid channel were measured using a Zeiss optical microscope at 5× magnification and non-contact surface profilometer. Figures 1.4 and 1.5 show the channel no. 8 and 13 as per CCRD inputs (Table 1.3). The first channel corresponds to I = 8 A, P = 20 µs and S = 2 µs. The micrograph and profilometer images for this channel are shown in Fig. 1.4a and b, respectively. The same is depicted for channel no. 13 along with its channel width and depth measurements in Fig. 1.5a–c, respectively. Channel 8 has different peak current and spark time as that were used to fabricate channel 13; however, it was fabricated using

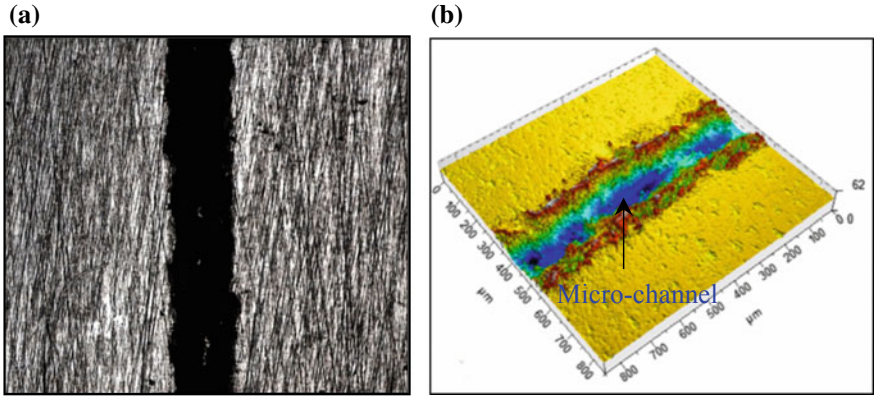

Fig. 1.4 Micro-fluidic channel no. 8: **a** surface micrograph and **b** 3D surface profile

a lower pulse-on time. Channel 8 recorded a lower *Ra* (2.9 μm) value than channel 13 (3.6 μm), which shows that surface roughness increases as the pulse-on time is increased. It is also observed that the channel width and depth increased with an increase in the value of pulse-on time.

1.3.1 Channel Width

As per CCRD, the following relation was obtained for the channel width with the input parameters;

$$\text{Channel width } (C_w) = 305.68 + 43.17I - 28.67P - 2.61S - 0.32IP + 0.77IS - 0.11PS - 2.08I^2 + 0.71P^2 - 1.01S^2 \quad (1.3)$$

with coefficient of determination (R^2) value of 0.9217, where I = peak current (A), P = pulse-on time (μs), S = spark time (μs).

It was observed from Fig. 1.6 that the channel width increases when more current is applied during the machining process. As heat produced is proportional to the square of input current value, the crater size produced is more leading to greater roughness, which also results in increased channel width. The slope becomes less steep with increasing value of current. Figure 1.7 illustrates that the value of pulse-on time increases, channel width first decreases and then begins to increase in a parabolic fashion. Here the largest channel width is obtained for the channel with highest peak current value. It is evident from Figs. 1.6 and 1.7 that channel width increases with peak current. It may be attributed to the increment in thermal energy which further

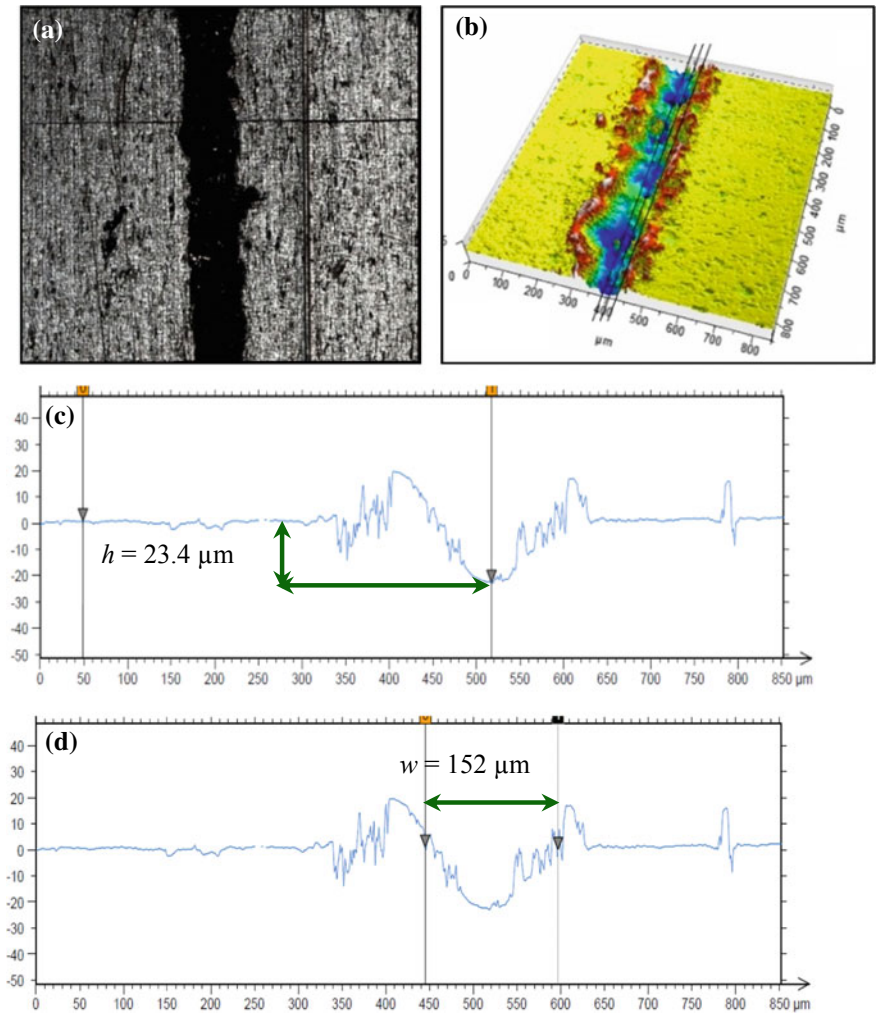

Fig. 1.5 Micro-fluidic channel no. 13: **a** surface micrograph, **b** 3D surface profile, **c** channel depth measurement and **d** channel width measurement

causes increase in working temperature. This causes more metal to melt and forms a wider crater, thereby increasing the channel width.

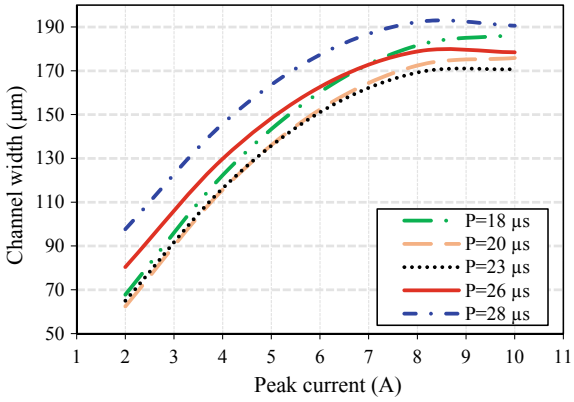

Fig. 1.6 Effect of peak current on channel width for constant spark time

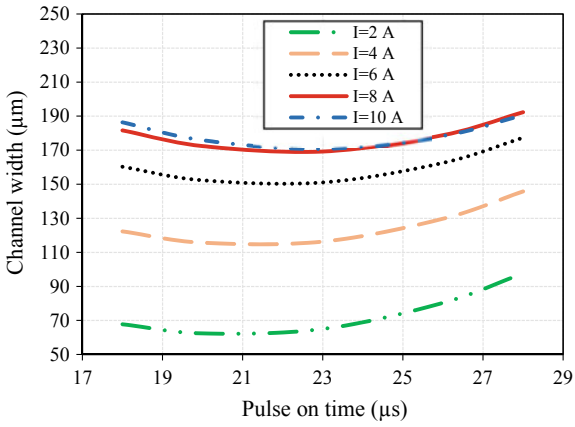

Fig. 1.7 Effect of pulse-on time on channel width for constant spark time

1.3.2 Channel Depth

As per CCRD, the channel depth is related to the input parameters as follows:

$$\text{Channel depth } (C_d) = 214.16 + 0.26I - 16.14P - 11.8S + 0.16IP - 0.7IS + 0.72\,PS + 0.22I^2 + 0.28\,P^2 - 0.18S^2 \quad (1.4)$$

with an R^2 value of 0.9573, where I = peak current (A), P = pulse-on time (μs), S = spark time (μs).

It is observed that the effect of input parameters on channel width is somewhat similar to that on the channel depth. The increase in channel depth with increasing current and pulse-on time can be seen in Fig. 1.8. Also, the slope of the curve increases with increasing value of current. Figure 1.9 shows the effect of peak current

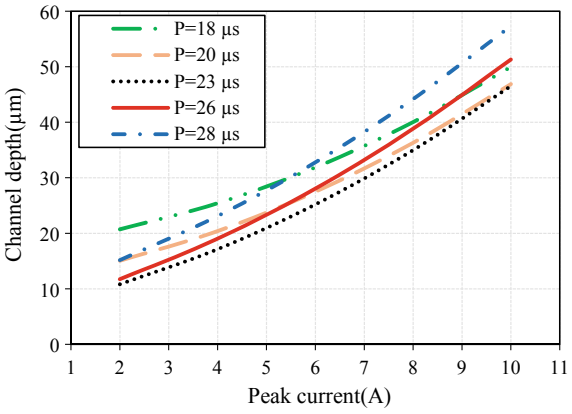

Fig. 1.8 Effect of peak current on channel depth for constant spark time

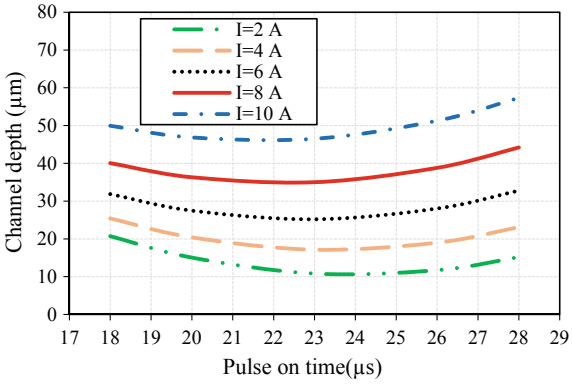

Fig. 1.9 Effect of pulse-on time on channel depth for constant spark time

on channel depth which first decreases and later increases with increasing value of pulse-on time.

1.3.3 Average Surface Roughness (R_a)

For getting a smooth channel, all the three parameters need to be optimized. From the data obtained, the dependence of *Ra* (µm) with peak current, pulse-on time and sparking time is studied and is given as follows:

$$R_a\ (\mu m) = 16.4I + 0.14I + 1.51P - 0.2S - 7.08e^{-3}IP + 0.32IS - 5.84e^{-3}PS - 0.053I^2 - 0.03P^2 - 0.21S^2 \quad (1.5)$$

with R^2 value of 0.9175, where I = peak current (A), P = pulse-on time (µs), S = spark time (µs).

This relationship of R_a with each input parameter is discussed subsequently. It is observed from Fig. 1.10 that when the peak current is increased, the channel surface roughness increases initially, and then it decreases. The increase in peak current causes an increase in the discharge heat energy at the point where the discharge takes place. At this point, a pool of molten metal is formed and overheated.

The molten metal evaporates and the forming gas bubbles explode when the discharge takes place, so taking the molten material away. Successive discharges will result in craters, thus increasing the surface roughness. The channel roughness increases with increasing pulse-on time, as shown in Fig. 1.11. Figure 1.11 also reveals that roughness value for I = 10 A is the highest. The slope of the curve decreases with increasing value of pulse-on time. Also, the effect of current becomes less pronounced on roughness at its higher values. Sparking time affects R_a in an inconsistent manner. The R_a value increases up to a spark time, which lies between 4 and 5 μs; after which it decreases.

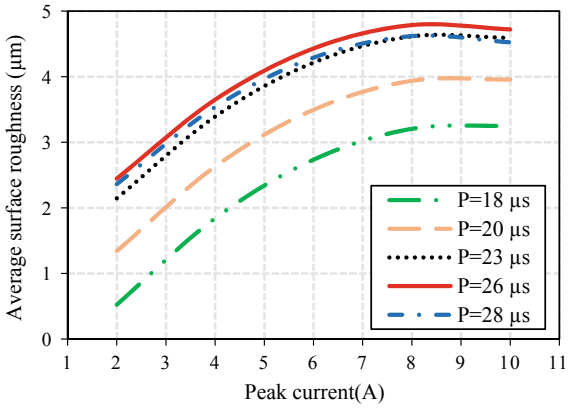

Fig. 1.10 Effect of peak current on surface roughness for constant pulse-on time

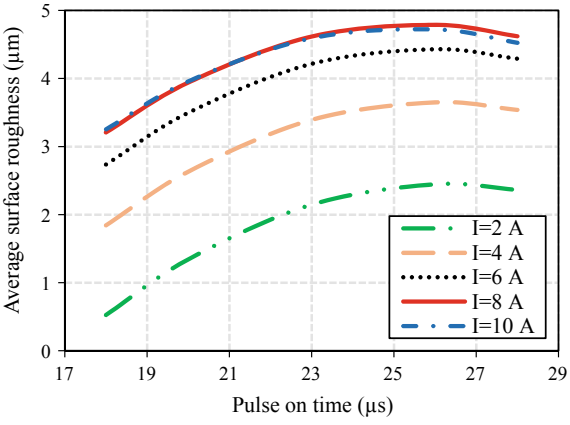

Fig. 1.11 Effect of pulse-on time on surface roughness for constant spark time

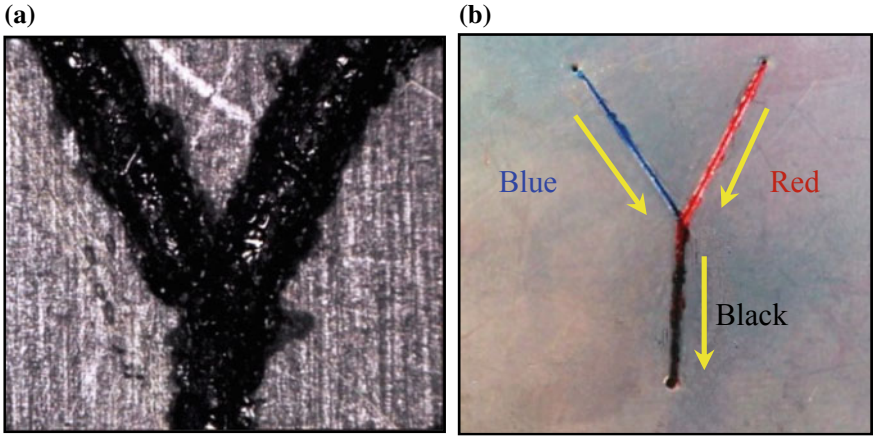

Fig. 1.12 Y-shaped micro-fluidic system. **a** Optical micrograph of the junction and **b** fluid flow and mixing in the micro-channels

1.3.4 Flow of Fluids in the Micro-fluidic System

In the present study the input parameters that yielded optimal and low roughness, channel width and depth for fabricating the micro-fluidic device were selected (Ra = 2.9 μm, C_w = 38.2 μm, C_d = 170 μm).

The mixture was collected through another syringe at the outlet. Figure 1.12a shows an image of the junction where the three channels meet, and is taken using an optical microscope at 5×. The flow in the micro-channel device is crucial to the three micro-channels being concurrent. Figure 1.12b shows the flow of two miscible liquids in the device. The mixing of a blue and a red liquid to yield a black mixture was studied. It can be clearly seen that the blue fluid mixes more readily than its red counterpart. This device was designed keeping in mind a typical biomedical application of liquid testing and mixing. Varying the roughness of mixing channel can alter the homogeneity of the mixture and mixing time.

1.4 Conclusion

Micro-fluidic devices have seen rapid development in the present years. In this paper, micro-channels of dimension within the micrometre scale were fabricated using EDM. Y-shaped micro-fluidic system was also developed for mixing of different fluids. The salient findings are as follows:

- Micro-channels and micro-holes were successfully fabricated using die sinking EDM.

- Peak current has considerable effect on channel width, depth and its surface roughness.
- At 8 A peak current, 20 μs pulse-on time and 2 μs spark time, lowest surface roughness of micro-channel was obtained.
- Y-shaped micro-fluidic system was fabricated using optimized parameters to mix different fluids.

References

1. Mao, X., Huang, T.J.: Microfluidic diagnostics for the developing world. R. Soc. Chem. **12**, 1412–1416 (2012)
2. Kovarik, M.L., Ornoff, D.M., Melvin, A.T., Dobes, N.C., Wang, Y., Dickinson, P.C., Shah, P.K., Albritton, N.L.: Micro total analysis systems: fundamental advances and applications in the laboratory, clinic, and field. Anal. Chem. **85**(2), 451–472 (2013)
3. Graber, N., Manz, A., Widmer, H.M.: Miniaturized total chemical analysis system: a novel concept for chemical sensing. Sens. Actuators B: Chem. **1**, 244–248 (1990)
4. Arora, A., Simone, G., Georgette, B., Beugelaar, S., Kim, J.T., Manz, A.: Latest development in micro total analysis system. Anal. Chem. **82**, 4830–4847 (2010)
5. Balagadde, F.K., You, L.C., Hansen, C.L., Arnold, F.H., Quake, S.R.: Long-term monitoring of bacteria undergoing programmed population control in a micro chemo stat. Science **309**, 137–140 (2005)
6. Lee, C.C., Sui, G, Elizarov, A., Shu, C.J., Shin, Y.S., Dooley, A.N., Huang, J., Daridon, A., Wyatt, P., Stout, D., et al.: Multistep synthesis of a Radio labelled imaging probe using integrated micro fluidics. Science **310**, 1793–1796 (2005)
7. Bhattacharyya, B., Munda, J., Malapati, M.: Advancement in electrochemical micro-machining. Int. J. Mach. Tools Manuf. **44**, 1577–1589 (2004)
8. Schuster, R., Kirchner, V., Allongue, P., Ertl, G.: Electrochemical machining. Science **289**, 98–101 (2000)
9. Bhattacharya, B., Jain, V.K.: Introduction to Micromachining. Narosa Publication, pp. 17.1–17.32 (2009)
10. Jain, V.K., Lal, G.K., Kanetkar, Y.: Stray current attack and stagnation zones in electrochemical drilling. Int. J. Adv. Manuf. Technol. **26**, 527–536 (2005)
11. Gunther, A., Jhunjhunwala, M., Thalmann, M., Schmidt, M.A., Jensen, K.F.: Micro mixing of miscible liquids in segmented gas-liquid flow. Langmuir **21**, 1547–1555 (2005)
12. Hong, W.J., Quake, S.R.: Integrated nanoliter system. Nat. Biotechnol. **21**, 1179–1183 (2003)
13. Weibel, D.B., Kruithof, M., Potenta, S., Sia, S.K., Lee, A., Whitesides, G.M.: Torque actuated valves for microfluidics. Anal. Chem. **77**, 4726–4733 (2005)
14. Nguyen, N.T., Wu, Z.: Micromixers—a review. J. Micromech. Microeng. **15**, R1–R16 (2005)
15. Garstecki, P., Fischbach, M.A., Whitesides, G.M.: Design for mixing using bubbles in branched microfluidic channels. Appl. Phys. Lett. **86** (2005)
16. Gajrani, K.K., Sankar, M.M.: State of the art on micro to nano textured cutting tools. Mater. Today: Proc. **4**(2A), 3776–3785 (2017)
17. Behera, R.R., Babu, P.M., Gajrani, K.K., Sankar, M.R.: Fabrication of micro-channels on 304 stainless steel (SS-304) using Nd:YAG laser beam micro-machining. Int. J. Addit. Subtractive Mater. Manuf. **1**(3/4), 338–359 (2017)
18. Gajrani, K.K., Suresh, S., Sankar, M.R.: Environmental friendly hard machining performance of uncoated and MoS_2 coated mechanical micro-textured tungsten carbide cutting tools. Tribol. Int. **125**, 141–155 (2018)

19. Gajrani, K.K., Reddy, R.P.K., Sankar, M.R.: Tribo-mechanical, surface morphological comparison of un-textured, mechanical micro-textured (MμT) and coated-MμT cutting tools during machining. Proc. Inst. Mech. Eng. Part J: J. Eng. Tribol. (2018). https://doi.org/10.1177/1350650118764975
20. Gajrani, K.K., Sankar, M.R., Dixit, U.S.: Environmentally friendly machining with MOS_2 filled mechanically micro-textured cutting tools. J. Mech. Sci. Technol. **32**(8), 3797–3805 (2018)
21. Gajrani, K.K., Sankar, M.R.: Sustainable machining with self-lubricating coated mechanical micro-textured cutting tools. In: Reference Module in Materials Science and Materials Engineering. Elsevier. https://doi.org/10.1016/b978-0-12-803581-8.11325-6
22. Reynaerts, D., Meeusen, W., Brussel, H.V.: Machining of three-dimensional microstructures in silicon by electro-discharge machining. Sens. Actuators **67**, 159–165 (1998)
23. Zeid, O.A.A.: On the effect of electro discharge machining parameters on the fatigue life of AISI d6 tool steel. Curr. Adv. Mech. Des. Prod. VI **68**, 27–32 (1997)
24. Mohri, M., Suzuki, M., Furuya, M., Saito, N., Kobayashi, A.: Electrode wear process in electrical discharge machining. CIRP Ann. 165–168 (1995)

Chapter 2
Compression and Diametral Tensile Strength Analysis of Graphene–Al_2O_3 Reinforced AA 2024 and AA 2219 Hybrid Nanocomposites

P. Ashwath and M. Anthony Xavior

Abstract Aluminum-matrix nanocomposites (AMNCs), in particular the graphene particle reinforced AMNCs, have received considerable attention due to their attractive physical and mechanical properties, such as high strength, tensile strength, compressible property, improved wettability and improved tribological characteristics. Carbon and ceramic filler reinforcement is an active method to enhance the strength of aluminum and its alloy, nevertheless, the homogeneous dispersion, and controlled interfacial reactions in the matrix during processing. In the current research work, composites with graphene of average particle size 10 nm and Al_2O_3 of particle size 10 μm as reinforcement combinations in various proportions (wt%) in aluminum alloy (AA) AA 2024 and AA 2219 matrix materials are carried out through powder metallurgy approach. Homogeneous dispersion of reinforcement in the matrix is achieved through ultrasonic dispersion followed by ball milling. Thus, the prepared precursors are consolidated by uniaxial hot compaction in a universal tensile testing machine and microwave sintered in inert gas atmosphere. Rockwell hardness studies were carried out on the samples as per ASTM standards. SEM, X-ray diffraction analysis, and microstructure analysis were done on developed composites. Further, compression and diametrical tensile strength were evaluated on developed composites according to the standard testing conditions. Enhancement in the bulk strength, strengthening mechanism and probable motives for crack initiations were widely examined to study the effect of graphene–Al_2O_3 addition and its combinations in the composites matrix. The addition of fine particles of Al_2O_3 enhances the nanocomposites reinforced with graphene to further improve the strength properties.

Keywords Hybrid nanocomposites · Diametral tensile strength · Graphene reinforcement · Powder metallurgy · Hybrid composites

P. Ashwath · M. Anthony Xavior (✉)
Manufacturing Engineering, Department of Mechanical Engineering, Vellore Institute of Technology, Vellore 632014, India
e-mail: manthonyxavior@vit.ac.in

M. S. Shunmugam and M. Kanthababu (eds.), *Advances in Micro and Nano Manufacturing and Surface Engineering*, Lecture Notes on Multidisciplinary Industrial Engineering,
https://doi.org/10.1007/978-981-32-9425-7_2

2.1 Introduction

Today, one of the active areas of researches in materials engineering field is that of fabrication of new class of advanced materials. The advanced materials should possess high strength with improved material and mechanical stiffness properties. The fabrication of the composites with ceramic particle reinforced is purely based on the level of homogeneity achieved while processing the powder samples. In particular, focusing on nanocomposites, the nature of nano-reinforcement material used and the homogeneous mixing and the bonding of the nano-reinforcement with the matrix are the key factors governing the outcome of the composites developed. At nanocomposite level, various application challenges like micro and nanometer range can be used to achieve specific properties required. These metal–matrix composites and nanocomposites can be engineered with different fabrication methods and processing methods without sacrificing specific engineering properties [1–3]. It was delicate for the recent researchers to take extra effort in narrowing the selection of type of reinforcing material used in line with the aluminum alloy matrix used. Selection and using of the reinforcement is the key factor that determines the overall property of the composites [4]. Most of the recent research works are focused on developing hybrid composites by varying the nano reinforcements, like nano alumina, graphene nano platelets and carbon nano tubes at different combinations. More frequently, carbides and oxides of ceramic materials are reinforced and studied for mechanical and microstructural improvements [5], of which alumina is majorly used as a ceramic reinforcement in line with aluminum matrix for engineering application. Alumina because of the good thermal stability and good load-bearing capacity was used more in structural application and frictional application [6]. Carbon-based reinforcements such as graphene and CNT exhibit mixed challenges while processed through powder metallurgy method because of low surface contact area and wettability [7, 8].

In carbon-based composites where graphene is allotrope of carbon and actively used in the fabricating hybrid composites for recent research work in structural and frictional-based application, choosing graphene as a reinforcement is driven by its specific higher physical and mechanical properties, such as tensile strength 130 (GPa), elastic modulus (0.5–1 TPa), and thermal conductivity (5.3×10^3 W m^{-1} K^{-1}). In addition, it exhibits strong sp^2-hybridized 2D-nanomaterial (sheet-like morphology) which is a key factor as a unit of composites with extreme strength [9]. In the past decades, a few or no attempts were tried to characterize on the aluminum metal matrix hybrid composites reinforced with Al_2O_3 and graphene. Recent research works have reported the difficulties in achieving the homogeneous dispersion of nano graphene in the matrix, which is achieved by several methods such as ultrasonication and magnetic stirring methods.

2.2 Experimentation and Methods

2.2.1 Dispersion of Graphene and Al_2O_3

The aluminum alloy powder AA 2024 and AA 2219 manufactured by gas atomized method with average particulate size 30–35 μm (from Ampal Inc.) was taken as a matrix material and the corresponding chemical composition is given in Tables 2.1 and 2.2: Al_2O_3 with density 3.20–3.70 g/cm^3 and graphene 1.5–2.0 g/cm^3 (from Angstron Materials) are used as reinforcements. Ultrasonic liquid processor and ball milling is used to achieve homogeneous dispersion of reinforcements into the metal matrix. The structure and morphology of all precursors are shown in Fig. 2.1a–d. Table 2.3 shows the combinations of various reinforcements and matrix materials (reinforcements and matrix blending parameters) used for the current research work in weight percentage (wt%). Initially, dispersion of graphene particulates is achieved by using ultrasonic dispersion method. Graphene with various weight percentage (0.25, 0.5, 0.75 and 1.0 wt%) were added into the acetone and sonicated for 1 h. Later, calculated quantity of Al_2O_3 (8.0 wt%) were added to solvent containing graphene which is dispersed in an acetone and continued the sonication for 30 min by keeping the slurry beaker on magnetic stirrer to avoid the sedimentation due to difference in densities. Figure 2.2 explains the processing of precursors, and thus the obtained mixtures are ball milled by adding aluminum alloy powders (AA 2024 and AA 2219) separately followed by drying the powder mixtures in oven at 90 °C for 24 h.

2.2.2 Composite Preparation

Powder metallurgy method was used to fabricate the metal matrix composites. The fabricated composites are compacted according to ASTM standard B925-08. The dies are made up of carbide material and die case with chromium hot-work tool steel (40–48 HRC). Compaction was performed with compaction pressure of 460 MPa (holding the pressure for 15 min) for all the samples and high temperature lubricant such as boron nitride is used between the die walls. Subsequently, the samples were sintered using microwave sintering furnace at 610 °C in an inert gas atmosphere for 30 min followed by furnace cooling.

2.2.3 Testing and Characterization

A portion of the alloy powder (AA 2024 and 2219), graphene and Al_2O_3 was analyzed under scanning electron microscope (SEM). XRD analysis is carried out on sintered composites. Vickers hardness (VH) values are measured for all the sintered

Table 2.1 Chemical composition of aluminum alloy 2024 used as matrix material (wt%)

Element	Si	Fe	Cu	Mn	Mg	Cr	Zn	Ti	Al
(%)	0.5	0.5	4.0	0.4	1.50	0.1	0.25	0.15	Bal.

Table 2.2 Chemical composition of Al 2219 used as matrix material (wt%)

Element	Si	Fe	Cu	Mn	Mg	Cr	Zn	Ti	Zr	V	Al
(%)	0.2	0.3	5.8	0.3	0.02	0.1	0.1	0.1	0.2	0.1	Bal.

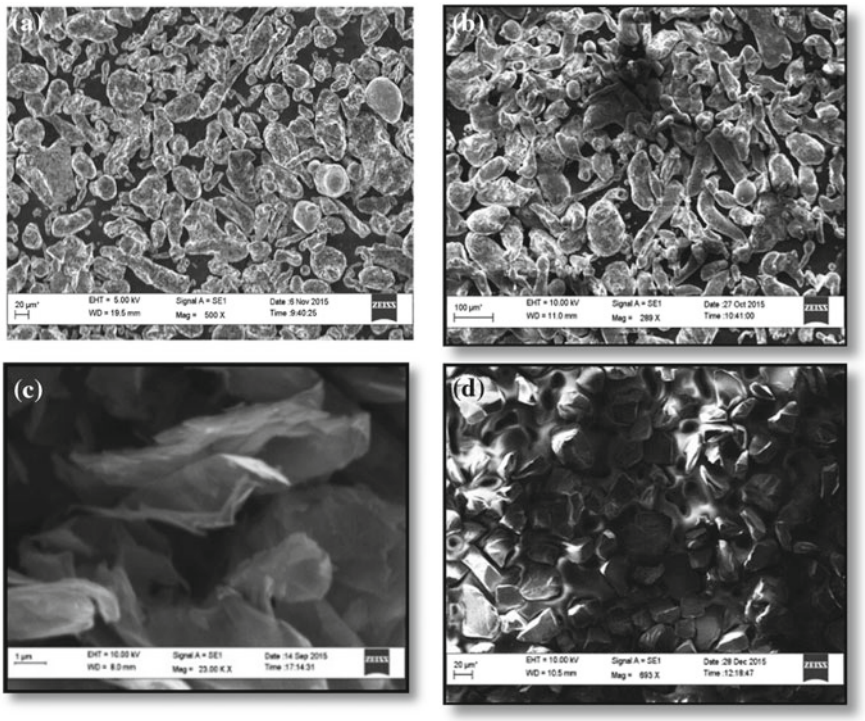

Fig. 2.1 Scanning electron microscope (SEM) image of **a** Al 2024, **b** Al 2219, **c** graphene and **d** Al_2O_3 particulates

Table 2.3 Powders blending parameters

AA alloy	Al_2O_3 (Weight %)	Graphene (Weight %)
AA 2024	0.8	0.25, 0.5, 0.75 and 1.0
AA 2219	0.8	0.25, 0.5, 0.75 and 1.0
(Sonication time, ball milling time: 30 min for each sample)		

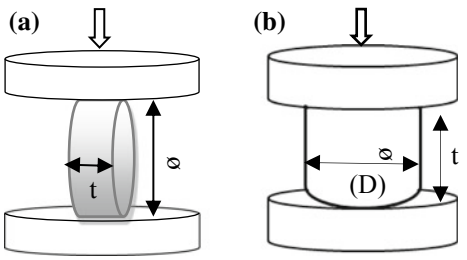

Fig. 2.2 Schematic illustration of **a** diametrical tensile strength and **b** compressive strength analysis

composites samples after fine polishing. Minimum of five measurements were done on different surface areas on the composites surface and average of the measured values are reported. Densities are measured on each sample by calculating mass and volume for all the fabricated composites. Theoretical densities (g/cm^{-3}) of various configurations are calculated according to ground rule illustrated by hybrid mixture relation (RoHM) applied to composite fabricated and sintered density (g/cm^{-3}) calculated by Archimedes' principle adapting an electronic density measurement equipment with measuring sensitivity of 0.0001 mg for graphene composites. Diametrical tensile test samples (Ø 25 mm × 50 mm) are polished (mirror finish) and checked for the cracks. Thus, the checked samples are positioned vertically, and the test was performed using universal axial loading at cross-head rate of 0.5 mm/min, as illustrated in Fig. 2.2a. Destructive-type (procedure) compressive strength analysis is adapted to characterize the powder metallurgy sample. Compressive strength testing of the alloy (AA 2024 and 2219), graphene, Al_2O_3 and the three composites was conducted at room temperature in INSTRON-8801 axial loading testing machine, using samples of dimensions 25 mm dia × 50 mm long and lubricating compression loading cells (plates) by boron nitride spray (from Momentive, USA) to reduce the friction. The tests were carried out at a constant strain rate (v = 0.04 mm/min) with controlled compressive load rating perpendicular to its central axis of the solid composite sample, as illustrated in Fig. 2.2b.

$$\text{Diametrical tensile strength (DTS)R} = \frac{2P}{\pi Dt} \tag{2.1}$$

2.3 Results and Discussion

The SEM micrographs observations of Al 2024 and Al 2219 alloy powders show that most of the particles have smooth curved edges and also layered morphology of the graphene which are loaded one over the other and curl-free. Ultrasonicated followed by ball milling powder mixture exhibits, most of graphene exist in flake form, mono-layered wrapped on other particles and homogeneously dispersed in the matrix. The predecessors are hot compacted and thus fabricated compacts are successfully sintered using microwave sintering furnace in which the mixed powder samples are heated at higher heating rate. Figure 2.3 shows the XRD analysis of (a) Al 2024–graphene–Al_2O_3 and (b) Al 2219–graphene–Al_2O_3. It is clear that the presence of graphene peaks at 2θ equal to 26.50° (related to graphene shown by arrow mark). Diffraction phase is found only in the samples with higher graphene concentrations (>0.5 wt% and above) and also it depends on the level of sensitivity of the XRD apparatus used. The aluminum carbide peaks are not detected in any of the aluminum hybrid samples of any compositions which are sintered through microwave heating method. Theoretical densities (g/cm^{-3}) of hybrid compositions measured according to ground rule are illustrated by hybrid mixtures (RoHM) relation, as shown in Eq. 2.1

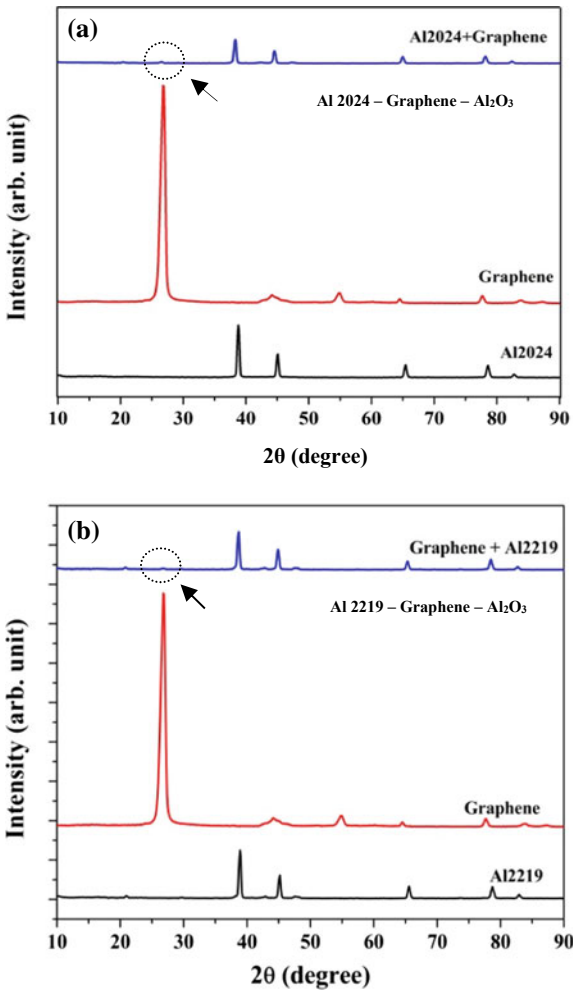

Fig. 2.3 X-ray diffraction analysis of **a** Al 2024–graphene–Al_2O_3 and **b** Al 2219–graphene–Al_2O_3 composite after microwave sintering

[10]. Experimental values of theoretical and sintered density (g/cm^{-3}) are shown in Tables 2.4 and 2.5, respectively.

$$D_{Theoretical} = D_{Matrix} * V_{Matrix} + D_{Particulate} * V_{Particulate} + D_{Graphene} * V_{Graphene...} \quad (2.2)$$

where D = density and V = volume fraction.

Comparison of densities demonstrates that adding graphene would not give significant difference but combination with Al_2O_3 leads to slightly higher than the theoretical values. The minor improvement in the density values is attributed to the strong

Table 2.4 Theoretical and experimental densities with graphene

Composition Al 2219–Al_2O_3–graphene (graphene in various concentrations A-0.0, B-0.25, C-0.5, D-0.75, E-1.0 wt%)	Theoretical density (g/cm^{-3})	Sintered density (g/cm^{-3})
A	2.7	2.378 ± 0.02
B	2.69	2.454 ± 0.03
C	2.68	2.501 ± 0.03
D	2.66	2.447 ± 0.02
E	2.64	2.501 ± 0.03

Table 2.5 Theoretical and experimental densities with graphene

Composition Al 2024–Al_2O_3–graphene (graphene in various concentrations: A-0.0, B-0.25, C-0.5, D-0.75, E-1.0 wt%)	Theoretical density (g/cm^{-3})	Sintered density (g/cm^{-3})
A	2.7	2.356 ± 0.04
B	2.69	2.546 ± 0.03
C	2.68	2.461 ± 0.04
D	2.66	2.567 ± 0.02
E	2.64	2.651 ± 0.04

interfacial bonding with homogeneously dispersed Al_2O_3 and graphene in combination with the microwave sintering process. This is in good consistency with improved hardness values, which is discussed further in this paper. Moreover, the graphene weight fraction is varied and highest density is achieved in the range 0.25–0.75 wt% in both Al 2024–graphene–Al_2O_3, and Al 2219–graphene–Al_2O_3. The marginal variation or lesser in densities for higher weight fractions (>0.75 wt% graphene) may be due to occurrence of graphene cluster and oxidation of aluminum [11]. Further, addition of Al_2O_3 in the composite decreases the compressibility of the precursor due to higher hardness value. Also, difference in huge melting point may lead to inadequate sintering mechanism. Vickers hardness measured for various concentrations of graphene in Al 2024–graphene–Al_2O_3, Al 2219–graphene–Al_2O_3 hybrid composites and same values are summarized in Fig. 2.4. From the hardness values comparison (Fig. 2.4) of microwave sintered composites, significant improvement is witnessed when compared to monolithic alloy, as reported in the literatures [12, 13]. Graphene is evoked with excellent potential candidate for microwave absorption [14] and when it is encapsulated/coated with alumina at lower concentrations (<1 wt%) improved microwave absorption is witnessed, which is attributed to change of dielectric properties. The micro particle size Al_2O_3 and graphene flakes also possess higher surface area, which helps in effective interfacial bonding, better densification

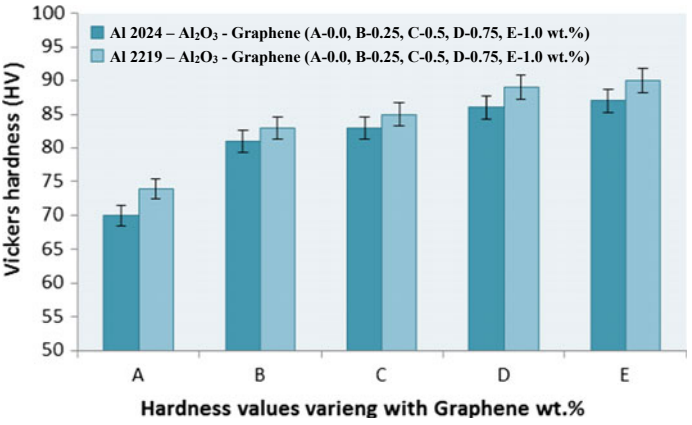

Fig. 2.4 Hardness with varying graphene content in Al 2024–graphene–Al_2O_3, Al 2219–graphene–Al_2O_3 hybrid composites

and decrease in the porosity. The improvement in the hardness values is due to formation of aluminum carbide in the developed composite. But XRD analysis reveals the formation of no such peaks to confirm [8] due to usage of pristine Al_2O_3 and graphene in the matrix combination with microwave sintering. From the hardness comparison, it reveals that the Al 2024–graphene–Al_2O_3 hybrid composites have significant improvement in the hardness compared to Al 2219–graphene–Al_2O_3 due to difference in the percentage of copper content and same trend of hardness values are seen in various weight fractions of graphene.

Figures 2.5 and 2.6 show the comparative study of compressive behavior and diametrical tensile strength of Al 2024–graphene–Al_2O_3, Al 2219–graphene–Al_2O_3

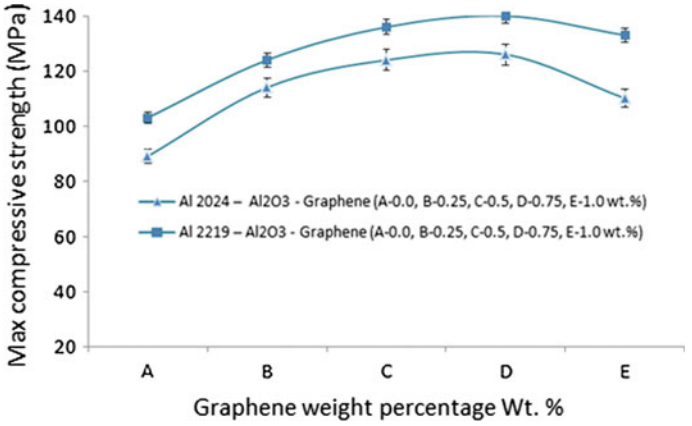

Fig. 2.5 Compressive behavior of Al 2024–graphene–Al_2O_3, Al 2219–graphene–Al_2O_3 hybrid composites due to addition of graphene (wt%)

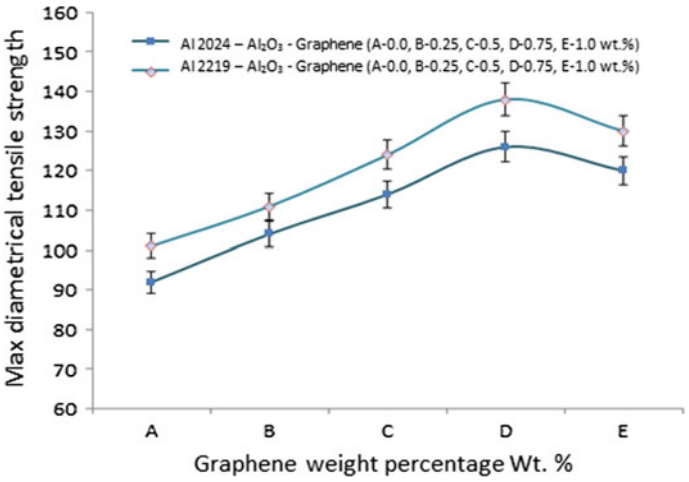

Fig. 2.6 Diametrical tensile strength behavior of Al 2024–graphene–Al_2O_3, Al 2219–graphene–Al_2O_3 hybrid composites due to addition of graphene (wt%)

hybrid composites, respectively. The tests are carried out at room temperature to study the influence of Al_2O_3 (8.0 wt%) and graphene addition (0.25–1.0 wt%) on the composites which are processed through ultrasonic liquid processor and microwave sintering. Maximum strengths (compressive strength—140 MPa for AA2219 and 126 MPa for AA 2024, diametrical tensile strength—128 MPa for AA 2219 and 123 MPa for AA2024 at 0.75 graphene and 8.0 Al_2O_3) are achieved for the hybrid composite. A significant improvement in compressive and diametrical tensile strength of the hybrid composites is observed on increasing the concentration of the graphene. The increasing trends of strengths which are seen in both the AA alloys hybrid composite is due to combination of Al_2O_3 and graphene, compared to monolithic alloy and microwave sintering method. Also, it is observed that the strength of AA 2219 with the 5.8 wt% of Cu content exhibits more strength compared to AA 2024 with 4.0 wt% of Cu. Typically, the presence of lower percentage (0.1–6.0 wt%) of Cu provides a substantial improvement of the strength in the developed composites, which are found to be promising data with the current research work. In AA alloy hybrid composites, improvement in bulk properties during bulk microwave sintering is attributed to heat developed from inside, and the material flow is supported by diffusion mechanism that takes place due to vacancy concentration gradient. This criterion similarly depends on time temperature and chemical potential gradient. For the active grain, great amount of high energized movement of atoms should be present at the matrix vacancies but this movement is suppressed by graphene platelets by making barrier against grain growth by covering. So, densification increases due to increase in the diffusion rate and it is directly proportional to sintering temperature, which can be related by Arrhenius equation as shown in Eq. 2.3.

$$N = N_o e^{-q/RT} \tag{2.3}$$

where N is the number of vacancy sites, N_o is the total number of lattice sites, q is the activation energy and RT is the average kinetic energy.

During testing and analysis, the error percentage is considered more due to discrepancies in the flakes orientations and unavoidable clustering or agglomerations in the developed composites, which occurs at higher concentrations (>0.75 wt% and above). Since graphene possess high tensile strength and being 2D material, processing of these materials and incorporating into the matrix is very challenging. Under compressive testing condition, graphene nano particulates are experiencing perpendicular buckling and deformation as the reinforced particle is aligned parallel to the direction of the load. Also, no effect in strength values are noted for the graphene flakes aligned perpendicular to loading direction. In both the cases composites are exposed to more strain rate during deformation compared to parent alloy and this can be detained by the addition of Al_2O_3 particles (ceramic particle) in both compressive and diametrical loading conditions. It is also probable to attain the improved properties when the graphene flake is inlined approximately at 45° to the loading direction. The probabilities of attaining the strength are conceivable only in specific directions but achieving in all directions is quite incredible when graphene alone is reinforced in the composite. But combination of Al_2O_3 and graphene is very much advantageous to bring the strength in the developed Al 2024–graphene–Al_2O_3 and Al 2219–graphene–Al_2O_3 hybrid composites.

Also, experiments are repeated for at least five samples for individual compositions and the highest compressive strength attained is considered for examination. It is expected that addition of graphene and Al_2O_3 leads to dislocation pile which gives rise to increase in strengths. Moreover, flake morphology of graphene is contributing to the obstruction of the particle movement which leads to narrowing the distance between them, and this is in good agreement with the increase in hardness and density, as discussed in the previous section. Also, the improvement in the strengths due to addition of one or more reinforcing particle/flakes with various combinations can be related and is shown in Eq. 2.4 [15].

$$\sigma_c = \sigma_m f_m + \sigma_{r1} f_{r1} + \sigma_{r2} f_{r2} \tag{2.4}$$

where σ_c = strength of the composites, σ_m = compressive strength of matrix, f_m = volume fraction of the matrix, σ_{r1} = strength of reinforcement, Al_2O_3, f_{r1} = volume fraction of the Al_2O_3, σ_{r2} = strength of reinforcement, graphene, f_{r2} = volume fraction of the graphene.

2.4 Conclusion

In this research work study, Al 2024–graphene–Al_2O_3, Al 2219–graphene–Al_2O_3 hybrid composites were processed through ultrasonic liquid processing of Al_2O_3

and graphene, followed by ball milling successfully. The precursor is preheated and compacted in the semi-solid regime. Finally, the compacts are microwave sintered. XRD analysis has exposed the presence of all major alloying elements of aluminum alloys, including graphene particulate (peak at 26.50°) in the fabricated composite and no sign of carbide formation at the surface. On comparing AA 2219 with AA 2024, AA 2219 exhibits good hardness characteristics, compressive strength and diametrical tensile strength, where higher amount of copper present in the alloy facilitated the processing method. Microwave processing of the hybrid composites leads to excellent diffusion mechanism in a controlled atmosphere where the oxidation of the composite samples is prevented, which enhances the properties. Al_2O_3 at 8.0 wt% leads to increase in hardness and compressive strength. Further, graphene addition leads to improvement in strength of the composites and the amount of graphene is kept low (approximate or <0.75 wt%) because of its agglomeration and clustering in the matrix which reduces the strength of the nanocomposites. Microwave sintering technique can effectively increase the diffusion of ions and thus speed up the sintering process, causing the grain growth and the densification of matrix.

References

1. Umasankar, V., Xavior, M.A., Karthikeyan, S.: Experimental evaluation of the influence of processing parameters on the mechanical properties of SiC particle reinforced AA6061 aluminium alloy matrix composite by powder processing. J. Alloy. Compd. **582**, 380–386 (2014)
2. Bastwros, M., Kim, G.Y., Zhu, C., Zhang, K., Wang, S., Tang, X., Wang, X.: Effect of ball milling on graphene reinforced Al6061 composite fabricated by semi-solid sintering. Compos. B Eng. **60**, 111–118 (2014)
3. Baradeswaran, A., Perumal, A.E.: Wear and mechanical characteristics of Al 7075/graphite composites. Compos. B Eng. **56**, 472–476 (2014)
4. Madakson, P.B., Yawas, D.S., Apasi, A.: Characterization of coconut shell ash for potential utilization in metal matrix composites for automotive applications. Int. J. Eng. Sci. Technol. **4**(3), 1190–1198 (2012)
5. Yigezu, B.S., Mahapatra, M.M., Jha, P.K.: Influence of reinforcement type on microstructure, hardness, and tensile properties of an aluminum alloy metal matrix composite. J. Miner. Mater. Charact. Eng. **1**(04), 124 (2013)
6. Singh, G., Goyal, S.: Microstructure and mechanical behavior of AA6082-T6/SiC/B4C-based aluminum hybrid composites. Part. Sci. Technol. **36**(2), 154–161 (2018)
7. Rashad, M., Pan, F., Hu, H., Asif, M., Hussain, S., She, J.: Enhanced tensile properties of magnesium composites reinforced with graphene nanoplatelets. Mater. Sci. Eng. A **630**, 36–44 (2015)
8. Bartolucci, S.F., Paras, J., Rafiee, M.A., Rafiee, J., Lee, S., Kapoor, D., Koratkar, N.: Graphene–aluminum nanocomposites. Mater. Sci. Eng. A **528**(27), 7933–7937 (2011)
9. Kumar, H.P., Xavior, M.A.: Graphene reinforced metal matrix composite (GRMMC): a review. Procedia Eng. **97**, 1033–1040 (2014)
10. Thostenson, E.T., Chou, T.W.: Microwave processing: fundamentals and applications. Compos. A Appl. Sci. Manuf. **30**(9), 1055–1071 (1999)
11. Thakur, S.K., Srivatsan, T.S., Gupta, M.: Synthesis and mechanical behavior of carbon nanotube–magnesium composites hybridized with nanoparticles of alumina. Mater. Sci. Eng. A **466**(1–2), 32–37 (2007)

12. Ashwath, P., Joel, J., Xavior, M.A., Kumar, H.P.: Effect of SiC and Al_2O_3 particles addition to AA 2900 and AA 2024 MMC's synthesized through microwave sintering. Mater. Today: Proc. **5**(2), 7329–7336 (2018)
13. Xavior, M.A., Ashwath, P., Rajendran, R.: Effect of precipitation hardening on particle reinforced aluminum alloy composites. In: ASME 2015 International Mechanical Engineering Congress and Exposition, pp. V02AT02A046–V02AT02A046 (2015)
14. Leonelli, C., Veronesi, P., Denti, L., Gatto, A., Iuliano, L.: Microwave assisted sintering of green metal parts. J. Mater. Process. Technol. **205**(1–3), 489–496 (2008)
15. Sherif, E.S.M., Latief, F.H., Junaedi, H., Almajid, A.A.: Influence of exfoliated graphite nanoplatelets particles additions and sintering temperature on the mechanical properties of aluminum matrix composites. Int. J. Electrochem. Sci. **7**(5), 4352–4361 (2012)

Chapter 3
A New Approach for Fabrication of Complex-Shaped Arrayed Micro Electrodes

Hreetabh, C. K. Nirala and A. Agrawal

Abstract This work reports a new approach for fabrication of complex-shaped arrayed micro electrodes using reverse micro electro-discharge machining (R-μEDM) in combination with LASER micromachining. The proposed technology for fabrication of such micro electrodes is evaluated for its process capabilities based on several responses. The responses which are considered for evaluating the process capability are—aspect ratio, cross-sectional profile and cross-sectional area of the micro electrodes. High aspect ratio electrodes find a lot of potential applications in the miniaturized engineering components, including, biomedical and MEMS devices, fuel injectors and jewelry crafting. Apart from these applications, the complex-shaped arrayed micro electrodes act as micro pin-fins heat exchangers for effective cooling of electronic components. In this regard, a novel aerofoil cross-section of pin-fins, which are highly anticipated for an effective cooling of electronic components, is modeled and numerically simulated for higher heat transfer rate.

Keywords LASER micromachining · R-μEDM · Micro electrodes · MEMS devices · Aerofoil cross-section

3.1 Introduction

Requirements of complex-shaped miniaturized metallic products in engineering systems have risen in recent times. These products include mechanical components such as micro gears, electrodes, shaft, cam and follower [1]. Micro features such as micro detailing in jewelry and micro pin-fins for effective heat transfer in micro electronics are other potential applications. The fabrication processes available for such components are mainly—LIGA, Roll molding and R-μEDM. Apart from many advantages in fabrication of micro featured components, LIGA has some challenges like highly expensive setup, limited aspect ratio of the fabricated part up to 1000 μm. In addition,

Hreetabh · C. K. Nirala (✉) · A. Agrawal
Department of Mechanical Engineering, Indian Institute of Technology Ropar, Rupnagar 140001, India
e-mail: nirala@iitrpr.ac.in

M. S. Shunmugam and M. Kanthababu (eds.), *Advances in Micro and Nano Manufacturing and Surface Engineering*, Lecture Notes on Multidisciplinary Industrial Engineering,
https://doi.org/10.1007/978-981-32-9425-7_3

synchrotron radiation required in LIGA is not easily available and the design procedure itself is very complex [2, 3]. Apart from these limitations, the products fabricated by this process undergo phase changes (solid–liquid–solid) which may bring metallurgical changes in the fabricated component. The roll molding also has limitations in fabrication of micro electrodes, as it has potentiality in 1D/2D surface patterns only and the height of micro fins is also limited to 600 μm [4]. Recent advancements in micromachining techniques allow more complex three-dimensional micro-size components to be fabricated directly for the material having higher thermal conductivity. Alternatively, it has been tried to explore the potentiality of micro electro-discharge machining (μEDM) which is anticipated to be more suitable than the other manufacturing methods used for such purpose. μEDM is further derived as R-μEDM to meet the process requirement of 3D-shaped micro electrodes. It shows its potential in fabrication of 3D-shaped micro electrodes dominating over the above-said process. This process allows effective fabrication of a single and multiple arrayed electrode, which can be used as a tool for the fabrication of arrayed micro holes or even high aspect ratio blind holes that are extremely difficult to fabricate. Furthermore, these electrodes could potentially be used as extended surfaces (arrayed micro pin-fins) for effective cooling of micro electronic components, an example of which is shown in Fig. 3.1. The existing R-μEDM process used for fabrication of micro electrodes is detailed in the next section.

Figures 3.2 and 3.3 demonstrate the basic configuration of R-μEDM processes with respect to μEDM-drilling. The process is meant for fabrication of single and/or arrayed micro electrode using a pre-drilled single and/or arrayed micro hole. The differences between the μEDM-drilling and R-μEDM in various aspects are summarized here. The workpiece of the μEDM-drilling is in the form of a plate, whereas it is cylindrical in case of R-μEDM. The workpiece in R-μEDM is kept rotating with certain RPM which is dissimilar from the μEDM-drilling as it is kept stationary in this case. The cylindrical workpiece of R-μEDM process is eroded from its circumference to form a micro electrode of comparatively less cross-sectional area. In contrast, in μEDM-drilling, the materials are eroded from a flat surface to form a cylindrical hole by a rotating tool. The debris accumulated on the circumference of

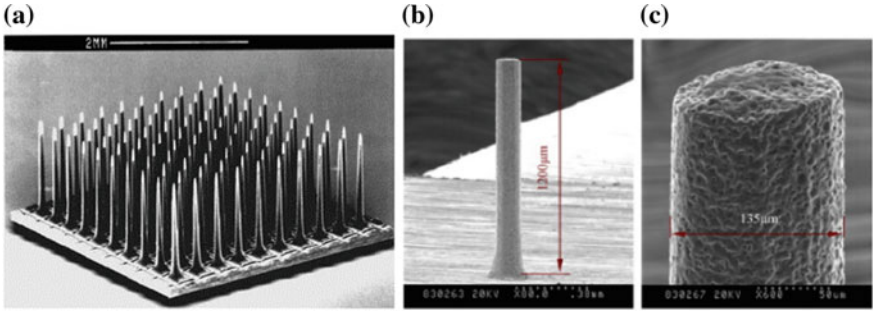

Fig. 3.1 **a** Arrayed microelectrodes [5], **b** fabricated micro rods (steel), **c** partial cylindrical rod [6]

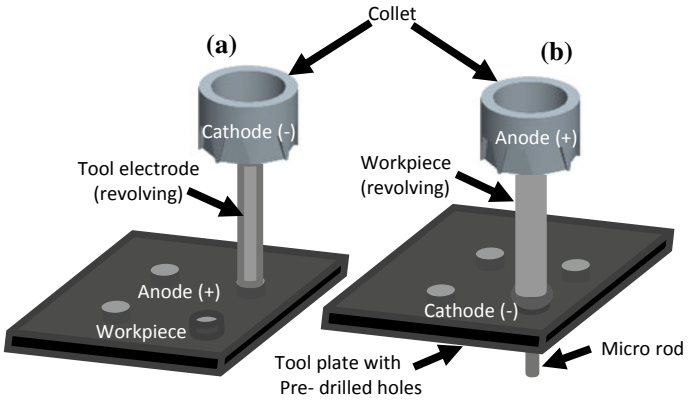

Fig. 3.2 Tool workpiece orientation in **a** μEDM-drilling and **b** R-μEDM [8]

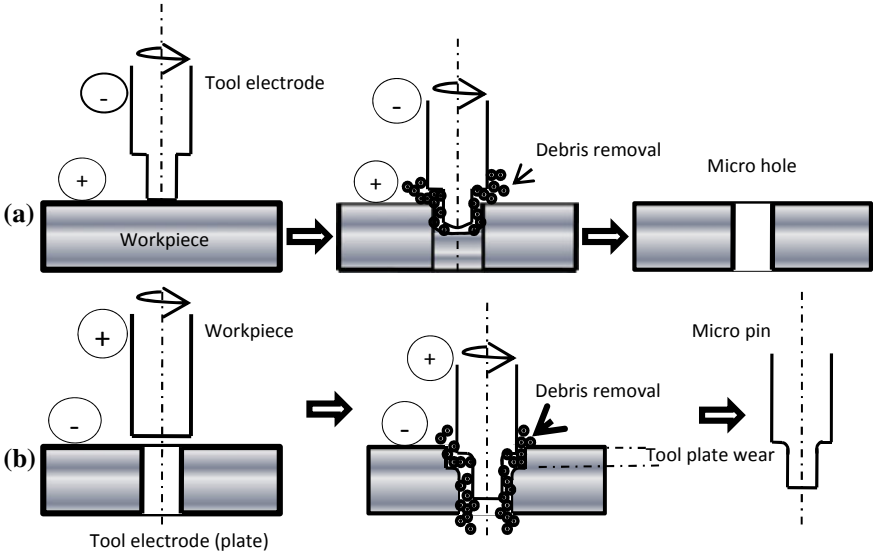

Fig. 3.3 Representation of **a** μEDM-drilling and **b** R-μEDM process and debris removal [10]

the cylindrical workpiece gets removed by centrifugal action, evacuation and gravitational effect as the tool plate in this case has a through hole [7]. μEDM-drilling, on the other hand, provides facility of debris removal mostly by evacuation. Refer to Fig. 3.3 for comparative schematic of these processes.

The micro-scale fabrication by reverse polarity EDM (R-μEDM) utilizes an energy lower than that of the conventional EDM to achieve the volume removal per discharge. The μEDM employs an RC circuit in which the discharge energy for unit material removal is given as shown in Eq. 3.1.

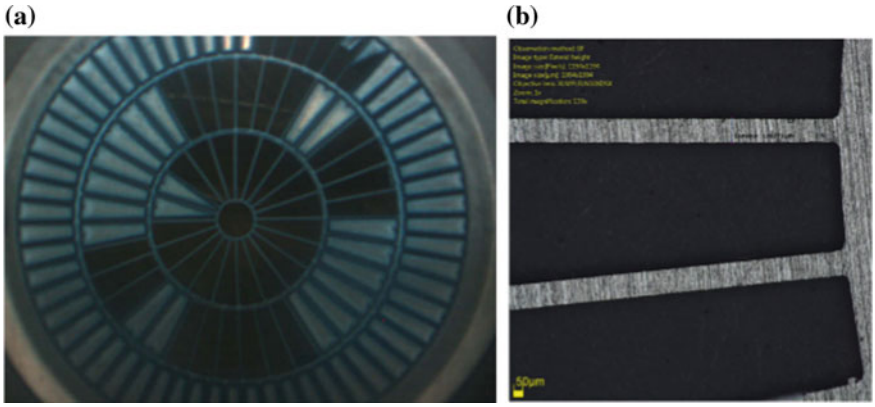

Fig. 3.4 Applications of LASER micro machining **a** slots in control grids. **b** SEM image of slots [17]

$$E = \frac{1}{2}CV^2 \tag{3.1}$$

Here, "V" represents the value of open-circuit voltage and "C" represents the value of the capacitance. Several researchers have shown the potentiality of micro electrode fabrication by using R-μEDM. Mastud et al. [9] fabricate similar-textured surfaces on Ti6Al4V rods using a vibration-assisted R-μEDM process. The textured surfaces contain micro pillars of 40–50 μm in diameter with inter-pillar spacing of 35 μm. They analyzed process stability and erosion rate depending upon voltage, capacitance, amplitude and frequency of the anode (plate electrode) vibrations. They also obtained process stability in terms of variation in the normal, the open-circuit and the short-circuit voltage–current (V–I) during the process. It was further studied by Mujumdar et al. [10]. They analyzed the effect of voltage, capacitance and the threshold of the spark circuit on the erosion rate, dimensional accuracy and the surface finish during the machining of brass using R-μEDM process. It was found that voltage and capacitance were dominating factors that affect the erosion rate and dimensional accuracy. Further studies on material removal during processing were done by Nirala et al. [11] using the actual volume removal per discharge method proposed by Bissacco et al. [12], which significantly applied to R-μEDM approach for the machining of required height micro rods.

The R-μEDM process has, however, shown capability in fabrication of significant micro features but also encounters some challenges such as: (i) it is difficult to achieve the optimum aspect ratio of micro electrodes; (ii) the height of the micro electrode, beyond an allowable limit, is difficult to achieve as the height is restricted by the tool-plate thickness; and (iii) fabrication of a complex cross-sections such as elliptical, aerofoil and water droplet arrayed micro pin-fins is not attempted yet. It requires a tool plate having pre-drilled holes in a pattern similar to the one which is required for the 3D micro pin-fins. It is worthy to mention here that these arrayed complex-shaped

pre-drilled holes are not possible to fabricate by using mechanical micro drilling. LASER micro machining is anticipated as a possible substitute of mechanical micro drilling in this regard. The capability of the LASER micro machining dedicatedly for the above purpose is explained in Sect. 3.3.

3.2 Proposed Technology

The proposed technology for arrayed micro electrodes fabrication utilizes two different micro machining processes. The R-μEDM, which is the principle processes for such fabrication, is discussed earlier whereas the LASER micro machining, as a supporting process to fabricate complex-shaped pre-drilled tool plate is discussed in Sect. 3.3. This pre-drilled tool plate is a key component of R-μEDM. It is worthy to mention that the existing technologies were able to produce only a very regular shape of cross-sectional profile for the pin-fins heat exchangers. The proposed technology, on the other hand, is able to produce any irregular cross-sectional profile of the pin-fins heat exchangers.

3.3 LASER Micro machining

LASER in micro machining has significant contributions. Klotzbach et al. [13] reported that LASER has excellent beam quality which gives high precision for material micro machining undergoing micro scale other than excellent beam quality. LASER technology has compact installation, higher efficiency, reasonable system price and easy to be collaborate with other processes. Typical applications of LASER micro machining include drilling, cutting, structuring, lateral material removal as well as marking. Other applications were highlighted by Singh et al. [14]. They described LASER micro machining as a stable process for the fabrication of micro channels to generate ridge formation along the edges accompanied by ripples. They conducted systematic experiments using the second harmonics of Q-switched Nd:YAG LASER to fabricate micro channels having depth of 43.39 μm, width up to 64.49 μm and surface quality was nano-level finish having average surface roughness (Ra) value of 370 nm for SS 316L. Another experimental study performed by Caiazzo et al. [15] achieved the application of the CO_2 LASER cutting process to three thermoplastic polymers layers of thicknesses ranging from 2 to 10 mm. They examined the effect of LASER process parameters and the values of kerf widths on top and bottom thicknesses of solid polymer layers. They also measured melted transverse area, the melted volume per unit time and surface roughness values (Ra) on cut edges. Recent studies done by Mishra et al. [16] used short and ultra-short LASER pulses for the micro machining applications and proved as evolving fabrication technology.

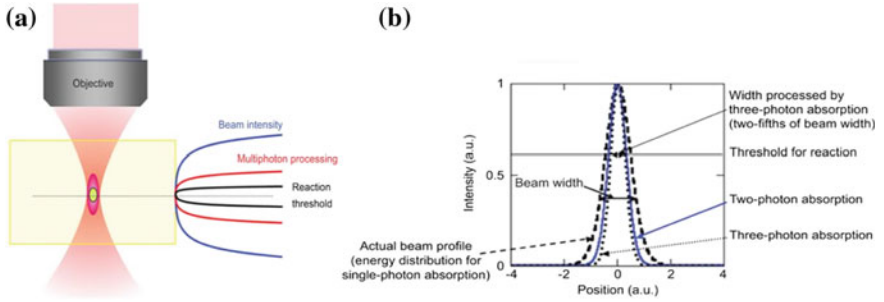

Fig. 3.5 **a** Schematic of sub-diffraction-limited fabrication based on multiphoton absorption. **b** Beam profile and spatial distributions of LASER energy [18]

They overviewed LASER beam micro machining (LBMM), its capabilities up to sub-micron size and performed experiments with nanosecond, picosecond and femtosecond, and critical experimental parameters are involved in LBMM.

The LASER intensity and the profile for LBMM are very much defined for micron and sub-micron level. The reaction between the beam and the workpiece is defined by the threshold intensity and spot diameter of the beam. The solid horizontal line depicting the reaction threshold is shown in Fig. 3.5. Micro-ablation due to LASER-based vaporization of materials has been used in a large number of miniaturized component fabrications like micro molds, functional components in electronics applications and so on. Some practical examples of LASER micro machining are shown in Fig. 3.4. LASER radiation is used as a tool to fabricate at a faster rate by thermal vaporization.

A model of 3D-arrayed micro pin-fins is prepared by using SOLIDWORKS15. SOLIDCAM module of the SOLIDWORKS is further used for generating the respective CNC machine codes for micron-level machining. Fabrication of these micro pin-fins requires highly accurate and precise machine with optimal machining parameters. Subsequently, the LASER micro machining parameters have been defined and coded for making the holes of desired complex-shaped profile of micro pin-fins over the tool plate using LASER micro machining. The R-μEDM experiments have been performed on a multipurpose micro machining setup (Hybrid-μEDM DT-110i, Make: MikroTools Pte Ltd.). The machine setup has got a LASER micro machining attachment which is used to fabricate complex-shaped holes profile on the tool plate. The LASER machining used here produces class IV LASER, where the LASER type is YLR-150/1500QCW-MN-AC-Y11 having an average power of 150 W and a wavelength of 1070 nm. The photographic view of LASER along with complete setup is shown in Fig. 3.6.

The multipurpose hybrid-μEDM machine uses RC-type pulse generator with a well-established setup dedicated to the fabrication of miniaturized components having an accuracy of 1 μm. Ideally, an RC-type pulse generator in μEDM is supposed to provide the pulses with identical discharge durations and peak values. This process takes place when the fully charged capacitor is used for the continuous discharges. A brass rod of 6 mm diameter is used as workpiece which is conductive in nature and

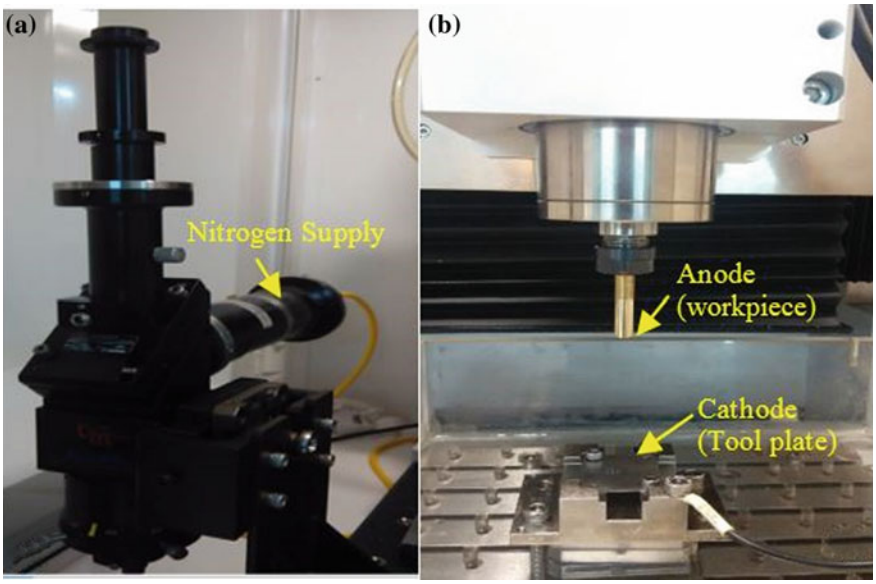

Fig. 3.6 Experimental setup: **a** LASER; **b** R-μEDM

having optimal thermal properties. On the other hand, a SS304 steel plate of 0.4 mm thickness is used as tool electrode. The fabrication of arrayed micro fins is done by using R-μEDM technique where the tool electrode is used as cathode (−ve) and the workpiece electrode is used as anode (+ve), as shown in Fig. 3.6b. In R-μEDM an arrayed LASER cut micro holes are arranged over the tool electrode which is directed against the workpiece electrode at controlled feed rate. Hydrocarbon oil is used as a liquid dielectric for uniform flushing and removal of debris. When the gap between the workpiece and tool electrode is small, a spark is generated between them due to the formation of electric field, and hence erosion occurs from the surface of workpiece electrode at an elevated temperature.

Micro fins are fabricated by eroding the periphery of the electrode that has the diameter larger than the existing holes fabricated by LASER micro machining. It is important to mention that the part of the workpiece which is exposed directly to the holes will not get eroded during discharging, which eventually will lead to formation of micro fins of the respective cross-section profile. The dimensions of these fabricated micro fins are comparatively lower than the respective holes. This is due to the discharge gap which is maintained throughout the surface interface. These pre-drilled arrayed and complex-shaped holes are used for making protruding structures of different shapes which has height in the range of 50–1000 μm or more, depending on the thickness of tool electrode. These fabricated complex-shaped micro pin-fins are used as a heat transfer body inside the electronic circuits where escaping heat is a great challenge. Different shapes of micro pin-fins arrangement of inline and staggered pattern is fabricated for verifying the process capability and process

parameters. Micro fins can be made of several materials but it should be conductive in nature. Figure 3.7 shows a complete flowchart of proposed methodology.

Feasibility Test

First, the tool plate is micro machined using fiber (Nd:YAG) LASER having minimum spot size of 50 μm. Further different profile pre-drilled holes are generated in stainless steel plate and cleaned using liquid acetone. The complex-shaped micro pin-fins profiles are fabricated using R-μEDM process, which consists of two parts: the tool plate and the rod of cylindrical shape. The rod used is of 6 mm diameter, which is held at spindle side and the tool plate was screwed in the fixture facing each other. The R-μEDM process showed its salient potential features for actual fabrication of the micro pin-fins array. The machining has been done at the optimal parameter obtained by different test runs. Different micro pin-fins profiles with tool plates have been shown in Fig. 3.8. The SEM image of aerofoil pin-fin (APF) is

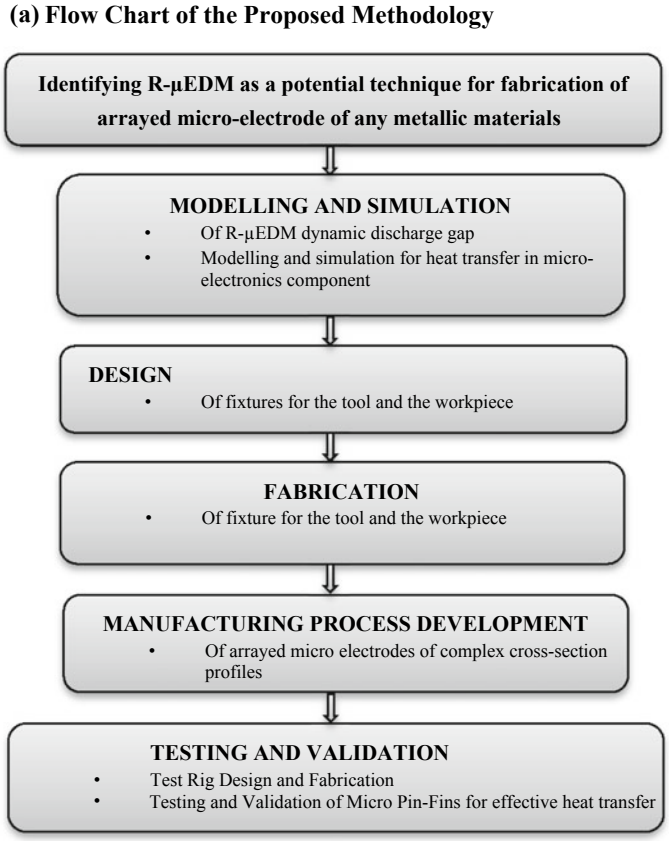

Fig. 3.7 Process flowchart of present work

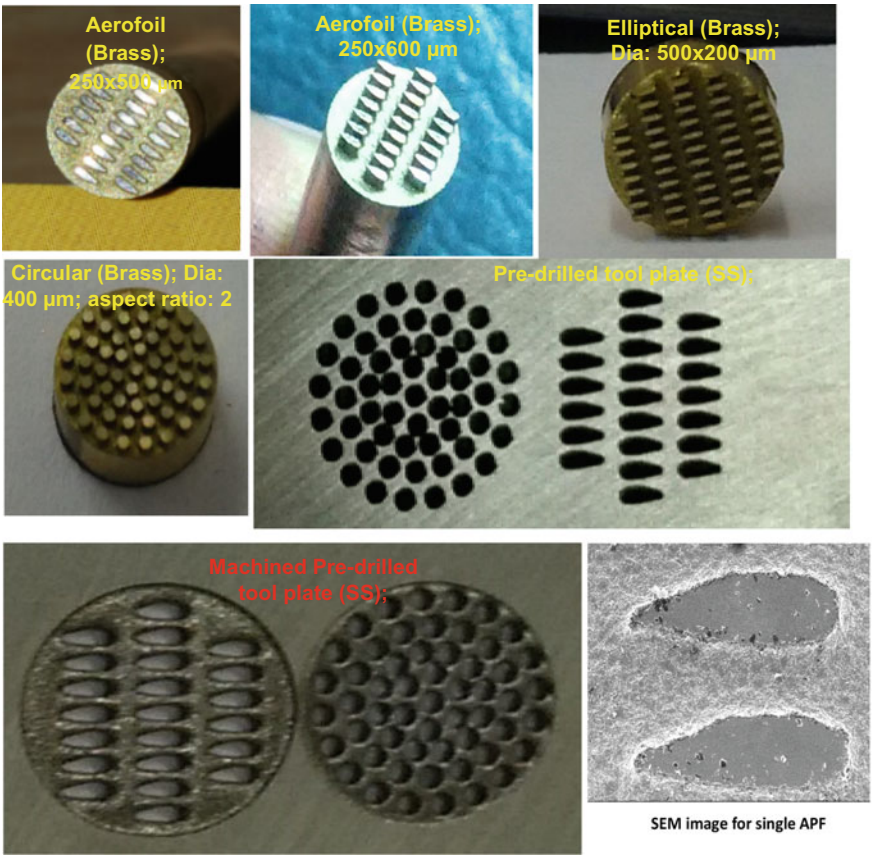

Fig. 3.8 Different fabricated micro fins profiles with tool plate

also provided in the same figure. Characterization of these fabricated micro features could be a future work plan.

3.4 Results and Discussions

3.4.1 Influence of Pin-Fins Aspect Ratio

In order to understand the heat transfer behavior through arrayed micro pin-fins, the simulation and experimental studies of different literature have been analyzed. Based on the analysis, this work found to be suitable to simulate numerical domain consisting of micro pin-fins and heated base plate. The thermal performance of the

domain has been analyzed using five values of aspect ratio "ϒ" in the range of 1.2–2.2, including both the values. The micro pin-fins with $\Upsilon = 1.5$ is simulated here, for both inline and staggered arrangements and compared their influence on heat transfer rate. The difference in the simulation results reveals that with the increasing micro pin-fins aspect ratio up to certain value, thermal performance of the heat sink in both the arrangements remains enhancing. Beyond $\Upsilon = 2$ and up to $\Upsilon = 2.2$, diminishing results have been observed for different shaped micro pin-fins heat sink. At optimum aspect ratio and arrayed fins arrangement, there has been an enhanced thermal performance for staggered arrangement by 10–25%, as compared to inline arrangement.

The simulation results give a clear conception of heat transfer characteristics of fabricated micro pin-fins at optimum aspect ratio. The numerical simulation proved to be an alternative solution to analyze the hydraulic and thermal performances of micro pin-fins used in electronic components. Researchers simulated the model to study the effect of natural and forced convection on the average heat transfer rate along the longitudinal direction of the micro fins.

Tuckerman and Pease [19] were the first who studied single-phase fluid flow in the micro channel in 1981. They reported the highest value of heat flux of 790 W/cm^2 which was reduced using water. Maximum bulk temperature rise was 71 °C, which is above the input water temperature and is further analyzed using different fin profiles defined by Tullius et al. [20] who modeled finned mini-channels to optimize the fins configuration and increased heat transfer dissipation by convection from a heated base plate surface. They used six pin-fins shapes, that is, circle, square, triangle, ellipse, diamond and hexagon in their staggered arrangement placed upon the heated base surface.

In this paper, a novel pin-fin named aerofoil pin-fin is introduced and shown in Fig. 3.9a. With the addition of these micro pin-fins in a micro heat sink plate, the heat transfer area of electronic components has increased. At the same time, arrangement of pin-fins can change the fluid flow and enhance the heat transfer further using larger surface area involvement, as shown in Fig. 3.9b. Also, the asymmetrical profile design in the body of aerofoil pin-fin (APF) can realize large-scale surface impingement of working fluid based on operating conditions. Table 3.1 shows various parameters used for simulation study. Furthermore, in consideration of dissipating

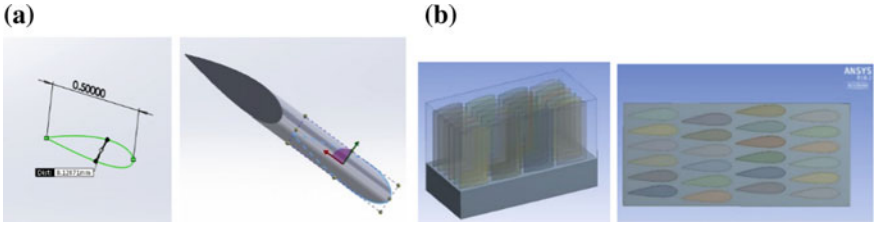

Fig. 3.9 Representation of model and its dimensions and APF array. **a** Single micro airfoil design with dimensions; **b** inline and staggered arrangement of the APF array

Table 3.1 Simulation parameters

S. no.	Parameters	Range/values
01	Reynolds number	Re < 200
02	Heat flux	2–3 × 10^6 W/m^2
03	Inlet temperature	293 K
04	Fluid velocity	0–0.353 m/s
05	Degree of freedom	6–7 × 10^6
06	Outlet temperature	300–350 K

even higher heat flux, this profile can be utilized in convective heat flow region and increase in frictional resistance of flow. For the following part, the ANSYS 18.2 fluent module has been used for simulation [21]. Good agreement between experimental and numerical results has been obtained. The heat transfer characteristics with their proper explanations for convective heat transfer through aerofoil micro pin-fins profile are analyzed numerically.

Figure 3.10a, b shows the temperature profile of the two different obligatory arrangements of pin taken from one side of the imaginary box inscribing the array of pin-fins. The temperature profile ranges from 300 to 350 K shown here through legend color from dark blue to red. The inlet temperature was set at 293 K at the inlet surface of the domain. The rise in temperature starts from leading part of APF domain, and the fluid flow layer gets heated and denser as it approaches nearer to the trailing side (outlet). The temperature profile and fluid flow behavior get changes in the longitudinal direction according to the APF configuration. At low Reynolds numbers Re < 200, wake regions at the interaction point between flowing fluid and pin-fins are not desired. Therefore, symmetrical unit cell has been used in which the flow velocities changes from one MPFs row to another due to developed flow conditions as it may result in more possibility for pressure drop at the outlet wall.

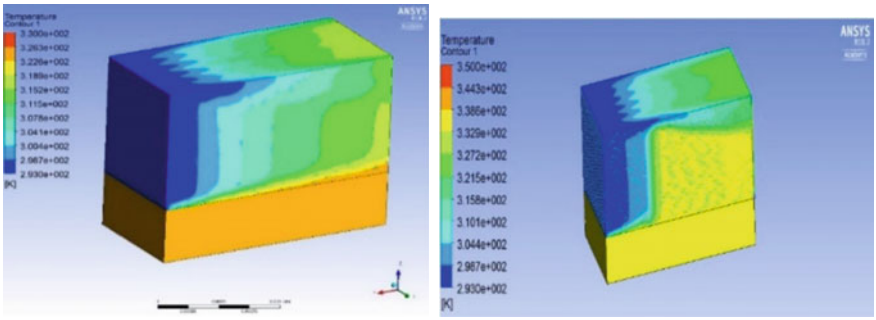

(a) Inline arrangement (b) Staggered arrangement

Fig. 3.10 **a** and **b** Temperature (in K) distribution in different APF array arrangement. **a** Inline arrangement, **b** staggered arrangement

3.4.2 Heat Transfer Characteristics

The simulated results are shown in Fig. 3.11. The variation of convective heat transfer increases in the regions at the pin-fins cross-sectional surface around its periphery in both the arrangements. The local convective heat transfer in the rear wake regions of aerofoil pin-fins shows higher values due to the strong interaction of fluid with its curvature. Dimensional average heat transfer rate (h) has been represented here against the dimensional mass flow rate which is more dominant than the one simulated with dimensionless Reynolds number (Re). The APF with staggered arrangement has the highest heat transfer rate over the mass flow rate in comparison to their inline arrangement. The former has 13% higher performance than the latter one. The heat transfer rate increases with the fluid flowing through both the arrangements. The amount of h depending on total mass flow rate is developed due to the profile of micro pin-fins. This phenomenon in APF is stronger than other profiles due to its configuration. During the validation of model, there is observed difference in the values of h in experimental and simulation results which were possibly because of the difference in the model setup and parametric conditions.

The thin edges of micro APFs accelerate separation effects for the fluid flowing results in heat transfer enhancement with inter-mixing of the fluid in the domain. Despite of it, APFs have larger surface area as compared to other fin shapes. Hence in this study staggered arrangement has been observed having large wake zone downstream of the micro APFs. The downstream wake zone in staggered arrangement shows higher heat transfer coefficients compared to the inline arrangement.

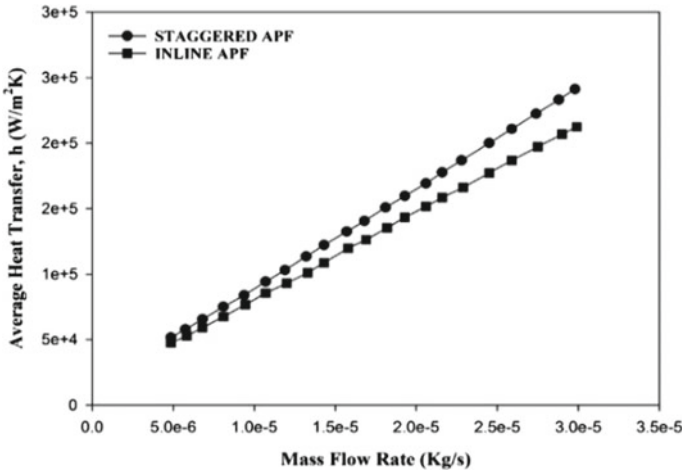

Fig. 3.11 Average heat transfer coefficient over mass flow rate for different APF array

3.5 Conclusions

The main objective to establish a promising technology for fabrication of complex-shaped arrayed micro electrodes has been achieved successfully. The technology brought the R-μEDM and the LASER micro machining processes together for the purpose. The methodology discussed has been thoroughly evidenced for such fabrication by feasibility tests. Multiple arrays of micro electrodes (highlighted as micro pin-fin) explicitly circular, elliptical and aerofoil, all in micron range and aspect ratio of more than two, have been successfully fabricated and presented as evidence. In order to highlight the applicability of these fabricated micro electrodes, the numerical simulation of effective heat transfer for inline and staggered arrangement for the array of aerofoil cross-section micro electrodes has been performed. Heat transfer rate using micro fins having aerofoil cross-section has been reported to be enhanced by a significant figure of 10–25%. The staggered arrangement has shown a heat transfer rate higher (enhanced by 13%) than the inline arrangement of micro pin-fins. A future scope for improvement in fabrication technology for even more complex products has been proposed which further has to be experimentally validated for effective heat transfer.

References

1. Loh, N.H., Tor, S.B., Tay, B.Y., Murakoshi, Y., Maeda, R.: Fabrication of micro gear by micro powder injection molding. J. Microsyst. Technol. **14**, 43–50 (2007)
2. Malek, C.K., Saile, V.: Applications of LIGA technology to precision manufacturing of high-aspect-ratio micro-components and systems: a review. J. Micro-Electron. **35**, 131–143 (2004)
3. Winick, H.: Synchrotron Radiation Research, Chapter 2: Properties of Synchrotron Radiation. Plenium Press, New York (1980)
4. Philip, P.A., Zhang, B., Zhang, X., Miller, J., Meng, J.W., Pratik, C.K., Arden, M.L.: Aluminum-based one-and two-dimensional micro fins array structures: high-throughput fabrication and heat transfer testing. J. Micromech. Microeng. **27**(02), 5–12 (2017)
5. Seung, K.J., Sandeep, M.C., David, W.J., Richard, N.A.: Electrophysiological mapping of cat primary auditory cortex with multi electrode arrays. J. Ann. Biomed. Eng. **34**(2), 300–309 (2006)
6. Peng, Z., Wang, Z., Dong, Y., Chen, H.: Development of a reversible machining method for fabrication of microstructures by using micro-EDM. J. Mater. Process. Technol. **210**, 129–136 (2010)
7. Nirala, C.K., Saha, P.: Evaluation of μEDM-drilling and μEDM-dressing performances based on online monitoring of discharge gap conditions. Int. J. Adv. Manuf. Technol. **85**, 1995–2012 (2016)
8. Sachin, M., Mayank, G., Ramesh, S., Johnson, S., Suhas, J.: Experimental characterization of vibration-assisted reverse micro electrical discharge machining (EDM) for surface texturing. In: Proceeding of the ASME International Manufacturing Science and Engineering Conference, MSEC2012-7314, Notre Dame, Indiana, USA, pp. 1–10 (2012)
9. Mujumdar, S.S., Mastud, S.A., Singh, R.K., Joshi, S.S.: Experimental characterization of the reverse micro-electro discharge machining process for fabrication of high-aspect-ratio micro-rod arrays. J. Eng. Manuf. **224**, 777–794 (2015)

10. Nirala, C.K., Saha, P.: Evaluation of μEDM-drilling and μEDM-dressing performances based on online monitoring of discharge gap conditions. Int. J. Adv. Manuf. Technol. **85**(9–12), 1995–2012 (2016)
11. Nirala, C.K., Saha, P.: A new approach to tool wear monitoring and compensation in R-μEDM process. J. Mater. Manuf. Process. **31**(4), 483–494 (2015)
12. Bissacco, G., Tristo, G., Hansen, H.N., Valentincic, J.: Reliability of electrode wear compensation based on material removal per discharge in micro EDM milling. CIRP Ann. Manuf. Technol. **62**, 179–182 (2013)
13. Klotzbach, U., Lasagni, A.F., Panzner, M., Franke, V.: Fabrication and characterization in the micro-nano range. J. Adv. Struct. Mater. **10**, 29–46 (2011)
14. Singh, A.K., Patowari, P.K., Deshpande, N.V.: Experimental analysis of R-μEDM for machining microtool. J. Mater. Manuf. Process. **31**(4), 530–540 (2016)
15. Caiazzo, F., Curcio, F., Daurelio, G., Minutolo, F.M.C.: LASER cutting of different polymeric plastics (PE, PP and PC) by a CO_2 LASER beam. J. Mater. Process. Technol. **159**, 279–285 (2005)
16. Mishra, S., Yadava, V.: LASER beam micromachining (LBMM)—a review. J. Opt. LASERs Eng. **75**, 89–122 (2015)
17. Mathew, M.M., Bathe, R.N., Padmanabham, G., Padmanaban, R., Thirumalini, S.: A study on the micromachining of molybdenum using nanosecond and femtosecond lasers. Int. J. Adv. Manuf. Technol. 1–11 (2017)
18. Sugioka, K., Cheng, Ya.: Ultrafast LASERs—reliable tools for advanced materials processing. J. Light Sci. Appl. **3**(e149), 1–12 (2014)
19. Tuckerman, D.B., Pease, R.F.W.: High-performance heat sinking for VLSI. IEEE Electron. Device Lett. **2**(5), 126–129 (1981)
20. Tullis, J.F., Tullis, T.K., Bayazitoglu, Y.: Optimization of short micro pin-fins in minichannels. Int. J. Heat Mass Transf. **55**, 3921–3932 (2012)
21. ANSYS Fluent Theory Guide (2018). http://ansys.com/products/simulation+Technology/ComputationalFluidDynamics

Chapter 4
Fabrication of Micro-holes Array Through Multiple Electrodes with Distributed M-Pulsed Electrochemical Machining

Mahesh Thalkar, D. S. Patel, J. Ramkumar and V. K. Jain

Abstract Electrochemical micro-machining (ECM) has tremendous potential on account of versatility of its applications in different domains of engineering. Micro-machining of large surface area by ECM process is one of the challenging tasks on the current date—such as production of perforated sheets for filtering specific dimensioned micro-particles needs to generate millions of identical micro-holes in small area. As in the case of electrochemical micro-machining (ECMM), high-resolution micro-features are achieved when a low duty cycle pulsed voltage is used. When a low duty cycle pulsed voltage is supplied for machining of micro-holes, the pulse off time will increase the effective machining time by significant amount. To minimize the machining time when machining large number of micro-features, we hypothesize multiple electrodes EC drilling with sequentially distributed micro-second pulses. By providing the sequential firing-order-based pulse distribution, pulse off time is zero because at any instant at least one or more number of electrodes would be in the pulse on mode. This study outlines a numerical and experimental study of micro-holes array drilling through multiple electrodes in ECM process. A novel approach of sequential pulse distribution to each electrode is studied to improve the machining efficiency by reducing the machining time. Simultaneously four electrodes of 65 μm tip diameter are used to pierce micro-holes in stainless steel sheet of 100 μm thickness. Micro-holes of 121 and 149 μm diameters with spacing of 200 μm are machined. The study shows there is a close fit between the simulated and experimental diameters of machined holes.

Keywords ECMM · Multiple electrodes · Pulse distribution

M. Thalkar · D. S. Patel (✉) · J. Ramkumar
Micromanufacturing Laboratory, Department of Mechanical Engineering, Indian Institute of Technology Kanpur, Kanpur 208016, India
e-mail: divy@iitk.ac.in

V. K. Jain
Department of Mechanical Engineering, Maulana Azad National Institute of Technology, Bhopal 462003, India

M. S. Shunmugam and M. Kanthababu (eds.), *Advances in Micro and Nano Manufacturing and Surface Engineering*, Lecture Notes on Multidisciplinary Industrial Engineering,
https://doi.org/10.1007/978-981-32-9425-7_4

4.1 Introduction

Over the past several years, in response to the demand of miniatured products, various industries are developing advanced technologies to fulfil the requirements of customer of society in order to sustain their growth. The demand of miniatured products is not new for today's micro-engineering field. Without affecting performance capability of product or with increased number of functions, its size is decreased to a much smaller scale, mostly in mechatronics, biomedical and robotics industries. Most products of these industries are manufactured at the micron, sub-micron or up to nano level. Endoscopy and micro-neurography are examples of visualizing techniques used in bio-medical field, where micro-products are used [1]. The biggest advantage of ECM process over all other non-conventional process is the process is unaffected by the hardness and thermal conductivity of the workpiece material, and surface properties of base material remain unchanged [2].

Many key structural components in the field of aerospace industries such as turbine engine blades, optical fibre connectors in electronics industry, printer nozzles, high-density flexible printed circuit boards, gratings for electronic microscopes and chemical fiber spinneret structures contain array of micro-holes with progressively smaller sizes. Ink ejector nozzle used in digital printers is typical example of components that require array of micro-holes made with a high machining accuracy [3]. Micro-filters with holes ranging from 1 to 100 μm are used in filtration or separation, and also for sieving of powder in predefined size [4]. Micro-holes with high precision are used in nozzle plates for the conversion of liquid into mist or in the form of finely divided droplets [4]. Interference or resonance effect of light is one of the immensely studied fields in optical science. Aperture of micro-holes is used to eliminate stray light, and to correct light beam micro-hole structures are mostly used. But conventional machining produces some burrs on the edge of the hole which creates obstruction to the light path; therefore, non-conventional machining processes can be effectively used for the production of micro-apertures with highest quality [5]. In PVD and CVD process shallow masks are used on the substrate for the selective deposition of required material. These deposition masks can be made by ECM in required dimensions. In ink jet printing devices, highly corrosive ink is used for printing purposes. Therefore, highly corrosion-resistant material is needed for nozzle plate of printhead. The printhead or nozzle usually consists of an array of micro-holes with diameters smaller in size [2]. Typical material includes stainless steel and bronze. Therefore, in this work, stainless steel is used as primary workpiece material for the machining of micro-holes.

Many researchers have used different methods to fabricate micro-holes. Among all, micro-EDM is the mostly used process for micro-hole drilling, but this process has problem of taper and roundness of edges [1]. Use of kerosene and deionized water shows good results over the processing capability of EDM [6]. Fang et al. used new method of optimized electrolyte dividing manifolds for electrochemical drilling of micro-holes (≈1 mm diameter). Flushing efficiency of electrolyte can be improved by this method in case of multiple-hole drilling [7]. Precision-filled wax

deposition method is another hybrid process of micro-hole drilling. In this process initially holes are made on SU8 substrate, and then the holes are filled with wax and extruded. After extrusion the mold is deposited with required material to make micro-holes at wax-filled bars, which are later removed by heating [3]. Kim et al. [8] fabricated multiple electrode of tungsten carbide (WC) material by using reverse EDM process up to 35 μm diameter and used that electrodes as a tool in micro-ECM process to drill holes and to make grooves. Productivity of machining process can be increased by this process. Wang and Zhu [9] also fabricated array of square-shaped tools by using wire EDM process. After fabrication of square-shaped electrodes they processed through electrochemical bath to make circular cross-section to make micro-holes on SS304 steel.

In this work multiple electrodes are used to fabricate micro-holes by the electrochemical drilling process. Electrochemical drilling process uses micro-tool with side wall insulted by an insulating material and fed against workpiece in vertical direction. Micro-tools are fabricated by electrochemical etching process where initial diameter of shaft used was 800 μm to obtain micro-tool-tip diameters ranging from 50 to 90 μm.

Although the use of multiple tool electrodes can help to reduce the machining time of larger surface areas, it has some disadvantages. As the number of electrodes increases, it also decreases the impedance of system due to increased area of tools. As the tool electrode becomes larger, the cell impedance decreases and the actual rising time of the double-layer potential increases [10]. If the impedance of system decreases then it increases the rising time of signal from zero to maximum or signal fluctuates from its original parameters due to mismatching of source impedance and load impedance. Most of the time high-frequency DC pulse supply is used in ECM machining process. Mithu et al. [11] showed that charging constant of double layer increases in case of long tool and decreases for short tool length and the same for large and small diameter tool—effect of this is to increase in machining time. Owing to increased capacitance of double layer, pulse voltage across double layer will not reach to its peak value, which will result in improper machining or formation of passive layer due to low voltage. It also leads to power loss in circuit resulting in heating of electrolyte.

As mentioned above, off time of first electrode is used to switch on other electrodes serially: considering four electrodes E-1, E-2, E-3 and E-4, switching them serially with high frequency and keeping duty ratio of 25 to minimize the impedance of the circuit. Implementing this methodology results in double-layer capacitance of only single electrode and therefore reduces the rising time of high-frequency pulse. Charging profile of double layer around the tool surface depends upon the shape of pulse or rising characteristics of pulse. As pulse rises from zero to some predefined value, voltage across double layer also increases but it takes finite time to reach up to predefined value. This rising time of double layer voltage depends on time constant, that is, product of charging resistance and capacitance of double layer.

Charging equation of double layer is used to find out rising time for particular capacitance and resistance of electrode and electrolyte, respectively. Rising time is the time required to fully charge electric double, and time constant value of double

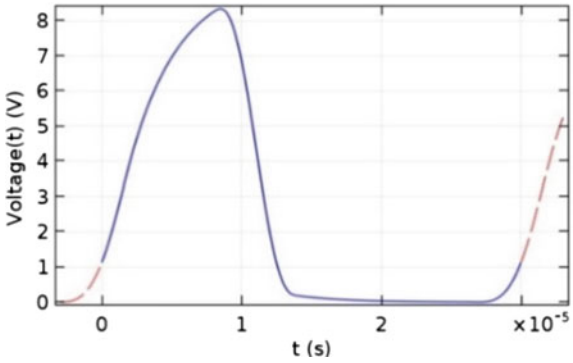

Fig. 4.1 Charging and discharging time for pulse

layer can be determined by the inter electrode gap and from size of electrode, hence frequency of pulse can be easily determined. Equation is given by [12]:

$$V_c = V_o\left(1 - e^{\frac{-t}{RC}}\right) \tag{4.1}$$

$$V_d = V_0 \cdot e^{\left(\frac{-t}{RC}\right)} \tag{4.2}$$

Considering 0.75 M concentration of $NaNO_3$ in water and conductivity $\sigma = 70$ mS/cm, permittivity of space $\varepsilon_o = 8.85 \times 10^{-12}$ F/m, and relative permittivity of electrolyte solution $\varepsilon_r = 48$, length of Helmholtz layer, that is, radius of solute ion is 3.2 Å [13]. The estimated value of Helmholtz capacitance equals 1.32 μF/mm^2. Helmholtz capacitance is given by the following equation [13]. For cylindrical electrode of radius R_0

$$C_H = \frac{\varepsilon_0 \varepsilon_r}{R_0 \log\left(1 + \frac{H}{R_0}\right)} \tag{4.3}$$

For high value of voltage (9 V in this experiment) Gouy–Chapman model gives very high value of capacitance; therefore, it is neglected in stern model. Equivalent capacitance is equal to 3.07 μF/mm^2. For conductivity of 70 mS/m and IEG of 10 μm, ohmic resistance between two electrodes is 250 Ω. Plotting profile for charging and discharging of double layer is shown in Fig. 4.1.

4.2 Numerical Simulation of EC Drilling

COMSOL Multiphysics 5.2 is used for numerical simulation of electrochemical drilling. Three-dimensional model is studied by using the electric current sub-module under its AC/DC module; deformed mesh sub-module is used to check deformed

shape of hole. Electric current and deformed geometry physics are solved simultaneously in this simulation process. Electric current physics is applied to all three domains. Local charge density in electrolyte varies with divergence of current density and is given by:

$$\nabla \cdot J = Q_j \tag{4.4}$$

Vector of current density results is given by:

$$J = \left(\sigma + \varepsilon_0 \varepsilon_r \cdot \frac{\partial}{\partial t}\right) E + J_e \tag{4.5}$$

where σ is the electrical conductivity, $\varepsilon_0\varepsilon_r E$ is the electric displacement field and J_e is the externally supplied vector of current density.

E in Eq. (4.5) is the electrical field defined by the negative gradient of electric voltage:

$$E = -\nabla v \tag{4.6}$$

Water as a material for electrolyte is chosen with conductivity equal to 70 mS/cm, SS304 for workpiece and copper for tools.

Faraday's equation ($V_n = A \cdot J/z \cdot F \cdot \rho_w$) is used to find normal dissolution rate, that is, V_n, where A is the atomic weight, z is valency, F is Faraday's constant equal to 96,500 C/mol, ρ is the density of workpiece material and J is the current density vector in the normal direction at tool surface, which can be obtained from Eq. (4.5).

$$V_n = \frac{A \cdot J}{z \cdot F \cdot \rho_w} \tag{4.7}$$

In the above expression, current density J is a variable parameter; all other parameters are constants and can be expressed as:

$$V_n = -(k) \cdot J \tag{4.8}$$

where $k = (A/z \cdot F \cdot \rho_w)$ dissolution constant for anode material. We know that most commercial materials in use are alloys. Thus, the expression of V_n modified for alloy material is

$$V_n = -\frac{1}{F}\left(\sum_i \frac{\left(\frac{W_i}{100}\right) A_i}{\rho_{wi \cdot Z_i}}\right) \cdot J \tag{4.9}$$

where i is the summation index denoting number of elements in the alloy and W_i is the weight percentage of a particular element in the alloy.

Spacing between two electrodes is fixed to 200 μm. Diameter of tool used in geometry is 90 μm. Boundary conditions are given as follows (illustrated in Fig. 4.2):

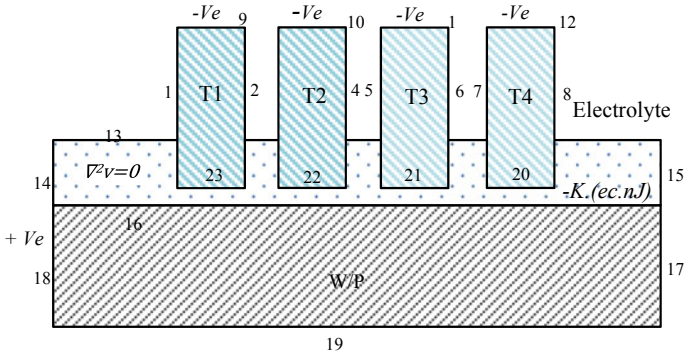

Fig. 4.2 Initial boundary conditions employed to the geometry of multiple electrodes, electrolyte and the workpiece

At workpiece surface

$$v|\Gamma_{16} = 0\,V \tag{4.10}$$

At tool surface,

$$v|\Gamma_{9,10,11,12} = -Ve\ pulses \tag{4.11}$$

Mesh velocity in x-direction is

$$V_x|\Gamma_{1,2,3,4,5,6,7,8,14,15,17,18} = 0 \tag{4.12}$$

Mesh velocity in y-direction is

$$V_y|\Gamma_{9,10,11,12,13,19} = 0 \tag{4.13}$$

All the outer surfaces are insulated,

$$n \cdot J|\Gamma_{1,2,3,4,5,6,7,8,17,18} = 0 \tag{4.14}$$

Feed is given to tool surface,

$$V_y|\Gamma_{20,21,22,23,} = 7\mu\text{m/s} \tag{4.15}$$

Mesh degradation velocity is given by faradays law:

$$V_n|\Gamma_{16} = -k \cdot (ec \cdot nJ) \tag{4.16}$$

For SS304 material dissolution constant value, that is, k = 3.35 × 10^{-11} m^3/A s.

Figure 4.3 shows the domains considered in the simulation through 3-D geometry of COMSOL. The workpiece and four electrodes are considered to be submerged in the electrolyte of known electrical conductivity. As shown in Fig. 4.4, individual pulses of 10 μs pulse width and 25% duty ratio are applied at each electrode. Workpiece potential is kept at zero and negative pulses are applied on each electrode. Figure 4.5 shows time-dependent current density plot of each electrode. Current density is different at electrodes because of distributed pulse at each electrode. Distribution of current density is Gaussian; maximum at the center of electrode and gradually decreases along the radial direction. The observed maximum current density is 2.5 × 106 A/m^2 at the center of tool. Figure 4.6 shows the final machining

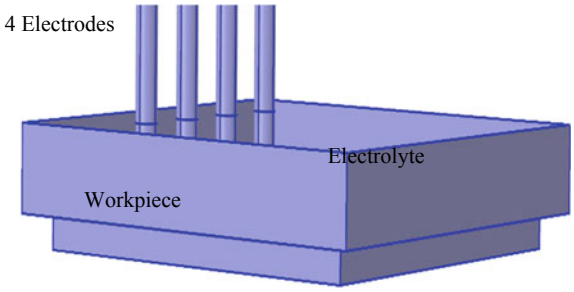

Fig. 4.3 Three-dimensional geometry showing different domains used in simulation process

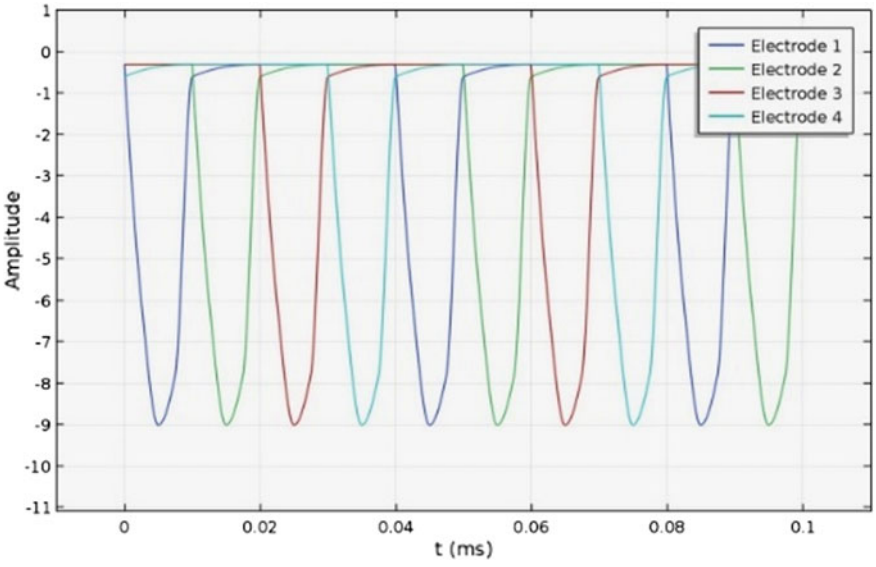

Fig. 4.4 Sequential distribution of pulses for simulation to four electrodes

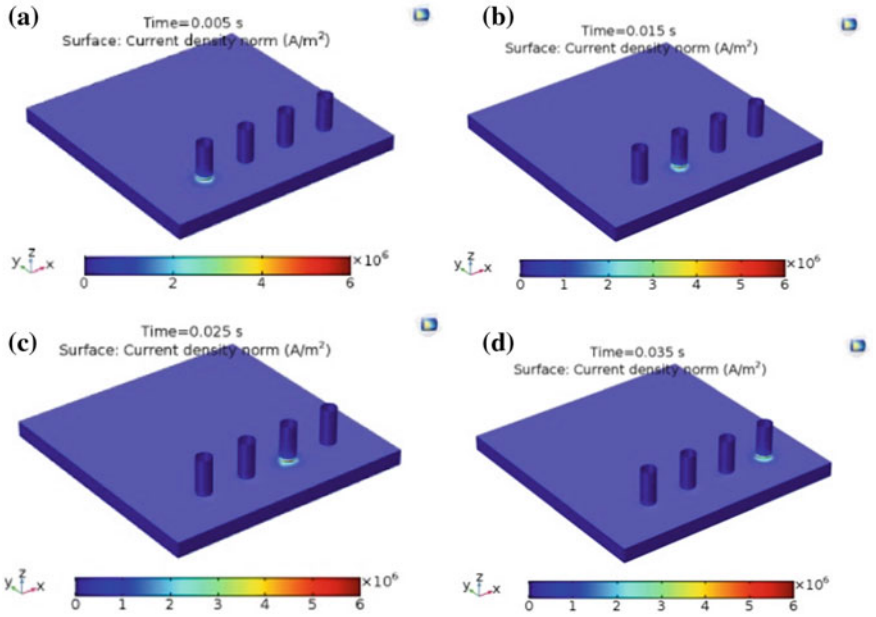

Fig. 4.5 Current density on sequentially distributed pulses to four electrodes during EC drilling

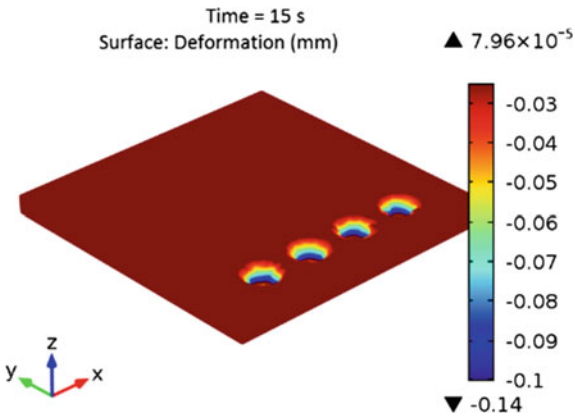

Fig. 4.6 Final simulated profile of holes drilled by four electrodes in 15 s

profile of holes. Average diameter of holes obtained is 158.58 μm with the tool of 90 μm at input voltage of 9 V and at other parameters as shown in Table 4.1.

Table 4.1 Constants and their values utilized in the analysis

S. no.	Para.	Description	Value
1	σ	Electrical conductivity	70 mS/cm
2	k	Dissolution constant	3.35×10^{-11} m^3/A s
3	ρ_w	Density of anode	8000 kg/m^3
4	v	Applied potential	9 V
5	IEG	Inter-electrode gap	10 μm
6	z	Valency number of ions	2
7	F	Faraday's constant	96,500 C/m
8	ε_0	Electrical field constant	1
9	ε_r	Relative permittivity	48

4.3 Experimental Setup

Figure 4.7 shows the experimental setup and parts employed in sequentially distributed pulsed multiple electrode electrochemical micromachining center. Setup has been built by modifying a three-axes CNC stage by mounting a cantilever tool arm, electrolyte feed tube and an acrylic tank for collecting the electrolyte. Experiments are performed on SS304 foil of thickness 100 μm. Four parallel tool of tip diameter 90 μm is used for the drilling process. $NaNO_3$ is used as electrolyte of conductivity 70 mS/cm.

Electronic pins connector with female pins is used to hold four electrodes. Initial spacing between two electrodes used is 1.8 mm. These socket connectors are fabricated with isolated electrical contacts, which are used to supply pulse voltage.

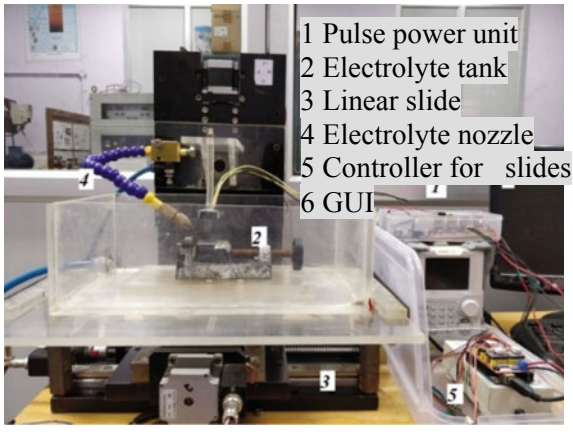

Fig. 4.7 Experimental setup used in machining

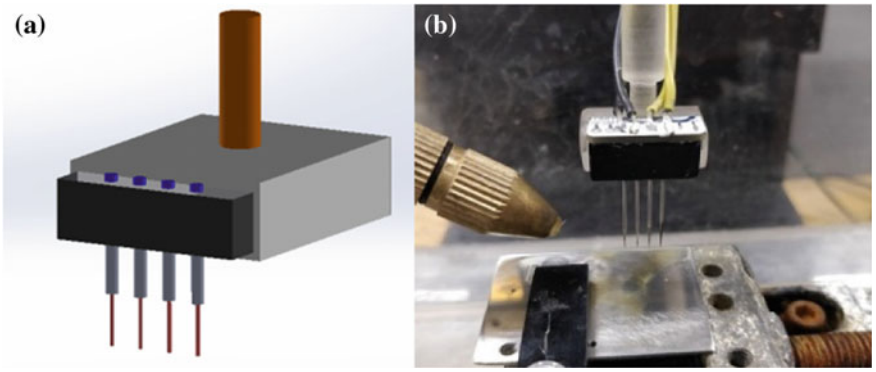

Fig. 4.8 **a** 3-D cad model of **b** multiple tools used in experiments pulses

Detail image of tool holder is shown in Fig. 4.8a, b. Distributed pulses, as shown in Fig. 4.10, are used for machining.

4.3.1 Development of the Power Supply

IRFP150N MOSFET is used to generate output pulses. MOSFET is driven by high-frequency pulse output of Arduino UNO microcontroller through MOSFET driver TC4429. ATMEGA 328 microcontroller is used to generate switching pulses. Buck converter is used to power up microcontroller with 5 V DC supply. Detailed circuit diagram of power supply is shown in Fig. 4.9.

Figure 4.10 shows the distribution of microsecond pulses to the four electrodes. As it can be seen from the image, at the instant where pulse is being off in first electrode after 5 μs, another pulse is sent to electrode 2. At the same time, sequential pulses are distributed in all four electrodes continuously. There is no pulse off time since at least one electrode is machining at any instant. The distribution of pulses can

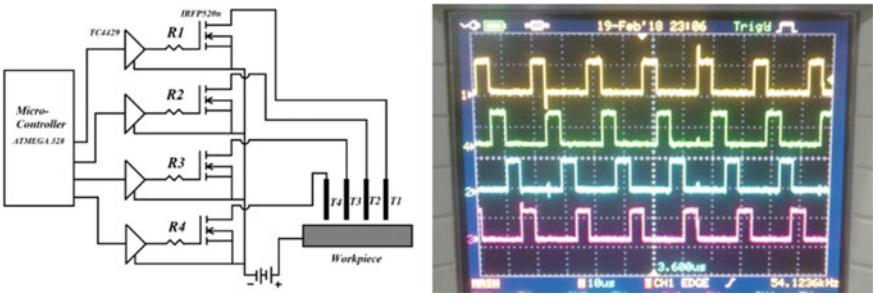

Fig. 4.9 Circuit diagram of power supply for distribution of four pulses (left) and screenshot of sequential distribution of pulses at 54 kHz frequency (right)

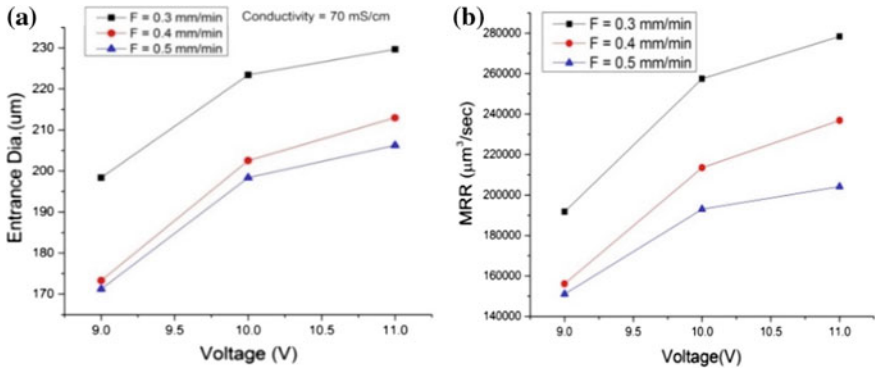

Fig. 4.10 Variation in diameters of holes and average (**a**), and MRR at different feed rates and voltages (**b**)

be modified as the number of electrodes increases, such as two alternative electrodes can get the same pulse in case of large number of tools.

4.4 Experimental Results

Figure 4.10 shows average entrance diameter of drilled hole for different feed rate. Maximum overcut value observed is 139 μm at 11 V and 0.3 mm/min feed, and minimum value of overcut is 81 μm; observed at 9 V and 0.5 mm/min feed. For minimum hole diameter, machining condition of 9 V and 0.5 mm/min feed was opted and array of holes are drilled in SS304 foil with spacing of 200 μm. Micro-holes of 121 μm diameters are machined by using 65 μm tool tip diameter. Figure 4.12 shows the entrance and exit diameters of holes. Table 4.2 presents the effect of tool feed rate and input voltage on the diameter of the micro-holes.

It can be seen from Fig. 4.11a, b that entrance diameter and exit diameter of drilled holes are almost the same. Holes are exact concentric to the center point. Burrs around the edges of drilled hole is absent. Table 4.3 shows entrance and exit diameter of selected nine holes shown in Fig. 4.11. Taper angle is 0.001° because of very less thickness of workpiece foil. Stray current effect is more if the side walls of tool are non-insulated, and pitting of area nearby to holes can be seen from Fig. 4.12a. Pitting due to stray current at the back side can be seen from Fig. 4.12b. This is due to; as tool comes out of foil, stray current from tip starts to machine nearby area.

Figure 4.12b shows the range of diameter for drilled holes is between 120 and 122 μm with maximum deviation of 0.4531 μm from mean value. Figure 4.13 demonstrates the pictorial view of a sieve fabricated through the above process.

Table 4.4 demonstrates the deviation % of the diameters of micro-holes at different input voltages.

Table 4.2 Experimental results at increasing feed and input voltage

Diameters of micro-holes at varying feed	Input voltage		
	9 V	10 V	11 V
Entrance diameter at F = 0.3 mm/min		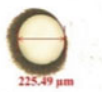	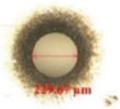
Exit diameter at F = 0.3 mm/min		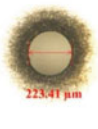	
Entrance diameter at F = 0.4 mm/min	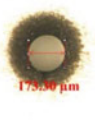		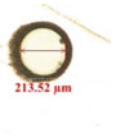
Exit diameter at F = 0.4 mm/min	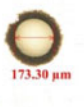		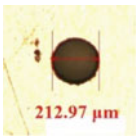

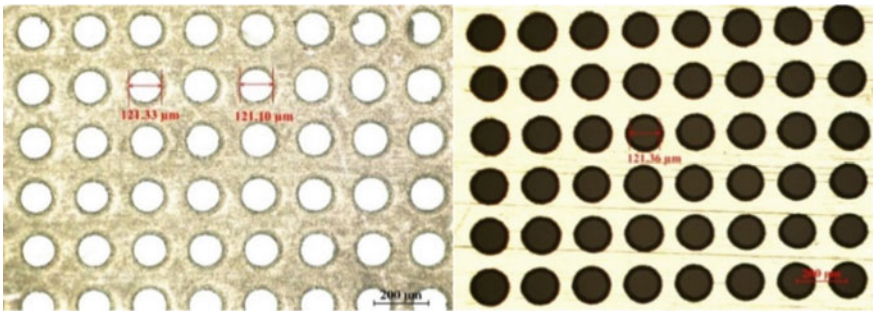

Fig. 4.11 Optical microscopy images of micro-holes drilled at entrance (left) and exit (right)

4.5 Conclusions

Simulations and experiments were conducted on the electrochemical drilling by multiple electrodes. The simulated results of holes drilling fit closely with the experimental drilled holes. The deviation in simulation and experiments observed was 8–11%. The difference in overcut is significantly high due the assumptions made

Table 4.3 Taper variations of micro holes

Hole	Entrance dia. (μm)	Exit dia. (μm)	Taper angle (°)
H1	120.83	120.70	0.000
H2	121.76	120.96	0.004
H3	120.73	120.40	0.002
H4	121.33	121.33	0.000
H5	120.52	120.25	0.001
H6	120.69	120.28	0.002
H7	121.36	121.10	0.000
H8	121.71	121.71	0.000
H9	121.10	121.10	0.000

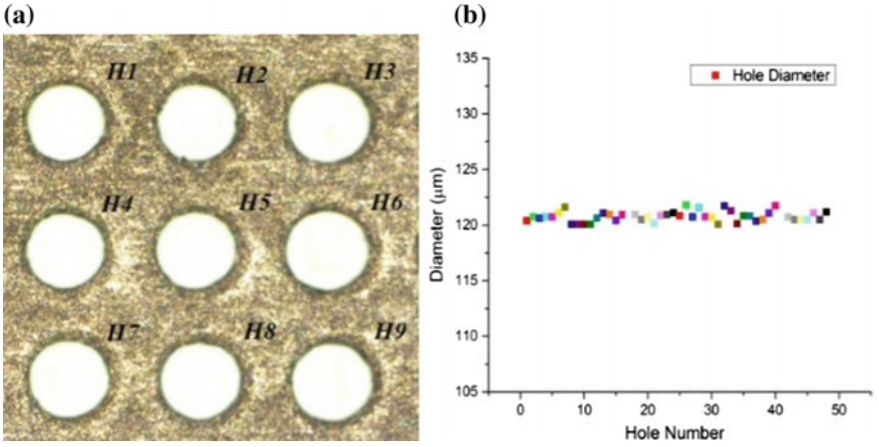

Fig. 4.12 **a** Micrograph of holes array **b** variation of diameters of holes

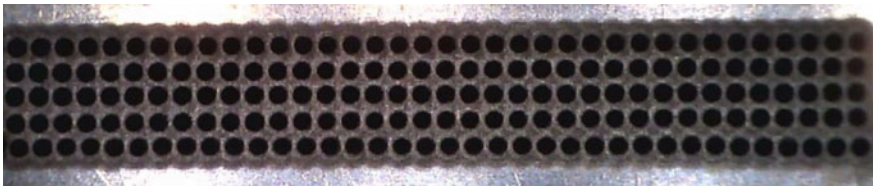

Fig. 4.13 Micrographic image of micro-hole array (36 × 5) with diameter of 149 μm and spacing between two holes of 200 μm

Table 4.4 Comparison of simulated and experimental results

Machining voltage	Simulated dia.	Experimental dia.	% deviation
9	158.56	173.3	8.505482
10	179.56	202.53	11.34153
11	195.18	212.97	8.353289

in the simulations do not consider the effect of electrochemical byproducts such as gas bubbles, temperature and sludge. Owing to distribution of voltage pulses, load on power supply is found to be decreased to one-fourth of original. By using optimum voltage and feed rate, micro-hole with precision is machined by the process. By the use of four electrodes, machining time is reduced by 75% and productivity is increased by 300%. Different-sized array of micro-holes with high circularity index are successfully drilled by ECM process. Micro-sieves of 120 and 153 μm are fabricated with standard deviation of 0.453 μm from mean.

References

1. Allen, D.M., Almond, H.J.A., Bhogal, J.S., Green, A.E., Logan, P.M., Huang, X.X.: Typical metrology of micro-hole arrays made in stainless steel foils by two-stage micro-EDM. CIRP Ann. Manuf. Technol. **48**(1), 127–130 (1999)
2. Patel, D., Jain, V., Ramkumar, J.: Micro texturing on metallic surfaces: state of the art. Proc. Inst. Mech. Eng. Part B J. Eng. Manuf. (2016)
3. Chen, S.T., Luo, T.S.: Fabrication of micro-hole arrays using precision filled wax metal deposition. J. Mater. Process. Technol. **210**(3), 504–509 (2010)
4. ECM Technologies: Product and showcase [Online]. http://electrochemicalmachining.com/showcase/micro-reactor. Accessed 20 May 2018
5. Huang, H., Liu, J., Yang, L.M.: Micro-hole drilling and cutting using femtosecond fiber laser. Opt. Eng. **53**(5), 051513 (2014)
6. Zhu, G., Bai, J., Guo, Y., Cao, Y., Huang, Y.: A study of the effects of working fluids on micro-hole arrays in micro-electrical discharge machining. Proc. Inst. Mech. Eng. Part B J. Eng. Manuf. **228**(11), 1381–1392 (2014)
7. Xiaolong, F., Xindi, W., Wei, W., Ningsong, Q., Hansong, L.: Electrochemical drilling of multiple small holes with optimized electrolyte dividing manifolds. J. Mater. Process. Technol. **247**(April), 40–47 (2017)
8. Kim, B.H., Park, B.J., Chu, C.N.: Fabrication of multiple electrodes by reverse EDM and their application in micro ECM. J. Micromech. Microeng. **16**(4), 843–850 (2006)
9. Wang, M.H., Zhu, D.: Fabrication of multiple electrodes and their application for micro-holes array in ECM. Int. J. Adv. Manuf. Technol. **41**(1–2), 42–47 (2009)
10. Park, M.S., Chu, C.N.: Micro-electrochemical machining using multiple tool electrodes. J. Micromech. Microeng. **17**(8), 1451–1457 (2007)
11. Mithu, M.A.H., Fantoni, G., Ciampi, J.: How microtool dimension influences electrochemical micromachining. Int. J. Adv. Manuf. Technol. **70**(5–8) (2014)
12. Schuster, R.: Electrochemical Microstructuring with Short Voltage Pulses, pp. 34–39 (2002)
13. Wang, H., Pilon, L.: Accurate simulations of electric double layer capacitance of ultramicroelectrodes. J. Phys. Chem. C **115**(33), 16711–16719 (2011)

Chapter 5
Effect of Water and KOH Aqueous Solution on Micro-slot Grinding of Silicon

Ashwani Pratap and Karali Patra

Abstract This study deals with the micro-slot fabrication of silicon wafer using mechanical micro-machining. Polycrystalline diamond micro-grinding tool is used to create three-dimensional micro-slots in silicon where the effectiveness of water and KOH is observed in terms of grinding force and surface roughness reduction. Grinding forces were lesser on using KOH as compared to pure water. It is attributed to increased lubricating property of KOH solution and its reaction with silicon surface creates a hydrated layer. Surface roughness was compared using water as well as KOH solution but surface generated with KOH solution shows some heat-affected marks. This is due to low heat-carrying capacity of KOH solution as compared to water. KOH aqueous solution shows better performance in terms of force reduction, whereas pure water shows better cooling property during silicon micro-grinding.

Keywords Micro-grinding · Silicon · PCD tool · KOH · Grinding force

5.1 Introduction

In the present-day advanced manufacturing scenario, the components produced must strictly adhere to the dimensional, positional and form specifications, in order to have an edge over competitor's products [1]. Silicon, being the mostly used bulk material in solar panels and semiconductor devices, demands a capable and fast process to create damage-free micro-features on its surface. Owing to its adverse material properties, micro-machining of silicon is never easy. Many unconventional fabrication processes such as LBM (laser beam machining) [2], USM (ultrasonic machining) [3], FIB (focused ion beam) [4], μ-EDM (electro discharge machining) [5], LIGA (lithography, electroplating and molding) [6] and chemical micro-machining were adopted in the past to manufacture micro-features or cutting with high accuracy. But these processes have some process-specific problems such as workpiece thermal damage,

A. Pratap (✉) · K. Patra
Micro-Fabrication Laboratory, Department of Mechanical Engineering, Indian Institute of Technology Patna, Bihta 801 103, India
e-mail: ashwani.pme15@iitp.ac.in

M. S. Shunmugam and M. Kanthababu (eds.), *Advances in Micro and Nano Manufacturing and Surface Engineering*, Lecture Notes on Multidisciplinary Industrial Engineering,
https://doi.org/10.1007/978-981-32-9425-7_5

high cost and low productivity. Mechanical micro-machining is another technique to create micro-features in silicon but is limited due to probability of early tool failure and brittle fractures on surface. Tanaka et al. [7] established that amorphous phase change in silicon is the primary mechanism for inelastic deformation and stable shearing is required for ductile mode machining. They also emphasized on the use of sharp cutting edge tool having large negative rake angle for ductile mode machining of silicon. These works paved the way for more mechanical micro-machining of silicon using large negative rake angles. Micro-grinding process employs abrasive tools where sharp abrasives, for example, diamond always cut the material with negative rake angles. Micro-grinding is progressing as a new alternative technique to create and finish 3D micro-features. Many recently published literatures show the increasing acceptability of the process and its capability [8]. Cheng et al. [9] discriminated material removal regimes and performed a parametric experimental study to correlate the undeformed chip thickness with edge crack length during micro-slot grinding of silicon. Variation in grinding force with undeformed chip thickness and material crystal structure was also noticed. Aurich et al. [10] performed micro-slot grinding in monocrystalline silicon using ultra-small micro-grinding tools where micro-slots with width 40 and 4 μm were produced. Significant brittle cracks were observed on the edge of 4 μm wide micro-slot. It happened due to limited achievable cutting speed of 0.03 m/s for 4 μm diameter tool with available spindle speed of 160,000 rpm. Such small setting of cutting speed was not able to excite complete ductile mode machining. Jin et al. [11] established the surface roughness model for silicon crystal micro-grinding and verified it with experimentation at various feed rates and cutting speed combinations.

From the available literature, it is evident that silicon micro-grinding is very challenging and more efforts are further needed to simplify and optimize the process. Reduction of feature damage, grinding force, surface roughness and tool wear are the primary concerns in silicon micro-grinding.

Different chemical media lead to reduction in grinding forces as well as surface quality improvement. Park et al. [12, 13] proposed chemical-assisted mechanical micro-machining of silicon where 10 wt% KOH solution was used to alter the surface hardness and to create ductile hydrated layer on the silicon surface, which could further help to improve micro-machining performance. But their study was mostly confined to determine the changes in silicon surface properties due to pre-treatment and no further examinations were made on machining forces and surface quality. 10 wt% KOH solution was able to create a ductile hydrated layer up to nanometric depths.

The current study, therefore, is an attempt to investigate the effects of different media on grinding forces and surface roughness. Micro-grinding performances in the presence of 10 wt% KOH solution and pure water were compared with those of dry grinding of silicon surface.

5.2 Experimental Procedure

To find the effect of medium (dry or wet) micro-grinding on silicon, a systematic approach is followed consisting of micro-grinding experiments, followed by measurements and post analysis of results. The complete experimental methodology followed during the study is shown in Fig. 5.1.

5.2.1 Machining Conditions and Methodology

Machining parameters for micro-grinding are adopted in a manner such that ductile mode machining could be observed. Undeformed chip thickness limit for ductile mode machining of silicon is instituted as 20 nm in the literature. The undeformed chip thickness in terms of cutting speed, feed rate and dynamic grit density is given in Eq. 5.1.

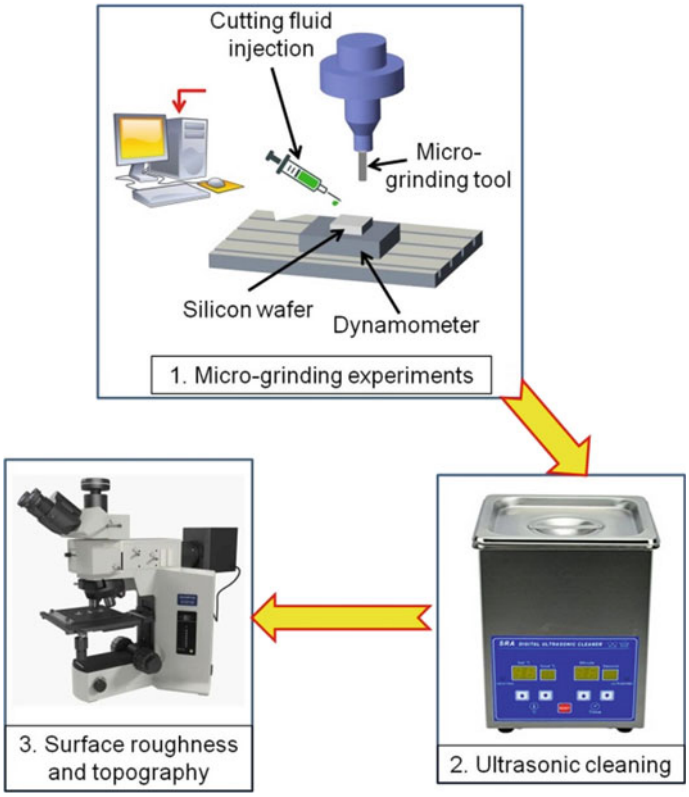

Fig. 5.1 Experimental procedure

Table 5.1 Machining conditions for single factor experiments

Tool	PCD, 0.7 mm dia
Workpiece	Silicon
Feed rates (mm/min)	0.6, 1.2, 1.8, 2.4, 3.0, 4.0
DOC (μm)	15
Speed (rpm)	2500
Experimental conditions	(1) Dry micro-grinding (DG) (2) KOH-assisted micro-grinding (KAG) (3) Water-assisted micro-grinding (WAG)
Total experiments (18)	Feed rates (6 values) * Experimental conditions (3)

$$h_m = \frac{v}{VC\left[1 + \left(\frac{B}{2D}\right)^2\right]^{1/2}} \tag{5.1}$$

where v is the feed rate, V is the cutting speed, C is the dynamic cutting edge density, B is the width to be cut and D is the tool diameter. Rotational speed during all the experiments was constant at 2500 rpm, whereas feed rate values varied from 0.6 to 4 mm/min. Micro-grinding tool used in the study is a 0.7 mm diameter polycrystalline diamond tool having abrasive grit size of 5 μm. This combination of tool geometry, feed rate and spindle rotational speed restricts the undeformed chip thickness below 20 nm. The total three conditions were selected for comparison of different parameters. All the machining conditions and parameters are presented in Table 5.1. Total number of experiments performed is 18.

5.2.2 Experimental Setup

Experiments were performed on hybrid micro-machining centre (Model: DT-110, Make: Mikrotools Pte Ltd, Singapore) which has programmable multi-axis controller (PMAC) and maximum allowable movements of 200, 100 and 100 mm in x, y and z directions, respectively. Positional accuracy of the machine is 1 μm/100 mm. Experimental setup used for micro-grinding is shown in Fig. 5.2. The main components of the setup are machine spindle, cutting fluid injection setup and dynamometer to capture the grinding force signals. Kistler mini-dynamometer 9256C2 coupled with charge amplifier 5070 is used. Sampling rate of data acquisition with dynamometer is kept at 10 kHz.

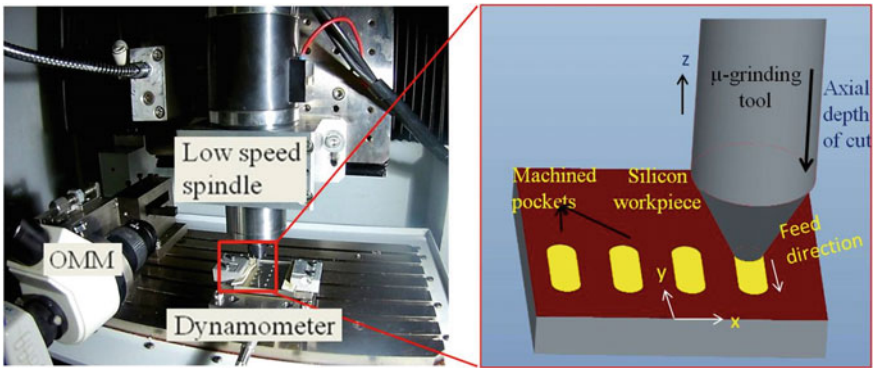

Fig. 5.2 Experimental setup for micro-grinding

5.3 Experimental Procedure

5.3.1 Grinding Forces

Raw force signature with respect to time is captured and then root mean square of the data points is taken to compare the grinding forces at different conditions. Force signature with respect to time for a particular machining condition is presented in Fig. 5.3. Normal force (z direction) signature is more complex and noisy as compared with 'x' and 'y' due to prevalent friction and rubbing on the tool bottom surface.

Root mean square values of the grinding forces in x, y and z directions were plotted against feed rate and shown in Fig. 5.4a, b and c, respectively, for different conditions. It can be observed that magnitudes of F_X and F_Y are within 0.4 N and much lesser than that of F_Z due to more rubbing and ploughing force addition between tool bottom and

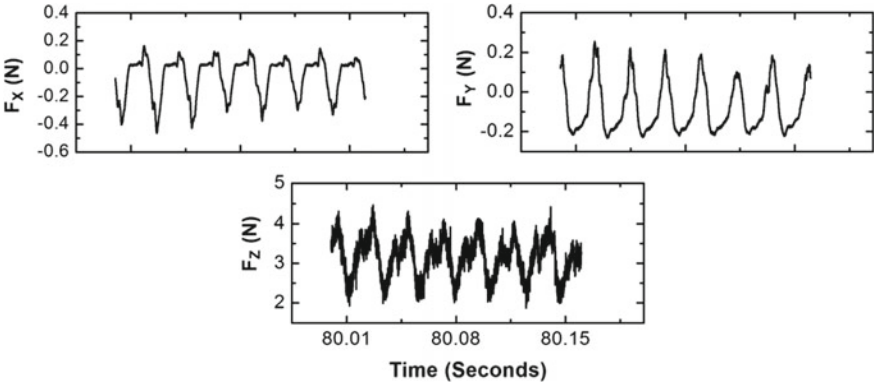

Fig. 5.3 Grinding force signature in all directions: (micro-grinding with KOH aqueous solution cutting fluid at speed 2500 rpm and feed rate 1.8 mm/min)

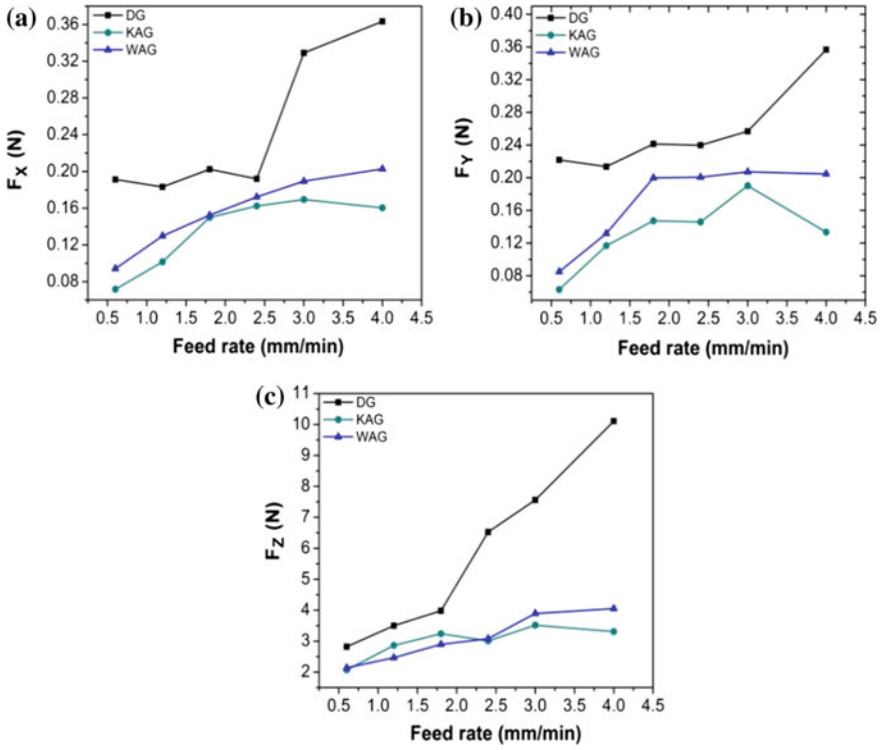

Fig. 5.4 Comparison of grinding forces at different conditions

workpiece surface. Dry grinding produces high magnitudes of forces in all directions. Grinding forces in dry condition are high and even increasing drastically at higher feed rates as compared to those of wet grinding conditions. Forces with KOH and water are lesser and increase in force at higher feed rates is gradual as compared to random increase under dry grinding. Lubrication has higher effect on z direction force rather than x and y direction forces. It can be inferred that it helps in reducing frictional and rubbing forces between tool and workpiece at larger scale as compared to cutting forces. Cutting forces with KOH solution are always lesser than those of with water lubrication and it is attributed to high lubricating property of KOH pallets suspended in solution and hydrated ductile layer formation due to KOH reaction with silicon material.

5.3.2 Grinding Force Ratio

Grinding force ratio is another important parameter which actually indicates the tool stability and probable tool life during application of miniature-sized micro-grinding

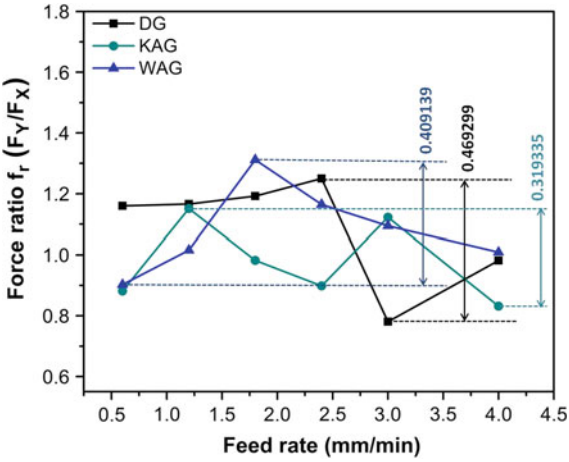

Fig. 5.5 Comparison of grinding force ratios

tools. More unbalanced the forces will be, higher are the chances of tool failure. Grinding force ratio (F_Y/F_X) should be stable and close to unity at all machining conditions so that radial vibrations of the tool due to force dynamics could be arrested. Force ratio for all lubricating conditions with respect to feed rate is shown in Fig. 5.5. It is observed that force ratio is close to unity and most stable when using KOH solution. Maximum variation in force ratio with KOH solution and water is 0.3193 and 0.4091, respectively. It can be inferred that KOH solution is able to lubricate the cutting zone, weaken the silicon bonds as well as evacuate the micro-chips from the cutting zone and makes the process more stable.

5.3.3 Surface Roughness and Topography

Topography and surface roughness of the machined pockets are measured using 3D profilometer. Average area surface roughness (S_a) values of the machined pockets are compared and shown in Fig. 5.6a. Surface roughness in dry grinding is hundreds of nanometers, which is not the acceptable quality for precision components, whereas roughness values in wet micro-grinding is tens of nanometers which can be accepted as high quality surface. Surface roughness of surfaces machined in the presence of KOH solution and water is almost comparable. Better lubrication and reduction in frictional rubbing between tool and workpiece led to higher surface finish in wet grinding. Specifically, KOH reacted with silicon and enhanced the machinability and thereby reduced vibrations and chatter, which in turn helped in achieving lower surface roughness. Surface roughness with respect to feed rate shows the obvious increasing trend. On increasing feed rate, undeformed chip thickness gets increased and brittle mode cutting may prevail. During cutting of brittle materials like silicon

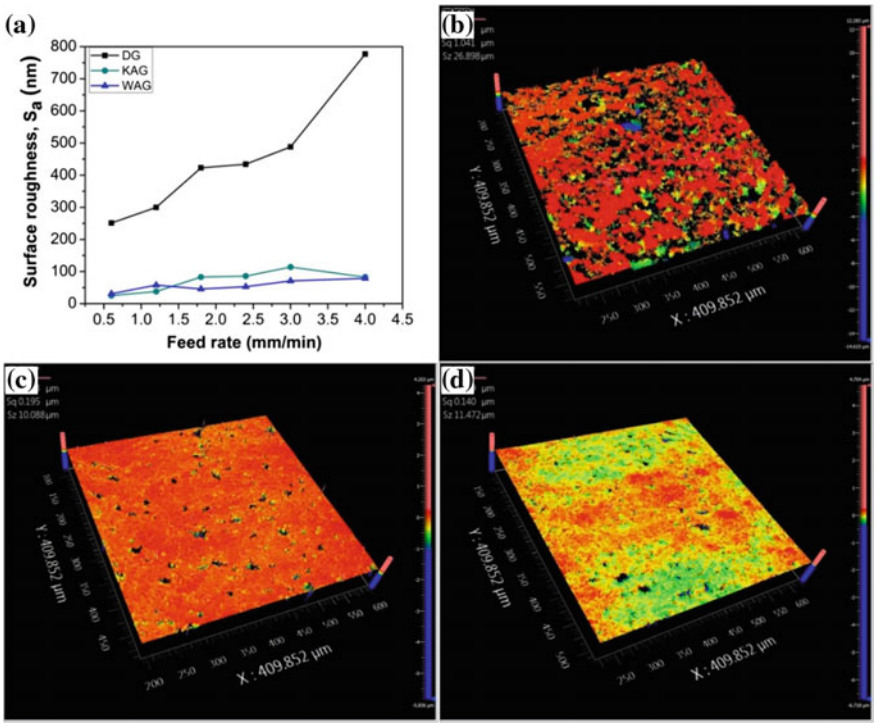

Fig. 5.6 **a** Surface roughness comparison at different conditions and surface topography under, **b** dry micro-grinding, **c** KOH lubrication, **d** water lubrication

and glass, there may be direct transition from ploughing-dominant region to brittle mode cutting region without showing of ductile mode cutting region.

Three-dimensional topography of the generated surfaces under three conditions is shown in Fig. 5.6b, c, d. It can be observed that surface formed during dry conditions is broken and brittle fractures are found, as shown in Fig. 5.6b. These fractures on the surface are due to high friction and rubbing between tool and workpiece. Secondly, poor evacuation of micro-chips and their crushing in the machining zone adds to the indentation and fractures on the surface. On the contrary, surfaces in wet micro-grinding have lesser breakages and shows throughout consistent nature, which again shows the effective evacuation of chips and smooth cutting.

Microscopic images of the machined surface are shown in Fig. 5.7a, b. Yellowish texture on the surface ground with KOH solution is clearly observed as compared to whitish and clear texture of the surface ground in the presence of water lubrication. Yellowish texture occurs due to heat generation in tool–workpiece contact and poor cooling effect of KOH solution. Poor cooling characteristic of KOH solution may be attributed to the exothermic reaction between KOH pallets and water which increases the temperature of solution. Moreover, water-assisted grinding produces clear and smooth surface without any burnt marks due to better cooling property of water.

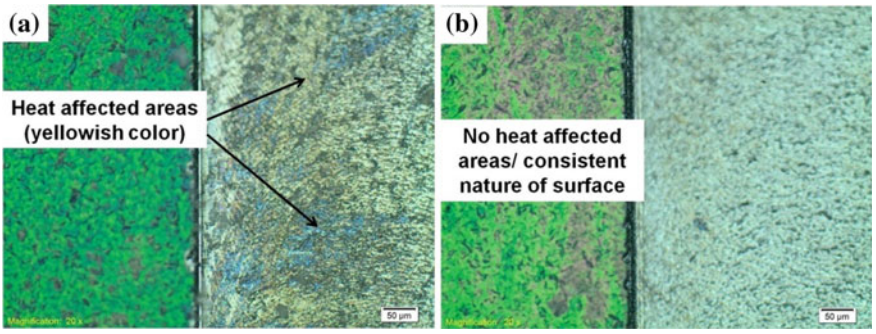

Fig. 5.7 Surface condition after micro-grinding in the presence of **a** KOH aqueous solution and **b** pure water

5.4 Conclusions

- 10 wt% KOH solution as a lubricant and chemical reactant during micro-grinding produced lesser grinding force as compared to that produced with water. It is due to better lubricating property and chemical reaction of KOH pallets suspended in solution.
- Grinding force ratio is also most stable with KOH solution, which indicates the probability of higher tool life and lesser machining vibrations.
- Surface obtained by micro-grinding with water as a lubricant was found to be consistent and free of thermal damage/burn marks due to high cooling capacity of water. On the other hand, surface produced using KOH solution got a yellowish texture due to thermal damage as KOH pallets mixed with water is an exothermic reaction and results in poor heat capacity of KOH solution.
- Further work in this area will be characterization of the KOH-dipped silicon surface and correlating the surface properties with micro-grinding performance. Physical properties such as zeta potential and mechanical properties such as hardness will be of utmost important.

References

1. Pratap, A.: Manufacturing miniature products by micro-grinding: a review. Procedia Eng. **150**, 969–974 (2016)
2. Dubey, A.K.: Laser beam machining-a review. Int. J. Mach. Tools Manuf. **48**, 609–628 (2008)
3. Thoe, T.B.: Review on ultrasonic machining. Int. J. Mach. Tools Manuf. **38**, 239–255 (1998)
4. Reyntjens, S.: A review of focused ion beam applications in microsystem technology. J Micromech. Microeng. **11**, 287–300 (2001)
5. Joshi, K.: Ultra thin silicon wafer slicing using wire-EDM for solar cell application. Mater. Des. **124**, 158–170 (2017)
6. Malek, C.K.: Applications of LIGA technology to precision manufacturing of high-aspect-ratio micro-components and -systems: a review. Microelectron. J **35**, 131–143 (2004)
7. Tanaka, H.: Requirements for ductile-mode machining based on deformation analysis of mono-crystalline silicon by molecular dynamics simulation **56**, 53–56 (2007)
8. Pratap, A.: Enhancing performances of micro-grinding of BK-7 glass through modification of PCD micro-tool. Procedia Eng. **206**, 1365–1370 (2017)
9. Cheng, J.: Experimental study of surface generation and force modeling in micro-grinding of single crystal silicon considering crystallographic effects. Int. J. Mach. Tools Manuf. **77**, 1–15 (2014)
10. Aurich, J.C.: Micro grinding with ultra small micro pencil grinding tools using an integrated machine tool. CIRP Ann.-Manuf. Technol. **64**, 325–328 (2015)
11. Jin, Y.: Experimental investigation on surface generation mechanism of micro-grinding of hard brittle crystal materials. Int. J. Adv. Manuf. Technol. **91**, 3953–3965 (2017)
12. Park, J.M.: A study on the micro machining of Si wafer using surface chemical reaction. Key Eng. Mater. **257–258**, 459–464 (2004)
13. Park, J.: A study on the fabrication of micro groove on Si wafer using chemical mechanical machining. J. Mech. Sci. Technol. **19**, 2096–2104 (2005)

Chapter 6
Magnetic Effect on High-Speed Electrochemical Discharge (HSECD) Engraving

Mukund L. Harugade, Sachin D. Waigaonkar, Nikhil S. Mane and Narayan V. Hargude

Abstract Machining operation of hard and brittle materials is a challenging task with conventional machining processes. Use of electrochemical discharge machining (ECDM) for machining of hard materials like glass and composites is a promising option due to the efficient cutting ability of the process. But the ECDM process is also suffering from limitations like low material removal rates and heat-affected zones. Material removal rate (MRR) can be increased by providing high-speed rotation of the tool electrode as high-speed ECDM process showed promising results for an increase in MRR. Further improvement in ECDM can be done by using magneto hydrodynamic (MHD) force on the machining zone. With MHD force more stable gas film can be obtained which will increase the thermal discharge. MHD force also increases the cooling of the surface around the machining zone which reduces the heat-affected zone (HAZ) and increases MRR. In this research work machining zone of high-speed electrochemical discharge engraving process (HSECD engraving) is exposed using magnetic elements of 3000 gauss capacity. Performance of HSECD engraving process is studied with and without magnetic field using different process variables, like voltage, tool rotation speed and feed rate. The results of this work show that the performance of the HSECD engraving process is improved with the use of the magnetic field. It is observed that MRR is increased by a maximum value of 0.17 mg/min and HAZ is decreased by a maximum value of 16 μm when magnetic field is applied.

Keywords High speed · MHD · MRR · HAZ

M. L. Harugade (✉) · S. D. Waigaonkar
Department of Mechanical Engineering, Birla Institute of Technology, Pilani, K. K. Birla, Sancoale 403 726, Goa, India
e-mail: mukundharugade86@gmail.com

N. S. Mane · N. V. Hargude
Department of Mechanical Engineering, Padmabhooshan Vasantraodada Patil Institute of Technology, Budhgaon (Shivaji University), Sangli 416 304, India

M. S. Shunmugam and M. Kanthababu (eds.), *Advances in Micro and Nano Manufacturing and Surface Engineering*, Lecture Notes on Multidisciplinary Industrial Engineering,
https://doi.org/10.1007/978-981-32-9425-7_6

6.1 Introduction

Making channel and engraving on glass material is quite difficult due to the properties of the glass, like hardness and brittleness. Owing to the extensive use of glass material in manufacturing and engineering applications, it is necessary to provide reliable machining processes with precision and accuracy. ECDM is a promising option for machining of glass. Though ECDM can be used to generate micro channels on materials like glass [1], it also suffers from limitations like low MRR, HAZ and overcut (OC). These limitations are the result of a lack of electrolyte circulation [2], lack of heat dissipation [3] and excessive thermal erosion of the surface. All these problems are associated directly and indirectly with lack of electrolyte circulation in the machining zone, and hence by improving electrolyte circulation these limitations can be overcome. High-speed electrochemical discharge machining (HSECDM) is an improvement in the conventional ECDM process which provides higher capacity, low tool wear [4] and high MRR. Because of increasing demand for precise and fast ECDM process, the field of HSECDM is becoming popular among researchers. Zhang et al. [5, 6] conducted a study on the machining of a film cooling hole in a single crystal super alloy by high-speed electrochemical discharge drilling (HSECDD). The findings of the study show that ECDM provides better surface quality and eliminates the recast layer. The study also shows that HSECDM improves machining accuracy of the holes. Dong et al. [7] conducted HSECDD for micro holes on beryllium copper alloy and it shows the promising result for machining speed and precision of the work. Further improvement in ECDM can be done by using magneto hydrodynamic effect. The magneto hydrodynamic force produces convection currents in electrolytes which enhances electrolyte circulation in a machining zone and improves machining accuracy [8]. The improvement in electrolyte circulation also improves material removal rate of the process up to 200% [9, 10]. The improvement in the ECDM process with magnetic field is dependent on magnetic field orientation and electrolyte concentration; it is also observed that magnetic field is more effective at lower electrolyte concentration [11]. Some researcher also observed that magnetic field efficiently removes debris from sparking zone which provides uniform spark generation which leads to better accuracy and surface quality of the work [12]. Magnetic field assistance can be useful for maintaining the quality of the work and a faster machining speed [13]. A combination of high-speed and magnetic field assistance for electrochemical discharge (ECD) can provide more accurate and faster machining process. In this paper, an experimental investigation is conducted to study the effect of high-speed tool rotation and magnetic field assistance on MRR and HAZ. Results obtained in this study show that the magnetic field-assisted high-speed tool rotation has a positive impact on the quality of work produced by ECD engraving. Table 6.1 shows the work of different researchers on MHD-assisted ECDM.

Table 6.1 Literature review of the magnets used during ECDM process

Authors	Machining process	Workpiece	Magnet
Cheng et al. [8]	Drilling	Pyrex glass	Permanent Nd–Fe-B ring magnet
Rattan and Mulik [9, 10, 12]	Travelling wire—electrochemical spark machining (ECSM)	Quartz	Permanent Nd–Fe-B disc magnet
Hajian et al. [11]	Milling	Soda lime glass	Permanent Nd–Fe-B rectangular regular shape magnet
Xu et al. [13]	Drilling	Soda lime glass	N-52 disc neodymium magnet

6.2 Experimentation

A mini CNC machine controlled by GRBL 0.9 software is used for machining of the work. The setup also includes electrolyte bath and work-holding fixture placed below the tool in machining area. Work-holding fixture is placed such that it ensures proper electrolyte circulation along the work. A tool electrode is supplied with the negative terminal from a direct current (DC-supply) transformer and the positive terminal is placed inside the electrolyte bath as an auxiliary electrode. Magnetic elements are placed around the tool electrode to ensure magnetic field exposure to machining area. Figure 6.1a shows the schematic arrangement of the experimental setup and Fig. 6.1b shows the actual experimental setup used for the research work. Relative positions of the machine elements, a magnetic element, tool and workpiece can be observed in Fig. 6.1b. This experimental setup is developed for the engraving of width 500 μm channel. A total of 24 experiments are conducted in this study to find the results, and each experiment is repeated three times (three trials) to obtain the results. Finally, the average values of the results are presented in this paper.

Figure 6.2 shows the geometry of the engraving tool used in magnetic field-assisted high-speed electrochemical discharge (MF-HSECD) engraving. The specifications of magnetic elements and workpiece material are shown in Tables 6.2 and 6.3. Table 6.4 shows the chemical composition of soda lime glass.

Table 6.5 shows the range of process parameters and specifications of the different elements of the MF-HSECD engraving process selected for the experimentation of this study.

Average HAZ thickness is calculated using the following Eq. (6.1):

$$Avg.HAZ\ Thickness = \frac{l_1 + l_2 + l_3 + \cdots + l_n}{n} \tag{6.1}$$

where $l_1, l_2, l_3, \ldots, l_n$ = thickness of HAZ at different points

n = number of points considered for the thickness of HAZ (in this case 18)

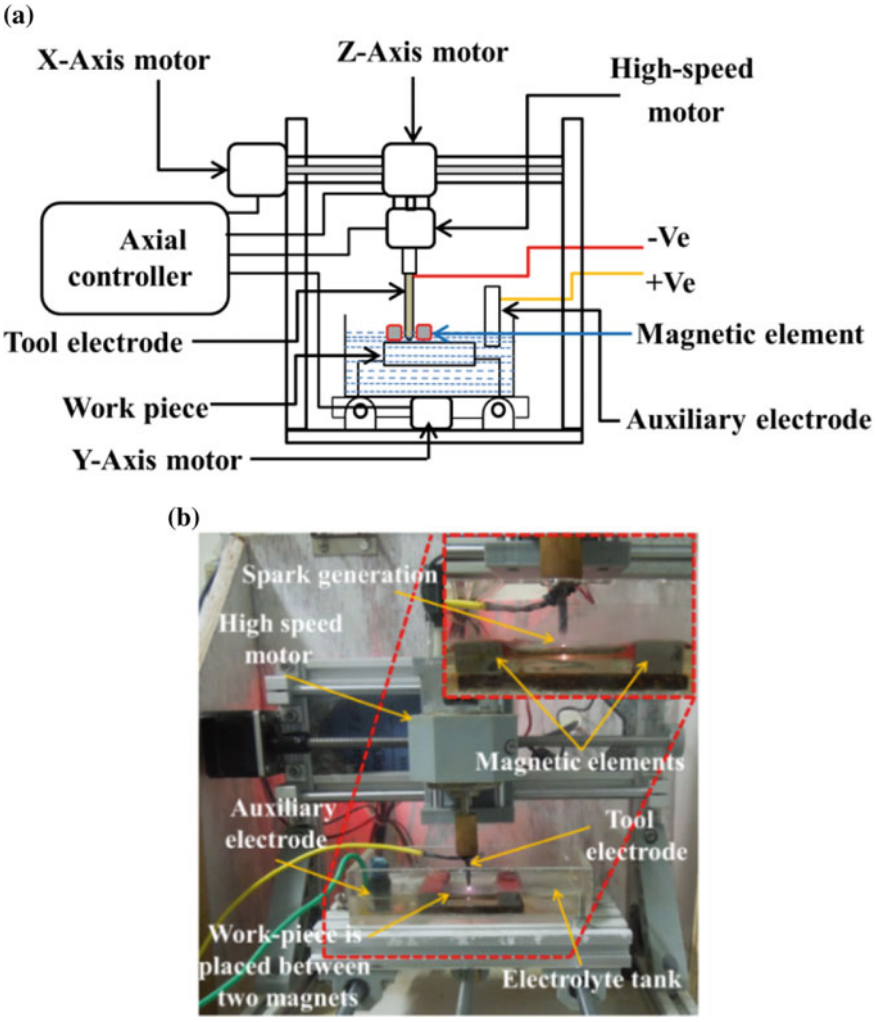

Fig. 6.1 **a** Schematic view. **b** Pictorial view. Experimental setup

The amount of metal removed (MR) was measured by taking the difference in weight of the specimen before machining weight (W_1) and after machining weight (W_2). The MRR is evaluated using the following Eq. (6.2):

$$MRR = \frac{MR}{T} OR \frac{(W_1 - W_2)}{T} \tag{6.2}$$

where

T is the machining time.

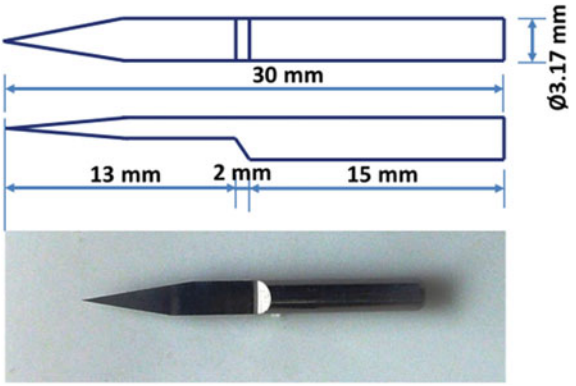

Fig. 6.2 Schematic diagrams of the engraving tool and photographic view

Table 6.2 Details of Nd–Fe-B permanent magnet

Specifications	Details
Material	Nd–Fe-B rectangular block magnet
Dimensions	25 mm × 12 mm × 8 mm

Table 6.3 Material properties of soda lime glass

Characteristic	Value
Thermal conductivity (J/KgK)	1.4
Specific heat capacity (Wm/K)	840
Mass density (Kg/m^3)	2440

Table 6.4 Chemical composition of soda lime glass

Composition of soda lime glass						
Composition	SiO_2	Na_2O	CaO	MgO	Al_2O_2	K_2O
wt%	73	14	9	4	0.15	0.03

Table 6.5 Details of the experimental arrangement

Tool electrode	Tungsten carbide
Auxiliary electrode	Copper
Work piece material	Soda lime glass
Electrolyte solution	KOH
Tool tip diameter	500 μm
Electrolyte concentration (wt%)	25
Tool rotation speed (rpm)	1000, 2000, 3000, 4000
Feed rate (mm/min)	0.1, 0.5, 1, 1.5
Voltage (V)	40, 50, 60, 70

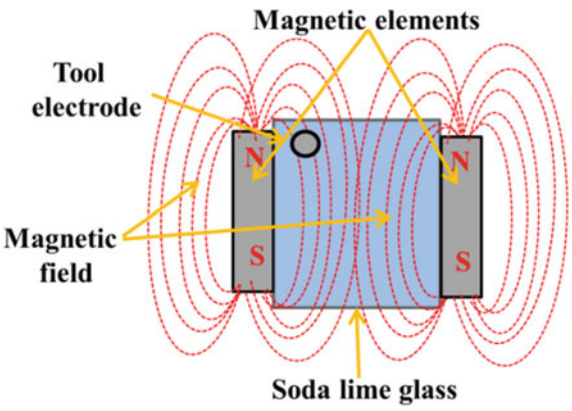

Fig. 6.3 Mechanism of MF-HSECD engraving

Figure 6.3 shows the relative positions of a magnetic element, tool electrode and machining zone in MF-HSECD engraving. The figure also shows the magnetic field lines present in the machining zone which influences the electrolyte present between magnetic elements and generates convection currents known as MHD convection. The magnetic field generates the MHD convection along the field lines which removes debris present in the machining zone effectively.

6.3 Results and Discussion

6.3.1 Effect of Voltage With and Without Magnetic Field

Figure 6.4a, b shows the effect of voltage and magnetic field on MRR and HAZ thickness of the MF-HSECD engraving. Figure 6.4a shows that with the increase in voltage from 40 to 70 V, the MRR increases from 0.72 to 1.15 mg/min without magnetic field and from 0.76 to 1.20 mg/min with magnetic field. With the increase in voltage, a gas film is more stable due to an increased rate of electrolysis which leads to stable discharge. Hence, more thermal erosion of the material takes place which gives higher material removal rate. At the same time, more heat will be conducted in the material around the machining zone which increases the thickness of the HAZ. It can be observed that with the increase in voltage from 40 to 70 V, the HAZ increases from 210 to 232 μm without magnetic field and from 201 to 229 μm with magnetic field.

Figure 6.4a also shows that the MRR of the work increases with the application of the magnetic field on the machining area. This increase in the MRR occurs due to efficient debris removal from the cutting zone. The magnetic field when applied to the machining zone generates the MHD convection currents in the electrolyte present in the machining zone. Owing to this MHD convection currents, debris generated during thermal erosion will be removed continuously. This provides a more stable

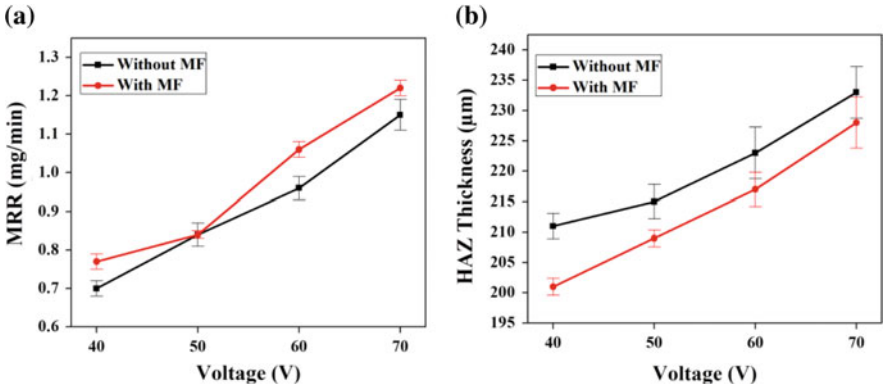

Fig. 6.4 **a** Effect of voltage on MRR. **b** Effect of voltage on HAZ (tool rotation speed = 2000 rpm, feed rate = 1 mm/min, electrolyte conc. = 20%)

gas film which results in strong spark generation at the tip of the tool electrode. With strong spark generation, more material is removed and MRR increases. Figure 6.4b shows that with the application of the magnetic field, a thickness of HAZ decreases. HAZ observed during the HSECD engraving is a result of heat conduction around the machining area. With magnetic field exposure, the MHD currents are generated in the electrolyte; due to this, more heat is removed by the electrolyte through convection. Hence, less heat is conducted inside the work material which reduces the thickness of HAZ.

6.3.2 *Effect of Tool Rotation Speed With and Without Magnetic Field*

Figure 6.5a, b shows the increase in the MRR and decrease in the thickness of HAZ with the application of magnetic field and increase in tool rotation speed. At high speed, a strong bubble layer is formed around the tooltip due to the centrifugal effect provided by tool rotation.

This strong bubble layer ensures for higher breakdown voltage and discharges, which finally result in high MRR. High tool rotation speed also provides higher electrolyte circulation in the machining zone due to which more heat will be removed by the electrolyte and less heat will be conducted into the work material. This will reduce the thickness of heat-affected zone at higher tool rotation speed. Figure 6.5b shows that with increase in tool rotation speed from 1000 to 4000 rpm, the HAZ decreases from 238 to 212 μm for without magnetic field and from 228 to 205 μm with magnetic field condition.

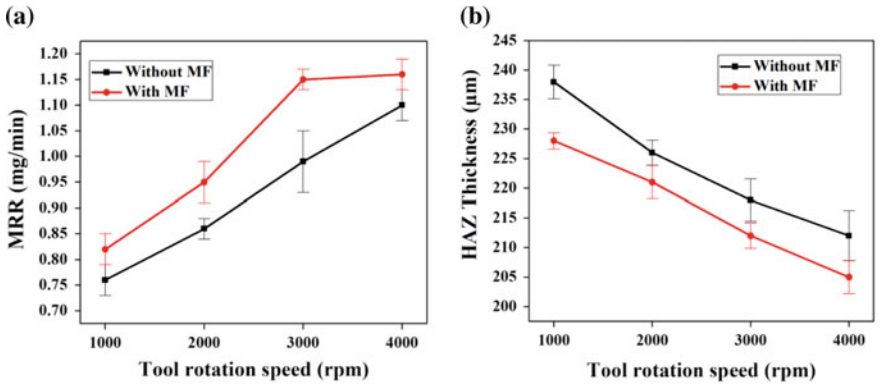

Fig. 6.5 **a** Effect of tool rotation on MRR. **b** Effect of tool rotation on HAZ (voltage = 50 V, feed rate = 1 mm/min, electrolyte conc. = 20%)

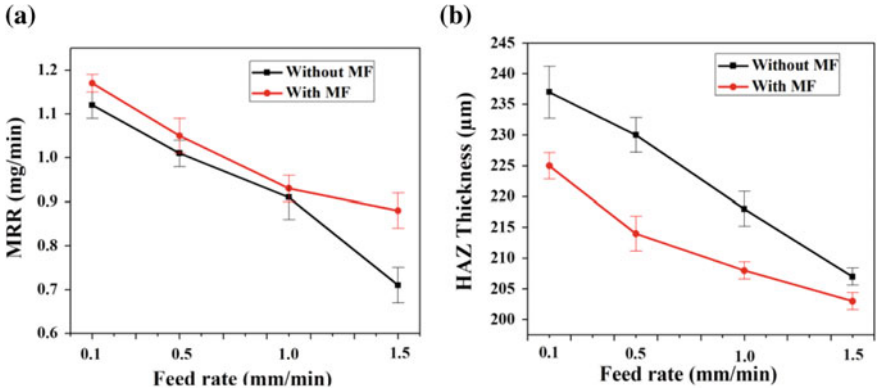

Fig. 6.6 **a** Effect of feed rate on MRR. **b** Effect of feed rate on HAZ (voltage = 50 V, tool rotation speed = 2000 rpm, electrolyte conc. = 20%)

6.3.3 Effect of Feed Rate With and Without Magnetic Field

The effect of feed rate and magnetic field on MRR and thickness of HAZ can be observed from the Fig. 6.6a, b, that with an increase in feed rate MRR decreases. The material removal in the MF-HSECD engraving is done by thermal erosion of the material and hence when feed rate increases the exposure time of material to thermal discharge decreases. The decrease in exposure time further reduces the melting of the material and heat conduction, hence MRR and thickness of HAZ decreases. The MRR increases by 0.41 mg/min without magnetic field and by 0.28 mg/min with magnetic field condition when feed rate is increased from 0.1 to 1.5 mm/min. Also, the MRR increases with the application of a magnetic field due to debris removal.

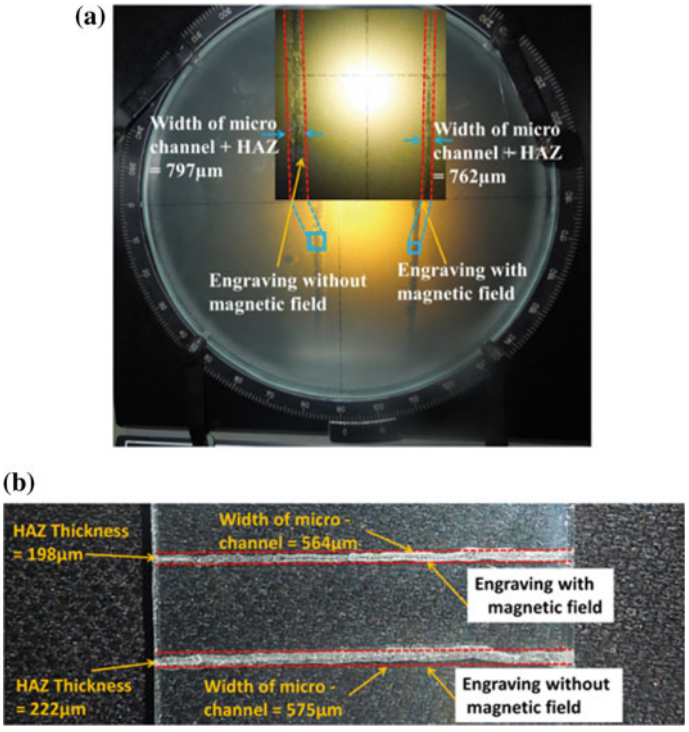

Fig. 6.7 **a** Optical profile image of micro-channel. **b** Actual image of micro-channel. Workpiece

HAZ decreases with the magnetic field due to heat removal by the electrolyte through MHD convection.

The optical profile image of the engraving done with and without the magnetic field can be observed from Fig. 6.7a, b, which shows that the thickness of HAZ for HSECD engraving without the magnetic field is 222 µm, and which decreases up to 198 µm with the magnetic field. It can also be observed that the overcut in the HSECD engraving without the magnetic field is 75 µm, and the overcut with the magnetic field is 64 µm.

6.4 Conclusions

In this research study, the effect of the magnetic field on MRR and HAZ of the HSECD engraving process on soda lime glass is studied with different operating variables. The results observed in this work are very promising for obtaining efficient, fast and precise machining operations. Following are the conclusions drawn from this study:

- The application of magnetic field increases the MRR of the HSECD engraving process by removing debris from the machining zone, building a strong and steady discharge. The experimental result shows that with magnetic field, MRR can be increased up to 6.5%.
- The thickness of HAZ is also decreased with the magnetic field due to effective heat removal from the machining zone; it is observed that the thickness of HAZ can be decreased up to 7.5%.
- The study also investigates the effect of different operating variables on the performance of HSECD engraving. With an increase in voltage, MRR and thickness of HAZ increases.
- With an increase in tool rotation speed, MRR increases and the thickness of HAZ decreases. Feed rate is also an important operating parameter of the HSECD engraving process, with an increase in feed rate both MRR and HAZ decreases.

References

1. Mallick, B., Tayade, R.M., Sarkar, B.R., Doloi, B., Bhattacharyya, B.: Effects of process variables on ECDM performances during micro-channel cutting on glass. In: Proceedings of the All India Manufacturing Technology Design and Research Conference, College of Engineering, Pune, Maharashtra, India, pp. 1580–1584 (2016)
2. Jui, S.K., Kamaraj, A.B., Sundaram, M.M.: High aspect ratio micro machining of glass by electrochemical discharge machining (ECDM). J. Manuf. Process. **15**, 460–466 (2013). https://doi.org/10.1016/j.jmapro.2013.05.006
3. Wuthrich, R., Fascio, V., Viquerat, D., Langen, H.: In situ measurement and micromachining of glass. In: Proceedings of 1999 International Symposium on Micromechatronics and Human Science, Nagoya, Japan, pp. 185–191 (1999). https://doi.org/10.1109/mhs.1999.820004
4. Huang, S.F., Liu, Y., Li, J., Hu, H.X., Sun, L.Y.: Electrochemical discharge machining micro-hole in stainless steel with tool electrode high-speed rotating. J. Mater. Manuf. Process. **29**, 634–637 (2014). https://doi.org/10.1080/10426914.2014.901523
5. Yan, Z., Zhengyang, X., Yun, Z., Di, Z.: Machining of a film cooling hole in a single-crystal super alloy by high speed electrochemical discharge drilling. Chin. J. Aeronaut. **29**(2), 560–570 (2016). https://doi.org/10.1016/j.cja.2015.06.021
6. Yan, Z., Zhengyang, X., Di, Z., Jun, X.: Tube electrode high-speed electrochemical discharge drilling using low-conductivity salt solution. Int. J. Mach. Tools Manuf. **92**, 10–18 (2015). https://doi.org/10.1016/j.ijmachtools.2015.02.011
7. Dong, S., Wang, Z., Wang, Y.: High-Speed electrochemical discharge drilling (HSECDD) for micro holes on C-17200 Beryllium copper alloy in deionized water. Int. J. Adv. Manuf. Technol. **88**(1–4), 827–835 (2016). https://doi.org/10.1007/s00170-016-8645-x
8. Cheng, C.P., Wu, K.L., Mai, C.C., Hsu, Y.S., Yan, B.H.: Magnetic field assisted electrochemical discharge machining. J. Micromech. Micro Eng. **20**, 1–7 (2010). https://doi.org/10.1088/0960-1317/20/7/075019
9. Rattan, N., Mulik, R.S.: Improvement in Material Removal Rate (MRR) using magnetic field in TW-ECSM Process. J. Mater. Manuf. Process. **10**, 21–44 (2016). https://doi.org/10.1080/10426914.2016.1176197
10. Rattan, N., Mulik, R.S.: Experimental set up to improve machining performance of silicon dioxide (Quartz) in magnetic field assisted TW-ECSM process. Silicon 1–9 (2018). https://doi.org/10.1007/s12633-018-9818-z

11. Hajian, M., Razfar, M.R., Movahed, S.: An experimental study on the effect of magnetic field orientations and electrolyte concentrations on ecdm milling performance of glass. J. Precis. Eng. **45**, 322–331 (2016). https://doi.org/10.1016/j.precisioneng.2016.03.009
12. Rattan, N., Mulik, R.S.: Experimental investigations and multi-response optimization of silicon dioxide (Quartz) machining in magnetic field assisted TW-ECSM process. Silicon **9**(5), 663–673 (2017). https://doi.org/10.1007/s12633-016-9521-x
13. Xu, Y., Chen, J., Jiang, B., Liu, Y., Ni, J.: Experimental investigation of magneto hydrodynamic effect in electrochemical discharge machining. Int. J. Mech. Sci. **142–143**, 86–96 (2018). https://doi.org/10.1016/j.ijmecsci.2018.04.020

Chapter 7
Bactericidal Nanostructured Titanium Surface Through Thermal Annealing

D. Patil, M. K. Wasson, V. Perumal, S. Aravindan and P. V. Rao

Abstract Inspired from nature, the antibacterial titanium (Ti6Al4V) alloy surface is developed through thermal annealing at 750 °C for 15 min. The titanium sample was coated with 5 nm thickness silver film using DC sputter coating and the thermal annealing was carried out in two different annealing environments (atmospheric and argon gas environment). The annealed samples were characterized through field-emission scanning electron microscope (FESEM). The formation of nanostructured topography on the annealed samples depends on the annealing environment. The polygonal-shaped surface structure is observed when annealed in atmospheric condition, and nanospikes were seen on titanium surface after annealed in an argon environment. The X-ray diffraction (XRD) analysis was carried out in order to investigate the phase formation during annealing. Plate counting method was used to study the bactericidal capability of modified titanium surfaces. The modified titanium surface in argon gas environment has shown better bactericidal property compared to surface annealed in an atmospheric environment. The physical contact killing mechanism of nanospike with the bacterial cell is dominant on the nanospike-structured titanium surface.

Keywords DC sputtering · Thermal annealing · Surface topography · Bactericidal surface · Biofilm

7.1 Introduction

In biomedical field, the biofilm formation on surgical implants is a critical challenge and it causes infection at surgical sites. Such infection is caused due to bacterial

D. Patil · S. Aravindan (✉) · P. V. Rao
Department of Mechanical Engineering, Indian Institute of Technology, New Delhi 110 016, Delhi, India
e-mail: aravindan@mech.iitd.ac.in

M. K. Wasson · V. Perumal
Kusuma School of Biological Sciences, Indian Institute of Technology, New Delhi 110 016, Delhi, India

M. S. Shunmugam and M. Kanthababu (eds.), *Advances in Micro and Nano Manufacturing and Surface Engineering*, Lecture Notes on Multidisciplinary Industrial Engineering,
https://doi.org/10.1007/978-981-32-9425-7_7

attacks, which can result in costly and traumatic surgery. The number of surgeries for hip replacement grew by 50% in USA during the period 1993–2004 [1]. Recently, from 1999 to 2016, the Australian Orthopedic Association has reported that 23% of surgeries are carried out after implantation (especially hip and knee implant) due to failure of implants because of bacterial infection [2]. Therefore, it is very important to make implants that can prevent such infection without sacrificing some of the basic functions of implants. There are different ways through which one can achieve the antibacterial titanium and titanium alloy surfaces. The titanium surfaces are modified with antimicrobial peptides, antibiotics [3], nanoparticles [4, 5] and so on. However, any slight increase in the concentration of these antibacterial agents would cause serious health-related issues. It has been also shown that the nanostructures are able to damage bacterial cells by penetrating into the bacterium cell membrane [6]. The nanopillar structure available on wings of cicada's surface has a bacteria-killing ability. The nanopillar physically damages the outer membrane of the bacterial cell and prevents the formation of biofilm [7]. Many researchers have made a layer of nanotitania tube through anodization on pure titanium and its alloy surfaces [8]. The photocatalytic property of nanotitania (TiO_2) makes it useful to decompose or kill organic compounds such as bacteria. Moreover, the chemically synthesized silver nanoparticles can be loaded into this titania nanotube in order to kill the bacteria efficiently [9]. High aspect ratio nanostructured surfaces can be fabricated by different nanomanufacturing processes, such as focused ion beam machining (FIB), nanoimprint lithography (NIL) and reactive ion etching (RIE) [10]. However, the FIB process has low throughput, while the RIE process requires costly mask and NIL is applicable to polymers only. The nanostructures fabricated by these processes are highly ordered and limited to very small area. Therefore, the alternate solution to fabricate high aspect ratio nanostructure is hydrothermal etching [11] and thermal annealing [12] of titanium alloy. However, the etching route is costly and hazardous. In this study, the bactericidal titanium surface is fabricated through DC sputtering followed by thermal annealing which can effectively kill both classes of bacteria: *Staphylococcus aureus* and *Escherichia coli*. The effects of environments used during thermal annealing process on the bactericidal property of titanium alloy were also studied.

7.2 Experimental Procedure

7.2.1 Materials and Methods

Ti6Al4V specimens of dimensions 12 mm × 12 mm × 8 mm were cut from the Ti6Al4V bock using wire-cut electric discharge machine. The SiC grit papers of different sizes starting from 200, 400, 600, 800, 1000, 1200 and 2000 were used for mechanical polishing of Ti6Al4V specimens. Subsequently, fine polishing with alumina particles of average sizes 1–0.5 μm was done on the polishing machine. The

polished samples were cleaned in ultrasonication bath of deionized water and ethanol for 15 min. The samples were dried using hot air and then taken into DC sputter coater (Q150 RS, Quorum Tech., Lewes, UK) chamber for deposition of the thin silver metallic film. The metallic silver film of 5 nm thickness was deposited on Ti6Al4V at 50 mA current and 5 mbar chamber pressure. After the deposition, the coated samples were transferred to a microprocessor-based temperature-controlled furnace. The samples were annealed at 750 °C for 15 min in two different environments. One set of samples was annealed in atmospheric conditions and another set in argon gas environment. The flow rate of argon gas is maintained at 1 lit/min. The samples were immediately taken out from the furnace after 15 min and allowed to cool in the air until it reaches the room temperature. The plain and modified Ti6Al4V samples were characterized using FESEM and XRD analysis.

7.2.2 Antibacterial Testing

The plate counting method was adopted for testing bactericidal property of nanostructured Ti6Al4V surface [13]. *E. coli* and *S. aureus* cultured was kept in a shaking incubator with 200 rpm at 37 °C. The ultrasonically clean samples are placed into a 12-well plate after sterilization. The bacterial culture of 100 μL was dropped on each sample with an approximate concentration of 1×10^5 colony forming unit per milliliter (CFU/mL). Then, the 12-well plates were kept in the incubator for 12 h. After incubation, the samples were gently washed and diluted with 2 mL volume of phosphate buffer saline (PBS). Simultaneously, standard agar plates of Luria broth were prepared. Out of diluted solution, 100 μL volume of bacterial culture was spread into agar plate and kept inside the incubator for 24 h at 37 °C. The experiments were conducted for three times in order to get standard error of the results.

$$\text{The CFU/mL of culture solution is calculated as CFU/mL} = \frac{\text{No. of colonies}}{\text{Vol. of culture in the plate}} \times \text{dilution factor.}$$

7.3 Results and Discussion

7.3.1 Samples Characterization

The FESEM images of plain and annealed Ti6Al4V samples are shown in Fig. 7.1.

Figure 7.1b, c shows annealed silver-deposited Ti6Al4V surface for film thicknesses of 5 nm in ambient condition and argon gas environment, respectively. From SEM images, it is observed that the silver-deposited Ti6Al4V samples surface shows

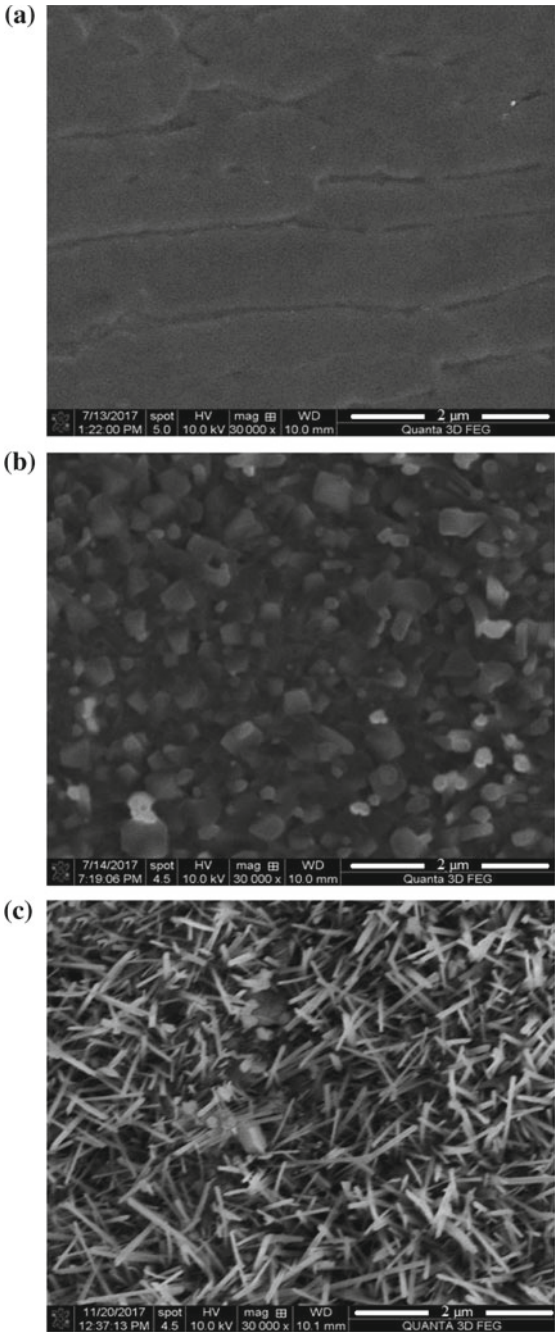

Fig. 7.1 FESEM micrographs of **a** plain Ti6Al4V and 5 nm Ag-coated annealed Ti6Al4V in **b** ambient condition **c** argon environment

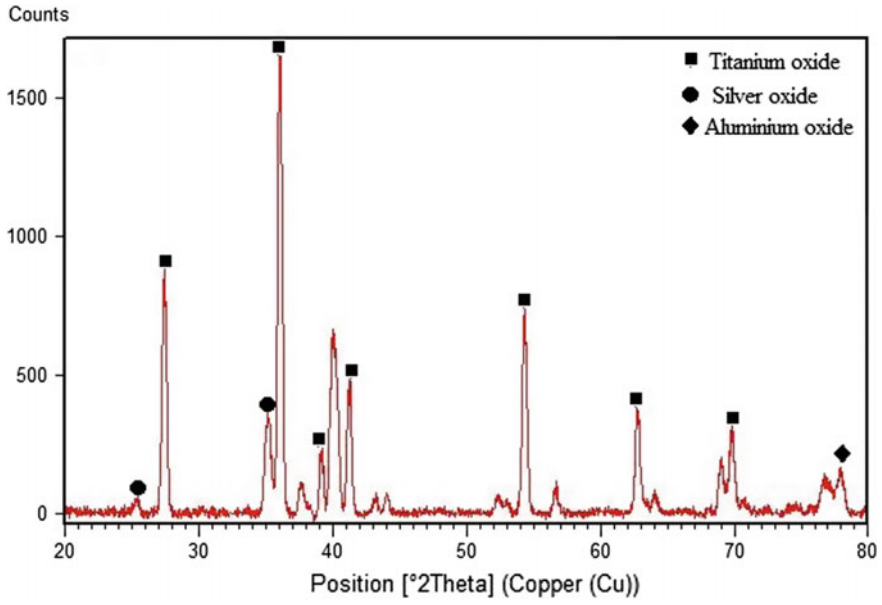

Fig. 7.2 XRD spectra for 5 nm Ag-Ti6Al4V annealed sample in argon gas environment

the polygonal nanoparticles formed during the heating process in an oxygen-rich environment (ambient condition). Thin rode-like structures called nanospikes are observed when annealed in oxygen-deficient environment. From XRD analysis it is confirmed that the nanospiked-structured titanium surface consists of titanium, silver and aluminum oxide, as can be seen from Fig. 7.2.

The mechanism behind the formation of nanospike in oxygen-deficient environment is explained by Xinsheng et al. [14]. A thin oxide layer is formed, which is a combination of TiO_2 and Al_2O_3. The titanium atoms from the oxide surface will have a much higher chemical affinity than the surrounding alumina and will react with the oxygen present in the environment and form titanium oxide nuclei. This process of diffusion of titanium outward from the bulk surface continues as long as the sample remains at elevated temperature. However, in case of oxygen environment, the growth rate of TiO_2 formation is faster. Oxygen diffusion is very high due to its high concentration. Thus the formation of TiO_2 takes place at the interface between initial formed TiO_2 grains and metal surface. Hence large crystal grains of TiO_2 are observed in oxygen-rich environment.

7.3.2 Antibacterial Testing

Plate counting method was used to quantify the antibacterial property of plain and modified Ti6Al4V sample. The steps mentioned in Sect. 7.3.2 were carried out. After 24 h, the optical micrographs of colony forming units were recorded. On polished titanium sample, both the bacteria form bacterial lawn, whereas on modified titanium sample, only a few countable colonies are formed, as can be observed from Fig. 7.3. The number of colonies formed on nanospike-structured sample is significantly less than colonies formed on titanium sample annealed in ambient conditions (Fig. 7.3a–f).

The CFU/mL of the culture solution was calculated and can be seen from Fig. 7.4. The significant reduction in number of colonies was observed on the nanospike-structured surface compared to the plain and polygon-structured titanium surface. There are two possible mechanisms that take place on a nanostructured surface which actively inhibits the growth of bacteria. One is the presence of silver content, the release of silver ion which comes into contact with the cell membrane and induces oxidative stress with the help of reactive oxygen species and subsequently damages cell membrane [4]. Once a membrane gets disrupted, the next Ag + ion enters the cytoplasm to destroy the intracellular structures like mitochondria and DNA, resulting in bacterial death. The leaching of silver ion is a common mechanism on both modified titanium samples. However, the physical contact killing is dominant on the nanospike-structured titanium surface. The bacterium comes into contact with nanospikes and creates sufficient stress on the bacterial cell membrane. The surface contact area between the bacterial cell membrane and the nanospike tip surface is very less. Once local stress exceeds the strength of bacterial cell wall, the membrane gets disrupted and nanospike pierces into the cell body. Finally, it results in complete rupture of the cell membrane and cell lysis takes place. This mechanism is schematically explained with the help of Fig. 7.5. Moreover, it is observed that the modified Ti6Al4V surface is more prone to kill *S. aureus* compared to *E. coli* bacterium due to the spherical shape of *S. aureus*. The round shape of *S. aureus* provides minimum surface area for stress concentration due to penetration of nanospikes and also for silver ion to interact with bacterium membrane. It was proposed that the spacing between the high aspect ratio nanostructures should be in the range of 130–380 nm in order to kill both classes of bacteria effectively [12]. The bioinspired structures such as cicada wings (nanopillars: L: 159–146 nm and D: 82–148) and Dragonfly wings (nanopillars: L: 80–90 nm and D: 20–150) act as bactericidal surfaces. However, cicada wings are efficient against gram-negative bacteria while inefficient against gram-positive bacteria due to thick wall structure. Dragonfly wings are efficient in killing both classes of bacteria [15]. Hence in order to kill both classes of bacteria efficiently, a small amount of silver content was encapsulated into the matrix of nanospike and the modification made was significantly effective against both bacteria. The fabricated nanospikes in our study are more closely packed. Because of the apparently random positions of nanospikes, the bacteria can be exposed in many possible directions. This is the reason behind the better antibacterial property

	Escherichia coli	*Staphylococcus aureus*
Plain Ti6Al4V	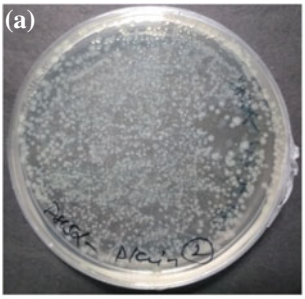	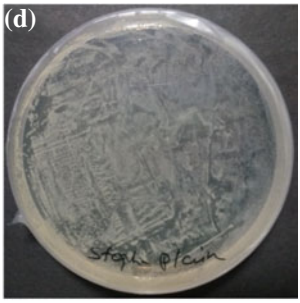
5nm Ag_ annealed in presence of atmospheric	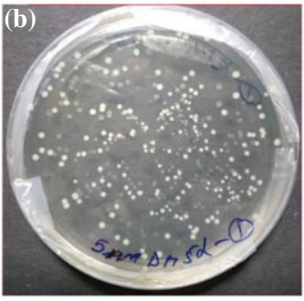	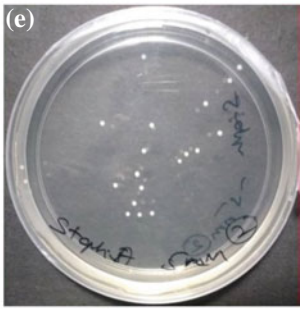
5nm Ag_ annealed in presence of Argon	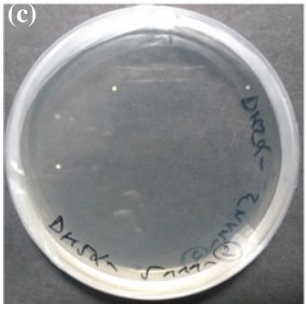	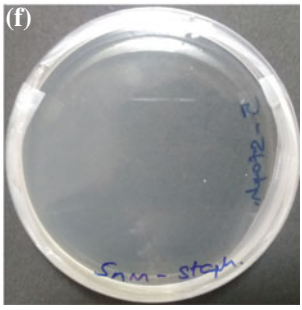

Fig. 7.3 Surface colonization results for **a** *E. coli* **b** *S. aureus* for 24 h

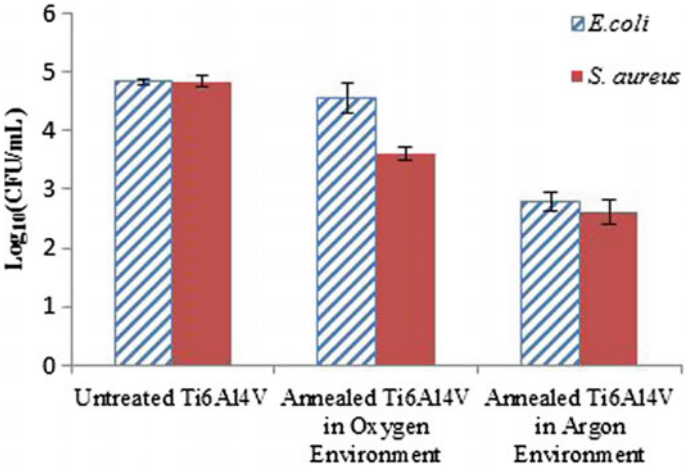

Fig. 7.4 The quantitative result (in $\log_{10}$ (CFU/mL)) of antibacterial property of modified Ti6Al4V surface against *E. coli* and *S. aureus*

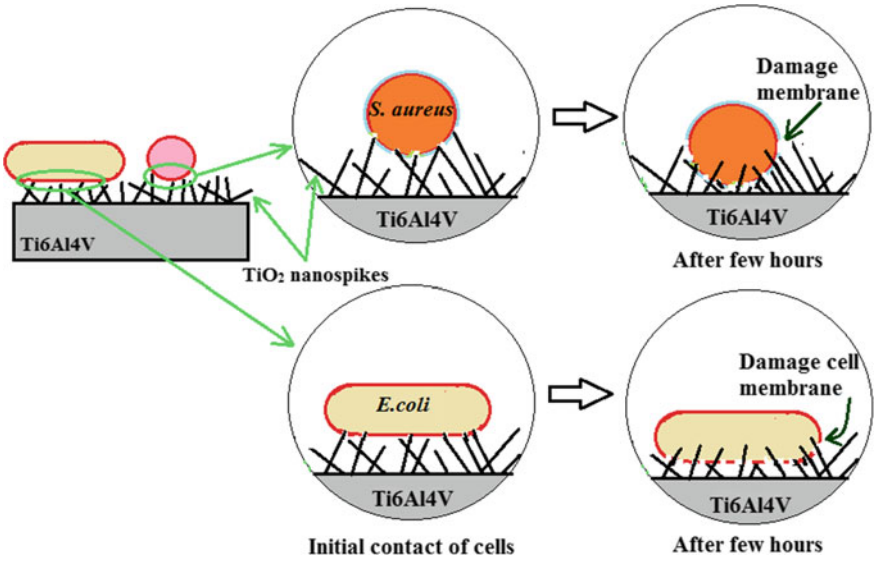

Fig. 7.5 Mechanism explains the bactericidal activity on nanospike structures

of the nanospike-structured sample compared to acicular-shaped particles formed on titanium surface annealed in an ambient environment with the same amount of silver content. Moreover, the aspect ratio of titanium oxide nanospike depends on the annealing time, annealing temperature and argon flow rate [12]. Hence incorporation of small quantity of bactericidal agent (like silver) with high aspect ratio nanostructure surfaces can enhance the bacterial killing ability of titanium implants.

7.4 Conclusions

In order to avoid the complications caused due to bacterial infection after implantation, simple and effective approach was proposed to make high efficient antibacterial titanium surfaces against a wide range of bacteria. The thermal annealing process was used to fabricate high aspect ratio random nanostructures on Ag-coated Ti6Al4V surface. The fabricated surface has shown effective bactericidal property that combines the two mechanisms of bacterial killing; one is through physical contact killing and another is through leaching of silver ion. Therefore, such surface can be able to kill two different classes of bacteria effectively. Moreover, it could be effective against multi-resistant bacteria. This new approach of combining the minimum amount of silver content in the nanostructured surface is beneficial in dental and orthopedic implants so as to avoid the infection.

References

1. Alka, J., Hesam, S., Asha, M., Prasad, K.D.V.Y.: Biomimicking nano and microstructured surface fabrication for antibacterial properties in medical implants. J. Nanobiotechnol. **15**(64), 64–84 (2017). https://doi.org/10.1186/s12951-017-0306-1
2. Australian Orthopaedic Association.: Hip, knee and shoulder arthroplasty: annual report. In: Australian Orthopedic Association National Joint Replacement Registry (2016). https://aoanjrr.sahmri.com/documents/10180/275066/Hip%2C%20Knee%20%26%20Shoulder%20
3. Jenny, A.L., Krystyn, J.V., Michael, F.R.: Design of antibacterial surfaces and interfaces: polyelectrolyte multilayers as a multifunctional platform. Macromolecules **42**(22), 8573–8586 (2009). https://doi.org/10.1021/ma901356s
4. Gianluigi, F., Annarita, F., Stefania, G., Luciana, P., Mahendra, R., Giancarlo, M., Massimiliano, G.: Silver nanoparticles as potential antibacterial agents. Molecules **20**(5), 8856–8874 (2015). https://doi.org/10.3390/molecules20058856
5. Patil, D., Wasson, M.K., Aravindan, S., Perumal, V., Rao, P.V.: Fabrication of silver nanoparticles-embedded antibacterial polymer surface through thermal annealing and soft molding technique. Mater. Res. Express **6**(4), 045010 (2018). https://doi.org/10.1088/2053-1591/aaf916
6. Aaron, E., Russell, J.C., Elena, P.I.: Nano-structured antimicrobial surfaces: from nature to synthetic analogues. J. Colloid Interface Sci. **508,** 603–616 (2017). https://doi.org/10.1016/j.jcis.2017.07.021

7. Kelleher, S.M., Habimana, O., Lawler, J., Reilly, B.O., Daniels, S., Casey, E., Cowley, A.: Cicada wing surface topography: an investigation into the bactericidal properties of nanostructural features. ACS Appl. Mater. Interfaces **8**(24), 14966–14974 (2016). https://doi.org/10.1021/acsami.5b08309
8. Demetrescu, I., Ionita, D., Pirvu, C., Portan, D.: Present and future trends in TiO2 nanotubes elaboration, characterization and potential applications. Mol. Cryst. Liquid Cryst. **521**, 195–203 (2010). https://doi.org/10.1080/15421401003715918
9. Shenglin, M., Huaiyu, W., Wei, W., Liping, T., Haobo, P., Changshun, R., Qianli, M., Mengyuan, L., Huiling, Y., Liang, Z., Yicheng, C., Yumei, Z., Lingzhou, Z., Paul, K.C.: Antibacterial effects and biocompatibility of titanium surfaces with graded silver incorporation in titanianotubes. Biomaterials **35**(14), 4255–4265 (2014). https://doi.org/10.1016/j.biomaterials.2014.02.005
10. Patil, D., Sharma, A., Aravindan, S., Rao, P.V.: Development of hot embossing setup and fabrication of ordered nanostructures on large area of polymer surface for antibiofouling application. Micro Nano Lett. **13**, 1–5 (2018). https://doi.org/10.1049/mnl.2018.5462
11. Huan, H., Vince, S.S., Stacey, M.G., Sungcheol, K., Minhua, L., Pablo, M., Gustavo, A.S.: Bio-inspired silicon nanospikes fabricated by metal-assisted chemical etching for antibacterial surfaces. Appl. Phys. Lett. **111**(25), 253701, pp. 1–5 (2017). https://doi.org/10.1063/1.5003817
12. Terje, S., Angela, H.N., Bo, S.: Bactericidal nanospike surfaces via thermal oxidation ofTi alloy substrates. Mater. Lett. **167**, 2–26 (2016).https://doi.org/10.1016/j.matlet.2015.12.140
13. Zhu, Y., Cao, H., Qiao, S., Wang, M., Gu, Y., Luo, H., Meng, F., Liu, X., Lai, H.: Hierarchical micro/nanostructured titanium with balanced actions to bacterial and mammalian cells for dental implants. Int. J. Nanomed. **10**, 6659–6674 (2015). https://doi.org/10.2147/IJN.S92110
14. Xinsheng, P., Aicheng, C.: Aligned TiO_2 nanorod arrays synthesized by oxidizing titanium with acetone. J. Mater. Chem. **14**, 2542–2548 (2004). https://doi.org/10.1039/B404750H
15. Alka, J., Hesam, S., Asha, M., Prasad, K.D.V.Y.: Bio-mimicking nano and micro-structured surface fabrication for antibacterial properties in medical implants. J. Nanobiotechnol. **15**, 64–84 (2017). https://doi.org/10.1186/s12951-017-030-1

Chapter 8
A Study on the Effect of Oxalic Acid Electrolyte on Stainless Steel (316L) Through Electrochemical Micro-machining

J. R. Vinod Kumaar, R. Thanigaivelan and V. Dharmalingam

Abstract Stainless steel 316L (SS 316L) finds numerous applications in various industries, such as pharmaceuticals, marine, architectural, medical implants and fasteners. Owing to its excellent mechanical, physical and chemical properties, stainless steel finds application in manufacture of micro-electro-mechanical system (MEMS)-based devices. The machining of SS (316L) through conventional way still remains a problem owing to its poor surface characteristics. In this paper, an attempt is made to machine SS (316L) using electrochemical micro-machining (ECMM) with oxalic acid as an electrolyte. The effect of voltage in machining, duty cycle and concentration of electrolyte on material removal rate (MRR) and overcut is studied. Furthermore, scanning electron microscope (SEM) analysis technique has been carried out to study the parametric effect on machined surface. The use of oxalic acid as an electrolyte contributes for low MRR and smaller overcut. The use of weak electrolyte protects the machining setup and increases the lifespan of the machine.

Keywords Electrochemical micro-machining · Stainless steel SS (316L) · Oxalic acid

8.1 Introduction

There are several unconventional machining processes available for machining stainless steel (316L), like electro discharge machining (EDM), laser beam machining (LBM), and these processes are not suitable because they cause thermal distortion of the machined surface. Electrochemical micro-machining (ECMM) process is one

J. R. Vinod Kumaar (✉) · R. Thanigaivelan
Department of Mechanical Engineering, Mahendra Engineering College (Autonomous), Namakkal 637503, Tamilnadu, India
e-mail: jrvinod@gmail.com

V. Dharmalingam
Department of Chemistry, Mahendra Engineering College (Autonomous), Namakkal 637503, Tamilnadu, India

M. S. Shunmugam and M. Kanthababu (eds.), *Advances in Micro and Nano Manufacturing and Surface Engineering*, Lecture Notes on Multidisciplinary Industrial Engineering,
https://doi.org/10.1007/978-981-32-9425-7_8

of the best suited methods to machine extremely difficult-to-cut materials like SS (316L).

In ECMM, electrolytes play a prominent role, and various electrolytes and its effects are found in the literatures. In line with that, oxalic acid is a natural compound quiet commonly found in many plants and vegetables. It is an organic acid, which is colourless crystalline solid and forms a colourless solution, when mixed up with distilled water. In manufacturing industries, it is used as a bleaching agent and for rust removal. In this research work, to develop a chemical process, an ethane-dioic acid, also known as oxalic acid ($C_2H_2O_4$) and with condensed formula HOOCCOOH, is used as an electrolyte with distilled water.

In ECMM, the researchers had used many electrolytes, such as strong electrolytes and weak electrolytes, in their research to machine the materials. Shi Hyoung Ryu [1] performed experiments on stainless steel 304 using citric acid as an electrolyte through ECMM to machine micro-hole diameter of 60 μm to the depth of 50 and 90 μm in diameter. They also produced the cavities in the form of square and circular shape. Yang et al. [2] suggested an eco-friendly micro-machining method with mineral water and fabricated the tungsten carbide micro-pin to the diameter of 20–30 μm. Lin Tang et al. [3] have chosen NaCl and $NaNO_3$ and their admixture solutions to machine stainless steel material. The surface roughness and MRR increases with electrolyte flow pattern. Ryu [4] machined high aspect ratio micro-holes using citric acid electrolyte in ECMM. Ayyappan and Sivakumar et al. [5] experimented and improved the surface quality and MRR using oxygenated aqueous sodium chloride (NaCl) electrolyte and potassium dichromate ($K_2Cr_2O_7$) mixed with aqueous NaCl in ECMM. Thanigaivelan et al. [6] investigated on the comparison of sodium nitrate with acidified sodium nitrate in ECMM. The use of acidified sodium nitrate electrolyte for machining stainless steel 304 shows better results for machining rate and overcut. Thanigaivelan et al. [7] suggested a new technique by infrared heating of sodium nitrate ($NaNO_3$) electrolyte for machining copper material and they studied the parametric effect on overcut and MRR. Sandip Kunar et al. [8] proposed a novel approach to ECMM maskless SS 304 material using NaCl, $NaNO_3$ and NaCl + $NaNO_3$ as electrolytes. Among these electrolytes, NaCl + $NaNO_3$ electrolyte was found to be better in influencing the factor for mean radial overcut and mean machining depth. Kalaimathi et al. [9] investigated the machining of Monel 400 alloy through travelling-wire electrochemical machining with ozonated aqueous NaCl as an electrolyte. MRR was observed to be increased to 90% and surface roughness was decreased up to 32%. Lin tang et al. [10] conducted an orthogonal experiment on S-03 stainless steel material with $NaNO_3$ and $NaClO_3$ as electrolyte. They found that the increase in voltage and cathode feed rate increases MRR and decreases the surface roughness and the side gap. Anasane et al. [11] investigated the performance of electrolytes on titanium material and chose seven electrolytes, namely sodium bromide (NaBr), sodium chloride (NaCl), sodium perchlorate ($NaClO_4 \cdot H_2O$), hydrochloric acid (HCI), sulphuric acid (H_2SO_4), ethylene glycol (EG) and sodium bromide (EG + NaBr), ethylene glycol (EG), sodium bromide and sodium chloride (EG + NaBr + NaCl). In addition to these five electrolytes, they had also used two non-aqueous electrolytes to find out various criteria, like material removal rate, radial overcut and

conicity of micro-hole. Among these electrolytes, they proved that the combination of ethylene glycol and sodium bromide shows outstanding results for machining titanium material.

From the above literature review, researchers had tried using of strong and weak electrolytes in machining the materials. This research mainly emphasise on machining of SS (316L) using oxalic acid as an electrolyte with its influential effect on MRR, and overcut was studied under the parametric conditions of machining voltage, duty cycle and electrolyte concentration.

8.2 Experimental Arrangement of ECMM

The experimental arrangement of ECMM was indigenously developed for this research work, as shown in Fig. 8.1. The setup consists of different parts, namely pulse generator, micro controller unit, stepper motor, electrolyte tank, tool feeding arrangement to control the inter-electrode gap, pump and filter. The work-holding fixture is fixed in the electrolyte tank to hold the workpiece. Tool and workpiece is submerged in the electrolyte. Pulsed power supply system has been used to vary the duty cycle, voltage and current. The voltage is applied between workpiece (anode) and tool (cathode). Several electrochemical reactions occur at the cathode, the anode

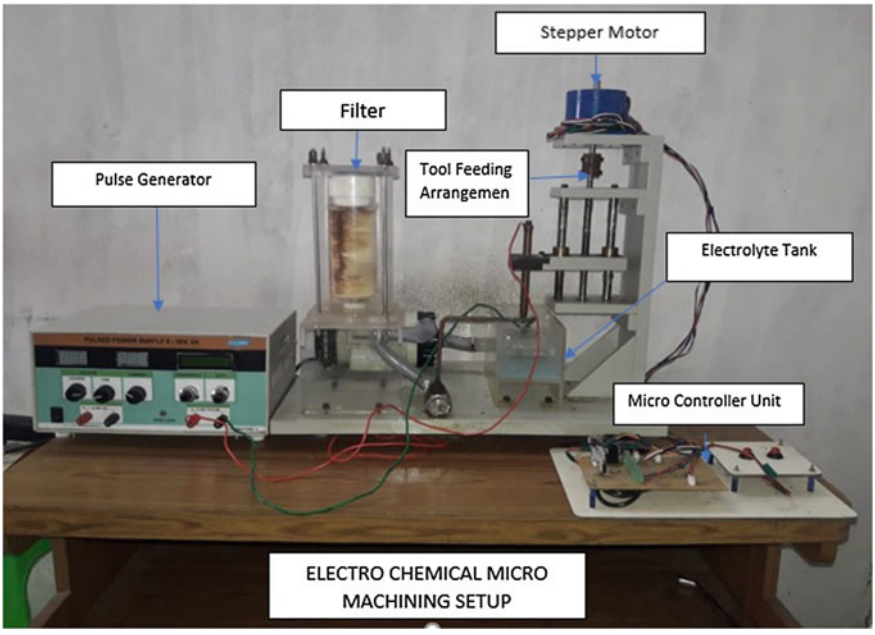

Fig. 8.1 Experimental arrangement of ECMM

Table 8.1 Parameters and their levels considered for machining SS (316L) through ECMM

S. No.	Parameters	Symbol	Unit	Range
1	Voltage	V	V	7–11
2	Duty cycle	D	%	25–85
3	Electrolyte concentration	C	g/l	40–80

and in electrolyte, thereby causing chemical erosion in ECMM. Pump is driven by an electric motor used to transfer the electrolyte from the tank to the filter. Filter purifies the electrolyte by removing the tiny machined particles in the form of sludges.

Oxalic acid solution ($C_2H_2O_4$) as electrolyte of varying concentrations, stainless steel electrode of size φ 460 μm and stainless steel SS (316L) workpiece of thickness 500 μm were used to conduct the experiments. The chemical composition of SS 316L is presented in Table 8.2. A constant stand-off distance of 20 μm is maintained throughout the experiments. Oxalic powder of varied grams is mixed with 1 litre of distilled water to prepare the electrolyte solution. Properties of Oxalic acid is presented in Table 8.3. Based on the literature review, the process parameters and ranges were chosen for this research work are presented in Table 8.1. MRR is calculated using the Eq. (8.1). Overcut of the machined hole is seen through SEM analysis and is calculated using the Eq. (8.2).

Calculation of MRR is done using the following formula:

$$\begin{aligned} \text{MRR} &= \text{Material removal rate} \\ &= \text{Thickness of the work piece} \\ &\quad /\text{Time taken to machine the micro hole in } \mu\text{m/sec} \end{aligned} \tag{8.1}$$

Overcut is calculated using the following formula:

$$\text{OC} = \text{Observed diameter} - \text{Actual diameter} \tag{8.2}$$

8.3 Chemical Reactions of Oxalic Acid Solution on SS (316L)

The material removal in ECMM is attained through controlled anodic dissolution of the workpiece. In ECMM, the workpiece is connected to an anode and the tool is connected to the cathode. In the metallic workpiece (M) oxidation occurs at the anode, which releases the electrons. This reaction is known as anodic reaction.

$$\text{M} \rightarrow \text{M}^{\text{n}+} + \text{ne}^- \quad \text{(Anodic dissolution)} \tag{8.3}$$

Table 8.2 Chemical composition of SS (316L)

Grade	Level (%)	C	Mn	Si	P	S	Cr	Mo	Ni	N
316L	Min	–	–	–	–	–	16.0	2.00	10.0	–
	Max	0.03	2.0	0.75	0.045	0.03	18.0	3.00	14.0	0.10

Table 8.3 Properties of oxalic acid

S. no.	Property	Value
1	Appearance	White crystals
2	Odour	Odourless
3	Density	1.90 g/cm^3 (anhydrous); 1.653 (de-hydrous)
4	Melting point	189–191
5	Solubility in water	143 g/l (25°C)

where n denotes the number of electrons released during reaction.

$$C_2H_2O_4 \rightarrow C_2O_4^{2-} + 2H^+$$
$$M^{n+} + C_2O_4^{2-} \rightarrow [M(C_2O_4)] \quad (8.4)$$

$$2H^+ + ne^+ \rightarrow H_2 \quad \text{(Hydrogen evolution)} \quad (8.5)$$

At the cathode, the oxalic acid from the electrolyte dissociates into oxalate ions and thereby hydrogen evolution takes place. These oxalate ions react with the metallic ions produced during anodic reaction and precipitate as sludge. The continuous flushing of electrolyte removes the precipitate from the machining zone and gets filtered by the filter tank for efficient ECMM process.

8.4 Results and Discussion

8.4.1 Influence of Voltage on Material Removal Rate and Overcut

Figure 8.2 shows the mapping of voltage, overcut and MRR. ECMM works based on Faraday's laws of electrolysis in which the material removal rate is directly proportional to its voltage. The increase in voltage level shows the increasing trend for MRR and overcut. The increase in voltage improves the current density required for material removal rate resulting in higher MRR. At machining voltage 7 V along with 80 g/l of electrolytic concentration, the MRR is found to be 0.508 μm/s and increases to highest value of 0.678 μm/s at 11 V with 80 g/l of electrolyte concentration, which is comparatively less when compared to acidified sodium nitrate and sodium nitrate solution [6]. The use of oxalic acid as an electrolyte contributes to lower MRR, and it is evident from Fig. 8.2 that no drastic change in the trend of MRR curve is witnessed. It is due to the fact that oxalic acid takes longer time to create micro-pore structure on the work surface. These regular micro-pores join together to create large pits and further extend as a micro-hole [12]. This mechanism of micro-hole formation also

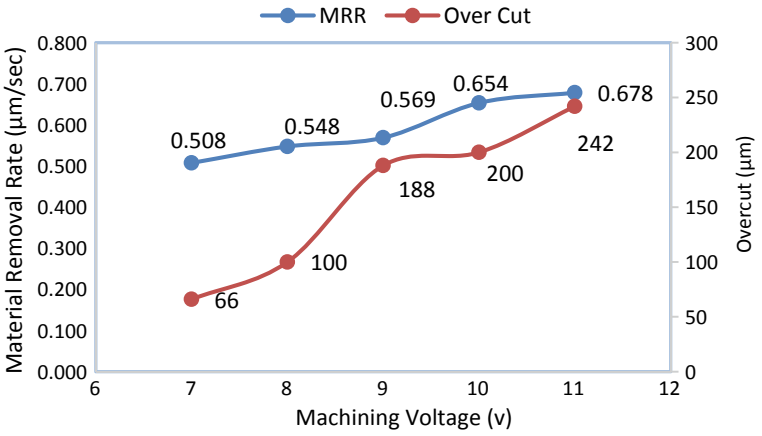

Fig. 8.2 Influence of voltage on material removal rate and overcut

aids for smaller overcut. The use of oxalic acid produces less sludges and it improves the accuracy of the micro-hole.

8.4.2 *Influence of Duty Cycle on Material Removal Rate and Overcut*

The duty cycle increases as the MRR also increases and overcut, as shown in Fig. 8.3. For the fixed frequency, the increase in duty cycle increases the current density required for the machining. This increase in pulse on time provides sufficient current for machining. Higher percentage of duty cycle contributes to the availability of longer duration of machining current on the workpiece, resulting in increasing MRR.

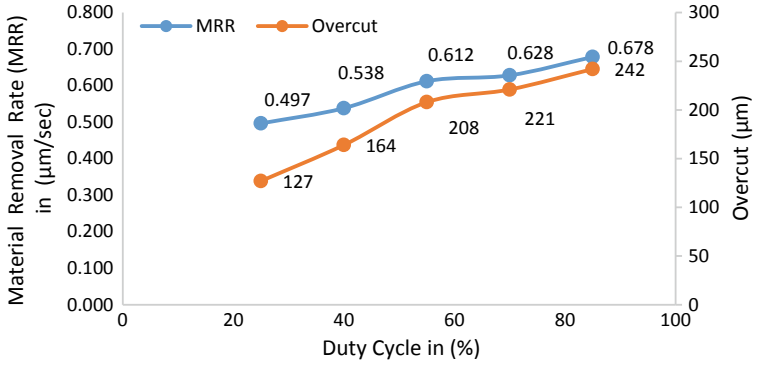

Fig. 8.3 Influence of duty cycle on material removal rate and overcut

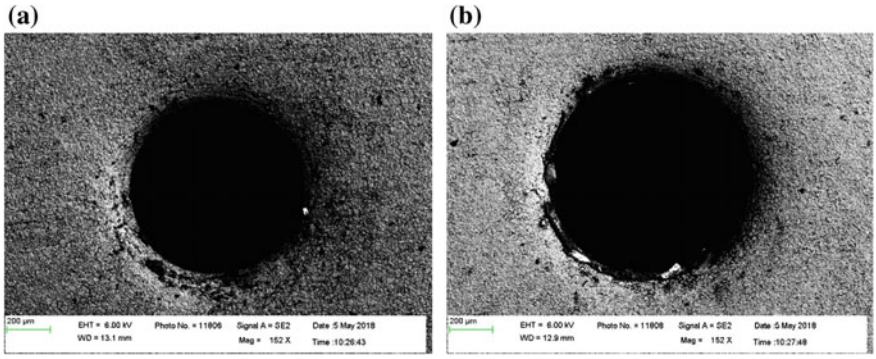

Fig. 8.4 (**a** and **b**) SEM images of the machined hole

The use of weak electrolyte along with the required current density contributes to accurate micro-hole. A gradual increase in graph for overcut is observed due to the lesser sludge generation which is removed continuously by flushing process. The proper evacuation of debris avoids micro-sparks and over-etched surfaces, as seen in Fig. 8.4a, b.

The SEM analysis of the machined surface SS (316L) is shown in Fig. 8.4a, b, in which we can observe the clear image of the machined hole of SS (316L) material having lesser overcut. Figure 8.4a illustrates the overcut under the following parametric conditions: voltage of 11 V, duty cycle of 85% and 80 g/l of oxalic concentration. Figure 8.4b illustrates the overcut under the following parametric conditions: voltage of 11 V, duty cycle of 85% and 40 g/l of oxalic concentration.

8.4.3 Influence of Electrolyte Concentration on Material Removal Rate and Overcut

When the concentration of the electrolyte increases, the number of ions associated in the machining process increases, and thus results in higher machining rate. Figure 8.5 clearly shows that as the concentration of the electrolyte increases material removal rate also increases. On comparing with other concentrated electrolytes, the overcut is less for oxalic acid [6]. At lower electrolyte concentration of 40 g/l, the material removal rate and overcut are found to less. Pores of the machined surface were found to be uniform and regular when compared to other electrolytes [12], which indicates that constant machining takes place without any striking of sludges. This less-concentrated electrolyte has been useful to enhance the surface texture characteristics, by restricting the current passage through increased electrolyte resistance. The SEM shown in Fig. 8.6 shows a circular hole with less density of micro-pores. It is obvious from the figure that the MRR and overcut are found to be increasing

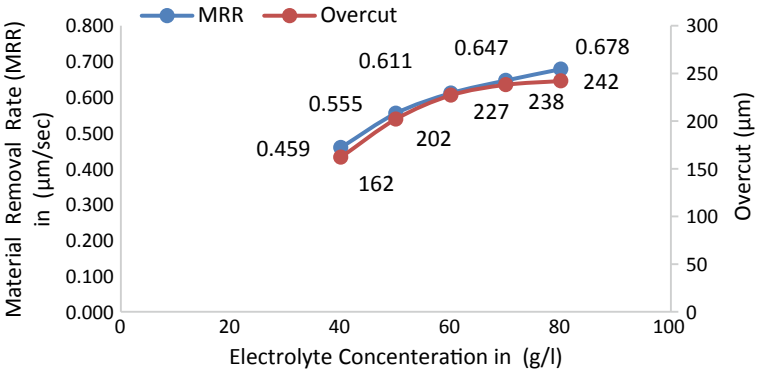

Fig. 8.5 Influence of electrolyte concentration on material removal rate and overcut

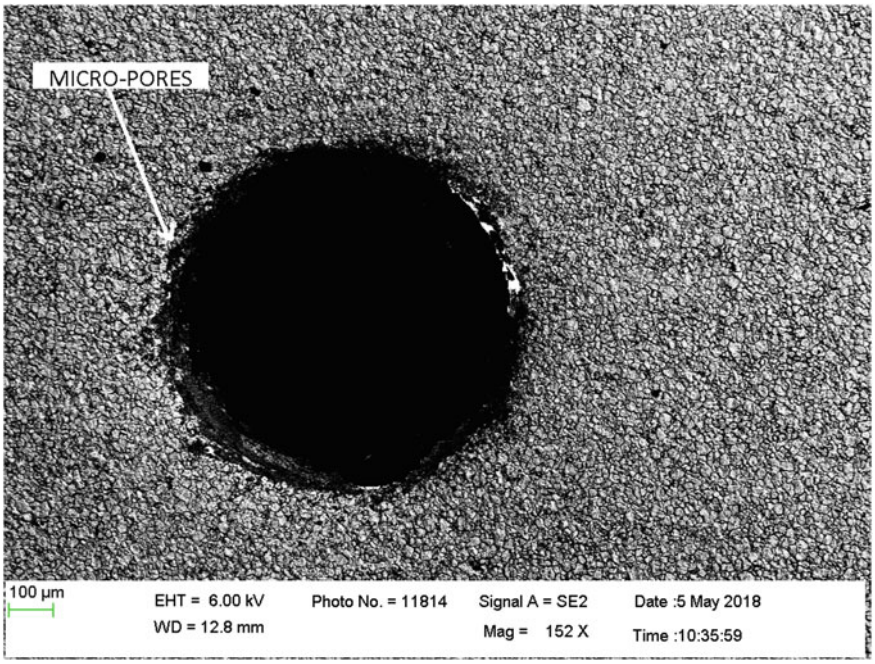

Fig. 8.6 SEM analysis with minimum voltage of 7 V, duty cycle of 85% and electrolytic concentration of 80 g/l

with concentration, and both the curves stabilize after the electrolyte concentration of 60 g/l.

8.5 Conclusions

On the basis of preliminary experiments conducted with oxalic acid electrolyte, the following conclusions are made:

1. It is possible to machine SS (316L) material using oxalic acid as an electrolyte solution.
2. The use of oxalic acid as an electrolyte contributes to low MRR and smaller overcut.
3. Micro-pores of the machined surface was found to be uniform and regular when compared to other electrolytes, which indicates constant machining is taking place without any striking of sludges.
4. An electrolyte which is strong in the base could corrode the machinery over time. This paper recommends the use of oxalic acid as an electrolyte solution for ECMM of SS (316L), which is a less concentrated electrolyte and has been recommended to enhance the surface texture characteristics, by restricting the current passage through increased electrolyte resistance.

References

1. Ryu, S.H.: Micro fabrication by electrochemical process in citric acid electrolyte. J. Mater. Process. Technol. **209**(6), 2831–2837 (2009)
2. Yang, Ye, Natsu, Wataru: WanshengZhao,: Realization of eco-friendly electrochemical micro-machining using mineral water as an electrolyte. Precis Eng. **35**(2), 204–213 (2011)
3. Tang, L., Li, B., Yang, S., Duan, Q., Kang, B.: The effect of electrolyte current density on the electrochemical machining S-03 material. Int. J. Adv. Manuf. Tech. **71**(9–12), 1825–1833 (2014)
4. Ryu, S.H.: Eco-friendly ECM in citric acid electrolyte with microwire and micro foil electrodes. Int. J. Precis. Eng. Man **16**(2), 233–239 (2015)
5. Ayyapan, S., Sivakumar, K.: Experimental investigation on the performance improvement of electrochemical machining process using oxygen-enriched electrolyte. Int. J. Adv. Manuf. Tech. **75**(1–4), 479–487 (2014)
6. Thanigaivelan, R., Arunachalam, R.M., Karthikeyan, B., Loganathan, P.: Electrochemical micromachining of stainless steel with acidified sodium nitrate electrolyte. Procedia CIRP **6**, 351–355 (2013)
7. Thanigaivelan, R., Arunachalam, R.M., Kumar, M., Dheeraj, B.P.: Performance of electro-chemical micromachining of copper through infrared heated electrolyte. Mater. Manuf. Process **33**(4) (2018)
8. Kunar, S., Mahata, S., Bhattacharyya, B.: Influence of electrolytes on surface texture characteristics generated by electrochemical micromachining. J. MicroManuf. 1–10 (2018)

9. Kalaimathi, M., Venkatachalam, G., Sivakumar, M., Ayyappan, S.: Experimental investigation on the suitability of ozonated electrolyte in travelling wire electrochemical machining. J. Braz. Soc. Mech. Sci. Eng. **39**(11), 4589–4599 (2017)
10. Tang, L. and Guo, Y.F.: Experimental study of special purpose stainless steel on electrochemical machining of electrolyte composition. Mater. Manuf. Process **28**(4) (2013)
11. Anasane, S.S., Bhattacharyya, B.: Experimental investigation on suitability of electrolytes for electrochemical micromachining of titanium. Int. J. Adv. Manuf. Tech. **86**(5–8), 2147–2160 (2016)
12. Keshavarz, A., Parang, Z.: The effect of sulfuric acid, oxalic acid, and their combination on the size and regularity of the porous alumina by anodization. J. Nanostruct. Chem. 2193-8865-3-34 (2013)

Chapter 9
Inkjet Printing-Based Micro-manufacturing of the Thin Film Electrodes for Flexible Supercapacitor Applications

Poonam Sundriyal, Pankaj Singh Chauhan and Shantanu Bhattacharya

Abstract Inkjet printing is one of the most promising micro-manufacturing techniques to develop thin film and flexible electronics. The selective area deposition and efficient integration of all components of an electronic device on a flexible substrate are major challenges for the existing flexible electronics field. Also, the wide spread of the portable electronics, with features such as compactness, lightweight, low cost, environment friendliness, and high-performance electronic devices, raises the demand for the more research attention in using smart manufacturing techniques to achieve the required performance of the flexible devices. Here, we have reported a micro-supercapacitor device on a filter paper substrate with ~8 μm thick electrode layer. The reduced graphene oxide (rGO) and rGO–MnO_2 nanocomposite materials were converted to water-based printable inks using ethylene glycol and ethanol. The rGO ink was used to make the conducting patterns, while rGO–MnO_2 nanocomposite ink is used to fabricate interdigital electrodes for the supercapacitor device. The developed device shows excellent electrochemical performance with the poly(vinyl alcohol) (PVA) 4 M KOH gel electrolyte within a voltage range of 1 V. The device shows ideal supercapacitor behavior with a highest areal capacitance of 390 mF/cm^2 at one mA/cm^2 current density. The developed device also exhibits excellent cycle stability with 96% capacitance retention up to 1000 cycles. Also, the excellent performance of the device in various flexibility conditions facilitates its huge potential for high-performance flexible electronics applications.

Keywords Micro-manufacturing · Inkjet printing · Flexible electronics · Supercapacitors

P. Sundriyal · P. S. Chauhan · S. Bhattacharya (✉)
Department of Mechanical Engineering, Microsystems Fabrication Laboratory, Design Programme, Indian Institute of Technology, Kanpur 208 016, India
e-mail: bhattacs@iitk.ac.in

M. S. Shunmugam and M. Kanthababu (eds.), *Advances in Micro and Nano Manufacturing and Surface Engineering*, Lecture Notes on Multidisciplinary Industrial Engineering,
https://doi.org/10.1007/978-981-32-9425-7_9

9.1 Introduction

Micro-manufacturing techniques evolved with the growth of micro-electromechanical systems (MEMS) [1]. MEMS systems were used to integrate sensors and actuators with electronic circuits. Usage of MEMS-based devices was successful due to small, low cost, and efficient fabrication methods. Till date, most of the MEMS fabrications are based on the photolithography technique on silicon-based semiconductors. However, the inherent limitations of the lithography technique, such as the requirement of a patterned mask, waste generation, environmental pollution, and expensive processing, make it unsuitable for the low-cost electronics. On the contrary, the brittle nature of the silicon substrates is unfavorable for the flexible devices [2]. In recent times, the demand for the flexible/portable electronics needs a more industrial and scientific attention to explore different manufacturing techniques for the electronics manufacturing. Therefore, exploration of the smart manufacturing techniques is required to fabricate the highly flexible devices.

Inkjet printing is one of the best alternative methods for the micro-manufacturing of smart and flexible electronic devices [3, 4]. It is a direct deposition tool, hence only the desired quantity of material is printed at the required location. Also, the low wastage of material eliminates environmental hazards. The requirement of cost and time for mask fabrication in the photolithography process is eliminated by the fundamentally digital, data-driven process of inkjet printing. Inkjet printing is quite useful in flexible electronics, which is an emerging industry for making flexible devices. Inkjet printing can be easily done on any thin film and flexible substrate. However, the major challenge of this method is the need for the printing inks which have the rheological properties within a fixed range. The Fromm number (related to the viscosity, density, and surface tension of the inks) should be between 4 and 14 for a printable ink [5]. Besides the high-cost special purpose industrial printers, some inexpensive inkjet printers have also been reported for the low-cost electronics [6]. Out of the various components of the electronic devices, energy storage unit is one of the essential parts of the device. It should be highly flexible to be integrated into a flexible device. The solid-state supercapacitors are gaining much attention as energy storage devices due to their attractive features, such as high energy density, high power density, high electrochemical stability, and the long cycle life [3]. The proper integration of the supercapacitor components (including a conducting layer, an electrode layer, and the electrolyte) on the flexible substrates is still a major challenge. The commercially available carbon-based inks and some metal oxides are reported for the printed supercapacitors. Additionally, for the environmental sustainability and the low cost, the waste recycled carbon and plant extracts [7, 8] can be used in the printed electronics application.

In this work, we have described a planar micro-supercapacitor device on a filter paper substrate. The water-based rGO ink was used to make the conducting layer and the rGO–MnO_2 nanocomposite ink to construct the interdigital electrodes for the

planar supercapacitor device. The developed device shows excellent electrochemical performance with the highest areal capacitance of 390 mF/cm^2 at 1 mA/cm^2 current density. The micro-supercapacitor device also displays excellent cycle stability with 96% capacitance retention up to 1000 cycles. Most of the previous reports are based on the sandwich structures. These make the energy storage devices bulky and complex. This research reports the use of a planar micro-supercapacitor device which reduces the weight and complexity of the system. Other than that, the use of a water-based ink makes the process more environment-friendly. This study shows that the inkjet printing technique could highly benefit the printed and flexible electronics area.

9.2 Experimental

9.2.1 Preparation of the Conducting Layer and Electrode Layer Inks

The conducting ink was prepared by the oxidation of graphite and its further exfoliation with the water–ethylene glycol–ethanol (8:1.5:0.5) mixture solution. The rGO was synthesized using modified Hummer's method [9]. The printed patterns are dried at 85 °C for 8 h in a vacuum oven to get the conducting patterns. The rGO–MnO_2 nanocomposite was prepared by a hydrothermal method. Typically, a mixture of 0.4 g $KMnO_4$ and 100 mL of rGO ink was transferred to the Teflon-lined autoclave and maintained at 150 °C for 4 h. The obtained nanocomposite was mixed in the water–ethylene glycol–ethanol (8:1.5:0.5) mixture solution to prepare the electrode ink.

9.2.2 Fabrication of the Device

The planar and symmetric micro-supercapacitor device was fabricated by using the inkjet printing method. Typically, the interdigital electrode patterns were printed on the filter paper substrate to make the conducting patterns. These conducting patterns were reprinted with the electrode layers by using the electrode inks. The PVA 4M KOH gel electrolyte was further coated on the printed electrodes to make the full device.

9.2.3 Characterization

The crystal structures of the prepared materials are characterized by X-ray diffraction (XRD, X'Pert Pro, PAN Analytical, The Netherlands). The microstructure and surface morphology are examined by field-emission scanning electron microscopy (FESEM, ZEISS Supra 40VP) and transmission electron microscopy (TEM, FEI Technai G2, USA). The surface tensions are measured by contact angle goniometry (Kruss), and viscosities of the inks are examined by Rheometer (Anton Paar). The electrochemical analysis of the printed device was investigated by cyclic voltammetry (CV), and galvanostatic charge/discharge (GCD) tests were performed using potentiostat/galvanostat (Autolab 302 N, Metrohm, The Netherlands).

9.3 Calculations

As discussed earlier, the quality of printing depends upon the rheological properties of ink, such as surface tension, viscosity, and density. These properties are evaluated by some dimensionless numbers which are as follows:

Reynolds number (Re) is the ratio of inertia force and viscous force.

$$\mathbf{Re} = \frac{\mathbf{Inertia\ force}}{\mathbf{Viscous\ force}} = \frac{\boldsymbol{\rho l V}}{\boldsymbol{\eta}} \tag{9.1}$$

Weber number (We) is the ratio of inertia force and surface tension force.

$$\mathbf{We} = \frac{\mathbf{Inertia\ force}}{\mathbf{Surface\ tension}} = \frac{\mathbf{v^2 a \rho}}{\boldsymbol{\sigma}} \tag{9.2}$$

Fromm number (Z) is the ratio of Reynolds number and the square root of the Weber number.

$$\mathbf{Z} = \frac{\mathbf{Reynolds\ number}}{\sqrt{\mathbf{Weber\ number}}} = \frac{\sqrt{\mathbf{l \rho \sigma}}}{\boldsymbol{\eta}} \tag{9.3}$$

where ρ, l, V, η, and σ are density, characteristic length (nozzle diameter), velocity, dynamic viscosity, and surface tension of the printing fluid, respectively.

The areal capacitance (C) is calculated from the GCD curves using the following equation:

$$\mathbf{C} = \frac{\mathbf{I_c \Delta t}}{\mathbf{A \Delta V}} \tag{9.4}$$

Here, I_c is the constant current, $\mathbf{\Delta t}$ is the total discharge time, A is the total surface area of the device and $\mathbf{\Delta V}$ is the operational voltage range.

9.4 Results and Discussion

9.4.1 Material Characterization

The crystallographic structures of the prepared materials were characterized by XRD. The XRD patterns of the rGO and rGO–MnO_2 nanocomposite are displayed in Fig. 9.1a. All the peaks of the rGO–MnO_2 nanocomposite corresponding to the (001), (002), (−111), (020), and (−220) are related to the birnessite-type MnO_2 structure. For the rGO sample, the peaks at 22.6° and 42° confirm the formation of graphene oxide. The surface morphology and the microstructure of the prepared materials were examined by SEM and TEM. Figure 9.1b, c shows the SEM images of the rGO and GO–MnO_2, respectively. These images clearly show the formation of rGO sheets and the presence of MnO_2 on the rGO layers. Also, the TEM image of the GO–MnO_2 nanocomposite as shown in Fig. 9.1d further confirms the formation of MnO_2 structures on the rGO sheets.

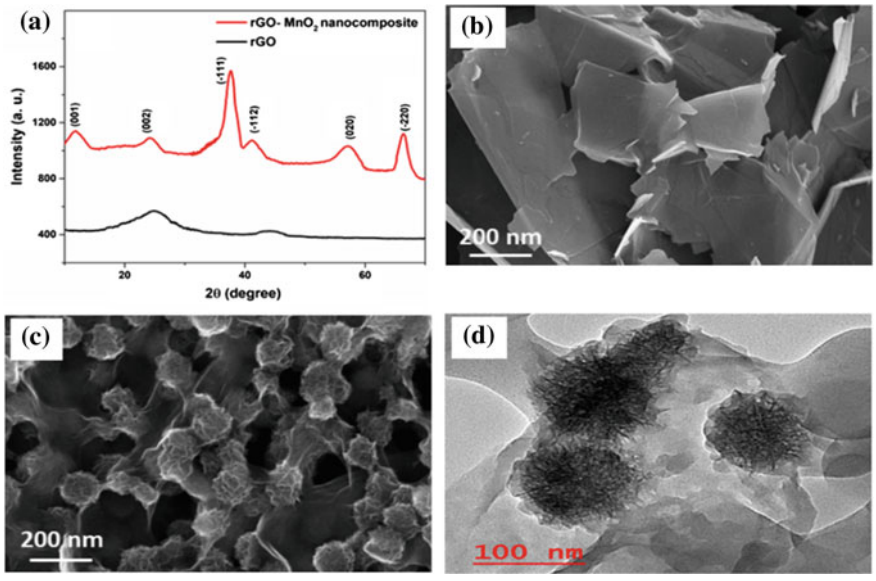

Fig. 9.1 **a** XRD patterns of rGO, rGO–MnO_2 nanocomposite, **b** SEM image of the rGO, **c** SEM image of the rGO–MnO_2 nanocomposite, and **d** TEM image of the rGO–MnO_2 nanocomposite

Table 9.1 Physical properties of the inks

S. No.	Ink composition	Density (kg/m^3)	Surface tension (mN/m)	Viscosity (mPa-s)	Fromm number (Z)
1.	GO (in water + EG + ethanol)	1085	52	5.6	6
2.	GO–MnO_2 (in water + EG + ethanol)	1150	56	5.8	6.12

9.4.2 Micro-Manufacturing of the Thin Film Electrodes

The electrodes for the supercapacitors were fabricated using an inkjet printing technique. The prepared rGO and rGO–MnO_2 nanocomposites were converted to water-based inks and used as a conducting layer and electrode layers, respectively. A filter paper was used as a printing substrate and a desktop printer EPSON L130 was used for printing. The printing quality of the drop-on-demand printers depends on the physical properties of the injected inks. The inks should have a specific range of the surface tension, viscosity, and the solution density which are jointly governed by the Fromm number. We have prepared rGO and rGO–MnO_2 nanocomposite inks in a water–ethylene glycol–ethanol mixture (8:1.5:1). The rheological properties of these inks and the calculated Fromm number from Eq. 9.3 are displayed in Table 9.1 (at a fixed nozzle diameter of ~20 μm). The Fromm numbers for both the inks are within the required range of the inkjet printing; therefore these inks are directly used for inkjet printing. Also, these inks are filtered with a 450 nm syringe filter to remove the large size particles to prevent the nozzle from clogging.

The interdigital electrode patterns were first printed on the filter paper using rGO ink. The width of the printed electrode patterns is 150 μm (as shown in Fig. 9.2a) and the thickness of the electrode layer was ~8 μm (as shown in Fig. 9.2b). The sheet resistance drastically reduced with increase in the number of printing layers. The 50 layers of the ink converted the patterns to a highly conducting matrix. The electrode's ink was further printed over the rGO pattern to fabricate the anode and the cathode for the symmetric supercapacitor. The PVA 4M KOH gel electrolyte was coated over the printed electrodes to complete a solid-state and flexible GO–MnO_2//GO–MnO_2 symmetric micro-supercapacitor device.

9.4.3 Electrochemical Analysis

The prepared solid-state micro-supercapacitor device was tested in a two-electrode configuration. The CV and GCD analyses were conducted to check its electrochemical performance. Figure 9.3a shows the CV curves of the GO–MnO_2//GO–MnO_2

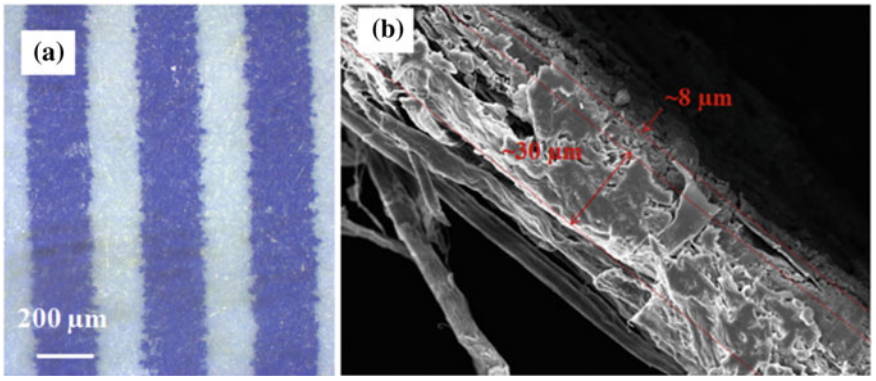

Fig. 9.2 **a** Optical micrograph of the printed electrode patterns on the filter paper, and **b** cross-sectional SEM image of the printed electrodes showing conducting and electrode layers thickness

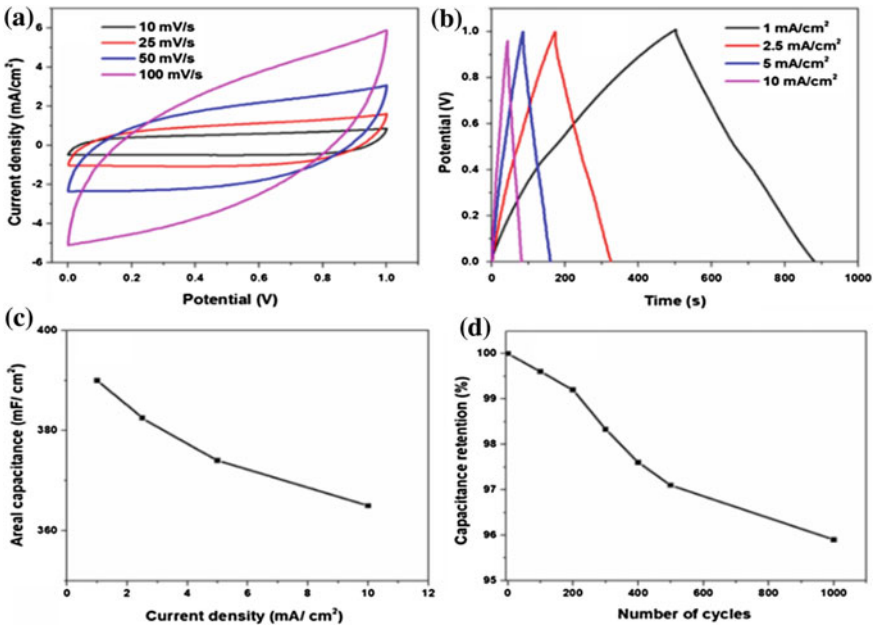

Fig. 9.3 **a** CV curves of the device at different scan rates, **b** GCD curves of the device at various current densities, **c** change in the areal capacitance of the device at various current densities, and **d** capacity retention with charge–discharge cycles

symmetric micro-supercapacitor device at different scan rates. The rectangular shape of the curves exhibits the ideal supercapacitor performance of the device.

The GCD curves, as shown in Fig. 9.3b, are triangular shaped with negligible resistive drops, which again indicates good electrochemical performance of the device. According to Eq. 9.4, the device displays the maximum areal capacitance of 390 mF/cm^2 at 1 mA/cm^2 current density within a voltage window of 1 V (as shown in Fig. 9.3c). Additionally, the device shows a rate capability of 93.58% when the current density increased from 1 to 10 mA/cm^2. The cyclic stability is an essential requirement of an energy storage system. The developed device was examined for the cyclic stability by performing the GCD measurements up to 1000 charge–discharge cycles. Figure 9.3d shows capacitance retention versus cycle numbers at 10 mA/cm^2 current density. The micro-supercapacitor device displays excellent stability with 96% capacity retention after 1000 cycles. The outstanding cycle stability of the device validates its feasibility for practical applications.

Also, the mechanical flexibility of the micro-supercapacitor device was further tested to evaluate its feasibility for flexible electronics. Therefore, the electrochemical performance of the developed device was investigated at a scan rate of 50 mA/cm^2 under different mechanical deformation conditions, such as folding, rolling, bending, and cutting (as shown in Fig. 9.4). All the CV curves were almost similar in shape with negligible deviation from the flat position. The device shows capacitance retentions as 98.6, 98.9, and 99.2% under folding, rolling, and cutting conditions, respectively. These remarkably high capacitance retention values show the excellent performance of the device in the flexible conditions. The device also shows energy storage capability in the cutting condition which indicates its energy storage capability even when the device suffers from any accidental tearing during its service life.

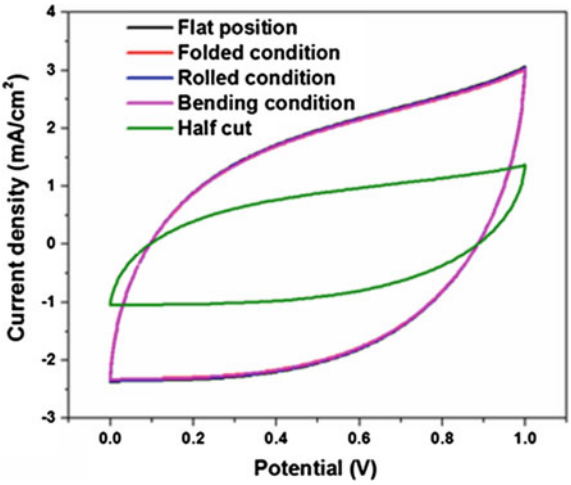

Fig. 9.4 Variation in the CV profiles of the micro-supercapacitor device in various test conditions: **a** Flat position, **b** folded condition, **c** rolled condition, **d** bending condition, and **d** cutting condition

9.5 Conclusions

In summary, inkjet printing is an effective tool for the micro-fabrication of thin film devices. The developed conducting patterns using the rGO inks were highly conducting, and the fabricated asymmetric micro-supercapacitor device also shows excellent performance even at the flexed conditions. Therefore, the combination of the micro-manufacturing techniques with the thin film electronics devices could effectively improve the performance of flexible electronics.

Acknowledgments The authors would like to thank the Nanoscience unit of DST, IIT Kanpur for material characterizations, and PG Research Lab, Chemical Engineering Department, IIT Kanpur for the electrochemical analysis of the supercapacitor device. The authors would also like to thank DST for providing the research grant (DST/TMD/MES/2K17/05).

References

1. Tseng, A.A., et al.: NSF 2000 workshop on manufacturing of micro-electro-mechanical systems. J. Mater. Process. Manuf. Sci. **8**, 292–360 (2000)
2. Smith, P.J., Shin, D.H.: Inkjet-Based Micromanufacturing. Wiley (2012)
3. Liu, W., et al.: Flexible and stretchable energy storage: recent advances and future perspectives. Adv. Mater. **29**(1) (2017)
4. Sundriyal, P., Bhattacharya, S.: Inkjet-Printed Sensors on Flexible Substrates, in Environmental, Chemical and Medical Sensors. 2018, Springer. p. 89–113
5. Jang, D., Kim, D., Moon, J.: Influence of fluid physical properties on ink-jet printability. Langmuir **25**(5), 2629–2635 (2009)
6. Sundriyal, P., Bhattacharya, S.: Inkjet-printed electrodes on A4 paper substrates for low-cost, disposable, and flexible asymmetric supercapacitors. ACS Appl. Mater. Interfaces **9**(44), 38507–38521 (2017)
7. Sundriyal, P., Bhattacharya, S.: Polyaniline silver nanoparticle coffee waste extracted porous graphene oxide nanocomposite structures as novel electrode material for rechargeable batteries. Mater. Res. Express **4**(3), 035501 (2017)
8. Patel, V., Sundriyal, P., Bhattacharya, S.: Aloe vera versus poly (ethylene) glycol-based synthesis and relative catalytic activity investigations of ZnO nanorods in thermal decomposition of potassium perchlorate. Part. Sci. Technol. **35**(3), 361–368 (2017)
9. Marcano, D.C., et al.: Improved synthesis of graphene oxide. ACS Nano **4**(8), 4806–4814 (2010)

Chapter 10
Multiresponse Optimization of Electrochemical Micro-machining Process Parameters of Micro-dimple Using TOPSIS Approach

B. Mouliprasanth, N. Lakshmanan and P. Hariharan

Abstract Electrochemical micro-machining (ECMM) is generally used to effectively machine hard materials in mass production that are challenging to machine using the traditional approach. This process can pierce intricate contours, small or odd-shaped angles, or hollow craters in metals. The machining is restricted to electrically conductive materials. In this paper, techniques for producing micro-dimple are discussed. Producing a micro-hole is simple while a pit formation or micro-dimple formation needs a lot of study with respect to machining parameters. Optimization techniques are carried out so that form errors in creating micro-dimples are eradicated. Several researchers have studied the process and tried to improve various process parameters and factors affecting it. The paper focuses on producing a micro-dimple of 0.5 mm by varying the input parameters, namely voltage, feed rate, and duty ratio to get exceptional output response in MRR and S_a. The methods for handling ECMM and its parameters optimization using TOPSIS are shown in this paper.

Keywords SS304 · Micro-dimple · TOPSIS · Inter-electrode gap (IEG) · Material removal rate (MRR) · Surface roughness (S_a)

10.1 Introduction

In the existing advanced manufacturing platform, electrochemical micro-machining (ECMM) belonging to the electrochemical category is based upon Faraday's laws of electrolysis, which by theory states that the quantity of a material removed is proportional to the amount of electrical charges transferred to that of the electrode. Electrochemical micro-machining is a material removal or etching process through localized corrosion. The workpiece and tool are retained with a certain micron-level gap (IEG). Material is removed by corrosion action from the workpiece so

B. Mouliprasanth (✉) · N. Lakshmanan · P. Hariharan
Department of Manufacturing Engineering, College of Engineering Guindy, Anna University, Chennai 600 025, India
e-mail: bmouliprasanth@gmail.com

M. S. Shunmugam and M. Kanthababu (eds.), *Advances in Micro and Nano Manufacturing and Surface Engineering*, Lecture Notes on Multidisciplinary Industrial Engineering,
https://doi.org/10.1007/978-981-32-9425-7_10

that in the anode, oxidation reactions take place by virtue of the workpiece to be etched is connected to the anode and the corresponding micro-tool is connected to the cathode; as a result, it forms an electrolytic cell together with water-based salt solutions. Inclusively, it is a concept of a controlled anodic dissolution at atomic level with the flow of current passed through electrolyte by a negative-shaped tool at a comparatively low potential difference. ECMM is different from electroplating or deposition process as the polarity and basic concept changes. Minghuan Wang et al. discussed that the applied voltage is the major factor that influences the diameters of the dimples, while the depth is affected by the feeding speed [1]. S. Mahata et al. developed micro-dimple arrays that play a significant role in performance and reliability enhancement of mechanical systems and also stated that the presence of micro-dimples on the workpiece surfaces has created a positive impact on the friction control and wear resistance of sliding surfaces [2].

Zhibao Hou et al. used polydimethylsiloxane mask to fabricate micro-dimples of depth 19 μm, width 95 μm with the diameter 40 mm, and obtained large-area micro-dimple arrays with high machining accuracy by feasible standard deviations of the micro-dimple width and depth of about 0.84 and 0.23 μm [3]. G. Q. Wang et al. used the appropriate mask (through-mask EMM technique) and simulated micro-dimples in a series of experiments in which the aspect ratio is found for fabricating semicircular micro-grooves [4]. Qu Ningsong et al. generated micro-dimples for a fixed dimple depth, and showed with passivating sodium nitrate electrolyte combined with lower current density and higher machining time, smaller dimple diameter can be obtained [5]. Sebastian Skoczypiec discussed the special attention paid toward the results of the application of voltage pulses and integration with other technologies that micro-features are created by ECMM, ECDM, hybrid micro-machining, and laser micro-machining [6]. Divyansh Singh Patel et al. created micro-pillars, micro-channels, micro-dimples and electrochemical texturing in stainless steel and briefly compared laser surface texturing (LSTex) and electrochemical surface texturing (ECSTex) [7]. Ningsong Qu et al. used PDMS technique and conducted experiments to validate the feasibility of producing micro-dimples, so that an array of micro-dimples with 109 μm in diameter and 9.7 μm deep are fabricated and its effect of applied voltage and machining time on the diameter and depth of the micro-dimple is studied [8].

Low potential difference is retained in IEG, so the present ions in the electrolytes travel toward the contradictory electrodes. With the potential difference, the positive ions diverge themselves to their opposite electrode cathode and similarly, negatively ions diverge themselves to their opposite electrode anode; by virtue ions migrate, thus flow of current is triggered with respect to the electrolyte. The anticipated quantity of metal is removed because of ion migration, which indirectly leads the workpiece in localized corrosion while keeping the tool safe from damage as hydrogen bubbles evolve due to electrochemical reactions in the intentional micro-gap present between the electrodes. A constant supply of electrolyte is established by pushing it at high pressure with an external setup in the interest to remove adulterated electrolyte with the metal oxides. The tool electrode approaches the workpiece for the machining in the presence of electrolytic medium, so the temperature generated is very low, and

no heat-affected zone is formed; therefore no possibility of metallurgical changes in the workpiece.

If the IEG is small, the tool feed will result in local contact between the anode and the cathode that leads to short circuit, or if the IEG is large, it will result in improper machining. In both the cases, the machine attains unanticipated stoppage of the machining process. Sadagopan et al. carried out experiments and analyzed using ANOVA for an L9 orthogonal array in EDM [9]. Machining zone consists of suspended precipitates and oxides due to the removal of ions. In spite of the removal of ions in the machining zone, electrolyte reaches its lower pH, which ultimately leads to the accumulation of debris. In order to completely eradicate the short-circuit problem, an electrolyte pumping system fitted with filter is used to exchange the electrolyte as it diffuses the machined products apart. Yuvaraj et al. carried their experiments in AWJM using the technique for order preference by similarity ideal solution (TOPSIS) approach for finding the optimal parameter settings [10]. The IEG plays a vital role in machining of SS304 in case of both MRR and S_a. The IEG potential is the reason to produce the micro-dimple.

10.2 Experimental System and Experimental Methods

10.2.1 Experimental Setup

The workpiece stainless steel 304 alloy is cut according to the dimensions of the fixture. Then the tool was inserted into the tool holder using appropriate means. The composite electrolyte mixture was poured into the electrolytic tank. Then, the workpiece along with the fixture is lowered into the electrolyte bath with the workpiece polarity as anode and copper tool polarity as cathode. The experiments are carried out by varying the supply voltage, duty ratio, and feed rate and with some of the fixed machine input parameters using a pulsed power supply. The setup of the machine is shown in Fig. 10.1. The setup is kept stationary and the tool is fed linearly. The electrolyte flushing is ensured between the electrodes.

10.2.2 Process Parameters

The various process parameters in electrochemical micro-machining are electrolyte concentration, voltage, feed rate, duty ratio, inter-electrode gap, and electrolyte flow rate, which influence the main machining conditions, such as metal removal rate, surface finish, profile accuracy, and so on. The selection of proper process parameters for electrochemical micro-machining process is crucial to have the efficient and exceptional output response. Predetermining optimal machining parameters for better machining and improving the output quality is a complex process because of

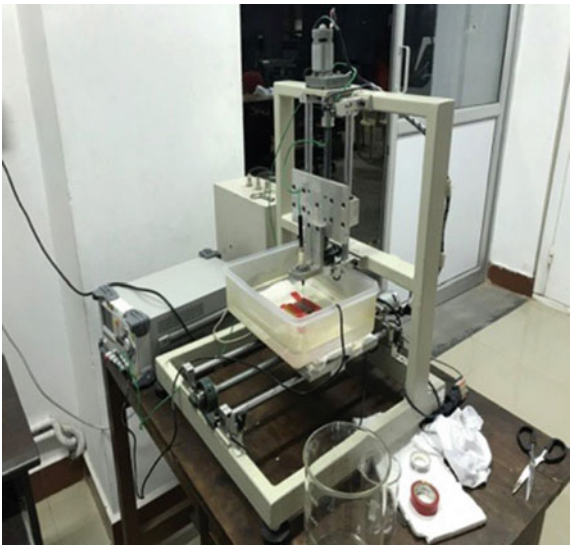

Fig. 10.1 Developed ECMM machine setup

Table 10. 1 Levels considered for design of experiments

S. no	Factors		Levels		
		Unit	1	2	3
1	Voltage	V	16	17	18
2	Duty ratio	%	60	70	80
3	Feed rate	mm/min	0.5	0.6	0.7

the intricacy of the electrochemical micro-machine and its process. Multiobjective optimization of voltage, feed rate, duty ratio and IEG was done for improving MRR and S_a.

The input parameters are fixed to a constant value based on the machine conditions and the trial experiments are performed. Experiments are conducted based upon Taguchi's DOE, considering the levels shown in Table 10.1.

10.2.3 Selection of Electrolyte and Electrolyte Concentration

The selection of electrolytes primarily relies on micro-machining principle and material properties of chosen anode to achieve performance criteria, such as machining rate, accuracy, and surface integrity. The machining performance and desired quality can be achieved by the electrolyte as it is the reason that machining happens because it tends to close the electric circuit by the flow of ions. By providing the flow of electrolyte between the electrodes, anodic films are formed on workpiece

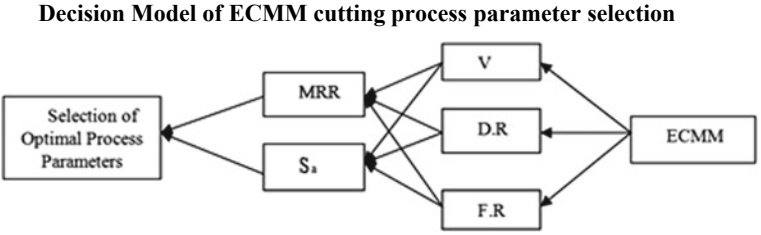

Fig. 10.2 Decision model

surface, which are the foremost barrier for the anodic dissolution. Intermittently, uncontrolled machining may take place due to change in electrolyte conductivity because of the improper flushing of sludge, increased pH and development of gas bubbles, which increases the possibilities of short circuit in-between the narrow IEG. The tool diameter is of 500 μm and the tool tip is well polished. The chosen electrolytic concentration for machining of SS304 alloy of 0.4 mm thickness is about 15 g/L. The electrolytic concentration is kept constant. The electrolyte chosen for machining is composite electrolyte of the combined mixture of polyethylene glycol and sodium nitrate. Under such conditions, a micro-dimple which is approximately reciprocal to that of the cathode tip will be replicated on the anode (Fig. 10.2).

10.2.4 Experimental Results

See Table 10.2.

Table 10.2 Experimental results for multiresponse L9 array

Expt. no.	Voltage (V)	Feed rate (mm/min)	Duty ratio	MRR (mg/min)	S_a(μm)
1	16	0.5	0.6	0.0163	0.382
2	16	0.6	0.7	0.0415	1.293
3	16	0.7	0.8	0.0862	3.07
4	17	0.5	0.7	0.0440	0.465
5	17	0.6	0.8	0.0512	0.754
6	17	0.7	0.6	0.0708	0.561
7	18	0.5	0.8	0.0432	1.735
8	18	0.6	0.6	0.0599	0.766
9	18	0.7	0.7	0.0748	0.612

10.3 Multiresponse Optimization

10.3.1 Optimization Steps Using TOPSIS Approach

The technique for order preference by similarity ideal solution method is selected among the optimization practices. In this paper, Simos' procedure is used to provide the subjective input weights of the considered output responses and equal weightage is provided for both output responses, along with that the computational steps of this technique are carried out. The weighting criteria are calculated as follows:

$$\textbf{Definite set of criteria} = [\textbf{MRR and } \mathbf{S_a}]$$

The design set of criteria is ranked from least to most important by the decision maker based on their importance from output responses MRR and S_a. The TOPSIS optimization is calculated by means of the successive stages.

Stage 1.
Normalized values are taken by eliminating the units of all criteria, and selecting the alternatives. Table 10.3 also represents the normalized performance matrix (r_{ij}) attained by the following formula:

$$r_{ij} = \frac{X_{ij}}{\sqrt{\sum_{i=1}^{m} X_{ij}^2}} \quad i = 1, 2, \ldots 9;\ j = 1, 2, 3$$

such that

i is the number of experimental alternatives,
j is the number of output responses,

Table 10.3 Design of experiment and normalized values of output response parameters

Expt. no.	A	B	C	Normalized matrix values (r_{ij})	
				MRR	S_a
1	16	0.5	0.6	0.09405655	0.0945779
2	16	0.6	0.7	0.23946913	0.3201287
3	16	0.7	0.8	0.49740335	0.7600891
4	17	0.5	0.7	0.25389498	0.1151275
5	17	0.6	0.8	0.29544143	0.1866799
6	17	0.7	0.6	0.4085401	0.1388958
7	18	0.5	0.8	0.24927871	0.4295618
8	18	0.6	0.6	0.34564339	0.1896509
9	18	0.7	0.7	0.43162147	0.1515227

Table 10.4 Computational steps of SIMOS weighting procedure

Subset criteria	Number of criteria	Number of position	Non-normalized weighted matrix	Total
MRR	1	1	½ * 100 = 50	50
S_a	1	1	½ * 100 = 50	50
Total	2	2		100

x_{ij} is the normalized value of *i*th experimental run associated with *j*th output response.

Stage 2.
The weighted normalized matrix (w_{ij}) is calculated in this stage as the product of the normalized value and the weighted values, which is given by the following equation:

$$\vartheta_{ij} = w_j * r_{ij} : i = 1, 2, \ldots 9;\ j = 1, 2, 3$$

For giving weightage to the response, parameters from least to most important by Simos' procedure are calculated and displayed in Table 10.4. Equal weightage is provided to both MRR and S_a.

Stage 3.
An ideal alternative to the best alternative performance (S^+) and the worst alternative performance (S^-) for every output response is identified.

If the *j*th criteria have a better performance.

$$S^+ = \left\{\left[\max\left(S_{ij}\right)|j \in J\right] or \left[\min\left(S_{ij}\right)\middle|j \in J'\right], i = 1, 2, \ldots 9\right\}$$

where

S^+ denotes a positive ideal solution
$S^+ = [0.332765]$.

Correspondingly, the S^- values were determined if the *j*th criteria are worst performances.

$S^- = [0.182543]$.

whereas S^- denotes a negative ideal solution.

Stage 4.
The significance of every criterion has been measured in this step: (D_{ij}^+) from S^+ values as the best distance, and (D^-) from S^- values as the worst alternative distance. The values of D_{ij}^+ and D_{ij}^- are calculated by means of below equation. Table 10.5 shows the performance of every alternative under the best and worst conditions.

$$D_i^+ = \sqrt{\sum_{i=1}^{9}\left(\vartheta_{ij} - S_j^+\right)^2}$$

Table 10.5 Closeness coefficient values and ranking of alternatives

Expt. no.	D_i^+	D_i^-	C_i	Rank
1	0.040671	0.110697	0.622608	6
2	0.029352	0.053659	0.574843	7
3	0.110732	0.040675	0.377366	9
4	0.014929	0.110354	0.731093	5
5	0.012318	0.092315	0.732444	4
6	0.002465	0.12117	0.875164	2
7	0.043448	0.033322	0.466882	8
8	0.008018	0.097151	0.776829	3
9	0.001893	0.121051	0.888851	1

$$D_i^- = \sqrt{\sum_{i=1}^{9}\left(\vartheta_{ij} - S_j^-\right)^2}$$

where i = 1, 2, 3, …, 9.

Stage 5.
The closeness coefficient (C_i) values are calculated in this step for every alternative, by means of following equation:

$$C_i = \frac{D_i^-}{D_i^- + D_i^+} \quad i = 1, 2, \ldots, 9; 0 \le C_i \le 1$$

The preference rank is arranged according to the best alternative by the C_i value, that is, very nearest to the ideal solution (Table 10.6).

To find the optimal level of the machining parameters, TOPSIS method is carried out and the average closeness coefficient is found; then using that, the optimal parameters setting is found. Experiment 9 showed rank no. 1, so the same setting of optimized process parameters is found in the mean response table. Hence no confirmation test is required for this study (Table 10.7).

With the help of optimal level of ECMM machining parameters, the expected response value ($\gamma_{predicted}$) can be calculated by means of following equation:

Table 10.6 Mean response table for closeness coefficient

Symbols	Process parameters	Average closeness coefficient			Max.–Min.
		Level 1	Level 2	Level 3	
V	Voltage	0.524939	0.779567	0.710854	0.254628
D	Duty ratio	0.606861	0.694705	0.713794	0.106933
F	Feed rate	0.7582	0.731596	0.525564	0.232636

Table 10.7 Results of ANOVA for multiresponse parameters

Source	DOF	SS	MS	F	*P* value
Voltage	2	1.4702	0.7351	1.27	0.440
Duty ratio	2	0.5397	0.2698	0.47	0.682
Feed rate	2	2.8255	1.4127	2.44	0.291
Error	6	1.1571	0.5786		
Total		5.9924			

$$\Upsilon_{\text{predicted}} = \Upsilon_{\text{m}} + \sum_{j=1}^{n} (\gamma_o - \gamma_m)$$

10.4 Results and Discussion

10.4.1 Fabrication of micro-dimple

Video measuring system (VMS) image of machined SS304 alloy with the optimized feed rate, voltage, and duty ratio is shown in Fig. 10.3 (1–9). From Fig. 10.3 (1–9), it has been observed that voltage of 16 V with reciprocating feed (0.5 mm/min) as well as duty ratio (0.6) aids to develop circular micro-dimple on SS304 alloy. The same parameters except for duty ratio (0.7) maintain high current density, which

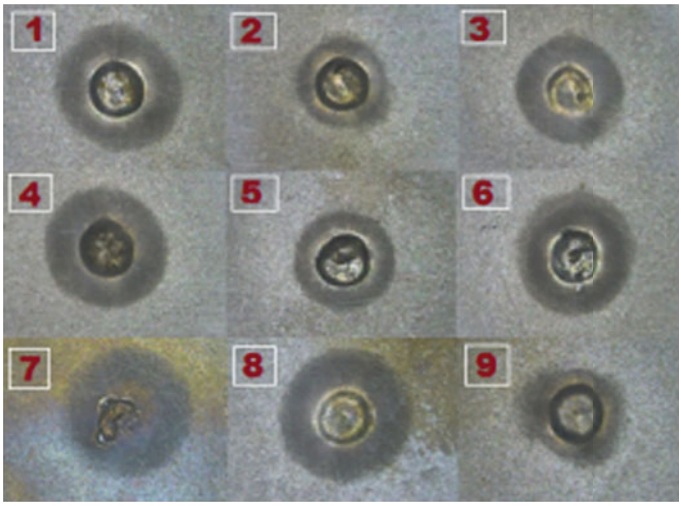

Fig. 10.3 (1–9) VMS image of micro-dimple array

tends to higher material removal with less time taken on machining zone. Using the same parameters namely voltage, feed rate, with a higher duty ratio makes difficult to maintain the IEG. So either increase or decrease of the duty ratio with respect to feed rate as well as voltage is needed.

10.4.2 Effect of Applied Voltage on Micro-Dimple

The shape and surface finish of generated circular micro-dimples can be controlled using dominant factor voltage. The supplied voltage effect on MRR, overcut, and taper during micro-finishing can be controlled by using a proper power supply. When voltage increases, the potential difference between the cathode and the anode increases the electrolyte ionization, so it tends the MRR to increase as dissolution increases. The overcut and taper is also a major concern to be taken care of in producing such complicated circular micro-dimples since they both directly increase with an increase in supply voltage. With higher voltage, the micro-gap between the tool and workpiece gets heated and the joule heat is generated which is not maximum. The composite electrolyte makes varying local conductivity with a non-uniform current density, so it tends to create non-uniform dissolution of metal. This is because the electric field intensity between the tool and electrode is in the tip tool, so sidewall is larger in some experiments. The electric field intensity at the tip of the tool is more when compared to other tool area, leading to poor dimensional uniformity of the micro-dimple. Because of the usage of composite electrolyte, the electric field intensity is low, so the current density at the edge is low leading to the creation of less machining products.

10.4.3 Effect of Duty Ratio on Micro-Dimple

The shape and surface finish of the produced circular micro-dimples can also be controlled with the input factor duty ratio. With the increase in duty ratio without pulse-off time, the MRR gradually increases, and with some intervals of pulse-off time, the geometrical aspects and surface finish can be controlled. With the increase in duty ratio, undercut increases gradually up to a certain value and then decreases. The diameters of the micro-dimple should not be increased in order the pulse-on time is supplied to reproduce it. During pulse power, the sludge formed due to dissolution adhered in the IEG is obviously pulled off by the composite electrolyte since the viscosity is also very high during the pulse-off time, so for the next cycle fresh electrolyte comes into contact in the machining gap. As the duty ratio changes from 60 to 70%, depth of the micro-dimples gradually decreases. A localized removal should not happen in this case of producing circular micro-dimple because it tends to form a circular hole, so the power pulse should be given with a certain amount of pulse-off time to control the depth of the dimple. When duty ratio increases up to 80%, the

pulse-off time accordingly decreases, causing complication in electrolyte exchange mechanism. This leads to a reduction in duty ratio and the depth of the formed micro-dimples. The applied pulse-on time with certain pulse-off time hinders electrolyte refreshment, so the dimple diameter gets decreased and the depth is controlled. So, material removal happens during pulse-on time, and the controlled etching with better surface finish is obtained that increases the efficiency. Thus, for machining micro-dimple, appropriate pulse-on time and pulse-off time must be selected for the effect of localization, surface finish, taper angle, and material removal rate.

10.4.4 Effect of Feed Rate on Micro-dimple

The shape and size of micro-dimple can be controlled using the input factor feed rate. Increasing the feed rate causes tool and workpiece to interact easily. So, as the machining time decreases, only less material on the sidewalls gets eroded, which ultimately decreases the diameter of the circular dimple followed by the taper. Micro-dimple with better surface finish, minimum taperness, and better accuracy can be fabricated at high feed rate as the interaction of both positive and negative ions is faster. Higher feed rate, specifically above 0.9 mm/min, causes frequent contact between the tool and workpiece that leads to short circuit and made the machining process unstable. ECMM can produce better experimental results with the recommended optimal feed rate in the range of 0.3–0.7 mm/min. The circular dimple depth is kept constant so that the contact between tool and workpiece should be completely avoided. It could be observed that when the feed rate increases the circular dimple formed is more precise than that of the lower feed rate.

10.4.5 Surface Roughness Profile of Micro-Dimple

Average surface roughness (S_a) is measured by means of non-contact Talysurf CCI3000A, as shown in Fig. 10.4(1–9). The 3D surface roughness of the micro-dimple is taken. It has been observed from the figures that at a lower voltage, less feed rate and lower duty ratio helps to enhance the surface quality for developing micro-dimple area. At higher voltage, current density increases which tend to higher MRR so that the depth of the micro-dimple cannot be controlled. Higher MRR occurs due to rough machining which affects the surface quality of produced micro-dimple area.

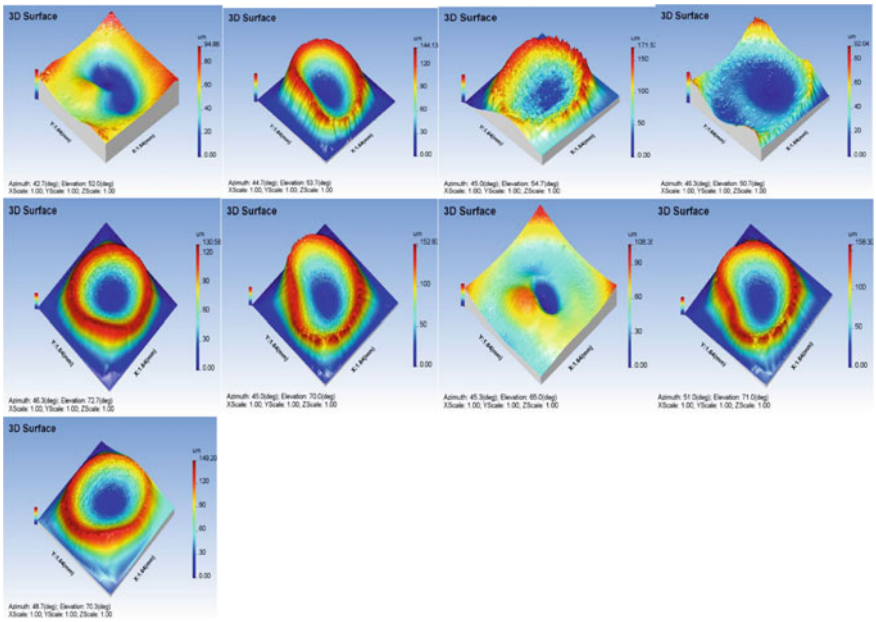

Fig. 10.4 (1–9) 3D-surface roughness of micro-dimple on SS304

10.5 Conclusions

In this work, TOPSIS optimization method with L9 orthogonal array is carried out, to optimize the process parameter for creating micro-dimples in ECMM and finishing of the SS304 alloy.

The combination of the ECMM finishing parameters and their levels are identified for achieving higher material remove rate (MRR) and lower surface roughness (S_a). It is found that experiment number 9 conceded the maximum closeness coefficient value for the multiresponse optimization of ECMM machining parameter, as follows: Voltage (V) at 18 V, feed rate (FR) at 0.7 mm/min, and duty ratio (DR) at 70%.

The optimum levels of the input process parameter combinations were identified by the response of the closeness coefficient values. The optimum parameter level combinations such as voltage (V) at 18 V, feed rate (FR) at 0.7 mm/min, and duty ratio (DR) at 70% were obtained for the ECMM finishing process. ANOVA is carried out for the analysis using the Minitab software to find and experimentally study the significant parameter for the multiperformance characteristics of ECMM. From the ANOVA analysis, the *P* value is established to be the most significant factor in the multiperformance characteristics. It is noticed that the proposed combination of TOPSIS and ANOVA is more effective, for creating micro-dimples and for solving Multiresponse problems in ECMM.

Acknowledgments The authors sincerely thank DST-FIST for providing the instrument "Non-contact 3D roughness measurement", Department of Manufacturing Engineering, Anna University.

References

1. Wang, M., Bao, Z., Qiu, G., Xu, X.: Fabrication of micro-dimple arrays by AS-EMM and EMM. Int. J. Adv. Manuf. Technol. **93**, 787–797 (2017). https://doi.org/10.1007/s001170-017-0538-0
2. Mahata, S., Kunar, S., Bhattacharyya, B.: Micro dimple array fabrication by through mask electrochemical micromachining utilizing low-aspect-ratio mask. J. Electrochem. Soc. **165**(3), E129–E137 (2018). https://doi.org/10.1149/2.0521803jes
3. Hou, Z., Qu, N., Chen, X.: Electrochemical micromachining of large-area micro-dimple arrays with high machining accuracy. Proc. Inst. Mech. Eng. Part B: J. Eng. Manuf. https://doi.org/10.1177/0954405416682280
4. Wang, G.Q., Zhu, D., Li, H.S.: Fabrication of semi-circular micro-groove on titanium alloy surface by through-mask electrochemical micromachining. J. Mater. Process. Tech. **258**, 22–28 (2018). https://doi.org/10.1016/j.jmatprotec.2018.03.015
5. Qu, N., Chen, X., Li, H., Zeng, Y.: Electrochemical micromachining of micro-dimple arrays on cylindrical inner surfaces using a dry-film photoresist. Chin. J. Aeronaut. **27**(4), 1030–1036 (2014). https://doi.org/10.1016/j.cja.2014.03.012
6. Skoczypiec, S.: Electrochemical methods of micro part's manufacturing. In: Micro and Precision Manufacturing, Engineering Materials. https://doi.org/10.1007/978-3-319-68801-5_2
7. Patel, D.S., Jain, V.K., Shrivastava, A., Ramkumar, J.: Electrochemical micro texturing on flat and curved surfaces: simulation and experiments. Int. J. Adv. Manuf. Technol. https://doi.org/10.1007/s00170-016-9700-3
8. Qu, N., Chen, X., Li, H., Zhu, D.: Fabrication of PDMS micro through-holes for electrochemical micromachining. Int. J. Adv. Manuf. Technol. **72**, 487–494 (2014). https://doi.org/10.1007/s00170-014-5702-1
9. Sadagopan, P., Mouliprasanth, B.: Investigation on the influence of different types of dielectrics in electrical discharge machining. Int. J. Adv. Manuf. Technol. **92**, 277–291 (2017). https://doi.org/10.1007/s00170-017-0039-1
10. Yuvaraj, N., Pradeep Kumar, M.: Multiresponse optimization of abrasive water jet cutting process parameters using TOPSIS approach. Mater. Manuf. Process. https://doi.org/10.1080/10426914.20

Chapter 11
Investigations into Micro-Hole Drilling on SS-304 by Sequential Electro-Micro Machining

R. M. Tayade, B. Doloi, B. R. Sarkar and B. Bhattacharyya

Abstract This paper focuses on the improvement of performances in sequential electro-micro-machining (SEMM) which consists of micro-EDM and micro-ECM processes during drilling micro-holes on SS-304 stainless steel sheet. In the first phase of experimentation, through micro-holes drilling on SS-304 material was done by applying micro-EDM process. As EDM being a thermal process, shaping of an object takes place rapidly due to high intensity spark discharges, but these spark discharges also create heat-affected zone consisting of recast layer, craters, cracks, and so on. These defects are then ameliorated by micro-ECM process performed sequentially after micro-EDM. This paper investigates the effects of machining time on the post electro-discharge machined holes for the various machining responses, such as radial overcut, circularity and hole taper. The experiments revealed that with the increase in machining time, there is an improvement in hole circularity as well as hole taper angle, but undesirable radial overcut also escalates with the passage of time.

Keywords SEMM · Micro-EDM · SS-304 · Radial overcut · Hole circularity · Hole taper angle

11.1 Introduction

Micro-machining in non-conventional domain is gaining importance due to the relentless demand of micro-parts which are made of highly sophisticated materials. Micro-parts are manufactured by applying different micro-machining techniques. These micro-parts are then assembled to form micro-structures which can be used to manufacture miniature instruments required extensively in the various fields of applications. Generally non-traditional micro-machining techniques are preferred to fabricate micro-features on the micro-parts; these micro-machining techniques offer several advantages, such as machining of conducting, non-conducting and semiconducting materials, irrespective of their stiff mechanical properties, like hardness or

R. M. Tayade (✉) · B. Doloi · B. R. Sarkar · B. Bhattacharyya
Production Engineering Department, Jadavpur University, Kolkata 700032, India
e-mail: rmtayade@vjti.org.in

M. S. Shunmugam and M. Kanthababu (eds.), *Advances in Micro and Nano Manufacturing and Surface Engineering*, Lecture Notes on Multidisciplinary Industrial Engineering,
https://doi.org/10.1007/978-981-32-9425-7_11

toughness, maintenance of close dimensional tolerances, high material removal rate, excellent surface finish, and so on. Each and every non-traditional micro-machining process has its own advantages and disadvantages. The processes such as laser beam machining (LBM), electro-discharge machining (EDM) and electron beam machining (EBM) have high rate of material removal but being a thermal process, heat generated during machining imparts some inherent flaws such as resolidified material, burrs, cracks, white layers and residual stresses in heat-affected zone (HAZ). ECM imparts excellent surface finish with high material removal rate but non-conducting materials cannot be machined by this process and uncontrolled stray corrosion affects machining accuracy. Controlling input parameters during machining may provide relief to some extent but in lieu of this some flaws still exists due to the inherent characteristic of the process.

In sequential machining technique, two or more than two micro-machining processes are applied in sequence on single or different machine tools. The prime motto behind sequencing is to extract the advantages and to minimize the disadvantages present in individual machining process. The technology implemented here for micro-hole drilling is specifically termed as "sequential electro-micro machining" (SEMM). SEMM is a new terminology applied specifically for electro-micro-machining processes which involve the non-conventional micro-machining processes, such as micro-EDM, micro-ECM, micro-ECDM, and so on. In SEMM, the tool–workpiece interaction takes place through the media of conducting fluids such as electrolytes, non-conducting fluid-like dielectric and other semiconducting fluids also. Thus, SEMM appears as the most appealing technology to fulfill the ever-progressing demand of miniaturized components.

In this paper the experiments are carried out on difficult-to-cut SS-304 grade stainless steel material, as it is one of the most versatile and widely used of all stainless steels. Its chemical composition, mechanical properties, weldability and resistance to corrosion provide the best all-round performance at relatively low cost. It also has excellent low temperature properties and it responds well to hardening by cold working. It can be successfully used from cryogenic temperatures to the red-hot temperatures of jet engines and furnaces. It readily breaks or rolled into variety of components for applications in industrial, architectural and transportation fields. Grade 304 with higher carbon content finds application at elevated temperature. SS-304 is specifically chosen for machining by considering its above-mentioned genuine properties, advantages and applications in various fields. As it is noted that very few sequential machining combinations are developed so far, there is a need of assimilation of different machining processes. The research work carried out in this area is less; hence the research material available in this particular domain is scanty. Nonetheless, some researchers have extended their research in order to exploit the potential involved in this particular machining technique.

Sebastian and Ruszaj [1] designed and developed a unique machine tool to investigate the effects of application of electrochemical and electro-discharge micro-milling in sequence for manufacturing 3-D sculptured surfaces. The application of electrochemical/electro-discharge (EC/ED) micro-sinking operation in sequence has been performed. Almost double decrease in machining time required for milling a cavity

in comparison to electro-discharge micro-machining was observed. Zeng et al. [2] investigated the combination of micro-EDM and micro-ECM in sequential manner for milling 3-D micro-structures on the same machine tool with the same tool electrode. The methodology applied during experimentation was micro-EDM for shaping the cavities and micro-ECM for finishing the micro-electro-discharge machined surfaces. The process was accomplished successfully by controlling the process parameters such as optimal machining voltage as 10 V, initial machining gap of 10 μm and tool feed rate of 10 μm/s during micro-ECM. This results in reduction of micro-EDM-shaped surface roughness (Ra) from 0.707 to 0.143 μm drastically as it eliminated the recast layer, burrs and craters completely. Implementation of sequential micro-EDM and micro-ECM milling processes results in improvement of machining efficiency, surface quality and mechanical properties of the workpiece.

Fleischer et al. [3] performed sequential combination of laser micro-ablation and micro-EDM to manufacture wear-resistant mold inserts. The mold cavity was shaped by applying pulsed laser beam and then finished precisely by micro-EDM process. The micro-features to be produced were machined using high ablation power of nanosecond pulsed laser, which cut micro-profile very rapidly. Laser is a thermal process; it generates HAZ and highly rough surface in machined area. Post application of micro-EDM then removed surface defects formed due to laser ablation process. Saeed et al. [4] classified sequential machining processes into five major categories on the basis of purpose of operations, such as (i) micro-tool-making-oriented processes, (ii) enhancement of material removal rate, (iii) machining surface quality improvement processes, (iv) energy efficiency, and (v) microstructure improvement-oriented processes. Xiaolong et al. [5] applied EDM–ECM combined processes for drilling micro-hole on SS-304 material. Initially, the tool electrode of 500 μm, diameter reduced to 100 μm, by using block electrical discharge grinding (BEDG) process, and then through hole drilled by applying micro-EDM process. The various surface defects were observed on the hole surface due to thermal effects of EDM process. These defects were eliminated by applying ECM finishing operation. Ghoshal et al. [6] generated micro-channels in SS-304 stainless steel by using different concentration of sulfuric acid (H_2SO_4) solution. It was observed that with least concentrated H_2SO_4 (0.1 M) solution, width overcut of channel was greater than the width overcut obtained by using 0.2 and 0.3 M of sulfuric acid. The micro-ECM sinking and milling was applied for generation of different types of taper less through micro-channels on SS-304. The least overcut with reduced taper on micro-channel was obtained by using 0.2 M of H_2SO4 solution. Das et al. [7] studied the surface integrity of micro-holes drilled on SS-304 stainless steel plate by micro-EDM and made a comparative analysis of material removal with and without providing ultrasonic vibrations to the workpiece. The variation in the thickness of recast layer, micro-hardness and other metallurgical transformations including HAZ were analyzed. The thickness of the recast layer which was in the range of 9–23 μm earlier reduces to 6–20 μm after providing ultrasonic vibrations. Thus, it was concluded that the application of vibrations to the workpiece enhances the surface characteristics of hole. Widodoa et al. [8] studied the effect of three cutting parameters such as spindle speed, feed rate, depth of cut on hole roundness while drilling holes on AISI 304 austenitic stainless

steel. Thus better hole roundness is possible with low spindle speed and low feed rate.

The two micro-machining processes such as micro-EDM for cutting and micro-ECM for finishing the electro-discharge machined holes were applied in a sequential manner. In order to find suitable sequential machining combination, the experiments were performed to find the effects of machining time on radial overcut, circularity and hole taper.

11.2 Experimental Details

To carry out the experiments and to predict suitable machining conditions, compatible system setup was developed indigenously. The developed micro-ECM setup was a combination of three major functioning units, such as a power supply unit, electrolyte circulation unit and machining unit. The ratings of available power supply line are three-phase 440 V alternating current (AC) with 50 Hz frequency. Although both the power supply units are connected to the same source line, but their individual power supply ratings are different. The micro-EDM power supply unit is connected to the mains through voltage stabilizer and the holes are drilled at machining voltage of 50 V, peak current 2 A and T_{on} time 7.50 μs. The micro-ECM process adopted for subsequent operation demands low-voltage DC (full-wave rectified) or pulsed DC power supply.

The voltage and current ratings of micro-ECM pulsed DC power supply are: 50 V and 5 A, respectively. The reduction of input voltage and conversion of it from AC to DC was accomplished by step down transformer and silicon diode-controlled rectifier, respectively, by connecting them one after the other in the circuit. Similarly, to measure current, applied voltage in the system and to generate desired type of pulses, voltmeter, ammeter and pulse generator units are connected at the required places. Japan-made digital storage oscilloscope (DL 1520 Yokogawa) is used to observe the pulses formed and to monitor the machining conditions. The machining unit comprises different subunits such as workpiece mounting unit, tool electrode holding and feeding arrangement, online monitoring microscope, desktop computer, and so on. The X–Y–Z translation stage (Mettler Toledo, Switzerland) having resolution of 0.1 μm, with position controlling unit is operated by software named APT (automated programmed tool), which plays a significant role during machining. The stage is equipped with micro-processor control unit to execute controlled movements of all the three stages in co-ordination with one another to feed the tool electrode and stepper controlling unit which in actual provides mechanical movements to the stages through the stepper motors attached at the end of each stage. The maximum travel distance of the stages in X, Y and Z direction is limited to 100 mm.

The workpiece mounting unit remains submerged in corrosive electrolytes; therefore it is made up of acrylic glass. The workpiece locating platform was made precisely in such a way that after unloading the workpiece from EDM setup, it was possible to place it exactly at the same location in ECM setup. The tool holding

attachment provided on the front face of the Z axis of the stage has a provision of fixing the tool electrode perpendicular to the workpiece surface. The online monitoring microscope facilitates the checking of quality and progress of tool electrode, density of bubble formation, occurrence of sporadic sparks if any. Measurement of machined features on the workpiece without removing it from the workpiece holder becomes possible. It also helps in recording actual machining operations; micro-feature profile measurement without unloading workpiece from its position, thus recording of actual machining process videos and photographs is achievable by such versatile equipment. The third major unit which is essential from the point of view of machining to occur is an electrolyte flow system. The main purpose of introducing electrolyte circulation unit was to supply fresh electrolyte and to regulate the flow of fluid at the tool–workpiece interface. The electrolyte completes the electrical circuit which is essential for machining reactions to take place by forming an electrolytic cell [9]. It also cools the machining zone and removes reaction products efficiently. This unit consists of a main machining chamber, electrolyte tank and pump. The main chamber is made of electric-resistant and corrosion-resistant transparent perspex material having dimensions 220 × 200 × 110 mm. The size of the main machining chamber is kept in such a way that it can accommodate the workpiece of maximum size, similarly, it will hold the optimum amount of electrolyte. The electrolyte tank which serves as a reservoir has 37 W, 0.5 HP pump in it for circulating electrolyte through the main chamber during machining. The opening valves are set in such a way that the flow speed of electrolyte would be less than 3 m/s. Strainer is provided at the suction side of the pump to restrict entry of sludge/and foreign particles in the main machining chamber.

11.3 Experimental Planning

To fulfill the aim of investigating the influences of sequential machining approach on the micro-holes drilled in SS-304, all the experiments in micro-ECM were conducted by keeping the duty ratio 90% and current amplitude 0.75 A constant. The effects of test parameter such as machining time while finishing micro-holes in SS-304 stainless steel plates are studied. The machining parameters considered in shaping holes in micro-EDM are: Open circuit voltage = 220 V, peak current = 2 A, machining voltage = 50 V, pulse-on time (T_{on}) = 7.5 μs. The machining with micro-EDM took place in the medium of dielectric oil. The micro-features generated on the hole surface due to micro-EDM and micro-ECM were measured by a Leica digital microscope. The weight of tool electrode and workpiece before and after the machining is weighed by precision weighing machine (Mettler Toledo, Switzerland). The various parameters related to experimentation are measured by the equipments such as multimeter (TX3 Tektronix, USA), online monitoring microscope and precision stop watch (Baker, India). First, the micro-holes were drilled by micro-EDM process by placing the workpiece in a highly precise workpiece-holding attachment; the same attachment can be accommodated precisely in developed micro-ECM setup to maintain the

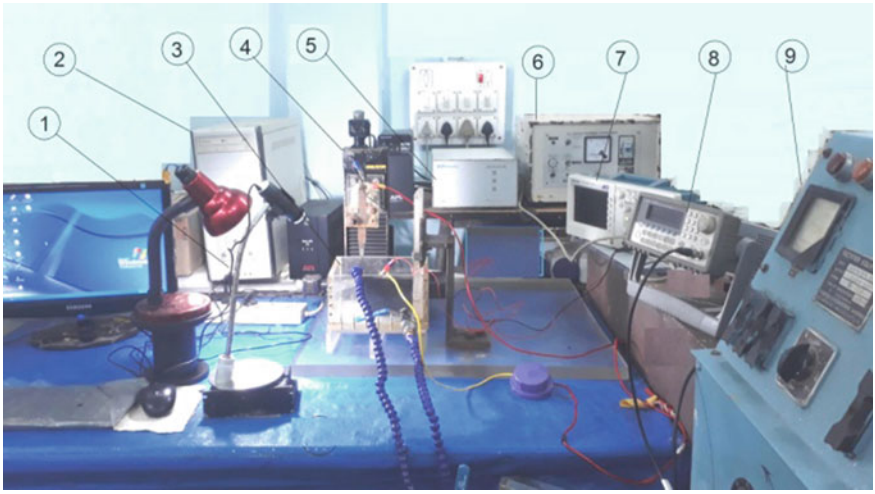

(1) Online monitoring microscope, (2) Central processing unit, (3) machining chamber, (4) X-Y-Z translation stage, (5) Stepper motor controller, (6) Voltage stabilizer, (7) Digital storage oscilloscope, (8) Function generator, (9) Power supply unit.

Fig. 11.1 Micro-ECM setup photograph

positioning accuracy. The photographic view of the experimentation set up is shown in Fig. 11.1. Three sets of experiments are carried out by keeping machining time value 2, 3, 4, 5, and 6 min, respectively. All the machining operations are performed by using electrolyte of 0.1 M of sulfuric acid (H_2SO_4) solution prepared in distilled water.

11.3.1 Tool Electrode and Workpiece Specifications

The SS-304 grade stainless steel comes under the category of difficult-to-cut materials and machining it by classical conventional methods pose many challenges. This application of non-conventional methods for machining SS-304 is a better option. The workpiece specimens of size 30 × 10 × 0.4 mm for length, width and thickness were prepared using a standard diamond cutter grinder machine: Struers, Secoton 15. The hardness value of the AISI 304 is 35 HRC, the chemical composition of AISI 304 includes 0.021% C, 18.75% Cr, 8.18% Ni, 1.81% Mn, 0.290 Si, 0.268% Mo, 0.018% P and 0.008% S. The tool electrode used in micro-ECM experimentation is of 250 μm diameters and made up of tungsten carbide (WC) material having composition 94% tungsten carbide (WC) with 4% cobalt (Co). The tool electrode used in micro-EDM experimentation is about 200 μm diameter and made up of electrolytic copper, which constitutes 99.8% copper.

11.4 Results and Discussion

The machining was carried out according to the planned scheme for different duration of machining time by keeping the duty ratio constant at 90% and current amplitude at 0.75 A. Three experiments are conducted for each time duration, and the final value is obtained by calculating average to get the most precise reading. The effects of the above-mentioned control parameter on machining performance characteristics such as radial overcut, circularity and hole taper are then analyzed to find the best sequential machining parametric combination.

The formula for calculating the taper angle (α) after completion of micro-EDM and micro-ECM operations is as follows:

$$\alpha = \tan^{-1}(D_t - D_b)/2L \,\text{degree}. \tag{11.1}$$

In formula (11.1), Dt is the diameter of hole measured on the top surface of sheet, Db is the diameter of hole measured on the bottom surface of the sheet and l represents the thickness of the sheet. The hole roundness or circularity is one of the important attribute which needs to be taken care of while machining. In conventional micro-machining, low spindle speed and low feed rate correspond to better roundness of hole. According to the definition of International Standard ISO 1101 [10], circularity error is defined as the radial distance between two concentric circles separated by minimum possible distance and containing all the measurement points on the given profile, as shown in Fig. 11.2. The circularity of holes drilled after micro-EDM and micro-ECM is calculated by applying formula di/do, where di represents the inner hole diameter and do is the outer diameter encompassing all the irregularities as shown in Fig. 11.2. The MRR of micro-EDM was obtained as 11.458 mm^3/min which results in reduced machining time by giving impetus to the machining efficiency. On the other hand, the MRR of micro-ECM was 0.042 mm^3/min., which is too less as compared to that in EDM process, this is because the micro-ECM process was applied for finishing operation only. The finishing of micro-hole was performed after the completion of micro-EDM operation.

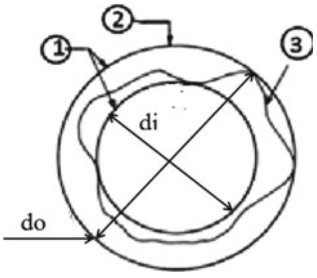

Fig. 11.2 Schematic representation of circularity error

1. Assessment features, 2. Circularity error, 3. Circular feature

Table 11.1 Values of machining performance characteristics after micro-EDM

Sr. No.	Radial overcut (ROC) μm	Hole circularity	Hole taper angle (°)
1	73	0.942	1.60
2	70	0.948	1.58
3	72	0.946	1.59
4	70	0.943	1.52
5	71	0.940	1.56

To find out the influence of machining time on a radial overcoat (ROC), hole taper angle (HT) and circularity, number of operations are performed in micro-ECM. The machining is carried out by keeping the current value constant at 0.75 A and duty ratio fixed at 90%. In micro-ECM, along with voltage, type and concentration of electrolyte, machining time is also an important process parameter which dictates the rate of anodic dissolution. Thus the effect of above-mentioned control parameter on machining performance characteristics is then analyzed by varying the time duration. The micro-hole cutting operation is carried out by applying micro-EDM process, in which the holes are shaped in few seconds. Thus EDM ensures hole drilling operation with high machining efficiency, but when these holes observed through a microscope, show some surface defects. The electro-discharge-machined hole surface becomes rough due to repetitive action of spark discharges which erodes material rapidly, but leaves a multitude of craters, layer of resolidified material, including micro-cracks, micro-pores, etc. The piled up recast layer surrounding the periphery of electro-discharge-machined hole with heat-affected zone is clearly visible in the actual photograph taken, as shown in Figs. 11.6a and 11.7a. The thermal effect in the heat-affected zone (HAZ) alters the mechanical properties of material and induces residual stresses. In order to reduce these shortcomings, the electro-discharge-machined holes are then treated by micro-ECM for different time periods and the effects of machining time on hole surface characteristics such as ROC, circularity and HT are studied. Table 11.1 indicates the values of machining characteristics obtained after drilling holes by micro-EDM process. The holes drilled by EDM process do not show much variation in the ROC, circularity and HT values, as they are shaped at particular standard machining conditions, whereas the difference in above parametric values in micro-ECM takes place due to variation in machining time. Table 11.2 indicates the values of performance characteristics after finishing the holes in micro-ECM for different time periods. Figure 11.3 represents the effects of machining time on ROC. A gradual increment in ROC is observed till the machining time reaches to 4 min, whereas rapid increment in ROC is observed after 4 min. The ROC is admissible till it levels the value of HT; exceeding ROC beyond that limit may affect the dimensional accuracy of the hole. It is observed from Fig. 11.4 that the circularity of the holes increases with the increase in machining time because the inner diameter of the hole increases as the stay of tool electrode increases for a longer period of time giving rise to the increased anodic dissolution which reduces the spacing between the inner and outer diameters encompassing the circularity errors.

Table 11.2 Values of machining performance characteristics after micro- ECM

Sr. No.	Machining time (min.)	Radial overcut (ROC) μm	Hole circularity	Hole taper angle (°)
1	2	80	0.932	1.58
2	3	83	0.938	1.30
3	4	85	0.943	1.15
4	5	96	0.952	0.80
5	6	105	0.960	0.72

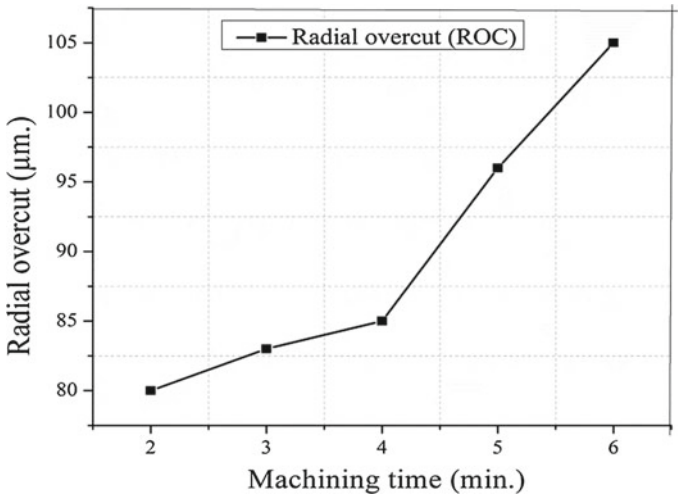

Fig. 11.3 Effect of machining time on radial overcut

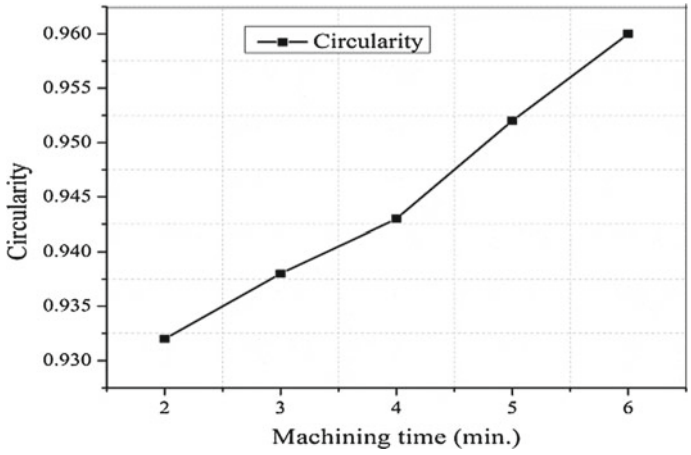

Fig. 11.4 Effect of machining time on circularity

The graphical representation of machining time corresponding to HT is shown in Fig. 11.5. With the increased machining time the period available for anodic dissolution of material surrounding the tool electrode is more which results in reduced hole taper with the passage of time.

Thus, by the increased machining time, there is an improvement in the values of circularity and HT, but the increase of ROC beyond the acceptable limit may affect the dimensional accuracy of the holes. Figures 11.6 and 11.7 show the actual photographs of micro-holes taken with Leica microscope. In Figs. 11.6a and 11.7a, the holes shaped by micro-EDM process are shown.

The presence of heat-affected zone and accumulated recast layer surrounding the periphery of the elecrto-discharge machined holes as it is visible in Figs. 11.6 and

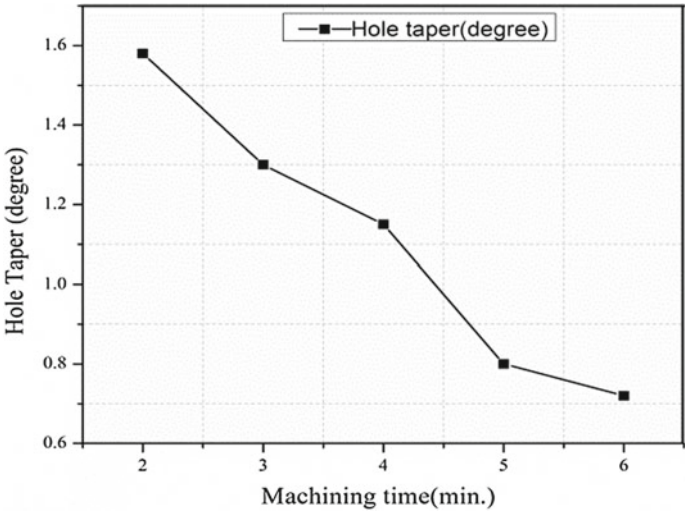

Fig. 11.5 Effect of machining time on hole taper

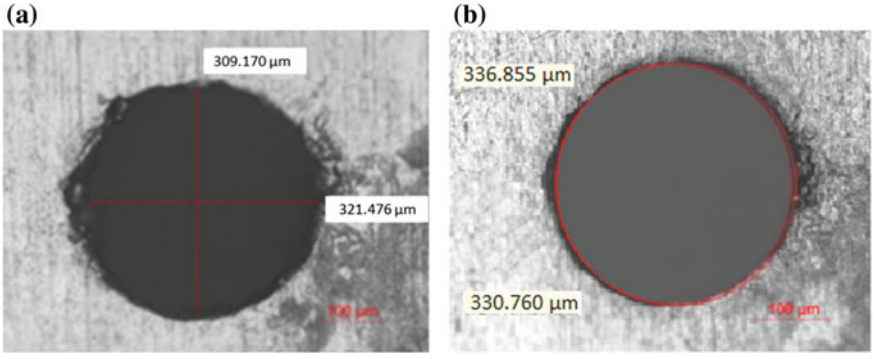

Fig. 11.6 **a**. Hole condition after EDM, **b**. Hole condition after 2 min of ECM

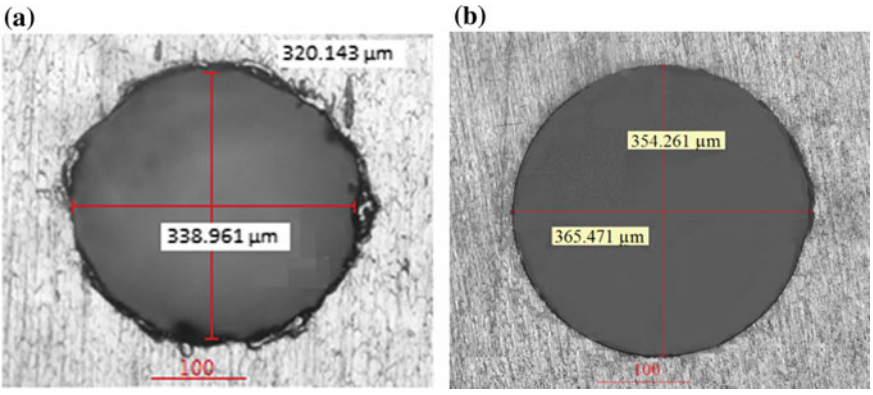

Fig. 11.7 **a**. Hole condition after EDM, **b**. Hole condition after 6 min of ECM

11.7a makes the hole surface rough and uneven. Figure 11.6b shows the removal of a recast layer up to a certain extent, since the machining time allotted was 2 min, time available for anodic dissolution was not sufficient for removing a recast layer completely. Figure 11.7b shows hole condition after 6 min of micro-ECM finishing operation which results in smooth hole surface by removing a recast layer completely at given machining conditions.

11.5 Conclusions

The sequential electro-micro-machining system has been developed indigenously to carry out micro-ECM finishing of micro-hole followed by micro-EDM hole drilling on SS-304 sheet. The plan of action of sequencing two diverse techniques for drilling micro-holes on the SS-304 stainless steel sheet was executed successfully. The machining time in micro-ECM is one of the dominant control parameters which dictate the terms of machining. The main motive behind conducting the experiments in micro-ECM after micro-EDM processing was to find the proper sequential machining combination. To achieve this goal, the effect of machining time on the various machining performance characteristics such as radial overcut, circularity, and hole taper angle was studied. After micro-EDM drilling operation on SS-304 sheet, the lower values of radial overcut, higher value of hole circularity and lower value of hole taper angle were obtained as 70 µm, 0.948 and 1.52°, respectively. It is revealed in the experimental investigation that 6 min of micro-ECM finishing operation is performed after micro-EDM operation. The lower value of hole taper and higher values of hole circularity were obtained at 0.72° and 0.960, respectively. After micro-ECM lower value of radial overcut was obtained as 80 µm which is higher than that obtained after micro-EDM hole drilling operation. Hence there is an improvement in hole taper and hole circularity during sequential electro-micro-drilling on the SS-304 sheet while

micro-ECM finishing operation has been carried out after micro-EDM operation sequentially. From the photographic views of micro-hole by SEMM, it is concluded that the surface quality of the periphery of micro-hole on SS-304 has been improved by micro-ECM finishing followed by micro-EDM hole drilling. Research on this sequential electro-micro-machining is also needed to carry out an in-depth study for sequential combination of processes, considering the effects of applied voltage, pulse frequency and duty ratio etc. which may lead towards further improvement of machining performances.

References

1. Sebastian, S., Ruszaj, A.: A sequential electrochemical-electro-discharge process for micropart manufacturing. Precis. Eng. **38**, 680–690 (2014)
2. Zeng, Z., Wang, Y., Wang, Z., Shan, D., He, X.: A study of micro-EDM and micro-ECM combined milling for 3D metallic micro-structures. Precis. Eng. **36**, 500–509 (2012)
3. Fleischer, J., Schmidt, J., Haupt, S.: Combination of electric discharge machining and laser ablation in microstructuring of hardened steels. Microsyst. Technol. **12**, 697–701 (2006). https://doi.org/10.1007/s00542-006-0095-1
4. Chavoshi, S.Z., Goel, S., Morantz, P.: Current trends and future of sequential micro-machining processes on a single machine tool. Mater. Des. **127**, 37–53 (2017)
5. Xiaolong, H., Yukui, W., Zhenlong, W., Zhaoqi, Z.: Micro-hole drilled by EDM-ECM combined processing. Key Eng. Mater. (2013). ISSN: 1662-9795, 562-565, 52-56
6. Ghoshal, B.B.: Micro electrochemical sinking and milling method for generation of micro-features. Proc. Instit. Mechan. Eng. Part B: J. Eng. Manuf. **227**(11), 1651–1663 (2013)
7. Das, A.K., Pankaj Kumar, A., Sethi, P.K., Singh, M.H.: Influence of process parameters on the surface integrity of micro-holes of SS304 obtained by micro-EDM. J Braz. Soc. Mech. Sci. Eng. **38**, 2029–2037 (2016). https://doi.org/10.1007/s40430-016-0488-8
8. Widodoa, N.R., Kurniawan, D.: Evaluation of hole quality on micro drilling AISI 304 austenitic stainless steel. Procedia Manuf. **2**, 465–469 (2015)
9. Bhattacharyya, B., Munda, J., Malpati, M.: Advancement in electrochemical micro-machining. Int. J. Mach. Tools Manuf. **44**, 1577–1589 (2004)
10. Murthy, T.S.R., Abdin, S.Z.: Minimum zone evaluation of surfaces. Int. J. Mach. tool Des. Res. **20**, 123–136 (1980)

Chapter 12
Experimental Investigations to Evaluate Machining Accuracy of Ultrasonic-Assisted Milling on Thin-Walled Structures

Girish Chandra Verma, Pulak Mohan Pandey and Uday Shanker Dixit

Abstract Ultrasonic vibration-assisted milling (UAM) process is one of the most recent advancements in the area of milling. In axial UAM process, milling cutter is rotated and simultaneously vibrated in axial direction with high frequency and small amplitude. As observed experimentally, the superposition of axial ultrasonic vibrations in milling operation improved the performance of the process by reducing cutting forces and enhancing surface quality. This study intended to evaluate the machining accuracy of thin-walled structures milled with and without the assistance of ultrasonic vibration. Two different types of thin-walled (with straight and curved geometry) structures were machined by UAM and conventional milling to compare their machining accuracy. Accuracy of machined components was assessed following a reverse engineering technique. Experimental results indicated that the superposition of axial ultrasonic vibrations improved the machining accuracy of the typical milling process of up to 33%.

Keywords Axial ultrasonic vibration-assisted milling · Thin-walled structure · Machining accuracy · Reverse engineering

12.1 Introduction

Accuracy in machining is one of the important requirements in the modern manufacturing era. The dimensional and geometric accuracy is one of the most key factors affecting the functional performance of the product. Machining of parts having low rigidity (thin-walled structure) with dimensional and geometric accuracy is a major challenge for the existing manufacturing processes. Accuracy of the machined part is highly dependent on tool paths and cutting strategies [1].

G. C. Verma (✉) · P. M. Pandey
Department of Mechanical Engineering, Indian Institute of Technology Delhi, Delhi 110016, India
e-mail: girish.verma3139@gmail.com

U. S. Dixit
Department of Mechanical Engineering, Indian Institute of Technology Guwahati, Assam 781 039, India

M. S. Shunmugam and M. Kanthababu (eds.), *Advances in Micro and Nano Manufacturing and Surface Engineering*, Lecture Notes on Multidisciplinary Industrial Engineering,
https://doi.org/10.1007/978-981-32-9425-7_12

Thin-walled structures have large aspect (height to thickness) ratio. A typical example of thin-walled structure machining is the peripheral milling of a blade of an impeller. The peripheral milling of such components is difficult, as varying cutting forces periodically excite vibrations in cutter as well as the product. These process-generated vibrations in milling process results in dimensional deviation and poor surface finish [2]. Variation in the cutting force is the major cause of the vibrations [3]. The vibrations become detrimental when the frequency of the cutting force variation comes close to the natural frequency of the milling system. This results in chattering, which has adverse effect on tool and workpiece [4].

Several advancements in the area of milling were made in the recent time to improve the stability lobes [4]. One of the newly developed techniques is cryogenic cooling during milling. Experimental studies [5, 6] showed that application of cryogenic cooling reduced the secondary shear zone length resulting in lower cutting forces and improved tool life. Huang et al. [6] studied the effect of cryogenic cooling on the stability lobes in milling of 7075-T6 aluminum alloy. Their experimental results showed an improvement of 50–100% in stability limits.

Minimum quantity lubrication (MQL) has also been tried with milling in order to improve the machining responses. Lee et al. [7] applied MQL mixed with nanoparticles and found reduction in surface roughness and cutting forces. The experimental results [8] confirmed that the formation of thin film in the secondary shear zone reduced the friction, leading to a better machining performance.

Ultrasonic vibration-assisted milling (UAM) is another technique for improving the machining performance. In UAM, milling cutter is rotated and vibrated simultaneously with high frequency and small amplitude [9]. However, most of the researchers applied ultrasonic vibration to the workpiece in place of cutting tool [10–13]. The effect of ultrasonic vibration-assisted cutting on different kind of materials like steel, glass and brittle ceramics resulted in better surface finish, longer tool life and lower cutting forces [9, 14, 15]. The researchers [10–12, 16] attributed these advantages to intermittent cutting effect, which occurs during UAM for a certain range of machining parameters.

The application of ultrasonic vibrations in milling operation results in reduced cutting forces and better surface finish [17, 18]. Experimental results [18] showed that the application of ultrasonic vibration in different direction yielded different results. Ko et al. [18] observed that the application of ultrasonic vibration in axial, feed as well as cross-feed directions resulted in reduced cutting forces. However, vibration in axial and feed direction resulted in high surface finish due to ironing effect [18]. Furthermore, axial vibration was found to be more advantageous as it provided flexibility to perform UAM in any direction with uniform surface finish. Shen et al. [11] evaluated the effect of ultrasonic vibrations in feed direction by measuring cutting forces, surface roughness and chip morphology in UAM. Their experimental results showed that application of ultrasonic vibration caused intermittent cutting, which allowed cutting fluid to reach the processing area resulting in improved machining responses. Li and Wang [19] studied the effect of process parameters on tool wear and surface roughness in UAM of SKD61 tool steel. Their experiments showed that using axial ultrasonic vibration improved the milling process by reducing tool wear,

surface roughness and burr height. They also demonstrated that effect of ultrasonic vibration decreased with increase in rotational speed.

In literature, there is no study on the effect of ultrasonic vibration-assisted milling on the accuracy of thin-walled components. This work intends to fill up this research gap by performing ultrasonic vibration-assisted milling on a thin-walled structure and measuring the dimensional deviation after machining. Al6063 aluminum alloy was chosen as a work material because of its use in heat conducting fins, which are thin-walled structures. Two types of thin-walled structures (compound curved and straight) were machined to evaluate the ultrasonic-vibration effect. These structures were designed using Creo-parametric software whose machining module was used to generate the part program (in terms of G and M codes) for milling. Optimized process parameters from the literature were chosen for machining the structure. Further, point cloud data of these structures were captured using reverse engineering technique and compared with the designed CAD (computer-aided design) model. A 3D white light scanner (Steinbichler, Comet 5 1.4 M) was used for the reverse engineering. The cross-sectional view of the point cloud data and CAD showed that employing axial-ultrasonic vibration in milling process improved its machining accuracy.

12.2 Design and Fabrication of Experimental Setup and Design of Experiments

In order to perform the UAM with axial vibration, an experimental setup was designed and fabricated. The setup consisted of an ultrasonic vibration-assisted milling assembly, which can be mounted on the head of CNC (computer numerical control) milling machine. The assembly consisted of four major components as given in Table 12.1.

Brass provided rigidity to the horn and metalon provided electric insulation. Copper rings provided on the collar were for electric connection to supply power to piezoelectric crystal. The schematic diagram and actual photo of the designed and

Table 12.1 Description of all the major components of ultrasonic vibration-assisted milling assembly [20]

Component of the assembly	Material of the component	Purpose
Collar	Metalon	Acts as an attachment between casing and collet
Casing	Brass	Acts as an attachment between collar and tool
Tool	HSS	Acts as a apart of the horn and performs cutting
Horn assembly	AISI 316	Generates and transmits vibration to the tool through horn

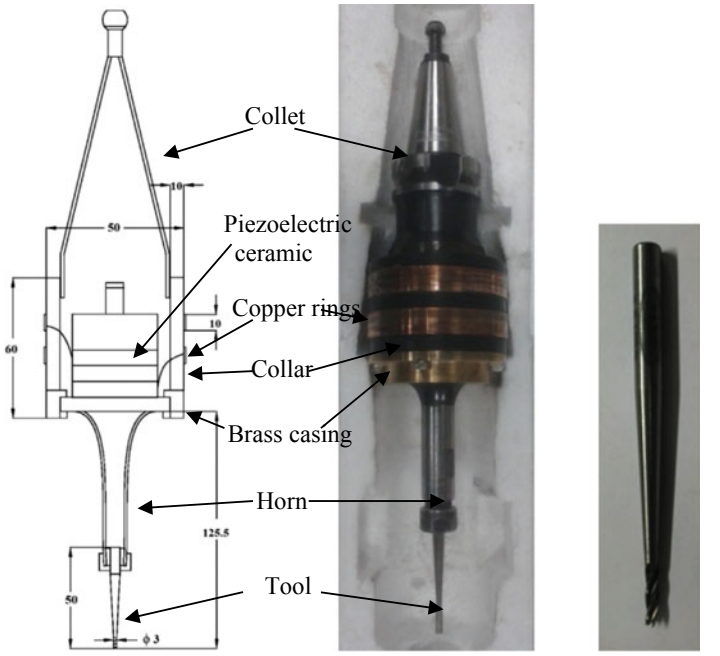

(a) Schematic diagram (b) Actual assembly (c) Milling tool

Fig. 12.1 Ultrasonic horn and tool assembly for end milling [20, 21]

fabricated assembly to perform ultrasonic vibration-assisted milling are shown in Fig. 12.1 [20, 21].

The experimental setup for ultrasonic vibration-assisted milling mainly consisted of the designed UAM assembly and three-axis vertical CNC milling machine. UAM assembly was mounted on the head of CNC milling machine (Hytech CNC machines) with carbon brush arrangement for the power supply. Workpiece was rigidly mounted on the CNC work table with the help of vice. Figure 12.2 shows the designed experimental setup for UAM. Workpieces (of size $70 \times 50 \times 10$ mm^3) used in the experiments were prepared from the same billet (made of Al6063 aluminum alloy) to avoid any error due to difference in material properties. Also, the experiments were performed in the same ambience with fresh tool (Table 12.2) to minimize the errors.

Previous studies [22, 23] suggested that machining accuracy of thin-walled structure depended on the cutting forces and the structure stiffness. Therefore, to compare the machining accuracy of UAM and conventional milling (CM), optimal set of milling parameters (for lower cutting forces) were chosen. These optimized set of process parameters (Table 12.3) are based on the previous experimental results [21] (Fig. 12.3).

The ultrasonic power in all the UAM experiments was kept at 1200 W (20 μm amplitude). The tool path was planned in such a way that in final pass side milling with optimized machining parameter can be performed on the thin-walled structure.

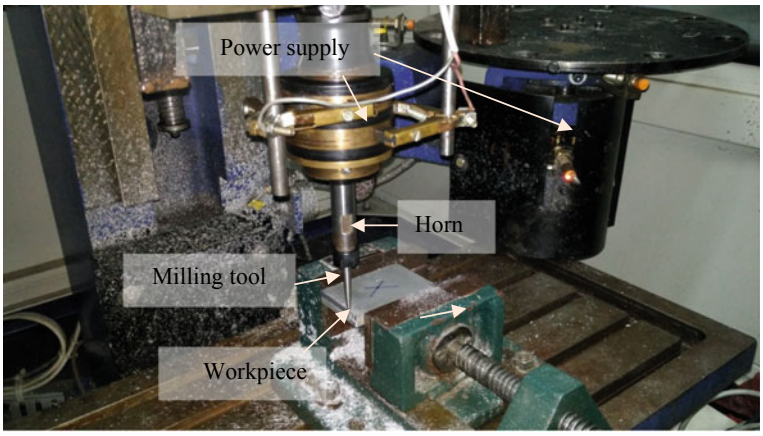

Fig. 12.2 Experimental setup for UAM

Table 12.2 Specification of the tool used in the experiments [20]

Tool material	Diameter (mm)	No. of tooth	Helix angle	Rake angle	Clearance angle
HSS	3	4	30^o	10^o	5^o

Table 12.3 UAM parameters used in the experiment

Rotational speed	Feed rate	Radial depth of cut
2625 RPM	10 mm/min	0.2 mm

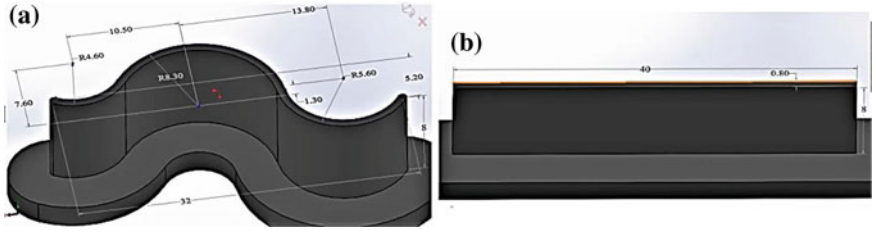

Fig. 12.3 CAD design of the thin-walled structure, **a** curved and **b** straight

In order to evaluate the effect of ultrasonic vibration assistance on the machining accuracy, two different types (straight and curved) of thin-walled structure were machined with and without the ultrasonic vibration assistance. After machining, burs and chips were removed from all the machined components for the measurements. Figure 12.4 shows the thin-walled structures machined by UAM and CM.

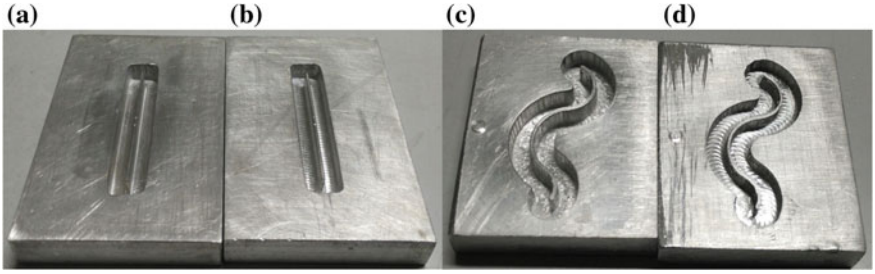

Fig. 12.4 Machined thin-walled structures: **a** straight structure machined with UAM, **b** straight structure machined with CM, **c** curved structure machined with UAM and **d** curved structure machined with CM

12.3 Measurement and Comparison

In order to measure the accuracy of the machined thin-walled structure, reverse engineering methodology was used. Reverse engineering refers to the process of creating the CAD model by acquiring the surface data (by using point cloud data) of an existing part using a scanning or measurement device. White light scanner (Steinbichler, COMET 5) (Fig. 12.5) was used for the reverse engineering in the present case. The obtained CAD models were further used for the inspection of the accuracy of the machined components.

By measuring the deviation of the machined components with respect to CAD model, the accuracy was compared. Polyworks®16 software was used for comparing the obtained point cloud data with the CAD (for G code generation) model. CAD and point cloud data were further superimposed on each other to evaluate the deviation. Furthermore, average deviation at the top and bottom sections was calculated from the sectioned view. Table 12.4 shows the average, maximum and minimum deviation obtained at the top and the bottom portion of both type of thin-walled structure

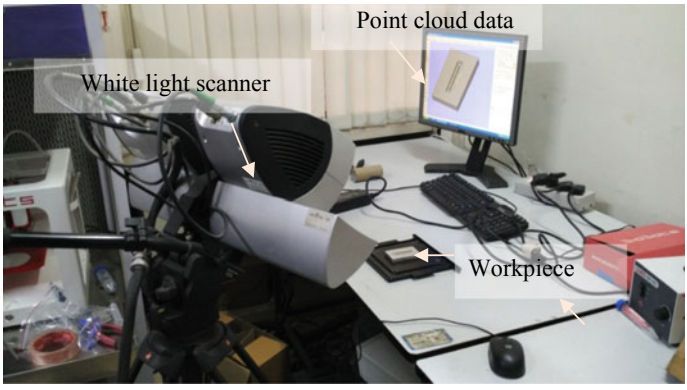

Fig. 12.5 Setup for reverse engineering

Table 12.4 Comparison of dimensions (all dimensions in mm)

	Straight (UAM)	Straight (CM)	Curved (UAM)	Curved (CM)
CAD dimension	0.8	0.8	0.8	0.8
Average measured dimension (at top)	0.862	0.885	0.832	0.848
Maximum measured dimension (at top)	0.867	0.893	0.838	0.856
Minimum measured dimension (at top)	0.856	0.878	0.828	0.842
Average measured dimension (at bottom)	0.792	0.790	0.788	0.787
Maximum measured dimension (at bottom)	0.790	0.788	0.786	0.785
Minimum measured dimension (at bottom)	0.793	0.792	0.790	0.788

machined by UAM and CM. It can be seen that the deviation in the thin-walled structure is higher at top as compared to the bottom. It is due to bending of thin-walled structure during machining, resulting in higher deviation at the top and lower deviation at the bottom [24]. It can also be observed from the results that deviation at the top is higher for straight thin-walled structure as compared to curved thin-walled structure (for both UAM and CM). Low rigidity of straight thin-walled structure caused more bending during machining and resulted in much thicker section at the top. However, at the bottom, the deviation is almost equal and it is very less as compared to deviations at the top section.

It can also be seen from the results that the deviations in the thin-walled produced by UAM are less as compared to those produced by CM. This is due to the lower average cutting forces in UAM which causes lesser deflection in thin-walled structure and milling tool during machining. As suggested by many researchers [10–12, 16, 21, 25], the lower cutting force in UAM is mainly due to intermittent cutting effect. From the previous theoretical studies [21, 25], it was found that cutting force in the UAM reduced up to 50% and it depended on the amplitude of vibration. However, in present condition an improvement of 33% in dimensional accuracy (in the case of curved structure) was achieved with application of ultrasonic vibrations (of 20 μm amplitude). Further, to obtain how deviation varies throughout the machined component, variation between point cloud data and CAD was mapped (Figs. 12.6a, b, 12.7a, b). Figures 12.6 and 12.7 show the comparison results (3D and cross section) for straight and curved thin-walled structure.

Figure 12.6a, b shows the mapped deviation in the straight thin-walled structure prepared by UAM and CM (gray color for prepared CAD and colored for STL from reverse engineering). Maximum and minimum deviation is also shown in Fig. 12.6c, e for UAM and Fig. 12.6d, f for CM. The result shows that in both the cases the deviation on the machined thin wall is the highest at the edge (93 μm for conventional milling and 67 μm for UAM) and lowest at middle portion (78 μm for conventional

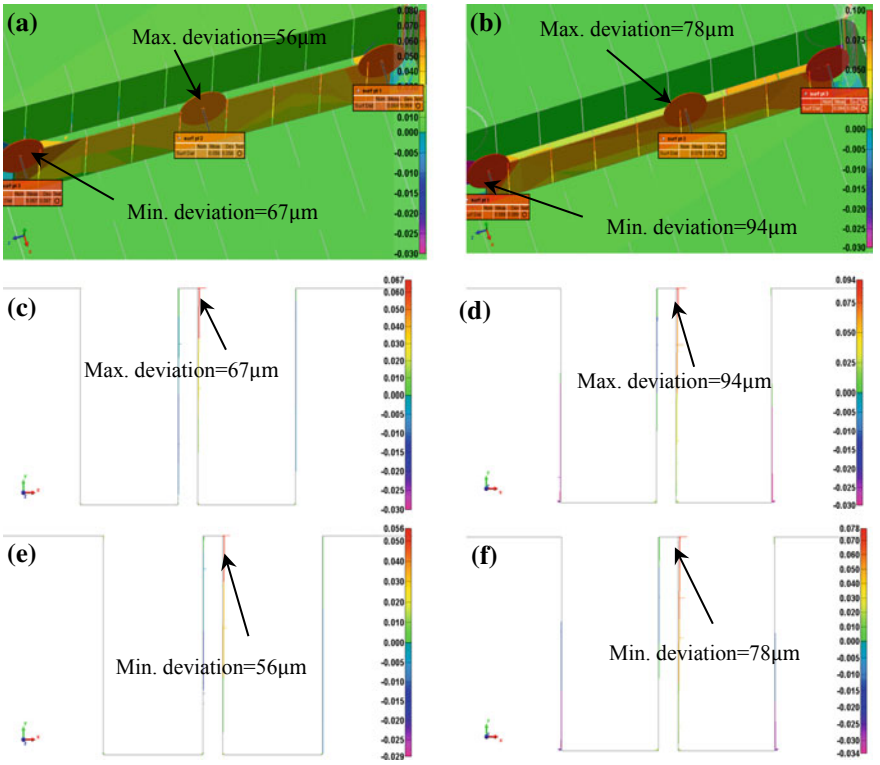

Fig. 12.6 Comparison results for straight thin-walled structure **a**. with UAM, **b**. with CM, **c**. max deviation at the edge with UAM, **d**. max deviation at the edge with CM, **e**. min at the middle with UAM, **f**. min at the middle with CM

milling and 56 µm for UAM). This is due to higher stiffness at the middle portion as compared to the edge which resulted in lower dimensional deviations at middle portion. However, due to lower rigidity at the edges thin wall is more susceptible to deformation. Therefore, reduction in milling forces (due to vibration assistance) has more effect at the edges which results in higher improvement in the dimensional accuracy.

Figure 12.7a, b shows the mapped deviation in the curved thin-walled structure prepared by UAM by CM. Maximum and minimum deviations are also shown in Fig. 12.7c, e for UAM and Fig. 12.7d, f for CM. It was also verified from the comparison of curved thin-wall structure that application of ultrasonic vibration resulted in lower deviations in the machined thin-walled structure. The result also shows that in both the cases the deviation is highest at the edge (56 µm for conventional milling and 38 µm for UAM) and lowest at middle portion (42 µm for conventional milling and 28 µm for UAM) similar to straight thin wall.

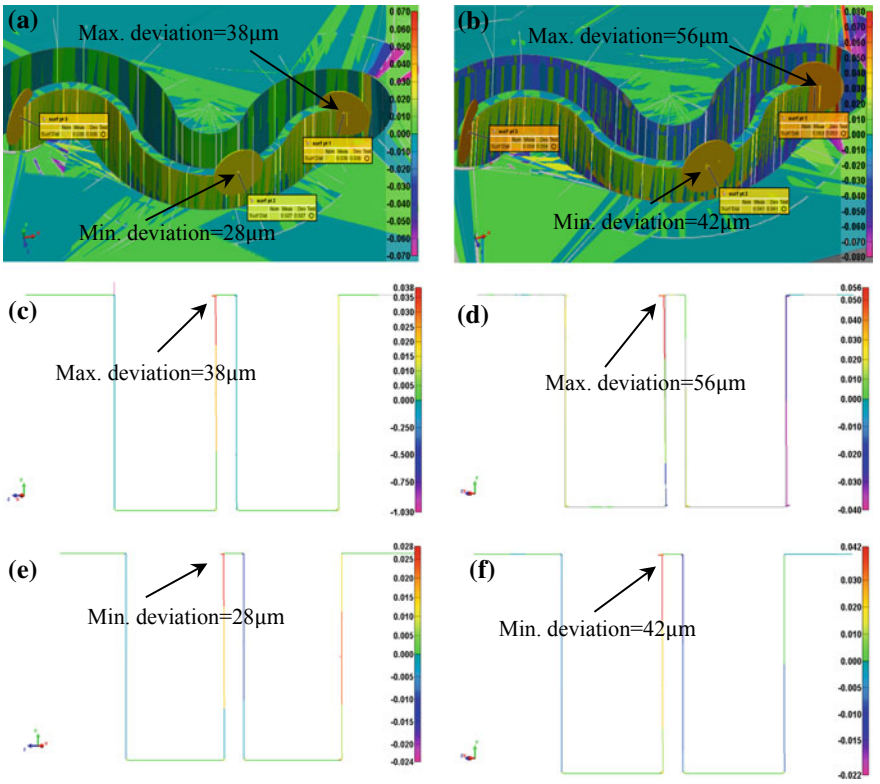

Fig. 12.7 Comparison results for curved thin-walled structure, **a**. with UAM, **b**. with CM, max deviation at the edge with UAM, **d**. max deviation at the edge with CM, **e**. min at the middle with UAM, **f**. min at the middle with CM

12.4 Conclusions

In this work, reverse engineering technique was used to compare the dimensional accuracy of milled thin-walled structures and has been found very effective in evaluating the machining accuracy. The machining accuracy of UAM is higher as compared to conventional milling, resulting in more accurate thin-walled structure. Maximum improvement of 33% in machining accuracy was achieved in case of curved thin-walled structure and is mainly due to ultrasonic-vibration assistance. The deviations at the bottom are lesser as compared to top portion and have insignificant effect of ultrasonic vibration assistance.

Acknowledgements Funding from the Engineering and Physical Sciences Research Council (UK) through grant EP/K028316/1 and Department of Science and Technology (India) through grant DST/RCUK/14-AM/2012 for project "Modeling of Advanced Materials for Simulation of Transformative Manufacturing Processes (MAST)" is gratefully acknowledged.

References

1. Wang, P., Zhang, S., Li, Z., Li, J.: Tool path planning and milling surface simulation for vehicle rear bumper mold. Adv. Mech. Eng. **8**, 1–10 (2016). https://doi.org/10.1177/1687814016641569
2. Ginting, A., Nouari, M.: Experimental and numerical studies on the performance of alloyed carbide tool in dry milling of aerospace material. Int. J. Mach. Tools Manuf. **46**, 758–768 (2006). https://doi.org/10.1016/j.ijmachtools.2005.07.035
3. Altintaş, Y., Budak, E.: Analytical prediction of stability lobes in milling. CIRP Ann. Manuf. Technol. **44**, 357–362 (1995). https://doi.org/10.1016/S0007-8506(07)62342-7
4. Quintana, G., Ciurana, J.: Chatter in machining processes: a review. Int. J. Mach. Tools Manuf. **51**, 363–376 (2011). https://doi.org/10.1016/j.ijmachtools.2011.01.001
5. Wang, Z.Y., Rajurkar, K.P.: Cryogenic machining of hard-to-cut materials. Wear **239**, 168–175 (2000). https://doi.org/10.1016/S0043-1648(99)00361-0
6. Huang, X., Zhang, X., Mou, H., Zhang, X., Ding, H.: The influence of cryogenic cooling on milling stability. J. Mater. Process. Technol. **214**, 3169–3178 (2014). https://doi.org/10.1016/j.jmatprotec.2014.07.023
7. Lee, P.H., Nam, J.S., Li, C., Lee, S.W.: An experimental study on micro-grinding process with nanofluid minimum quantity lubrication (MQL). Int. J. Precis. Eng. Manuf. **13**, 331–338 (2012). https://doi.org/10.1007/s12541-012-0042-2
8. Dhar, N.R., Ahmed, M.T., Islam, S.: An experimental investigation on effect of minimum quantity lubrication in machining AISI 1040 steel. Int. J. Mach. Tools Manuf. **47**, 748–753 (2007). https://doi.org/10.1016/j.ijmachtools.2006.09.017
9. Brehl, D.E., Dow, T.A.: Review of vibration-assisted machining. Precis. Eng. **32**, 153–172 (2008). https://doi.org/10.1016/j.precisioneng.2007.08.003
10. Razfar, M.R., Sarvi, P., Zarchi, M.M.: Experimental investigation of the surface roughness in ultrasonic-assisted milling, Proc. Inst. Mech. Eng. Part B: J. Eng. Manuf. **225**, 1615–1620 (2011). https://doi.org/10.1177/0954405411399331
11. Shen, X.H., Zhang, J.H., Li, H., Wang, J.J., Wang, X.C.: Ultrasonic vibration-assisted milling of aluminum alloy. Int. J. Adv. Manuf. Technol. **63**, 41–49 (2012). https://doi.org/10.1007/s00170-011-3882-5
12. Abootorabi Zarchi, M.M., Razfar, M.R., Abdullah, A.: Investigation of the effect of cutting speed and vibration amplitude on cutting forces in ultrasonic-assisted milling. Proc. Inst. Mech. Eng. Part B: J. Eng. Manuf. **226**, 1185–1191 (2012). https://doi.org/10.1177/0954405412439666
13. Abootorabi Zarchi, M.M., Razfar, M.R., Abdullah, A.: Influence of ultrasonic vibrations on side milling of AISI 420 stainless steel. Int. J. Adv. Manuf. Technol. **66**, 83–89 (2013). https://doi.org/10.1007/s00170-012-4307-9
14. Halim, N.F.H.A., Ascroft, H., Barnes, S.: Analysis of tool wear, cutting force, surface roughness and machining temperature during finishing operation of ultrasonic assisted milling (UAM) of carbon fibre reinforced plastic (CFRP). Procedia Eng. **184**, 185–191 (2017). https://doi.org/10.1016/j.proeng.2017.04.084
15. Uhlmann, E., Protz, F., Stawiszynski, B., Heidler, S.: Ultrasonic assisted milling of reinforced plastics. Procedia CIRP **66**, 164–168 (2017). https://doi.org/10.1016/j.procir.2017.03.278
16. Nath, C., Rahman, M.: Effect of machining parameters in ultrasonic vibration cutting. Int. J. Mach. Tools Manuf. **48**, 965–974 (2008). https://doi.org/10.1016/j.ijmachtools.2008.01.013
17. Ko, J.H., Tan, S.W.: Chatter marks reduction in meso-scale milling through ultrasonic vibration assistance parallel to tooling's axis. Int. J. Precis. Eng. Manuf. **14**, 17–22 (2013). https://doi.org/10.1007/s12541-013-0003-4
18. Ko, J.H., Shaw, K.C., Chua, H.K., Lin, R.M.: Cusp error reduction under high speed micro/meso-scale milling with ultrasonic vibration assistance. **12**, 15–20 (2011). https://doi.org/10.1007/s12541-011-0002-2

19. Li, K.-M., Wang, S.-L.: Effect of tool wear in ultrasonic vibration-assisted micro-milling. Proc. Inst. Mech. Eng. Part B: J. Eng. Manuf. **228**, 847–855 (2013). https://doi.org/10.1177/0954405413510514
20. Verma, G.C., Pandey, P.M.: Machining forces in ultrasonic-vibration assisted end milling. Ultrasonics **94**, 350–363 (2019). https://doi.org/10.1016/j.ultras.2018.07.004
21. Verma, G.C., Pandey, P.M., Dixit, U.S.: Modeling of static machining force in axial ultrasonic-vibration assisted milling considering acoustic softening. Int. J. Mech. Sci. **136**, 1–16 (2018). https://doi.org/10.1016/j.ijmecsci.2017.11.048
22. Budak, E.: Analytical models for high performance milling. Part I: Cutting forces, structural deformations and tolerance integrity. Int. J. Mach. Tools Manuf. **46**, 1478–1488 (2006). https://doi.org/10.1016/j.ijmachtools.2005.09.009
23. Kline, W.A., DeVor, R.E., Shareef, I.A.: The prediction of surface accuracy in end milling. J. Eng. Ind. **104**, 272 (1982). https://doi.org/10.1115/1.3185830
24. Ratchev, S., Liu, S., Huang, W., Becker, A.A.: Milling error prediction and compensation in machining of low-rigidity parts. Int. J. Mach. Tools Manuf. **44**, 1629–1641 (2004). https://doi.org/10.1016/j.ijmachtools.2004.06.001
25. Verma, G.C., Pandey, P.M., Dixit, U.S.: Estimation of workpiece-temperature during ultrasonic-vibration assisted milling considering acoustic softening. Int. J. Mech. Sci. **140**, 547–556 (2018). https://doi.org/10.1016/j.ijmecsci.2018.03.034

Chapter 13
High-Speed Conduction-Mode Micro-Laser Welding of Thin SS-304 Sheets: Modeling and Experimental Validation

S. Patel, A. Aggrawal, A. Kumar and V. K. Jain

Abstract In this work, an experimental investigation has been carried out to identify the set of process parameters that leads to the formation of conduction-type micro-welds in thin SS-304 sheets. Thereafter, a 3-D computational model has been developed to understand the process physics in-depth and to clarify the influence of various process parameters on the weld bead profile quantitatively. The phenomena of heat transfer, fluid flow, melting and solidification are incorporated into the model. The model is used to describe the thermo-fluid behavior (temperature and velocity field) and the melt pool characteristics. The simulated weld pool geometry agreed well with the corresponding experimental observations. The developed computational model can be effectively used to quantify the influence of different processing conditions in conduction-mode micro-laser welding and to develop a process map.

Keywords Micro-laser welding · High scanning speed · Conduction mode

13.1 Introduction

Laser micro-welding is a joining technique by fusion of micro-parts or micro-features using precisely controlled minimal laser beam energy. The continuous miniaturization of systems and devices with cost reduction, reliability, high controllability, less distortion and repeatability, and better performance creates difficulties and challenges to the welding of micro-parts. Thus, the laser micro-welding is widely used in microelectronics, medical, aerospace, defense, packaging and interconnection in micro-electro-mechanical systems (MEMS), where mechanical, electrical and optical components are connected and coupled [1, 2].

S. Patel · A. Aggrawal · A. Kumar (✉)
Department of Mechanical Engineering, Indian Institute of Technology Kanpur, Kanpur 208016, India
e-mail: arvindkr@iitk.ac.in

V. K. Jain
Mechanical Engineering Department, M.A.N.I.T, Bhopal, India

M. S. Shunmugam and M. Kanthababu (eds.), *Advances in Micro and Nano Manufacturing and Surface Engineering*, Lecture Notes on Multidisciplinary Industrial Engineering,
https://doi.org/10.1007/978-981-32-9425-7_13

Several computational as well as experimental works have been reported to investigate the high-speed laser micro-welding. Okamoto et al. (2008) reported that a small focus diameter beam produces a good welding seam without pulse control. They also found that narrow welding region can be obtained with large focus diameter using high scanning laser beam speed for thin stainless sheet [3]. Ascari et al. (2017) explained that the peak pulse power is a highest influencing process parameter on penetration depth and width of a weld bead of commercially pure titanium thin sheets. Therefore, to attain good weld morphology, the peak pulse power should be relatively low and the depth of penetration can be achieved by averaging high pulse durations [4]. Caiazzo et al. (2013) have done the experimental analysis of butt laser welding of thin aluminum alloy sheet to evaluate the mechanical and geometrical features of laser welding [5]. Baruah and Bag (2017) investigated the effect of laser pulse parameters of butt welding of 500-μm titanium alloy by experimental and thermo-mechanical finite-element numerical modeling. They also explained that an increase of heat input increases distortion of weld joint due to more amount of heat available at a particular area, and also the hardness of fusion zone is very high due to the formation of fine martensitic structure [6]. Ismail et al. (2012) investigated experimentally and numerically that the controlling of pulse wave form of laser heat source produces good weld joint without defect, which increases the shear strength. They also observed that the zinc present in the brass evaporates easily and forms porosity in the weld using rectangular pulse waveform of laser beam during micro-welding of thin copper circuit and thick brass electrode [7]. Rohde et al. (2010) attempted to control aspect ratio and quality of the weld pool using laser beam-shaped pulse on two different aluminum alloy foils using numerical model and experimental data [8]. He et al. (2005) numerically predicted the evolution of temperature and velocity fields, weld thermal cycles, weld pool geometry and many weld parameters during spot and linear laser micro-welding of stainless steel 304 (SS-304) using three-dimensional heat transfer and fluid flow model [9]. Hozoorbakhsh et al. (2016) developed a three-dimensional computational fluid dynamics model to investigate the thermal and fluid flow phenomena of a weld pool in laser micro-welding [10].

In spite of the fact that post-build microstructural and mechanical characterization of the welded sample gives an adequate measure of data about the weld quality, but real-time data of melt pool dimension, thermal and fluid behavior are difficult to get. Additionally, by advanced technique (such as pyrometer or infrared cameras) real-time monitoring is difficult as the high-speed micro-welding process is localized (<200 μm melt pool dimension), transient (<5 m/s traversal velocity) and due to rapid solidification (>105 K/s cooling rate) [11]. Therefore, a different approach such as mathematical modeling along with experiments is a better way to understand high-speed micro-laser welding process, effect of the process parameters and process optimization.

In this study, a transient three-dimensional simulation of high-speed conduction-mode micro-laser welding for stainless steel 304 has been performed. The objective is to develop a computational model that can be effectively used to understand the thermo-fluidic transport phenomenon and to quantify the influence of different processing conditions in conduction-mode micro-laser welding. The effect of Marangoni

Table 13.1 Process parameters used in experiments

Parameter	Value
Laser spot diameter (μm)	50
Laser power (W)	50
SS304 sheet thickness (μm)	100
Scanning speed (mm s^{-1})	1000, 1200, 1400, 1600

convection on melt pool thermal behavior, flow dynamics and geometry is described. For validation of the model, a comparison of melt pool shape and dimensions under various processing conditions is made with the in-house experimental results.

13.2 Experimental Procedure

Experiments were performed on a SS-304 sheet having thickness of 100 μm using a 50 W single-mode continuous-wave Yb:YAG fiber laser. The 1070 nm wavelength laser beam has been delivered by the optical fiber and focused by an f-θ lens to a focus diameter of 50 μm. The high-speed laser traversal has been achieved by a galvano scanner. The experiments have been carried out in shielding atmosphere of argon gas. Varying combination of power and scanning speed was considered in the experiments. Parameters used during the experiments are listed in Table 13.1.

After the micro-laser welding, the cross-section and top of the samples were prepared using the standard metallographic polishing method and then etched in aqua regia before performing the optical microscopy.

13.3 Model Description

A three-dimensional finite-element heat transfer and fluid flow model is developed to study the transport phenomenon in the high-speed micro-laser welding process. The model was implemented using COMSOL Multiphysics™ software. The schematic and dimensions of the computational domain are given in Fig. 13.1. In this case, the laser beam travels in positive X direction. Only half-domain was simulated to reduce the computational cost because of symmetry in the x–z plane. The process parameters used for the simulation of welding stainless steel 304 workpiece are given in Table 13.1, and the thermo-physical properties of stainless steel 304 workpiece are given in Table 13.2.

The following assumptions were made in the model:

(1) Incompressible and laminar flow was considered in the melt pool.
(2) Vaporization was not considered as evaporation temperature for SS304 is very high and it was not reached in many cases.

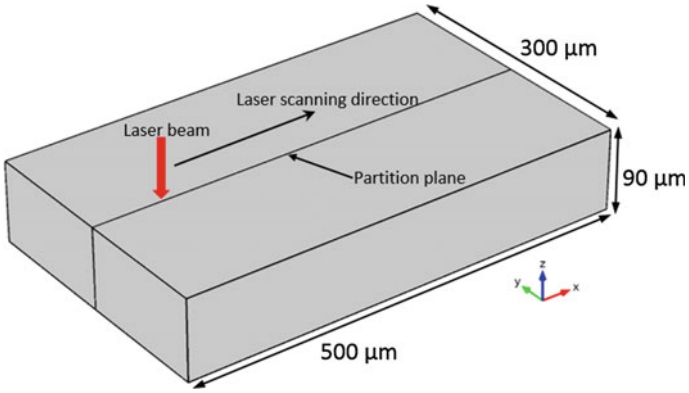

Fig. 13.1 Schematic of computational domain

Table 13.2 Thermophysical properties of stainless steel 304 [9]

Liquidus temperature (K)	1727
Solidus temperature (K)	1697
Solid specific heat (J kg^{-1} K^{-1})	711.8
Liquid specific heat (J kg^{-1} K^{-1})	837.4
Solid thermal conductivity (W m^{-1} K^{-1})	19.63
Liquid thermal conductivity (W m^{-1} K^{-1})	167.5
Density (kg m^{-3})	7200
Latent heat of fusion (kJ K^{-1})	246
Dynamic viscosity (N m^{-1} s^{-1})	0.06
Thermal expansion coefficient (K^{-1})	1.96×10^{-5}
Surface tension coefficient (N m^{-1} K^{-1})	-0.43×10^{-3}
Absorptivity	0.27

(3) The thermo-physical properties of SS304 are considered as constant with different values for solid and liquid phases.

13.3.1 Governing Transport Equations

Mass Conservation. The continuity equation is given by:

$$\nabla \cdot (\vec{u}) = 0 \tag{13.1}$$

where $\vec{u}$ is the velocity vector.

Energy Conservation. The energy conservation equation is given by:

$$\frac{\partial(\rho C_P T)}{\partial t} + \vec{u} \cdot \nabla(\rho C_p T) = \nabla \cdot (K \nabla T) - \rho L \frac{\partial f_l}{\partial t} \tag{13.2}$$

where T denotes the temperature, t denotes the time, K denotes the thermal conductivity, C_p denotes the heat capacity of the material, ρ denotes the density, L denotes latent heat and f_l represents liquid fraction.

Momentum Conservation. The momentum conservation equation is given by

$$\frac{\partial(\rho \vec{u})}{\partial t} + \vec{u} \cdot \nabla(\rho \vec{u}) = -\nabla p + \nabla \cdot (\mu\left(\nabla \vec{u} + (\nabla \vec{u})^T\right) + \overrightarrow{F_T} + \overrightarrow{F_N} \tag{13.3}$$

The source term $\overrightarrow{F_T}$ in Eq. (13.3) brings down the velocity of un-melted solid zone to zero, according to the Carman-Kozeny equation for flow through the porous media, and it is defined by Eq. (13.4).

$$\overrightarrow{F_T} = \frac{(1 - f_l)^2}{f_l^3 + c} B \vec{u} \tag{13.4}$$

The value of mushy zone constant B in Eq. (13.5) of current model is 100,000 kg m^{-3} s^{-1}. The term c is a constant with very small value to prevent division by zero when liquid fraction f_l becomes zero. Liquid fraction f_l is defined as

$$f_l = \begin{pmatrix} 0 & T < T_{solidus} \\ \frac{T - T_{solidus}}{T_{liquidus} - T_{solidus}} & T_{solidus} \leq T < T_{liquidus} \\ 1 & T \geq T_{liquidus} \end{pmatrix} \tag{13.5}$$

where $T_{solidus}$ and $T_{liquidus}$ represent solidus and liquidus temperature, respectively.

Natural Convection. The thermo-buoyant flow is included in this model according to Boussinesq approximation. The source term $\overrightarrow{F_N}$ in Eq. (13.3) is given as

$$\overrightarrow{F_N} = \rho_{liq} \vec{g} \beta (T - T_{ref}) \tag{13.6}$$

where $\rho_{liq,}$ β and T_{ref} are density of liquid, coefficient of thermal expansion and reference temperature, respectively.

Marangoni Convection. The shear force on the top surface because of surface tension gradient induces the Marangoni convection, which is defined by following equations.

$$\tau_{xz} = -\mu\left(\frac{\partial u}{\partial z}\right) = \left(\frac{\partial \gamma}{\partial T}\right)\left(\frac{\partial T}{\partial x}\right) \tag{13.7}$$

$$\tau_{yz} = -\mu\left(\frac{\partial v}{\partial z}\right) = \left(\frac{\partial \gamma}{\partial T}\right)\left(\frac{\partial T}{\partial y}\right) \tag{13.8}$$

where μ and γ are viscosity and surface tension, respectively.

13.3.2 Boundary and Initial Conditions

At the top surface of the substrate, the laser heat energy is approximated by a Gaussian distribution and the heat flux (W m^{-2}) due to the laser beam is given by the following expression:

$$q = \frac{2\eta P}{\pi R_o^2} e^{\left(-2\left((x-Vt)^2+(y)^2\right)/R_o^2\right)} \tag{13.9}$$

where q is the input heat flux, η is the absorptivity, P is the power of laser beam, V is the laser scanning speed, t is the time and R_o is the laser spot radius.

The heat energy balance at the top surface leads to the following boundary condition:

$$K\frac{\partial T}{\partial n} = q - h(T - T_a) - \varepsilon\sigma\left(T^4 - T_a^4\right) \tag{13.10}$$

where the value of convective heat transfer coefficient, $h = 10$, the value of emissivity, $\varepsilon = 0.45$, σ is the Stefan–Boltzmann constant and T_a is ambient temperature.

The right-hand side terms of Eq. (13.10) are heat flux from the laser beam, convective heat loss and radiation heat loss to the surroundings, respectively. The symmetric plane and the bottom side, as shown in Fig. 13.1, were modeled as thermally insulated wall and the other vertical sides of the computational domain were modeled as convective heat loss. Initially, the whole domain was at the ambient temperature of 300 K and zero velocity.

13.3.3 Numerical Implementation

The mathematical model is simulated using finite-element analysis software COMSOL Multiphysics™. In this case, the entire domain is divided into three subdomains. The continuity and momentum conservation equations are solved only in the melt pool sub-domain in order to keep the computational cost as low as possible. The whole domain is meshed with free tetrahedral element. Melt pool sub-domain is meshed finely (max. size 6.16 μm, min. size 1.16 μm and total element 68,375) in order to obtain accurate results of melt pool evolution. To minimize the computational cost, the remaining domains are meshed with coarse elements (max. size

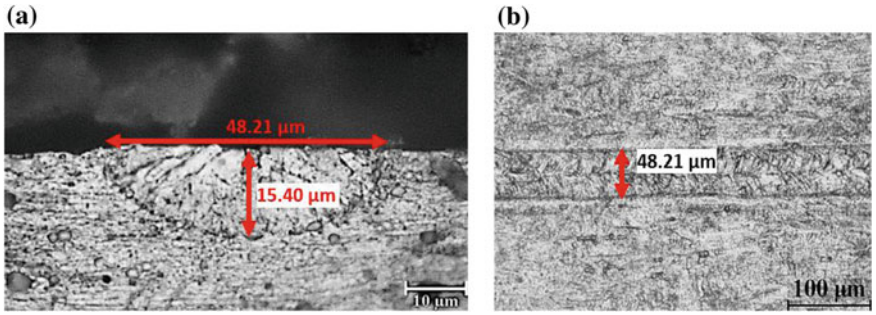

Fig. 13.2 Experimental result of melt pool for $P = 50$ W, **a** cross-section view and **b** top view

250 µm, min. size 35 µm and total element 26,365). The effect of elements size on the computational results is performed by running test simulations for different mesh size for the case of laser power, P = 50 W. However, a decrease in the element size required enormous increase in the computational time.

A workstation with 8 × 3.50 GHz Intel Xeon processor with 32 GB RAM was used for running the simulations. The time step used in the simulation was 0.001 ms. For each time step, continuity, momentum and energy transport equations were solved.

13.4 Results and Discussion

13.4.1 Experimental Results

The laser micro-welded SS-304 sheets were prepared using standard polishing technique and then etched in Aqua regia very carefully. Figures 13.2a and 13.2b show the cross-sectional and top view of melt pool, respectively. The welded regime is clearly evident from the etched specimen. It can be clearly observed from Fig. 13.2a that the melt pool shape is wider and shallower, which confirms the conduction-mode laser micro-welding. Also, it can be observed that the grain growth is toward the center of melt pool because of heat which is diffusing opposite to the grain growth.

13.4.2 Modeling Results

Figure 13.3 shows the simulated fluid flow pattern of the molten metal at t = 0.17 ms at laser power scanning speed of 1000 mm/s. The maximum velocity was observed along the free surface, which tends to pull the molten metal from center to outward of the melt pool. This is due to the temperature gradient present inside the melt pool which causes a surface tension-driven flow, often called thermo-capillary fluid flow

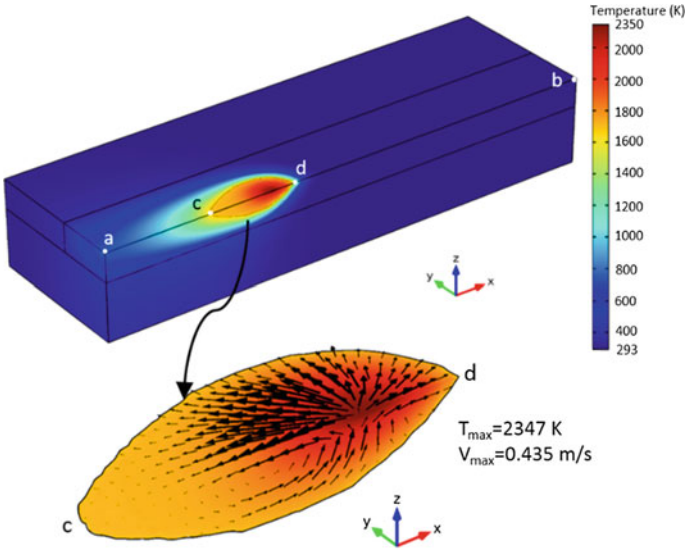

Fig. 13.3 Temperature field and flow field in the melt pool for $P = 50$ W at $t = 0.17$ ms

(or Marangoni convection). This flow is from a region having low surface tension (high temperature region at the center) to regions having high surface tension (low temperature regions in the outward direction). This Marangoni convection tends to recirculate the flow within melt pool. The velocity magnitude of this recirculating flow within the melt pool is of the order of 0.434 m/s, which is quite significant. A shallow melt pool geometry is formed as a result of liquid melt displacement caused due to high surface velocity in the melt pool. This flow is more responsible for increasing the width than the depth of the melt pool because it is confined close to the top free surface and not toward the deeper portion of the melt pool. A large portion of the melt pool region exhibited negligible velocity. The melt pool width and depth were 49.768 and 15.345 μm, respectively.

Figure 13.4 shows the temperature variation between the points a and b shown in Fig. 13.3. It can be observed that there is large a variation of temperature along the line ab. The maximum thermal variation is between melt pool zone c–d, because of phase change and fluid flow zone. Right behind the center of the melt pool, a strong outward fluid flow (just before the end of the melt pool) is built up driven by the Marangoni shear stress. The temperature gradient in the rear part of the melt pool is relatively low. Therefore, the convection is negligible in the tail portion of the melt pool.

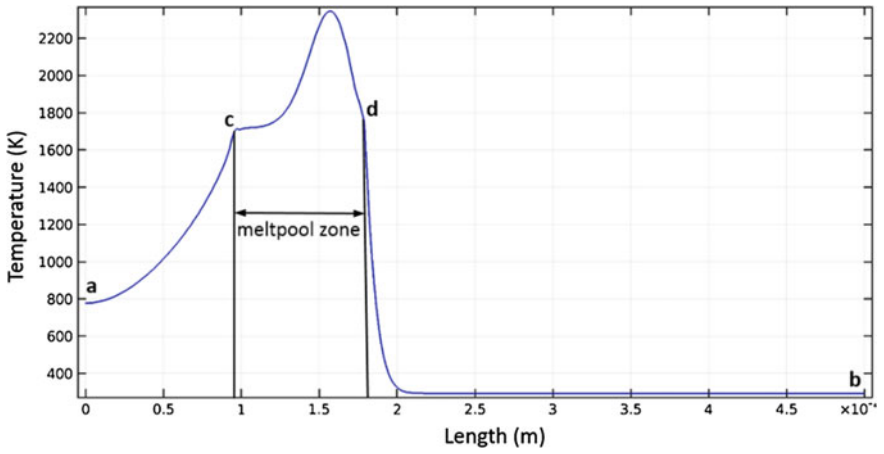

Fig. 13.4 Temperature plot along the line *ab* shown in Fig. 13.3 for $P = 50$ W

13.4.3 Model Validation

Weld pool geometry in cross-sectional view obtained from the developed numerical model of conduction mode continuous laser welding is compared with an in-house experimental observation as shown in Fig. 13.5. The shape and size of cross-sectional view of the computed melt pool geometry by numerical model is in well agreement with the experimental result. The simulation result is taken at 170 μs after fully developed melt pool.

The melt pool geometry obtained from the developed transient numerical model for different welding conditions is compared with the in-house experimental work, and the result is shown in Fig. 13.6. The width and depth of the numerically simulated melt pool geometry are in well agreement with the experimental results, thus validating the present numerical model. The experimental and numerical results confirm

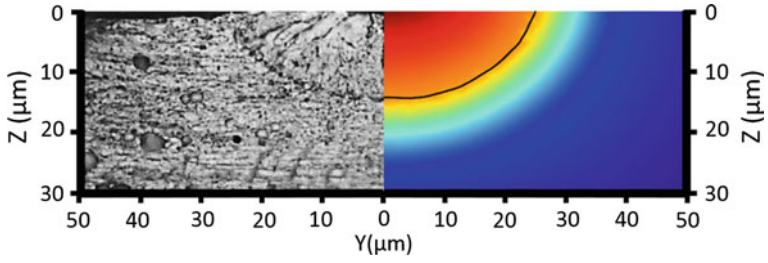

Fig. 13.5 Comparison of melt pool geometry in the cross-sectional view as estimated from numerically predicted solidus isotherm in the temperature map and experimentally measured weld micrograph at laser power. Process conditions: $P = 50$ W, time, $t = 170$ μs, laser beam spot radius, $r_0 = 25$ μm and laser scanning speed 1000 mm/s

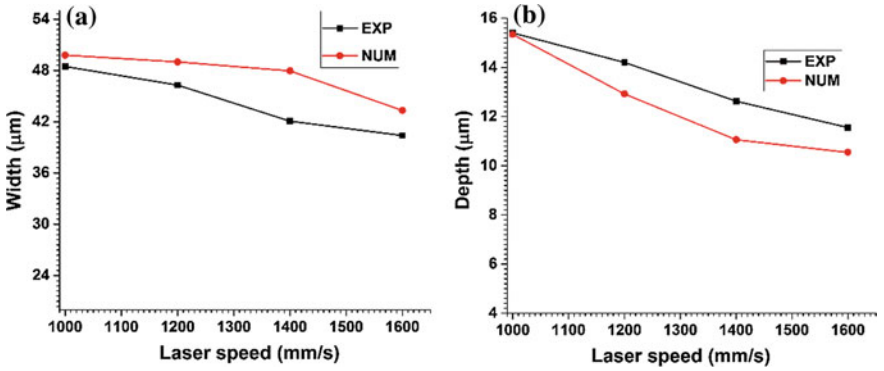

Fig. 13.6 Comparison experimental and simulated results with reference to **a** melt pool width, **b** melt pool depth, with laser speed at laser power, $P = 50$ W

that the wide and shallow melt pool geometry evolves for the considered process parameters and thermo-physical properties of SS-304. This is because of the negative value of surface tension coefficient, causing the outward fluid flow of molten metal near the top surface in the melt pool. It is also suggested from Fig. 13.6 that the melt pool width and depth decrease with an increase of laser scanning speed due to the decrease of laser–matter interaction time.

The experiments were performed on a SS304 sheet having thickness 100 μm using a 50 W single-mode continuous wave Yb:YAG fiber laser of 1070 nm wavelength, for different scanning speed. The focused laser beam spot radius 25 μm has been selected to avoid the vaporization of the workpiece during experimentation. The melt pool geometry (shape and size) has been measured using Nikon eclipse LV100 optical microscope after the standard polishing technique and then carefully etching of samples in Aqua regia.

Table 13.3 shows a comparison of experimentally measured and numerically predicted melt pool dimensions for different welding parameter. The comparison shows that the present numerical model is able to calculate the melt pool geometry accurately, thus validating the present numerical model for continuous laser micro-welding. Thus, the current numerical simulation is capable of predicting the weld characteristics for continuous laser micro-welding.

Figure 13.7 shows a plot of the maximum temperature and the maximum velocity in the melt pool for different laser scanning speeds for the laser beam of 50 W. The result is shown at $t = 0.17$ ms when the melt pool achieved a quasi-static state in its shape and size. It can be seen that the maximum temperature and maximum velocity in the melt pool decreases almost linearly with increase in the laser scanning speed within the prescribed range. This is because as the laser scanning speed increases the laser–matter interaction time decreases resulting in less thermal energy absorption by the workpiece. Similarly, the variation in melt pool half-width and depth of penetration with the laser scanning speed is presented in Table 13.3. For a constant laser beam radius of 25 μm and laser power of 50 W, the size of the melt pool

Table 13.3 Comparison of melt pool dimensions obtained from experiments and numerical model for continuous laser micro-welding

Process parameters P = 50 W, R_o= 25 μm, t = 0.17 ms,	Half-width (Expt), W_{Expt} (μm)	Half-width (Num), W_{Num} (μm)	$\frac{W_{Expt}-W_{Num}}{W_{Expt}}$ (%), difference	Depth of penetration (Expt), D_{Expt} (μm)	Depth of penetration (Num), D_{Num} (μm)	$\frac{D_{Expt}-D_{Num}}{D_{Expt}}$ (%), difference
Scanning speed = 1000 mm/s	24.10	24.88	−3.2	15.40	15.35	0.32
Scanning speed = 1200 mm/s	22.05	24.5	−11.11	14.20	12.92	9.01
Scanning speed = 1400 mm/s	21	23.98	−14.19	12.62	11.06	12.36
Scanning speed = 1600 mm/s	19.55	21.66	−10.79	11.55	10.54	8.74

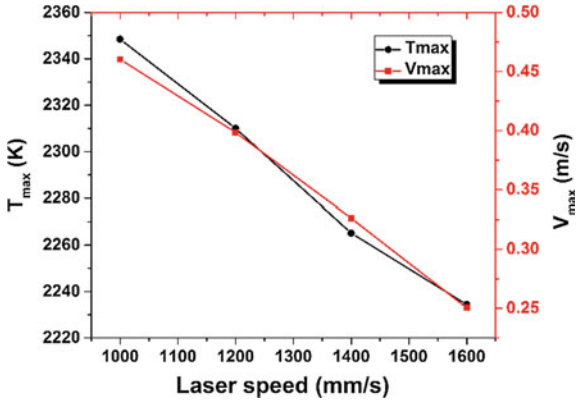

Fig. 13.7 Variation of maximum temperature and maximum velocity in the melt pool with the laser scanning speed

width and depth decreases with the increases of laser scanning speed from 1000 to 1600 mm/s. Thus, these results suggest that there is a strong dependency of the melt pool geometry on laser scanning speed.

13.5 Conclusions

A three-dimensional computational FEM model has been developed for simulating the transport phenomenon associated with the conduction-mode continuous laser micro-welding process. In this model, phase change thermodynamics, heat transfer and fluid flow have been implemented to predict the thermo-fluidic behavior of the melt pool with the help of thermal and velocity fields. From the experimental results, it can be observed that the grain growth is toward the center of the melt pool. The melt pool configuration obtained from the numerical simulation for the continuous laser welding shows a good degree of consistency compared to its respective experimentally obtained values for various welding conditions. By performing a quantitative analysis on the reported half-width and penetration depth, a maximum of 14.19 and 12.36% deviation was obtained. This further conforms to the consistency of the reported numerical model. It was also observed that the maximum velocity in the melt pool is present at the top surface and away from the center of laser beam spot. The maximum temperature and maximum velocity in the melt pool increases almost linearly when the laser scanning speed decreases. It was found that Marangoni convection was a dominant factor causing fluid flow, which in turn influences the melt pool geometry and the maximum temperature in the melt pool.

References

1. Jain, V.K., Dixit, U.S., Paul, C.P., Kumar, A.: Micromanufacturing: a review—part II. Proc. Inst. Mech. Eng., Part B: J. Eng. Manuf. **228**(9), 995–1014 (2014)
2. Sluzalec, A.: Thermal effects in laser microwelding. Comp. Struct. **25**(1), 29–34 (1987)
3. Caiazzo, F., Alfieri, V., Cardaropoli, F., Sergi, V.: Butt autogenous laser welding of AA 2024 aluminium alloy thin sheets with a Yb: YAG disk laser. Int. J. Adv. Manuf. Technol. **67**(9–12), 2157–2169 (2013)
4. Ascari, A., Fortunato, A., Guerrini, G., Liverani, E., Lutey, A.: Long pulse laser micro welding of commercially pure titanium thin sheets. Procedia Eng. **184**, 274–283 (2017)
5. Okamoto, Y., Gillner, A., Olowinsky, A., Gedicke, J., Uno, Y.: Fine micro-welding of thin stainless steel sheet by high speed laser scanning. J. Laser Micro/Nanoeng. **3**(2), 95–99 (2008)
6. Baruah, M., Bag, S.: Influence of pulsation in thermo-mechanical analysis on laser micro-welding of Ti6Al4V alloy. Opt. Laser Technol. **90**, 40–51 (2017)
7. Ismail, M.I.S., Okamoto, Y., Okada, A., Uno, Y., Ueoka, K.: Direct micro-joining of flexible printed circuit and metal electrode by pulsed Nd: YAG laser. Int. J. Precis. Eng. Manuf. **13**(3), 321–329 (2012)
8. Rohde, M., Markert, C., Pfleging, W.: Laser micro-welding of aluminum alloys: experimental studies and numerical modeling. Int. J. Adv. Manuf. Technol. **50**(1–4), 207–215 (2010)
9. He, X., Elmer, J.W., DebRoy, T.: Heat transfer and fluid flow in laser microwelding. J. Appl. Phys. **97**(8), 084909 (2005)

10. Hozoorbakhsh, A., Ismail, M.I.S., Sarhan, A.A.D.M., Bahadoran, A., Aziz, N.B.A.: An investigation of heat transfer and fluid flow on laser micro-welding upon the thin stainless steel sheet (SUS304) using computational fluid dynamics (CFD). Int. Commun. Heat Mass Transfer **75**, 328–340 (2016)
11. Aggarwal, A., Kumar, A.: Particle scale modelling of selective laser melting-based additive manufacturing process using open-source CFD code OpenFOAM. Trans. Indian Inst. Met. **71**(11), 2813–2817 (2018)

Chapter 14
Surface Roughness Improvement by Removal of Recast Layer on Wire Electrical Discharge Machined Surface Through Abrasive Flow Finishing Machine

M. A. Manjunath, A. Murugan, Prakash Vinod and N. Balashanmugam

Abstract Wire electrode discharge machining (WEDM) is a widely accepted process for machining of precision and complex geometry. Generally the spark produced during the WEDM process on the workpiece surfaces forms a layer of recast. It is one of the challenging aspects to remove this recast layer from a complex surface. The present research investigates the removal of WEDM recast layer and surface roughness improvement on the components having internal complex geometry on stainless steel (SS 410) material. The study also explores the effect of abrasive flow finishing for multiple components by stacking parallel to each other for simultaneous finishing through suitable fixture. The featuring of WEDM machined surface before and after AFFM process is examined through scanning electron microscope (SEM). Additionally, EDS reveals the noticeable amount of electrode material deposited on the component, which is removed after AFFM. The improvement in the surface roughness has been also noticed through surface roughness tester, Form Talysurf.

Keywords EDM recast layer · Abrasive flow finishing machine (AFFM) · Surface roughness · SEM analysis · EDS

14.1 Introduction

Today, owing to the advancement in modern manufacturing sector, the requirement of better surface finish is an increasing demand. The surface integrity of WEDM process has a detrimental impact, as each spark melts a small portion of workpiece. A portion of these molten material yields gets flushed away, and the remaining material resolidifies to form a surface layer known as recast layer. These layers may

M. A. Manjunath (✉) · A. Murugan · P. Vinod · N. Balashanmugam
Nano Manufacturing Technology Centre, Central Manufacturing Technology Institute, Bangalore 560022, India
e-mail: manjunathma.cmti@gov.in

M. S. Shunmugam and M. Kanthababu (eds.), *Advances in Micro and Nano Manufacturing and Surface Engineering*, Lecture Notes on Multidisciplinary Industrial Engineering,
https://doi.org/10.1007/978-981-32-9425-7_14

contain an altered micro-structure, tensile stress, micro-cracks and impurities which adversely affect the performance of the component [1, 2].

The automation in finishing operation is always an advantage to achieve the process in reliable and economical way. Abrasive flow finishing technology is established for micro-/nano-finishing, deburring, radiusing and also for the removal of recast layer in wide range of applications. The AFFM can process many selected passages on a single workpiece or multiple parts simultaneously. Inaccessible areas and complex internal passages can be finished economically and productively. It reduces the surface roughness by 75–90% on cast machined or EDM surfaces [3]. The effects of AFFM process on various machined surfaces, like WEDM, milling, grinding and turning are seen in the surface roughness profile, where wire EDM surfaces are well suited for abrasive flow finishing. The result shows that medium viscosity considerably affected surface improvements while extrusion pressure did not have a major effect on this [4]. The precision micro-slit fabricated by WEDM is subsequently fine-finished by identifying optimal combination of AFFM parameters, and the surface is elucidated using SEM [5]. The obstacle to shape precision strictly restricts the development of EDM process in micro-manufacturing. The AFFM process has the potential to improve the shape precision and surface roughness of the micro-hole fabricated by EDM [6]. The EDM machine for tool steel component of 59HRC is successfully processed in AFFM to improve the surface roughness; the result proves that the AFFM process is also capable of inducing high-compressed residual stress to the machined surface [7]. The effect of WEDM surfaces is experimentally investigated, by mixing suitable material, that is, aluminium oxide and chromium powder with dielectric fluid. The decrease in the surface roughness is observed with the workpiece materials like tool steel, stainless steel and copper [8, 9]. The characteristics of WEDM surface for cylindrical jobs are evaluated using micro-hardness tester and SEM. The study explores the feasibility of removing thermal recast layers through magnetic abrasive finishing [10]. The quantification of normal and axial forces generated during abrasive flow finishing process through CFD technique. The material loss is evaluated theoretically and experimentally for varying pressure and grit sizes [11].

Several researchers have studied the AFFM process and other techniques to improve the surface quality by removal of recast layers. The present research investigates the effect of AFFM on wire electrode discharge machined internal gear components, to achieve nanometric surface finish. Abrasive flow finishing with sophisticated fixture design demonstrates the simultaneous finishing process for multiple components. The work evaluates the impact on surface roughness (Ra, Rt and Rz) with varying abrasive mesh size and selected AFFM process parameters. The improvements of surface roughness through removal of EDM recast layers is characterised utilising the equipments like SEM, EDS, Talysurf and micro-hardness tester.

Fig. 14.1 AFFM-150D setup

14.2 Experimental Work

14.2.1 Abrasive Flow Finishing Machine

An indigenously developed AFFM-150D at CMTI, Bangalore, as shown in Fig. 14.1, is used for the present experimentation. The process involves extruding an abrasive-filled semi-solid media through a workpiece passage. The machine hydraulically clamps the work-holding fixtures between two vertically opposed media cylinders. These cylinders extrude the media back and forth through the workpiece(s). Two cylinder strokes, one from the lower cylinder and another from the upper cylinder, make up one process cycle (Table 14.1).

14.2.2 Abrasive Polymer Media

An essential component in the abrasive flow finishing is the viscoelastic polymer media. Basically, the media consists of base material/carrier, abrasives and suitable

Table 14.1 Technical specification of AFFM-150D

Parameter	Value
Hydraulic clamping range	10–300 mm
Hydraulic pressure range	15–100 bar
Media cylinder bore diameter	150 mm
Media piston stroke	250 mm
Media	Viscoelastic abrasive laden polymer
Controller	PLC and HMI based

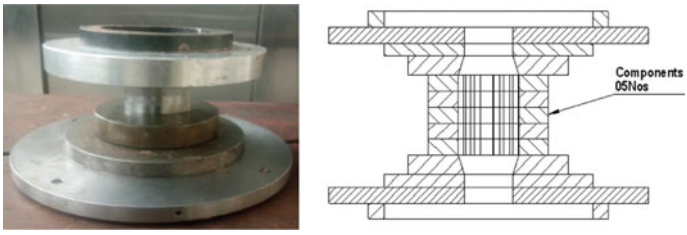

Fig. 14.2 Assembled fixture with components

additives. The present experimentation involves medium viscous polymer media with viscosity of 20,000 Pa-s. The concentration of media and abrasive is in the weight ratio of 1:1.

14.2.3 Work-Holding Fixture

The fixture is designed and fabricated to finish five components simultaneously in the AFFM process. The assembled fixture with the components to be finished is as shown in Fig. 14.2. Fixture directs the pressurised abrasive polymer media from abrasive flow finishing machine to the internal WEDM profile of the components where surface improvements are desired.

14.2.4 Component

The workpiece is of material stainless steel (SS-410) and has been pre-machined by wire electrical discharge machining. The material is machined for internal gears, as shown in Fig. 14.3. The overall dimension of the component is: length 75 mm, width 50 mm and thickness 10 mm. The surface roughness on WEDM surfaces is Ra = 1.529 μm, Rt = 13.597 μm and Rz = 11.637 μm.

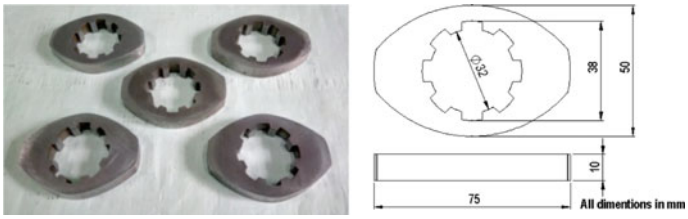

Fig. 14.3 Workpiece material

14.2.5 Experimental Procedure

The experiments were conducted on the internal surfaces of components pre-machined through WEDM process. The fixture is assembled along with the components in AFFM-150D. The machining and media parameter as mentioned in Table 14.2 is selected based on the successful results achieved in initial studies with AFFM-150D.

Initially, the characterisation of WEDM surface is conducted through Form Talysurf Series-2 (Taylor Hobson) for Ra, Rt and Rz. The recast layer thickness/surface topography and elemental study has been carried out using SEM (Carl Ziess, Neon-40) and EDS (Oxford Instruments, X-act). The hardness of the recast surface is also recorded using micro-hardness tester (Matsuzawa, MMT-X7B).

The cycle time is estimated using 60 mesh size abrasive media at 30 bar hydraulic pressure. The number of components is incremented from 1 to 5 numbers by stacking parallel to each other in the AFFM fixture to achieve best possible finish. The cycle time in minutes is recorded for individual increment in component numbers. The selected AFFM process parameters as per Table 14.2 with estimated cycle time is then used for different abrasive polymer media of SiC mesh size of 60, 220, 400 and 800 for simultaneous finishing of the components. The characterisation on AFFM finished surfaces is recorded and performed initially for comparative study.

Table 14.2 Technical specification of AFFM-150D

	Parameters	Value
Machine parameters	Hydraulic pressure	30 bar
	Stroke length	250 mm
	Media cylinder temperature	25 °C
Abrasive media	Viscosity	20,000 Pa-s
	Abrasive mesh size	60, 220, 400, 800

14.3 Results and Discussion

The increase in the number of components has influence on consumption of AFFM cycle. As the number of components increased up to five numbers by stacking parallel, the internal surface area to be finished also increased gradually. The time consumption of AFFM cycle is 15 min to achieve the uniform finish of Ra 0.585 μm from Ra 1.529 μm on the components of five numbers (Fig. 14.4).

The effect of varying abrasive media mesh size on surface roughness—Ra, Rt and Rz—is determined through AFFM experimental results (Table 14.3). Surface roughness was taken at different positions and directions at the surfaces of all five components, and the maximum recorded roughness values are considered.

The individual abrasive media mesh size has shown a predominant improvement on surface roughness. With increase in abrasive mesh size, the surface roughness decreases. The result indicates that surface roughness has improved apparently with selected hydraulic pressure and cycle time. The initial roughness of WEDM surface, Ra = 1.529 μm, Rt = 13.597 μm and Rz = 11.637 μm, has improved to Ra = 0.073, Rt = 0.944 and Rz = 0.375 after the completion of AFFM process uniformly in all five components.

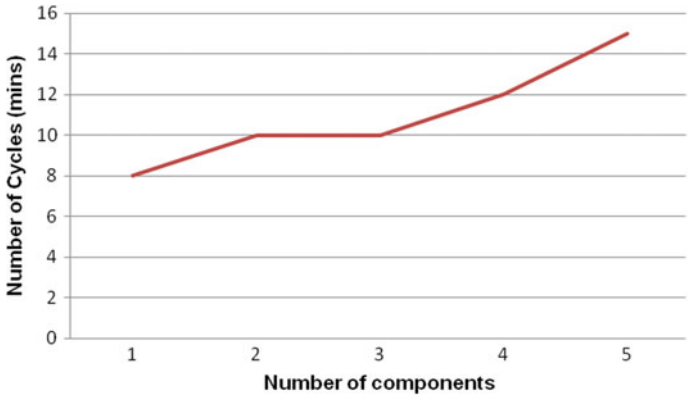

Fig. 14.4 Variations in the number of cycle, with number of components @60 mesh abrasive size and pressure of 30 bar

Table 14.3 AFFM experimental results

Hydraulic pressure (bar)	Abrasive media (mesh)	Cycle time (min)	Ra (μm)	Rt (μm)	Rz (μm)
30	60	15	0.585	5.668	4.382
	220	15	0.232	4.696	2.446
	400	15	0.180	2.273	1.154
	800	15	0.073	0.944	0.375

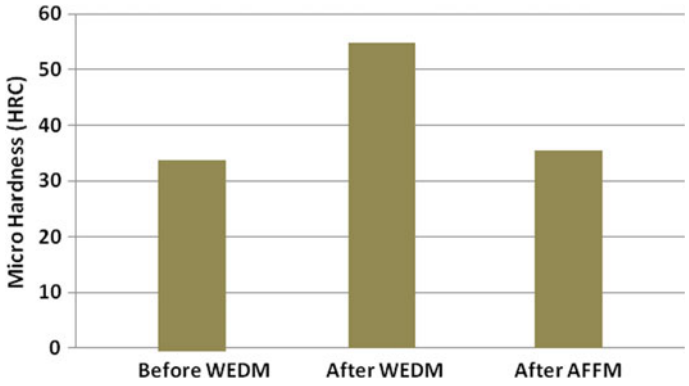

Fig. 14.5 Hardness of the surface at different stages

14.3.1 Micro-hardness Analysis

The surface hardness on the recast layers formed due to the WEDM process and after AFFM process is evaluated using micro-hardness tester, at Vickers hardness 100 g/s. It is observed that the hardness of the heat-affected zone of recast layer is high, compared to the hardness of the raw materials (Fig. 14.5). With the removal of react layer through AFFM process, the surface hardness decreased gradually.

14.3.2 Scanning Electron Microscopic Analysis

The surface morphology of WEDM surface and AFFM finished surface are analysed through comparative study of SEM images (Fig. 14.6).

The recast layer thickness can be visualised at cross-section of WEDM surface through proper sample preparation. Figure 14.6a indicates that the recast layer thickness is approximately around 13–15 μm at the machined surfaces of the component. The elimination of these recast layers after AFFM can be observed in Fig. 14.6b. The microstructures of a wire electrode discharge machined surface are complex and differ from that of the parent metal. At different magnification a large number of craters are observed in Fig. 14.6c, e. The flow path of abrasive media formed during the finishing is seen (Fig. 14.6d, f). It would seem that the abrasive flow finishing process can produce very fine finish over the rough WEDM surface.

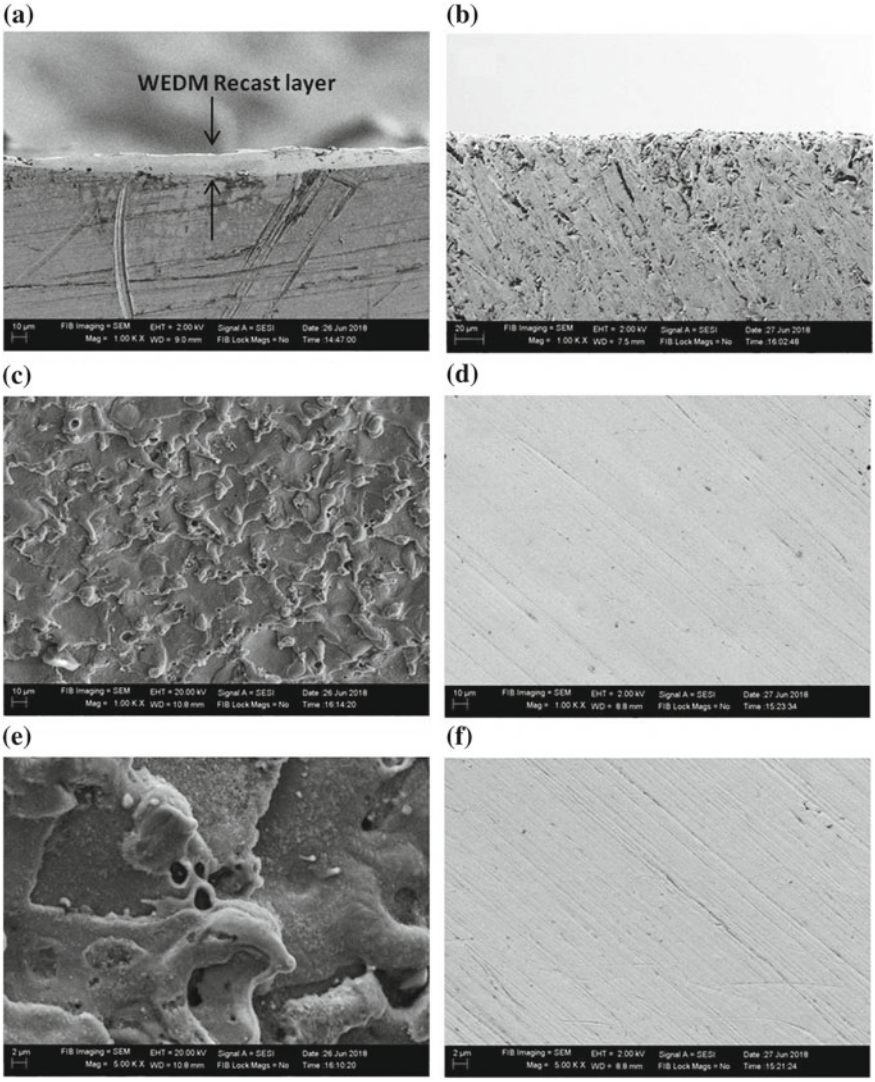

Fig. 14.6 **a** Cross-sectional view of WEDM recast layer. **b** Cross-sectional view of AFFM processed surface. **c** WEDM surface at 1000×. **d** AFFM finished surface at 1000×. **e** WEDM surface at 5000×. **f** AFFM finished surface at 5000×

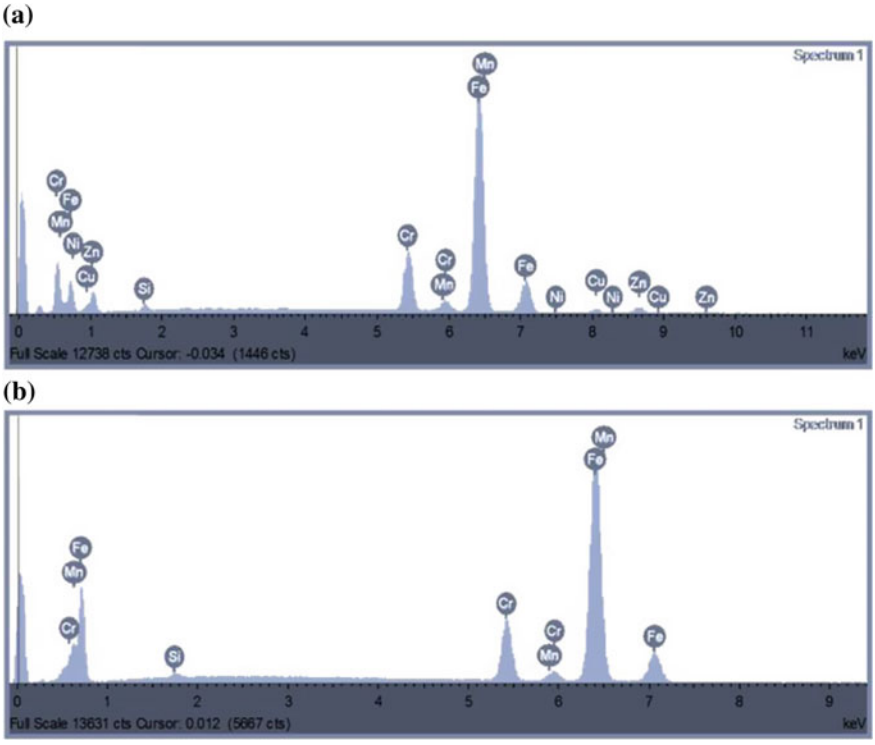

Fig. 14.7 EDS analysis of **a** WEDM surface and **b** AFFM finished surface

14.3.3 EDS Analysis

The constituent element in the WEDM surface and finished surface is analysed through energy-dispersive spectrometer (EDS).

Figure 14.7a shows the EDS analysis of WEDM surfaces. The peaks quantitatively show the traces of impurities in the surfaces. It is observed that there is a pickup of material like Cu and Zn from brass wire tool during WEDM process. Similar examination is held for AFFM surfaces, as shown in Fig. 14.7b, where contamination of Cu and Zn materials is clearly eliminated. This observation in the EDS plots proves the removal of recast layers during the AFFM process.

14.4 Conclusions

The present work attempts the abrasive flow finishing process simultaneously for multiple components, pre-finished through WEDM. The AFFM fixturing with selective process parameters improves the surface roughness in the range of nanometres,

by removing recast layer. The conclusions drawn from the experimental results and characterisation study of WEDM/AFFM finished surface are as follows:

(1) The AFFM process is suitable to remove the WEDM recast layer simultaneously for multiple components through proper fixturing.
(2) The AFFM cycle time of 15 min is consumed for individual abrasive media of mesh sizes to achieve uniform surface finish in all the five components.
(3) The selected process parameter of AFFM hydraulic pressure of 30 bar and the higher abrasive polymer media of size 60 mesh has shown the predominant improvement over initial WEDM recast layer.
(4) The surface roughness has improved gradually with varying abrasive polymer media mesh size. At 800 grits the roughness has improved to Ra 0.073 μm.
(5) The micro-hardness test reveals the higher surface hardness of recast layer up 55HRC, which are removed through AFFM.
(6) The comparative study on SEM/EDS results significantly determines the elimination of WEDM recast layer for the surface after AFFM process.

References

1. Williams, R.E., Rajurkar, K.P.: Study of wire electrical discharge machined surface characteristics. J. Mater. Process. Technol. **28**, 127–138 (1991)
2. Sachin, B., Shrinivas, S., Vishal, B.: Study and analysis of recast layer formation during wire electo discharge machining process. Int. J. Innov. Res. Sci., Eng. Technol., 8032–8039
3. Kohut, T.: Surface finishing with abrasive flow machining. SME technical paper, 35–43 (1989)
4. Loveless, T.R., Williams, K.P., Rajurkar, K.P.: A study of the effect of abrasive-flow finishing on various machined surfaces. J. Mater. Process. Technol. **47**, 133–151 (1994)
5. Tzeng, H.-J., Yan, B.-H., Hsu, R.-T., Cho, H.-M.: Finishing effect of abrasive flow machining on micro slit fabricated by wire EDM. Int. J. Manuf. Technol. **34**, 649–656 (2007)
6. Lin, Y.-C., Chow, H.-M., Yan, B.-H., Tzeng, H.-J.: Effects of finishing in abrasive fluid machining on microholes fabricated by EDM. Int. J. Manuf. Technol. **33**, 489–497 (2007)
7. Kenda, J., Pusavec, F., Kermouche, G., Kopac, J.: Surface integrity in abrasive flow machining of hardened tool steel AISI D2. Procedia Eng. **19**, 172–177 (2011)
8. Toshimitsu, R., Okada, A., Kitada, R., Okamoto, Y.: Improvement in surface characteristics by EDM with chromium powder mixed fluid. In: 18th CIRP Conference on Electro Physical and Chemical Machining (ISEM XVIII), vol. 42, pp. 231–235 (2016)
9. Khan, A.A, Mohiuddin, A.K.M., Latif, M.A.A.: Improvement of MRR and surface roughness during electrical discharge machining (EDM) using aluminium oxide powder mixed dielectric fluid. In: IOP Conference Series: Materials Science and Engineering, vol. 290, p. 012063 (2018)
10. Amineh, S.K., Tehrani, A.F., Mohammadi, A.: Improving the surface quality in wire electrical discharge machined specimens by removing the recast layer using magnetic abrasive finishing method. Int. J. Manuf. Technol. (2012)
11. Manjunath, M.A., Abhinav, K., Vinod, P., Balashanmugam, N.: Simulation of force generated and material removal in abrasive flow finishing for aluminium material. COPEN **10**, 765–768 (2017)

Chapter 15
Investigations on the Influence of Size Effect on Surface Characteristics During Micro-End Milling of Inconel 718

N. Anand Krishnan, G. Venkatesh and Jose Mathew

Abstract Micro-end milling is one of the widely used micromachining techniques in industries and research organizations to produce microfeatures having complex 3D shapes with high flexibility and high material removal rate. The analysis of areal surface roughness, surface defect, and microhardness are important for understanding the surface characteristics of the machined surface. This paper focused on the analysis of areal surface roughness, surface defect, and microhardness during micro-end milling on Inconel 718. Inconel 718, a nickel-based superalloy, was used as the workpiece material due to the superior properties such as high hardness, high strength to weight ratio, resistance to high-temperature loading, and corrosion resistance. Areal surface roughness and microhardness were taken as responses to understand their variations with feed per tooth at a constant depth of cut and speed. The feed per tooth is selected by giving importance to both inside and outside the size effect zone. It was observed that the areal surface roughness shows a decreasing trend initially at lower feed per tooth and then it shows an increasing trend outside the size effect region. The minimum value of areal surface roughness (Sa) was found to be in the range of 3 μm, which is the cutting edge radius of the tool. Inside the size effect zone, severe strain hardening was observed. Size effect in microhardness was also found. Inside the size effect region, the microhardness increases with feed per tooth and outside size effect region microhardness shows a decreasing trend.

Keywords Micro-end milling · Areal surface roughness · Microhardness · Inconel 718

15.1 Introduction

The increasing demand for microfeatures in the industry as well as research organizations has led to the development of the high-quality microfabrication techniques.

N. Anand Krishnan (✉) · G. Venkatesh · J. Mathew
Department of Mechanical Engineering, National Institute of Technology Calicut, Kozhikode 673601, Kerala, India
e-mail: anandkrish487@gmail.com

M. S. Shunmugam and M. Kanthababu (eds.), *Advances in Micro and Nano Manufacturing and Surface Engineering*, Lecture Notes on Multidisciplinary Industrial Engineering,
https://doi.org/10.1007/978-981-32-9425-7_15

Micromachining has a very critical role in today's manufacturing sectors especially in MEMS, optics, electronics, biomedical devices, communication, and avionics due to the high requirement of the micro-parts. The micromachining is not at all a downscaled version of conventional machining; it has its own features like size effect, minimum uncut chip thickness, ploughing effect, etc. One of the significant differences between conventional machining and micromachining is the formation of chips, which depends on the concept of minimum uncut chip thickness (MUCT). Whenever the chip thickness exceeds MUCT, only the chips were formed. Micro-milling is one of the preferred micromachining techniques capable of fabricating 3D complex parts very accurately with high precision. In the micro-milling process, the value of minimum uncut chip thickness depends upon the feed per tooth as well as cutting edge radius. In the micro-end milling process, the diameter of the milling cutter will be up to 500 μm only. Inconel 718 is widely used in aircraft gas turbines, reciprocating engines, rocket engine parts, high-temperature fasteners, etc., due to the superior properties such as the high strength-to-weight ratio and corrosion resistance. Inconel is mainly useful in high-temperature applications and maintains strength over large temperatures. Inconel is used when aluminum and steel fail to resist pressure to creep failure which will lead to thermally induced crystal vacancies. The machining of Inconel 718 causes metallurgical damage to its surface due to high cutting temperature and pressure [1]. The Inconel 718 comes under the difficult to cut material due to these reasons.

Many researchers have been rapidly extending their focus on micromachining due to the greater applications in this area. Vijay et al. [2] conducted extensive studies on various microscale machining processes and its performance characteristics. They discussed the micromachining simulation techniques in detail. Boswell et al. [3] critically analyzed the micro-mechanical cutting and discussed the potential of these processes. They emphasize the application of micro-milling for creating 3D free-form surfaces. Ng et al. [4] investigated micro- and nanoscale machining characteristics of aluminum alloy through cutting experiments. They explained the idea of effective rake angle in detail. Min and Takeuchi [5] discussed the modeling of machining processes and effect of microstructure on the cutting mechanism, surface finish, built-up edge formation, etc. Many industries are facing critical issues like costs for manufacturing of complex parts by machining of Ni-based superalloys. So the systematic investigations are necessary to identify the influence of machining parameters on the machining characteristics of Inconel 718. Xavior et al. [1] determined the effect of machining parameters on machining characteristics of Inconel 718 and achieved the optimum parameters for turning. Lu et al. [6] identified the interrelationship between Vickers hardness, flow strain, and the flow stress values for the prediction of surface hardness of Inconel 718 during micromachining with the help of the simulation results. In micromachining, it is very important to calculate the value of minimum uncut chip thickness. Fernando et al. [7] analyzed the size effect behavior in micro-milling by applying ANOVA on the cutting force and they related it with surface roughness and cutting edge radius of the tool. They found that the MUCT varies from one-third to one-fourth of the cutting edge radius and which is independent of workpiece material and tool material. Vipindas et al. [8] analyzed

the effect of cutting edge radius on the machining parameters. They identified the importance of size effect in machining performance. Hamed et al. [9] determined the smallest undeformed chip thickness by conducting experiments on Ti-6Al-4V in different cutting conditions. They have predicted the smallest uncut chip thickness to get the material removal rate by using an analytical model. Also considered are the various material removal mechanisms and transition from one to other mechanisms related to relative tool sharpness.

The surface roughness value has great importance in surface quality which will play a critical role in the functional operation and life of the microfeature/part. Many researchers have done extensive efforts on optimizing machining parameters in microscale machining using different optimization techniques and developed models for predicting the surface roughness. Kuram and Ozcelik [10] conducted a Taguchi-based gray-relational analysis to reduce the surface roughness, machining force, and tool wear during micro-milling of Al. On the other hand, these types of statistical modeling of surface roughness and optimization of machining parameters based on experimentation are extremely costly and time consuming. To overcome these problems, a few researchers concentrated on developing mathematical models for surface roughness prediction. Vogler et al. [11] developed a surface generation model to calculate the surface roughness based on MUCT concept during micro-end milling process for both single- and multiphase workpiece materials. Iturbe et al. [12] proposed a coupled model to explain the material behavior of Ni-based alloys at high strain rates and high temperatures. For estimating the surface roughness value, they developed a mathematical model for the effect of cutting mechanisms on surface nonuniformity. Only a few researchers have discussed the areal surface roughness parameters and surface defect in the micromachining process [13–15]. Aramcharoen and Mativenga [13] studied the impact of the size effect on the quality of the machined surface during micro-milling of steel. Liu et al. [14] explored the 3D roughness parameter (Sa) in micro-end milling and developed a model for the prediction of surface roughness. Elkaseer et al. [15] observed severe strain hardening, cracks, and burrs on the machined surface at low feed per tooth of 0.75 μm/tooth due to the ploughing action.

The main objective of this paper is to investigate the influence of the size effect on the surface characteristics such as areal surface roughness, surface defect, and microhardness during micro-end milling of Inconel 718. The experiments were performed by varying the feed per tooth so as to explore the size effect in the machined surface characteristics such as areal surface roughness, surface defect, and microhardness. The feed per tooth is selected in such a way that it accommodates both inside and outside the size effect region. In most of the literature, 2D parameters were used for the surface roughness evaluation. But in this work, the 3D surface roughness parameter (Sa) was used, which gave a better idea about the machined surface quality. The size effect in areal surface roughness and microhardness were analyzed in detail. SEM analysis on the micromachined surfaces at lower feed per tooth was conducted to get a better idea regarding the size effect and ploughing.

Table 15.1 Properties of Inconel 718

Properties	Value
Density (Kg/m^3)	8200
Young's modulus (GPa)	210
Thermal conductivity (W/mK)	6.5
Vickers hardness	350
Yield strength (MPa)	915
Melting temperature (°C)	1225

15.2 Experimental Work

15.2.1 Workpiece Material

Inconel 718 is used as the workpiece material for this work due to its greater properties like high hardness, high strength to weight ratio, resistance to high-temperature loading, and high corrosion resistance. Inconel 718 has a wide range of applications in chemical, nuclear, and automobile industries because of its superior mechanical and chemical properties at high temperatures. Table 15.1 shows the physical and mechanical properties of Inconel 718 material.

15.2.2 Cutting Tool

AlTiN coated WC end mill with 500 μm cutter diameter, 80 rake angle, and 100 clearance angles were used for this study. Since edge cutting radius of the tool has a great influence on size effect in micromachining, it has been measured physically using an optical microscope. The measured cutting edge radius of the micro-end mill cutter was in the range of 3 μm. Figure 15.1 shows the optical images of micro-end mill cutter and the detailed view of the cutting edge.

15.2.3 Experimental Setup

The micro-end milling experiments were performed on micromachining center (Make: Mikrotools, Model: DT110) with AlTiN-coated WC micro-end mill cutter with an effective diameter of 500 μm. Micro-channels of 10 mm length were machined on Inconel 718 workpiece at a constant depth of cut of 0.1 mm and cutting speed of 7.85 m/min. The areal surface roughness was measured by using a 3D noncontact optical profiler (Infinite focus G5, Alicona, Austria) and microhardness of the micro-machined surfaces were measured using microhardness tester (Make:

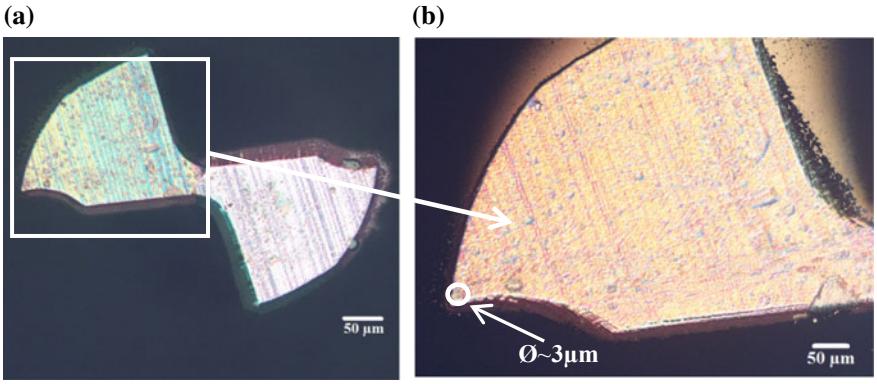

Fig. 15.1 Optical images of **a** top view of micro-end mill cutter, **b** detailed view of cutting edge of the tool

Matsuzawa, Model: VMT-X7) by Vickers hardness method. Figure 15.2 shows the detailed experimental setup and Table 15.2 shows the experimental plan.

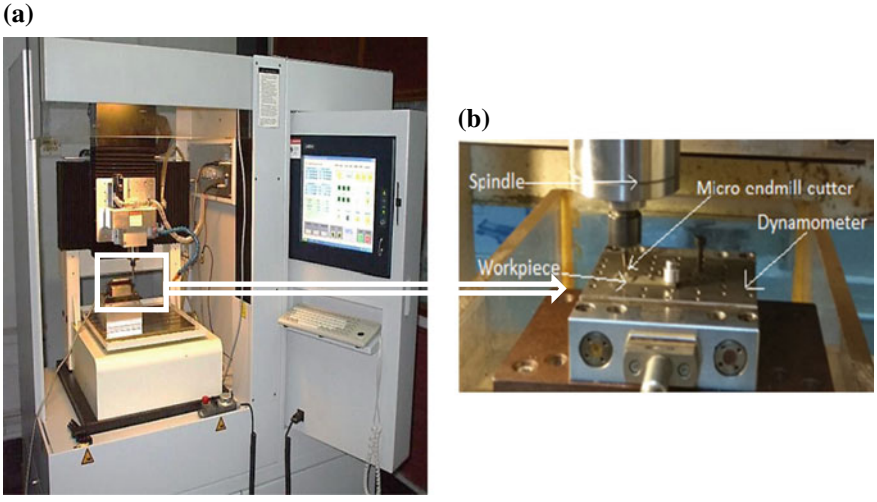

Fig. 15.2 **a** Micromachining center. **b** Experimental setup

Table 15.2 Experimental plan

Item	Description
Machine tool	Micromachining center (DT110, Mikrotools, Singapore)
Cutting speed (m/min)	7.85
Feed rate (μm/tooth)	0.3, 0.7, 1.1, 1.5, 2, 3, 4, 5
Depth of cut (mm)	0.1
Cutting tool	AlTiN coated WC end mill cutter with 500 μm cutter diameter
Workpiece material	Inconel 718
Optical profiler	Infinite focus G5, Alicona
SEM	SU 6600 FESEM, Hitachi

15.3 Results and Discussion

15.3.1 Areal Surface Roughness

The areal surface roughness of the machined slots of 10 mm length on Inconel 718 was characterized by using a 3D noncontact optical profiler (Alicona, Infinite Focus G5) in terms of areal roughness parameter Sa. Figure 15.3 shows the experimental setup for the areal surface roughness measurement. The areal surface will give the surface roughness based on an area. So it gives a more realistic value than that of 2D surface roughness parameters.

Figure 15.4 shows the variation of areal surface roughness with feed per tooth at the constant cutting speed of 7.85 m/min and depth of cut of 100 μm. Experimentations were carried out without the application of any lubricants (dry machining).

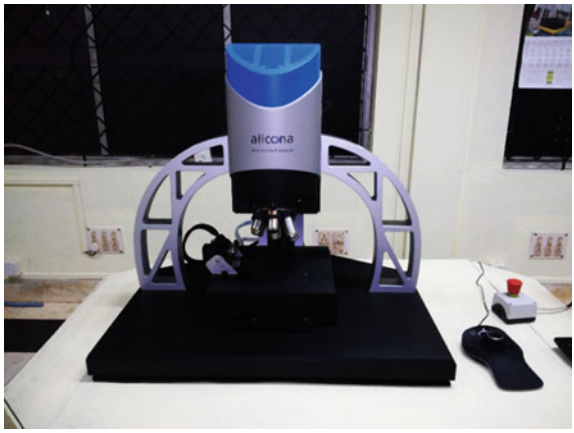

Fig. 15.3 Setup for measurement of the areal surface roughness of the micro-slot

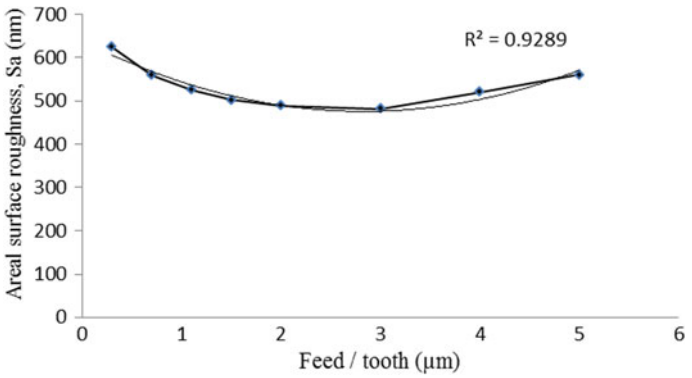

Fig. 15.4 Deviation of areal surface roughness (Sa) with feed per tooth for a cutting speed of 7.85 m/min and 0.1 mm depth of cut

From Fig. 15.4, it is noticed that the areal surface roughness (Sa) initially decreases with an increase in feed per tooth and then increases with the increase of feed per tooth. When the feed per tooth increases in the beginning, the areal surface roughness reduces and reaches a minimum roughness value. But above the cutting edge radius value, the areal surface roughness increases with the increase in feed per tooth. This is mainly due to the fact that ploughing is dominant in the region where feed per tooth is lesser than the edge radius of the cutting tool and shearing is dominant in the region where feed per tooth is higher than edge radius of the cutting tool. Near to 3 μm, the edge radius of the end mill cutter, the minimum value of areal surface roughness was obtained. Similar kind of variation was observed in Aramcharoen and Mativenga [13]. The higher value of the areal surface roughness obtained at small feed per tooth is mainly due the ploughing effect.

15.3.2 Surface Defect

In order to understand the reason behind the high areal surface roughness value inside the size effect zone, a detailed analysis of the micro-machined surfaces on Inconel 718 were inspected and analyzed using Scanning Electron Microscope (SEM). Figure 15.5 shows the SEM images of the micro-slot at lower feed per tooth of 0.3 μm. Inside the size effect zone, a large number of surface texturing and features like severely strain hardened parts of workpiece material (prows), micro-voids, cracks, and burrs were observed. Similar conclusions were observed in Elkaseer et al. [15] during micro-milling. The high strain hardening at lower feed per tooth on the machined slot was mainly due to the change of cutting mechanism from shearing to ploughing. As the feed per tooth decreased (inside the size effect zone), the rake angle becomes highly negative and as a result, the shearing was changed by ploughing. As a result of ploughing, severe strain hardening will occur in the machined surface.

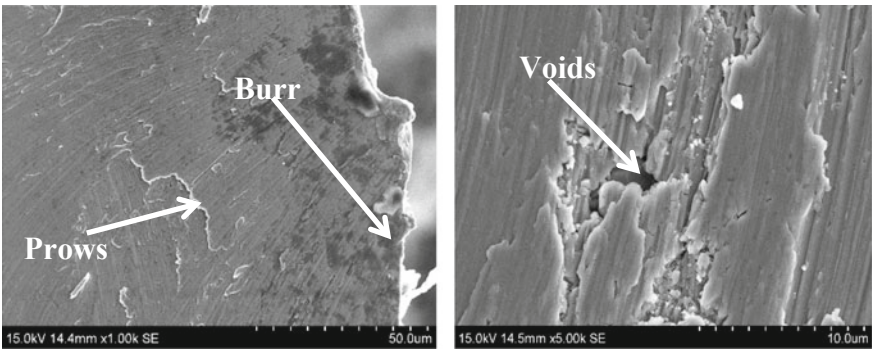

Fig. 15.5 Surface defect on the machined surface at a feed per tooth of 0.3 μm

Figure 15.5 shows the large number surface cracks/voids at lower feed per tooth due to severe strain hardening and ploughing effect.

Figure 15.6 shows the SEM images of machined slot at lower feed per tooth. From Fig. 15.6, it was clear that inside the size effect zone the machined surface contains more prows due to severe strain hardening as a result of ploughing. As the feed per tooth reaches close to edge radius of the micro-end mill cutter, the surface is clearer and the areal surface roughness result shows the same trend. For feed per tooth above cutting edge radius, the machined surface becomes rough again due to shearing. Higher strain hardening was the major reason behind the poor surface quality inside the size effect region.

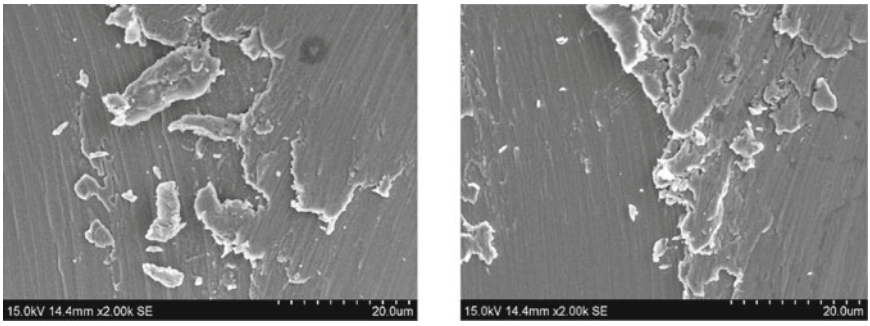

(a) 0.3 μm/tooth (b) 0.7μm/tooth

Fig. 15.6 Machined surfaces at lower feed per tooth

15.3.3 Microhardness

Microhardness of the micro-machined Inconel 718 surfaces was measured using Microhardness tester (Make: Matsuzawa, Model: VMT-X7) by Vickers hardness method as shown in Fig. 15.7. The load of 10 kgf is applied for 5 s for the purpose of the indentation for microhardness measurement.

Figure 15.8 shows the variation of the microhardness with feed per tooth at constant spindle speed of 5000 rpm (7.85 m/min) and depth of cut of 100 μm. It was found that at lower feed per tooth the microhardness of the micro-machined surface shows an increasing trend with the feed per tooth. Then the microhardness reaches

Fig. 15.7 Matsuzawa VMT-X7 for measuring Vickers hardness

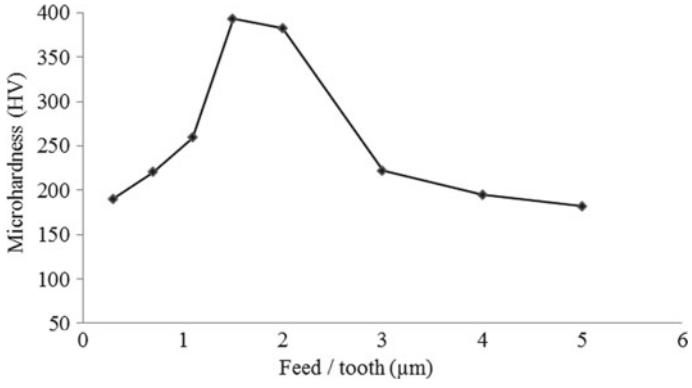

Fig. 15.8 Variation of feed per tooth with microhardness

a maximum value. Finally, the microhardness decreases with the feed per tooth at a higher feed rate or the feed rate above size effect zone. The maximum value of microhardness obtained in between 1 μm and 2 μm feed per tooth, which is near to be the cutting edge radius of the micro-end mill cutter. According to Fernando et al. [7], the MUCT value varies from one-third to one-fourth of the cutting edge radius of the tool irrespective of the tool-workpiece material and properties. In this work, the cutting edge radius of the tool was in the range of 3 μm. So, the size effect in microhardness was observed for micro-end milling on Inconel 718. From the microhardness analysis, it was observed that near to 1.5 μm feed per tooth, the transition from ploughing to shearing will occur.

When the feed per tooth is lesser than the edge radius of the end mill cutter, the ploughing effect will decrease the work hardening in micromachining. Due to the ploughing effect, the material was plastically deformed and new dislocations were generated. So, the work hardening increases. When feed per tooth is further increased, the shearing action starts and ploughing effect decreases. As the ploughing area decreases with an increase in feed per tooth, the extrusion friction effect of the tool decreases and it will lead to a decrease in work hardening. Due to these reasons, the surface produced in the ploughing region was severely strain hardened. As a result of that, the surface may contain a large number of prows, burrs, defects, etc.

15.4 Conclusions

In this paper, a detailed analysis of areal surface roughness, surface defect and microhardness of the micro-machined Inconel 718 surface was presented. The size effect in areal surface roughness and microhardness were observed. Within the size effect region, the severe strain hardening was observed. This is the major reason for higher surface roughness value above size effect region. It was found that during machining, inside the size effect zone, the areal surface roughness shows a decreasing trend with feed per tooth. However, outside the size effect region, the areal surface roughness increases with feed per tooth like conventional machining. The minimum value of areal surface roughness was obtained near to the 3 μm, which is the cutting edge radius of the micro-end mill cutter. Size effect in microhardness was also observed. At lower feed per tooth, the microhardness increases with feed per tooth and then after a particular value of feed per tooth microhardness shows a decreasing trend. Near to 1.5 μm feed per tooth, maximum microhardness was obtained.

Acknowledgements The authors would like to sincerely thank the Department of Science and Technology (DST), Govt. of India, and Centre for Precision Measurements and Nano mechanical Testing, Department of Mechanical Engineering, National Institute of Technology Calicut, for providing support to carry out this work under the scheme "Fund for Improvement of Science and Technology" (No. SR/FST/ETI-388/2015).

References

1. Xavior, M.A., Patil, M., Maiti, A., Raj, M., Lohia, N.: Machinability studies on Inconel 718. Mater. Sci. Eng. Conf. **149**, 1–8 (2016)
2. Vijay, V., Niharika, S., Srinivas, G., Praveen, K., Harish, C.B.: Review on machining characteristics and research prospects of conventional microscale machining operations. Mater. Manuf. Processes **32**, 235–262 (2016)
3. Boswell, B., Islam, M.N., Davies, I.J.: A review of micro-mechanical cutting. Int. J. Adv. Manuf. Technol. **94**, 789–806 (2018)
4. Ng, C.K., Melkote, S.N., Rahman, M., Kumar, A.S.: Experimental study of micro- and nano-scale cutting of aluminium 7075-T6. Int. J. Mach. Tools Manuf. **46**, 929–936 (2006)
5. Min, S., Takeuchi, Y.: Recent advances in micro machining. Ann. CIRP **64**, 134–141 (2006)
6. Lu, X., Jia, Z., Lu, Y., Feng, Y., Liang, S.Y.: Predicting the surface hardness of micro-milled nickel-base super alloy Inconel 718. Int. J. Adv. Manuf. Technol. (2017). https://doi.org/10.1007/s00170-017-0512-x
7. Fernando, B.O., Alessandro, R.R., Reginaldo, T.C., Adriano, F.S.: Size effect and minimum chip thickness in micro milling. Int. J. Adv. Manuf. Technol. **89**, 39–54 (2015)
8. Vipindas, K., Annand, K.N., Mathew, J.: Effect of cutting edge radius on micro end milling: force analysis, surface roughness, and chip formation. Int. J. Adv. Manuf. Technol. **97**, 711–722 (2018)
9. Hamed, R., Sadeghi, M.H., Budak, E.: Determination of minimum uncut chip thickness under various machining conditions during micro-end milling of Ti-6 Al-4V. Int. J. Adv. Manuf. Technol. **95**, 1617–1634 (2018)
10. Kuram, E., Ozcelik, B.: Multi-objective optimization using Taguchi based grey relational analysis for micro-milling of Al 7075 material with ball nose end mill. Measurement **46**(6), 1849–1864 (2013)
11. Vogler, M.P., DeVor, R.E., Kapoor, S.G.: On the modelling and analysis of machining performance in micro-end milling, part i: surface generation. J. Manuf. Sci. Eng. **126**, 685–694 (2004)
12. Iturbe, A., Giraud, E., Hormaetxe, E., Garay, A., Germain, G., Ostolaza, K., Arrazola, P.J.: Mechanical characterization and modelling of Inconel 718 material behavior for machining process assessment. Mater. Sci. Eng., A **682**, 441–453 (2017)
13. Aramcharoen, A., Mativenga, P.T.: Size effect and tool geometry in micro milling of tool steel. Precis. Eng. **33**(4), 402–407 (2009)
14. Liu, X., DeVor, R.E., Kapoor, S.G.: Model-based analysis of the surface generation in micro end milling-part II: experimental validation and analysis. J. Manuf. Sc. Eng. **129**, 461–469 (2007)
15. Elkaseer, A.M., Dimov, S.S., Pham, D., Popov, K.P., Olejnik, L., Rosochowski, A.: Material Microstructure Effects in Micro-End milling of Cu99.9E. Proc. Inst. Mech. Eng., Part B: J. Eng. Manuf. **232**(7), 1143–1155 (2018)

Chapter 16
Machining of Borosilicate Glass Using Micro-End Milling

K. Vipindas and Jose Mathew

Abstract Increasing demand on optical components in various fields such as consumer electronics and medical images requires fast and efficient machining of optical materials. This paper presents machining of brittle borosilicate glass in ductile mode to produce crack-free slots with good surface quality. Micro-end milling process was adopted in this study for machining. Three different cutters with diameter 0.3, 0.5, and 0.8 mm were selected to study the influence of the size of the cutter on the machining performance. Machining performance was assessed based on the surface roughness, slot profile, and chip formation. Finally, a brittle mode machining was performed with 1 mm diameter cutter and machining performance was compared with ductile mode machining. It was found that ductile mode machining produced a crack-free surface with surface roughness in the range of 250 nm and edge wall of the slots were free from cracks and damages.

Keywords Micro-end milling · Brittle mode · Ductile mode · Undeformed chip thickness · Borosilicate glass · Surface roughness · Chip

16.1 Introduction

There is increasing demand on optical components in various fields such as manufacturing of micro-lens arrays, aspheric lenses, and polygon mirrors. [1] machining of brittle materials such as silicon, optical glasses, and germanium is a topic of interest in the industry. However, there are a lot of challenges in machining brittle materials and achieving an optical quality surface due to their low fracture toughness [2]. It is reported in the literature that by maintaining ductile mode machining while machining brittle materials, high-quality surface finish can be attained.

K. Vipindas (✉)
Department of Mechanical Engineering, Pandit Deendayal Petroleum University, Gandhinagar, Gujarat, India
e-mail: vipindas.k@gmail.com

J. Mathew
National Institute of Technology Calicut, Kozhikode 673601, Kerala, India

M. S. Shunmugam and M. Kanthababu (eds.), *Advances in Micro and Nano Manufacturing and Surface Engineering*, Lecture Notes on Multidisciplinary Industrial Engineering,
https://doi.org/10.1007/978-981-32-9425-7_16

It has been proved that at very small depth of cut, brittle material will undergo plastic deformation rather than fracture [3]. Hence by machining at a small depth of cut, any brittle material can be machined in ductile mode and a mirror finish surface can be obtained [4]. Fang and Chen [5] have studied the machining of ZKN7 glass material. A new cutting strategy was proposed to obtain the nanometric surface finish. Experiments were conducted with three different undeformed chip thicknesses to study brittle mode, semi-ductile mode, and ductile mode machining. It was found that with 25 nm undeformed chip thickness, a mirror-finish surface with Ra = 14.5 nm was achieved in ductile mode cutting. Since undeformed chip thickness in micromachining is very small, sometimes less than the critical depth of cut required for brittle to ductile mode transition, micromachining can be used to machine brittle materials [6]. Egashira and Mizutani [7] studied critical depth of cut for ductile mode micro-drilling of single-crystal silicon.

Yu et al. [1] have presented a new method to determine the subsurface damage depth during diamond turning of brittle materials. With the proposed model, subsurface damage depth can be determined with only one structured surface with sinusoidal wave along the radial direction (SWR), which considerably reduces the effort for the determination of subsurface damage depth. Based on the subsurface damage depth, minimum feed rate for machining a crack-free micro-structured surface can be obtained before machining. Nakasuji et al. [8] have proposed a model of brittle to ductile transition during machining of brittle materials and discussed factors influencing the process. Also suggested that, with ductile mode chip removal, mirror-finished surface can be obtained. It was found that the tool rake angle and feed rate have significant influence on the surface finish. Owen et al. [9] have made an experimental investigation on the ultraprecision diamond machining of chalcogenide glass. It was suggested that there is a change in brittle to ductile mode machining at length scale of approximately 1 μm. The change in the cutting mechanics corresponds to increased fracture in the machined surface and a change in the shape of the machining chips. Choi et al. [10] developed a method to determine the critical point in the ductile–brittle transition of the single-crystal silicon. Yoon et al. [11] observed ductile–brittle transition in terms of cutting direction. Xiao et al. [12] attempted MD simulation of ductile mode machining. Wang et al. [13] investigated temperature dependence on critical ductile–brittle transition load during machining of fused silica.

This study mainly focused on the feasibility of micro-end milling in machining brittle borosilicate glass in ductile mode. Since brittle to ductile mode transition takes place at very small undeformed chip thickness, experiments were conducted at 0.1, 0.2, and 0.3 μm feed per tooth. Machinability of borosilicate under ductile mode machining was evaluated based on the quality of the surface roughness, slot profile, and chip formation. Since the cutting edge radius of the tool also influences the ductile mode machining, experiments were also conducted at three different diameter tools (0.3, 0.5, and 0.8 mm). In order to compare the performance of ductile mode machining with brittle mode machining, a conventional milling was performed with 1 mm diameter end mill tool with 7, 9, and 11 μm feed per tooth.

16.2 Brittle to Ductile Mode Transition Mechanism

While machining of brittle materials, the material is removed either due to plastic deformation of the material on the slip plane or due to the brittle fracture on the cleavage plane whichever happens first depending on the stress level under a particular machining condition [14]. Figure 16.1 shows a schematic representation of these processes.

When machining homogeneous materials, the slip or cleavage planes coincide with the plane of maximum shear or tensile stresses. However, when machining crystalline materials, plastic deformation takes place when the resolved shear stress in the easy slip direction exceeds a certain critical value, which depends on the workpiece material before a cleavage takes place (Fig. 16.1a). Whereas a cleavage takes place when the resolved tensile stress normal to the cleavage plane exceeds a certain critical value before slip (Fig. 16.1b). Hence it can be concluded that the mode of material removal depends on a predominant criterion in a particular cutting condition. When a plastic deformation takes place before cleavage, a smooth surface finish can be achieved. However, a cleavage process would result in a surface with cracks.

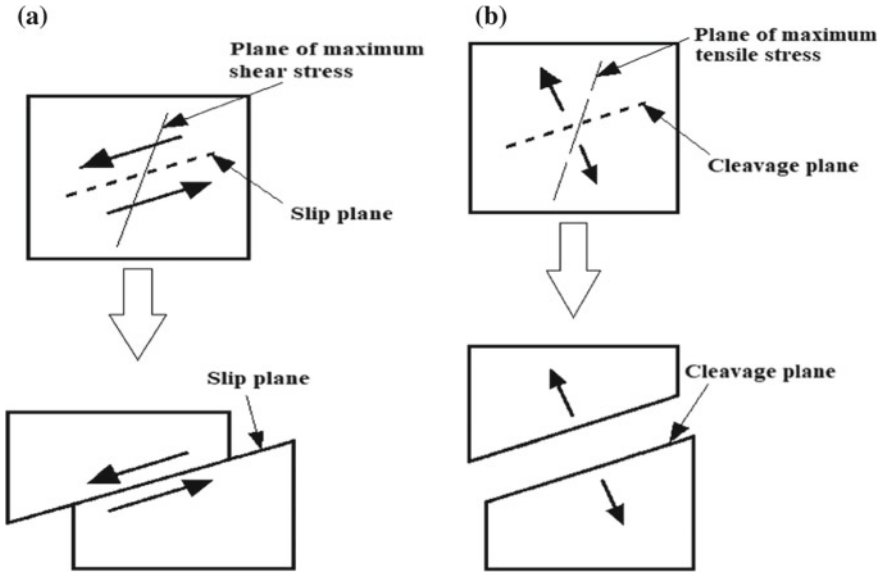

Fig. 16.1 Material removal mechanism in brittle materials

16.3 Experimental Setup

Experiments were conducted on a micromachining center (MIKROTOOLS—DT110 micromachining center, Singapore). The workpiece used is a borosilicate glass. Micro-end milling process was adopted for machining purpose. Since cutting edge radius of the tool has got significant influence on the machining mechanism of brittle materials, especially for brittle to ductile transition, micro-end mill cutter with three different diameters was chosen in this study. Solid tungsten carbide tools coated with TiAlN with 0.3, 0.5, and 0.8 mm diameter tools were used for the experiments. Figure 16.3 shows the measurement of the edge radius of the tools. Cutting edge radius of the tool was measured by fitting a circle to the image of the cutter edge and radius of the circle was taken as the cutting edge radius of the tool as shown in Fig. 16.3. Table 16.2 shows the measured edge radius of the fresh tools. Cutting parameters were also selected in such a way that feed per tooth (chip load) is very small, because brittle to ductile transition is possible only at very small undeformed chip thickness [4]. Experiments were conducted with 0.1, 0.2, and 0.3 μm feed per tooth. Also a conventional macro-end milling was performed to compare the results with brittle mode machining with 1 mm diameter tool. Conventional macro-end milling was performed with feed per tooth of 7, 9, and 11 μm. Figure 16.2 shows the experimental setup and machined workpiece.

3D optical profile meter (Alicona Infinite Focus G5) was used for characterizing the machined slots in terms of surface roughness and slot profile. SEM was used to visualize the chips (Fig. 16.3).

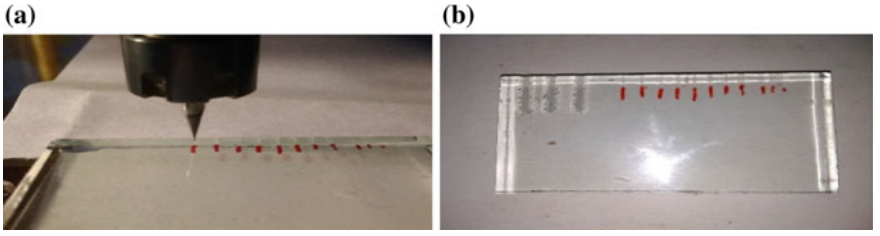

Fig. 16.2 Experimental setup **a** micro-end milling, **b** machined component

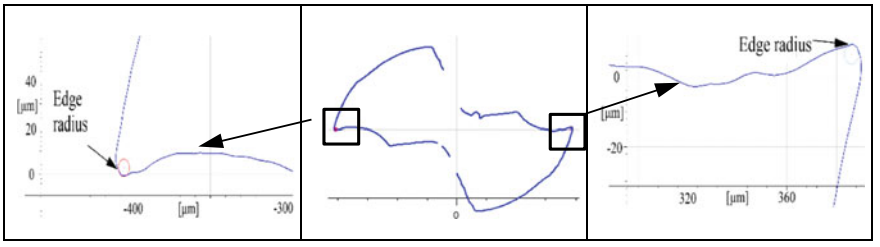

Fig. 16.3 Measurement of cutting edge radius of 0.8 mm diameter end mill cutter

16.4 Results and Discussion

Borosilicate glass is a highly brittle material. In order to machine such brittle material using conventional machining method, material needs to be removed in ductile mode. It has already been reported in the literature that ductile to brittle transition is always associated with increased surface roughness because of the presence of cracks on the machined surface and the chip formation is also influenced by this transition [15]. Hence in this study, in order to investigate the brittle to ductile transition during the machining process, the chips, machined surface, and slot profiles were examined at different feed per tooth values. Figure 16.4 shows the SEM images of the chips produced in brittle and ductile mode machining conditions as given in Table 16.1. Figure 16.4a shows the image of the chip produced in brittle mode machining, i.e., with 1 mm diameter tool with 11 μm feed per tooth and 0.15 mm axial depth of cut. It can be noticed that the chips are irregular in shape. This indicates that the chips are formed by brittle fracture. Figure 16.4b, c shows the images of chip produced with 0.8 mm diameter tool under 0.1 and 0.2 μm feed per tooth, respectively. It can be noted that in both cases, sawtooth segmented chips are produced, which indicates the occurrence of periodic shear deformation. Hence it is evident that under low feed per tooth, even though the material is brittle, it is removed by plastic deformation and ductile mode machining is prevalent (Fig. 16.4b, c). Similar results were obtained

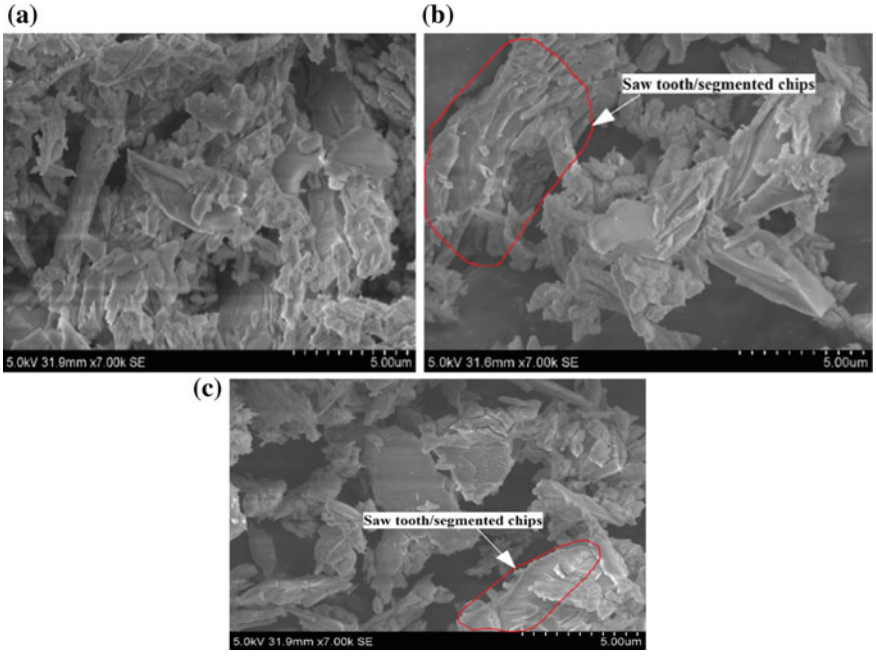

Fig. 16.4 SEM images of the chips at different feed per tooth, **a** 1 mm diameter tool, f/t-11 μm, **b** 0.8 mm diameter tool, f/t-0.1 μm **c** 0.8 mm diameter tool f/t-0.2 μm

Table 16.1 Experimental condition

Item	Details
Machine tool	Micromachining center (Mikrotools—DT110)
Workpiece material	Borosilicate glass
Cutting tool	TiAlN coated tungsten carbide tool
End mill tool diameter for brittle mode machining	1 mm
Feed per tooth for brittle mode machining	7, 9 and 11 μm
Axial depth of cut for brittle mode machining	0.15 mm
End mill tool diameter for ductile mode machining	0.3, 0.5, and 0.8 mm
Feed per tooth for ductile mode machining	0.1, 0.2, and 0.3 μm
Axial depth of cut for ductile mode machining	0.05 mm

Table 16.2 Cutting edge radius of the tool

Sl. No.	Tool diameter (mm)	Edge radius (μm)
1	0.3	2.5883
2	0.5	3.2529
3	0.8	3.6897

with 0.3 and 0.5 mm diameter tool when machined with 0.1, 0.2, and 0.3 μm feed per tooth (Table 16.2).

Brittle to ductile mode transition in micromachining could be due to stress state transition in the cutting region. When undeformed chip thickness is very large, near the cutting edge a tensile stress region is developed, whereas the upper region remains at low stress state [15]. Because of the low fracture toughness of borosilicate glass, cracks will be initiated in the tensile stress region before plastic deformation takes place. As the undeformed chip thickness decreases below the cutting edge radius of the tool, the effective rake angle of the tool becomes highly negative. This would result in the development of compressive stress on the workpiece material in front of the tool edge. This situation is very similar to hydrostatic pressure under sharp intender in an indentation test. It has already been proved that under high hydrostatic pressure, brittle material behaves like ductile material. Owen et al. [9] have reported that brittle materials such as silicon and germanium undergo plastic deformation under hydrostatic pressure. Similarly, in any machining process when undeformed chip thickness is less than the tool edge radius, material in front of the tool will be in a hydrostatic pressure condition. This facilitates the ductile mode machining in

micromachining processes as undeformed chip thickness is very small compared to cutting edge radius of the tool.

Figure 16.5 shows the images of the machined surface under conventional macro-machining condition, i.e., with 1 mm end mill cutter with a feed per tooth value of 7, 9, and 11 μm. It can be clearly noticed that the machined surface is severely damaged with a fractured surface for all three feed per tooth. Figure 16.6 shows the cross-sectional view of the machined slots, when machined with 1 mm diameter tool at 7 and 9 μm feed per tooth. It can be observed that the edges of the slots were completely damaged and machining did not produce a proper rectangular slot. Figure 16.7 shows the image obtained from 3D optical profile meter; cracks formed on the machined surface as well as broken slot edges due to brittle fracture of the material are clearly visible in this image. Figure 16.8 shows the surface roughness of the machined surface under brittle mode machining. As the cutting progresses, cutting edge radius of the tool increases and it may reach very close to 9 μm. At this point, machining mechanism changes from shearing to ploughing which results in excessive rubbing of flank face and elastic recovery of the machined surface. Also rubbing of flank face increases the critical stress field which initiates cleavage fractures. This could be a probable reason for increase in surface roughness at 9 μm feed per tooth.

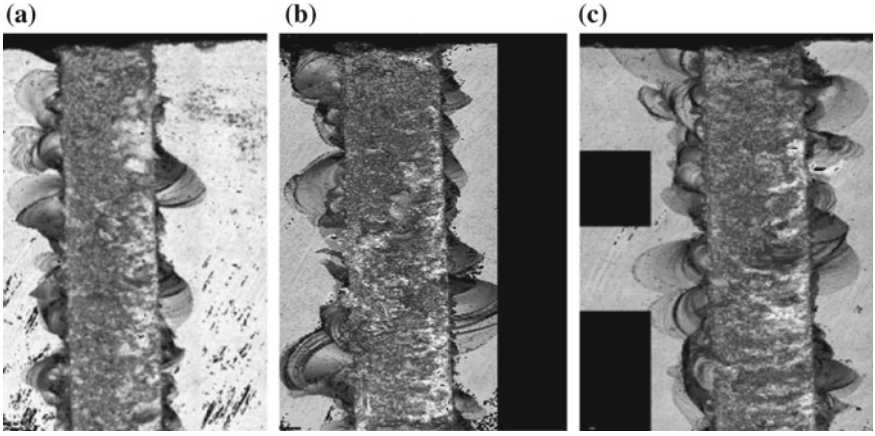

Fig. 16.5 Machined slot with 1 mm diameter tool at **a** 7 μm feed per tooth, **b** 9 μm feed per tooth, **c** 11 μm feed per tooth

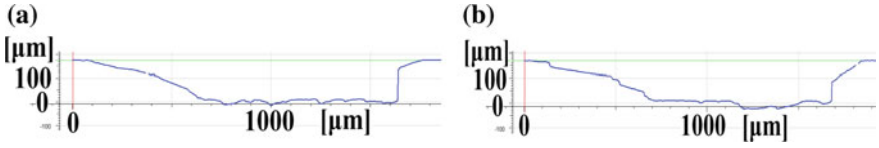

Fig. 16.6 Cross-sectional profile of the machined slot with 1 mm diameter tool at **a** 7 μm feed per tooth, **b** 9 μm feed per tooth

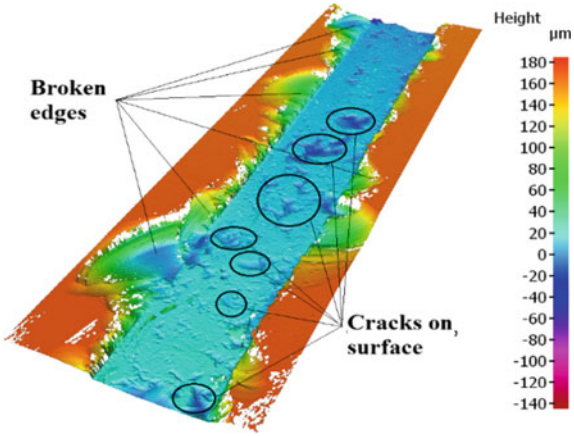

Fig. 16.7 Image from 3D optical profile meter of machined slot with 1 mm diameter tool and 9 µm feed per tooth

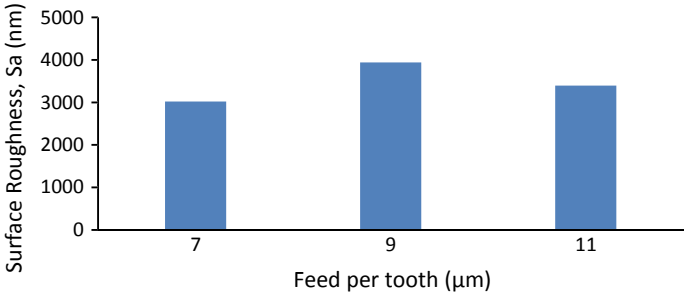

Fig. 16.8 Surface roughness under conventional macro-end milling process

As feed per tooth increases to 11 µm, feed per tooth shearing mechanism dominates and the surface roughness reduces. Surface roughness was found to be in the range of 3000–4000 nm when machined under the brittle mode.

Figure 16.9 shows some of the images of the slots machined under ductile mode. Figure 16.9a–c shows the slots machined with 0.8, 0.5, and 0.3 mm diameter tools with 0.1 µm feed per tooth. It can be clearly noted that the machined surface is free from cracks and slot edge walls were also not damaged. Cutting edges of the small tool may easily break up/wear out which would result in an increase in cutting edge radius of the tool. This results in increased ploughing and excessive rubbing of the tool flank face with the workpiece. Consequently, there is a possibility of critical stress field size to increase and cleavage fracture initiates at the defects. This could be one probable reason for presence of minor cracks on the surface when machined with a 0.3 mm diameter tool. Figure 16.10 shows the cross-sectional profile of the slots machined under ductile mode. It can be noted that a rectangular cross-sectioned slot

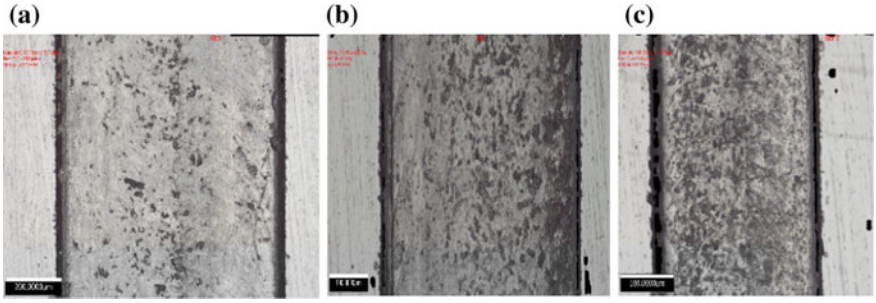

Fig. 16.9 Machined slot with 0.1 μm feed per tooth with **a** 0.8 mm diameter tool, **b** 0.5 mm diameter tool, **c** 0.3 mm diameter tool

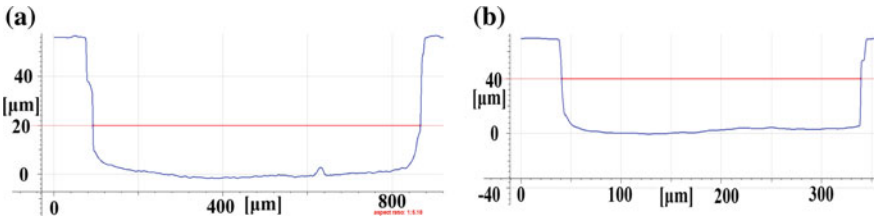

Fig. 16.10 Cross-sectional profile of the machined slot with 0.1 μm feed per tooth with **a** 0.8 mm diameter tool, **b** 0.3 mm diameter tools

without edge breakage were produced when machined in ductile mode. As shown in Fig. 16.11a tool mark can be clearly seen on the machined surface, which indicates that the material is removed in ductile mode during machining and brittle fracture of the material has not taken place. Figure 16.11b shows the image from the 3D optical profile meter which also confirms the crack-free machined surface as well as the sidewalls of the slot were not damaged.

Figure 16.12 shows the variation of surface roughness with micro-end mill cutter with 0.8, 0.5, and 0.3 mm diameter machined at 0.1, 0.2, and 0.3 μm feed per tooth. It was noted that for all the three end mill cutters, minimum surface roughness was obtained at 0.1 μm feed per tooth. Also, 0.8 mm diameter tool produces minimum surface roughness compared to 0.3 and 0.5 mm diameter tool. This could be due to the fact that smaller tools have very sharp cutting edges which may easily break. This would result in the increase in cutting edge radius of the tool and ploughing mechanism will be predominant. This results in increase in surface roughness. Table 16.3 shows the experimental conditions used to compare the brittle and ductile mode machining in terms of surface roughness (Sa). Figure 16.13 shows a comparison between surface roughness of the machined slots under brittle mode and ductile mode machining. It can be clearly observed that ductile mode machining generates a better surface when machining borosilicate glass.

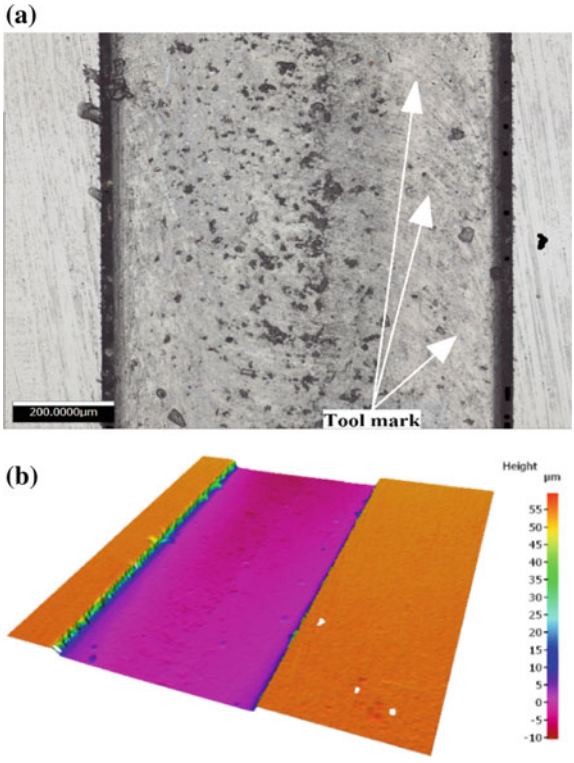

Fig. 16.11 Machined slot with 0.8 mm diameter tool and 0.1 µm feed per tooth, **a** slot surface, **b** image from 3D optical profile meter

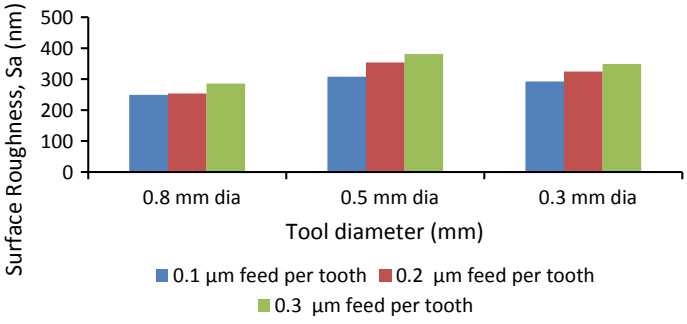

Fig. 16.12 Variation of surface roughness with different tool diameters

Table 16.3 Comparison between brittle and ductile mode machining

Exp. No.	Spindle speed (rpm)	Brittle mode			Ductile mode		
		Feed per tooth (μm)	Depth of cut (mm)	Surface roughness, Sa (nm)	Feed per tooth (μm)	Depth of cut (mm)	Surface roughness, Sa (nm)
1	5000	7	0.15	3019.5	0.1	0.05	249.0181
2	5000	9	0.15	3941.8	0.2	0.05	253.7528
3	5000	11	0.15	3397.1	0.3	0.05	285.6606

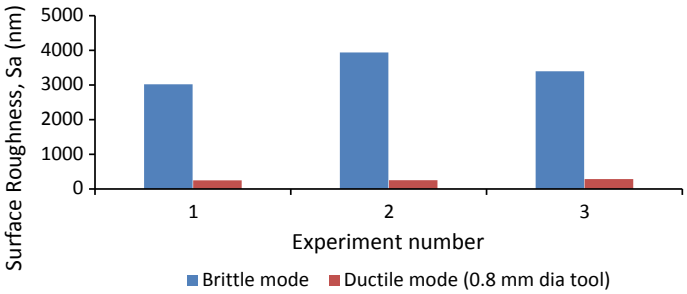

Fig. 16.13 Comparison of surface roughness between brittle mode and ductile mode machining

16.5 Conclusions

This study mainly focused on machining of brittle borosilicate glass in ductile mode. Since ductile mode machining is possible at very small undeformed chip thickness, 0.1, 0.2, and 0.3 μm feed per tooth was chosen as machining parameter and three micro-end mill cutters with diameters 0.3, 0.5, and 0.8 mm were used for machining. A conventional machining condition, where brittle mode material removal dominates, was also carried out to compare the results with ductile mode machining. Machining performance was assessed based on surface roughness, slot profile, and chip formation. Following conclusions can be drawn from this study.

- Under brittle mode machining, machined surface quality was very poor due to the presence of cracks on the machined surface. Also, slot edge walls were severely damaged and cross-sectional view of the slot does not have a proper rectangular shape.
- With 0.1, 0.2, and 0.3 μm feed per tooth, all three tools (0.3, 0.5, and 0.8 mm diameter) were able to machine borosilicate glass with good surface finish free from cracks and produced a slot without any edge breakage of the side walls. When machined in ductile mode, sawtooth/segmented chips were observed. This clearly indicates that the materials are removed by plastic deformation rather than crack propagation. Tool marks were clearly visible on the machined surface when feed

per tooth is 0.1, 0.3, and 0.5 μm. This indicates that the material is removed in ductile fashion at low feed per tooth.

- Under conventional machining conditions, the surface roughness of the machined slots was found to be in the range of 3000–4000 nm. Whereas in ductile mode machining, surface roughness of the machined surface was found to be in the range of 250–400 nm.
- In ductile mode machining, for all three tools, minimum surface roughness was obtained with 0.1 μm feed per tooth. 0.8 mm diameter tool with 0.1 μm feed per tooth produced a surface with minimum surface roughness.

Acknowledgements Authors would like to sincerely thank the Department of Science & Technology(DST), Govt. of India and Centre for precision measurements and Nano mechanical Testing, Department of Mechanical Engineering, National Institute of Technology Calicut, for providing support to carry out this work under the scheme "Fund for improvement of Science & Technology" (No. SR/FST/ETI-388/2015).

References

1. Yu, D.P., Wong, Y.S., Hong, G.S.: A novel method for determination of the subsurface damage depth in diamond turning of brittle materials. Int. J. Mach. Tools Manuf. **51**, 918–927 (2011)
2. Blake, P.N., Scattergood, R.O.: Ductile-regime machining of germanium and silicon. J. Am. Ceram. Soc. **73**(4), 949–957 (1990)
3. Bifano, T.G., Dow, T.A., Scattergood, R.O.: Ductile-regime grinding: a new technology for machining brittle materials. Trans. ASME—J. Eng. Ind. **113**, 184–189 (1991)
4. Takeuchi, Y., Sata, T.: Ultraprecision 3D micromachining of glass. Ann. CIRP **45**(1), 401–404 (1996)
5. Fang, F.Z., Chen, L.J.: Ultra-precision cutting for ZKN7 glass. Ann. CIRP **49**(1), 17–20 (2000)
6. Dornfeld, D., Min, S., Takeuchi, Y.: Recent advances in mechanical micromachining. Ann. CIRP **55**(2), 745–768 (2006)
7. Egashira, K., Mizutani, K.: Micro-drilling of monocrystalline silicon using a cutting tool. Precis. Eng. **26**(3), 263–268 (2002)
8. Nakasuji, T., Kodera, S., Hara, S., Matsunaga, H., Ikawa, N., Shimada, S.: Diamond turning of brittle materials for optical components. Ann. CIRP **39**(1), 89–92 (1990)
9. Owen, J., Davies, M., Schmidt, D., Urruti, E.: On the ultra-precision diamond machining of chalcogenide glass. CIRP Ann.—Manuf. Technol. **64**, 113–116 (2015)
10. Choi, D.H., Lee, J.R., Kang, N.R., Je, T.J., Kim, J.Y., Jeon, E.: Study on ductile mode machining of single-crystal silicon by mechanical machining. Int. J. Mach. Tools Manuf. **113**, 1–9 (2017)
11. Yoon, H.S., Lee, S., Min, S.: Investigation of ductile-brittle transition in machining of yttrium-stabilized zirconia (YSZ). Procedia Manuf. **26**, 446–453 (2018)
12. Xiao, G., To, S., Zhang, G.: The mechanism of ductile deformation in ductile regime machining of 6H SiC. Comput. Mater. Sci. **98**, 178–188 (2015)
13. Wang, W., Yao, P., Wang, J., Huang, C., Zhu, H., Zou, B., Liu, H., Yan, J.: Crack-free ductile mode grinding of fused silica under controllable dry grinding conditions. Int. J. Mach. Tools Manuf **109**, 126–136 (2016)
14. Shimada, S., Ikawa, N., Inamura, T., Takezawa, N., Ohmori, H., Sata, T.: Brittle-ductile transition phenomena in microindentation and micromachining. Ann. CIRP **44**(1), 523–526 (1995)
15. Yan, J., Maekawa, K., Tamaki, J., Kubo, A.: Experimental study on the ultraprecision ductile machinability of single-crystal germanium. JSME Int. J. **47**(1), 29–36 (2004)

Chapter 17
Parametric Optimization of Micro-electrical Discharge Drilling on Titanium

Siddhartha Kar and Promod Kumar Patowari

Abstract This paper aims to perform an experimental study of drilling micro-holes on titanium grade 2 alloy using micro-electrical discharge machining (μEDM) process. Key process parameters such as capacitance, feed rate (FR) and tool rotation speed (TRS) are varied during machining. Machining time, diameter at entry and diameter at exit are the response measures evaluated to examine the effect of chosen process parameters on them. A Taguchi L-9 orthogonal array design of experiment has been employed to frame the parametric combination of the process parameters, based on which experiments are conducted. Furthermore, analysis of variance (ANOVA) is carried out to find significant process parameters. Deviation of 14.16, 0.03 and 2.14% is observed between the experimental and predicted results at optimum condition of machining time (10^4 pF, 15 μm/s and 1000 rpm), diameter at entry (10^2 pF, 5 μm/s and 500 rpm) and diameter at exit (10^2 pF, 10 μm/s and 1500 rpm), respectively.

Keywords Drilling · Micro-holes · Machining time · Diameter · Titanium

17.1 Introduction

Nowadays, micromachining is the most demanding manufacturing practice due to the upsurge in the use of micro-devices and components. As a result of this, micromachining technique such as micro-drilling is finding tremendous importance. Conventional micro-drilling process requires tool material of superior hardness and strength to inhibit self-wear and actuate removal of material from the workpiece. Such perplexity restricts the variety of materials that can be machined by conventional micro-drilling process. Furthermore, manufacturing of micro-drill bit is also a tedious task which requires high amount of cost and advanced technology. Electrical discharge machining (EDM) process has the potential to negate all these issues, wherein it can

S. Kar (✉) · P. K. Patowari
Department of Mechanical Engineering, National Institute of Technology Silchar, Assam 788010, India
e-mail: siddkar.nita@gmail.com

M. S. Shunmugam and M. Kanthababu (eds.), *Advances in Micro and Nano Manufacturing and Surface Engineering*, Lecture Notes on Multidisciplinary Industrial Engineering,
https://doi.org/10.1007/978-981-32-9425-7_17

machine any material which is a conductor of electricity regardless of its hardness [1]. It is a non-contact machining process, where the material is removed by melting and vaporization due to a series of discharges occurring between the tool electrode and workpiece. Micro-electrical discharge machining (μEDM) process works on the same principle as EDM with the exception of less amount of energy supplied (compared to macro-EDM process) in the inter-electrode gap (IEG) between the two electrodes (tool and workpiece). The use of lower energy allows fabrication of micro-features with superior accuracy and precision [2]. Over the last few decades, μEDM has been highly used for drilling micro-holes in components of superior strength and hardness such as inkjet and nozzle. Several researches have been carried out and are still ongoing on drilling of such materials using μEDM. However, the fundamental concern is optimizing the various process parameters of μEDM to achieve superior quality of micro-holes (which would possess dimensional accuracy and precision) along with higher machining efficiency. Generally, resistance–capacitance (RC) pulse generator is used in μEDM to provide lower discharge energy in the IEG. Apart from discharge energy, other parameters such as feed rate (FR), tool rotation speed (TRS) and polarity also play a vital role in μEDM process. At present, titanium and its alloys are in high demand due to their distinctive properties such as high stiffness, strength, outstanding toughness and lower density [1]. Moreover, these materials offer corrosion resistance at very low to high temperatures and are biocompatible in nature, which enhances their applicability in biomedical implants and devices.

Conventional machining methods are not suitable to machine titanium and its alloys due to their high hardness. Therefore, several researchers have chosen some alternative approach to machine such materials. EDM process has been one of those alternatives which has been successfully utilized for machining such materials of higher hardness. Wansheng et al. [3] successfully fabricated micro-holes of *diameter* $< 200\,\mu m$ and *aspect ratio* > 15 in Ti-6Al-4V using ultrasonic vibration and single-notch rotating tool in μEDM. Hasçalık and Çaydaş [4] executed EDM of Ti-6Al-4V with diverse electrode materials (copper, graphite and aluminium) and varied process parameters such as current and pulse duration to investigate surface integrity of the machined workpiece. They observed increase in surface roughness (SR), tool wear and material removal rate (MRR) with increase in process parameters with an exception in case of lengthy pulse duration of 200 μs. Graphite yielded highest MRR and tool wear, whereas aluminium exhibited lowest SR. Pradhan et al. [5] studied the effect of current, pulse duration, duty ratio and flushing pressure on MRR, tool wear rate (TWR), overcut and taper in μEDM of Ti-6Al-4V. They found pulse duration to be most influential in case of MRR, overcut and taper, whereas current to be most influential in TWR. Kibria et al. [6] examined the use of different dielectrics on MRR, TWR, overcut, variation of entry and exit diameters and surface topography in μEDM of Ti-6Al-4V. MRR was high with deionized water in comparison to kerosene. Accuracy of the micro-holes was higher with the use of lower discharge energy in deionized water as compared to the use of higher discharge energy in kerosene. Azad and Puri [7] performed simultaneous optimization of MRR, TWR and overcut in μEDM of Ti-6Al-4V, wherein the process parameters varied

were pulse duration, current, voltage and frequency. Among all the process parameters, voltage and current were the most significant, affecting each response measure. In another study, Meena and Azad [8] utilized grey relational analysis to optimize multiple responses such as TWR, MRR and overcut in μEDM of Ti-6Al-4V. They found voltage to be the most crucial process parameter affecting the overall process followed by current, pulse duration and frequency. Kumar et al. [9] performed powder mixed EDM of titanium grade 2 with the use of cryogenic treated tool electrodes. Further, they also explored the effect of current and pulse duration on MRR, TWR, SR and microhardness. They found current to be the most important parameter followed by pulse duration, whereas tool electrode material had negligible effect. Baroi et al. [10] investigated MRR, TWR and SR in EDM of titanium grade 2 alloy. MRR, TWR and SR increased with an increment in current. Elsewhere, TWR exhibited a decreasing trend, SR exhibited an increasing trend and MRR initially increased up to a critical limit, then decreased with increment in pulse duration.

In regards to the existing literature, it can be seen that proper value of the process parameters is the foremost to achieve higher machining efficiency and superior quality of holes in titanium alloy. As per the literature, very limited works have been reported on micro-hole drilling of titanium and its alloy, which possesses a potential to play a significant role in aerospace and biomedical industries. Thus, in the present work, micro-holes are drilled on titanium grade 2 alloy using μEDM process which is very hard to machine by conventional machining processes. Key process parameters such as capacitance, FR and TRS are varied to investigate their effect on response measures such as machining time and hole diameter (at entry and exit).

17.2 Materials and Methods

The experimentation is done on a μEDM setup which is of table top type (Make: Sinergy Nano Systems; Model: Hyper-15). Through pilot experiments, it has been inferred that negative polarity of tool electrode incurs higher material removal from the workpiece as compared to positive polarity. Therefore, polarity of the tool is connected to the negative terminal throughout the experimentation. Moreover, voltage is kept fixed at 180 V, whereas capacitance is varied in three levels due to the higher impact of the latter as observed by Jahan et al. [11]. FR and TRS are also varied in three levels throughout the experimentation. Taguchi L-9 orthogonal array is used to frame the design of the experiment based on which the experimentation is carried out. The process parameters consisting of both variable parameters and fixed parameters are depicted in Table 17.1. The response measures evaluated are machining time and hole diameter (at entry and exit). In each experiment, the tool electrode is penetrated to a depth of 2 mm, which is significantly higher than the thickness of titanium sheet (0.7 mm) to ensure drilling of holes.

Table 17.1 Experimental condition

Variable parameters		
Parameters	Level	Values
Capacitance (pF)	3	10^2, 10^3, 10^4
FR (μm/s)	3	5, 10, 15
TRS (rpm)	3	500, 1000, 1500
Fixed parameters		
Workpiece	Titanium sheet, 0. 7 mm thick	
Tool electrode	Tungsten (518 μm diameter)	
Polarity	Tool (−ve); Workpiece (+ve)	
Voltage	180 V	
Dielectric medium	Hydrocarbon oil	
Flushing type	Jet	

Machining time is observed by a stopwatch from the initiation of spark till the fixed depth is achieved by the tool electrode. Thereafter, the diameter of the micro-holes is observed by an optical microscope from which the overcut (at entry and exit) can also be calculated. The mathematical formulation of overcut is depicted by Eq. (17.1) and its corresponding schematic diagram is shown in Fig. 17.1.

$$Overcut = \frac{Diameter\ of\ hole - Diameter\ of\ tool}{2} \tag{17.1}$$

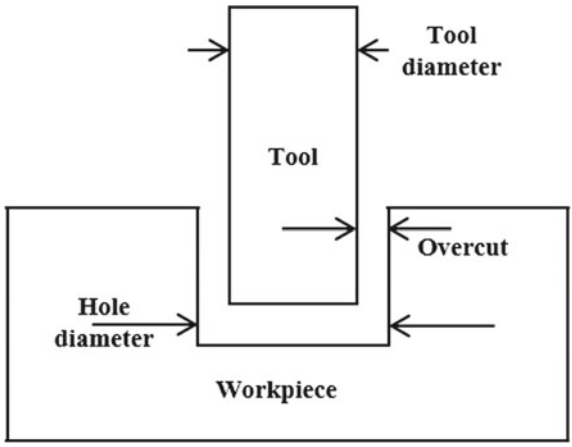

Fig. 17.1 Schematic diagram showing overcut

17.3 Results and Discussion

The experimental results of machining time and hole diameter (at entry and exit) are shown in Table 17.2. The photographic image of the fabricated micro-holes on titanium using μEDM is shown in Fig. 17.2.

The outcome of the response measures due to change in process parameters is discussed in the subsequent subsections.

17.3.1 Machining Time

The mean effect of process parameters on machining time is shown in Fig. 17.3. Increment in capacitance gives rise to the discharge energy, which leads to a decrease in machining time. With an increment in FR, the speed of retraction and forward movements of the tool increases (after encountering short circuit), which reduces the idle time and consequently reduces the machining time. With an increment in TRS from 500 to 1000 rpm and then to 1500 rpm, there is no significant change in

Table 17.2 Taguchi L-9 design of experiment with the corresponding result

Exp. No.	Cap (pF)	FR (μm/s)	TRS (rpm)	Machining time (s)	Diameter at entry (μm)	Diameter at exit (μm)
1	10^2	5	500	1842	547.40	515.48
2	10^2	10	1000	1772	552.14	524.64
3	10^2	15	1500	1455	552.28	525.82
4	10^3	5	1000	1470	596.58	562.02
5	10^3	10	1500	1646	600.90	542.78
6	10^3	15	500	1389	595.08	577.54
7	10^4	5	1500	722	633.72	579.02
8	10^4	10	500	538	633.08	580.04
9	10^4	15	1000	510	633.90	581.50

Note Cap—Capacitance

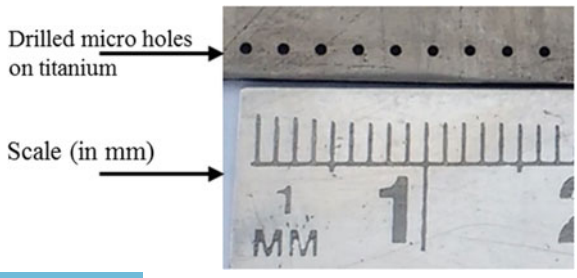

Fig. 17.2 Micro-holes drilled on titanium

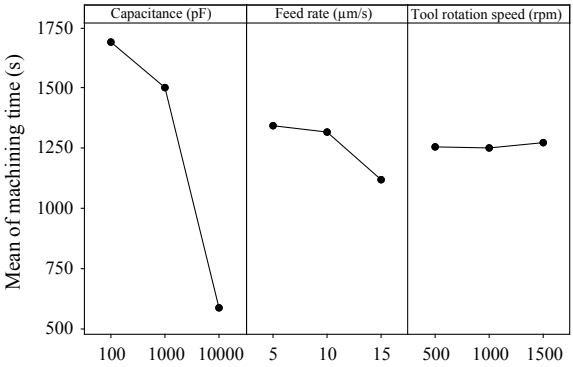

Fig. 17.3 Mean effect of process parameters on machining time

the machining time. From Fig. 17.3, the optimum condition of machining time is observed at capacitance of 10^4 pF, FR of 15 µm/s and TRS of 1000 rpm.

17.3.2 Diameter at Entry and Exit

The mean effect of process parameters on diameter at entry and exit is depicted in Figs. 17.4 and 17.5, respectively. With an increment in capacitance, diameter at both entry and exit increases. The increase in diameter can be attributed to rise in plasma channel radius due to higher discharge energy. With the rise in FR from 5 to 10 µm/s, diameter at exit decreases, but further rise in FR from 10 to 15 µm/s causes a slight increment in diameter due to secondary sparking. In case of entry diameter, no significant variation is observed with change in FR. With increment in TRS, the entry diameter increases but the exit diameter decreases. The variation of increment in case of entry diameter is very less as evident from Fig. 17.4. The decrement in exit diameter with rise in TRS may be attributed to reduction in the wobbling effect due to higher spin stability at higher TRS. In each parametric combination, it can be seen

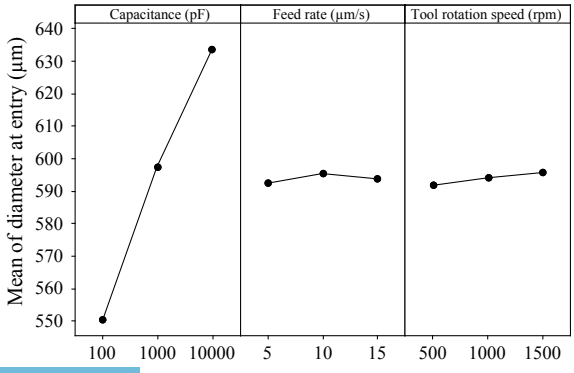

Fig. 17.4 Mean effect of process parameters on diameter at entry

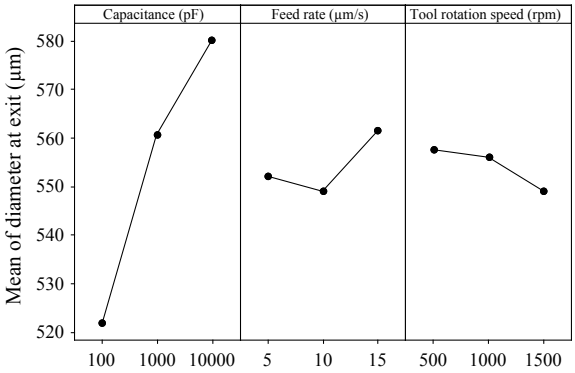

Fig. 17.5 Mean effect of process parameters on diameter at exit

that the exit diameters are less than the entry diameters. Tool wear can be attributed for such deviation in entry and exit diameter which is inevitable in any variant of EDM [2].

From Fig. 17.4, the optimum condition of diameter at entry is observed at a capacitance of 10^2 pF, FR of 5 μm/s and TRS of 500 rpm. Similarly, the optimum condition of diameter at exit observed from Fig. 17.5 is capacitance of 10^2 pF, FR of 10 μm/s and TRS of 1500 rpm. The microscopic images of the lowest diameter at entry (547.40 μm) and exit (515.48 μm) are depicted in Fig. 17.6a and b, respectively.

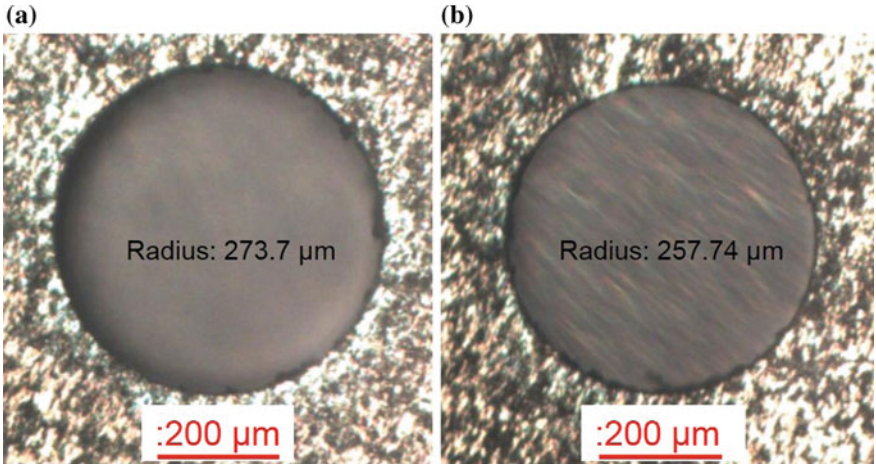

Fig. 17.6 Microscopic image of the lowest diameter (180 V, 10^2 pF, 5 μm/s, 500 rpm) **a** at entry and **b** at exit

Table 17.3 ANOVA of response measures

Source	DOF	Sum of square	Mean square	F-ratio	P value	Contribution (%)
1. Machining time						
Cap	2	2,075,747	1,037,873	39.26	0.025	93.42
FR	2	92,321	46,160	1.75	0.364	4.16
TRS	2	916	458	0.02	0.983	0.04
Error	2	52,872	26,436	–	–	2.38
Total	8	2,221,856	–	–	–	100
$R^2 = 97.62\%$, $R^2(adj) = 90.48\%$						
2. Diameter at entry						
Cap	2	10382.6	5191.29	35192.55	0.000	99.67
FR	2	11.9	5.95	40.37	0.024	0.11
TRS	2	21.9	10.93	74.10	0.013	0.21
Error	2	0.3	0.15	–	–	0.00
Total	8	10416.7	–	–	–	100
$R^2 = 100\%$, $R^2(adj) = 99.99\%$						
3. Diameter at exit						
Cap	2	5270.1	2635.04	17.66	0.054	88.67
FR	2	253.8	126.89	0.85	0.540	4.27
TRS	2	121.5	60.73	0.41	0.711	2.04
Error	2	298.4	149.19	–	–	5.02
Total	8	5943.7	–	–	–	100
$R^2 = 94.98\%$, $R^2(adj) = 79.92\%$						

Note Cap—Capacitance; DOF—Degree of freedom

17.3.3 Analysis of Variance

Analysis of variance (ANOVA) is carried out for all the response measures to find the importance of process parameters. The result of ANOVA is shown in Table 17.3. Capacitance is the most significant process parameter affecting all the response measures. The correlation coefficient (R^2) and adjusted correlation coefficient ($R^2(adj)$) values are higher for all the three responses, with the diameter at exit possessing the lowest $R^2 = 94.98\%$ and $R^2(adj) = 79.92\%$ values. Such high R^2 and $R^2(adj)$ values indicate that the models are fairly significant.

17.3.4 Confirmation Test

Test is conducted at optimum setting of all the response measures and compared to the predicted values. Table 17.4 depicts the optimum condition, predicted and

Table 17.4 Confirmation test result

Response	Optimum condition			Predicted	Experimental	Observed deviation%
	Cap (pF)	FR (μm/s)	TRS (rpm)			
Machining time (s)	10^4	15	1000	437.78	510	14.16
Diameter at entry (μm)	10^2	5	500	547.23	547.40	0.03
Diameter at exit (μm)	10^2	10	1500	511.71	522.90	2.14

Note Cap—Capacitance

experimental values and deviation between experimental and predicted values. In case of machining time and diameter at entry, their optimum condition matches with Exp. no. 9 and Exp. no. 1, respectively, from initial set of Taguchi L-9 experiments. So, no separate tests are conducted and their initial values are taken as the experimental ones to calculate deviation from the predicted values. Deviation of 14.16% and 0.03% is observed between experimental and predicted values of machining time and diameter at entry, respectively. In case of diameter at exit, confirmation test is conducted at optimum condition (10^2 pF, 10 μm/s and 1500 rpm), wherein deviation of 2.14% is achieved between the experimental and predicted value. Thus, overcut of 14.7 and 2.45 μm is observed at optimum condition of diameter at entry and exit, respectively.

17.4 Conclusions

Micro-holes have been successfully drilled in titanium by μEDM process. Process parameters such as capacitance, FR and TRS have been varied during experimentation to investigate their effect on response measures such as machining time and diameter at entry and exit. Within the range of parameters considered in this study, the following conclusions are drawn.

- With increase in capacitance, machining time decreases, whereas both diameter at entry and exit increases due to rise in discharge energy.
- With increase in FR, the machining time decreases due to faster movement of the tool. But, there is no significant change in machining time with increase in TRS.
- In case of diameter at entry, the effect of FR and TRS is very low.
- The exit diameter initially decreases with increase in FR up to a certain limit, then it increases with further increase in FR due to secondary sparking.
- With increase in TRS, the exit diameter decreases due to decrement in wobbling effect.

- From ANOVA, capacitance unfolded as the most significant process parameter impacting all the response measures.
- At the optimum condition of machining time, diameter at entry and diameter at exit, deviation of 14.16%, 0.03% and 2.14% is observed between the experimental and predicted results, respectively.

References

1. Qudeiri, J.E.A., Mourad, A.-H.I., Ziout, A., Abidi, M.H., Elkaseer, A.: Electric discharge machining of titanium and its alloys: review. Int. J. Adv. Manuf. Technol. **96**(1–4), 1319–1339 (2018). https://doi.org/10.1007/s00170-018-1574-0
2. Kar, S., Patowari, P.K.: Electrode wear phenomenon and its compensation in micro electrical discharge milling: a review. Mater. Manuf. Process. **33**(14), 1491–1517 (2018). https://doi.org/10.1080/10426914.2018.1453144
3. Wansheng, Z., Zhenlong, W., Shichun, D., Guanxin, C., Hongyu, W.: Ultrasonic and electric discharge machining to deep and small hole on titanium alloy. J. Mater. Process. Technol. **120**(1–3), 101–106 (2002). https://doi.org/10.1016/S0924-0136(01)01149-9
4. Hasçalık, A., Çaydaş, U.: Electrical discharge machining of titanium alloy (Ti–6Al–4 V). Appl. Surf. Sci. **253**(22), 9007–9016 (2007). https://doi.org/10.1016/j.apsusc.2007.05.031
5. Pradhan, B.B., Masanta, M., Sarkar, B.R., Bhattacharyya, B.: Investigation of electro-discharge micro-machining of titanium super alloy. Int. J. Adv. Manuf. Technol. **41**(11–12), 1094–1106 (2009). https://doi.org/10.1007/s00170-008-1561-y
6. Kibria, G., Sarkar, B.R., Pradhan, B.B., Bhattacharyya, B.: Comparative study of different dielectrics for micro-EDM performance during microhole machining of Ti-6Al-4V alloy. Int. J. Adv. Manuf. Technol. **48**(5–8), 557–570 (2010). https://doi.org/10.1007/s00170-009-2298-y
7. Azad, M.S., Puri, A.B.: Simultaneous optimisation of multiple performance characteristics in micro-EDM drilling of titanium alloy. Int. J. Adv. Manuf. Technol. **61**(9–12), 1231–1239 (2012). https://doi.org/10.1007/s00170-012-4099-y
8. Meena, V.K., Azad, M.S.: Grey relational analysis of micro-EDM machining of Ti-6Al-4V alloy. Mater. Manuf. Process. **27**(9), 973–977 (2012). https://doi.org/10.1080/10426914.2011.610080
9. Kumar, S., Singh, R., Batish, A., Singh, T.P.: Multi-objective parametric optimization using the grey-taguchi approach for powder mixed electric discharge machining of grade-II titanium alloy with cryogenically treated electrodes. Indian J. Eng. Mater. Sci. **24**(5), 339–350 (2017)
10. Baroi, B.K., Kar, S., Patowari, P.K.: Electric discharge machining of titanium grade 2 alloy and its parametric study. Mater. Today: Proc. **5**(2), 5004–5011 (2018). https://doi.org/10.1016/j.matpr.2017.12.078
11. Jahan, M.P., Wong, Y.S., Rahman, M.: A study on the quality micro-hole machining of tungsten carbide by micro-EDM process using transistor and RC-type pulse generator. J. Mater. Process. Technol. **209**(4), 1706–1716 (2009). https://doi.org/10.1016/j.jmatprotec.2008.04.029

Chapter 18
Numerical Simulation of Micro-EDM Process by Incorporating a Novel Approach of Multi-sparks

Mahavir Singh, Devesh Kumar Chaubey and J. Ramkumar

Abstract Due to the stochastic nature of the EDM process, limited knowledge of material removal mechanism as well as the progression of sparks is available. For complete utilization of the micro-EDM process, a concrete study is needed to understand the physics associated with the process such as the formation of crater, multiple-sparks generation, and overlapping of craters for uniform material removal. The scarcity of the models to simulate multi-sparks with appropriate crater overlap in the micro-EDM process is the motivation for the present work. This work presents a numerical simulation of the micro-EDM process based on the generation of multiple-sparks. The sparks are assumed to be occurring at a point of minimum inter-electrode gap (IEG) based on the arbitrary surface roughness assigned to the tool as well as the workpiece. Using the thermal ablation model as a mechanism of material removal and adopting Gaussian distribution of input heat flux to the workpiece, the crater radius, depth, and pulse frequency are determined by creating single sparks. The data obtained from the simulation of the single spark has been applied to develop a multi-spark approach for the removal of a single layer of material from the workpiece. The sparks are generated uniformly across the tool–workpiece contact length with appropriate crater overlapping.

Keywords Micro-EDM · Multi-spark · Crater overlap · Numerical simulation · SS-EN 24

M. Singh · J. Ramkumar (✉)
Department of Mechanical Engineering, Indian Institute of Technology Kanpur, Kanpur 208016, India
e-mail: jrkumar@iitk.ac.in

D. K. Chaubey
Materials Science Programme, Indian Institute of Technology Kanpur, Kanpur 208016, India

M. S. Shunmugam and M. Kanthababu (eds.), *Advances in Micro and Nano Manufacturing and Surface Engineering*, Lecture Notes on Multidisciplinary Industrial Engineering,
https://doi.org/10.1007/978-981-32-9425-7_18

18.1 Introduction

Over a period, conventional machining processes have been evolved for micromachining application, in which tool and workpiece are in direct contact with each other [1]. Conventional machining processes have certain advantages over the nontraditional processes of having high material removal rate and ability to fabricate 2D and 3D micro-features. However, conventional machining processes have some limitations such as difficulty to fabricate complex geometry, inability to machine advanced and hard materials, and low precision and accuracy.

To overcome these limitations, nonconventional machining processes are developed as revolutionary techniques for micromachining. Among the different nontraditional machining processes, Electrical Discharge Machining (EDM) process is considered one of the more resourceful and reliable techniques for micro-fabrication in a vast array of applications. The process of material removal by controlled erosion due to a series of rapid sparks occurring in a small gap between electrodes is known as the Electric Discharge Machining process [2]. To machine microparts, intricate geometries, and micro-features with high precision, downscaling of electric discharge machining is required, and it is termed as a micro-EDM process. This can be achieved by minimizing the discharge energy between the tool and workpiece and using an extremely short pulse of the discharge current, etc. Micro-EDM is a versatile process to produce products with micro-dimensions with high precision and geometric accuracy. A lot of theoretical models have been developed to predict the performance of the micro-EDM process by FEM analysis of a single crater formed due to the generation of a solitary spark. An anode erosion model has been developed to show that the removal of material in the EDM process is due to the thermal melting of electrodes. A constant fraction of the total discharge power is supplied to the anode, the distribution of which can be approximated by the Gaussian distributed heat flux. The flux area and therefore the plasma channel radius increases with discharging time (pulse-on duration) [3]. In another model called the cathode erosion model, it has been suggested that the electrons in the plasma channel move with higher velocity than that of positive ions which results in the formation of larger melt pool at anode at the initial stage of discharge duration. As a result, anode melts faster than the cathode. The plasma channel expands further and due to its expansion, the heat flux density at the anode decreases which results in resolidification of molten material at anode [4]. Superheating phenomenon is a dominating factor for electrode material removal; hence the formation of superheated and highly pressurized plasma channel causes the heat transfer to the electrodes, and this results in the material removal due to erosion [5]. Simulation of single discharge crater in the EDM process has been studied to predict MRR of the process. A good correlation can be found by considering thermophysical properties of materials, latent heat of fusion, and evaporation. It is suggested that using an expanding heat source would give more accurate results [6]. An electrothermal model incorporating temperature-dependent thermal properties of the workpiece and plasma channel expensing with a pulse duration

has been developed to predict the percentage of energy distribution to the tool and workpiece [7].

A modified numerical model has been developed for micro-EDM to show the effect of sparking ratio on temperature profile in the workpiece. Also, the numerical analysis of multi-spark micro-EDM has been performed in order to observe the temperature distribution along the normal and axial direction in the workpiece. The model confirms that the rate of decrease in temperature is high during spark off time due to surface convection [8]. The thermal damage to the workpiece surface has been investigated by modeling of progressive random discharge in die-sinking EDM on NiTi workpiece. The temperature profile on the surface has been analyzed, and a large temperature gradient is found on the surface [9]. Evaluation of thermal phase transformation and residual stresses in the recast layer along with HAZ is predicted using a single-spark EDM model [10].

Single-spark numerical simulation has been performed by the researches. However, in actual practice to create a feature in the workpiece, multiple sparks are required to be generated in a sequence dictated by the minimum gap between two electrodes. In view of that, an effort has been made to develop a novel model to account for the generation of multiple progressive sparks based on the minimum IEG. The IEG between tool and workpiece is determined through the arbitrary surface roughness induced to both the electrodes' surfaces.

18.2 Multi-sparks in the EDM Process

Tool and workpiece surface have irregularities and asperities due to which the localized gap between them is not constant everywhere. The asperities to both the surfaces are assigned by the random surface roughness value (Ra). Figure 18.1 shows a schematic representation of the tool and workpiece surface with random asperities. Point 1 is the position where the localized gap is minimum, so the first spark generates at that point and lasts for the pulse-on duration. The spark switches its occurrence to position 2 which happens to be the next minimum gap. In a similar manner, the continuous sparks are generated between the tool and workpiece according to the ascending order of IEGs which results in the machining of a layer of material from both the surfaces.

The number of sparks corresponding to the set of open-circuit voltage and capacitance is determined by the crater radius of single sparks with certain crater overlap (10%). The total time of the simulation for a single layer of machining is the number of spark times the duration of a single spark. Duration of single sparks has been assumed to be the sum of pulse-on and pulse-off duration.

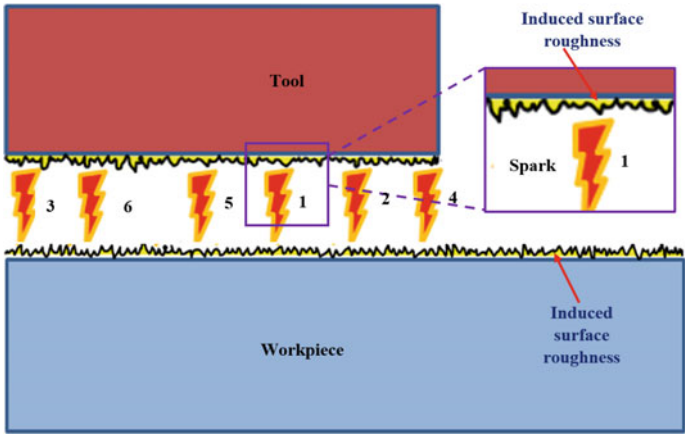

Fig. 18.1 Schematic diagram showing the formation of multiple sparks in the EDM process

18.3 Model Description

The electrothermal model is generally used to describe the micro-EDM process wherein a plasma channel formation results in superheating of the workpiece electrode. The consequence of superheating is the generation of a crater on the workpiece as well as the tool surface. Superheating involves melting and vaporization, so the mechanism for crater formation is the result of melting and vaporization of electrically conductive material. In the current work, the thermal conduction model and thermal ablation model are combined to make a more realistic model.

Certain assumptions are applied to the model due to the stochastic nature of the EDM process. The uncertainty arises due to some governing factors such as energy distribution between the tool and workpiece, plasma radius, and the shape of the plasma channel.

The following assumptions are made for the model generation:

1. Thermophysical properties of the workpiece material do not depend on temperature.
2. The material of the workpiece is homogenous and isotropic in nature.
3. The discharge would occur at an instantaneous voltage (50%) of the open-circuit voltage.
4. A certain fraction of the total discharge energy is conducted to the workpiece. This fraction of energy varies with different conditions of the tool, workpiece combination, and dielectric medium.
5. The plasma breakdown has already taken place, and the condition in the inter-electrode gap is such that certain percentage of total discharge energy is going into the workpiece electrode and the tool electrode.

6. Flushing efficiency is assumed to be 100%. It implies that the total volume of the workpiece material having a temperature above the melting temperature of the workpiece is removed.

18.3.1 Boundary Conditions

Figure 18.2 shows a 2D axisymmetric domain considered for the current study. Boundaries 2, 3, and 4 are assumed to be insulated as the pulse-on duration is very low in the micro-EDM process for the diffusion of heat to these boundaries. The fraction of discharge energy going into the workpiece (anode) is approximated by the Gaussian distribution and applied to Boundary 1.

At Boundary 1, the condition during the discharge time is

$$K\frac{\partial T}{\partial y} = q(r)\ [\text{at r} \leq \text{R}]$$

The distribution of the heat input to the workpiece is approximated by the Gaussian heat flux distribution as follows:

$$q(r) = q_0\, exp\left\{-4.5 \times \left(\frac{r}{R}\right)^2\right\} \tag{18.1}$$

The heat conducted to the workpiece is the fraction of the total discharge energy. The maximum of that heat is expressed as

$$q_0 = \frac{(\eta \times 4.45 \times E)}{t_{on} \times \pi \times R^2}\ \left(\text{W/m}^2\right) \tag{18.2}$$

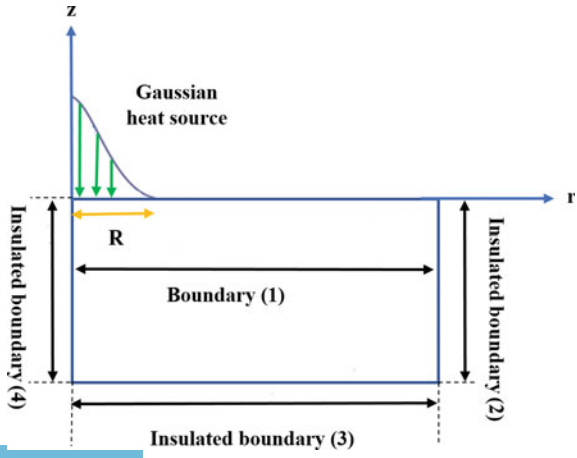

Fig. 18.2 Schematic of the 2D physical domain used

where q_0 is the maximum heat flux at r = 0.

E is the discharge energy per pulse = { $\frac{1}{2} \times C \times (V_d)^2$}, R is the plasma channel radius which is a function of pulse-on time, t_{on} is pulse-on time or discharge duration, and η is the fraction of the total energy going into the workpiece. In the current model, η is taken as 0.39 [11].

The plasma radius expands with an increase in pulse-on time and is given by the relations [11]

$$R_a = 0.0284\ (t_{on})^{0.9115} \tag{18.3}$$

$$R_c = 0.0425(t_{on})^{0.0895} \tag{18.4}$$

where R_a and R_c represent plasma radius at the anode (workpiece) and cathode (tool).

Boundaries 2, 3, and 4 are insulated. Therefore, no heat loss occurs at these boundaries.

$$\frac{\partial T}{\partial n} = 0$$

where *n* is normal to the boundaries.

18.3.2 Thermal Conduction Model

The governing equation used for heating the workpiece is the thermal conduction equation without any heat generation and is given by

$$\frac{\partial T}{\partial t} = \alpha\left(\frac{\partial^2 T}{\partial x^2} + \frac{\partial^2 T}{\partial y^2}\right) \tag{18.5}$$

where α is thermal diffusivity expressed as $(\frac{K}{\rho \times C_p})$, K is the thermal conductivity, C_p is the specific heat capacity, and ρ is the density of workpiece material. T and t represent temperature field and time, respectively.

18.3.3 Thermal Ablation Model

In order to measure the dimensions of the crater formed due to the melting and even evaporation of the workpiece material, it is difficult to obtain it employing only the thermal conduction model as the conduction of heat results into melting as well as evaporation. With the addition of thermal ablation model, the portion of the melt pool having a temperature above melting temperature is removed to comply with the

100% flushing efficiency. The formed crater geometry and its depth, as well as the radius, are comparable with the crater formed using only the conduction model [6].

For applying the thermal ablation model to the micro-EDM process, some boundary conditions have to be applied in order to satisfy the mechanism of thermal ablation. The first boundary condition is related to ablation temperature condition which constrains the temperature on the workpiece during machining not to exceed above melting temperature. This is because the volume of material inside the crater, having a temperature above the melting point, is assumed to flush out from the crater. For applying this approach, the temperature of material inside the crater should not reach above its melting point as melted part of the crater, in accordance with the assumption, should not be present inside the crater.

At Boundary 1 during pulse-off time:

$$K\frac{\partial T}{\partial y} = q_a = h_a \times (T_m - T)\,[\text{at r} \le \text{R}] \tag{18.6}$$

where q_a is ablative heat flux, T_m is melting temperature, h_a is ablative heat transfer coefficient, and T is ambient temperature.

The ablative heat transfer coefficient (h_a) in this model is assumed to be temperature-dependent and linearly increases with increase in temperature. This temperature dependency of ablative heat transfer coefficient is necessary for proper functioning of the initial boundary condition. So, the value of h_a be defined as

h_a is zero when $T < T_m$ and linearly increases when $T > T_m$.

The above condition implies that the portion of the crater above melting point temperature releases heat by convection, and the amount of heat release is equal to the ablative heat flux. With the increase in temperature inside the crater (above melting point temperature), the value of ablative heat transfer coefficient increases and consequently the convective heat transfer rate increases. Deformed geometry feature with a normal ablation velocity is used to reduce the solid boundary.

18.4 Results and Discussion

Numerical simulation has been performed employing FEM solver COMSOL Multiphysics considering SS-EN 24 as the workpiece material. The process parameters used in the simulation of single as well as multi-spark micro-EDM process are shown in Table 18.1. The thermophysical properties of SS-EN 24 are given in Table 18.2.

Table 18.1 Process parameters and their levels

S. No.	Parameter	Unit	Levels		
1.	Open-circuit voltage	V	90	105	120
2.	Capacitance	nF	0.1	1	10

Table 18.2 Thermophysical properties of workpiece material

Material	Melting point (K)	Thermal conductivity (W/mK)	Specific heat capacity (J/kgK)	Density (kg/m^3)	Latent heat of fusion (kJ/kg)
SS-EN 24	1427	42	460	7850	265

18.4.1 Results of the Crater Formed Due to Single Spark

Crater diameter and crater depth have been calculated by the numerical simulation of the single-spark micro-EDM process at different combinations of process parameters (open-circuit voltage and capacitance), and then the effect of these input parameters on crater geometry is analyzed. A typical crater formed during the single-spark EDM process is shown in Fig. 18.3.

Variation of Crater Depth with Open-Circuit Voltage and Capacitance

Figure 18.4a and b show the variation in crater depth with open-circuit voltage and capacitance, respectively. With an increase in open-circuit voltage and capacitance, the crater depth increases continuously as both the parameters define the discharge energy per pulse. The increased discharge energy results in the formation of a crater with higher depth. The increased value of the capacitor also increases the discharging time which allows the large penetration of heat into the workpiece. The variation in crater depth with open-circuit voltage is not much significant as the discharging time invariably remains constant for a constant value of capacitance. However, the discharge energy depends on the supplied voltage for maximum heat delivered to the gap.

Variation of Crater Diameter with Open-Circuit Voltage and Capacitance

The open-circuit voltage has a very less effect on crater diameter as compared to the capacitance value. This is due to the fact that for the RC-based power generator, the charging time is invariably constant with constant capacitance value. Since the discharging time (pulse-on time) is assumed to be 10% of the charging time, it also remains constant. The plasma radius is directly related to discharging time given

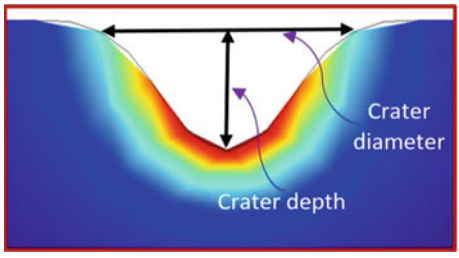

Fig. 18.3 Representation of crater diameter and crater depth (SS-EN 24, 120 V, 1nF)

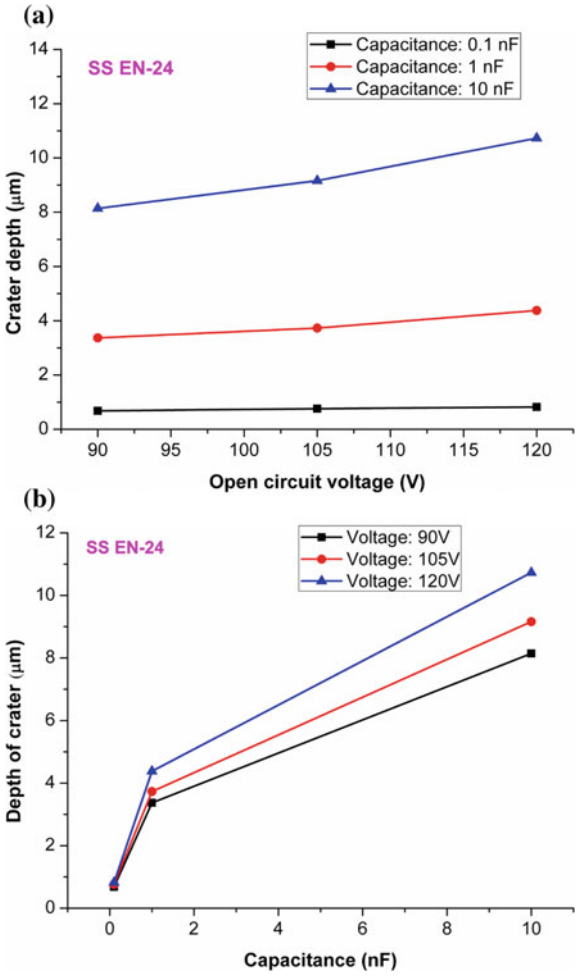

Fig. 18.4 Variation of crater depth, **a** with open-circuit voltage, **b** with capacitance

by $R_a = 0.0284\ (t_d)^{0.9115}$. Therefore, the formed crater diameter is a function of discharging time which increases with the capacitance value. The effect of open-circuit voltage is very small on discharging time, and thus the crater diameter shows a very less variation with it (Fig. 18.5a). However, the discharge energy as well as discharging time increases with capacitance which results in a larger diameter of the crater formed as shown in Fig. 18.5b.

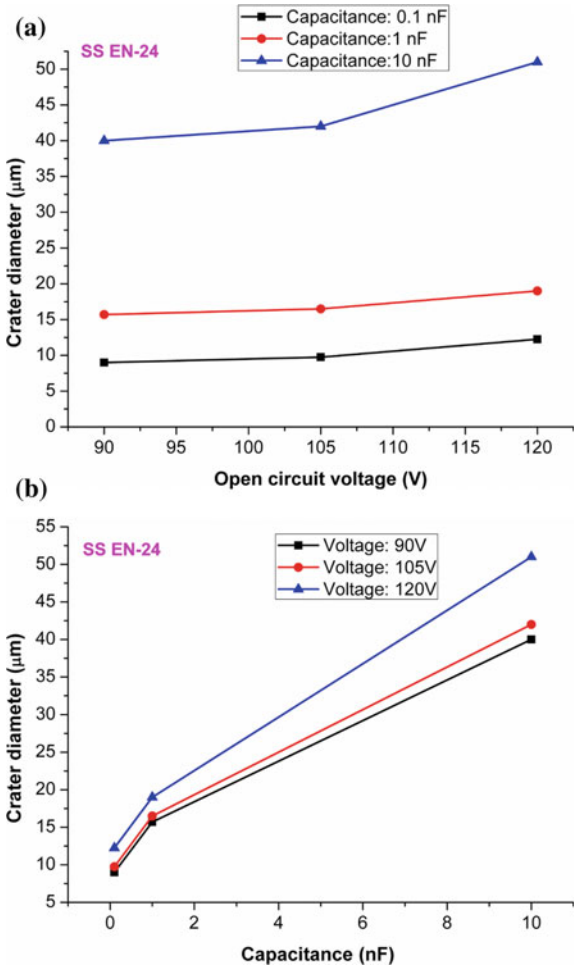

Fig. 18.5 Variation of crater diameter, **a** with open-circuit voltage, **b** with capacitance

18.4.2 Results of Multi-spark Micro-EDM Simulation

Based on the crater geometry observed at different values of capacitance, open-circuit voltage, and incorporation of 10% of crater overlap, the number of sparks required to remove a layer of material from workpiece has been calculated. The generation of spark at least inter-electrode gap results into the formation of a crater. The switching code generated in MATLAB determines the occurrence of subsequent sparks at the next locations. Therefore, the accurate prediction of overlapping between two adjacent sparks and the total number of sparks removes a layer of material from the workpiece surface. The progression of sparks in multi-spark numerical simulation is shown in Figs. 18.6, 18.7, and 18.8. The simulated images show the workpiece

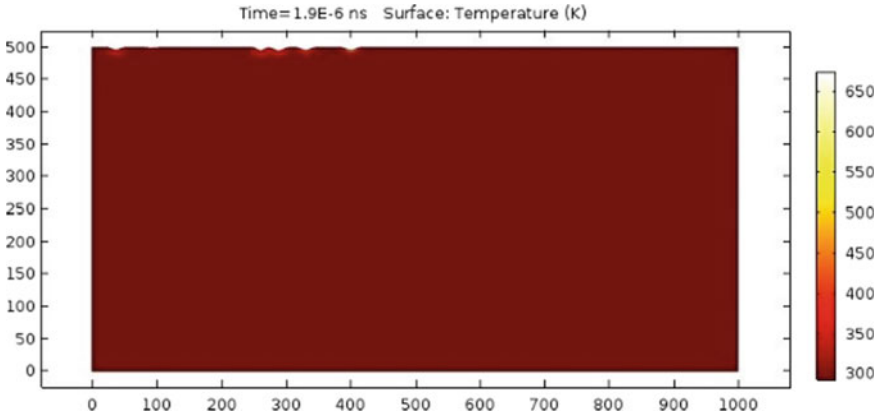

Fig. 18.6 Workpiece profile after five sparks

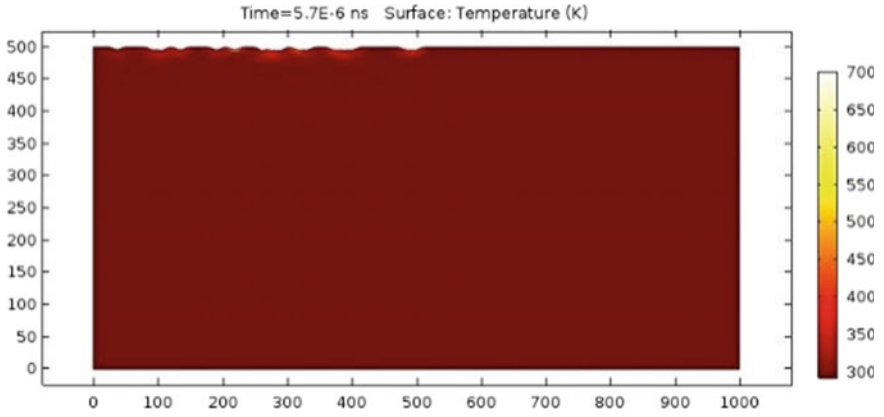

Fig. 18.7 Workpiece profile after 15 sparks

surface after 5, 15, and final spark, respectively. The workpiece material is SS-EN 24 machined at 120 V and 0.1 nf.

The total time for a single layer of machining has been calculated by the product of the total number of sparks and the average time required for the machining of a single spark. The capacitor charging time is calculated using standard RC circuit and discharging time is assumed to be 10% of the charging time.

Variation of Material Removal Rate with Capacitance

Figure 18.9 depicts the variation on material removal rate with the capacitance at different levels of open-circuit voltage.

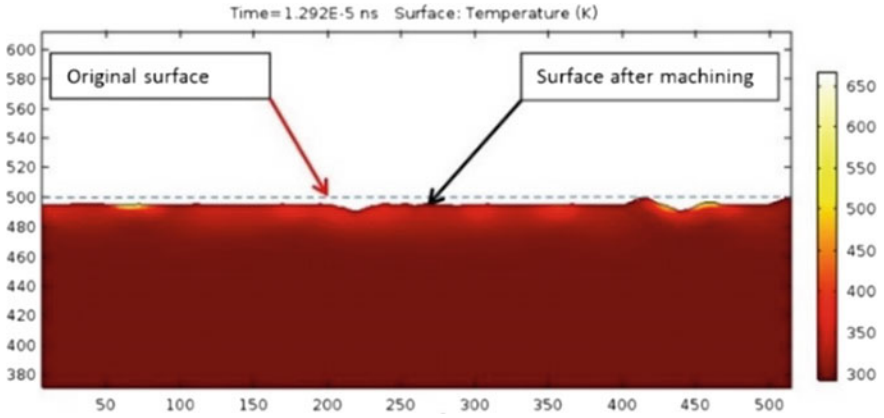

Fig. 18.8 Initial workpiece surface and the machined surface after the final spark

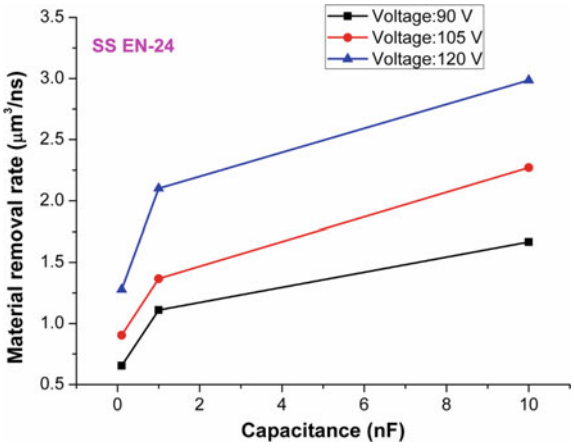

Fig. 18.9 Variation of MRR with capacitance

Material removal rate increases with both open-circuit voltage as well as capacitance as the energy per pulse increases with both the input parameters. It is evaluated by the ratio of the average volume of a single layer removed and the total time of machining per layer. The third dimension of the workpiece is assumed to be unity.

Variation of Material Removal Rate with Open-Circuit Voltage

The variation of MRR with open-circuit voltage at different capacitance levels is shown in Fig. 18.10. The MRR increases with open-circuit voltage at constant capacitance value. This variation is a consequence of rising discharge energy with open-circuit voltage. More material is removed with increased discharge energy and as a result of this the MRR increases.

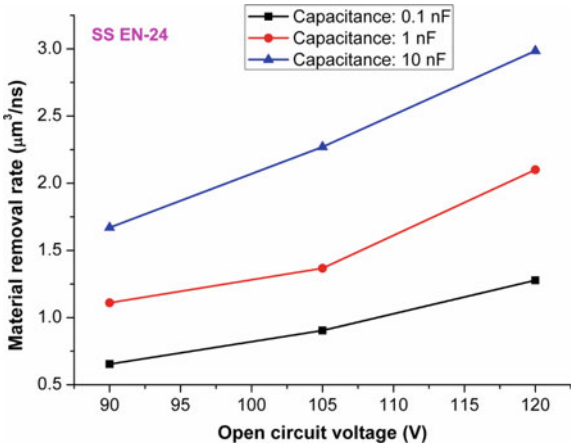

Fig. 18.10 Variation of MRR with open-circuit voltage

18.5 Conclusions

In this work, a novel approach of multiple spark generation has been used for simulation of micro-EDM process to analyze the consequences of process parameters, viz., capacitance value, open-circuit voltage on the performance of the micro-EDM process. It is observed that the capacitance value has a critical effect on crater geometry. Large variations in crater diameter and crater depth with capacitance have been found. Open-circuit voltage has a small effect on crater dimensions. Material removal rate directly depends on the open-circuit voltage and capacitance. With the increase in either open-circuit voltage or capacitance, MRR increases because increasing any one process parameter results in increasing discharge energy. This is an exploratory work in the direction of multiple sparks in EDM process. Further investigations would incorporate crater overlap, workpiece thermophysical property, etc., to explore the material removal in micro-EDM process.

References

1. Liu, X., DeVor, R.E., Kapoor, S.G., Ehmann, K.F.: The mechanics of machining at the microscale: assessment of the current state of the science. J. Manuf. Sci. Eng. **126**(4), 666–678 (2005)
2. Ho, K.H., Newman, S.T.: State of the art electrical discharge machining (EDM). Int. J. Mach. Tools Manuf. **43**, 1287–1300 (2003)
3. Patel, M.R., Barrufet, M.A., Eubank, P.T., DiBitonto, D.D.: Theoretical models of the electrical discharge machining process. II. The anode erosion model. J. Appl. Phys. **66**(9), 1 (1989)
4. DiBitonto, D.D., Eubank, P.T., Patel, M.R., Barrufet, M.A.: Theoretical models of the electrical discharge machining process. I. A simple cathode erosion model. J. Appl. Phys. **66**(9), 4095–4103 (1989)

5. Eubank, P.T., Patel, M.R., Barrufet, M.A., Bozkurt, B.: Theoretical models of the electrical discharge machining process. III. The variable mass, cylindrical plasma model. J. Appl. Phys. **73**(11), 7900–7909 (1993)
6. WeingäLrtner, E., Kuster, F., Wegener, K.: Modeling and simulation of electrical discharge machining. Procedia CIRP **2**, 74–78 (2012)
7. Shao, B., Rajurkar, K.P.: Modelling of the crater formation in micro-EDM. In: 9th CIRP Conference on Intelligent Computation in Manufacturing Engineering - CIRP ICME'14 (2015)
8. Somashekhar, K.P., Panda, S., Mathew, J., Ramachandran, N.: Numerical simulation of micro-EDM model with multi-spark. Int. J. Adv. Manuf. Technol. **76**(1–4), 83–90 (2015)
9. Liu, J.F., Guo, Y.B.: Thermal modeling of EDM with progression of massive random electrical discharges. Procedia Manuf. **5**, 495–507 (2016)
10. Tang, J., Yang, X.: Simulation investigation of thermal phase transformation and residual stress in single pulse EDM of Ti–6Al–4V. J. Phys. D: Appl. Phys. **51**, 135308, (12 pp) (2018)
11. Yeo, S.H., Kurnia, W., Tan, P.C.: Electro-thermal modelling of anode and cathode in micro-EDM. J. Phys. D: Appl. Phys. **40**, 2513–2521 (2007)

Chapter 19
Analysis of Fiber Laser Micro-grooving on 316 L Stainless Steel

A. Sen, B. Doloi and B. Bhattacharyya

Abstract Within the domain of austenitic stainless steel, 316 L stainless steel is widely used in both biomedical and automotive industries due to its superior mechanical properties. In the present research study, the performance of the fiber laser micro-grooving process with regard to kerf width and surface roughness R_a has been analyzed. The process parameters, i.e., laser power (7.5–20 W), pulse frequency (55–80 kHz), and cutting speed (0.5–3 mm/s) are considered to examine the aforesaid responses. The results of the experiments exhibit that the presence of flowing condition of the high-pressure assist air in combination with varying aforesaid process parameters, have a considerable effect on the kerf width characteristics along with the average surface roughness R_a of microgroove cut on 316 L stainless steel.

Keywords Fiber laser · Micro-grooving · Stainless steel · Kerf width · Surface roughness

19.1 Introduction

Over the past decade, it has been observed that fiber lasers have played an essential role in the laser industries ranging from high to low power laser sources required for various engineering applications. Although the number of research works utilizing fiber lasers has increased in the previous years, the research works integrating fiber lasers have not yet obtained their optimum utilization in the domain of micromachining. At present, the utilization of fiber laser micromachining process on 316 L stainless steel (SS) for the manufacturing of stents has increased rapidly. The previous research works involving 316 L showcase various aspects of geometrical features such as kerf width, depth in order to achieve desired profiles, etc.

A pulsed fiber laser setup was utilized by Meng et al. [1] in order to fabricate stents on 316 L. Laser output power, pulse frequency, pulse length, assist gas pressure (oxygen) along with cutting speed were considered as the primary process parameters for

A. Sen (✉) · B. Doloi · B. Bhattacharyya
Production Engineering Department, Jadavpur University, Kolkata 700032, India
e-mail: abhishek.sen1986@gmail.com

M. S. Shunmugam and M. Kanthababu (eds.), *Advances in Micro and Nano Manufacturing and Surface Engineering*, Lecture Notes on Multidisciplinary Industrial Engineering,
https://doi.org/10.1007/978-981-32-9425-7_19

the analysis of the kerf width. With the change in laser power along with the cutting speed, the kerf width dimensions were varied significantly. The authors found that at a laser power 7 W, 0.15 ms pulse duration, cutting speed of 8 mm/s, assist oxygen pressure of 0.3 MPa, and pulse frequency of 1500 Hz, the kerf width along with surface roughness and heat-affected zone (HAZ) width was minimized. A comparative study of fiber laser micro-cutting on 316 L under different conditions was performed by Muhammed et al. [2]. The authors derived that, in the wet condition, kerf width was low in comparison to that of the dry condition. The back wall damages along with HAZ width were reduced significantly during the wet condition. Kleine et al. [3] further utilized single-mode fiber laser in order to micro-cut stainless steel stents. The considered responses were kerf width and surface quality on the sidewall of the micro-cut profiles. The authors concluded that during high settings of pulse frequency, spot overlap was a dominant factor which in turn produced low and good quality kerf widths. However, when the spot overlap reached over 85%, the factor was insignificant for surface roughness parameters. Sen et al. [4] on the other hand, carried out a fiber laser micro-grooving operation on 316 L SS at 200, 250 °C as well as at room temperature to assess the influence of cutting speed and laser beam focal position on the kerf width in combination with HAZ width. The authors also found out that at 250 °C, the uniformity of the micro-groove profiles was higher compared to the other temperatures. However, at room temperature, kerf width along with the HAZ width dimension was relatively lower compared to the elevated temperatures. Further, the uniformity and waviness of the profiles were also affected considerably in the room temperature compared to the higher temperatures. The authors concluded that the formation of taper notably affected the uniformity as well as the kerf width of the micro-groove profiles. Fuss et al. [5] showcased that when micro-grooves were generated on the surface of 316 L, the rate of human aortic endothelial cells (HAEC) increased significantly. Thus, it is essential to fabricate micro-grooves on 316 L in order to utilize the stent with its specific geometrical features to improve the biocompatibility as well as the tissue response time.

In this regard, the assessment of fiber laser on the machinability of 316 L SS (at room temperature) in atmospheric condition and in flowing assist air condition is yet to be carried out by the researchers. The high range of pulse frequency which leads to an increment in the laser spot overlapping factor has also not been studied extensively. From the trial runs, the selection of process parameters is carried out for the present study. Further, laser beam sawing angle, along with the laser beam opening type (the offset value between the micro-groove cut width and micro-groove wall), is correlated to the surface profiles of the fiber laser fabricated micro-grooves with the considered process parameters to study their effects on the performance criteria.

In this present research study, a comparative analysis has been conducted in order to find out the effect of fiber laser process parameters, i.e., cutting speed, laser power, and pulse frequency in atmospheric condition as well as in condition of flowing assist air pressure on kerf width and surface roughness R_a of micro-groove cut on 316 L SS by fiber laser micromachining process.

19.2 Experimental Plan

In the present research study, a total of 18 experiments has been carried out on 316 L SS (50 mm × 50 mm × 1 mm) without the supply of assist air, i.e., in atmospheric condition. In addition to this, with a similar set of process parameters, the same number of experiments is repeated with assist airflow at a pressure of 4 kgf/cm^2. In each set of experiment, one process parameter is kept as a variable while the remaining two process parameters are kept as constants at their lowest values, considered in the experimental investigation. A total of 36 experiments is carried out with multi-diodes pumped 50 W nanosecond pulsed fiber laser system. However, in the present research work, due to the Gaussian beam profile of the laser beam, straight cut micro-groove profiles have been fabricated with the triangle-shaped formation at the depth edges. The experiments are categorized into three sets in which one set of the process parameter is varied with and without the supply of high-pressure assist air. The experiments are carried out by utilizing software designed for micro-cutting applications, in which the offset value (based on the sawing angle) between the micro-groove width and micro-groove wall in combination with the sawing angle has a notable influence. The higher the sawing angle, the higher is the opening of the micro-groove profile. Thus, in order to achieve smaller dimensions of kerf width, a low sawing angle is preferred. As a result, in the present research study, the sawing angle is made constant at 0.01°. In Fig. 19.1, a schematic diagram comprising the movement of the laser beam inside a micro-groove is exhibited. The micro-groove profiles are measured by Leica optical microscope at 1.25×, 20× and 50× optical lenses. The surface roughness (R_a) is measured by a Mitutoyo SJ 410 surface roughness tester with a Gaussian filter. Parameters related to surface roughness measurements are as follows: sampling length (l) of 4 mm and cut-off length (λ_c) of 0.8. The measurements of both the kerf width and surface roughness are carried out at five reference lines, and the result is the average of these values. The array of fiber laser fabricated micro-grooves is shown in Fig. 19.2.

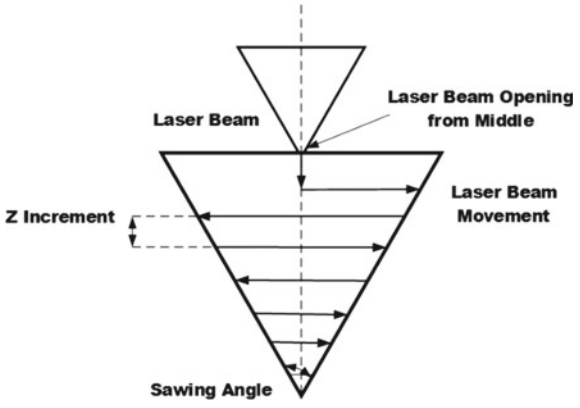

Fig. 19.1 Schematic diagram of laser beam movement during micro-groove formation

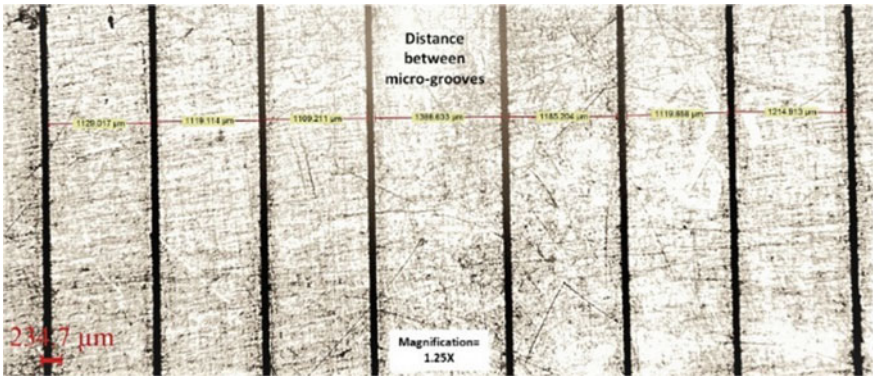

Fig. 19.2 Microscopic view of an array of fiber laser fabricated micro-grooves

19.3 Experimental Results

A total of 18 experiments (corresponds to three sets of experiments) has been performed without assist air along with another 18 experiments, which have been repeated with the aid of high-pressure assist air. The effect of laser power, pulse frequency, and cutting speed with respect to surface roughness parameters of fiber laser produced micro-grooves on 316 L SS are discussed and analyzed subsequently.

19.3.1 Effect of Laser Power on Kerf Width and Surface Roughness, R_a

In the first set of experiments, the laser power is varied from 7.5 to 20 W while the other fixed parameters are set at a pulse frequency of 55 kHz, cutting speed of 0.5 mm/s and the duty cycle of 99%. The high value of the duty cycle is considered for all the 36 experiments in order to achieve high laser power corresponding to the input laser power value. Figure 19.3 corresponds to the effect of laser power on kerf width during the supply of assist air and without the assist air supply. Figure 19.4 represents the effect of laser power on surface roughness R_a with and without the supply of high-pressure assist air. The average value of R_a to assist air supply and without assist air is found at 2.13 μm and 2.09 μm, respectively.

In Fig. 19.3, it can be observed that in the presence of assist air supply, the kerf width dimensions tend to increase more compared to the experiments conducted without the supply of assist air. However, the maximum kerf width dimension is found to be 97.44 μm in the absence of assist air at a laser power of 20 W. Advancement of high laser power causes high laser peak power in the machining zone. Subsequently, a high amount of energy is further generated by an increase in the laser peak power. Therefore, immediate melting and vaporization occur in the machined

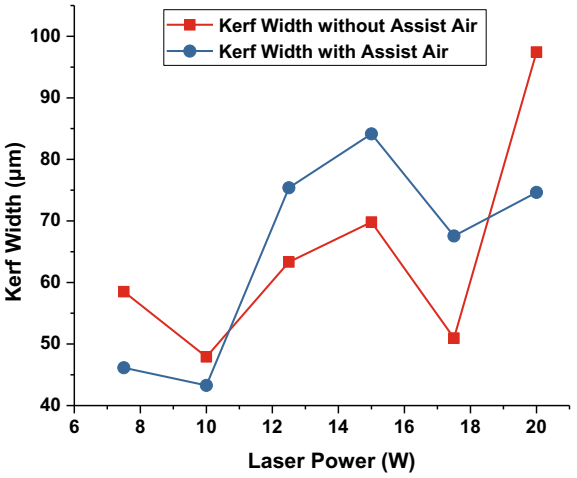

Fig. 19.3 Effect of laser power on kerf width

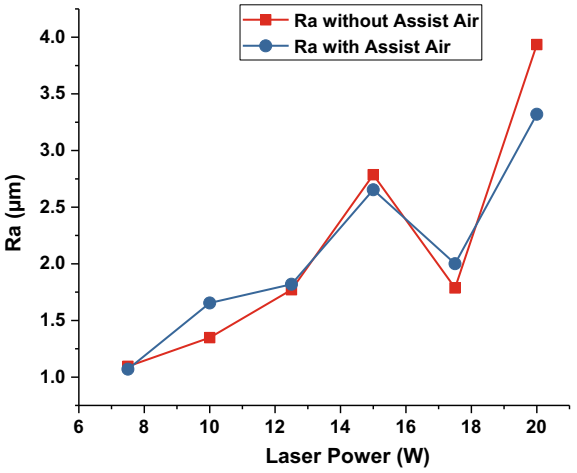

Fig. 19.4 Effect of laser power on R_a

zone subsequently. Furthermore, a high amount of material is removed and leads to high kerf width dimensions. The presence of a high-pressure flow of assist air has attributed less formation of resolidified material at the micro-groove edges which in turn has increased the kerf width dimensions. However, when the laser power reaches 20 W, sufficient amount of laser pulse energy, as well as laser beam peak power, can remove the resolidified material from the edges and lead to a steep rise in the kerf width dimension.

From Fig. 19.4, it is noted that when laser power increases up to 15 W, R_a tends to increase irrespective of the supply of assist air. A drop in values of R_a can be observed at a laser power of 17.5 W in which the high flow of assist air aids in lowering of R_a value considerably. This phenomenon can be the effect of resolidified material

along the micro-groove zone which lowers the surface roughness. Furthermore, with the increment in laser power, there is a rapid increase in R_a value in both the conditions due to the reason that the machining zone gets the suitable energy to melt and evaporate instantly. Thus, the laser peak power intensity can penetrate furthermore. However, simultaneous evaporation of the surfaces may occur in the irradiated spot center, and therefore, the irradiated laser surface shows a bumpy surface. The high amount of removal of material is observed during the flow of high pressurized assist air while combining with high laser power. It is also observed that the homogeneity of the micro-groove profiles is inconsistent throughout the entire length of the micro-groove.

19.3.2 Effect of Pulse Frequency on Kerf Width and Surface Roughness, R_a

In the second set of experiments, pulse frequency varies from 55 to 80 kHz, whereas the constant parameters are laser power of 7.5 W, cutting speed of 0.5 mm/s with and without the supply of assist air. Figure 19.5 shows the effect of pulse frequency on kerf width with and without the supply of assist air whereas the effect of pulse frequency on surface roughness R_a is shown in Fig. 19.6. The effect of the supply of high-pressure assist air with the increment of pulse frequency is found to be more predominant than the laser power. From Fig. 19.5, it is observed that in the presence of assist air supply, kerf width dimensions are reduced with the high values of pulse frequency. On the contrary, a reverse phenomenon is observed with the absence of assist air. During pulse frequency of 75 and 80 kHz, a notable decrease in the values of kerf width dimensions is observed in the presence of assist air supply, although the

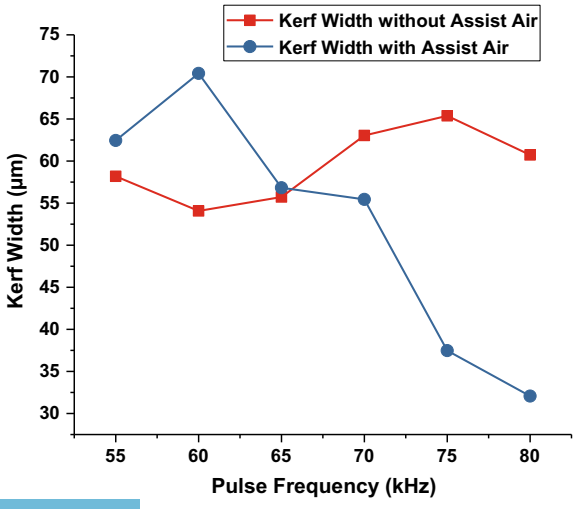

Fig. 19.5 Effect of pulse frequency on kerf width

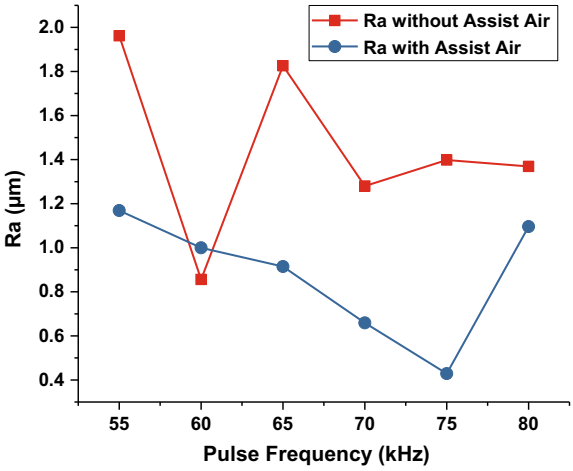

Fig. 19.6 Effect of pulse frequency on R_a

drop in laser peak power is inevitable at a high pulse frequency setting. A high number of laser pulses induce high laser material interaction time while keeping the pulse energy constant. In the absence of assist air supply, high laser material interaction time provides a sufficient amount of time for the ablation of material removal. The resolidification phenomenon along with HAZ are the dominant factors in absence of assist air. Resolidification phenomenon revereses and leads to the lowering of kerf width dimensions due to high spot overlapping factor in combination with the flow of high-pressure assist air. In addition to this, the changes in kerf width dimensions without assist air are not as high as compared to the assist air supply. High-pressure assist air forces the extra amount of molten material from the machining zone, leading to the reduction in kerf width dimension along with the thicker cut width.

When pulsed laser beam irradiates on 316 L SS surface, a thin melted layer is formed on the machined surface. Further, the machined surface is found to be less interrupted by the liquid displacement on the micro-machined zone. This phenomenon is due to the action of recoil pressure [6], formed during the fiber laser interaction with 316 L surface. As a result, smooth machined surfaces can be observed at a high pulse frequency. The effect is prominent when a high jet flow of assist air is applied to remove the molten material from the micro-groove zone. As the material removal rate is low at high pulse frequency due to low laser beam peak power, the flow of high-pressure assist air reduces the attributes of sputtering as well as HAZ width from the micro-groove profiles. The absence of assist air supply leads to high values of R_a in comparison to the presence of assist air supply. Thus, high peak power in combination with assist air significantly reduces R_a in a considerable amount. Only when the pulse frequency is kept as 80 kHz in the presence of assist air supply, R_a tends to showcase an observable rise as compared to the previous set of values.

At 50× magnification, a microscopic view of the micro-grooves profiles cut at the variation of pulse frequency in the presence of assist air supply has been shown

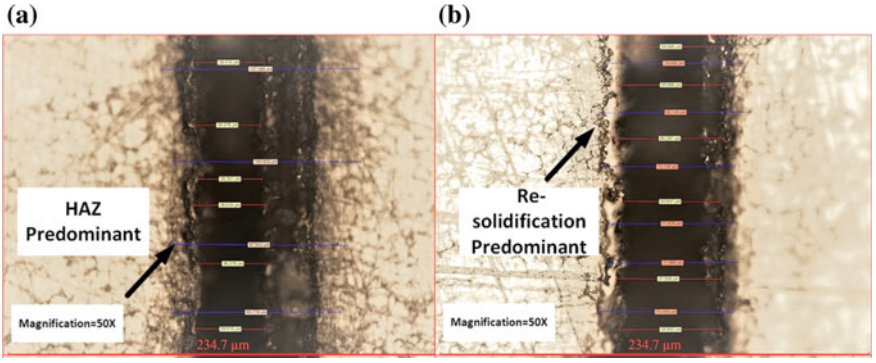

Fig. 19.7 **a** Microscopic view of a micro-groove profile at 50× magnification at a pulse frequency of 80 kHz. **b** Microscopic view of micro-groove profile at 70 kHz of pulse frequency during assist air pressure (constants: laser power of 7.5 W and cutting speed of 0.5 mm/s)

in Fig. 19.7. From Fig. 19.7a, b, it is evident that HAZ is a detrimental factor which hinders while obtaining a uniform and smooth micro-groove profile.

19.3.3 Effect of Cutting Speed on Kerf Width and Surface Roughness, R_a

In this set of experiments, pulse frequency of 80 kHz and laser power of 7.5 W are kept as constants. The effects of cutting speed with and without assist air supply on kerf width are shown in Fig. 19.8. Figure 19.9 depicts the effect of cutting speed on average surface roughness R_a of the cut surface of micro-groove with and without assist air supply. The supply of high-pressure assist air has considerably improved micro-groove homogeneity by reducing the surface roughness. At higher cutting speed, kerf width without assist air follows a gradual decrease in the kerf width dimension as observed from Fig. 19.8.

On the contrary, a kerf width dimension in the presence of assist air is higher at cutting speed of 1.5 mm/s, followed by a gradual decrease in the kerf width dimensions. The average dimensions of the kerf width are comparatively higher when the assist air is supplied at high pressure. This increment in kerf width dimension suggests that assist air supply has partially blown away the molten material from the machining zone to facilitate more penetration of the laser beam in the machining zone. Machining time in combination with the assist air determines the homogeneity and uniformity of the micro-groove profiles. When the cutting speed increases, it is evident that the machining time is subsequently reduced, which in turn lowers the kerf width dimensions. When the laser beam moves to and fro with the machining zone as shown in Fig. 19.1, some amount of molten material is accumulated at the machining zone which ultimately reduces the laser beam penetration rate. At

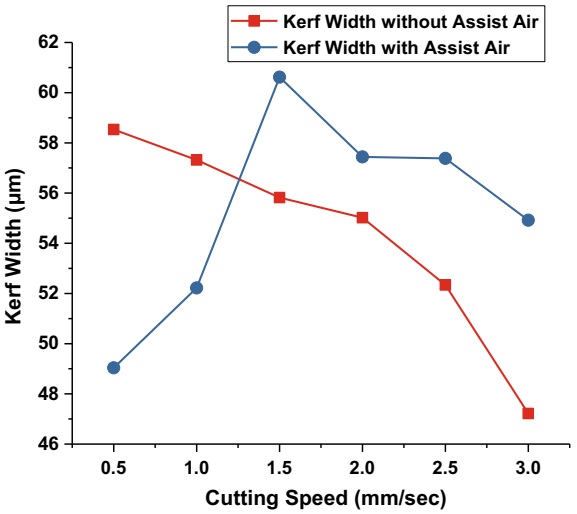

Fig. 19.8 Effect of cutting speed on kerf width

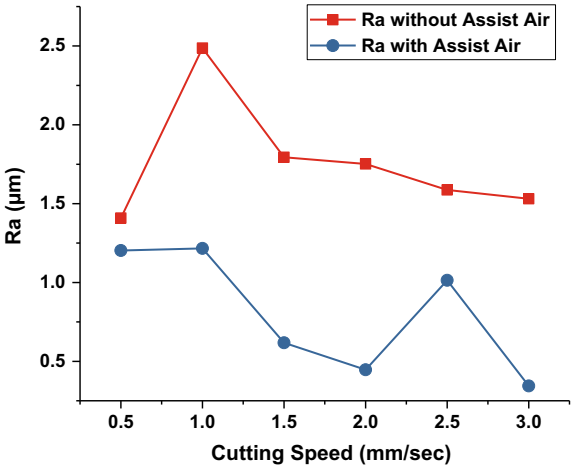

Fig. 19.9 Effect of cutting speed on R_a

each pass, the penetration rate is decreased with or without the supply of assist air. However, a sufficient amount of assist air pressure leads to the removal of the molten material and subsequently increases the kerf width dimensions. This increment in kerf width dimensions holds true at higher assist air pressure in combination with cutting speed of 1.5 mm/s. Nevertheless, low machining time along with low penetration rate ultimately reduces the kerf width dimension as observed from Fig. 19.8.

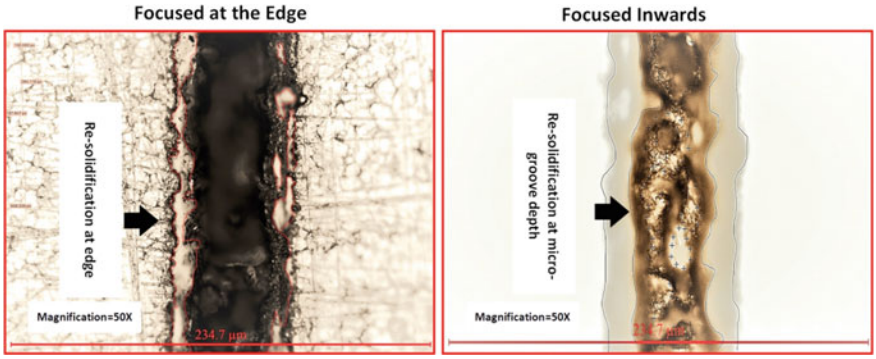

Fig. 19.10 Microscopic view of fiber laser fabricated micro-groove profiles at 50× magnification

Selection of cutting speed along with pulse frequency determines the laser spot overlapping factor and laser–material interaction time. The lower laser material interaction time during high cutting speed helps to reduce the surface roughness parameters considerably. When high cutting speed (low MRR) in combination with high-pressure assist air comes into effect, the excess amount of molten material is blown away [7]. In the presence of assist air, heat can quickly go out from the machining zone. This loss of energy successively produces resolidified material on the inner surfaces of the micro-grooves as shown in Fig. 19.10. Without the supply of assist air, it is difficult to remove the extra amount of molten material from the micro-groove periphery. Furthermore, in the absence of assist air, the excess amount cannot be blown away completely which results in high surface roughness, R_a.

19.4 Conclusions

Fiber laser micro-grooving of 316 L SS has been studied to analyze the effect of the flow of high-pressure assist air on micro-groove kerf width and average surface roughness R_a. In the presence of assist air supply at high laser power, the kerf width dimensions tend to increase more rapidly as compared to the experiments conducted without assist air supply. The effect of assist air supply is more on the kerf width dimensions in combination with high values of pulse frequency. Without the presence of assist air, the kerf width dimensions tend to increase with the increase in pulse frequency, whereas the reverse phenomenon is observed with the aid of assist air. At cutting speed of 1.5 mm/s, the presence of the jet of assist air results in a larger kerf width of micro-groove. Higher ranges of kerf width dimensions are observed when the assist air is supplied during the fiber laser micro-grooving on 316 L SS.

The experimental results also indicate that the effect of assist air is prominent in order to achieve a low average surface roughness of the cut profiles. In the presence of high-pressure assist air, the average surface roughness R_a of the cut profiles increases

with the increment of laser power. The similar phenomenon is also observed in the experiments conducted without the presence of assist air supply. However, it is observed that the difference in the obtained surface roughness values in both the cases does not exhibit observable differences. Due to the supply of high-pressure assist air, surface roughness values decrease for high values of pulse frequency. An opposite set of the phenomenon is observed in the experiments conducted without the supply of assist air. At higher cutting speed in the presence of a jet flow of assist air supply, surface roughness values lower at a considerable amount as compared to the experiments conducted without the supply of assist air.

The research findings are useful in order to analyze other surface characteristics such as waviness, tapering of the micro-grooves, and also to obtain the desired micro-groove geometries with respect to the considered process parameters during fiber laser micro-grooving on 316 L stainless steel.

Acknowledgements The authors would like to express their gratitude toward the assistance and financial support aided by CAS Ph-IV Programme of the Production Engineering Department of Jadavpur University under the University Grants Commission, New Delhi, India.

References

1. Meng, H., Liao, J., Zhou, Y., Zhang, Q.: Laser micro-processing of cardiovascular stent with fiber laser cutting system. Opt. Laser Technol. **41**(3), 300–302 (2009). https://doi.org/10.1016/j.optlastec.2008.06.001
2. Muhammad, N., Whitehead, D., Boor, A., Li, L.: Comparison of dry and wet fibre laser profile cutting of thin 316 L stainless steel tubes for medical device applications. J. Mater. Process. Technol. **210**(15), 2261–2267 (2010). https://doi.org/10.1016/j.jmatprotec.2010.08.015
3. Kleine, K.F., Whitney, B., Watkins, K. G.: Use of fiber lasers for micro cutting applications in the medical device industry. International Congress on Applications of Lasers & Electro-Optics (2002)
4. Sen, A., Doloi, B., Bhattacharyya, B.: Fiber laser micro-grooving of 316 L stainless steel utilizing variable temperature heating apparatus. In: Proceedings of the All India Manufacturing Technology Design and Research Conference, Pune, India, pp. 285–289 (2016)
5. Fuss, C., Sprague, E.A., Bailey, S.R., Palmaz, J.C.: Surface micro grooves (MG) improve endothelialization rate in vitro and in vivo. J. Am. Coll. Cardiol. **37**(2), 70A–70A (2001)
6. Soveja, A., Cicală, E., Grevey, D., Jouvard, J.M.: Optimization of TA6V alloy surface laser texturing using an experimental design approach. Opt. Lasers Eng. **46**(9), 671–678 (2008). https://doi.org/10.1016/j.optlaseng.2008.04.009
7. El Aoud, B., Boujelbene, M., Bayraktar, E., Salem, S.B., Miskioglu, I.: Studying effect of CO_2 laser cutting parameters of titanium alloy on heat affected zone and kerf width using the Taguchi method. In: Mechanics of Composite and Multi-functional Materials, 6th edn. Springer, Cham (2018). https://doi.org/10.1007/978-3-319-63408-1_14

Chapter 20
Characterization of Cutting Edge Radius of a Single Crystal Diamond Tool by Atomic Force Microscopy

Akhilesh Gupta, G. Ganesan, Sonal Sonal, A. S. Rao, Rakesh G. Mote and R. Balasubramaniam

Abstract Single crystal diamond (SCD) is the ideal tool material in ultra-precision machining because of its high hardness, wear resistance, chemical stability, and the ability to sharpen the cutting edge in nanometers. The sub-micron level in the cutting edge profile could affect the accuracy of the fabricated surfaces, since cutting edge radii strongly influence the specific cutting energy, cutting forces, cutting temperature, residual stress in the workpiece. Therefore, cutting edge profile of an SCD tool should be checked periodically. The measurements of cutting edge radii of SCD tools are very difficult because of their geometric features (angles, radius... etc) and their dimensions in the nanometric level. This paper deals with various methods of cutting edge characterization of SCD tool by Atomic Force Microscopy (AFM). The change to measurement of the cutting edge radii has been done based on the methodology of the least square circle fit over cutting edge radius with error minimization in the calculation and determined iteratively.

Keywords Atomic force microscope (AFM) · Single crystal diamond tool (SCD) · Cutting edge radius · Least square method (LSM)

20.1 Introduction

Ultra-precision machining of the non-ferrous metal optical mirrors like Fresnel lenses, Infrared aspherical lenses and molding dies for diffractive optical lenses by using diamond turning is most preferable. Here, high accuracy, complicated shapes

A. Gupta · A. S. Rao
Department of Mechanical Engineering, Veermata Jijabai Technological Institute, Matunga, Mumbai 400031, India

G. Ganesan (✉) · S. Sonal · R. G. Mote
Department of Mechanical Engineering, Indian Institute of Technology Bombay, Mumbai 400076, India
e-mail: ganeshguna91@gmail.com

R. Balasubramaniam
Bhabha Atomic Research Centre, Trombay, Mumbai 400085, India

M. S. Shunmugam and M. Kanthababu (eds.), *Advances in Micro and Nano Manufacturing and Surface Engineering*, Lecture Notes on Multidisciplinary Industrial Engineering,
https://doi.org/10.1007/978-981-32-9425-7_20

and micro-surface structures are commonly achieved. Measurement resolution and movement accuracy of the machine have been improved from nanometric level to sub-nanometric (10^{-10} m) level in the last two decades but the fabrication of SCD tool is still a challenging issue. The quality of cutting edge of the SCD tool is an important factor to determine the surface roughness and form accuracy of the machined surface. Since it is greatly influenced by sharpness and contour accuracy of the cutting edge of the SCD tool [1]. Hence, the measurement of cutting edge radius deserves with very accurate method. From the intersection of rake and flank face, three fundamental cutting edge radius shapes are defined and those are sharp, rounded, and chamfered. A cutting edge radius is a transition between the flank and rake face [2]. The highly precise method is required for assuring the accuracy of the cutting edge profile.

The undeformed chip thickness of the material must be smaller than the cutting edge radius in ductile mode machining of brittle materials [3]. Thus, nanoprecision measurement of the SCD tool has become a key issue in ductile mode cutting of brittle materials. The larger cutting edge radius creates a larger contact area and consequently, heat generation in workpiece increases due to friction [4]. The shear stress decreases with increase in the cutting edge radius and when it is beyond the critical limit, the insufficient shear will cause subsurface damage on the machined workpiece.

Characterization of the SCD tool cutting edge radius has been done by many researchers using many equipments such as optical microscope, AFM, and Scanning Electron Microscope (SEM). It is a challenging task to measure the cutting edge radius of the tool by using an optical microscope which can suffer low contrast images as a result of light coming from outside of the focal plane, measurement noise, the transparency of diamond and uncertainty of measurement. Due to constrains of lateral and vertical resolution of laser interferometer microscope and step height profilometer, the measurement of nano-scale feature is limited. Some researchers have used SEM as the most effective and most accurate approach to measure cutting edge radius due to the very high magnification of SEM [5]. Electron Beam Induced Deposition (EBID) is a direct method and an effective way to obtain tool edge radius and wear land without coating on the surface of the tool.

The SEM images are unable to show 3*D* structure topographical data points, so SEM is not capable of getting cutting edge radius data and evaluation of cutting-edge radius [6]. AFM is one of the best tools to measure the cutting edge radius since it has an excellent resolution in 3*D* measurement and capable of carrying out the measurement in the air [7] but the alignment of cutting edge of the SCD tool and AFM tip were tedious and time consuming. Additionally, there is the possibility of loss of contact between the AFM tip and cutting edge of the SCD tool. A newly developed laser-based AFM instrument for alignment of AFM tip with cutting edge was developed for obtaining 3*D* topology of the tool with high accuracy, high resolution, and reliability.

20.2 Least Square Method (LSM) of Circle Fitting with Error Minimization

The general form of the circle can be given as [8],

$$x^2 + z^2 + 2(ax + cz) + \mathrm{c} = 0 \tag{20.1}$$

By arranging the above equation in the general circle equation with radius and center data as given in Eq. 20.2.

$$(x + a)^2 + (z + b)^2 - \left(a^2 + b^2 - c\right) = 0 \tag{20.2}$$

Hence, it can be seen that the center of the circle is (−a, −b) and the radius is $\mathrm{r} = \sqrt{a^2 + b^2 - c}$. If this circle is used to approximate a collection of set of points, the shortest distance from point P (x_i, z_i) to the circle is

$$d_i = \sqrt{(x_i + a)^2 + (z_i + b)^2} - r \tag{20.3}$$

Consequently, the squared distance is

$$D_i{}^2 = (x_i + a)^2 + (z_i + b)^2 - 2r\sqrt{(x_i + a)^2 + (z_i + b)^2} + r^2 \tag{20.4}$$

It is noted that $\mathrm{r} - \sqrt{(x_i + a)^2 + (z_i + b)^2} = 0$ when P lies on the circle. Instead of solving a nonlinear least square problem formed from the above equations, we may measure the deviation from p to the circle as

$$(x_i + a)^2 + (z_i + b)^2 - r^2 = x_i{}^2 + z_i{}^2 + 2ax_i + 2\mathrm{b}z_i + c \tag{20.5}$$

The sum of the squared error is given by Eq. 20.5 as

$$\varepsilon = \sum_{i=1}^{n}\left(x_i{}^2 + z_i{}^2 + 2ax_i + 2\mathrm{b}z_i + c\right)^2 \tag{20.6}$$

From the equation of maxima and minima, ε is minimized if

$$\frac{d\varepsilon}{da} = 0, \quad \frac{d\varepsilon}{db} = 0, \quad \frac{d\varepsilon}{dc} = 0 \tag{20.7}$$

Explicitly. we need to solve

$$2\sum_{i=1}^{n}\left(x_i{}^2 a\right) + 2\sum_{i=1}^{n}(x_i z_i b) + \sum_{i=1}^{n}(x_i c) + \sum_{i=1}^{n}(x_i{}^2 + z_i{}^2)x_i = 0 \tag{20.8}$$

$$2\sum_{i=1}^{n}(x_i z_i a) + 2\sum_{i=1}^{n}(z_i{}^2)b + \sum_{i=1}^{n}(z_i c) + \sum_{i=1}^{n}(x_i{}^2 + z_i{}^2) = 0 \tag{20.9}$$

$$2\sum_{i=1}^{n}(x_i a) + 2\sum_{i=1}^{n}(z_i{}^2)b + nc + \sum_{i=1}^{n}(x_i{}^2 + z_i{}^2) = 0 \tag{20.10}$$

For simplification, let us take

$$\left.\begin{aligned}
a_0 &= 2\sum_{i=1}^{n} x_i{}^2 \\
a_1 &= 2\sum_{i=1}^{n} x_i z_i \\
a_2 &= \sum_{i=1}^{n} x_i \\
b_0 &= -\sum_{i=1}^{n}(x_i{}^2 + z_i{}^2)x_i \\
a_3 &= 2\sum_{i=1}^{n} x_i z_i \\
a_4 &= 2\sum_{i=1}^{n} z_i{}^2 \\
a_5 &= \sum_{i=1}^{n} z_i \\
b_1 &= -\sum_{i=1}^{n}(x_i{}^2 + z_i{}^2)z_i \\
a_6 &= 2a_2 \\
a_7 &= 2a_5 \\
a_8 &= nb_2 = -\sum_{i=1}^{n}(x_i{}^2 + z_i{}^2)
\end{aligned}\right\} \tag{20.11}$$

Then the least square circle is obtained by solving the following system of linear equation by putting the values of the above-defined constants as

$$\begin{bmatrix} a_0 & a_1 & a_2 \\ a_3 & a_4 & a_5 \\ a_6 & a_7 & a_8 \end{bmatrix} \begin{bmatrix} a \\ b \\ c \end{bmatrix} = \begin{bmatrix} b_0 \\ b_1 \\ b_2 \end{bmatrix} \tag{20.12}$$

20.3 Experimentation

20.3.1 Equipment Specifications

Scanning of cutting edge radius of SCD tool has been done with AFM (ASYLUM Research Company, model MFP 3*D* Bio). Table 20.1 shows the detailed description of the AFM probe.

20.3.2 Diamond Tool Specifications

A SCD tool of type II B with nose radius 1.5 mm was used for measurement of cutting edge radius. The flank and rake angles are 10° and 0°, respectively. The cutting edge radius is 150 nm.

20.3.3 Experimental Setup

Figure 20.1 shows the experimental setup which is used for the characterization of cutting edge radius of the SCD tool with the help of a small tool holder.

20.3.4 Scanning of Cutting Edge Radius

The cutting edge of the SCD tool is scanned for the position as shown in Fig. 20.1 in tapping mode with a scanning frequency of 50 Hz, the lowest value of frequency so as to avoid damage of silicon-based AFM tip due to the sharpness of the cutting edge. Scanning of the area (30 μm * 30 μm) is selected so as to get a better magnification of the scan.

Table 20.1 Probe specifications

Spring k (N/m)	2
Frequency (kHz)	70
Shape	Rectangular
Material	Silicon
Tip radius (nm)	7
Tip height (μm)	15
Tip shape	Three-sided
Tip coating (nm)	None

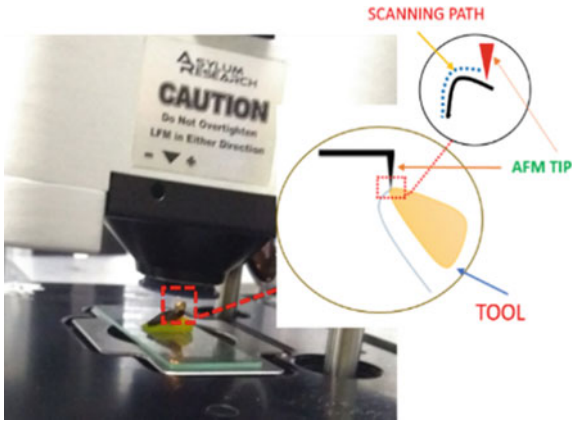

Fig. 20.1 Experimental setup

20.4 Result and Discussion

20.4.1 Data Processing

The data obtained from AFM scanning has been filtrated using the Gwydion software for the noise reduction. From the captured 2D profile, the small area has been chosen inorder to reduce the computational time. Different 2*D* profiles were plotted for different regions of the small selected region so as to reduce error in the characterization of the tool. The Fig. 20.2 shows the data without noise reduction, with noise reduction, and the small region selected for calculation purpose, and in that, different 2*D* plots were obtained which were used further for calculation of cutting edge radius.

The 2*D* profiles of actual surface profile for different regions were plotted with the profile of roughness and form for the same selected region. The cutting edge of the tool is mainly associated with the form of the tool; hence, the form has been selected for further characterization as shown in Fig. 20.3.

20.4.2 Characterization of Cutting Edge Radius

20.4.2.1 By Form Factor Method

The form factor method is the simplest approximation method to calculate the radius of any curvature [9]. This method is simple and the ambiguity in the calculation is less. It is suitable for approximation where the accuracy is not required.

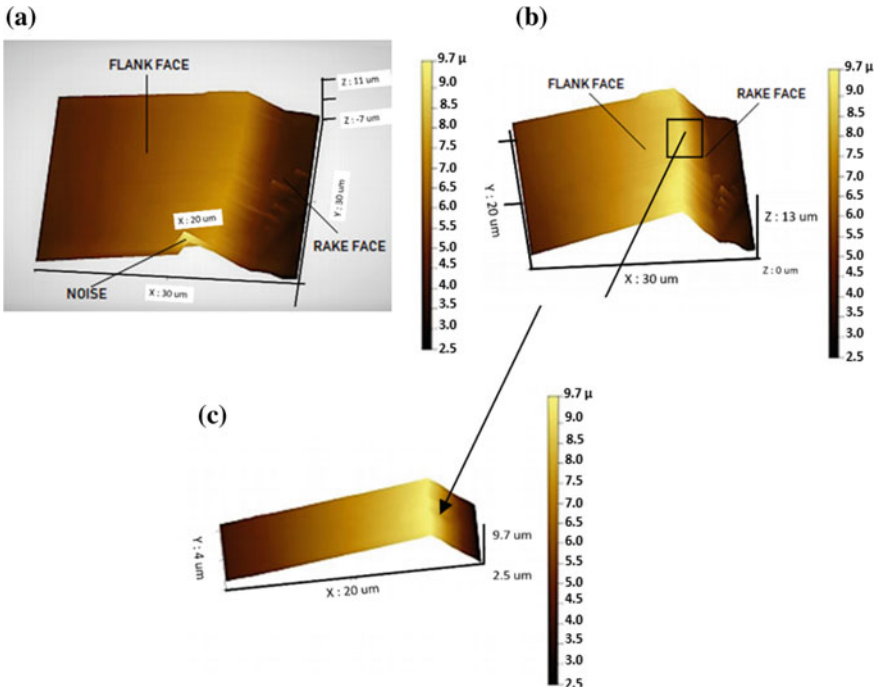

Fig. 20.2 3*D* profile of AFM data, **a** before filtration, and **b** after filtration, **c** small region of area for the measurement

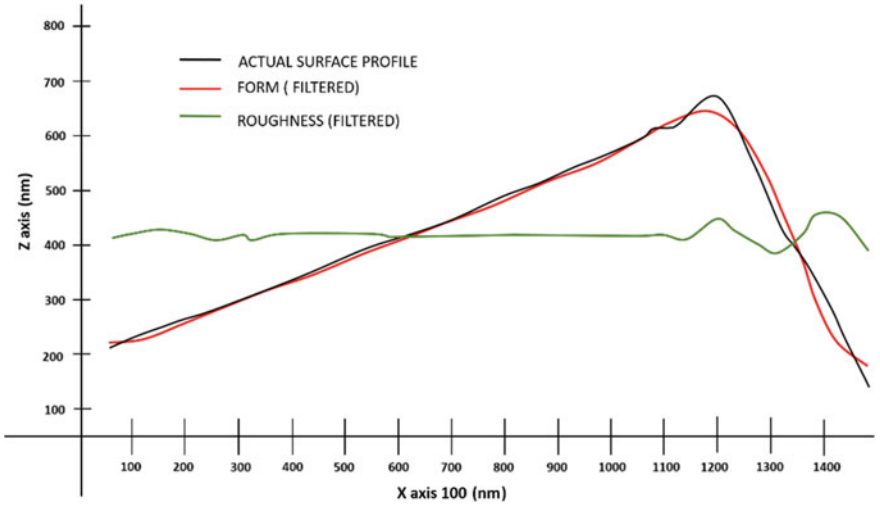

Fig. 20.3 2*D* profile of actual surface profile with form and roughness

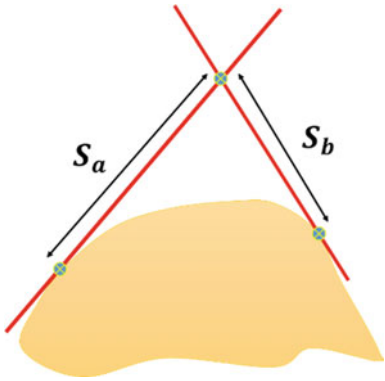

Fig. 20.4 Schematic diagram for form factor method

As shown in Fig. 20.4, the two tangents were drawn on a waving curve and let two tangents passes through point A (x_1, z_1) and B (x_2, z_2) and let point C be the point where the two tangents cross each other. An angular bisector is drawn from point C and let it intersect the curve at point D (x_3, z_3) and thus, these three coordinates were obtained. The distance between points A and C is called S_a and the distance between points B and C is called S_b which is measured. The values of S_a and S_b are obtained for various 2D profiles and it is found to be different for different 2D profiles which are obtained and the values of the radius were calculated using

$$R = \frac{S_a + S_b}{2} \tag{20.13}$$

The average of all the radii was calculated to minimize the error. The cutting edge radius for the different curve was calculated and its average is found to be 205 nm which was quite higher than the expected value of the cutting edge radius.

20.4.2.2 Calculation by the Radius of Curvature Formula

Various order polynomial were fitted to obtained data and it was found that second-order polynomial is fitting best to obtained data in a red color curve and the black curve represents the form profile as illustrated in Fig. 20.5.

As we know that for plane curves given by the explicit equation $Z = f(x)$, the radius of curvature at a point (x, z) is given by the following expression.

$$R = \frac{(1 + (f'(x))^2)^{\frac{3}{2}}}{f''(x)} \tag{20.14}$$

From the fitting curve for 2D profile, equation of curvature was obtained in general form as Eq. 20.15.

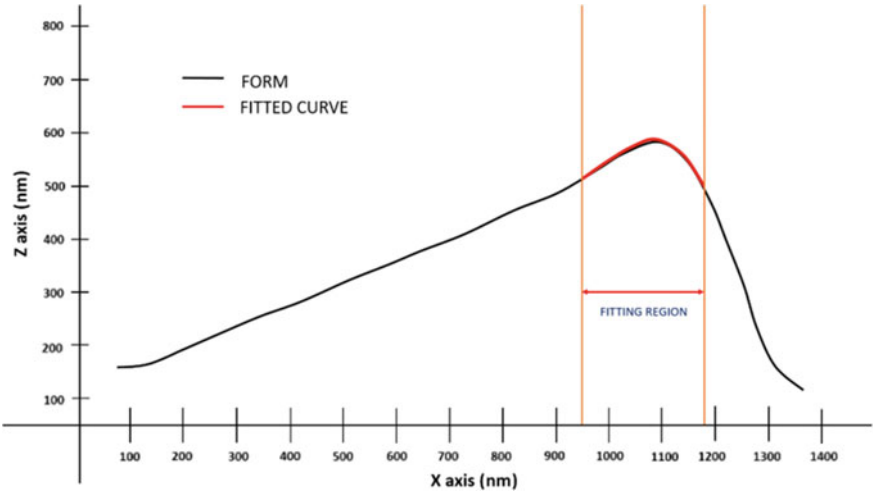

Fig. 20.5 Second-order polynomial curve fitting

$$Z = a + bx + cx^2 \tag{20.15}$$

By using Eq. 20.14, the radius of curvature equation of cutting edge radius can be calculated.

The second-order graphs were fitted for a selected region of the curve and for various 2*D* profiles. The average value of cutting edge radius was calculated and it is found around 198 nm which is still higher than the expected value of cutting edge radius and this is mainly due to the selection of region for 2*D* curve fitting which affects the constant values of the fitted curve and cutting edge radius calculation.

20.4.2.3 Calculation by the Least Square Method

In this method of calculation of cutting edge radius for a set of values of *X* and *Z*, the fitted radius of the fitted circle is calculated by the formula:

$$x^2 + z^2 - 2(ax + cz) + a^2 + c^2 = r^2 \tag{20.16}$$

In a given formula, a and c are the centers of circle and r is the radius of the fitted circle which can be calculated for the given set *X* and *Z* values.

For various set of values of *X* and *Z*, the fitted radius r was calculated and mean of that radii was calculated to reduce error in the calculation. LSM is the widely used method for fitting the circle but its constant values of the fitted circle are affected by the selection of fitting points; to minimize this variation in calculation, authors have selected only 3 sets of points i, j, and k as shown in Fig. 20.6, for the calculation which is the most widely used point for geometrical manual fitting. It is assumed that

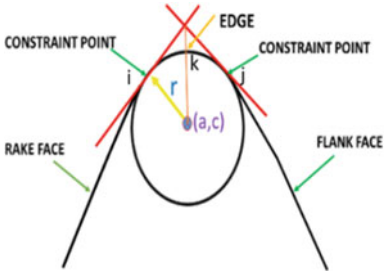

Fig. 20.6 Schematic diagram for the least square fitting

the circle passing through points of the tangent drawn to curvature and intersection of the angular bisector of angle traced by two tangents and curve is a best-fitted circle for the given set of values of X and Z. In this method, radius of curvature is calculated directly by the formula for various 2*D* curves obtained at different regions. By averaging the calculated values, cutting edge radius was found to be 187 nm which is closer to the expected value of cutting edge radius.

20.4.2.4 Calculation by Least Square Method with Error Minimization

The three points *A*, *B*, and *C* are considered for circle fitting method because circle passing through these three points are considered to best-fitted circles as shown in Fig. 20.7. The above process is repeated for the various 2*D* profiles to obtained three crucial points for each plot.

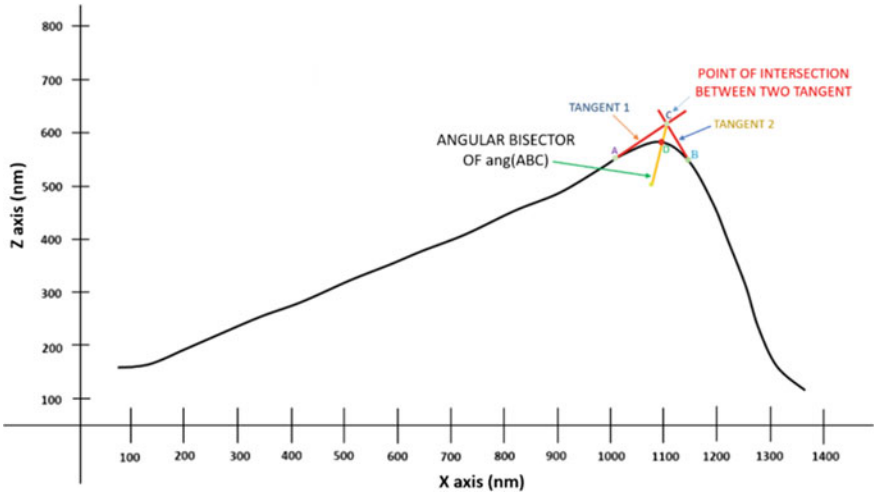

Fig. 20.7 Fitting of three points for calculation

Table 20.2 Calculation of cutting edge radius by different methods

Method	Cutting edge radius (nm)
Cutting edge radius form factor method	205
Calculation by the radius of curvature formula	198
Calculation by the least square method	187
Calculation by the least square method with error minimization	160

By using Eq. 20.12, values of constants a, b, and c were calculated. The radius of the circle can be calculated by averaging the values of r ($r = \sqrt{a^2 + b^2 - c}$). The fitting of circle with the LSM gives an approximate nearby value of cutting edge radius but there some error exists in this calculation method; hence, authors were tried to put the mathematical error minimization method through which the error in calculation of constants a, b, and c can be directly minimized to give exact value of cutting edge radius by reducing error in the LSM. By using this method of calculation, cutting edge radius was found to be 160 nm after averaging all values of cutting edge radius of the SCD tool has been calclulated from the same method.

The calculations of cutting edge radius by different methods are tabulated as given in Table 20.2. As mentioned by tool specifications, cutting edge radius should be around 150 nm and it is clear that by the new approach of calculation, error in calculation is minimized and the approximately exact value of the cutting edge radius was obtained. There is still a small variation in the cutting edge radius because the uncertainty in measurement and calculation are not considered here.

20.5 Conclusion

The special fixture is used to keep the tool at a particular angle to scan the cutting edge profile directly by using the AFM without damaging its probe. The authors were tried to compare different methods of circle fitting and proposed a method of circle fitting by using the error minimization approach so as to reduce error in the calculation of the cutting edge radius. The previous works of calculating cutting edge radius using various approximation methods like form factor method, least square method, and curvature formula are not taken care of for mathematical fitting error at the time of characterization of the cutting edge. But in this paper, authors have taken care of the minimization of error and to get the most accurate result for the cutting edge radius,160 nm, which is 10 nm more than the actual value of the tool due to uncertainty in calculation and further improvement in process, is expected so as to get the exact value of the cutting edge radius.

Acknowledgements The authors gratefully acknowledge the support and grant provided for this work by the Board of Research in Nuclear Sciences (BRNS), India via project no. 34/14/06/2015/BRNS.

References

1. Arif, M., Rahman, M., San, W.Y.: A study on the effect of tool-edge radius on critical machining characteristics in the ultra-precision milling of tungsten carbide. Int. J. Adv. Manuf. Technol. **67**(5–8), 1257–1265 (2013)
2. Li, X.P., Rahman, M., Liu, K., Neo, K.S., Chan, C.C.: Nano-precision measurement of diamond tool edge radius for wafer fabrication. J. Mater. Process. Technol. **140**(1–3 SPEC), 358–362 (2003)
3. Yue, X., Xu, M., Du, W., Chu, C.: Effect of cutting edge radius on surface roughness in diamond tool turning of transparent $MgAl_2O_4$ spinel ceramic. Opt. Mater. (Amst) **71**, 129–135 (2017)
4. Zhao, T., Zhou, J.M., Bushlya, V., Ståhl, J.E.: Effect of cutting edge radius on surface roughness and tool wear in hard turning of AISI 52100 steel. Int. J. Adv. Manuf. Technol. **91**(9–12), 3611–3618 (2017)
5. Asai, S., Taguchi, Y., Horio, K., Kasai, T., Kobayashi, A.: Measuring the very small cutting edge radius for a diamond tool using a new kind of SEM having two detectors. Ann. CIRP **39**(l), 85–88 (1990)
6. Drescher, J.: Scanning electron microscopic technique for imaging a diamond tool edge. Precis. Eng. **15**(2), 112–114 (1993)
7. Li, Z.Q., Sun, T., Li, P., Zhao, X.S., Dong, S.: Measuring the nose roundness of diamond cutting tools based on atomic force microscopy. J. Vac. Sci. Technol. B Microelectron. Nanometer Struct. **27**(3), 1394 (2009)
8. Umbach, D., Jones, K.N.: A few methods for fitting circles to data. IEEE Trans. Instrum. Meas. **XX**, 5 (2000)
9. Denkena, B., Biermann, D.: Cutting edge geometries. CIRP Ann. Manuf. Technol. **63**(2), 631–653 (2014)

Chapter 21
Effect of Different Electrodes on Micro-feature Fabrication in Biomedical Co-29Cr-6Mo Alloy Machined Using μ-EDM Process

Siddhartha K. Singh and H. S. Mali

Abstract μ-EDM is a versatile non-conventional machining process that is used to machine any difficult-to-cut material. In this process, material is removed due to sparking, which causes localized melting and evaporation. Beginning with metals, application of μ-EDM has now been extended to most materials, such as non-metals, alloys, composites, and ceramics. Co-29Cr-6Mo is a biomedical alloy which offers industrial/medical applications like hip implants, knee implants, drug delivery, and so on. For these applications, various micro-features are required on the surface along with different micro-devices. In the present work, machinability of Co-29Cr-6Mo using different popular electrode materials, namely copper, brass, and tungsten carbide is investigated. Micro-sized holes of equal dimension are machined at the same machining parameters using the three different electrodes and resulting cavities are imaged using optical microscope. Material removal rate, tool wear rate, and overcut between the three electrodes are evaluated, analysed, and compared. Use of tungsten carbide results in most accurate micro-features but consumes most time.

Keywords Micro-EDM · Co-29Cr-6Mo · Electrode

21.1 Introduction

Micro-fabrication is a rapidly evolving field of technology that aims at fabricating features that are in the micro-domain (<1 mm). There are various techniques that are employed to create such features or devices. One such technique is micro-electric discharge machining (μ-EDM). It is an electro-thermal-type non-conventional machining process which removes material by bombardment of electrons and ions. When an electrical field is applied between the electrode and the workpiece in the presence of a dielectric medium, eventually the dielectric between them breaks down and the flow of electrons and ions is established in a narrow zone called plasma

S. K. Singh (✉) · H. S. Mali
Malaviya National Institute of Technology Jaipur, Jaipur 302017, Rajasthan, India
e-mail: sid.sks@gmail.com

M. S. Shunmugam and M. Kanthababu (eds.), *Advances in Micro and Nano Manufacturing and Surface Engineering*, Lecture Notes on Multidisciplinary Industrial Engineering,
https://doi.org/10.1007/978-981-32-9425-7_21

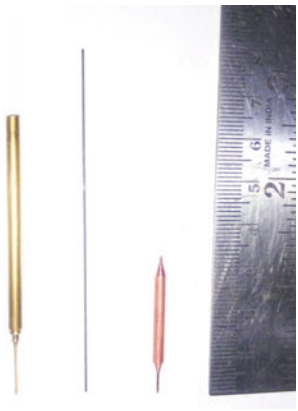

Fig. 21.1 Different electrodes for machining

channel, which causes removal of material from both the workpiece and the electrode, as shown in Fig. 21.1. This process is highly versatile in the sense that one could machine any material irrespective of the hardness of the material, provided it is electrically conductive. Hence, this technique is used to machine many hard and difficult-to-cut materials. Co-29Cr-6Mo is one such material that is difficult to machine using conventional machining techniques. Co-29Cr-6Mo is a biomedical alloy that has applications in various fields, like aviation, aerospace, gas turbines, medical implants, and so on. It is widely used to make components of hip, shoulder, and knee replacement [1]. Apart from this, Co-29Cr-6Mo is also used in the drug delivery system by employing devices like micro-pumps, and so on.

Constant attempts are being made by different investigators to ascertain the feasibility of machining various kinds of metals, alloys, composites, and ceramics using μ-EDM. Chiou et al. [2] performed μ-EDM on SKH59 steel alloy with tungsten carbide electrodes and then compared it to machining using highly conductive Ag and Cu electrodes coated with WC. Cu electrode coated with WC exhibited superior behaviour in material removal compared to other electrodes while lowest tool wear was observed in WC electrodes which also has the highest melting point. Moreover, the best surface finish was obtained while using WC-coated Ag electrodes. Gosavi et al. [3] machined titanium wrought alloy VT-20 used in aerospace industry, using hollow, tubular brass electrode of diameter 500 μm. They found that an increase in pulse-off time reduces both the material removal rate (MRR) and electrode wear rate (EWR). Also, discharge energy was observed as the most significant factor affecting MRR, EWR, taper angle, and overcut. Kibria et al. [4] analysed the effect of different dielectric by fabricating micro-holes in titanium alloy Ti-6Al-4V using a cylindrical, 300 μm electrode of tungsten. Deionized water was found to be a better dielectric compared to kerosene in terms of MRR. Addition of B4C additive with deionized water further enhanced the MRR and also resulted in thinner recast layer. Mali et al. [5] used ultrasonic vibration with μ-EDM to machine superalloy Inconel 718 and titanium nitride-aluminium oxide ($TiN\text{-}Al_2O_3$) ceramic composite. The investigation revealed that use of vibration significantly improves the MRR,

which in turn is significantly affected by capacitance. Schubert et al. [6] conducted experiments on a non-conducting zirconia (ZrO_2) ceramic using 115 μm tungsten electrode and compared the results with the machining of chromium-nickel steel. To make the machining feasible and to begin, a layer of silver varnish of about 20 μm was applied on the surface of the workpiece. They achieved stable machining, though after formation of a second recast layer. The final surface roughness of the part too was observed and was found to be two to three higher than in steel.

The process of EDM which began with machining of conducting metals has been extended to machining of alloys, composites, and non-conducting ceramics as well. Keeping in line with the same, coupled with the recent rise of biomaterials and the imbibed need of micro-features in biomaterials, the feasibility of using μ-EDM to machine and generate such features is being widely explored. However, the availability of literature on this topic is minimal and despite the extensive application of Co-29Cr-6Mo alloy, the authors found no literature investigating the feasibility and ease of machining Co-29Cr-6Mo with different types of electrodes via μ-EDM process. Hence to fill such void, this work is undertaken.

21.2 Experimentation

In order to perform the investigation, cobalt-chromium-molybdenum alloy, also known as stellite, was used. Its constituents are listed in Table 21.1.

The alloy was cut into a machinable block of dimension 20 mm × 10 mm × 5 mm. The block was then abraded using emery paper and then finally polished before carrying out the machining. Table 21.2 lists down the properties of Co-29Cr-6Mo alloy.

For investigating the machinability of Co-29Cr-6Mo, same micro-feature was machined using different electrodes and three iterations were carried out with each electrode. To carry out the machining, three most popular electrode materials, namely

Table 21.1 Composition of Co-29Cr-6Mo alloy

Element	Cr	Mo	C	Mn	Fe	Co
Weight (%)	29.4	6	0.6	0.5	0.4	Rest

Table 21.2 Co-29Cr-6Mo properties

Property	Value
Melting point	1350–1450°C
Density	8.5 g/cm^3
Hardness	40–45 HRC
Coefficient of thermal expansion	13.6 × 10^{-6} m/m/°C
Young's modulus	220 GPa

copper, brass, and tungsten carbide (WC) were selected. Cylindrical WC electrode of diameter 0.50 mm was procured, while the rest two were fabricated by micro-turning copper and brass rods of diameter 3 mm. The final obtained diameter of copper electrode was 0.52 mm and that of brass electrode was 0.53 mm, as measured using Mitutoyo digital vernier calliper with a least count of 0.01 mm. Figure 21.2 shows the different electrodes as obtained after micro-turning.

All the experiments were carried out on MIKROTOOLS DT 110i hybrid micro-EDM machine. The experimental setup is shown in Fig. 21.3. The electrode which is taken as the negative terminal to keep tool wear to a minimum is connected to a RC circuit for pulse generation. The workpiece acts as the positive terminal, while the dielectric is fed between the electrodes through a nozzle so as to impart it velocity high enough to take out debris and molten material from the machining zone. The electrode has the Z-motion while the workpiece which is kept on the machine bed can move in X- and Y-directions. To ascertain the effect of electrodes, blind micro-holes of depth 1 mm were drilled. With each electrode, three separate holes were drilled, while all the parameters were kept constant. These parameters are listed in Table 21.3.

All the experiments were carried out in commercially available SUN EDM Oil 100 as the dielectric medium. The dielectric was supplied using a nozzle for localized

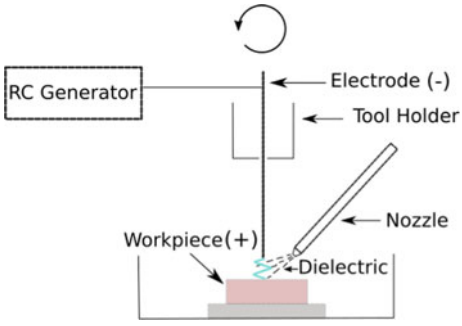

Fig. 21.2 Schematic of experimental setup

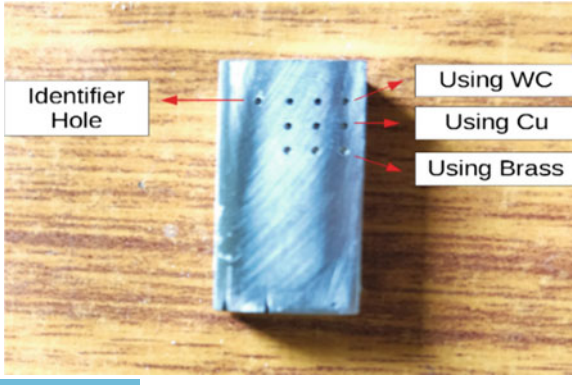

Fig. 21.3 Machined micro-holes

Table 21.3 Parameters and their values

Parameter	Value
Capacitance	0.1 μF
Peak voltage	120 V
Electrode speed	1000 rpm
Feed	0.2 mm/min

effect and flushing. To evaluate the material removal rate (MRR), machining time for each hole was noted down using a stopwatch. To evaluate tool wear rate (TWR), dimensions of the electrode were taken using Z-axis of the μ-EDM machine which has a resolution of 0.1 μm. Further, in all experiments, the tool was made as cathode and the workpiece as anode. After machining the micro-holes, diameter of each individual hole was measured using AxioCam AX10 ZEISS optical microscope.

21.3 Results and Discussion

In μ-EDM, apart from the electrical parameters, the influence of electrode and workpiece material on machining characteristics is quite significant. The thermal and electrical properties of the materials in use affect every machining output parameter such as MRR, TWR, and overcut. The difference in the profiles of the micro-holes obtained with different electrodes is also visible with naked eye, as observed in the block after machining. The three holes with the same electrode were machined in a row at a gap of 2 mm from each other. Thus nine micro-holes were finally machined as shown in Fig. 21.3. For identification, column 1–3 progresses from left to right.

21.3.1 Material Removal Rate

While machining with WC, an initial delay was observed in establishment of stable spark compared to machining with Cu and brass electrodes. This initial delay leads to an overall increase in machining time comparatively. The delay in spark may be a consequence of the lower electrical conductivity of the WC electrode as compared to the other two electrodes. It can be observed from Fig. 21.4 that of all the three electrodes, WC electrode has the least MRR and thus takes the maximum time to fabricate a micro-feature. This may also be due to relatively less electrical conductivity of WC compared to Cu and brass. The highest MRR, initially, was obtained with brass electrode although the MRR with Cu electrode too was much higher than with WC electrode. Further, it can be observed that variation in MRR between Cu and brass electrode is minimal, and initially brass provides better MRR but is superseded by copper as machining progresses. Also, with all three electrodes an increasing trend in MRR can be observed, which is due to the increase in overcut as machining

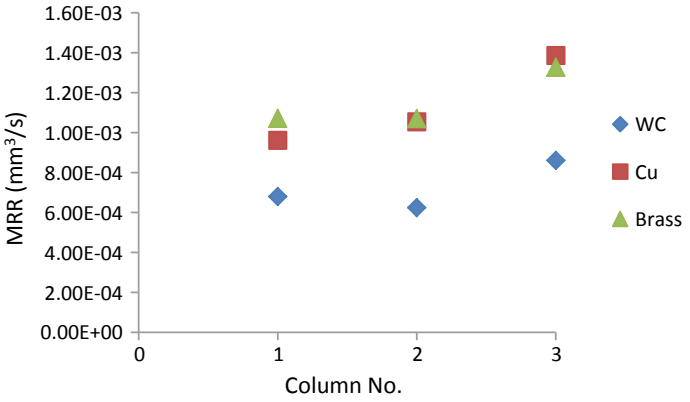

Fig. 21.4 Comparision of material removal rate

continues. This enhanced material removal is a result of increased energy transfer between the electrodes with the progression of machining. As machining progresses, wear out of the tool and workpiece leads to removal of oxide layer present initially on the surface of the electrodes, thus bringing fresh material to the surface. As a result, enhanced energy transfer occurs between the electrodes leading to greater material removal.

21.3.2 Tool Wear Rate

In terms of wear out of the tool material, it can be observed from Fig. 21.5 that in the first two columns of micro-holes, WC offers the lowest tool wear followed by brass, while copper has the highest tool wear. However, while machining the third column,

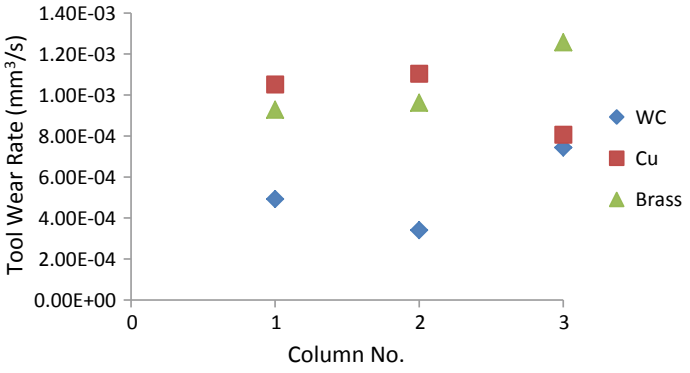

Fig. 21.5 Comparision of tool wear rate

considerably high tool wear is observed in WC which almost coincides with the wear in Cu electrode, while brass surpasses the other two electrodes in terms of wear. The comparatively low wear of WC tool may be due to its relatively higher melting point as compared to copper and brass electrodes. Moreover, it is interesting to note that lowest MRR obtained while machining the hole at column 2 using WC coincides with the lowest TWR. This means that while machining the second micro-hole minimum exchange of energy has taken place between the electrodes. Further, a drastic increase in tool wear is observed in WC for machining the micro-hole at column 3. It may have a correlation with comparatively larger size of micro-hole at column 3. As a general trend, it can be observed that TWR increases with continued machining except when copper electrode is used. The three iterations were re-performed using copper electrode to confirm whether the sudden drastic reduction in tool wear while machining the third micro-hole was not obtained erroneously. But during the repeated iterations too, a similar trend was observed. This confirms that although tool wear increases with repeated machining with WC and brass electrodes, tool wear reduces if copper electrode is used for repeated machining.

21.3.3 Overcut

The third parameter that was evaluated to compare the performance of different electrodes is overcut. Overcut is an unavoidable and undesirable phenomenon in electric discharge machining. Figure 21.6 shows the distribution of overcut obtained in all the holes. It can be observed that use of WC electrode results in maximum overcut, while the use of brass electrode causes minimum overcut, and overcut while using Cu electrode remains in between WC and brass electrode. Moreover, an increasing trend in overcut is observed as machining progresses from column 1 towards 3.

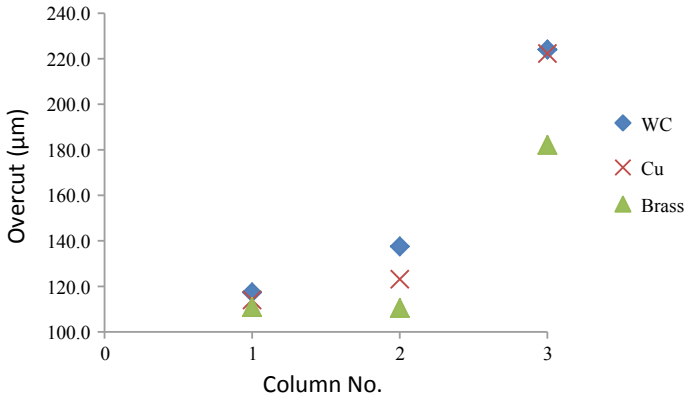

Fig. 21.6 Comparison of overcut

An increase in overcut is an indicator of increase in material removal and thus the trend of overcut corresponds to the trend observed for MRR. This trend is observed for all the three electrodes, so it may be said that electrode material does not have a significant effect on this observed trend. One possible reason for this trend may be deposition of material on the electrode surface as machining progresses over time, thus causing a change in dimension of the electrode and hence greater overcut. Another possible reason may be the increased presence of loose electrons and ions as machining progresses, which may result in greater material removal and consequently more overcut. However, to analyse with certainty, the reason of this obtained trend, further investigation is required.

21.4 Conclusions

In this investigation, machinability of a biomedical material, Co-29Cr-6Mo using different electrodes via micro-EDM process is studied. For this purpose, WC, Cu, and brass electrodes were selected and similar microstructure was fabricated using these different electrodes. From this study, the following remarks may be drawn:

- WC electrode takes the longest time to machine a micro-feature, but also results in lowest wear in the tool. However, using WC also causes relatively largest overcut in the machined micro-feature.
- When using Cu electrode, which has the highest electrical conductivity among the three, time taken to machine a micro-feature is relatively much lower than WC but minutely larger than brass. But, it is also prone to more tool wear than other electrodes.
- Brass electrode takes the least amount of time to machine a micro-feature among the three, and also leads to least overcut. However, tool wear in brass is found to be much greater than WC.

So, to conclude, μ-EDM technique is highly feasible for generating micro-features on Co-29Cr-6Mo which is used for several biomedical applications. For this purpose different type of electrodes may be selected depending upon the requirement of output parameters. For generation of precise features in less time, brass electrode may be used but will also cause greater tool wear. Additionally, lowest wear is obtained using the electrode with relatively higher melting point and less conductivity.

Acknowledgements The authors would like to acknowledge the financial support provided by DST SERB through the grant EMR/2016/003372.

References

1. Yamanaka, K., Mori, M., Chiba, A.: Mechanical properties of as-forged Ni-free Co-29Cr-6Mo alloys with ultrafine-grained microstructure. Mater. Sci. Eng. A **528**, 5961–5966 (2011)
2. Chiou, A.H., Tsao, C.C., Hsu, C.Y.: A study of the machining characteristics of micro EDM milling and its improvement by electrode coating. Int. J. Adv. Manuf. Technol. **78**, 1857–1864 (2015)
3. Gosavi, V., Phafat, N., Deshmukh, S.: Investigation of effect of process parameters in micro hole drilling. Int. J. Mod. Trends Eng. Res. **2**(6), 583–588 (2015)
4. Kibria, G., Sarkar, B.R., Pradhan, B.B., Bhattacharyya, B.: Comparative study of different dielectrics for micro-EDM performance during microhole machining of Ti-6Al-4 V alloy. Int. J. Adv. Manuf. Technol. **48**, 557–570 (2010)
5. Mali, H.S., Baghel, R., Unune, D.R.: Experimental investigation on hybrid micro-electro discharge machining of Inconal 718 and ceramics materials. Int. J. Concept. Mech. Civ. Eng. **5**, 1–6 (2017)
6. Schubert, A., Zeidler, H., Hahn, M., Hackert-Oschätzchen, M., Schneider, J.: Micro-edm milling of electrically nonconducting zirconia ceramics. Procedia Cirp **6**, 297–302 (2013)

Chapter 22
Micro-tool Fabrication and Micro-ED Milling of Titanium Nitride Alumina Ceramic–Composite

Rupali Baghel, H. S. Mali and Vivek Baghela

Abstract Titanium Nitride Alumina Ceramic–Composite has potential applications in aerospace, tool industries, and thermal shielding. However, it has poor machinability using conventional machining processes. This article presents a novel approach of on-machine fabrication of high aspect ratio micro-electrodes ($\Phi = 500\,\mu m$) and studies the machining characteristics of TiN-Al_2O_3 ceramic–composite by micro-EDM. Micro-electrodes of diameter 500 μm are successfully fabricated using micro-turning process. Micro-channels are also fabricated with those electrodes on TiN-Al_2O_3 ceramic–composite by micro-ED Milling. The surface topography of micro-channels is studied by scanning electrode microscope. The machined surfaces were filled with droplets of debris, craters, and micro-pores, indicating melting and vaporization as a mechanism of material removal.

Keywords ED milling · Micro-tool · Ceramics · Turning · Discharge energy

22.1 Introduction

Miniaturization of components needs micro-features, like micro-holes, micro-channels, high aspect ratio holes, and micro-groves, and so on, to be fabricated on its parts. Such micro-components have applications in many industrial products like ultra-precision die-molds for lenses of digital cameras, fuel injection nozzle membrane, and so on. Micro-electro-discharge machining (μ-EDM) comes out to be a promising method for machining micro-components [1]. The μ-EDM technology basically depends on a series of electric discharge between the tool and the workpiece caused by the pulsed voltage in the presence of dielectric fluid. EDM provides some remarkable advantage, that is, no contact between electrode and workpiece which justify the use of this manufacturing method for machining of very hard or fragile materials because the only force is an impulse produced by the flash-over.

R. Baghel (✉) · H. S. Mali · V. Baghela
Department of Mechanical Engineering, Malaviya National Institute of Technology Jaipur, Jaipur 302017, India
e-mail: 2014rme9009@mnit.ac.in

M. S. Shunmugam and M. Kanthababu (eds.), *Advances in Micro and Nano Manufacturing and Surface Engineering*, Lecture Notes on Multidisciplinary Industrial Engineering,
https://doi.org/10.1007/978-981-32-9425-7_22

EDM is helpful in generating micro-features such as 3D cavities, micro-holes with high aspect ratio, accuracy and fine surface quality [2]. Advanced ceramics are the emerging class of material known for its high strength, chemical inertness, high toughness, and excellent wear resistance. They have high potential for a wide variety of industrial applications such as wear parts, micro-sensors, micro-fuel pump, bearings, and medical implants. Advanced ceramic–composite is a diverse family of materials, including both conventional and advanced ceramics, like alumina, silica, and so on, and their composites. Applications of ceramics are as vast as refractories, pottery, cutting tools, aerospace components, hybrid engine, fuel cell, metal matrix composites, orthopedic implants, dentistry, armor plates, a shield for security cameras and communication equipment, and so on. Ceramics are inorganic and non-metallic materials with ionic and covalent bonds. These kinds of bonding are the causes of unique properties of ceramics, like low ductility, low tensile strength, high hardness, low conductivity, and so on. These properties of ceramics lead it as a very difficult-to-machine material compared to metal. Ceramics are very hard, non-combustible, and chemically inert [3]. Ceramics can be used at very high temperatures as compared to metals, but full-scale applications of these ceramics are always inhibited as they are very hard to machine. Advanced ceramics are developed by controlling their micro-structures to improve machinability.

Advanced materials like ceramics alloy and composites are used for complex design requirements (high precision, good surface quality) but manufacturing industries are facing challenges for micro-machining these advanced and difficult-to-cut ceramic–composites in terms of machining process as well machining cost. Conventional machining processes have limitations to machine complex shapes, like turbine blades, complex cavities, die-molds, non-circular and curved holes, low rigidity structures, and micro-mechanical components with tight tolerances and good surface finish. Expensive equipment, tooling, and high processing time make conventional machining processes economically unviable, so the new process comes into consideration. Unconventional machining process, that is, electro-discharge machining (EDM) has been used to machine non-conductive ceramics [4, 5] as well as conductive ceramics [6, 7] in present days. The unconventional machining processes have been continuously improving by developing hybrid machining processes. Hybrid machining processes (HMPs) are becoming more preferred while machining advance materials and composites. In HMPs, two or more processes work together in a controlled manner and show a significant effect on process performances [6]. HMPs are becoming more popular in recent years because they enhance the advantages and diminish the disadvantages of each process. HMPs are based on the simultaneous and controlled interaction of process mechanisms having a significant effect on the process performance [8]. Although EDM is one of the most significant machining processes among non-conventional machining processes for hard to machine materials such as ceramic and composites, rare studies have reported on a fundamental understanding of on-machine fabrication of electrodes and electro-discharge machining ceramic–composite.

22.2 Materials and Methods

Titanium Nitride Aluminum Oxide (TiN-Al_2O_3) ceramic–composite is a new generation of advanced ceramic–composite. TiN-Al_2O_3 ceramic–composite is prepared by hot pressing the starting powders (TiO_2 and AlN) at 1450 °C for 30 min with graphite die and punch (70 mm diameter). The inside wall of the die and outside wall of the punch were coated with boron nitride for lubrication and protection of the powders from reaction with graphite. The product was then characterized by X-ray diffraction for phase analysis, ultrasonic test for elastic modulus, universal testing apparatus for four-point flexural strength, hardness tester for micro-hardness and laser flash test for measuring thermal diffusivity. Bulk densities were measured by Archimedes method. It has high resistance to thermal degradation, high mechanical strength, and electrical conductivity. The composite is prepared by high-temperature reaction sintering technique. TiN-Al_2O_3 also shows high resistance to various kinds of abrasion, chemical inertness, low friction coefficient, high hardness. TiN-Al_2O_3 is an aerospace material and also has applications in the tool industry and heat shielding [9]. It is being used in high-end areas, that is, medical implants, drug delivery systems, gas turbines, aerospace parts, and micro-pumps. Owing to its high hardness, it faces difficulty in machining by traditional machining methods. The conventional machining of this ceramic–composite is challenging due to low fracture toughness and high hardness at elevated temperature. Generation of high tool wear and surface damage due to high cutting forces hinder full-scale applications of advanced ceramics in different engineering areas. Hybrid μ-EDM process is used because of its merits of machining hard conductive material [10]. All the experiments are performed on hybrid μ-EDM DT-110i machine. The DT-110i machine has the ability to perform multiple micro-machining processes on the same machine, allowing the machine to excel at hybrid μ-EDM. "SUN EDM oil" is used in Mikrotools® DT110i Hybrid μ-EDM machine. It is made of de-aromatized hydrocarbons and additives. SUN EDM oil is a high-quality, odorless, low-viscosity dielectric, which is a superior alternative to smoky, smelly viscose traditionally used EDM oil. The micro-electrodes are fabricated by brass rods (3 mm diameter and 60 mm in length), as shown in Fig. 22.1. The micro-tool fabrication is done on micro-turning machine setup. The details of the tool material and workpiece are given in Table 22.1.

Fig. 22.1 Initial brass tool electrode ($\Phi = 3$ mm)

Table 22.1 Details of the tool and workpiece

Electrode material	Brass
Length (mm)	60
Diameter (μ)	500
Machining process	Micro ED-milling and micro-turning
Workpiece	TiN-Al_2O_3 ceramic–composite

22.3 Experimentations

During miniaturization, the handling of micro-electrodes is a challenge as they tend to bend and get damaged during manual handling. In this regard, on-machine tool-fabrication techniques lower the risk of damaging the tool electrodes. The tool electrodes are fabricated on micro-turning setup on Mikrotools® DT110i Hybrid μ-machine.

The initial diameter of the brass tool was 3.0 mm that was reduced to 500 μ by micro-turning process, as shown in Fig. 22.1. The carbide insert is used as a single-point cutting tool for micro-turning process. The spindle is rotated at the speed of 1200 rpm for micro-turning process. The brass rod is turned in five steps. The depth of cut for machining is varying from higher to lower values. The depth of cut during tool turning is 300, 300, 250, 250 and 150-μ sequentially and feed rate is taken as 0.2 mm/min. After the micro-turning process, the micro-tool is prepared, as shown in Fig. 22.2. The micro-tool ($\Phi = 500$ μ) prepared is shown in Fig. 22.3.

The micro-tools prepared are used as tool electrodes during the micro-ED milling process. In this process, micro-channels of length 60 mm and depth 500 μ are fabricated on TiN-Al_2O_3 ceramic–composite. The fabricated micro-channels are as shown in Fig. 22.4. Devices containing micro-channels in ceramics are gaining importance for the miniaturization and reducing the weight to volume ratio. Micro-channels have applications in micro-electro-mechanical system (MEMS), micro-chemical reactor (MCR), and biomedical systems. These micro-channels could also be used in heat exchangers to provide rapid heat transfer. The input parameters responses selected for this study are shown in Table 22.2. The material removal rate (MRR) is measured by total volume lost per unit machining time. Electrode wear rate (EWR) is also measured by total volume loss per unit time for each experiment. Tool wear ratio is measured as the ratio of MRR to EWR. The discharge energies during micro-channel fabrication are measured by Eq. 22.1.

$$\textit{Discharge energy}\ (E) = \frac{1}{2}CV^2\ \mu\text{J} \tag{22.1}$$

where

C capacitance in micro-farad
V voltage in volt.

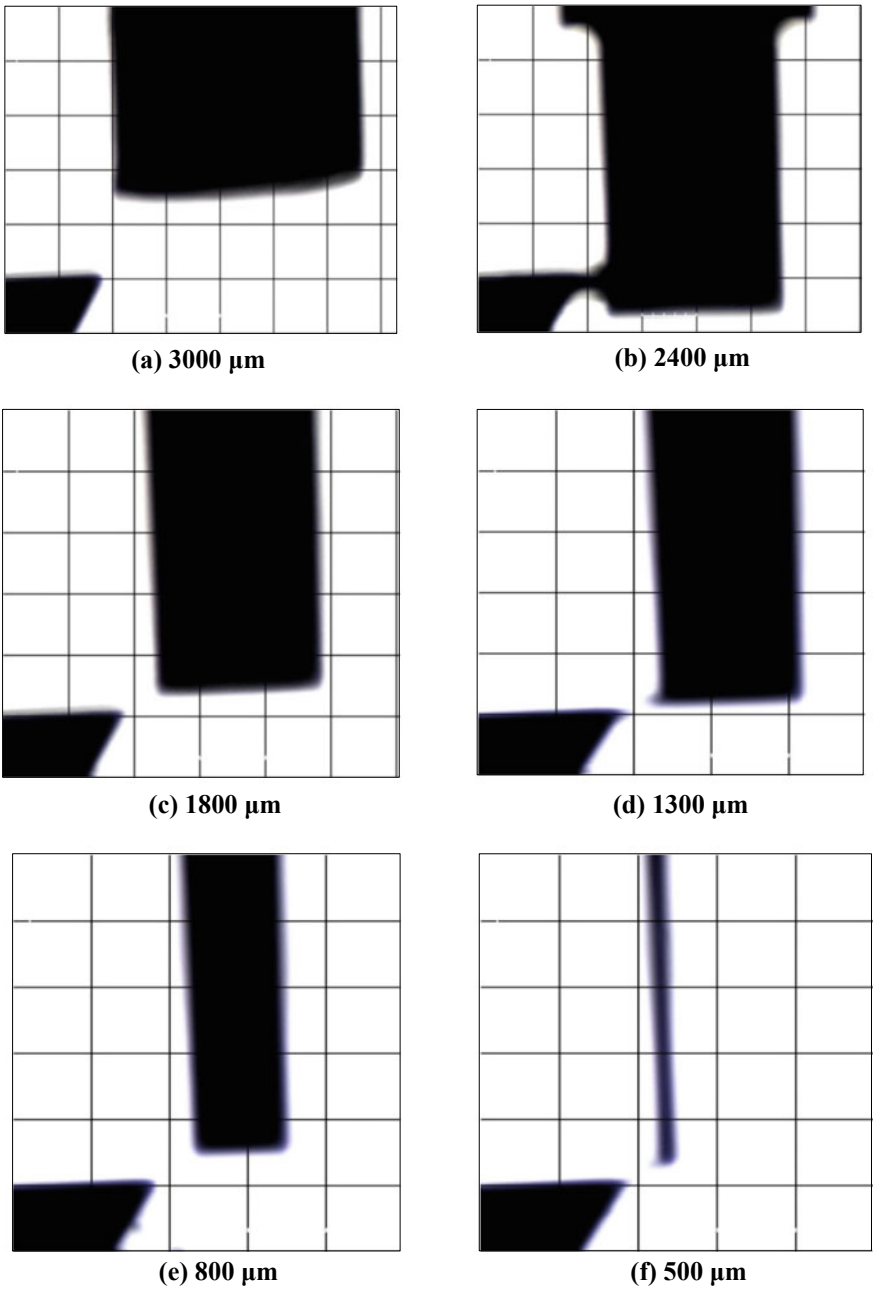

Fig. 22.2 Fabrication of micro-electrode in steps (**a**, **b**, **c**, **d**, **e**, and **f**) by the micro-turning process

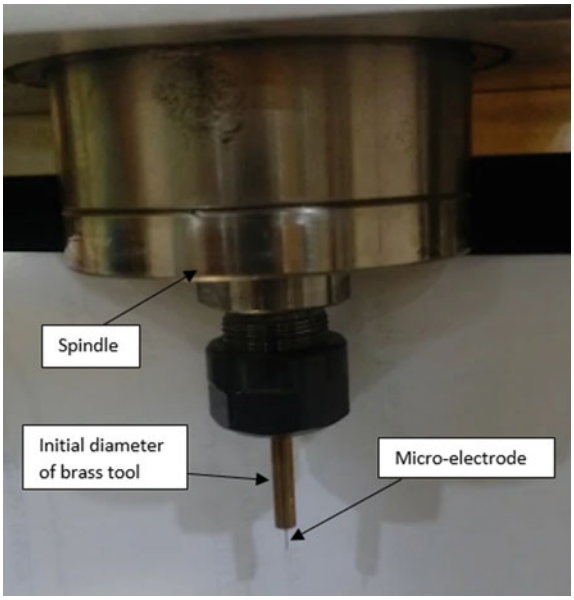

Fig. 22.3 Fabricated micro-electrode ($\Phi = 500\ \mu m$)

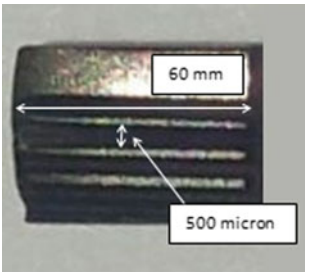

Fig. 22.4 Micro-channels fabricated by μ-EDM

Table 22.2 EDM parameters and response parameter for micro-channels

S. no.	Energy (μJ)	Spindle speed (rpm)	MRR (mm^3/min)	TWR (mm^3/min)	TW ratio
1	500	1000	0.0001390	0.0052124	0.026667178
2	605	1000	0.0003250	0.005440062	0.059741967
3	720	1000	0.0002570	0.005540664	0.046384335
4	845	1000	0.0001396	0.0041679	0.033494084

22.4 Results and Discussion

The advanced ceramics TiN-Al_2O_3 has been machined and micro-channels are fabricated by the on-machined fabricated brass tool. The dimensions of micro-channels are 6 mm in length and cross-section area is of 500 × 500 μ. The study indicated that the on-machine fabricated tool could be used to create micro-features on hard-to-cut materials so that chances of tool damage can be reduced. The results also show that the material removal rate is very less, that is, 0.000325 mm^3/min as shown in Fig. 22.5. ED milling of TiN-Al_2O_3 also shows that there is a very high TW ratio, which indicates that there is excessive tool worn out while machining. The EWR plot with discharge energy shows that from 500 to 700 μJ electrode wear rate increases and after that EWR suddenly falls, as shown in Fig. 22.6.

More tool wear is due to the very high melting temperature of TiN-Al_2O_3 as compared to brass. The results also show that MRR is the highest at 600 μJ and after that MRR decreases (Fig. 22.5). This is due to high discharge energy, at which the brass tool could not sustain high temperature. The EWR also shows a similar trend, that is, increases up to approximately 600 μJ and a sudden decrease is noticed afterword. Further investigations may be required to ascertain the exact cause of the sudden decrease in both EWR and MRR at higher energy levels (Fig. 22.6).

Based on the experimental investigation, the mechanism of material removal is also discussed for the EDM process. The study on surface morphology of machined surface is also conducted. The surface was examined by scanning electron microscopy (SEM). The SEM images provide the glimpse of surface defects and effects of input parameters on the machined surface. The SEM image in Fig. 22.7 shows microspores and droplets type of debris, indicating that melting and vaporization are the mechanisms of material removal. The presence of a metal particle on the machine surface also confirms the material migration mechanism. The machined surface is also filled with micro-cracks that shows the contraction mechanism of molted metal.

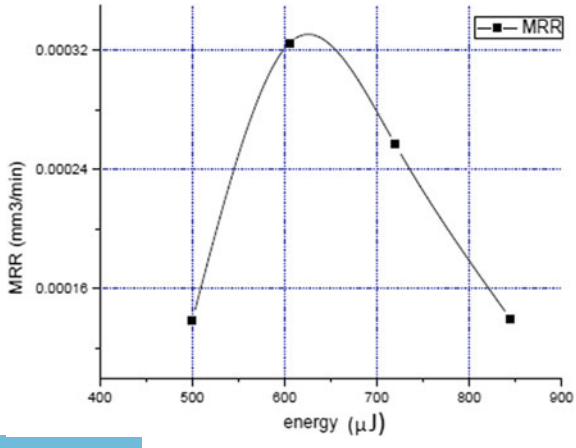

Fig. 22.5 Plot of MRR with discharge energy

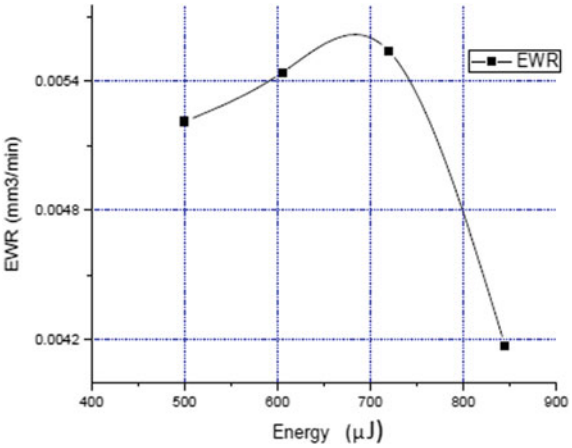

Fig. 22.6 Plot of EWR with discharge energy

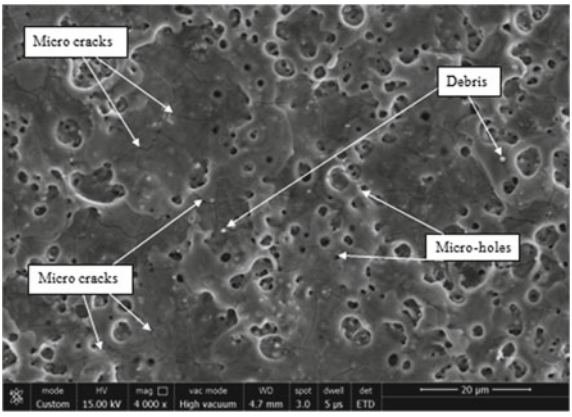

Fig. 22.7 SEM image of the machined surface

22.5 Conclusions

In this study, micro-tools are fabricated by "on-machine fabrication technique" to avoid micro-electrode damage by manual handling, and micro-channels are fabricated on TiN-Al_2O_3 ceramic–composite by these micro-electrodes. The machined surface of fabricated channels is also studied. The machined surfaces are filled with irregular debris, microcracks, and droplets. This study also shows that machining of TiN-Al_2O_3 ceramics using brass electrode at higher energy leads to lower MRR and hence machining at low energy is advised. For better MRR, a material with a higher melting point should be used as tool electrode as brass cannot sustain high temperature.

Acknowledgments The authors would like to acknowledge the financial support provided by DST SERB EMR_2016_003372 for this work.

References

1. Baghel, R., Mali, H.S., Biswas, S.K.: Study of vibration-assisted micro electro-discharge milling of titanium nitride-aluminum oxide composite. In: Proceedings of 6th International & 27th All India Manufacturing Technology, Design and Research Conference, pp. 276–279, Pune, India (2016)
2. Baghel, R., Mali, H.S., Biswas, S.K.: Parameter optimization of diamond grinding assisted EDM of TiN-Al_2O_3 ceramics using Taguchi method. In: Proceedings of 6th International & 27th All India Manufacturing Technology, Design and Research Conference, pp. 272–276, Pune, India (2016)
3. Baghel, R., Mali, H.S., Biswas, S.K.: Parametric optimization and surface analysis of diamond grinding-assisted EDM of TiN-Al_2O_3 ceramic composite. Int. J. Adv. Manuf. Technol. **1**, 1–10 (2018)
4. Sabur, A., Ali, M.Y., Maleque, M.A., Khan, A.A.: Investigation of material removal characteristics in EDM of nonconductive ZrO_2 ceramic. In: 5th BSME International Conference on Thermal Engineering, pp. 696–701, Procedia Engineering 56, Dhaka Bangladesh (2013)
5. Schubert, A., Zeidler, H., Hahn, M., Hackert-Oschätzchen, M., Schneider, J.: Micro-EDM milling of electrically nonconducting zirconia ceramics. In: The Seventeenth CIRP Conference on Electro Physical and Chemical Machining (ISEM), Procedia CIRP 6, pp. 297–302 (2013)
6. Yoo, H.K., Ko, J.H., Lim, K.Y., Kwon, W.T., Kim, Y.W.: Micro-electrical discharge machining characteristics of newly developed conductive SiC ceramic. Ceram. Int. **41**(1), 3490–3496 (2015)
7. Luis, C.J., Puertas, I.: Methodology for developing technological tables used in EDM processes of conductive ceramics. J. Mater. Process. Technol. **189**(1), 301–309 (2007)
8. Koshy, P., Jain, V.K., Lal, G.K.: Mechanism of material removal in electrical discharge diamond grinding. Int. J. Mach. Tools Manuf. **36**(10), 1173–1185 (1996)
9. Bhaduri, D., Kuar, A.S., Sarkar, S., Biswas, S.K., Mitra, S.: Electro discharge machining of titanium nitride-aluminium oxide composite for optimum process criterial yield. Mater. Manuf. Process. **24**(12), 312–1320 (2009)
10. Baghel, R., Mali, H.S.: A study on effects of discharge energy on geometric characteristics of high aspect ratio micro-holes on TiN-Al_2O_3 ceramics. In: 8th International Conference on Materials Manufacturing and Characterization, Materials Today: Proceedings, Hyderabad, India (2018)

Chapter 23
Experimental Investigations on the Effect of Energy Interaction Durations During Micro-channeling with ECDM

Tarlochan Singh and Akshay Dvivedi

Abstract In the present study, the effect of feed rate (that implies the energy interaction durations), applied voltage and pulse on time on performance characteristics of machined micro-channels was experimentally investigated. One factor at a time approach was used to perform the experiments. The width of micro-channels (WOC) and depth of penetration (DOP) were considered as the response characteristics. Additionally, the mechanism of energy interaction during fabrication of micro-channels has also been discussed with appropriate illustrations. DSO-recorded voltage signals were used to describe the discharge characteristics as well as their respective gas film behavior. During experimentation, the maximum DOP and minimum WOC were found 104 and 480 μm, respectively.

Keywords ECDM · Energy interaction durations · Micro-channels

23.1 Introduction

These days, the use of micro-fluidic devices in various applications (such as biomedical, lab-on-a-chip devices and drug delivery systems) grabbed great attention of the manufacturers. The micro-fluidic devices comprise a set of micro-channels and micro-holes on a single substrate. Micro-channels are the important part of micro-fluidic devices. The connection of various micro-channels over single substrate can be used to perform multiple operations, such as mixer, micro-pump, sorter and controller [1]. Literature revealed the use of various non-conventional micro-machining processes (like electric discharge machining, laser beam machining, electrochemi-

T. Singh (✉) · A. Dvivedi
Mechanical and Industrial Engineering Department, Indian Institute of Technology Roorkee, Roorkee 247667, India
e-mail: tsingh.iitr@yahoo.com

M. S. Shunmugam and M. Kanthababu (eds.), *Advances in Micro and Nano Manufacturing and Surface Engineering*, Lecture Notes on Multidisciplinary Industrial Engineering,
https://doi.org/10.1007/978-981-32-9425-7_23

cal machining and ultrasonic machining) for the machining of micro-channels for micro-fluidic devices [2]. However, the above-mentioned machining processes possess some limitations in regards to the material properties, economical aspects and machining accuracy. Electrochemical discharge machining (ECDM) process is a non-conventional micro-machining method that can be used to machine any kind of materials irrespective of their electrical conductivity, hardness and strength [3]. The basic configuration of ECDM is quite similar to the electrochemical cell (ECC). It consists of two electrodes, DC power supply and electrolytic chamber. The tool electrode (cathode) has to be immerged in the electrolyte up to 2–3 mm. The work material has to be placed below the tool electrode. Auxiliary electrode is fully immerged in the electrolyte. The electrolyte connects both the electrodes and develops electrochemical cell circuit (ECC). As the voltage is supplied across both the electrodes of ECC, the hydrogen and oxygen bubbles evolved from the tool and auxiliary electrodes, respectively. The coalescence of hydrogen bubbles over the tool electrode generates gas film. The formation of a gas film over the tool electrode ceases the flow of electrons across the circuit and develops high dynamic resistance. Owing to high dynamic resistance, the ohmic heating of gas film takes place, and as a consequence, gas film breaks down. The breakdown of gas film results in spark discharging. The thermal energy liberated by spark discharges over the work material results in material removal due to melting and vaporization [4]. The tracing of these spark discharges in a predefined direction result in the generation of micro-channels over the work material [2]. During micro-channeling, the energy liberated by spark discharges and the tracing speed of tool electrode are important process parameters that mainly control the geometry of micro-channels and material removal rate. Literature reveals two strategies that have been used to machine the micro-channels. In the first strategy, the tool electrode has to be placed just above the work material at some working gap [5]. In the second strategy, the tool electrode has to be placed inside the work material and then, it moves over the work material. In order to effectively utilize the ECD energy, the second strategy seems very appropriate [2]. But, in case of small applied voltage, the tool electrode experienced bending forces and thereby it leads to the failure of tool electrode [5]. Apart from this, the effect of feed rate also contributes in influencing the machine performance during micro-channeling. Several researchers performed various experimental studies to investigate the effect of feed rate during micro-channeling [2, 5, 6]. But, all the studies were limited to just investigate the effect of feed rate on the geometry of machined features. The effect of feed rate on discharge characteristics (energy interaction durations) is yet not explained. Thus, in the present investigation, feed rate, applied voltage and pulse on time were selected as process parameters and the effect of above-mentioned process parameters on discharge characteristics and their respective energy channelization/interaction behavior has also been discussed. The materials and methods that were used to perform the study are given in the subsequent section.

23.2 Materials and Methods

In the present study, an in-house developed ECDM setup was used to perform the experiments. A schematic view of the experimental setup is shown in Fig. 23.1. It consists of various components such as tool electrode, auxiliary electrode, X-Y slider, electrolytic bath and DC-pulsed power supply. A stainless steel (SS-304) cylindrical rod of diameter 400 μm was used as a tool electrode and was mounted in a chuck. Borosilicate glass was used as a work material and it was positioned below the tool electrode at zero working gap. The graphite block was placed below the work material and it was connected to the positive terminal of the power supply. In ECDM, the electrical signals in terms of current versus time and voltage versus time have been used to describe the discharge characteristics and their respective gas film behavior [7, 8]. In the current investigation, a digital storage oscilloscope (DSO) (Model: DSOX3034A, Agilent) was used to record voltage signals and it was connected to both the electrodes of the electrochemical cell circuit (ECC). The photographic view of the voltage signals recorded during experimentation is shown in Fig. 23.1. Here, the peak voltage represents the maximum voltage (V_{max}) and it corresponds to the intensity of spark discharges.

On the basis of preliminary experimentation and literature review, the process parameters and their selected ranges to machine the micro-channels are given in Table 23.1. Seterozoom microscope (Model: SMZ745T, Nikon) was used to capture and measure the dimensions of the machined micro-channels.

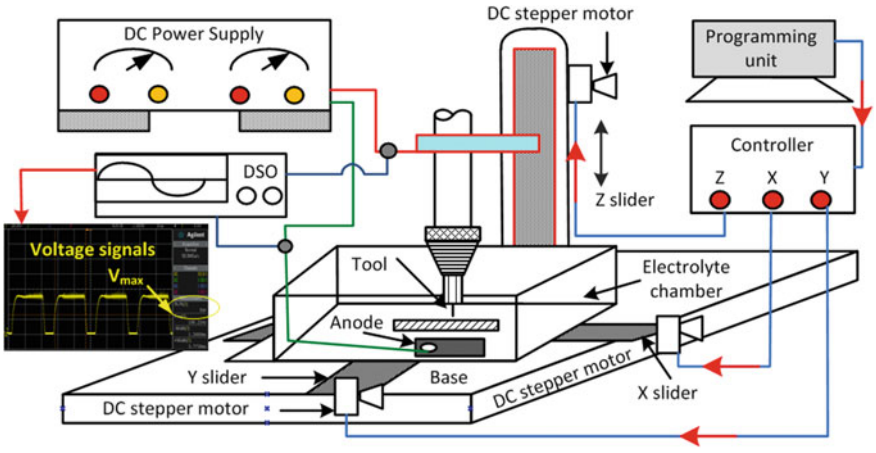

Fig. 23.1 Schematic view of the ECDM setup

Table 23.1 Process parameters and their levels

S. no.	Process parameters	Levels
1	Applied voltage (V)	50–70 (in steps of 5 V)
2	Feed rate (mm/min)	6–14 (in steps of 2 mm/min)
3	Pulse on time (ms)	1–5 (in steps of 1 ms)
4	Pulse off time (ms)	1
5	Electrolyte concentration (%)	20 (sodium hydroxide (NaOH))
6	Inter-electrode distance (IED) (mm)	25

23.3 Results and Discussion

In ECDM, feed rate decides the interaction durations between tool electrode and work material to liberate the electrochemical discharge (ECD) energy. In order to fabricate the accurate micro-channels, the synchronization between applied ECD energy and feed rate is very essential. Thus, in the present study, the feed rate was varied from 6 to 14 mm/min while the rest of other process parameters were fixed at constant levels, such as applied voltage = 60 V, pulse on time = 3 ms. The effect of feed rate on width and depth of machined micro-channels is shown in Fig. 23.2. The discharge characteristics recorded at different feed rates are also depicted in Fig. 23.2. The optical images to depict the machined micro-channels at different feed rates are shown in Fig. 23.3.

It was observed that at low feed rate of 6 mm/min, the WOC and DOP is at maximum value. The reason thereof is the maximum interaction time between the tool electrode and work material. Moreover, it can also be observed from the voltage

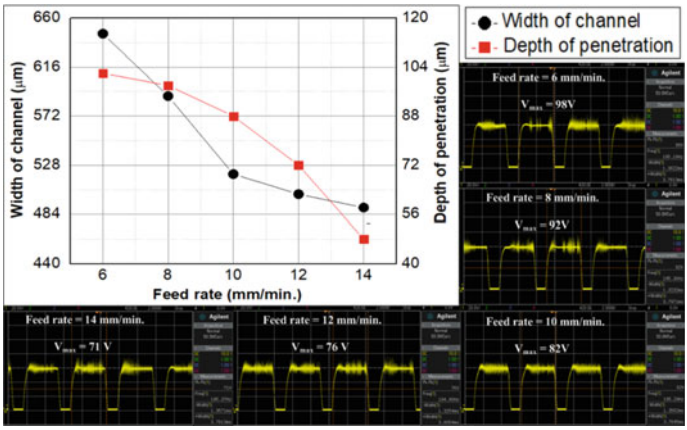

Fig. 23.2 Influence of feed rate on machined features and discharge characteristics

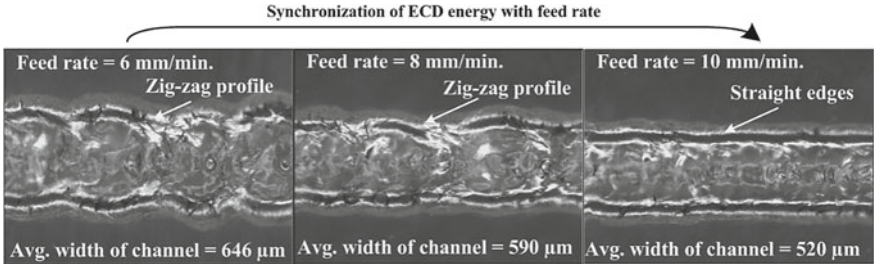

Fig. 23.3 Influence of feed rate on profile of machined micro-channels

signals shown in Fig. 23.2 that at low feed rate the intensity of discharges is very high ($V_{max} = 98$ V), but as the feed rate increases the intensity of discharge decreases. It means that at low feed rate, the thick gas film is formed around the tool electrode due to the accumulation of more gas bubbles in per unit time period. Thus, the breakdown of thick gas film produced high-intensity low-frequency discharges, as depicted in Fig. 23.2. The discontinuous flow of electrochemical discharge energy produced by these high-intensity low-frequency discharges results in zig-zag profiles of micro-channels. As the feed rate increases beyond 6 mm/min, the WOC and DOP decrease sharply. The reason thereof is the effective synchronization between applied ECD energy and feed rate. Hence, a feed rate of 10 mm/min produces micro-channels with straight edges, as shown in Fig. 23.3.

During ECDM, the applied voltage plays an important role as it directly controls the supply of electrochemical discharge (ECD) energy. In this study, the effect of applied voltage on width of channel and depth of penetration was analyzed by conducting the experiments. The experimentation was conducted by varying the applied voltage from 50 to 70 V, while the rest of other process parameters were fixed at constant levels (pulse on time = 3 ms, electrolyte concentration = 20% and feed rate of 10 mm/min).

The effect of applied voltage on WOC and DOP is depicted in Fig. 23.4, and on discharge characteristics and material removal mechanism during micro-channeling are given in Figs. 23.4 and 23.5, respectively. It was observed that at low applied voltage of 50 V, the DOP and WOC are at its lower values. The reason thereof is the availability of low ECD energy at machining zone. The lower applied voltage produces low-frequency, low-intensity spark discharges, as can be seen from the Fig. 23.4. The intensity of spark discharges is 59 V at applied voltage of 50 V. Thus, the energy liberated by low-intensity spark discharges is not sufficient to remove the material from work surface. Hence, the energy liberated by the tool electrode in the form of rings overlapped with each other, as can be seen from the Fig. 23.5, and thereby it results in low DOP. The overlapping of discharging rings at low ECD energy is also reported by Saranya et al. (2017) [9].

As the applied voltage increases from 50 to 60 V, the rate of bubbles accumulation around the tool electrode also increases, and, as a consequence, results in the formation of a thick gas film. Further, the breakdown of thick gas film produces

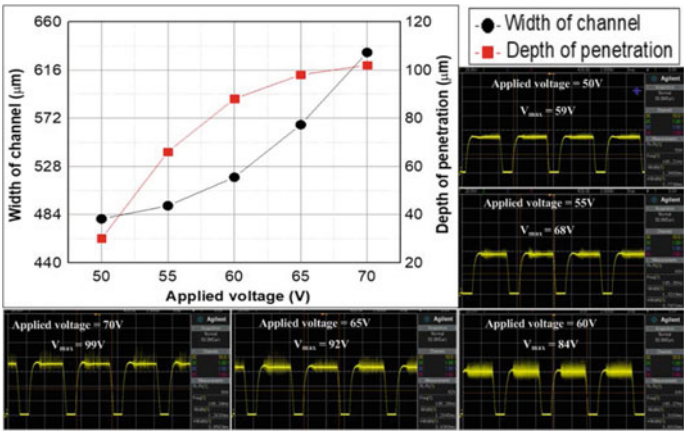

Fig. 23.4 Influence of voltage on machined features and discharge characteristics

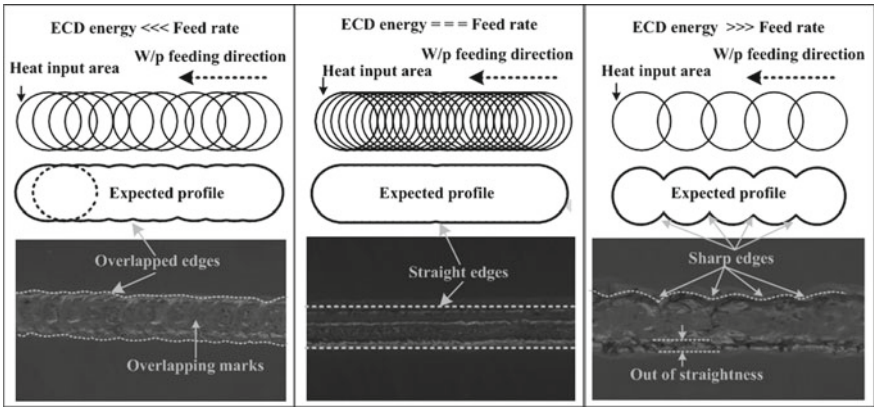

Fig. 23.5 Mechanism of energy interaction during electrochemical discharge milling

high-intensity spark discharges, as can be seen from the Fig. 23.4. The energy liberated by these discharges synchronizes the ECD energy with feed rate in such a way that it developed straight micro-channels as depicted in Fig. 23.5. On the other hand, the increase in applied voltage increases the WOC and DOP, simultaneously (refer Fig. 23.4). However, the rate of increase for DOP is higher than the rate of increase for WOC. But beyond 60 V, the increase in applied voltage produces high-intensity, low-frequency spark discharges, as depicted in Fig. 23.4. The energy liberated by these spark discharges results in zig-zag profiles of micro-channels, as shown in Fig. 23.5. The reason thereof is the liberation of high ECD energy per unit interaction period, and the applied ECD energy is used to increase the WOC at a higher rate than the DOP as illustrated in Fig. 23.4. The discharge patterns obtained during experimentation concur with the findings reported by Gupta et al. [10].

In ECDM, the use of pulse power supply is recommended over the continuous power supply [10]. The pulse power supply provides pulse on and pulse off phases, where pulse on phase is used to liberate the ECD energy over the work material, and pulse off is used to flush out the sludge and debris from machining zone [10]. An appropriate combination of pulse on and pulse off time for the effective machining is very essential. Thus, in this study, the pulse on time was varied from 1 to 5 ms, while the pulse off time was fixed at a constant level of 1 ms.

The effect of pulse on time on WOC, DOP and discharge characteristics is shown in Fig. 23.6. The profile of machined micro-channels is depicted in Fig. 23.7. It was observed that with an increase in pulse on time, the width of channels and depth of penetration increases simultaneously. The reason thereof is the increase in heat energy per unit pulse time [10]. It can also be seen from the discharge signals depicted in Fig. 23.2 that the intensity as well as frequency of discharges increases with an increase in pulse on time. Thus, the energy liberated by these high-intensity, high-frequency spark discharges increases the material removal, which in turn results in an increase in both WOC and DOP. However, the rate of increase for DOP is higher as compared to the rate of increase for WOC.

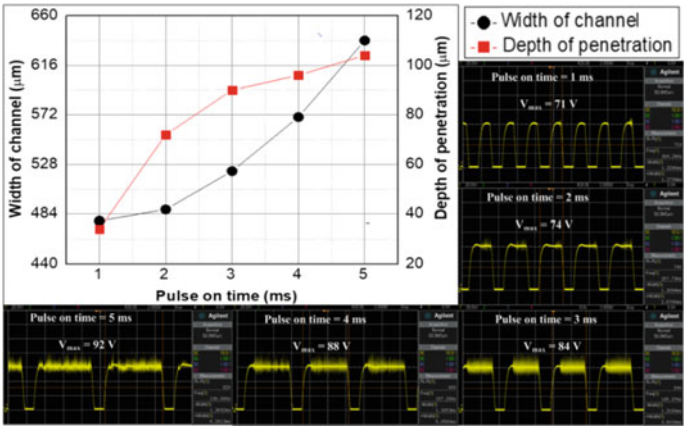

Fig. 23.6 Influence of pulse on time on machined features and discharge characteristics

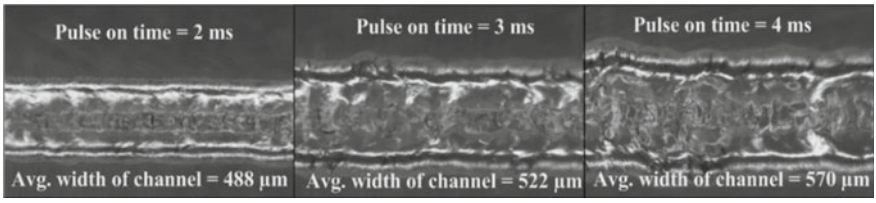

Fig. 23.7 Effect of pulse on time on profile of machined micro-channels

Beyond 3 ms pulse on time, the increase in pulse on time also increases the DOP and WOC simultaneously. But, the rate of WOC is quite higher than the rate of increase in DOP. It means that the beyond 3 ms pulse on time, the applied ECD energy is used to increase the width of the micro-channels instead of the depth. The effect of ECD energy on width of micro-channels can also be seen from the machined micro-channel profiles shown in Fig. 23.7.

23.4 Conclusions

In ECDM, the interaction durations play an important role to control the form of machined micro-features. Low feed rate provides more interaction time; thereby, it develops thick gas film around the tool electrode. The breakdown of thick gas film produces high-intensity low-frequency discharges and thereby results in wider micro-channels. The feed rate of 10 mm/min synchronizes with the applied ECD energy; therefore it develops micro-channels with straight edges instead of zig-zag profiles. Low applied voltage provides insufficient ECD energy to generate the micro-channels. Thus, the micro-channels fabricated at low applied voltage provide low WOC and DOP with zig-zag profiles. However, higher applied voltage provides excessive thermal energy at machining zone. Thus, it also leads to the fabrication of micro-channels with inaccurate profiles. The maximum DOP of 104 μm was obtained at the parametric combination of applied voltage = 60 V, pulse on time = 5 ms and feed rate = 10 mm/min. However, the minimum WOC was found to be 480 μm for applied voltage of 50 V, pulse on time of 3 ms and feed rate of 10 mm/min.

References

1. Judy, J.W.: Microelectromechanical systems (MEMS): fabrication, design and applications. Smart Mater. Struct. **10**, 1115–1134 (2001)
2. Singh, T., Dvivedi, A.: On performance evaluation of textured tools during micro-channeling with ECDM. J. Manuf. Process. **32**, 699–713 (2018)
3. Singh, T., Dvivedi, A.: Developments in electrochemical discharge machining: a review on electrochemical discharge machining, process variants and their hybrid methods. Int. J. Mach. Tools Manuf. **105**, 1–13 (2016)
4. Pawariya, K., Dvivedi, A., Singh, T.: On performance enhancement of electrochemical discharge trepanning (ECDT) process by sonication of tool electrode. Precis. Eng. (2018). https://doi.org/10.1016/j.precisioneng.2018.08.016
5. Hajian, M., Razfar, M.R., Etefagh, A.H.: Experimental study of tool bending force and feed rate in ECDM milling. Int. J. Adv. Manuf. Technol. **91**(5–8), 1677–1687 (2017)
6. Singh, T., Dvivedi, A.: An ecdm approach for the development of 3d microchannels on glass substrates. Int. J. Res. Eng. Technol. **5**, 125–127 (2016)
7. Singh, T., Dvivedi, A.: A pressurized feeding approach for effective control on working gap in ECDM of borosilicate glass. Mater. Manuf. Process. **33**(4), 462–473 (2018)

8. Elhami, S., Razfar, M.R.: Study of the current signal and material removal during ultrasonic-assisted electrochemical discharge machining. Int. J. Adv. Manuf. Technol. **92**(5–8), 1591–1599 (2017)
9. Saranya, S., Nair, A., Sankar, A.R.: Experimental investigations on the electrical and 2D-machining characteristics of an electrochemical discharge machining (ECDM) process. Microsyst. Technol. **23**(5), 1453–1461 (2017)
10. Gupta, P.K., Dvivedi, A., Kumar, P.: Effect of pulse duration on quality characteristics of blind hole drilled in glass by ECDM. Mater. Manuf. Process. **31**(13), 1740–1748 (2016)

Chapter 24
Influence of Chip Thickness Models on Deflection Aspects of an End Mill Cutter and a Spindle Bracket of a Miniaturized Machine Tool

Kadirikota Rajesh Babu

Abstract The forces generated during micro milling are relatively small (<10 N) due to the limited size and strength of the tool edge. Force model can be combined with tool stiffness to estimate the deflection of the tool as a function of depth of cut, the up-feed per revolution and the geometry of the part. In view of the importance attributed to the tool deflection in achieving the high-quality surface of a micro component, in the present study an attempt is made to utilize the different chip thickness models in characterizing the micro end milling operations from the viewpoint of static deflection of a cutter and spindle bracket of a miniaturized machine tool (MMT) by including cutter stiffness in force model. The variation of cutting force and the consequent tool deflection as a function of tooth position angle are illustrated graphically.

Keywords Chip thickness models · Tool deflection · Spindle bracket

24.1 Introduction

In the recent past, micro-sized products with complex miniaturized features manufactured in small volumes are in full demand for many industries, such as optics, electronics, biomedical, defense and so on [1]. Indeed, micro meso-mechanical manufacturing (M4) systems are perceived by many as potentially promising machine tools of the twenty-first century. Furthermore, mechanical manufacturing will generate free form and three-dimensional (3D) surfaces in metal and non-metal components. The widely used micro mechanical manufacturing process in an industry is micro end milling [2]. Being one of the most flexible components in micro machining system, micro scale tools commonly dominate the static and dynamic characteristics of a machine tool during micro milling. It is a well-known fact that in end milling,

K. Rajesh Babu (✉)
Department of Mechanical Engineering, S.V.U. College of Engineering, Tirupati 517502, AP, India
e-mail: rajesh.babuiit@gmail.com

M. S. Shunmugam and M. Kanthababu (eds.), *Advances in Micro and Nano Manufacturing and Surface Engineering*, Lecture Notes on Multidisciplinary Industrial Engineering,
https://doi.org/10.1007/978-981-32-9425-7_24

chip thickness changes as the cutter rotates and therefore the path of cutter (trajectory) would affect the surface topography of the workpart [3]. This implies that chip thickness is a function of tooth position angle. Therefore, there is a need to study the deflection aspects of a micro end mill cutter from the point of view of chip thickness models [4]. And another vital component of a miniaturized machine tool (MMT) is a spindle bracket as it directly affects the mounting of a cutter into the spindle assembly of a milling machine. The work herein also focuses on the deflection aspects of the spindle bracket.

24.2 Chip Thickness Models

Assuming the path of a cutter is circular, Martelloti expressed the chip thickness as [3]

$$h = f_t \sin\theta + R - \sqrt{R^2 - f_t^2 \cos\theta} \tag{24.1}$$

In most milling processes, feed per tooth is smaller than the cutter radius (R), thus Eq. (24.1) can be further simplified as

$$h = f_t \sin\theta \tag{24.2}$$

where h is the undeformed chip thickness, f_t is the feed per tooth, and θ is the angular position of the tooth. This equation of chip thickness model is widely used in the analysis of traditional milling process. As far as true path (trochoidal path) of the cutter tooth is concerned, Bao and Tansel model [5] is used in the present analysis and it is of the following form:

$$h = f_t \sin\theta - \frac{z}{2\pi R} f_t^2 \sin\theta \cos\theta + \frac{1}{2R} f_t^2 \cos^2\theta \tag{24.3}$$

with z = number of teeth, R is the radius of the cutter and other notations have same meaning as indicated for Eq. (24.2).

24.2.1 Tooth Position Angle (θ) Calculation

Chebyshev's spacing method of approximate selection, in which the optimum location of the angular positions $\theta_1, \theta_2, \theta_3, \theta_4$, and θ_5 are given by [6]

$$\theta_j = \frac{\theta_f + \theta_o}{2} - \frac{\theta_f - \theta_o}{2} \cos\left[\frac{\pi}{2m}(2j-1)\right] \tag{24.4}$$

Table 24.1 Selected angular positions by Chebyshev's spacing and equal spacing method

Spacing method	θ_1 (°)	θ_2 (°)	θ_3 (°)	θ_4 (°)
Chebyshev spacing	4.40	37.09	90	142.90
Equal spacing	0	45	90	135

where $j = 1, 2, \ldots, m$; m is the number of angular positions to be selected, that is, $m = 5$. θ_o and θ_f represent the entry angle and exit angle during cutting, respectively. In the full range of angular positions $\theta_o = 0^{\circ}$ and $\theta_f = 180^{\circ}$. Table 24.1 gives the values obtained for θ_j.

24.3 Cutting Force Models

In end milling, the mechanistic cutting force model is used because the chip load and cutting forces are evaluated based on the cutting geometry and the machining conditions. In this model, the cutting force is directly proportional to the chip area of the cut [4]. The equations which relate the elemental chip loading to the cutting forces contain empirical constants or simply cutting constants.

24.3.1 Specific Cutting Force Model

In an end milling operation, the conventional or specific cutting force models (based on chip load) in tangential and radial directions of cutting are given as follows [4].

Tangential cutting force,

$$F_t = K_t h b \tag{24.5}$$

Radial force,

$$F_r = k_r F_t \tag{24.6}$$

where K_t is a specific cutting pressure and is constant for a specific tool–work pair and has a unit of $\mathrm{N}/\mu\mathrm{m}^2$, and k_r is the dimensionless constant called force ratio and relates radial force to tangential force, and b is the axial depth of cut.

24.3.2 Cutting Force Model with Cutter Stiffness Included

The present work also focuses on evaluating cutter deflection by including cutter stiffness in the force model. This implies that a closed-loop form of control is established between the cutter deflection and its force component [7]. And if the deflection of the cutter is considered, then Eq. (24.5) now becomes,

$$F_t = K_t b\left[h - \frac{F_t}{K}\right] \tag{24.7}$$

where K is the stiffness of the cutter and $\frac{F_t}{K}$ is the deflection of the cutter. Then $\left[h - \frac{F_t}{K}\right]$ is the chip thickness for the first pass. Solving for the force, we have

$$F_t = \frac{K_t bh}{\left[1 + \frac{K_t b}{K}\right]} \tag{24.8}$$

The ratio between cutting stiffness ($K_t b$) and cutter stiffness (K) controls whether or not the effect of the deflection of cutter will be significant [7].

24.4 Tool Deflection of a Micro End Mill

The features of large shank, taper and reduced diameter at the cutting edges, as shown in Fig. 24.1, are unique characteristics of a micro end mill. This design is required for micro end mills to provide tool holding with the shank and to keep the length to diameter ratio small in the fluted region for stiffness. Fig. 24.2 illustrates the idealized model of vertical MMT depicting vital components of a machine tool.

Comparison of the cutting force models has been carried out by assuming the following numerical data and by considering two cases, namely, circular tooth path and trochoidal tooth path. In the present study, the effect of the cutter runout has been neglected and also assumed that end milling taking place at constant cutting constants.

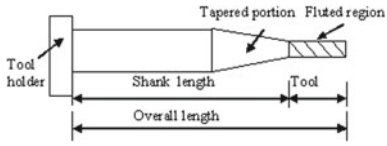

Fig. 24.1 Fig. 24.2. Micro end mill [8]

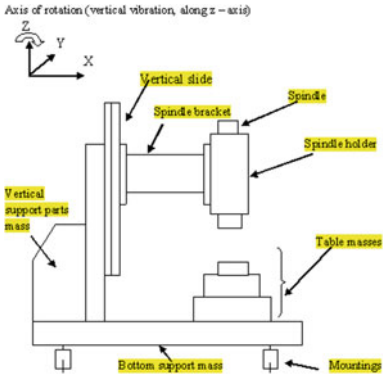

Fig. 24.2 Idealized structure of MMT [9]

24.4.1 Path of Cutter Tooth—Circular

Assume the following data for the purpose of comparing the above-cited two models. Feed per tooth, $f_t = 2\,\mu\text{m}$; specific cutting pressure, $K_t = 1.2\,\frac{\text{N}}{\mu\text{m}^2}$; axial depth of cut, $b = 10\,\mu\text{m}$.

In case of circular tool path, the required equation for an uncut chip thickness of an end milling operation is given by Eq. (24.2). The radial stiffness (K_r) of the cutter is $K_r = \frac{3EI}{L^3}$, where flute length of the cutter (assuming aspect ratio as 3:1), $L = 3d$, diameter of the cutter, $d = 200\,\mu\text{m}$ with $E =$ Young's modulus of the cutter $\left(E = 6 \times 10^5\,\text{N}/\text{mm}^2\right)$, $I =$ section modulus of the cutter $\left(\frac{\pi}{64}d^4\right)$.

Table 24.2 illustrates the tangential force and radial force values of the micro end mill cutter by considering the circular cutter path and cutter stiffness in the cutting force models.

As a rule, for the second pass, radial force is 20% less than the first pass, that is, 80% of the radial force of the first pass [9]. The corresponding deflection values are tabulated as shown in Table 24.3.

From the above tables, it is clear that as the cutting force decreases the deflection of the end mill cutter also decreases. The associated plots representing the variation

Table 24.2 Cutting forces and static deflection values of a cutter for different tooth position angles (θ) (Chebyshev's spacing method)

θ (°)	Uncut chip thickness (μ)	Tangential force (N)	Radial force $F_r = 0.3F_T$ (N)	Deflection $\delta = \frac{F_r}{K_r}$ (μ)
4.40	0.1534	0.09523	0.02857	0.04365
37.09	1.2064	0.74878	0.22460	0.34316
90	2.0000	1.24130	0.37240	0.56898
142.90	1.2064	0.74878	0.22460	0.34320
175.60	0.1534	0.09523	0.02857	0.04365

Table 24.3 Cutter deflection values during the second pass of the cutter

θ (°)	Radial force $F_{r2} = 0.8F_r$ (N)	Deflection $\delta = \frac{F_{r2}}{K_r}$ (μ)
4.40	0.022856	0.03492
37.09	0.179680	0.27453
90	0.297920	0.45518
142.90	0.179704	0.27456
175.60	0.022856	0.03492

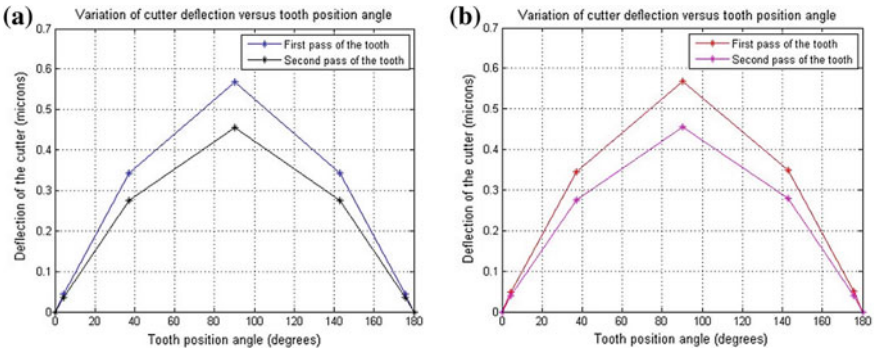

Fig. 24.3 Variation of cutter deflection as a function of tooth position angle

of deflection of the end mill cutter with respect to the different tooth position angles were illustrated in Fig. 24.3a.

24.4.2 Trajectory of Cutter Tooth—Trochoidal

By using the same numerical data as assumed for circular tool path, one can easily estimate the cutter deflections even for the trochoidal cutter path, and the estimated values were tabulated as in Tables 24.4 and 24.5, respectively.

The corresponding deflection plots as a function of tooth position angle were depicted in Fig. 24.3b.

24.5 Static Deflection of Spindle Bracket of a MMT

Say, for a given geometrical configuration of a machine tool and assuming that the machine tool uses micro end milling cutter, we can model the spindle bracket as a cantilever beam (see Fig. 24.4) whose end deflection has to be estimated by an analytical approach [10].

Table 24.4 Cutting forces and static deflection values of a cutter for different tooth position angles (θ) (Chebyshev's spacing method)

θ (°)	Uncut chip thickness (μ)	Tangential force (N)	Radial force $F_r = 0.3F_T$ (N)	Deflection $\delta = \frac{F_r}{K_r}$ (μ)
4.40	0.1723	0.10696	0.03208	0.04903
37.09	1.2130	0.75287	0.22586	0.34508
90	2.0000	1.24130	0.37240	0.56898
142.90	1.2253	0.76050	0.22815	0.34858
175.60	0.1743	0.10818	0.03245	0.04958

Table 24.5 Cutter deflection values during the second pass of the cutter

θ (°)	Radial force $F_{r2} = 0.8F_r$ (N)	Deflection $\delta = \frac{F_{r2}}{K_r}$ (μ)
4.40	0.026316	0.04021
37.09	0.180688	0.27607
90	0.297920	0.45518
142.90	0.182520	0.27887
175.60	0.025963	0.03966

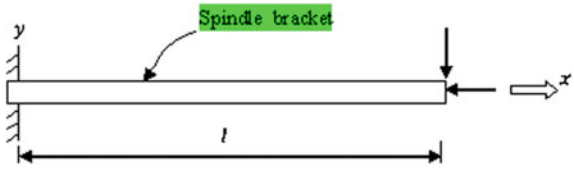

Fig. 24.4 Cantilever beam subjected to radial and tangential (axial) loads

For a specific combination of tool and work material, and letting $\theta = 25.84°$, axial depth of cut, $b = 10\,\mu\text{m}$ feed per tooth, $f_t = 2\,\mu\text{m}$, specific cutting pressure, $K_t = 1.2\,\text{N}/\mu\text{m}^2$. Substitution of the above numerical data in the 'specific cutting force model' equation yields tangential cutting force, $F_t = K_t hb = 10.46\,\text{N}$, radial force, $F_r = k_r F_t = 0.3F_t = 3.138$ N. Further substitution of the above force values together with material (aluminum) properties, E and I in the following static deflection equation will result in end deflection of a spindle bracket [10].

$$\delta_{\text{static}} = \frac{F_r l^3}{3EI\left[1 - \frac{2F_t l^2}{5EI}\right]} \tag{24.9}$$

with $l = 127\,\text{mm}$; $EI = 82.10724 \times 10^{10}\,\text{N-m}^2$ and hence the static deflection of a spindle bracket is $\delta_{\text{static}} = 2.61$ nm.

Table 24.6 Cutter maximum tool deflection values of circular and trochoidal trajectories of a cutter path

Tooth position angle (90°)	Maximum tool deflection (μm)	
	Circular path	Trochoidal path
First pass	0.56898	0.56898
Second pass	0.45518	0.45518

24.6 Results and Discussion

Micro end mill cutter static deflections were determined analytically by considering circular and trochoidal cutter tooth trajectories. In calculating the tooth position angles of a cutter, Chebyshev's approximation technique has been used (Table 24.6).

From the above table, it is evident that maximum deflection values were the same in both the trajectories. As far as deflection of the spindle bracket is concerned, the end deflection of the same was determined analytically by modeling it as a cantilever beam and it was found to be 2.61 nm. This numerical value is also in agreement with the static deflection of a cantilever beam model (spindle bracket) for the given geometrical data and cutting conditions.

24.7 Conclusions

In this research study, micro end mill cutter deflections were estimated by considering two different chip thickness models—circular tooth path and trochoidal cutter path—and two cutting force models—specific cutting force model and an instantaneous force model (inclusion of cutter stiffness). To say explicitly, Chebyshev's approximation technique has been used in determining the tooth position angles of the cutter and then the cutter deflections were found at these tooth position angles. It was observed that maximum deflection (of the same value) of the cutter (for both circular cutter path and trochoidal cutter path) had occurred at tooth position angle of 90°. This implies that chip thickness models have little or no impact as far as maximum deflection of the cutter is concerned. The associated deflection plots were drawn as a function of tooth position angles. In addition, the static (end) deflection of a spindle bracket of MMT has also been estimated by classical cantilever beam theory. Finally, the work herein will aid the design engineer to assess the deflection aspects of a cutter and a spindle bracket by closed-form solutions in a more systematic way.

References

1. Liu, X., et al.: The mechanics of machining at the microscale: assessment of the current state of the science. Trans. ASME **39**, 666–676 (2004)
2. Huo, D., et al.: Modelling the influence of tool deflection on cutting force and surface generation in micromilling. Micromachines **188**(8), 1–10 (2017)
3. Martellotti, M.E.: An analysis of the milling process. Trans. ASME, 677–700 (1941)
4. Tulsty, J., Elbestawi, M.: Constraints in adaptive control with flexible endmills. CIRPAnnals **28**(1), 253–255 (1979)
5. Bao, W.Y., Tansel, I.N.: Modelling of microendmill operations, Part 1: analytical cutting force model. Int. J. Mach. Tools Manuf. **40**, 2155–2173 (2000)
6. Kang, Y.H., Zheng, C.M.: Mathematical modelling of chip thickness in micro-end-milling: a Fourier modeling. Appl. Math. Model. **37**, 4208–4223 (2013)
7. Smith, S., Tlusty, J.: An overview of modelling and simulation of the milling process. J. Eng. Ind. **113**, 169–175 (1991)
8. Uhlmann, E., Schauer, K.: Dynamic load and strain analysis for the optimization of microend-mills. CIRP Ann. **54**, 75–78 (2005)
9. Dow, T.A., et al.: Tool force and deflection compensation for small milling tools. Precis. Eng. **28**, 31–35 (2004)
10. Budynas, R.G.: Advanced Strength and Applied Stress Analysis. McGraw-Hill Book Company, NY, U.S.A (1977)

Chapter 25
Micro-hardness Improvement of HSS Using Tungsten Tool Through Micro-electrical Discharge Process

S. Mohanty, Avijit Roy, Brij Bhushan, A. K. Das and Amit Rai Dixit

Abstract In the present state of work, a tungsten tool is used for alloying of HSS workpiece material by depositing a hard carbide layer of tungsten and iron through micro-electrical discharge machining (μ-EDM) process. Commercial EDM oil was used as a dielectric that reacts with the tungsten tool electrode to form tungsten carbide over HSS work material. The micro-hardness values and the Energy Dispersive Spectroscopy (EDS) plots proved the appearance of carbide phase of the tool on HSS. X-ray diffraction (XRD) plot suggest the formation of hard carbide phase of tungsten (tungsten carbide) and iron (cementite) on the alloyed surface. The diffusion of tool and dielectric material from the base material (HSS) towards the transition region has been studied by EDS reports.

Keywords Micro-hardness · EDS · M-EDM · XRD · Diffusion

25.1 Introduction

Micro-electrical discharge machining process (μ-EDM) has craved to develop hard coatings over miniaturized tools to be profoundly used for micro-manufacturing [1]. The micro-tools find application in cutting, drilling, turning, boring, etc. The life of such tools can degrade with prolonged use. Thus increasing the strength and life of the particular surface exposed to the cutting environment is a major challenge these days. μ-EDM process has made it convenient for local alloying of miniaturized parts wherein reverse polarity of electrode (tool positive and workpiece negative) helps the deposition possible on workpiece from the tool.

A lot of research has been conducted for improving the micro-hardness of engineering materials [2]. Kumar et al. [3] carried a review on various methods of surface modification in EDM. Prakash et al. [4] carried out experiments on Nickel sheets using Ti6Al4V micro-tool electrodes using EDM oil and kerosene to form a hard

S. Mohanty (✉) · A. Roy · B. Bhushan · A. K. Das · A. R. Dixit
Department of Mechanical Engineering, Indian Institute of Technology (ISM), Dhanbad 826001, Jharkhand, India
e-mail: shalinimohanty5@yahoo.com

M. S. Shunmugam and M. Kanthababu (eds.), *Advances in Micro and Nano Manufacturing and Surface Engineering*, Lecture Notes on Multidisciplinary Industrial Engineering,
https://doi.org/10.1007/978-981-32-9425-7_25

carbide layer of TiC on work surface. In another study, Aspinwall et al. [5] used W/CrC/Co, TiC/WC/Co, and WC/Co tool to increase the surface hardness of steel (2% Cr), reason being the presence of W, C, and Co. Bleys et al. [6] reported the pyrolysis of dielectric occurs with the transfer of both electrode material over the workpiece surface to form hard phase recast layer. Kumar et al. [7] conducted EDM alloying experiments on OHNS die steel using Inconel electrode and results indicate 88% improved micro-hardness of the alloyed surface. The SEM and XRD results indicate the transfer of chromium and nickel from the tool material to the workpiece surface.

A number of research articles suggest the surface modification using conventional electrical discharge machining process. The large tool size cannot be used for micron sized components since a large discharge energy damages the workpiece. On other hand, μ-EDM involves microsize tool electrodes wherein less discharge energy is generated and hence, the diffusion depth is less as compared to that of the conventional one. Thus, the present study involves the alloying of miniature components made of HSS using μ-EDM to improve its micro-hardness. The work focusses on localized alloying of miniaturized tool components made from HSS material which are prone to extreme environmental conditions during machining operations. This further can find application in various miniaturize tool and die industries.

25.2 Methodology

The experiments were carried out with in-house developed micro-electrical discharge machine setup taking high-speed steel (HSS) as workpiece, tungsten as tool electrode with commercial EDM oil as dielectric liquid. The 3D model of the setup used for alloying process is shown in Fig. 25.1. It constitutes of a rotating chuck that holds the tool and the workpiece is submerged in the dielectric tank fitted with arrangements to give linear movements in X-Y direction. The tool electrode is attached to a DC motor for giving rotational motion. LAB-View software is employed for controlling the directional movement of the X, Y, and Z stages. Transistor pulse power unit is adopted for the process. The μ-EDM works on the principle of generation of sparks between electrodes in a dielectric medium and hence necessary material melting, vaporization, and solidification take place on the workpiece surface. Figures 25.2 and 25.3 show the workpiece and the tool used for experimentation. The workpiece dimensions were 40 mm × 20 mm × 3 mm whereas the tool was cylindrical in shape with 1 mm diameter. A reverse polarity (tool positive and workpiece negative) was ensured for carrying out the alloying process as such more material melting takes place from the tool surface. The pilot experiments were conducted to define the optimal range of parameters before the actual start of experiments. A total of 27 experiments were conducted using parametric settings at different levels of duty factor (DF), voltage (V), and alloying time (T_m) shown in Table 25.1. Duty factor indicates the ratio of total pulse on time to the total pulse duration.

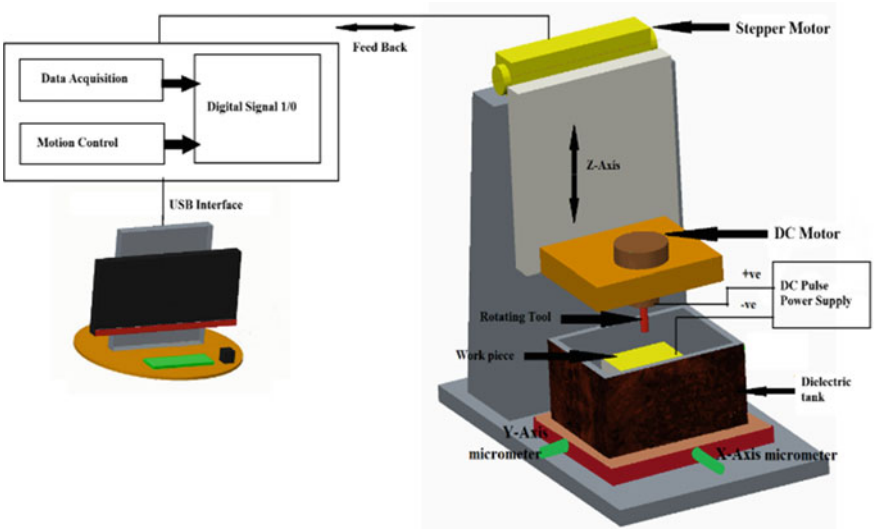

Fig. 25.1 Experimental setup used for alloying

Fig. 25.2 HSS workpiece after alloying in μ-EDM

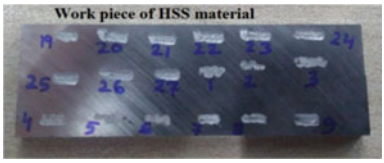

Fig. 25.3 Tungsten tool electrode used in alloying

Table 25.1 Parametric settings for alloying

Parameter	Range
Voltage (V)	30, 45, 60
Duty factor (%)	45, 55, 65
Alloying time (min)	5, 10, 15

25.3 Results and Discussion

25.3.1 Micro-hardness

The experimental results (shown in Table 25.2) constituting the micro-hardness parameter were assessed by Economet micro-hardness testing machine (Model number- VH-1 MD, Make - Chennai Metco), measuring range lying between 8 and 2900 HV. The hardness testing was carried out at a load-bearing 0.1 kgf with a dwell time of 10 s using a diamond indenter (a pyramid with square base). The

Table 25.2 Observation table for micro-EDM alloying of HSS

Sl No	Voltage	Duty factor	Alloying time	HV
1	30	0.45	5	621.06
2	30	0.45	10	667.58
3	30	0.45	15	728.589
4	30	0.55	5	771.06
5	30	0.55	10	752.06
6	30	0.55	15	790.31
7	30	0.65	5	789.10
8	30	0.65	10	813.33
9	30	0.65	15	847.17
10	40	0.45	5	878.64
11	40	0.45	10	911.01
12	40	0.45	15	935.01
13	40	0.55	5	940.28
14	40	0.55	10	947.08
15	40	0.55	15	959.27
16	40	0.65	5	910.28
17	40	0.65	10	947.08
18	40	0.65	15	981.27
19	60	0.45	5	1130.81
20	60	0.45	10	1174.22
21	60	0.45	15	1268.52
22	60	0.55	5	1192.97
23	60	0.55	10	1300.11
24	60	0.55	15	1339.80
25	60	0.65	5	1381.35
26	60	0.65	10	1429.31
27	60	0.65	15	1446.38

observations were recorded and relationship between the micro-hardness values and the input alloying parameters were derived as shown in Fig. 25.4. The average micro-hardness values lie in the range of 621.06–1446.38 HV which is almost three times more than the base material (611.21 HV). It implies the mean micro-hardness values of the recast layer of the alloyed region can be up to three times to that of the base material [8, 9]. The increase in hardness of the alloyed sample could have been due to the presence of tungsten carbide and other intermetallic compound formed on the recast layer. This has been verified by the X-ray diffraction (XRD) results.

In addition to this, with the increase in voltage and duty factor (as shown in Fig. 25.4 a–c), high melting of material takes place as a result, the hardness values of the average recast layer increases [4]. The other reason for improved hardness is the sudden cooling of the melted material from the tool and workpiece on the recast layer within the dielectric medium [10]. The prolonged exposure of the workpiece surface to the tool and dielectric results in more and more deposition of the carbide phase on the recast layer. Thus, an increase in alloying time results in increase in width of recast layer and micro-hardness value.

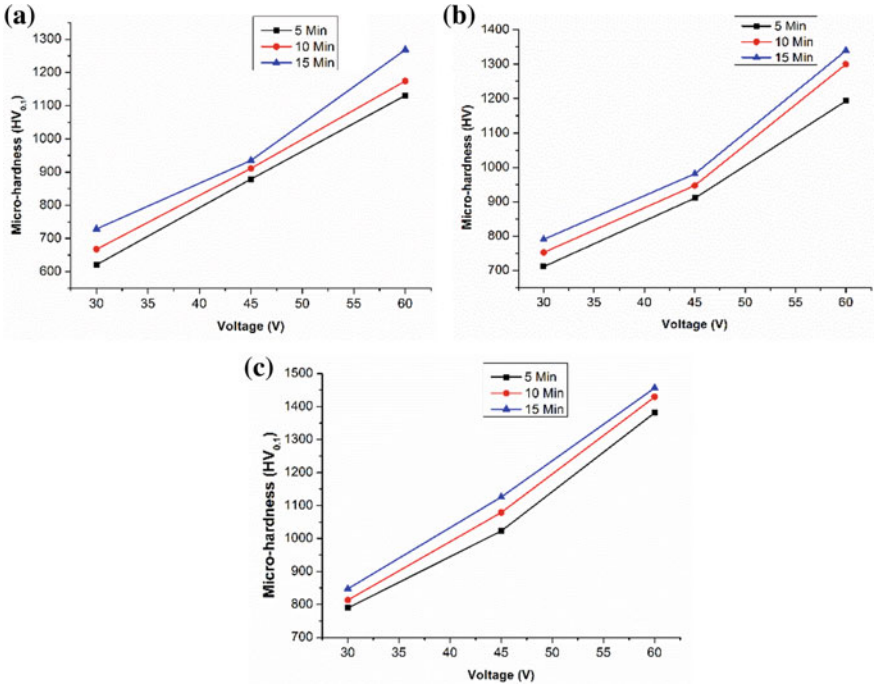

Fig. 25.4 Effect of voltage and alloying time on micro-hardness at duty factors **a** 0.45, **b** 0.55, and **c** 0.65

25.3.2 EDS Analysis

The energy dispersive spectroscopy (EDS) report shown in Fig. 25.5 suggests the presence of iron (Fe), tungsten (W), chromium (Cr), carbon (C), molybdenum (Mo), vanadium (V), cobalt (Co), and oxygen (O) for a sample alloyed at 45 V, 0.55 duty factor and 10 min alloying time. The presence of carbon element confirms the carbide phase formed on the recast layer of the workpiece surface. Since the experiments have been carried out in an open atmosphere, oxygen content has been found in the EDS report. The presence of carbide and oxide phase of elements may be one of the reasons responsible for an improvement in micro-hardness of HSS work surface which has been confirmed in XRD results.

25.3.3 XRD Analysis

The XRD plot of a sample prepared with parametric setting voltage 60 V, duty factor 65% and alloying duration of 10 min is shown in Fig. 25.6. It indicates the presence of tungsten carbide (WC) and cementite (Fe_3C) that is responsible for increase in micro-hardness of the HSS specimen. The dissociation of elements from the tool, workpiece, and the dielectric takes place which results in formation of intermetallic compounds. It is clear that there is carrying away of the tool and dielectric fluid material to the alloyed work surface.

25.3.4 Diffusion

The elemental diffusion into the recast layer of the alloyed specimen from the tool and the dielectric is examined by EDS reports. A sample prepared at 60 V, 0.55

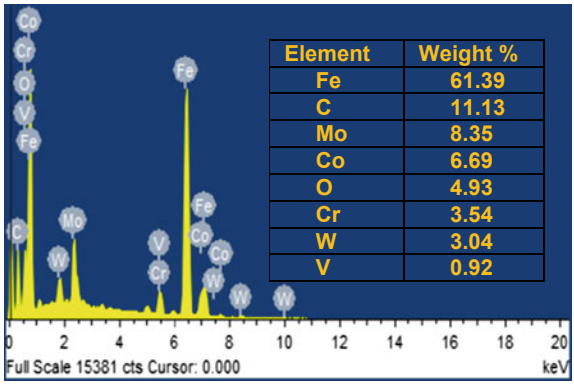

Fig. 25.5 EDS report of the alloyed specimen prepared at 45 V, 0.55 DF, and 10 min alloying duration

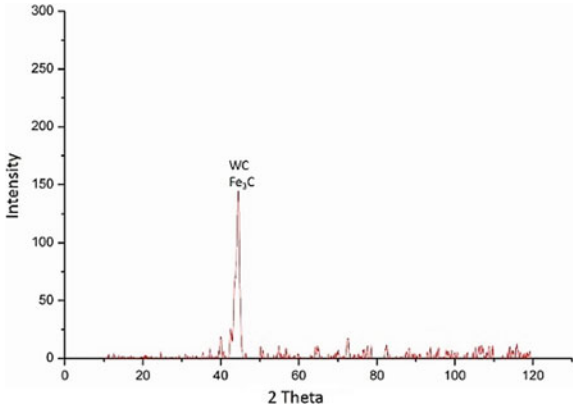

Fig. 25.6 XRD plot showing the alloyed workpiece sample at 60 V, 0.65 duty factor and 10 min alloying time

duty factor, and 10 min parametric setting was taken up for the diffusion study. A smaller portion of area is considered for analysis starting from HSS base material and proceeding towards the alloyed recast layer on the work surface, covering the transition region. Each of the spectra gives the elemental content of that particular area taken into consideration. Figure 25.7 shows the spectra produced for each of the area of transition phase with corresponding EDS report (Fig. 25.7a–d). Figure 25.7e depicts the FESEM image of the alloyed recast layer formed over the base metal indicating area considered for each of the spectra. Figure 25.7f shows the variation in weight percentage of major elements from the base material (region 1) towards the alloyed surface (region 4). It is evident that carbon content increases from the base metal towards the recast alloyed layer since the formation of tungsten carbide and cementite takes place. Moreover, a decrease in tungsten up to the transition region indicates its dissociation and again its increase denotes the formation of tungsten intermetallic compound with carbon that gets deposited over the alloyed surface. A similar trend is followed by iron that dissociates to form iron oxide and iron carbide that is one of the reasons for the improvement in hardness. This confirms the transmission of tool and dielectric material to the alloyed surface of the workpiece post alloying using micro-electrical discharge process.

25.4 Conclusions

The experimental results reveal the formation of a hard phase of tungsten and iron on the HSS die steel work surface. The micro-hardness was seen to be increased along with the voltage, duty factor, and alloying duration. More melting of material allows more deposition on the work surface in the form of recast layer. Prolonged exposure to the sparks (due to an increase in alloying duration) leads to higher deposition on the recast region. The micro-hardness value was increased from 1.61 to 136.64% compared to that of the base material (HSS). The Energy Dispersive

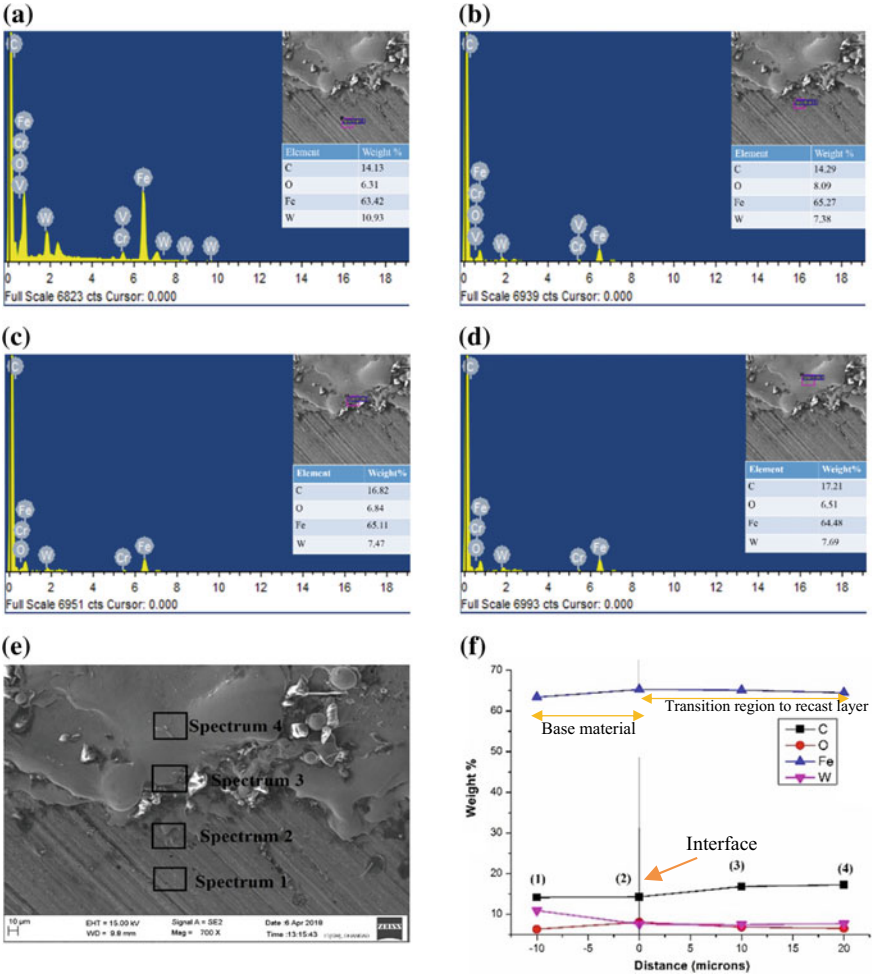

Fig. 25.7 EDS images showing elemental diffusion in the recast layer at **a** region 1, **b** region 2, **c** region 3, **d** region 4, **e** different regions, and **f** change in weight % with distance from transition region

Spectroscopy (EDS) results also confirmed the presence of basic elements of tool and substrate material. X-ray Diffraction analysis (XRD) identified the nature of intermetallic compounds formed on the substrate material, i.e., tungsten carbide and cementite that is responsible for increasing the micro-hardness of the HSS specimen. The elemental diffusion from the tungsten tool and the dielectric on the workpiece material was studied by EDS results by considering area of each spectrum initiating from HSS base material and continuing towards the alloyed region. The aim of the study to produce hard surface over HSS material has been successfully accomplished

by micro-electrical discharge process. Thus, the locally alloyed miniaturized HSS parts find application in micromachining of various engineering materials such as in case of micro-tools, micro dies, micro-punch, etc.

References

1. Prakash, V., Kumar, P., Singh, P.K., Hussain, M., Das, A.K., Chattopadhyaya, S.: Micro-electrical discharge machining of difficult-to-machine materials: a review. In: Proceedings of the Institution of Mechanical Engineers, Part B: Journal of Engineering Manufacture. https://doi.org/10.1177/0954405417718591 (2017)
2. Abbas, N.M., Solomon, D.G., Bahari, M.F.: A review on current research trends in electrical discharge machining (EDM). Int. J. Mach. Tools Manuf. **47**(7), 1214–1228 (2007)
3. Kumar, S., Singh, R., Singh, T.P., Sethi, B.L.: Surface modification by electrical discharge machining: a review. J. Mater. Process. Technol. **209**(8), 3675–3687 (2009)
4. Prakash, V., Shubham, Kumar, P., Singh, P.K., Das, A.K., Chattopadhyaya, S., Dixit, A.R.: Surface alloying of miniature components by micro-electrical discharge process. Mater. Manuf. Process. 1–11 (2017)
5. Aspinwall, D.K., Dewes, R.C., Lee, H.G., Simao, J., McKeown, P.A.: Electrical discharge surface alloying of Ti and Fe workpiece materials using refractory powder compact electrodes and Cu wire. CIRP Ann. Manuf. Technol. **52**(1), 151–156 (2003)
6. Bleys, P., Kruth, J.P., Lauwers, B., Schacht, B., Balasubramanian, V., Froyen, L., Van Humbeeck, J.: Surface and sub-surface quality of steel after EDM. Adv. Eng. Mater. **8**(1–2), 15–25 (2006)
7. Kumar, S., Singh, T.P., Sethi, B.L.: Surface alloying of OHNS die steel by EDM process using inconel electrode. Int. J. Mach. Mach. Mater. **6**(3–4), 176–193 (2009)
8. Rahang, M., Patowari, P.K.: Parametric optimization for selective surface modification in EDM using Taguchi analysis. Mater. Manuf. Process. **31**(4), 422–431 (2016)
9. Gill, A.S., Kumar, S.: Surface roughness and microhardness evaluation for EDM with Cu–Mn powder metallurgy tool. Mater. Manuf. Process. **31**(4), 514–521 (2016)
10. Mohanty, S., Kumar, V., Das, A.K., Dixit, A.R.: Surface modification of Ti-alloy by micro-electrical discharge process using tungsten disulphide powder suspension. J. Manuf. Process. **37**, 28–41 (2019)

Chapter 26
Nano-finishing of Internal Surface of Power Steering Housing Cylinder Using Rotational Magnetorheological Honing Process

S. K. Paswan and A. K. Singh

Abstract The rotational magnetorheological honing (MRH) process is an advanced finishing process. The MRH tool is designed and developed for nano-finishing the internal cylindrical surfaces of ferromagnetic parts. The magnetorheological polishing fluid is used as a finishing medium. The power steering housing cylinder is finished in this work. Rotational motion is given to the cylindrical workpiece through the servomotor using the automatic centering 3-jaw chuck in the opposite direction to the rotational motion of the MRH tool. The relative speed of an active abrasive gets enhanced and continuous shuffling of the active abrasives takes place in this process. The change in surface roughness was found to be 71.87% at the rotational speed of workpiece at 40 rpm which is measured with Mitutoyo Surftest. The scanning electron microscopy is conducted on the finished cylinder internal surface for analysing the surface texture. The surface textures and roughness profiles revealed that the rotational MRH is more capable and productive.

Keywords Rotational · Magnetorheological · Honing · Power steering housing cylinder · Internal surface

26.1 Introduction

Initially for finishing the internal cylindrical surfaces, cylindrical grinding, conventional honing, etc., are some traditional finishing processes which are used to finish the inner cylindrical surfaces [1]. These finishing processes are having less controllability and unwanted high heat generation due to direct contact of the rigid tool during finishing [2]. These things enforce the products in residual thermal stress,

S. K. Paswan · A. K. Singh (✉)
Department of Mechanical Engineering, Thapar Institute of Engineering and Technology, Patiala 147004, India
e-mail: anantsingh@thapar.edu

S. K. Paswan
e-mail: spaswan_phd16@thapar.edu

M. S. Shunmugam and M. Kanthababu (eds.), *Advances in Micro and Nano Manufacturing and Surface Engineering*, Lecture Notes on Multidisciplinary Industrial Engineering,
https://doi.org/10.1007/978-981-32-9425-7_26

heat affected zone, subsurface damage, microcracks, and changes in microstructures [3, 4]. In these finishing processes, various surface defects such as deeper grooves, pits or cavities, torn and folded, etc. on the internal cylindrical surface take place. [5, 6]. These imperfections diminish the internal surface integrity of cylindrical parts in both grinding and conventional honing process [7]. To get rid of these limitations and to enhance the quality of interior cylindrical surfaces, various types of advanced finishing operations have been introduced [2]. To achieve the nanolevel of finishing over the internal surface of the power steering cylinder, the rotational magnetorheological honing (R-MRH) process is used. The power steering housing cylinder is an essential component of a power steering system which encloses hydraulic piston, rack, and pinion gear, etc. The hydraulic piston is mounted on rack shaft and is reciprocated over the inner surface of the power steering housing cylinder. The inner surface of the power steering housing cylinder requires nano-finished surface quality to reduce friction, lower oil consumption, less efforts for turning the steering and to avoid the oil leakage from piston ring surface. In present work, nano-finishing of inner surface of power steering cylinder takes place in reduced finishing time as compared to the existing MR polishing fluid-based finishing processes. In this process, rotational motion is also given to the power steering cylinder along with the rotational and reciprocation movement of the magnetorheological honing tool as shown in Fig. 26.1. The magnetorheological (MR) polishing fluid is a mixture of the carbonyl iron particles (CIPs) powder and non-magnetic silicon carbide (SiC) abrasive particles in carrier base fluid (AP3 grease and heavy paraffin oil) which is used in MR polishing fluid-based finishing processes as a finishing agent [8].

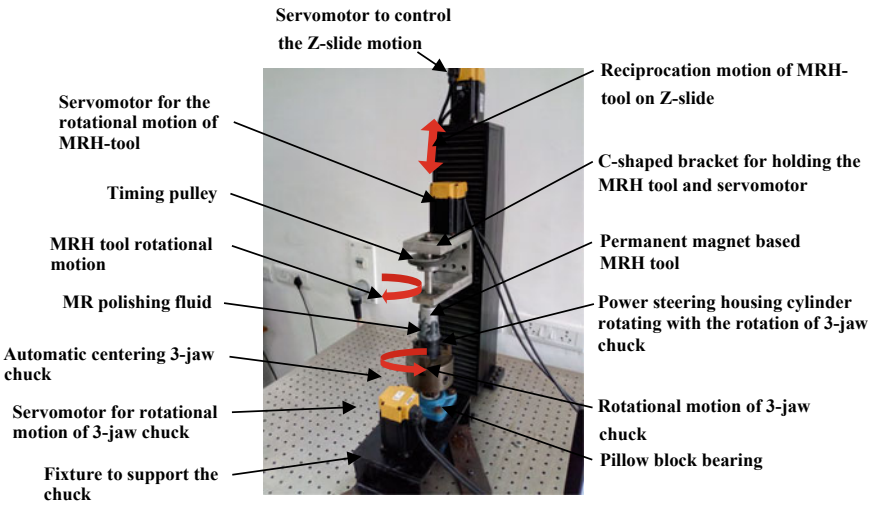

Fig. 26.1 Photograph of the experimental setup of the rotational magnetorheological honing (R-MRH) process

26.2 Design of Magnetorheological Honing Tool and Experimental Setup

For designing the magnetorheological honing (MRH) tool, the magnetostatic simulation of the CAD modelled MRH tool is performed. The CAD model of the MRH tool is as shown in Fig. 26.2. The uniform distribution of magnetic field density over the finishing end surface plays a crucial role in finishing. There are three curved (NdFeB) permanent magnets used in the present magnetorheological honing tool.

From the magnetostatic simulation in Maxwell Ansoft V13 software the optimized dimensional specification of the magnets is considered. The dimensional specification of magnets is 70 mm outer diameter, 55 mm inner diameter, the axial length is 60 mm, and the arc length of the curved magnet is 15 mm. The internal diameter of the power steering housing cylindrical workpiece is 38 mm and the workpiece sample made for the experimentations is of height 60 mm. The gap between the finishing surface of the MRH tool and the housing cylinder is kept 1 mm. The two-dimensional magnetostatic simulation for magnetic flux distribution from the finite element analysis (FEA) performed in Maxwell Ansoft V13 software using the input parameters from Table 26.1, exposes that the outer surface of the finishing end of the MRH tool in front of the permanent magnet is uniformly distributed as shown in Fig. 26.3a. It also shows the pattern of flow of the magnetic flux line in the MRH

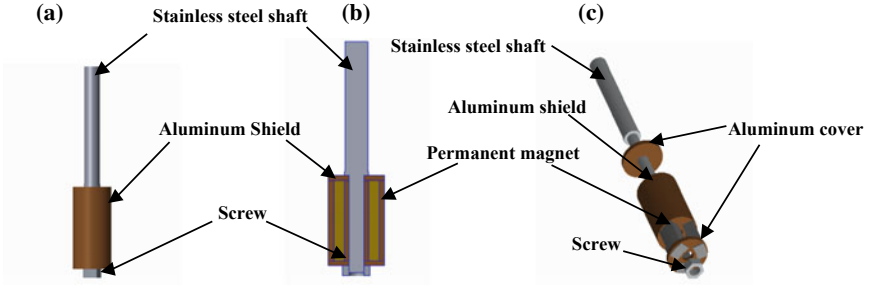

Fig. 26.2 CAD model of magnetorheological honing (MRH) tool **a** complete assembled tool, **b** cross section view of the tool, and **c** exploded view of the tool

Table 26.1 Input parameters for the magnetostatic finite element analysis (FEA) of the magnetological honing (MRH) tool

Parameters	Materials	Relative permeability
Tool holding shaft	Stainless steel	1
Shield for magnet	Aluminium	1.000021
Permanent magnet	NdFeB	1.091000
Power steering housing cylindrical workpiece	Iron alloy	100
Finishing medium	MR polishing fluid	5

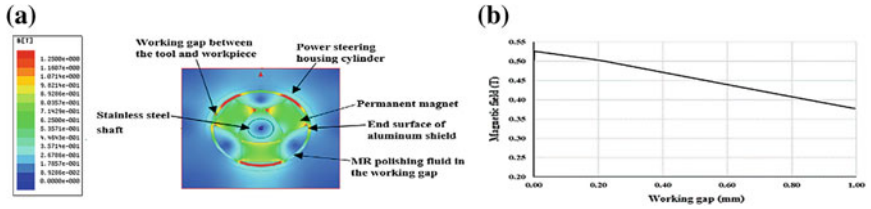

Fig. 26.3 Magnetostatic finite element analysis (FEA) **a** magnetic flux distribution in present finishing operation and **b** variation of the magnetic field in the working gap

tool. As per the pattern of magnetic lines followed, it is observed that in the first magnets the lines are emerging out normal to the inner surface of the workpiece. Therefore, the magnetic flux attracts the magnetorheological (MR) polishing fluid from one side of the tool and repels on another side, which causes the indentation of active abrasive particles into the workpiece surface.

Fig. 26.3b showed the trend of the magnetic field distribution. The trend of magnetic field distribution is desirable for finishing as it makes capable of performing the relative motion of active abrasives by resisting the sticking of the CIP on the finishing surface of the workpiece. This relative motion of abrasive particles causes finishing action over the finishing surface.

The experimental setup is made of the three servomotors, one fixture for holding an automatic three-jaw chuck, a Z-slide for performing the reciprocation motion of the MRH tool, and a breadboard to mount all the aforesaid components of the experimental setup as shown in Fig. 26.1. The motions in the present work are given by the three servomotors and are governed by the programmable logic controller (PLC). The workpiece used in the present work is power steering housing cylinder on which spectroscopy was performed to analyze its composition. The major composition of the workpiece material is Fe 98.3%, C 0.426%, Si 0.2313 %, and Mn 0.4670%. In the present work, magnetorheological (MR) polishing fluid is utilized as a finishing agent which is made of magnetic carbonyl iron particles (CIPs), silicon carbide and base medium in percentage volumetric proportion of 20%, 20%, and 60%, respectively. The base medium is made by mixing AP3 grease (20% wt) and heavy paraffin oil (80% wt) and by stirring soundly in the mixing chamber.

26.3 Experimentation

With designed and fabricated magnetorheological honing (MRH) tool the experimentation is performed. The power steering housing cylinder workpiece is rotated by the servomotor mounted on mild steel fixture rigidly fixed on the breadboard. There are three workpiece samples that are made from a power steering housing cylinder, are used for the experimentation. The workpiece cylinders were tightly clamped in the automatic three-jaw chuck mounted on the fixture as shown in Fig. 26.1. The gap

between the end surface of the tool and workpiece is maintained and measured by the wire gauge. In the present work, the surface roughness parameters (Ra, Rq, and Rz) were measured using the Mitutoyo surface roughness tester (model- SJ 400) with a cut-off length of 0.25 mm. The original surface of the workpiece was finished for the working condition of power steering housing cylinder during its manufacturing. Before the start of experimentations, roughness parameters were measured at 12 different positions on the internal surface of the workpiece cylinder. The initial measured surface roughness parameters at a random location were Ra = 0.320 μm, Rz = 2.1 μm, and Rq = 0.390 μm as shown in Fig. 26.4a. The first experimentation was conducted by rotating and reciprocating the magnetorheological honing (MRH) tool and keeping stationary the workpiece cylinder. During this experimentation, a uniform gap of 1 mm is maintained. The rotation and reciprocation speed of the tool was kept constant as reported in Table 26.2 throughout all four experimentations. The MRH tool is rotated with 400 rpm, reciprocating speed of 70 cm/min and at the same time, the workpiece cylinder is kept stationary for the first experiment. To analyze the surface texture of the inner surface of the power steering housing cylinder (workpiece cylinder) before and after finishing, the scanning electron microscopic (SEM) examination was also performed on the Zeiss Scanning Electron Microscope.

The relative motion between the active abrasive particles stuck in the carbonyl iron particle (CIP) chain structure and the workpiece surface causes a shearing action on the ploughed grain of the workpiece. This shearing action causes to material removal from the vicinity of ploughed grains, and finishing activity takes place. Experimentation was conducted for the 80 min with four sets of finishing cycle of 20 min each. After completion of each set of finishing cycles, the surface roughness of the finished surface was measured. Also, the MR polishing fluid was changed after each set of finishing cycle to provide fresh edged SiC abrasive particle for finishing and avoid the blunted abrasives. After finishing the internal surface on

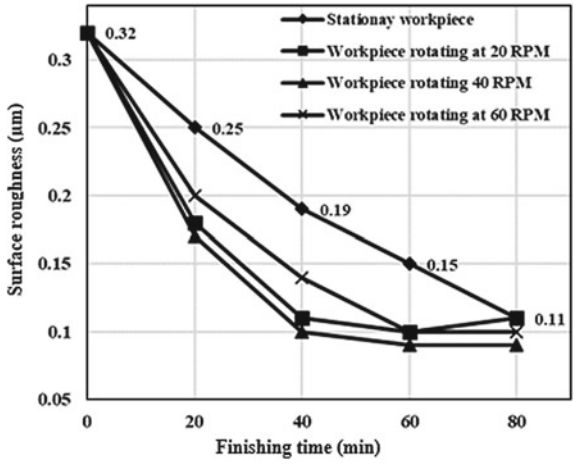

Fig. 26.4 Change in the surface roughness values Ra (μm) of the internal surface of the power steering housing cylinder in all the type of experimentations performed

Table 26.2 Experimental process parameters and conditions

Process parameters	Conditions
MRH tool rotational speed	400 rpm
MRH tool reciprocation speed	70 cm/min
Rotational speed of cylindrical workpiece	0, 20, 40, 60 rpm
Working gap	1 mm
SiC abrasive particles	20% by volume (800 mesh size)
Carbonyl iron particles	20% by volume (500 mesh size)
Base fluid medium	60% by volume
Cylindrical workpiece material	Ferromagnetic medium carbon alloy steel

different parameters for 80 min with the MR honing tool, the final surface roughness parameter Ra was measured on 12 different positions but at the same position where the measurement of the initial surface was done.

26.4 Results and Discussion

From the magnetostatic finite element analysis (FEA) as shown in Fig. 26.3a and b, it is observed that in front of the permanent magnet the magnetic field density is uniform and high whereas on the edges of the magnets the magnetic field is extremely high due to the edge effect. The slope of magnetic flux density from the tool end surface to the workpiece is negative. This results the magnetic CIP particle to stick on the tool surface more stiffly than sticking on workpiece surface which favours the relative motion of active abrasive particles on the finishing surface.

The average surface roughness values (Ra) after each set of finishing cycle (i.e., 20, 40, 60, and 80 min) for all the experimentations were measured and plotted their variation as in Fig. 26.4. It was observed that after each set of finishing cycle the surface roughness was decreasing. But, the rate of diminishing the surface roughness in experimentation with rotating workpiece with 40 rpm is significantly higher than all other cases of experimentations under same finishing condition.

It is observed that the relative speed of active abrasives against the inner surface of the power steering housing cylinder due to its rotation in the opposite direction to the rotation motion of magnetorheological honing tool influences the finishing rate and capability of the process.

The measurement of roughness profile was performed with the Mitutoyo Surftest (SJ-400 model) for all the types of experiment. But, in the present work the roughness profile of the initial surface, after finishing the workpiece for 80 min by keeping it

stationary and after finishing the rotating cylindrical workpiece at 40 rpm for 60 min are given as in Fig. 26.5a–c, respectively.

As the workpiece cylinder is given rotational motion in the opposite direction to the rotational motion of the MRH tool, the relative motion of active abrasive particles gets enhanced, and hence shear force also increased. Therefore, with the provision of rotational movement to the workpiece cylinder, the finishing rate and the finishing capability get increased. After a specific value of the rotational speed of the workpiece cylinder, the finishing rate and capacity both start decreasing because of the more increased relative motion of an active abrasive particle confirms to the decreased interacting time for cutting the grain. Due to the optimum enhancement in relative speed of the active abrasive particle by providing the rotational motion to the workpiece cylinder the best surface roughness parameters were found as Ra = 0.09 μm, Rq = 0.13 μm, and Rz = 0.7 μm at the rotational speed 40 rpm of the workpiece cylinder in 60 min of finishing time as it is given in Fig. 26.5c.

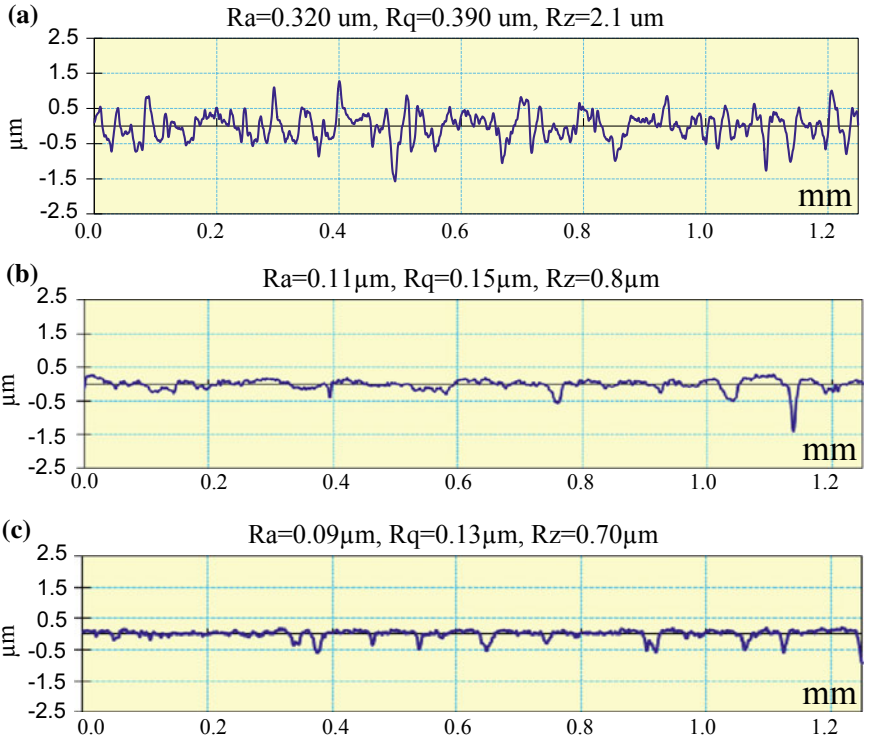

Fig. 26.5 Surface roughness profiles of **a** initial internal surface of the power steering housing cylinder, **b** MR finished surface after 80 min while cylindrical workpiece kept stationary, and **c** MR finished surface after 60 min while cylindrical workpiece kept at rotational speed of 40 rpm using the rotational magnetorheological honing process

Figure 26.6a shows the SEM images of the initial internal surface of the present workpiece cylinder. The initial internal surface of the power steering housing cylinder was already finished with the cylindrical grinding process and the measurement is used as the initial surface before conducting the experiment. The initial surface has a large number of grinding marks, pit holes, and surface irregularities. The Fig. 26.6b is the SEM image of the finished inner surface of workpiece cylinder after 80 min by keeping it stationary during the present MR finishing operation, which had some finishing marks as it has been indicated in its image. By providing the rotational motion to the workpiece cylinder, the surface roughness got decreased and improved surface textures, as it can be observed with roughness profile and SEM image shown in Figs. 26.5c, and 26.6c, respectively. Therefore, from the results obtained in the form of roughness profiles and surface textures in SEM images, it is found that the present MR finishing process is highly applicable to reduce the friction, lower oil consumption, easier turning the steering and to avoid the oil leakage from piston ring surface the inner surface of the power steering housing cylinder.

26.5 Conclusions

From the magnetostatic finite element analysis and experimentations in the present rotational magnetorheological honing (R-MRH) process following conclusions are made and ensured the improvement in productivity.

- The higher magnetic field (0.53 T) at the end surface of the MRH tool and lower magnetic field (0.38 T) on the inner surface of the ferromagnetic power steering housing cylinder, results in relative motion between active abrasive particle and workpiece which favours the better finishing of the surface.
- With increase in rotational speed of workpiece cylinder in the present finishing process, the surface finishing rate and its finishing capability were found better, but after a limit of increase in rotational speed.

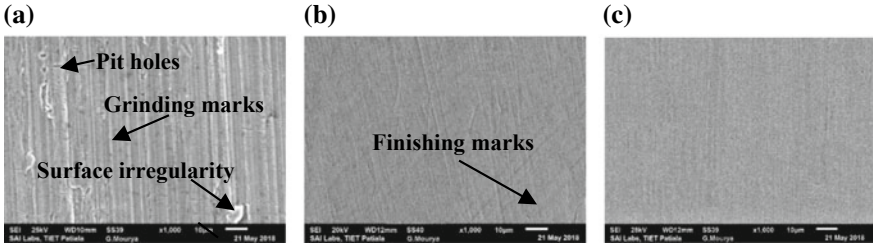

Fig. 26.6 Scanning electron microscopy images of **a** initial surface of power steering housing cylinder, **b** final MR finished surface of stationary workpiece cylinder after 80 min, and **c** final MR finished surface after 60 min at rotational speed of cylindrical workpiece of 40 rpm using the rotational magnetorheological honing process

- The maximum percentage change in surface roughness (%ΔRa) was seen as 65.62 and 71.87% in 80 and 60 min of finishing over the internal surface of the stationary cylindrical workpiece and rotating cylindrical workpiece (at 40 rpm), respectively which revealed the supremacy of R-MRH process over the existing MRH process.
- Roughness profile and SEM images of the finished surface revealed the capability of the R-MRH process to achieve the nano-finishing of the internal surface of the power steering housing cylinder with higher productivity.

References

1. Tawakoli, T., Rasifard, A., Rabiey, M.: High-efficiency internal cylindrical grinding with a new kinematic. Int. J. Mach. Tools Manuf. **47**, 729–733 (2007)
2. Jain, V.K.: Abrasive based nano finishing techniques: an overview. Mach. Sci. Technol. **12**, 257–294 (2008)
3. Singh, M., Singh, A., Singh, A.K.: A rotating core-based magnetorheological nanofinishing process for external cylindrical surfaces. Mater. Manuf. Process. **33**(11), 1160–1168 (2018)
4. Bedi, T.S., Singh, A.K.: Magnetorheological methods for nanofinishing—a review. Part. Sci. Technol. **34**(4), 412–422 (2016)
5. Bedi, T.S., Singh, A.K.: A new magnetorheological finishing process for ferromagnetic cylindrical honed surfaces. Mater. Manuf. Process. **33**(11), 1141–1149 (2018)
6. Gupte, P.S., Wang, Y., Miller, W., Barber, G.C., Yao, C., Zhou, B., Zou, Q.: A study of torn and folded metal (TFM) on honed cylinder bore surfaces. Tribol. Trans. **51**, 784–789 (2008)
7. Liu, M., Nguyen, T., Zhang, L., Wu, Q., Sun, D.: Effect of grinding-induced cyclic heating on the hardened layer generation in the plunge grinding of a cylindrical component. Int. J. Mach. Tools Manuf. **89**, 55–63 (2015)
8. Singh, G.S., Singh, A.K., Garg, P.: Development of magnetorheological finishing process for external cylindrical surfaces. Mater. Manuf. Process. **32**(5), 581–588 (2016)

Chapter 27
Investigation and Evaluation of Erosion Efficiency in Micro-EDM Dressing of Biocompatible Ti6Al7Nb Material

M. S. Shah and P. Saha

Abstract Machinability of Ti6Al7Nb by Micro-EDM dressing was investigated and evaluated with and without vibration of the tool plate. Experiments were conducted at three discharge energy settings. Using a simple electrical energy model, the erosion efficiency of contributing pulses was calculated at those energy settings. It was found thaterosion efficiency is highly influenced by the discharge energy. From the experimental results, it was also noticed that erosion efficiency of normal pulses gets lower at higher discharge energy, whereas there was a continuous increase in the erosion efficiency of effective pulses with the increment in discharge energy. Moreover, the processes under vibration at any discharge energy settings yield higher erosion efficiency for both normal and effective pulses.

Keywords Discharge energy · Vibration · Erosion efficiency · Normal pulse · Effective pulse

27.1 Introduction

The Micro-EDM dressing is one of the emerging variants of micro-EDM process that allows fabricating complex three-dimensional arrays of micro-rods. This process is well accepted for machining any conductive materials independent of their hardness, brittleness, and wear resistance. However, occurrence of varying high-frequency repetitive sparks inconsistently erodes the material from electrodes that in turn generate different shapes or sizes of micro-craters. This drives the process toward instability by drastically bringing change in the breakdown strength of the dielectric fluid. Also, generation of bubbles and improper flushing of debris and carbon particles (from cracked dielectric fluid) contaminate the interelectrode gap (IEG)

M. S. Shah · P. Saha (✉)
Department of Mechanical Engineering, Indian Institute of Technology Patna, Bihar 801103, India
e-mail: psaha@iitp.ac.in

M. S. Shah
e-mail: shamim.pme15@iitp.ac.in

M. S. Shunmugam and M. Kanthababu (eds.), *Advances in Micro and Nano Manufacturing and Surface Engineering*, Lecture Notes on Multidisciplinary Industrial Engineering,
https://doi.org/10.1007/978-981-32-9425-7_27

and hence lower the erosion efficiency. The process can be driven under a stable condition with high-erosion efficiency either by introducing techniques such as vibration assistance electrode, magnetic field assistance, jet flushing, rotating electrodes, or geometrically modified electrodes. However, vibration assistance micro-EDM has proved to be effective compared to others due to dimensional constraints [1].

Endo et al. [2] implemented vibration on the micro-EDM process and successfully produced a small square shaft to investigate the machining stability. The experimental results showed an increase in machining stability with a large reduction in machining time. Jahan et al. [3] machined micro-holes with the application of vibration and observed significant increase in effective discharge ratio. In addition, the effective discharge ratio significantly improves at lower discharge energy setting compared to higher one. Only a few literature exist in which the researchers attempted for evaluating the machining erosion efficiency of micro-EDM process. Using the fundamental erosion mechanism of material, Wong et al. [4] estimated erosion efficiency of material due to vaporization, melting, and by both. They showed that with higher efficiency, the material gets removed by vaporization at lower energy levels. They also concluded that for any discharge energy settings, erosion efficiency due to only melting is found to be always less compared to erosion efficiency due to vaporization alone. However, the work was limited to only single discharge and the erosion efficiency determined by them would not reveal any information on the stability of the process. In another literature, Mastud et al. [5] have done computational modeling of the debris motion and its interaction with the dielectric fluid under low-amplitude vibrations imparted via a magnetorestrictive actuator by using single-pulse micro-EDM dressing process. It was again based on single discharge. However, single discharge cannot describe the whole process.

Thus, the above literature reveals no work on evaluating the stability of Micro-EDM dressing process in terms of erosion efficiently and subsequently improving it. Investigation and evaluation of this parameter may assist in improving the productivity and economics of micro-EDM dressing process.

27.2 Experimental Details

Experiments were conducted on a DT-110 Mikrotools machine. The machine had an optical linear scale with a resolution of 0.1 μm and positional accuracy of ±1 μm for each of the three axes. Both electrodes were submerged in dielectric fluid during micro-EDM dressing process. EDM oil was used as a dielectric. A NI digitizer card (model: 5122) with 100 MS sampling rate was used to capture the signals from current probe (model: i30; make: Fluke) and voltage probe (model: 701938; make: Yokogawa). Signals from current and voltage probes were imported via the digitizer card to the LabView software. Now the pulses were discriminated based on an algorithm written in LabView [6]. The flowchart 1 and 2 as shown in Fig. 27.1, respectively depicts the pulse classification strategy and calculation of average energy associated

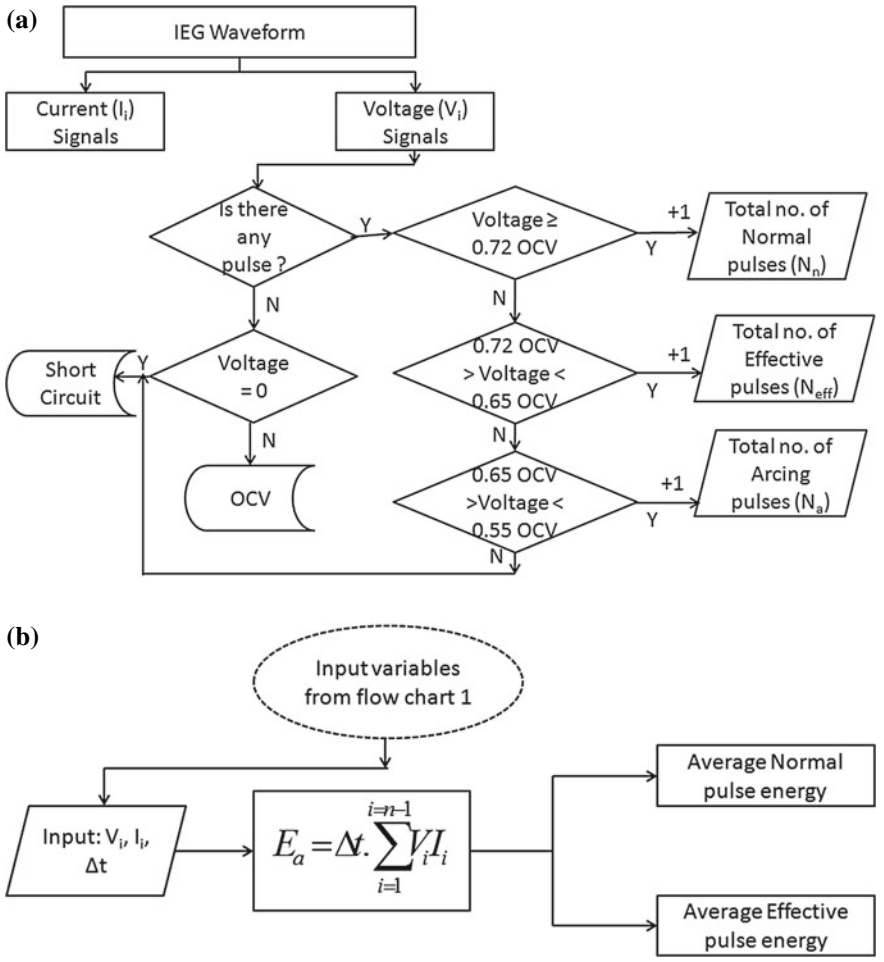

Fig. 27.1 Flow chart of micro-EDM dressing **a** pulse classification strategy and **b** energy per corresponding pulse

with each pulse used in this work. Experimental conditions and materials for workpiece and tool are listed in Table 27.1. Further to carry out the process with vibration, a setup was designed and developed in-house and integrated with the micro-EDM machine. It consists of a fixture and a PZT actuator (P-885.55 Physic Instrumente). The PZT actuator was driven from a DC power supply, function generator, and power amplifier. First, conventional micro-drilling was done on multipurpose micromachining setup. Then, finally micro-EDM dressing was conducted to fabricate length of 100 μm micro rod at each energy setting. To evaluate erosion efficiency, average energy for different pulses can directly be obtained from the PD system. Machining

Table 27.1 Machining Conditions

Material	
Ti6Al7Nb (Workpiece, 500 μm diameter) and Brass (Tool plate, 500 μm thickness with 300 μm predrilled hole)	
Experimental conditions	
Total supplied spark energy (E_T)	E_1 (110 V, 0.1 nF) = **0.605 μJ** E_2 (100 V, 1.0 nF) = **5.000 μJ** E_3 (090 V, 10 nF) = **40.500 μJ**
Feed rate	10 μm/s

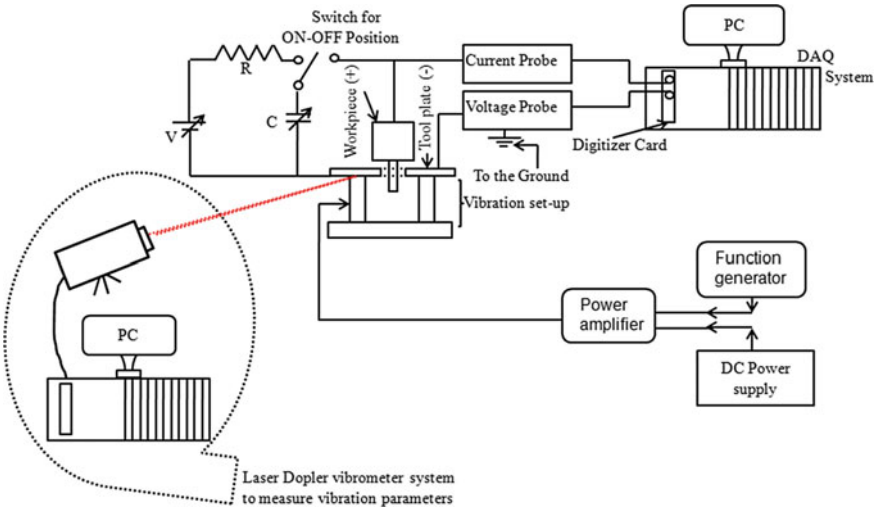

Fig. 27.2 Schematic diagram of experimental setup

was done with and without vibration at three different discharge energy settings. Amplitude and frequency of vibration were used as 1 μm and 600 Hz, respectively which was calibrated through Laser Doppler Vibrometer. The schematic diagram of the whole experimental setup is shown in Fig. 27.2.

27.3 Errosion Efficiency of Micro-EDM Dressing

27.3.1 Assumptions

In order to derive simple theoretical model for evaluating erosion efficiency, following assumptions were made:

- A constant sampling rate, i.e., 100 Ms/s is used for all discharge energy settings.
- Presence of negative current data due to parasitic capacitance of the system is filtered before arrays of voltage and current data get multiplied and program gets executed.
- The pulses discriminated based on above 72% of open-circuit voltage (OCV) are called normal pulses and those between 72 and 65% of OCV are called effective pulses. Therefore, effective pulses appear similar to normal pulses but contribute less in material removal.
- For one particular discharge energy, all normal pulses are assumed to be identical in shape and sizes and same for effective pulses.
- Breakage of dielectric fluid occurs only when voltage crosses above 55% of the OCV.

27.3.2 Theoretical Modeling

The total supplied spark energy (E_T) per pulse of the RC pulsed circuit delivered to the machining gap, as given in Eq. (27.1)

$$E_T = \frac{1}{2} C V^2 \tag{27.1}$$

where C is the capacitance and V is the applied open circuit voltage. A part of total supplied energy from the spark erodes the material, which determines "erosion efficiency" (η). Therefore, erosion efficiency can be defined as the ratio of the actual energy (E_a) used to erode the material to the total supplied energy in the gap (E_T), as given in Eq. (27.2).

$$\eta = \frac{\text{actual erosion energy}}{\text{total supplied energy}} = \frac{Ea}{ET} \tag{27.2}$$

Experimentally, actual erosion energy for different pulses can be obtained from developed PD system. The expression for E_a can be written as

$$E_a = \frac{\Delta t}{N_x}\left[\sum_{i=1}^{i=n_1-1} V_i I_i + \sum_{i=1}^{i=n_2-1} V_i I_i + \sum_{i=1}^{i=n_3-1} V_i I_i + \ldots\ldots\ldots\ldots + \sum_{i=1}^{i=n_n-1} V_i I_i\right] \tag{27.3}$$

where Δt = Time interval between two consecutive data points, N_x = Total number of either normal (N_n) or effective pulses $\left(N_{eff}\right)$, V_i, I_i = ith data points of discharge voltage and current signatures, respectively, and i = Number of data points within single pulse.

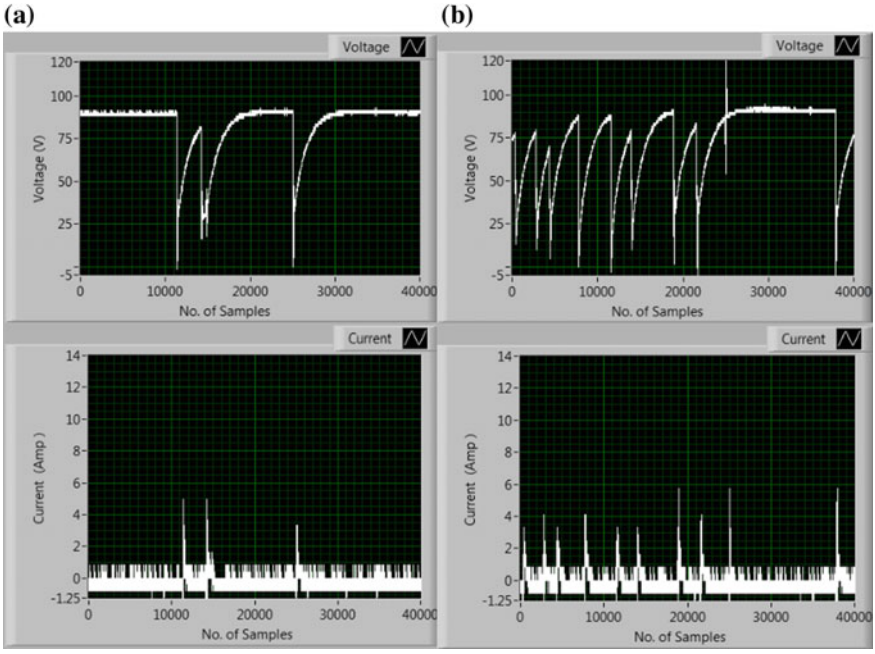

Fig. 27.3 Voltage and current waveforms **a** without vibration and **b** with vibration

It is well-known that normal pulse contributes mostly in material removal due to its high voltage amplitude value, whereas effective pulse contributes the least due to its low voltage amplitude range. This can be confirmed from Eq. (27.3) also. Thus, amplitudes of voltage, corresponding current, and shape and size of the pulses decide the amount of energy contained per pulse. From this, one can conclude that normal pulses will have always higher average energy compared to the effective pulses.

It is obvious that with no flushing across IEG, erosion efficiency will always be less in comparison with flushing condition. Figure 27.3 shows a snap shot of the voltage and current signatures taken with and without vibration condition. The signatures reveal that the existence of more number of normal pulses occurs with high discharge points (>80 V) and charging points (close to zero voltage) in case of with vibration. Thus, vibration has been provided to the tool plate to enhance the erosion efficiency in micro-EDM dressing process.

27.4 Results and Discussion

27.4.1 Erosion Efficiency of Normal Pulses

Erosion efficiency was calculated using Eq. (27.2). Figure 27.4 depicts erosion efficiency of normal pulses at three different discharge energy settings with and without vibration of the tool plate. It can be noticed from this figure that erosion efficiency is comparatively less in E_1 and E_3. That means maximum normal pulse energy is utilized by the work material that is set at E_2. The cause of low erosion efficiency at E_1 can be due to poor ionization and deionization effect owing to low plasma explosive force [4]. Thus, trapping of debris is more common at low-energy setting. On the other hand, at higher energy setting (E_3) removes material in the form of cluster that contaminates the IEG and results to more arcing and sometime short-circuiting [7] that again reduces the erosion efficiency. These large populated debris reduce the IEG and lower the dielectric strength; hence, cause arcing. This phenomenon further worsens if physical contact takes place between tool and workpiece; hence, causes short-circuiting.

It can also be observed from Fig. 27.4 that efficiency of normal pulses under vibration is always higher irrespective of any energy settings. This is because vibration further improves ionization and deionization effect due to the existence of larger variations in dielectric pressure as well as the act of large momentum to the dielectric fluid and debris particles across IEG [5]. This phenomenon reduces the debris agglomeration across IEG that further reduces the arcing or short-circuiting and allows the capacitor to get charged and discharged up to the maximum possible level. Therefore, increase in erosion efficiency of the normal pulse is being observed with vibration-assisted micro-EDM dressing. Inother words, IEG condition gets improved by the application of vibration to the process.

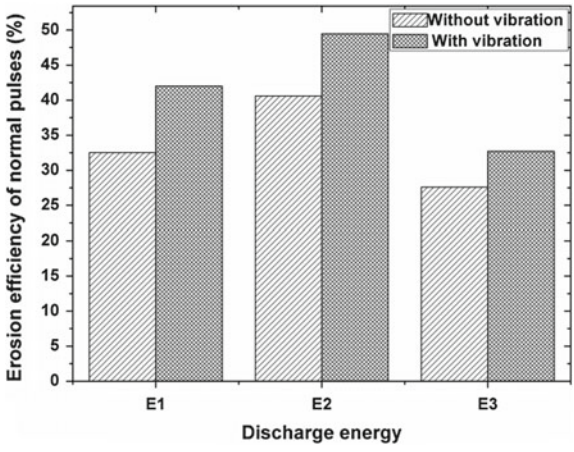

Fig. 27.4 Erosion efficiency of normal pulse with vibration versus without vibration

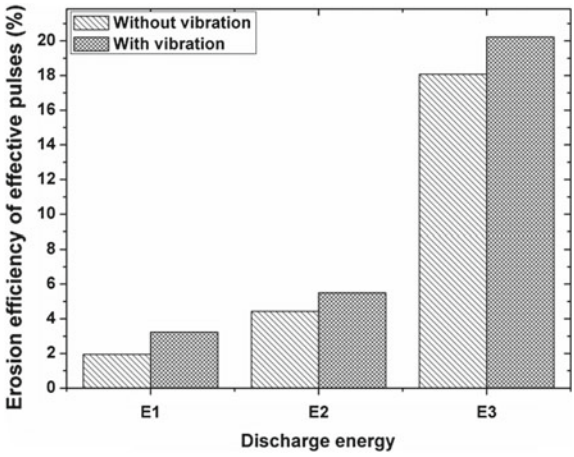

Fig. 27.5 Erosion efficiency of effective pulse with vibration versus without vibration

27.4.2 Erosion Efficiency of Effective Pulse

Erosion efficiency was calculated using Eq. (27.2). Figure 27.5 depicts erosion efficiency of effective pulses at three different discharge energy settings with and without vibration of the tool plate. Effective pulse energy is the low-strength plasma energy that also contributes to material removal but lesser than normal pulse. Thus, it is obvious that debris with less concentration gets generated under such pulses. It can be noticed from this figure that erosion efficiency due to effective pulse increases with discharge energy. This may be due to higher plasma explosive force at higher discharge energy [8], which is able to reduce localized debris-rich region and maintain an acceptable IEG condition.

Further, with the aid of vibration at any discharge energy level, the erosion efficiency of effective pulse increases. It can be understood from the fact that repetitive suction and pumping action during vibration are able to trap less gas bubbles, carbon particles, and debris across IEG [9]. This repetitive suction and pumping movement of vibration continuously provides, both positive and negative thrusts to keep the polluted particles in the dynamic condition. In this way, by achieving a stable machining gap condition, the magnitude of effective amplitude voltage rises that in turn leads to higher pulse energy and ultimately, contributes to larger erosion efficiency.

27.5 Conclusions

Following important conclusions are drawn:

- Erosion efficiency of normal pulses degrades for too low and too high discharge energy setting.
- With the aid of vibration, erosion efficiency of normal pulses increases.

- Erosion efficiency of effective pulses increases with discharge energy.
- With the aid of vibration, erosion efficiency of effective pulses increases.

27.6 Future Directions

In order to broaden the application of the micro-EDM dressing with flexibility in process to the industries, a deep understanding of material removal mechanism across dynamic IEG at different energies under vibration is necessary. In this regard, research work must focus on determining and understanding the fundamental science of effect of different plasma explosive forces at different vibration parametric forces.

References

1. Billa, S., Sundaram, M., Rajurkar, K.: A study on the high aspect ratio micro hole drilling using ultrasonic assisted micro-electro discharge machining. Aspe.Net
2. Endo, T., Tsujimoto, T., Mitsui, K.: Study of vibration-assisted micro-EDM-the effect of vibration on machining time and stability of discharge. Precis. Eng. **32**(4), 269–277 (2008)
3. Jahan, M.P., Wong, Y.S., Rahman, M.: Evaluation of the effectiveness of low frequency workpiece vibration in deep-hole micro-EDM drilling of tungsten carbide. J. Manuf. Process. **14**(3), 343–359 (2012)
4. Wong, Y.S., Rahman, M., Lim, H.S., Han, H., Ravi, N.: Investigation of micro-EDM material removal characteristics using single RC-pulse discharges. J. Mater. Process. Technol. **140**(1–3 SPEC.), 303–307 (2003)
5. Mastud, S.A., Kothari, N.S., Singh, R.K., Joshi, S.S.: Modeling debris motion in vibration assisted reverse micro electrical discharge machining process (R-MEDM). J. Microelectromecha. Syst., 1–9 (2014)
6. Nirala, C.K., Saha, P.: Evaluation of μEDM-drilling and μEDM-dressing performances based on online monitoring of discharge gap conditions. Int. J. Adv. Manuf. Technol. **85**(9–12), 1995–2012 (2016)
7. Yang, X., Guo, J., Chen, X., Kunieda, M.: Molecular dynamics simulation of the material removal mechanism in micro-EDM. Precis. Eng. **35**(1), 51–57 (2011)
8. Tong, H., Li, Y., Wang, Y.: Experimental research on vibration assisted EDM of micro-structures with non-circular cross-section. J. Mater. Process. Technol. **208**(1–3), 289–298 (2008)
9. Abdullah, A., Shabgard, M.R.: Effect of ultrasonic vibration of tool on electrical discharge machining of cemented tungsten carbide (WC-Co). Int. J. Adv. Manuf. Technol. **38**(11–12), 1137–1147 (2008)

Chapter 28
Correlation Between Mechanical Properties and Microstructure of Fe-Ti-Zn Alloys Fabricated by Powder Metallurgy

D. Arthur Jebastine Sunderraj, D. Ananthapadmanaban, K. Arun Vasantha Geethan and S. Vijayananth

Abstract Two Iron-based alloys namely, 93Fe-5Ti-2Zn and for 88Fe-10Ti-2Zn, Specimens were prepared using powder metallurgy techniques. XRD results on both alloys showed the presence of intermetallic phase in 88Fe-10Ti-2Zn. The hardness of 88Fe-10Ti-2Zn samples was higher than that of 93Fe-5Ti-2Zn sample. Impact value for Sample 1 (93Fe-5Ti-2Zn) was 66 J and for Sample 2 (88Fe-10Ti-2Zn) was 73 J. Mechanical property values were correlated to the XRD and microstructures obtained.

28.1 Introduction

Iron melts at 1538 °C and Titanium at 1668 °C. This being the case, manufacturing an alloy of Iron and Titanium with minor alloying addition of Zn becomes very cumbersome and energy consuming if it is done by the normal casting process. Powder metallurgy is a route which has been followed for the last 30–40 years in order to manufacture such high melting alloys. While mechanical properties obtained are comparable to alloys manufactured by casting techniques, reduction in porosity is an added advantage if powder metallurgy is used. Titanium was chosen as the major alloying element in order to reduce weight of the alloy and Zinc was chosen

D. Arthur Jebastine Sunderraj (✉) · K. Arun Vasantha Geethan
Department of Mechanical Engineering, St. Joseph's Institute of Technology, Chennai 600119, India

D. Ananthapadmanaban
Department of Mechanical Engineering, SSN College of Engineering, Chennai 603110, Tamil Nadu, India

S. Vijayananth
Department of Mechanical Engineering, Vels Institute of Science, Technology and Advanced Studies, Chennai 600117, India

M. S. Shunmugam and M. Kanthababu (eds.), *Advances in Micro and Nano Manufacturing and Surface Engineering*, Lecture Notes on Multidisciplinary Industrial Engineering,
https://doi.org/10.1007/978-981-32-9425-7_28

as the minor alloying element in order to reduce corrosion resistance. Many high melting alloys have been fabricated by using Powder Metallurgy, most commonly Aluminium and Titanium based refractory alloys and Nickel-based Superalloys. Fe-35 Mn alloys have been manufactured for use in stents [1]. Iron-Copper Tin Lead alloys have been fabricated using P/M for use in self-lubricating bearings [2, 3]. On studying the Iron-Titanium phase diagram, it is found that up to 15% Titanium, we have ferrite at higher temperatures. Since Ferrite is soft and not so strong, it is not possible to strengthen Iron-Titanium alloys using casing techniques [4]. Hence, it is more important that powder metallurgy techniques are made use of. Iron-Titanium system which is known to show the presence of intermetallics, namely Fe-Ti and Fe_2Ti.

28.2 Experimental Work

28.2.1 Manufacture of Alloy Using Powder Metallurgy

In this process, the final component is made from a mixture of powders. Usually, metal removal rates can be drastically reduced as the process is a near net manufacturing process. Thus it is clear that yield will be more and losses are reduced, thereby reducing costs. But, on the other hand, the high volume to the surface area of the powders renders the powders more reactive to the atmosphere. Highly reactive powders like Titanium and Iron are more prone to oxidation.

Many special products are possible with powder metallurgy technology. A non exhaustive list includes Al_2O_3 whiskers coated with very thin oxide layers for improved refraction; iron compacts with Al_2O_3 coatings for improved high temperature creep strength; light bulb filaments made with powder technology; linings for friction brakes; metal glasses for high-strength films and ribbons; heat shields for spacecraft reentry into Earth's atmosphere; electrical contacts for handling large current flows; magnets; microwave ferrites; filters for gases; and bearings which can be infiltrated with lubricants.

One should be extra careful of metal powders and adequate safety precautions should be taken, especially when bulk powders are handled. This is because in the finely divided form many powders pose health hazards. The same powder which may be benign in bulk form can be dangerous in fine powder form (Fig. 28.1).

Powder metallurgy consists of the following process.

- Mixing of powder
- Compacting
- Sintering
- Secondary Finishing.

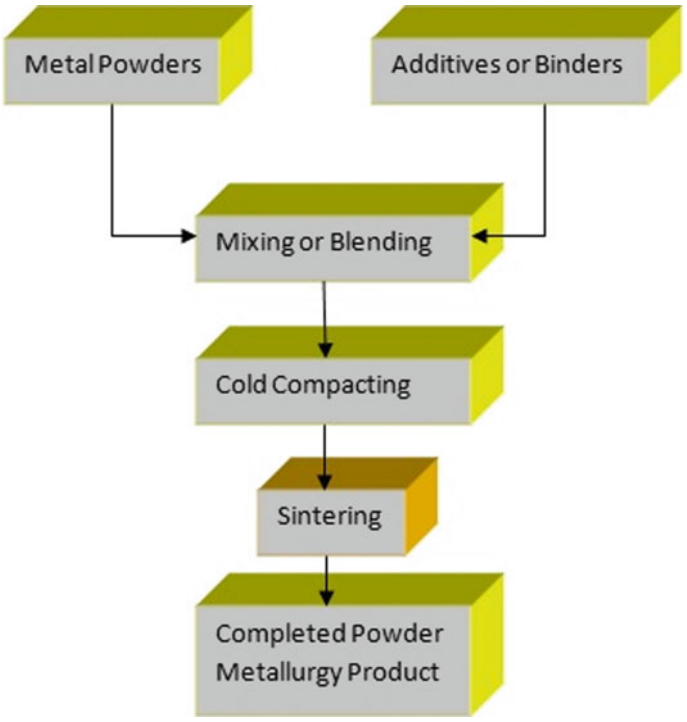

Fig. 28.1 Flow chart indicating the powder metallurgy process

28.2.2 Mixing of Powders

Mixing of the powders is the most important step since proper mixing will ensure uniform distribution of the constituents. If the constituents are not mixed properly, there is a possibility of obtaining non-uniform mechanical properties, while mixing and compacting, lubricants like stearic acid added to help in lubrication. The alloy is mixed under two different proportions and compacted. The two alloys are tested for various mechanical properties and microstructure and were compared.

The powders of iron, zinc and titanium are mixed in the planetary ball miller. Ball mills are of different types like horizontal, vertical, tumbler mill, cement mill, etc. Here, a laboratory scale model has been used. The number of balls and the number of hours of milling are important variables. Normally, research is performed varying the number of hours of milling as 5, 10, 15 and 20 h. In this case, 8 h of milling has been used. 0–2 wt% stearic acid or magnesium stearate have been used in literature to mill Titanium-based powders. This internal lubricant improves compressibility [5]. A lubricant such as stearic acid, stearin, metallic stearates or other organic compound of a waxy nature is added to the mixture. The mixture is milled in the planetary ball mill for about 8 h. Finally, the mixture is taken out. Graphite has also been added

as a lubricant during Powder Metallurgy manufacture of alloys [6]. Stearic acid and Molybdenum disulfide are some of the other lubricants commonly used in powder metallurgy. The mixed powder may be injected into a die or a press.

28.2.3 Compacting the Mixture

The mixture of iron, titanium and zinc powders obtained from the planetary mill is then compacted to solid of 40 × 15 × 10 mm rectangle. First, the die cavity is filled with the powder mixture. The die is pressed in the hydraulic pallet press. The pressure of about 650 N/mm^2 is applied on the die. Then the compacted powder mixture is ejected out of the die and left for some time. Generally, it is enough if cold compaction is performed [7]. However, in case where very high accuracy and surface finish is required, for example in defence applications hot compaction is resorted to attain high accuracy and surface finish [8]. Hot compaction is sometimes referred to as Hipping or Hot isostatic pressing [9]. The word isostatic means applying equal pressure from all directions. This ensures uniformity of properties.

28.2.4 Sintering

Sintering can be considered to proceed in three stages. During the first, neck growth proceeds rapidly but powder particles remain discrete. During the second, most densification occurs, the structure recrystallizes and particles diffuse into each other. During the third, isolated pores tend to become spheroidal and densification continues at a much lower rate. The words 'solid state' in solid state sintering simply refers to the state the material is in when it bonds, solid meaning the material was not turned molten to bond together as alloys are formed [11].

One recently developed technique for high-speed sintering involves passing a high electric current through a powder to preferentially heat the asperities. Most of the energy serves to melt that portion of the compact where migration is desirable for densification; comparatively little energy is absorbed by the bulk materials and forming machinery. Naturally, this technique is not applicable to electrically insulating powders.

Titanium and Iron are both highly reactive with Iron. So, extra care should be taken while melting. Sintering in commonly conducted in party ovens and Tab. ovens [10, 11]. These sintering systems are called conventional sintering. The compacted metal powder needs to be sintered in order to gain mechanical strength. There is also some porosity present in compacted specimens. This can be reduced by sintering since the titanium in the alloy is highly reactive to the atmospheric gases such as oxygen, nitrogen, etc. the tubular furnace with inert gas supply is chosen. The compacted alloy is sintered at 1320 °C for 45 min. The sintered workpiece is cooled to room temperature and then the secondary finishing operations are done. In our case, no

secondary operation was performed. Sintering is usually done at 2/3 rds of the melting point. Assuming the Melting point of this alloy to be around 1350 °C, the right sintering temperature works out to 900 °C. Most literature on sintering of Iron-Titanium alloys gives sintering temperatures of between 950 and 1200 °C. Literature is available only for Titanium alloys mixed with Iron powder and not Iron mixed with Titanium. Hence, our work is a new work and for this combination, sintering data are not available. Here, the sintering temperature chosen is very high at 1320 °C. Hence, some partial melting is to be expected, which has happened as seen in Fig. 28.3. The dendrites seen in Fig. 28.3 confirm partial melting.

Normally, Powder metallurgy gives the final finished product. But, Secondary finishing may be performed in rare cases. This may just consist of some fine surface finishing. A sintered product can be finished in a way similar to cast products. Normally, finishing is done to improve corrosion resistance, mechanical properties, wear resistance, porosity and surface finish. Various finishing operations include–plating, coating, deburring, brazing, welding furnace treatment, etc. Oil or resin impregnation is also used in some cases, especially in self-lubricating bearings. Oil to the extent 20–30% is absorbed in this case. Resin impregnation is also used to improve machinability. Coining or sizing is sometimes done to modify surface properties. This process also provides stricter dimensional control.

28.2.5 Testing of the Alloy

Testing consists of mechanical tests like hardness, tensile and impact tests. Here only hardness and impact tests have been carried out. After this, the material is normally characterized using XRD, SEM, Microstructure analysis, SEM-EDS, etc. and the mechanical properties are correlated to the structure. In our case, XRD and microstructural analysis were done.

X-Ray Diffraction

X-Ray diffraction (XRD) is one of the simplest characterization techniques, which can be used to give information about the presence of phases or perform elemental analysis. Electron Dispersive Spectra is also sometimes used as an attachment to XRD.

XRD for both the alloys was carried out. Hardness was taken for four locations and the average was computed. Impact test was done on both the samples and microstructures of the samples were taken with the help of metallurgical microscope.

28.3 Results and Discussion

28.3.1 XRD Results

XRD shows one major peak in both samples. As seen in the XRD peaks, and one peak in the first sample and two peaks in the second sample. The hardness as seen from Table 28.1 is also more in the second sample. So, we can infer from these two data that there is a possibility of some intermetallic formation in both samples, with higher volume of intermetallic in the second sample. The XRD peak in the second sample is also strained, with the horizontal striated part being broader. This again is an indication that there may be more of intermetallics in the second sample. Intermetallics being brittle, in all probability also give rise to strain, which is reflected in the XRD pattern. Higher Iron content in the second sample could have led to intermetallic formation (Fig. 28.2).

The peak in the second sample is slightly lower in intensity. Combined with the hardness results, which indicate the presence of intermetallic, it is possible that a Ti-Zn intermetallic has formed. But a very high sintering temperature chosen could have softened the hardening effect of the intermetallic and so hardness values are lower than that reported in literature. Literature has reported intermetallics of hardness 250 HV as has been already mentioned. $TiZn_{16}$ and Ti_3Zn_{22} are two of the intermetallics mentioned in literature.

Table 28.1 Shows hardness comparison for 88Fe-10Ti-2Zn and 93Fe-5Ti-2Zn

Sample	Hardness HV 0.5				Average hardness HV
Sample 1 88Fe-10Ti-2Zn	131.23	129.56	130.66	132.66	131.027
Sample 2 93Fe-5Ti-2Zn	139.66	141.05	138.02	140.05	139.57

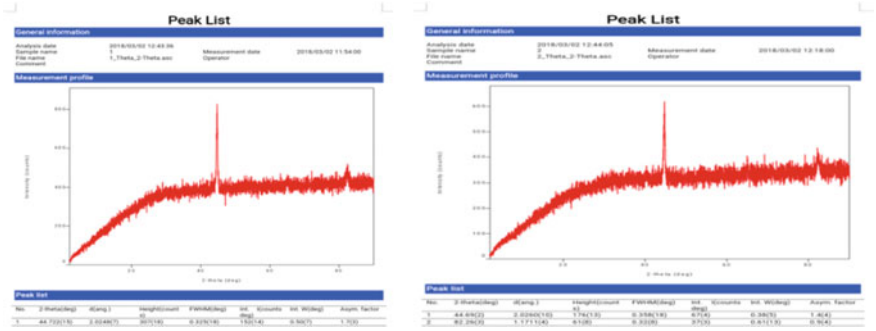

Fig. 28.2 XRD for: 93Fe-5Ti-2Zn sample and for 88Fe-10Ti-2Zn samples, respectively

28.3.2 Microstructure

Normally, powder metallurgy structures show spherical or nodular morphology of structure, especially when seen under the Scanning Electron Microscope. Figure 28.3 shows a dendritic structure. Generally, components manufactured by powder metallurgy do not exhibit dendrites. But, the presence of dendrites, in this case, can be attributed to some partial melting and cooling.

So, it is possible that at the high temperature of 1325 °C, some partial melting of lower melting elements has occurred. In Sample 1, this partial melting could have softened or dissolved some intermetallics. However, Fig. 28.3 does not show any dendrites and so it can be assumed that partial melting has not occurred, with the result that the Sample 2 is harder Zinc has a melting point of 420 °C and since Zinc is present in this powder mixture, we can say with fair degree of certainty that Zinc powder has melted and solidified. It is also seen from the microstructures that porosity is less.

28.3.3 Hardness Test Results

Hardness tests are the simplest tests, which give wealth of relevant information. They are generally used to give an idea of precipitates or intermetallics. Hardness tests should be used in conjunction with XRD or SEM in order to give meaningful results and come to accurate conclusions.

Literature reports a hardness of around 250 HV for conventionally sintered Iron powder. There is a lot of work available on Ti-Al intermetallic sand and Ti-Cu intermetallics. Ti-Cu intermetallics have hardness of the order of 630 HV. This could be due to the presence of nanoparticles. When the compaction pressure is very high, nanoparticles have been reported in literature. It is a known fact that nanoparticles show unusual properties like very high hardness. In our work, since hardness is on the lower side, there is very little possibility of nanoparticle formation. There is very little

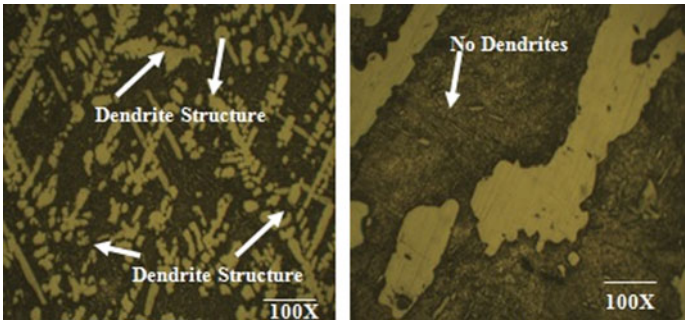

Fig. 28.3 Microstructures for samples 1 and 2, respectively

published work on Ti-Zn intermetallics, especially pertaining to hardness. Studies pertaining to phase stability are reported in literature [6]. In our work, hardness is on the lower side. The alloy has been sintered at 1320 °C. Normally, sintering temperature should be above 2/3 rd of the melting point of the constituent elements. The melting point of Iron is 1500 °C So, choice of sintering temperature is correct, but sintering time is only 45 min. It is possible that a higher sintering time could improve hardness values. Literature shows the hardness value of Titanium increases up to 0.13 wt% of Iron [12]. But, generally, Titanium being softer than Iron, we can expect Fe-Ti alloys to be less harder than Pure Iron. Better control over the sintering time and temperature could also yield better hardness values.

28.3.4 Impact Test Results

Impact value for Sample 2 (93Fe-5Ti-2Zn) was 66 J and for Sample 1 was 73 J (88Fe-10Ti-2Zn). Impact values are a combination of strength and ductility. Earlier it was enough to have good strength or good ductility but in recent times a good combination of both the properties is very much essential for a material to be accepted by the customer. A good impact value indicates a good combination of strength and ductility. However, from the microstructure analysis, Sample 1 shows some partial melting and solidification (as evidenced by the dendrites) and hence, ductility could be more in Sample 1. So, even though hardness is slightly low, it is made up by the higher ductility and as Impact strength the overall effect is higher impact strength is evident in Sample 1. Sample 2, though having higher hardness could possibly be exhibiting very low ductility due to the presence of intermetallics and also absence of any melting. XRD data also confirm strain hardening due to intermetallics. This could be the reason for brittleness in Sample 2. So, even though strength may be high, the bad impact of low ductility could have resulted in lower impact strength in Sample 2.

28.4 Conclusions

Hardness value for the second alloy 93Fe-5Ti-2Zn is higher showing that probably intermetallics are more in this alloy. However, the overall hardness in both alloys is on the lower side. This may be due to the high sintering temperature used and possibility of some partial melting. Impact strength of the first alloy 88Fe-10Ti-2Zn is slightly higher possibly due to lower amount of intermetallics in this sample. The microstructure of 88Fe-10Ti-2Zn shows some partial melting and presence of dendrites, which are not seen in Sample 2, 93Fe-5Ti-2Zn.

Acknowledgements The authors wish to acknowledge the encouragement given by the management, St. Josephs Institute of Technology, Semmancherry. They also thank the Management, SSN College of Engineering for providing a conducive atmosphere for doing research.

References

1. Moravej, M., Mantovani, D.: Biodegradable metals for cardiovascular stent application: interests and new opportunities. Int. J. Mol. Sci. **12**, 4250–4270 (2011). https://doi.org/10.3390/ijms12074250
2. Teisanu, C., Gheorghe, S.: Development of new PM iron-based materials for self-lubricating bearings. Adv. Tribol. **2011**, 11 pp. (Article ID 248037) (2011). http://dx.doi.org/10.1155/2011/248037
3. Xiao, Z.Y., Ke, M.Y., Fang, L., Shao, M., Li, Y.Y.: Die wall lubricated warm compacting and sintering behaviors of pre-mixed Fe–Ni–Cu–Mo–C powders. J. Mater. Process. Technol. **209**, 4527–4530 (2009). https://doi.org/10.1016/j.jmatprotec.2008.10.018
4. Gakkaishi, K.: ASM alloy phase diagrams center, 2007; data from Murakami Y., An investigation on the titanium-iron-carbon system (1st Report). On the Titanium Iron System, Nippon, vol. 21, 1957, pp. 665–669 (2007)
5. Lou, J., Gabbitas, B., Zhang, D.L.: Effects of lubrication on the powder metallurgy processing of titanium. In: Key Engineering Materials, vol. 520, pp. 133–138 (2012). https://doi.org/10.4028/www.scientific.net/KEM.520.133
6. Fogagnolo, J.B., Robert, M.H., Torralba, J.M.: The effects of mechanical alloying on the extrusion process of Aa 6061 alloy reinforced with Si3n4, the Brazilian Congress of Mechanical Engineering, November 1999. Print version ISSN 1678-5878 On-line version ISSN 1806-3691. http://dx.doi.org/10.1590/S1678-58782003000200015
7. Çavdar, U., Atik, E., Ataç, A.: Mechanical properties and hardness results of the medium frequency induction sintered iron based powder metal bushings. Sci. Sinter. **46**, 195–203 (2014). https://doi.org/10.2298/sos1402195c
8. Górny, M., Kawalec, M., Effects of titanium addition on microstructure and mechanical properties of thin-walled compacted graphite iron castings. J. Mater. Eng. Perform. **22**(5), 1519–1524 (2013). https://doi.org/10.1007/s11665-012-0432-8
9. Gelfi, M., Gorini, D., Pola, A., La Vecchia, G.M.: Effect of titanium on the mechanical properties and microstructure of gray cast iron for automotive applications. J. Mater. Eng. Perform. **25**(9), 3896–3903 (2016). https://doi.org/10.1007/s11665-016-2227-9
10. Yu, W-T., Li, J., Shi, C-B., Zhu, Q-T.: Effect of titanium on the martensitic stainless steel 8Cr13MoV. Metals **6**(8), 193 (2016). https://doi.org/10.3390/met6080193
11. Gelfi, M., Gorini, D., Pola, A., La Vecchia, G.M.: Effect of titanium on the mechanical properties and microstructure of gray cast Iron for automotive applications. J. Mater. Eng. Perform. **25**(9), 3896–3903 (2016)
12. Yu, W-T., Li, J., Shi, C-B., Zhu, Q-T.: Effect of titanium on the martensitic stainless steel 8Cr13MoV. ZhuMetals **6**, 1–15 (2016)

Chapter 29
Experimental Investigations into Wire Electrical Discharge Machining Process for the Machining of Ti-6Al-4V

Mahavir Singh, V. K. Jain and J. Ramkumar

Abstract In the present work, an experimental investigation on Ti-6Al-4V is conducted for micro-slit cutting operation using wire electrical discharge machining process. The objective is to analyse the effect of different input parameters such as discharge energy per pulse, wire feed rate and wire speed on the typical responses such as average cutting/machining rate and average kerf loss. Further, the machining rate and kerf loss are also compared by performing the machining operation at different angles of inclination from the horizontal axis. Finally, applying the kerf loss data obtained at a certain set of input parameters (discharge energy and wire feed rate) a multi-slit operation has been performed to fabricate ultra-thin wall. A minimum wall thickness of 8.78 μm between two adjacent slits was accomplished using wire displacement approach.

Keywords WEDM · Kerf loss · Cutting rate · Feed rate · Multi-slit · Thin wall

29.1 Introduction

Wire electrical discharge machining (WEDM) process has got a considerable impetus in the machining of hard electrically conductive materials. It is conceived as a variation of the traditionally used EDM process wherein a thin wire of diameter generally ranging from 30 to 300 μm is used as a tool electrode [1]. The capability to machine intricate geometries with a superior degree of dimensional accuracy and surface integrity has been the driving force in the well acceptance of the process in the last several decades. WEDM process extensively being used in enormous array of industries for various applications such as slicing of thin silicon wafer used in photovoltaic solar cell [2, 3], precise cutting of Titanium alloys (Ti-6Al-4V),

M. Singh · V. K. Jain · J. Ramkumar (✉)
Department of Mechanical Engineering, Indian Institute of Technology Kanpur, Kanpur 208016, India
e-mail: jrkumar@iitk.ac.in

V. K. Jain
Department of Mechanical Engineering, M.A.N.I.T. Bhopal, 462003 Bhopal, India

M. S. Shunmugam and M. Kanthababu (eds.), *Advances in Micro and Nano Manufacturing and Surface Engineering*, Lecture Notes on Multidisciplinary Industrial Engineering,
https://doi.org/10.1007/978-981-32-9425-7_29

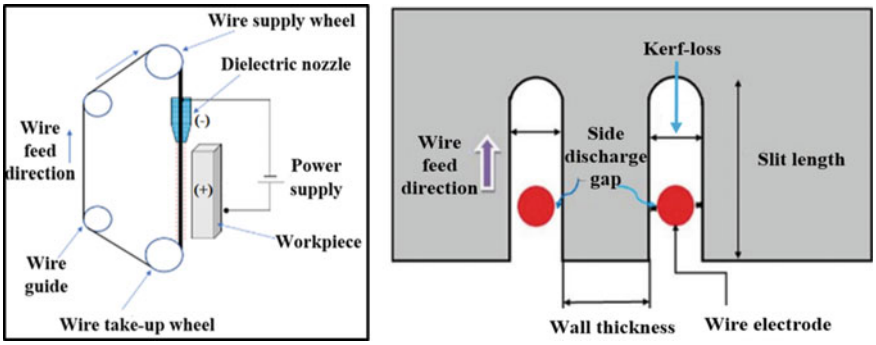

Fig. 29.1 Schematic diagram of the WEDM process and concept of kerf loss

machining of Inconel (Ni-based superalloy) used in turbine blade, manufacturing of precise components, viz., micro gears, shafts, pins, etc. To evaluate the performance characteristics of a typical WEDM process, the kerf loss/kerf width is one of the utmost criteria besides average cutting/machining rate, average surface roughness, heat affected zone (HAZ) and so on. The kerf loss in WEDM process can be expressed as the width of the material that is removed during the operation. This includes the diameter of the wire and the lateral discharge gap on either side of the wire (the gap between the wire and the workpiece in the lateral direction). As wire progresses in the cutting direction, secondary sparks happen in the gap between wire and workpiece which results in the overcut in the machined profile. This overcut contributes to the undesirable removal of material known as kerf loss. The minimum amount of overcutting is essential as it eliminates the short circuit and flushes the debris out of the machining zone. However, it also deteriorates the dimensional accuracy of the machined feature. The wire vibration in the lateral direction besides secondary sparks also increases the kerf loss [4]. Figure 29.1 shows a schematic diagram of a typical WEDM system and the conception of kerf loss. It is to be noted that the unmachined width of the material between two successive passes of wire travel is known as wall thickness or wafer thickness.

29.2 Experimental Details

For conducting the experiments, hybrid micro-EDM machine tool: DT-110 (Make Mikrotools Pte. Ltd., Singapore) equipped with wire-EDM attachment has been used. The experiments were performed by varying the parameters using one factor at a time approach. The various input parameters and their levels are given in Table 29.1.

The constant parameters used in the present work are as follows:

Wire electrode: Tungsten (Diameter: 70 μm), Workpiece: Ti-6Al-4V (800 μm thickness), Initial inter-electrode gap: 20 μm and Slit-length: 500 μm. Wire-tension: 10%, Dielectric fluid: EDM-Oil.

Table 29.1 Input parameters and their levels

S. no.	Parameters	Unit	Levels				
1.	Discharge energy	(μJ)	0.072	0.72	7.2	72	720
2.	Wire feed rate	(μm/s)	2		4	6	
3.	Wire speed	(%)	10		15	20	

29.3 Results and Discussion

This section describes the variation of average cutting rate and average kerf loss with discharge energy per pulse, wire feed rate and wire speed.

29.3.1 Variation of Average Cutting Rate with Discharge Energy and Feed Rate

Discharge energy is varied at five different levels from 0.072 to 720 μJ. The discharge energy per pulse in RC-based power generator is given by $E_d = \frac{1}{2} \times C \times V^2$. This expression is applicable for the condition of maximum energy delivered to the discharge gap such that $V_d = \frac{V}{2}$, where C is the capacitance of the capacitor used, V is the open-circuit voltage and V_d is the discharge/breakdown voltage.

From Fig. 29.2a it is evident that there is an increase in the cutting rate with an increase in the discharge energy except at 7.2 μJ. The increase in cutting rate with discharge energy can be explained by the formation of larger size crater per pulse and hence the higher volume of material removed per pulse. But the increase in discharge energy is governed by the increase in the capacitance which in turn reduces the frequency of sparks as the charging-time and discharging-time of the

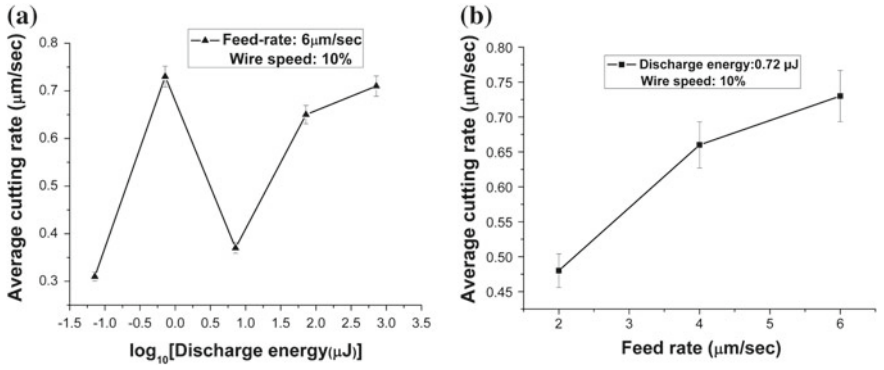

Fig. 29.2 Variation of the average cutting rate with **a** discharge energy, **b** feed rate

capacitor is higher for higher capacitance value. Therefore, there is always a trade-off between higher discharge energy and lower frequency of the sparks. This could lead to the reduction in cutting rate at discharge energy of 7.2 μJ. At a certain level of discharge energy if the feed rate is not appropriate, then there is a tendency of the frequent short circuit or wire takes more time for maintaining the gap between wire and workpiece which may lead to low cutting rate. The cutting rate increases with an increase in the wire feed rate because the non-productive time associated with short circuit and compensation of the gap due to the formation of the crater is minimized. However, beyond a certain wire feed rate, a frequent short circuit occurs which deteriorate the machining accuracy.

29.3.2 *Variation of Average Kerf Loss with Discharge Energy and Feed Rate*

Figure 29.3a, b represents the variation of average kerf loss with discharge energy and wire feed rate, respectively. As the discharge energy increases the material removal per pulse would also increase. Therefore, the secondary sparks occurring in the gap between the wire and side of the kerf would experience the larger volume of material being removed. Whereas, the kerf loss decreases continuously with the increase in wire feed rate as the higher feed rate would facilitate less time for secondary sparks to occur in the side-discharge gap. However, frequent short circuit beyond a certain limit of feed rate would result in increased kerf loss.

Figure 29.4a shows the SEM image of the micro-slit machined on the Ti-6Al-4V workpiece. The image depicts uniformity of the slit width along the length as well as the thickness of the workpiece. Hence, it can be concluded that the taper free slit machining is possible by the WEDM process. The semi-circular end radius of the slit is due to the equal length of the sparks from the centre of the wire electrode. The utmost significance of kerf loss is indicated in the male–female miniature gear

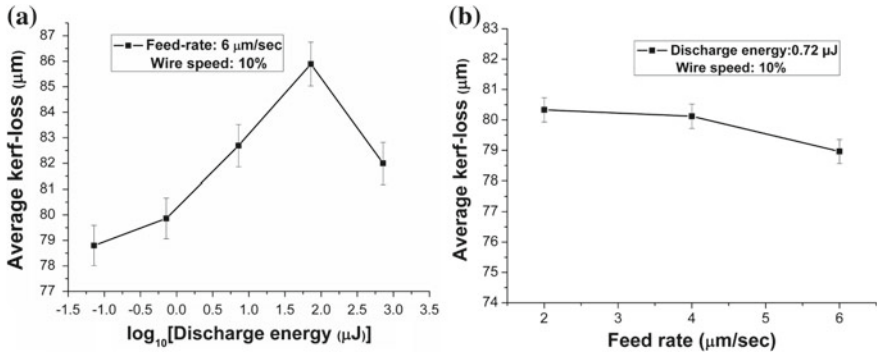

Fig. 29.3 Variation of kerf loss with **a** discharge energy, **b** wire feed rate

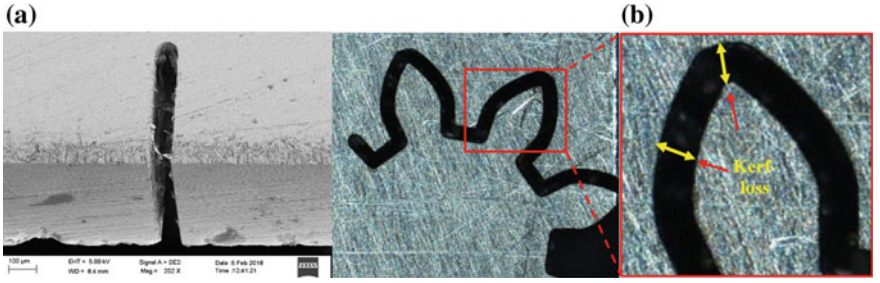

Fig. 29.4 **a** SEM image of the micro-slit machined on Ti-6Al-4V, **b** miniature spur gear profile machining (discharge energy: 0.72 μJ and wire feed rate of 6 μm/s)

cutting operation shown in Fig. 29.4b where higher kerf loss would lead to the larger clearance between internal and external gears. The higher kerf loss consequences into the functional problems in the meshing of two gears.

29.3.3 Effect of Wire Speed

Wire speed determines the relative speed of the wire with which it circulates through the workpiece. Figure 29.5a shows a slight increase in average cutting rate with wire speed due to improved flushing of the gap. Whereas the kerf loss reduces with wire speed due to a reduction in short circuits caused by better flushing (Fig. 29.5b). It has also established that the wire speed has a little impact on machining rate and kerf loss as compared to other input parameters [5, 6].

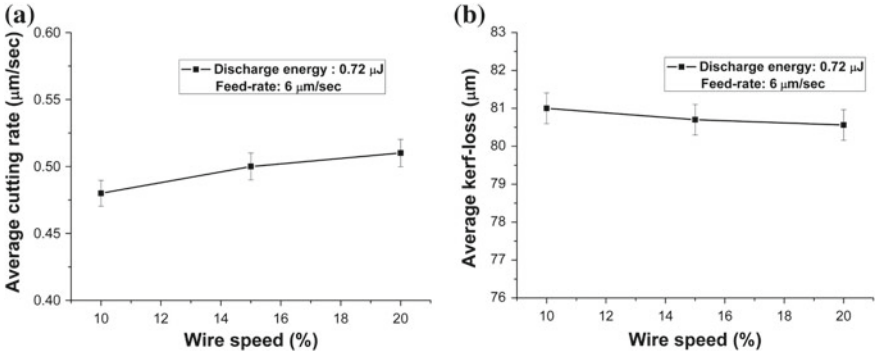

Fig. 29.5 Variation of **a** average cutting rate, **b** average kerf loss with wire speed

29.4 Comparative Assessment of Micro-slit Machining at Different Inclination Angles

Micro-slit machining has been performed by varying the angle of inclination with the horizontal axis as shown in Fig. 29.6a. The slit inclination angle has been changed from 30° to 45°, 60° and finally to 90° (straight cutting). The primary aim is to assess the variation in machining characteristics such as average cutting rate and kerf loss obtained at different inclination angles. This study could be useful in the machining of compliant structures predominantly used in the handling and manipulation of delicate micro-objects. The machining is required to be performed at various angles to machine these structures [7].

The results obtained from the experimental investigations are shown in Fig. 29.7a, b. The results include the variation of the average cutting rate as well as average kerf loss for machining of slits at varying inclination angles.

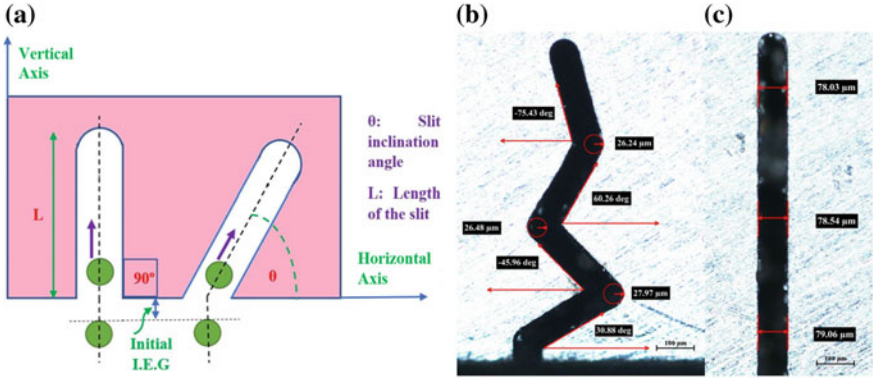

Fig. 29.6 **a** Schematic diagram representing the slit machining at different inclination angles, **b** slit cutting operation at various angles, **c** straight cutting (at 90°) (discharge energy = 720 μJ, feed rate = 6 μm/s)

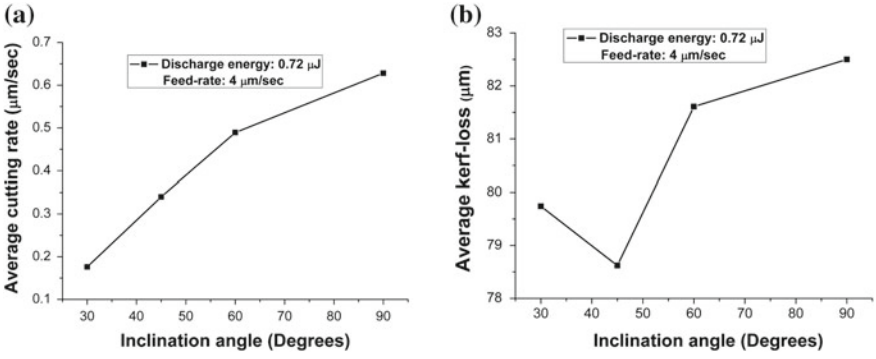

Fig. 29.7 Variation of **a** average cutting rate, **b** average kerf loss with varying angle of inclination (discharge energy: 0.72 μJ, feed rate: 4 μm/s)

The experimental investigation reveals that the average cutting rate is continuously increasing with the increase in inclination angle from the horizontal direction. The cutting rate is found to be maximum at 90° inclination angle where the only unidirectional motion of wire is required for cutting. Other than 90° the wire moves in such a manner that both x- and y- coordinates of the subsequent points changes. This causes a continuous change in the inter-electrode gap (IEG). The simultaneous movement of wire in both x- and y- directions may cause the striking of it with the workpiece surface. Therefore, more short circuits and poor dielectric flushing can reduce the performance of the process. To verify it, the slit cutting operation at 30°, 45°, 60° and 75° angles are performed in a single experiment and number of short circuits were counted (Fig. 29.6b). The same operation is done for straight cutting (90°) using the same input parameters (Fig. 29.6c). The number of short circuits is reduced while cutting at 90°. The machining time is also found to be slightly less while machining at 90° due to a smaller number of short circuits.

The kerf loss is consistent with the machining rate observed with inclination angles. The lower kerf width at smaller inclination angle can be attributed to the small spark length of the secondary discharges though the accurate explanation will require detailed investigations of the process. Therefore, the material removal from the side surface of the wire is small. The results show a slight decrease in kerf loss while machining at 45° probably due to an equal change in the x- and y-coordinates while moving forward from one point to another.

29.5 Machining of Micro-slits with Thin Wall

Thin wall machining or generation of thin wafers from the ingots of various materials such as Silicon, Titanium and Graphite are getting substantial popularity in various fields. The commonly used methods of thin wafer slicing include wire-saw method, internal diameter saw method, etc. These methods are limited by the large mechanical force acting on the wafer [8, 9]. Therefore, the minimum thickness of the wafer is limited by the mechanical forces, brittle-fracture and hardness of the material.

The kerf loss analysis performed in Sect. 3.2 which aids in determining the appropriate wire displacement from the previous pass to create a structure with suitable wall thickness.

Figure 29.1 shows schematically the concept of wall thickness wherein the wire is displaced by some suitable distance from the centre of the previous path. At the different set of process parameters, the kerf loss is different. Therefore, the wire displacement includes the kerf loss and the approximate thickness of the intended wall. If the displacement is less than the kerf loss generated at the certain discharge energy and feed rate, then the next wire-pass would overlap (partially) the first pass and no wall thickness is achieved. Lower the kerf loss higher will be the thickness of the wall and lesser will be the material loss for a constant displacement of wire.

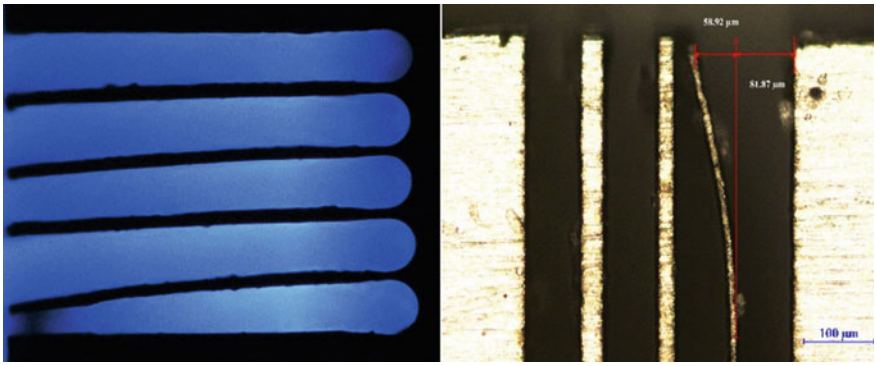

Fig. 29.8 Multi-slit machining with a minimum wall thickness of 8.78 µm (machining conditions: discharge energy = 0.72 µJ, feed rate = 6 µm/s)

Figure 29.8 shows a multi-slit thin wall machining operation. Displacement of wire from its previous path results in the generation of a thin wall of thickness less than 10 µm (wall dimensions: 8.78 × 300 × 800 µm). If the thickness of the wall is not sufficient to withstand the thermal deformation caused by the high temperature and wire vibration, then it will deform severely.

29.6 Conclusions

The following conclusions have been drawn from the experimental investigations presented in the current work:

- The average cutting rate is influenced by the discharge energy and frequency of the pulses in the RC-based power generator. Flushing also plays a significant role in the improvement in average cutting rate.
- The wire feed rate has a considerable impact on the machining rate as well as kerf loss improvement. However, there is a maximum limit of wire feed rate beyond which frequent short circuit occurs.
- Wire speed has less effect on cutting rate and kerf loss as compared to other parameters.
- The machining characteristics of the slit machined at various inclination angles are different than that with the slit machining at 90°. However, the detailed investigation of accurate machining behaviour while cutting at angles other than 90º is needed.
- Reducing discharge energy to 0.72 µJ and applying a wire feed rate of 6 µm/s an ultra-thin wall of thickness 8.78 µm is fabricated using wire displacement approach.

References

1. Ho, K.H., Newman, S.T.Ã., Rahimifard, S., Allen, R.D.: State of the art in wire electrical discharge machining (WEDM). Int. J. Mach. Tools Manuf. **44**, 1247–1259 (2004)
2. Joshi, K., Ananya, A., Bhandarkar, U., Joshi, S.S.: Ultra thin silicon wafer slicing using wire-EDM for solar cell application. Mater. Des. **124**, 158–170 (2017)
3. Luo, Y.F., Chen, C.G., Tong, Z.F.: Investigation of silicon wafering by wire EDM. J. Mater. Sci. **27**(21), 5805–5810 (1992)
4. Di, S., Chu, X., Wei, D., Wang, Z., Chi, G., Liu, Y.: Analysis of kerf width in micro-WEDM. Int. J. Mach. Tools Manuf. **49**(10), 788–792 (2009)
5. Tosun, N., Cogun, C., Tosun, G.: A study on kerf and material removal rate in wire electrical discharge machining based on Taguchi method. J. Mater. Process. Technol. **152**, 316–322 (2004)
6. Scott, D., Boyina, S., Rajurkar, K.: Analysis and optimization of parameter combinations in wire electrical discharge machining. Int. J. Prod. Res. 37–41 (1991)
7. Miller, S.F., Kao, C.C., Shih, A.J., Qu, J.: Investigation of wire electrical discharge machining of thin cross-sections and compliant mechanisms. Int. J. Mach. Tools Manuf. **45**(15), 1717–1725 (2005)
8. Struth, W.F. Steffens, K.: Wafer slicing by internal diameter sawing. Precis. Eng. 29–34 (1988)
9. Chen, C.C.A., Chao, P.H.: Surface texture analysis of fixed and free abrasive machining of silicon substrates for solar cells. Adv. Mater. Res. **126–128**, 177–180 (2010)

Chapter 30
Design and Development of Tool Electrode for Electrochemical Micromachining Using Reverse EMM Technique

S. Sangeethakrishnan, E. Rajkeerthi, P. Hariharan and G. Bhavesh

Abstract The leaning of micro components is being utilized in various fields such as electronics, aerospace, automotive, biomedical, avionics, and optics industry. The surface finish of micro parts is enhanced by using electrochemical micro machining (EMM). Tool shape and size plays a major role in dimensional accuracy and shape of micro parts being produced. This paper presents design and fabrication of micro tool in reverse electrochemical micro machining with a usage of special fixture arrangement. Micro conical tools were fabricated by reverse polarity or reverse electrochemical micro machining aids to enhance material removal rate (MRR) and reduce overcut during machining processes. EMM is more favorable in the fabrication of a microelectrode due to no heat affected zone, lower machining time, absence of residual stress, and good surface quality. A hollow conical shaped micro tool of ϕ300 μm was fabricated from a hollow cylindrical shaped micro tool of Φ800 μm and the same hollow conical micro tool was used to machine the micro holes on 304 stainless steel of 400 μm thickness by EMM. The effect of electrolyte concentration with and without reciprocating feed was studied. The fabricated micro tools by reverse EMM is analyzed with output responses like MRR and overcut. It is inferred that hollow conical tool gives more MRR and produces lesser overcut.

Keywords Reverse EMM · Hollow conical tool · Material removal rate (MRR) and overcut

30.1 Introduction

Unconventional machining is a process of removing material in which there is no direct contact between the tool and the workpiece. In unconventional machining, a form of energy is used to remove unwanted material from a given workpiece (Example: Electrochemical micro machining). Electrochemical micro machining is

S. Sangeethakrishnan (✉) · E. Rajkeerthi · P. Hariharan · G. Bhavesh
Department of Manufacturing Engineering, College of Engineering Guindy, Anna University, Chennai 600025, India
e-mail: sangeethkrishnan11@gmail.com

M. S. Shunmugam and M. Kanthababu (eds.), *Advances in Micro and Nano Manufacturing and Surface Engineering*, Lecture Notes on Multidisciplinary Industrial Engineering,
https://doi.org/10.1007/978-981-32-9425-7_30

a process of removing material by the mechanism of anodic dissolution. When power source is given and an optimum interelectrode gap is maintained between tool and workpiece, owing to Faraday's law of electrolysis the ion will start to displace from the workpiece and deposits over the tool. Before they deposit on the tool electrolyte present between the tool and workpiece will be pumped out continuously, so that ions will move out along with electrolyte without depositing on to the tool. Due to this no disturbance will occur to the tool hence the same tool can be used to produce the number of components. Depending upon the above process, the mechanism of material removal is based on ion displacement. EMM process is reverse of electroplating process where dissolution takes place at anode. The surface of atoms in machined surface becomes ions which migrate in electrolyte between anode and cathode into the interelectrode gap.

The material removal rate (MRR) in EMM process depends on the number of ions displaced from the workpiece, gram atomic weight of workpiece material, the valency of electrons, and electrical conductivity of the electrolyte.

Reverse EMM can be utilized for the development of the tool electrode in electrochemical micromachining. In Reverse EMM, the tool act as anode against the cathodic fixture. A very few kinds of research on advancements in EMM, an influence of tool shapes and process parameters in EMM have been made worldwide. Bhattacharyya et al. [1] explored the effect of voltage and electrolyte concentration on the anode material. It is concluded that machining voltage range of 7–10 V and electrolyte concentration of 15–25 g/l, which generate higher MRR and minimum overcut. Bhattacharyya et al. [2] described the effect of various EMM process parameters such as voltage, concentration of electrolyte, duty cycle and frequency on material removal rate, accuracy, and surface finish. High pulse off-time is endorsed for improving the accuracy and surface finish. Geethapriyan et al. [3] studied the most impelling process parameters to machine an anode material using NaCl and $NaNO_3$ electrolyte. Mithu et al. [4] examined the effect of tool shape on a nickel plate and compared the shape and size of micro holes with tool shape. Rathod et al. [5] developed disc shaped micro tool by Reverse electrochemical micromachining in order to reduce overcut, taper angle, and stray current effects in EMM. Thanigaivelan et al. [6] investigated the influence of process parameters. According to the study they found that the most efficient range for machining voltage, pulse on-time, machining current, and electrolyte concentration which aids to enhance MRR and reduce overcut. Liu et al. [7] analyzed model and development of micro hole by electrochemical micromachining to enhance machining accuracy using the retracted tip tool by reducing stray current effect and bell mouth entrance. Based on the experiments it is inferred that MRR, machining time, and shape of micro holes were effectively influenced by tool dimension. From the literature survey available in electrochemical micro machining (EMM) of various areas such as advancement in EMM, influence of tool shapes, influence of process parameters in EMM were studied and learnt major ideas such as a tool design not only depend on cathode dimension but also depend on electrolyte flow path as well as the machining rate and overcut are also depend on suitable tool electrode profile.

30.2 Experimentation Details

The EMM machine setup available in the laboratory consists of machining structures, power supply unit, and Inter-Electrode Gap (IEG) control system as shown in Fig. 30.1. The machine work table has a size of 260 mm × 110 mm × 100 mm. The maximum work table range is 130 mm × 75 mm × 75 mm. ECM power controller module has a voltage range 1–25 V, Current rating up to 2.5 A, Pulse on-time, Pulse off-time and pulse width modulation is controlled by pulse generator. Gap control has a constant current condition by setting target value.

The sacrificial tool electrode used for fabrication of conical tool with a rounded tip for electrochemical micro machining (EMM) is a copper tube. Fixture and tool electrode both are made by copper of thickness 5 mm and diameter of 800 μm, respectively. Tool material is same as that of workpiece material, the electron affinity of both materials will be same for the ease of ion displacement which will be easier. Experimental conditions for the development of conical tool electrode with rounded tip as shown in Table 30.1.

In reverse EMM, a tool (copper tube) is fixed in tool holder which act as anode and a fixture which act as a cathode is fixed in the machining chamber with $NaNO_3$ electrolyte. In the present work, the fixture is designed in order to develop a tool electrode for electrochemical micro machining as shown in Fig. 30.2.

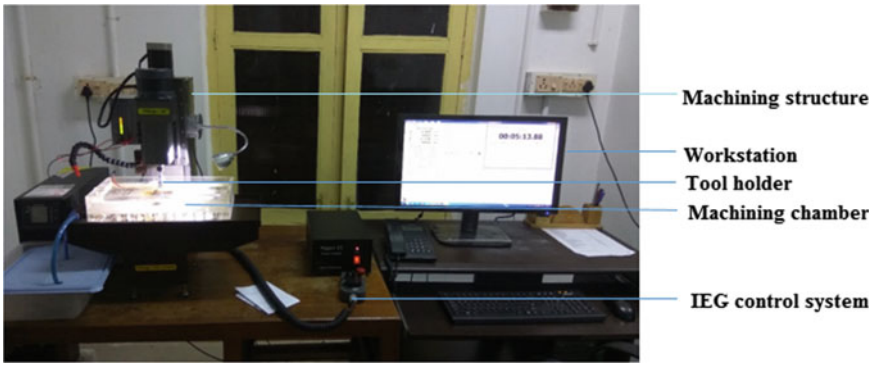

Fig. 30.1 Electrochemical micromachining setup

Table 30.1 Experimental conditions of reverse EMM

Fixture material	Copper
Workpiece material	Copper
Power supply	DC Pulsed
Electrolyte	$NaNO_3$
Electrolyte concentration	1 g/l to 4 g/l

Fig. 30.2 Fixture setup

30.3 Results and Discussion

Trial Experiments were performed to find the optimized process parameters namely machining voltage, concentration of electrolyte, reciprocating feed, and duty ratio. A conical shaped hollow tool electrode with rounded tip was developed using reverse EMM by varying concentration of electrolyte with and without reciprocating feed.

30.3.1 Effect of Electrolyte Concentration (2 and 2.5 g/l) on Tool Shape—Without Reciprocating Feed

A conical shaped hollow tool electrode with rounded tip was developed using reverse EMM by varying concentration of electrolyte without reciprocating feed. Sacrificial hollow tool electrode was machined for 15 and 30 min. Taper angle as well as tip portion of tools were measured in video measuring system (VMS) at fixed intervals to examine the effect of machining time on tool shape. Figure 30.3a (i–ii) shows that sodium nitrate as electrolyte (2.5 g/l) without reciprocating feed has produced needle like shape at tooltip due to high exposure of tool at higher machining time and level of electrolyte concentration was more. Figure 30.3b (i–ii) explored that the same parameters with less machining time have produced conical shape but the sharp edge was observed at tip portion of tool electrode. Diffusion layer was formed around the tool. Due to presence of gravity the diffusion layer was developed along tool length and accumulated at the tooltip which affects the tip portion of the tool. From Fig. 30.3c (i–ii), it has been observed that sodium nitrate used as electrolyte (2 g/l) without feed rate has produced higher taper angle with high aspect ratio and a diffusion layer around the tool. The deposition of dirt was observed at tool electrode tip.

From the experimental results, it was found that the tip portion of the hollow tool electrode gets affected due to the absence of reciprocating feed and higher exposure of tooltip at machining domain.

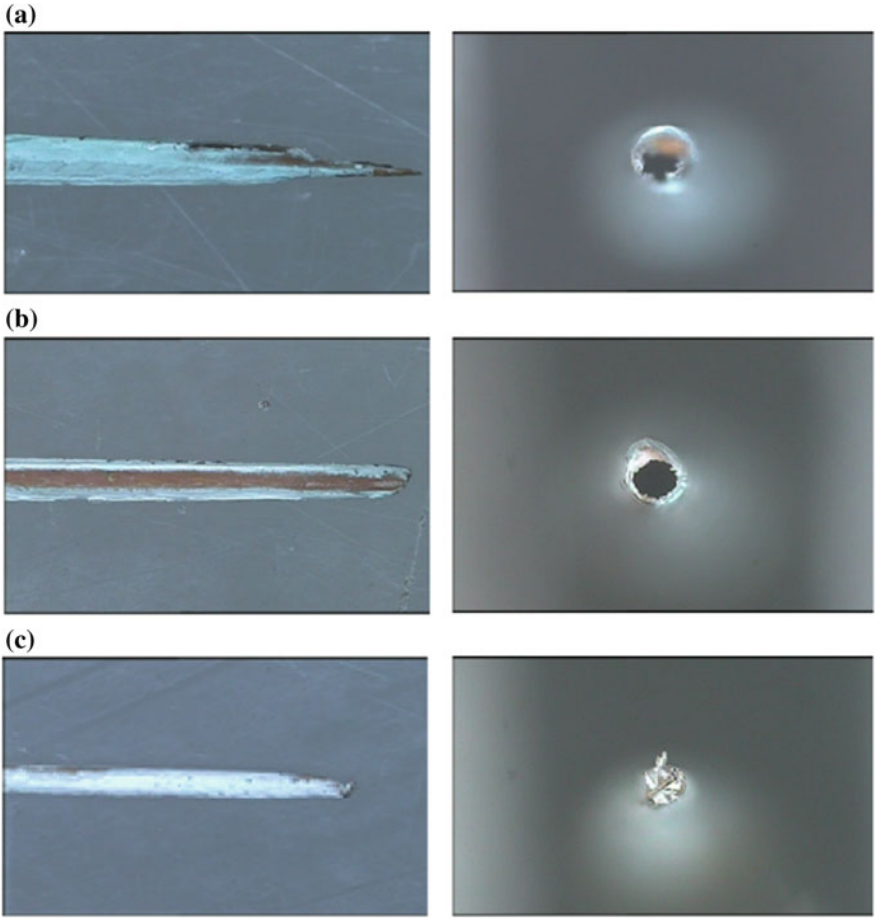

Fig. 30.3 **a** (i–ii) VMS image of copper tool (2.5 g/l, 30 min) **b** (i–ii) VMS image of copper tool (2.5 g/l, 15 min) **c** (i–ii) VMS image of copper tool (2 g/l, 30 min)

30.3.2 Effect of Electrolyte Concentration (2–2.5 g/l) on Tool Shape—With Reciprocating Feed

A conical shaped tool with a rounded tip by varying electrolyte concentration and machining time with reciprocating feed using revere EMM was fabricated. The Fig. 30.4a–b reveals that sodium nitrate used as an electrolyte (2 g/l) with a feed rate of 0.5 mm/min, a hollow conical shaped micro tool of ϕ300 μm was fabricated from hollow cylindrical shaped micro tool of Φ800 μm. The tool exposed to machining was less due to constant feed rate which aids to reduce the formation of the diffusion layer around the tool. The unit material removal rate was uniform to avoid short circuit as it severely damages the topography of the workpiece material.

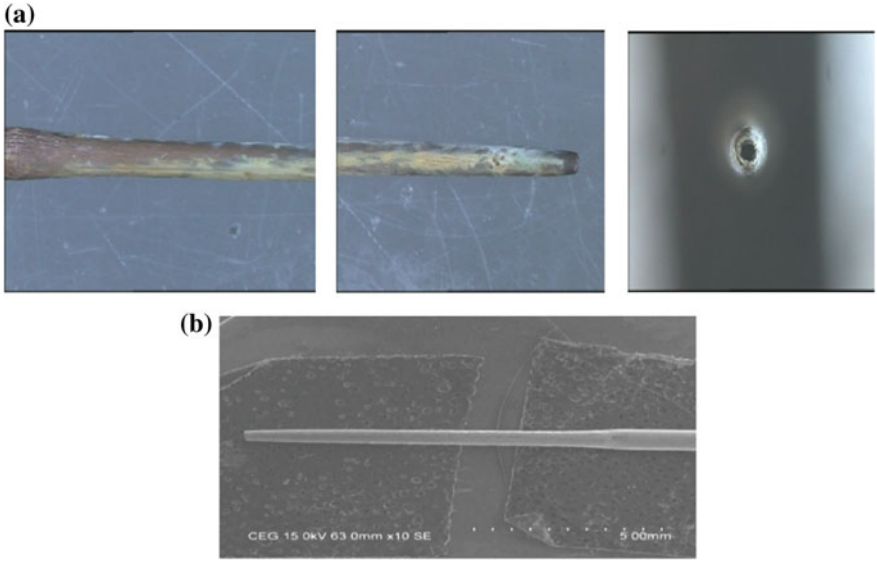

Fig. 30.4 **a** VMS image of copper tube with reciprocating feed. **b** SEM image of the fabricated hollow conical tool

30.3.3 Surface Roughness Profile of Micro Tools

Average Surface Roughness (Ra) was measured by means of Non-Contact Talysurf CCI 3000A. The surface roughness (Ra) of cylindrical copper tube and fabricated conical copper tube were measured at the different portions such as tip, mid, and air-electrolyte interface. Then the surface roughness of tools was compared (cylindrical and conical) and concluded that fabricated conical copper tube has lower surface roughness value than cylindrical copper tube due to ion displacement and constant feed rate as shown in Fig. 30.5a–b.

30.3.4 Machining of Micro Holes on 304 SS

The outcome of Fig. 30.6a reveals that the fabricated conical copper tube with a circular tip is used to machine 304 SS of thickness 400 μm and compare the MRR with a cylindrical copper tube. It was concluded that MRR gets enhanced by the usage of fabricated conical copper tube electrode with circular tip due to the diameter of tooltip is lesser which confines the potential and increases the current density to remove the material from sacrificial material by localized machining. Hence, the machining rate is faster by localized machining compared to a hollow cylindrical tool. Figure 30.6b shows the variation of overcut with respect to hollow tool electrode shapes. The optimum gap is maintained between the tool and workpiece for ion displacement.

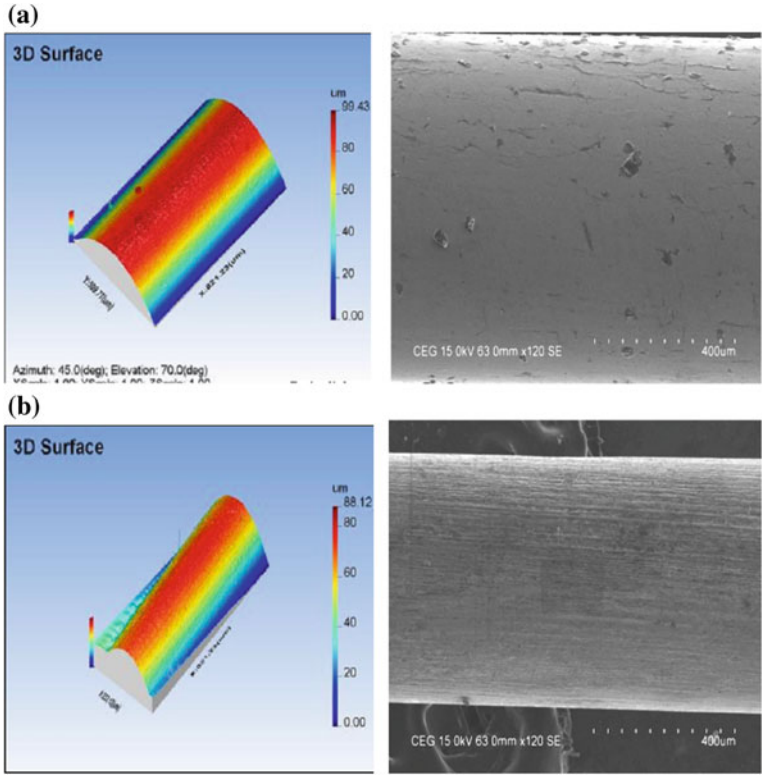

Fig. 30.5 **a** Surface quality of microtool before machining (Sa = 23.627 μm & Ra = 0.196 μm). **b** Surface quality of microtool after machining (Sa = 16.016 μm & Ra = 0.188 μm)

The current density increases in machining gap results in higher overcut due to localization and stray current effect lead to insufficient flow of electrolyte which makes difficult to remove the debris in the machining gap. The time of tool stay along the length of developed fixture during travel is dependent on reciprocating feed. It shows that the overcut can be reduced by using hollow conical shaped tool electrode with rounded tip due to sufficient flow of electrolyte which helps to remove the debris in the machining zone.

30.4 Conclusions

In the present study, experiments were conducted and an investigation has been carried out to find the effect of process parameters such as applied voltage, feed rate, pulse on-time, pulse off-time, and duty cycle to develop tool electrode. Hollow conical shaped tool electrode was fabricated by Reverse EMM and the fabricated

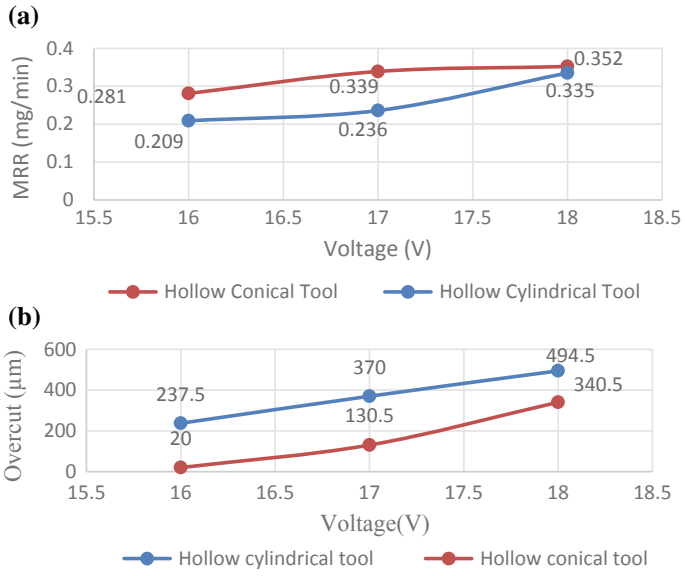

Fig. 30.6 **a** Variation of MRR with respect to hollow tool electrode shape, **b** variation of overcut with respect to hollow tool electrode shape

micro tool was used to machine the micro holes on 304 stainless steel. From the experimental results, the following conclusions were drawn

(i) Experimental outcome reveals that the choice of NaCl electrolyte is less suitable for the development of copper tool electrode because it affects tool electrode surface in reverse polarity.

(ii) Presence of diffusion layer was observed on tool electrode during reverse electrochemical micro machining (EMM).

(iii) Diffusion layer formed around the tool makes it less conductive. It hinders the movement of hydroxide ion towards the tool electrode which reduces the dissolution rate. The reciprocating feed should be synchronized so that proper electrolyte flushing may take place with a constant interelectrode gap in machining domain.

(iv) Tip portion of the tool gets affected when there is no feed given during fabrication of tool electrode.

(v) Sodium nitrate used as the electrolyte (2 g/l) with feed rate (0.5 mm/min) has produced hollow conical tool electrode with high taper angle as well as high aspect ratio and there is no sharp and crosscut edge observed at the tooltip.

(vi) From the experimental results, machining micro holes on the workpiece (304 SS) by using fabricated hollow taper shaped tool electrode with a rounded tip at experimental conditions 16 to 18 V, the material removal rate (MRR) gets enhanced and overcut was reduced compared with a hollow cylindrical shaped tool.

(vii) The surface roughness of fabricated hollow conical tool electrode was taken at three different portions (Tip, Middle, and Air-electrolyte interface portion). At tip portion surface Roughness (Ra) is less compared to mid and interface portion due to constant feed.

References

1. Bhattacharyya, B., Munda, J.: Experimental investigation into electrochemical micromachining (EMM) process. J. Mater. Process. Technol. **140**, 287–291 (2003)
2. Bhattacharyya, B., Malapati, M., Munda, M.: Experimental study on electrochemical micromachining. J. Mater. Process. Technol. **169**, 485–492 (2005)
3. Geethapriyan, T., Kalaichelvan, K., Muthuramalingam, T.: Multi performance optimization of electrochemical micro-machining process surface related parameters on machining Inconel 718 using Taguchi-grey relational analysis
4. Mithu, M.A.H., Fantoni, G., Ciampi, J.: How microtool dimension influences electrochemical micromachining. Int. J. Adv. Manuf. Technol. **70**(2014), 1303–1312 (2014)
5. Rathod, V., Doloi, B., Bhattacharyya, B.: Fabrication of disc shaped micro tool by electrochemical micromachining for micromachining applications. In: All India Manufacturing Technology, Design and Research Conference (AIMTDR 2014). IIT Guwahati, Assam, India, 12th–14th Dec 2014
6. Thanigaivelan, R., Arunachalam, R.M., Natarajan, N.: Investigation of machining characteristics of electrochemical micromachining machine (EMM). In: All India Manufacturing Technology, Design and Research Conference (AIMTDR 2014). IIT Guwahati, Assam, India 12th–14th Dec 2014
7. Liu, W., Ao, S., Li, Y., Liu, Z., Luo, Z., Wang, Z., Song, R.: Modelling and fabrication of micro hole by electrochemical micromachining using retracted tip tool. Precis. Eng. (2017)
8. Mi, D., Natsu, W.: Design of ECM tool electrode with controlled conductive area ratio for holes with complex internal features. Precis. Eng. **47**, 54–61 (2017)

Chapter 31
Micro-dimple Array Fabrication by Through Mask Electrochemical Micromachining

S. Mahata, S. Kunar and B. Bhattacharyya

Abstract Micro-dimple arrays are a common mechanical structure in engineering components. Surface texturing is an attractive approach for improving the friction and tribological performance of mechanical components. Through-mask electrochemical micromachining (TMEMM) has shown good feasibility in the field of machining difficult-to-cut metal parts with micro-patterned arrays. Experiments have been carried out utilizing mask thickness of 16 μm to search out for the respective contributions of principle input parameters, viz. input voltage, pulse frequency and duty ratio in controlling the machining performances, such as undercut (U_c) and dimple depth (D_d) of the fabricated micro-dimples. An experimental plan designed based on the standard L_9 orthogonal array have been incorporated to recognize the best possible combination of machining parameters of TMEMM using Taguchi Methodology. By applying Taguchi design, the time required for experimental investigation can be significantly reduced, as it is effective in investigating the effects of multiple factors on performance. In this study, the best possible parametric combinations have been found with the help of signal-to-noise (S/N) ratio and ANOVA analyses that minimize the undercut and maximize the dimple depth respectively. Input voltage has been varied from 8 to 12 V whereas the machining frequency and the duty ratio has been altered from 2 to 10 kHz and 20 to 40% respectively during experimentation. Confirmation experiments under most favorable parametric combination are carried out to certify the certainty in the enrichment in quality characteristics of TMEMM process. Both the performance characteristics are found to be mostly influenced by Duty Ratio followed by Machining Frequency and Input Voltage.

Keywords TMEMM · Micro-dimple · Machining depth · Mask · Orthogonal array

S. Mahata (✉) · S. Kunar · B. Bhattacharyya
Department of Production Engineering, Jadavpur University, Kolkata 700032, India
e-mail: subrata.2k9@gmail.com

M. S. Shunmugam and M. Kanthababu (eds.), *Advances in Micro and Nano Manufacturing and Surface Engineering*, Lecture Notes on Multidisciplinary Industrial Engineering,
https://doi.org/10.1007/978-981-32-9425-7_31

31.1 Introduction

In the present industry, with the drastic technological advancements, the parts' size has become smaller and there is a requirement of a precision machined surface for the parts that include micro or nano-scale. Further, stainless steel is widely used in automobiles, bio-products, electric and electronic appliances, and an airplane etc. as its surface is pretty and it's easy to process. The surface texture, such as micro-dimples or grooves, has been a well-known approach to improve tribological performances of sliding surfaces. It was experimentally investigated that metal surfaces with micro-dimples of appropriate geometry are more effective for reducing the coefficient of friction as compared to the smooth surface [1]. It has been established by researchers that ECM is a viable method for generating micro-dimple in micron range because of its merit of high efficiency; good surface quality; stress-free and no tool wear [2]. In one of the ECM method, 10% NaCl electrolyte with an electrolyte flow pattern of forward flow along with added backpressure was found to be a handy method for increasing the MRR and improving surface roughness [3]. Electrochemical Micro-machining (EMM) removes materials by electrochemical reaction selectively at the anode. TMEMM is a variant in EMM utilized for generation of micro-dimple arrays with controlled size, shape, and geometry of dimple. It is a precise and relatively prompt process which is competent of producing well-defined surface topographies from the micro- to the macro range, also compatible with chemically resistant metals. Using this method, micro-hole arrays with hemispherical cavities were fabricated on titanium [4]. Moreover, it was experimentally demonstrated that a sheet of an insulation layer, closely attached to a workpiece surface, could be used as a mask to electrochemically etch microstructures. Dimple-arrays in the scale of several hundred microns have been produced with the help of a modified through-mask EMM process [5]. In another study, multilevel cavities with a narrow opening as well as large aspect ratio cavities have been produced by isotropic electrochemical etching of titanium in an electropolishing electrolyte by using oxide film laser lithography (OFLL) [6].

The thickness of the mask plays a crucial role in the shape evolution of the fabricated microstructures. It was learned from previous works of literature that during TMEMM, the current distribution at the anode surface is highly non-uniform when the aspect ratio of the mask is <1. Machining with low aspect ratio mask has been previously considered to be a restraint in TMEMM. Some studies have been carried out using a 250 μm thick PDMS mask for generation of micro-dimple array wherein it was stated that sound micro-dimples can be fabricated only by increasing the mask thickness i.e. >200 μm [7]. Because of the hydrophobic nature of PDMS mask, the electrolyte may not stream into the mask's micro-holes averting ECM. This may not generate a sound dimple surface. As such, AZ4903 have been considered as mask in the present research work due to its flexibility as well as compatibility during the experimentation. Moreover, the thickness of the mask has been restricted to 16 μm to establish the viability of TMEMM using low aspect ratio mask.

In this paper, Taguchi methodology has been applied to study the best parameter settings for fabrication of micro-patterned arrays during TMEMM process. The process input parameters taken are input voltage (V), machining frequency (ν) and duty ratio (%) whereas the quality characteristics analyzed are U_c and D_d. Based on the robust design concept, an L_9 orthogonal array (OA) has been used for conducting the experiments to search out the suitable process parametric combinations for minimizing undercut (U_c) and for maximizing the dimple depth (D_d) separately. Moreover, ANOVA on the basis of S/N ratio has been used to determine the percentage contribution of each input parameters on the responses. Confirmation experiments validate the parametric combination for minimization of undercut as well as maximization of dimple depth respectively.

31.2 Experimentation

31.2.1 Experimental Conditions

Experiments were performed using the developed TMEMM setup. The schematic diagram of the developed set up for TMEMM is given in Fig. 31.1. SS 304 sheets of 200 μm thickness are coated with a negative photoresist AZ4903 using Spin Coater for achieving coat of specific thickness. The coated samples are then baked followed by exposure through UV-Lithography and developed for obtaining micro-

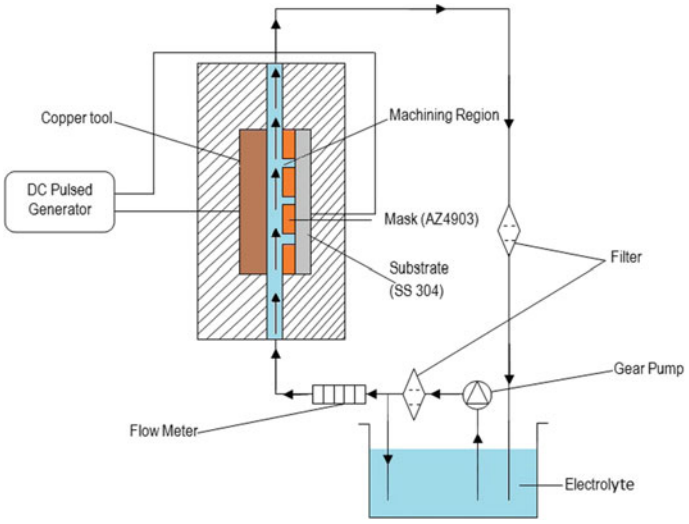

Fig. 31.1 Schematic representation of developed TMEMM set-up

scale pattern. Each sample consists of micro dimple arrays of 65 μm diameter. A cylindrical copper tool having 12 mm diameter is utilized as the cathode during experimentation.

31.2.2 Experimental Planning

After proper understanding of the TMEMM fundamentals along with a survey of the literature of the past research works, the experimental scheme has been designed according to Taguchi method for three input factors, each one having three levels. The various important TMEMM process parameters like input voltage, machining frequency, and duty ratio are considered as varying parameters by keeping other machining parameters such as inter-electrode gap, flushing pressure and electrolyte concentration etc. as constant. Considering these input factors with their multiple levels and according to the orthogonal array of Taguchi method minimum 9 experiments should have to be conducted. So, 9 experimental runs have been carried out and the subsequent machining performances are recorded and utilized for statistical analyses. Each experiment has been performed thrice and average values of the responses are considered during analysis. The detailed experimental conditions are shown in Tables 31.1 and 31.2. Further, Table 31.3 shows the levels of various process parameters along with the experimental layout and results for U_c and D_d according to the L_9 orthogonal array of Taguchi method respectively.

Table 31.1 Fixed machining parameters during experiments

Average diameter of micro-holes on the mask	65 μm
Thickness of the patterned mask	20 μm
Workpiece	SS 304
Thickness of the workpiece	200 μm
Material of the mask	AZ 4903
Inter electrode gap (IEG)	2000 μm
Flow velocity	3.8 m/s
Concentration of electrolyte	NaCl (10%) + $NaNO_3$ (10%)
Machining time	120 s

Table 31.2 Variable machining parameters with their levels

Symbol	Machining parameters	Level 1	Level 2	Level 3
A	Input voltage (V)	8	10	12
B	Machining frequency (kHz)	2	6	10
C	Duty ratio (%)	20	30	40

Table 31.3 Design of experiments along with results

Expt. No.	Design of experiments			Undercut (μm)	Dimple depth (μm)
	Input voltage (V)	Machining frequency (kHz)	Duty ratio (%)		
1	8	2	20	9.10554	19.83
2	8	6	30	5.73767	11.46
3	8	10	40	5.53923	16.14
4	10	2	30	10.4696	21.92
5	10	6	40	21.0483	34.04
6	10	10	20	3.84037	7.58
7	12	2	40	28.2651	41.46
8	12	6	20	6.18792	13.44
9	12	10	30	13.8909	21.84

31.2.3 Measurement of Experimental Outcomes

Experiments are carried out as per chalked out plan and the outcomes are recorded for every experimental run. Here, undercut and dimple depth are considered as two performance criteria of the fabricated micro-dimples where undercut has been calculated by simply calculating the difference in radius of a micro-dimple before (with mask) and after machining (upon mask removal). This is accomplished initially with the help of Leica DM2500 optical precision microscope. Precise measurements of depth along with the diameter of the generated micro-dimples are carried out with the help of Talysurf CCI Non-Contact Profilometer (Taylor Hobson). For achieving accuracy in measurements, the values have been taken at various positions of the sample and the average results are used for analyses.

31.3 Taguchi's Robust Methodology and Investigation of the Machining Parameters

The current analysis comprises parametric optimization technique based on Taguchi method to find out the effects of different controllable parameters considered during machining, on the TMEMM quality characteristics and to investigate the most favorable parametric combination for optimizing the responses. Design of experiments (DOEs) is a statistical method used to effectively plan and execute experiments [8, 9]. In order to minimize the total number of experiments, Taguchi uses DOE by constructing a special table known as Orthogonal Arrays (OA). Experimental results are analyzed by using the S/N ratio and ANOVA. The analyses of S/N ratio and ANOVA have been done to examine the significance of the input parameters on U_c

and D_d of the micro-dimples generated by TMEMM process. Based on S/N ratio and ANOVA analysis, the best possible parameter setting for U_c and D_d of the fabricated micro-dimples are obtained and verified. Statistical analysis has been accomplished on the experimental information obtained through Taguchi design using statistical software MINITAB 16.

31.3.1 Orthogonal Array Selection

At first, the total degrees-of-freedom (DOF) for the experiments is computed for selection of a suitable OA for experimentation. Input voltage, Machining frequency, and Duty ratio are the three controllable parameters that have been considered during the experimentation. Three levels of values have been taken for each factor. The total DOFs with three factors and three levels can be computed as 7. In this experimental investigation, the interaction among the machining parameters has been neglected. It is established from the DOF value (7), that minimum seven experiment needs to be carried out to investigate the effect of each input parameter. The standard OA which possess at least three columns at three levels i.e. L_9 has been selected for carrying out the experimentation. The selected OA has four columns and nine rows. As such, it can include four machining parameters having three-level each. Each machining parameter can be allocated to a column pertaining to the availability of nine parametric combinations in the standard L_9 OA matrix. Therefore, only nine experiments need to be carried out as per L_9 OA to study the effects of the controllable input parameters on the performance of TMEMM process.

31.3.2 Analysis of Signal-to-Noise (S/N) Ratio

In robust design, Taguchi philosophy of orthogonal arrays determines the effects of various process parameters efficiently. The analyses of experimental results have been carried out based on the values of signal to noise (S/N) ratios. The term signal represents the desired mean value of the output parameters and the term noise signifies the undesirable value for the responses. Three categories of S/N ratio are lower-the-better, higher the better, and nominal-the-best. In order to attain the most favorable machining outcome for U_c, the lower-the-better quality characteristic is considered. The S/N ratio for U_c, for jth experiment, can be calculated as

$$\eta_j = -10 * \log_{10}\left(\frac{1}{m}\sum_{i=1}^{m} y_{ij}^2\right) \tag{1}$$

where m is the total number of replications and y_{ij} represents the value of U_c of ith replication run for jth no. of experiment. Table 31.3 reflects the results obtained

from the experimental design for U_c and the respective S/N ratio calculated using MINITAB 16. Being an orthogonal experimental design, it is feasible to figure out the effect of each input parameter at various levels. The average S/N ratio for each of the levels for all input parameters taking U_c as the response is graphically shown in Fig. 31.2. U_c is minimum at the highest average S/N ratio. It is clear from the S/N ratio graph that for achieving minimum U_c, the best parametric machining combination is $\mathbf{A_1B_3C_1}$ i.e., 8 V input voltage, 10 kHz machining frequency, and 20% duty ratio. On the other hand, for obtaining the best machining performance for dimple depth the higher-the-better quality characteristic is taken into consideration. The S/N ratio for jth experimental run, n taking D_d as the response can be computed as,

$$\eta_j = -10 * \log_{10}\left(\frac{1}{n}\sum_{i=1}^{m}\frac{1}{y_{ij}^2}\right) \tag{2}$$

where y_{ij}, is the value of D_d for ith test of replication for jth no. of experiment. Table 31.3 also contains the experimental results for D_d. The S/N ratio can be obtained through MINITAB 16. The mean S/N ratio for D_d for all the factors at various levels is calculated. The S/N ratio graph for D_d is revealed in Fig. 31.3.

The maximum depth is represented by a greater S/N ratio (average). From the S/N ratio graph (Fig. 31.3), it can be concluded that the most suitable parametric combination for maximization of dimple depth is $\mathbf{A_3B_1C_3}$ i.e. input voltage of 12 V, machining frequency of 2 kHz and 40% duty ratio.

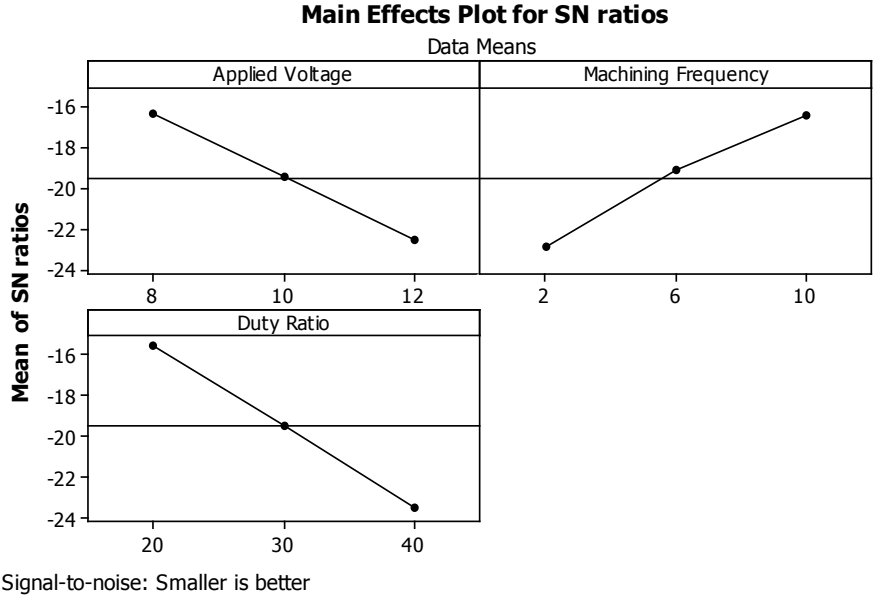

Fig. 31.2 S/N ratio graph for undercut

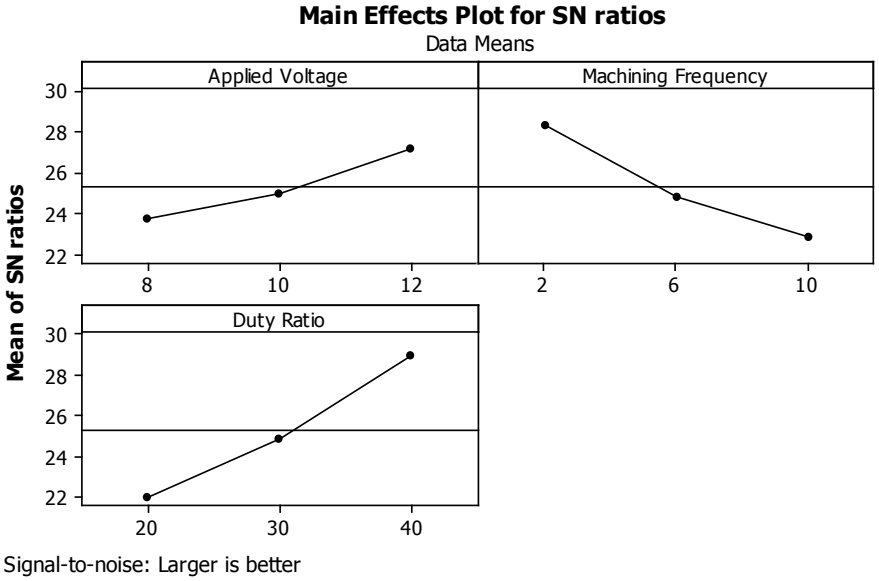

Fig. 31.3 S/N ratio graph for dimple depth

31.3.3 Analysis of Variance (ANOVA)

In this study, the ANOVA has been carried out not only to determine the significant TMEMM parameters and also to figure out the respective machining parameters' contribution in controlling the responses of the TMEMM process. To carry out ANOVA, SS_T i.e. the total sum of squared deviation can be calculated from the total mean S/N ratio (η_m) as

$$SS_T = \sum_{j=1}^{P} (\eta_j - \eta_m)^2 \tag{3}$$

where P represents the total experiments as per experimental design.

$$(SS_T) = \left(\sum_{j=1}^{N} \eta_j \right) / P \tag{4}$$

The total SS_T can be differentiated into two sources: (i) the sum of squared deviations for each machining characteristics i.e. SS_A, SS_B and SS_C and (ii) the sum of the squared error (SS_E).

The mean squared deviation for each design parameter is calculated for performing the F test. It can be computed as SS_T divided by the total no. of DOFs associated

with the machining variables. For each machining parameter, F is the ratio of the mean squared deviation to the mean squared error. The percentage contribution by each of the controllable machining parameters can be calculated as the ratio of the F value of each input parameter to the total sum of the values of F for all the input parameters. The result for ANOVA analysis for undercut is depicted in Table 31.4. The larger the F value, the more significant that factor becomes for controlling the respective response of the TMEMM process. So the value of F can be utilized to rank order the contribution of different factors. From ANOVA analysis, it is revealed that the duty ratio is the most significant factor for influencing U_c. The input voltage and machining frequency approximately contribute equally to the U_c during the generation of a micro-dimple array in TMEMM.

The result of ANOVA for D_d is depicted in Table 31.5. It is also observed that the duty ratio has the most significant effect on the dimple depth fabricated by TMEMM process. Out of the other machining parameters, the machining frequency has a moderate effect on D_d followed by the input voltage. The order of contribution by the input parameters for D_d is duty ratio, machining frequency and input voltage which is identical for U_c.

Table 31.4 ANOVA analysis results for undercut (U_c)

Symbol	Input parameter	DOF	Sum of squares (SS)	Mean squares (MS)	F	Contribution (%)
A	Input voltage (V)	2	56.92	28.46	1.06	26.8313
B	Machining frequency (kHz)	2	61.96	30.98	1.15	29.2071
C	Duty ratio (%)	2	93.25	46.63	1.73	43.9616
Error		2	53.90	26.95		
Total		8	266.04			

Table 31.5 ANOVA analysis results for dimple depth (D_d)

Symbol	Input parameter	DOF	Sum of squares (SS)	Mean squares (MS)	F	Contribution (%)
A	Input voltage (V)	2	18.55	9.276	0.66	13.2273
B	Machining frequency (kHz)	2	47.13	23.565	1.68	33.6067
C	Duty ratio (%)	2	74.55	37.277	2.66	53.1660
Error		2	28.03	14.016		
Total		8	168.27			

31.3.4 Confirmation Tests

After the selection of the best controllable parameters, the ultimate step is to forecast and authenticate the improvement in the selected responses of the TMEMM process during the generation of a patterned micro-dimple array. The optimum value (predicted) of S/N ratio η_{opt} can be computed from Eq. 5 as

$$\eta_{opt} = \eta_m + \sum_{j=1}^{q} (\eta_j - \eta_m) \tag{5}$$

where η_m is the total mean of S/N ratio, n_J denotes the mean S/N ratio at the optimum level, and q is the number of major design parameters that influences the quality characteristics.

The predicted S/N ratio using the best machining parameters for U_c can be obtained and minimum undercut can be formulated using Eq. (1). Table 31.6 shows a comparison between the predicted U_c with the experimental U_c using the most favorable machining parametric combination where it could be judged that there is a good liaison between the actual U_c obtained through experiments and predicted U_c calculated theoretically.

The positive difference in S/N ratio between the primary machining parameters to the best parameters is 1.9355 dB which establishes the fact that the U_c of the micro-dimple array decreases to 0.58 times of the primary value. Microscopic image of a micro-dimple array fabricated at optimized parametric combination is shown in Fig. 31.4a. An undercut of 2.5395 μm could be observed when TMEMM was conducted at the most favorable parametric combination of $A_1B_3C_1$ i.e., input voltage of 8 V, machining frequency of 10 kHz and duty ratio of 20%. Figure 31.4b shows the magnified image of a single dimple.

A comparison between the theoretically predicted D_d and the experimentally found D_d using the finest machining parameter setting is described in Table 31.7. The predicted D_d is reasonable with the actual D_d. The increment in the S/N ratio from the primary to the best machining parameters is 14.384 dB and hence the final value of D_d after improvement is 4 times that of the primary value.

Table 31.6 Confirmation experiment results for undercut

	Primary machining parameters	Best machining parameters	
		Predicted	Experimental
Level	$A_2B_2C_2$	$A_1B_3C_1$	$A_1B_3C_1$
Undercut (μm)	3.1734	2.9684	2.5395
S/N ratio	−10.0305	−9.4505	−8.0950

Improvement in S/N ratio = **1.9355 dB**
Prediction error in S/N ratio = −1.355 dB

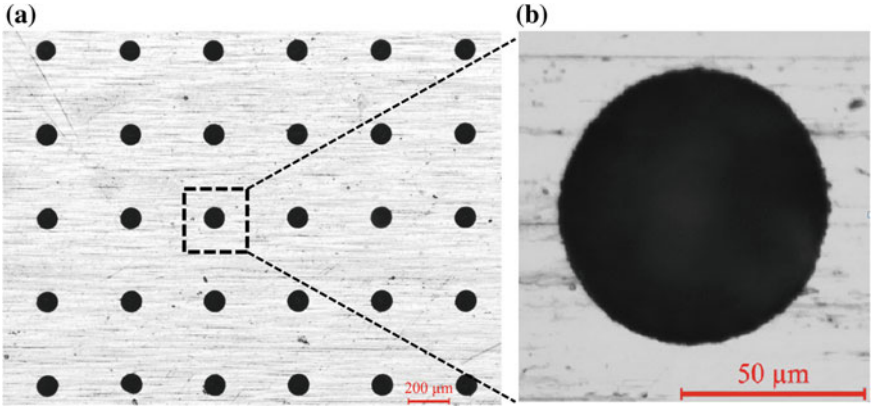

Fig. 31.4 Micro-dimples formed at best parametric combination **a** Patterned array **b** Single dimple

Table 31.7 Confirmation experiment results for dimple depth

	Primary machining parameters	Best machining parameters	
		Predicted	Experimental
Level	$A_2B_2C_2$	$A_3B_1C_3$	$A_3B_1C_3$
Dimple depth (µm)	9.656	50.0086	41.46
S/N ratio	19.6959	33.9809	32.3526

Improvement in S/N ratio = **14.384 dB**
Prediction error in S/N ratio = 1.6283 dB

31.4 Conclusions

Design optimization of the machining parameters is firstly introduced for generation of micro-dimple arrays of TMEMM process. From the experimental findings, S/N ratio and ANOVA analyses along with the results of the confirmation test; the following conclusions can be put up:

(a) On the basis of percentage contribution, the duty ratio, machining frequency and input voltage are the three influential parameters which significantly influence the U_c as well as D_d of TMEMM process. The input voltage has the least effective among the input variables on the selected outputs of TMEMM process.
(b) The best level of parameter setting for attaining minimum U_c, is $A_1B_3C_1$ i.e., input voltage = 8 V, machining frequency = 10 kHz and duty ratio = 20%.
(c) For achieving dimple depth to its maximum, the best level of the parametric combination is $A_3B_1C_3$, i.e., input voltage of 12 V, machining frequency of 2 kHz and duty ratio of 40%.
(d) From the results acquired through the confirmation test, it is accomplished that under most favorable parametric combination, the least value of the 2.5395 µm could be observed in the U_c whereas a fourfold increase with reference to the

initial value could be noticed in dimple depth. The confirmation test results verify the best parametric combinations suitable for improvement in the different experimental outcomes of the Through Mask EMM process.

TMEMM is a process in which microstructure patterning is accomplished by selective material removal through photoresist masks. It is a process with reasonably high accuracy and a fast machining process that produces micro-dimple arrays with a specified size on the workpiece surface. Various geometries to be effectively utilized for various industrial applications e.g. Micro-square arrays etc. can be effectively machined with this methodology of Through-Mask EMM (TMEMM).

References

1. Wakuda, M., Yamauchi, Y., Kanzaki, S., Yasuda, Y.: Effect of surface texturing on friction reduction between ceramic and steel materials under lubricated sliding contact. Wear **254**(3–4), 356–363 (2003). https://doi.org/10.1016/S0043-1648(03)00004-8
2. Bhattacharyya, B.: Electrochemical micromachining for nanofabrication. MEMS Nanotechnol. **270** (2015)
3. Tang, L., Li, B., Yang, S., Duan, Q., Kang, B.: The effect of electrolyte current density on the electrochemical machining S-03 material. Int. J. Adv. Manuf. Technol. **71**(9–12), 1825–1833 (2014). https://doi.org/10.1007/s00170-014-5617-x
4. Madore, C., Landolt, D.: Electrochemical micromachining of controlled topographies on titanium for biological applications. J. Micromech. Microeng. **7**(4), 270–275 (1997). https://doi.org/10.1088/0960-1317/7/4/002
5. Zhu, D., Qu, N.S., Li, H.S., Zeng, Y.B., Li, D.L., Qian, S.Q.: Electrochemical micromachining of microstructures of micro hole and dimple array. CIRP Ann. Manuf. Technol. **58**(1), 177–180 (2009). https://doi.org/10.1016/j.cirp.2009.03.004
6. Chauvy, P.F., Landolt, D.: Unusual cavity shapes resulting from multistep mass transport controlled dissolution: numerical simulation and experimental investigation with titanium using oxide film laser lithography. J. Appl. Electrochem. **33**(2), 135–142 (2003). https://doi.org/10.1023/A:1024034404509
7. Chen, X., Qu, N.S., Li, H.S., Zhengyang, X.: Electrochemical micromachining of micro-dimple arrays using a polydimethylsiloxane (PDMS) mask. J. Mater. Process. Technol. **229**, 102–110 (2016). https://doi.org/10.1016/j.jmatprotec.2015.09.008
8. Montogomery, D.C.: Design and analysis of experiments (1996)
9. Phadke, M.S.: Quality engineering using robust design (1989)

Chapter 32
Parametric Optimize and Surface Characterisation of Micro Electrical Discharge Machining Drilling Process

Jush Kumar Siddani, C. Srinivas and N. N. Ramesh

Abstract Micro electrical Discharge Machining Drilling (MEDM Drill) technology has recently come into existence. The MEDM Drill process is an amalgamation of electromagnetic, thermodynamic and hydrodynamic behaviour and stochastic in nature. Optimize the course of action parametric combination, modelling the method, employ Artificial Neural Network (ANN) as well as to characterize the MEDM Drill external from end to end time progression technique. Therefore feed—forward reverse dissemination neural network base on top of very important composite rotatable investigational drawing mechanism, developed to model machining procedure. The best possible parametric combination is particular for development.

Keywords MEDM Drill · ANN · Process optimization · Surface characterization

32.1 Introduction

MEDM Drill is an upcoming process to drill micro holes with high accuracy, no cutting forces capability to attain small holes in workpiece and remains unaffected material hardness. Electrical discharge machining is a thermoelectric method, wear away bits and pieces from workpiece by series, cut off spark among the gap of workpiece and electrode immersed (tool) in liquid dielectric in-between workpiece and tool [1]. The electrical discharge vaporizes and assembles tiny amount of work material, which are flushed as well as driven out away by dielectric fluid.

Therefore augment of voltage or reduce of the gap connecting the workpiece and electrode result within vaporization and ionization dielectric into the important conductivity link and form, spark channel linking the two surfaces. The spark channel is

J. K. Siddani (✉)
Acharya Nagarjuna University, Guntur 522508, Andhra Pradesh, India
e-mail: jushkumar.siddani@gmail.com

C. Srinivas
RVR & JC College of Engineering, Guntur 522019, Andhra Pradesh, India

N. N. Ramesh
Anurag Group of Institutions, Hyderabad 500088, Telangana, India

M. S. Shunmugam and M. Kanthababu (eds.), *Advances in Micro and Nano Manufacturing and Surface Engineering*, Lecture Notes on Multidisciplinary Industrial Engineering,
https://doi.org/10.1007/978-981-32-9425-7_32

caused by the high amount of current. The pressure and temperature augment within the spark channel. Therefore spark duration is extremely short and little quantity of material of electrode and workpiece is melted and vaporized at a very high temperature spark. In this process the spark and heating exploit to come to an end instantly, at the end of electrical pulse, voltage is isolated resulting in vapour bubble collapse and explosive removal, melted material commencing both electrode and workpiece surface. The EDM's process is an arrangement of electromagnetic action, thermodynamic action, electrodynamic exploit and hydrodynamic exploit within the period of microseconds to milliseconds.

In Micro EDM drilling procedure has differed from sinking EDM procedure with the aim of a Nanotube as itengages as the tool electrode. The workpiece is mounted on the clamp frame. The dielectric medium delivering at the gap between the tube (tool) and workpiece is flushed through the Nanotubes in the sparking area. This gap among tool and workpiece range from 0.025 close to 0.05 mm [2] frequently maintained by a computer restricted position system. The producer and customer for eternity desire to attain better-quality machining productivity through a wanted precision along with surface finish. This typical MEDM Drill drilling rate is 200 mm^2/min for a 30 mm substantial tool steel along with 600 mm^2/min for a 100 mm substantial aluminium [3] as well as surface finish feature is at the same time as well as 0.03–0.20 R_a. MEDM Drill uses deionised water as dielectric fluid contain surrounded by sparking zone. In this process the deionised water is not appropriate for Sinking EDM because it cause- electrode wear, except—low viscosity and rapid cooling rate create it perfect for MEDM Drill [4]. The investigation into persuading of machining input parameter lying on performance of Sinking EDM and Wire—EDM has subsisted broadly reporting [5–8]. Numerous attempt to be prepared to represent the process [9, 10].

32.2 Experimental Procedure

Process Modelling by Artificial Neural Network, this process consists of two operations. One is finishing operation and the other is surface finishing operation. In the final and surface finishing operation, in the surface finishing is introductory significance. The elevated cutting speed as well as smooth surface finish can be reached at the same time, no meticulous recipe of matching.

The reproduction expressive connection between machining condition and process performance is vital. The MEDM Drill process the intricate and stochastic environment has made it complex to establish certain notional form; a practical method is adopted for the progress. This lead to the development of an observed replica able to predict and measure the presentation. The procedure used to further optimize, research, a reasonable setup of parameter is particularly similar to inputs through other parameters affecting the performance of the process fixed. Generally, a smaller setup of input parameter yields simpler replica; on the other hand, larger number of parameter may give the model additional accurate projecting control and wider

function spot. The experiment is carried out on a Rapid Drill (electronic) schematic of the tool-workpiece system, the dielectric medium supply of the machine and the spark gap is shown in Fig. 32.1.

Parameters to locale the Rapid Drill are planned in Table 32.1. Therefore input and fixed parameter have been employed in the present study which is listed in Table 32.1. These are selected in the course of review of knowledge, record survey, and some preliminary investigation.

Therefore factor and their level are shown in Table 32.2, composite rotatable investigation mechanism of design and uniform precision for modelling the micro EDM Drill was designed as shown in Tables 32.3 and 32.4. The experimental runs were randomly designed for Sixteen factorial (inherent level ±1) run shown in Tables 32.3 and 32.4 (Tables 32.5 and 32.6).

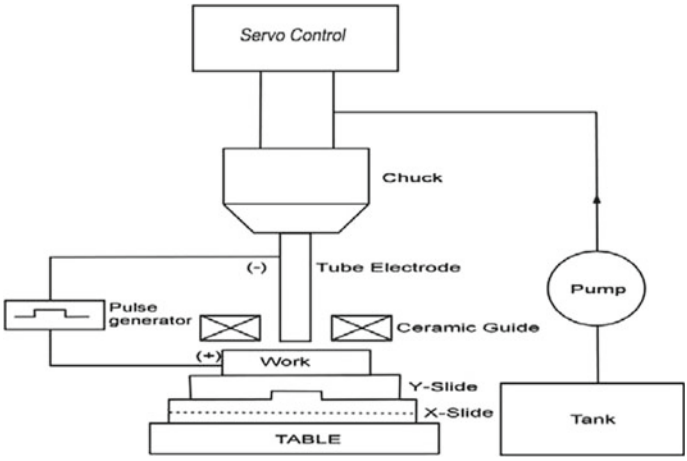

Fig. 32.1 Schematic illustration of micro EDM drill

Table 32.1 Parameters of the machine setup

S. No	Parameters	Setting	
1	Input	Pulse width (A)	Factor (A)
		Time between two pulses (B)	Factor (B)
		Tool feed space (WS)	Factor (WS)
2	Fixed	Tool (Nano tube) copper or brass	0.5–1.9 mm
		Temporary reduction in frequently (FF)	80%
		Current voltage (V)	−60 V
		volts pulse time (T_{ac})	0.2 μs
		Mean voltage	22 V
		Dielectric (deionization)	10

Table 32.2 Factor and level for operation

Key factors	Level/code					
	1/−2	2/−1	3/0	4/+1	5/+2	Unit
Pulse width (A)	0.4	0.6	0.8	1.0	1.1	μs
Time between two pulses (B)	2	4	6	8	10	μs
Tool Feed Alacrity (WS)	4.0	5.5	6.4	8.2	10.0	mm/min

Table 32.3 Result of alacrity on top of roughness indices (material: H.S.S)

S. No	Index	Alacrity (mm/rev)			
		1.834	1.834	1.946	1.946
1	R_a (μm)	2.84	3.96	4.38	6.66

Table 32.4 Effect of alacrity on roughness indices (material: titanium)

S. No	Index	Alacrity (mm/rev)			
		0.948	0.948	1.64	1.64
1	R_a (μm)	1.51	2.75	5.13	5.46

Table 32.5 Experimental design for H.S.S

Exp. No	A (μs)	B (μs)	WS (m/min)	R_a (μm)	W_a (μm)	Alacrity (mm/min)
1	0.6	4	5.5	2.660	1.845	1.845
2	1.0	4	5.5	2.745	1.394	1.946
3	0.6	8	5.5	2.008	1.126	1.866
4	1.0	8	5.5	1.895	1.149	1.807
5	0.6	4	5.5	2.454	1.185	1.908
6	1.0	4	5.5	2.324	1.199	1.962
7	0.6	8	5.5	1.466	0.129	1.833
8	1.0	8	5.5	1.108	0.127	1.834
9	0.6	4	8.2	1.245	0.154	1.844
10	1.0	4	8.2	1.306	0.166	1.856
11	0.6	8	8.2	1.346	0.163	1.840
12	1.0	8	8.2	1.464	0.158	1.843
13	0.6	4	8.2	2.100	1.368	1.836
14	1.0	4	8.2	2.147	1.239	1.932
15	0.6	8	8.2	1.955	0.136	1.944
16	1.0	8	8.2	1.986	0.133	1.868
Total	12.8	96	109.6	30.209	11.671	29.964
Average	0.8	6	6.85	1.888	0.729	1.873

Table 32.6 Experimental design for titanium

Exp. No	A (μs)	B (μs)	WS (m/min)	R_a (μm)	W_a (μm)	Alacrity (mm/min)
1	0.6	4	5.5	1.804	0.148	1.640
2	1.0	4	5.5	1.665	0.167	1.543
3	0.6	8	5.5	1.060	0.148	1.548
4	1.0	8	5.5	1.006	0.143	1.499
5	0.6	4	5.5	1.768	0.146	1.467
6	1.0	4	5.5	1.456	0.144	1.489
7	0.6	8	5.5	1.398	0.136	1.463
8	1.0	8	5.5	1.387	0.138	0.987
9	0.6	4	8.2	0.946	0.045	0.948
10	1.0	4	8.2	0.956	0.066	0.936
11	0.6	8	8.2	0.988	0.059	0.944
12	1.0	8	8.2	0.974	0.054	0.942
13	0.6	4	8.2	1.179	0.198	0.952
14	1.0	4	8.2	1.180	0.147	1.400
15	0.6	8	8.2	1.199	0.155	1.501
16	1.0	8	8.2	1.204	0.158	1.581
Total	12.8	96	109.6	20.170	2.052	20.840
Average	0.8	6	6.85	1.260	0.128	1.302

32.3 Results and Discussions

The experimental result is performed at random (i.e.., commence illustrate in first column of Table 32.3 and 32.4). The specified input parameter is set and the work piece of H.S.S and Titanium was drilled completely through for each run. The time for drill through the workpiece is recorded. Then cutting speed is calculated according to depth of drill and cutting time. H.S.S and Titanium workpieces revealed that speed of 1.834 and 0.987 mm/min are the most suitable. The surface roughness Ra of H.S.S and Titanium are best suitable at 1.108 and 1.387 μm and then average values if Ra was recorded in Tables 32.3 and 32.4. The surface waviness Wa 0.127 and 0.138 μm are recorded in Tables 32.3 and 32.4. The conclusion that Ra, Wa and cutting speed are useful to remodel R_a, W_a as well as cutting speed which are measured as yield parameter of representation. The investigational results in Tables 32.3 and 32.4 by using logical neural network by means of the single form 3-4-3 to 3-16-3. The hyperbolic tangent function is experienced as transfer function in neural network.

$$f(z) = \frac{e^2 - e^{-1}}{e^2 + e^{-1}}$$

and logistic sigmoid function

$$f(z) = \frac{1}{1 + e^{-1}}$$

The hyperbolic tangent role is improved than logistic sigmoid function as well as 3-8-3 be nearly all fitting size for the neural network. In the 3-8-3 extent neural network are shown in Fig. 32.2. Figures 32.3 and 32.4 show R_a, W_a and cutting speed

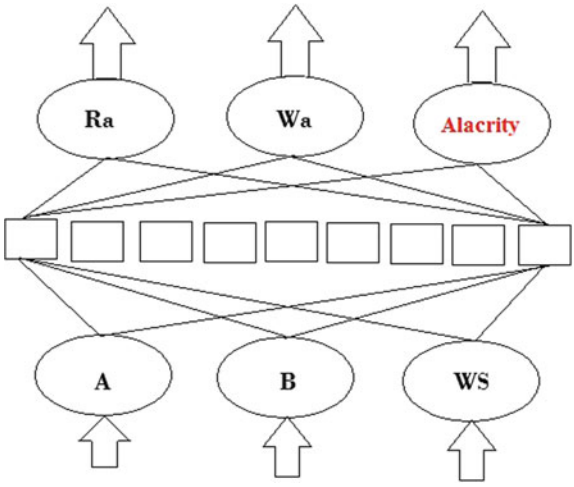

Fig. 32.2 Neural networks for micro EDM drill

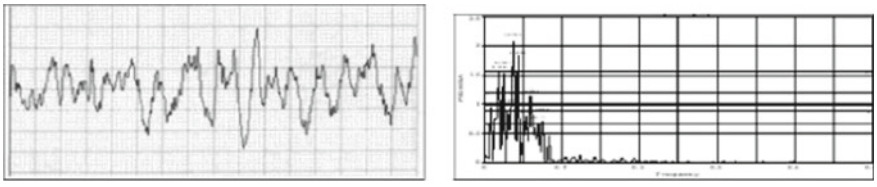

Fig. 32.3 Roughness and Fourier spectra of H.S.S material sample workpiece 1

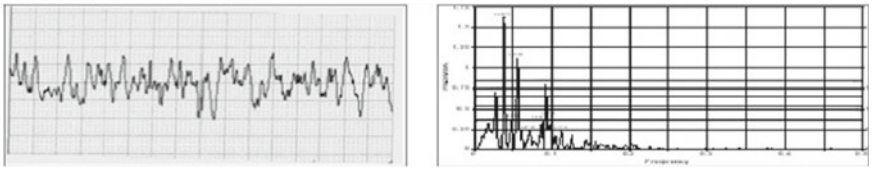

Fig. 32.4 Roughness and Fourier spectra of H.S.S material sample workpiece 2

response, the fitted ANN replica by means of value toward input control factor A and B.

A large amount of factor is production of surface roughness. In this the effect of drive, the roughness profiles, as well as their Fourier spectra, are exposed in Figs. 32.3, 32.4, 32.5 and 32.6. Therefore roughness indices are listed within Tables 32.3 and 32.4. Meanwhile predictable roughness increase by means of feed rate. Taking place the roughness, profile impetus characters as well turn out to be clearer and major. The subordinate momentum rate roughnesses become independent to speed as well as function the tip of the tool only [1]. Cause's more micro roughness, i.e., superimpose irregularity greater than the grooves generated through chip removal. Therefore artificial stream part is reasonably added. Similarly when alacrity is more and tip of the tool radius is small. This shows artificial flow is contrary to momentum track by means of elevated low alacrity in the direction and lead to elevated roughness next to small speed. An associated irregularity has been reported with lesser roughness and advanced momentum due to pure drilling achievement and comparative absence of bulge. Therefore the similar way next to small alacrity, material gets ploughed rather than in the shape of chips. The existences of optimum speed, speculation suggest roughness to be a function, the open area of momentum, within put into practice; it is further like openly related to rapidity rate. This shows outstanding in the direction of knocking down of ridge side flow or tool-workpiece relative vibrations. The possessions are corroborated by Fourier transforms. Creation of more than a few harmonics next to lower speed rates owing to ploughing achievement is seen evidently in the direction of the influence presented in micro roughness next

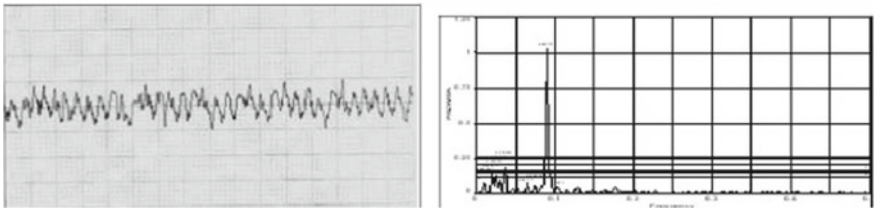

Fig. 32.5 Roughness and Fourier spectra of titanium material sample workpiece 1

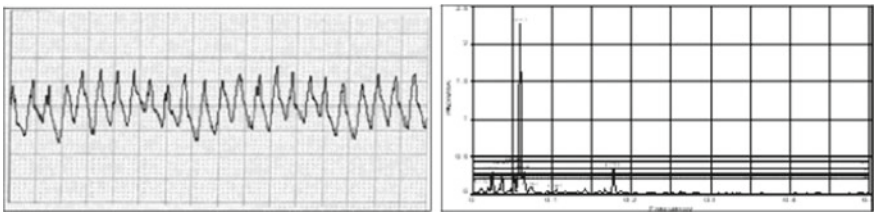

Fig. 32.6 Roughness and Fourier spectra of titanium material sample workpiece 2

to high rapidity. Therefore decrease in micro roughness and marked periodicity is to see by means of the retreating harmonics as it finally reduces to single harmonic matching in the direction of speed. This is added to skewness in a positive way which shows the roughness shape to be partial valley at elevated rapidity that indicates metal otherwise chip taking away mechanism of roughness making next to high alacrity. These consequences are extremely alike to H.S.S specimen as well and elevated credibility in the direction of the preceding outcome compared, to Titanium in addition to conversation.

32.4 Conclusions

The performance productivity and the surface texture of the workpieces H.S.S and Titanium were performed with uniform precision and optimization of the Micro EDM Drill process in order to model the process. Between the two pulses, pulse width and tool feed speed were chosen at the same time as that of control factor. Callous speed, waviness and surface roughness of workpieces of H.S.S and Titanium were selected as process outputs. The 3-15-3 feed forward back propagation ANN model was developed to represent the Micro EDM Drill process. The developed ANN replica which shows, the best possible procedure of parametric combination en route for dissimilar waviness and surface roughness. The factors such as tool-workpiece thickness and material may be attempted for further research as input parameters. The output such as topological surface, hardness, etc. might be investigated. The Micro EDM Drilling or any other Drilling operations may be suggested for further studies in drilling operations (Figs. 32.7 and 32.8).

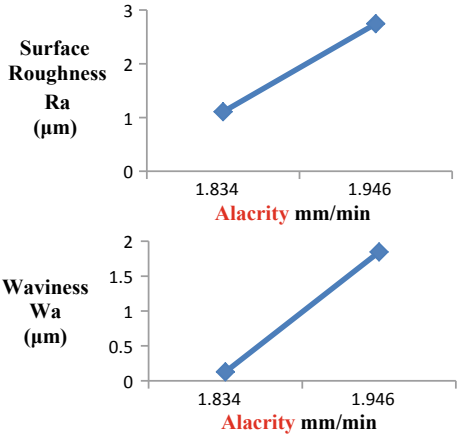

Fig. 32.7 Graphic display of factor effects of R_a, W_a and alacrity corresponding to Table 32.5

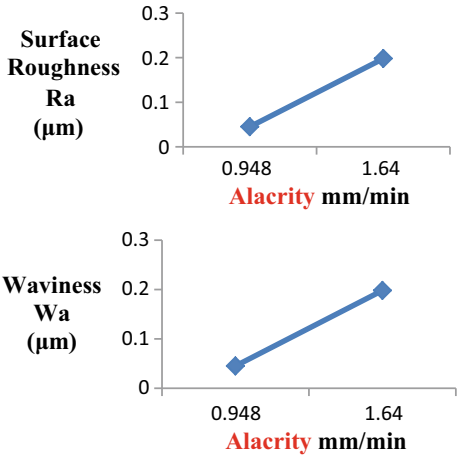

Fig. 32.8 Graphic display of factor effects on R_a, W_a and Alacrity corresponding to Table 32.6

References

1. Nagabhushana Ramesh, N., Neeraja, A., Chaitanya Krishna Chowdary, P., Ashwini Shanthi, A.: Gap in the knowledge base of electro discharge machining. Int. J. Sci. Res. **6**, 1346–1349 (2017)
2. Benedict G.F.: Non-traditional Manufacturing Processes. Marcel Dekkar, New York (1987)
3. Kalley Harinarayana, N., Ramesh, N.N., Balu Naik, B.: Experimental investigations of process parameters of electrodischarge sawing, a modified EDM using Taguchi approach. Int. J. Emerg. Technol. Adv. Eng. **2**, 620–626 (2012)
4. Narayan, Y.S., Ramesh, N.N., Balu Naik, B.: Effect of process parameters on tool wear rate in micro drilling of maraging steel 300 Alloy. In: 4th International and 25th (AIMTDR) Conference, Jabalpur University (2012)
5. Kunieda, M., Furioya, S.: Improvement of EDM efficiency by supplying oxygen gas into gap. Ann. CIRP **40**, 215–218 (1991)
6. Weck, M., Dehmer, J.M.: Analysis and adaptive control of EDM sinking process using the ignition delay time and fall time as parameter. Ann. CIRP **41**, 243–246 (1992)
7. Soni, J., Chakraverti, G.: Machining characteristics of titanium with rotary electro—discharge machining. Wear **171**, 51–58 (1994)
8. Dauw, D.F. Beltrami, I.: High precision wire—EDM by online wire positioning control. Ann. CIRP **43**, 193–197 (1994)
9. Rajurkar, K.P., Wang, W.M.: Thermal modeling and on-line monitoring of wire—EDM, J. Mater. Process. Technol. **38**, 417–430 (1993)
10. Indurkhya, G. Rajurkar, K.P.: Artificial neural network approach in modeling of EDM process. In: Proceedings of the Artificial Neural Networks in Engineering (ANNIE)

Chapter 33
Experimental Study of Nanosecond Fiber Laser Micromilling of Ti6Al4V Alloy

A. K. Sahu, H. A. Patel, J. Malhotra and S. Jha

Abstract Fiber Laser micromachining technique has a great ability to because of high laser beam intensity, good focusing characteristics with lesser maintenance. In laser micromilling for higher depth, multiple scans of laser beam are required. In this study, controllable factor like pulse overlap, number of scans were considered to determine the depth of Ti6Al4V. The central composite designed (CCD) technique based on response surface methodology (RSM) is employed to plan the experiment and to develop mathematical regression model. A significant parameter has been selected based on the analysis of variance (ANOVA). The depth is achieved between 49 and 163 μm. Maximum average surface roughness was measured up to 19.95 μm.

Keywords Laser micromilling · RSM · Depth · Microgroove

33.1 Introduction

Titanium and its alloy have wide application in medical implants, aerospace, biomedical, and automotive industries because of their high strength-to-weight ratio and better corrosion resistance properties at room and elevated temperatures. Ti6Al4V alloy is most widely used as its application of 50% of total titanium alloy production. Aluminum (Al) increases phase stabilization and hardness of alloy. Vanadium (V) provides hot workability of the alloy. Titanium and its alloys are hard to machine due to their properties by conventional and nonconventional machining processes. Machining of titanium and its alloys by conventional methods require high running costs (tool cost and coolant) with low productivity [1].

There are different method to machine titanium like EDM, ECM or by conventional machining. By which EDM is a very popular method but this is a very slow process. The MRR in EDM is very low although surface quality of machined part is better. Conventional micro machining having very limited area to machine

A. K. Sahu · H. A. Patel · J. Malhotra · S. Jha (✉)
Department of Mechanical Engineering, Indian Institute of Technology Hauz Khas, Delhi 110016, India
e-mail: suniljha@iitd.ac.in

M. S. Shunmugam and M. Kanthababu (eds.), *Advances in Micro and Nano Manufacturing and Surface Engineering*, Lecture Notes on Multidisciplinary Industrial Engineering,
https://doi.org/10.1007/978-981-32-9425-7_33

hard to machine material and also cost of tooling is so high because of high tool manufacturing cost and tool wear. So laser micromachining can be opted for faster micromachining of Titanium.

Laser micromachining (LMM) is a highly precise, fast, and force-free technology for micromilling of hard to machine material, alloys, and composites. In LMM process high energy collimated laser beam focused by optics to a selected surface of material which cause melting and vaporization of material to create the desired feature. LMM involves machining of microns and submicron size feature with nanometer (nm) tolerances and high precision on metals and nonmetals substrates. In LMM, the feature size highly depends on beam quality (M^2), wavelength, and focusing lens and aperture of lens [2]. LMM is widely used in mold and die making industry, microfluidics to fabricate 3-D submicron sized structures. Microfluidics and microreactors have application of microchannels, hollow channel for miniature flow of liquids and gasses.

Biffi et al. performed percussion microdrilling on Ti (0.5 mm thick) with 50 W pulsed fiber ns laser to study the effect of pulse energy and pulse frequency on quality of machined through holes, i.e., diameters, taper, circularity, area of top spatter, and surface morphology. They developed adequate regression model for D_{top} and D_{bottom} [3]. They also analyzed effect of microdrilling on material microstructure of region in close proximity. Exit hole found free from spatter and drop. D_{top} and D_{bottom} increased due to higher heat input. Taper depends only on pulse energy and no effect of pulse frequency. Spatter, i.e., molten metal inside hole and expelled on top surface also increases as average power increases (i.e., pulse energy * frequency). Higher value of nano hardness usually measured in internal walls which shows significant modification occurs on Ti property after laser processing on entrance and exit surface of hole [4]. Lash et al. used copper laser to drill holes in 0.025–0.127 mm thick foil of Cu, Ti, and Fe at atmospheric pressure air and argon. They used a photodiode to detect no. of pulses to drill holes. They found that with 0.032 mm thick Ti foil. Drilling time in argon (Ar) reduced by factor 4. No machining was observed on the surface of aluminum foil in argon [5]. Biswas et al. investigated Nd-Yag laser microdrilling process considering hole taper and circularity at entry and exit, through response surface methodology based experiments on titanium nitride alumina ($TiN–Al_2O_3$) composite. For investigation lamp current, pulse repetition rate, airflow pressure, pulse width, and focal length considered as process parameter. The parameter optimum condition for hole taper and circularity has been evaluated. Only significant parameters have been selected based on the analysis of variance (ANOVA) in model [6].

Singh et al. optimized parameters of the electrical discharge machining process, i.e., pulse on time (Ton), pulse off (Toff), and current (I) to improve the surface roughness of Ti-6AL-4V by analysis of variance. Copper (Cu) electrode used as tool EDM tool [7]. Arnaboldi et al. investigated laser micro cutting of nickel-titanium-copper (Ni40Ti50Cu10) alloy. It is a ternary Shape memory alloy derived from NiTi binary alloy [8]. Cutting edge quality features, such as the amount of spatter and the kerf width considered as response. The number of laser passes, type of shielding gas, gas pressure, and process speed has been opted for micro cutting analysis.

Table 33.1 Composition of Ti6Al4V

Composition	Ti	Al	V	C	O	N	H	Fe
%	90	6	4	<0.1	<0.2	<0.05	<0.0125	<0.3

Finally, functional characterization, i.e., differential scanning calorimetry (DSC) and mechanical measurements (nano indentations), of the laser cutting edge were performed. Nitrogen (N) and Argon (Ar) assist gasses at 2 and 5 bar pressure were investigated. Process speed varied between 1 and 50 mm/s. Zhou et al. has fabricated microchannels of different size and shape to investigate the surface morphology and geometrical measurements by Scanning Electron Microscope using different process parameters of micromilling operation. The outcome shows the surface morphology of micro features is affected by scanning speed and laser power, also the depth of microchannel is increased by increasing laser power and number scans [3]. Kasman et al. performed micromilling on AISI H13 using 30 W fiber laser to investigate optimal process parameters for minimum roughness and maximum depth of channels. The result shows with decreasing laser power and pulse frequency at high speed will decrease the roughness. Also, the combination of the fill spacing and lower scan speed decreases the roughness and increases the depth of channel [9].

Consequently, few researcher were reported to use laser micromachining of Titanium and its alloy by Nd-Yag laser. The aim of this study is to model response depth in terms of input parameter, i.e., pulse overlap and No. of scans on Ti6Al4V of thickness 10 mm by fiber laser. Composition of Ti6Al4V shown in Table 33.1.

33.2 Experimental Setup

Laser micromachining having a fiber laser source with optics system were mounted on precision linear positioners. A 50 W fiber laser source of nanosecond pulse width (SPI lasers) of near infrared wavelength (1064 nm) and cutting head with suitable optics were mounted on the system. Cutting head has focusing lens and provision to assist gas supply. The purpose of optics containing focusing lens to guide collimated beam and is to focus on the surface of substrate with small spot size. Fiber laser is operated in continuous mode for fabrication of microgroove. The workpiece of Ti6Al4V of size 50 × 100 × 10 mm was placed horizontally on motorized stage. The stage translates while keeping the laser spot stationary. To ensure laser beam focus on workpiece surface the stage height can be adjusted relative to focus position by z axes movement. The accuracy of height adjustment of axis is 10 μm. All the experiments were performed in assist gas medium as air supplied at a pressure of 5 bar by air compressor. Length of microgroove fabricated is 40 mm each. Pulse overlap calculated as per Eq. 33.1. For No. of scans each groove scanned by laser beam one over another. LMM system specification Shown in Table 33.2. After laser processing

Table 33.2 LMM system specification

Laser type	Fiber
Avg. power	50 W
Mode	CW
M^2	1.3
Pulse energy	1 mJ
Pulse duration	290 ns
Assist gas	Air (5 bar)
Wavelength	1064 nm

the workpiece was removed for depth and surface roughness measurement. Zeta 3d optical Profilometer has been used at 20 X condition for measurements.

33.3 Experimental Plan Based on Response Surface Methodology

Experiments have been designed according to the central composite rotatable (CCD) second-order design based on response surface methodology. Response surface modeling was used to establish the mathematical relationship between the response, y_u and the various machining parameters [10]. A general second-order polynomial response surface model as shown by Eq. (33.1) was considered to analyze the parametric influences on the various response:

$$y_u = \beta_0 + \sum_{i=1}^{n} \beta_{ii} x_{iu}^2 + \sum_{i<j} \beta_{ij} x_{iu} x_{ju} + e_u \tag{33.1}$$

here y_u is the corresponding response, e.g., depth of microgroove of the laser beam micromilling process, xiu is the coded value of the *i*th machining parameter of the *u*th experiment, n is the number of machining parameters and βi, βii, βij are the second-order regression coefficients, the residual e_u is a measure of experimental error of the *u*th observations.

For response surface methodology two parameters, i.e., pulse overlap and No. of scans having three level each has been selected considering FCC ($\alpha = 1$) and experiment has been designed and analyzed by design expert. Selected parameter and levels are shown in the table below. Total 13 experiments has been designed as shown in Table 33.3 and each experiment has been carried out two times and an average of response has been considered for analysis. Levels of parameters considered for experiments is shown in Table 33.4.

Pulse overlap (%) depends on scanning speed and pulse repetition rate. It has been calculated as per Eq. 33.2.

Table 33.3 DOE of process parameter and observed response

S. No	Run	Pulse overlap (%)	No. of scans	Depth (μm)
1	13	99.94	1.00	49
2	7	99.98	1.00	103
3	5	99.94	3.00	139
4	1	99.98	3.00	163
5	8	99.94	2.00	80
6	12	99.98	2.00	137.5
7	6	99.96	1.00	61
8	2	99.96	3.00	132
9	4	99.96	2.00	102
10	11	99.96	2.00	110
11	3	99.96	2.00	102
12	9	99.96	2.00	101.5
13	10	99.96	2.00	103.5

Table 33.4 Actual level of parameter

Parameter	Levels		
	−1	0	1
Pulse overlap (%)	99.94	99.96	99.98
No. of scans	1	2	3

$$Pulse\ Overlap\,\% = 1 - \frac{U}{f * d} \times 100 \tag{33.2}$$

where

U Scanning speed (mm/s)
f Pulse repetition rate in Hz
d Spot Size (μm)

Similarly, for No. of scans microgroove scanned one over another subsequently.

33.4 Results and Discussion

33.4.1 Parametric Influence on Depth

Pulse overlap and no. of scans effect on depth of microgroove shown in Fig. 33.1. Depth has been varied between 49 and 163 μm with pulse overlap and No. of scans. From the surface plot, it has been observed that by increasing pulse overlap the depth

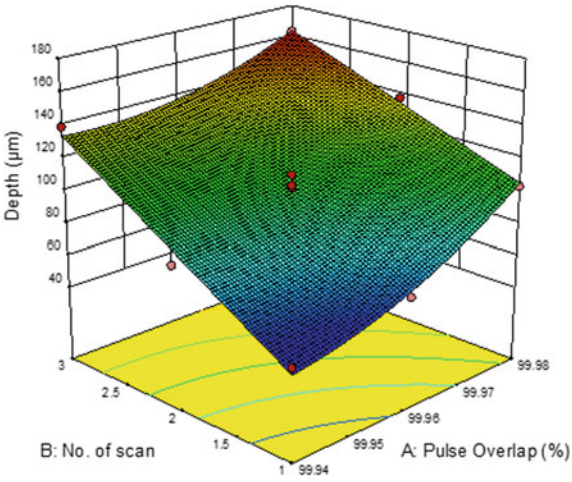

Fig. 33.1 Response surface interaction plot of scans and pulse overlap for depth

increases. This is because higher overlap occurs at low scanning speed, so the laser beam pulses interaction per unit length is higher, so laser ablation increases due to melting and vaporization. The melted material removed from groove by high-pressure air. So higher depth is achieved.

Similarly, by increasing the no. of scans the depth increases. This is because of multiple scans at same surface achieved higher depth. Although removal of depth in second and third scan is comparatively lower than first scan, which can be explained by focusing condition which remains the same and depth of focus limits more depth of removal.

It is because of the laser beam having constant depth of focus which is limited to certain depth. Also at higher depth removal of melted material by assist gas pressure is limited and not effective due to groove wall. Images of microgroove fabricated by laser micromachining has shown in Fig. 33.2.

33.4.2 Mathematical Regression Model

The experimental result of the depth of microgroove is listed in Table 33.3 from the designed experiment which is used for development of mathematical regression model for depth. Equation 33.3 shows model in actual parameter.

$$\begin{aligned}\textbf{Depth}(\mu\,\textbf{m}) = {} & \mathbf{101.71} + \mathbf{22.58} * \textbf{Pulse Ovelap} + \mathbf{36.83} * \textbf{No. of Scans} \\ & + \mathbf{10.20} * \textbf{Pulse Overlap}^2 - \mathbf{7.50} * \textbf{Pulse Overlap} * \textbf{No. of Scans}\end{aligned} \tag{33.3}$$

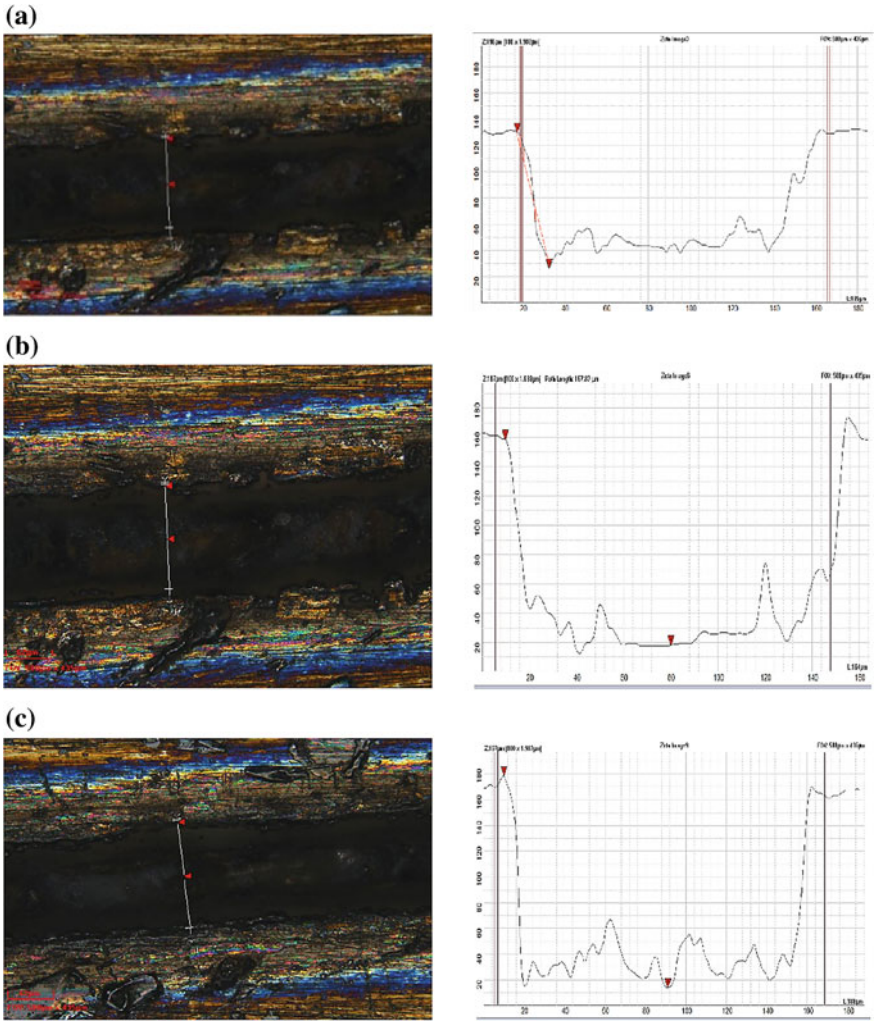

Fig. 33.2 Fabricated microgroove at 99.98% pulse overlap profile and corresponding depth graph at **a** one **b** two and **c** three scans

In the model only significant terms were considered. Analysis of variance has been carried out to test adequacy of developed mathematical model for depth. Analysis of variance is shown in Table 33.5 by analysis of variance it is clear that most influencing parameter is No. of pulses. For developed model R-squared 0.9771, Pred R-Squared of 0.8362, and Adj R-Squared of 0.9616 has been found after analysis. The Pred R-Squared is in reasonable agreement with the Adj R-Squared.

Table 33.5 Analysis of variance (ANOVA) for depth

Source	Sum of squares	DF	Mean source	F value	Prob > F	
Model	11761.49	4	2940.37	85.25	<0.0001	Significant
Pulse overlap	3060.04	1	3060.04	88.72	<0.0001	
No. of scans	8140.17	1	8140.17	236.01	<0.0001	
Pulse overlap^2	336.29	1	336.29	9.75	0.0142	
Pulse overlap * No. of scans	225.00	1	225.00	6.52	0.0340	
Residual	275.93	8	34.49			
Lack of fit	225.63	4	56.41	4.49	0.0876	Not significant
Pure error	50.30	4	12.58			
Cor total	12037.42	12				

33.4.3 Roughness Measurement Inside Groove

Roughness was measured with the help of Zeta 3d profiler inside microgroove. For measurement average surface roughness value Ra has been evaluated at 99.96% overlap and 1–3 scans over 500 μm along the length of microgroove Fig. 33.3. It has been found that Ra value increased by increasing No. of pulses as more metal get melted and vaporized so crater observed as roughness shown in Fig. 33.4. There is significant variation that has been observed at third scan compared to first and second. It is because of in third scan depth increased significantly and at higher depth the material gets melted but it has not been removed out with assist gas due to unreachability of gasses and groove walls. Recast layer redeposition of melted material and material get resolidified and higher roughness is achieved. Roughness measured is 1.703, 4.27, and 19.95 μm for first to third scans at 99.96% pulse overlap. Roughness profile is shown in Fig. 33.4 for three grooves.

33.5 Conclusions

In the present research Fiber laser micromilling of Ti6Al4V has been carried out and the effect of process parameter on response variable has been explained in detail. For depth mathematical model is developed based on response surface methodology. The analysis of variance test done to identify the process parameter that contributes most significantly on depth. The No. of scans having the most significant effect on Depth. The maximum depth achieved was 163 μm. After three scans roughness increases drastically as compared to one and two scans. Maximum average surface roughness was 19.95 μm. Parameters need to optimize for higher depth and lower surface roughness.

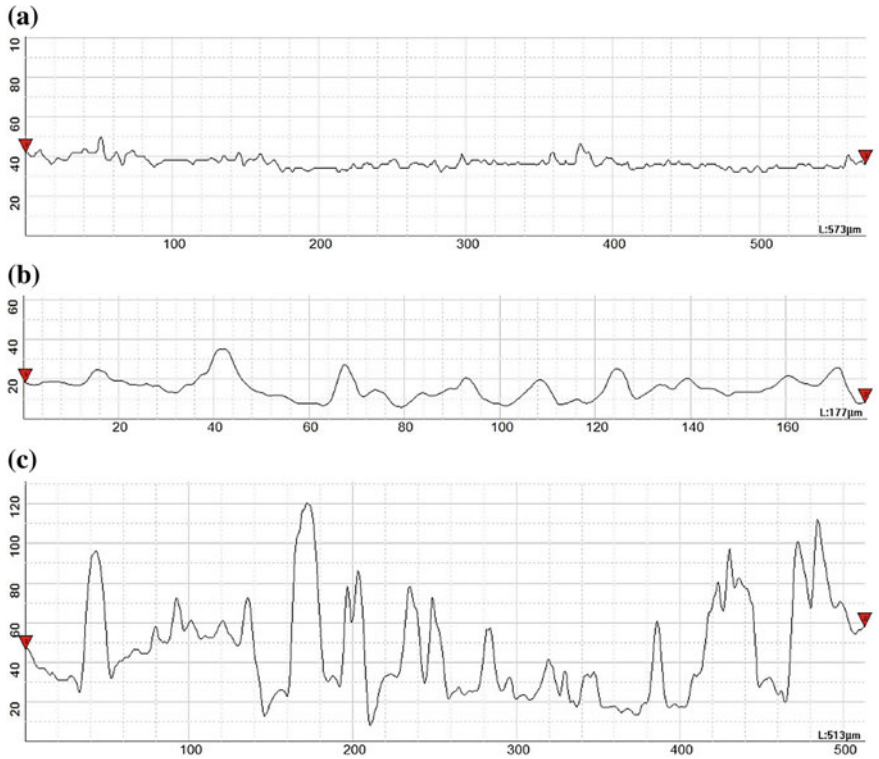

Fig. 33.3 Roughness profile (R_a) inside microgroove at 99.96% overlap. **a** 1 scan, **b** 2 scan, **c** 3 scan

Fig. 33.4 Roughness Ra at 99.96% overlap

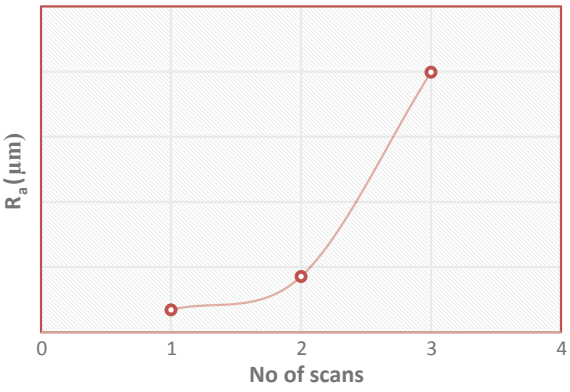

References

1. Rahman, M., Wang, Z., Wong, Y.: A Review on High-Speed Machining of Titanium Alloys ∗ **49**(1), 11–20 (2006)
2. Schaeffer, R.D.: Fundamentals of Laser Micromachining. Taylor & Francis Group, Llc CRC Press is an Imprint of Taylor & Francis Group, p. 49 (2012)
3. Zhou, W., Deng, W., Lu, L., Zhang, J., Qin, L., Ma, S., Tang, Y.: Laser micro-milling of microchannel on copper sheet as catalyst support used in microreactor for hydrogen production. Int. J. Hydrog. Energy **39**(10), 4884–4894 (2014). https://doi.org/10.1016/j.ijhydene.2014.01.041
4. Biffi, C.A., Lecis, N., Prevital, B., Vedani, M., Vimercati, G.M.: Fiber laser microdrilling of titanium and its effect on material microstructure. Int. J. Adv. Manuf. Technol. **54**(1–4), 149–160 (2011). https://doi.org/10.1007/s00170-010-2918-6
5. Lash, J.S., Gilgenbach, R.M.: Copper vapor laser drilling of copper, iron, and titanium foils in atmospheric pressure air and argon. Rev. Sci. Instrum. **64**(11), 3308–3333 (1993)
6. Biswas, R., Kuar, A. S., Biswas, S. K., Mitra, S.: Artificial neural network modelling of Nd: YAG laser microdrilling on titanium nitride-alumina composite. Proc. Inst. Mech. Eng. Part B J. Eng. Manuf. **224**(3), 473–482 (2010). https://doi.org/10.1243/09544054jem1576
7. Singh, S.K., Kumar, N.: Optimizing the EDM parameters to improve the surface roughness of titanium alloy (Ti-6AL-4V). Int. J. Emerg. Sci. Eng. **10**, 10–13 (2013)
8. Arnaboldi, S., Bassani, P., Biffi, C.A., Carnevale, M., Lecis, N., Conte, A.L., Tuissi, A.: Microcutting of NiTiCu alloy with pulsed fiber laser. In ASME 2010 10th Biennial Conference on Engineering Systems Design and Analysis. American Society of Mechanical Engineers, pp. 593–602 (2010)
9. Saklakoglu, I.E., Kasman, S.: Investigation of micro-milling process parameters for surface roughness and milling depth. Int. J. Adv. Manuf. Technol. **54**(5–8), 567–578 (2011). https://doi.org/10.1007/s00170-010-2953-3
10. Montogomery, design and analysis of experiment Arizona (2013)

Chapter 34
Evaluation of Side Wall Roughness and Material Removal Rate in Vibration Assisted Powder Mixed Micro-EDM Drilling on Inconel 718

Deepak G. Dilip, Satyananda Panda and Jose Mathew

Abstract Micro-EDM drilling on difficult to machine materials has disadvantages like low MRR, high surface roughness, and others. In this manuscript the effect of two variants, workpiece vibration frequency and powder concentration in dielectric was applied together with the normal micro-EDM drilling operation. Voltage, Electrode Rotation Speed, Feed Rate, Workpiece Vibration Frequency, and Powder Concentration in Dielectric were taken as the five factors with Material Removal Rate (MRR) and Surface roughness along the sidewalls of the hole as the responses. Box Behnken design for five factors varied in three levels was taken as the experimental design. ANOVA was done on both the responses to find the significant factors and it was observed that all five factors were significant in both the cases. Multi-objective optimization using desirability approach was done and the optimum parameter setting was obtained. The optimized results were then validated with experiments and the relative error obtained was less than 4%.

Keywords Micro-EDM · SiC · Optical profiler · Areal surface roughness

34.1 Introduction

The society's demand for high precise minute components has prompted the manufacturing industries to go for newer materials and high precision operations. Micro machining has emerged to be a very important methodology for precision machining

D. G. Dilip (✉) · J. Mathew
Department of Mechanical Engineering, National Institute of Technology Calicut, Kozhikode 673601, Kerala, India
e-mail: deepakgd1@yahoo.co.in

D. G. Dilip
Department of Mechanical Engineering, Mar Baselios College of Engineering and Technology, Trivandrum 695001, Kerala, India

S. Panda
Department of Mathematics, National Institute of Technology Calicut, Kozhikode 673601, Kerala, India

M. S. Shunmugam and M. Kanthababu (eds.), *Advances in Micro and Nano Manufacturing and Surface Engineering*, Lecture Notes on Multidisciplinary Industrial Engineering,
https://doi.org/10.1007/978-981-32-9425-7_34

of minute parts. Micro machining can be defined as the methodology to manufacture components in the size range of 1–500 μm. Micro machining is basically a scaled down version of the original manufacturing process [1]. The advent of new materials which are capable to withstand the arduous environments without much wear has called upon the manufacturing industries to look for newer machining techniques, as almost all these materials come under the category of difficult to machine materials. Electrical Discharge Machining (EDM), which due to its unique ability to machine any electrically conductive material irrespective of their mechanical properties is an ideal method to machine these new materials. EDM is a thermal process where material removal happens via melting and vaporization. EDM works on the principle of spark machining. The two electrically conductive electrodes are connected to the positive and negative terminals, respectively; a gap is maintained between them, which is filled with a dielectric fluid. The negative tool electrode is moved downwards and when a certain optimum gap is reached the dielectric breaks down making the gap conductive in nature and sparking occurs [2]. Micro-EDM is a scaled down form of EDM where the material removal mechanism is similar to that of EDM with certain small differences like small unit removal to facilitate for accurate machining, increased frequency of sparks, etc.

One of the major applications of micro-EDM comes in deep hole drilling. The conventional drilling process has some inherent disadvantages like high cutting and thrust forces, burr formation, poor surface finish, etc. In micro-EDM drilling, the tool electrode is rotated and the holes are made using the spark discharge mechanism of EDM which eliminates the disadvantages of the normal drilling process. Before going to the main content of the paper, a brief overview of various works conducted in this regard is presented as follows.

The micro-EDM drilling process is associated with poor surface finish, low MRR, high overcut, and taper. One important methodology to overcome this issue is to mix semiconductor powder particles in the dielectric. This variant is known as powder mixed micro-EDM (PMMEDM). Here the conducting powder particles in the dielectric provide a bridging effect between the tool and the workpiece thereby the plasma channel becomes enlarged and widened. The spark is uniformly distributed among the powder particles, hence electric density of the spark decreases. Due to uniform distribution of the spark among the powder particles, shallow craters are produced on the workpiece surface. This results in improvement in surface finish [3]. Kibria et al. [4] concluded that there is a great influence of mixing of boron carbide additive in deionized water dielectrics for enhancing machining performance characteristics in micro-EDM during micro hole generation on Ti-6Al-4V alloy. Kuriachen et al. [5] studied the effects of EDM parameters like voltage, capacitance, and Silicon carbide powder concentration in dielectric on MRR and tool wear rate (TWR) during micro-EDM milling. From the obtained results, it was recommended to use powder concentration of 5 g/L, capacitance of 0.1 μF, and voltage of 115 V for achieving highest material removal and lowest tool wear.

Another variant which has been extensively applied in improving micro-EDM drilling process stability is providing axial vibration to the workpiece while machining. There are two important methods by which ultrasonic vibration to the tool or

workpiece can improve the overall performance of EDM/micro-EDM. One is by direct contribution to the material removal and the other by assistance in dielectric flushing. Sundaram et al. [6] conducted a study on process parameters of ultrasonic assisted Micro-EDM based on Taguchi Method and observed that a good reduction of machining time was observed which results in reduced tool wear. Li et al. [7] studied the morphology of micro holes and linear grooves made on cemented carbide tools using micro-EDM assisted with high frequency vibration. Results showed that micro holes and linear grooves with high dimension accuracy and exact position were machined by micro-EDM assisted with high frequency vibration. Jahan et al. [8] investigated the feasibility of drilling deep micro holes in difficult-to-cut tungsten carbide by means of low frequency workpiece vibration assisted micro-EDM. He observed that the workpiece vibration has a significant effect on the removal of debris particles from the machining zone. The arcing and short-circuiting was reduced considerably, thus improving the overall machining conditions.

Prihandana et al. [9, 10] conducted the effect of ultrasonic vibration in powder mixed micro-EDM studies and concluded that there was a drastic improvement in the overall machining performance with respect to the MRR. The literature survey conducted points to the fact that the overall machining stability can be improved by the addition of powder in the dielectric and imparting vibration on the workpiece surface.

In the present work, an attempt has been made to combine the effectiveness of both powder mixed dielectric and vibration assisted workpiece on the micro-EDM drilling of Inconel 718. The MRR and sidewall roughness (SWR) were taken as the responses with Voltage, Feed rate, Electrode Rotation Speed (ERS), Workpiece Vibration frequency, and Powder concentration in dielectric being the five factors. Here the vibration frequency and powder concentration are varied along with other factors to find the optimum combination which gives the highest MRR and lowest surface roughness on the sidewalls.

34.2 Experimental Setup

The experiments were conducted on DT-110 Multipurpose micro machining centre, make: Mikrotools Singapore. Voltage, Feed Rate, ERS, Vibration frequency and Powder concentration were taken as the factors with MRR and SWR being the responses. All the factors were varied in three levels and they are as shown in Table 34.1.

Response surface methodology was used to formulate the experimental design and Box Behnken design for five factors all varied in three levels was selected amounting to a total of 45 runs. In order to do the experiments, an external dielectric circulation system was made. The low frequency vibration device is kept in the dielectric tank and the workpiece was fixed on top of it. The nozzle fed the dielectric onto the machining zone and continuous circulation takes place during drilling. The powder particle used is SiC. Tungsten carbide rod of 0.4 mm diameter was taken as the tool electrode with Inconel 718 sheets of thickness 2 mm as the workpiece. Through

Table 34.1 Factors and their various levels

Factor	−1	0	+1
Voltage (A)	80 V	115 V	150 V
ERS (B)	800 rpm	1600 rpm	2400 rpm
Feed rate (C)	8 μm/s	16 μm/s	24 μm/s
Frequency (D)	300 Hz	650 Hz	1000 Hz
Powder con: (E)	2 g/l	4 g/l	6 g/l

holes were drilled with the experimental setup as per the experimental design and the MRR and Surface roughness along the sidewalls were measured and analyzed.

34.3 Results and Discussion

The holes were drilled as per the experimental design and the major factors which determine the feasibility of the process, MRR, and surface roughness along the sidewalls of the holes were measured. The results were analyzed and then multi-objective optimization was done on the obtained MRR and surface roughness to identify the ideal combination for machining.

34.3.1 Analysis of Material Removal Rate

Material Removal Rate (MRR) is the most important parameter which determines the economic feasibility of a process. During micro-EDM drilling using a cylindrical electrode, though we expect a cylindrical hole with dimensions equal to that of the tool, errors due to side sparking and improper flushing of debris lead to a shape similar to a frustum of a cone. The MRR was calculated using Eq. (34.1).

$$MRR = \frac{Volume\ of\ the\ cone}{time} = \frac{\frac{1}{3}\pi\left(x_1^2 + x_2^2 + x_1x_2\right)h_1}{t}, \tag{34.1}$$

where x_1 and x_2 are the top and bottom radii of the hole, respectively, h1 is the depth of the hole and t is the total time taken for drilling the hole. The top and bottom diameter were measured using a noncontact 3D optical profiler, Make: Alicona and the thickness of the sheet was taken as the depth. Experiments were conducted, and Analysis of Variance (ANOVA) with 95% confidence interval was done for the obtained MRR to find out the significant factors. Minitab was used for the analysis.

The regression equation in terms of coded factors considering only the significant terms has been shown in Eq. (34.2).

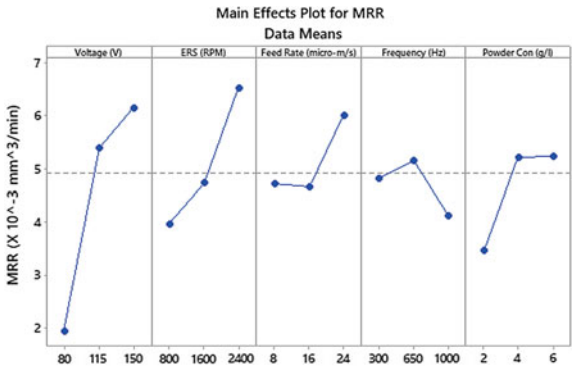

Fig. 34.1 Main effects plot for MRR

$$MRR = +6.44 + 2.11 \times A + 1.28 \times B + 0.6455 \times C - 0.3442 \times D + 0.8875 \times E + 1.42 \times AB + 1.02 \times BC - 0.9792 \times BD + 0.8551 \times BE - 0.8543 \times CE - 1.76 \times A2 - 1.19 \times D2 - 1.35 \times E2 \quad (34.2)$$

The R^2, Adj. R^2 and Pred. R^2 values are 0.9199, 0.8825, and 0.8061, respectively. This shows that the equation is valid in the design space and all the factors are significant. The main effects plot showing the average variation of MRR with respect to all factors individually are shown in Fig. 34.1.

The MRR is directly dependent on the discharge energy, so when the voltage increases the intensity of each spark increases resulting in more material removal per spark, leading to an increased MRR. The ERS also positively influences the MRR, as the electrode rotation helps in flushing the debris particles and continuous circulation of the powder particles within the discharge zone. Thus as ERS increases MRR also increases. MRR stays almost constant initially on increasing the feed rate till 16 μm/s and increases on increasing it further. Thus by increasing the feed rate the sparking rate increases and the overall MRR increases. The workpiece vibration frequency provides an axial motion onto the debris particles facilitating its easy removal from the discharge zone during machining. As we increase the frequency to 1000 Hz, the very high workpiece vibration results in high undulation within the dielectric leading to the debris and the powder particles being scattered towards the sides and thus resulting in more side sparking and reduction in MRR. The powder in dielectric has a positive influence on the MRR. The powder particles create a bridge between the tool and the workpiece, thus reducing the dielectric strength. This results in an increased spark gap which in turn increases the MRR.

34.3.2 Analysis of Surface Roughness Along Sidewall

The applications for a machining process are directly dependent upon the quality of the surfaces generated by it. In this study, the surface finish of the micro-EDM drilled holes was evaluated by calculating the sidewall roughness (SWR). Sa is the extension of Ra (arithmetical mean height of a line) to a surface. It expresses, as an absolute value, the difference in the height of each point (Z(x, y)) compared to the arithmetical mean of the surface. It can be expressed mathematically as

$$Sa = \frac{1}{A} \iint_A |Z(x, y)| dx dy \tag{34.3}$$

The measured roughness values were analyzed by ANOVA and the regression equation considering the significant factors is given by Eq. (34.4).

$$SWR = +1.69 + 0.3860 \times A + 0.0395 \times B + 0.1171 \times C + 0.0641 \times D - 0.1668 \times E + 0.2114 \times AC - 0.0704 \times B^2 - 0.1609 \times E^2 \tag{34.4}$$

The R^2, Adj. R^2, and Pred. R^2 values are 0.883, 0.857, and 0.796, respectively. This shows that the equation is valid in the design space and all the factors are significant. The main effects plot showing the average variation of SWR with respect to all factors individually are shown in Fig. 34.2.

The increase in voltage results in more material being removed per spark as we observed from Fig. 34.1; more material removed means increased crater depth and higher surface roughness. ERS does not have much of an influence in the SWR and it remains almost a constant within the design space. As the feed rate increases the rate of sparking increases, which in turn attributes to the increased SWR.

The workpiece vibration adversely affects the surface finish. An increase in vibration frequency attributes to the powder particles axially being moved in the discharge

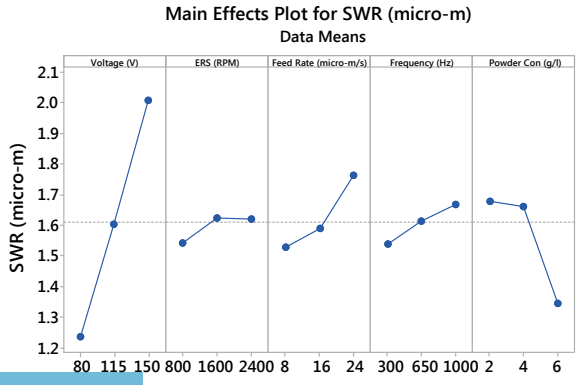

Fig. 34.2 Main effects plot for sidewall roughness

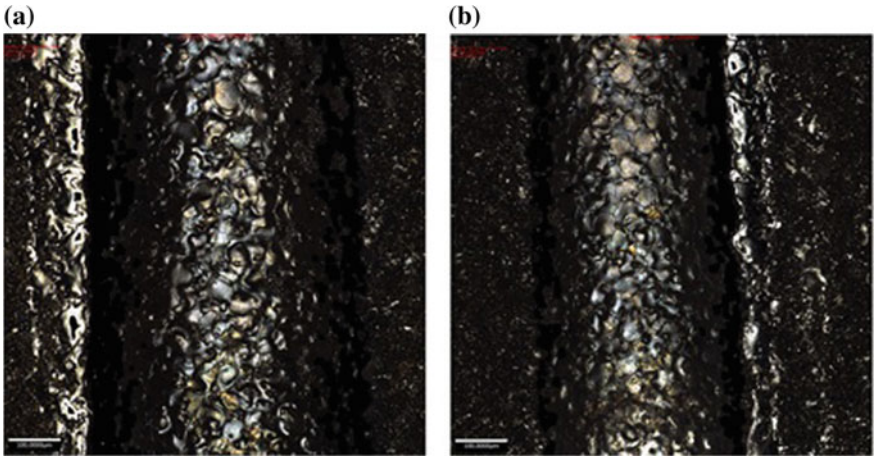

Fig. 34.3 Sidewall of hole drilled at **a** 115 V, 1600 rpm, 8 μm/s, 1000 Hz and 4 g/l **b** 80 V, 1600 rpm, 16 μm/s, 650 Hz and 6 g/l

zone. This may lead to the powder particles being embedded onto the surface causing unevenness or the powder particles causing surface damage due to the impact force leading to increased SWR. As we increase the powder concentration, the surface roughness reduces due to the multiple bridges being formed in the discharge zone which in turn results in shallower craters. Figure 34.3a, b bear testimony to the fact that shallower craters are seen in the low voltage high powder concentration condition.

34.3.3 Multi-objective Optimization of MRR and SWR

The multi-objective optimization with the aim of maximizing MRR and minimizing SWR was done using Minitab. Desirability approach was followed and the optimum condition obtained was Voltage 126 V, ERS 2400 rpm, Feed rate 12.7 μm/s, Vibration Frequency 392 Hz, and Powder concentration 6 g/l. The composite desirability was obtained as 0.81. The obtained reading was then validated experimentally and is as shown in Table 34.2. The relative error percentage was observed to be less than 4% validating the same.

Table 34.2 Predicted versus experimental readings for optimized result

Response	Predicted	Experimental
MRR ($\times 10^3$ mm^3/min)	8.8861	8.571
SWR (μm)	1.3306	1.3611
Error (%)	3.67	2.24

34.4 Conclusions

Vibration assisted powder mixed micro-EDM drilling was done on Inconel 718 with Voltage, Electrode Rotation speed, Feed rate, Vibration frequency, and Powder concentration in dielectric as the main factors and Material Removal Rate and Sidewall roughness as the responses. The major conclusions drawn were

- For all the factors except vibration frequency, the MRR increased by increasing the factors in the design space. For vibration frequency the local maxima were 650 Hz, beyond which the MRR reduced as very high vibration frequency leads to unwanted undulation within the dielectric resulting in inhibition of proper sparking.
- The powder concentration in the dielectric attributes in improving the surface finish by bridging the discharge from the tool onto the workpiece. This results in the distribution of the discharge channel which in turn leads to shallow craters on the workpiece resulting in better surface finish.
- Multi-objective optimization to maximize MRR and minimize SWR was done using desirability approach and the optimum condition was found to be Voltage 126 V, ERS 2400 rpm, Feed rate 12.7 μm/s, Vibration Frequency 392 Hz, and Powder concentration 6 g/l. The relative error between predicted and actual response was less than 4%.

Acknowledgements Authors would like to sincerely thank the Department of Science & Technology (DST), Govt. of India & Centre for Precision Measurements & Nanomechanical Testing, Department of Mechanical Engineering, National Institute of Technology Calicut, for providing support to carry out this work under the scheme 'Fund for improvement of Science & Technology' (No. SR/FST/ETI-388/2015).

References

1. Masuzawa, T.: State of the art of micromachining. CIRP Ann. Manuf. Tech **49**, 473–488 (2000)
2. Kunieda, M., Lauwers, B., Rajurkar, K.P., Schumacher, BM.: Advancing EDM through fundamental insight into the process. CIRP Ann.-Manuf. Tech. **54**(2), 64–87 (2005)
3. Kansal, H.K., Sehijpal, S., Pradeep, K.: Technology and research developments in powder mixed electric discharge machining (PMEDM). J. Mater. Process. Technol. **184**(1–3), 32–41 (2007)
4. Kibria, G., Sarkar, B.R., Pradhan, B.B., Bhattacharyya, B.: Comparative study of different dielectrics for micro-EDM performance during microhole machining of Ti-6Al-4V alloy. Int. J. Adv. Man. Tech. **48**(5), 557–570 (2009)
5. Kuriachen, B., Mathew, J.: Effect of powder mixed dielectric on material removal and surface modification in micro electric discharge machining of Ti-6Al-4V. Mater. Manuf. Process. **31**(4), 439–446 (2016)
6. Sundaram, M.M., Pavalarajan, G.B., Rajurkar, K.P.: A study on process parameters of ultrasonic assisted micro EDM based on Taguchi method. J. Mater. Eng. Perform. **17**, 210–215 (2008)
7. Li, Y., Deng, J., Chai, Y., Fan, W.: Surface textures on cemented carbide cutting tools by micro EDM assisted with high-frequency vibration. Int. J. Adv. Manuf. Technol. **82**(9–12), 2157–2165 (2016)

8. Jahan, M.P., Wong, Y.S., Rahman, M.: Evaluation of the effectiveness of low frequency workpiece vibration in deep-hole micro-EDM drilling of tungsten carbide. J. Manuf. Process. **14**(3), 343–359 (2012)
9. Prihandana, G.S., Mahardika, M., Hamdi, M., Wong, Y.S., Mitsui, K.: Effect of micro-powder suspension and ultrasonic vibration of dielectric fluid in micro-EDM processes—Taguchi approach. Int. J. Mach. Tool Manuf. **49**, 1035–1041 (2009)
10. Prihandana, G.S., Tutik, S., Mahardika, M.: Improvement of machining time in micro-EDM with workpiece vibration and graphite powder mixed in dielectric fluid. Indian J. Eng. Mater. Sci. **19**(6), 375–378 (2012)

Chapter 35
Analysis of Effect of Heat Treatment on Machining Characteristics During Micro-end Milling of Inconel 718

Ankit Awasthi, N. Anand Krishnan and Jose Mathew

Abstract Miniaturized products are getting great importance in highly growing industries such as aerospace, automobile, and biomedical due to the high demand and great applications of micro part/feature. Out of the different micromachining techniques, micro-end milling is one of the preferred processes because of its flexibility, ability to produce complex part, and high material removal rate. A detailed analysis of cutting force and areal surface roughness during micro-end milling of Inconel 718 is performed to analyze the effect of heat treatment on machining characteristics. The different heat treatments were performed on Inconel 718 at 920 °C. Micro-end milling experiments on different heat-treated samples by varying feed per tooth were conducted. The cutting force was measured using KISTLER dynamometer (9256C2) and areal surface roughness is measured using Alicona 3D optical profiler (Infinite Focus G5). Comparative analyzes of different heat-treated samples were analyzed. It was found that the cutting force, as well as areal surface roughness, shows a similar trend under different heat treatment conditions. At lower feed per tooth higher cutting force was observed with nonlinear pattern due to the higher plowing force. Size effect in cutting force was observed near to 1 μm feed per tooth. Outside the size effect region, both cutting force and areal surface roughness show the trend similar to macro-machining. The minimum value of areal surface roughness is obtained for water quenching condition. The minimum value of areal surface roughness obtained near to 3 μm, which is the cutting edge radius of the micro endmill cutter.

Keywords Micro-end milling · Microstructure · Heat treatment · Cutting force · Areal surface roughness · Inconel 718

A. Awasthi · N. Anand Krishnan (✉) · J. Mathew
Department of Mechanical Engineering, National Institute of Technology Calicut, Kozhikode 673601, Kerala, India
e-mail: anandkrish487@gmail.com

M. S. Shunmugam and M. Kanthababu (eds.), *Advances in Micro and Nano Manufacturing and Surface Engineering*, Lecture Notes on Multidisciplinary Industrial Engineering,
https://doi.org/10.1007/978-981-32-9425-7_35

35.1 Introduction

Micro parts/features are getting great attention in industries due to the high demand in the fields such as aerospace, automobile, biomedical, communication, and biomedical. The micro-milling is one of the most preferred micromachining techniques because of high material removal rate, low cost, great flexibility, and ability to produce complex three-dimensional features. Inconel 718, a nickel-base superalloy, is mainly intended for high-temperature applications. This property owns a complex microstructure formed by a matrix of Ni and a variety of precipitates. The type, the form, and the amount of these phases significantly affect the resulting properties of these alloys. At sufficiently long exposure to high temperatures, the transformation phase can occur, which can lead to degradation of properties of these alloys. So it is important to study the effect of heat treatment on mechanical properties of Inconel 718.

Inconel 718 has a very complex phase transformation mechanism which helps it to retain its strength even at elevated temperatures. The main matrix phase of Inconel 718 is cubic face centered. γ' is having the cubic structure and it is the equilibrium phase. γ'' is the main strengthening phase of Inconel 718 which makes it as a high strength material but it is metastable and undergoes dissolution to different phases at high temperature. The γ'' phase is having the tetragonal structure. The stable phase corresponding to the γ'' phase at high temperature is δ phase. Although the δ phase is not as such strengthening phase, it stabilizes grain size and also enhances its high-temperature rupture properties. As the high temperature is reached, the γ' and γ'' phase will dissolve and δ phase is also having a low-volume fraction, so the strength of Inconel 718 starts decreasing. But during aging, the γ'' starts converting to δ phase which results in stabilizing its mechanical properties. The δ phase is having the orthorhombic structure.

Researches have been done to analyze the behavior of Inconel 718 under different machining conditions. Iturbe et al. [1] have done the analysis to assess the machinability of Inconel 718 by microhardness measurement and microstructural analysis of samples at high temperature and strain rate. The correlation is also developed for relating mechanical properties of Inconel 718 with the microstructural state. The effect of microstructure on flow stress and cutting force on Inconel 718 is also analyzed for the milling process. The analysis is done considering the effect of grain growth and dynamic recrystallization due to the high temperature generated during machining. The grain growth improves machinability due to reduced flow stress. Softening effect such as preheating is also used to reduce the cutting force. The grain size-dependent cutting force model was developed to consider the recrystallization effect [2]. Venkatachalam et al. [3] analyzed the influence of grain boundaries, grain size, and crystallographic orientation on flow stress and cutting forces. Rahman et al. [4] investigated the effect of chip thickness and grain size on flow stress. The variation of surface quality and chip morphology due to varying tool sharpness and grain size is also analyzed. The microstructure effect on machinability of hard to machine material is also analyzed at different cutting speeds. Effect of different grain sizes,

obtained by varying annealing conditions, on cutting forces is investigated and it is observed that for large grain size, deformation twinning occurs. The effect of microstructure on tool wear is also very significant when it comes to micromachining [5]. Vipindas et al. [6] investigated the effect of cutting edge radius on cutting force, surface roughness, and chip formation during micro end milling of titanium alloy. This paper explained the cutting edge radius in detail.

A few modeling works were observed by considering the microstructure analysis in machining. Pan et al. [7] developed the model having the thermal, mechanical, and microstructural coupled analysis during machining. The analysis is also considered the microstructural changes occurred in the workpiece during machining. The changes in surface integrity and mechanical properties due to microstructure changes were also investigated. Vogler et al. [8] developed the algorithm for considering the influence of minimum uncut chip thickness. The slip line plasticity model for finding force is used when uncut chip thickness is more than the minimum chip thickness, and elastically deformable model for force is used when uncut chip thickness is less than the minimum chip thickness. Simulations were also performed at microstructure level for finding the parameters of force model. In micro-end milling, since the process inputs such as feed and depth of cut are comparable with the grain size, so it is very important to analyze the microstructure of the workpiece material too.

This work is mainly focused on the effect of heat treatment on the machining characteristics such as cutting force as well as areal surface roughness during micro-end milling of Inconel 718. Most of the literature was focused on the effect of heat treatment on the material properties only. This work describes the heat treatment effects on machining characteristics by considering microstructure and microhardness of the Inconel 718. The Inconel 718 sheets were heat treated to 920 °C (Above the recrystallization temperature); held for 15 min and then water and furnace cooling was performed. Micro-end milling experiments were performed on both heat-treated and the normal workpiece. Then the variation of the effect of feed per tooth on cutting forces, microhardness and areal surface roughness were analyzed.

35.2 Experimental Work

35.2.1 Workpiece Material

Inconel 718 is used as the workpiece material for this work because of its superior properties like high hardness, lightweight, high strength to weight ratio, high resistance to high-temperature loading, and high resistance to corrosion. Table 35.1 shows the mechanical and physical properties of Inconel 718.

Table 35.1 Properties of Inconel 718

Mechanical properties	Inconel 718
Density (kg/m^3)	8200
Thermal conductivity (W/mK)	6.5
Vickers hardness	350
Yield strength (MPa)	915
Melting temperature (°C)	1225

35.2.2 Cutting Tool

AlTiN-coated WC end mill with an effective cutter diameter of 500 μm, 80 rake angle and 100 clearance angles were used for this work. Since edge radius of the cutting tool has a major effect on size effect in micromachining, it has been physically measured using a non-contact 3D optical profiler (Make: Alicona, Model: Infinite Focus G5). The measured edge radius of the micro endmill cutter was near to 3 μm.

35.2.3 Experimental Setup

Experiments were performed using micromachining center (Make: Mikrotools, Model: DT110) with AlTiN-coated WC micro endmill tool with a diameter of 500 μm. Micro slots of 10 mm length and 0.1 mm depth of cut were machined on Inconel 718. Figure 35.1 shows the experimental setup for the cutting force measurement. Muti-component mini-dynamometer (Make: KISTLER, Model: 9256C2) was used for the cutting force measurement and areal surface roughness was measured using Alicona non-contact 3D optical profiler. Inconel 718 sheet was directly

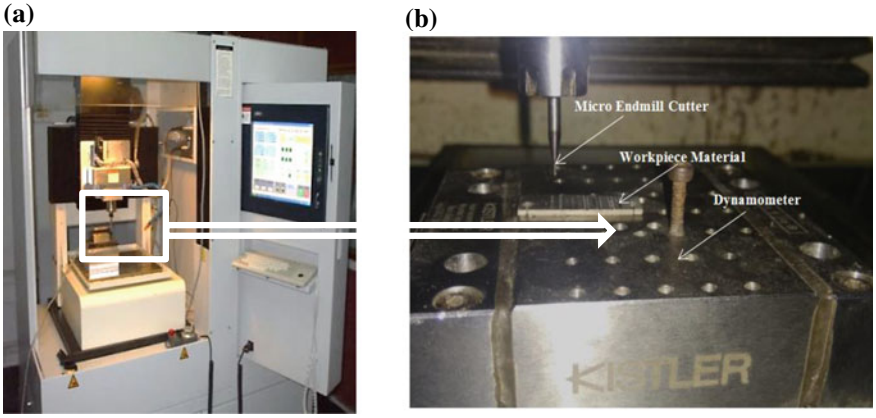

Fig. 35.1 **a** Micromachining center **b** detailed experimental setup

Table 35.2 Experimental plan

Item	Description
Machine tool	Micromachining center (DT110, Mikrotools, Singapore)
Cutting speed (m/min)	7.85
Depth of cut (mm)	0.1
Feed rate (μm/tooth)	0.1, 0.3, 0.5, 0.7, 0.9, 1.1, 1.3, 1.5,2, 2.5, 3, 3.5, 4, 4.5, 5, 5.5, 6

mounted on to the KISTLER dynamometer as shown in Fig. 35.1. Microhardness of the heat-treated and normal samples were measured using microhardness tester (Make: Matsuzawa Model: VMT-X7) by Vickers hardness method.

Workpiece samples were prepared with a dimension of 30 mm × 10 mm × 3 mm using wire EDM for performing the heat treatment and then performing the micro-end milling experiments. The heat treatment was done on the samples according to the standard heat treatment procedure. The samples were heated to 920 °C in the induction furnace and maintained at 920 °C for 15 min. Glycergia etchant was used for getting the microstructure of Inconel 718. The etching is done to obtain the grain size and to visualize the grain boundaries. Table 35.2 shows the detailed experimental plan.

35.3 Results and Discussion

35.3.1 Effect of Grain Size on Heat-Treated Samples

For Inconel 718 glycergia is used as the etchant (15 cc HCl + 10 cc Glycerol + 5 cc HNO_3) and held it for 5 s to perform the etching on the workpiece surface. The etching was done to obtain the grain size and visualize the grain boundaries. The metallurgical microscope is used to analyze the microstructure and to obtain the grain size. The line interception method is used to find the grain size. The analysis is done using ASTM E 112-2013 standards. Table 35.3 shows the grain size of the different heat-treated and normal samples.

Table 35.3 Effect of heat treatment on grain size

SI. no.	Workpiece	Grain size (μm)
1	Normal workpiece	18.5
2	Water quenching	16.5
3	Furnace cooling	20.75

Table 35.4 Effect of heat treatment on microhardness

SI. no.	Workpiece	Hardness (HV)
1	Normal workpiece	258
2	Water quenching	309
3	Furnace cooling	208

35.3.2 Effect of Microhardness on Heat-Treated Samples

Microhardnesses of the normal and heat-treated workpiece surfaces were measured using microhardness tester (Matsuzawa VMT-X7) by Vickers hardness method. The load of 10 kgf is applied for 5 s for indentation. The microhardness at three different positions on the workpiece was taken and the average was used for the comparison. The results were compared for water-quenched, furnace-cooled, and normal workpiece of Inconel 718.

The hardness value for the water quenched sample is observed to be the highest among the three because of the fast quenching rate which results in the increase in hardness value. The grain size is reduced due to fast cooling in quenching causes increase in grain boundaries. These grain boundaries act as the hindrance during machining which results in an increase in cutting force requirement. Table 35.4 shows the effect of heat treatment on microhardness.

35.3.3 Effect of Heat Treatment on Areal Surface Roughness

The areal surface roughness of the micromachined slots was measured using a non-contact 3D optical profiler (Alicona, Infinite Focus G5) using areal surface roughness (Sa). Figure 35.2 shows the variation of areal surface roughness with feed per tooth. It was found that the areal surface roughness value was minimum at a feed per tooth

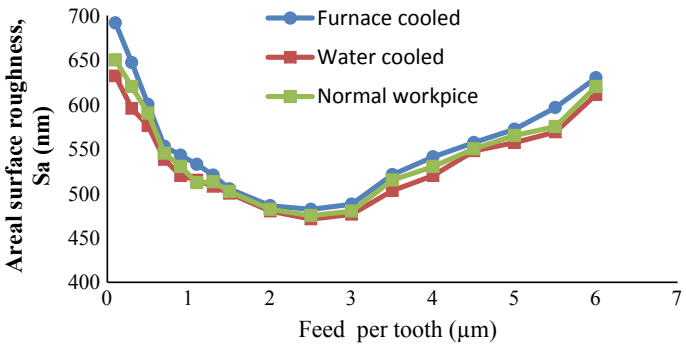

Fig. 35.2 Effect of heat treatment on the areal surface roughness

close to the cutting edge radius as the trend followed in the micromachining process. The roughness values obtained for water quenched is always higher than the furnace-cooled sample for corresponding feed per tooth. The cooling rate in furnace cooling is slow as compared to water quenching results in the grain growth and the refinement of the microstructure, which results in the development of coarse grains.

The coarse grains result in the ease in machining which results in the poor surface finish. Due to these reasons, the furnace-cooled specimens got higher areal surface roughness values as compared to water quenched specimens. While comparing the areal surface roughness results of heat-treated samples with actual workpiece sample (without heat treated), it was found that the lower value of surface roughness was obtained for water quenched samples. This is due to the fact that water quenching has a high cooling rate, which results in the removal of impurities, internal stresses, and refinement of grain structure which leads to the rearrangement of grain structure and causes the grain growth. At lower feed per tooth, the areal surface roughness obtained was very high due to high plowing in the size effect region. As the feed per tooth increased above 3 μm, the areal surface roughness showed an increasing trend as like macro-machining.

35.3.4 Effect of Heat Treatment on Cutting Force

The cutting force during micro-end milling was obtained with the help of KISTLER mini-dynamometer (9256C2). Figure 35.3 shows the variation of cutting force with the feed per tooth. In all cases, the cutting force shows a similar trend with the feed per tooth. The cutting force was observed to be minimum for all cases, where the feed per tooth is close to the minimum uncut chip thickness. The minimum uncut chip thickness is varied from one-third to one-fourth of the cutting edge radius [9]. The cutting force values obtained for water quenched was observed to be higher than the furnace-cooled sample for corresponding feed per tooth due to the lower grain size value. In the case of furnace cooling, the cooling rate is slow as compared to water

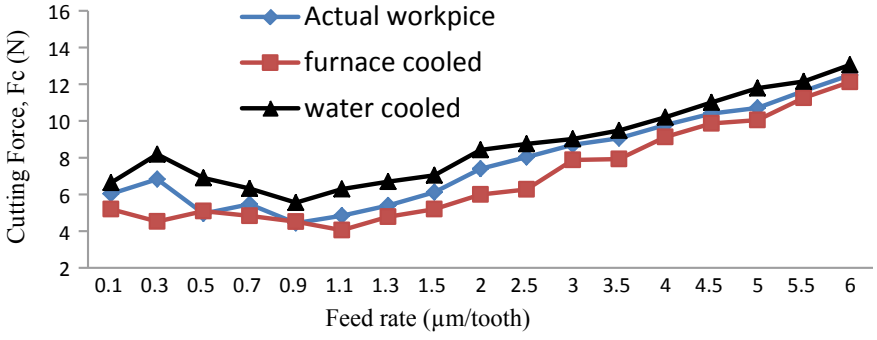

Fig. 35.3 Effect of heat treatment on cutting force

quenching which results in the grain growth and the refinement of the microstructure which results in the development of coarse grains.

The coarse grains results in the ease in machining which results in a lower cutting force. That is why, the furnace-cooled specimens have lesser cutting force values as compared to actual specimens and water quenched specimens. The cutting force at lower feed per tooth shows a nonlinear trend due to high-plowing effect in the size-affected region. Then near 1 μm feed per tooth, the cutting force shows its minimum value. So it can be observed that near to 1 μm the plowing to shearing transition occurs. According to Fernando et al. [9], the minimum uncut chip thickness varies from one-third to one-fourth of the cutting edge radius irrespective of the workpiece material and tool material. Here, the cutting edge radius of the endmill cutter is 3 μm. After 1 μm feed per tooth the cutting force shows the linear increasing trend similar to conventional machining.

35.4 Conclusions

This paper presents a detailed analysis of the effect of heat treatment on machining characteristics in micro-end milling of Inconel 718. The microstructure analysis of Inconel 718 is performed to analyze the effect of heat treatment on microhardness, cutting force, and areal surface roughness. Experimental investigation of cutting forces clearly showed the size effect in the micro-end milling process in all heat treatment conditions. For all the cases the cutting force, as well as areal surface roughness, shows a similar trend with feed per tooth. The size effect in cutting force was observed to near to 1 μm. The heat treatment of the Inconel 718 leads to change in microstructure which changes the machining characteristics. These changes are occurring mainly because of grain recrystallization and grain refinement effects. For water quenching, higher grain size was obtained due to the high cooling rate. Within the size effect region, the cutting force shows a nonlinear trend unlike macro-machining due to size effect. It was found that inside the size effect zone the areal surface roughness reduces with feed per tooth. However, outside the size effect region, the areal surface roughness showed an increasing trend with feed per tooth-like macro-machining. The minimum value of surface roughness obtained near to 3 μm, which is the edge radius of the cutting tool.

Acknowledgements The authors would like to sincerely thank Department of Science and Technology (DST), Govt. of India, and Centre for Precision Measurements and Nanomechanical Testing, Department of Mechanical Engineering, National Institute of Technology Calicut, for providing support to carry out this work under the scheme "Fund for Improvement of Science and Technology" (No. SR/FST/ETI-388/2015).

References

1. Iturbe, A., Giraud, E., Hormaetxe, E., Garay, A., Germain, G., Ostolaza, K., Arrazola, P.J.: Mechanical characterization and modelling of Inconel 718 material behavior for machining process assessment. Mater. Sci. Eng. A **682**, 441–453 (2017)
2. Pan, Z., Feng, Y., Lu, Y.T., Lin, Y.F., Hung, T.P., Hsu, F.C., Liang, S.: Force modeling of Inconel 718 laser-assisted end milling under recrystallization effects. Int. J. Adv. Manuf. Technol. **92**(5–8), 2965–2974 (2017)
3. Venkatachalam, S., Fergani, O., Li, X., Yang, J.G., Chiang, K.N., Liang, S.Y.: Microstructure effects on cutting forces and flow stress in ultra-precision machining of polycrystalline brittle materials. J. Manuf. Sci. Eng. **137**(2), 0210201-8 (2015)
4. Rahman, M.A., Rahman, M., Kumar, A.S.: Modelling of flow stress by correlating the material grain size and chip thickness in ultra-precision machining. Int. J. Mach. Tools Manuf. **123**, 57–75 (2017)
5. Nouari, M., Makich, H.: Experimental investigation on the effect of the material microstructure on tool wear when machining hard titanium alloys: Ti–6Al–4V and Ti-555. Int. J. Refract. Met. Hard Mater. **41**, 259–269 (2013)
6. Vipindas, K., Anand, K.N., Mathew, J.: Effect of cutting edge radius on micro end milling: force analysis, surface roughness, and chip formation. Int. J. Adv. Manuf. Technol. **97**, 711–722 (2018)
7. Pan, Z., Feng, Y., Liang, S.Y.: Material microstructure affected machining: a review. Manuf. Rev. **4**, 1–12 (2017)
8. Vogler, M.P., DeVor, R.E., Kapoor, S.G.: On the Modeling and analysis of machining performance in micro-endmilling, part I: surface generation. J. Manuf. Sci. Eng. **126**(4), 685–694 (2005)
9. Fernando, B.O., Alessandro, R.R., Reginaldo, T.C., Adriano, F.S.: Size effect and minimum chip thickness in micromilling. Int. J. Adv. Manuf. Technol. **89**, 39–54 (2015)

Chapter 36
Modeling of Mechanical Residual Stresses in Micro-End Milling of Ti-6Al-4V Alloy

Y. Rahul, K. Vipindas, Kattari Muni Sekhar and Jose Mathew

Abstract Wide range applications of micro-components make micromachining an important manufacturing method in industry. The distribution of machining-induced residual stresses has significant effects on the fatigue life, corrosion resistance, precision, and durability of parts. This study is focused on the modeling and validation of the residual stress induced in the workpiece after micro-end milling of Ti-6Al-4V. A coupled elasto-plastic model of mechanical stress inside the workpiece was developed to predict the residual stress. The contact between the cutter edge and the shear plane are considered a rolling contact which admits isotropic hardening only. In order to validate the developed residual stress model on the machined surface was evaluated by comparing the published literature result with similar cutting condition. It was found that the experimental and predicted values of both model and experimental results show hook-shaped distribution, with good agreement.

Keywords Micro-end milling · Ti-6Al-4V · Effective rake angle · Residual stress · Stress relaxation

36.1 Introduction

Nowadays, there is an increasing demand for micro-components in many industries such as electronics, optics, aerospace, and medicine and biotechnology. Micro-end milling, one of the micromachining methods, that utilizes end mill cutter typically vary in diameter from 1 to 500 μm and have edge radii that vary from 1 to 10 μm [1]. In micromachining as the depth of cut is become the same order as the tool edge radius, size effect come into picture and assumption that tool edge radius is

Y. Rahul · K. M. Sekhar · J. Mathew
Department of Mechanical Engineering, National Institute of Technology Calicut, Kozhikode 673601, Kerala, India

K. Vipindas (✉)
Department of Mechanical Engineering, Pandit Deendayal Petroleum University, Gandhinagar, Gujarat, India
e-mail: vipindas.k@gmail.com

M. S. Shunmugam and M. Kanthababu (eds.), *Advances in Micro and Nano Manufacturing and Surface Engineering*, Lecture Notes on Multidisciplinary Industrial Engineering,
https://doi.org/10.1007/978-981-32-9425-7_36

perfectly sharp is no longer valid. Micromachining may involve significant sliding on the flank face and plowing due to large effective negative rake angle. Plowing effect is responsible for higher surface roughness, high cutting, and thrust forces during machining [2]. It is well known that machining processes such as turning, milling, etc. create undesirable residual stresses on the surface of the workpieces. Depending upon their nature, these residual stresses can have significant effects on component life by influencing fatigue, creep, and stress corrosion cracking resistance [3]. Stress induced due to applied load higher than the material yield strength, plastic deformation of the material will be occurred. This leads to plastic strain suffered by the surface will be greater than the core. This particular behavior is associated to the different strain hardening rates of the surface layer and the core, owing to residual stress which is interlock inside the material even after external loading has been removed. Research effort has been composed of finding out induced residual stress in machining by analytical modeling, FEM modeling.

Zeng et al. [2] developed an analytical model to predict residual stress induced in workpiece during micro-end milling process. It was observed that maximum residual stress located at a depth of 2 μm from the surface and residual stress reaches to zero at depth of 12 μm. Ulutan et al. [3] and Lazoglu et al. [4] studied about the development of residual stress in machining processes. A thermomechanical model was used to predict the residual stress. Jacobus et al. [5] have proposed a model to predict in-plane biaxial residual stress developed in a machining process using incremental plasticity model. Su et al. [6] incorporated cutting force and thermal model to propose a model to predict surface and subsurface residual stress profile developed during milling process.

Zhipeng et al. [7] considered the effect of microstructural evolution on residual stress and proposed a model to predict residual stress in orthogonal turning process.

This paper presents a mathematical model to predict residual stress during micro-end milling of Ti-6Al-4V. Most of the literature on residual stress were concentrated on conventional macro machining process. In spite of widely used material in aerospace and biomedical industries, because of superior properties such as high tensile strength, low weight density, outstanding corrosion resistance, and high toughness, Ti-6Al-4V is considered to be one of the difficult machine materials due to its low thermal conductivity, high chemical affinity to tool materials, and rapid tool wear. Few works were reported in literature on modeling of residual stress especially during micro-end milling of Ti-6Al-4V. In this study Ti-6Al-4V was selected as workpiece material. An elasto-plastic model is developed to finding out the residual stress distribution in the workpiece during micro-end milling process. Governing equations would be required to relate the elastic and plastic deformation at the surface to corporate the residual stress. Generalized hooks law and associate flow rule have been used to establish the relation between increments of stress and strain. Governing equations were solved by MATLAB simulation with plane strain and isotropic hardening assumption. Simulated results were validated with the experimental observation reported in the literature.

36.2 Elastic Loading

Mechanical stress induced due to contact between the tool edge and the workpiece, and the other is due to shearing at shear plane. The tool edge contributes to a normal load coupled with a tangential load. The shear zone adds shear stress and normal stress. Combined state of stress induced at the contact of tool and the workpiece is shown in Fig. 36.1. Following assumptions have been taken during modeling that workpiece is treated as a semi-infinite, homogeneous, isotropic, and elastic-plastic material. The tool is treated as a rigid body and the workpiece deforms in a plane strain manner. Effect of heat generation in primary shear zone (due to shearing at shear plane), secondary zone (due to friction between tool and chip at the rake face of tool), and tertiary zone (rubbing between clearance face and machined surface) are neglected. Only isotropic hardening is in consideration with orthogonal machining.

36.3 Loading Beyond Yielding

From Fig. 36.2, the rectangular workpiece on which end milling operation has been performed and aim to find out the residual stress inside the workpiece at the point of interest (z) and the surface. The cutting tool tip moves in the positive x-direction as

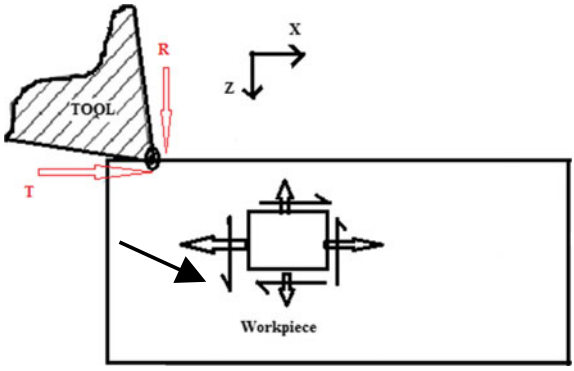

Fig. 36.1 2D model of workpiece

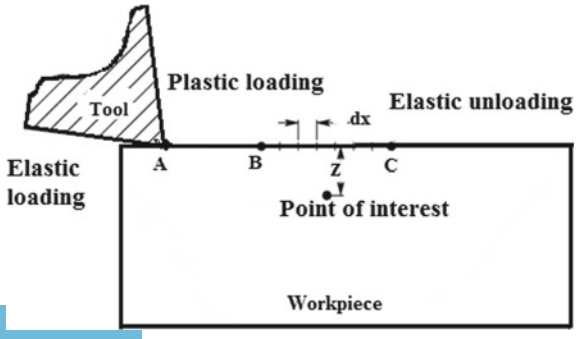

Fig. 36.2 Domain of workpiece

shown in Fig. 36.1. During this motion of the tool, stresses induced at the point of interest, initially tool is at point (A) at which elastic loading started and imparted the elastic residual stress which is recoverable and finally, say at point B in Fig. 36.2, plastic deformation starts and continues until the onset of elastic unloading at point C. In this section, the analytical approach applied within plastic zone (BC) to find out the residual stress at point of interest (z). From the fundamental elasto-plastic strain Eqs. (36.13)–(36.22), for a small movement of cutting tool in x-directions, dx, stress increments $d\sigma_{xx}$, $d\sigma_{zz}$, $d\sigma_{yy}$, and $d\sigma_{xz}$ can be calculated using Eqs. (36.13)–(36.22). The increment $d\sigma_{yy}$ can be calculated using plane strain condition during machining. Total strain increment due to elastic and plastic deformation, in the y-direction should be zero.

$$d\varepsilon_{yy} = d\varepsilon^e + d\varepsilon^p = 0 \tag{36.1}$$

Beyond the point C as shown in Fig. 36.2, elastic unloading takes place. Once the elastic unloading is completed, cutting forces reduced to zero, and it will not induce any stresses at the point of interest. Following section deals relating induced stresses during machining to the residual stresses through a relaxation procedure. Figure 36.1, shows the state of stress at a point of contact between workpiece and tool. Initially, the strain and stress developed at the point of contact are elastic in nature. From Hooke's law, the relation between stress and strain can be written as Eqs. (36.2)–(36.5).

$$d\varepsilon_{xx} = \frac{(1-\mu^2)}{E} d\sigma_{xx} - \frac{\mu(1+\mu)}{E} d\sigma_{zz} \tag{36.2}$$

$$d\varepsilon_{zz} = \frac{(1-\mu^2)}{E} d\sigma_{zz} - \frac{\mu(1+\mu)}{E} d\sigma_{xx} \tag{36.3}$$

$$d\varepsilon_{xz} = \frac{1}{2G} d\sigma_{xz} \tag{36.4}$$

$$d\varepsilon_{yy} = 0 = \frac{\boldsymbol{d\sigma_{yy}}}{E} - \frac{\mu(\boldsymbol{d\sigma_{xx}} + \boldsymbol{d\sigma_{zz}})}{E} \tag{36.5}$$

36.4 Increment in Plastic Strain Due to Plastic Loading

When the material is loaded beyond yield strength, plastic deformation initiated. To predict the exact behavior of plastic deformation, associate flow rule has been used to finding out yield function [2]. Associate flow rule is utilized to formulate the relationship between increment in stress and strain with isotropic hardening (yield

surface expansion or contraction uniformly without changing shape). Assuming that the workpiece behaves as an isotropic material and follows the Von Mises yield criteria. The yield function is defined by

$$F = \frac{1}{2} S_{ij} S_{ij} - K^2 \tag{36.6}$$

where K is yield shear strength

$$S_{ij} = \sigma_{ij} - \sigma_{kk}(\delta_{ij}/3) \tag{36.7}$$

where σ_{ij} is a resultant state of stress at a point and σ_{kk} is the sum of normal stresses as given Eq. (36.8).

$$\sigma_{kk} = (\sigma_{xx} + \sigma_{yy} + \sigma_{zz}) \tag{36.8}$$

Associated flow rule from the theory of plasticity is used to finding out the increment in plastic strain and stress in a direction normal to the yield surface. So that

$$d\varepsilon^p = d\lambda \left(\frac{dF}{d\sigma} \right)_Y \tag{36.9}$$

where $d\lambda$ is nonnegative multiplier. Using associate flow rule of plastic strain, plastic strain increment can be written as

$$d\varepsilon^p = \frac{1}{2HK^2} S_{ij} d\sigma_{kl} \tag{36.10}$$

where H is the plastic modulus, depends on plastic strain and gives the information about the change of the shape and size of the yield surface.

$$d\sigma_{kl} = \frac{(2\sigma_{xx} - \sigma_{yy} - \sigma_{zz})}{3} d\sigma_{xx} + \frac{(2\sigma_{yy} - \sigma_{xx} - \sigma_{zz})}{3} d\sigma_{yy} + \frac{(2\sigma_{zz} - \sigma_{yy} - \sigma_{xx})}{3} d\sigma_{zz} + \frac{2(3\sigma_{xz} - \sigma_{yy} - \sigma_{zz} - \sigma_{xx})}{3} d\sigma_{xz} \tag{36.11}$$

Total strain = Elastic strain + plastic strain

$$d\varepsilon_T = d\varepsilon^e + d\,\varepsilon^p \tag{36.12}$$

The total increment of strain by including elastic and plastic deformation during machining can be obtained from Eq. (36.12), as follows:

$$d\varepsilon_{xx} = \frac{(1-\mu^2)}{E} d\sigma_{xx} - \frac{\mu(1+\mu)}{E} d\sigma_{zz} + \frac{(2\sigma_{xx} - \sigma_{yy} - \sigma_{zz})}{2(H)\sigma^2} d\sigma_{kl} \tag{36.13}$$

Similarly

$$d\varepsilon_{zz} = \frac{(1-\mu^2)}{E}d\sigma_{zz} - \frac{\mu(1+\mu)}{E}d\sigma_{xx} + \frac{(2\sigma_{zz} - \sigma_{yy} - \sigma_{xx})}{2(H)\sigma^2}d\sigma_{kl} \tag{36.14}$$

$$d\varepsilon_{xz} = \frac{1}{2G}d\sigma_{zx} + \frac{(3\sigma_{xz} - \sigma_{yy} - \sigma_{zz} - \sigma_{xx})}{2(H)\sigma^2}d\sigma_{kl} \tag{36.15}$$

$$d\varepsilon_{xy} = 0 = \frac{(\boldsymbol{\sigma_{xx}} + \boldsymbol{\sigma_{yy}} + \boldsymbol{\sigma_{zz}})}{2(H)\sigma^2}d\sigma_{kl} \tag{36.16}$$

Levi–Mises relation is used to relate the increment in strain with stress within plastic deformation zone as written in Eqs. (36.17) and (36.18).

$$\frac{d\varepsilon^p_{xx}}{\sigma_{xx}} = \frac{d\varepsilon^p_{zz}}{\sigma_{zz}} \tag{36.17}$$

$$\frac{d\varepsilon^p_{zz}}{\sigma_{zz}} = \frac{d\varepsilon^p_{zx}}{\sigma_{xz}} \tag{36.18}$$

where

$$d\varepsilon^p_{xx} = \frac{(2\sigma_{xx} - \sigma_{yy} - \sigma_{zz})}{2(H)\sigma^2}d\sigma_{kl} \tag{36.19}$$

$$d\varepsilon^p_{yy} = \frac{(2\sigma_{zz} - \sigma_{yy} - \sigma_{xx})}{2(H)\sigma^2}d\sigma_{kl} \tag{36.20}$$

$$d\varepsilon^p_{xz} = \frac{(3\sigma_{xz} - \sigma_{yy} - \sigma_{zz} - \sigma_{xx})}{2(H)\sigma^2}d\sigma_{kl} \tag{36.21}$$

$d\sigma_{yy}$ can be solved by Eq. (36.22) given as

$$d\varepsilon_{yy} = 0 = \frac{d\sigma_{yy}}{E} - \frac{\mu(d\sigma_{xx} + d\sigma_{zz})}{E} + \frac{3}{2(H)\sigma^2}\left(\frac{2\sigma_{yy} - \sigma_{zz} - \sigma_{xx}}{3}\right)d\sigma_{kl} \tag{36.22}$$

36.5 Relaxation Procedure

Relaxation procedure is used to relax the variable to satisfying the boundary condition and it relates the increment of stress to residual stress. At end of relaxation, cutting forces reduced to zero. Thus, corresponding stress remained in workpiece would be residual stress [2, 9, 10]. According to Merwin and Johnson [8], plane strain has been

taken along the y-direction which leads to $\sigma_{zy} = \varepsilon_{yy} = \varepsilon_{yz} = \varepsilon_{xy} = 0$. The remaining stress and strain components will not vary with y-direction because (width of cut $\gg$ depth of cut). Further, surface remains planar after deformation; therefore, strain in x-direction (ε_{xx}) at the workpiece surface treated as zero and other remaining stress and strain components will not vary with x-direction. It is assumed that the equilibrium condition exists and the surface is treated as traction-free, such that σ_{zz} and σ_{zx} cannot exist. The outcome from the above discussion can summarized as follows:

$$(\varepsilon_{xx})_r = \left(\varepsilon_{yy}\right)_r = 0, (\sigma_{xx})_r = f_{1(z)}, \left(\sigma_{yy}\right)_r = f_{2(z)}, (\varepsilon_{zz})_r = f_{3(z)}, (\sigma_{zz})_r = 0,$$
$$(\varepsilon_{xz})_r = f_{4(z)}, (\sigma_{xz})_r = 0$$

Generally, during the loading, equilibrium condition does not exist. The component of residual stress should not be neglected. During relaxation, for purely elastic relaxation, yield function (F) < 0 and for elastic-plastic relaxation, yield function (F) = 0.

36.6 Simulations and Validation

In order to validate the simulated residual stress model, Simulation results are compared with the published literature experimental result [7] with similar cutting condition (Spindle speed-5000 rpm, Feed-4 mm/min, Depth of cut-100 μm, Length of slot-50 mm) and same material. Simulated model is developed for the residual stress prediction in the orthogonal end milling of Ti-6Al-4V material using associate flow rule and compared the result with published literature experimental results.

From Figs. 36.3 and 36.4, it can be observed that simulated maximum residual stress is compressive in nature at the machined surface because of high strain rate. In general, in micromachining the effect of plastic deformation dominant over thermal stress results compressive residual stress induced at the surface. The magnitude of the compressive residual stress decreases to zero at the depth 200 μm because strain hardening rate decreases with the depth. Experimentally, it was found that from published literature, maximum compressive residual stress located at the 25 μm depth from the machined surface because in actual case at the surface, less material hindered the plastic deformation owing to stress relaxation. At certain depth, bulge of material prevents the plastic deformation leading to accumulation of stress.

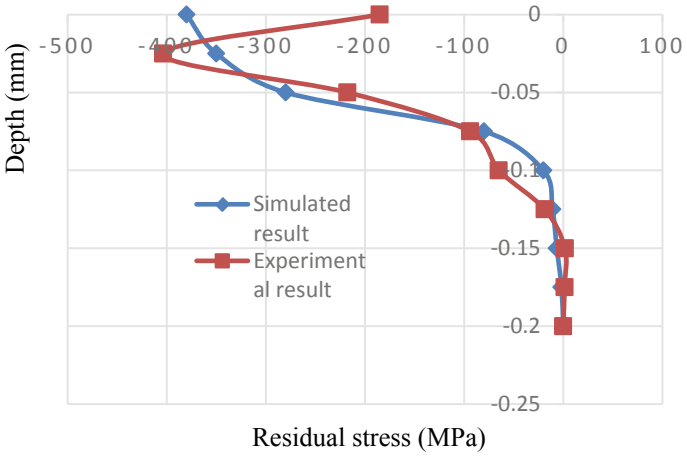

Fig. 36.3 Residual stress in transverse direction (σ_{yy})

Fig. 36.4 Residual stress in cutting direction (σ_{xx})

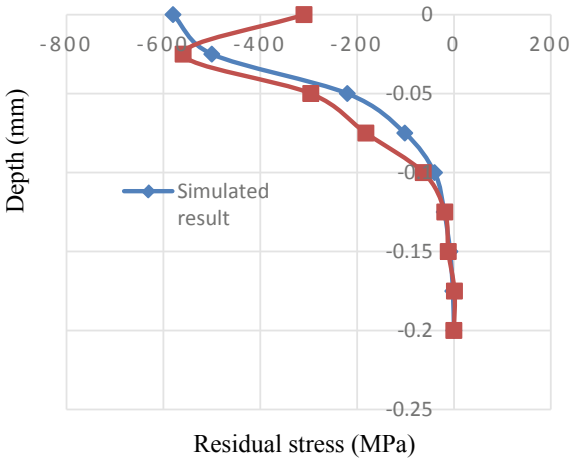

36.7 Conclusions

This study presents a method to predict residual stress during micro-end milling of Ti-6Al-4V based on the concept of theory of elasticity and plasticity. Following conclusions can be drawn from this study

1. From Figs. 36.3 and 36.4, it was observed that simulated result from the model and the experimental result from the published literature, profile and the magnitude of the residual stress beneath the surface matching better, whereas the error becomes less evident when compare residual stresses at deeper levels.

2. It was found that from the simulated results, maximum residual stress in cutting direction and in the transverse direction, located at the machined surface which is compressive in nature with a magnitude of 380 MPa and 580 MPa, respectively.
3. From the published literature experimental results, maximum residual stress in cutting direction and transverse direction, located at 25 μm below the machined surface which is compressive in nature, because of the bulge of material prevent plastic deformation at certain depth compare to surface.

Acknowledgements Authors would like to sincerely thank Department of Science and Technology (DST), Govt. of India and Centre for Precision Measurements And Nanomechanical Testing, Department of Mechanical Engineering, National Institute of Technology Calicut, for providing support to carry out this work under the scheme "Fund for improvement of Science and Technology" (No. SR/FST/ETI-388/2015).

References

1. Liu, X., Devor, R.E., Kapoor, S.G.: An analytical modeling for the prediction of minimum chip thickness in micro machining. ASME J. Manuf. Sci. Eng. **128**, 474–481 (2008)
2. Zeng, H., Yan, F., Peng, L., Zhou1, B.: An investigation of residual stresses in micro-end-milling considering sequential cuts effect. Int. J. Adv. Manuf. Technol. **91**, 3619–3634 (2017)
3. Ulutan, D., Alaca, B., Lazoglu, I.: Analytical modelling of residual stresses in machining. J. Mater. Process. Technol. **183**, 77–87 (2007)
4. Lazoglu, I., Ulutan, D., Alaca, B.E., Engine, S., Kaftanoglu, B.: An enhanced analytical model for residual stress prediction in machining. CIRP Ann. Manuf. Technol. **57**, 81–84 (2008)
5. Jacobus, K., Kapoor, S.G., Devor, R.E.: Machining-induced residual stress: experimentation and modeling. J. Manuf. Sci. Eng. **122**, 20–31 (2000)
6. Su, J.C., Young, K.A., Ma, K., Srivatsa, S., Morehouse, J.B., Liang, S.Y.: Modeling of residual stresses in milling. Int. J. Adv. Manuf. Technol. **65**, 717–733 (2013)
7. Zhipeng, P., Donald, S., Hamid, G., Steven, Y.: Residual stress prediction for turning of Ti-6Al-4V considering the microstructure evolution. Int. J. Mech. Sci. **23**, 1–9 (2017)
8. Merwin, E., Johnson, K.: An analysis of plastic deformation in rolling contact. Proc. Inst. Mech. Eng. **177**, 676–690 (1963)
9. Fergani, O., Lazoglu, I., Makddem, A.: Analytical modeling of residual stress and the induced deflection of milled thin plate. Int. J. Adv. Manuf. Technol. **75**, 455–463 (2014)
10. Peng, F.Y., Dong, Q., Yan, R., Zhou, L., Zhan, C.: Analytical modeling and experimental validation of residual stress in micro-end-milling. Int. J. Adv. Manuf. Technol. **87**, 3411–3424 (2016)

Chapter 37
Machining of High-Quality Microchannels on Ti6Al4V Using Ultra-Short Pulsed Laser

Murugesh Munaswamy and G. L. Samuel

Abstract Design and development of microscale features are found to be an evolving field of interest in various manufacturing industries including aerospace, automobile, spacecraft, and biomedical. Even though there are various advancements in ultraprecision machining techniques, accomplishment of microscale features with higher geometrical quality is still found to be the critical area of research, which needs to be explored as it affects the performance of the micro-components. Hence, in the present work a detailed investigation on the lasing parameter with respect to the surface integrity of microfeature has been carried out, and it is discussed in detail. Microfeatures in the form of channels and circular profile were machined on Ti6Al4V using ultra-short pulsed laser trepanning technique at various scan speeds. All the laser processed surfaces were analyzed using an optical microscope and 3D profilometer to evaluate the formation of heat-affected zone. Experimental results show a significant reduction in the width of heat-affected zone with the increase in scan speed from 2 to 2000 mm/s. Further analysis on the profile of the microfeature depicted the occurrence of higher order distortions at scan speed of 2 mm/s, which can be attributed to the occurrence of re-solidification layer and debris entrapment. A benchmark can be set from the current observations for the future investigations in selecting the optimal scan speed for achieving high-quality microfeatures on Ti6Al4V.

Keywords Ultrafast pulsed laser · Trepanning · Microfeatures · Characterization

37.1 Introduction

In recent years, laser micromachining is playing a major role in the field of advanced material processing. Conventional short pulse lasers (nanosecond, picosecond) are having limitation to produce the high accuracy microfeatures due to thermal damage

M. Munaswamy · G. L. Samuel (✉)
Manufacturing Engineering Section, Department of Mechanical Engineering, Indian Institute of Technology Madras, Chennai 600036, India
e-mail: samuelgl@iitm.ac.in

M. S. Shunmugam and M. Kanthababu (eds.), *Advances in Micro and Nano Manufacturing and Surface Engineering*, Lecture Notes on Multidisciplinary Industrial Engineering,
https://doi.org/10.1007/978-981-32-9425-7_37

and recast layer. The development of pulsed laser technology gives a way to achieve precise control over feature size [1]. Nowadays, the importance of microchannels is rapidly increasing due to their numerous advantages. The application areas of microchannels include micro heat exchangers, micro-coolers, micro heat pipes and micropumps which are extensively used in the field of aerospace, automotive, refrigeration and air conditioning, solar system, and biomedical sectors [2]. In the present decade, developments in short pulsed laser technologies are playing a major role in micro- and nanomanufacturing due to its capabilities in controlled removal of material, which lead to a wide range of industrial applications. The ultra-short pulse lasers have the cutting-edge capabilities in producing precise microfeatures in submicron range. Various studies are available on production of microchannels on nonmetallic materials, such as Polycarbonate (PC) [3], Polymethylmethacrylate (PMMA) [4], and glass [5], but very less research activities have been reported on fabrication of microfeatures in hard to machine materials like titanium and nickel alloys. Titanium alloy Ti6Al4V is an extensively used material in industries, such as the medical field for prosthetics and surgical instruments, as well as in the other industries as diverse as aerospace and the automotive industries [6]. The micromachining/micro-drilling by nanosecond (ns) or longer pulsed lasers may be good at achieving geometrical precision but it leads to the formation of melting and recast layer. Even in picosecond pulse laser drilling, ablated surfaces display large heat-affected zones and recast layers due to high energy input and thermal stress, which affects the accuracy and reliability of the process [7, 8].

Though the ultra-short pulsed laser micromachining is having the capability of producing microfeatures without re-solidification or thermal damage, systematic investigations are essential. It is required to analyze the effects of parameters which influence the quality of the microfeatures. The key parameters include average power, fluence, and scanning speed. Effect of scanning speed on the ablation quality was investigated on regular metals such as tungsten carbide and its alloys and reported that the low scanning speed yields larger heat accumulation—ablation to recast volume ratios [9]. Hydrophobicity of micro/nano-patterned morphologies on stainless steel also infers the dependency of scanning speed. Four distinctly different nano-patterns observed at different lasing parameters, namely, nano-rippled, parabolic-pillared, elongated sinusoidal-pillared, and triple roughness nanostructures [10].

An investigation in micromachining of glass with fs pulses states the occurrences of micro-cracks at low scanning speeds. At low scanning speeds, greater number of pulses were delivered on one laser spot and more laser spots were overlapped resulting in stronger shock wave and thermal heat due to longer laser interaction time. This results in thermal cracks debris deposition as droplets at the ablation area. The results recommend the optimal scanning speed for laser ablation of Gorilla glass without cracks and debris was above 200 mm/s [11]. Very less investigations are conducted on high-temperature materials such as Ti6Al4V and Nickel alloys. In the current paper, the experiments were performed to produce microchannels (linear and circular) at various levels of scan speed with a constant average power of 8 Watts (W). The analysis of the produced microchannels is explained systematically in the subsequent sections.

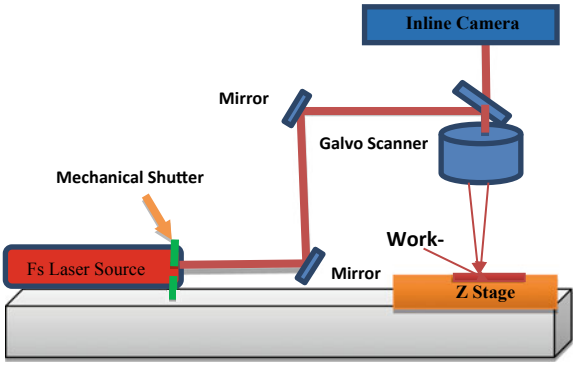

Fig. 37.1 Schematic diagram of ultrafast laser set up

37.2 Experimental Setup

37.2.1 Experimental Setup and Materials

Femtosecond (fs) laser system used for the present investigations is a commercial diode-pumped fiber laser (SATSUMA HP2, Amplitude Systems, France) with a pulse width of 350 fs at a wavelength of 1030 nm wavelength and the repetition rate of 2 kHz–2 MHz with an Acusto-Optic Modulator (AOM). The output of the collimated beam is a Gaussian profile with M 2 < 1.2 and of pulse energy 40 μJ. The polarized laser beam can be focused on the workpiece at a focal length of 255 mm at a spot size of 121 μm. The installed beam delivery unit minimizes the losses in pulse energy and ensures a higher quality laser output. The precise motion of Z-axis with a μm resolution helps to achieve the required depth by ensuring the focusing of fs laser precisely at each layer. Synchronization of Galvo scanner X- and Y-axes motion with Z-axis motion was programmed with the Kyla Software. The software was also used to flexibly control the laser path taking multiple parameters of the laser as input. The high-speed inline camera was used to monitor the process during machining. Figure 37.1 shows the schematic diagram of the micromachining facility.

The microchannels were produced on titanium alloy (Ti6Al4V). The samples of required geometry (20 × 40 × 2 mm) were prepared with the help of wire-cut electrical discharge machine (WEDM). Figure 37.2 shows the elemental composition of Ti6Al4V.

37.2.2 Characterization of Microfeatures

Microtopography of the channels was characterized by stereomicroscope (Make: Carl Zeiss™ Stemi 2000-C) and 3D optical profiling system (Wyko NT1100, Veeco Instruments). The quality of microchannels was affected by the debris entrapment,

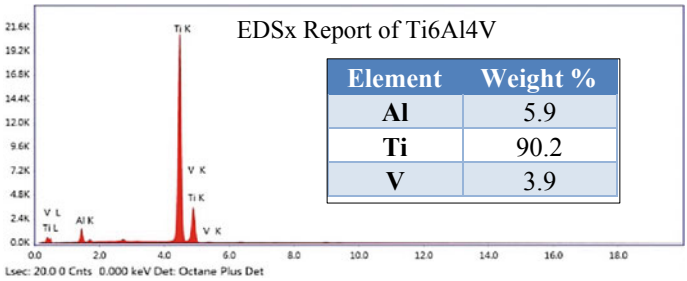

Fig. 37.2 Elemental investigations by EDSx

recast layer, and width of heat-affected zone (HAZ), altering the geometry. Achieving accurate results from the produced microfeature is possible only by removing the entrapped nanoparticles over machined surface, and hence, each sample has undergone an ultrasonic cleaning for 5 min at room temperature (25 °C). Microcracks were observed using Field Emission Scanning Electron Microscope (FESEM) (Make: Inspect™ SEM, FEI).

37.3 Results and Discussions

Computing the feasible operating range of least thermal damage and better geometrical accuracies is crucial for the mass production of microchannels. Microchannels (linear and circular) were produced at various intervals of scanning speeds. The average power was maintained at 8 W for all the experiments. The effect of scanning speed had to be investigated before deciding the full set of observations because it is one of the most significant process parameters which has a direct impact on the geometrical accuracy. Further, a poor selection of working range in scan speed leads to higher order distortions on the laser processed surfaces. The observations from the experiments are shown in Table 37.1. The full set of fixed parameters of the laser are as follows: Average power: 8 W, Pulse Repetition frequency (RR): 500 kHz for the experiments 1–3, and 200 kHz RR for experiments 4–8 (in Table 37.1). The fluence (pulse energy per unit area) will be increasing with the increase in the number of pulses. The number of pulses is calculated from Eq. (37.1).

Equation (37.1) states that there is an inverse relationship between the number of pulses and the scan speed. The number of passes (repetitions) was relatively increased to keep stable machining conditions considering the decreasing number of pulses. Observations made on both slot and circular profile.

$$\text{Number of pulses} = \frac{\text{Pulse repetiition frequency (Hz)} \times \text{Spot size (mm)}}{\text{Scanning Speed}} \quad (37.1)$$

Table 37.1 Matrix of the investigated parameters

S. no.	Scan speed (mm/s)	No. of passes	No. of pulses	Linear channel (slot)		Circular channel	
				Width of HAZ (μm)	Depth (μm)	Width of HAZ (μm)	Depth (μm)
1	2	3	90750	77.93	108	79	108
2	10	7	42350	62.94	82	60	113
3	50	11	13310	41.77	89	42	54
4	400	101	6111	22.37	92	22	93
5	800	101	3055	22.58	69	22	65
6	1200	101	2037	17.57	55	19	61
7	1600	101	1528	16.23	43	16	54
8	2000	101	1222	13.30	32	13	46

37.3.1 Micro Channel—Slot

The investigations were performed at default width of laser spot size, i.e., 121 μm. The inferences can be used in microscale up to feature size in range up to 500 μm. The experiments were started with the scanning speed of 2 mm/s (Fig. 37.3a) resulting in 90750 pulses for the span of 3 mm. It can be inferred that more overlap of each laser spots which caused a thermal shock resulted in high heat accumulation consequently higher heat-affected zone (77.93 μm). From the image, it can be noted that the width of the channel is 70.22 μm which is lower than the width of HAZ, this is due to the redeposition of debris. The second observation at 10 mm/s (Fig. 37.3b) resulting in 42350 pulses shows the reduction in the width of heat-affected zone (62.94 μm) with the channel width of 69.29 μm. Further, the third experiment at 50 mm/s (Fig. 37.3c) with 13310 pulses shows a further reduction in the width of HAZ (41.77 μm) at channel width of 65.54 μm. The trend of reduction in heat accumulation can be noticed.

It is also found the occurrence of micro-cracks at a low scanning speed of 50 mm/s and below), Fig. 37.4. Shows the micro-crack found at scan speed of 50 mm/s. This

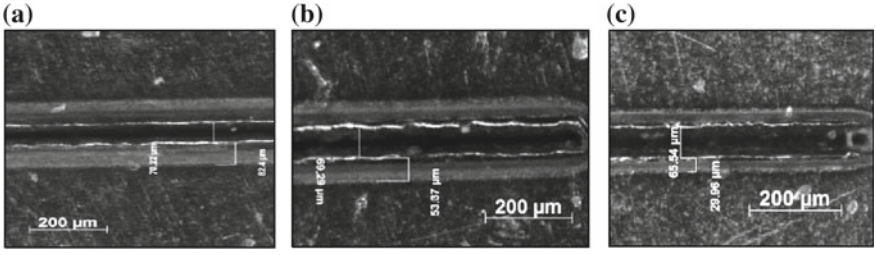

Fig. 37.3 Microchannel at low scan speeds. **a** 2 mm/s, **b** 10 mm/s, **c** 50 mm/s

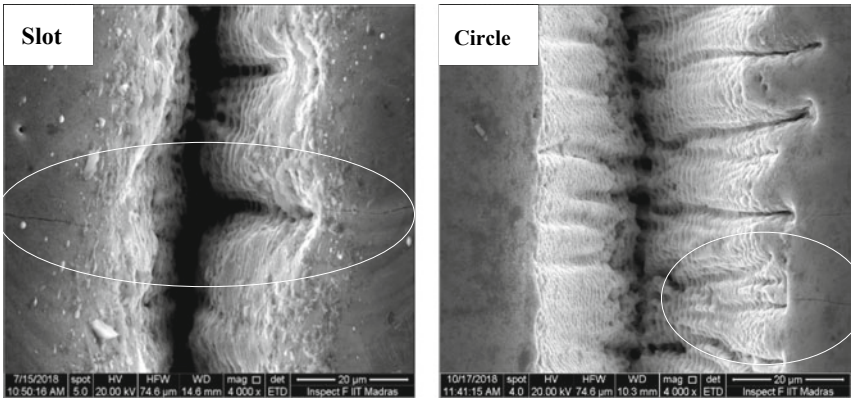

Fig. 37.4 Micro-crack found at scanning speed: 50 mm/s

is due to the thermal shock that occurs at deposition of more pulses per same laser spot [11]. The occurrence of crack was also noticed 2 mm/s and 10 mm/s. The redeposition at the ablation area can also be the oxides formed during the machining at high temperatures with vanadium element. Vanadium does not react with oxygen at room temperature but it does at elevated temperatures above 600–700 °C. The contrast of color in Fig. 37.3a–c shows the oxide layer [12].

The subsequent observations were performed at 400 mm/s (5A), 800 mm/s (5B), 1200 mm/s (5C), 1600 mm/s (5D), and 2000 mm/s (5E). It is evident that the heat accumulation is reducing with increasing scanning speed resulting in a quality channel at the scanning speed of 2000 mm/s. As mentioned earlier, the increase in scan speed results in less number of pulses per spot. The width of the channel also increased (117.64 μm at 400 mm/s) close to the programmed width of microchannel, i.e., 120 μm (123.84 μm at 2000 mm/s) (Fig. 37.5).

3D surface profile of the microchannel produced at 2 mm/s (Fig. 37.7a) and 2000 mm/s (Fig. 37.7b) is considered for additional evidence to recommend the suitable working zone of scanning speed for achieving better quality. The width of HAZ plotted against scanning speed (Fig. 37.6) confirms the decreasing trend against increasing scanning speed. As discussed above with stereo microscope images, here 3D surface also shows the evidence of resolidification with higher order debris/distortions at 2 mm/s (Fig. 37.7a) and a clear surface at 2000 mm/s (Fig. 37.7b). From 3D scan surfaces cross-sectional profile can be extracted, which can be used to find the depth of removal and the distortions on the feature; for the current observations, the cross sectional profile is shown in Fig. 37.8, the variation in depth of removal against scan speed is shown in Fig. 37.9. Considering the observations from the stereomicroscope and 3D surface profiler, the scan speed of 2000 mm/s is recommended for producing the superior quality microchannels.

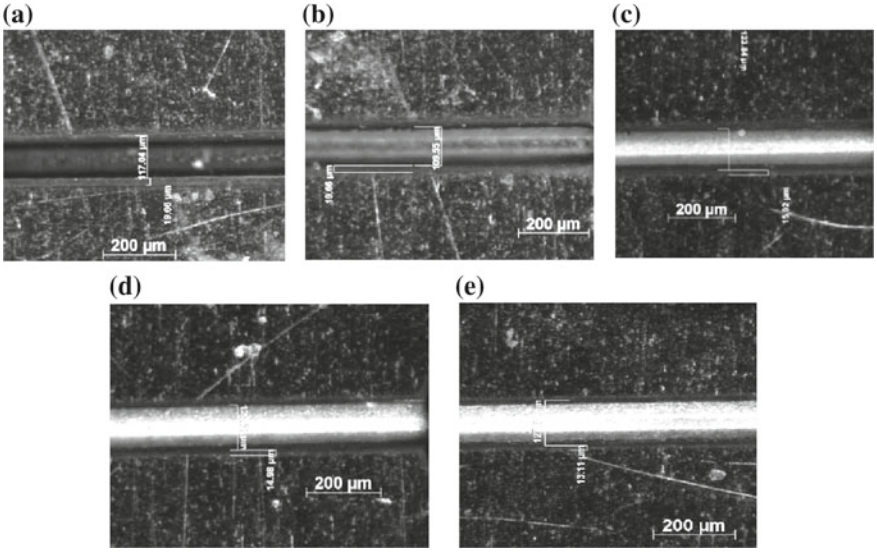

Fig. 37.5 Microchannel at higher scan speeds. **a** 400 mm/s **b** 800 mm/s **c**1200 mm/s **d** 1600 mm/s **e** 2000 mm/s

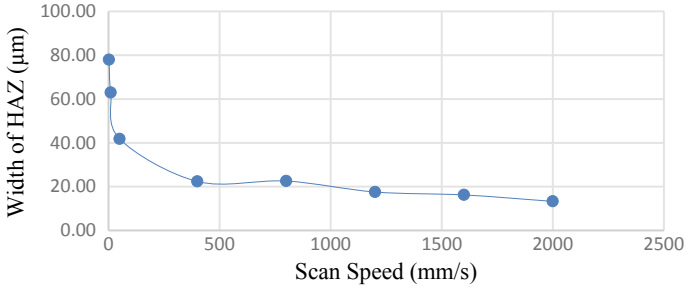

Fig. 37.6 Change in width of HAZ against scanning speed

37.3.2 Microchannel—Circular

The experimental investigations for circular microchannels were performed at the same lasing parameters as linear (slots). The microchannels produced at low scanning speeds 2 mm/s (Fig. 37.10a), 10 mm/s (Fig. 37.10b) and 50 mm/s (Fig. 37.10c) reveal the similar effects as in slots; micro-cracks, re-solidifcation, and oxidation layer. The width of HAZ at 2 mm/s found to be 79 µm, at 50 mm/s the width of HAZ reduced to 42 µm. Similar to microchannels (slots) as shown in Sect. 37.3.1, the heat accumulation is reducing with increasing scanning speed, resulting in a quality circular microchannel at the scanning speed of 2000 mm/s (Fig. 37.11).

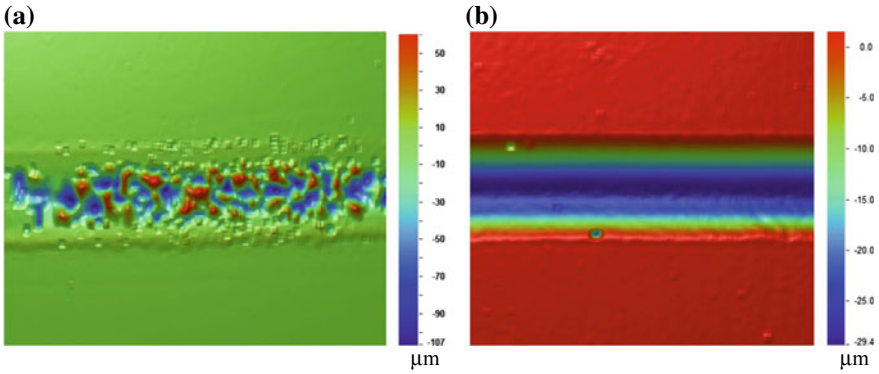

Fig. 37.7 3D surface profile. **a** 2 mm/s and **b** 2000 mm/s

Fig. 37.8 Cross-sectional profile from 3D surface date for 2 and 2000 mm/s

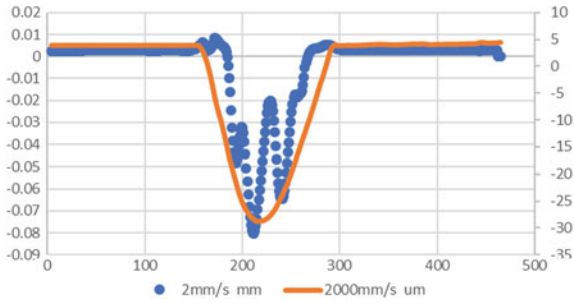

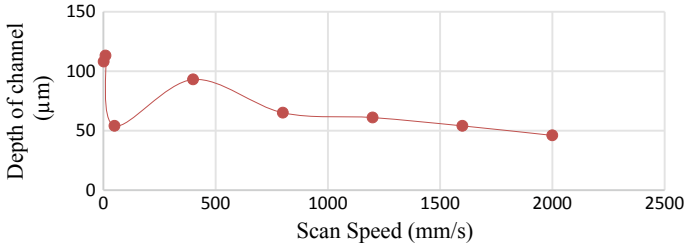

Fig. 37.9 Variation in depth of removal against scanning speed

The observation confirms the trend of change in width of HAZ and heat accumulation. The recorded values of width of HAZ shown in the plot in Fig. 37.12. The experiments at higher scanning speeds from 400 to 2000 mm/s infer the reduction in heat accumulation/thermal damage on the ablation surface. 3D Surface plots observed (Fig. 37.13) for the circular channels produced at 2 mm/s and 2000 mm/s. Similar to slots, here also the profile shows higher order distortions at 2 mm/s and uniform removal at 2000 mm/s.

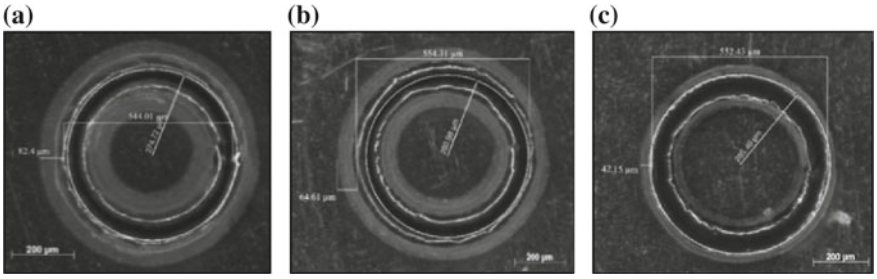

Fig. 37.10 Circular channels at scan speeds. **a** 2 mm/s, **b** 10 mm/s and **c** 50 mm/s

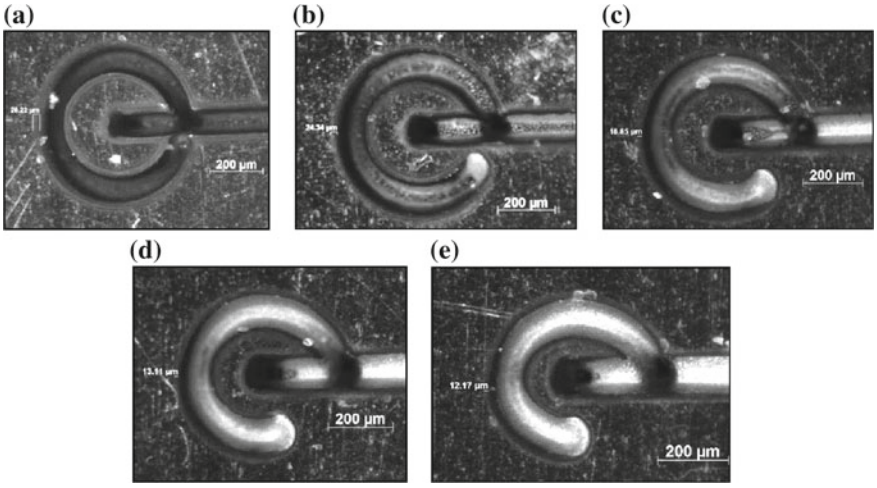

Fig. 37.11 Circular microchannels. **a** 400 mm/s, **b** 800 mm/s, **c** 1200 mm/s, **d** 1600 mm/s and **e** 2000 mm/s

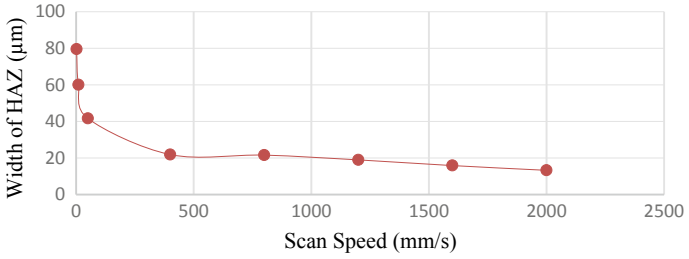

Fig. 37.12 Variation in the width of HAZ with increase in scanning speed

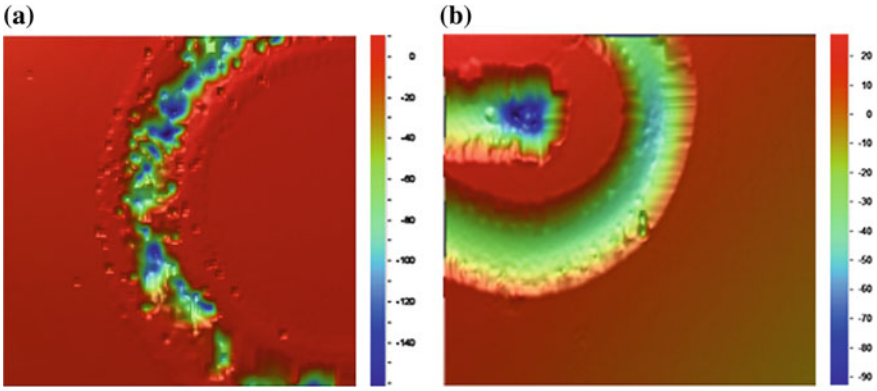

Fig. 37.13 3D surface profile of circular channels. **a** 2 mm/s, **b** 2000 mm/s

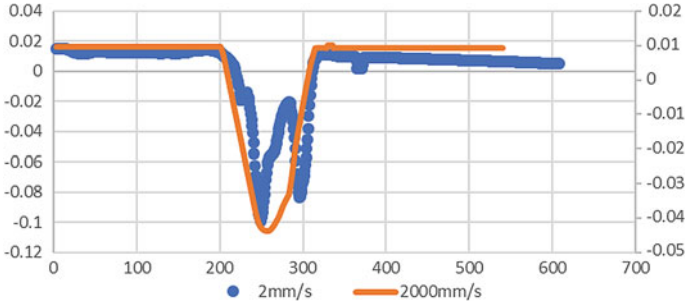

Fig. 37.14 Cross-sectional profile acquired from 3D surface profile

3D Surface profile (Fig. 37.13) with the cross-sectional profile (Fig. 37.14) shows the evidence of higher order distortions at scanning speed 2 mm/s and uniform removal at 2000 mm/s. Figure 37.15 shows the decreasing trend of the depth of removal against increase in scanning speed. From the observations, the recommended range of scanning speed for circular microchannels also can be 2000 mm/s.

37.4 Conclusion

The investigations on the effect of scanning speed in generating microfeatures (slot and circle) on Ti6Al4V confirm that the recommended scanning speed should be 2000 mm/s for uniform material removal with least heat accumulation. The thermal damage and recast layer were found to be high at the scanning speed of 2 mm/sec and was noticed to be decreasing with increase in scanning speed to 2000 mm/s (no evidence of molten component was observed). It also found that there were occurrences

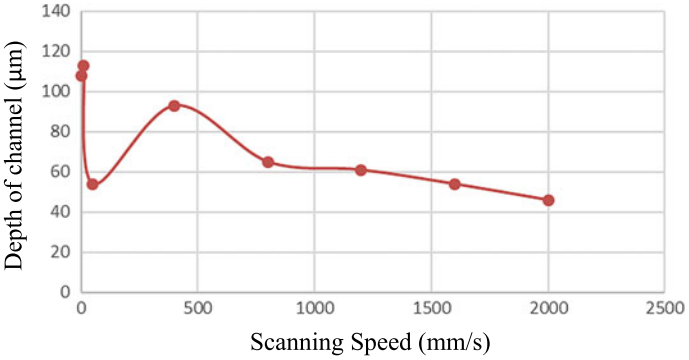

Fig. 37.15 Variation of the depth of circular channel against scan speed

of micro-cracks due to thermal shock at lows scanning speeds up to 50 mm/s. From Eq. (37.1) it can be inferred that at higher scan speeds, the number of pulses will be less which directly implies spot to spot overlap. From the current observations, it can be noted that pulses in the range of 1200 numbers provide good quality microchannels; hence, pulse duration in this range can be used for machining microfeatures. Variation in ablation rate and the lower thermal conductivity of titanium metal are found to be the predominant factors which deteriorate the geometrical quality of microfeatures. The findings from the present work can be referred as a benchmark in choosing appropriate lasing parameters for mass production of micro/nano square or rectangular fins and microchannels. The observations from the circular profiles will be helpful in adopting for micro- and nano-drilling of micro holes. The literature also confirms that an investigation on scan speed is required for producing nano-fillers or nano-texturing.

Acknowledgements The author would like to thank the financial support received from Aeronautics Research and Development Board (ARDB), Government of India, Project Number: ARDB/01/2031768/M/I dated August 10, 2015, and also scanning electron microscope at HRSEM facilities, IIT Madras.

References

1. Kiran Kumar, K., Samuel, G.L., Shunmugam, M.S.: Theoretical and experimental investigations of ultra-short pulse laser interaction on Ti6Al4V alloy. J. Mater. Process. Technol. (2018) (S0924-0136(18)30370-4)
2. Naveed, A., Saied, D., Alahmari, A.M.: Experimental investigation of dimensional variation in laser machined micro-channels produced in titanium alloy. J. Laser Micro/Nanoeng. **11**(2), 210–225 (2016)
3. David, G., Igor, G.: On the incubation effect on two thermoplastics when irradiated with ultrashort laser pulses: Broadening effects when machining microchannels. Appl. Surf. Sci. **253**, 2230–2236 (2006)

4. Shashi, P., Subrata, K.: Fabrication of microchannels on transparent PMMA using CO2 laser (10.6 μm) for microfluidic applications: an experimental investigation **16**(2), 361–366 (2015)
5. Patrik, H., Valdas, P., Michael, F.: Study of incubation effects during surface ablation using picosecond pulses at a wavelength of 800 nm. Phys. Status Solidi C **8**(9), 2862–2865 (2011)
6. Elisa, V., Daniel, T.K., Pedro, Y.N., Jorge, V.L.D.S., Joaquim, C.: Computer fluid dynamics analysis for efficient cooling and lubrication conditions in micromilling of Ti6Al4V alloy. Mater. Manuf. Process. **29**, 1494–1501 (2014)
7. Weck, A., Crawford, T.H.R., Wilkinson, D.S., Haugen, H.K., Preston, J.S.: Laser drilling of high aspect ratio holes in copper with femtosecond, picosecond and nanosecond pulses. Appl. Phys. A (90), 537–543 (2008)
8. Ancona, A., Doring, S., Jauregui, C., Röser, F., Limpert, J., Nolte, S., Tünnermann, A.: Femtosecond and picosecond laser drilling of metals at high repetition rates and average powers. Opt. Lett. **34**(21), 3304–3306 (2009)
9. Mensink, K., Penilla, E.H., Martınez-Torres, P., Cuando, N., Mathaudhu, S., Aguilar, G.: High repetition rate femtosecond laser heat accumulation and ablation thresholds in cobalt-binder and binderless tungsten carbides. J. Mater. Process. Technol. (2018) (S0924-0136(18)30427-8)
10. Moradi, S., Kamal, S., Englezos, P., Hatzikiriakos, S.G.: Femtosecond laser irradiation of metallic surfaces: effects of laser parameters on superhydrophobicity. Nanotechnology **24**, 415302 (2013)
11. Wang, Z.K., Seow, W.L., Wang, X.C., Zheng, H.Y.: Effect of laser beam scanning mode on material removal efficiency in laser ablation for micromachining of glass. J. Laser Appl. (S2), S28004-1 to 6 (2015)
12. Frangini, S., Mignone, A., de Riccardis, F.: Various aspects of the air oxidation behaviour of a Ti6Al4V alloy at temperatures in the range 600–700 °C. J. Mater. Sci. **29**(3), 714–720 (1994)

Chapter 38
Investigation of Electrochemical Micromachining Process Using Ultrasonic Heated Electrolyte

M. Soundarrajan and R. Thanigaivelan

Abstract Electrochemical micromachining (EMM) is one of the important machining methods for fabrication of micro-components on alloys and composites materials. Fabrication of micro hole is the important micro-machined feature, which are used in many components that find application in various fields such as aerospace, automobile, power circuit board (PCB), Ink jet nozzle, and the electronics industries. In this research, micro-hole is generated on 300 μm thick copper workpiece using 460 μm diameter stainless steel electrode. Sodium nitrate ($NaNO_3$) is considered as electrolyte and during machining process, the electrolyte is heated using Ultrasonic Vibration (USV). The experiments are planned according to L_{18} Orthogonal Array (OA) using the machining parameters such as electrolyte concentration, machining voltage, duty cycle, and electrolyte temperature. The machining parameters are optimized using Multi-Objective Optimization of Ratio Analysis (MOORA) method. Weight of each response is calculated using entropy method as w_j for Material Removal Rate (MRR) = 0.4941 and w_j for Overcut (OC) = 0.5051. The optimal combination obtained using MOORA is 30 g/l of electrolyte concentration, 9 V of machining voltage, 55% of duty cycle, and 36° of electrolyte temperature. According to Analysis of Variance (ANOVA) results, the machining voltage contributes about 55% of overall performance. Additionally, Scanning Electron Microscope (SEM) images are taken for the further understanding of micro-hole profile.

Keywords Electrochemical · Heated electrolyte · Ultrasonic · Entropy · MOORA

M. Soundarrajan (✉)
Department of Mechanical Engineering, Muthayammal Engineering College (Autonomous), Rasipuram, Namakkal (Dt) 637408, India
e-mail: soundarrajan05@gmail.com

R. Thanigaivelan
Department of Mechanical Engineering, Muthayammal Engineering College (Autonomous), Rasipuram, Namakkal (Dt) 637408, India
e-mail: tvelan10@gmail.com

M. S. Shunmugam and M. Kanthababu (eds.), *Advances in Micro and Nano Manufacturing and Surface Engineering*, Lecture Notes on Multidisciplinary Industrial Engineering,
https://doi.org/10.1007/978-981-32-9425-7_38

38.1 Introduction

Due the operational method of traditional machining, manufacturing of burr-free surface in the copper material is the difficult task due to the geometry of the tool, rotational speed, and vibration [1]. EMM is one of the dependable methods for micro-machining of copper with accuracy [2]. In the last decade, various research works has been carried out worldwide to improve the machining performance of EMM. Bhattacharyya et al. [3] have studied the machining performance of EMM on a copper plate in addition to vibration of the tool. They found that sludge removal from the machining zone significantly improved the machining rate and accuracy. Liu et al. [4] have used two types of electrolytes such as aqueous NaCl and ethylene glycol mixed NaCl in EMM on titanium alloy. These electrolytes significantly influence the taper angle and surface roughness. Zhang et al. [5] have used as quasi-solid electrolyte (agarose hydrogel) in NaOH solution to fabricate the micro-tools in EMM. They noted that the accuracy of micro-tool increased significantly in quasi-solid electrolyte than the liquid electrolyte. Guodong et al. [6] have investigated the effect composite electrolyte at different concentration levels for machining stainless steel. They found that the mixture of sodium nitrate with sodium citrate stimulates the ion attraction in the electrolyte. Therefore, disposal of dissolved material is unhindered in the inter-electrode gap which leads to high material removal and better accuracy. Sekar et al. [7] have blended the nanocopper particles in aqueous NaCl electrolyte to machine high carbon and high chromium die steel. The copper particle crashes the hydrogen bubbles in the machining area resulting in an increase in the material removal rate and good surface quality. The optimization of process parameters plays a vital role in manufacturing for reducing the machining time and cost. Therefore, various optimization techniques has been followed by the researchers since the last decade. Jeykrishnan et al. [8] have used the Taguchi technique in ECM on D3 die steel to optimize the machining parameters. From the above literatures, it is understood that the researchers have improved the EMM performance with various types of electrolytes and optimized the process parameters with different techniques. This research focuses on electrolyte heating and in electrochemical machining, the electrolyte temperature plays s significant role in material removal [9]. Different methods are adapted by the researchers to heat the electrolyte and all those methods have disadvantages of heating the subsystems of the EMM setup. Considering this difficulty, a detailed experiment is planned to introduce USV to simultaneously heat and vibrate the electrolyte [10]. Here the USV is kept in the electrolyte tank and heating of the other EMM subsystems is averted The effect of electrolyte temperature on EMM process is studied with L_{18} OA experiment design and the process parameters are optimized by the MOORA method.

38.2 Experimental Method

Figure 38.1 shows the EMM system used for conducting experiments. The experiments are carried out using an indigenously developed system. The EMM system operated with the subsystems such as tool feeding system, pulse rectifier, and electrolyte supply system. Stainless steel of Φ 460 μm is used as electrode, and 300 μm thick copper plate is used as a work-piece. The electrode is insulated with epoxy resin to reduce overcut. The aqueous sodium nitrate ($NaNO_3$) is used as an electrolyte. The machining time has been noted using a stop watch for through-hole machining. The completion of through hole is witnessed by evaluation of hydrogen gas bubbles beneath the workpiece. The experiments are carried out on the basis of L_{18} OA and the temperature of the electrolyte is measured using a digital thermometer. Commercially available 24 V ultrasonic mist maker is used as the ultrasonic vibrator, which is fixed in the electrolyte tank in a partially submerged position. The ultrasonic vibrator inbuilt with 110 kHz piezoelectric transducer and Φ 20 mm ceramic plate to generate high-frequency vibration is passed beneath the electrolyte surface. The high-frequency vibration creates rapid collision among the water molecules; consequently, the kinetic energy of the water molecules increases; due to this, the electrolyte heat increases in the machining zone (Fig. 38.2).

The machining parameters are varied for different levels during the experiments and MRR and OC are evaluated for the assessment of the machining performance. From the preliminary study, the machining parameters and their levels are fixed as shown in Table 38.1. The variable machining time and hole diameter of each experiment have been displayed in Table 38.2. The MRR has been evaluated by the ratio of constant thickness of work material in μm to the variable machining time in seconds and the difference between the tool and hole diameter is considered for OC in μm. Optical microscope image is used for the evaluation of hole diameter [11].

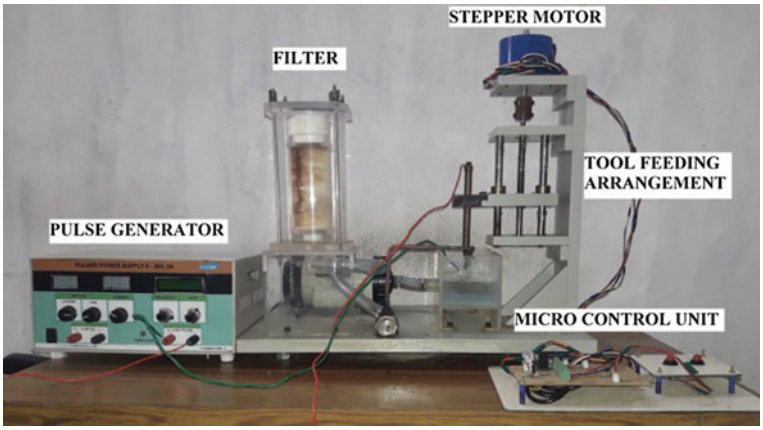

Fig. 38.1 EMM system

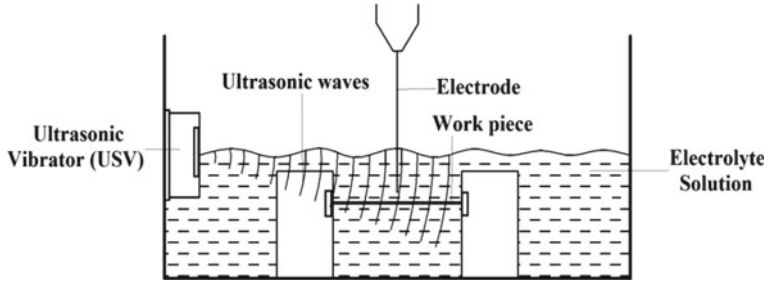

Fig. 38.2 Electrolyte tank attached with ultrasonic vibrator

Table 38.1 Machining parameters and their levels

Symbol	Factors	Level 1	Level 2	Level 3
EC	Electrolyte concentration (g/l)	20	25	30
MV	Machining voltage (V)	7	8	9
DC	Duty cycle (%)	45	55	65
ET	Electrolyte temperature (°C)	32	34	36

Machining parameters and their responses are shown in Table 38.2, which are considered to evaluate the optimal combination using entropy-weighted MOORA method.

38.3 MOORA (Multi-objective Optimization on the Basis of Ratio Analysis) Optimization Method

MOORA is one of best and simple tools to find the optimal parametric combination from the experiment results. The following steps are followed for the ranking [12].

Step 1: The decision matrix consist of 'n' attributes and 'm' alternatives and the responses are kept in the matrix as shown in the Eq. 38.1.

$$Y = \begin{bmatrix} y_{11} & y_{12} & y_{13} & \cdots & y_{1n} \\ y_{21} & y_{22} & y_{23} & \cdots & y_{2n} \\ y_{31} & y_{32} & y_{33} & \cdots & y_{3n} \\ \vdots & \vdots & \vdots & \ddots & \vdots \\ \vdots & \vdots & \vdots & \ddots & \vdots \\ y_{m1} & y_{m2} & y_{m3} & \cdots & y_{mn} \end{bmatrix} \tag{38.1}$$

Step 2: The matrix responses are normalized using Eq. 38.2.

Table 38.2 L_{18} OA and their responses with MOORA rank

Ex. no	EC (g/l)	MV (V)	DC (%)	ET (°C)	Machining time (s)	Hole dia (μm)	MRR (μm/s)	OC (μm)	MOORA value (Yi)	Rank
1	20	7	55	32	986.84	565.60	0.304	105.6	0.0514	18
2	20	8	45	34	582.52	563.22	0.515	103.22	0.0871	15
3	20	9	65	36	432.90	604.02	0.693	144.02	0.1171	3
4	25	7	55	34	568.18	596.82	0.528	136.82	0.0892	13
5	25	8	45	36	391.13	547.61	0.767	87.61	0.1032	8
6	25	9	65	32	360.14	539.21	0.833	79.21	0.0933	10
7	30	7	45	32	552.49	564.41	0.543	104.41	0.0918	11
8	30	8	65	34	412.09	558.41	0.728	98.41	0.1159	4
9	30	9	55	36	321.54	562.01	0.933	102.01	0.1202	1
10	20	7	65	36	657.89	530.81	0.456	70.81	0.0770	16
11	20	8	55	32	391.13	548.80	0.767	88.8	0.1046	7
12	20	9	45	34	342.08	546.40	0.877	86.4	0.1018	9
13	25	7	45	36	704.23	539.21	0.426	79.21	0.0720	17
14	25	8	65	32	562.85	584.82	0.533	124.82	0.0902	12
15	25	9	55	34	356.29	551.21	0.842	91.21	0.1075	6
16	30	7	65	34	574.71	553.61	0.522	93.61	0.0883	14
17	30	8	55	36	431.03	561.62	0.696	101.62	0.1176	2
18	30	9	45	32	307.38	552.41	0.976	92.41	0.1089	5

$$k_{ij} = \frac{y_{ij}}{\sqrt{\sum_{i=1}^{m} y_{ij}^2}} \quad \mathrm{j} = 1, 2, \ldots, \mathrm{n} \tag{38.2}$$

where k_{ij} is a dimension-less number which belongs to the interval [0, 1] for ith alternative and jth attribute which represents the normalized performance.

Step 3: The maximum normalized performance values are should added (for beneficial attributes) and minimum normalized values are should subtracted (non-beneficial attributes) as in Eq. 38.3

$$q_i = \sum_{j=1}^{g} k_{ij} - \sum_{j=g+1}^{n} k_{ij} \tag{38.3}$$

where g is the no. of attributes to be maximized, $(n - g)$ is the number of attributes to be minimized, and q_i is the normalized assessment value.

Step 4: The importance of responses to the attributes w_j are be multiplied with the corresponding weight.

$$q_i = \sum_{j=1}^{g} w_j k_{ij} - \sum_{j=g+1}^{n} w_j k_{ij} \; (\mathrm{j} = 1, 2, \ldots, \mathrm{n}) \tag{38.4}$$

where w_j is the weighted value obtained using the entropy method. Then these q_i values are ranked as per the preference values, in which higher value deserves the optimal combination.

38.4 Result and Discussion

38.4.1 Input Parameters Effect on MRR

The machining parameters and their mean responses are plotted in the graph as depicted in Figs. 38.3, 38.4, 38.5, and 38.6. It is evident from the figures that higher parameter level deserves the higher MRR. The ultrasonic vibration heats the electrolyte by creating the molecular collision. Due to heating, the ions in the electrolyte experience higher displacement, resulting in higher MRR [13]. Additionally, the USV dispels the debris produced during machining from the machining zone. This continues the removal of debris that helps to improve the machining, resulting in higher MRR.

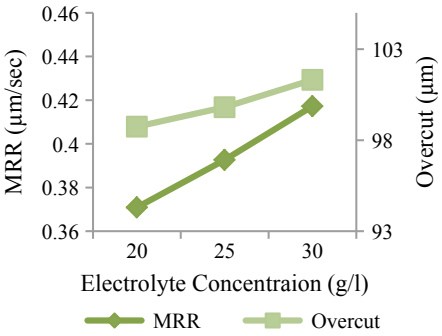

Fig. 38.3 EC versus MRR and OC

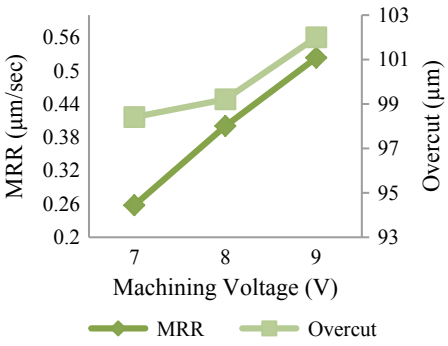

Fig. 38.4 MV versus MRR and OC

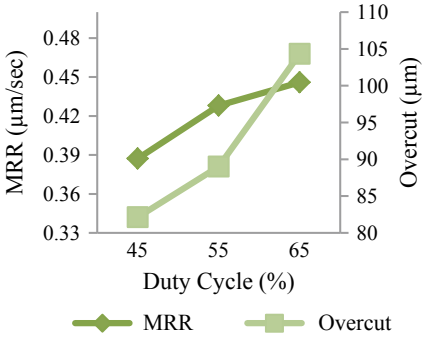

Fig. 38.5 DC versus MRR and OC

38.4.2 Input Parameters Effect on OC

The USV-heated electrolyte produces the overcut ranging from 75 to 110 µm. This range is comparatively lesser with the existing literatures [9]. USV electrolyte contributes for two times better overcut compared to the other electrolyte heating technique. The use of USV removes the debris continuously and possibilities of stray

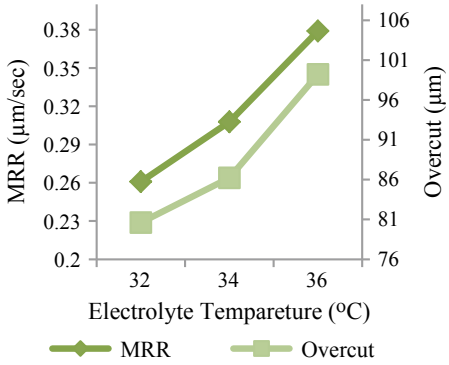

Fig. 38.6 ET versus MRR and OC

attack are reduced. The responses against the machining parameters are displayed in Figs. 38.3, 38.4, 38.5, and 38.6.

38.4.3 MOORA

Entropy-weighted MOORA method has been adopted for the optimization of MRR and OC using USV-heated electrolyte. Equations 38.1–38.4 are used for the MOORA values and its ranking, which is indexed in Table 38.2. The attribute weights are assigned using the entropy method as $w_j = 0.4941$ for MRR and $w_j = 0.5051$ for OC. The highest MOORA value is considered as the best value, which holds the first rank and considered as the optimal combination for the best machining performance. Therefore, experimental run 9 holds the highest MOORA value 0.1202. The experimental run 9 shows better result—0.933 µm/s MRR and 102.01 µm OC—compared to other experimental runs using MOORA. Also, the experimental runs 17 (0.1176) and 3 (0.1171) are the next two optimal combinations. Therefore, 30 g/l of electrolyte concentration, 9 V of machining voltage, 55% duty cycle, and 36° of electrolyte temperature are recommended for better machining performance.

38.4.4 ANOVA Table for MOORA

MOORA values are statically studied by ANOVA which identifies the significant process parameters and its contribution toward the machining performance. Therefore, machining voltage contributes about 55.51% in machining performance. Table 38.3 shows the percentage contribution of electrolyte concentration and temperature as 18.78% and 7.28%, respectively. According to ANOVA Table 38.3, duty cycle is insignificant compared to other parameters.

Table 38.3 ANOVA table for MOORA

Symbol	DF	Seq SS	Adj MS	F	% of contribution
EC	2	0.0010356	0.0005178	4.86	18.78
MV	2	0.0030605	0.0015302	14.3	55.51
DC	2	0.0000572	0.0000286	0.27	1.04
ET	2	0.0004013	0.0002006	1.88	7.28
Error	9	0.0009588	0.0001065		17.39
Total	17	0.0055133	0.015		100

38.5 SEM Analysis

SEM graphs that are shown in Figs. 38.7 and 38.8 are for the first and second optimal combinations. Figure 38.7 shows the round circumference micro-hole without any irregularity in major areas. Although one side of its circumference had an over-etched surface, the profile of the micro-hole is circular without any irregularities. It is due to the fact that the ultrasonic vibrations passed beneath the electrolyte from one side of tank and the smaller tank capacity makes way for debris encounter resulting in

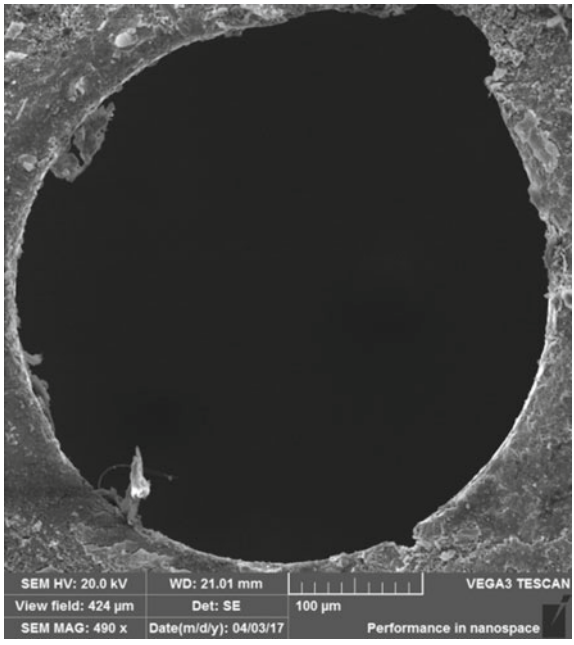

Fig. 38.7 SEM for the first optimal solution (30 g/l, 9 V, 55%, 36 °C)

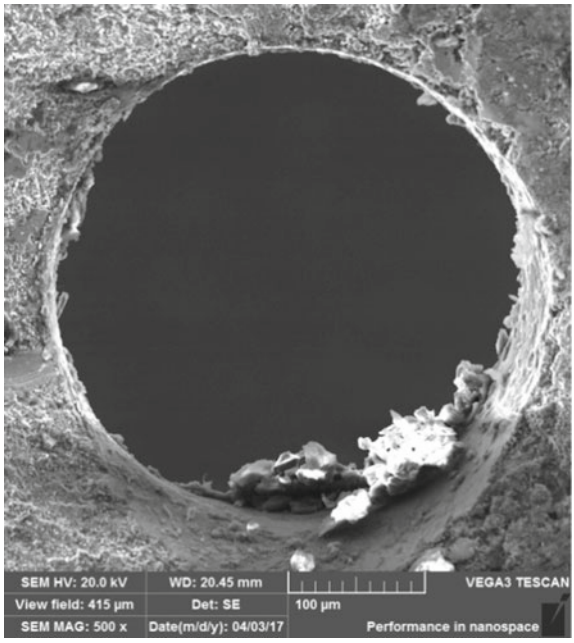

Fig. 38.8 SEM for the second optimal solution (30 g/l, 8 V, 55%, 36 °C)

few stray cuts. Figure 38.8 shows the better circularity, machined under the second optimal combination.

38.6 Conclusion

EMM performance is enhanced with aids of USV heated electrolyte. The experiments is planned based on the L_{18} OA. Entropy method is used to identify the weight of each response. MOORA method has been used to calculate the optimal combination.

- Weight for each responses are calculated using as w_j for MRR = 0.4941 and w_j for OC = 05051 using entropy method.
- The optimal combinations for better performance are 30 g/l of electrolyte concentration, 9 V of machining voltage, 55% duty cycle, and 36° of electrolyte temperature.
- Based on ANOVA, the machining voltage contributes about 55% in the overall machining performance.
- USV-heated electrolyte shows two times lesser overcut compared to the other methods.

- USV heated electrolyte is more suitable for better MRR and accuracy. Further experiments can be planned to hinder the over-etching surface in the machining area.

Acknowledgements The authors thank the Government College of Engineering, Salem, for providing the SEM facilities. The authors thank the management of Muthayammal Engineering College, Rasipuram, Tamil Nadu, for the encouragement and support. The authors are grateful to the management of Sona College of Technology, Salem, for providing the optical microscope facilities to verify the overcut.

References

1. Venkatesh, V., Swain, N., Srinivas, G., Kumar, P., Barshilia, H.C.: Review on the machining characteristics and research prospects of conventional micro-scale machining operations. Mater. Manuf. Process. **32**(3), 1042–6914 (2017). https://doi.org/10.1080/10426914.2016.1151045
2. Anasane, S.S., Bhattacharyya, B.: Electrochemical micromachining of titanium and its alloys. In: Kibria, G., Bhattacharyya, B., Davim, J. (eds.) Non-traditional Micromachining Processes. Materials Forming, Machining and Tribology. Springer, Cham (2017)
3. Bhattacharyya, B., Malapati, M., Munda, J.: Influence of tool vibration on machining performance in electrochemical micro-machining of copper. Int. J. Mach. Tools Manuf. **47**(2), 35–342 (2007). https://doi.org/10.1016/j.ijmachtools.2006.03.005
4. Liu, W., Zhang, H., Luo, Z., Zhao, C., Ao, S., Gao, F., Sun, Y.: Electrochemical micromachining on titanium using the NaCl-containing ethylene glycol electrolyte. J. Mater. Process. Technol. **255**, 784–794 (2018). https://doi.org/10.1016/j.jmatprotec.2018.01.009
5. Zhang, H., Ao, S., Liu, W., Luo, Z., Niu, W., Guo, K.: Electrochemical micro-machining of high aspect ratio micro-tools using quasi-solid electrolyte. Int. J. Adv. Manuf. Technol. **91**(9–12), 2965–2973 (2017). https://doi.org/10.1007/s00170-016-9900-x
6. Guodong, L., Yong, L., Quancuna, K.: Selection and optimization of electrolyte for micro electrochemical machining on stainless steel 304. Procedia CIRP **42**, 412–417 (2016). https://doi.org/10.1016/j.procir.2016.02.223
7. Sekar, T., Arularasu, M., Sathiyamoorthy, V.: Investigations on the effects of nano-fluid in ECM of die steel. Measurement **83**, 38–43 (2016). https://doi.org/10.1016/j.measurement.2016.01.035
8. Jeykrishnan, J., Vijaya Ramnath, B.: Optimization of process parameters in electro-chemical machining (ECM) of D3 die steels using Taguchi technique. Mater. Today Proc. **4**(8), 7884–7891 (2017). https://doi.org/10.1016/j.matpr.2017.07.124
9. Thanigaivelan, R., Arunachalam, R.M., Kumar, M.: Performance of electrochemical micromachining of copper through infrared heated electrolyte. Mater. Manuf. Process. **33**(4), 383–389 (2018). https://doi.org/10.1080/10426914.2017.1279304
10. Yaralioglu, G.: Ultrasonic heating and temperature measurement in microfluidic channels. Sens. Actuators A Phys. **170** (1–2), 1–7 (2011). https://doi.org/10.1016/j.sna.2011.05.012
11. Soundarrajan, M., Thanigaivelan, R.: Intervening variables in electrochemical micro machining for copper. In: International Conference on Precision, Meso, Micro and Nano Engineering (COPEN 10), Indian Institute of Technology Madras, Chennai, India (2017)

12. Chakraborty, S.: Application of the MOORA method for decision making in manufacturing environment. Int. J. Adv. Manuf. Technol. **54** (9–12), 1155–1166 (2011). https://doi.org/10.1007/s00170-010-2972-0
13. Van Deconinck, D., Damme, S., Deconinck, J.: A temperature dependent multi-ion model for time accurate numerical simulation of the electrochemical machining process. Part II: Numerical simulation. Electrochimica Acta **69**, 120–127 (2012). https://doi.org/10.1016/j.electacta.2012.02.079

Part II
Surface Engineering

Chapter 39
Microstructure and Mechanical Properties of Atmospheric Plasma Sprayed 8YSZ Thermal Barrier Coatings

N. R. Kadam, G. Karthikeyan and D. M. Kulkarni

Abstract Thermal Barrier Coatings (TBCs) are favorable to provide better thermal insulation to hot components of gas turbine and aero engines leading to improve durability. The TBCs were prepared using a NiCoCrAlY as a bond coat and 8YSZ as a top coat with the thickness range of 100 ± 25 μm and 250 ± 25 μm respectively, by atmospheric plasma spray. This paper presents the study of surface microstructure and mechanical properties of 8YSZ TBC. The surface microstructure was examined by scanning electron microscopy and microhardness was by the microindentation test. Also, the surface roughness and elemental composition present in the coating was studied with surface profilometer and energy dispersive x-ray spectrometry. At the high-temperature conditions, PYSZ has a good combination of thermal, physical, and mechanical properties. Therefore, it is favorable to select the partially stabilized zirconia coatings as TBCs for improvement in the thermal insulation and protection from high inlet gas temperature.

Keywords Thermal barrier coatings · Atmospheric plasma spray · Microstructure · Mechanical property · Yttria stabilized zirconia

39.1 Introduction

The development of Thermal Barrier Coatings (TBCs) started early in the 1950s for defense engine components [1]. Later this technology was adopted and applied in commercial services such as prototype planes, X-15 manned rocket exhaust nozzle, gas turbine, aero engines, diesel engine, and exhaust system components operating at high-temperatures [2, 3]. The TBC allows improving high-temperature capability which leads to increase in thermal efficiency thereby achieving a lower substrate temperature. The actual image of the civil jet engine and gas turbine components which are produced with TBCs are shown in Fig. 39.1.

N. R. Kadam (✉) · G. Karthikeyan · D. M. Kulkarni
Department of Mechanical Engineering, BITS Pilani, K. K. Birla Goa Campus, Zuarinagar 403726, Goa, India
e-mail: p20150410@goa.bits-pilani.ac.in

M. S. Shunmugam and M. Kanthababu (eds.), *Advances in Micro and Nano Manufacturing and Surface Engineering*, Lecture Notes on Multidisciplinary Industrial Engineering,
https://doi.org/10.1007/978-981-32-9425-7_39

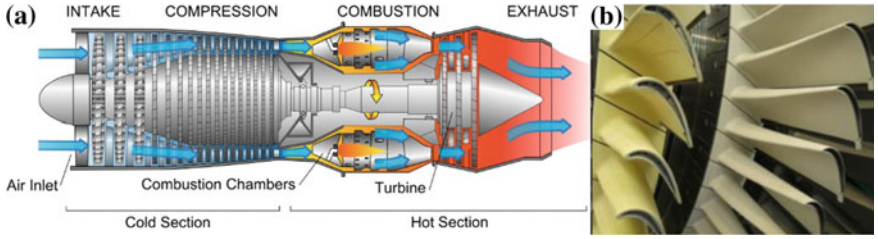

Fig. 39.1 **a** The actual image of the civil jet engine [3] and **b** TBC coated gas turbine blade [4]

The schematic representation of the TBC system consisting of a multilayer structure is as shown in Fig. 39.2. It is made up of four layers namely the superalloy substrate, metallic bond coat followed by Thermal Grown Oxides (TGO) and final thermal barrier layer called a ceramic topcoat. Typically, the bond coat is of thickness ranging from 30 to 100 μm and consists of MCrAlY (M-Ni/Co) providing an irregular surface for good adhesion between the substrate and the ceramic topcoat, with better oxidation and corrosion protection to the underlying substrate reducing thermal expansion coefficient. When the bond coat is subjected to high temperature, it leads to oxidation forming TGO layer of a thickness ranging from 2 to 10 μm which acts as an oxidization barrier. The ceramic topcoat with a thickness ranging from 120 to 200 μm provides actual thermal barrier forming a thermally insulating ceramic layer for protection of the hot component surface against high inlet gas temperatures and erratic environments [5, 6].

Partially Yttria Stabilized Zirconia (7–8% YSZ) is the most common candidate material used as TBC material to protect the gas turbine components from high-temperature. The most widely and common deposition processes applied to deposit TBCs are Atmospheric Plasma Spraying (APS) and Electron-Beam Physical Vapor Deposition (EB-PVD). The microstructure developed by APS represents a splat layer structure and by EB-PVD represents a columnar structure.

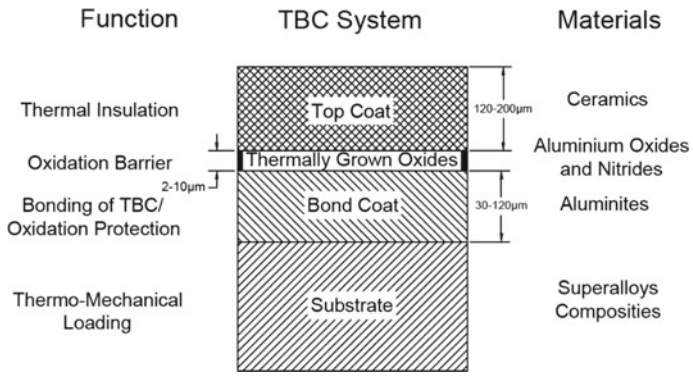

Fig. 39.2 A schematic of a multilayer TBC system

In the present study, the combination of 8YSZ TBCs with NiCoCrAlY bond coat applied on Ni-based superalloy (Inconel 718) was prepared by the atmospheric plasma spray process. To improve the mechanical properties of 8YSZ TBCs, the surface microstructure of 8YSZ TBC with NiCoCrAlY bond coat were examined and studied by Scanning Electron Microscopy (SEM). Along with SEM, Energy dispersive X-ray spectrometry (EDS) was used to determine the elemental composition present in the coating. The microindentation and surface roughness test were carried out to study the mechanical properties such as microhardness and surface roughness for improving the properties of TBCs.

39.2 Experimental Procedure

39.2.1 Preparation of TBCs

The flat plate Ni-based superalloy (Inconel 718) as shown in Fig. 39.3a was used as the substrate material and the dimensions were 20 × 20 × 3 mm. The chemical

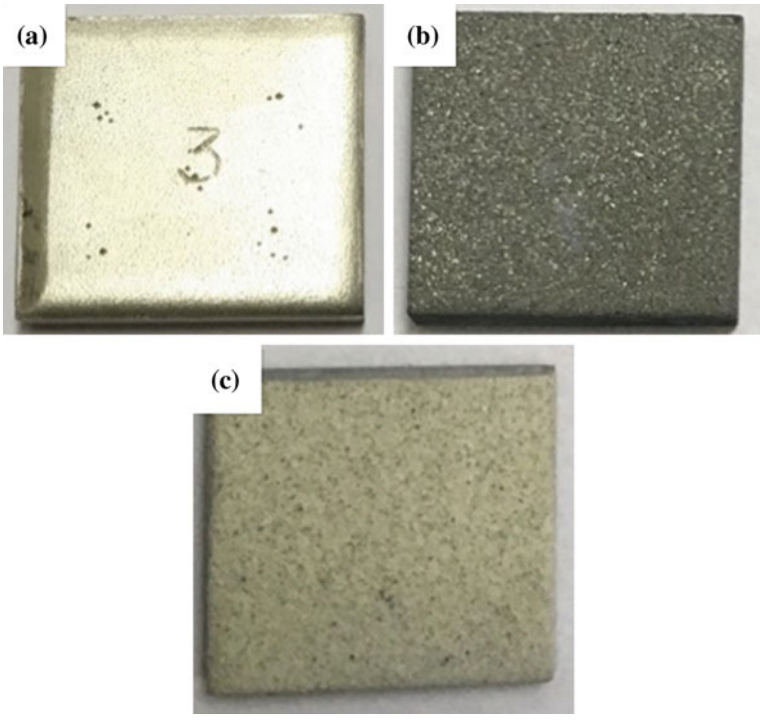

Fig. 39.3 **a** Inconel 718 substrate, **b** NiCoCrAlY bond coat applied by APS and **c** 8YSZ topcoat applied on the bond coat by APS

composition of Inconel 718 by wt%: Ni-58.5%, Cr-13.6%, Mo-0.9%, Fe-bal, Nb + Ta-2.6%. Prior to the thermal spraying, the substrate surface was grit blasted with alumina abrasive powder to increase the rough surface resulting in better mechanical interlocking between substrate and coating. Further, the substrate was ultrasonically cleaned with distilled water and acetone, and dried before the thermal spray coating deposition.

A commercially available feedstock powder with different composition and particle size distribution were used as a bond coat and topcoat for depositing TBCs. The metallic NiCoCrAlY powder (AMDRY 997, Sulzer Metco Inc., USA) with a nominal composition of Ni-26Co-23Cr-11Al-0.9Y (in wt%) having a spherical morphology and a particle size ranging from 40 to 80 μm in diameter was used to apply a bond coat. Similarly, ZrO_2 with 8 wt% Y_2O_3 i.e. 8 wt% Yttria Stabilized Zirconia (8YSZ) ceramic powder (Metco 233B, Sulzer Metco Inc., USA) with spherical morphology and particle size ranging from 22 to 45 μm in diameter was used to apply topcoat. The thermal spraying was carried out using an APS equipment, with 40 KW plasma spray system using 3MBM (Make-Sulzer Metco AG, Switzerland) plasma gun with a 6 mm internal diameter nozzle. The above facilities were available in Spraymet Surface Technologies, Bangalore which was used to deposit bond coat and topcoat. The bond coat of NiCoCrAlY (see Fig. 39.3b) was applied by atmospheric plasma sprayed with a thickness of 100 ± 25 μm in order to improve the adhesion and minimize the thermal expansion match. The topcoat of 8YSZ (see Fig. 39.3c) was applied with a thickness of 250 ± 25 μm on the bond coat in order to protect the component from high-temperature. The detailed deposition and spray parameters for bond coat and topcoat used for TBC deposition by APS are listed in Table 39.1.

Table 39.1 Spray parameters used for APS-TBCs

Parameters	Bond coat	Top coat
Feedstock powder	NiCoCrAlY	8YSZ
Current (A)	400	500
Voltage (V)	60	65
Primary gas flow rate—Ar (slpm)	100	80
Secondary gas flow rate—He (slpm)	5	15
Primary gas pressure—Ar (MPa)	0.69	0.69
Secondary gas pressure—He (MPa)	0.35	0.35
Powder feed rate (g/min)	100	40
Spray distance (mm)	150	75
Spray angle (°)	90°	90°
Particle velocity (m/s)	≤450	≤450
Gas temperature (°C)	12,000–16,000	12,000–16,000

39.2.2 Characterization

The 8YSZ TBCs samples with the layered structure were used to study the surface microstructure and mechanical properties. The microstructural examination of 8YSZ TBCs was observed by SEM (Make: Quanta FEG 250, Hillsboro, USA) which was operated at low accelerating voltage conditions. In order to improve the imaging of the samples, gold/palladium (Au/Pd) is applied using magnetron sputtering (Leica EM ACE200, Germany). As nonconductive sample requires an Au/Pd coating to create a conductive layer to inhibit charging, reducing thermal damage and to improve the secondary electron signal required for topographic examination in the SEM. The thickness of Au/Pd deposited on to the TBC samples was in the range of 5 ± 1 nm. The EDS unit attached to the SEM was used to find the elemental composition of the bond coat and topcoat of the TBC samples. The reported values of elemental composition present in the coating were the average of the three values randomly selected on the surface of the bond coat and a topcoat of TBCs.

The microindentation test was carried in order to determine the hardness value of the coating surface. The measuring system of indentation equipped with quadrangular pyramid diamond indenter (Make: Matsuzawa MMT-X7, Japan) and two objective lenses (with the magnitude of 40× and 210×) was used. The microindentation test was conducted with the maximum applied load of 20 N with a dwell period of 10 s. In order to perform the indentation test, the substrate samples were polished and finished with grid paper and ultrasonically cleaned with acetone and distilled water. The bond coat and topcoat samples were directly considered for indentation test. Each reported values of Hardness (HV) is the average of the five values made on each TBC sample. Figure 39.3a indicates the microindentation marks on the surface of the Inconel 718 substrate. The similar, test was carried on a bond coat and top coat to determine the hardness value of the coating surface.

The surface roughness of NiCoCrAlY-8YSZ TBCs was measured by Mitutoyo surf test profilometer (Mitutoyo SJ 410, Japan) with a cutoff length of 800 μm, measurement length of 16 mm with tracing speed of 0.5 mm/s. The reported values of the arithmetic mean roughness (R_a) was the average of six values scanned from different areas of each TBC sample. The microindentation and surface roughness test was performed in air at room temperature.

39.3 Results and Discussion

39.3.1 Microstructure

SEM study shows the surface microstructure of as-sprayed NiCoCrAlY bond coat and 8YSZ topcoat as shown in Fig. 39.4a and 39.5a. The APS deposited TBCs presents a characteristic splat and dense microstructure. The networks of the microcracks and pores formed in the APS-TBCs were observed. Figure 39.4a represents the plasma

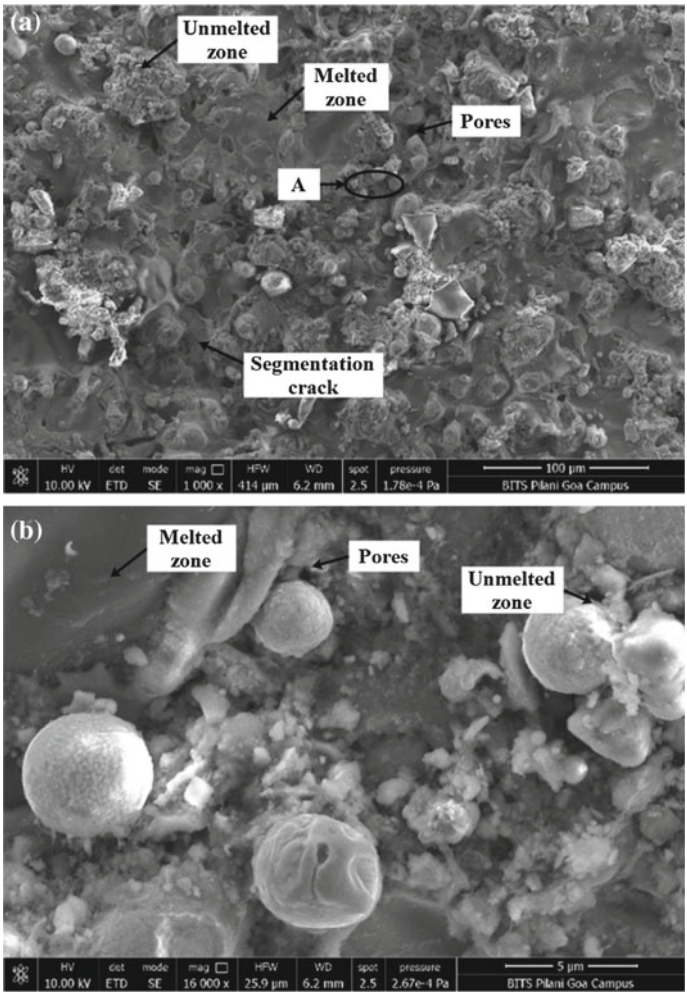

Fig. 39.4 **a** The microstructure of the as-sprayed NiCoCrAlY bond coat obtained by SEM. **b** The magnified microstructure of NiCoCrAlY bond coat from point A of Fig. 39.4a

sprayed surface microstructure of NiCoCrAlY bond coat in which unmelted particles, irregular voids, and pores are identifiable. Thus creating a rough surface which leads to mechanical bonding for the ceramic topcoat to improve the adhesion property of the coating. The magnified view of the surface microstructure of NiCoCrAlY bond coat is shown in Fig. 39.4b which represents point A in Fig. 39.4a. The irregular voids and pores formed are resulted from unmelted particles and gas entrapment. Also, the particle velocity and melting temperature of particles play an important role in the formation of voids and pores. Similarly, the intersplat voids and pores are resulted due to poor adhesion between splats.

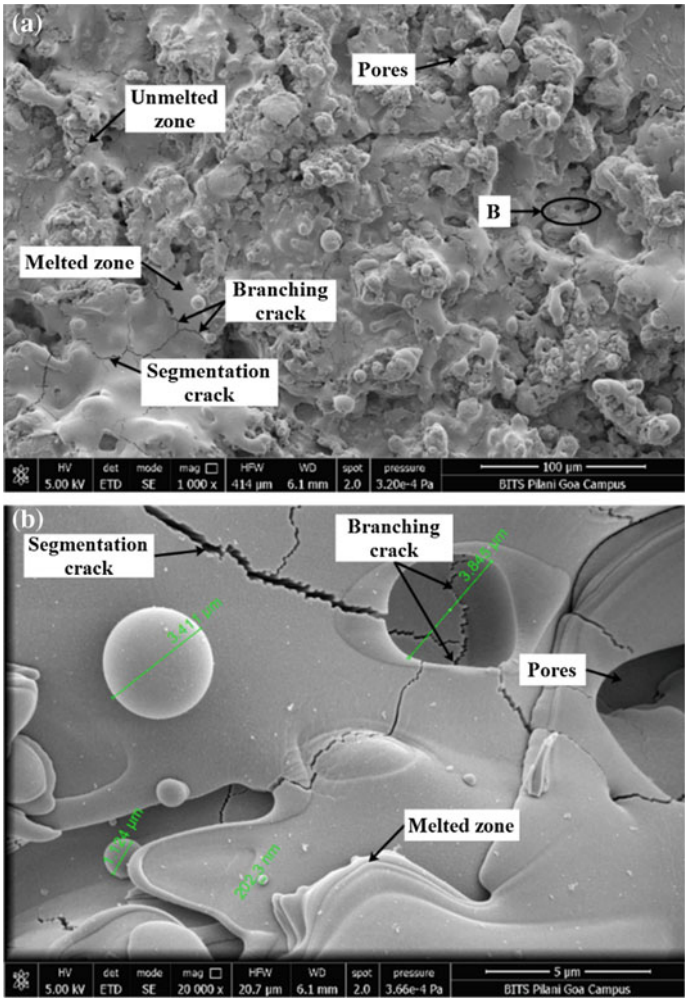

Fig. 39.5 **a** The microstructure of the as-sprayed 8YSZ topcoat obtained by SEM. **b** The magnified microstructure of 8YSZ topcoat from point B of Fig. 39.5a

Figure 39.5a represents the plasma sprayed surface microstructure of 8YSZ top coat. From Fig. 39.5a, it can be seen the presence of segmentation cracks which improves the strain tolerance of the coating. Further, the segmentation cracks lead to branching cracks which extend horizontally from the segmentation cracks. The development of segmentation crack with branching cracks in the 8YSZ can be seen in Fig. 39.5b which represents point B in Fig. 39.5a. The width of both segmented and branching cracks is in the order of micrometer. Similarly, the length of branching cracks is more than 50 μm.

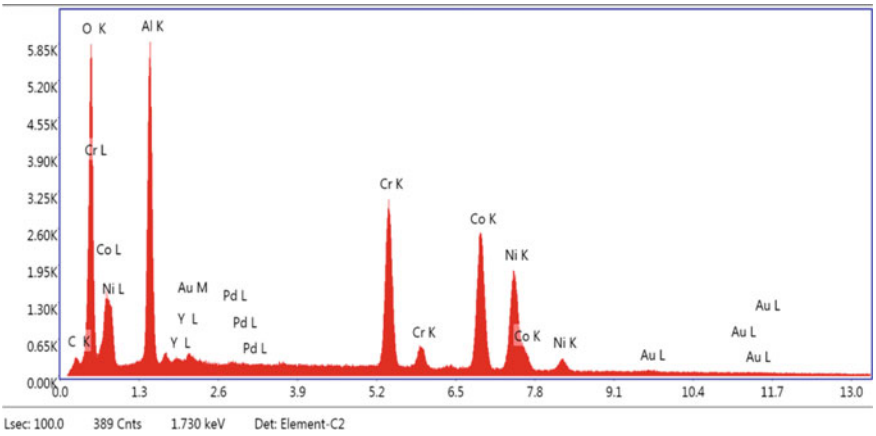

Fig. 39.6 EDS analysis of NiCoCrAlY bond coat from point A in Fig. 39.4a

In comparison, NiCoCrAlY bond coat has finer and fewer microcracks and pores like that of the 8YSZ topcoat. The 8YSZ surface has more microcracks and pores which results in strain tolerance in the coating. Also, the branching of segmentation cracks is seen in 8YSZ topcoat compared to the NiCoCrAlY bond coat. The bond coat surface is smooth as compared to topcoat due to the high degree of splat flattering. The 8YSZ TBCs has dense splat layer microstructure as compared to NiCoCrAlY bond coat.

In thick TBCs, the presence of microcracks near the defects can be observed when the surface is analyzed in high detail. The APS-TBCs has some spherical defects present on the surface which further were analyzed with EDS and found to be the same elemental composition as that of the bulk coatings. The examination of bond coat and topcoat by EDS was observed at low energy (1.730 keV) out in order to determine and the elemental compositions present. The bond coat exhibits a high percentage of Co, Cr, Al, and O as shown in Fig. 39.6 and a small amount of Ni and Y elements plus some presence of Au/Pd due to the sputtering for creating a conductive layer over the bond coat samples. Thus the bond coating comprises mainly of NiCoCrAlY. Similarly, the topcoat exhibits a high percentage of Zr and Y as shown in Fig. 39.7 and a small amount of O element with the presence of Au/Pd due to the sputtering for creating a conductive layer over the topcoat samples as same as bond coat samples.

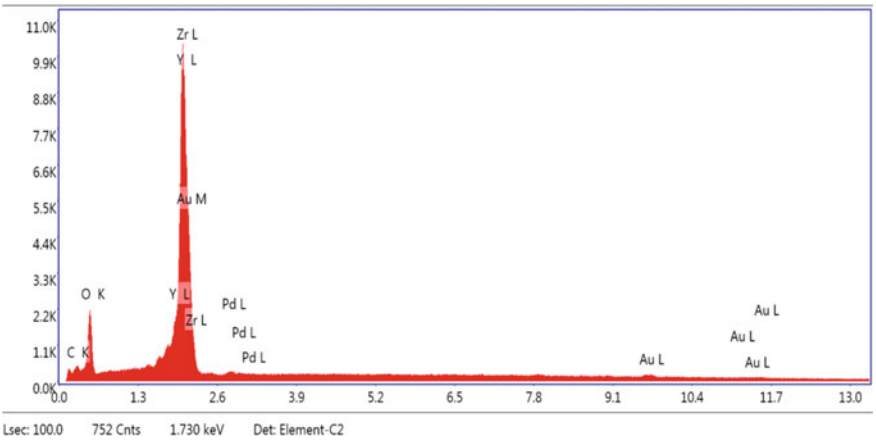

Fig. 39.7 EDS analysis of 8YSZ topcoat from point B in Fig. 39.5a

39.3.2 Mechanical Properties

Table 39.2 represents the hardness properties of Inconel 718 substrate, NiCoCrAlY bond coat, and 8YSZ ceramic topcoat. Four samples were selected for deposition and characterization of NiCoCrAlY-8YSZ TBCs. From which two samples were NiCoCrAlY bond coat and two samples were NiCoCrAlY-8YSZ TBCs. The microindentation test was conducted and the results are consolidated in Table 39.2. It can be seen that the hardness of the 8YSZ topcoat TBC sample is more in the range of 649.30–654.95 HV as compared to NiCoCrAlY bond coat (in the range 625.03–645.60 HV).

The surface roughness test was used to determine the smoothness, i.e., arithmetic mean roughness value (R_a) of the coated surface which is the result of fully melted particles and the presence of fewer microcracks and pores. The R_a is the average deviation of the surface profile from the centerline over the measuring length. The same samples were considered for the surface roughness test and the results obtained were consolidated in Table 39.3. From Table 39.3, it is clear that the 8YSZ top coat has a rough surface which can lead to nonuniform contact with the contour surface resulting in nonuniform wear and uneven temperature drop across the TBC surface.

Table 39.2 The hardness of APS deposited NiCoCrAlY bond coat and 8YSZ top coat

Sample No.	Hardness (HV)		
	Substrate	Bond coat	Top coat
1	362.14	625.03	–
2	375.22	635.20	–
3	345.14	629.03	649.30
4	355.04	645.60	654.95

Table 39.3 The surface roughness of APS deposited NiCoCrAlY bond coat and 8YSZ topcoat

Sample No.	Surface roughness (μm)		
	Substrate	Bond coat	Top coat
1	2.08	6.22	–
2	1.96	6.19	–
3	1.92	6.70	7.15
4	1.79	6.73	7.41

39.4 Conclusions

The surface microstructure and mechanical properties such as microhardness and roughness of 8YSZ TBC deposited using APS have been studied. The experimental observations are summarized below,

The APS-TBCs shows splat layer structure consisting of nano-micro sized particles with the presence of unmelted zone. The presence of unmelted zone in the coating structure can result in improvement in bond strength. The presence of segmentation cracks leads to improve strain tolerance and Young's modulus resulting in better thermal performance. Similarly, the segmented coatings result in lower porosity which leads to decrease in the volume of intersplat pores due to the elimination of splat boundaries. The coated surface results in a rough surface which leads to low cohesion, a low degree of flattering, and low microhardness. Therefore, to improve the cohesion property, the surface produce must be smooth with a high degree of flattering creating large contact area between splats. Therefore, the microstructure and properties are more dependent on the deposition process and selection of spraying parameters such as particle size, particle feed rate, particle velocity, and spraying distance.

References

1. Cao, X.Q., Vassen, R., Stoever, D.: Ceramic materials for thermal barrier coatings. J. Eur. Ceram. Soc. **24**(1), 1–10 (2004)
2. Vaβen, R., Jarligo, M.O., Steinke, T., Mack, D.E., Stover, D.: Overview on advanced thermal barrier coatings. Surf. Coatings Technol. **205**(4), 938–942 (2010)
3. Hille, T.S., Nijdam, T.J., Suiker, A.S.J., Turteltaub, S., Sloof, W.G.: Damage growth triggered by interface irregularities in thermal barrier coatings. Acta Mater. **57**(9), 2624–2630 (2009)
4. Miller, R.A.: Thermal barrier coatings for aircraft engines: History and directions. J. Therm. Spray Technol. **6**(1), 35–42 (1997)
5. Zhang, D., Zhao, Z., Wang, B., Li, S., Zhang, J.: Investigation of a new type of composite ceramics for thermal barrier coatings. Mater. Des. **112**, 27–33 (2016)
6. Karlsson, A.M.: Modeling failures of thermal barrier coatings. Key Eng. Mater. **333**, 155–166 (2007)

Chapter 40
Decoding the Grinding Zone—A Study on Track Grinding Wheels

Debaditya Chattopadhyay and Suresh Venkatraman

Abstract Grinding plays a major role in the manufacturing of majority of industrial parts like cutting tool, camshafts, crankshaft, connecting rods, etc. Bearing is one such part where every individual component is ground before final assembly. Grinding of Inner Ring (IR) track of bearing assembly offers a great challenge due to high grinding stock, good surface finish requirement, and profile accuracy. What happens at the grinding zone has always been a black art for years due to lack of scientific understanding. This paper presents an approach to develop Bearing Inner Ring (IR) track grinding wheels by using the output of the grinding diagnostic tools and relating to the microscopic interactions at grinding zone with right combination of grains with special focus on grain shape and structure. Here using the diagnostic tool, signals were collected from grinding interface, data was analyzed and inferences were drawn.

Keywords Grinding zone · Microscopic interaction · GrindTrak · IR track grinding

40.1 Introduction

There is always a need for a more precise surface generation with every new or emerging technology. Grinding is basically a surface generation process that involves an abrasive which acts as a multipoint cutting tool. The main purpose of the grinding process is to remove material from the workpiece to achieve the required form, dimensions, surface finish, and other desired quality parameters. "Trial and error" approach is often used to control various grinding parameters to achieve desired results.

D. Chattopadhyay (✉) · S. Venkatraman
Department of Technology, Bonded Abrasives Division, Carborundum Universal Limited, Chennai 600019, India

S. Venkatraman
e-mail: sureshv@cumi.murugappa.com

M. S. Shunmugam and M. Kanthababu (eds.), *Advances in Micro and Nano Manufacturing and Surface Engineering*, Lecture Notes on Multidisciplinary Industrial Engineering,
https://doi.org/10.1007/978-981-32-9425-7_40

The interference region between the grinding wheel and the workpiece is called the "Grinding zone". In the grinding zone, grinding wheel interacts with the workpiece to remove material in the form of chips. This is a complex process and can be characterized into six microscopic interactions [1] as follows.

Interaction 1.1: Cutting happens when the depth of penetration of grain on the workpiece is intense and hence the workpiece material is removed in the form of chips.

Interaction 1.2: Plowing takes place when the depth of penetration is small and the workpiece is mainly experiencing plastic deformation instead of material removal.

Interaction 1.3: Sliding takes place when the depth of penetration is extremely shallow resulting in sliding of abrasive grain against the workpiece material at high contact stress.

Interaction 2 and 3: Finally, the chips that are produced at the grinding zone, are likely to be trapped between the adjacent grains in the grinding wheel and the workpiece material. Hence they will be forced to slide against the bond material or work material, causing chip/bond and chip/work interactions.

Interaction 4: If the bond is not recessed, and it remains close to the periphery of the wheel, it is likely to slide against the work material, leading to bond/work interaction (Fig. 40.1).

Reference: *"Microscopic interactions in surface generation processes using abrasive tools"* by Dr. K. Subramanian et al. Year of Publication: December 2017

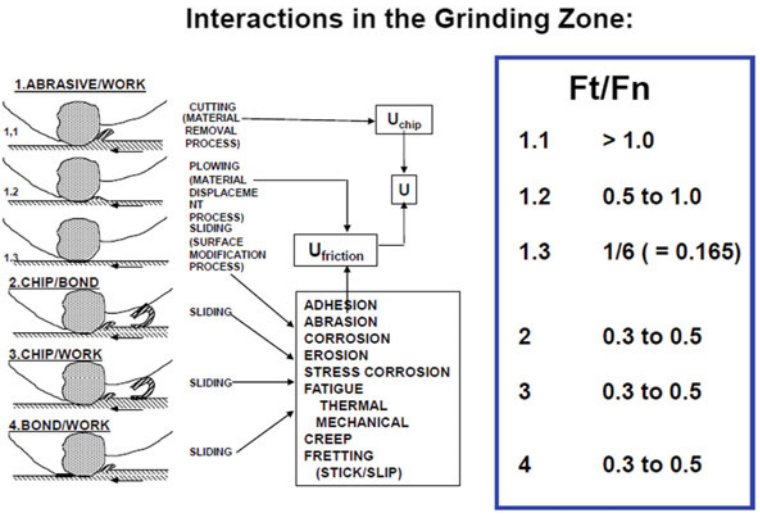

Fig. 40.1 Interactions in the grinding zone

Fig. 40.2 Bearing inner ring (IR)

Inner Ring (IR) Track grinding of bearing is always a challenging task. It involves high stock removal, profile accuracy, fine surface finish, and other desired quality parameters. This study was made to arrive at right combination of grains with particular emphasis on its shape for this grinding application. This was done by studying microscopic interactions [1] at the grinding zone using a diagnostic tool (Grind Trak [2]) on a cylindrical grinding machine (Micromatic Model No-SH40). This study involved (i) process monitoring and data acquisition, (ii) data analysis, and (iii) inferences for further action (Fig. 40.2).

The component used was made of SAE52100 steel having hardness range 58–62 HRc. The diagnostic tool monitors the power drawn by the spindle motor in a typical grinding cycle of roughing, semi finishing, and finishing. The dresser feed rate was also varied. Based on this, the power drawn, dressing frequency, and surface finish were studied for the two different grain combinations.

40.2 Experiments

Combination of White Aluminum oxide (99% Pure) and Microcrystalline grains of two different shapes namely "blocky" and "needle" were used as given in Table 40.1. A vitrified bond system, fusible in nature was used. The grinding wheels were of dimensions 450 mm outer diameter, 20 mm thickness, and 127 mm inner diameter. Dimension details of components used in lab study are given in Fig. 40.3. Property comparison of Needle shaped and blocky shaped microcrystalline grains are given in Table 40.2. Grinding cycle parameters for the test are given in Table 40.3.

The first set of trials were taken with the above grinding cycle for both wheels T1 & T2. During grinding process, grinding wheel is subjected to attritious wear, abrasive grain fracture, bond fracture and loading of chips on to the grain, bond, and pores.

Table 40.1 Combination of White Aluminum oxide and Microcrystalline grains

Trial wheel	Wheel details	Type of grain	Wheel photos
T1	Needle shaped Microcrystalline Abrasives + White Aluminum Oxide	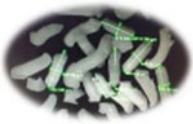	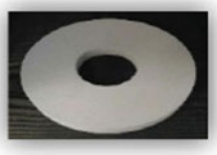
T2	Blocky shaped Microcrystalline Abrasives +White Aluminum Oxide	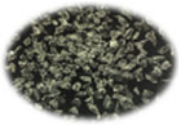	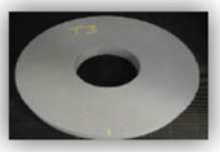

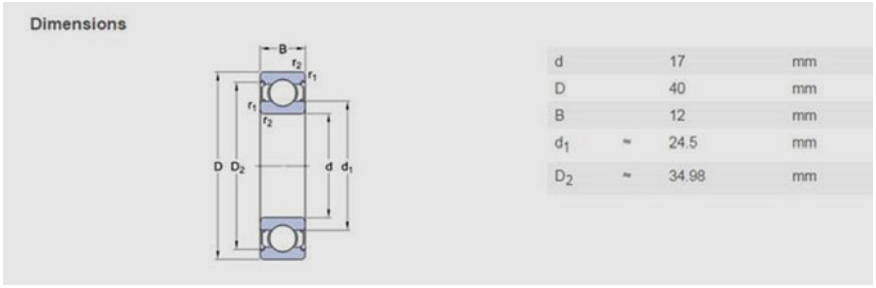

Fig. 40.3 Component details for lab study

Table 40.2 Property comparison of Needle versus Blocky shaped grains

Parameters	Needle shaped microcrystalline	Blocky shaped microcrystalline
Loose packed density (g/cc)	1.76	1.82
Aspect ratio	1:7	1:1.5
Knoop hardness (Gpa)	2100	2100
True density (g/cc)	3.92	3.90
Crystal size (micron)	0.26–0.30	0.26–0.30

Table 40.3 Grinding cycle and dresser feed rate

Cycle	Stock (mm)	Feed rate (mm/min)	Time (s)	Dresser feed rate (mm/min)
Rough	0.1	6	1	200
Semi finish	0.075	4.5	1	
Finish	0.025	1.5	1	
Total	0.2		3	

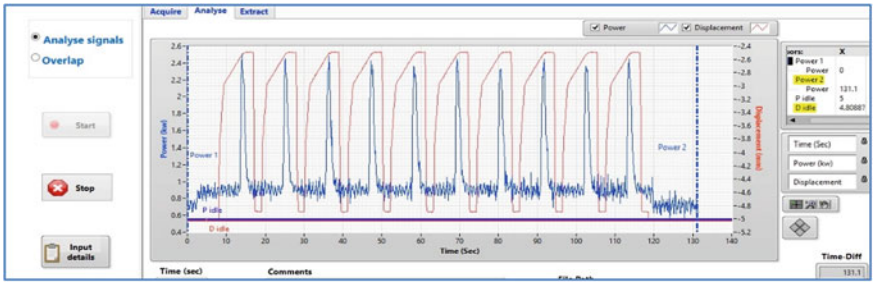

Fig. 40.4 Grinding signal from the diagnostic tool

40.2.1 Diagnostic Tool

The diagnostic tool (Grind Trak of Micromatic Make) has an arrangement of a power cell to monitor the power drawn by the spindle motor and a LVDT to measure the infeed of wheel head during grinding of workpieces. Power drawn and LVDT with respect to the feed were measured for grinding every workpiece. Figure 40.4 shows a typical signal captured during grinding cycle. This depicts the signature of grinding process.

40.2.2 Derivatives of Power and Material Removal

The diagnostic tool provides the power and infeed of the wheel in real time. Grinding power is an indication of the energy consumed (Pc) for a given material removal rate (MRR) Qw. Qw is calculated by using process parameters such as work velocity (v_w), depth of cut (a_e), and grinding width (b_w).

$$Q_w = a_e \cdot v_w \cdot b_w$$

The variation of MRR along with power can be used to derive the specific cutting energy (SCE) Uc during grinding of the workpiece [3] (Fig. 40.5).

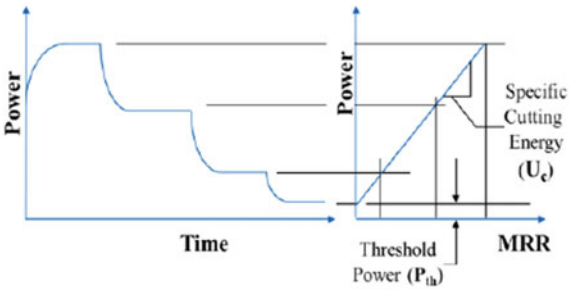

Fig. 40.5 Specific cutting energy [3]

$$Uc = \left[(P_c)/Q_w\right]$$

Assuming power associated with chip making process is P_c, any change in it over time $P_c(t)$ can be attributed to frictional effects of the chip (Microscopic Interactions 2 and 3) with varying time. This is denoted as $P_f(t)$.

The power after time "t" at a given MRR consists of four components. The initial threshold power P_{th} (0), changes in threshold power with time P_{th} (t), the power for cutting or chip making P_c and the change in the cutting power caused by the chip friction effects P_f (t). The connection between these parameters and their corresponding microscopic interactions are illustrated [4] in Fig. 40.6.

Specific cutting energy (SCE) obtained for individual components ground for both test wheels T1 & T2 are shown in Figs. 40.7 and 40.8.

Surface finish (Ra) on each of the ground components was measured using a roughness measuring equipment (Mitutoyo surf test SJ210). Values obtained for both wheels are shown in Figs. 40.9 and 40.10.

The next set of experiments were done by maintaining the same grinding cycle as mentioned in Table 40.3 and varying the dresser feed rate as mentioned in Table 40.4. Here the dressing depth was maintained the same.

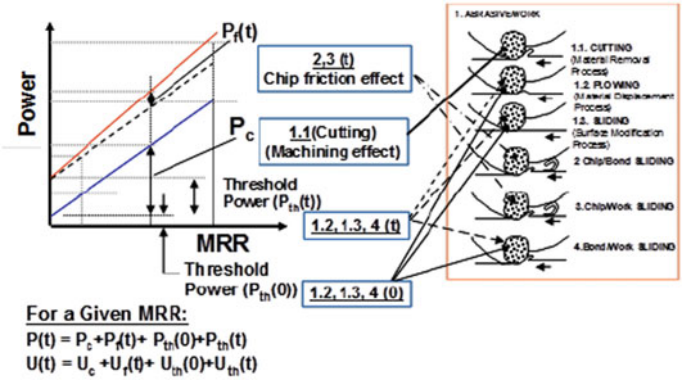

Fig. 40.6 Components of power and microscopic interactions [4]

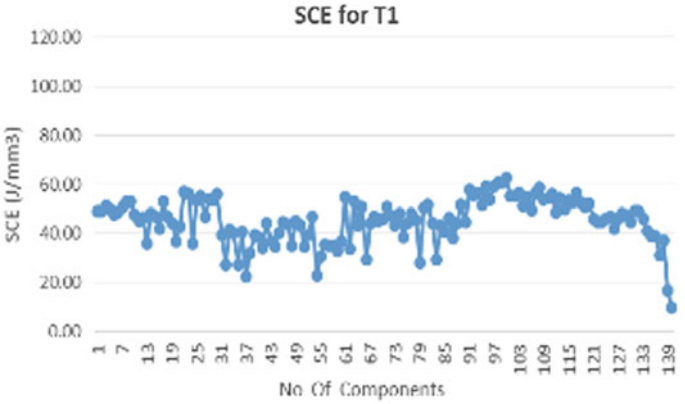

Fig. 40.7 SCE for T1 wheel

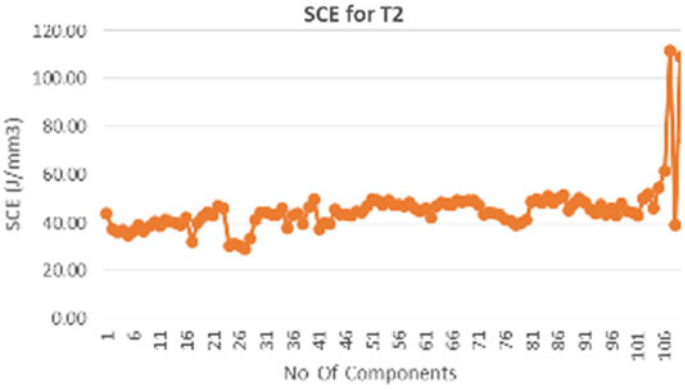

Fig. 40.8 SCE for T2 wheel

Figure 40.11 shows the specific cutting energy values obtained for grinding each component at different dresser feed rate for test wheel 1. It also shows the number of components ground at each dresser feed rate before next dressing was warranted. Figure 40.12 shows corresponding data for test wheel 2. Figures 40.13 and 40.14 show surface finish (Ra) values obtained on the components for test wheels T1 and T2, respectively, at different dresser feed rate.

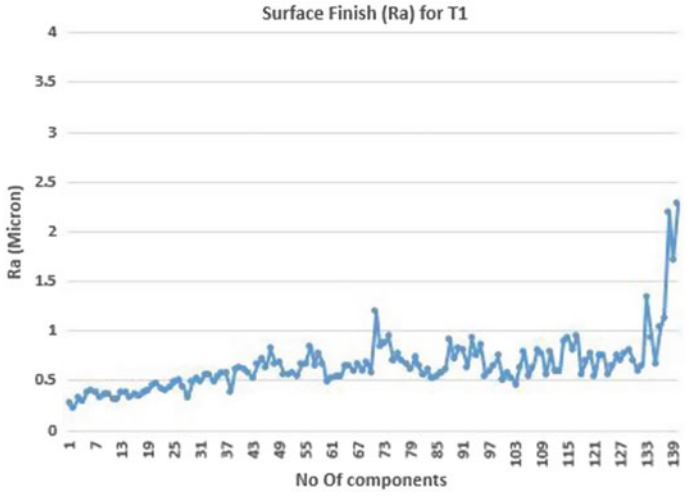

Fig. 40.9 Surface finish for T1 wheel

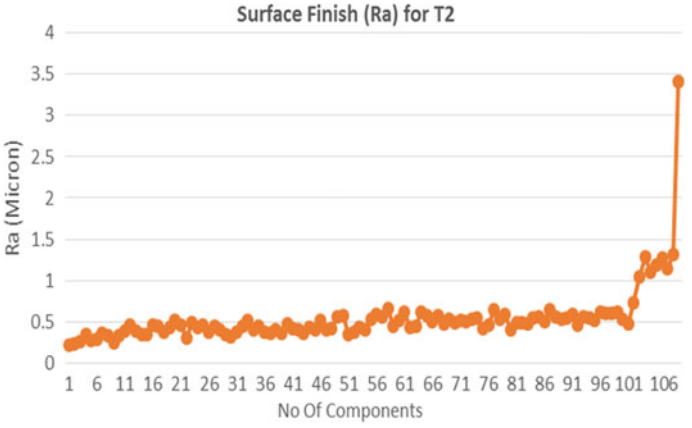

Fig. 40.10 Surface finish for T2 wheel

Table 40.4 Dresser feed rate

Sl. No.	Feed rate (mm/min)
1	50
2	100
3	200
4	250

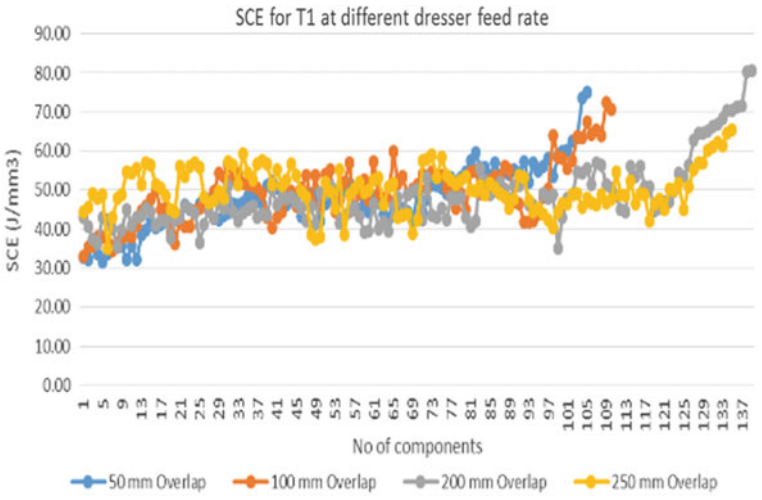

Fig. 40.11 SCE at different dresser feed-T1

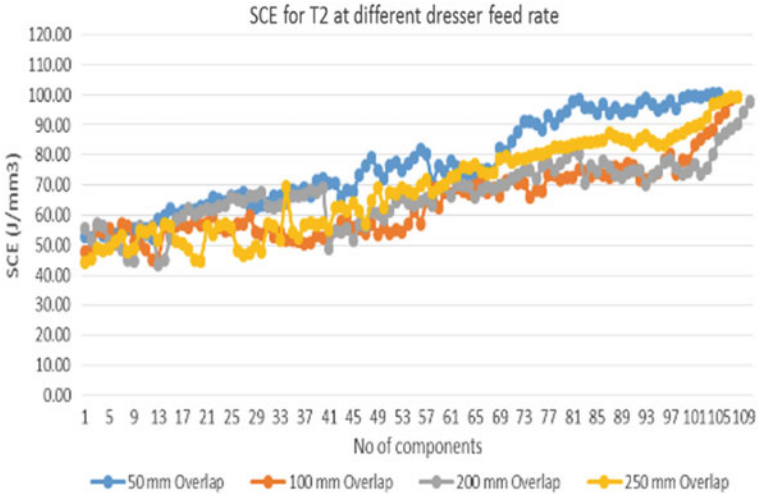

Fig. 40.12 SCE at different dresser feed-T2

40.3 Results and Discussion

40.3.1 Needle Shaped Versus Blocky Shaped Grains

In general, microcrystalline grains have high fracture resistance. The grain does not fracture at lower loads. Even at higher loads, the fracture would be at a microlevel.

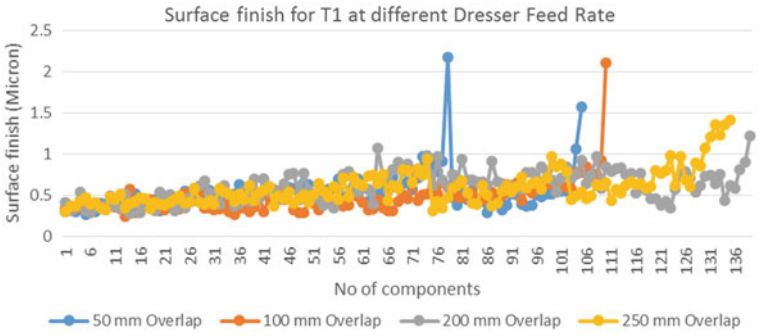

Fig. 40.13 Ra at different dresser feed-T1

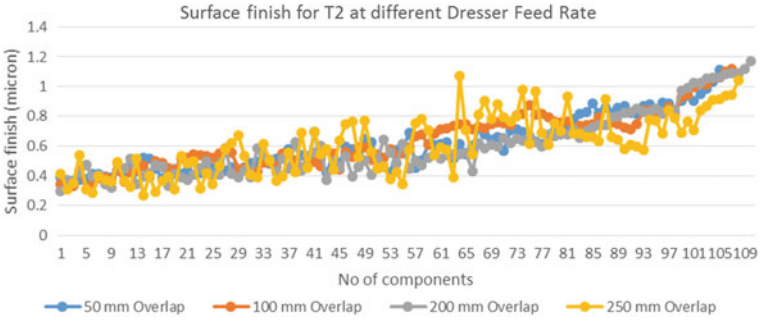

Fig. 40.14 Ra at different dresser feed-T2

Here interactions 1.1 (cutting) is maintained for a longer duration due to its high fracture resistance along with interactions 1.2 (plowing) and 1.3 (sliding). Also, micro fracturing help grains retain the sharpness leading to lower SCE over a sustained period. Surface finish (Ra) also gets maintained during this period.

Between needle shaped grain and regular blocky grain, the needle shaped grain has a higher aspect ratio as per Table 40.2. This leads to lower loose packed density (LPD) that naturally introduces a larger porosity and grain spacing in the grinding wheel as per Table 40.5. This spacing between grains can accommodate more chips, which dramatically influences and lowers chip related tribological interactions 2 (chip/bond)

Table 40.5 Wheel Porosity comparison between Needle and Blocky shaped grains

Type of grain	Porosity (%)
Needle shaped microcrystalline	37.21
Blocky shaped microcrystalline	32.76
4.45% porosity increase in needle shaped microcrystalline grain	

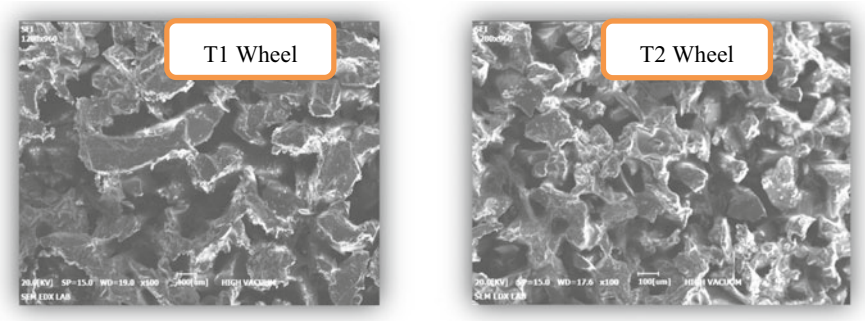

Fig. 40.15 SEM analysis of grinding wheels

and 3 (chip/work). This means that interactions 1.1 (cutting), 1.2 (plowing), and 1.3 (sliding) are sustained over a longer period when compared to blocky grains. This is reflected in lower SCE and more no of components ground between dressings with needle shaped grains.

In the case of blocky grains, the porosity level is comparatively low. Even though this grain also fractures at microcrystal level, the ability to accommodate chips is reduced due to closer packing. So interactions 2 and 3 sets in early leading to increase in SCE and lesser no of components ground before next dressing.

Scanning Electron Microscope (SEM) pictures of these grinding wheels indicate more porosity for needle grains (T1 wheel) as shown in Fig. 40.15.

Surface finish (Ra) values of both experimental wheel T1 and T2 are fairly stable till the endpoint where it shoots up drastically. This was coupled with a heavy grinding noise. This could be attributed to interactions 2 (chip/bond) and 4 (bond/work). As the grinding continues, more material removal also leads to more chips getting deposited on the wheel surface over time. This leads to more of interaction 2 (chip/bond) though interaction 3 (chip/work) also comes into play. Meanwhile over a period of time, the protrusion of grain comes down due to its wear and slowly the bond gets in contact with the workpiece leading to interaction 4 (bond/work). Vitrified bond is glassy and brittle in nature. At higher grinding force, it starts fracturing at a rapid rate. This leads to vibration and noise while grinding. Surface finish deteriorates as shown in Fig. 40.10 at a comparatively lesser number of components ground.

It may be noted that the major difference between these two grains is that the needle shaped grains can accommodate more chips due to its porous structure so that the onset of bond fracture is delayed. This leads to lower specific cutting energy and more number of components ground between dressing cycles.

Chemical Analysis of grinding wheel surface before and after dressing for these two wheels reveals the presence of more iron in wheel with needle shaped grain (Table 40.6). This shows accommodation of more chips in the pores. These chips do not interfere with grinding process for a considerable period of time.

Table 40.6 Fe content comparison before and after dressing

Wheel	Type	Fe content before dressing (%)	Fe content after dressing (%)
T1	Needle shaped microcrys-talline	6.3–7.0	1.0–1.3
T2	Blocky shaped microcrys-talline	4.4–4.7	1.0–1.3

Table 40.7 Dresser feed rate versus dressing frequency

Dresser feed rate (mm/min)	Dress frequency (No. of components) for T1 wheels	Dress frequency (No. of components) for T2 wheels
50	105	105
100	110	107
200	139	110
250	135	108

40.3.2 Varying the Dresser Feed Rate

A comparison of dress frequency at different dresser feed rate for both T1 and T2 wheels are shown in Table 40.7.

For T1 Wheels, The maximum number of components ground was achieved at a dresser feed rate of 200 mm/min closely followed by 250 mm/min. Whereas at a lower dresser feed rate, the number of components ground before next dressing is comparatively lesser. It was evident from the previous experiment that the needle shaped grain had a lot of naturally introduced porosity due to its specific shape and it can accommodate more chips.

While dressing, it has to be ensured that the chips loaded deep in the pores had to be fully cleared off. At a higher dresser feed rate, the dressing force is more, leading to more grain fracture and clearance of chips. This results in sharper edges on the wheel periphery with pores without any metal loading.

When grinding starts with such surface texture, interactions 1.1 (cutting) will be predominant, followed by interactions 1.2 (plowing) and 1.3 (sliding). Since the porous structure is reinstated on the surface due to the clearing of chip, onset of interactions 2 and 3 are delayed. All these factors lead to more number of components being ground before next dressing cycle sets in.

At lower dresser feed rate of 50 and 100 mm/min, this phenomenon of chip clearance from deep inside the pores is not effective. This leads to earlier onset of interactions 2 (chip/bond), 3 (chip/work), and 4 (bond/work). This has resulted in lesser number of components being ground before next dressing.

For T2 wheels, As can be seen from Table 40.7, there is no appreciable difference in no of components between the different dresser feed rates for blocky microcrystalline grains. As these grains are more blocky in shape, the loose pack density (LPD) is high. The structure is more closed contrary to the porous structure of needle shaped grains. The extent to which it can accommodate chips is limited.

Initially, interactions 1.1, 1.2, and 1.3 are good due to microcrystalline fracture. As the chips start loading the wheel, interactions 2, 3, and 4 come into picture earlier than for needle shaped grains. The penetration of chips onto the grinding wheel surface is also shallow due to lack of porous structure. Owing to this, dressing force required to dislodge the chip is also less. Hence even at a lower dresser feed rate of 50 mm/min, the wheel surface is clean. A fair amount of grain fractures along with recessing of bond leading to sharper surface which will enhance cutting action. At higher dresser feed rates, the microfracture of grains is more, leading to sharper surfaces. However, the overall number of components ground between dressing intervals is comparatively lesser than needle shaped grains.

40.4 Conclusions

This paper attempts to arrive at the right combination of grains for Inner Ring (IR) Track grinding wheel for bearing. Both needle and blocky shaped microcrystalline grains were tried. The dresser feed rate was varied. Using a diagnostic tool, the process signals were captured for all the experiments. The specific cutting energy (SCE), surface finish (Ra) were compared along with dressing frequency obtained for each experiment. Inferences were made from the above data through analysis of microscopic interactions at the grinding zone. This study concludes that the needle shaped microcrystalline grains give much better grinding efficiency and quality parameters than a blocky shaped microcrystalline grain for this particular grinding application. These learnings can further lead to solving process related issues or development of new products for the bearing industry. The methodology and understanding the importance of grinding zone will lead to a more "cause and effect" scientific approach in surface generation techniques than treating them as a "black art".

Acknowledgements We express our sincere thanks to the management of Carborundum Universal Limited, Chennai for supporting us during this development. We are also thankful to Dr. K. Subramanian, President, STIMS Institute Inc., USA for his valuable guidance, mentoring, and continuous support to the team through thought-provoking discussion during this development.

References

1. Subramanian, K.: Microscopic Interactions, the System Approach for Precision Components Manufacturing, STIMS Institute (Science Based Technology Innovation and Management Solutions), pp. 3–7
2. Subramanian, K.: Measurement and Analysis, the System Approach for Precision Components Manufacturing, STIMS Institute (Science Based Technology Innovation and Management Solutions), pp. 8–9
3. Vairamuthu, R., Brij Bhushan, M., Srikanth, R., Ramesh Babu, N.: Performance analysis of cylindrical grinding process with a portable diagnostic tool, p. 2
4. Subramanian, K., Jain, A., Rajagopal, V., Bhushan, B.M.: Tribology as an enabler for innovation in surface generation process, pp. 4–6

Chapter 41
Three Turn ECAP Processing of AA6061 Alloy: Microstructure and Mechanical Properties

Atul Dayal, Ankit Sahai, K. Hans Raj and R. S. Sharma

Abstract A popular Severe Plastic Deformation (SPD) process known as Equal Channel Angular Pressing (ECAP), is envisaged as the best method for large volume and at low cost for obtaining UltraFine Grain (UFG) in bulk metals, due to its low pressing force requirement and the resulting low pressure on pressing tool (plunger) and die. High-strength semifinished products produced from ECAP have a high potential for application for the manufacture of fasteners for aircraft, components of aircraft fuselage, medical devices, sports equipment, and microsystems. The usefulness of experimental and FEM analysis in developing practical ECAP process with innovative dies is demonstrated. Practical problems faced during single turn ECAP experimentations are identified (i.e., labour intensive process, reduction in billet size, billet jamming, etc.) and remedies are suggested in this work. A Multi-turn (Three Turn) ECAP process to increase the process efficiency and for upscaling the procedure is developed. Microstructural results indicate that AA6061 aluminium billet processed through innovative Multi-Turn ECAP die after four repetitive passes show the significant reduction in average grain size i.e., 10 μm (Fresh billet) to 0.3 μm (Processed billet after 4 passes), and smaller grain size helps substantially to increase the yield strength and tensile strength.

Keywords ECAP · SPD · UFG materials

41.1 Introduction

Ultrafine grain materials/Bulk nano materials are among the interest areas of research today to meet present engineering challenges. Traditionally bulk nano materials are made by nano scale synthesis i.e., self-assembly, nontraditional lithography, template growth and biomimetics. In these processes, nanoparticles, delivered in the form of nanotubes, nanopowders, quantum dots, and biomaterials are staked into final product in a designed way. These processes are quite expensive, time-consuming and

A. Dayal (✉) · A. Sahai · K. Hans Raj · R. S. Sharma
Department of Mechanical Engineering, Dayalbagh Educational Institute, Agra, India
e-mail: atuldayal333@gmail.com

M. S. Shunmugam and M. Kanthababu (eds.), *Advances in Micro and Nano Manufacturing and Surface Engineering*, Lecture Notes on Multidisciplinary Industrial Engineering,
https://doi.org/10.1007/978-981-32-9425-7_41

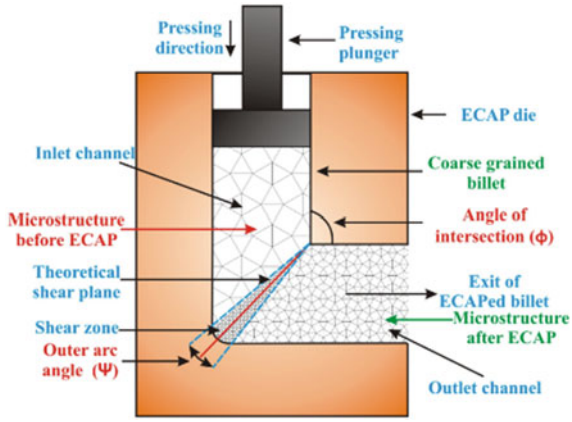

Fig. 41.1 Schematic diagram of ECAP process

chemically unstable [1]. Recently a top-down grain refinement approach known as Severe Plastic Deformation (SPD) [2, 5, 7, 8] has been adopted to produce bulk nanomaterial at a commercial level. Among different SPD approaches, one approach known as Equal Channel Angular Pressing (ECAP) (Fig. 41.1) [3] attracted a lot of attention recently because of its potential to be used at an industrial level, but still its applications are restricted to laboratory level only. Larger pressing load, heavier dies, large experimental setup and labour intensiveness are the major hurdles before the commercialization of an ECAP process [4–8]. In this work practical problems faced during single turn ECAP process is analyzed and A new multi-turn ECAP process is designed, developed and experimentally tested to overcome the process shortcomings. The outcome of this work certainly provides momentum in the commercialization of ECAP process.

41.2 Experimental Setup

ECAP experimentations are performed on conventional single turn ECAP die and newly developed three turn ECAP die. Split ECAP dies are used for the experimentation and experiments are performed on commercially available AA6061 aluminium alloy. Since AA6061 is ductile in nature, all forming experiments are carried out at room temperature. Plunger speed kept low (2 mm/s), to avoid heating up the material, which could lead to grain growth. A computerized hydraulic press with a pressing capacity up to 100 tonnes is used for experimental analysis. An 80 kg weight cast iron fixture is used for holding the vertically split ECAP die, this fixture had added extra strength to the ECAP die for hard material to be processed. The fixture also facilitates the rapid engagement and disengagement of an ECAP die for multiple passes.

All experiments are carried out at room temperature with or without molybdenum disulfide (MoS_2) lubricant.

Circular cross section, AA6061 billets with 10 mm diameter and 100 mm length are used for analysis. Tolerance between plunger and ECAP channel kept very low to prevent material flow through the joint cavity. To avoid cup formation at top portion of the billet, top and bottom portions are grinded into a conical shape.

41.3 Limitations in Conventional Single Turn Ecap Process

During single turn ECAP experimentations few shortcomings have been faced like:

41.3.1 Labour Intensive Process

In single turn ECAP process, after each pass, ECAP die is to be dismantled for extracting of ECAPed billet as shown in Fig. 41.2. For the next pass, the extracted billet is surfaced finished and inserted into tightly closed ECAP die (Fig. 41.3). Due to these activities of dismantling, surface finishing and billet rotation, the process becomes quite labour intensive.

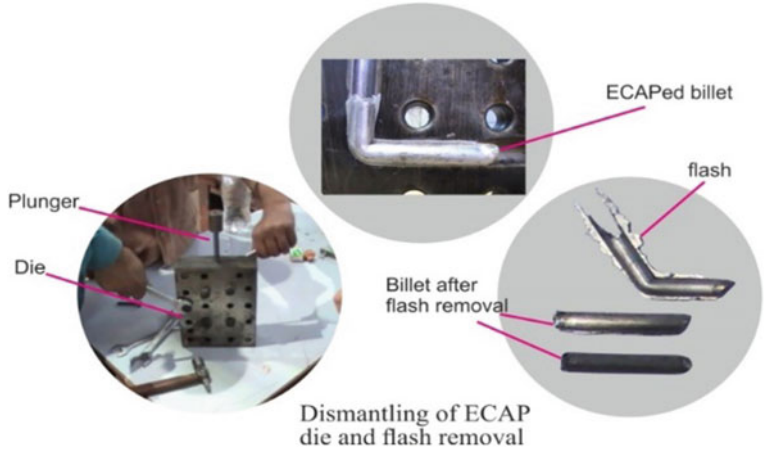

Fig. 41.2 Illustrative images of dismantling of ECAP die and flash removal of ECAPed billet

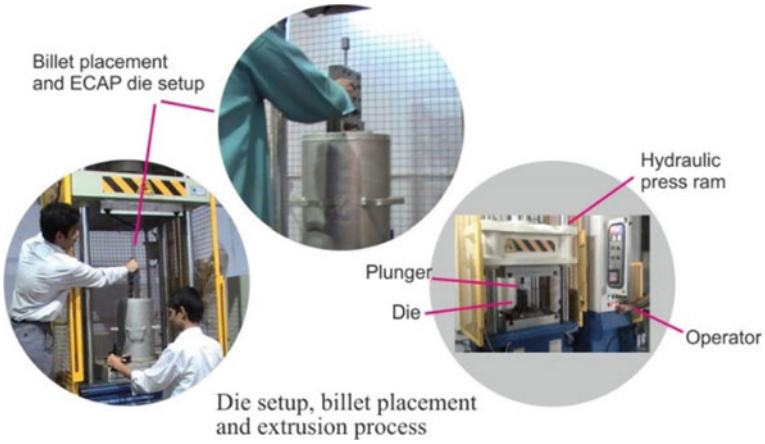

Fig. 41.3 Illustrative images of die and billet placement and extrusion process for repetitive ECAP passes

41.3.2 Reduction in Billet Size

In a single turn ECAP process, in order to obtain uniform grain refinement, the billet has to follow the processing routes (i.e., A, BA, BC, C) as shown in Fig. 41.4. Therefore, the ECAP die need to be dismantled and billet has to be extracted out and again reinserted into the die after grinding of flash and removal of end portion of the billet (Fig. 41.2). By the repetition of this process the size of processed billet gradually reduces. The size reductions in AA6061 aluminium alloy billet during four repetitive ECAP passes are shown in Fig. 41.5.

Therefore, the above challenges encountered in single turn ECAP process encouraged us to design a novel multi-turn ECAP process to resolve these process limitations.

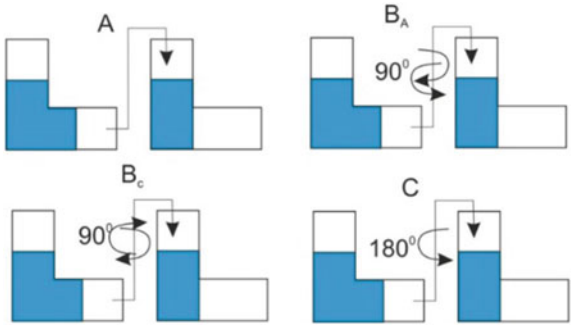

Fig. 41.4 Schematics of ECAP processing routes, A, B_A, B_C and C

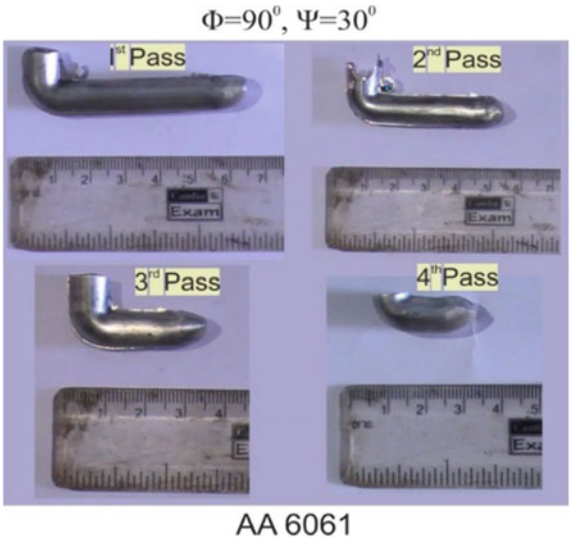

Fig. 41.5 Experimental illustration of billet size reduction during four repetitive ECAP passes

41.4 Three Turn ECAP

The three turn ECAP design is presented in Fig. 41.6a, b, this design consists of three channels, one in each direction X, Y and Z respectively.

The main advantage of three turn ECAP process over convention single turn ECAP is its 3-dimensional channel profile which enables the indie rotation of processed billet as per route 'Bc' during one complete cycle (Fig. 41.7b). Whereas, in single

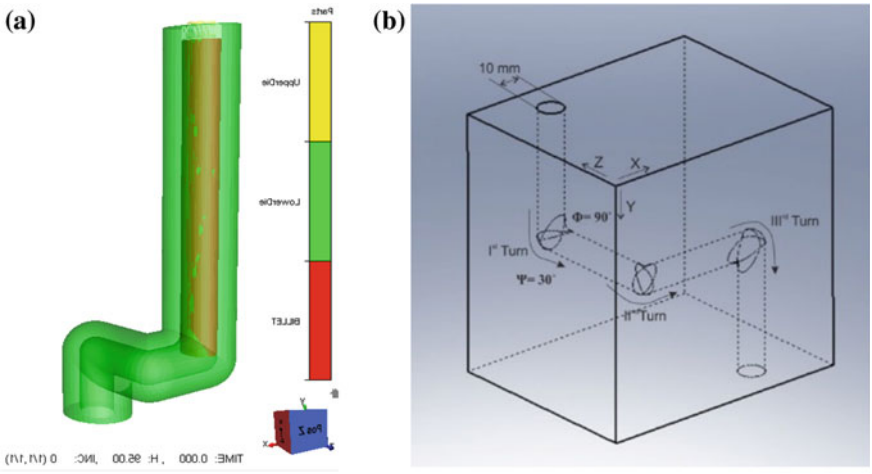

Fig. 41.6 Schematics of **a** Three turn ECAP die assembled view in FORGE FE environment, **b** Isometric view of three turn ECAP die

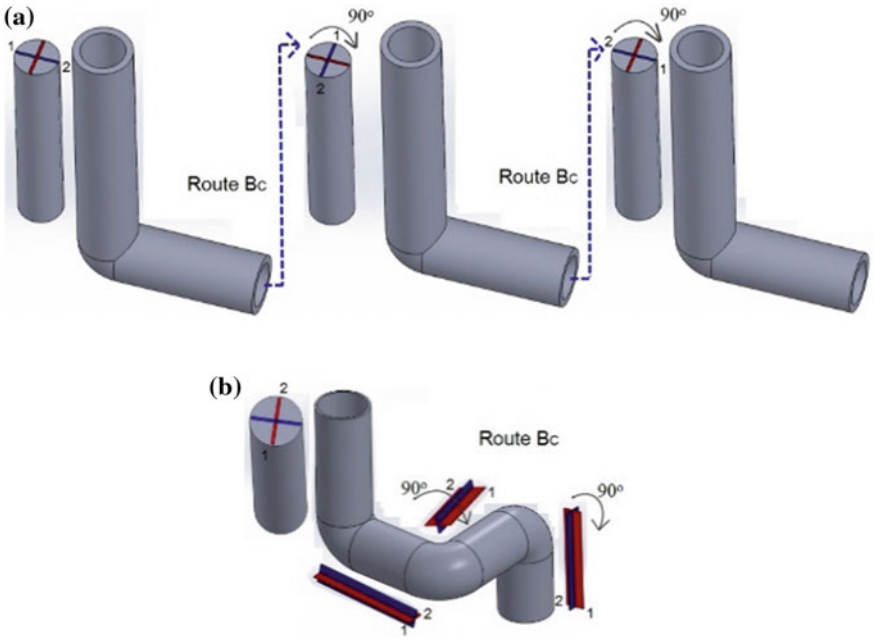

Fig. 41.7 Schematics of **a** Manual billet rotation during consecutive passes in single turn ECAP die, **b** automatic indie billet rotation in three turn ECAP die

turn, ECAP die billet needs to be rotated manually and reinserted in the ECAP die during consecutive passes (Fig. 41.7a).

Three billets pressed inside the die in a continuous manner one after another, each billet pushes its successor along the channel and eventually out of the die. Since billets used in three turn ECAP trials were shorter than the total passages, therefore during continuous pressing operation two billets always remain inside the die which is extended over three turns. Since AA6061 is ductile in nature, the forming experiments were carried out at room temperature. The forming speed kept low (2 mm/s), to avoid heating up the material, which could lead to grain growth. Three turn die is designed in two segments. These segments were kept together by two holding rings; these rings are pressed on the die segments and then tightly bolted in order to prevent the die segments to going apart during forming operation. The outer surface of the die is kept slightly conical in order to force it into the holding rings. The die is made of high-speed steel and manufactured by CNC milling process.

Experimental design of three turn die and processed AA6061 billets after one complete cycle is shown in Fig. 41.8a and b, respectively. Three turn die contains longer channel length. Therefore, after one complete three turn cycle, a considerably full length processed billet is obtained, unlike single turn ECAP. The concealed and tightly closed design of three turn ECAP die also helps in reducing the flash generation.

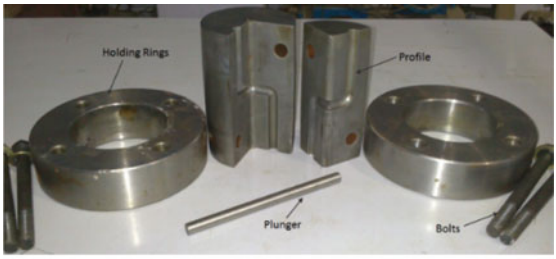

(a) Three turn die

(b) Processed AA6061 aluminium billet after one complete three turn cycle

Fig. 41.8 Experimental images results and discussion

Commercially available AA6061 aluminium alloy is used for numerical and experimental analysis. Raw specimen billet has been grinded up to 0.5–1 mm in diameter to permit loose fit in the die channel. It facilitates billet to slide properly into the tightly closed ECAP die. Before placing the processed billet into the die for next pass, processed billet needs to be finished properly and extra flash is removed by filing, as shown in (Fig. 41.9a), removal of the flash is necessary because this flash gets inserted into the die's joint cavities, and tightly sticks with the die and leads to plunger failure.

Extrusion process has been carried out using a tool steel plunger guided by a hydraulic press. Tolerance between plunger and ECAP channel kept very low to prevent material flow through the joint cavity and cup formation at the top portion of the billet. To avoid cup formation at top portion of a billet, top and bottom portion of billet are grinded into a conical shape as shown in figure (Fig. 41.9b).

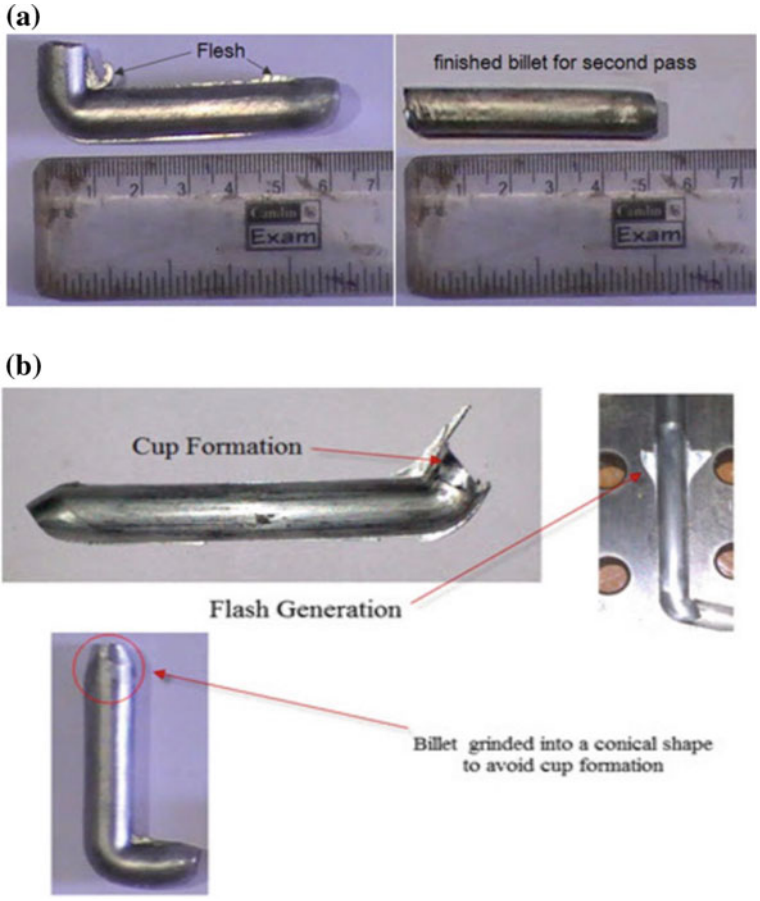

Fig. 41.9 Billet fabrications for experimental analysis

41.4.1 Tensile Testing

The engineering stress-strain curves of AA6061 alloy before ECAP and after ECAP are presented (Fig. 41.10). Ductility and strength are measured by uniaxial tensile test. It is apparent that the initial coarse-grained billet is in itself an extruded rod having grain size of about 10–15 μm and shows yield strength up to 250 MPa and a large elongation to failure or ductility (25%). At the same time aluminium alloy (AA6061) subjected to two passes of ECAP with route 'A' shows significant increase in strength (400 MPa), but dramatically decrease in elongation to failure or ductility (10%). Billet subjected to two passes of ECAP with route 'Bc' shows almost similar results. This result is consistent with the classical mechanical behaviour of metals that are deformed plastically. However, with further straining up to four passes, it shows that there is an increase in both strength (Yield strength—475 MPa) and

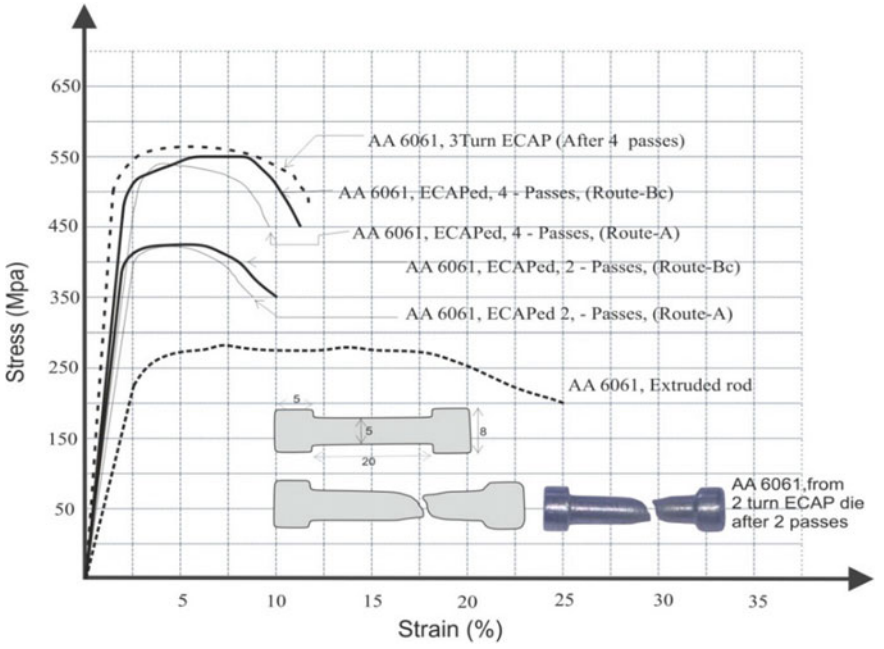

Fig. 41.10 Stress strain curve of unprocessed and ECAPed AA6061 aluminium alloy

ductility (12.5%). Stress-strain curve (Fig. 41.10) indicates that material processed with three turn ECAP die after four complete turns show slight improvement in ductility in comparison with conventional single turn ECAP die after four repetitive passes with route 'Bc'. It can be seen that pressing route also helps in retaining ductility; route 'Bc' shows greater retention of ductility than route 'A'. This satisfies the effect called 'Paradox of Strength and Ductility in SPD processed material' [5, 6]. It is also observed that pressing route also helps in retaining ductility; route (Bc) shows greater retention of ductility than route (A).

41.4.2 Microstructural Analysis

The scanning electron microscope is employed to study the microstructure produced in the processed billet. For microstructural analysis, a segment is cut from the processed billet and properly electropolished.

Microstructural results of unprocessed billet before ECAP and ECAPed billet after four passes with route 'Bc' are presented in Fig. 41.11. Results showed that the unprocessed billet (extruded rod) contains grain with size of 10–15 μm (Fig. 41.11a), and after four passes with processing route 'Bc' (with single turn ECAP die ($\Phi = 90°$, $\Psi = 0°$)), the average grain size reduces to 0.4–0.5 μm (Fig. 41.11b). The

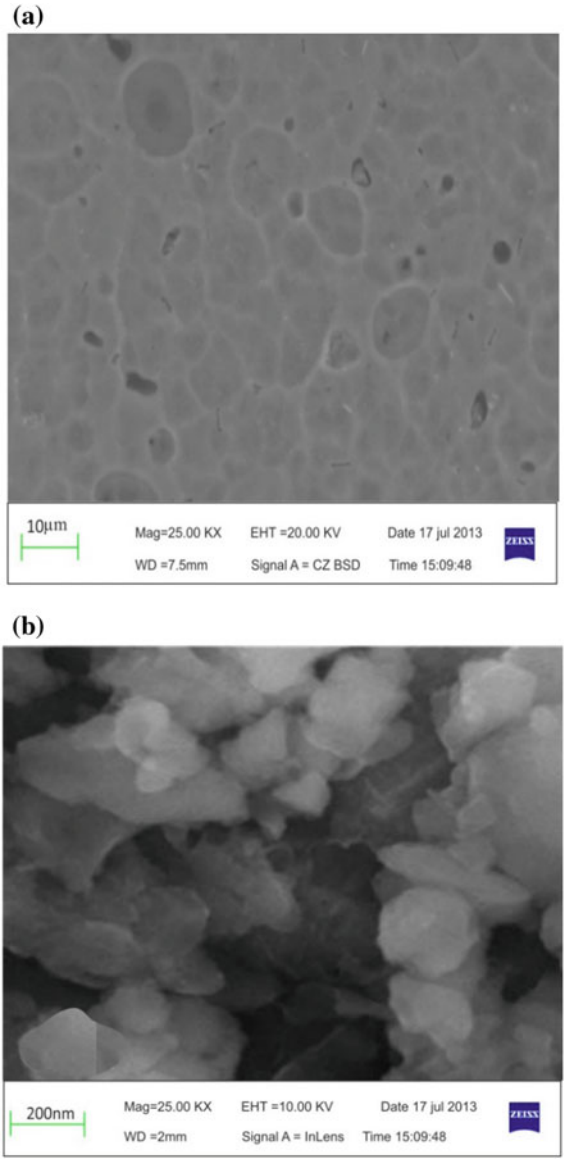

Fig. 41.11 **a** Unprocessed billet. **b** ECAPed billet after 4 passes with processing route 'Bc'

result showed that after four passes, the subgrain boundaries evolve into high angle grain boundaries and arrays of subgrains get transformed into an array of equiaxed ultrafine grain.

The microstructure result of ECAPed aluminium (AA6061) billet processed through three turn ECAP die during four passes are shown in Fig. 41.12a–d for Ist, IInd, IIIrd and IVth pass, respectively. It is observed that after first pass metal grains get elongated along the shear plane and with further repetitive passes as per route 'Bc' the subgrains get transformed into ultrafine grain with high angle grain boundaries. It is observed that after IVth ECAP pass the ultrafine grains with an average grain size of 0.3–0.4 μm are present in the processed billet (Fig. 41.12d).

The microstructural results presented in Fig. 41.12, have suggested that material processed with route 'BC' shows the presence of equated grain with high angle grain boundaries thus demonstrates the better mechanical properties.

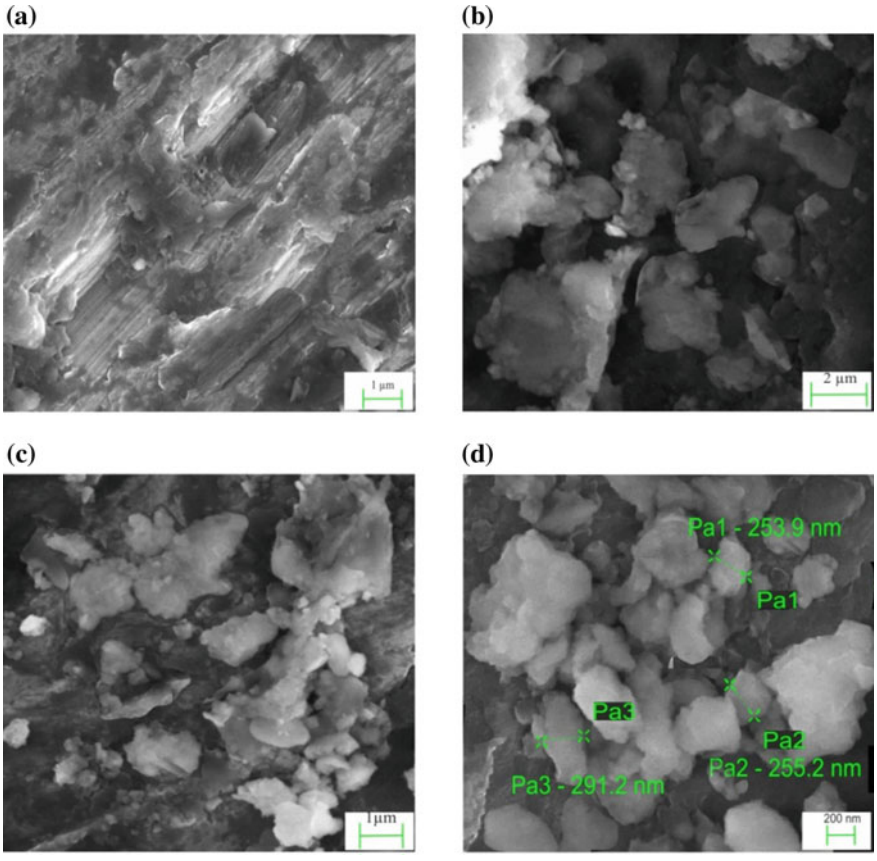

Fig. 41.12 Microstructure of AA6061 aluminium billet processed through three turn ECAP die after—**a** First pass, **b** Second pass, **c** Third pass, **d** Fourth pass

41.5 Conclusions

Uniaxial tensile test performed on AA6061 aluminium alloy indicates that after 4 repetitive ECAP passes with processing route 'Bc', yield strength increases from 240 to 475 MPa.

Mechanical test performed on ECAPed billet processed through three turn ECAP die after four passes show that the yield strength of AA6061 billet increases from 240 to 500 MPa and ultimate tensile strength increases from 280 to 565 MPa. The billet processed through three turn ECAP die follows route 'Bc' and it has already proven that processing route 'Bc' helps in getting better mechanical properties.

It can be observed that for AA6061 alloy, with route 'A' percentage elongation to failure decreases 25 to 9, while for route 'Bc', percentage elongation to failure decreases from 25 to 11.5. Therefore, it is observed that the billet process with route 'Bc' shows slight retention in ductility in comparison with route 'A'.

Microstructure characterization performed on AA6061 aluminium alloy shows the presence of large grain size with an average grain size of 10–15 μm in an unprocessed billet (extruded rod). After four repetitive ECAP passes through conventional single turn ECAP die with route 'Bc', it is evident that the average grain sizes get refined up to 400–500 nm.

The microstructural characterization results of ECAPed billet processed through three turn ECAP die shows the presence of ultrafine grains with an average grain size of 300–500 nm.

Acknowledgements The authors gratefully acknowledge the help rendered by NIT Tiruchirappalli for using the experimental facility and ACMS, IIT Kanpur for allowing to perform EBSD and Scanning Electron Microscopy. Support for this research from the MHRD, under NMEICT–Virtual Labs is deeply appreciated.

References

1. Olejnik L., Rosochowski A. Methods of fabricating metals for nano-technology. Bull. Polish Acad. Sci. **53**, 1–11 (2005)
2. Zhu Y.T.: Nanomaterials by severe plastic deformation. Scr. Mater. **51**, 825–830 (2004)
3. Valiev, R.Z.: Bulk nanostructured materials from severe plastic deformation. Prog. Mater. Sci., **45**, 103–189 (2005)
4. Parshikov, R.A., Rudskoy, A.I., Zolotov, A.M.: Technological problems of equal channel angular pressing. Rev. Adv. Mater. Sci. **34**, 26–36 (2013)
5. Dayal, A., Sahai, A., Raj, K.H., Sharma, R.S.: Comprehensive study of effect of process parameters in equal channel angular pressing. Indian J. Eng. Mater. Sci. **25**(2), 113–121 (2018)
6. Valiev, R.Z., Langdon, T.G.: Principles of equal-channel angular pressing as a processing tool for grain refinement. Prog. Mater. Sci. **51,** 881–981 (2006)
7. HansRaj, K., Sharma, R.S., Sahai, A., Gupta, N.K.: Different die designs for processing of Al alloy using equal channel angular pressing. Proc. Indian Natn. Sci Acad. **79**, 829–836 (2013)
8. Sahai, A., Sharma, R.S., HansRaj, K., Gupta, N.K.: Mechanical properties of Al6061 processed by equal channel angular pressing. Adv. Mater. Res. **585**, 392–396 (2012)

Chapter 42
Wear Performance Evaluation of AlCrN Based Coating Deposited by PVD Technique Under Dry and Cryogenic Environments

Abhishek Singh, S. Ghosh and S. Aravindan

Abstract The current study investigates the wear performance of the AlCrN based coatings deposited by conventional cathodic arc evaporation (CAE) technique and arc enhanced high impulse magnetron sputtering (HiPIMS) technique. The formation of the defect (holes, pores and droplet formation) on the coated surface due to continuous movement of cathode spot make the surface topography of the coating uneven in comparison to the later thus causing reduction of tool performance. The performance of the coating was evaluated in two environments for better understanding of the basic mechanics involved in wear phenomenon for AlCrN based coating deposited by different techniques. The results have demonstrated that the coating deposited by hybrid technique has performed better in comparison to conventionally deposited coating in both the environment.

Keywords Cathodic arc evaporation · HiPIMS · Topography · Flank wear

42.1 Introduction

More than hundred years have been passed since from its development the cutting tool is going through continuous evolution for improving its performance and economic aspects during the machining of various difficult to machine materials. The easiest way possible to optimize both is by coating the cutting tools. Wear minimization has been persuaded by various means like using high hardness cutting tools like PCD and CBN but high cost associated with them makes it a non-viable option in terms of economic aspects in comparison to sintered carbides [1]. PVD hard coatings are used to enhance the wear behaviour of the cutting tools while operating in severe environments for machining of nickel-based superalloys [2]. However, the

A. Singh · S. Ghosh · S. Aravindan (✉)
Department of Mechanical Engineering,
Indian Institute of Technology Delhi, Delhi 110 016, India
e-mail: aravindan@mech.iitd.ac.in

M. S. Shunmugam and M. Kanthababu (eds.), *Advances in Micro and Nano Manufacturing and Surface Engineering*, Lecture Notes on Multidisciplinary Industrial Engineering,
https://doi.org/10.1007/978-981-32-9425-7_42

improved wear behaviour of these coatings over the edge integrity depends on the optimized physical and mechanical characteristics of the coating material over the cutting tool. Aluminum-based multifunctional multicomponent coatings like AlCrN and AlTiN have gained popularity among the researchers. These coatings provide better wear resistance in comparison to the coatings which are aluminum deficient such as CrN and TiN at elevated temperature due to its high hot hardness, low thermal conductivity and improved oxidation resistance [3]. But when we compare AlTiN with AlCrN it can be found that the addition of the higher content of aluminum in the titanium-based nitride composition the crystal structure of the coating changes. The formed hexagonal lattice from cubic lattice of TiN, makes the less favourable properties in comparison with the chromium-based coatings which can hold more amount of aluminum without altering the structure. These properties prove AlCrN based coating a viable or efficient option for high-speed machining applications [4]. These coatings deposited by the conventional PVD deposition technique make the process easier in comparison to other methods but has certain limitations in terms of surface morphology and coating structure [5]. In order, to overcome these limitations and to harness the advantages of both the magnetron and cathodic arc techniques are amalgamated to deposit a coating which offers surface defect-free topography along with excellent wear and other tribological characteristics.

However, some of the properties of these obtained coatings are available in the literature but their behaviour in terms of wear performance is still unknown in comparison to AlCrN based coating deposited by CAE-PVD process. The wear performance of the coatings can't be better judged while machining difficult to cut material like nickel-based superalloy which offer so many difficulties because of its properties such as high work hardening rate, high hardness and presence of hard abrasive carbide particles and strong tendency to weld the tool and for a built-up edge [6–8].

This study focuses on the wear behaviour of AlCrN based coatings deposited by conventional and novel hybrid deposition technique under dry and cryogenic environment. Both the environments were selected concerning the sustainability aspects, i.e. environmental concerns, manufacturing cost, and other machining parameters. The study also emphasizes on the analysis of how the varied surface morphology of the coating and elemental composition affects the wear performance of the tools.

42.2 Experimental Details

42.2.1 Coating Deposition

The coatings were deposited on the K Grade cemented carbide inserts of geometry CNMA 120408. Coating A and Coating B were deposited using cathodic arc evaporation technique and are of 3.4 μm and 3.1 μm thickness and were deposited in 128 min and 100 min respectively. The samples were cleaned and ultrasonicated before placing inside the vacuum chamber. The substrate/tool holders were rotated

Table 42.1 Chemical composition of the workpiece material Nimonic C 263

Element	Mass (%)	Element	Mass (%)
Carbon	0.0480	Silicon	0.2100
Manganese	0.3900	Sulphur	0.0060
Chromium	20.1400	Molybdenum	5.8500
Nickel	50.5800	Aluminum	0.3900
Cobalt	19.8700	Copper	0.0640
Titanium	1.9500	Iron	0.2600

at fixed rpm so that the uniformity in the coating thickness can be achieved. The deposition temperature for both the coatings are in the range of 600–6500 C and 450–5500 C, respectively. Coating C was deposited using arc enhanced HiPIMS technique and it took 51 min for depositing a layer of 1.5 μm thickness. The thickness of the coating was measured using x-ray florescence technique (XRF).

42.2.2 Machining Test

The experimental investigation was carried out on the nickel-based superalloy Nimonic C 263 workpiece. Table 42.1 shows material composition, evaluated through the mass spectrometry.

The machining tests were performed on Leadwell T6 turning center under dry and cryogenic conditions. The machining parameters were kept constant at speed of 60 m/min, feed 0.12 mm/rev and depth of cut 1 mm for both the conditions. Six passes each of 25 mm length was performed to cut a length of total 150 mm with a single cutting edge. For cryogenic environment, liquid nitrogen was supplied at the cutting zone by means of the nozzle of 2 mm, through a vacuum jacketed line of cryogenic dewar at a constant pressure of 4 bar.

42.2.3 Tool Wear Characterization

The flank wear was measured under an optical microscope after every length of cut for each environment and coating. The flank and rake surfaces after 150 mm of cut were analyzed under scanning electron microscope and optical microscope for detailed analysis of the wear modes involved during the process.

42.3 Results and Discussion

42.3.1 Coating Morphology and Composition

The coatings deposited by conventional and hybrid physical vapor deposition techniques exhibited excellent surface characteristics. Though the surface morphology of conventionally deposited Coating A and Coating B have some surface defects in the form of holes and pores at some localized sites. The presence of these surface defects not only impart unevenness to the surfaces but also causes hindrance to the performance of the coated surface during its applications in the machining operation. Coating C is free from surface defects and its surfaces are much smoother in comparison to the former. Figure 42.1 shows the surface morphology for all the coatings. The Coating A is a multilayer coating with TiAlN as the base layer while AlCrN as the top layer. Coating B is a monolayer of AlCrN while Coating C being the same with different deposition technique and thickness. Table 42.2 represents the coating details in a descriptive way.

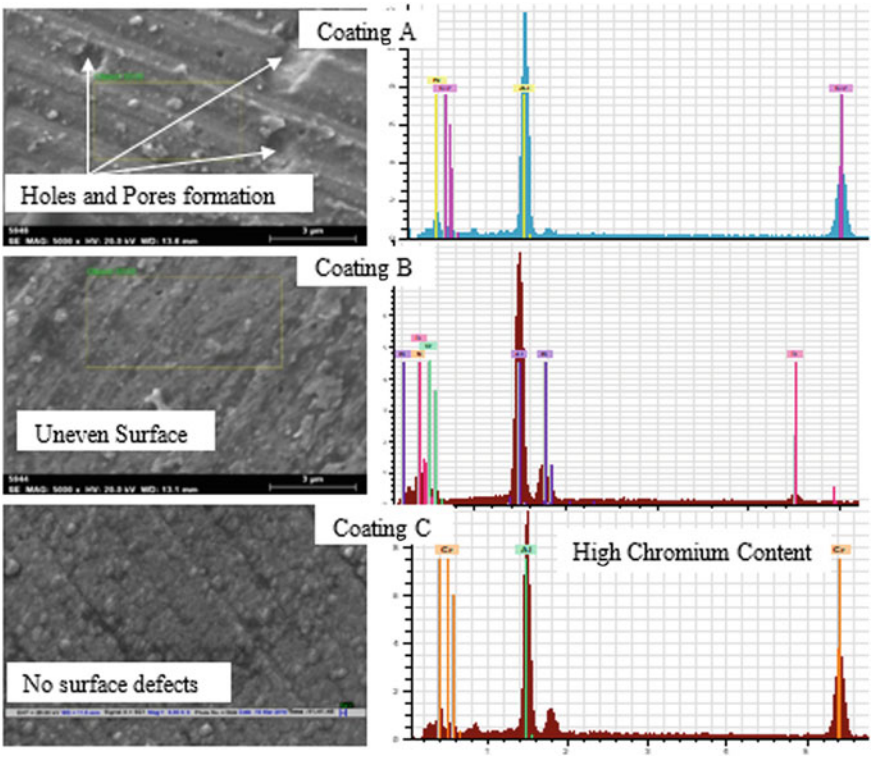

Fig. 42.1 Surface morphology and elemental analysis of AlCrN based coating

Table 42.2 Cutting tool coatings and properties

Description	Coating A	Coating B	Coating C
Deposition technique	CAE	CAE	Arc Enhanced HiPIMS
Hardness	~28.0 GPa	~28.8 GPa	~32.0 GPa
Coating structure	Dual layer	Mono layer	Mono layer
Colour	Blue-Grey	Bright-Grey	Grey

Energy dispersive x-ray spectroscopy was carried out to confirm the elemental composition. It can be seen that the Coating C has high Chromium content in comparison to aluminum while in case of other coating aluminum carries more weightage, thus making it better in terms of resistance to oxidation at elevated temperature. This is due to the fact that chromium oxide is one of the most stable oxides in comparison to aluminum oxide formed in aluminum rich coatings. In the initial stage, the formed oxide is CrO_2 which converts to highly stable Cr_2O_3 at a later stage.

42.3.2 Flank Wear Studies

Though the cost of the cutting tool may be very insignificant in comparison to cost of workpiece in most of the cases, studying their wear behaviour is of prime importance as it affects the surface integrity of the machined surface. Cemented carbide tools work quite well for low or medium speed machining of nickel-based superalloys but when machining them at higher speed their hardness reduces approximately by 50% as compared to its hardness at room temperature [9]. So, in this study coated carbide tools are utilized. Progressive flank wear was observed for all types of tools under both the environments. Figure 42.2 represents the progressive flank wear for all the three coatings. While Fig. 42.3 indicate the scanning electron microscopic images of wear obtained during the final cut. In the beginning, the tool underwent gradual wear with the machining length. However, after 125 mm length of cut it can be seen that the cutting edge for Coating A underwent a catastrophic failure which becomes more prominent at 150 mm length of machining under dry condition. This failure can be correlated to high stresses exerted on the cutting tool during the process. While under cryogenic condition no such wear was observed. Coating B doesn't undergo any type of failure at the later stages, but the obtained flank wear values were subsequently higher than that of Coating A. Severe chipping can be seen during the dry condition for the Coating B at later stages and is due to entangling of the flowing hard particles in the form of chip during the machining of nickel-based superalloy. This behaviour was not observed in case of cryogenic conditions.

The use of cryogenic helps in achieving high chip breakability by increasing the chip curling. The high chip breakability during the machining process thus helps in better penetration of the cryogenic into the primary cutting zone (effective cooling)

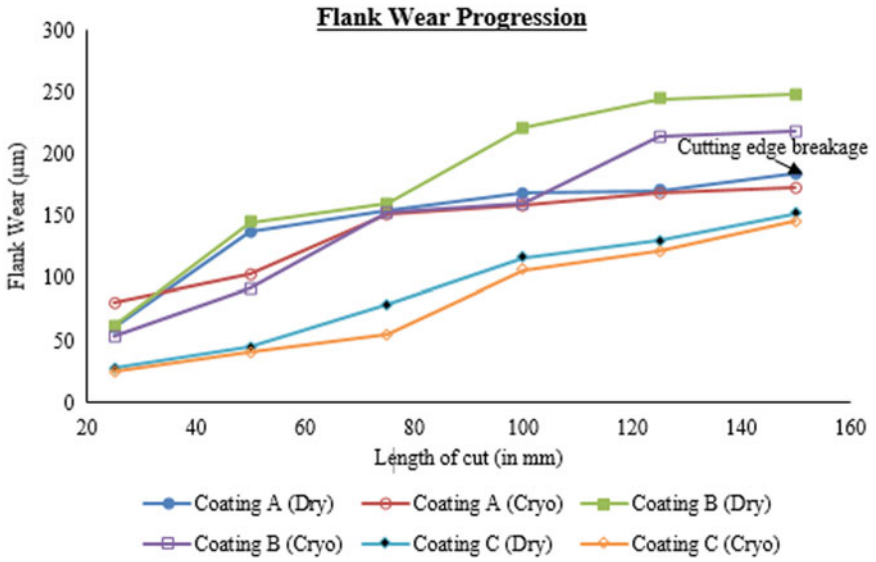

Fig. 42.2 Flank wear progression for the coated samples under dry and cryogenic conditions

as shown in Fig. 42.4. The improvement of the chip breakability in the cryogenic cutting is due to formation of chips of reduced thickness in comparison with dry cutting. This can be explained by the expression for chip reduction coefficient (£)

$$£ = e^{\mu\,(\pi/2-\alpha)} \text{ and } £ = t_2/t_1 \tag{42.1}$$

While for both cutting conditions t_1 and α are same.
Here t_1 is uncut chip thickness and α is rake angle.

So, the chip thickness (t_2) is dependent on the value of the coefficient of friction at the contact zone if other parameters are kept constant.

$$\mu(\text{cryogenic}) < \mu(\text{dry}) \text{ due to cushioning effect}$$

For the coating C deposited by the hybrid technique, the wear on the flank surface reduced to minimum, i.e. 28.12 and 25.37 µm in the starting of the cut. It's the smooth surface properties and better adhesion of the coating helps in achieving desired results. During the machining using Coating C built-up-edge formation can be seen during the machining length of 50 mm but due to its instability as it gets removed during the third pass. Though the use of cryogenic helps in reducing the flank wear by some amount but didn't help in reducing the progressive notch wear, which plays and an important role in determining the tool life.

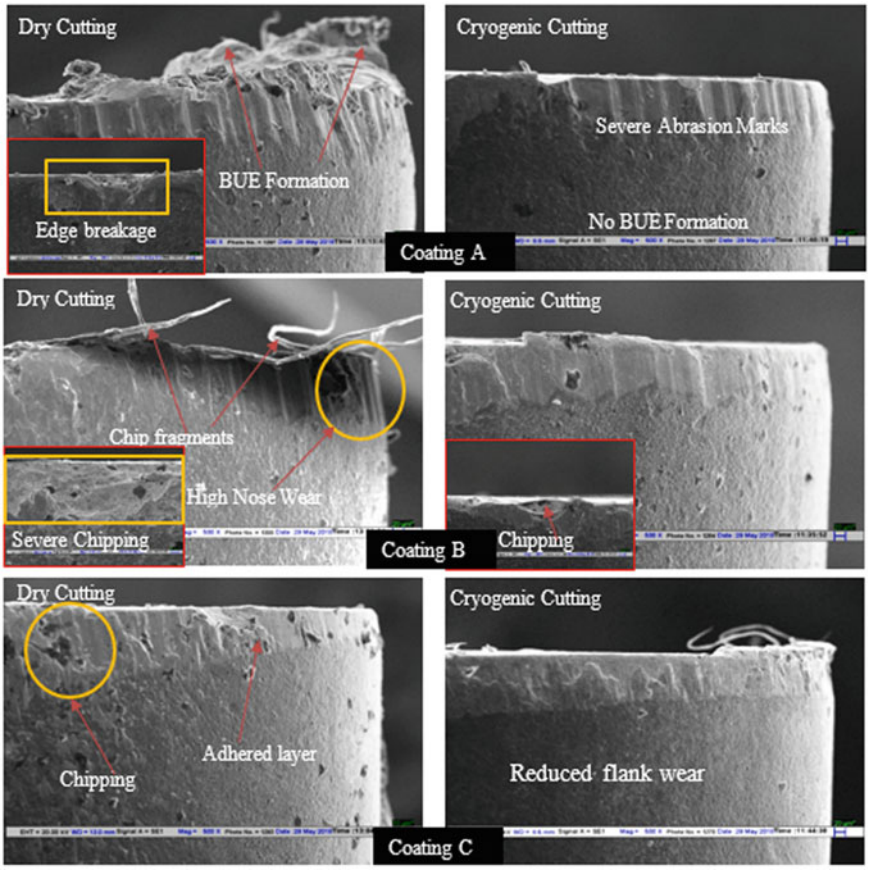

Fig. 42.3 Scanning electron microscopic images for flank wear under dry and cryogenic environment for AlCrN based coating

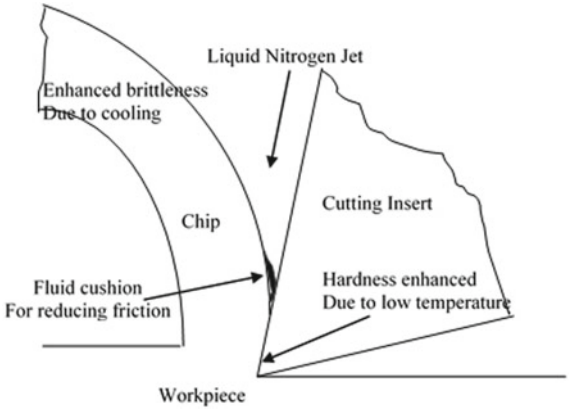

Fig. 42.4 Schematic of chip formation in cryogenic cooling (adapted from [10])

42.3.3 Rake Wear Studies

Though the flank wear is always considered as the criterion for the tool wear selection and rejection during the machining process the condition on the rake face also affects its performance during the machining operation. It was observed that when machining was performed under the dry condition the chips produced carry very high temperature that not only oxidizes the tool surface but also causes their adhesion nearby the cutting edge. During the study at the rake surface it was found that formation of the crater could be seen for both the multilayer and single layer Coating A and Coating B, respectively (Fig. 42.5). This behaviour is more prominent in the case of single-layer coating. However, in the case of Coating C no such behaviour

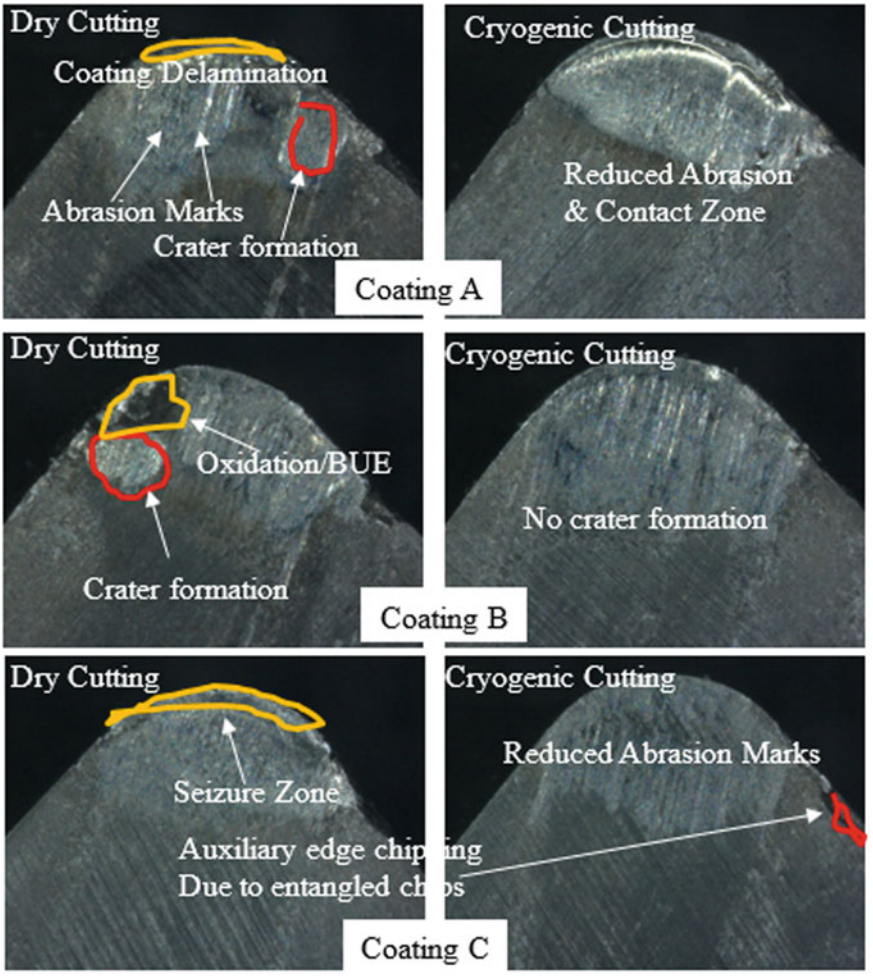

Fig. 42.5 Optical microscopic images for rake surface under dry and cryogenic environment for AlCrN based coating

was observed. Due to absence of chip breaker the formed chips always keep on entangling with the workpiece and tool thereby causing chipping at the auxiliary cutting edge. The use of the cryogenic, i.e. liquid nitrogen doesn't only diminish the formation of red hot chips (and thereby oxidation) but also reduces the contact area of the flowing chips with the tool surface. The obtained surfaces are much smoother in comparison to dry cutting environment as seen in the obtained microscopic images. High heat carrying capacity of the cryogenic reduces the temperature at the cutting zone and also provides a cushion at the rake surface thereby reducing the friction between the tool and flowing chips [9, 10]. The failure modes for all the coatings were same but it's the hardness and the adhesion of the coating which affects its wear performance during the machining process. The high hardness of the Coating C enables it to withstand severe dynamic stresses while the better adhesion provides resistance against the coating peel off by the flowing chips.

42.4 Conclusions

The study has focused on the wear behaviour of the AlCrN based coating under dry and cryogenic cutting environment correlating to its surface characteristics. The following conclusions can be drawn from the experimental results.

- The evenness in the surface morphology of the Coating C not only reduces the friction with the flowing chips but also enhances its wear performance.
- This improved wear performance was obtained with the coating of thickness approximately half that of Coating A and Coating B.
- Multilayer coating performed better in comparison to single-layer coating but this behaviour is limited to coatings deposited by conventional PVD technique.
- The use of cryogenic during the machining operation reduces the wear both at the flank and rake surface in terms of abrasion, chip tool contact area and oxidation behaviour.

All the coated tools underwent chipping at the auxiliary cutting edge in the absence of the chip breaker. However, this doesn't affect the cutting tool performance during the machining.

References

1. El-gallab, M., Sklad, M.: Machining of Al/SiC particulate metal-matrix composites Part I : tool performance **83**, 151–158 (1998)
2. Kursuncu, B., Caliskan, H., Guven, S.Y., Panjan, P.: Improvement of cutting performance of carbide cutting tools in milling of the Inconel 718 superalloy using multilayer nanocomposite hard coating and cryogenic heat treatment. Int. J. Adv. Manuf. Technol. 1–13 (2018). https://doi.org/10.1007/s00170-018-1931-z

3. Endrino, J.L., Fox-Rabinovich, G.S., Gey, C.: Hard AlTiN, AlCrN PVD coatings for machining of austenitic stainless steel. Surf. Coatings Technol. **200**, 6840–6845 (2006). https://doi.org/10.1016/j.surfcoat.2005.10.030
4. Viana, R., de Lima, M.S.F., Sales, W.F., da Silva, W.M., Machado, Á.R.: Laser texturing of substrate of coated tools—performance during machining and in adhesion tests. Surf. Coatings Technol. **276**, 485–501 (2015). https://doi.org/10.1016/j.surfcoat.2015.06.025
5. Čekada, M., Panjan, P., Kek-Merl, D., Panjan, M., Kapun, G.: SEM study of defects in PVD hard coatings. Vacuum **82**, 252–256 (2007). https://doi.org/10.1016/j.vacuum.2007.07.005
6. Zhu, D., Zhang, X., Ding, H.: Tool wear characteristics in machining of nickel-based superalloys. Int. J. Mach. Tools Manuf **64**, 60–77 (2013). https://doi.org/10.1016/j.ijmachtools.2012.08.001
7. Arunachalam, R., Mannan, M.A.: Machinability of nickel-based high temperature alloys. Mach. Sci. Technol. **4**, 127–168 (2000). https://doi.org/10.1080/10940340008945703
8. Akhtar, W., Sun, J., Sun, P., Chen, W., Saleem, Z.: Tool wear mechanisms in the machining of Nickel based super-alloys: a review. Front. Mech. Eng. **9**, 106–119 (2014). https://doi.org/10.1007/s11465-014-0301-2
9. Kaynak, Y.: Evaluation of machining performance in cryogenic machining of Inconel 718 and comparison with dry and MQL machining. Int. J. Adv. Manuf. Technol. **72**, 919–933 (2014). https://doi.org/10.1007/s00170-014-5683-0
10. Hong, S.Y., Markus, I., Jeong, W.: New cooling approach and tool life improvement in cryogenic machining of titanium alloy Ti-6Al-4 V. Int. J. Adv. Manuf. Technol. **41**, 2245–2260 (2001). https://doi.org/10.1016/s0890-6955(01)00041-4

Chapter 43
Numerical and Experimental Analysis of Plasma Nitrided XM-19 Stainless Steel

Shivanshu Dixit, R. K. Mishra and B. Ganguli

Abstract An experimental study of plasma nitriding and numerical simulation on XM-19 stainless steel is done in this work. PN conducted at various process temperatures ranging from 340 to 580 °C. The process parameters taken for PN were 4 h and in a ratio of N_2:H_2 = 1:4. The surface modification is done for the purpose of increasing the service life of the material. Numerical simulation is done on ABAQUS CAE and validated using the results of Guo et al. A numerical model is simulated for the different rates of compression (high and low) test using coupled temperature-displacement. The experimental work evaluated for microhardness and optical microscopy. Since the material found application to a highly corrosive environment, so a protective coating can be suggested for such material. This will be in the interest of both the research and industrial point of view which uses plasma nitriding on a large scale.

Keywords Plasma nitriding (PN) · XM-19 · Coupled temperature-displacement · Microhardness · Optical microscope

43.1 Introduction

The austenitic stainless steel [1] XM-19 (UNS S20910), when compared with other stainless steel (316 and 317), is having higher strength as well as it is cost-effective. It has high corrosion resistance, which makes the application of this material in extremely corrosive environments [2, 3]. Other physical, chemical, and mechanical

S. Dixit (✉)
Department of Mechanical Engineering, Indian Institute of Technology Ropar, Rupnagar 140001, Punjab, India
e-mail: 2017mez0018@iitrpr.ac.in

R. K. Mishra
Department of Mechanical Engineering, Gautam Buddha University, Greater Noida 201310, Uttar Pradesh, India

B. Ganguli
Institute for Plasma Research, Near Indira Bridge, Bhat, Gandhinagar 382428, India

M. S. Shunmugam and M. Kanthababu (eds.), *Advances in Micro and Nano Manufacturing and Surface Engineering*, Lecture Notes on Multidisciplinary Industrial Engineering,
https://doi.org/10.1007/978-981-32-9425-7_43

properties such as its nonmagnetic behavior, high work hardening rate, ductility, high strength, and corrosion resistance make this material high applicable in all types of working environments. The application of XM-19 SS is shown in Fig. 43.1. The alloying element composition of XM-19 by (%wt): 0.06% C (max), 0.010% S (max), 0.04% P (max), 0.10–0.30% Va, 0.10–0.30% Nb, 0.20–0.40% N, 1% Si (max), 20.5–23.5% Cr, 11.5–13.5% Ni, 1.5–3% Mo, 4–6% Mn, and balance is Fe [4].

The commercial names which are used by different industries are UNS S20910, 22-13-5, and XM-19 SS. This work presented in this paper includes plasma-based nitriding experiment. Literature available shows the little use of the plasma-based nitriding for XM-19 material while some uses gas nitriding process or liquid bath nitriding [4–8]. Chidambaram et al. [9] studied stainless steel 316 and XM-19 type for corrosion behavior under extreme condition of the nuclear- and coal-based power plant. Trester et al. [10] reported tribological properties of inconel 718 and nitronic 60. Another work by Williamson [11] studied different types of metals (total-16) having the same crystal structure (FCC). Guo [5] tested Nitronic 50 (XM-19) under uniaxial compression test. Their study includes the response of the material in thermomechanical testing and obtained results under a different range of strain rates, i.e., ranging from 0.001/s to 8000/s, and temperature ranges from 77 to 1000 K show the value of stain (true) overshoot more than 60%. Another article by Kumar [12] includes a coating on 23-8-N (Nitronic) stainless steel by the process of HVOF (high-velocity oxy-fuel). The coating of metal with WC–10Co–4Cr was tested for hardness and erosion. Schneider [13] talked about the better edge of XM-19 against more commercially available stainless steel (316 and 17-4 PH types). Since XM-19 remains nonmagnetic and has corrosion resistance as high the aforementioned steels, this can be a good alternative material in stainless steels.

From the literature mentioned above about the material XM-19 alloy, it was found that the work available is generally related to pulse RF technique or gas nitriding.

Fig. 43.1 Application of XM-19 stainless steel

Plasma-based nitriding can also be employed on such material as it falls under nitridable category [7]. Present work includes the surface modification of XM-19 and evolution of material for desired properties of high hardness and wear resistance through material characterization. Guo [5] worked on the flow behavior of nitronic 50 at various rates, and temperature is replicated through FEA simulations. The material properties found in the paper and other condition essential for the test were used as same to conduct a numerical simulation on commercially available software Abaqus 6.10-1 CAE. A close match of paper results and simulation results under coupled temperature-displacement Step used for different strain rates (high and low) and the temperature-dependent problem is used. Other important data is found in the literature available for the materials.

43.2 Experimental Procedure

The experiment requires sample preparation. To make sample free from scratch, first, rough grinding is done. Second, different emery papers 240, 600, 1200, and 2000 grit sizes are used. Finally, diamond paste 0.25-μ size is used for mirror polishing and cleaning with petroleum ether. The finished samples were used for plasma nitriding. A final sample will appear as shown in Fig. 43.2, while experimental step-up used for plasma nitriding is shown in Fig. 43.3.

XM-19 stainless steel was plasma nitrided with nascent [N] by glow discharge method. The detailed process parameter includes the creation of a vacuum of 0.05–0.10 Torr. The part on which the sample is placed is made up of cathode. The flow of the gas mixture of N_2 and H_2 is controlled by flow meter at a pressure reduced to 1–10 Torr. N_2 gas on the application of high voltage dissociates into N_2 ion that is accelerated toward the cathode. When these ions strike the metal surface, they form a glow of bluish color as shown in Fig. 43.4 also known as glow discharge plasma. Important parameters of DC voltage and current are continuously checked

Fig. 43.2 Polished XM-19 (substrate material)

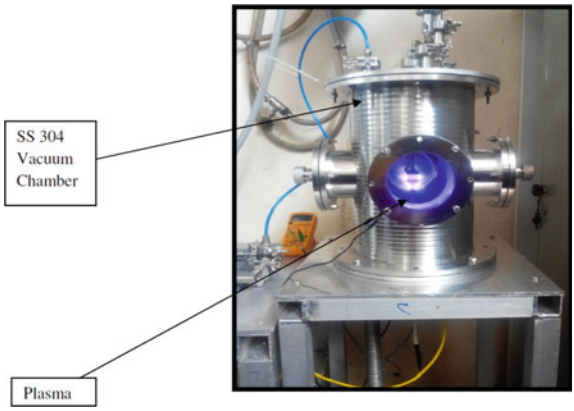

Fig. 43.3 Plasma nitriding experimental setup

Fig. 43.4 Glow discharge envelops the part

for continuous plasma region. This establishes the glow between cathode and anode and starts nitriding. This nitriding process is controlled by current, flow rate of gases, time, and temperature.

43.2.1 Hardness Measurement

Vickers's microhardness machine is used for hardness testing shown in Fig. 43.5. The machine is coupled with a microscope to measure the indentation dimensions.

$$HV = 1.854F/d2 \tag{43.1}$$

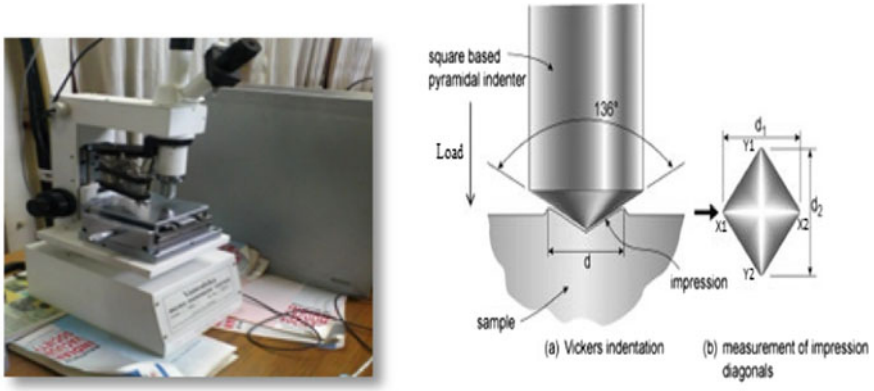

Fig. 43.5 Micro hardness tester and Vickers hardness test diamond indenter

Table 43.1 XM-19 property used in the simulation [6]

Property	Values
Density (ρ)	7888 kg/m^3
Elasticity modulus (E)	1.99E + 05
Poisson's (μ) ratio	0.312
Conductivity (K)	15.6 W/mK

Equation 43.1 defines load F in Kg arithmetic mean of the two diagonals d1 and d2 for calculating "d".

43.2.2 Simulation Problem

Guo [5] performs uniaxial compression tests at different strain rates and temperature conditions. A physics-based model is also discussed by the author. This paper is simulated on Abaqus CAE using coupled temperature-displacement scheme, and the results were compared within the accuracy range of 10% (Table 43.1).

43.3 Outcomes and Discussion

43.3.1 Physical Appearance

Figure 43.6 shows the difference between the untreated and nitride sample. Where treated sample shows some ring-type structure due to the effect of direct current

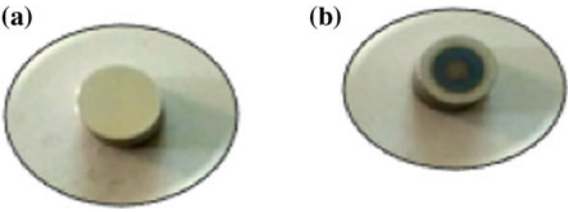

Fig. 43.6 Appearance **a.** Bare **b.** PN Sample

plasma nitriding comparing to no effect on the bare sample. The rings in the treated sample are slightly dark blue in color.

43.3.2 Optical Microscopy

In Fig. 43.7, PM XM-19 samples were cut to see the surface morphology under a microscope. A layer of nitrogen which is shown in Fig. 43.7 diffuses on the surface, while the etched sample observed precipitated nitrides under an optical microscope (500x) (Fig. 43.8).

PN 460 °C sample nitrided layer thickness = 20 μm (approx.)

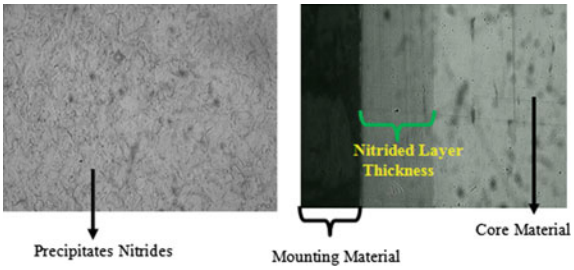

Fig. 43.7 Top layer of nitrided surface and nitrided layer thickness

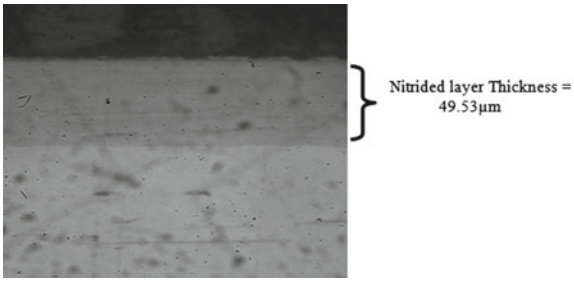

Fig. 43.8 A view of sample 50 μm (approx. thickness) treated at 560 °C

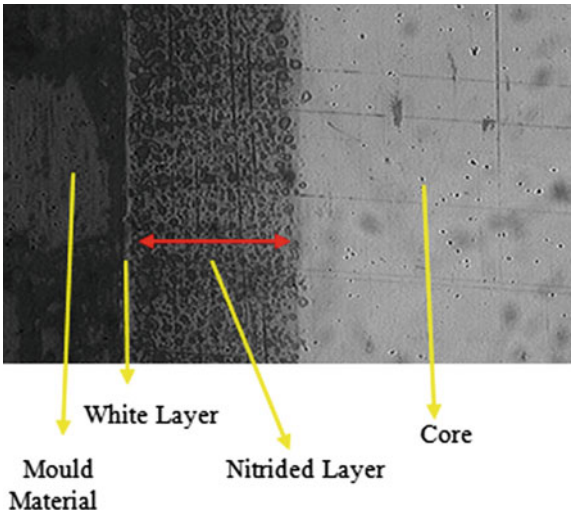

Fig. 43.9 Different layers in the PN sample

For PN 540 °C sample nitrided layer thickness found 40.59 μm (approx.)
PN 560 °C sample nitrided layer thickness found 49.53 μm (approx.)

PN sample at different temperature treatments of 460, 540 and 560 °C is compared to show the influence of temperature in PN. As from the observation from the above-mentioned points as the temperature of treatment increases nitriding thickness is also increased. Low-temperature PN observes no nitrided layer, i.e., below 400 °C. A significant layer of nitrided layer is clearly observed in high-temperature PN samples as the rate of nitrogen diffusion is enhanced at high temperature. A white layer (Fe_2N and Fe_4N phases) is visible at a temperature high at 560 °C. The sample in which white layer is formed is shown in Fig. 43.9.

When PN was done in lesser time period, i.e., ½ h or less, this PN treatment of grain boundaries was found which is due to the etching action in which nitrogen atmosphere of PN reacts with the elements present in the metal substrate, and the formation of grain boundaries takes place which is clearly observed when the treated sample is etched with nital solution as shown in Fig. 43.10. The adjacent picture captures the indentation mark within the grain as the hardness of the grain boundary is more than the substrate; the indentation was observed between the two grain boundaries.

43.3.3 Hardness Measurement and Profile Plot

The hardness of each plasma nitrided sample was performed on Vickers's hardness test clearly mention in Table 43.2. The hardness values increase with temperature up

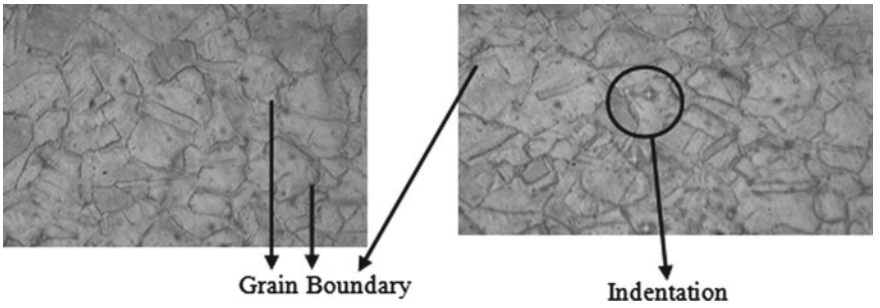

Fig. 43.10 ½ h PN sample shows different layers morphology with grain boundary

Table 43.2 PN sample surface hardness each under the parameter of 4 h nitriding time and N_2:H_2 1:4

S. No.	Treatment parameters (°C)	Times (Nitride) (h)	Hardness (HV)
1.	340	4	373.5
2.	380	4	364.6
3.	420	4	547.58
4.	460	4	1609.2
5.	480	4	1412
6.	500	4	1636.6
7.	540	4	912.8

Hardness measurement of untreated XM-19 = 430.78HV

to certain temperature limit like in this case maximum hardness is achieved in 500 °C PN sample (1632.36 HV). Before which, hardness value of the sample from 340 to 500 °C shows gradual increment. After 500 °C hardness value shows decrement, i.e., in case 540 °C, it is 912.8 HV. In Fig. 43.11, the plot hardness under the same process parameter against the bare sample is shown.

43.3.4 Case Depth Hardness Measurement Graph of PN Treated Specimens

Figures 43.12, 43.13, and 43.14 describe the hardness value in the core of the nitrided thickness whose value is maximum in this vicinity (Fig. 43.15). Whereas, when the case depth increase or distance from the nitrided layer is increase the following graph gives decrement in the hardness value and equalizes with the hardness value of the bare material in the center of the specimen. For example, in PN 560 °C sample, almost 0 μm distance, i.e., in the core of nitrided layer the hardness value, was found 1308 HV, while in the center at the distance of 305 μm of the specimen, it was found 370 HV. Similar with the case of other samples also. The hardness value of 1636.62

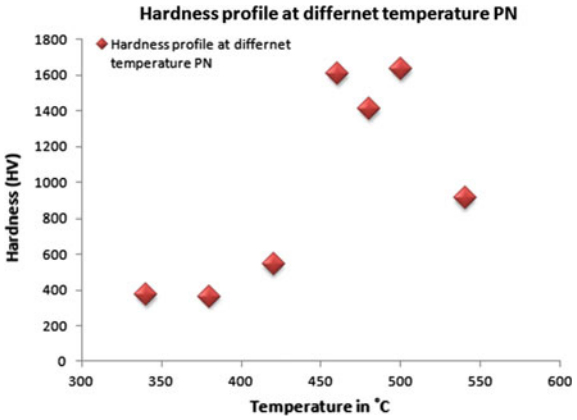

Fig. 43.11 The plot of hardness profile using data from Table 43.2

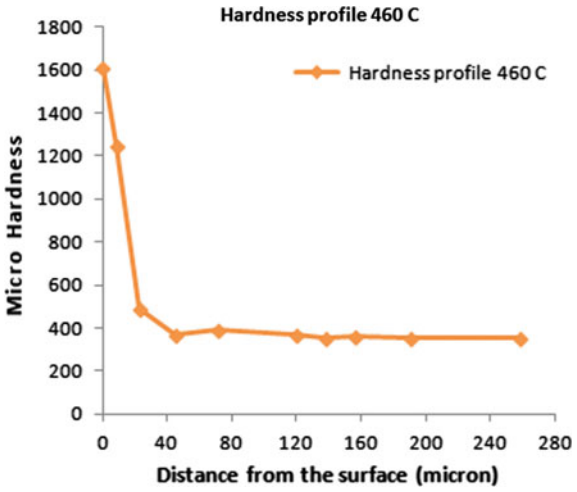

Fig. 43.12 Microhardness versus depth from the nitrided layer for PN 460 °C

HV was found in PN sample treated at 500 °C. It is evident from the chemical composition of material that material contains a large amount of chromium (Cr). At high temperature above 400 °C, the sample shows high hardness value which is reasoned by reaction of nitrogen with chromium and forming a hard compound CrN which is the reason of high hardness at a higher temperature. When the temperature of the process is increased more reaction takes place and thus at a higher temperature, high hardness value is obtained. Increasing the nitriding temperature increases the nitrided layer thickness. The hardness profile graphs of plasma nitrided treated sample at different temperature of 460, 540 & 560 °C shows that the hardness of the nitrided layer is far better than the core material, e.g., case of 460 °C plasma nitrided sample

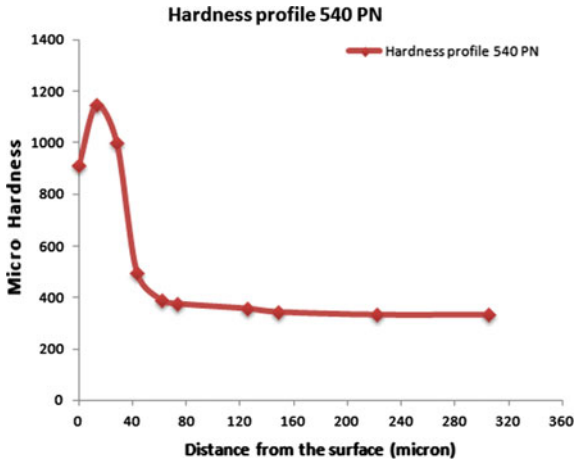

Fig. 43.13 Microhardness versus depth from the nitrided layer for PN 540 °C

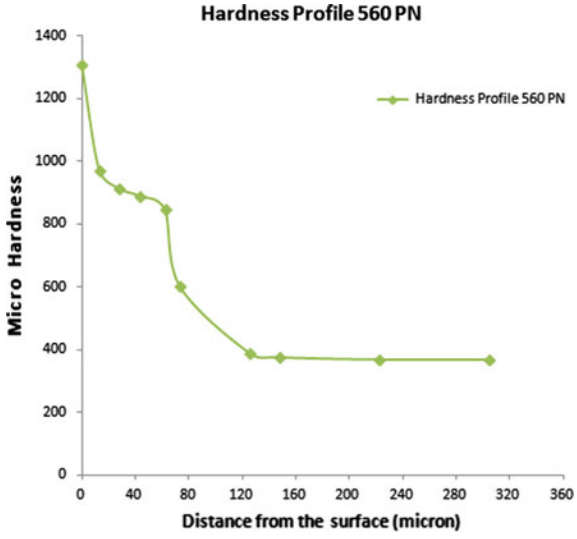

Fig. 43.14 Microhardness versus depth from the nitrided layer for PN 560 °C

inside the nitrided layer the hardness was found to 1609 HV at 0 μm while 1250 HV at 9 μm and then there is drastic decrease in the hardness value as the data taken far from the nitrided layer as in 493 HV at distance of 23 μm and goes on decreasing as the distance increases. This is followed in all the case which is clearly observed from the graph plotted in Figs. 43.12, 43.13, and 43.14.

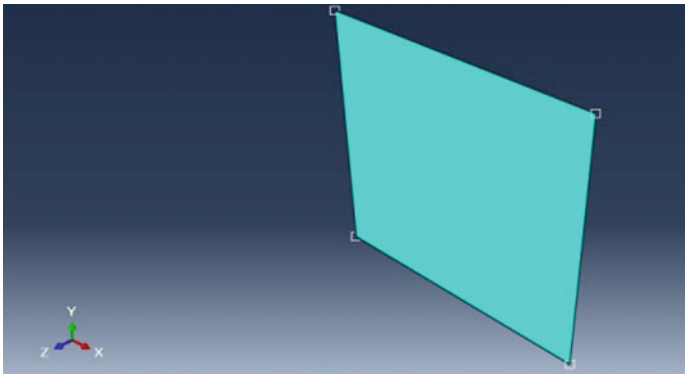

Fig. 43.15 FE model to simulate the test [14]

43.3.5 Numerical Simulation

Simulation to validate the results of Guo [5] was carried out in Abaqus 6.10-1. To formulate the similar problem of different rates of compression (high and low), a coupled temperature-isplacement scheme was used to solve that problem. Simulation results were also compared with the physical model shown in the paper.

Material properties of XM-19 are already defined in the experimental procedure. Various other parameters used in the Abaqus are step type of coupled temperature-displacement, element-type quad, and aspect ratio that was found to be 1.

Element type selected is CPE4RT, which is default element type for plane strain thermally coupled four-node quadrilateral, displacement-type bilinear, and temperature with RI (reduced integration) and hourglass control. XM-19 material properties used in simulation in ABAQUS CAE include damage of ductile material assign using stress triaxiality (Figs. 43.16, 43.17, and 43.18).

43.3.6 Results Comparisons

Figures 43.19 and 43.21, these results are compared with paper [5] from Figs. 43.18 and 43.20. The following figure below helps in understanding the link between the numerical simulation and experiment results of the paper.

Comparison of other results such as true stress versus strain at different rates is shown in series of Figs. 43.22, 43.23, 43.24, 43.25, 43.26, and 43.27. The author had also worked and gave a physical model to predict the flow behavior of metal which is shown in Figs. 43.26 and 43.27. These predicted results were also matched with the simulation problem done in Abaqus.

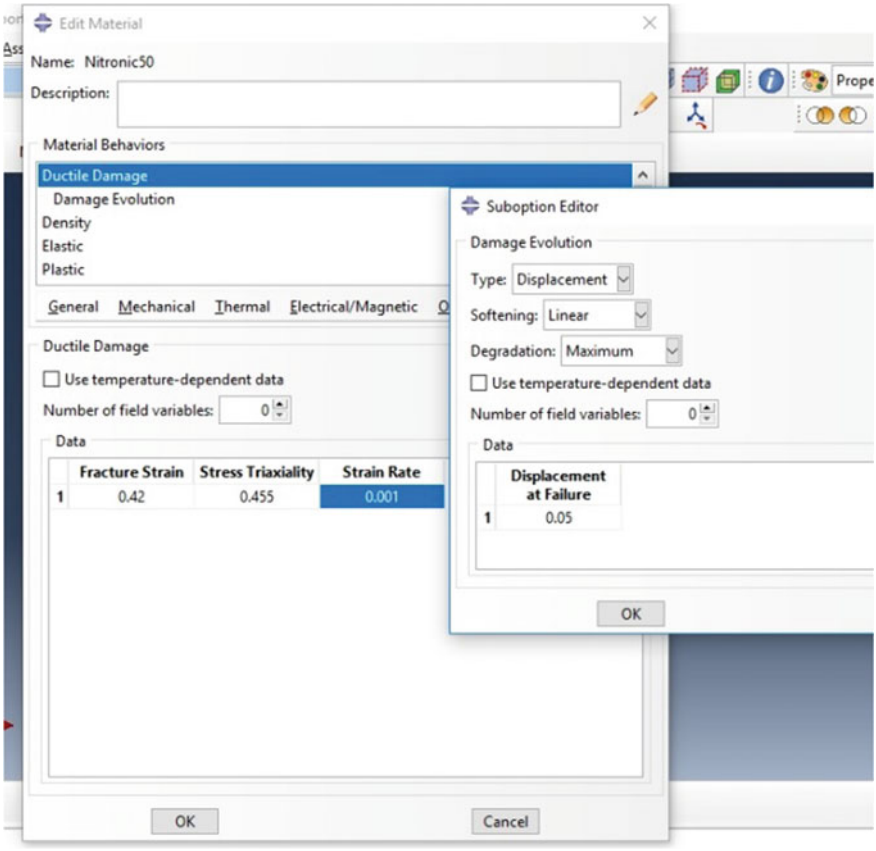

Fig. 43.16 The material definition in Abaqus CAE [14]

43.4 Conclusions

The experimental and numerical simulation is performed XM-19 materials and following notable conclusion can be drawn as follows:

- Plasma nitriding sample was evaluated for the thickness of the nitrided layer under optical microscopy followed by in-depth hardness measurements using microhardness tests. While low-temperature treatment shows now nitrided layer, i.e., $\leq$400 °C PN, whereas the thickness layer of 20, 40, and 50 μm was found in treated samples at a temperature of 460, 540, and 560 °C
- White layer iron nitrides phases Fe_2N and Fe_4N in the treated temperature of 560 °C are seen. Low time for half an hour treatment gives grain boundary on surface morphology in the sample observed in the microscope.

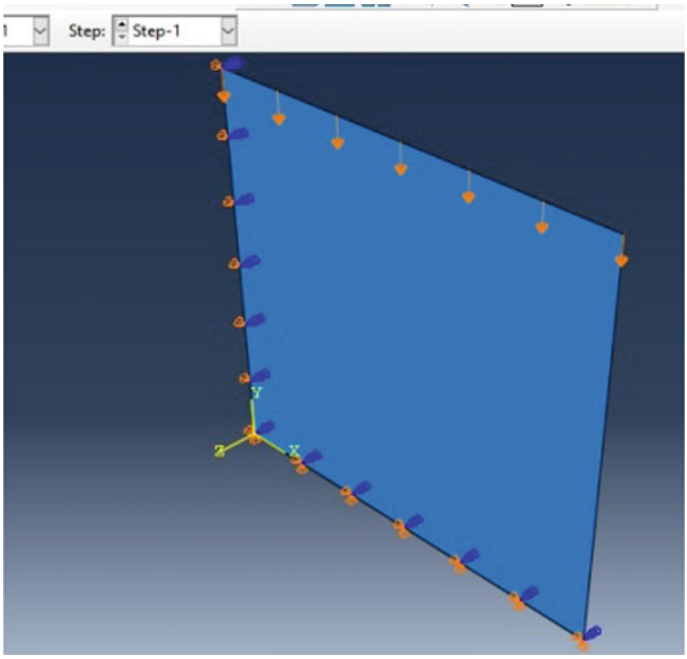

Fig. 43.17 Boundary condition and loading amplitude [14]

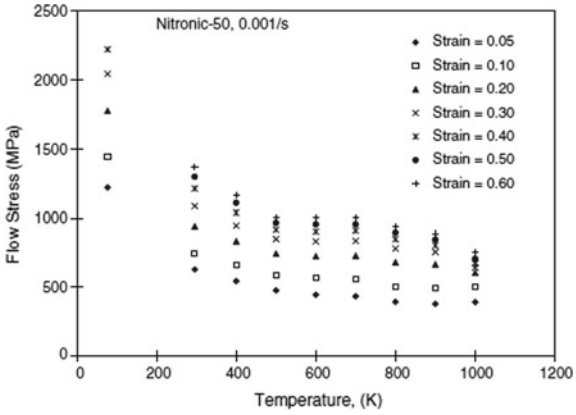

Fig. 43.18 Paper results of stress versus temperature at rate of 0.001/s [5]

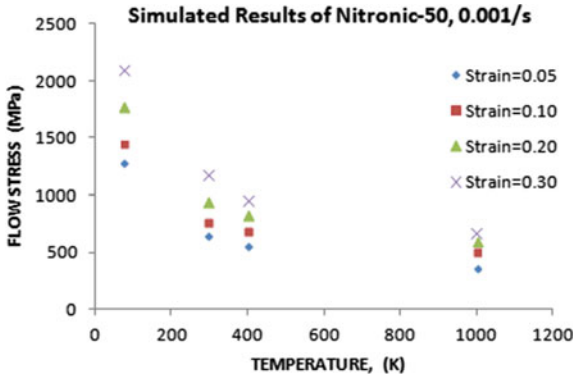

Fig. 43.19 Simulated results from Abaqus at same rate 0.001/s and different temperatures

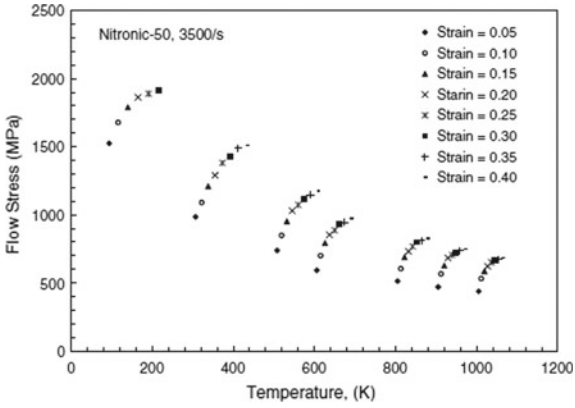

Fig. 43.20 Paper results of stress versus temperature at rate of 3500/s [5]

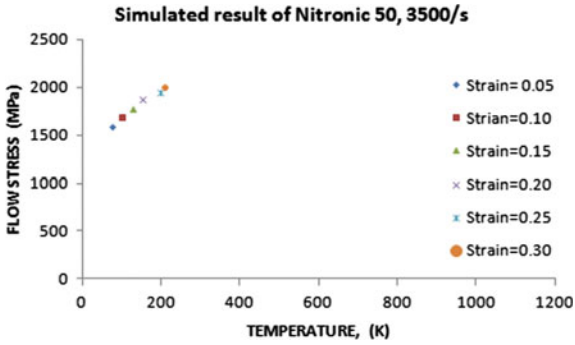

Fig. 43.21 Simulated results from Abaqus at same rate 3500/s and different temperatures

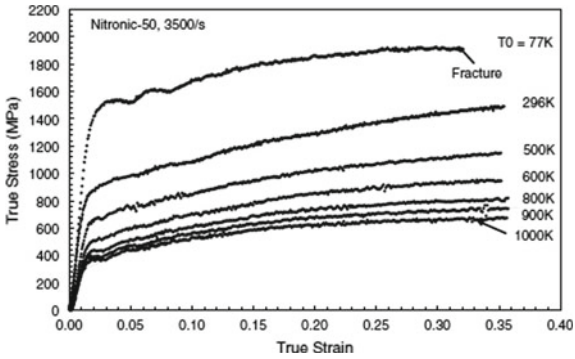

Fig. 43.22 Result from paper in which experimental stress–strain curves is obtained at rate 3500/s [5]

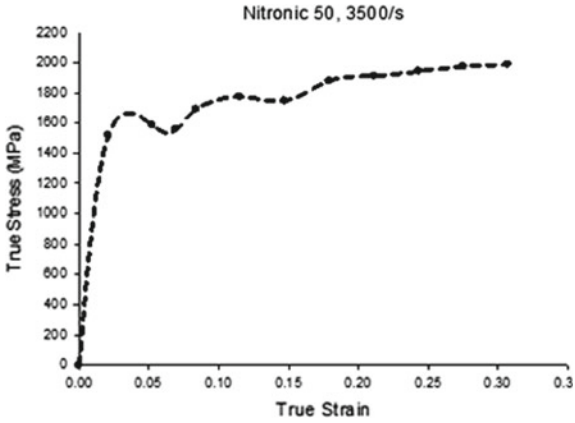

Fig. 43.23 Simulated result for temperature ($T_0 = 77$ K) is in a close match with above graph keeping the rate same

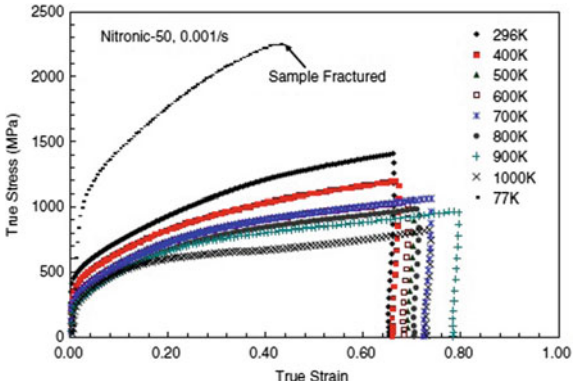

Fig. 43.24 Paper results at a rate of 0.001/s taken from the paper show different values with increase and decrease in the temperature [5]

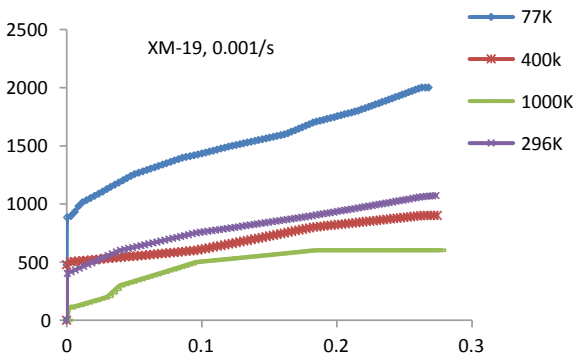

Fig. 43.25 Simulated result for temperature ($T_0 = 77, 296, 400, 1000$ K) is tried to match with above graph (Fig. 43.24) at rate 0.001/s

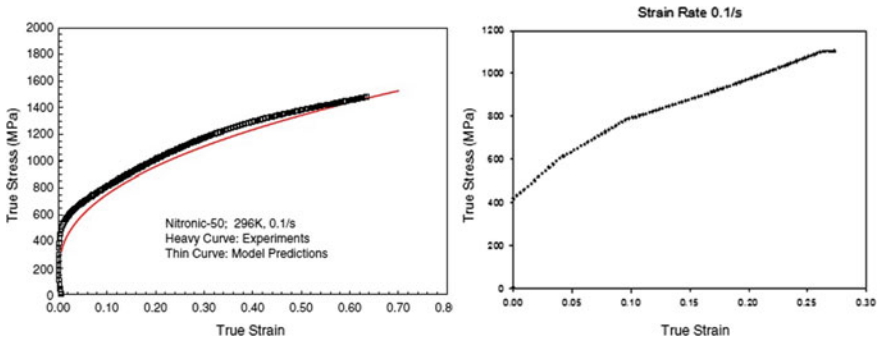

Fig. 43.26 Comparison between simulated and model proposed by author results keeping the rate similar, i.e., 0.1/s [5]

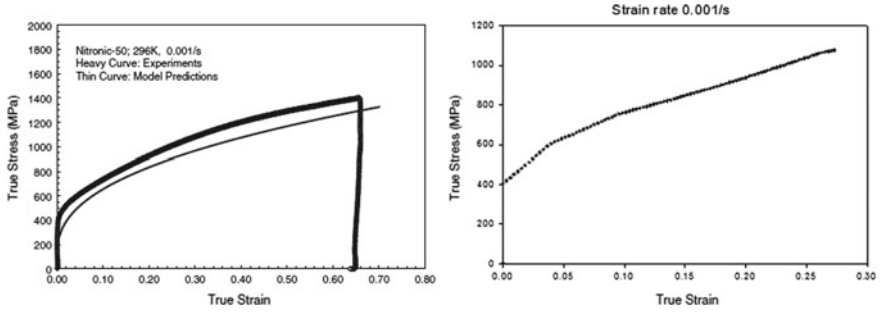

Fig. 43.27 Comparison between simulated and model proposed by author results keeping the rate similar, i.e., 0.001/s at 296 K temperature [5]

- Before any PN treatment, the value of hardness of bare material was found 430.78 HV. Under the prescribed procedure followed in the following experiment of PN the maximum hardness value of 1636 HV in 500 °C sample.
- Hardness plot shows the maximum hardness value in nitrided layer thickness. While the core of material observed constant hardness value.
- Numerical simulation results for various strain rates 0.001/s and 3500/s are done on Abaqus and results are closely matched within the accuracy of 10% which predicts the flow behavior of metal using software saving material from destructive testing and proofing cost-effective as well as time-saving.

Thus, from the above conclusion, it can easily be noted that XM-19 which founds application in high corrosion and high strength environment, its properties can be altered by surface modification techniques like plasma nitriding, after which material can be proposed for the applications like biomedical and marine application which requires material to be high corrosion resistance and retain its strength and hardness at both elevated and subzero temperature.

Acknowledgements Authors would like to express their deepest sense of gratitude in thanking Dr. B. Ganguli, Sr. Scientist at IPR, Bhat, Gandhinagar and IPR facility without this project, it would not be possible, and for Dr. Sia Nemat-Nasser Distinguished Professor, University of California, San Diego for granting permission.

References

1. W. S. Association: www.worldsteel.org/steelstory/
2. Bardes, B.P.: Properties and Selection: Irons and Steels, vol. 1. American Society for Metals (1978)
3. Callister W.D., Rethwisch, D.G.: Fundamentals of Materials Science and Engineering: an Integrated Approach. Wiley, New York (2012)
4. Nelson, C.W., Weir, R.D.: Tulip Memory Systems Inc, 1999. Method for manufacturing austenitic stainless steel substrate for magnetic recording media. U.S. Patent 5,900,126
5. Guo, W.G., Nemat-Nasser, S.: Flow stress of Nitronic-50 stainless steel over a wide range of strain rates and temperatures. Mech. Mater. **38**, 1090–1103 (2006). https://doi.org/10.1016/j.mechmat.2006.01.004
6. High Performance Alloys, Inc. March 1997. Product data bulletin HP Alloys: Nitronic 50. Volume 2, Issue 1
7. Langeslag, S.A.E.: Extensive characterisation of advanced manufacturing solutions for the ITER central solenoid pre-compression system. Fusion Eng. Des. **98–99**, 2015–2019 (2015). https://doi.org/10.1016/j.fusengdes.2015.06.007
8. Du, H., Somers, M.A.J., Agren, J.: Metall. Mater. Trans. A **31**, 195 (2000). https://doi.org/10.1007/s11661-000-0065-7
9. Rodriguez, D., Chidambaram, D.: Oxidation of stainless steel 316 and Nitronic 50 in supercritical and ultrasupercritical water. Appl. Surf. Sci. **347**, 10–16 (2015). https://doi.org/10.1016/j.apsusc.2015.03.127
10. Trester, P.W., McKelvey, T.E., Ulrickson, M.A.: Selection and qualification of materials for relative motion and electrical isolation in a vacuum environment. Thin Solid Films **119**, 113–120 (1984). https://doi.org/10.1016/0040-6090(84)90163-9

11. Williamson, D.L., Davis, J.A., Wilbur, P.J.: Effect of austenitic stainless steel composition on low-energy, high-flux, nitrogen ion beam processing. Surf. Coatings Technol. **103–104**, 178–184 (1998). https://doi.org/10.1016/S0257-8972(98)00389-2
12. Sharma, A., Goel, S.K.: Applied surface science erosion behaviour of WC–10Co–4Cr coating on 23-8-N nitronic steel by HVOF thermal spraying. Appl. Surf. Sci. **370**, 418–426 (2016). https://doi.org/10.1016/j.apsusc.2016.02.163
13. Schneider, S.: Nitronic 50—an austenitic steel with near to perfect properties (2011)
14. Smith, M.: ABAQUS/Standard User's Manual, Version 6.9. Providence, RI: Simulia (2009)

Chapter 44
Study on Actuation Characteristics of NiTiCu SMA Thin Film Deposited on Flexible Substrate

S. Jayachandran, A. Brolin, M. Harivishanth, K. Akash and I. A. Palani

Abstract In this work, the actuation of NiTiCu Shape Memory Alloy (SMA) bimorph is studied using Joule heating setup. The characterization of NiTiCu SMA thin film is carried out using Scanning Electron Microscope (SEM), X-Ray Diffraction (XRD), optical microscope and scotch tape analysis. The actuation study was carried out and the maximum displacement was found at 4 V and 3 A which was about 1.2 mm. The optical microscope images taken after the actuation studies show the removal of the film where contacts are made. The film burnt when the voltage is further increased resulting in the reduction in displacement. The NiTiCu film can be used for Micro Electro Mechanical System (MEMS) application considering the power requirement will be low when compared to NiTi thin film and also can be used for various applications.

Keywords Shape memory alloy · NiTiCu · Bimorph · Thermomechanical · Joule heating

44.1 Introduction

Shape Memory Alloys (SMA) are the special class of alloys which changes its shape when exposed to temperature and returns backs to its shape once the heat source is withdrawn [1]. NiTiCu thin film has been widely used for various applications because of several reasons like ability to recover large transformation stress and strain upon heating and cooling, high damping capacity, great shape restoring force and biocompatibility. The NiTiCu thin film exhibits small thermal mass to heat or

S. Jayachandran (✉) · A. Brolin · M. Harivishanth · K. Akash · I. A. Palani
Mechatronics and Instrumentation Lab, Discipline of Mechanical Engineering, Indian Institute of Technology Indore, Indore, India
e-mail: jayachandransubbian@gmail.com

I. A. Palani (✉)
Metallurgical Engineering and Materials Science, Indian Institute of Technology Indore, Indore, India
e-mail: Palaniia@iiti.ac.in

M. S. Shunmugam and M. Kanthababu (eds.), *Advances in Micro and Nano Manufacturing and Surface Engineering*, Lecture Notes on Multidisciplinary Industrial Engineering,
https://doi.org/10.1007/978-981-32-9425-7_44

cool as compared to NiTi bulk and results in reduced response time and increased operation speed. Fast natural cooling and large retention of actuation stresses and strains are possible due to large surface to volume ratio in NiTi [2]. Application of SMA thin film in MEMS aids simplification of mechanisms with flexibility of design and creation of clean, friction-free and non-vibration movement. These SMA thin films are fabricated using physical vapor deposition techniques such as laser ablation, ion beam deposition, arc plasma ion plating, and sputtering. The thin film deposition usually made using lithography technique which is time-consuming process where they can be developed using physical vapor deposition technique using masking on to the substrate. The problem with these techniques was nonuniformity in film thickness and composition, low deposition rate or incompatibility with MEMS process, etc. The thin films are mostly developed on silicon substrate provided various applications on semiconductor industry but the actuation characteristics can be only done through Differential Scanning Calorimetry (DSC), four-probe method, etc.; however, thin film developed on flexible substrate helped to study the actuation characteristics through Joule heating [3]. SMA thin film fabricated on flexible substrates finds more applications in MEMS field as an actuator than bulk material fabrication. NiTiCu deposited on flexible substrate helps to overcome the complex process of obtaining the free-standing film when deposited on rigid substrates such as glass and silicon wafer.

MEMS actuators primarily utilize Joule heating due to its convenience and simplicity as compared to other actuation sources such as laser beam and hot fluid. The actuation characteristics of copper-based shape memory alloys have been studied using Joule heating by varying the thickness of substrate and substrate temperature [4]. They also reported copper-based shape memory alloy showed increased displacement due to lesser resistance in the SMA thin film. Woongweerayoot et al. [5] studied NiTiCu shape memory alloy for microgripper application where they lift a load of 0.5 mg. They showed that at annealing temperature of 650 °C for 30 min provided the desired crystalline structure. From the literature, the actuation characteristics are studied through stress–strain behavior and there is less report on actuation study of fully deposited bimorph through thermomechanical behavior. There is no report on the thermomechanical behavior of patterned NiTiCu deposited bimorph through Joule heating. In this work, we have deposited NiTiCu SMA bimorph on the flexible substrate to study the actuation characteristics and also to study the crystal structure, surface morphology, and adhesion test using scotch tape analysis.

In this study, the deposition is made on the thin film using the flash evaporation technique [6]. This technique enables the deposition of multicomponents of the alloys whose constituents have different vapor pressures. The evaporation process is done with only one boat that is maintained at a sufficiently higher temperature to evaporate the components of the alloy. This technique has an added advantage of controlling the composition of the alloy components that need to be deposited with the help of a powder feeder wherein the alloying components are controlled by the vibrating powder feeder. The surface quality of the deposited thin film can also be directly related to the grain size of the powder that is being used for the deposition. The powder feeder also helps in controlling the thickness of deposition. The amount of

material that is fed into the crucible can be controlled by controlling the feeder which in turn controls the thickness of deposition.

44.2 Experimental Setup

Kapton polyimide of dimension 7 × 7 cm^2 was used for deposition as substrate material and NiTiCu of small pellets was used as source material. The pellets were fabricated through arc melting unit. The vacuum pressure was maintained at 2 × 10^{-3} mbar. The argon gas was purged thrice to reduce the deposition of carbon. The possibility of reaction between the crucible and the source due to high temperature can overcome by the use of water-cooled copper crucible. The NiTiCu pellets were precisely measured using precision balance. In order to obtain proper adhesion, the Kapton polyimide was cleaned using ultrasonic cleaning with acetone, isopropyl alcohol, and distilled water. Hydrophilic treatment was done on the glass substrate to enhance the adhesion between the source and the substrate. The solutions used for this treatment were water, ammonium hydroxide (NH_4OH), and hydrogen peroxide in a ratio of 5:1:1, respectively. The process parameter used for deposition is shown in Table 44.1.

The background pressure was evacuated from the chamber before deposition to about 5 × 10^{-5} mbar using diffusion and rotary pump. Figure 44.1a shows the

Table 44.1 Deposition parameters

S. No.	Parameter	Value
1	Vacuum pressure	5 × 10^{-5} mbar
2	Source material	NiTiCu
3	Current applied	80 A
4	Deposition time	5 min

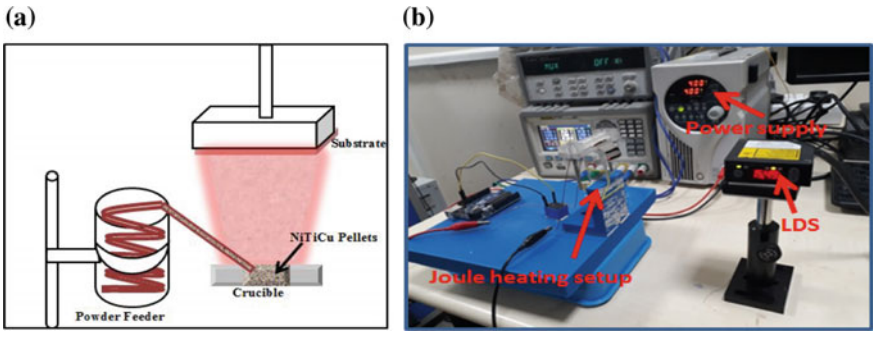

Fig. 44.1 **a** Schematic of powder feeder arrangement of Flash evaporation, **b** photographic image of actuation setup for Joule heating

schematic of flash evaporation equipment. The substrate was cleaned with acetone and properly baked before deposition. The thickness of the thin film was 1.75 μm which was measured using the optical microscope.

The surface morphology was investigated using SUPRA55 Zeiss Scanning Electron Microscope (SEM). The crystallographic phase structure of the deposited bimorph was examined using X-Ray Diffractometer (XRD). The thermomechanical behavior study was done to study the actuation behavior of SMA thin film. The bimorph of 3 × 2 cm^2 was cut and used for analyzing the thermomechanical behavior with the help of Joule heating setup. Joule heating setup helps to log the displacement data from the laser displacement sensor. Experiments were carried by varying the voltages to study the influence of bimorph in MEMS application.

Figure 44.1 shows the actuation setup that was used to check the actuation of the thin film. The actuation was checked by varying the voltage and current until an optimum value of voltage and current was reached that showed maximum deflection, i.e., actuation.

44.3 Results and Discussion

The NiTiCu shape memory alloy bimorph developed using flash evaporation technique shows Two-way Shape Memory Effect (TWSME). The TWSME was obtained without any tedious process of shape setting or training. During heating the bimorph changes from its curved shape to flat position due to its shape memory effect. The thermal stresses developed in the bimorph during deposition help to recover its shape from flat position to curved shape thus resulting in two-way shape memory effect. The process of deposition was carried out in two steps: (i) raising the temperature till the eutectoid point that allows the thorough mixing of the alloy components in the molten state and (ii) then rapidly increasing the temperature which leads to the evaporation of materials and results in the deposition on the substrate.

The surface morphology examined using Scanning Electron Microscope (SEM) exhibited surface with no pores and cracks, and there are a large number of precipitates which are present within the grains and along the grain boundary [7]. X-Ray Diffraction (XRD) shows peaks at the range between 40° and 50° and also it revealed that some crystalline peak phases attributed to Ti_2Cu and Ni_3Ti [8] (Fig. 44.2).

The scotch tape analysis [9] was used to check the adhesion of the bimorph. The experiment was performed by sticking a 2 × 2 cm^2 tape on the SMA bimorph of 3 × 3 cm^2 to test the adhesion of the deposited thin film. The scotch tape is weighed before sticking and also after removing from the substrate. Table 44.2 shows the weight of the tape before and after the analysis. The developed thin film showed good adhesion and less removal of the film from the surface as there as only 0.1 mg of material on the scotch tape. The weight of the tape before sticking was 17.8 mg and weight of the scotch tape after testing was 17.9 mg. The diffusion of the copper layer on to the Kapton bare polyimide resulted in better adhesion.

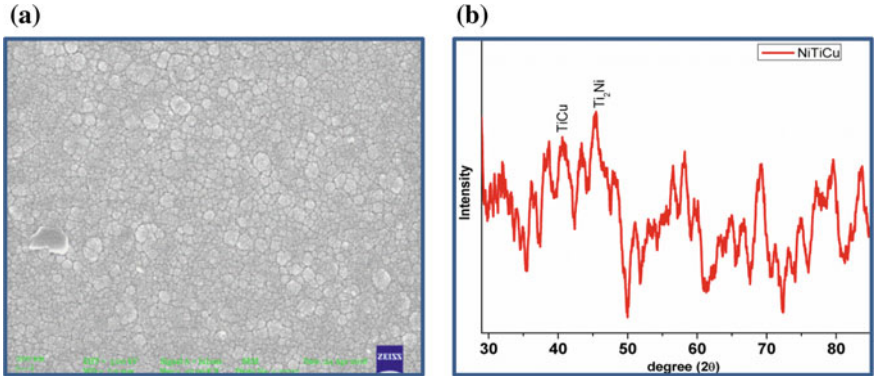

Fig. 44.2 **a** Microstructure of NiTiCu bimorph, **b** XRD crystal structure of NiTiCu

Table 44.2 Scotch tape results

Content	Weight of tape before testing (mg)	Weight of tape after testing (mg)	Weight of adhered material (mg)
NiTiCu	17.8	17.9	0.1

Joule heating results in heat generation by converting electrical energy into heat energy in the SMA/Kapton composite which aids in actuation. In Joule heating, the actuation largely depends on the electrical resistivity of the material. Copper contacts are provided to the Joule heating setup which reduces the contact resistance and also helps in regulating the current flow. The amount of heat generated in the composite film based on the resistance is given in Eq. (44.1).

$$Q = \frac{V^2}{R} \tag{44.1}$$

where

Q quantity of heat obtained in SMA/Kapton Composite (J)
V applied voltage (V)
R resistance of thin film (Ω).

The thermomechanical behavior of the film was studied through Joules heating setup. A suitable amount of voltage was passed throughout the film placed in the setup and the actuation of the film was studied at various voltages and at constant frequency of 0.5 Hz. The current was fixed at a constant value of around 3 A and the voltage was varied to study its behavior at various steps. The frequency was selected such that the bimorph has sufficient time to heat and cool [10]. Frequency of 0.5 Hz was set since the displacement of the bimorph was maximum. For the purpose of plotting the data points, the actuation of the bimorph was studied for 10 cycles. Then experiments were also carried out to study the behavior of the bimorph

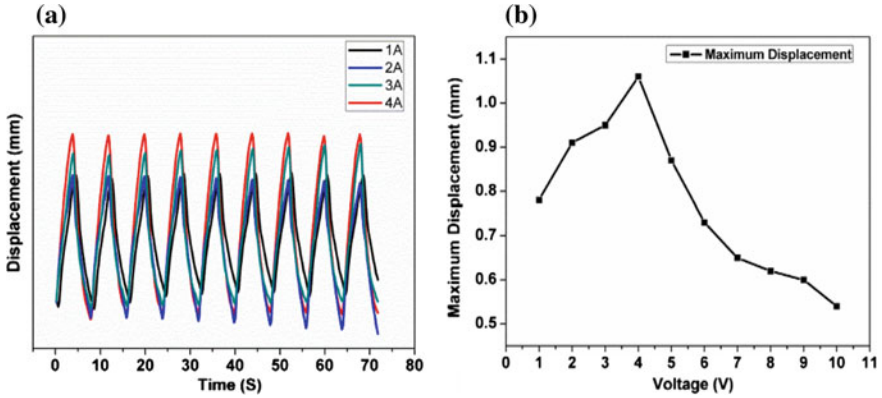

Fig. 44.3 **a** Thermomechanical behavior of bimorph for varying voltage at 3 A and 0.25 Hz, **b** maximum displacement versus voltage graph

during an extended period of actuation. Iterative experiments on the film show that the maximum value was observed at 4 V. Figure 44.3a shows the displacement of the film from 1 to 4 V. At 1 V the displacement was about 0.5 mm and as the voltage increases, the displacement gets increased. At 2 V the actuation was slightly higher up to 0.9 mm and further increasing the voltage to 3 V the deflection was 0.95 mm. The maximum displacement was 1.2 mm at 4 V. It was observed that as the voltage was increased beyond 4 V, the actuation started to decrease. Figure 44.3b shows a decrease in displacement with an increase in voltage.

The decrease in displacement may be due to delamination of NiTiCu thin film from the contact point. The actuation mainly depends on the electrical resistivity of the NiTiCu thin film which is in the order of 6×10^{-7} Ωm. The resistivity decides the amount of current flow through the bimorph film. The current completely flows throughout the film up to 4 V but increasing it further damages the contact region which gets delaminated from the surface of the bare polyimide.

The decrease in displacement with an increase in voltage is due to the delamination of the film from the surface due to repeated cyclic testing on the bimorph. Figure 44.4a shows the optical microscope image of surface of the film before the start of the experiment. The micrograph shows proper uniform surface without any cracks. The delaminated bimorph after actuation at more than 4 V is shown in Fig. 44.4b.

44.4 Conclusions

The actuation characteristic study on NiTiCu SMA bimorph developed using flash evaporation operation has been studied using Joule heating. The results can be summarized as follows:

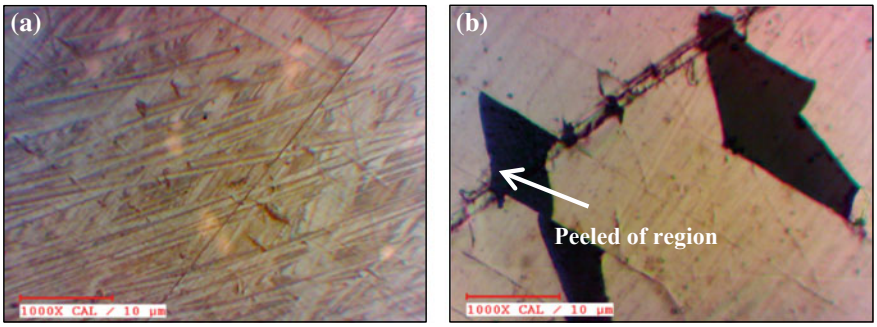

Fig. 44.4 Optical microscope image **a** before actuation and **b** after actuation for 3 A and 4 V for 0.25 Hz frequency

- The bimorph shows maximum actuation of 1.2 mm at 4 V and 3 A at a working frequency of 0.5 Hz.
- The displacement of the bimorph decreases with increase in voltage beyond 4 V and the film delaminates when repeatedly actuated for more cycles which are seen in the optical microscope image. The micrograph shows the peeled off region after a certain number of actuation cycles.
- The surface morphology showed a smooth surface without any pores and cracks. The crystalline structure showed presences of Ni_3Ti and Ti_2Cu which can be seen from XRD. The scotch tape analysis proved the adhesion was better quality.

References

1. Lagoudas, D.C.: Shape Memory Alloys: Modeling and Engineering Applications. Springer (2008). https://doi.org/10.1007/978-0-387-47685-8
2. Choudhary, N., Kaur, D.: Sensors and actuators a: physical shape memory alloy thin films and heterostructures for MEMS applications: a review. Sens. Actuators A Phys. **242**, 162–181 (2016). https://doi.org/10.1016/j.sna.2016.02.026
3. Akash, K., Shukla, A.K., Mani Prabu, S.S., Narayane, D.C., Kanmanisubbu, S., Palani, I.A.: Parametric investigations to enhance the thermomechanical properties of CuAlNi shape memory alloy Bi-morph. J. Alloys Compd. **720**, 264–271 (2017). https://doi.org/10.1016/j.jallcom.2017.05.255
4. Akash, K., SS, M.P., Shukla, A.K., Nath, T., Karthick, S., Palani, I.A.: Investigations on the life cycle behavior of Cu-Al-Ni/polyimide shape memory alloy bi-morph at varying substrate thickness and actuation conditions. Sens. Actuators, A Phys. **254**, 28–35 (2017). https://doi.org/10.1016/j.sna.2016.12.008
5. Wongweerayoot, E., Srituravanich, W., Pimpin, A.: Fabrication and characterization of nitinol-copper shape memory alloy bimorph actuators. J. Mater. Eng. Perform. **24**, 635–643 (2014). https://doi.org/10.1007/s11665-014-1334-8
6. Mineta, T., Kasai, K., Sasaki, Y., Makino, E., Kawashima, T., Shibata, T.: Flash-evaporated TiNiCu thick film for shape memory alloy micro actuator. Microelectron. Eng. **86**, 1274–1277 (2009). https://doi.org/10.1016/j.mee.2008.12.032

7. Ishida, A., Sato, M., Ogawa, K., Yamada, K.: Shape memory behavior of Ti–Ni–Cu thin films. Mater. Sci. Eng. A **440**, 683–686 (2006). https://doi.org/10.1016/j.msea.2006.02.154
8. Ishida, A., Sato, M.: Ti–Ni–Cu shape-memory alloy thin film formed on polyimide substrate. Thin Solid Films **516**, 7836–7839 (2008). https://doi.org/10.1016/j.tsf.2008.04.091
9. Akash, K., Jain, A.K., Karmarkar, G., Jadhav, A., Narayane, D.C., Patra, N., et al.: Investigations on actuation characteristics and life cycle behaviour of CuAlNiMn shape memory alloy bimorph towards flappers for aerial robots. Mater. Des. **144**, 64–71 (2018). https://doi.org/10.1016/j.matdes.2018.02.013
10. Rodrigue, H., Wang, W., Han, M.W., Quan, Y.J., Ahn, S.H.: Comparison of mold designs for SMA-based twisting soft actuator. Sens. Actuators A Phys. **237**, 96–106 (2016). https://doi.org/10.1016/j.sna.2015.11.026

Chapter 45
Influence of Laser Shock Peening on Wire Arc Additive Manufactured Low Carbon Steel

M. Manikandan, S. S. Mani Prabu, S. Jayachandran, K. Akash, I. A. Palani and K. P. Karunakaran

Abstract This paper attempts to investigate the effect of laser shock peening on mild steel structures developed by Wire Arc Additive Manufacturing (WAAM). This process has employed in fabricating the desired samples with an argon environment which has a feed rate of 15 cm/min, 16 V, 80 A, argon flow pressure and wire diameter 1.2 mm. Nd-YAG pulsed laser source has used for the shock peening process with the wavelength of 532 nm and power of 2 W. The optical microscope images represent microstructure of the surface before and after laser shock peened samples. The sample shows uniform grain refinement and reduced pores level after laser shock peening. Further X-ray diffraction has used for analyzing the confirmation of crystalline phase and structures in detail.

Keywords Wire arc additive manufacturing · Laser shock peening · Microstructure · Low carbon steel

45.1 Introduction

In past decades, an additive manufacturing technique is a vital process for fabricating the product with sufficient amounts of raw materials consumption, improved production rate, and less intake of post-processing time. As compared to additive manufacturing process, the conventional manufacturing process has various defects, such as misrun, closed pack porosity, scars, and thermal distortion, which occur due

M. Manikandan · S. Jayachandran · K. Akash · I. A. Palani (✉)
Mechatronics Instrumentation Lab, Discipline of Mechanical Engineering, Indian Institute of Technology Indore, Indore, Madhya Pradesh, India
e-mail: palaniia@iiti.ac.in

S. S. Mani Prabu · I. A. Palani
Metallurgy Engineering and Materials Science, Indian Institute of Technology Indore, Indore, Madhya Pradesh, India

K. P. Karunakaran
Rapid Manufacturing Laboratory, Department of Mechanical Engineering, Indian Institute of Technology Bombay, Bombay, Maharashtra, India

M. S. Shunmugam and M. Kanthababu (eds.), *Advances in Micro and Nano Manufacturing and Surface Engineering*, Lecture Notes on Multidisciplinary Industrial Engineering,
https://doi.org/10.1007/978-981-32-9425-7_45

to environmental conditions and human errors. Therefore, to overcome these defects the additive manufacturing process is a suitable process. This technique differentiated into various categories, which based on material and fabrication process such as stereolithography, fused deposition modeling, selective laser melting/sintering and wire arc additive manufacturing, etc. Among these, selective layer melting/sintering (SLM) method has high potential for developing complex structures and porous structures with high ultimate strength. However, SLM is a low deposition rate-based method, which is a major limitation due powder particles variation and scanning speed. The unmelted powder particles are included in final product, which no advisable because it will reduce the mechanical strength of SLM fabricated sample. WAAM is an arc-based fabrication method that can fabricate dense parts with low lead time and it will improve production rate. WAAM is a modern technology used to gas arc controlled process that fabricates desired complex structure with auto cad model. Therefore, WAAM technique is an entirely suitable method to produce high-rate deposition thin wall structure multilayered samples with single pass. This method can be used to manufacture aerospace components, turbine blades, and nuclear reactor structures [1, 2] because the WAAM developed samples were of superior quality with full dense, high mechanical strength, and reducing defects as compared with conventional method [3]. If there is a solidification time variation in between two layers, then thermal distortion defects initiating to develop in the samples. In WAAM process, the electrical energy highly influenced in thermal-based defects is affecting final product, so post-processing has been used to retain the properties [4].

There are various post-process techniques have consumed to attain the final product, such as the machining process to remove excess materials for attaining good surface finish [5, 6]. Heat treatment process enhances the surface properties and corrosion behavior. That behavior depended on the annealing temperature of about 1100–1200 °C; this assists to varying phase between σ and δ phases of 316L steel microstructure [7, 8]. However, the heat treatment process has some limitation to accomplish such properties. Plastic deformation-based post-process is suitable method for enhancing physical properties of as-fabricated samples. There are various methods used to improve the mechanical properties by plastic deformation such as shot peening, laser shock peening, warm shock peening, and ultrasonic peening. In shot peening, the spherical ball shot on the sample surface that induces micro-dimples on the surface and compressive residual stress induced inside samples that occur due to mechanical plastic deformation for fatigue strength. Shot peening has low depth penetration of compressive residual stress. Laser shock peening has many advantages such as high amplitude penetration of compressive residual stress, complex geometry samples can be employed, high precision laser pulse energy can be used on the samples, and reducing damages on the sample coating has been used as protective layer. Therefore, LSP has widely applied in automobile industrial components. In LSP process, laser as a source used to induce the compressive residual stress for improving the fatigue strength and surface properties [9, 10]. LSP causes three different mechanisms such as (i) different stress formations (compressive or tensile loading) (ii) high amplitude cyclic loading and (iii) thermal cyclic loading. LSP is a suitable method for enhancing corrosion resistance, wear resistance, and

superior attainment in grain refinement of the surface microstructure. In LSP process, two sacrificial layers have been used for protecting surface of the samples which is opaque and transparent layer. The transparent layer has been used to increase plasma range on the sample, which aid to improve the compressive residual stress. When compare to other LSP with the conventional surface treatment, they require coating or cladding technique has augmented the properties.

In this paper, motivation is enhancing the surface quality and reducing the surface defects of WAAM fabricated parts using laser shock peening. Governing the parameters of WAAM process has accomplished to reduce the number of experiment level. Further, Nd-YAG nanosecond laser is a source for laser shock peening which accomplishes the surface treatment to augment the microstructure refinement and mechanical properties.

45.2 Materials and Methods

45.2.1 Materials

The AWS ER70S-6 grade copper coated wire was used to fabricate in WAAM technique, for which chemical composition as shown in Table 45.1. This material has mainly used for structural application which has high strength.

45.2.2 Methods

WAAM and LSP:
The illustration of WAAM setup is shown in Fig. 45.1. WAAM process has retained with argon gas pressure at 28 Psi for making oxygen-free parts, and the parameters of the WAAM process shown in Table 45.2 are at optimum level.

The MS wire emanates from feeder to WAAM torch, which assists to fabricate thin wall structure with governed welding parameters. The argon gas has supplied to same torch nozzle for avoiding oxidation to the samples shown in Fig. 45.2. The above-optimized parameter has used to obtain the thin wall structure sample negligible spatter defects. After fabrication, the samples were employed to wire electrical discharge machining for cutting into 1 × 2 cm samples. Further which are done with surface polishing by metallography polishing machine with different grades of Sic paper. Subsequently, these samples have examined for surface treatments with

Table 45.1 Chemical composition

Elements	C	P	Si	Mn	S	Cu	Fe
% wt	0.09	0.012	0.95	1.65	0.018	0.35	Remaining

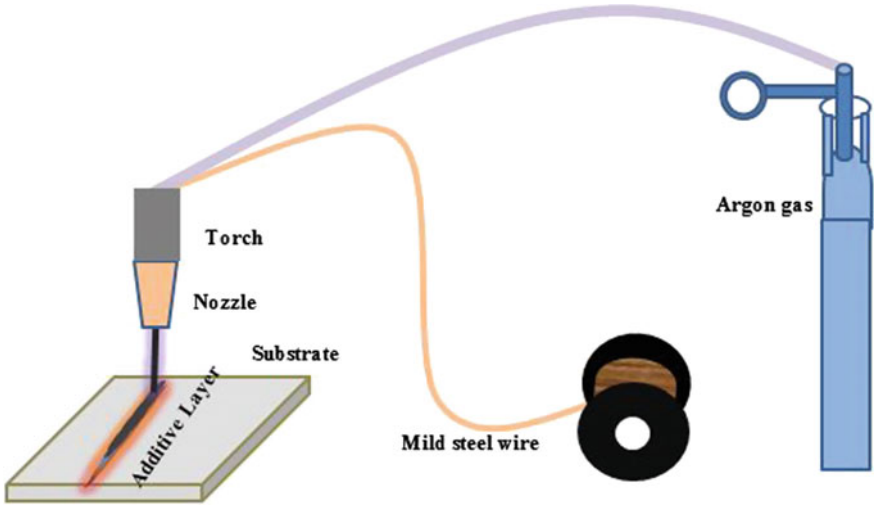

Fig. 45.1 Schematic representation of WAAM setup

Table 45.2 WAAM parameters

Parameters	Wire feed rate (m/min)	Ar. Gas Flow pressure (Psi)	Volt. (V)	Current (A)	Dia. (mm)
Quantity rate	1	28	16	80	1.2

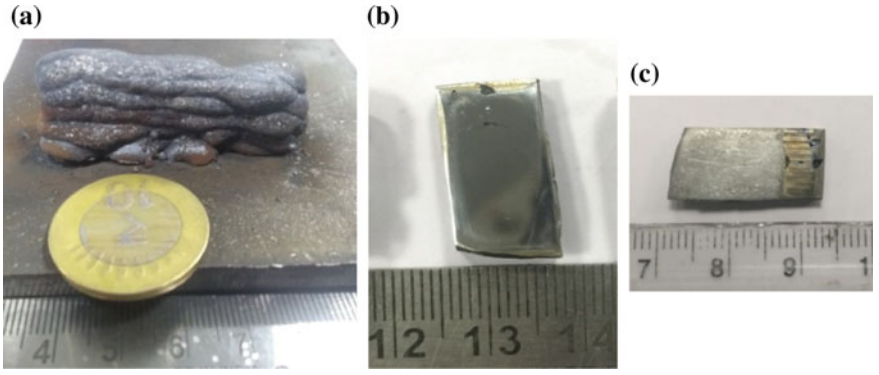

Fig. 45.2 WAAM fabricated samples. **a** WAAM fabricated six-layer sample. **b** Conventionally polished sample before shock peening. **c** After laser shock peened sample

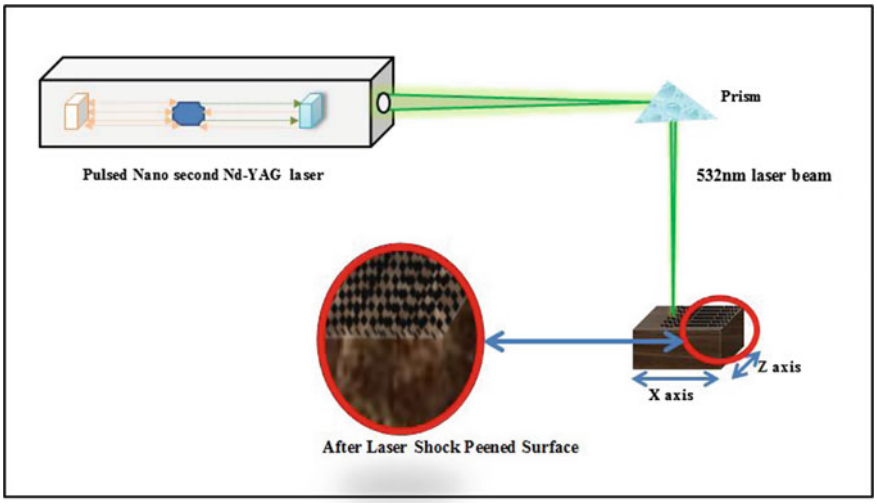

Fig. 45.3 Illustration of laser shock peening setup

the assistance of nanosecond Nd-YAG laser, the schematic arrangements of LSP are shown in Fig. 45.3.

The power of the laser shock peening process has maintained about 2 W of 532 nm wavelength, standoff distance 30 cm, without transparent overlay, and absorbent coating. The laser beam impinges able to ablate the atoms from WAAM sample which assist in changing the surface structure, and this effect helps to induce the compressive residual stress on the sample surface. An overlap of 90% between two layers can enhance wear resistance and fatigue life of the WAAM fabricated parts. The sample surfaces have characterized by an optical microscope. The crystalline structure and chemical element confirmations of as-fabricated samples have been investigated by X-ray diffraction. Before and after LSP samples surface has X-ray scanned by CuKα radiation ($\lambda = 0.1548$ nm) with an angle between 20° and 80°.

45.3 Result

45.3.1 Optical Microscope

The optical microscope has used for characterizing the surface morphology of WAAM fabricated samples before and aftershock peening which can magnify up to 0.2 μm. Figures 45.4 and 45.5 show the microstructure of WAAM fabricated low carbon steel samples which illustrates the micropores of the sample's surface. Nd-YAG solid-state pulsed laser has used for laser shock peening process with maximum laser power (2 W). The LSP process assisted to induce the residual stress and

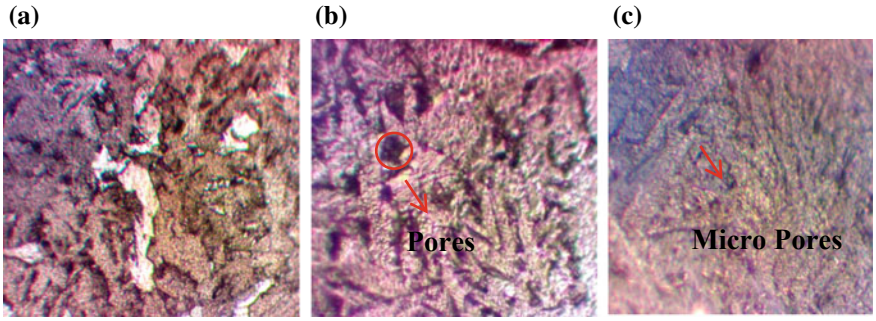

Fig. 45.4 Microstructure of before laser shock peened wire arc additive manufactured sample

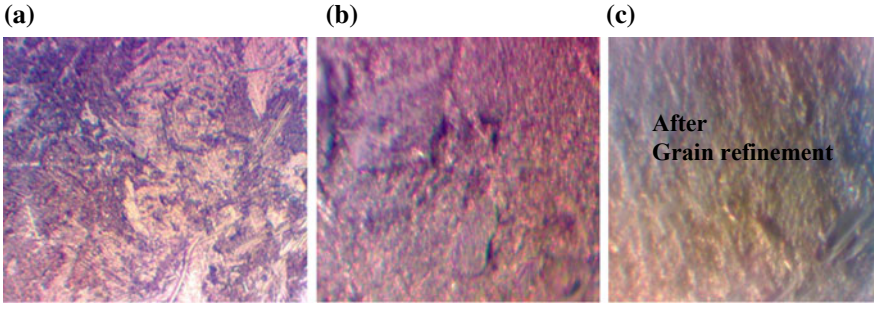

Fig. 45.5 Microstructure of after laser shock peened wire arc additive manufactured sample

to refine the grains. Figure 45.5a–c illustrate the grain refinement and enhancing the dense samples, and also the pores were decreased in laser shock peened WAAM fabricated sample. Finally, the LSP process achieved enhancing the surface topologies and internal structures of grains.

45.3.2 X-Ray Diffraction

The X-ray diffraction has used for characterizing crystalline orientation and crystal phases of the WAAM samples before and after the LSP process. When varying electron intensity concerning an angle between from 20° to 90°, the Bragg's law has illustrated grain orientation of the samples. Before LSP samples peaks in XRD graph (Fig. 45.6) were discover the conformation iron(Fe) element at an angle 45(2 0 0), 65(2 0 0) degree also the alpha and gamma iron as the same angles, which angles were observed absence of iron oxide elements. After the LSP processed samples (Fig. 45.7) were characterized the XRD peaks observed at 42.4(2 0 0) and 82.3(2 1 1), which illustrate that the peaks were shifted, due to the which laser-material

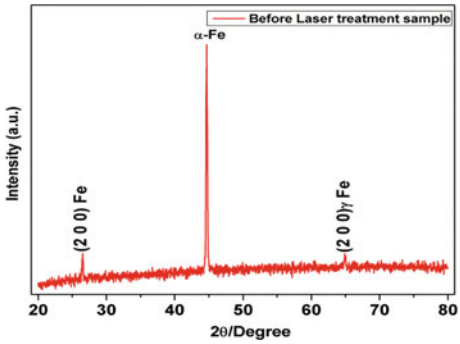

Fig. 45.6 XRD graph of before laser shock peened sample

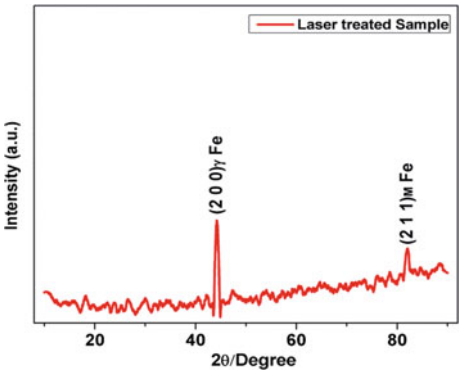

Fig. 45.7 XRD graph of after laser shock peened sample

interaction has induced the sufficient shock waves for phase transition from alpha to gamma phase. The Gaussian profile of 82.3 angles observed (211) Fe martensite phase. Hence, the LSP treated samples show good results as compared with non-LSP treated samples.

45.4 Conclusion

Summary of this research work,

1. The samples have successfully manufactured by WAAM process with the assistance of governed parameters, which are 16 V, 80 A, 1 m/min, and 28 psi.
2. The sample was laser shock peened with the source from Nd-YAG pulsed laser 10 ns pulse width and without transparent overlay an absorbent coating.
3. After the LSP process, the sample surface was enhancing the tribology properties.
4. Optical microscope showed the grain refinement and reduced micropores in laser-treated samples as compared with non-treated samples.

5. XRD peaks have observed phase changes between laser-treated to non-treated which transforms from Gamma iron to alpha iron.

Acknowledgements The authors thank the sophisticated instrumentation center of IIT Indore for their continuous support in providing characterization facilities. We also thank under DST Sponsored project DST/RC-UK/34-AM/2012 for providing financial support for carrying out the work. The authors acknowledge the support from Mr. Nithin of IIT Indore for helping XRD measurement.

References

1. Xiong, J., Lei, Y., Chen, H., Zhang, G.: Fabrication of inclined thin-walled parts in multi-layer single-pass GMAW-based additive manufacturing with flat position deposition. J. Mater. Process. Technol. **240**, 397–403, ISSN 0924-0136 (2017)
2. Busachi, A., Erkoyuncu, J., Colegrove, P., Martina, F., Ding, J.: Designing a WAAM based manufacturing system for defence applications. Procedia CIRP **37**, 48–53 (2015). ISSN 2212-8271
3. Xu, X.: Microstructural evolution and mechanical properties of maraging steel produced by wire+ arc additive manufacture process. Mater. Character. (2017). https://doi.org/10.1016/j.matchar.2017.12.002
4. Williams, S.W., Martina, F., Addison, A.C., Ding, J., Pardal, G., Colegrove, P.: Wire+ arc additive manufacturing. Mater. Sci. Technol. **32**(7), 641–647 (2016)
5. Song, Y.A.: 3D welding and milling: Part I–a direct approach for freeform fabrication of metallic prototypes. Int. J. Mach. Tools Manuf. **45**, 1057–1062 (2005)
6. Shen, C., Pan, Z., Ma, Y., Cuiuri, D., Li, H.: Fabrication of iron-rich Fe–Al intermetallics using the wire-arc additive manufacturing process. Addit. Manuf. **7**, 20–26 (2015). ISSN 2214-8604
7. Chen, X., Jia Li, X., Cheng, H.W., Huang, Z.: Effect of heat treatment on microstructure, mechanical and corrosion properties of austenitic stainless steel 316L using arc additive manufacturing. Mater. Sci. Eng. A **715**(7), 307–314 (2018)
8. Chen, S.: Arc welding processes for additive manufacturing: a review. Trans. Intell. Weld. Manuf. ISBN 978-981-10-5355-9
9. Lim, H.: Enhancement of abrasion and corrosion resistance of duplex stainless steel by laser shock peening. J. Mater. Process. Technol. **212**, 1347–1354 (2012)
10. Luo, K.Y.: Characterization and analyses on micro–hardness, residual stress and microstructure in laser cladding coating of 316L stainless steel subjected to massive LSP treatment. J. Alloys Compd. (2016)

Chapter 46
Fluidity of A206 Cast Alloy with and Without Scrap Addition Using Thin Cross-Sectional Fluidity Test: A Comparison

Srinivasa Rao Pulivarti and Anil Kumar Birru

Abstract The fluidity of the aluminium alloys decreases by increasing the volume fraction of oxide inclusions while recycling aluminium alloys and which in turn affects the castability of the materials. In the present investigation, the influence of scrap additions of A206 and Al–4Ni alloys on the fluidity of A206 alloy has been investigated for recycling. The measurements of the fluidity were achieved with plus type thin cross-sectional fluidity test. The pattern consists of cross sections 2, 4, 6 and 8 mm in order to make green sand moulds with respectable reproducibility. The effect of recycled alloys on fluidity has been compared with soapstone powder mould coating to that of the A206 alloy without coating. The results revealed that the fluidity decreased by an increase in the recycled alloy. It was observed that the fluidity was noticeably increased at 750 °C pouring temperature, particularly for the green sand moulds coated with soapstone powder.

Keywords A206 alloy · Fluidity · Thin wall castings · Mould coating · Pouring temperature · Recycling

46.1 Introduction

The aluminium alloy recycling causes substantial cost-effective benefits, energy savings, ecological benefits, etc. It was examined that secondary metal formed from recycled metal needs around 2.8 kWh/kg of metal formed, whereas the energy required for the production of primary aluminium is around 45 kWh/kg of prepared metal. It was significant to increase the use of recycled metal from the ecological point of view from the time when producing aluminium [1]. The change in environment is a rising issue of global concern. A new technique was adopted for the recycling process of aluminium alloy scrap with the purpose of less energy consumption and cost-effective production processes. By this technique, it can be observed that the

S. R. Pulivarti · A. K. Birru (✉)
Mechanical Engineering Department, National Institute of Technology, Lamphelpat, Imphal 795004, Manipur, India
e-mail: anilbirru@gmail.com

M. S. Shunmugam and M. Kanthababu (eds.), *Advances in Micro and Nano Manufacturing and Surface Engineering*, Lecture Notes on Multidisciplinary Industrial Engineering,
https://doi.org/10.1007/978-981-32-9425-7_46

less emission of air pollution as well as great saving of metal, in comparison with other processing techniques. The production of aluminium by recycling produces about 4–5% of the gas emitted in major production [2].

The fluidity is most commonly measured by either spiral mould or vacuum tests [3]. However, these tests are suitable for molten metal which flows in constant cross sections. But, the test results might be varied if the molten metal flows in different cross sections, and hence, the optimization of fluidity test procedure is essential [4]. The mould design with various cross sections proposed by Kwon and Lee [5] has given reproducible results. And, it was also observed that the grain refinement and oxide inclusions were found to be a significant impact on the castability of aluminium copper alloy with a low level of manganese at lower casting temperatures.

Few researchers made an attempt to enumerate the variables affecting the fluidity and concluded that the metallurgical factors, metal composition and degrees of superheat have a major impact on the fluidity [6]. Mollard et al. [7] reviewed the progress of fluidity in foundry technology and its applications in thin wall, high-integrity aluminium castings. Di Sabatino and Arnberg [8] studied the phenomena and effect of alloy composition, which reduces the fluidity of aluminium alloys. Yang et al. [9] investigated that fluidity and mechanical properties of Al–Si–Ni alloys. It was observed that the fluidity was increased by the addition of silicon and decreased by the addition of nickel at certain levels, whereas the addition of silicon and nickel both enhanced the ultimate tensile strength of the said alloy.

Sharma et al. [10] studied the tensile properties, fractography analysis and fluidity of the composites made iron oxide particulate composites. It was observed that the fluidly was increased linearly with the pouring temperature from 700 to 740 °C. Also, the fluidity was not having appreciable change for A518 alloys when the pouring temperature crosses beyond 715 °C [11]. However, the authors observed that much work has not been published on the effect of scrap on the fluidity of A206 alloy, especially for different thin cross sections. Therefore, in the present study, the authors made an attempt to study the effect of scrap and compare the fluidity of recycled A206 alloy for coated and uncoated moulds at different pouring temperatures.

46.2 Experimental Procedure

The A206 alloy was used to test the fluidity of different thin cross sections in the present investigation. The chemical composition of the A206 alloy is shown in Table 46.1.

Table 46.1 Composition of A206 alloy

The composition of elements (wt%)						
Cu	Mn	Mg	Si	Ti	Sr	Al
4.5	0.2	0.15	0.05	0.15	0.20	Balance

The A206 master alloy was made by green sand casting in an ingot form with ordinary crucible melting furnace. In order to make that, initially, 5 kg 99.7% purity aluminium was taken and melted in a graphite crucible at a temperature of 750 °C and then 4.5 wt% copper (99.8% purity) was introduced in a rod form to the molten aluminium at 800 °C. Later, the grain refiner Al–2.5Ti–0.5C was prepared with 2.5 wt% of titanium metal powder (99.8% purity) mixed with 0.5 wt% carbon powder (150 μm size) for 1 kg aluminium. The fluidity of the A206 alloy was tested by the addition of the aluminium scrap (5–15 wt%), which was made in the form of turning chips. Also, Al–4Ni master alloy was prepared with the nickel (Ni) metal which was processed into chips by drilling machine for 1 kg aluminium. The scrap of A206 alloy and Al–4Ni were added into virgin A206 alloy molten metal along with grain refiner at different percentages so as to study their effect on fluidity.

The fluidity test castings were made with the aid of green sand moulds. It was made from silica sand bonded with binders, namely, bentonite clay and molasses, and additives such as fly ash and water were taken in proportionate quantities in order to enhance the properties of green sand. Moreover, the soapstone powder mould coating was applied to mould surface due to the fact that their contact angles are large, and the wettability is low between the molten metal and mould, which in turn might increase the fluidity of thin cross section. The effect of thin cross section on the fluidity and mechanical properties of the A206 alloy is the motive behind the present investigation. Borouni et al. [12] have taken a cross-type pattern with different cross sections to test the fluidity. The same kind of fluidity test pattern has been selected in the current investigation as depicted in Fig. 46.1a.

The pattern was made with the mild steel and its design consists of four rectangular thin cross sections of 250 mm long and 30 mm wide with different thickness 2, 4, 6 and 8 mm thickness. Figure 46.1b shows the sand mould consists of mould cavity prepared by the designed pattern. The prepared green sand moulds which are coated with soapstone powder of a chosen pattern for the fluidity tests.

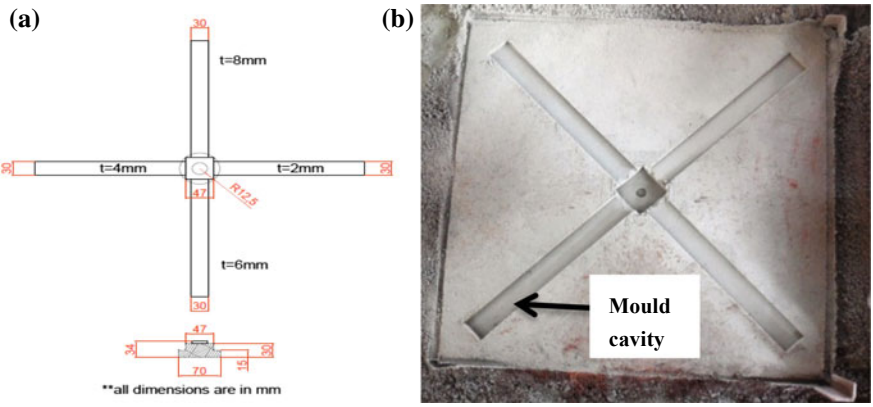

Fig. 46.1 **a** The pattern chosen for the fluidity investigation. **b** Sand mould

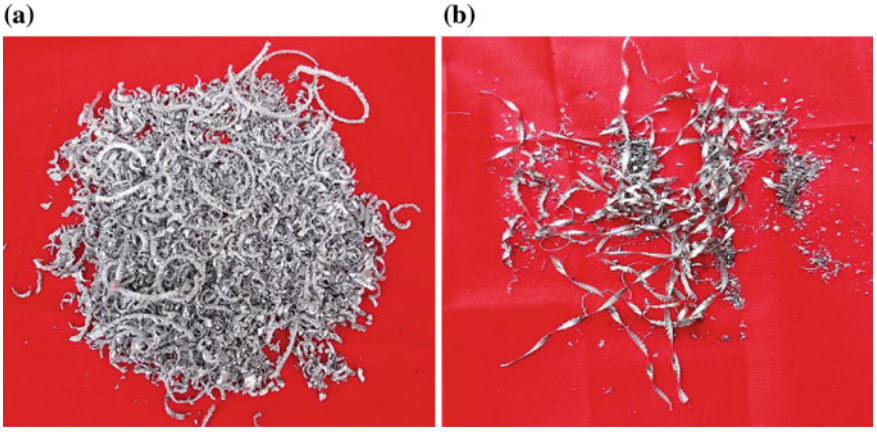

Fig. 46.2 Scrap used: **a** A206 alloy scrap, **b** nickel metal scrap

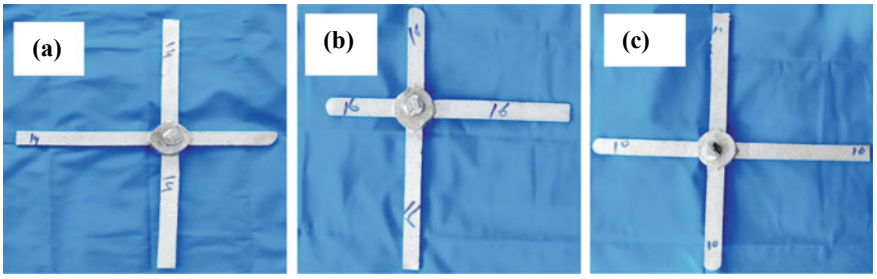

Fig. 46.3 Fluidity test castings: **a** A206 virgin alloy, **b** 15% A206 alloy scrap, **c** 4% Al–4Ni scrap

Figure 46.2 shows the scrap used for fluidity test and Fig. 46.3 shows castings made with different scraps.

46.3 Experimental Results

46.3.1 Fluidity Results of the A206 Alloy at Without Addition of Scrap

The results revealed that once the pouring temperature was raised from 700 to 750 °C, the fluidity length improved from 38.7 to 49.5 cm. Further increase of pouring temperature from 750 to 780 °C leads to enhance the fluidity length from 49.5 to 57.7 cm. Also, for the soapstone powder-coated moulds, Fig. 46.5 describes that while the pouring temperature was raised from 700 to 750 °C, the fluidity length

Table 46.2 Fluidity results of a thin cross section of the A206 alloy at without scrap addition

Pouring temperature (°C)	Fluidity length (cm)		Increase in fluidity	% Increase in fluidity (%)
	Uncoated	Coated		
700	38.7	67.6	28.9	74.68
750	49.5	76.1	26.6	53.74
780	57.7	81.2	23.5	40.73

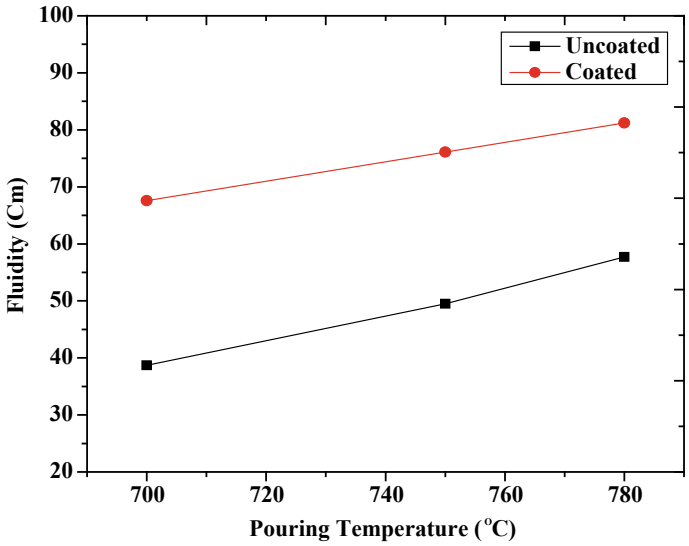

Fig. 46.4 Fluidity results of a thin cross section of the A206 alloy at without scrap addition

improved from 67.4 to 76.1 cm. As the pouring temperature increased from 750 to 780 °C, the fluidity length further improved from 76.1 to 81.2 cm as displayed in Table 46.2. The A206 alloy for thin cross sections with and without coating is as depicted in Fig. 46.4.

46.3.2 Fluidity Results of the A206 Alloy with 15% A206 Alloy Scrap Addition

Figure 46.5 depicts the results of the fluidity of the A206 alloy at 15% scrap addition. It was revealed that for uncoated cross-sectional mould, the fluidity was increased from 45.5 to 56.1 cm while the pouring temperature was raised from 750 to 780 °C. Likewise, the fluidity increased from 49.6 to 69.2 cm while the pouring temperature increased from 700 to 750 °C for the soapstone powder-coated moulds. Further

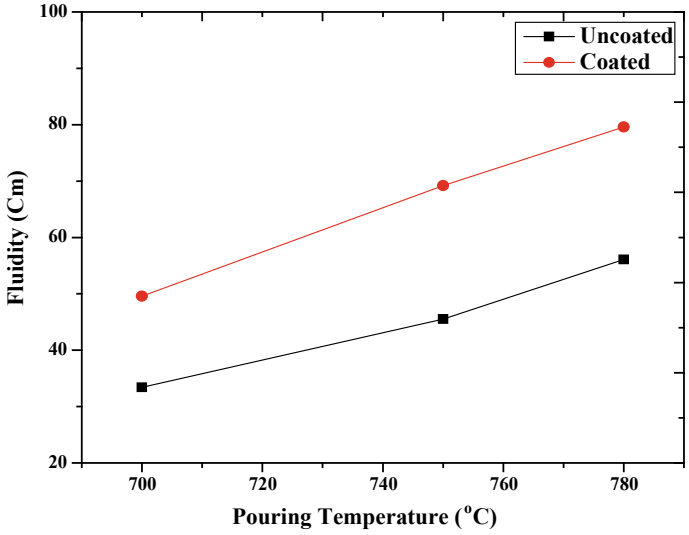

Fig. 46.5 Fluidity results of a thin cross section of the A206 alloy at 15% A206 scrap addition

Table 46.3 Fluidity of thin cross-sectional test results of A206 alloy with 15% scrap addition

Pouring temperature (°C)	Fluidity length (cm)		Increase in fluidity	% Increase in fluidity (%)
	Uncoated	Coated		
700	33.4	49.6	16.2	48.50
750	45.5	69.2	23.7	52.09
780	56.1	79.6	23.5	41.89

increase of pouring temperature from 750 to 780 °C leads the fluidity length enhanced to 79.2 cm as represented in Table 46.3.

46.3.3 Fluidity Results of the A206 Alloy with 15% A206 Alloy Scrap Addition

Figure 46.6 depicts the results of the fluidity of the A206 alloy at 15% scrap addition. It was revealed that for uncoated cross-sectional mould, the fluidity was increased from 45.5 to 56.1 cm while the pouring temperature was raised from 750 to 780 °C. Likewise, the fluidity increased from 49.6 to 69.2 cm while the pouring temperature increased from 700 to 750 °C for the soapstone powder-coated moulds. Further increase of pouring temperature from 750 to 780 °C leads the fluidity length enhanced to 79.2 cm as represented in Table 46.4.

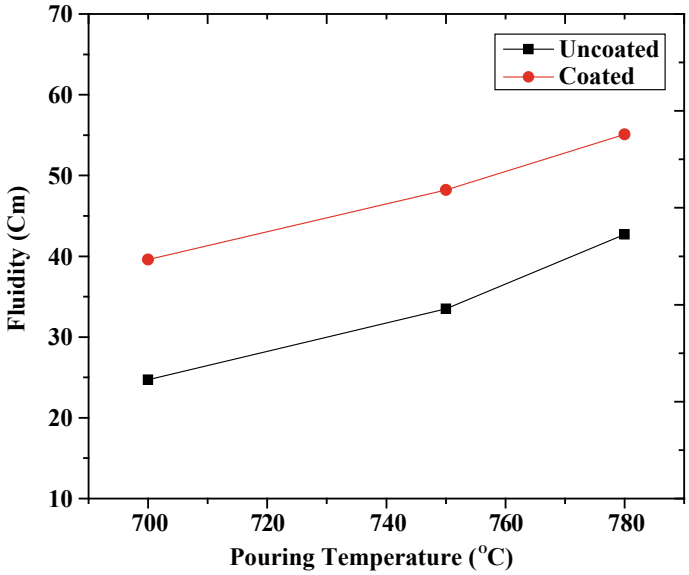

Fig. 46.6 Fluidity results of a thin cross section of the A206 alloy at 4% Al–4Ni scrap addition

Table 46.4 Fluidity of thin cross-sectional test results of 4% Al–4 Ni alloy without scrap addition

Pouring temperature (°C)	Fluidity length (cm)		Increase in fluidity	% Increase in fluidity (%)
	Uncoated	Coated		
700	24.7	39.6	14.9	37.63
750	33.5	48.2	5.5	11.41
780	42.7	55.1	21.6	39.20

46.4 Discussions

The fluidity results of the virgin A206 alloy obtained by the soapstone powder mould coating and mould without coating are compared at without scrap additions. It was observed that the fluidity was increased by 74.68% from uncoated to the coated thin cross section at the pouring temperature at 700. The fluidity was further increased by 53.74% at 750 °C pouring temperature and 40.73% at a pouring temperature of 780 °C. Likewise, for 15% scrap addition at 700 °C pouring temperature, the fluidity was increased by 48.50% when the results are compared at without coating and with soapstone powder coating. It was examined that the fluidity was further increased by 52.09% at 750 °C and 41.89% at 780 °C. So, recycling of A206 alloy with and without scrap additions might be recommended for industrial use because the fluidity was increased by the addition of 15% scrap of the A206 alloy. For the A206 alloy with 15% scrap addition, the oxide particles were weakened, which might

be the cause for least alterations in the fluidity at higher pouring temperature. Also, the addition of the A206 alloy scrap does not considerably affect fluidity at higher pouring temperatures with the 15% scrap addition. Conversely, with the increase in the pouring temperature, the fluidity has increased. Moreover, it can be expected that the inclusion of oxide particles was influenced by the mould coatings due to the pouring temperature. Authors, however, identified that further investigations may be needed to check the kind of oxide elements.

46.5 Conclusions

As per the investigations carried out, the following conclusions have been drawn as follows:

1. An appreciable improvement in the fluidity of A206 alloy without scrap addition was observed due to soapstone powder mould coating, particularly at minimum pouring temperature of 700 °C.
2. The fluidity was decreased by the addition of scrap at lower pouring temperatures. However, the fluidity was considerably increased at higher pouring temperatures. Therefore, the addition of scrap might be permissible up to 15% in case of A206 and 4% in the case of Al–4Ni alloy.
3. The percentage of A206 alloy scrap does not have a significant influence on fluidity at the higher pouring temperatures with the 15% scrap and 4% Al–4Ni additions. Therefore, it is recommended to the casting industries that scrap addition of the said alloy is beneficial with proper control of alloy composition.

References

1. Birru, A.K., Benny Karunakar, D., Mahapatra, M.M.: Fluidity of A713 cast alloy with and without scrap addition using double spiral fluidity test: a comparison. Int. Sch. Sci. Res. Innov. **6**, 128–132 (2012)
2. Samuel, M.: A new technique for recycling aluminum scraps. J. Mater. Process. Technol. **135**, 117–124 (2003)
3. Di Sabatino, M., Syvertsen, F., Arnberg, L., Nordmark, A.: An improved method for fluidity measurement by gravity casting of spirals in sand moulds. Int. J. Cast Met. Res. **18**, 59–62 (2005)
4. Colak, M., Kayikci, R., Dispinar, D.: Influence of different cross sections on fluidity characteristics of A356. Trans. Indian Inst. Met. **68**, 275–281 (2014)
5. Kwon, Y.D., Lee, Z.H.: The effect of grain refining and oxide inclusion on the fluidity of Al–4.5Cu–0.6Mn and A356 alloys. Mater. Sci. Eng., A **360**, 372–376 (2003)
6. Ravi, K.R., Pillai, R.M., Amaranathan, K.R., Pai, B.C., Chakraborty, M.: Fluidity of aluminum alloys and composites: A review. J. Alloy. Compd. **456**, 201–210 (2008)
7. Mollard, F.R., Flemings, M.C., Niyama, E.F.: Aluminum fluidity in casting. J. Metals 34–37 (1987)

8. Di Sabatino, M., Arnberg, L.: Castability of aluminium alloys. Trans. Indian Inst. Metals **62**, 321–325 (2009)
9. Yang, L., Li, W., Du, J., Wang, K., Tang, P.: Effect of Si and Ni contents on the fluidity of Al–Ni–Si alloys evaluated by using thermal analysis. Thermochim. Acta (2016). http://dx.doi.org/10.1016/j.tca.2016.10.013
10. Sharma, S.C., Girish, B.M., Kamath, R., Satish, B.M.: Fractography, fluidity, and tensile properties of aluminium/hematite particulate composites. J. Mater. Eng. Perform. **8**, 309–314 (1999)
11. Birru, A.K., Mahapatra, M.M., Karunakar, D.B., Kumar, P.: A study on fluidity and hot-tearing of A206, A518 and A713 cast alloys. Indian Foundry J. **57**(2011), 38–45 (2011)
12. Borouni, M., Niroumand, B., Fathi, M.H.: Effect of a nano-ceramic mold coating on the fluidity length of thin-wall castings in Al4-1 alloy gravity sand casting. Mater. Technol. **48**, 473–477 (2014)

Chapter 47
Study on the Aesthetic Behavior of Anodic Oxidation in ADC12 Aluminum Alloy

S. Shanmugham, M. Kamaraj, S. K. Seshadri, V. P. Balaji and S. Karthi

Abstract Anodizing/Anodic oxidation is the most common surface treatment of aluminum and its alloys for automobile and aerospace applications. Poor aesthetic appearance (scattered patches on the surface) is the common problem in pressure die-cast ADC12 aluminum alloy when it is subjected to anodic oxidation at higher temperature due to surface segregation. Surface segregation is inevitable in this material where it is a commercial aluminum alloy and having a high level of impurity contents. High impurity will ease to form alloy segregation in surface and subsurface during pressure die-casting and reflect poor surface appearance like yellow color patches. This case study deals to solve the poor aesthetic behavior in ADC12 alloy during the anodic oxidation process. Process condition study was done to eliminate this problem.

Keywords Anodic oxidation · Segregation · Intermetallics · X-ray diffraction · SEM–EDAX analysis · Pressure die-casting

47.1 Introduction

Aluminum pressure die-cast components are widely used in automotive applications due to its lightweight and better castability. In braking system applications, aluminum–silicon alloys such as ADC12 alloy used in valve internal components and other structural housing parts. In general, the surface nature of an aluminum alloy is more complex than pure aluminum. In pressure die-casting, thermal contact between the die wall and the solidifying metal ensured by the applied pressure during solidification results in very high cooling rates. This will create changes in microstructure near the casting surface such as alloy segregation of higher volume

S. Shanmugham (✉) · V. P. Balaji · S. Karthi
Research & Development, WABCO India Limited, Chennai, India
e-mail: Shanmugam.subramaniam@wabco-auto.com

M. Kamaraj · S. K. Seshadri
Department of Metallurgical and Materials Engineering, Indian Institute of Technology Madras, Chennai, India

M. S. Shunmugam and M. Kanthababu (eds.), *Advances in Micro and Nano Manufacturing and Surface Engineering*, Lecture Notes on Multidisciplinary Industrial Engineering,
https://doi.org/10.1007/978-981-32-9425-7_47

fraction of intermetallic in solution due to impurity. Distribution of impurity will happen in a nonuniform manner and scatter in the different regions due to localized undercooling. It makes inhomogeneous mixture in the aluminum solid solution. This is called as segregation of impurities.

These segregation phases are mainly Fe-rich compounds consisting of Al, Fe, Mn, Cu, and Ni. In some cases, it will appear as large intermetallic particles with respect to cooling rate and appear in surface and subsurface which is connected with locally finer grain size. The effect of second phase particles on growth and properties of anodic oxide layer depends on their composition, structure, chemical and electrochemical properties, their morphology, volume fraction, and distribution [1]. In general, nonequilibrium solidification occurs in actual pressure die-cast part is due to component geometry, which will result several brittle and harmful intermetallic phases such as Fe_2SiAl_8, $FeAl_6$, Al_5FeSi, $FeSi_2Al_4$, and $FeSiAl_3$, and coexist with one another and with Si in Al–Si iron-containing alloys [2].

Among all the alloying elements, Fe is the most detrimental impurity in cast aluminum alloys due to the formation of brittle intermetallics progressively, which decreases the mechanical properties such as ductility and ultimate tensile strength. The cooling rate and addition of neutralizers such as Mn influence the critical Fe content determine the final quality and soundness of the cast component. Fe in the melt will adversely affect castability, corrosion resistance, and machinability of the casting components. Fe-rich intermetallic will act as stress raisers due to formation of porosity during solidification. Nevertheless, with increased Fe content, the hardness and the resistance to hot tearing seem to increase and die soldering issues are avoidable leading to longer tool lifetime [3].

Corrosion protection of the aluminum castings is achieved by chromating and anodic oxidation method. Compared to chromating, anodic oxidation will be the better option to enhance the corrosion resistance of the aluminum castings. Anodic oxidation is carried out to increase the wear resistance of aluminum and its alloys in addition to corrosion resistance. By applying an anodic current or voltage in a sulphuric acid bath, the natural oxide layer on the aluminum becomes thicker leading to a better corrosion and wear resistance. The anodic oxide structure originates from the aluminum substrate and is composed entirely of aluminum oxide. During anodic oxidation, an increase in temperature intensifies the dissolving action of the sulfuric acid, which is faster than that of oxide formation resulting in softer, more porous coatings [4]. Surface segregation is inevitable in the ADC12 aluminum alloy which is having high impurity content. Aluminum oxide formation is the combination of aluminum dissolution and the formation of aluminum oxide. Pore creation during anodic oxidation is purely on temperature enhanced, higher the temperature larger the pore sizes. Combination of larger the pore size and temperature-assisted faster reaction with the surface segregation results in yellow color patch formation which is shown in actual Pressure Die Casting (PDC) part in Fig. 47.1. No study was carried out on the formation of yellow color patches. This paper deals with the effect of surface segregation on poor aesthetic behavior and resolves the problem.

Fig. 47.1 Poor appearance as yellow color patches on the surface of the component

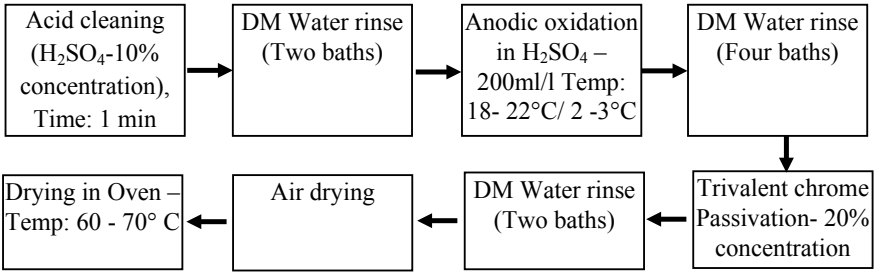

Fig. 47.2 Process flow for the anodic oxidation process

Table 47.1 Chemical composition of the ADC12 alloy

Composition wt%								
Specimen material	Si	Fe	Cu	Mn	Mg	Zn	Pb	Al
ADC12	10.78	0.93	1.97	0.46	0.17	0.89	0.061	Balance

47.2 Methodology

47.2.1 Materials Used

The material used for this study is ADC12 aluminum alloy, which is Al–Si cast alloy, enriched with copper. Chemical composition analysis was carried out using the spectroscopic method and the results are tabulated in Table 47.1. Anodic oxidation was carried out in actual production line using a sulphuric acid bath with the specific gravity of 1.12–1.16. Bath tank used for anodic oxidation is made out of high-density polyethylene plastic. Conventional power source mode is set up made with DC power source of 1000 A current and 24 V with thyristor controlled rectifier. The electrolyte is cooled using a cooling coil immersed in the bath and the bath temperature is maintained at 18–22 and 2–3 °C in different experiments. Titanium jigs were used to hold the substrate and ADC12 alloy component was used as an anode. Pure aluminum was used as cathode. The process flow of anodic oxidation is described in Fig. 47.2. Pre-etching and desmutting were done to clean the surface of the component.

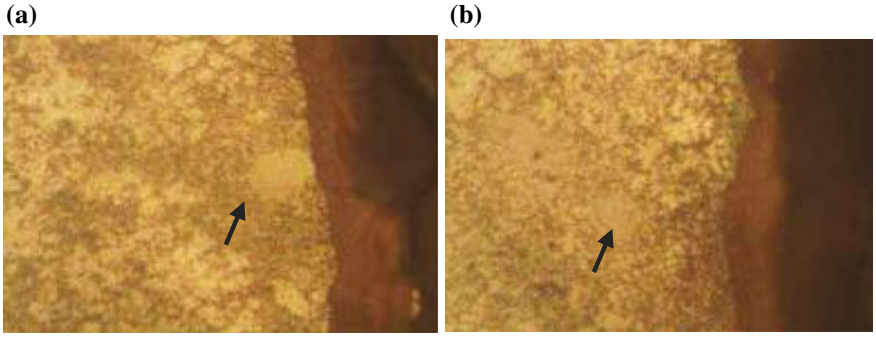

Fig. 47.3 The microstructure of the base material revealing intermetallic particle **a** at the surface **b** at subsurface

An optical microscope was used to study the microstructure of the castings in surface and subsurface metallographic studies using an optical microscope. The micro sample substrate for anodic oxidation was taken from the anodized component. A small sample size of 20 × 20 × 8 mm was cut from the actual cast component. Micro samples were cut using abrasive cutting machine and mechanically polished using 200, 400, 600, 800, and 1000 grade SiC papers. Final polishing was done using 0.5 μm diamond suspension. The morphology of the substrates and oxide layers was investigated using optical microscopy analysis of the cross sections. Images were captured by a digital camera type LU1176-CLX attached to the Carl-Zeiss Axio Scope k1 microscope was used for microscopic examination to measure the layer thickness. Anodic oxidation layer morphology was further analyzed using Scanning Electron Microscope (SEM). SEM–EDAX analysis done to quantify the elements present on the surface. In yellow color patches, to find out the intermetallic compound, X-Ray Diffraction (XRD) technique was used.

47.2.2 Process Improvements Outcome

Microstructure analysis revealed that large intermetallic particles are present in surface and subsurface as shown in Fig. 47.3. An anodized sample was analyzed in SEM and clearly revealed that the yellow color patch appeared as a fine layer on top of the anodized layer is shown in Fig. 47.4. The top surface formed on the top anodized layer due to the yellow color patch, which revealed by SEM examination.

SEM–EDAX examination confirmed that the yellow color patch layer is the complex intermetallic compound as shown in Fig. 47.5. XRD analysis is done on as cast as well as the anodized sample on alloy segregation where yellow color patches formed to find out the type of intermetallic compound. The XRD pattern of surface segregation is shown in Fig. 47.6. As the cast and anodized conditions, the intermetallic

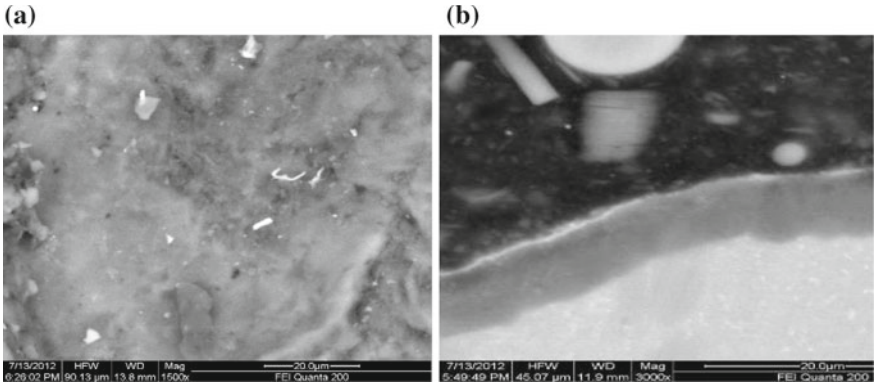

Fig. 47.4 SEM image of the anodized layer showing segregation at **a** at the surface **b** at subsurface

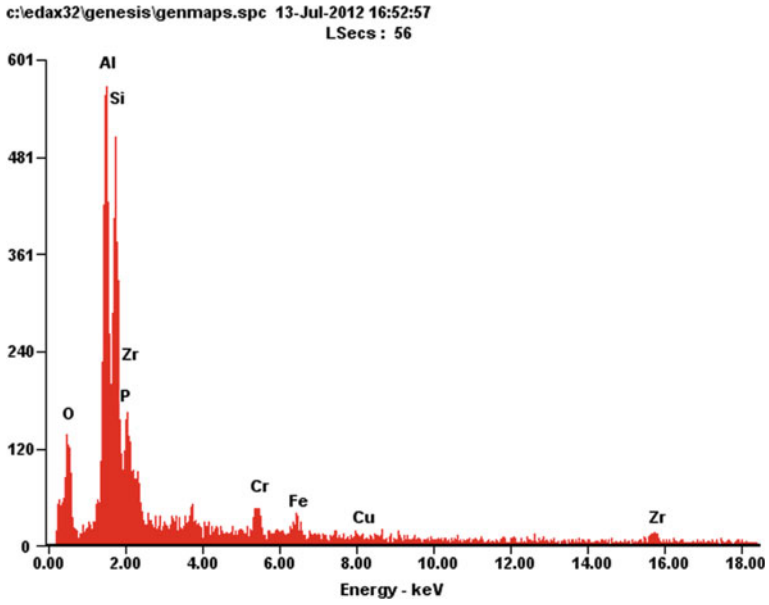

Fig. 47.5 EDAX pattern of silicon-rich intermetallic

compounds confirmed to $Al_9Fe_{0.84}Mn_{2.16}Si$, $Fe_2Al_3Si_3$, and $Al_{1.9}CuMg_{4.1}Si_{3.3}$ and corresponding Joint Committee on Powder Diffraction Standards (JCPDS) data as shown in Fig. 47.7. No changes happened in intermetallic compounds after anodic oxidation, since it is a very stable compound. Further XRD analysis revealed that the layer is silicon-rich, and $Al_9Fe_{0.84}Mn_{2.16}Si$, $Fe_2Al_3Si_3$, and $Al_{1.9}CuMg_{4.1}Si_{3.3}$ are intermetallic compounds. Yellow color patch formation was observed to be suppressed when anodic oxidation carried out in lower temperature such as 2–3 °C as

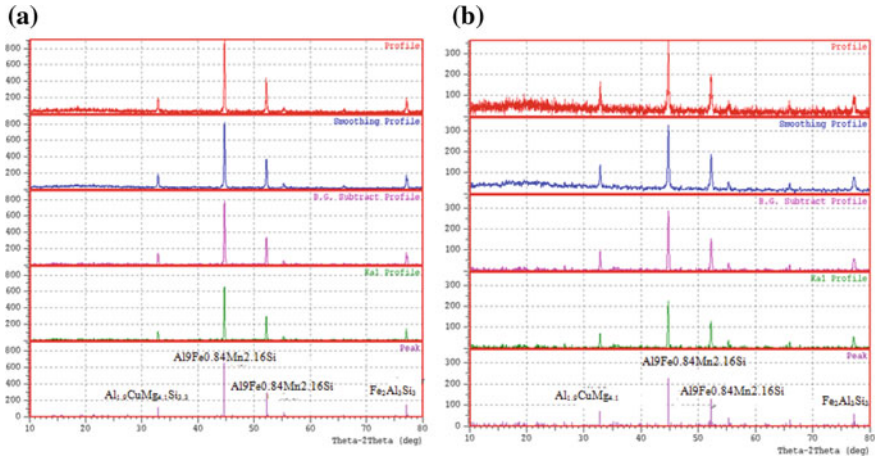

Fig. 47.6 X-ray diffraction pattern of yellow color patches **a** as cast **b** after anodic oxidation

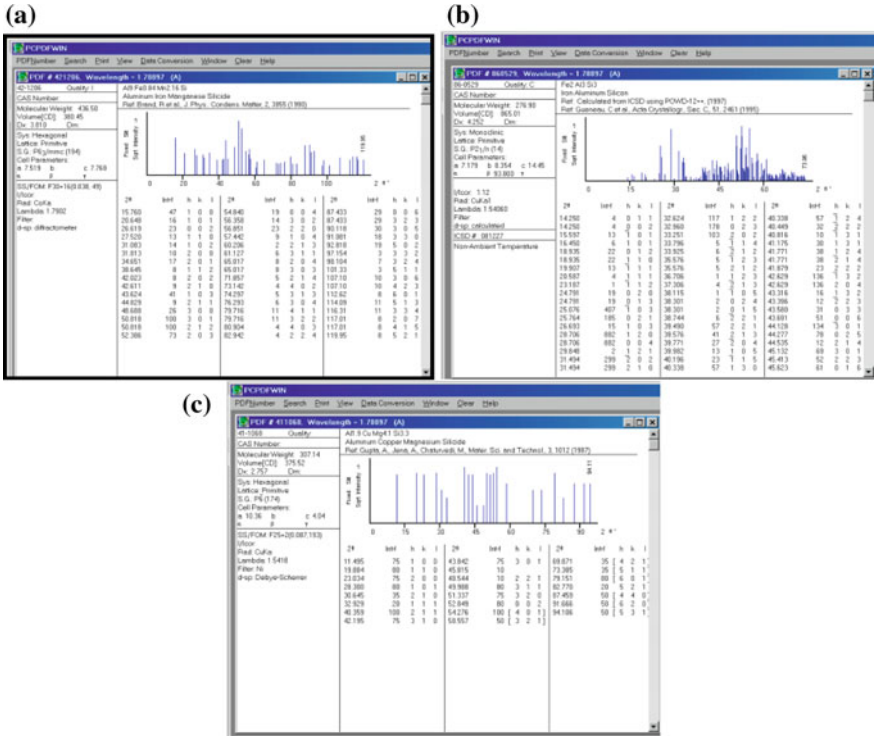

Fig. 47.7 JCPDS data for **a** $Al_9Fe_{0.84}Mn_{2.16}Si$ **b** $Fe_2Al_3Si_3$ **c** $Al_{1.9}CuMg_{4.1}Si_{3.3}$

Fig. 47.8 Image of the PDC part after improvement

shown in Fig. 47.8. Based on the observation, it can be seen clearly that high temperature can cause the higher dissolution rate of Al_2O_3 resulted in the segregation film to change the color of the surface.

High amount of heat released during the formation of oxide coating because of the exothermic reaction of anodic oxide formation and from the electric current. Due to this, the electrolyte near the component surface was heated to a maximum. At this maximum temperature, the electrolyte becomes more aggressive, and hence, its dissolution ability gets higher. At this condition, the formed anodic coating undergoes dissolution at a faster rate than that of its formation. At higher temperature, the dissolution of aluminum predominates, but at a lower temperature, the formation of oxide coating predominates. Because of the overheating, segregation reacts rapidly and changes its color. At high temperature, electrolyte temperature will increase due to the aggressiveness of the electrolyte toward the oxide, thereby, enhancing the chemical dissolution of the coating by the electrolyte [5].

47.2.3 Corrosion Testing

In order to check the effectiveness of the low-temperature anodic oxidation on corrosion resistance, Neutral salt spray test was carried out according to ISO-9227. Actual casting parts were subjected to salt spray testing. Test conditions of the neutral slat spray testing are tabulated in Table 47.2.

Three components in each high- and low-temperature anodic oxidized components were subjected to neutral salt spray testing till failure. In addition to elimination of yellow color patches, low-temperature anodized component was shown fourfold

Table 47.2 Neutral salt spray test parameters

Parameter	Specification
Salt concentration	5% NaCl
pH of solution in reservoir	6–7
pH of fallout	6.5–7.2
Air temperature	45 ± 2 °C
Cabinet temperature	35 ± 2 °C

Fig. 47.9 Casting component anodized with high temperature after NSS testing of 242 h

Fig. 47.10 Casting component anodized with low temperature after NSS testing of 1082 h

increase in corrosion resistance than high-temperature anodized component. Salt spray resistance of the low-temperature anodic oxidized shows 1082 h and 242 h of resistance, respectively, and salt spray tested components are shown in Figs. 47.9 and 47.10, respectively. In low temperature, the liberated heat during coating growth is completely and effectively dissipated from the specimen to the bulk of the solution. Hence, maximum thickness was obtained at low temperature as 12 μm, whereas high temperature resulted in only 7 μm. Higher thickness and tenacious anodic oxidation layer were resulted in higher corrosion resistance in the component. At this lower temperature, the formation of Al^{3+} and O^{2-} ions from the solution is maximum and they combined together to form various kinds of alumina compounds [6]. An increase in electrolyte temperature will increase proportionally the rate of dissolution of the anodic film resulting in a thinner, more porous and softer film. Low temperatures are used to produce hard coatings normally in combination with high current densities and vigorous agitation [7].

47.3 Conclusion

Surface segregation in aluminum alloy is more stable and no change even after anodic oxidation. Yellow color patch formation is caused by the reaction of the sulphuric acid electrolyte with cast surface segregation ($Al_9Fe_{0.84}Mn_{2.16}Si$, $Fe_2Al_3Si_3$, and $Al_{1.9}CuMg_{4.1}Si_{3.3}$ intermetallics) when anodic oxidation is done at 18–22 °C temperature. Yellow color patch formation prevented in anodic oxidation when electrolyte temperature is maintained at 2–3 °C.

In addition, low-temperature anodic oxidation results in remarkable improvement in corrosion resistance with salt spray hours of more than 1000 h in ADC12 alloy which is considered poor corrosion resistance material since higher copper content present in the material which generally prevents the formation of tenacious layer of aluminum oxide.

Acknowledgements The authors would like to thank WABCO India Limited to support this project.

References

1. Gourlay, C.M., Laukli, H.I., Dahle, A.K.: Segregation band formation in Al–Si die castings. Metall. Mater. Trans. A **35**(9), 2881–2891 (2004)
2. Seifeddine, S., Ingenjörshögskolan i Jönköping.: The influence of Iron on the microstructure and mechanical properties of cast Al–Si-alloys. Vilmer Project 5.2 Casting (2007)
3. Seifeddine, S., Ingenjörshögskolan i Jönköping.: The influence of Iron and Mn content on the microstructure and tensile properties of cast Al–Si–Mg. Vilmer Project 5.2, Casting (2007)
4. Shimizu, K., Brown, G.M., Habazaki, H., Kobayashi, K., Skeldon, P., Thompson, G.E., Wood, G.C.: Selective oxidation of aluminum and interfacial enrichment of iron during anodic oxide growth on an Al6Fe phase. Corros. Sci—CORROS SCI' **42**, 831–840 (2000)
5. Yang, K.V., Nagasekhar, A.V., Lumley, R., Caceres, C.H.: The skin effect of high pressure die casting Al alloys. In: Proceedings of the 12th International Conference on Aluminum Alloys, pp. 687–692 (2010)
6. Fratila-Apachitei, L.E.: Voltage transients and morphology of AlSi (Cu) anodic oxide layers formed in H2SO4 at low temperature. Surf. Coat. Technol. **157**, 80–94 (2002)
7. Henley, V.F.: Aluminum Oxidation of Aluminum and Its Alloy. Pergamon Press (1982)

Chapter 48
Development and Correlative Microstructural-Nanoindentation Investigation on Ni-Based + 10% Al_2O_3 Nanocomposite Microwave Clad on Hydroturbine Steel

Bhupinder Singh and Sunny Zafar

Abstract This work deals with the development of Ni-based + Al_2O_3 nanocomposite clads on CA6NM (hydroturbine steel) through microwave heating. In the present study, Ni-based + 10 wt% nanometric Al_2O_3 powders were used to develop clads on CA6NM grade hydroturbine steel using a multimode domestic microwave applicator of frequency 2.45 GHz operating at a power of 0.9 kW. A scanning electron microscope was used to evaluate the microstructure of the clad. The microstructural analysis and EDS confirm excellent metallurgical bonding between clad and the substrate. Nanoindentation was used to evaluate the nanoscale mechanical properties of the developed nanocomposite microwave clads. Nanoindentation analysis also revealed that the clad layer exhibit 74% higher hardness as compared to the substrate. The observations favor the deposition of the Ni-based + 10% Al_2O_3 nanocomposite microwave clads to minimize slurry erosion in CA6NM hydroturbine steel.

Keywords Nanocomposite · Microwave · Cladding · Microstructure · Nanoindentation

48.1 Introduction

The excellent corrosion resistance properties of CA6NM and good machinability make it a popular material in several applications including hydropower plants and petrochemical industries [1]. In hydropower plants, most of the components of the hydro turbine such as runner blades, guide vanes are exposed to high erodent particles flowing with water [2]. Therefore, the manufacturing of underwater components from high corrosion resistant material is not sufficient for long service life. There is also a requirement of high toughness that can resist the severe impact of erodent. To fulfill the strength requirements and also to reduce the cost of maintenance, hydro

B. Singh · S. Zafar (✉)
School of Engineering, Indian Institute of Technology Mandi, Kamand, Mandi 175005, India
e-mail: sunnyzafar@iitmandi.ac.in

M. S. Shunmugam and M. Kanthababu (eds.), *Advances in Micro and Nano Manufacturing and Surface Engineering*, Lecture Notes on Multidisciplinary Industrial Engineering,
https://doi.org/10.1007/978-981-32-9425-7_48

turbine steel (CA6NM) is usually coated with hard ceramics [3]. Although hard coatings are deposited using the thermal spray, laser cladding, etc., but thermally sprayed coatings are often mechanically anchored to the substrate and inherently have porosity. The regions with porosity trigger corrosion and erosion in the hydroturbine components during service [4]. On the other hand, popular laser cladding process has high initial cost. Furthermore, the oxide inclusion in thermal spray coating, the coating process seeks an alternative approach to modify the functional surfaces with higher efficiency and relatively lower cost. In this regard, low thermal stress and uniform microstructures are achievable with microwave cladding [5]. Microwave cladding is one of the innovative emerging techniques in surface engineering. In microwave cladding, it is possible to obtain a crack-free and metallurgically bonded surface layer. Processing of metallic material by microwave hybrid heating in the field of surface engineering has been widely reported [6].

Development of nanostructured cladding using a metallic material as matrix and a microwave transparent material as reinforcing material is a challenging task. The main reason behind this challenge is the poor coupling of these materials with microwave energy at room temperature. Furthermore, very limited work has been carried out in the case of reinforcing nanometric material in a metallic matrix.

Selection of cladding powder is highly dependent upon the application for which the material is to be used. Once the selection was made, proper grain size is recommended for improved mechanical properties of the coating. As per Hall-Petch relation, strength is greatly influenced by grain size. Several authors investigated the effect of reduced grain size on mechanical properties of the developed coating. Zafar and Sharma investigated the microhardness of nanostructured WC-12Co microwave clad. It was found to be 1564 ± 53 HV, which was 37% higher than the micrometric WC-12Co microwave clad (1138 ± 90 HV) [7, 8]. The difference in microhardness value of the clad developed from the same composition can be attributed to the increased grain boundaries that act as a barrier for dislocation in material in case of nanostructured clad.

In the present study, we demonstrated the development of microwave nanocomposite clad of Ni-based + 10% Al_2O_3 on CA6NM steel substrate. The average particle size of the Al_2O_3 powder was approximately 100 nm. The microstructure of microwave cladding was investigated through the scanning electron microscope (SEM). Nanohardness and Young's modulus of clad and substrate were evaluated by nanoindentation.

48.2 Experimental Procedure

48.2.1 Material Selection

In the present study, hydroturbine steel (CA6NM) was used as a substrate for developing the nanocomposite microwave clads. The hydroturbine steel substrate was

supplied by M/s Vaishnav Steels, Muzaffarnagar, Uttar Pradesh, India. The substrate was machined to prepare specimens of dimensions 25 × 25 × 6 mm^3. The Ni-based (EWAC) powder was sourced from EWAC Alloy powders, L&T, India, while the nanometric Al_2O_3 powder was supplied by Hongwu International, China. The nickel-based powder and Al_2O_3 powder has an average particle size of 40 μm and 100 nm, respectively. The Ni-based powder and 10 wt% nanometric Al_2O_3 powder were mixed mechanically in a powder mixer for 12 h at 23 °C to attain uniform composition. The typical morphology of Ni-based powder and nanometric Al_2O_3 powder are shown in Fig. 48.1a, b, respectively. The SEM images reveal the spherical morphology of Ni-based powder, whereas the nanometric Al_2O_3 exhibits irregular morphology. X-ray diffraction spectrum of Ni-based (EWAC) powder and nanometric Al_2O_3 powder is shown in Fig. 48.1c, d, respectively, that confirms the presence of Nickel and α-Al_2O_3 as a major phase. The nominal chemical composition of the CA6NM substrate was provided by the supplier, while energy dispersive spectroscopy was used to ascertain the elements in the clad powders and presented in Table 48.1.

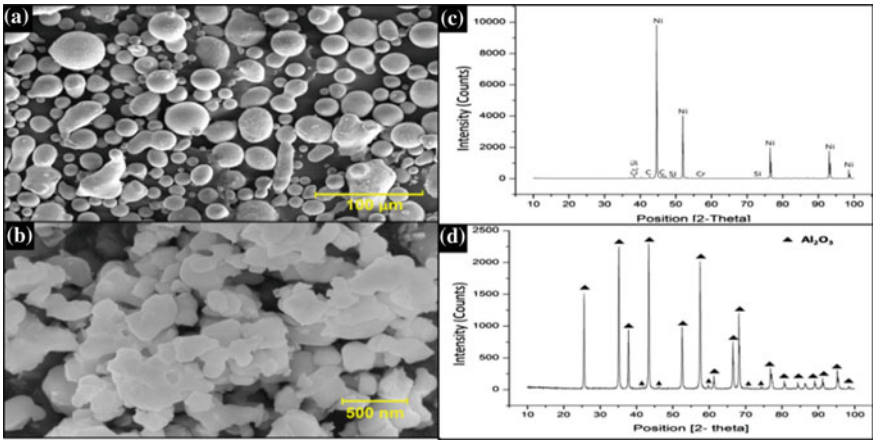

Fig. 48.1 Morphology of raw cladding powder **a** Ni-based powder and **b** nanometric Al_2O_3 powder, XRD spectrum of **c** Ni-based powder and, **d** nanometric Al_2O_3 powder

Table 48.1 Chemical composition of Ni-based powder, Al_2O_3 powder (nanometric) and CA6NM substrate

Material	Elements							
	Fe	Ni	Cr	O	C	Si	Mn	Al
CA6NM substrate	Bal.	3.70	12.5	–	0.05	0.6	0.6	–
Al_2O_3 powder (nanometric)	–	–	–	45.05	–	–	–	54.95
Ni-based powder	–	Bal.	0.17	–	0.2	2.8	–	–

48.2.2 Experimental Setup

The Ni-based + 10 wt% Al_2O_3 nanocomposite clads were developed in multimode domestic microwave applicator (Make: LG, model: MC2886BRUM) using microwave hybrid technique. Microwave hybrid heating technique was utilized considering the skin depth of the Ni-based powder as it was a matrix component in the clad powder (90 wt%). The skin depth of the Ni was found to be 0.12 μm at 2.45 GHz [5]. As the skin depth is less than the average particle size of the powder (44 μm), which eventually results in the reflection of the microwaves at room temperature. Therefore, to raise the temperature of the powder beyond its critical temperature the microwave hybrid heating was used. The critical temperature is a temperature beyond which the target material directly couples with the incident microwave irradiation owing to its increased skin depth. The charcoal powder was used as a susceptor for initial coupling. In order to prevent contamination of the clad powder with the susceptor, a 99% pure alumina sheet with the dimensions of 25 × 25 × 1 mm^3 was placed over the clad powder carefully before spreading the susceptor as shown in the schematic view of the experiment in Fig. 48.2. The exposure time was optimized by trial and error technique in order to achieve the optimized process parameters. The optimized process parameters selected in the present study are 0.9 kW with an exposure time of 700 s.

48.2.3 Characterization of the Nanocomposite Clad

In order to assess the mechanical and metallurgical properties, the microwave processed clad was sectioned along the thickness using low speed diamond saw. The sectioned specimen was polished by emery paper of 320 grit followed by 800, 1000, and 2000 grit and finally with fresh velvet cloth over which 1 μm diamond paste was spread to attain mirror finish.

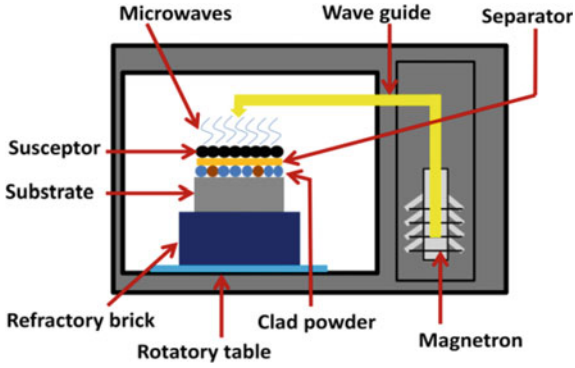

Fig. 48.2 Schematic view of microwave hybrid heating experimental setup

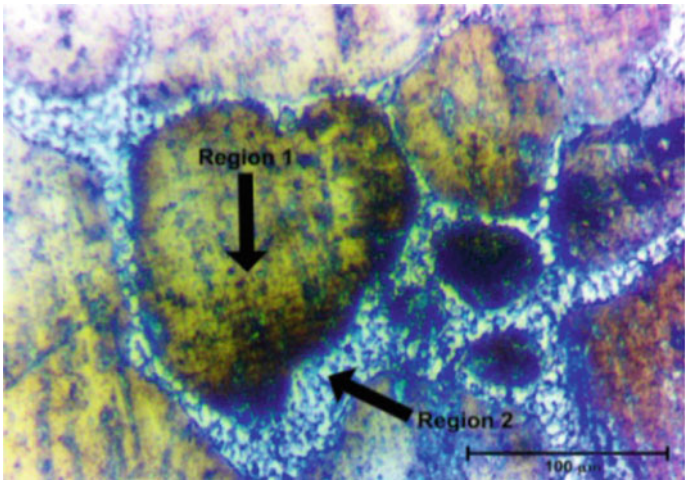

Fig. 48.3 Optical image of the top surface of the clad used to choose the region of interest for the nanoindentation. Region 1 depicts the intermetallic region whereas region 2 depicts the dendritic structure of the nanocomposite clad

A JFEI scanning electron microscope (Model: Nova Nano SEM-450) equipped with EDS was used for microstructural characterization of the clad specimens.

Nano Indentation. The hardness of a material indicates the wear resistance while Young's modulus of the material reflects its ability to deform elastically without fracture. A Berkovich nanoindenter [Hysitron triboindenter (TI950)] was used to evaluate the nanohardness and Young's modulus of the substrate and different regions of the clad layer. Visible light microscope interfaced with triboindenter was used to choose the region of interest for nanoindentation. Optical image of the top surface of the clad is shown in the Fig. 48.3.

48.3 Results and Discussion

48.3.1 Microstructure Analysis

Figure 48.4 shows the SEM micrograph of the clad developed over CA6NM substrate using domestic microwave applicator. A wavy interference separating the substrate and clad region can be clearly seen. The waviness can be attributed to the convective current produced during the process. It is a fact that convective current involves the movement of material thus this can be responsible for the diffusion of the elements between substrate and clad zone. The EDS analysis confirms the diffusion near the interference of the clad-substrate system. Electron dispersive X-ray spectroscopy line mapping shows the distribution of alloying elements throughout the line. The

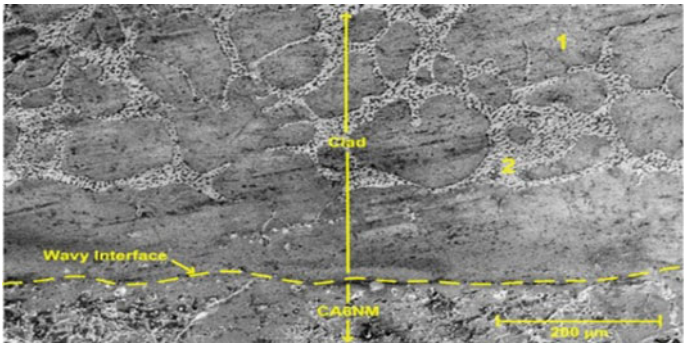

Fig. 48.4 SEM image showing a transverse section of Ni-based + 10% Al_2O_3 nanocomposite clad, substrate and interface

results of the line mapping over the distance of 1180 µm on the clad-substrate system are shown in Fig. 48.5.

It was analyzed that there was a sudden decrease in Ni element near the interference of the system. A constant proportion of Ni in the substrate zone was due to the presence of Ni element in the typical chemical composition of CA6NM steel substrate. It was noted that the decrease was subtle for Fe in the clad zone as the convective current associated with microwave heating allows the movement of Fe element in the clad zone. It can be observed from Fig. 48.5 that Fe diffuses strongly over the distance 40 µm in the clad zone.

The decrease in the proportion of Ni element in the clad zone near the interference can also be attributed to this diffusion. Thus, the bonding between the clad and substrate can be presumed to be metallurgical. Good metallurgical bonding between substrate and clad is signature for an ideal clad. The clad was free from visible interfacial and solidification cracks that will contribute to enhanced slurry erosion resistance during service in case of hydropower applications.

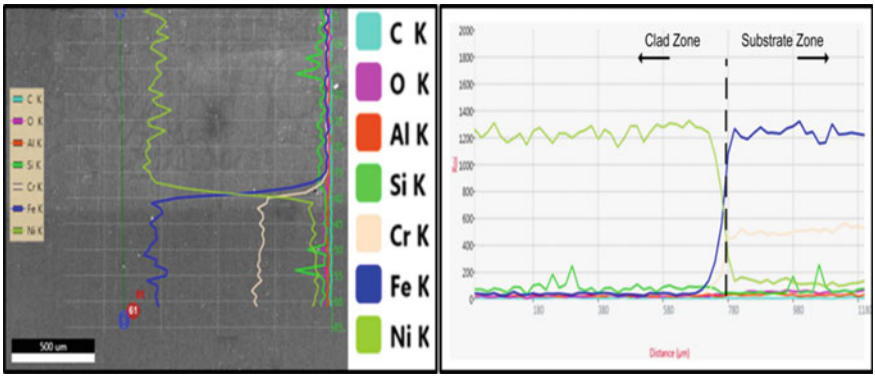

Fig. 48.5 EDS line mapping of developed Ni-based + 10% Al_2O_3 nanocomposite microwave clad

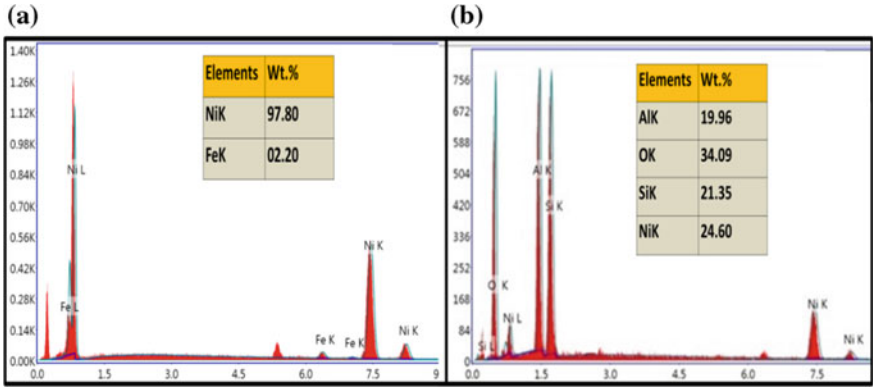

Fig. 48.6 **a** EDS spectrum of **a** clad matrix (point 1) and **b** clad reinforcement (point 2)

Figure 48.6a, b shows the elemental analysis of matrix and dendritic structure which are marked as 1 and 2 in Fig. 48.3. The dark contrast embedded in a brighter contrast matrix shows the composite nature of the clad. The elemental analysis of bright contrast confirms the presence of Al and O precipitates as a result of Al_2O_3 present in the composite clad powder whereas dark contrast was comprised of Ni and Fe that results into the formation of tough metallic matrix.

48.3.2 Nano Hardness

A Hysitron triboindenter (TI950) was used to obtain the load displacement curve and other results which are auto generated using Oliver and Pharr method.

Figure 48.7a shows the resulted load displacement curve obtained for the intermetallic phase, dendritic structure, and substrate during instrumented indentation testing. Table 48.2 shows the distribution of hardness across the intermetallic structure and dendrites structure in the clad zone. The hardness of the substrate was also obtained and presented in Table 48.2. It was found that dendritic structure owns hardness greater than intermetallic phase and substrate. Nanoindentation on microwave clad composites cut down the chances of indenter falling on different phases at once which was more readily observed during microhardness testing. Therefore, the resulted values are more accurate and quite differentiable for different phases. Figure 48.7a illustrate that there was an appreciable decrease in penetration depth for the clad zone. It can be attributed to the increase in nanohardness value of the nanocomposite cladding. In the clad zone, the curve shifting towards left for the dendritic structure indicates the possibility of strengthening and load sharing capability of various hard phases of nano alumina such as AlNi and $AlNi_3$ that were observed in the XRD spectrum of the nanocomposite clad.

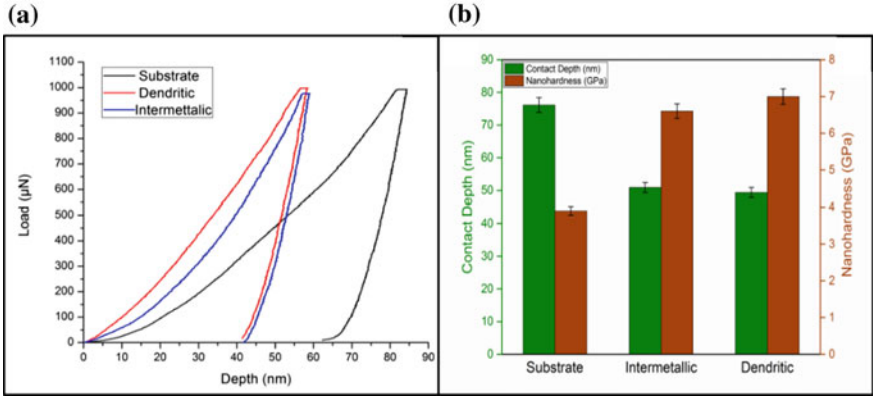

Fig. 48.7 **a** Load versus penetration depth plot obtained from nanoindentation on the substrate and different regions of clad. **b** Contact depth and nanohardness at different locations in the clad layer

Table 48.2 Results obtained from nanoindentation

Selected region	Nanohardness (GPa)	Modulus of Elasticity (GPa)	Contact depth (nm)
Substrate	3.9 ± 0.11	173 ± 5.1	76.17 ± 2.2
Intermetallic	6.6 ± 0.19	215 ± 6.4	50.92 ± 1.5
Dendritic	7.0 ± 0.21	219 ± 6.5	49.40 ± 1.4

The elemental analysis as shown in Fig. 48.7b confirms the presence of alumina elements in the dendritic structure. Results obtained from the load displacement curve represent that dendritic structure shows the least contact depth (49.40 ± 1.4 nm) whereas substrate shows the highest contact depth of 76.17 ± 2.2 nm. The slope of the unloading curve cast the elastic modulus of the material when fitted into the Oliver-Pharr method. The unloading curve consists the elastic recovery of the material, therefore, provides appreciable results of elastic modulus. The maximum elastic modulus that is 219 ± 6.5 GPa was calculated for dendritic region of the clad zone and in contrast, substrate shows the least value of elastic modulus that was found to be 173 ± 5.1 GPa. Elastic modulus is inversely proportional to contact depth therefore as h_c decreases, elastic modulus increases with a successive decrease in the contact area A_c. The difference in contact depth and hardness for substrate and different region of composite clad zone is shown in Fig. 48.7b. Overall results indicate that contact depth of clad zone was significantly less as compared to CA6NM substrate. The reduction in contact depth signifies the increased nanohardness and can be clearly seen in Fig. 48.7b. The dendritic structure possesses highest nanohardness value that is 7.0 ± 0.21 GPa whereas intermetallic region shows the nanohardness value of 6.6 ± 0.19 GPa.

Almost the same results from nanoindentation study of Nickel were reported by Jensen [9]. It has been already indicated by the EDS (Sect. 48.3.1), the intermetallic

region was mainly comprised of Nickel phase. The average nanohardness of the clad was found to be 74% more as compared to the substrate. The nanohardness of substrate was found to be 3.9 ± 0.11 GPa, thus the comparison showed the beneficial effect of depositing the clad over the CA6NM.

48.4 Conclusions

In the present study, Ni-based + 10% Al_2O_3 nanocomposite cladding over CA6NM substrate was successfully carried out using microwave cladding. Cladding was carried out in a domestic microwave applicator operating at 2.45 GHz at 0.9 kW. An optimized exposure time of 700 s was found to be sufficient for developing the nanocomposite clad. The major conclusions drawn from the discussion are as follows:

Clads were free from any type of visible solidification cracks. The microstructure of the clad exhibits dendritic structure reinforced in the intermetallic matrix.

Partial diffusion of elements from the substrate region to clad region and vice versa leads to metallurgical bonding between the substrate and clads.

The average nanohardness of clad was calculated to be 6.8 ± 0.2 GPa which was found to be 74% more than that of the substrate.

The dendritic structure of clad shows highest hardness among the intermetallic phase and substrate which could strengthen the clad.

The Ni-based + 10% Al_2O_3 nanocomposite microwave clads could be used to minimize slurry erosion in CA6NM hydroturbine steel.

Acknowledgements The authors gratefully acknowledge the financial support received from the Science and Engineering Research Board (SERB), Department of Science and Technology (DST), Government of India through project file number ECR/2016/001276.

References

1. Amrei, M.M., Monajati, H., Thibault, D., Verreman, Y., Germain, L., Bocher, P.: Microstructure characterization and hardness distribution of 13Cr4Ni multipass weld metal. Mater. Charact. **111**, 128–136 (2016)
2. Lin, M.C., Chang, L.S., Lin, H.C., Yang, C.H., Lin, K.M.: A study of high-speed slurry erosion of NiCrBSi thermal-sprayed coating. Surf. Coat. Technol. **201**, 3193–3198 (2006)
3. Zhao, H.X., Goto, H., Matsumura, M., Takahashi, T., Yamamoto, M.: Slurry erosion of plasma-sprayed ceramic coatings. Surf. Coat. Technol. **115**, 123–131 (1999)
4. Tucker, R.C., Inc, P.S.T.: Thermal spray coatings. Handbook Surf. Eng. **5**, 1446–1471 (1993)
5. Kaushal, S., Sirohi, V., Gupta, D., Bhowmick, H., Singh, S.: Processing and characterization of composite cladding through microwave heating on martensitic steel. Proc. Inst. Mech. Eng. Part L J. Mater. Des. Appl. **232**, 80–86 (2018)
6. Mondal, A., Upadhyaya, A., Agrawal, D.: Microwave sintering of W-18Cu and W-7Ni3Cu alloys. J. Microw. Power Electromagn. Energy **43**, 11–16 (2009)

7. Zafar, S., Sharma, A.K.: Abrasive and erosive wear behaviour of nanometric WC–12Co microwave clads. Wear **346**, 29–45 (2016)
8. Zafar, S., Sharma, A.K.: Development and characterisations of WC–12Co microwave clad. Mater. Charact. **96**, 241–248 (2014)
9. Jensen, J.A.D., Persson, P.O., Pantleon, K., Odén, M., Hultman, L., Somers, M.A.J.: Electrochemically deposited nickel membranes; process-microstructure-property relationships. Surf. Coat. Technol. **172**, 79–89 (2003)

Chapter 49
Evaluation of Surface Characteristics of PTAW Hardfacing Based on Energy and Powder Supplied

D. D. Deshmukh and V. D. Kalyankar

Abstract Wear, abrasion and erosion-corrosion are the dreadful mechanisms for the equipment and machineries working in the harsh environments. To cope up with these phenomena, various protections techniques are available and commonly employed for oil, gas, petroleum, nuclear, power and marine industries. The selection of appropriate protection technique depends on conditions of working environments and properties or behaviour of material exposed to it. Plasma transferred arc welding is one of the widely used technique for hardfacing by various superficial alloys. During hardfacing by welding the common problem faced by the manufacturer is to control the parameters to obtain smooth and acceptable coatings with no surface defects. Hence, present investigation is focused on the evaluation of surface characteristics of PTAW techniques based on energy and powder supplied per unit track of deposition. In this regard to understand and estimate the causes of surface variations, experiments are performed by varying energy levels and powder supplied then samples are examined by dye penetration test. Effects of energy and powder supplied per unit track on surface characteristics are evaluated. In addition, an attempt is made to study the issues of PTAW hardfacing techniques to understand its applicability based on evaluation of surface characteristics with acceptable processing conditions.

Keywords PTAW · Hardfacing · Stellite · Surface defects

49.1 Introduction

Hardfacing is the process of depositing wear resistance material on the substrate material by application of welding technology [1]. Hardfacing processes are widely applied to improve the substrate surface by depositing the specially designed alloy. High energy density sources compromises rapid heating and successive quenching

D. D. Deshmukh (✉)
Department of Mechanical Engineering, MET's I.O.E, Nashik, India
e-mail: dhirgajanan@gmail.com

V. D. Kalyankar
Department of Mechanical Engineering, S. V. N. I. T., Surat 295007, Gujarat, India

M. S. Shunmugam and M. Kanthababu (eds.), *Advances in Micro and Nano Manufacturing and Surface Engineering*, Lecture Notes on Multidisciplinary Industrial Engineering,
https://doi.org/10.1007/978-981-32-9425-7_49

from the melt, resulting to fine microstructures and good improvement of mechanical and tribological properties [2]. Use of welding techniques can be more suitable due to strong metallurgical bond formed between coating and substrate [3]. Hardfacing improves wear and corrosion resistance of substrate surface exposed to harsh working conditions, thus extending the service life of components [4].

The most commonly used welding techniques for the hardfacing are, submerged arc welding (SAW), tungsten inert gas welding or gas tungsten arc welding (TIG), oxyacetylene gas welding (OAW), plasma transferred arc welding (PTAW) and laser cladding [5, 6]. The applications of these welding processes are commonly observed in petrochemical, chemical, steels, marine, power, oil and aerospace industries [6]. Various researches on the coating characteristics and behaviour of material are going worldwide, to study the applicability and maintainability of these techniques for various kinds of material composition. Failure of the part at the vicinity of weld occurred due to improper welding techniques or defects in weld region such as porosity, blowholes, undercut and irregular heat affected zone (HAZ). Weldment characteristics like penetration, bead geometry, reinforcement, depth of penetration and HAZ which are extremely important characteristics for structural integrity and homogeneity of the joint in case of hardfacing. Superficial layers of the appropriate thickness free of cracks with required mechanical and tribological properties may be obtained by suitable control of the process variables as welding is termed as multi-input multi-output process. Investigation of a hardfacing process is important to know how strongly certain parameters influence low distortion, less porosity and crack free surface. Considering these aspects, it is necessary to understand the process and causes of surface defects. As, defects are the root causes hardfacing to fail because of damage with only a small surface resulted loss of the entire structure. In this regard, the hardfacing by PTAW process is studied with the effects of energy and powder supplied per unit track, which are responsible for the surface defects thereby causing failure of part. In-service modification and improvement of surface conditions of equipment to avoid the failure is core area of investigation. In these respects, the evaluation of surface characteristics PTAW hardfacing techniques is presented in this paper.

49.2 PTAW Hardfacing Technique

The PTAW technique is a derivation of plasma arc welding process. Use of non-consumable tungsten electrode is common in both the process and is located inside the torch. PTAW process uses powder as a filling material and inert gas, which is generally argon for its transportation to the arc area. PTAW technique has quite effectively been used as an outstanding surface deposition technique as a substitute to other thermal spray processes [6, 7] Hardfacing obtained by PTAW shows high quality, competitive wear and corrosion resistance and high retention of properties and characteristics of coating with better microstructure and stability of hardness at high temperature [6]. Also, PTAW hardfacings has a lower production cost and

higher productivity compared to thermal sprayed coatings. PTAW hardfacings are generally thicker than laser-induced hardfacings and there is a strong metallurgical bond between the substrate and coating, improving their impact-resistance [8]. Among the available techniques of hardfacing the most important differences lies in the welding efficiency and weld plate dilution rates. The composition and properties of hardfacing are strongly influenced by dilution obtained. Control of dilution is important in hardfacing process, where typical low dilution is desirable [5]. The dilution obtain is much lesser in PTAW coatings. The PTAW presents high quality, competitive wear-resistance, and high stability of properties at high temperature [6]. The uses probable with PTAW are hardfacing and cladding to protect against severe conditions in service life like heat, abrasion, corrosion, erosion, adhesive and abrasive wear etc. It is also used to repair of worn out parts or build-up of miss-machined parts. Recently, PTAW technique has gain tremendous attraction for deposition of superior alloys on the substrate material to impart wear and corrosion resistance thus improves the service conditions of equipment. Superior alloying materials always imparted the surface modification; Co and Ni based alloys are applied in numerous industries, including chemical and fertilizer plants, nuclear and steam power plants, pressure vessel, as it is convenient and practical. In this regard, the process of hardfacing is studied with the effect of process parameters, which are responsible for the producing tough and harder coating without any defects. Looking towards the literature on PTAW it is observed that several studies reported the investigations on PTAW. Bharath et al. [7] studied the effect of PTAW process parameters on the microstructure of Stellite F coating, where deposits are prepared on valves made of martensitic steel. Balasubrarnanian et al. [5] applied response surface methodology to predict and optimize the % dilution of iron-based hardfacing produced by the PTAW. Five process parameters were studied in their research and process is optimized by considering the effects on % dilution obtained in coating. Oxidation behavior of Ni-based coatings was investigated by Fernandes et al. [9] by PTAW on gray cast iron. TiC powder deposition and in situ mechanism on grey cast iron was studied by Gallo et al. [10] by PTAW hardfacing for enhanced wear resistance. Guoqing et al. [11] investigated the microstructure and tribological characteristics of Ni50 alloy powders coating deposited on AISI 304L stainless steel surface by using the PTAW process. Corujeira Deng et al. [8] investigate the influence of welding technique and temperature on fatigue properties of heat-resistant steel with hardfacing coatings. The PTAW and the OAW were employed.

49.3 Experimentations

To carry out the investigations, fully automated PTAW machine is utilized. This technique has been in use for the hardfacing of parts i.e. valve seat, collars, sleeve and couplings, employed for the pressure vessels, piping and valve components. Deposition is prepared on the surface of plate of thickness 16 mm in the form of multitrack layers by varying the process parameters. The electrode negative (DCEN)

according to the welding process specification (WPS) ASME21, with position of groove 1G. Tungsten electrode size of 4 mm diameter (2% Throated Tungsten), torch orifice diameter 25 mm, industrially pure argon (99.99%) is used at a constant flow rate of 15 L/min for shielding, 2.5 L/min for centre, and 3 L/min for powder feeding. The process parameters selected for the experimentations are, heat producing element i.e. transferred arc current (A), and filler material flow rate i.e. powder feed rate (gms/min). The effects of these process parameters with defects obtained are observed and examined by visual inspections and dye penetration test. Substrate material and hardfacing alloy used for the experimentation is explained in following subsection.

49.3.1 Hardfacing Alloy

The Cobalt based alloys are widely employed as wear-resistant hardfacing materials for combating wear in corrosive mediums and find applications in marine, gas, oil, petrochemicals, power, chemical, medical and food processing industries. Stellite alloy has nominal composition of Co—28 Cr—4 W—1.1C (wt%). Stellite alloys which are commonly used as hardfacing materials in a variety of industrial applications, as they are known to possess high hardness at high temperature, good resistance to sliding wear under elevated contact pressure and good corrosion resistance. Co–Cr alloy which is resistant to wear and corrosion and retains these properties at high temperatures [12]. Co–Cr alloy is a useful hardfacing alloy in which chromium provides corrosion resistance while carbides add strength to the alloy. From the literature it is found that Co–Cr alloy has excellent resistance to cavitation and corrosion, outstanding self-mating, anti-galling characteristics and it is used in valve, valve seats, plugs, pumps, bearings, shafts, erosion shields, rotors, etc. Considering the applicability of these materials (SS 316L and stellite 6) in various industrial applications these material is selected for the present investigations.

49.4 Result and Discussion

The prominent effect of energy and powder supplied per unit track on surface characteristics is observed in the investigations. The effect of these two principle parameters of hardcoding process is illustrated in next subsection under the effects of energy supplied and powder supplied per unit track of deposition.

49.4.1 Effects of Energy Supplied Per Unit Track of Deposition

During the process, heat energy supplied per unit track of deposition managed by the transferred arc current. The heat energy is responsible for melting the powder supplied and substrate material thereby forming a bond between weld pool and substrate. The effect of heat energy supplied can be observed prominently by track width and reinforcement. Following major inferences are drawn based on evaluation of deposited surface at varying energy supplied per unit track.

(1) When the heat supplied per unit length of track is excessive, (Which is the function of arc current, travel speed and powder feed rate) a rapid melting of powder supplied was observed where the width of deposit widens. On the other side, very narrow width of deposition is observed when the heat energy supplied per unit track is less.
(2) Insufficient arc current (Less than 100 A) leads to less amount of heat energy supplied to powder and substrate material. Which results incomplete melting of powder and base material, which results less bonding. It is also observed that transferred arc current less than 100 A results the incomplete melting of powders and lack of penetration on the substrate surface.
(3) In contrast, maximum arc current (Greater than 180 A) leads to more amount of energy supplied to the powder and substrate material. Which results complete melting of powder supplied and maximum penetration with strong bond possibly maximum dilution of coatings. It is also noticed that for the transferred arc current greater than 180 A, the undercut and spatter are noticed on the weld bead surface.
(4) The undercuts and spatter on the surface is attributed due to the fact that heat energy supplied for producing arc at constrictor nozzle increases as transferred arc current. With increasing current melting of substrate material increases leading to complete fusion of powder supplied at that instant with substrate surface causing higher deposition and undercuts. Consequently, at lower current, heat energy supplied is less causing incomplete melting of powder and less bonding with overlaid material this kind of surface characteristics is shown in Fig. 49.1.
(5) It is also identified that, the interaction time for forming the weld pool with substrate is also playing a vital role for the deposition. More interaction time resulted more amount of heat supplied at instant causing maximum melting of powder supplied. The interaction time can be control by travel speed of the work piece. Minimum travel speed leads to maximum concentration of heat energy to substrate and as a result, maximum melting of powder is observed before intersecting with the melt pool. In contrast, at maximum travel speed, powder supplied by nozzle interacted briefly with the available heat energy at that instant. However, maximum arc current is available at that instant, uneven and irregular weld bead was observed on the surface as shown in Fig. 49.2. This is because maximum current conditions contribute maximum melting of powder supplied, but higher travel speed reduces the interaction time between substrate

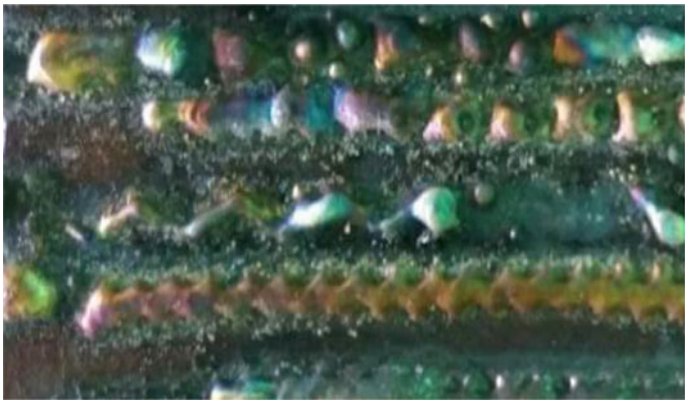

Fig. 49.1 Deposition characteristics with lower energy supplied per unit deposition (less current/lower energy)

Fig. 49.2 Deposition with irregular weld bead (lower energy and lower powder supplied per unit track)

and powder supplied for formation of weld pool. In this case nearly solid form of powder entered in melt pool and melt zone resulting in the collision of the powder particles with substrate material at the weld pool interface.

In addition to track characteristics, the prominent effects of heat supplied on dilution, penetration, deposition characteristics etc. observed in literature. This is attributed due to fact that with the increase in transferred arc current, the heat energy supplied at arc region increases which causes more melting of substrate material consequently % dilution in the coating increases. Darut et al. [13] noticed that increase in heat energy increases deposition rate, which leads to form porosity in the coatings,

which is significantly higher with higher arc current. Fernandes et al. [9] investigated the effect of arc current on oxidation behavior of coating. It was observed that coating produced with lower arc current exhibited more effective oxidation resistance than that produced with higher current furthermore; increasing the arc current, the oxidation resistance of coatings decreases. Buytoz et al. [14] investigated the effect of current on microhardness and it was found that the microhardness of the coating increases as a function of current. Celik [15] studied the effects current on the microstructure and wear properties, it was evaluated that increase in coating thickness with arc current. However, higher current resulted the lower hardness of coating that reduces the wear resistance correspondingly due to extended solubility of gases due to which porosity increases in of the overlay at higher current. Reinaldo and D'Oliveira [16] investigated that lower arc current and lower travel speed resulted hard coating with reduced mass loss. Ozel et al. [17] found that thickness of coating increases with current density. Katsich and Badisch [18] found that increasing current reduces the percentage of carbide area fraction thus higher wear rate was observed at higher current processed coating. Mandal et al. [19] reported that increase as current rises the plasma power as well as the energy density of the plasma beam rises that leads to maximum substrate surface melting. Consequently, the deposition width increases with the increase in current and subsequently dilution rate increases.

49.4.2 Effects of Powder Supplied Per Unit Track of Deposition

For deposition of coating, rate of powder supplied per unit track also plays an important role. The powder flow rate should be sufficient to form a complete molten pool and strong bond with substrate material. During the investigation the effects of powder flow rate are observed on surface characteristics, which are summarized as,

(1) Lower volume of powder supplied (less than 8 gms/min) leads to over melting of substrate material and results maximum % dilution in the coating. In contrast maximum volume of powder feed rate reduces the deposition efficiency by reducing the % melting of powder. Hence, powder supplied should be appropriate and should be supplied with reference to available energy at instant.
(2) It is observed that, if the powder flow rate was lower than 08 gms/min, over melting of base metal and overheating of tungsten electrode was noticed. This is attributed due to the reason that at lower powder flow rate, maximum heat energy is concentrates on the substrate material, which leads to undercut on the surface.
(3) Maximum powder flow rate (more than 20 gms/min) reduces the chances of undercuts on the substrate materials but contributes to deficiency in melting of powder supplied. This is attributed due to the reason that at maximum powder feed rate, minimum heat energy is concentrates on the substrate material and leads to incomplete bonding and melting.

(4) When the powder feed rate is more than 20 gms/min, the width and reinforcement of deposition increases. Also the weld bead formation was not smooth owing to incomplete melting of powders. Because, the amount of heat energy supplied at that instant is being utilised for melting of powder and forming a molten pool with possibly less melting of substrate material. This results less melting of substrate material, provided that the current supplied is sufficient to melt the powder supplied at that instant.

(5) Very thin layer of deposited surface is observed corresponding to lower powder feed rate (8 gms/min) and at lower current (100 A). This is attributed because at lower powder feed rate and lower arc current, heat energy supplied at instance decreases. When the powder feed rate is maximum with sufficient arc current wider bead width and smaller reinforcement height is observed. There was an over deposition of weld metal and higher reinforcement height was observed. At maximum heat energy and at maximum powder supplied.

(6) For lower powder feed rate and lower current, bead appearance and contours were not so smooth and very narrow bead was obtained as shown in Fig. 49.3. It is observed that, percentage melting of substrate decreases as arc current decreases giving less concentration at particular point on substrate surface. It is also observed that, there is variation in deposition parameters with the powder feed rate and it is identified that cross-section area of deposition rises with the increase in powder feed rate and due to this melting of substrate material decreases. Lower powder feed rate and higher current produces spatter and undercut on the surface with uneven layer of deposition. Whereas, higher powder feed rate and lower current reduces the melting of substrate material and resulted less bonding in the deposited layer.

(7) Time availability for deposition also plays a vital role, which correspond to relative displacement of material surface per unit time to the torch or arc current. Lower time availability produces very thin layer with zigzag pattern. In addition,

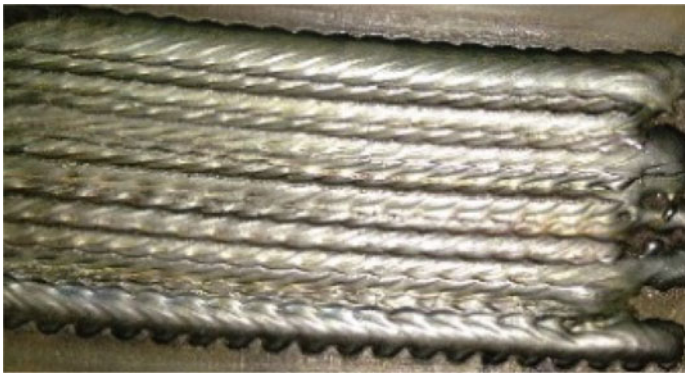

Fig. 49.3 Deposition showing narrow weld bead tracks (lower powder)

Fig. 49.4 Deposition showing spatter (lower energy, higher speed and higher powder feed rate)

less bonding and incomplete penetration is observed on the overlaid surface. Which resulted in spatter and cut-off of deposition as shown in Fig. 49.4.

In addition to track characteristics prominent effects of powder flow rate on dilution, penetration, deposition characteristics etc. were observed in literature. Balasubrarnanian et al. [5] investigated that, the % dilution of substrate decreases with when powder flow rate increases. It was noticed that, medium level of powder gas flow rate resulted the defect free coatings [7]. Mandal et al. [19] observed the variation of deposition parameters with the powder feed rate and it was identified that the variation in deposition width is much less as compared to the variation of deposition height. Moreover, cross-section area of deposition rises with the increase in powder feed rate, due to these factors the dilution decreases rapidly with the increase in powder feed rate. Variations in weld hardfacing contact angle and aspect ratio with processing parameters are also noticed in the present investigations. However, as far as track continuity is concerns, intermediate transferred arc current (100–140 A), and powder flow rate (10–14 gms/min) shows superior track geometry as shown in Fig. 49.5. Although for wear, abrasion and corrosion resistance offered by the materials to severe working conditions, the required qualification procedures for hardfacing suggest low % dilution level however, it should be enough to hold the overlaid material in working condition. Hence, considering the workability of overlaid surface it is prime requirement to have minimum weld hardfacing dilution but it should not leave the coating surface during working (if less than 1%). Control of dilution obtained is not major concern in PTAW hardfacing but getting optimum setting is of prior requirement to have maximum compositional material of superficial alloy in the coating. Thus, when subsequent hardfacing is required by multi-tracking, lower dilution and high contact angle both leads to increase the chances of producing lack of fusion type defects at the weld fusion zone (Fig. 49.6).

Fig. 49.5 Deposition showing smooth overlapping tracks (appropriate energy and powder)

Fig. 49.6 Deposition showing crack overlay (blowholes and gap due to insufficient energy and maximum powder feed rate)

49.5 Conclusions

Failure of components due to surface defects is main focusing issue for the various industrial equipment's such as, power, marine, oil and chemical industry. The cost of failure of equipment is not only related to failure of specific parts but it leads to decrease the productivity of plant also in many cases it leads to hazardous action. To avoid the hazards due to failure of parts it is necessary to investigate the possible failure mechanism and to concentrate the root cause of process. Hardfacing processes

are widely used for improvement in wear, tribocorrosion and mechanical properties of substrate surfaces, which are exposed to severe environmental condition. Uses of appropriate levels of hardfacing parameters are of prior importance to achieve desired properties of surface. In this investigation, an attempt is made to evaluate and investigate the causes of surface defects. Prominent effects of heat supplied and powder flow rate on melting of substrate materials is found in the investigations it is observed that hardfaced surface is greatly affected by influence of energy and powder supplied per unit track of deposition. By proper controlling the input process parameters and systematic investigations, causes of surface defects can be eliminated and smooth overlaid surface can be obtained.

References

1. Deshmukh, D., Kalyankar, V.: Recent status of overlay by plasma transferred arc welding technique. Int. J. Mater. Prod. Technol. **56**, 23–83 (2018)
2. Bourithis, E., Tazedakis, A., Papadimitriou, G.: A study on the surface treatment of "Calmax" tool steel by a plasma transferred arc (PTA) process. J. Mater. Process. Technol. **128**, 169–177 (2002)
3. Aghasibeig, M., Fredriksson, H.: Laser cladding of a featureless iron-based alloy. Surf. Coat. Technol. **209**, 32–37 (2012)
4. Shen, Z., Chen, Y., Haghshenas, M., et al.: Interfacial microstructure and properties of copper clad steel produced using friction stir welding versus gas metal arc welding. Mater. Charact. **104**, 1–9 (2015)
5. Balasubramanian, V., Lakshminarayanan, A., Varahamoorthy, R., Babu, S.: Application of response surface methodolody to prediction of dilution in plasma transferred arc hardfacing of stainless steel on carbon steel. J. Iron. Steel Res. Int. **16**, 44–53 (2009)
6. Deng, H., Shi, H., Tsuruoka, S.: Influence of coating thickness and temperature on mechanical properties of steel deposited with co-based alloy hardfacing coating. Surf. Coat. Technol. **204**, 3927–3934 (2010)
7. Bharath, R., Ramanathan, R., Sundararajan, B., Srinivasan, P.: Optimization of process parameters for deposition of stellite on X45CrSi93 steel by plasma transferred arc technique. Mater. Des. **29**, 1725–1731 (2008)
8. Deng, H., Shi, H., Tsuruoka, S., et al.: Influence of welding technique and temperature on fatigue properties of steel deposited with Co-based alloy hardfacing coating. Int. J. Fatigue **35**, 63–70 (2012)
9. Fernandes, F., Cavaleiro, A., Loureiro, A.: Oxidation behavior of Ni-based coatings deposited by PTA on gray cast iron. Surf. Coat. Technol. **207**, 196–203 (2012)
10. Corujeira Gallo, S., Alam, N., O'Donnell, R.: In situ synthesis of TiC–Fe composite overlays from low cost TiO_2 precursors using plasma transferred arc deposition. J. Therm. Spray Technol. **23**, 551–556 (2013)
11. Guoqing, C., Xuesong, F., Yanhui, W., et al.: Microstructure and wear properties of nickel-based surfacing deposited by plasma transferred arc welding. Surf. Coat. Technol. **228**, S276–S282 (2013)
12. Deshmukh, D., Kalyankar, V.: Deposition characteristics of multitrack overlay by plasma transferred arc welding on SS 316L with Co–Cr based alloy–influence of process parameters. High Temp. Mater. Process. (2018)
13. Darut, G., Liao, H., Coddet, C., Bordes, J., Diaby, M.: Steel coating application for engine block bores by plasma transferred wire arc spraying process. Surf. Coat. Technol. **268**, 115–122 (2015)

14. Buytoz, S., Orhan, A., Gur, A., Caligulu, U.: Microstructural development of Fe–Cr–C and B_4C powder alloy coating on stainless steel by plasma-transferred arc weld surfacing. Arab. J. Sci. Eng. **38**, 2197–2204 (2013)
15. Celik, O.: Microstructure and wear properties of WC particle reinforced composite coating on Ti6Al4V alloy produced by the plasma transferred arc method. Appl. Surf. Sci. **274**, 334–340 (2013)
16. Reinaldo, P., D'Oliveira, A.S.C.M.: NiCrSiB coatings deposited by plasma transferred arc on different steel substrates. J. Mater. Eng. Perform. **22**(2), 590–597 (2012)
17. Ozel, S., Kurt, B., Somunkiran, I., Orhan, N.: Microstructural characteristic of NiTi coating on stainless steel by plasma transferred arc process. Surf. Coat. Technol. **202**(15), 3633–3637 (2008)
18. Katsich, C., Badisch, E.: Effect of carbide degradation in a Ni-based hardfacing under abrasive and combined impact/abrasive conditions. Surf. Coat. Technol. **206**(6), 1062–1068 (2011)
19. Mandal, S., Kumar, S., Bhargava, P., Premsingh, C., Paul, C., Kukreja, L.: An experimental investigation and analysis of PTAW process. Mater. Manuf. Processes **30**(9), 1131–1137 (2014)

Chapter 50
Electroless Nickel–Phosphorus Plating on SS304 Substrate with Al_2O_3 and WS_2 Powder Suspended in Electrolytic Solution

Divit Saini, D. Taye, S. Mohanty, H. Bishwakarma, A. K. Das and N. K. Singh

Abstract An attempt has been made in this paper to study the synthesis of Ni–Al_2O_3–WS_2 coating on SS304 substrate with different levels of electroless coating process parameters. The electroless bath constitutes Nickel sulphate, Tri-sodium citrate, Sodium hypophosphite and Ammonium chloride (diluted in 1 litre of deionized water). The substrate with nickel plating showed microhardness value of 221.4 HV that was more than that of the base metal (113 HV). On addition of Al_2O_3 and WS_2 powders in the electroless bath solution, the microhardness value varied between 277.71 HV to 792.79 HV. The coating thickness increased from 10.2625 to 27.9482 μm with the addition of powders in the bath. The energy dispersive spectroscopy (EDS) and X-ray diffraction (XRD) analysis results confirmed the transfer of bath elements to the substrate surface.

Keywords Electroless plating · Microhardness · Coating thickness · Microstructure

50.1 Introduction

Electroless nickel plating is an autocatalytic chemical technique and a dignified way of coating by controlling the operating temperature and pH of the bath. Depositing layers of coating can intensify the performance of engineering components over their surface. Certain properties like wear resistance, microhardness, corrosion resistance, lubricity, etc. can be achieved by the deposition methods. The different coating methods used are electroplating, electroless coating, chemical vapour deposition (CVD) [1], etc. PVD and CVD are expensive as compared to electroplating and electroless coating process. Thus, electroplating methods are widely used these days. It is a method of deposition of metal onto the substrate surface by using electric current

D. Saini (✉) · D. Taye · S. Mohanty · H. Bishwakarma · A. K. Das · N. K. Singh
Department of Mechanical Engineering, Indian Institute of Technology (ISM) Dhanbad, Dhanbad 826004, India
e-mail: divit.saini@gmail.com

M. S. Shunmugam and M. Kanthababu (eds.), *Advances in Micro and Nano Manufacturing and Surface Engineering*, Lecture Notes on Multidisciplinary Industrial Engineering,
https://doi.org/10.1007/978-981-32-9425-7_50

that dissolves metal cations in order to form a thin metal plating on the substrate surface. The thickness of the electroplated component depends upon the current density and hence non-uniform deposition takes place. To this aspect, electroless plating avoids current source, cuts down the production costs, enables high deposition rate and uniform coating thickness [2]. Nickel Phosphorus electroless coating method is one such technique that finds wide application in machinery, electronics, automobiles, valves and aerospace industries due to its uniform coating and enhancement of excellent properties such as microhardness, wear resistance and frictional behaviour, corrosion resistance, low coefficient of friction, high reflectivity, etc. [3].

50.2 Literature Review

A lot of research work has been reported towards electroless plating of which few have been elaborated in this section. Krishnan et al. [4] studied electroless Ni–P plating and analyzed the overall features of its deposition, application and its advantages over other processes. This paper discusses different electroless nickel alloying, electroless bath techniques, characterization, nanoparticles plating, depositing mechanism and their significance, including short notes on difficult substrates. Li et al. [5] investigated electroless Ni–P plating procedure over Al matrix composite as its substrate to enhance the external substrate textures. Ni–P plating is deposited over the activated surface. Nickel and hypophosphite ion concentrations along with the rate of deposition were measured. Dong et al. [6] examined the effect of SiO_2 on electroless deposition on substrate. SiO_2 was heat-treated for 1 h at various temperatures to explore the wear resistance of Ni–P–SiO_2 composite plating. This process led to a significant improvement in the wear resistance and microhardness. It was observed that heat treatment at 380 °C led to structural changes due to reinforcing of SiO_2 nanoparticles. Shibli et al. [7] describe the use of nano zinc oxide particles for surface coatings, which result in surface uniformity and homogeneity of coated surface. Desirable results also included an improvement in microhardness and corrosion characteristics of the nanocomposite coatings.

Yang et al. [8] developed a novel technique to produce nanoparticle-reinforced metal plating. They incorporated ZrO_2 nanoparticle to Ni–P matrix by adding ZrO_2 sol to electroless plating bath. This increased microhardness of 1045 HV and wear resistance properties. Khalifa et al. [9] observed the behaviour of Ni–Sn–P/TiO_2 nanocomposite plating that is done by electroless plating technique on low carbon steel mainly. Incorporation of TiO_2 and $SnCl_2$ particles confirmed that a crystalline component could be implanted into the amorphous Nickel–Phosphorous matrix during the deposition. The study reported that addition of TiO_2 in coating significantly changed the surface morphology and increased the corrosion resistance. Zou et al. [10] performed an alteration of SiC nanoparticles through electroless nickel plating. A coating of nanoscale agglomerative nickel layer was observed by XRD, TEM and XPS. The dawn of improvement was debated and described through experimental aspects. Gu et al. [11] studied the acid pickling rate effect through electroless

Ni–P plating procedure over the alloy substrate of AZ91D. To analyze the morphology and nucleation mechanism of settled particles over the substrate SEM and XRD were used. Acid pickling time is directly proportional to the rate of deposition. First, the deposits were nucleated at β-$Mg_{17}Al_{12}$ stage and further expanded to eutectic and primary α stages of the substrate. Sivandipoor et al. [12] described that WS_2 particles, which have solid lubricant properties, were used in electroless plating of Nickel–Phosphorous to fabricate new plating with enhanced tribological behaviour. Plating degradation was carried out by heat treatment at 400 °C. In the pre-treatment, the stainless steel surface was polished to obtain even surface. After that, surface activation was carried out by acid cleaning, degreasing and preparation of WS_2 nanopowder before adding to the substrate for the electroless bath solution [13]. Liu et al. [14] examined the electroless nickel plating over magnesium and their alloys. The rate of deposition, chemical composition and microstructure of the electroless nickel coatings were evaluated. Surface roughness is significantly increased by the pretreatment of substrate chemically before being dipped into electroless bath plating solution. SEM was used to investigate the fabrications of nickel plating formed on the substrates. The critical load of AZ31 alloy reached about 14 N, i.e. the adhesion strength of the plating on magnesium alloys was higher than that on pure magnesium.

The literature suggests some electroless plating methods, yet little has been explored with the use of nanopowder suspension in the electroless bath. Thus, the present study throws light on the use of Al_2O_3 and WS_2 nanopowders suspended in Ni–P bath such that deposition is done on SS304 substrate for further industrial applications.

50.3 Methodology

50.3.1 Materials Used

The experiments were carried out on SS304 substrate with dimension 10 mm × 10 mm and thickness of 2 mm. The percentage composition and properties of the substrate are shown in Tables 50.1 and 50.2 respectively. It possesses certain distinct properties like corrosion resistance, good draw ability, versatility, better toughness even at very low temperature, etc., owing to which it is used as the substrate material.

Table 50.1 Composition of SS304 substrate

Steel grade	N	S	P	Si	Mn	C	Ni	Cr
304	0.1	0.03	0.045	0.75	2	0.08	8	18

Table 50.2 Mechanical properties of SS304 substrate

SS304		
	Typical	Minimum
Tensile strength (MPa)	600	515
Proof strength	310	205
Elongation	60	40
Hardness (Brinell)	170	–
Endurance limit	240	–

50.3.2 Experimental Set-Up

The experiments were carried out on a magnetic stirrer (Model: MC 03, Make: Tarsons Digital, India) with certain temperature variations. The constructed set-up is shown in Fig. 50.1. The set-up comprises of a magnetic stirrer with hot plate controlled manually. The temperature sensor records the temperature generated within the plating dip. The samples are held by the stand attached over the borosil beaker constituting the plating dip. The steps involved in the experimentation process are shown in the flow chart in Fig. 50.2.

Kemiclean SS is a soak cleaner designed for the removal of heavy oil and soil from steel. The operating condition is 70–80 °C for duration of 2–5 min with a concentration of 40 g/L of solution. The acid activator M1 is used for superior adhesion of the plating with the substrate thereby eliminating peeling off rejections. The nanoparticles used were Aluminium oxide (Al_2O_3) and Tungsten disulfide (WS_2). Increasing the phosphorous content can increase the corrosion resistance of the Ni–P coatings. The improvement in the tribological properties of the component can further be achieved by inclusion of micro/nanoparticles to the surface. These nanoparticles further increase the properties of the substrate surface (hardness, friction and wear resistance). Reducing agent supplies electrons to reduce metal ions in the bath composition. The reducing agent used in the bath is usually a hypophosphite compound

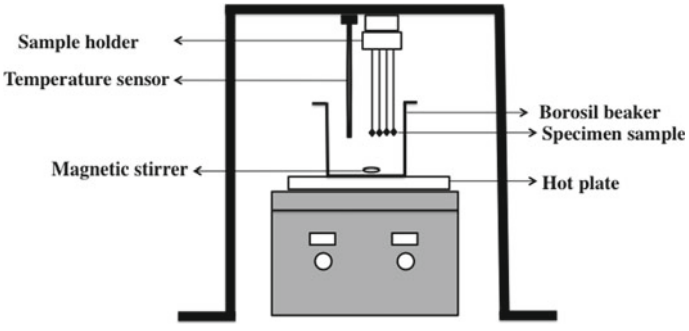

Fig. 50.1 Set-up arrangement of electroless plating

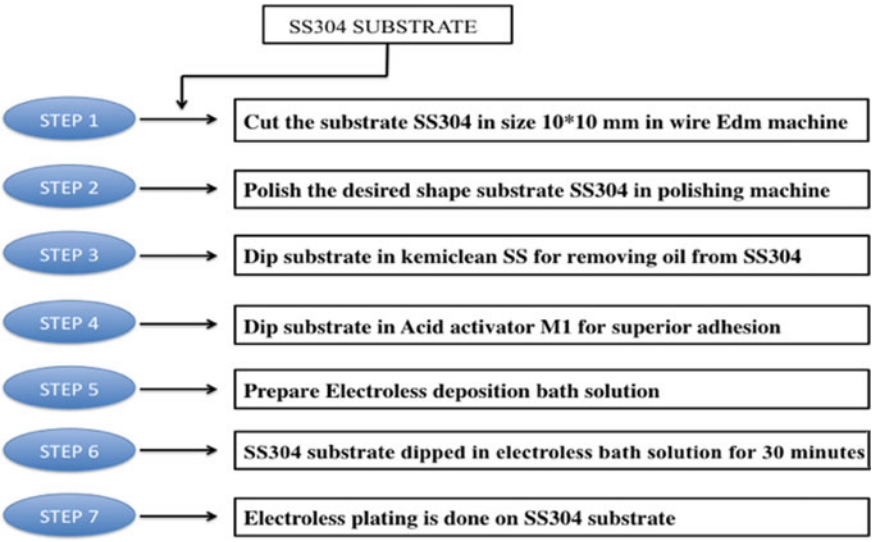

Fig. 50.2 Flow chart of electroless plating process of SS304

such as hydro-phosphorous acid or a bath soluble salt such as sodium hypophosphite, potassium hypophosphite and ammonium hypophosphite. Complexing agent such carboxylic acids, polyamines or sulfonic acids or mixture are also used such as carboxylic acids are mono-, di-, tri- and tetra-carboxylic acids or acetic acid is used because it acts as a buffering agent. It is used to prevent excess of free metal ion concentration. Stabilizing agents are added to prevent the bath from decomposition/breakdown of solution. The coating bath composition with constant and variable process parameters is given in Tables 50.3 and 50.4 respectively.

Table 50.3 Constant experimental parameters

Coating bath composition	Concentration (g L^{-1})
1. Nickel sulphate	40
2. Sodium hypophosphite	20
3. Tri-sodium citrate	25
4. Ammonium chloride	50
5. Bath temperature	(75–80) °C
6. Bath pH	4–4.8
7. Substrate immersion time	30 min

Table 50.4 Variable process parameters for electroless plating

Variable parameter	Description
Al_2O_3	(2, 3, 4) g/L
WS_2	(0.4, 0.8, 1.2) g/L

50.4 Result and Discussions

The microhardness and coating thickness are evaluated and recorded in Table 50.5. Various plots are drawn to determine the effect of the different powder concentration on response parameters.

50.4.1 Microhardness

Microhardness is determined for each of the coated specimens by using Vickers micro-hardness tester machine at a load of 0.1 kgf with dwell time of 10 seconds. The microhardness for the coated specimen (for different compositions of Al_2O_3 and WS_2 particle suspension in electrolytic bath) varied between 277.71 HV and 792.79 HV. An increase in microhardness denotes the presence of Al_2O_3 and tungsten carbide (WC) on the coated specimen surface that is responsible for the property variation. Figure 50.3 shows the effect of WS_2 powder concentration in electroless plating bath on microhardness at different Al_2O_3 concentrations. It is seen that with increase in Al_2O_3 concentration, the microhardness increases.

Table 50.5 Observation table for electroless plating of SS304

S. No.	Composition		Microhardness (HV)
1	$Al_2O_3 = 0$ g/L	$WS_2 = 0$ g/L	221.42
2	$Al_2O_3 = 2$ g/L	$WS_2 = 0.4$ g/L	277.71
3		$WS_2 = 0.8$ g/L	330.61
4		$WS_2 = 1.2$ g/L	405.15
5	$Al_2O_3 = 3$ g/L	$WS_2 = 0.4$ g/L	417.03
6		$WS_2 = 0.8$ g/L	479.65
7		$WS_2 = 1.2$ g/L	621.27
8	$Al_2O_3 = 4$ g/L	$WS_2 = 0.4$ g/L	552.74
9		$WS_2 = 0.8$ g/L	650.72
10		$WS_2 = 1.2$ g/L	792.79

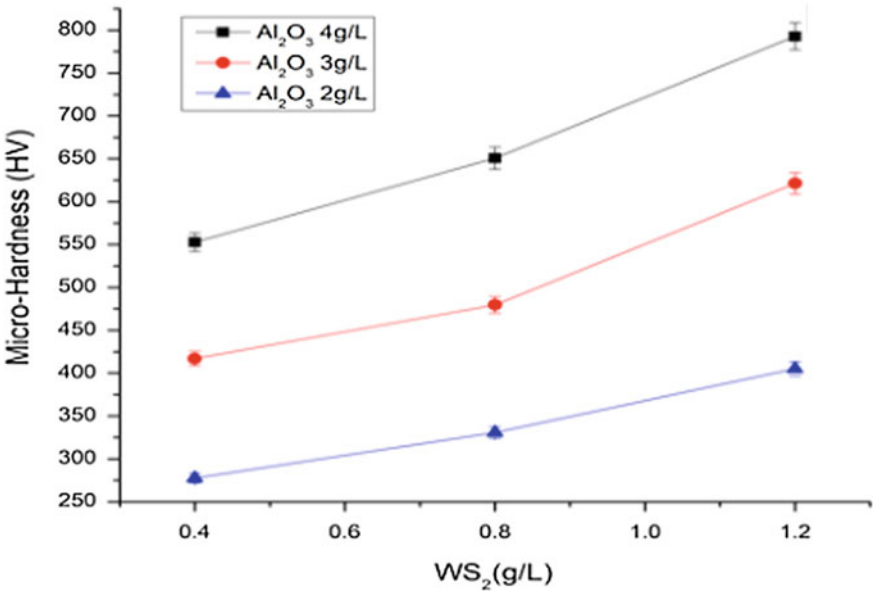

Fig. 50.3 Effect of Al_2O_3 and WS_2 powder concentration on microhardness

50.4.2 Coating Thickness

The transverse surface of a coated substrate is taken into account for the measurement of coating thickness by field emission scanning electron microscope (FESEM) images. Figure 50.4a–d shows the coating thickness of plating surface with different powder concentrations. The coating thickness increases with the addition of nanoparticles to the bath as shown in Fig. 50.5. Moreover, as the concentration of nanoparticles increases, i.e. Al_2O_3 and WS_2, the coating thickness further increases. It may be due to the fact that more agglomeration of particles takes place over the substrate material. Since tungsten disulphide is a solid lubricant, therefore, an increase in its content results in more deposition over the surface. A coating thickness of 27.9482 μm is obtained at 4 g/L with the incorporation of Al_2O_3 and 1.2 g/L of WS_2 in electroless bath with all the parameters of bath being same. Thus higher concentration of both the powders results in an increased value of coating thickness.

50.4.3 EDS Study

The energy dispersive spectroscopy (EDS) report suggests the elemental composition of the substrate surface after coating by electroless plating (Fig. 50.6). It is evident that nickel (Ni) composition is 79.52% in case of sample coated without

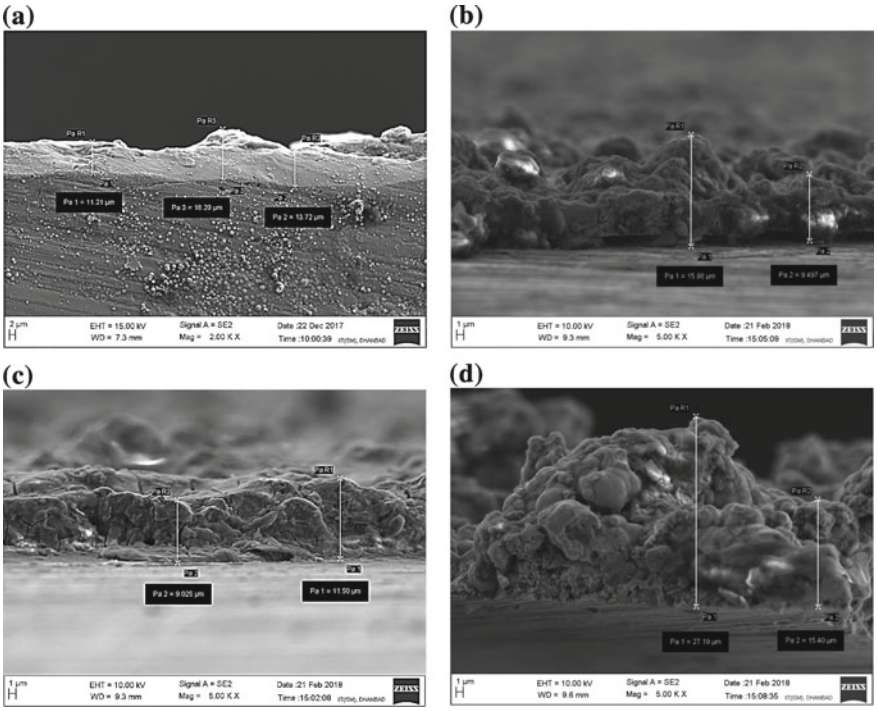

Fig. 50.4 FESEM images of the transverse section of coated surface, **a** without nanopowder concentration, with **b** $Al_2O_3 = 2$ g/L and $WS_2 = 0.4$ g/L, **c** $Al_2O_3 = 3$ g/L and $WS_2 = 0.8$ g/L, **d** $Al_2O_3 = 4$ g/L and $WS_2 = 1.2$ g/L

the addition of nanopowders whereas when the concentration of WS_2 increases, the nickel concentration is as high as 82.36%. The transfer of elements from the bath has also been seen such as phosphorus (P), sodium (Na), aluminium (Al), chromium (Cr), sulphur (S), carbon (C), oxygen (O), and the base material constituting iron (Fe).

50.4.4 Surface Morphology

The surface of the electroless Ni–P coated specimen was studied by field emission scanning electron microscopy (FESEM) machine (Make: Carl Zeiss, Germany, model: Supra 55). Figure 50.7 indicates the FESEM images of coated specimen at various concentrations of powder in the bath. It is seen that when the WS2 powder concentration is 1.2 g/L, more deposition on the surface takes place with more agglomeration of particles (Fig. 50.7c, g). The lower concentration of powders seen in Fig. 50.7a, b shows a lesser deposition on the surface yet uniform deposition.

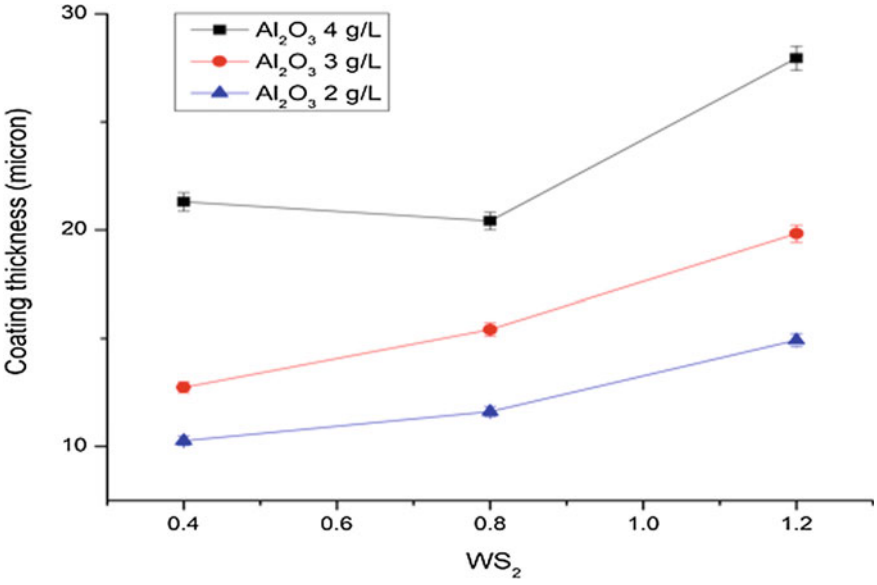

Fig. 50.5 Effect of Al_2O_3 and WS_2 powder concentration on coating thickness

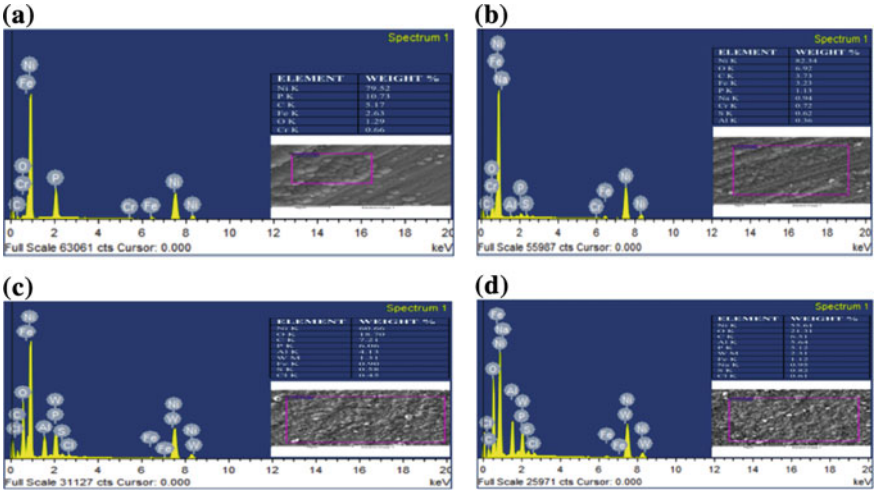

Fig. 50.6 EDS plot of sample coated, **a** without nanopowder concentration, **b** Al_2O_3 2 g/L and $WS_2 = 1.2$ g/L, **c** Al_2O_3 3 g/L and $WS_2 = 0.8$ g/L, **d** Al_2O_3 4 g/L and WS_2 0.4 g/L

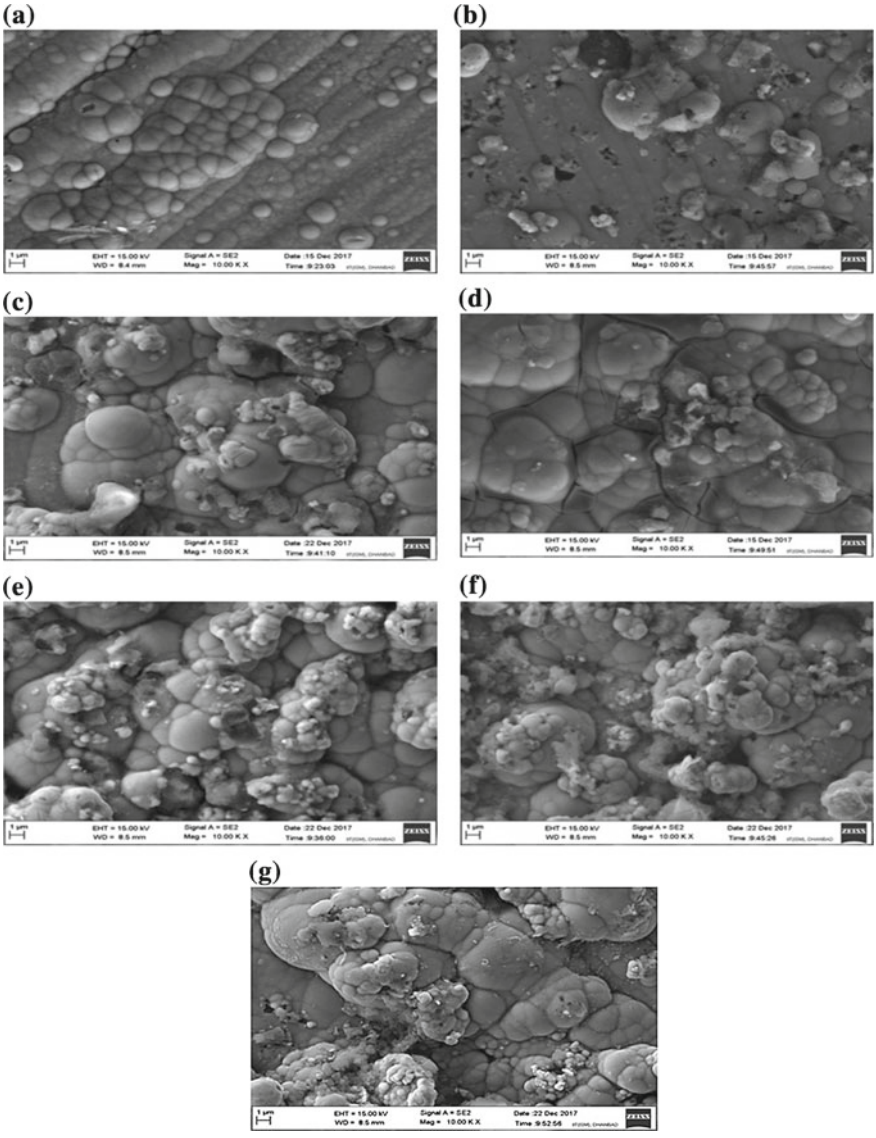

Fig. 50.7 FESEM images of samples coated, **a** without nanopowder concentration, with **b** Al_2O_3 = 2 g/L and WS_2 0.4 g/L, **c** Al_2O_3 = 2 g/L and WS_2 = 1.2 g/L, **d** Al_2O_3 = 3 g/L and WS_2 = 0.4 g/L, **e** Al_2O_3 = 3 g/L and WS_2 = 1.2 g/L, **f** Al_2O_3 = 4 g/L and WS_2 0.8 g/L, **g** Al_2O_3 = 4 g/L and WS_2 = 1.2 g/L

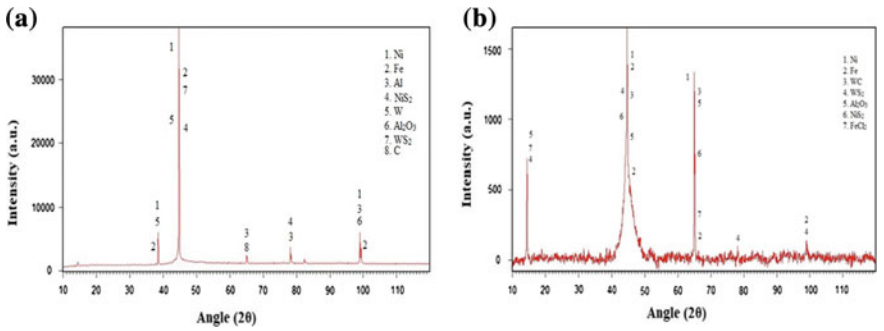

Fig. 50.8 XRD analysis of coated sample with, **a** $Al_2O_3 = 2$ g/L and $WS_2 = 0.4$ g/L, **b** $Al_2O_3 = 4$ g/L and $WS_2 = 1.2$ g/L

Thus, an increase in powders allows more deposition but more surface roughness is seen since agglomeration is more with non-uniform coating.

50.4.5 XRD Analysis

X-ray diffraction (XRD) analysis shows the different intermetallic compounds formed on the coated specimen. Figure 50.8a, b shows the XRD plot for powder concentration when Al_2O_3 is 2 g/L with WS_2 0.4 g/L and Al_2O_3 is 4 g/L with WS_2 1.2 g/L, respectively, where it is clear that there is deposition of nickel on the surface. Additional compounds such as Al_2O_3, WS_2 and WC have also been seen that improves the microhardness and lubricity properties of the coated samples.

Future scope in the present research, considering the effect of other solid lubricants on the tribological behaviour of the coating could be conducted and wear performance can be studied. A more comprehensive FESEM study of coated microstructures including the effect of heat treatment on the phase transformation.

50.5 Conclusions

In the present work, Ni–Al_2O_3–WS_2 coating was successfully deposited on SS304 through electroless plating process. The maximum coating thickness of 27.9482 μm is obtained at 4 g/L of Al_2O_3 and 1.2 g/L of WS_2 in electroless bath with all the parameters of bath being same. The microstructure study reveals that Ni–Al_2O_3–WS_2 surface consists of large number of Ni–Al_2O_3–WS_2 nodules. Microhardness values of the entire coated surface have increased nearly three times after coating.

References

1. Navinšek, B., Panjan, P., Milošev, I.: PVD coatings as an environmentally clean alternative to electroplating and electroless processes. Surf. Coat. Technol. **116**, 476–487 (1999)
2. McGeough, J.A., Leu, M.C., Rajurkar, K.P., De Silva, A.K.M., Liu, Q.: Electroforming process and application to micro/macro manufacturing. CIRP Ann. **50**(2), 499–514 (2001)
3. Sudagar, J., Lian, J., Sha, W.: Electroless nickel, alloy, composite and nano coatings—a critical review. J. Alloy. Compd. **571**, 183–204 (2013)
4. Krishnan, K.H., John, S., Srinivasan, K.N., Praveen, J., Ganesan, M., Kavimani, P.M.: An overall aspect of electroless Ni-P depositions—A review article. Metall. Mater. Trans. A. **37**(6), 917–1926 (2006)
5. Li, L., An, M.: Electroless nickel–phosphorus plating on SiCp/Al composite from acid bath with nickel activation. J. Alloy. Compd. **461**(1–2), 85–91 (2008)
6. Dong, D., Chen, X.H., Xiao, W.T., Yang, G.B., Zhang, P.Y.: Preparation and properties of electroless Ni–P–SiO_2 composite coatings. Appl. Surf. Sci. **255**(15), 7051–7055 (2009)
7. Shibli, S.M.A., Jabeera, B., Anupama, R.I.: Incorporation of nano zinc oxide for improvement of electroless nickel plating. Appl Surf. Sci. **253**(3), 644–1648 (2006)
8. Yang, Y., Chen, W., Zhou, C., Xu, H., Gao, W.: Fabrication and characterization of electroless Ni–P–ZrO_2 nano-composite coatings. Appl. Nanosci. **1**(1), 19–26 (2011)
9. Khalifa, O.R.M., El-Wahab, E.A., Tilp, A.: The corrosion behavior of electroless Ni-P-SiC and Ni-Sn-P-SiC nano-composite coating. J. Appl. Sci. Res. **6**(12), 2280–2289 (2010)
10. Zou, G., Cao, M., Lin, H., Jin, H., Kang, Y., Chen, Y.: Nickel layer deposition on SiC nanoparticles by simple electroless plating and its dielectric behaviors. Powder Technol. **168**(2), 84–88 (2006)
11. Gu, C., Lian, J., Li, G., Niu, L., Jiang, Z.: Electroless Ni–P plating on AZ91D magnesium alloy from a sulfate solution. J. Alloy. Compd. **391**(1–2), 104–109 (2005)
12. Sivandipoor, I., Ashrafizadeh, F.: Synthesis and tribological behaviour of electroless Ni–P-WS2 composite coatings. Appl. Surf. Sci. **263**, 314–319 (2012)
13. Chen, W.X., Tu, J.P., Xu, Z.D., Tenne, R., Rosenstveig, R., Chen, W.L., Gan, H.Y.: Wear and friction of Ni-P electroless composite coating including inorganic fullerene-WS2 nanoparticles. Adv. Eng. Mater. **4**(9), 686–690 (2002)
14. Liu, Z., Gao, W.: Electroless nickel plating on AZ91 Mg alloy substrate. Surf. Coat. Technol. **200**(16–17), 5087–5093 (2006)

Chapter 51
Influence of Heat Input on Corrosion Resistance of Duplex Stainless Steel Cladding on Low-Alloy Steel by FCAW

Manas Kumar Saha, Ajit Mondal, Ritesh Hazra and Santanu Das

Abstract Cladding is a popular surfacing process in which deposition of corrosion-resistant material on corrosion-prone structural steel is done to enhance the service life of different devices even under severe corroding atmosphere. Flux-cored arc welding is a successful process adopted for cladding. Duplex stainless steel is becoming an efficient cladding material in chloride atmosphere. Heat input is an important parameter for cladding process. In the present experiment, three sets of heat input are chosen by changing welding current and welding voltage, keeping voltage constant. Each set of heat input is constructed by three levels of current and voltage. Duplex stainless steel cladding is performed in a single layer with 50% overlap on low-alloy steel by flux-cored arc welding using 100% CO_2 as shielding gas. Metallography tests, corrosion test along with evaluation of chemical composition of clad samples have been performed. Theoretical values of chromium equivalent, nickel equivalent, ferrite number, and pitting corrosion equivalent number (PREN) obtained from chemical composition of clad samples suggest that Cr_{eq}, Ni_{eq}, ferrite number, and PREN (Pitting Corrosion Equivalent Number) do not change significantly with an increase in heat input. Corrosion rate increases with an increase in heat input within the experimental domain.

Keywords Cladding · Welding · Flux-cored arc welding · Heat input · Corrosion rate

51.1 Introduction

Cladding is a surfacing technic used to protect the base material from corrosion. In this process, corrosion-resistant filler material is deposited of a thickness of some millimeter on corrosion-prone base material by means of welding, rolling, etc. [1]. Cladding enhances the mechanical properties of the base material also. This technic

M. K. Saha · A. Mondal · R. Hazra · S. Das (✉)
Department of Mechanical Engineering, Kalyani Government Engineering College, Kalyani, Nadia 741235, West Bengal, India
e-mail: sdas.me@gmail.com

M. S. Shunmugam and M. Kanthababu (eds.), *Advances in Micro and Nano Manufacturing and Surface Engineering*, Lecture Notes on Multidisciplinary Industrial Engineering,
https://doi.org/10.1007/978-981-32-9425-7_51

is widely used in different engineering sectors, like petrochemical, paper and pulp, naval, chemical, etc. [2]. Among different types of welding, flux-cored arc welding (FCAW) is used to produce better quality clad parts due to some advantages relative to other processes. The clad portion is protected by inert gas and/or burnt flux from tubular core during welding. Instead of costly inert gas, cheap CO_2 gas is successfully used to protect the cladding layer from oxidation. FCAW is a semiautomatic, effective, and easy to use process [3].

Heat input is one of the most influential parameters for better quality cladding. Quality of cladding also depends upon weld bead geometry and chemical composition of filler and base material. Unlike welding, cladding requires wider bead, higher reinforcement, and lower penetration to minimize dilution. Cladding, which is basically dissimilar welding, requires optimum penetration for strong and durable joint without much hampering the corrosion resistance of filler material due to dilution. Heat input influences weld bead geometry a lot [4].

One of the major requirements for quality cladding is favorable microstructure which further depends upon chemical composition of both base and filler materials. Different phases, like ferrite, austenite, etc., are formed due to the presence of ferritiser and austenite in clad parts. Chromium equivalent (Cr_{eq}) and Nickel equivalent (Ni_{eq}) which are basically responsible for promoting ferrite and austenite phases respectively, determine the amount of different phases present in a ferrous metal theoretically [5]. Among different filler materials, duplex stainless steel has been reported to be having good corrosion resistance property in chloride atmosphere [6]. The clad part was produced by FCAW using duplex stainless steel as filler electrode with 100% CO_2 as shielding gas shows satisfactory corrosion resistance property [7]. Pitting corrosion equivalent number (PREN) of the clad part indicates pitting corrosion resistance property [8]. The more the PREN, the greater will be the pitting corrosion resistance. Heat input, as well as other parameters, plays a significant role for change in dilution, chemical composition, Cr_{eq}, Ni_{eq}, PREN of clad parts and so also, the corrosion resistance property of the same [9]. Different mechanical properties like hardness [10], toughness, etc., improve in clad part.

During the review of previous works done in this area, not many reports are found that relate corrosion rate, PREN, Cr_{eq}, Ni_{eq} with heat input. Mainly in some works done by this research group, the variation of rate of corrosion with heat input has been investigated. Considering this gap in this work, variation of Cr_{eq}, Ni_{eq}, PREN with heat input were investigated along with corrosion rate. In the present work, duplex stainless steel (E2209T01) cladding was produced on low-alloy steel (E250) by flux-cored arc welding process using 100% CO_2 as shielding gas. Cladding was done in single layer with 50% overlap. Process parameters like welding current and welding voltage were chosen in such a way that nine numbers of clad parts were produced in three levels. Chemical composition of each clad part was analyzed chemically using spectrometry. Metallographic test and corrosion test were performed. Cr_{eq}, Ni_{eq}.,and PREN were calculated theoretically and compared with heat input and corrosion rate.

51.2 Experimental Procedure

Weld cladding tests were performed using FCAW process on an ESAB, India-made MIG/MAG machine having voltage and current capacity in the range of 0–75 V and 0–400 A, respectively, on a low-alloy steel (E250) plate (composition shown in Table 51.1) using duplex stainless steel filler wire, E2209T01 (composition shown in Table 51.2). 100% CO_2 gas with a constant gas flow rate of 16 l/min was used as shielding gas throughout the cladding experiment. The cladding was done with single layer 50% overlap weld bead. The whole experiment was done twice to check more reliability of results obtained.

Three sets of welding current and welding voltage were selected, keeping travel speed constant at 450 mm/min. Three different rates of heat inputs were taken into consideration to get a total nine experiments. Parameters chosen for the experiments are shown in Table 51.3.

Table 51.1 Chemical composition of E250 low alloy steel

%C	**%Si**	**%Mn**	**%P**	**%S**	**%Mo**	**%Ni**
0.1985	0.1402	0.4976	0.0609	0.0308	0.0378	0.0253
%As	**%Co**	**%Cu**	**%Nb**	**%Pb**	**%Sn**	**%Fe**
0.0662	0.0059	0.0053	0.0096	0.0104	0.0137	<98.881

Table 51.2 Chemical composition of E2209 T01 duplex stainless steel electrode (in wt%) obtained by spectrometry

%Wt of C	0.02	%Wt of Cr	22.52
%Wt of Si	0.76	%Wt of Ni	9.09
%Wt of Mn	1.01	%Wt of Mo	2.91
%Wt of P	0.018	%Wt of N	0.125
%Wt of S 0.0087			

Table 51.3 Parameters of cladding experiment

Current (A)	Voltage (V)	Travel speed (mm/min)	Heat input (kJ/mm)
170	27	450	0.489
190	24	450	0.486
160	28	450	0.478
210	25	450	0.560
200	27	450	0.576
180	30	450	0.576
220	28	450	0.657
210	29	450	0.649
200	31	450	0.661

51.2.1 Calculation of Heat Input, Cr_{eq}, Ni_{eq}, Ferrite No., and PREN

Heat input plays a significant role in weld cladding. Proper heat input ensures proper penetration, favorable fusion, and sufficient bonding in cladding. Cooling rate, weld size, and material properties may all be influenced by the heat input [1]. Heat input is calculated by using Eq. (51.1).

$$Q = (60VI)/(1000S) \times \eta \tag{51.1}$$

where Q = Heat input (kJ/mm), V = Voltage (V), I = Current (Amp), S = Travel speed (mm/min), and η = Efficiency. For gas metal arc welding process, efficiency is taken to be 0.8 [8].

Calculation of Cr_{eq}, Ni_{eq}, Ferrite No., and PREN or Pitting Resistance Equivalent Number is performed by using Eqs. 51.2, 51.3, 51.4, and 51.5 respectively.

$$Cr_{eq} = Cr + Mo + 0.7\,Nb \tag{51.2}$$

$$Ni_{eq} = Ni + 35C + 20N + 25Cu \tag{51.3}$$

$$Ferrite\,No. = 15.2 + 2.2(Cr + Mo + 0.6Si + 15Ti + 0.8Nb) - 1.9(Ni + 17N + 30C) \tag{51.4}$$

$$PREN = Cr + 3.3(Mo + 0.5W) \tag{51.5}$$

51.2.2 Corrosion Test

Two sets of test samples consisting of nine number each, of size 15 × 15 × 25 mm were prepared from corresponding clad plates. Test samples were polished using 200, 400, 600, 800, and 1000 grades of emery papers followed by final polishing in the disk polishing machine. Each test sample was weighed by a digital weighing machine with a least count of 0.001 g. The corrosion test solution was a mixture of ferric chloride ($FeCl_3$, $6H_2O$), hydrochloric acid (HCl), and distilled water. After 24 h test, samples were weighed again and the difference in weight of each sample was calculated [9]. The corrosion rate was calculated using Eq. (51.6).

$$Corrosion\,Rate = W/(AxT) \tag{51.6}$$

where W = Weight loss (g), A = Exposed area (m^2), and T = Exposed time (h).

51.2.3 Metallographic Study

For the metallographic study, two sets of test samples (total number of eighteen) having size (15 × 15 × 25) mm were prepared. First, each sample was polished by using a belt grinder and then, on velvet cloth using alumina suspension as abrasive material to obtain mirror finish by using disk grinding cum polishing machine. Samples were then etched by waterless Kalling's reagent and Ralph's reagent one after another. Microstructure examination was carried out using metallurgical microscope. The photographs of the microstructure were taken at 200× magnification.

51.2.4 Chemical Composition

Chemical composition of each clad sample was tested using spectrometry and weight % of major alloying elements was evaluated as shown in Table 51.4.

51.3 Results and Discussion

Table 51.4 represents the chemical composition of nine test samples after cladding on the clad portion. Table 51.5 shows Creq, Nieq, Ferrite No., and PREN (Pitting Resistance Equivalent Number) of each clad part arranged according to ascending order of heat input. Table 51.5 also depicts corrosion rate of corresponding test samples. Depending on results obtained from Table 51.5, Creq is plotted against heat input in Figs. 51.1, 51.2, 51.3, 51.4, and 51.5 show plotting of Nieq, Ferrite No., PREN, and corrosion rate against heat input, respectively. From Figs. 51.1, 51.2, 51.3, and 51.4, it is observed that variation of each of Creq, Nieq, Ferrite No., and PREN with heat input is not remarkable. Figure 51.5 represents change in corrosion rate of two sets of clad parts against increasing heat input values. The figure clearly suggests that corrosion rate increases with increase in heat input. Diversion of values of corrosion rate is quite small for each heat input value suggesting strong relationship between corrosion rate and heat input.

Figure 51.6a–i shows the microstructure of nine clad samples. The etchant used was waterless Kalling's reagent and Ralph's reagent one by one. Magnification of the microstructure is 200×. From Fig. 51.6, it can be stated that white matrix represents ferrite phase and the blackish part represents austenitic phase. The extent of ferrite phase does not show remarkable change as in sample number 1 to sample 9

Table 51.4 Weight % of chemical composition of each clad part

	Sample No.	1	2	3	4	5	6	7	8	9
Weight % of chemical composition	% C	0.053	0.036	0.052	0.036	0.032	0.039	0.041	0.043	0.045
	% Mn	0.77	0.85	0.71	0.8	0.88	0.82	0.82	0.75	0.72
	% Si	0.58	0.69	0.52	0.6	0.78	0.63	0.64	0.55	0.52
	% S	0.014	0.009	0.004	0.008	0.008	0.011	0.009	0.005	0.013
	% P	0.021	0.018	0.019	0.018	0.016	0.019	0.018	0.018	0.02
	% Cr	17.14	19.75	17.37	19.47	21.38	18.17	18.97	18.11	17.64
	% Ni	6.84	7.83	6.96	7.82	8.3	7.46	7.63	7.33	7.07
	% Mo	2.38	2.55	2.26	2.46	2.85	2.29	2.28	2.36	2.28
	% Cu	0.065	0.071	0.061	0.07	0.073	0.067	0.068	0.065	0.065
	% W	0.016	0.019	0.017	0.015	0.017	0.012	0.017	0.014	0.009
	% Nb	0.052	0.047	0.050	0.049	0.050	0.053	0.519	0.053	0.051
	% Ti	0.041	0.0403	0.0333	0.0413	0.0477	0.0341	0.0375	0.0493	0.0428
	% N	0.094	0.105	0.092	0.102	0.112	0.1	0.092	0.097	0.096

Table 51.5 Creq, Ni_{eq}, Ferrite No., PREN, and corrosion rate of clad parts arranged in ascending order of heat input

Sample No.	1	2	3	4	5	6	7	8	9
Cr Eqv.	19.56	22.33	19.665	21.96	24.26	20.49	21.61	20.51	19.956
Ni Eqv.	12.2	12.97	12.15	12.87	13.49	12.5	12.61	12.65	12.19
Ferrite No.	10.77	15.71	10.586	14.95	19.42	12.09	14.59	12.47	11.6
PREN	26.52	29.88	26.328	29.24	32.61	27.34	27.99	27.47	26.716
Heat input	0.478	0.486	0.0.49	0.56	0.576	0.576	0.649	0.657	0.661
Corrosion rate first	256.4	254.3	254.3	261.9	267	274.9	289.7	322.8	332.8
Corrosion rate second	255.9	247.4	249.1	271.4	279.1	277.5	283.8	329.5	331.7
Average corrosion rate	256.1	260.8	251.7	266.6	273.1	276.2	286.8	326.2	332.25

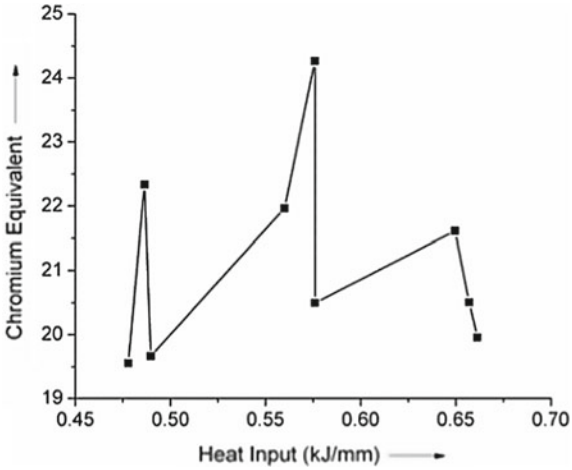

Fig. 51.1 Plot showing variation of Cr_{eq} with heat input

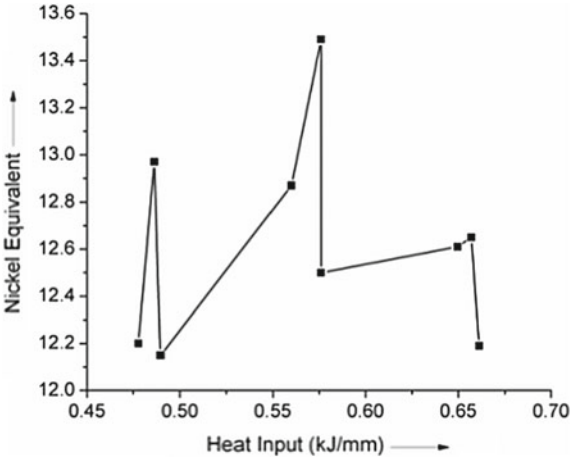

Fig. 51.2 Plot showing variation of Ni_{eq} with heat input

(corresponding to Fig. 51.6a–i). For every set of heat input, corrosion rate increases with the increase in current and decrease in voltage. The microstructure of clad layer contains blackish ferrite dendrite structure in lighter austenite matrix with incomplete grain boundaries. For each heat input value, ferrite phase decrease with increase in current and decrease in voltage as a whole.

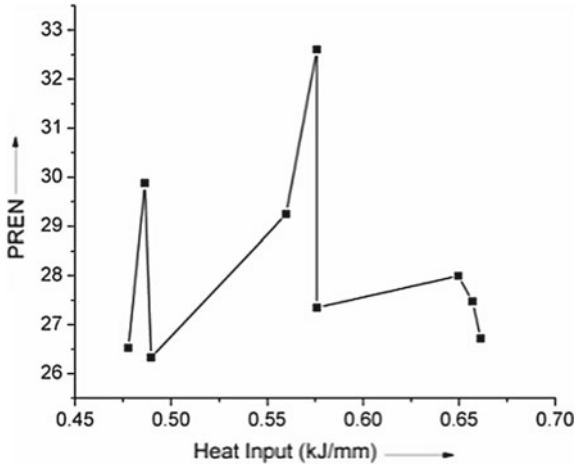

Fig. 51.3 Plot showing variation of Ferrite No. with input PREN

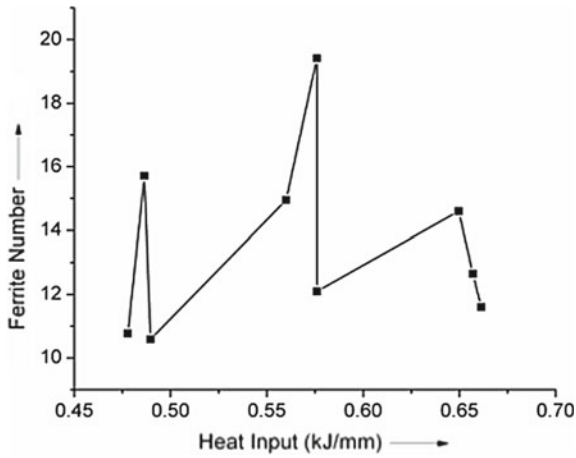

Fig. 51.4 Plot showing variation of heat with heat input

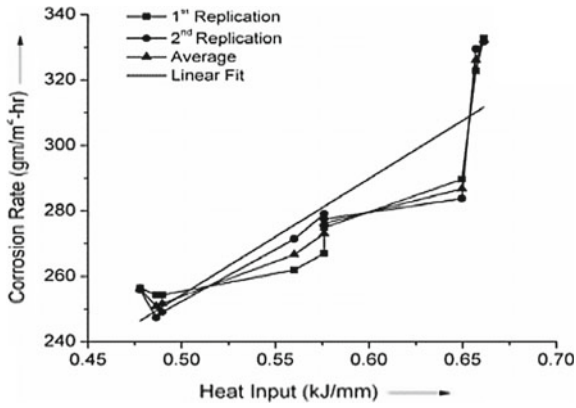

Fig. 51.5 Plot of variation of corrosion rate with increasing value of heat input

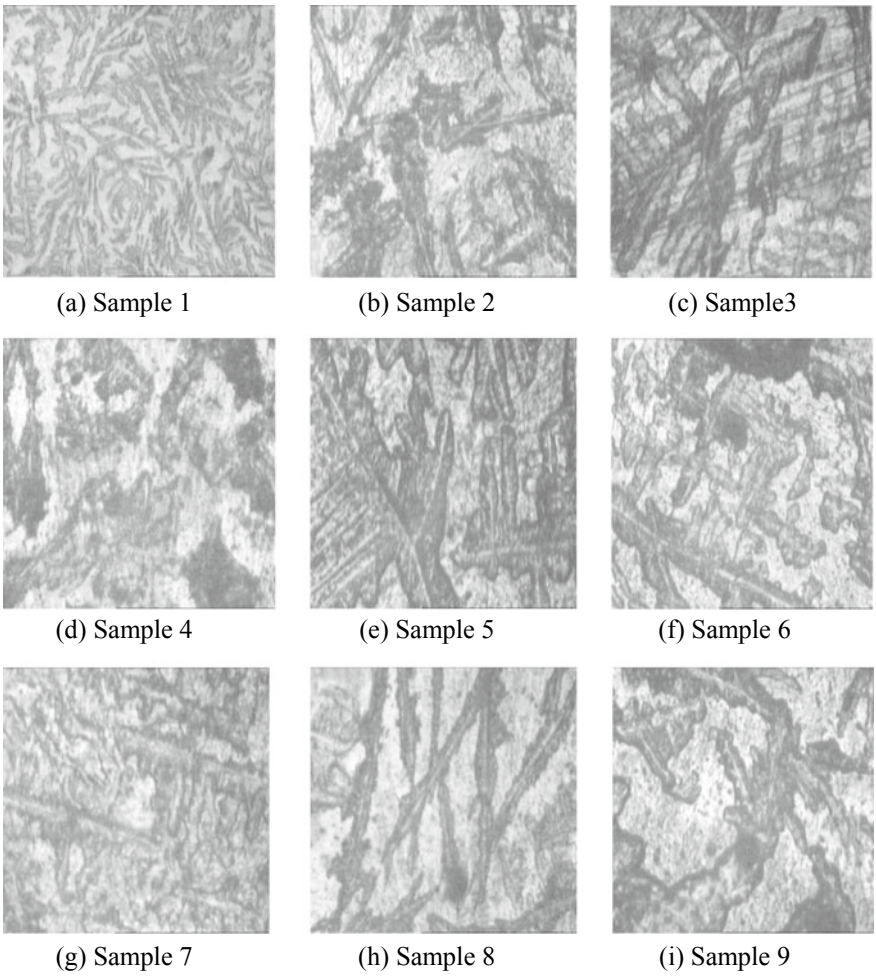

Fig. 51.6 Microstructure of nine clad sample

51.4 Conclusions

From the results obtained, the following conclusions may be drawn:

1. Within the experimental domain, ferrite phase present in the microstructure does not change remarkably with heat input. Ferrite number also changes not significantly with heat input.
2. Cr_{eq} indicating ferritising property and Ni_{eq} corresponding to austenizing characteristics both do not change significantly with heat input within the experimental domain. Also, pitting resistance equivalent number (PREN) which is the index for pitting corrosion resistance does not change remarkably with heat input.

3. However, corrosion resistance of duplex stainless steel cladding on low-alloy steel decreases with increase in heat input within the experimental domain.

Acknowledgements Authors would like to acknowledge Dr. ArijitDutta, Assistant Professor, Kalyani Govt. Engineering College, Kalyani, Nadia, India, for his active help in creating different plots used in this paper.

References

1. Saha, M.K., Das, S.: A review on different cladding techniques employed to resist corrosion. J. Assoc. Eng. India **86**(1&2), 51–63 (2016)
2. Saha, M.K., Das, S.: Gas metal arc welding cladding and its anti-corrosive performance—a brief review. Athens J. Technol. Eng. **5**(2), 155–174 (2018)
3. Senthilkumar, B., Kannan, T., Madesh, R.: Optimization of flux-cored arc welding process parameters by using genetic algorithm. Int. J. Adv. Manuf. Technol. **93**(1–4), 35–41 (2017)
4. Saha, M.K., Hazra, R., Mondal, A., Das, S.: Effect of heat input on geometry of austenitic stainless steel weld bead on low carbon steel. J. Inst. Eng. (Indian) Ser. C (2018). https://doi.org/10.1007/s40032-018-0461-7
5. Verma, A.K., Biswas, B.C., Roy, P., De, S., Saren, S., Das, S.: An investigation on the anti-corrosion characteristics of stainless steel cladding. Indian Weld. J. **50**(3), 52–63 (2017)
6. Duel-Phase Steel, Properties and Selection Iron Steel and High Performance Alloys. ASM Handbook, 10th edn (1993)
7. Saha, M.K., Kumar, M., Das, S.: Effect of heat input on pitting corrosion rate of duplex stainless steel cladding over low alloy steel by flux cored arc welding. In: Proceeding of the 1st International Conference on Mechanical Engineering, Jadavpur University, India (2018)
8. Chakrabarti, B., Das, S., Das, H., Pal, T.K.: Effect of process parameters on clad quality of duplex stainless steel using GMAW process. Trans. Indian Inst. Met. **66**(3), 221–230 (2013)
9. ASM International: Basic understanding of weld corrosion, Corrosion of Weldments: (#05182G). Accessed from 27 Dec 2017 at http://bit.ly/2BZa43k
10. Saha, M.K., Mondal, A., Hazra, R., Das, S.: On the variation of hardness of duplex stainless steel clad layer deposited by flux-cored arc welding. Reason Tech. J. **XVI**, 1–6 (2016). https://doi.org/10.21843/reas/2016/1-6/158768

Chapter 52
Study of Sliding Abrasive Wear Behaviour of TiC–TiB_2 Composite Coating Fabricated on Titanium Alloy by TIG Cladding Method

D. Tijo, Ajay Sivasankaran Menon and Manoj Masanta

Abstract Grade 5 Titanium alloy commonly known as Ti–6Al–4V is extensively used in various industries like aerospace, biomedical and chemical components owing to their low density, high strength and biocompatibility. Their application is limited in tribological components due to their low wear resistance. To increase the surface property of Ti–6Al–4V alloy, in this work first, a clad layer of TiC–TiB_2 composite was deposited by TIG cladding method through an in situ reaction between Ti and B_4C powder (mixed at 3:2 wt. ratio). The sliding abrasive wear performance of the coated substrate was done by a pin on disc type tribological test against an alumina disc. The effect of the applied normal load on the wear behaviour of the coating was studied by varying the normal load at 10, 20, 30 and 40 N. The assessment of wear was executed from the reduction of the height of coated pin-shaped samples as well as directly from the data acquisition system attached with the wear tester. The coefficient of friction of the coating was also noted, and the value was compared for different load conditions as well as with the uncoated Ti–6Al–4V alloy. It was found that the wear loss for the coating is sensibly lower than the Ti–6Al–4V substrate even at high load conditions.

Keywords TIG cladding · Titanium alloy · Sliding wear · TiC–TiB_2

52.1 Introduction

Ti–6Al–4V alloy also known as Grade 5 Titanium alloy exhibits properties like low density, high specific strength, high corrosion resistance and can withstand high temperature. Ti alloy has low resistance to plastic shearing and low work-hardening. Hence, wear phenomena caused due to abrasion, adhesion and delamination weaken

D. Tijo · A. S. Menon · M. Masanta (✉)
Department of Mechanical Engineering, National Institute of Technology Rourkela, Rourkela 769008, India
e-mail: manoj.masanta@gmail.com

M. S. Shunmugam and M. Kanthababu (eds.), *Advances in Micro and Nano Manufacturing and Surface Engineering*, Lecture Notes on Multidisciplinary Industrial Engineering,
https://doi.org/10.1007/978-981-32-9425-7_52

the material and reduces its service life. Hence, its applications become restricted in areas involving friction and wear [1, 2]. The properties of this alloy can be enhanced by employing a clad layer on it with a suitable material.

A layer of ceramic metal matrix composite or multicomponent ceramic composite is a suitable choice for wear-resistance coating by various research groups due to the combined effect of individual ceramic phases depending on the requirements. Among the ceramic composites, TiC–TiB_2 has acquired substantial attention owing to its extraordinary hardness, wear resistance and compatibility with Ti alloy [3]. Wang et al. [4] reported that with the enhancement of TiC and TiB_2 composition, the microhardness and wear resistance in of the coating improved significantly. TiC and TiB_2 have a high melting point, high abrasive resistance, low density and greater oxidation resistance. It was noticed that flexural strength and fracture resistance of TiC–TiB_2 coating are much superior to the individual ceramic phases [5].

There are many methods to deposit a hard and wear-resistant coating on the substrate material. Among them, TIG cladding is a developing method to create a hard and wear-resistant coating with sufficient thickness owing to its low cost, simplicity and applicability to a wide range of materials [6]. According to An et al. [7], TIG cladding is characterized by its low cost and valid for a range of materials, with accurately controlled heat input. Therefore, TIG cladding method can be implemented on various substrates to cut the manufacturing cost and to acquire an excellent surface property.

There are many methods to evaluate the wear resistance of a material in the form of a coating or as bulk. Pin-on-disc sliding wear test is the most widely used method for the study of wear and friction properties of a material. The method is used to study the wear behaviour of a cylindrical-shaped specimen by sliding against a rotating disc of a harder material or an abrasive wheel. The wear rate is measured from the height difference of the pin. Saroj et al. [8] performed the sliding abrasive wear test of TiC reinforced Inconel 825 coating fabricated by TIG cladding method and studying the effect of different processing conditions.

From the literature review, it was evident that several works have been done on Ti–6Al–4V alloy using mostly ceramic particle reinforcements. But, only a few studies show the wear characteristic of the fabricated coating under sliding abrasive condition. The objective of the present work is to study the sliding abrasive wear behaviour of TIG cladded TiC–TiB_2 composite coating deposited on Ti–6Al–4V alloy through in situ reaction. The wear test of the pin-shaped TiC–TiB_2-coated samples was performed by using a pin-on-disc tribological tester against an alumina disc by varying the normal load at 10, 20, 30 and 40 N.

52.2 Experimental Planning and Procedure

For the present experiment, the coating material was prepared by mixing of pure titanium and boron carbide (B_4C) powder with a weight ratio of 3:2. The powder precursor was prepared by ball milling process for three hours to make a uniform

powder mixture. The mixer was then combined with polyvinyl alcohol (PVA) to form a semisolid paste, which was then coated on Ti–6Al–4V alloy substrate of dimension 50 mm × 90 mm × 5 mm. Hence, a pre-deposited coating layer of 0.8 mm thickness was obtained.

The cladding was done by scanning the TIG arc on the pre-coated surface of the Ti–6Al–4V alloy. The schematic of the TIG cladding setup is shown in Fig. 52.1. For the present work, a single-line clad layer prepared with 100 A peak current and 2.3 mm/s scan speed was used. The details of the TIG cladding process may be available in the author's earlier work [9]. Due to the TIG arc heat source, Ti and B_4C powder reacted and produced TiC and TiB_2 as per Eq. (52.1).

After the fabrication of the clad layer, the specimen for wear test was prepared by cutting a cylindrical-shaped sample of 4 mm diameter using a wire electro-discharge machine (W-EDM). After the pin-shaped samples were taken out, the specimens were polished at the coated surface using 600 graded SiC emery paper to give the coated layer a smooth finish. The sliding abrasive wear test was performed in pin-on-disc test rig as per ASTM G99 standard (Make: Magnum). The conditions for the wear test are shown in Table 52.1.

$$3Ti + 2B_4C = TiC + 2TiB_2 \tag{52.1}$$

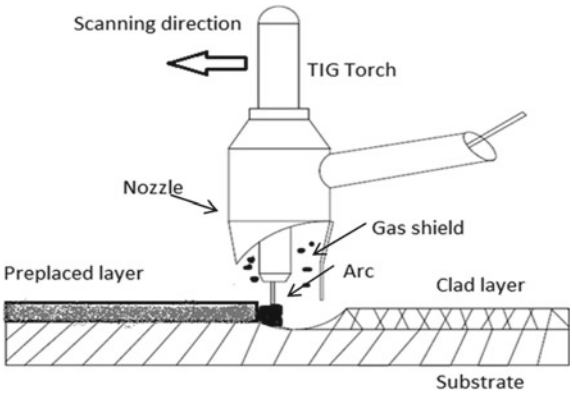

Fig. 52.1 Schematic representation of TIG cladding process

Table 52.1 Experimental condition for the wear test and assessment of coefficient of friction (COF)

Pin diameter	4 mm
Counter body	Alumina abrasive disc
Load (N)	10, 20, 30, 40
Track diameter	34 mm
RPM	112
Time of test	10 min
Sliding speed	200 mm/s

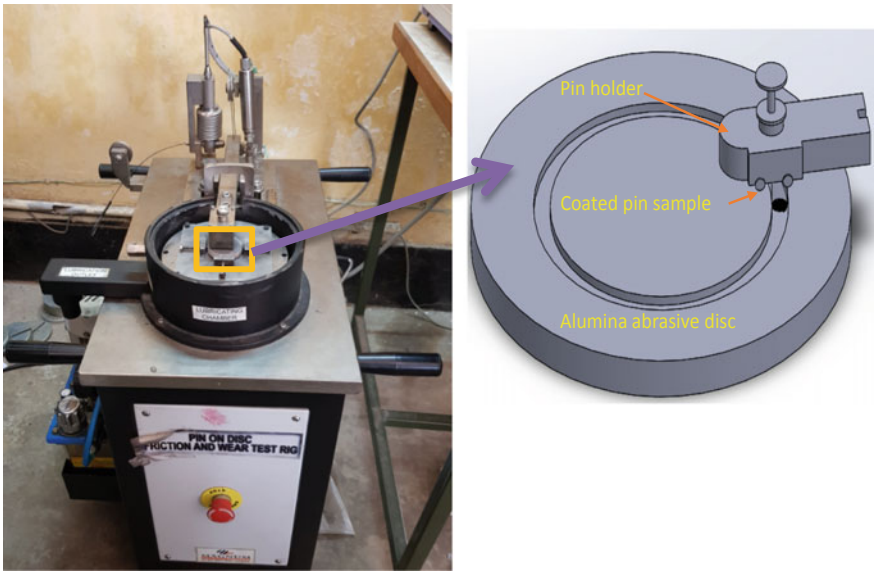

Fig. 52.2 Pin-on-disc setup for sliding abrasive wear test

Sliding velocity was calculated from rotational speed and diameter of the track. The load applied for each test was varied at 10, 20, 30 and 40 N maintaining the same rotational speed. The pin-shaped sample was sliding against the rotating abrasive disc as shown in Fig. 52.2. The height of the each coated pin sample was noted before and after the 10 min of the test, and the height loss or wear was calculated for each sample. Further, through an online data acquisition system, the wear value and the coefficient of friction (COF) were directly recorded.

52.3 Results and Discussion

Figure 52.3 shows the TiC–TiB_2 layer deposited on Ti–6Al–4V alloy and the extracted samples for the wear test. Figure 52.4 shows the SEM image of the cross section of the clad layer, which exhibits the composite structure of TiC–TiB_2 along with some other intermetallic components. From the image, approximately 1 mm thick coating layer can be visible. After the test, the wear or reduction of the height of the pin samples under different load conditions (10, 20, 30, and 40 N) and the uncoated Ti–6Al–4V alloy pin under 10 N load were measured by Vernier calliper and tabulated in Table 52.2.

Figure 52.5 shows the variation of height loss (wear) of the TiC–TiB_2 coating produced by TIG cladding technique against the applied load for performing the wear test counter to alumina disc under different loads and the Ti–6Al–4V alloy

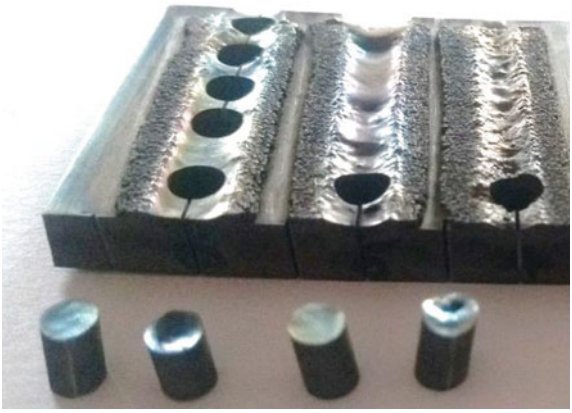

Fig. 52.3 Preparation of pin samples for sliding wear test

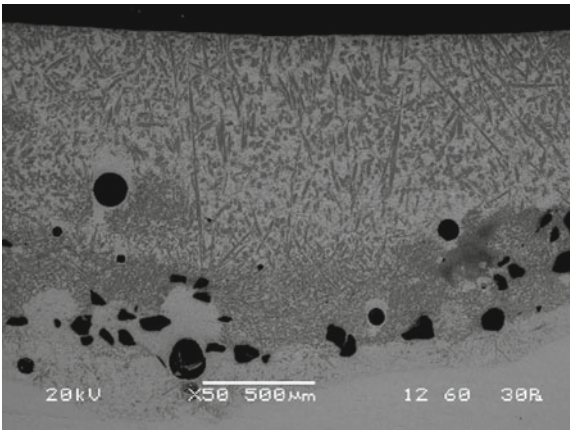

Fig. 52.4 SEM image of the TiC–TiB_2 clad layer deposited on Ti–6Al–4V alloy

Table 52.2 Wear or height loss values after the wear test

Material	Load (N)	Avg. initial height (mm)	Avg. final height (mm)	Average height loss (mm)
TiC–TiB_2 coating	10	5.02	4.9	0.12
	20	5.08	4.82	0.26
	30	5.04	4.66	0.38
	40	5.06	4.41	0.65
Uncoated Ti–6Al–4V alloy	10	5.01	4.17	0.84

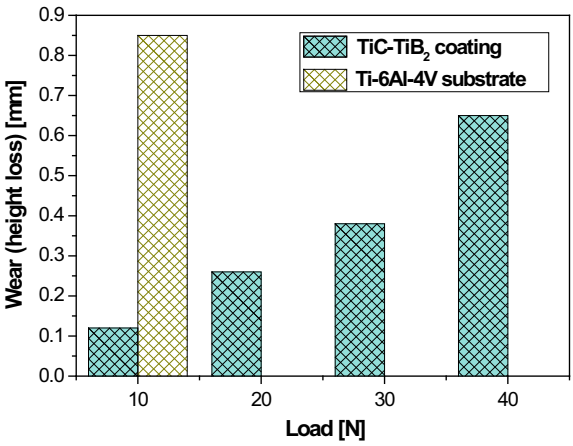

Fig. 52.5 Variation of height loss (wear) against alumina wheel for coating fabricated by the TIG cladding technique under different loads and for Ti–6Al–4V substrate under 10 N load

substrate under 10 N load. It is evident from the plot that the wear loss increases with increase in the load applied. The wear losses of the coated samples are between 0.12 and 0.56 mm for the variation of the normal load, while for uncoated Ti–6Al–4V alloy substrate (at 10 N load), the wear loss is more than 0.85 mm. The plot shows that the wear resistance of the coated samples is much better than the wear resistance of the uncoated Ti–6Al–4V alloy. The plot also shows that the wear value of the coating rises almost progressively with the employed normal load. As the coating layer consists of hard phases like TiC and TiB_2, during sliding abrasive wear, these particles resisted the abrasion of the coating layer and very low abstraction of the coating material occurred. However, with the increase in the employed normal load, the intensity of the scratches by individual alumina grits from the counter disc increased, and consequently augmented the removal of the material. On the contrary, the resistance against scratches by the Ti–6Al–4V alloy is relatively low due to its low hardness and increases the removal of the pin sample.

Further, from the data acquired from the online system, the plotted graphs (Fig. 52.6) against the wear test time shows that with time, the wear value increases gradually for all different normal loads. Due to the unevenness on the surface of the pin, the initial wear value of the pin shown in all the graphs is high, and then it increases steadily. The plots also show that with the increase in the applied normal load, the final wear value of the coated pin increases, which is almost equivalent to the wear or measured by Vernier calliper as shown in Fig. 52.5. From the graph, it is also evident that the wear rate increased at a higher load, but within the experimental domain, the coating did not get removed completely even at higher (40 N) load conditions. Hence, it is justified to conclude that the TiC–TiB_2 layer fabricated by TIG cladding technique is well enough to withstand high normal load even under an abrasive environment.

Figure 52.7 depicted the variation of coefficient of friction (COF) recorded during the sliding wear test for TiC–TiB_2 coating under different normal loads and the uncoated Ti–6Al–4V alloy at 10 N load. It is also apparent that the COF for uncoated

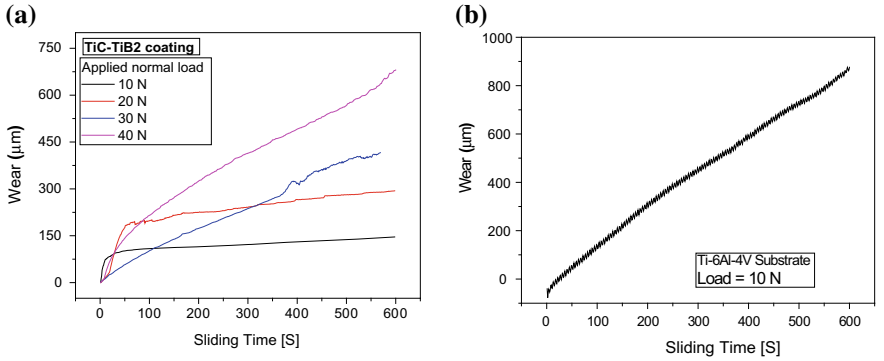

Fig. 52.6 Cumulative wear loss of the **a** coating (recorded through online system) with respect to the test time performed against alumina abrasive disc for different normal loads and **b** for Ti–6Al–4V alloy at 10 N load

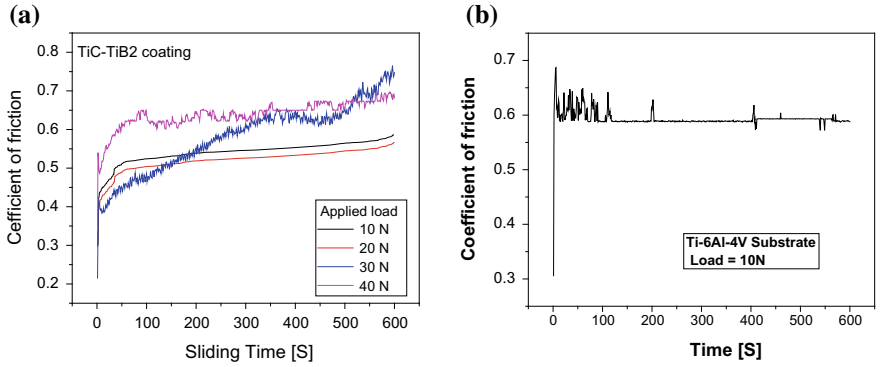

Fig. 52.7 Coefficient of friction of the coating (recorded through online system) with respect to the test time measured against alumina abrasive disc for different normal loads and Ti–6Al–4V alloy at 10 N load

Ti–6Al–4V alloy is almost steady at approximately 0.6. However, the COF value for TiC–TiB_2 coating was found marginally higher than the uncoated substrate material. It may also be observed that the COF value gradually increases with the sliding or test time for the coated surface for all different normal load conditions.

Figure 52.8 illustrates the SEM images of the coating surface after the wear test performed against the alumina abrasive disc under different normal loads. The images show that at relatively low load condition the scratches formed during the wear test are with low intensity. Whereas with the increase in applied load the intensity of the scratch marks is enhanced. At higher load condition, the applied pressure by the abrasives embedded in the alumina disc is larger, which causes more abstraction of the material from the coating surface. Consequently, the wear value increases with the increase in the applied load.

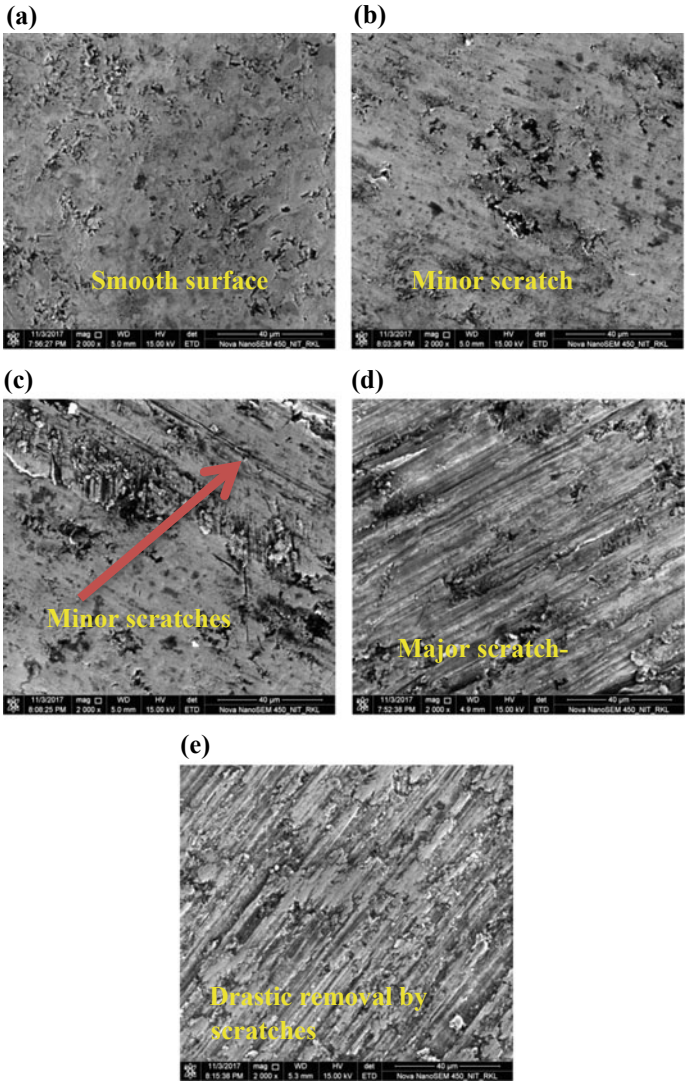

Fig. 52.8 SEM images of worn-out coating surface for different normal loads and Ti–6Al–4V alloy at 10 N load

52.4 Conclusions

The cladding of TiC–TiB_2 on Ti–6Al–4V alloy was done successfully using TIG cladding technique using Ti and B_4C as the precursor powder at 100 A current and 2.3 mm/s scan speed.

The sliding abrasive wear test performed using a pin-on-disc machine under different load shows that with an increase in the normal load, the wear in terms of height loss increases gradually. However, the wear rate even at a higher load is much lower than the wear value for uncoated Ti–6Al–4V alloy which performed at a lower load.

The experimental results performed show that the deposition of a hard TiC–TiB_2 coating on Ti–6Al–4V alloy significantly increased its surface property and consequently the wear resistance of the alloy against the alumina disc.

References

1. Mao, Y.S., Wang, L., Chen, K.M., Wang, S.Q., Cui, X.H.: Tribo-layer and its role in dry sliding wear of Ti-6Al-4V alloy. Wear **297**, 1032–1039 (2013)
2. Molinria, A., Straffelinia, G., Tesia, B.: Dry sliding wear mechanisms of the Ti-6Al-4V alloy. Wear **208**, 105–112 (1997)
3. Weng, F., Yu, H., Chen, C., Liu, J., Zhao, L., Dai, J.: Effect of process parameters on the microstructure evolution and wear property of the laser cladding coatings on Ti-6Al-4V alloy. J. Alloy. Compd. **692**, 989–996 (2016)
4. Wang, Z.T., Zhou, X.H., Zhao, G.G.: Microstructure and formation mechanism of in-situ TiC-TiB_2/Fe composite coating. Trans. Nonferrous Met. Soc. China **18**, 831–835 (2008)
5. Limei, W., Hanlian, L.: Microstructure and mechanical properties of TiC–TiB_2 composite cermet tool materials at ambient and elevated temperature. Ceram. Int. **42**(2), 2713–2717 (2016)
6. Chen, J.H., Chen, P.N., Lin, C.M., Chang, C.M., Chang, Y.Y., Wu, W.: Microstructure and wear properties of multicomponent alloy cladding formed by gas tungsten arc welding (GTAW). Surf. Coat. Technol. **203**, 3231–3234 (2009)
7. An, Q., Huang, L., Jiang, S., Li, X., Gao, Y., Liu, Y., Geng, L.: Microstructure evolution and mechanical properties of TIG cladded TiB reinforced composite coating on Ti-6Al-4V alloy. Vacuum **145**, 312–319 (2017)
8. Saroj, S., Sahoo, C.K., Tijo, D., Kumar, K., Masanta, M.: Sliding abrasive wear characteristic of TIG cladded TiC reinforced Inconel825 composite coating. Int. J. Refract. Met. Hard Mater. **69**, 119–130 (2017)
9. Tijo, D., Das, A.K., Masanta, M.: In-situ TiC-TiB_2 coating on Ti-6Al-4V alloy by tungsten inert gas (TIG) cladding method: part-I. Microstructure evolution. Surf. Coatings Technol. **344**, 541–552 (2018)

Chapter 53
Effect of Test Conditions on Tribological Behavior of NiTi–TiN-Coated Ti–6Al–4V Alloy Fabricated by TIG Cladding Method

Abhratej Sahoo, Dipak Tanaji Waghmare, Arti Sahu and Manoj Masanta

Abstract Ti–6Al–4V alloy is a versatile material widely used in aerospace, chemical, and marine industries owing to its properties like lightweight, high strength, and corrosion resistant. However, the alloy lacks inadequate hardness and wear resistance to ensure a long product life for its applications. In this study, the Ti–6Al–4V alloy was coated with a metal matrix composite coating that consists of NiTi and TiN by TIG cladding process, and the wear behavior of the coated specimen was studied by conducting a pin-on-disk type tribological wear test. The effect of the sliding speed (by altering the rotational the speed of the disk) and the normal load applied on the wear or height loss of the pin-shaped-coated sample, and the coefficient of friction were studied. It was found that within the experimental domain, the produced NiTi–TiN coating is suitable for application in high load—lower speed and medium load—high-speed combinations.

Keywords NiTi–TiN coating · Sliding wear · Coefficient of friction · TIG cladding

53.1 Introduction

Due to wide applications of Ti–6Al–4V alloy in aerospace, marine, power generation, and biomedical industries, it is referred to as the "workhorse alloy of the titanium industry." However, due to its poor tribological behavior, the application of Ti–6Al–4V is severely restricted under high wear and high-temperature conditions [1].

As demonstrated by Mao et al. [2], frictional wear of Ti–6Al–4V alloy is too high for diverse applications. Guo et al. [3] demonstrated that at high temperature, its oxidation and wear resistance are very poor, which further limits the application of Ti–6Al–4V. Weng et al. [4] suggested that these properties of Ti–6Al–4V alloy

A. Sahoo · D. T. Waghmare · A. Sahu · M. Masanta (✉)
Department of Mechanical Engineering, National Institute of Technology, Rourkela 769008, India
e-mail: manoj.masanta@gmail.com

M. S. Shunmugam and M. Kanthababu (eds.), *Advances in Micro and Nano Manufacturing and Surface Engineering*, Lecture Notes on Multidisciplinary Industrial Engineering,
https://doi.org/10.1007/978-981-32-9425-7_53

could be enhanced by the application of clad layer with suitable material, specifically a metal matrix composite (MMC) reinforced with ceramics.

NiTi is an intermetallic that owns excellent properties like shape memory effect, superelasticity, high fatigue strength, good corrosion resistance, and biocompatibility [5]. Its superelasticity and fatigue strength culminate to provide it the property of good wear resistance. Buehler and Wang [6] first reported the high wear resistance property of NiTi in their pioneering work on the development of NiTi.

Due to machinability issues and high cost, NiTi is generally not used in bulk to manufacture machine parts despite its superior properties. Cheng et al. [7] conducted cladding of NiTi on AISI 316 stainless steel and demonstrated that the usage of NiTi as a cladding material is feasible by avoiding its machinability issues. Considering the merits of ceramic reinforcement, Weng et al. [8] conducted experiments that involved the addition of TiN (Titanium Nitride) to Co-based alloy cladding over Ti–6Al–4V alloy. Hence, TiN can be added to NiTi to improve its hardness and wear resistance further.

Tungsten inert gas (TIG) welding is a well-established process used for welding and repairing purposes [9, 10]. Based on the review of prior research work carried out in this field, it was revealed that there is a lack of study on the deposition of NiTi–TiN composite coating on Ti–6Al–4V alloy by TIG cladding method and also the analysis of its tribological behavior.

The present work emphasizes on the study of the wear behavior of NiTi + TiN clad layer deposited on Ti–6Al–4V alloy by conducting the pin-on-disk wear test against harden steel disk with a hardness value of HRC 58, under different applied normal load and sliding speed conditions. The effect of the applied normal load and sliding speed was evaluated on the wear value and wear characteristic of the coated pins through an online data monitoring system and SEM of the worn surfaces.

53.2 Materials and Methodology

For the present work, at first, cladding of NiTi + TiN was deposited on Ti–6Al–4V alloy using Nickel, Titanium, and TiN powder mixed in a weight ratio of (10:10:2). The condition used for the cladding was TIG current of 70 A, arc scan speed of 2.3 mm/s, and Ar gas flow rate of 20 L/min. Figure 53.1 shows the SEM image of the NiTi + TiN clad layer at the cross section and the magnified image of the coating region.

After the cladding, the coating surface was tested to understand its wear characteristic. Wear test was performed using a pin-on-disk type wear test setup as per ASTM G99 standard. The NiTi + TiN cladded Ti–6Al–4V alloy plate was cut using a wire EDM to get cylindrical-shaped test samples for the wear test. Figure 53.2 shows the pin-on-disk wear tester and the pin-shaped samples extracted from the NiTi–TiN clad track for the wear test. The test specimen was then brought in contact with a

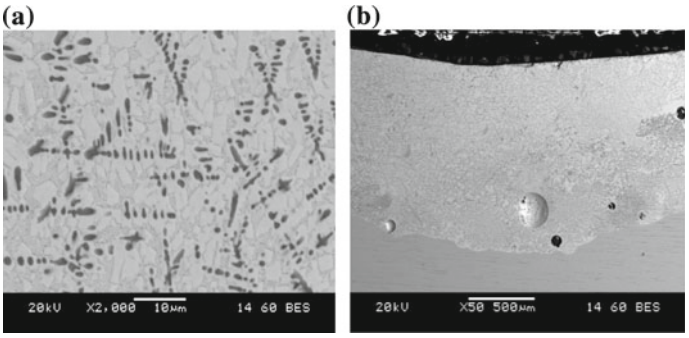

Fig. 53.1 SEM image of **a** NiTi + TiN clad layer at the cross section, **b** high magnified image of the coating region

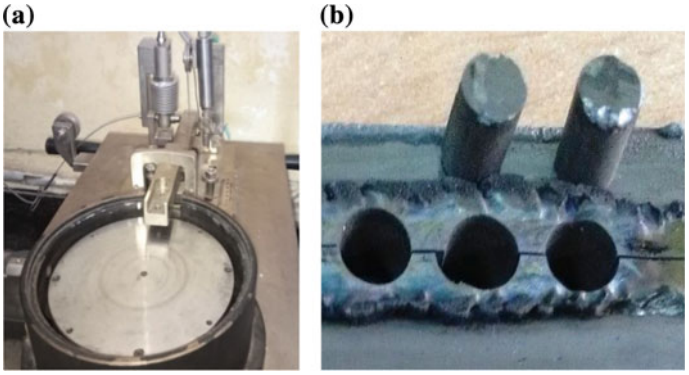

Fig. 53.2 **a** Pin-on-disk wear tester. **b** Pin-shaped specimen extracted from the coating track

rotating disk made of hardened steel (HRC 58). In order to measure the sliding wear of the sample, the pin is placed under some force using a pulley and a dead-weight loading mechanism that exerts an equivalent amount of force on the pin. Generally, a cylindrical pin is preferred to correlate the amount of wear directly with the average reduction in the height of the pin. The detail conditions used for the wear test are illustrated in Table 53.1.

For the present work, the wear test was performed by varying both sliding speeds and normal load was applied. The normal loads applied on the specimen were varied as 10, 20, and 30 N. The tests were carried out with two different rotational speeds, i.e., 250 RPM and 500 RPM so that, the sliding velocities of approximately 1000 mm/s and 2000 mm/s were obtained, respectively. After the test, the wear value was measured from the reduction in the height of the coated pin samples. In addition, the wear value and the coefficient of friction value were directly acquired with the help of an online monitoring system, which is furnished with the wear test setup. The

Table 53.1 Details of the wear test conditions

Counter body	Harden steel (HRC 58)
Pin diameter	4 mm
Track wear radius (D)	75 mm
RPM	250 and 500
Sliding speed (V)	1000 and 2000 mm/s
Test duration (T)	10 min
Sliding distance	590 and 1180 m

wear value obtained from the online monitoring system and height loss measured through Vernier caliper were correlated.

53.3 Results and Discussion

The height loss for every cylindrical-shaped samples measured by Vernier caliper after the sliding wear test as well as the final wear value recorded by the data acquisition system are tabulated in Table 53.2.

Figures 53.3 and 53.4 show the cumulative height loss for NiTi–TiN-coated Ti–6Al–4V pin against sliding time under different normal loads (10, 20, and 30 N) for sliding velocities of 1000 mm/s and 2000 mm/s, respectively. Form the plots, it may be evident that the wear value or height loss of the NiTi–TiN-coated Ti–6Al–4V pins are gradually increased for all different test conditions. However, with the increase of normal load for both the sliding velocity conditions, the wear rate increases, and a progressive final wear value is obtained. From the plots, it is also observed that for 2000 mm/s sliding velocity the wear values are also higher compared to the wear values obtained for 1000 mm/s sliding velocity.

As mentioned earlier, the thickness of the coating used for the present tribological test was approximately 800 μm. Hence, from the wear plot, it was seen that

Table 53.2 Wear values and COF of the NiTi–TiN-coated Ti–6Al–4V pins for different conditions

Sl. No.	Sliding velocity (mm/s)	Normal load (N)	Avg. height loss (measured by Vernier caliper) (mm)	Wear (from data acquisition system) (mm)
1	1000	10	0.018	0.019
2	1000	20	0.032	0.043
3	1000	30	0.185	0.196
4	2000	10	0.052	0.57
5	2000	20	0.158	0.167
6	2000	30	1.08	1.112

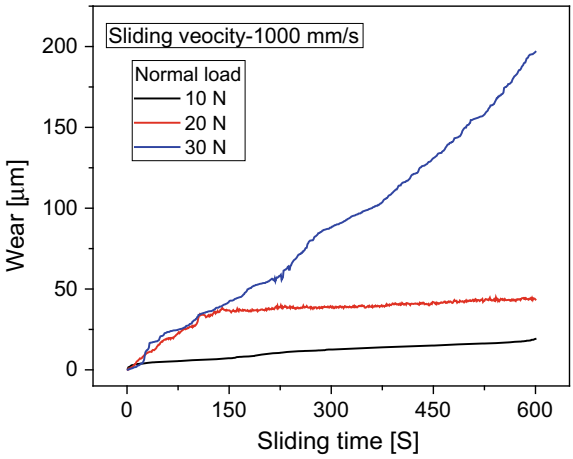

Fig. 53.3 Cumulative height loss against sliding time for NiTi–TiN-coated Ti–6Al–4V pin for sliding velocity of 1000 mm/s, under different normal loads (10, 20, and 30 N)

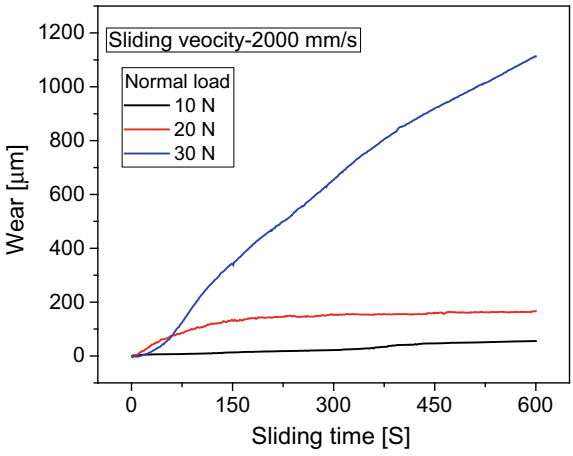

Fig. 53.4 Cumulative height loss against sliding time for NiTi–TiN-coated Ti–6Al–4V pin for sliding velocity of 2000 mm/s, under different normal loads (10, 20, and 30 N)

for employing 2000 mm/s sliding velocity and 30 N normal load, the final wear value exceeded the thickness of the coating or complete removal of the coating layer occurred. However, for all the other conditions, the coating remains to sustain under the employed sliding velocity and normal load conditions. Similarly, the wear values measured by Vernier caliper were plotted against applied normal load for two different sliding velocities that are depicted in Fig. 53.5.

Also, comparison of the final wear value measured by the data acquisition system (shown as a blue line in the plot), reveals that the wear values recorded by the data acquisition system are marginally higher than the wear value measured by Vernier caliper. It is perhaps due to the combined wear of the coated pin and the counter disk recorded by a data acquisition system, which is showing a higher value than the actual wear of the coated pin.

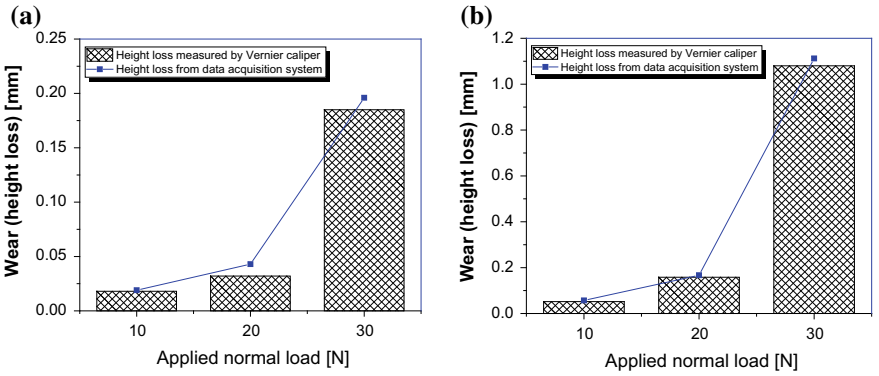

Fig. 53.5 Comparison of wear values of NiTi–TiN-coated Ti–6Al–4V alloy pins measured by Vernier caliper and obtained directly from data acquisition system after the abrasive wear test under different normal load conditions, for sliding velocity of **a** 1000 mm/s, and **b** 2000 mm/s

Figure 53.6 shows the comparison of wear or height loss of the NiTi–TiN-coated Ti–6Al–4V alloy pins for different sliding velocities (1000 and 2000 mm/s) under various normal loads. From the plots, it is clearly seen that the wear value is reasonably lower for sliding speed and normal load combination (1000 mm/s and 10 N), and the wear value is increasing with the increase of the applied normal load. From Fig. 53.4, a sharp increase in the wear value can be observed for 30 N load. Due to the high sliding velocity and normal load condition, catastrophic wear occurred on the coated pin, and extreme wear value was recorded.

From the plot, it can be inferred that the produced NiTi–TiN coating deposited on Ti–6Al–4V alloy is enabled to withstand the wear at the high sliding speed at lower

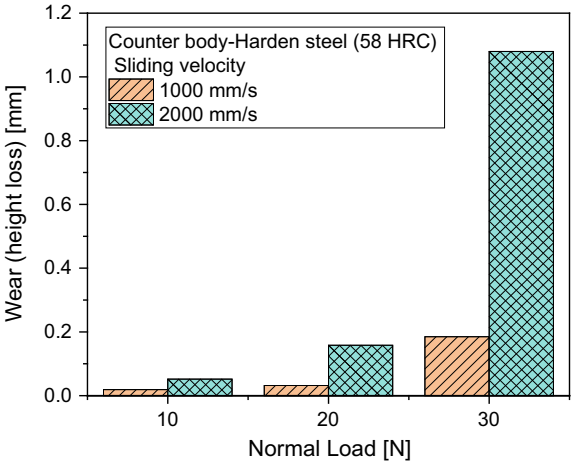

Fig. 53.6 Comparison of wear of the NiTi–TiN-coated Ti–6Al–4V alloy pins for different sliding velocities (1000 and 2000 mm/s) under various normal load conditions

load and above-average speed even at high load. However, the coating fails at high speed and high load combination within the experimental domain.

Figures 53.7 and 53.8 show the variation of coefficient of friction (COF) during the test for sliding velocities 1000 and 2000 mm/s for the alteration of normal load (10, 20, and 30 N). From the plots, for 1000 mm/s sliding velocity and relatively lower normal load (10 and 20 N), the steady-state COF value is approximately in the domain of 0.7. Whereas, for increasing the load (30 N) after a certain time, the COF value reduced to a value of approximately 0.5.

On the other side, for employing 2000 mm/s sliding velocity, it is evident that the steady-state COF value is approximately 0.7 for a normal load of 10 N. However, the COF value is found to have reduced after a certain time. Further, for employing

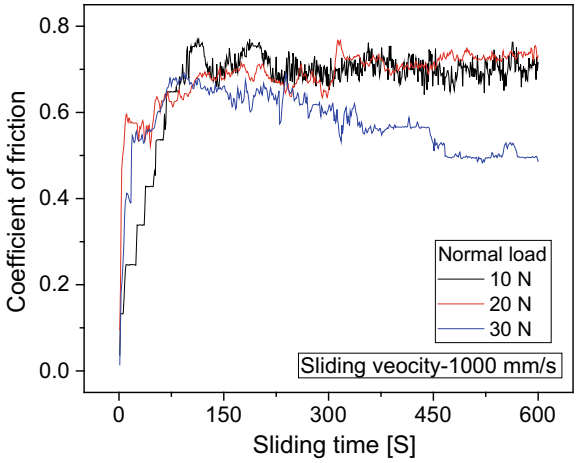

Fig. 53.7 Variation of the coefficient of friction (COF) during the test for sliding speed of 1000 mm/s, under different normal loads (10, 20, and 30 N)

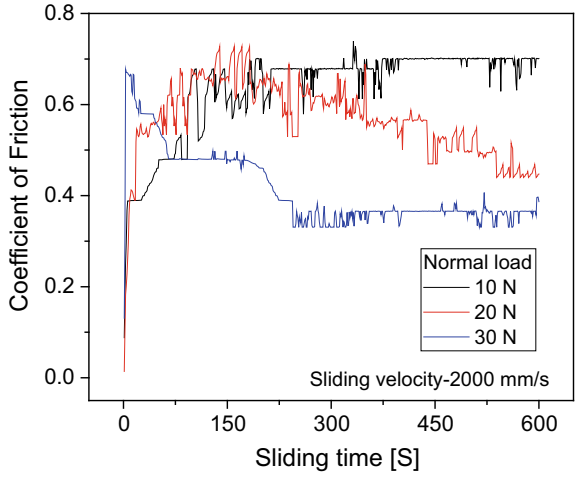

Fig. 53.8 Variation of the coefficient of friction (COF) during the test for sliding speed of 2000 mm/s under different normal loads (10, 20, and 30 N)

30 N load, it was found that the COF value reduced sharply and a lower steady-state COF value (0.38) was obtained after a specific time of the test.

53.4 Conclusions

From the analysis of the present tribological test of NiTi–TiN coating deposited by TIG cladding method on Ti–6Al–4V alloy, the following conclusions can be made.

The wear value of the coating gradually increases with the increase of normal load. At higher sliding velocity, the wear loss also was found larger for all different normal load conditions.

The produced NiTi–TiN coatings deposited on Ti–6Al–4V alloy were enabled to withstand the wear at high sliding speed and low normal load combination, and above-average speed even at high normal load within the experimental domain considered for the present study. However, the coating fails at high speed and high load combinations.

The steady-state coefficient of friction of the NiTi–TiN coating is in the range of 0.7, which is marginally higher than the COF value of the Ti–6Al–4V alloy. It was revealed that for higher load and sliding velocity combination, owing to the removal of the coating material, the COF value reduced down to 0.38, which is almost equivalent to the COF value of Ti–6Al–4V against the harden steel disk.

References

1. Dinesh, G.B., Melanie, K., Peter, J.B.: Effects of combined diffusion treatments and cold working on the sliding friction and wear behavior of Ti–6Al–4V. Wear **302**, 837–844 (2013)
2. Mao, Y.S., Wang, L., Chen, K.M., Wang, S.Q., Cui, X.H.: Tribo-layer and its role in dry sliding wear of Ti–6Al–4V alloy. Wear **297**, 1032–1039 (2013)
3. Guo, C., Zhou, J.S., Chen, J.M., Zhao, J.R., Yu, Y.J., Zhou, H.D.: Improvement of the oxidation and wear resistance of pure Ti by laser cladding at elevated temperature. Surf. Coat. Technol. **205**, 2142–2151(2010)
4. Weng, F., Chen, C., Yu, H.: Research status of laser cladding on titanium and its alloys: a review. Mater. Design **58**, 412–425 (2014)
5. Chiu, K.Y., Cheng, F.T., Man, H.C.: Laser cladding of austenitic stainless steel using NiTi strips for resisting cavitation erosion. Mater. Sci. Eng. A **402**, 126–134 (2005)
6. Buehler, W.J., Wang, F.E.: A summary of recent research on the Nitinol alloys and their potential application in ocean engineering. Ocean Eng. **1**, 105–120 (1968)
7. Cheng, F.T., Lo, K.H., Man, H.C.: NiTi cladding on stainless steel by TIG surfacing process: Part I. Corrosion behavior. Surf. Coat. Technol. **172**, 316–321 (2003)
8. Weng, F., Yu, H., Chen, C., Liu, J., Zhao, L: Microstructures and properties of TiN reinforced Co-based composite coatings modified with Y_2O_3 by laser cladding on Ti6Al4V alloy. J. Alloys Compd. **650**, 178–184 (2015)

9. Sahoo, C.K., Soni, L., Masanta, M.: Evaluation of microstructure and mechanical properties of TiC/TiC steel composite coating produced by gas tungsten arc (GTA) coating process. Surf. Coat. Technol. **307**, 17–27 (2016)
10. Tijo, D., Das, A.K., Masanta, M.: In-situ TiC-TiB_2 coating on Ti-6Al-4V alloy by tungsten inert gas (TIG) cladding method: Part-I. Microstructure evolution. Surf. Coat. Technol. **344**, 541–552 (2018)

Chapter 54
Sliding Abrasive and Adhesive Wear Behavior of TIG-Cladded NiTi–W Coating Deposited on Ti–6Al–4V Alloy

Jyotirmoy Singh Garbyal, Chinmaya Kumar Padhee, Abdu Raheem and Manoj Masanta

Abstract The wear characteristic of NiTi–W composite layer developed on Ti–6Al–4V alloy by using TIG cladding route was evaluated. The NiTi–W composite coating fabricated with preplaced Ni–Ti–W powder with 9:9:2 weight ratio and at 60 A current and 2.3 mm/s scan speed has been tested against an abrasive disk and hardened steel (HRC 58) under different normal load and sliding velocity conditions to analyze its sliding abrasive wear and adhesive wear behaviors. The effect of test conditions on the wear characteristic of the NiTi–W clad layer was analyzed in-depth and compared with the wear characteristic of the uncoated Ti–6Al–4V alloy. It was found that the NiTi–W composite coating shows up to eleven times better wear resistance than the uncoated Ti–6Al–4V alloy under abrasive wear test conditions and more than seven times under sliding adhesive test condition.

Keywords TIG cladding · NiTi–W coating · Ti–6Al–4V alloy · Wear resistance

54.1 Introduction

Titanium and its alloys find lots of applications in industries like aerospace, medical, and military due to some of its properties like specific strength, good corrosion resistance, and decent high temperature [1–3]. With the aim of reducing weight, Ti alloys are employed in spacecraft bearings instead of steel. But their relatively low surface hardness and poor wear resistance lead to a great problem in these applications [4]. An effective way to improve the surface properties of the Ti–6Al–4V alloy is the deposition of the ceramic reinforced hard coating layer by laser cladding or alloying route [5, 6]. However, laser processing is quite expensive and requires complicated arrangements. On the other hand, tungsten inert gas (TIG) cladding process stands apart due to its low-cost and easy-to-operate characteristics. It is pertinent to a range of

J. S. Garbyal · C. K. Padhee · A. Raheem · M. Masanta (✉)
Department of Mechanical Engineering, National Institute of Technology Rourkela, Rourkela 769008, India
e-mail: manoj.masanta@gmail.com

M. S. Shunmugam and M. Kanthababu (eds.), *Advances in Micro and Nano Manufacturing and Surface Engineering*, Lecture Notes on Multidisciplinary Industrial Engineering,
https://doi.org/10.1007/978-981-32-9425-7_54

materials, and the heat input can be controlled accurately by changing the processing current and scan speed [7, 8].

NiTi intermetallic alloy received enormous attention due to its shape memory and superelasticity properties in addition to its high hardness, excellent resistance to corrosion and ability to maintain stability at high temperature. Additionally, the NiTi coating is highly compatible with Ti–6Al–4V alloy [9]. Tungsten (W) is a dense metal with strength comparable to that of titanium and is also known for its high wear and corrosion resistance. Hence, it is expected that NiTi–W composite would increase the tribological properties of Ti–6Al–4V alloy substrate, without affecting its bulk properties. However, no definite work till now emphasizes the development of NiTi–W composite coating for wear-resistance applications.

The aim of this work is to analyze the wear characteristic of NiTi–W coating layer deposited on Ti–6Al–4V alloy by using the TIG cladding method. The NiTi–W composite coating layer fabricated at a specific processing condition has been tested against the abrasive disk and the hardened steel (HRC 58) disk under different normal load conditions to analyze its sliding abrasive wear and adhesive wear behaviors. The effect of test conditions on the wear behavior of the coating was analyzed in-depth and compared with the wear behavior of uncoated Ti–6Al–4V alloy.

54.2 Materials and Methodology

For the present work, TIG-cladded NiTi–W composite coating tracks deposited on Ti–6Al–4V alloy plate of 5 mm thickness were used. The deposition of the coating was performed by scanning the TIG arc on Ni–Ti–W (9:9:2 wt. ratio) pre-coated powder on Ti–6Al–4V alloy plate at 60 A current and 2.3 mm/s scan speed under atmosphere. Details of the TIG cladding procedure may be available elsewhere [10]. After the TIG cladding was done, the NiTi–W coating tracks were cut in the cylindrical shape of 4 mm diameter, so that the pin-on-disk wear test could be performed. The coated surfaces of pins were polished with polishing paper to flatten the surface and remove any oxidized layer and impurities.

The tribological tests were performed under sliding abrasive and adhesive conditions under different normal loads and sliding speeds. These are considered as variables using a pin-on-disk type tribometer as per the ASTM G99 standard. Sliding abrasive condition was created by attaching an abrasive disk on the rotating disk of the tribometer disk, and adhesive sliding wear test was done against the hardened steel disk. Figure 54.1 shows the pin-on-disk wear setup for sliding abrasive wear test and adhesive wear test arrangement. The detailed conditions for the sliding abrasive and adhesive wear tests are mentioned in Table 54.1. The wear values of the coated and the uncoated samples were assessed in terms of height loss during the wear test. The height loss due to wear was calculated from the height measurement of the pin samples before and after the test using a Vernier caliper. Additionally, the height loss of the pin samples was also noted against the test time using a data acquisition system equipped with the pin-on-disk wear test rig. After the wear test, SEM analysis on the

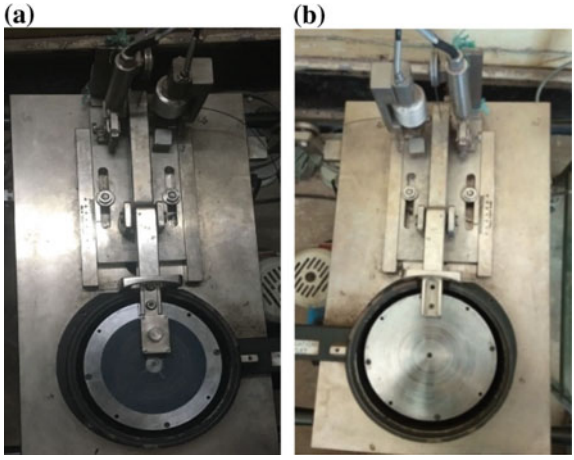

Fig. 54.1 Pin-on-disk wear test setup. **a** Abrasive type and **b** adhesive type

Table 54.1 Pin-on-disk wear test conditions

	Abrasive wear test	Adhesive wear test
Counter body	SiC abrasive disk (Ra = 15 μm)	Hardened steel (HRC 58)
Track wear radius (D) (mm)	75	75
Sliding speed (V) (mm/s)	260	1000
RPM	66	250
Test duration (T) (min)	5	10

worn surfaces was also carried out to study the wear characteristics under different test conditions.

54.3 Results and Discussion

54.3.1 Sliding Abrasive Wear Test

After the wear test, the height loss was calculated and recorded in Table 54.2. Figure 54.2 represents comparative height loss of NiTi–W-coated pins under various normal load conditions and uncoated Ti–6Al–4V alloy pin (tested at 5 N load) after the abrasive wear test. The graph clearly shows that the reduction of the height of the NiTi–W-cladded pins is significantly lower than the Ti–6Al–4V alloy pin. For 5 N load, the height loss of the Ti–6Al–4V alloy pin was found almost eleven times higher than NiTi–W coating. It may also appear that the wear of uncoated Ti–6Al–4V

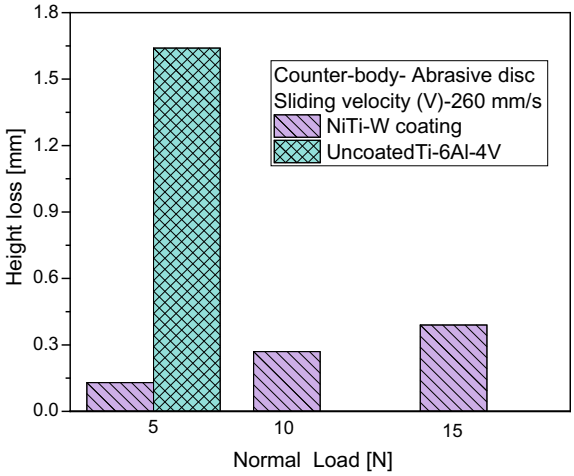

Fig. 54.2 Comparison of wear or height loss of the NiTi–W-coated pins and uncoated Ti–6Al–4V alloy pin after the wear test for various applied normal load

Table 54.2 Calculation of height loss for sliding abrasive wear test

Sample	Load (N)	Initial height of pin (mm)	Final height of pin (mm)	Height loss (mm)
NiTi–W-coated Ti–6Al–4V pin	5	5.66	5.51	0.15
	10	5.69	5.37	0.32
	15	5.67	5.28	0.39
Uncoated Ti–6Al–4V pin	5	5.22	3.58	1.64

alloy pin at 5 N load is also higher than the wear of coated pins performed at 10 or 15 N normal load.

These wear data signifies a considerable improvement in the wear value for deposition of NiTi–W coating on the Ti–6Al–4V alloy. The plot clearly shows that with an increase of normal load, the wear value of the coated pin gradually increases during the abrasive wear test. Further, the wear or height loss recorded directly by the data acquisition system was also plotted against the test time for the NiTi–W-coated pin under three different normal load conditions (5, 10, and 15 N), and for the Ti–6Al–4V alloy pin for 5 N normal load as illustrated in Fig. 54.3. From the plots, it is evident that the wear or height loss for all the samples increases gradually with the test time. However, depending on the applied normal load the rate of wear varyies, and it is revealed that for the enhancement of the applied load, the rate of wear increases considerably and higher final wear value is obtained for the high normal load. Figure 54.3b which represents the wear plot for Ti–6Al–4V alloy

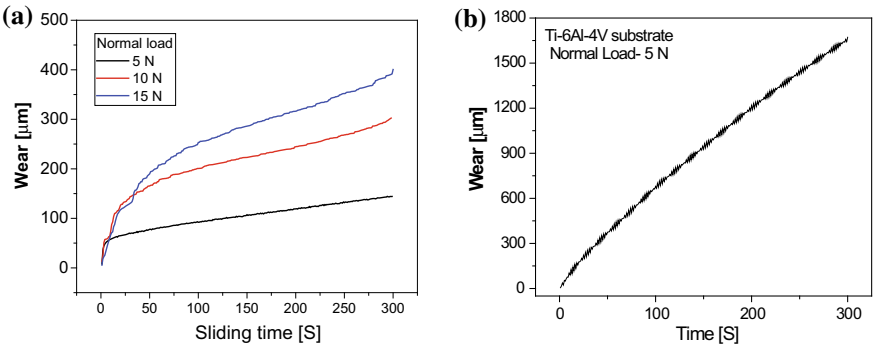

Fig. 54.3 Wear or height loss of **a** NiTi–W-coated Ti–6Al–4V pin for different normal loads (5, 10, and 15 N), **b** uncoated Ti–6Al–4V pin for 5 N

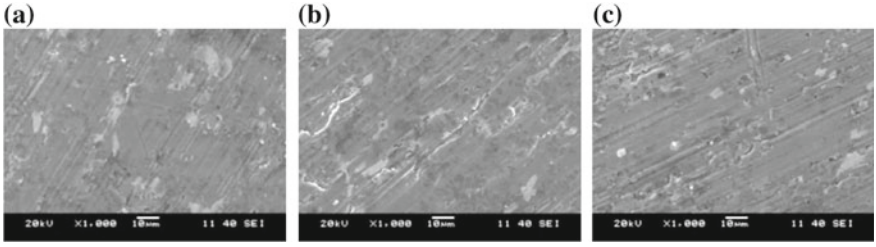

Fig. 54.4 SEM images of worn surfaces of the NiTi–W-coated Ti–6Al–4V pin after the wear test under different normal loads **a** 5, **b** 10, and **c** 15 N

pin shows a drastically higher wear rate and final wear value than that obtained for NiTi–W-coated Ti–6Al–4V alloy pin samples.

Figure 54.4 depicts the SEM images of worn surfaces of the NiTi–W-coated Ti–6Al–4V pin for employing various normal loads. From the images, it is noticed that at lower normal load (5 N), the scratch intensity on the worn out surface, which was created during the sliding of abrasive particles against the coated sample is relatively less. However, with the augmentation of normal load, the scratch intensity on the worn-out surface increases. Thus, there is an enhancement in the wear rate or overall wear is observed to increase with the employed load.

54.3.2 Sliding Adhesive Wear Test

Similarly sliding adhesive wear test was also performed on the pin-shaped coated as well as uncoated samples. However, after the test, the height loss was measured for both NiTi–W-coated and uncoated Ti–6Al–4V alloy pin and recorded as demonstrated in Table 54.3. Figure 54.5 represents the height loss of the NiTi–W-coated

Table 54.3 Calculation of height loss for adhesive wear

Sample	Load (N)	Initial height of pin (mm)	Final height of pin (mm)	Height loss (mm)
NiTi–W-coated Ti–6Al–4V pin	10	5.61	5.594	0.016
	20	5.64	5.612	0.028
	30	5.67	5.614	0.048
Uncoated Ti–6Al–4V pin	10	5.51	5.47	0.04
	20	5.65	5.51	0.14
	30	5.63	5.29	0.34

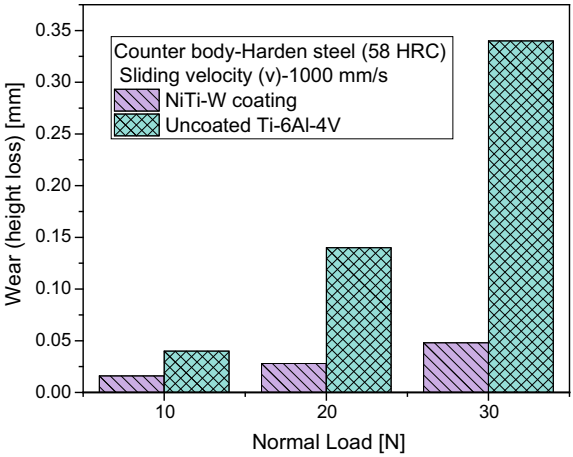

Fig. 54.5 Comparison of wear or height loss of the NiTi–W-coated pins and Ti–6Al–4V alloy pin after the adhesive wear test under different normal load conditions

pins and Ti–6Al–4V alloy pins after the sliding wear test against the hardened steel disk (HRC 58) under different normal load conditions as measured by a Vernier caliper. From the plot, it is clearly evident that the height losses of the NiTi–W-coated Ti–6Al–4V alloy pins are reasonably lower than the uncoated pin for all different normal load conditions. Comparing the wear values with the sliding abrasive wear as plotted in Fig. 54.2, it can be distinctly seen that the sliding wear against the hardened steel plate is much lower (almost ten times) than the sliding wear test performed against the abrasive disk, even when the tests against the hardened steel plate were performed at higher sliding velocity, higher normal load, and for a longer duration. The wear of the uncoated Ti–6Al–4V alloy was also found to be relatively lower compared to the wear value attained against the abrasive disk. For both NiTi–W coating and uncoated Ti–6Al–4V alloy pins, an incremental wear value was recorded for increasing the normal load from 10 to 30 N.

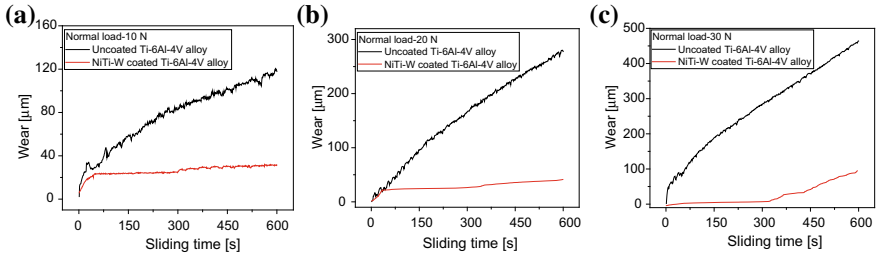

Fig. 54.6 Comparison of adhesive wear between NiTi–W-coated Ti–6Al–4V pin and uncoated Ti–6Al–4V pin for different normal loads **a** 10, **b** 20, and **c** 30 N

The aggregate wear or height loss for the NiTi–W-coated pin, and Ti–6Al–4V alloy was also recorded through a data acquisition system and compared for different normal load conditions (10, 20, and 30 N) as illustrated in Fig. 54.6a–c. The plots show that the cumulative wear for both NiTi–W-coated pin and uncoated Ti–6Al–4V alloy pin samples increases gradually with the sliding time for all different applied normal load conditions. However, the rate of wear for the uncoated pin sample is much higher than the NiTi–W-coated pin samples. It is also noted that with the enhancement of the employed normal load, the wear rates, as well as the final wear values, were increased considerably.

Figure 54.7 shows the SEM images of the NiTi–W-clad surface after the adhesive wear test under a normal load of 10, 20, and 30 N for using the sliding velocity of 1000 mm/s. The images show that at lower normal load, the worn surface is very smooth, without any scratches. However, with the increase of load, it is evident that some scratches are formed, which is probably created due to the removal of coating material and subsequent action of those particles on the coated surface at higher load. Hence, the wear value of the coated pin amplified with the rise of the employed normal load.

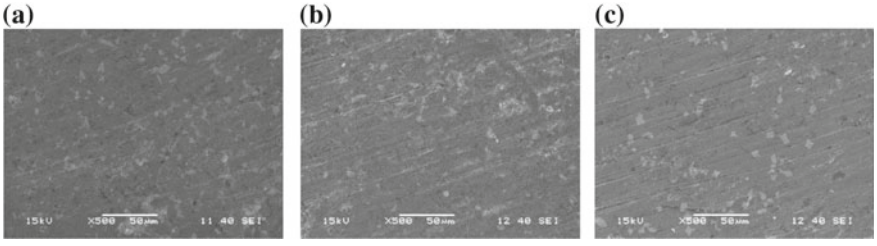

Fig. 54.7 SEM images of worn surfaces of the NiTi–W-coated Ti–6Al–4V pin after the sliding adhesive wear test under different normal loads **a** 10, **b** 20, and **c** 30 N

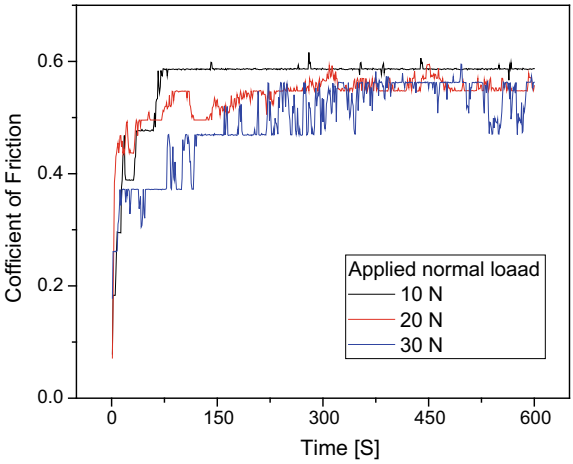

Fig. 54.8 Coefficient of friction of NiTi–W coating against the hardened steel (HRC 58) for different normal loads **a** 10, **b** 20, and **c** 30 N

54.3.3 COF for Adhesive Wear

In addition, during the sliding adhesive wear test, the coefficient of friction of the coated samples wear was also noted. Figure 54.8 depicts the coefficient of friction (COF) of NiTi–W coating as recorded with respect to the test time against the hardened steel disk (HRC 58) for different normal load conditions (10, 20, and 30 N). The plots show that the steady-state COF of the NiTi–W composite coating is in the range of 0.54–0.58.

54.4 Conclusions

From the present experimental analysis, the following conclusions can be made.

- The NiTi–W composite coating fabricated on Ti–6Al–4V alloy improves the wear resistance of the substrate material significantly against both, the sliding abrasive disk (abrasive wear) and the hardened steel disk (adhesive wear).
- The NiTi–W composite coating shows up to eleven times better wear resistance than the uncoated Ti–6Al–4V alloy under abrasive wear test condition and more than seven times better under sliding adhesive test condition.
- The sliding abrasive wear performance of the coating is much higher than the wear test carried out against the hardened steel plate.
- The steady-state COF of the NiTi–W composite coating developed by TIG cladding route was found in the range of 0.54–0.58.

References

1. Molinria, A., Straffelinia, G., Tesia, B.: Dry sliding wear mechanisms of the Ti-6Al-4V alloy. Wear **208**, 105–112 (1997)
2. Banerjee, D., Williams, J.C.: Perspectives on titanium science and technology. Acta Mater. **61**, 844–879 (2013)
3. Waghmare, D.T., Padhee, C.K., Prasad, R., Masanta, M.: NiTi coating on Ti-6Al-4V alloy by TIG cladding process for improvement of wear resistance: microstructure evolution and mechanical performances. J. Mater. Process. Technol. **262**, 551–561 (2018)
4. Kustas, F.M., Misra, M.S.: ASM Handbook: Friction and Wear of Titanium Alloys. ASM International (1991)
5. Galvan, D., Ocelík, V., Pei, Y., Kooi, B.J., De Hosson, J.T.M., Ramous, E.: Microstructure and properties of TiB/Ti-6Al-4V coatings produced with laser treatments. J. Mater. Eng. Perform. **13**, 406–412 (2004)
6. Lin, Y.H., Lei, Y.P., Li, X.Q., Zhi, X.H., Fu, H.G.: A study of TiB_2/TiB gradient coating by laser cladding on titanium alloy. Opt. Lasers Eng. **82**, 48–55 (2016)
7. Buytoz, S., Ulutan, M.: In situ synthesis of SiC reinforced MMC surface on AISI 304 stainless steel by TIG surface alloying. Surf. Coat. Technol. **200**, 3698–3704 (2006)
8. Saroj, S., Sahoo, C.K., Masanta, M.: Microstructure and mechanical performance of TiC-Inconel825 composite coating deposited on AISI 304 steel by TIG cladding process. J. Mater. Process. Technol. **249**, 490–501 (2017)
9. Gao, F., Wang, H.M.: Dry sliding wear property of a laser melting/deposited Ti_2Ni/TiNi intermetallic alloy. Intermetallics **16**, 202–208 (2008)
10. Sahoo, C.K., Masanta, M.: Microstructure and mechanical properties of TiC-Ni coating on AISI304 steel produced by TIG cladding process. J. Mater. Process. Technol. **240**, 126–137 (2017)

Chapter 55
Investigation of Surface Coating on Inconel 718 Alloy with Silicon Carbide Powder

S. S. Nivas and P. Balasubramanian

Abstract Inconel 718 is a nickel-based superalloy that is extensively used in a broad range of applications such as turbine blades, power generation, petroleum, and nuclear reactor technology due to its good mechanical properties at intermediate and high temperatures. It has been widely used because of its high plasticity and good corrosion resistance. But poor wear resistance of Inconel 718 limits its usage in some applications. In order to perform surface modification of Inconel 718, several surface treatment methods are used. Hence, Electrical Discharge Alloying was performed on Inconel 718 alloy with silicon carbide powder in a medium of dielectric fluid-like EDM oil using reverse polarity in an EDM machine. The experiments were conducted using orthogonal array of Taguchi L9 technique with the input process parameters like current, pulse on time, and pulse off time. The surface modification is studied by analyzing the surface roughness of the alloyed surface using Mitutoyo SJ-210 roughness tester. The alloyed layer of base material Inconel 718 is characterized by using SEM and EDAX. The experiment shows that pulse on time has a major role than other parameters like peak current and pulse off time.

Keywords Electrical Discharge Alloying · Inconel 718 · Surface roughness · Silicon carbide · Taguchi technique

55.1 Introduction

Surface coating is a practice to change the surface of the metals to accomplish the important mechanical properties like wear resistance, resistance at the elevated temperature, hardness, and impact strength without much change to the core. Some of the main processes are physical vapor deposition, chemical vapor deposition, lithography, laser cladding, etc. These methods need high vacuum and specialized devices.

S. S. Nivas (✉) · P. Balasubramanian
Department of Mechanical Engineering, A.V.C. College of Engineering, Mayiladuthurai 609305, India
e-mail: nivasmechanical@gmail.com

M. S. Shunmugam and M. Kanthababu (eds.), *Advances in Micro and Nano Manufacturing and Surface Engineering*, Lecture Notes on Multidisciplinary Industrial Engineering,
https://doi.org/10.1007/978-981-32-9425-7_55

Fig. 55.1 EDM machine

55.1.1 Electrical Discharge Alloying

Electro Discharge Alloying (EDA) is a new technique in this present scenario to coat the material over the surface adopting reverse polarity [1–4] using the electrical discharge machine [5]. Unlike others, here it needs only an electrical discharge machine with specified input parameters to increase wear resistance and hardness of the parent material. In this research work, surface modification has been done by alloying SiC powder on the surface of Inconel 718 by Electrical Discharge Alloying [10] process. High accuracy is needed to obtain the required mechanical properties for the concerned component in industries (Fig. 55.1).

55.1.2 Inconel 718 Alloy

Inconel 718 alloy is a kind of superalloy which belongs to Ni–Cr family which covers a wide range of compositions and mechanical properties. Ni and Cr give a struggle against corrosion, oxidation, carburizing, and other damage mechanism acting at high temperature. It has good cryogenic properties, good fatigue, and mechanical strength at moderate temperatures, and relatively good creep behavior. For this reason, it is widely used in gas turbine blades, nuclear power plant, submarine, rocket engines, heat exchangers, and cryogenic applications. The compositions of Inconel 718 are given in Table 55.1.

Table 55.1 Chemical compositions of Inconel 718

Metals	Composition (%)
Carbon (C)	0.08
Silicon (Si)	0.35
Manganese (Mn)	0.35
Phosphorus (P)	0.015
Sulfur (S)	0.015
Chromium (Cr)	21.00
Molybdenum (Mo)	3.3
Copper (Cu)	0.30
Niobium (Nb)	5.5
Aluminum (Al)	0.3
Titanium (Ti)	1.15
Nickel (Ni)	55.00
Iron (Fe)	Balance

55.1.3 Silicon Carbide

Silicon carbide means carborundum that contains silicon and carbon, popularly known as SiC. It is usually found in natural minerals namely moissanite. Silicon carbide has been using as an abrasive since 1893 because of its outstanding properties, such as good thermal shock resistance, brilliant oxidation resistance, strength retention to high temperatures, great wear resistance, and high thermal conductivity.

55.1.4 Surface Roughness

Roughness is one of the main functions to measure the texture of the surface. It is calculated by the vertical eccentricities of the real surface from the flawless surface. If the difference is large, the surface is said to be rough and if they are minor, the surface is smooth. While alloying, the melted material is not flushed away completely and considerable material solidifies to form discharge craters on the top surface of workpiece. Roughness measurement is attained using Mitutoyo SJ-210 roughness tester.

55.2 Experimental Details

The experimental details are shown in Table 55.2.

Table 55.2 Experimental details

Material	Electrode	Polarity
Inconel 718	Copper	Reverse

Table 55.3 Factors and levels

Factor/level	Peak Current (A)	Pulse On Time (μs)	Pulse Off Time (μs)
Low	6	25	3
Medium	8	50	6
High	10	75	9

The number of experiments to be run is set as 9 through Taguchi L9 orthogonal array [9]. The factors and levels for the L9 run are mentioned in Table 55.3.

55.2.1 Working Procedure

Electrical Discharge Alloying (EDA) was performed over the end surface of Inconel 718 alloy with silicon carbide powder mixed in the dielectric fluid EDM oil [7] to obtain better coating. The workpieces are prepared in the form of a cylindrical shape having diameter 8 mm, with the length 30 mm. A standard copper electrode of size 10 mm diameter is taken as a tool for EDM machine and it is immersed in the dielectric fluid. The semiautomatic EDM machine energized by 35 A pulse generators in reverse polarity is used for the alloying process. The recirculation dielectric fluid tank is provided in EDM machine which has capacity of 300 L. 75 g of the silicon carbide powder is suspended for the alloying process. A separate machining tank is provided for mixing the powder with EDM oil, which has a capacity of 10% of the main fluid tank. Dielectric fluid is recirculated by using a pump. Inconel 718 pin was locked in the fixture provided and then a standard copper electrode is fitted in the tool head against the top surface of the workpiece. Then the pump is switched ON and the machining tank is filled with EDM oil and preferred quantity of silicon carbide powder is mixed in it. The input parameters like peak current, pulse off and on time are set based on the Taguchi's L9 orthogonal array design which is shown in Table 55.3. Now the alloying process is performed for 7 min over the surface of Inconel 718 and accordingly, further workpieces are also alloyed. The structural properties of the alloyed surface were characterized by scanning electron microscope (SEM). The chemical composition of the alloyed surface was determined by energy dispersive spectroscopy (EDS). The surface roughness Ra is measured by means of Mitutoyo SJ-210 roughness tester (Figs. 55.2 and 55.3).

Fig. 55.2 Unalloyed Inconel 718

Fig. 55.3 Alloyed Inconel 718

55.2.2 Observation

A Taguchi design or orthogonal array is used to design the experimental procedure using different types of designs like two, three, four, five, and mixed level. Here, a three factor with two-level setup is chosen with a total of nine of experiments being conducted and hence the L9 was chosen. The orthogonal array for L9 and the output response were tabulated in Table 55.4.

Table 55.4 Response data

S. No.	Current (A)	PON (μs)	POFF (μs)	Ra (μm)
1	6	25	3	1.705
2	6	50	6	1.211
3	6	75	9	2.478
4	8	25	6	1.034
5	8	50	9	1.725
6	8	75	3	1.569
7	10	25	9	1.39
8	10	50	3	1.93
9	10	75	6	1.823

55.3 Results and Discussion

55.3.1 Surface Roughness

From the response Table 55.3, it clearly shows that, the minimum roughness value of 1.034 μm is obtained when the current is 8 A, pulse on time is 25 μs and pulse off time is 6 μs.

55.3.2 SN Ratio

The SN ratio for the surface roughness calculated using Minitab software is shown in Table 55.5.

Table 55.5 SN ratio

S. No.	Current (A)	PON (s)	POFF (s)	Ra (m)	SN ratio
1	6	25	3	1.705	−4.63449
2	6	50	6	1.211	−1.66288
3	6	75	9	2.478	−7.88203
4	8	25	6	1.034	−0.29041
5	8	50	9	1.725	−4.73578
6	8	75	3	1.569	−3.91246
7	10	25	9	1.39	−2.8603
8	10	50	3	1.93	−5.71115
9	10	75	6	1.823	−5.21573

55.3.3 Main Effects Plots

The main effect plot for mean and SN ratio for surface roughness is depicted in Figs. 55.4 and 55.5. The main effect plot for the mean roughness value reveals that the mean roughness is decreased when the current increases. The same is increased when the pulse on time increases and the same behavior happened to the pulse off time similar to the pulse on time (Table 55.6).

The SN ratio value is increased when the current increases, it decreases when the pulse on and pulse off decrease.

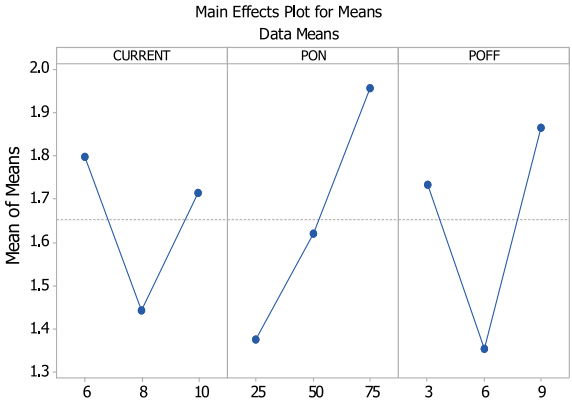

Fig. 55.4 Main effect plot for mean—surface roughness

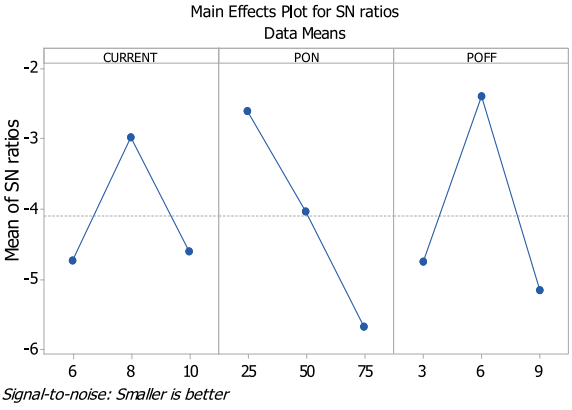

Fig. 55.5 Main effect plot for SN ratio—surface roughness

Table 55.6 Rank table

Level	current	PON	POFF
1	1.798	1.376	1.735
2	1.443	1.622	1.356
3	1.714	1.957	1.864
Delta	0.355	0.58	0.508
Rank	3	1	2

55.3.4 Surface Morphology

The scanning electron microscope [6] was carried out for the workpiece which consists of optimum parameters (current—6 A, pulse on time—25 μs, and pulse off time—6 μs) which is shown in Fig. 55.6.

The SEM image clearly shows that there were some blow holes [8] due to high current. SiC particles were also present on the alloyed layer. The surface was observed to be coarse because of debris which were not flowed away entirely from the specimen. The discharge between the workpiece and tool melts the metal and the metal vaporizes which creates thermally altered layers of the cavity. The white layer present over the surface shows the martensite, residual austenite, and some undissolved carbide.

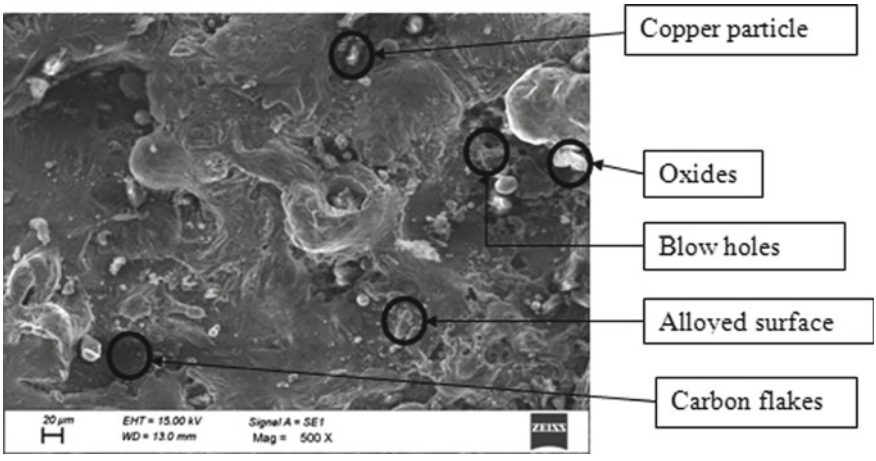

Fig. 55.6 SEM view of the alloyed layer of Inconel 718

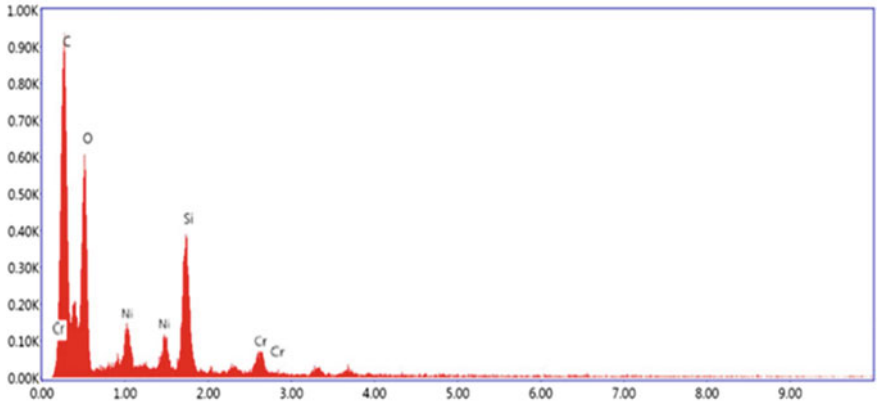

Fig. 55.7 Energy-dispersive X-ray spectroscopy

Table 55.7 Element composition through EDAX

Element	Weight %	Atomic %
C K	52.20	62.49
O K	32.90	29.57
Ni K	4.29	2.68
Si K	6.87	3.52
Cr K	1.99	0.81

55.3.5 Energy-Dispersive X-Ray Spectroscopy

The EDAX [6] spectroscopy was carried out in the same sample for the purpose of fiunding the compositions of elements present in the alloyed layer. It is shown in Fig. 55.7.

From the EDAX test, it is clearly shown that carbon is present around 63% and Si is present around 4%. Some other elements are also present in the alloyed layer as in Table 55.7.

55.4 Conclusion

The surface roughness is minimum when the current rate is 8 A, pulse on time is 25 μs, and pulse off time is 6 μs. Furthermore, it has been found that the current rate is fixed at 6 A with pulse on time of 75 μs and pulse off time of 9 μs getting higher surface roughness. It has been observed that of pulse on time and pulse off time decrease, even though increase of current minimizes the surface roughness. Silicon carbide is effectively deposited on the surface of Inconel with better bonding.

References

1. Chen, W.-C., Lin, H.-M., Uan, J.-Y.: Formation and characterization of self-lubricated carbide layer on AA6082 Al-Mg-Si aluminium alloy by electrical discharge alloying process. Trans. Nonferrous Metals Soc. China **26**, 3205–3218 (2016)
2. Bai, C.-Y., Koo, C.-H., Wang, C.-C.: Electrical discharge surface alloying of super alloy Haynes 230 with aluminium and silicon carbide. Corros. Sci. (ScienceDirect) **49**, 3889–3904 (2004)
3. Khan, A.A., Ndaliman, M.B., Zain, Z.M., Jamaludin, M.F., Patthi, U.: Surface modification using electric discharge machining (EDM) with powder addition. Appl. Mech. Mater. **110–116**(2012), 725–733 (2012). https://doi.org/10.4028/www.scientific.net/AMM.110-116.725
4. Ho, K.H., Newman, S.T.: State of the art electrical discharge machining (EDM). Int. J. Mach. Tools Manuf **43**, 1287–1300 (2003)
5. Balasubramanianan, P., Senthilvelan, T.: A comparative study on the performance of different sintered electrodes in electrical discharge machining. Trans. Indian Inst. Met. **68**(1), 51–59 (2015)
6. Algodi, S.J., Murray, J.W., Fay, M.W., Clare, A.T., Brown, P.D.: Electrical discharge coating of nanostructured TiC-Fe cermets on 304 stainless steel. Surf. Coat. Technol. **307**, 639–649 (2016)
7. Furutani, K., Sato, H., Suzuki, M.: Influence of electrical conditions on performance of electrical discharge machining with powder suspended in working oil for titanium carbide deposition process. Int. J. Adv. Manuf. Technol. **40**, 1093–1101 (2009). https://doi.org/10.1007/s00170-008-1420-x
8. Sumi, N., Kato, C., Shimada, K., Yuzawa, T., Teramoto, H., Mizutani, M., Kuriyagawa, T.: Mechanism of defect generation in the TiC layer and Si layer by electrical discharge coating. Procedia CIRP **42**, 221–225 (2016)
9. Arun, I., Duraiselvam, M., Senthilkumar, V.: Modelling and analysis of electrical discharge alloying through Taguchi technique. Appl. Mech. Mater. **592–594**, 521–524 (2014)
10. Janmanee, P., Muttamara, A.: Surface modification of tungsten carbide by Electrical Discharge Coating (EDC) using a titanium powder suspension. Appl. Surf. Sci. **258**(19), 7255–7265 (2012)

Chapter 56
Effect of Sensitization on Electroless Nickel Plating of MoS_2 Nanoparticles

N. Arunkumar, P. Eashwar Siddharth, Aravind Parthiban, K. Dhanapal, A. Stephen and N. E. Arun Kumar

Abstract In this work, the effect of the sensitization process on the electroless nickel coating over the MoS_2 particle surface was studied. The surface of the MoS_2 particles was coated with nickel (Ni) using the electroless plating method because it is relatively efficient and cost effective. Two samples were synthesized; while one of them was sensitized using SN, the other was not sensitized and both samples were annealed after the plating process. The XRD pattern of the surface of both samples showed the presence of Ni in *fcc* structural phase along with MoS_2 phase. The surface morphology of all the samples was observed using FESEM and it is observed that the treatment with SN forms a uniform coating over the MoS_2 particles along with rod-like structures whereas the non-sensitized sample shows irregular coating of Ni over MoS_2 particles without rod-like structures.

Keywords Electroless deposition · Surface sensitization · Structural information · Surface morphology

56.1 Introduction

Hybrid metal matrix composites are increasingly being used for their enhanced physical, chemical, and mechanical properties compared to monolithic metals [1]. These composites also exhibit reduced wear rate that can be attributed to the presence of ceramic and/or solid lubricant particulates [2, 3]. Graphite is a commonly used solid lubricant that significantly decreases the wear of the composite. Another widely used solid lubricant is MoS_2 and in an attempt to increase its wettability in the aforementioned composite, nickel coating is carried out [4]. The nickel coating on

N. Arunkumar (✉) · P. Eashwar Siddharth · A. Parthiban · N. E. Arun Kumar
Department of Mechanical Engineering, St. Joseph's College of Engineering, Chennai 600 119, India
e-mail: narunkumar72@gmail.com

K. Dhanapal · A. Stephen
Materials Science Centre, Department of Nuclear Physics, University of Madras, Guindy Campus, Chennai 600 025, India

M. S. Shunmugam and M. Kanthababu (eds.), *Advances in Micro and Nano Manufacturing and Surface Engineering*, Lecture Notes on Multidisciplinary Industrial Engineering,
https://doi.org/10.1007/978-981-32-9425-7_56

these particulates leads to an increase in the hardness of the composite and its load-carrying capacity [5, 6]. The most cost-effective and viable method for coating of transition metals over the surface of particles is the electroless deposition method [7–13]. Unlike graphite, MoS_2 does not require gases or vapors for effective lubrication [14].

In this paper, the MoS_2 particles are coated with Ni using the electroless method and the effect of the sensitization process on the surface morphology of MoS_2 particles were studied.

56.2 Experimentation

56.2.1 Pretreatment of MoS_2 Surface

Sensitized Ni–MoS_2 (Sample 1).

Cleaning:

The commercially available MoS_2 powder was first cleaned using ethanol. For the cleaning process, 1 g of MoS_2 was ultrasonically dispersed for 30 min in 40 ml of ethanol. After ultra-sonication, distilled water was added to the solution in order to rinse the particles. The rinsing was followed by decanting after allowing the particles to settle down; this process of rinsing and decanting was done in tandem. After the first rinse, the particles took nearly 3 h to settle down in the beaker. However, the time taken by the particles to settle down reduces with subsequent rinsing. In order to completely rinse the particles, the above-stated rinsing and decanting processes were carried out four times. Once the cleaning process was completed, the sample was dried using a heating mantle at 60 °C.

Oxidation:

After manually grinding the sample, it is then oxidized at 200 °C for 1 h in a tubular furnace. The sample was placed in an alumina boat and this boat was covered using aluminum foil in order to prevent spillage of the sample during material handling. The boat was placed inside a quartz tube which is strategically positioned in the tubular furnace. The furnace has a heating rate of 6 °C/min, but cooling was allowed to happen naturally. Once the furnace cools down to room temperature, the sample is transferred to a hydrophilic solution.

Hydrophilic treatment:

The sample is ultrasonically dispersed for 30 min in the hydrophilic solution which comprises 10% HF/10% HCl in 40 ml of distilled water. After ultra-sonication, distilled water was added to the solution in order to rinse the particles. The rinsing was followed by decanting after allowing the particles to settle down; this process of rinsing and decanting was done in tandem. The time taken by the particles to settle down reduces with subsequent rinsing. In order to completely rinse the particles, the

above-stated rinsing and decanting processes were carried out five times. Once the particles have been thoroughly rinsed, they are dried at 80 °C. The dried samples are then grounded using a mortar and pestle.

Sensitizing process (Sample 1):

The sensitizing process is a process in which the etched particles obtained from the hydrophilic treatment are ultrasonically dispersed for 30 min in a 24-h aged bath comprising 0.1 M SnCl2 and 0.1 M HCl. After ultra-sonication, distilled water was added to the solution in order to rinse the particles. The rinsing was followed by decanting after allowing the particles to settle down; this process of rinsing and decanting was done in tandem. The time taken by the particles to settle down reduces with subsequent rinsing. In order to completely rinse the particles, the above-stated rinsing and decanting process was carried out four times. Once the particles have been thoroughly rinsed, they are dried using a heating mantle at 60 °C.

Non-sensitized Ni–MoS_2 (Sample 2).

The cleaning, oxidizing, and hydrophilic treatment for non-sensitized Ni–MoS_2 was the same as that of sensitized Ni–MoS_2, however, the sensitizing step was not performed for the non-sensitized Ni–MoS_2 in order to understand the effect of the sensitizing process on the electroless nickel plating.

Electroless Ni plating:

Once the previously stated pretreatments are completed, the samples were individually subjected to electroless nickel plating. A sample of 0.672 g was immersed in the plating bath that comprises 0.12 M NiCl2.6H2O and 0.09 M NiSO4 6H2O as a source of metal ions along with 0.1 M C6H5Na3O7.2H2O and 0.45 M H8N2SO4 as complexing agents, while 0.04 M NaBH4 is used as a reducing agent. The sample is added to the bath only after all the constituents except NaBH4 are added. After the sample is added to the bath, it is magnetically stirred for 20 min before NaBH4 is added. Then, 1.5 g of NaBH4 was dissolved in 50 ml of distilled water and then gradually poured into the plating bath to promote the reduction process.

The plating bath was maintained at 85 °C and a pH of 9. The plating process was carried out for 2 h. During the entire process, the plating bath is continuously stirred to ensure uniform coating. Once the plating process is completed, distilled water was added to the solution in order to rinse the excess unreacted particles. The rinsing was followed by decanting after allowing the particles to settle down, this process of rinsing and decanting was done in tandem. The time taken by the particles to settle down reduces with subsequent rinsing. In order to completely rinse the particles, the above-stated rinsing and decanting process was carried out six times. Once the particles have been thoroughly rinsed, they are dried using a heating mantle at 60 °C.

After plating, the structural information of all the samples was examined using X-ray diffraction (XRD) measurement. The surface morphology of all the samples was observed using field emission scanning electron microscopy (FESEM).

56.3 Results and Discussion

56.3.1 Structural Information

The structure of the nickel-plated MoS_2 was calculated using the X-ray diffraction (XRD) instrument using Cu-Kα1 radiation of wavelength 1.5406 Å with the operating condition as 40 kV and 30 mA. The XRD pattern of pure MoS_2 sample is shown in Fig. 56.1. The XRD pattern of pure MoS_2 shows diffraction peaks at 14.5°, 29.1°, 32.7°, 33.6°, 35.9°, 39.6°, 44.2°, 49.8°, 58.4°, and 60.2° belonging to the hkl plans (200), (004), (100), (101), (102), (103), (006), (105), (110), and (008). These diffraction peaks confirm the MoS_2 with hexagonal structure with reference to the JCPDS file number 77-1716. The XRD pattern of pure MoS_2 also shows the well-crystalline nature which can be confirmed by the very sharp intense peaks. In the XRD pattern of pure MoS_2, no extra diffraction peak is observed, which confirms the absence of impurities in the material. The XRD pattern as plated MoS_2, prepared with two different pretreatment procedures are shown in Fig. 56.2. This shows diffraction peaks corresponding to the pure MoS_2 with reduced intensity due to the presence of nickel in the plated MoS_2 powder. The XRD pattern of annealed powder samples is shown in Fig. 56.3, which shows that the diffraction peaks at 44° and 52° belong to the hkl plane of (111) and (200) due to nickel [15]. This is confirmed with reference to the JCPDS file number 04-0850 and the plated nickel is in the fcc structure. The XRD pattern of annealed MoS_2 samples shows intense peak for Sample 2. The absence of extra peak confirms the absence of other impurities in the nickel-plated MoS_2 samples.

In the XRD pattern, the line broadening is due to the two major factors, instrumental and crystallite size. By subtracting the instrumental broadening, the crystallite size of the deposited MoS_2 can be calculated using the Scherer equation. The instrumental broadening of the peaks was subtracted with the standard annealed silicon peaks. The calculated crystallite size for pure MoS_2 is 12 nm, in as-plated condition

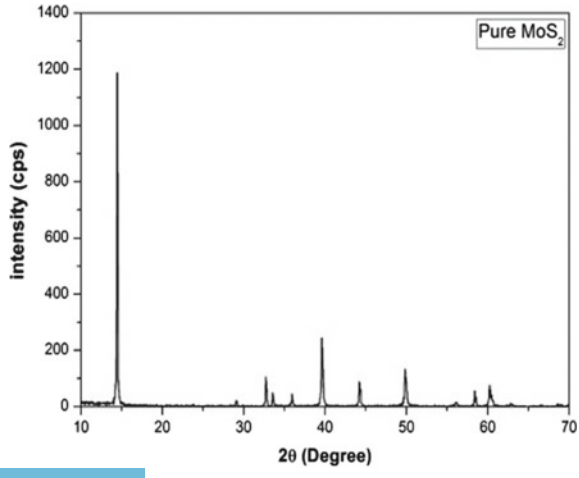

Fig. 56.1 XRD pattern of pure MoS_2 powder

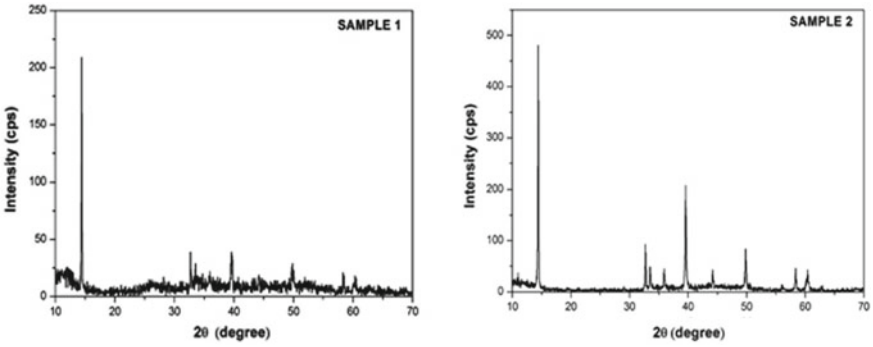

Fig. 56.2 XRD pattern of as-plated powder

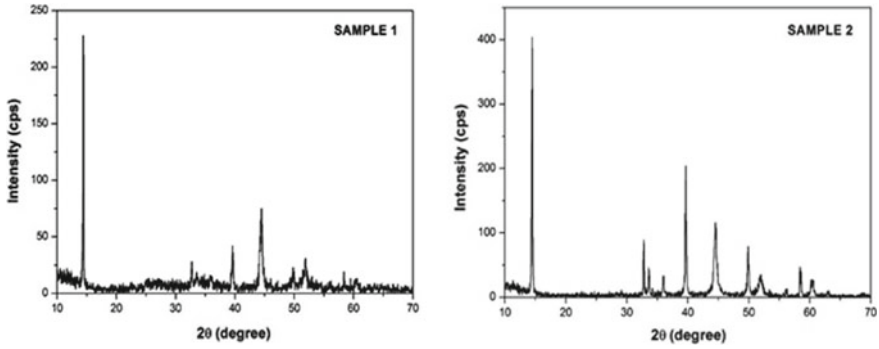

Fig. 56.3 XRD pattern of annealed powders

it is 80 nm for Sample 1 and 72 nm for the Sample 2. Similarly, the crystallite size for annealed Sample 1 is 72 nm for MoS_2 crystallite and 24 nm for nickel crystallite and for Sample 2 is 72 nm for MoS_2 crystallite and 23 nm for nickel crystallite. This shows that Sample 2 has higher crystallinity and reduced crystallite size. The presence of nickel in the samples indirectly confirms the coating of nickel in the MoS_2 powders.

The surface morphology of both, the pure MoS_2 and nickel-coated MoS_2 powders were observed using FESEM. The surface morphology of pure MoS_2 is shown in Fig. 56.4, which shows that the pure MoS_2 has flake-like surface morphology with random distribution of flakes. The surface morphology of etched MoS_2 samples is shown in Fig. 56.5. It is observed that the surface is no longer smooth, but, the overall flakes morphology remains unchanged. The surface morphology of the sensitized MoS_2 samples is shown in Fig. 56.6. This shows the same flake-like nature. However, the SN treatment has enabled active sites on the surface and also caused the rough surface to transform into a smooth surface.

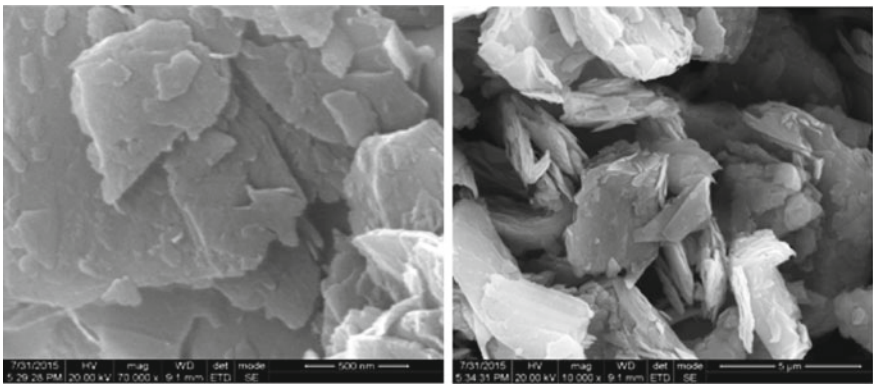

Fig. 56.4 Surface morphology of pure MoS_2

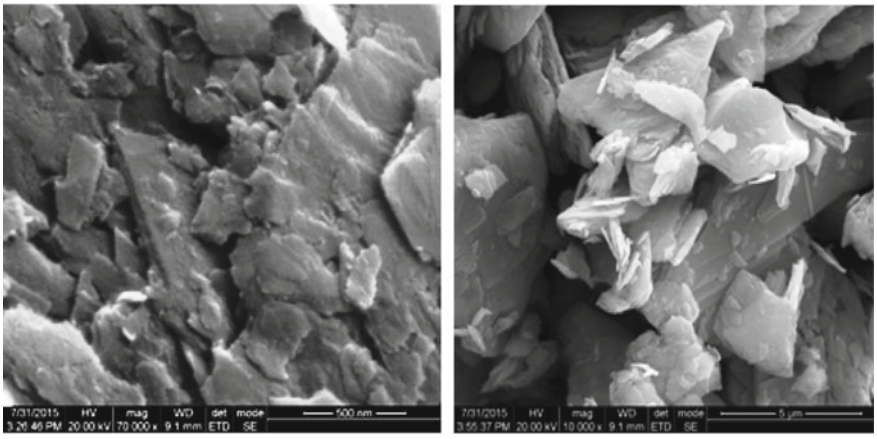

Fig. 56.5 Surface morphology of etched MoS_2

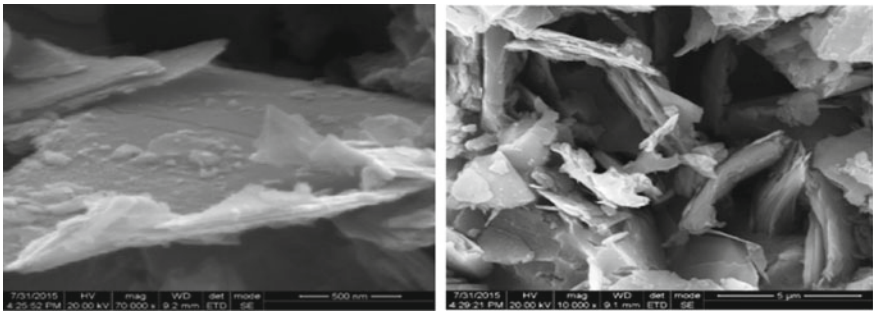

Fig. 56.6 Surface morphology of sensitized MoS_2

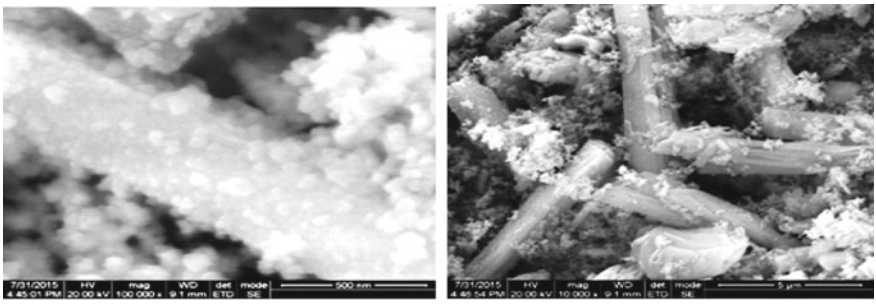

Fig. 56.7 Surface morphology of the sensitized nickel-coated MoS_2

The sensitized and nickel-coated MoS_2 samples are shown in Fig. 56.7. This shows the coating of nickel over MoS_2 rods. The flake-like MoS_2 particles are converted into rods due to the mismatch in the unit cell of MoS_2 and SN which develops a strain in the system. This strain is relieved by curling of the flake layer resulting in the rod formation. The thickness of the rod was calculated using ImageJ software and found to be 460 nm.

The free electrons that are released during the electroless nickel plating are attracted by both nickel and tin because of their similar electronegativity. Since tin has already been adsorbed on the surface (crevices) of MoS_2, a strain is developed between the unit cells of SN and MoS_2 that leads to the rolling of the lamellar MoS_2. Thus, nanotubes of MoS_2 are formed when it is subjected to sensitization before electroless nickel plating with random distribution across the sample. The nickel deposition is also randomly disturbed on the nanotubes as well as the rest of the sample. The sensitized samples show uniform coating of nickel when compared to the non-sensitized samples. In spite of following the same plating methodology, the non-sensitized samples show better coating of nickel, but, the sensitized samples form nano-rods.

The surface morphology of the non-sensitized (Sample 2) is shown in Fig. 56.8. This shows the coating of nickel over the MoS_2 particles, where the large grains are

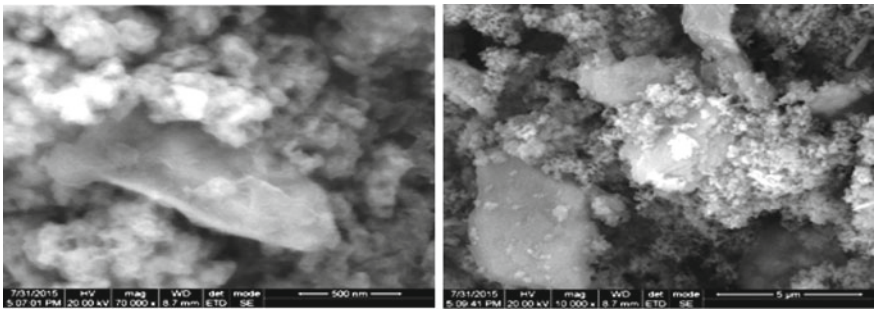

Fig. 56.8 Surface morphology of the non-sensitized nickel-coated MoS_2

of MoS_2 and small foam-like particles are nickel that are coated over the surface of the MoS_2 particles.

56.4 Conclusions

Nickel is successfully coated on the surface of the MoS_2 powder using the electroless plating method. The XRD pattern confirms the presence of Ni in the fcc structural phase along with MoS_2 phase for both samples. The surface morphology of all the samples was observed using FESEM. From the images, it is observed that sensitization induces uniform coating over the MoS_2 particles with rod formation while non-sensitized sample shows irregular coating of Ni over MoS_2 particles. This study concludes that the sensitization of the lamellar surface of the MoS_2 particles improves the coating distribution and leads to the formation of rod-like particles.

References

1. Chawla, N., Shen, Y.L.: Mechanical behavior of particle reinforced metal matrix composites. Adv. Eng. Mater. **3**, 357–370 (2001)
2. Suresha, S., Sridhara, B.K.: Effect of addition of graphite particulates on the wear behaviour in aluminium–silicon carbide–graphite composites. Mater. Des. **31**, 1804–1812 (2010)
3. Kumar, N.G.S., Ravindranath, V.M., Shankar, G.S.S.: Mechanical and wear behaviour of aluminium metal matrix hybrid composites. Procedia Mater. Sci. **5**, 908–917 (2014)
4. Clauss, F.J.: Solid Lubricants and Self-Lubricating Solids. Academic Press, New York (1972)
5. Estrada-Guel, I., Carreño-Gallardo, C., Cardoso-Cortés, J.L., Rocha-Rangel, E., Herrera-Ramírez, J.M., Martínez-Sánchez, R.: Effect of metallic addition on mechanical properties in an aluminum–graphite composite synthesized by means of mechanical milling. J. Alloy. Compd. **495**, 403–407 (2010)
6. Chen, H., Alpas, A.T.: Wear of aluminium matrix composites reinforced with nickel-coated carbon fibres. Wear **192**, 186–198
7. Palaniappa, M., Babu, G.V., Balasubramanian, K.: Electroless nickel–phosphorus plating on graphite powder. Mater. Sci. Eng. A **471**, 165–168 (2007)
8. Xu, X., Cui, Z.D., Zhu, S.L., Liang, Y.Q., Yang, X.J.: Preparation of nickel-coated graphite by electroless plating under mechanical or ultrasonic agitation. Surf. Coat. Technol. **240**, 425–431 (2014)
9. Zhang, S., Han, K., Cheng, L.: The effect of SiC particles added in electroless Ni–P plating solution on the properties of composite coatings. Surf. Coat. Technol. **202**, 2807–2812 (2008)
10. Rajkumar, K., Aravindan, S.: Tribological studies on microwave sintered copper–carbon nanotube composites. Wear **270**, 613–621 (2011)
11. Jiang, J.T., Zhen, L., Xu, C.Y., Wu, X.L.: Microstructure and magnetic properties of SiC/Co composite particles prepared by electroless plating. Surf. Coat. Technol. **201**, 3139–3146 (2006)
12. Zhu, S.L., Tang, L., Cui, Z.D., Wei, Q., Yang, X.J.: Preparation of copper-coated β-SiC nanoparticles by electroless plating. Surf. Coat. Technol. **205**, 2985–2988 (2011)
13. Luo, L., Wu, Y., Li, J., Zheng, Y.: Preparation of nickel-coated tungsten carbide powders by room temperature ultrasonic-assisted electroless plating. Surf. Coat. Technol. **206**, 1091–1095 (2011)

14. Flom, D.G., Haltner, A.J., Gaulin, C.A.: Friction and cleavage of lamellar solids in ultrahigh vacuum. ASLE Trans. **8**, 133–145 (1965)
15. Dhanapal, K., Revathy, T.A., Raj, M.A., Narayanan, V., Stephen, A.: Magnetic anisotropy studies on pulsed electrodeposited Ni/Ag/Ni trilayer. Appl. Surf. Sci. **313**, 698–703 (2014)

Chapter 57
Laser Beam Treatment of Nimonic C263 Alloy: Study of Mechanical and Metallurgical Properties

A. K. Sharma, M. Anand, Vikas Kumar, Shakti Kumar and A. K. Das

Abstract In the present research experiment was performed to study the penetration effect of laser treatment on Nimonic C263 alloy using 400 W fiber laser. The influence of input parameters on scanning bead geometry was examined and microstructures of the bead were investigated. The effects of laser beam diameter on laser treatment were studied and found to be significant during the laser beam treatment. Depth of penetration and width of heat affected zone (HAZ) increase with the increase in laser power. Micro-hardness of the Nimonic C263 alloys, after laser treatment, was investigated and found to be in the range of 250–285 HV, which is higher than the parent material. From this investigation, a very small heat affected zone (35–95 μm) was observed during laser beam treatment of nimonic 263 alloy. The good bead appearances and microstructures indicate that laser beam treatment of nimonic 263 alloys is feasible.

Keywords Fiber laser · Beam size · Nimonic 263 · Penetration depth

57.1 Introduction

Nimonic C263 is a nickel-based high temperature resistant superalloy, which possess superior material properties such as high mechanical strength, resistance to thermal creep deformation, excellent surface stability and high corrosion and oxidation resistance. It is having a centered cubic austenitic crystal structure and an age hardened alloy of nickel, chromium, molybdenum, and cobalt. In annealed condition, it shows the excellent characteristics of the fabrication work [1]. Further, aluminium and chromium present in Nimonic C263 endow with excellent oxidation and corrosion resistance properties. The formability and weldability of Nimonic C263 alloys are also good as compared to other nickel-based alloys such as Waspaloy and Rene 41. Nimonic C263 exhibits excellent ductile properties at an intermediate temperature

A. K. Sharma · M. Anand · V. Kumar · S. Kumar · A. K. Das (✉)
Department of Mechanical Engineering, Indian Institute of Technology (ISM) Dhanbad, Dhanbad 826004, Jharkhand, India
e-mail: eralok@yahoo.co.in

M. S. Shunmugam and M. Kanthababu (eds.), *Advances in Micro and Nano Manufacturing and Surface Engineering*, Lecture Notes on Multidisciplinary Industrial Engineering,
https://doi.org/10.1007/978-981-32-9425-7_57

and this property, in the annealed condition, makes it suitable for both cold forming and hot working processes. This alloy has wide applications in turbines combustion chamber, casing liner in aerospace and marine engines etc. [2]. Laser welding is an impactful assembling innovation utilized for the generation of precise items made of sheet metals. It is a speedy & exact joining process contrasted with the other customary welding process. Subsequently, laser welding of nickel-based superalloys needs a watchful choice of process parameters because of their poor thermal conductivity and this property empowers it for high temperature applications. Amid laser welding, a high temperature contrast introduces in short separation, so surface distortion happens. Facilitate plasma is created in the framed key hole. The power conveyed by the laser beam is specifically absorbed by the wall surface of the keyhole. However, another heat exchange happens amid the combination of the laser beam with the plasma, so interaction strength increases [3, 4]. At the point when the plasma pressure turns out to be high, at that point keyhole seems like a cavity.

Laser welding can be favored over other welding forms because of its points of interest, for example, narrow heat affected zone (HAZ), no cracks with less distortion due to thermal effects & less significant heating of the base material. Mazar Atabaki et al. (2017), examined the weld quality with respect to different welding parameters such as laser power, standoff distance, and scanning speed, and reported that at a higher welding speed and optimum standoff distance, a fully-penetrated sound weld can be obtained [5]. New generations of high brightness lasers (fiber and thin disk lasers) are advantageous as they simultaneously deliver good beam quality as well as high output power and high efficiency. Additionally, the maintenance cost of these lasers is very low, and it occupies a small floor area. Raghukandan et al. (2016) performed pulse laser welding operation on dissimilar grade steel and reported that porosity in weld bead increases with higher scanning speed. Zieliñska (2010) investigated the effects of laser power, scanning speed and standoff distance on the strength of welded zone for joining nickel-based superalloys. Further, it was reported that thermal conductivity of superalloys depends on the chemical composition and welding temperature [6]. The interaction of laser beam with any material can improve the micro-hardness of the material [7]. Many studies are devoted to microstructural change and mechanical properties of laser beam scanned superalloys. As very few literature reported the laser welding of the Nimonic C263 alloy, so the present research shows the effect of different laser welding parameters (i.e. laser power density, stand-off distance (SOD), scanning speed) on the penetration depth, width of HAZ of the superalloy. Further, the changes in microstructure during the laser treatment process have also been investigated. However, it may be noted that due to limited resources some important factors such as flow characteristics of molten metal in the melt pool and keyhole behavior at fusion zone are not considered in this study.

57.2 Experimental Procedure

57.2.1 Experimental Setup

The experiments were carried out using a fiber laser (electrical power supply equipment, single phase, continuous type), having a wavelength of 1070 nm. Figure 57.1 shows the laser machine setup. The laser beam is transmitted from the laser source through a fiber optic cable and is made to pass through a laser welding head. The welding head is facilitated with gas purging facility to protect the lens from the deposition of metal vapors and to prevent the oxidation of melt surface. The laser head can be moved in Z-axis only and the work table can be moved in X–Y axes of the CNC stage respectively. All the three motions can be controlled simultaneously through a CNC controller along with the starting and stopping of the laser at the desired time. The general specifications of the developed setup are presented in Table 57.1.

Further to estimate the power density of laser beam (laser power/beam spot area) at the working zone, a mathematical equation between laser power density and SOD

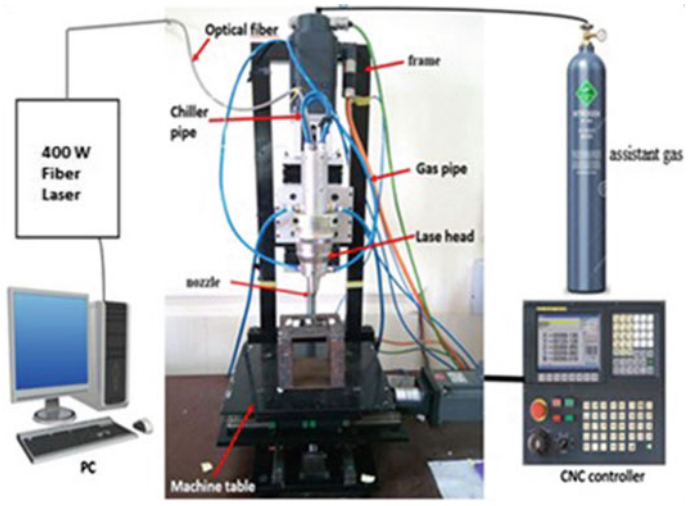

Fig. 57.1 Setup for laser beam operation

Table 57.1 Machine specification

Diameter of laser beam at optical lens (AB)	5 mm
Focal length of laser beam (L)	80 mm
Nozzle tip position from optical lens (L')	79.8 mm
Diameter of beam at nozzle tip (CD)	0.0125 mm
Focal point from nozzle tip (d)	0.2 mm
Angle AEB (Angle of convergence)	3.58°

has been established. The standoff distance (SOD) is the vertical distance between the top surface of the workpiece to machine's nozzle tip. It is an important parameter of laser beam operations as power density at working zone is mostly influenced by the beam diameter. Therefore to estimate the power density at a specific position, it is necessary to obtain the spot diameter of the laser beam at a different standoff distance. In this regard, a number of trial experiments have been conducted to find the geometrical relationship between standoff distance and laser beam diameter.

57.2.2 Workpiece Material

A nimonic C263 alloy of thickness 2 mm was used as the workpiece material. The workpiece samples were cut from the parent sheet through wire electrical discharge machining process to reduce the distortion of material as to of high heat generated during conventional cutting processes. Thereafter, the samples were cleaned thoroughly in an acetone bath under ultrasonic vibration.

57.2.3 Experimentation

In the experiment, the workpiece was kept under the laser beam in such a way that the focal point of the laser beam is always above the work surface. After a number of trial experiments, working ranges of different experimental parameters were found as laser power: 250–350 W, scanning speed: 300–700 mm/min and, stand-off distance: 3.2–7.2 mm. The parameter settings for the different experimental run are presented in Table 57.2. All the experiments were conducted in an argon gas environment (gas flow rate 6 L/min). After conducting experiments, the samples were cleaned and, thereafter, optical images were captured (as presented in Fig. 57.2).

Table 57.2 Experimental matrix

S. No.	Power (W)	Speed (mm/min)	Standoff distance (mm)	Beam diameter (mm)	Top width (mm)	DOP (mm)
1	250	300	3.2	0.2	0.762	0.312
2			5.2	0.32	0.767	0.292
3			7.2	0.45	0.828	0.207
4		500	3.2	0.2	0.721	0.298
5			5.2	0.32	0.748	0.31
6			7.2	0.45	0.685	0.308

(continued)

Table 57.2 (continued)

S. No.	Power (W)	Speed (mm/min)	Standoff distance (mm)	Beam diameter (mm)	Top width (mm)	DOP (mm)
7		700	3.2	0.2	0.686	0.238
8			5.2	0.32	0.651	0.225
9			7.2	0.45	0.699	0.199
10	300	300	3.2	0.2	0.668	0.367
11			5.2	0.32	0.47	0.356
12			7.2	0.45	0.599	0.334
13		500	3.2	0.2	0.751	0.36
14			5.2	0.32	0.852	0.325
15			7.2	0.45	0.754	0.255
16		700	3.2	0.2	0.799	0.285
17			5.2	0.32	0.773	0.255
18			7.2	0.45	0.761	0.232
19	350	300	3.2	0.2	1.02	0.602
20			5.2	0.32	0.955	0.57
21			7.2	0.45	1.152	0.461
22		500	3.2	0.2	0.868	0.414
23			5.2	0.32	0.892	0.401
24			7.2	0.45	0.878	0.383
25		700	3.2	0.2	0.977	0.36
26			5.2	0.32	0.957	0.345
27			7.2	0.45	0.987	0.332

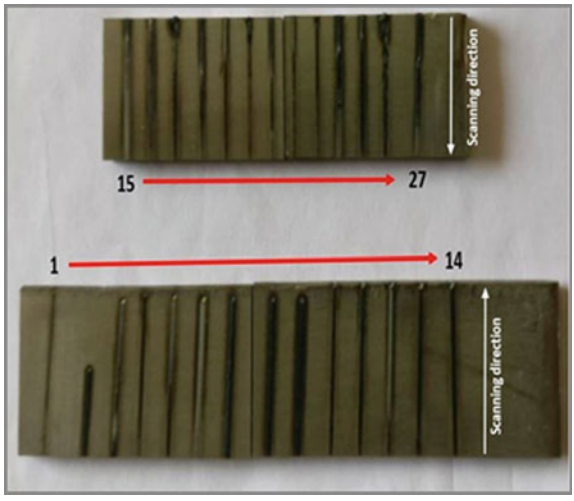

Fig. 57.2 Laser beam scanned Nimonic C263 specimen from run 1 to 27

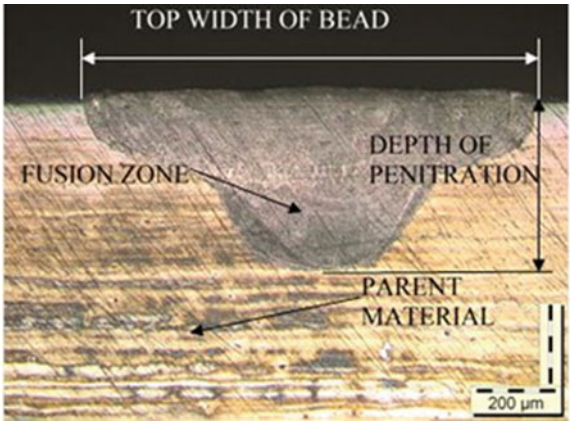

Fig. 57.3 Optical microscope image of running bead cross section after polishing and etching

57.2.4 Characterization of Samples

After collecting the samples, each sample was cut by using wire EDM across the direction of laser scan direction. After this, the cutting surfaces of all the samples were ground by emery paper. Further, these were polished by fine grit emery paper followed by cloth polishing with diamond paste to obtain mirror-like surface. Finally, all samples were etched using a solution of HCl (45%), HNO_3 (15%) and glycerol (40%) by swabbing for 30–40 s. After successful etching of all samples, a metallurgical optical microscope was used to investigate the weld beads, which were clearly visible on the polished surface. Microstructures, top width of the bead, depth of penetration (D.O.P) and heat affected zone (HAZ) were observed at 200× magnification as shown in Fig. 57.3. During the investigation, it was found that all the beads were different in term of bead width, penetration depth and heat affected zone.

57.3 Results and Discussion

57.3.1 Effect of Process Parameters on Bead Geometry

Effect of scanning speed

To analyze the effect of scanning speed on D.O.P and top width of beads scanning speed was varied in the range of 300–900 mm/min by keeping laser power and stand-off distance constant at 350 W and 3.2 mm respectively. At the scanning speed of 300 mm/min, D.O.P. is 0.60 mm which is the deepest among others. Similarly, the top width of the bead (1.02 mm) is also the largest at lowest scanning speed. This is because of higher interaction time between the laser beam and material hence more material melts at low speed for the same laser power density.

Effect of standoff distance

To examine the influence of stand-off distance on bead geometries, stand-off distance was varied from 3.2 to 9.2 mm by keeping laser power and scanning speed constant at 350 Wand 300 mm/min respectively. It is found that the D.O.P increases with shorter standoff distance. Whereas, the top width of bead decreases at shorter stand-off distances. The above trend can be explained by analyzing the laser beam diameter and power density. As the standoff distance increases the spot diameter of the beam also increases so the laser power density decreases. Therefore, at large standoff distance, less amount of materials is melted, as a result, lesser penetration depth. However, at the same time, top width of the bead is larger due to bigger beam diameter.

Effect of laser power

When the standoff distance and scanning speed remain constant and laser power was varied, variations in D.O.P with a change in laser power have been obtained as shown in Table 57.2. While keeping the standoff distance and scanning speed constant, D.O.P increases with laser power. Due to the fact that the increase in laser power at the constant standoff distance the power density of beam is increased so laser beam is capable to penetrate more depth into the material. Increase in top bead width was also observed with increasing laser power, more heat energy is developed at the higher laser power due to a high power density of beam [8].

Figure 57.4 represents the different depth of penetration with laser power under different scanning speed. The plot shows a clear increasing trend of DOP with laser power. However, the rate of increase of DOP is relatively much higher at lower scanning speed and high laser power which is due to the expanded span of the association about laser beam with that material. It is also observed that as the scanning speed increases, the depth of penetration decreases due to lesser interaction time of the beam with the material. There is an indication of optimum scanning speed for lower to medium laser power as not much considerable change in DOP is observed on decreasing scanning speed from 500 to 300 mm/min. Due to the high laser power,

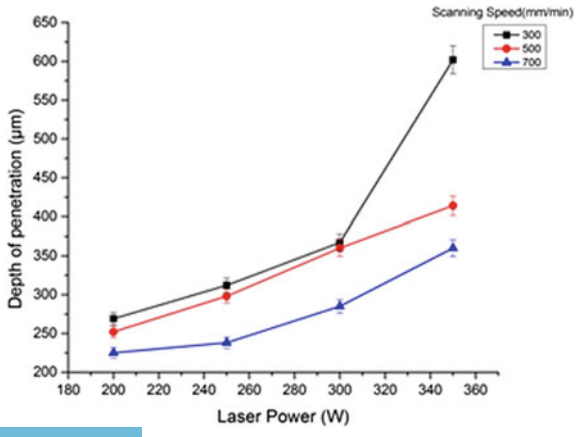

Fig. 57.4 Variations of DOP with laser power and scanning speed at SOD 3.2 mm

the width of bead becomes wider, but narrow and sharp beads are being preferred during laser beam welding. The ratio of the DOP to top width of bead should be high for the preferable process parameters of laser scanning operation.

Area of fusion zone follows an expected trend with variation in power and scanning speed. The fusion zone area increases with power and decreases with increase in scanning speed. The defocus point of the laser beam, however, does not have a significant effect on fusion zone if other two variables are kept constant. This makes it more useful for industrial use where a focal position may change due to robot inaccuracy on the complex path.

57.3.2 Microstructure and Heat Affected Zone (HAZ) at Weld Bead Cross Section

The Laser treated bead was examined by scanning electron microscope (SEM). Figure 57.5 represents the cross-section of the sample where microstructure of the laser scanning beads of nimonic C263 alloy can easily be seen at different laser scanning power but constant scanning speed and standoff distances. A very narrow heat affected zone is observed during the operation due to low laser power, and good

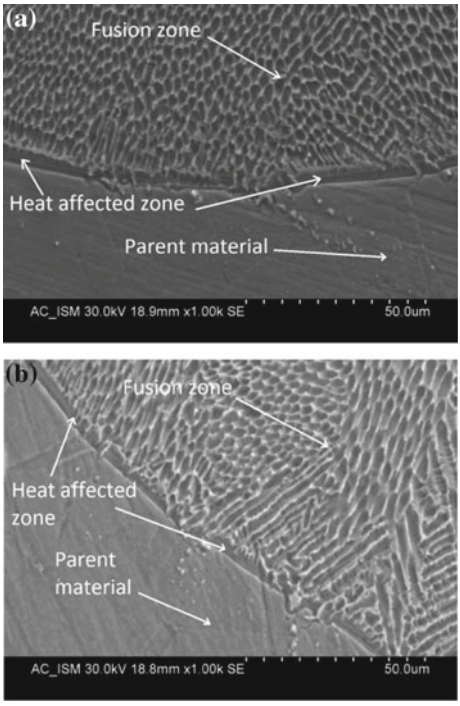

Fig. 57.5 Heat affected zone and microstructures of bead cross-section at different laser power and same scanning speed **a** 350 W, 500 mm/min. **b** Laser power 300 W, speed 500 mm/min

heat resistant nature of nimonic C263 alloy. At high laser power and low scanning speed, the larger grains appear in the microstructure. From the observation of SEM images of the Nimonic C263 parent material and melting zone can be easily identified. The noticeable metamorphous zone and HAZ between the substrate and melting zone are difficult to observe. The microstructures in the fusion zone are columnar, dendrites and directing towards the centre of the weld bead. At high laser power, fine grains were produced and the microstructural grain becomes coarse when laser power decreases. The formation of columnar dendrites is due to rapid cooling rate and heat input [9]. A fine grain of microstructure throughout the scanning bead is obtained at high laser power. From the Fig. 57.5, it is observed that width of HAZ is directly proportional to the laser power because HAZ is the function of temperature and directly proportional to the heat supply.

Figures 57.6 and 57.7 represent the effect of scanning speed on microstructure and heat affected zone when laser power and standoff distance remains constant. At low scanning speed due to the expanded span of the association about laser beam with that material so more heat is delivered to material hence fine grains are produced. In Fig. 57.6b the grain size of melting zone becomes linear directing away from the centre of the bead. It occurs due to low laser power of the beam which will not properly melt the base material. Due to high laser energy heat affected zone at lower scanning speed is larger as compared to the higher scanning speed. From

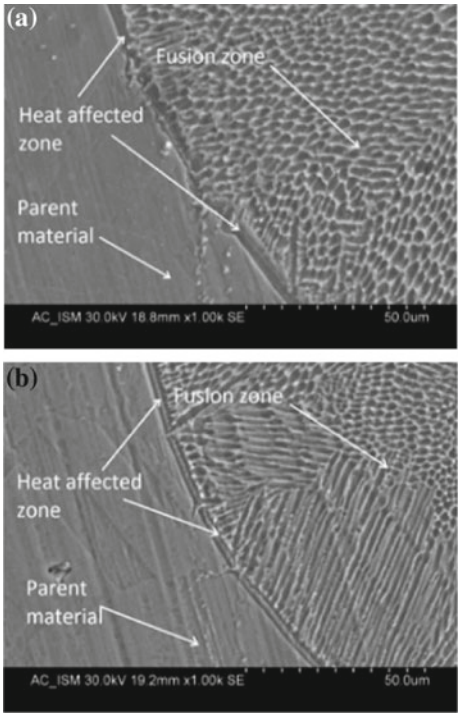

Fig. 57.6 Heat affected zone and microstructures of bead cross section at same laser power and different scanning speed **a** laser power 300 W and scanning speed 300 mm/min. **b** Laser power 300 W scanning speed 700 mm/min

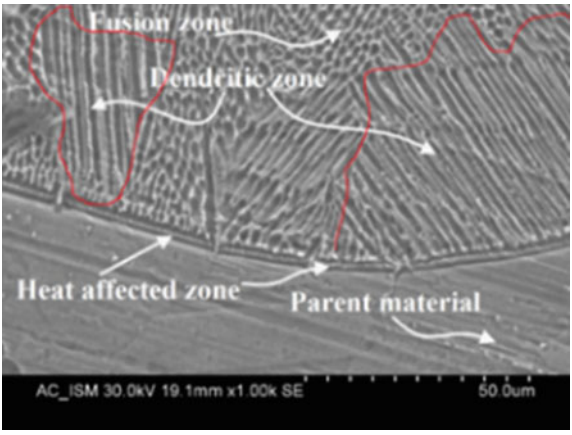

Fig. 57.7 Heat affected zone and microstructure of bead cross section at laser power 250 W and scanning speed 500 mm/min

Fig. 57.6a, b, it can be observed that HAZ is inversely proportional to scanning speed and directly proportional to laser power. The images of heat affected zone between fusion zone and parent material were taken by an optical microscope which is shown in Fig. 57.9.

After scanning, the laser treated samples were polished and cleaned to observe the change in microstructure in scanning zone. Figure 57.9 shows the optical images of microstructure for two different scanning beads. It is observed that microstructure of base metal, melting zone and heat affected zone are different. The average value of HAZ was taken into consideration. Figure 57.8 demonstrates the variety of HAZ with laser power at various scanning speed. With the expansion in laser power, HAZ increments (at steady scanning speed). The HAZ diminishes with increment in scanning speed at constant laser power. At constant laser power, with an expansion in scanning speed, the measure of heat energy diminishes at fusion zone, so the width

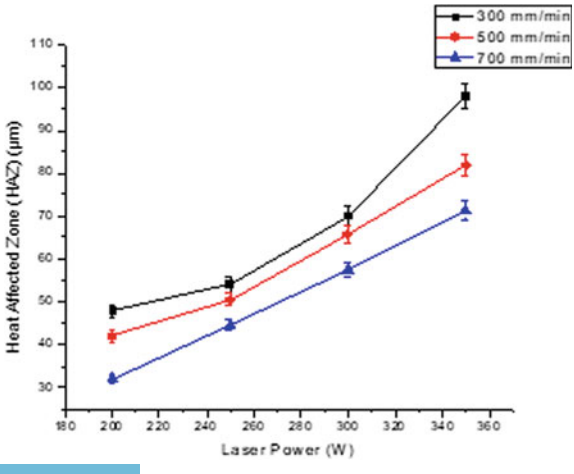

Fig. 57.8 Effect of laser power and scanning speed (mm/min) on HAZ

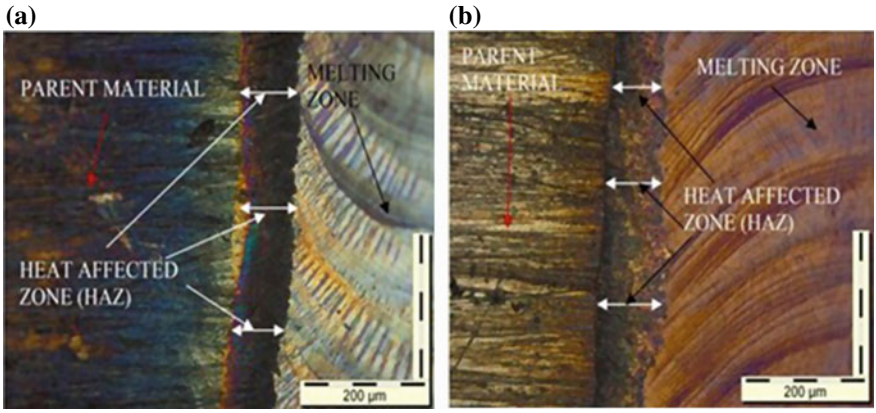

Fig. 57.9 Heat affected zone between melting zone and parent material

of HAZ diminishes. At consistent scanning speed with an expansion in laser power, the width of HAZ increments. During laser scanning operation the temperature of scanning zone increases to its melting point. Further increase in laser power increases the temperature of the nearest material to fusion zone and hence the width of HAZ increases. To minimize the width of HAZ, operational parameters should be selected as higher scanning speed and low laser power.

57.3.3 X-Ray Diffraction (XRD) Analysis

Figure 57.10 shows the X-ray diffraction (XRD) pattern of the laser treated surface of Nimonic C263 alloy at laser power 300 watts and scanning speed 500 mm/min. The laser treated surface was characterized by using X'pert high score plus software keeping diffraction angle (2θ) in the range of 20° to 140°. Different phases such as Ni_3Fe, Cr_2Fe_6 $Mo_{0.1}Ni_{1.3}$ $Si_{0.3}$, $Cr_{0.19}Fe_{0.7}Ni_{0.11}$, $Ni_{2.9}Cr_{0.7}Fe_{0.36}$ and C are formed during laser treatment process due to series of chemical reactions. The formation of Ni phase with Al and Fe could be attributed reveals that the percentage of Ni in Nimonic alloys is relatively higher. The phase formation intensity of Ni3Fe was found higher, with few another defined phases like FeNi, AlNi. At the position of 53° and 92°, the phase formation of Austenitic steel (Cr2Fe6.7Mo0.1Ni1.3Si0.3) and stainless steel is observed respectively due to the presence of Fe (0.07%), Si (0.3%) and Cr (20%) in the substrate.

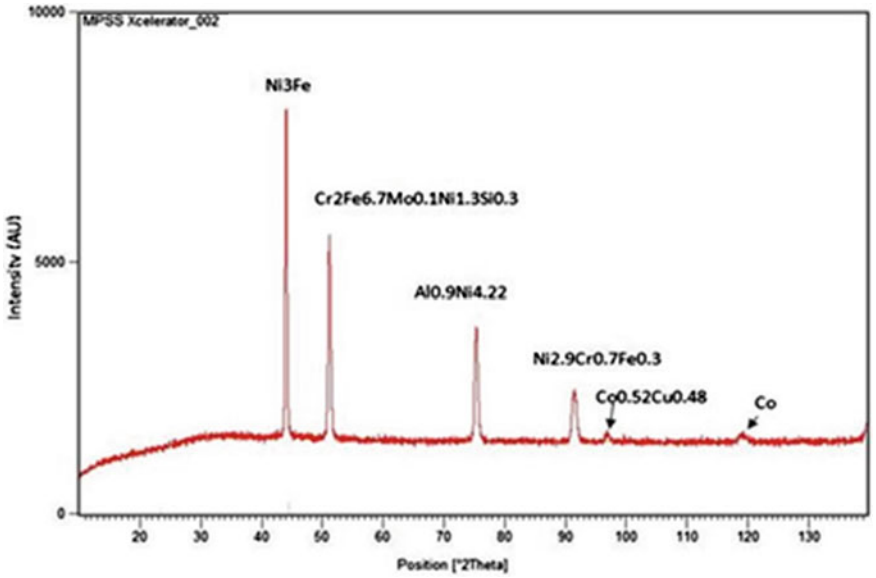

Fig. 57.10 X ray diffraction profile of top surface of laser scanning bead

57.3.4 Effect of Laser Power on Micro-Hardness

Micro-hardness testing was performed using Vickers hardness testing machine (Make: ECONOMET VH-1MD) having diamond pyramid shape of include angle 136°. 0.5 kg load is applying for 10 s and for each sample, the average of four readings was taken. The results show a slight increase in hardness (20–30 HV) of Nimonic C263 after laser scanning process. The results also show that hardness is the function of temperature. The micro-hardness of laser melted sample was markedly higher than the parent nimonic 263 alloy. The micro-hardness of parent material was obtained as 245 HV. A proper trend was obtained for the change in micro-hardness at varying process parameters. Micro-hardness of laser scanning beads of Nimonic C263 alloy was increasing with increase in laser power. The graphical representation of the change in micro-hardness with increasing laser power is shown in Fig. 57.11. The results show that the micro-hardness of the melted zone of Nimonic C263 alloys was 285 HV at laser power 350 W, at high laser power and short interaction time produced fine grain structure with the high value of micro-hardness. The increase in micro-hardness of laser scanned area could be due to recrystallization of the microstructure. No any proper trend was obtained for change micro-hardness of Nimonic C263 alloy at varying scanning speed and standoff distances. But after scanning, the micro-hardness slightly increases by 3–8 HV at decreasing scanning speed.

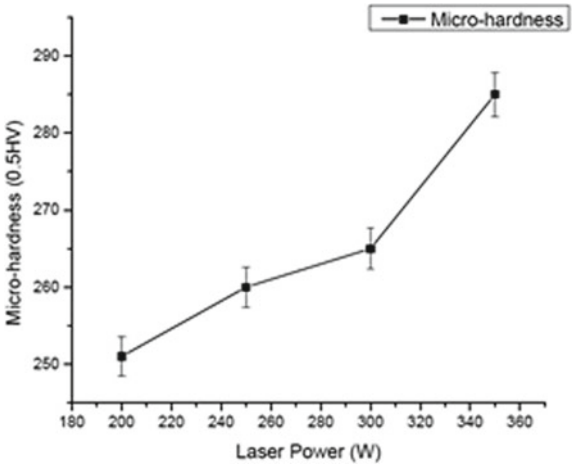

Fig. 57.11 Variation of micro-hardness with respect to laser power

57.4 Conclusion

In this experiment, running beads are successfully formed on 2 mm thick Nimonic 263 alloy using a 400 W fiber laser. For Low power laser scanning of nimonic alloy plates, the standoff distance plays a vital role. For high D.O.P and low top width of beads, low standoff distance is required. D.O.P increases proportionally to laser power and inversely to scanning speed and standoff distance. A very small HAZ (35–95 μm) has appeared between fusion zone and the Nimonic substrate due to the poor thermal conductivity of nimonic alloys. A slight increase in micro-hardness (20–30 HV) of laser treated Nimonic 263 alloy is observed. The microstructures of fusion zone are columnar in nature with the orientation towards the centre of the bead. The XRD pattern has indicated the formation of different phases of NiFe3, stainless steel and austenitic steel on the laser treated surfaces. The fiber laser scanning treatment has resulted in the better bead appearances and desired depth of penetration.

References

1. Zhao, S., Xie, X., Smith, G.D., Patel, S.J.: Microstructural stability and mechanical properties of a new nickel-based superalloy. Mater. Sci. Eng. A **355**, 96–105 (2003). https://doi.org/10.1016/S0921-5093(03)00051-0
2. Schubert, E., Klassen, M., Zerner, I., et al.: Light-weight structures produced by laser beam joining for future applications in automobile and aerospace industry. J. Mater. Process. Technol. **115**, 2–8 (2001). https://doi.org/10.1016/S0924-0136(01)00756-7
3. Kumar, V., Hussain, M., Raza, M.S., et al.: Fiber laser welding of thin nickel sheets in air and water medium. Arab. J. Sci. Eng. **42**, 1765–1773 (2017). https://doi.org/10.1007/s13369-016-2305-1

4. Torkamany, M.J., Hamedi, M.J., Malek, F., Sabbaghzadeh, J.: The effect of process parameters on keyhole welding with a 400 W Nd: YAG pulsed laser. J. Phys. D Appl. Phys. **39**(21), 4563 (2006)
5. Mazar Atabaki, M., Ma, J., Yang, G., Kovacevic, R.: Hybrid laser/arc welding of advanced high strength steel in different butt joint configurations. Mater. Des. **64**, 573–587 (2014). https://doi.org/10.1016/j.matdes.2014.08.011
6. Kapłonek, W., Nadolny, K.: The diagnostics of abrasive tools after internal cylindrical grinding of hard-to-cut materials by means of a laser technique using imaging and analysis of scattered light. Arab. J. Sci. Eng. **38**, 953–970 (2013). https://doi.org/10.1007/s13369-012-0374-3
7. Hussain, M., Mandal, V., Kumar, V., Das, A.K., Ghosh, S.K.: Development of TiN particulates reinforced SS316 based metal matrix composite by direct metal laser sintering technique and its characterization. Opt. Laser Technol. **97**, 46–59 (2017). https://doi.org/10.1016/j.optlastec.2017.06.006
8. Ghaini, F.Malek, Hamedi, M.J., Torkamany, M.J., Sabbaghzadeh, J.: Weld metal microstructural characteristics in pulsed Nd: YAG laser welding. Scripta Mater. **56**(11), 955–958 (2007)
9. Mahmoudi, B., Torkamany, M.J., Sabour Rouh Aghdam, A.R., Sabbaghzade, J.: Laser surface hardening of AISI 420 stainless steel treated by pulsed Nd: YAG laser. Mater. Des. (1980–2015) **31**(5), 2553–2560 (2010)

Chapter 58
Evaluation of Mechanical Properties of Ti6Al4V Built by Composite Coating of WS_2, CNT, Ni, and Ti6Al4V Powders Through Laser Cladding Process

Shakti Kumar, Umar Arif, Vikas Kumar, M. Anand, R. Tyagi, Amitava Mandal and A. K. Das

Abstract Titanium and its alloy have wide application in the field of aerospace and marine engineering. But due to it's poor tribological and weight to strength ratio make difficult to use in the critical working environment. To overcome this drawback a composite cladding of WS2, CNT, and Ni was formed on the Ti6Al4V substrate. In the present work select the process parameter at constant scanning speed (450 mm/min), laser power (125–250 W). The variations of layer thickness microhardness with respect to the input parameter have been analyzed and it was observed that laser power is the influential parameter to the output measure. Hence the maximum microhardness was found to be 1246 $HV_{.5\ kg}$ which is approximately three times more than that of the substrate material. Further characterization has been done for the morphological analysis which shows that strong bonding have been formed to the interface zone and there is no crack found but at a higher percentage of CNT some microcrack are observed. With the increase in WS2, wear resistance have been improved significantly in comparison to the substrate. XRD analysis observed that there are a number of a compounds like W_2C, WS_2, TiC, Ti_2S, NiS_2, and Al_4C_3 was formed which improve the mechanical properties of the substrate titanium alloy.

Keywords Laser cladding · Composite coating · Microhardness · Layer thickness · Wear

58.1 Introduction

Laser surface modification technique is one of the most advanced techniques to enhance the properties of the existing surface of the material. It produces a high-quality metallic coating with low dilution and strong intermetallic fusion bonding with the substrates. Titanium and its alloys are well-known engineering materials

S. Kumar (✉) · U. Arif · V. Kumar · M. Anand · R. Tyagi · A. Mandal · A. K. Das
Department of Mechanical Engineering, Indian Institute of Technology (Indian School of Mines) Dhanbad, Dhanbad, Jharkhand, India
e-mail: shaktimech10@gmail.com

M. S. Shunmugam and M. Kanthababu (eds.), *Advances in Micro and Nano Manufacturing and Surface Engineering*, Lecture Notes on Multidisciplinary Industrial Engineering,
https://doi.org/10.1007/978-981-32-9425-7_58

used extensively and frequently in aerospace, marine, chemical, biomedical, and power generation industries due to its high strength to weight ratio and good corrosion resistance. Although there are different type of surface modification process i.e. LMD (Laser Metal Deposition), Laser heat treatment, DMLS (Direct Metal Laser Sintering) are using now a days to improve surface mechanical properties [1, 2]. Among these different LMD processes, laser cladding techniques show economic and effective result. However, due to the lower affinity to wear and strength, it is restricted to use in various harsh environments in industries and aerospace engineering. Hence there are various surface modification techniques like cladding, coating, and case hardening which have been adopted to improve surface properties in the past literature. In this process, a high energy density laser beam is passing through the surface where the powder is placed to form a metallurgical bond with powder materials, which have been either preplaced above the substrate material or feed during the process. In order to avoid excessive dilution of the substrate, energy density needs to maintain and further process parameters like laser scanning speed and laser power hatching distance, and stand-off distance also affects the surface morphology and the clad geometry.

The fabrication of metal matrix compound is obtained by cladding of TiB_2 powder on titanium plate; it is observed that with the increase in distance from the coating surface microhardness and the elastic module of the coating decreases but the fracture toughness of the clad increase gradually due to de-bonding of the TiB_2 particle and short fiber of TiB [3]. Pure titanium (Ti6Al4V) was cladded on the titanium plate and it is found that under high scanning speed a very ultra-fine microstructure of α/α' phase up to 60–400 nm which justifies the high hardness increase in the substrate. Coefficient of friction reduces which improves the wear resistance. But the layer band zone consists of coarse basket weaves microstructure which decreases the uniformity of the top surface, it is also seen that at higher scanning speed lamellar structure change to circular which improves wear performance, hardness, and fatigue strength [4, 5].The effect of scanning speed of the laser deposited have been investigated and it is observed that microhardness increases with the scanning speed due to high rate of cooling, however, it can be seen that proper control of microhardness can be obtained with varying scanning speed. At lower scanning speed, the laser metal interaction time is higher, a large melt pool has been formed which results in higher solidification time that formed large grain size and hence decrease in microhardness [6]. A composite coating of powder mixed with nickel, carbon, TiN, and Mo on titanium alloy has been performed in which nickel-based composite coating has been made and different response outputs have been measured on the basis of variation of Mo (molybdenum), which results in increasing wear resistance as well as hardness of the base material [7]. Titanium alloy diffuses with the molybdenum and nickel to form NiTi, Ni_3Ti, and $NiTi_2$ which improve wear as well as microhardness of the material. However, due to increase in surface roughness higher coefficient of friction is produced during sliding, Ni diffused sample has higher friction coefficient than Molebdenum diffused sample and hence wear loss is lower in case of nickel diffuses clad [8]. In the composite cladding of Titanium alloy with TiC and TiC + NiCrBSi, with the addition of TiC microstructure of well-developed dendrite structure have

been formed, with an increase in energy density due to higher dilution of powder and the substrate microhardness decreases. However, with the addition of NiCrBSi to the TiC which dissolves with nickel in the clad zone leads to increase in the microhardness and wear resistance [9]. The composite cladding of Mo–WC powder on Ti6Al4V substrate is observed that with the increase in the wt% of WC particles in Mo–WC prepaste powder mixture leads to an increase in microhardness and wear resistance of the titanium alloys. Fabrications of metal matrix composites coating Ti–Si–C–N/TiCN on Ti6Al4V substrate improve microhardness up to 1400 HV which is found to be about four times higher than the base material. A composite coating of Ti and TiC have been formed on the titanium plate which leads to the formation of hard clad surface and high wear resistance that is found in [10, 11]. The fabrication of metal matrix composite Mo-WC on the Ti6Al4V through laser cladding process which improve the microhardness and wear resistance of the substrate (Ti6Al4V). Carbon nano tubes are the cylindrical carbon molecules which have novel properties that have wide application in the field of nanotechnology, optics and material science. It can sustain highly critical working environment, because of its capability to exhibit high strength and efficient for the heat conductivity [11–19]. Composite material systems consist of metals; ceramic and additive are effective in fabricating the coatings on Titanium alloys to improve the mechanical properties. The composite coating of TiC, SiC, and Ti_5Si_3 on titanium plate which improves hardness value up to two times in comparison to the base material [13, 14].

On study, the past research it is observed that there are very few works that have been done to improve hardness as well as tribological properties simultaneously. So the present work motive is to improve surface properties of titanium alloy. In this regards, it is observed that the combined effect of WS_2, CNT, and Ni in improving Ti6Al4V surface properties. The surface has been modified by using a laser cladding process with the composite of WS2, CNT, and Ni on Ti6Al4V plate. Tungsten Disulfide (WS_2) has been used due to its lower coefficient of friction which leads to higher solid lubrication effect till date which drastically improves the life of components. However, effect of its coatings deteriorates heavily under heavy load conditions due to their low hardness. Hence WS2 mixed with CNT and Ni to improve hardness and wear resistance of clad layer due to its high hardness and load-bearing capacity. Therefore, the experiment has been conducted to study layer thickness microhardness and wear resistance properties of the clade layer (Fig. 58.1).

58.2 Experimental Details

58.2.1 Setup for the Experiment

In order to perform the experiment, SPI fiber laser with a continuous wave having maximum power capacity 400 W, operating voltage 240 V, and laser beam wavelength of 1070 ± 10 nm was used. DMLS process setup includes a laser source, chiller,

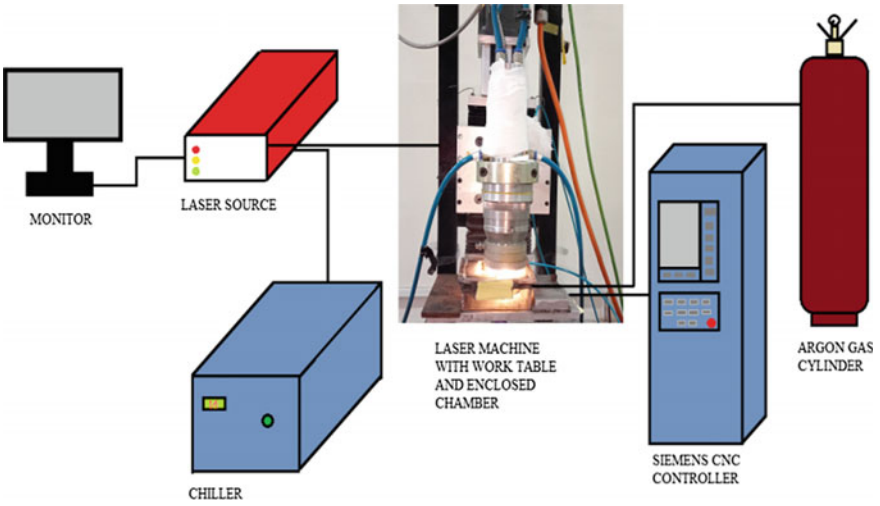

Fig. 58.1 Laser cladding operation setup

CNC-XY table and Siemens controller, and Argon gas cylinder. The laser source is for producing laser energy, chiller for cooling down and maintaining the temperature of the laser source. Two-dimensional CNC-XY table (SIEMENS Controller) is used for providing motion to the workpiece in XY direction while the motion of workpiece [V1].

58.2.2 Material Selection and Powder Preparation

Ti6Al4V substrate was taken and powder mixtures of varying wt (%) of WS2, CNT, Ni, and fixed composition of Ti6Al4V were prepared. The mixture contains WS2–CNT–Ni–Ti64 (50, 25, 20 and 5), WS2–CNT–Ni–Ti64 (60, 20, 15 and 5), and WS2–CNT–Ni–Ti64 (70, 15, 10 and 5). All powders are mixed properly using mortar pestle to make homogeneous powder mixture even though it takes long time approx. it takes 3–4 h to mixed properly. After mixing powders properly, powder paste is prepared using polyvinyl alcohol as binder then this powder paste is applied on the surface of Ti6Al4V substrate surface uniformly. After preparation of powder paste, it is applied to the substrate and left for drying in a hot air oven for 12 h.

58.2.3 Experimental Procedure

In the present work, fiber laser source with a range of 40–400 W (SM-S00051 SPI Fiber Laser Source) was used to conduct the experiments. The laser head was fixed on the Z-axis which can move up and down to adjust the spot diameter. The workpiece

was placed on the x-y CNC table. The program was created by using a SIEMENS controller to decide the traveled path of the laser beam over the substrate.

In order to avoid direct contact of machining zone to the atmosphere which can lead to severe defect and inclusion of gases, the experiment has been performed in a closed chamber with argon gas environment with a flow rate of 10 L/min. Focused beam spot dia. can be calculated by using formula, Focused beam spot diameter, $(d_o) = 1{:}27 \times \lambda \times f \times M^2/D$.

Where λ = wavelength of beam, D = diameter of the laser beam, and F = focal length of the laser beam (80 mm).

In all experiments spot dia. is fixed to 1 mm and about 50% overlapping of the beam path is done to ensure uniform cladding of the preplaced powder paste onto the substrate surface during the subsequent scanning paths (Fig. 58.2).

Samples are allowed to cool down to room temperature in the same argon gas atmosphere inside the enclosed chamber to avoid oxidation of the prepared sample. Samples were cut to ensure further testing using Wire Electro Discharge Machining (WEDM). The process parameters and observation table are shown in Tables 58.1 and 58.2.

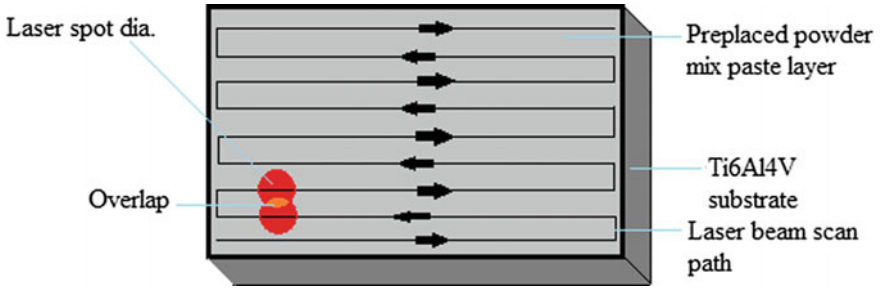

Fig. 58.2 Laser beam path and overlapping of consecutive laser beams

Table 58.1 Process parameter

Workpiece	Ti6Al4V	Argon gas flow	10 L/min
Workpiece thickness	5 mm	Binder	Polyvinyl alcohol
Clad material	WS_2, CNT, Ni, Ti64	Beam type	Continuous
Inert gas	Argon	Spot size	1 mm
Scanning speed	450 m/min		
Laser power	125–250 W		
Composition	WS_2 50–70%, CNT 15–25%, Ni 10–20%, Ti64 5%		

Table 58.2 Observation table

Sample no.	Composition (%)				Power (W)	Scanning speed (m/min)	Microhardness $HV_{.5\,kg}$	Clad layer thickness (mm)
	WS_2	CNT	Ni	Ti64				
1	50	25	20	5	125	450	730.21	0.311
2	50	25	20	5	150	450	785.29	0.322
3	50	25	20	5	175	450	903.82	0.341
4	50	25	20	5	200	450	934.5	0.372
5	50	25	20	5	225	450	959.63	0.402
6	50	25	20	5	250	450	991.49	0.432
7	60	20	15	5	125	450	791.48	0.296
8	60	20	15	5	150	450	852.62	0.303
9	60	20	15	5	175	450	958.32	0.337
10	60	20	15	5	200	450	1084.95	0.363
11	60	20	15	5	225	450	1118.81	0.388
12	60	20	15	5	250	450	1246.57	0.419
13	70	15	10	5	125	450	748.32	0.251
14	70	15	10	5	150	450	801.22	0.282
15	70	15	10	5	175	450	862.43	0.32
16	70	15	10	5	200	450	905.55	0.356
17	70	15	10	5	225	450	983.23	0.38
18	70	15	10	5	250	450	1040.87	0.404

58.2.4 Characterization of the Coated Layer

There was a number of trial experiments were done to know the bonding feasibility of the substrate material with a powder mixture of the cladding material. EDX analysis was done for each experiment to know the chemical composition of the cladding surface and FESEM images were taken and analyzed to know if bonding affinity of different materials exists or not to make strong metallurgical bonds for forming a good strength clad layer. Vickers microhardness of cladded surface was measured and compared with the substrate, i.e., Ti6Al4V to observe improvement in microhardness using "Econo met VH-1 MD" testing machine, Make: Chennai Metco, India. The load applied was 5 N for a dwell time of 10 s. Olympus metallurgical microscope (model-BX51) was used to capture optical images for doing a morphological study of clad layer. Microstructure, the presence of microcracks was studied with help of FESEM images (Model: Supra 55, Make: Zeiss, Germany). Clad layer thickness along with melt depth was observed in each sample using an Olympus BX51 optical microscope. At last wear test of each sample was carried out to find out wear rate of a clad layer formed and compared it with the substrate wear rate. DUCOM TR-201-M1 pin on disk machine which confirms to the ASTM G99 standard was used to analyze the

wear rates and friction monitoring at room temperature. The EN31 disk was used in the wear rate load was 2 N, RPM was 300, and test duration was 10 min, respectively, run out and flatness on disk was controlled within 10 microns.

58.3 Results and Discussions

58.3.1 EDX Analysis of Clad Layer

Energy dispersive X-ray analysis was done to know the chemical composition of cladded surface prepared over Ti6Al4V substrate. Figure 58.3 shows the EDX report of the top surface of cladded sample and Fig. 58.4 shows the EDX report of the cross-sectional surface of the cladded sample.

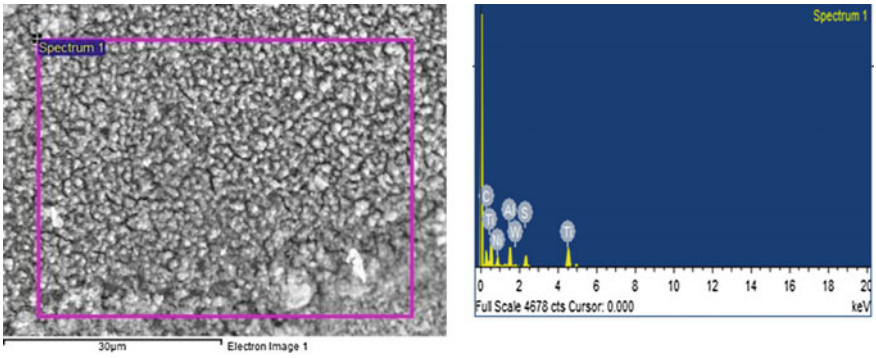

Fig. 58.3 EDX report of top cladded surface prepared at 125 W and scanning speed 450 m/min

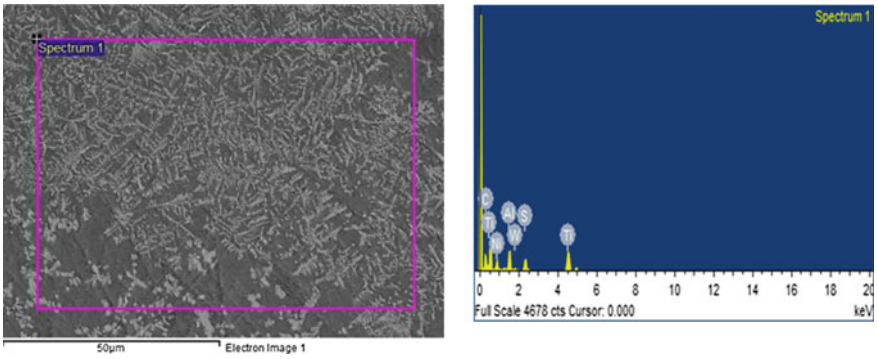

Fig. 58.4 EDX report of the cross-sectional surface of cladded at 125 W and scan 450 m/min

Table 58.3 Comparison of EDX report of the top surface (A) and cross-sectional surface (B) of cladded sample

Elements	C	Ti	Ni	Al	S	W
wt% A	38.44	35.15	7.08	9.65	7.78	1.90
wt% B	4.56	42.53	5.99	1.88	12.25	31.08

Metal matrix composite coatings were prepared on the Ti6Al4V substrate that consist of Tungsten, Carbon, Nickel, Aluminum, Sulfur, Titanium, and some minor constituents. Percentage of Tungsten in metal matrix composition is higher at inner region in comparison to the top surface of the metal matrix as shown in Table 58.3, i.e., EDX report of cross section of the metal matrix composite shows 31.08 wt% of Tungsten but EDX report of top surface of the metal matrix composite layer shows only 1.90 wt% of Tungsten. This is because Tungsten is a heavier particle with density 19.25 gm/cm3 in comparison to other elements. Hence this is settled at the bottom of the molten pool in higher concentration than the surface. It is also observed that percentage of Tungsten in metal matrix composite is higher at lower laser power than at higher laser power, this is due to the reason that at higher laser power greater melting of the substrate takes place which contributes higher dilution of the substrate in the melt pool. During laser cladding process preplaced tungsten powder and titanium powder reacts with carbon nanotubes in the molten pool to form carbides of tungsten, hence this leads to the formation of a hard compound like titanium carbide which contributes more to improve hardness up to 3–4 times hardness of the substrate. However, at a higher temperature, a chemical reaction took place between liquid titanium and tungsten with the carbon nanotubes in the melt pool [15]. Due to the higher temperature gradient between the cladding layer and substrate with the rapid heating and cooling result in the formation of fine titanium carbide particles precipitates easily due to higher cooling rate [16].

58.3.2 XRD Analysis of Clad Layer

X-Ray diffraction analysis was done on the prepared laser cladded samples to know the intermetallic compounds present in the metal matrix composite layer deposited on the Ti6Al4V substrate. XRD was performed on 2nd GEN D2 (BRUKER) machine. XRD analysis of WS_2–CNT–Ni–Ti6Al4V cladded sample with composition WS_2-60%, CNT-20%, Ni-15%, Ti6Al4V-5% is shown in Fig. 58.5. Various compounds like W_2C, WS_2, TiC, Ti_2S, NiS_2, Al_4C_3, and VS_2 are detected in XRD analysis in large amount which contributes to high hardness, less wear rate, and low coefficient of friction of the composite clad layer formed and some compounds are also detected in small amount, oxide formation in compounds is prevented by providing Argon gas atmosphere. Strong diffraction peak is seen at an angle of 40° and small peaks are seen in the graph at angles of 35°, 56.5°, 59.5°, 63.7°, 73.5°, and 101°. W_2C, TiC,

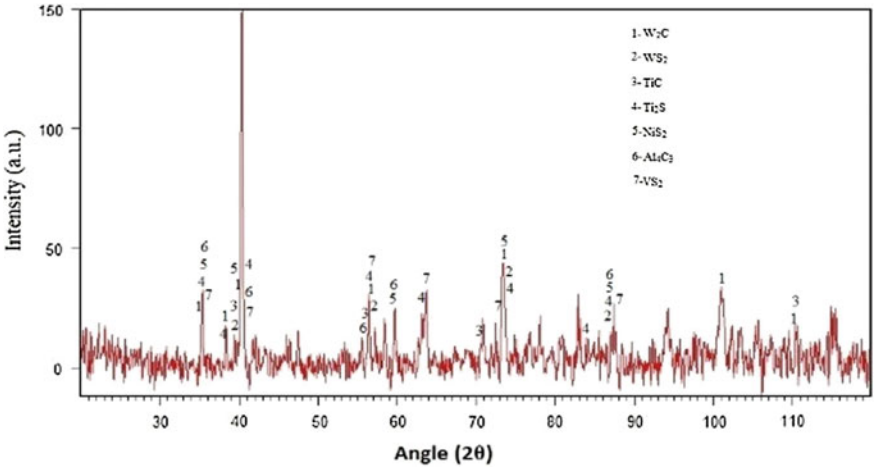

Fig. 58.5 XRD pattern of laser cladded sample with WS_2-60%, CNT-20%, Ni-15%, and Ti64-5%

and Al_4C_3 are the intermetallic compounds having high hardness value responsible for increasing the hardness of the metal matrix composite clad layer up to 3.5 times that of the substrate, i.e., Ti6Al4V. WS_2, NiS_2, Ti_2S, and VS_2 are the compounds contributing to the low coefficient of friction and less wear rate of the composite clad layer.

58.3.3 Microstructure

FESEM images of the top surface and cross section of the clad sample was taken to study the microstructure of the cladded sample. Presence of cracks, pores, bulk impurities, and particle shape generated are detected by analysis of top surface while the cross-sectioned surface was analyzed to check the presence of internal cracks in the cladded metal matrix composite layer. In Fig. 58.6 six FESEM images of top and cross-section surface of three different samples prepared with the same laser operating parameters but with different compositions are shown. It was observed that globular nanoparticles are formed in cladded layer and these are surrounded by other metals. Uniform metal matrix composite was formed by laser cladding. On comparing FESEM image (a), (c), and (e) in Fig. 58.6 it was observed that more uniform metal matrix composite coating with no cracks was formed in samples with (a) 15% CNT and (c) 20% CNT composition but sample with (e) 25% CNT composition shows crack formation. It is observed when CNT% composition increases beyond 20% then crack formation occurs in cladded layer.

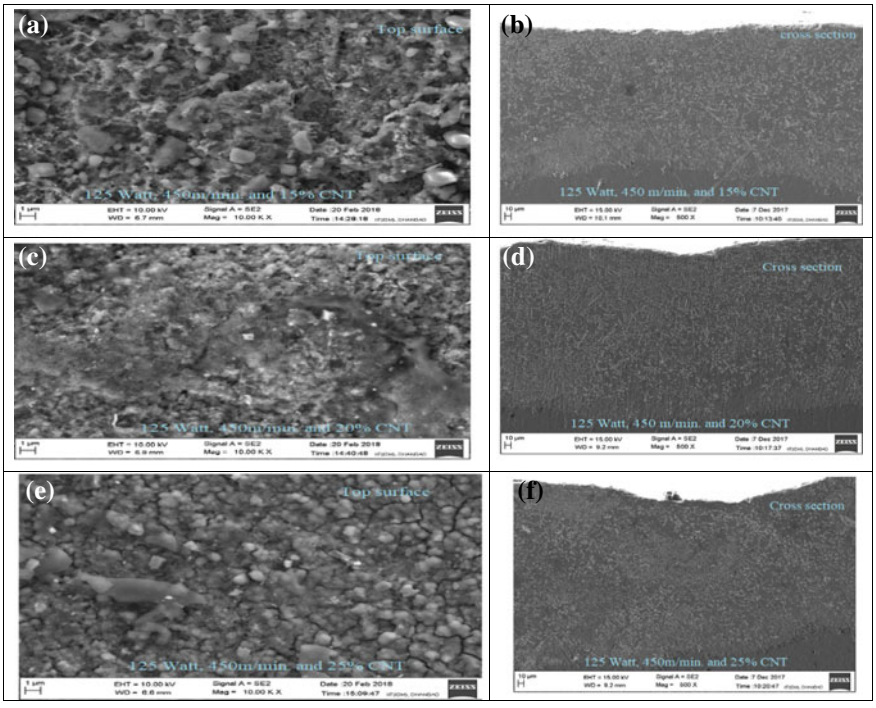

Fig. 58.6 FESEM images of the top surface and cross section of some cladded samples at a different composition percentages of CNT, i.e., 15 (**a**, **b**), 20 (**c**, **d**), 25 (**e**, **f**)

58.3.4 Microhardness of the Clad Layer

To detect the microhardness of the clad samples, Vickers microhardness indenter (ECONOMET VH-1, Chennai METCO) was used with a load of 500 kgf and dwell time of 10 s. Each cladded samples were polished with the fine grinding disk to get the accurate microhardness readings. On each sample, three indentations at different positions were made and an average of their microhardness reading was considered as microhardness of the sample. Microhardness of cladded layers was found to be increased 2–3.5 times (up to 1240 $HV_{.5\,kg}$) the microhardness of the substrate material, i.e., Ti6Al4V (360 $HV_{.5\,kg}$) due to the formation of hard compounds tungsten carbide and titanium carbide in the cladded layer by laser cladding. Variation in microhardness of the metal matrix composite clad layer with varying laser power and composition of WS_2, CNT, and Ni has been plotted in Fig. 58.7. It was observed that with increasing laser power microhardness of cladded layer increases as with the increase in laser power, size of melt pool increases due to which there is more heat transfer convection, this observation was reported by other researchers also [17]. With varying composition microhardness first increases and then decreases, this is

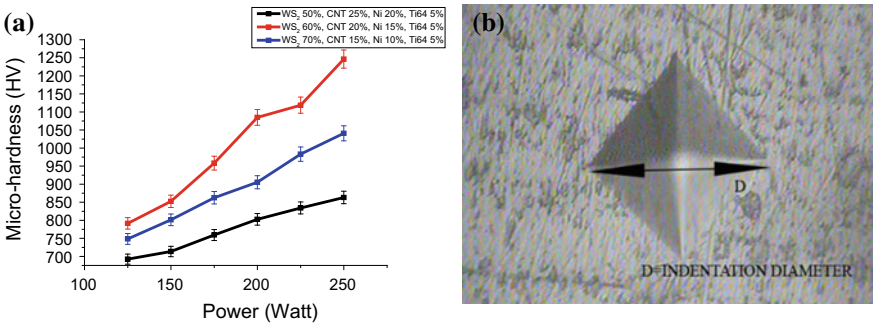

Fig. 58.7 **a** Variation of microhardness ($HV_{.5\ kg}$) with power (Watt) in cladded sample **b** diamond indentation on the cladded sample by Vickers microhardness intender

due to the reason that with increasing composition of CNT up to 20% microhardness increases but increasing it further to 25% leads to crack formation.

58.3.5 Clad Layer Thickness

Optical images using Olympus metallurgical microscope (model-BH2-UMA) at 5× magnification were taken and FESEM images of the cross section of the clad layers were taken to know the clad layer thickness along with melt depth and presence of pores inside the clad layer. It was observed that good clad layer is formed without pores inside the clad layer and the clad-substrate interface is clearly visible with no pore formation which indicates minimum dilution effect. At different experimental parameters, the different clad layer thickness is observed as shown in Table 58.1. With increasing laser power clad layer thickness increases because when laser power increases keeping scanning speed constant substrate melts in greater amount and more dilution effect takes place between the molten pool and molten substrate. As shown in Fig. 58.8b good metal matrix composite of average 251 μm thickness is formed without any pores and cracks in its depth by laser cladding of WS2, CNT, Ni, and Ti6Al4V powders on Ti6Al4V substrate. It is seen from Fig. 58.8a clad layer thickness along with melt depth increases when power increases, as with the increase in power more substrate melts and get mixed in the clad layer in molten form increasing the clad layer thickness. It was also observed as shown in the graph that as composition of CNT increases clad layer thickness increases, this may be because heat absorptivity of carbon is very high so the amount of heat energy absorbed by the melt pool is dependent on the weight% of CNT, as the weight % of CNT increases in composition of clad layer more amount of heat energy is absorbed which will melt more amount of substrate and in result clad layer thickness along with melt depth increases.

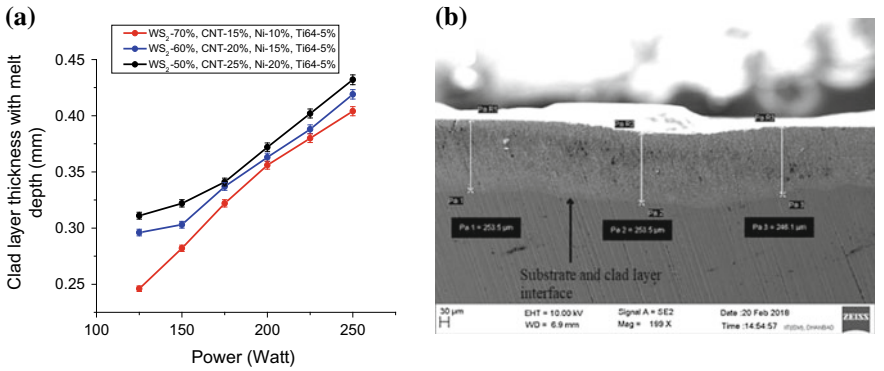

Fig. 58.8 **a** Variation of clad layer thickness (mm) with power (Watt) at different compositions. **b** FESEM image of cross section of cladded sample showing cladded layer at 150 W and 450 mm/min

58.3.6 Wear Analysis

Wear tests were performed on three coated samples of different compositions and the substrate material using pin and disk test rig wear testing machine (TR-20LE, DUCOM) using the SS304 disk on the wear testing machine. By pin and disk testing machine wear, the coefficient of friction and frictional force can be performed. For performing wear test of the coated samples, first samples were cut in small size 5 mm × 2.5 mm × 4 mm by wire-EDM machine then these small samples were polished by grit papers using grit number 1200. After polishing, samples acetone cleaning of the samples was done and then these samples were fixed to the cylindrical pins (6 mm in diameter and 30 mm in height) using adhesive. On wear testing machine parameters were fixed as angular speed 300 rpm, track dia. 110 mm, 2 kgf loads, and experiment on each sample was performed on for 10 min.

Wear analysis of three coated samples of different compositions is shown in Fig. 58.9a and wear analysis of substrate material, i.e., Ti6Al4V is shown in Fig. 58.9b. Wear of the coated samples is much lower than the wear of substrate material as we can see from both graphs, on an average wear of the coated samples has been reduced to about 20 times of the substrate material, i.e., Ti6Al4V which shows metal matrix composite coating has improved and much high wear resistance than the substrate. It was observed from the shown graph that initially wear rate in coated samples was high in comparison to wear rate after few seconds; it is because of the uneven contact surface while after some surface contact becomes uniform with disk and the wear rate decreases. Wear of the sample with 25% CNT composition was lowest and wear of sample with 15% CNT composition is highest which is due to the reason that as wt% of CNT increases in the composition of metal matrix composite there is more carbide formation in form of tungsten carbide and titanium carbide which improves more dispersion strengthening of the clad layer which enhances hardness and strength of the clad layer which results in improved wear resistance of

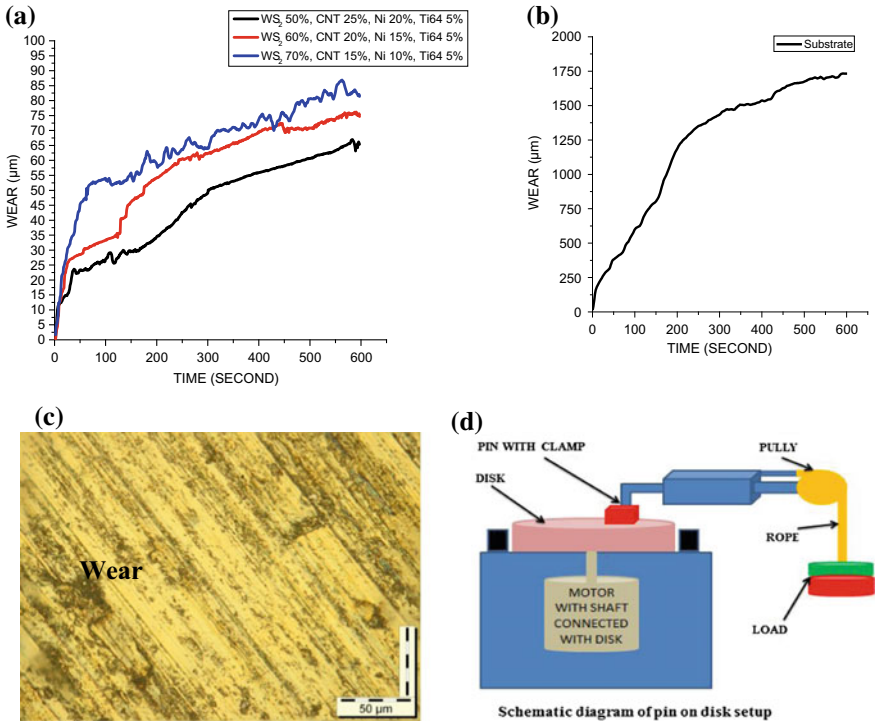

Fig. 58.9 Variation of wear of **a** coated samples with time at different compositions fabricated at same laser parameters, i.e., 125 W laser power and 450 m/min. Scanning speed **b** Ti6Al4V substrate. **c** Wear track of the wear out sample. **d** Schematics diagram of wear testing machine

the clad layer. Wear track has been seen in Fig. 58.9c. A similar result is also seen in other works of CNT on the titanium substrate.

Value of coefficients of friction of the samples lies in the range 0.3–0.35 which is not much improved than the coefficient of friction for substrate, i.e., 0.352. But it is the combined action of WS_2 and Ni used with CNT in this work which restricts coefficient of friction in this range as carbide formation having high hardness value due to the presence of CNT can lead to the higher coefficient of friction in 0.5–0.6 range. WS_2 is the solid lubricant which reduces friction value by providing lubricating effect and in situ formation of Nickel, sulfides have taken place during laser cladding operation, which also has good lubricating property and contributed to lowering down the coefficient of friction value of the metal matrix composite coating formed by laser cladding.

58.4 Conclusion

- Metal matrix composite coating was formed by laser cladding operation on Ti6Al4V substrate and characterization was carried out as reported to study the synergetic action of WS2, CNT, and Ni powders used to form a coating. By analysis of characterizations conclusions made are as follows:
- There is good metallurgical bond formation between the coated clad layer and the substrate, without very less pore formation in depth of clad layer.
- A metal matrix composite clad layer of thickness in the range 251–432 μm was deposited on the surface of Ti6Al4V substrate as observed with the help of an optical microscope and FESEM images.
- XRD analysis of the metal matrix composite coating shows the presence of compounds like W_2C, WS_2, TiC, and NiS_2 which are contributing to the combined effect of improving the hardness of the coated layer as well as reducing the coefficient of friction for improving wear resistance.
- Microhardness of the metal matrix composite coating formed shows a good increase from 360 $HV_{(0.5\ kg)}$ of the substrate up to 1118.18 $HV_{(0.5\ kg)}$ which indicates its good industrial usability.
- Wear of the coated samples is about 20 times less than the substrate wear, it shows that coated samples have much improved wear resistance than the substrate and has good scope for industrial utilization.
- It was found that due to the synergetic effect of WS_2, CNT, Ni, and Ti6Al4V powders coefficient of friction of coated layer was reduced up to 0.30 which is lower than the coefficient of friction of substrate, i.e., 0.352.

References

1. Hussain, M., Kumar, V., Mandal, V., Singh, P.K., Kumar, P., Das, A.K.: Development of cBN reinforced Ti6Al4V MMCs through laser sintering and process optimization. Mater. Manuf. Process. 1–11 (2017). https://doi.org/10.1080/10426914.2017.1303152
2. Hussain, M., Mandal, V., Singh, P.K., Kumar, P., Kumar, V., Das, A.K.: Experimental study of microstructure, mechanical and tribological properties of cBN particulates SS316 alloy based MMCs fabricated by DMLS technique. J. Mech. Sci. Technol. **31**(6), 2729–2737 (2017). https://doi.org/10.1007/s12206-017-0516-3
3. Zhu, Y., Wang, W., Jia, X., Akasaka, T., Liao, S., Watari, F.: Deposition of TiC film on titanium for abrasion resistant implant material by ion-enhanced triode plasma CVD. Appl. Surf. Sci. **262**, 156–158 (2012). https://doi.org/10.1016/j.apsusc.2012.03.152
4. Costa, M.Y.P., Venditti, M.L.R., Cioffi, M.O.H., Voorwald, H.J.C., Guimarães, V.A., Ruas, R.: Fatigue behavior of PVD coated Ti–6Al–4V alloy. Int. J. Fatigue **33**(6), 759–765 (2011). https://doi.org/10.1016/j.ijfatigue.2010.11.007
5. Kumar, S., Mandal, A., Das, A.K., Dixit, A.R.: Parametric study and characterization of AlN-Ni-Ti6Al4V composite cladding on titanium alloy. Surf. Coat. Technol. (2018). https://doi.org/10.1016/j.surfcoat.2018.05.053
6. Kundu, S., Hussain, M., Kumar, V., Kumar, S., Das, A.K.: Direct metal laser sintering of TiN reinforced Ti6Al4V alloy based metal matrix composite: fabrication and characterization. Int. J. Adv. Manuf. Technol. 1–12 (2018). https://doi.org/10.1007/s00170-018-2159-7

7. Yoon, S., Kim, H.J., Lee, C.: Deposition behavior of bulk amorphous NiTiZrSiSn according to the kinetic and thermal energy levels in the kinetic spraying process. Surf. Coat. Technol. **200**(20–21), 6022–6029 (2006). https://doi.org/10.1016/j.surfcoat.2005.09.022
8. Huang, N., Yang, P., Leng, Y.X., Wang, J., Sun, H., Chen, J.Y., Wan, G.J.: Surface modification of biomaterials by plasma immersion ion implantation. Surf. Coat. Technol. **186**(1–2), 218–226 (2004). https://doi.org/10.1016/j.surfcoat.2004.04.041
9. Candel, J.J., Amigó, V., Ramos, J.A., Busquets, D.: Sliding wear resistance of TiCp reinforced titanium composite coating produced by laser cladding. Surf. Coat. Technol. **204**(20), 3161–3166 (2010). https://doi.org/10.1016/j.surfcoat.2010.02.070
10. Kobryn, P.A., Semiatin, S.L.: Microstructure and texture evolution during solidification processing of Ti–6Al–4V. J. Mater. Process. Technol. **135**(2–3), 330–339 (2003). https://doi.org/10.1016/S0924-0136(02)00865-8
11. Wu, X., Liang, J., Mei, J., Mitchell, C., Goodwin, P.S., Voice, W.: Microstructures of laser-deposited Ti–6Al–4V. Mater. Des. **25**(2), 137–144 (2004). https://doi.org/10.1016/j.matdes.2003.09.009
12. Feng, S.R., Tang, H.B., Zhang, S.Q., Wang, H.M.: Microstructure and wear resistance of laser clad TiB–TiC/TiNi–Ti2Ni intermetallic coating on titanium alloy. Trans. Nonferrous Metals Soc. China **22**(7), 1667–1673 (2012). https://doi.org/10.1016/S1003-6326(11)61371-X
13. Pang, W., Man, H.C., Yue, T.M.: Laser surface coating of Mo–WC metal matrix composite on the Ti6Al4V alloy. Mater. Sci. Eng. A **390**(1–2), 144–153 (2005). https://doi.org/10.1016/j.msea.2004.07.065
14. Tu, J.P., Yang, Y.Z., Wang, L.Y., Ma, X.C., Zhang, X.B.: Tribological properties of carbon-nanotube-reinforced copper composites. Tribol. Lett. **10**(4), 225–228 (2001). https://doi.org/10.1023/A:1016662114589
15. Giraldo, L.F., López, B.L., Brostow, W.: Effect of the type of carbon nanotubes on tribological properties of polyamide 6. Polym. Eng. Sci. **49**(5), 896–902 (2009). https://doi.org/10.1002/pen.21386
16. Wu, W.L.: Dissolution precipitation mechanism of TiC/Ti composite layer produced by laser cladding. Mater. Sci. Technol. **26**(3), 367–370 (2010). https://doi.org/10.1179/174328408X395998
17. Yang, S., Liu, W., Zhong, M., Wang, Z.: TiC reinforced composite coating produced by powder feeding laser cladding. Mater. Lett. **58**(24), 2958–2962 (2004). https://doi.org/10.1016/j.matlet.2004.03.051
18. Wu, X.: In situ formation by laser cladding of a TiC composite coating with a gradient distribution. Surf. Coat. Technol. **115**(2–3), 111–115 (1999). https://doi.org/10.1016/S0257-8972(99)00045-6
19. Mandal, V., Hussain, M., Kumar, V., Das, A.K., Singh, N.K.: Development of reinforced TiN-SS316 metal matrix composite (MMC) using direct metal laser sintering (DMLS) and its characterization. Mater. Today: Proc. **4**(9), 9982–9986 (2017). https://doi.org/10.1016/j.matpr.2017.06.306

Chapter 59
Towards Extending ECAP Technology from Lab Scale to Manufacturing by Enhanced Multipass Continuous ECAP Process

Ankit Sahai, Atul Dayal and R. S. Sharma

Abstract Last two decades have witnessed innovations in the area of Equal Channel Angular Pressing (ECAP) for producing ultra-fine grained materials. But the manipulation of billets between consecutive passes of ECAP may cause problems in industrial set-ups where continuous processing is required. The paper examines developments related to modifying conventional ECAP with multipass continuous ECAP process to increase the process efficiency and techniques for upscaling the procedure. In first part, conventional ECAP is discussed with changes in mechanical properties of Al alloy, then, based on the problems encountered during experimentation, multipass continuous ECAP is proposed with FEM simulations carried out for 10 mm round Al7075 billet, simulating four passes in a single set-up. The equivalent strain after four passes in conventional ECAP for 70 mm billet is 5.21 which as compared to continuous ECAP for 1614 mm length is 7.4 (an increase of 48% for 1500% increase in length).

Keywords Equal Channel Angle Pressing (ECAP) · Finite Element Analysis (FEA) · Continuous ECAP · Mechanical properties

59.1 Introduction

It has been established that the grain size is the major factor in dictating the mechanical properties of polycrystalline material and last 20 years have witnessed considerable achievements in obtaining materials with these ultra-fine grain sizes through Severe Plastic Deformation (SPD) techniques [1–3]. The SPD work during last two decades was focussed on variety of alloys in lab scale for obtaining bulk nanostructured materials with superior mechanical properties which can be used in many industrial and engineering applications. Among them, aluminium alloys, being light weight and widely used in automobile, aerospace and military applications, are studied most thoroughly due to their high ductility and ease of processing.

A. Sahai (✉) · A. Dayal · R. S. Sharma
Faculty of Engineering, Dayalbagh Educational Institute, Agra, India
e-mail: sahaiankit@dei.ac.in

M. S. Shunmugam and M. Kanthababu (eds.), *Advances in Micro and Nano Manufacturing and Surface Engineering*, Lecture Notes on Multidisciplinary Industrial Engineering,
https://doi.org/10.1007/978-981-32-9425-7_59

Due to numerous processing parameters, various characteristics of structural changes caused by SPD have been the research themes in laboratories worldwide resulting in the publication of large amount of papers over the last 25 years [4, 5]. Apart from many experimental investigations, many researchers are also working on Finite Element Modelling (FEM) [6–8] to understand the deformation behaviour of materials and to estimate the developed strain in the ECAP process. Some have also discussed the optimization of dies in metal forming [9]. But, less attention has been paid for moving the SPD technology from lab scale to an industry. For example, the primary drawbacks of the ECAP process are that most material currently produced only billets of small cross sections and short lengths for laboratory studies, and there is a substantial amount of undeformed material at the leading and training end of each piece. The length of the workpiece is limited because of the development of very large frictional stresses in the entrance channel. This imposes high stresses on the dies, which may fracture at points of stress concentration. Also, with every pass, split dies are opened for taking out the billet and for cleaning purposes. Before experimentation, the die channels are again lubricated properly for smooth pressing of the material. Then, again the billet is pressed for subsequent pass and the same process is followed. This results in huge time involvement in opening, closing and cleaning of dies as the billet is pressed multiple times. The force required to press a billet through the die increases very rapidly with the length of the billet. Correspondingly, there is also a large increase in stresses experienced by the die. These two factors limit the length of the billet that can be practically processed by ECAE/P. The most scientific studies had been conducted on samples 10 mm diameter or smaller. These sizes are clearly not sufficient for use as stock material for most forging applications. As a result, commercialization of ECAP technology is not possible because of above-mentioned limiting factors which may be attributed to its discontinuity in experimentation.

The work in this paper presents how FEM analysis can be used to help assess technical feasibility of the existing ECAP process and develop new continuous ECAP technique process without committing to expensive tooling and machinery. In this research work, first, AlSiMg alloy was ECAPed to analyse its mechanical properties and then based on difficulties and limitations in set-up, the process is modified to multipass continuous ECAP and FEM simulations are performed to compare it with conventional ECAP with respect to the equivalent strain.

59.2 Experimental Set-up

AlSiMg alloy billets of 70 mm in length and diameter 10 mm were used in this research work. The ECAP was conducted at 30 °C with dies used in the experimentation consisted of two channels having equal channels intersecting at channel angle, $\phi = 90°$ and outer arc angle, $\psi = 12°$ as shown in Fig. 59.1. The multipass ECAP processing was performed using routes route C up to four passes. The lubricant used

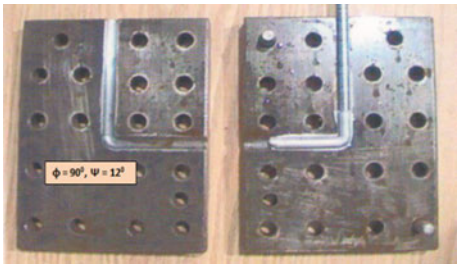

Fig. 59.1 ECAP dies

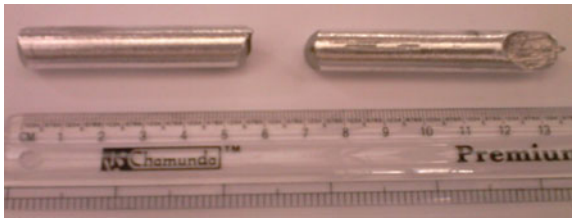

Fig. 59.2 Samples after ECAP

during the experimentation was Molybdenum Disulphide (MoS_2). The dies containing the specimen and plunger were placed on the platform of the hydraulic machine of 100 T capacity. After adjusting the height of plunger which is coming out of the dies, calculated load is applied and the plunger is pressed with constant speed of 1 mm/s at room temperature. The plunger is pressed till the entire specimen passes plastic deformation zone at the crossing of two channels. The die set is then taken out and unscrewed to take the sample out for further processing, Fig. 59.2.

59.3 Mechanical Properties and Microstructure

The X-ray diffraction analysis was done using RIGAKU X-ray diffractometer with a Co target. The samples were analysed for different passes and profiles are plotted in Fig. 59.3. The Al–Si–Mg alloy having FCC structure has peaks for 111, 200, 220, 311, 222, etc. The as-received sample has strong initial texture, so, no (220) peak and high intensity. During the deformation, there is increase in dislocation density and preferred orientation. This results in reduction of intensity but the relative intensity for 111 and 220 increases with number of passes indicating evolution of strong <111> and <220> texture fibres. The processed samples were evaluated for mechanical properties using tensile testing done with the help of tensometer. The tensile properties evaluated up to four passes are shown in Table 59.1. It can be seen that the tensile strength increases from 122 to 388 MPa (enhancement of 215%) up to four passes and also, there is significant enhancement of yield strength during the pressing of billet (105–330 MPa) while elongation to failure % decreases from 18.3 to 11.5% for route C.

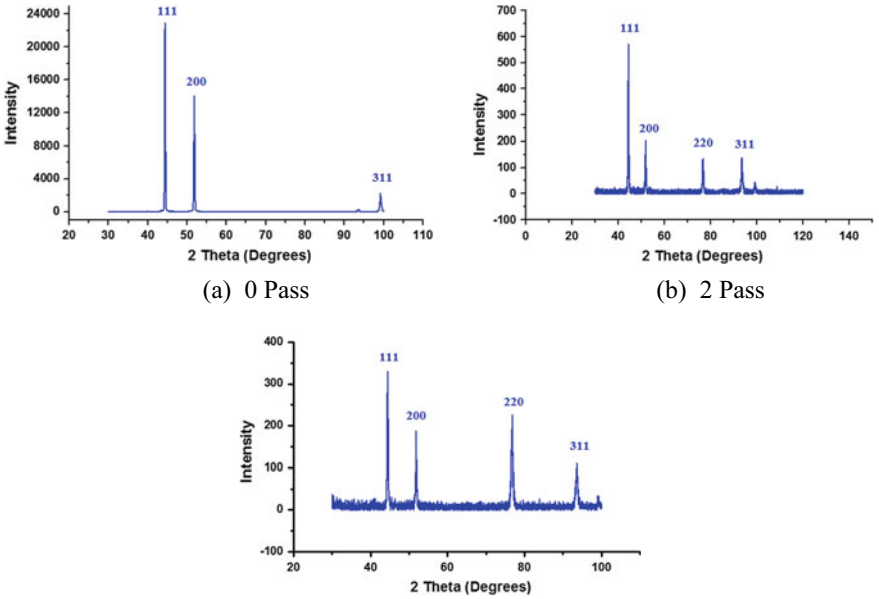

Fig. 59.3 XRD profiles of ECAPed specimens for different passes

Table 59.1 Mechanical properties of AlSiMg alloy after ECAP

Condition	Average microhardness (HV)	Ultimate tensile strength (MPa)	Yield strength (MPa)	Elongation (%)
As received	60	122	105	18.3
1-pass	80	220	195	15
2-pass	96	258	240	12.5
3-pass	108	335	285	13
4-pass	123	388	330	11.5

This significant enhancement in mechanical properties is due to refinement in grain size in the resulting microstructure as a result of large accumulated strain in the deformed material during multipass ECAP. Also, because the material is pressed multiple times during ECA pressing in different routes, which may lead to the evolution of shear systems that are responsible for the development of microstructures with substantial grain refinement. Figure 59.4 shows SEM images of the alloy at different passes. Before ECAP, the average grain size was 60 μm, which decreases to around 1 μm after four passes. This decrease in grain size is attributed to the subgrain formation due to severe deformation of the material, which further increases the misorientation along its boundaries during repeated pressing of workpiece. As

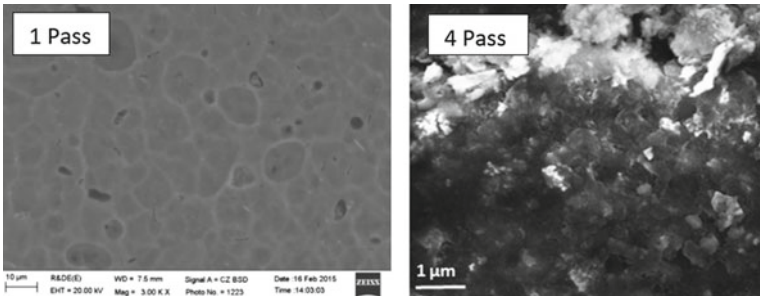

Fig. 59.4 SEM micrographs during ECAP processing through route C for different passes

a result, a stage will come when due to large plastic strains, a definite misorientation will cause subgrain to change to high angle grain boundaries resulting in grain refinement.

The average microhardness values are measured and depicted in Table 59.1, the as-received specimen exhibits Vickers hardness value of 60 HV which increases to 123 HV (an increase of 105%) after four passes during route C processing. This increase in hardness is also a result of refinement of grains during intensive deformation of material. The readings are average values of multiple positions in longitudinal direction.

59.3.1 Limitations of Conventional ECAP

In ECAP process if die design and process parameters are not planned properly, experimental difficulties can arise resulting in the breaking of plunger, dies and formation of cracks during multipass pressing of the billets, Fig. 59.5 and finally complete failure of the specimen after some passes. The process parameters need to be carefully studied and investigated properly before performing the experiments as wrong set of parameters may lead to the above-mentioned failures.

Also, with every pass, split dies are opened for taking out the billet and for cleaning purposes. Again the billet is pressed for subsequent pass and the same process is followed. This results in huge time involvement in opening and closing of dies as the billet is pressed multiple times. To solve this problem some researchers have proposed continuous ECAP [10], Fig. 59.6a, but they proposed the process for one pass. This work proposes enhanced continuous ECAP for four passes in one complete set-up, Fig. 59.6b. The process set-up has four rollers integrated with upper and lower dies which can smoothly push the material so that it can be pressed four times during one complete experimentation cycle.

(a) 1st Pass (b) 2nd Pass

(c) 3rd Pass (d) 4th Pass

Fig. 59.5 Crack formation during ECAP for route C in 90° die

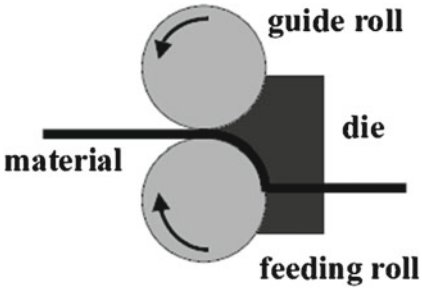

(a) Continuous ECAP

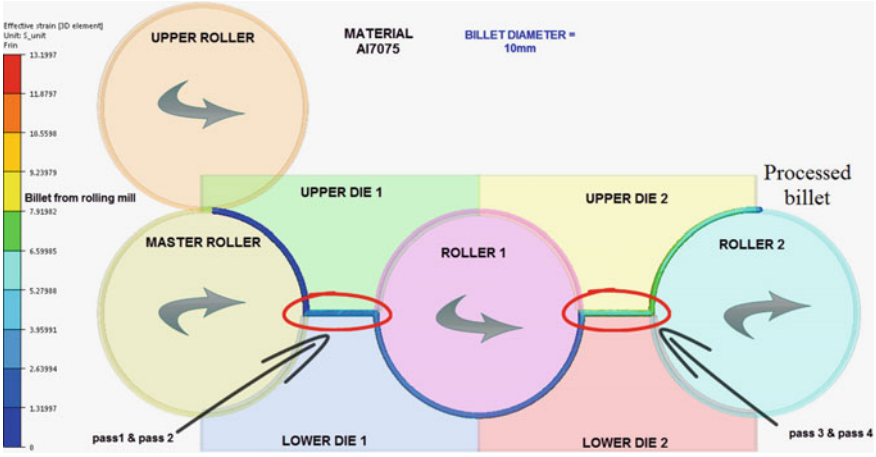

(b) Enhanced Multi-pass Continuous ECAP

Fig. 59.6 **a** Continuous ECAP proposed earlier and **b** enhanced continuous ECAP

59.4 Finite Element Analysis of Continuous ECAP

The billet used for the simulations is a cylindrical piece of 10 mm in diameter and 1614 mm in length (which has been processed) having the material properties of Aluminium alloy (Al7075). The meshing and FEM model is depicted in Fig. 59.7. Al7075 composition includes 5.6–6.1% zinc, 2.1–2.5% magnesium, 1.2–1.6% copper and traces of silicon, iron, manganese, titanium and chromium.

Here, thermo-mechanical conditions are governed by the Hansel Spittel rheology which can be defined by the following equation:

$$\sigma_f = Ae^{m_1 T} T^{m_9} \varepsilon^{m_2} e^{\frac{m_4}{\varepsilon}} (1+\varepsilon)^{m_5 T} e^{m_7 \varepsilon} \dot{\varepsilon}^{m_3} \dot{\varepsilon}^{m_8 T} \tag{59.1}$$

The equivalent strain contours during the deformation process for the complete process is shown in Fig. 59.8. The equivalent strain after pass 1 is 2.4 which increases to 7.4 at the end of fourth pass. The billet undergoes high plastic deformations during each pass and the same has been confirmed with colour maps depicting highly strained material exiting after final ECAP pass. The strain contour exhibits low strain values before first pass which increases during multiple pressing and reaching very high values after final ECAP pass.

The results are also depicted in Table 59.2 for $\text{Ø} = 90°$, $\Psi = 0°$, dia = 10 mm, temperature = 20 °C and material Al7075. It is clearly evident that after four passes equivalent strain in continuous ECAP reaches to 7.4 which is much higher than conventional ECAP process (5.21), Fig. 59.9. During conventional ECAP process for 70 mm length billet, equivalent strain after four passes is around 5.21 which as compared to continuous ECAP for 1614 mm length is 7.4 (an increase of 48% for 1500% increase in length). This multipass continuous ECAP process allows us to think an alternative solution to the conventional set-up with enhanced equivalent

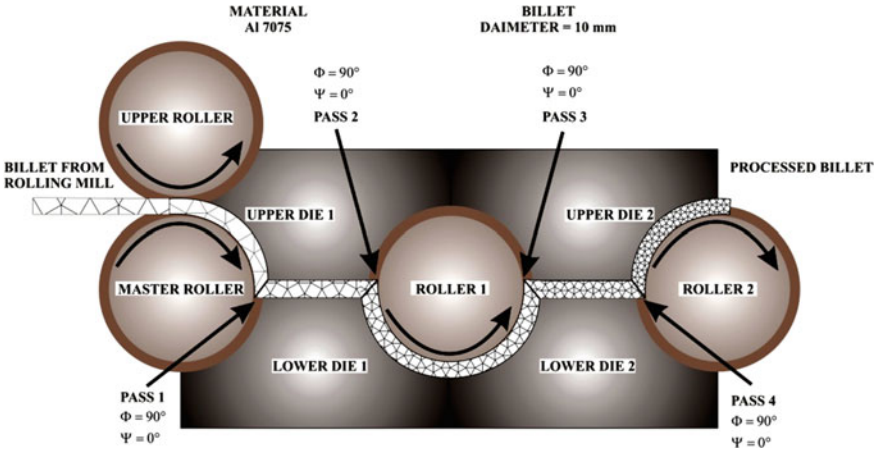

Fig. 59.7 FEM model of continuous ECAP set-up

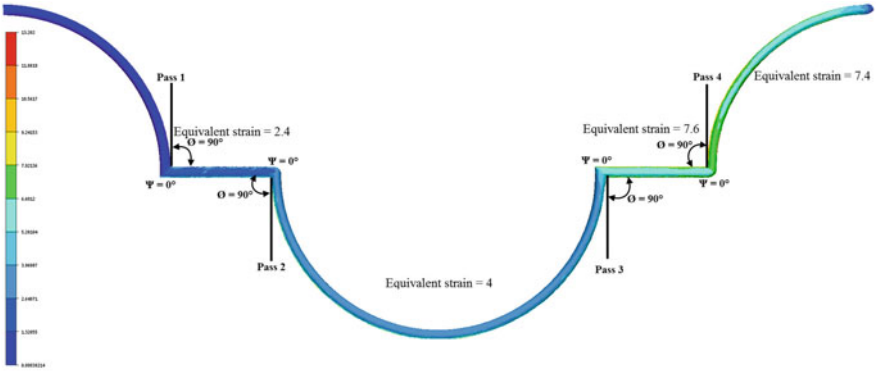

Fig. 59.8 Equivalent strain contours of Ccontinuous ECAP process

Table 59.2 Equivalent strain values for different passes

Passes	Pass 1	Pass 2	Pass 3	Pass 4	Conventional ECAP (4th pass)	
Eq. strain	2.4	4	5.6	7.4	5.21	See Fig. 59.9

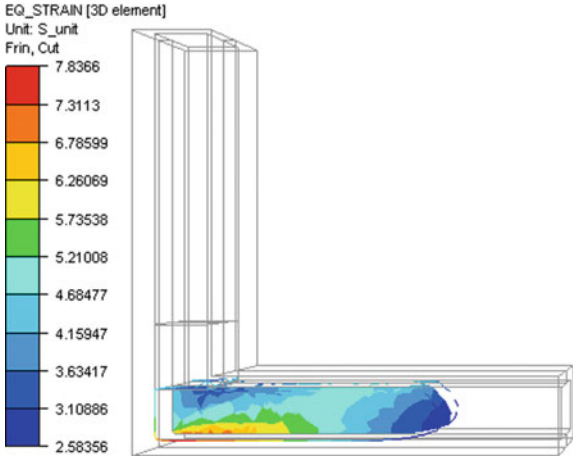

Fig. 59.9 Equivalent strain contours for conventional ECAP

strain (an indicative of grain size) with an added advantage of large length billets. So, this continuous set-up is far better than conventional lab set-up and can easily get integrated with manufacturing industry.

59.5 Conclusions

The research work outlines the following points:

(a) AlSiMg alloy was ECAPed up to four passes, increasing tensile strength and yield strength to 388 and 330 MPa but with difficulties in processing and crack formation, new enhanced continuous ECAP is proposed.
(b) This enhanced continuous severe plastic deformation process can accommodate four ECAP passes in one set-up as compared to conventional ECAP where we can perform one or maximum up to two ECAP passes.
(c) In this continuous process where billets of lengths 1600 mm can be easily processed as compared to conventional ECAP where mostly researchers work on 60–70 mm length billet (1500% increase in length as compared to conventional process).
(d) The equivalent strain produced after the complete process is 7.4 which is much higher (48%) than the conventional ECAP (5.21).
(e) It is proposed to integrate this set-up with any manufacturing industry so that nanostructured alloys can be prepared for large size billets which are not possible for lab scale ECAP set-up.

Acknowledgements The authors gratefully acknowledge the help rendered by NIT Tiruchirappalli and ACMS, IIT Kanpur for Scanning Electron Microscopy. Support for this research from MHRD, under NMEICT-Virtual Labs is deeply appreciated.

References

1. Langdon, T.G.: Research on bulk nanostructured materials in Ufa: twenty years of scientific achievements. Mater. Sci. Eng. A **503**, 6–9 (2009)
2. Dayal, A., Sahai, A., HansRaj, K., Sharma, R.S.: Comprehensive study of effect of process parameters in equal channel angular pressing. Indian J. Eng. Mater. Sci. **25**(2), 113–121 (2018)
3. Valiev, R.Z., Langdon, T.G.: Principles of equal-channel angular pressing as a processing tool for grain refinement. Prog. Mater Sci. **5**, 881–981 (2006)
4. Estrin, Y., Vinogradov, A.: Extreme grain refinement by severe plastic deformation: a wealth of challenging science. Acta Mater. **61**, 782–817 (2013)
5. Langdon, T.G.: The principles of grain refinement in equal-channel angular pressing. Mater. Sci. Eng. A **462**, 3–11 (2007)
6. Dixit, P.M., Dixit, U.S.: Modeling of Metal Forming and Machining Processes. Finite Element and Soft Computing Methods. Springer, London (2008)
7. HansRaj, K., Sharma, R.S., Sahai, A., Gupta, N.K.: Different die designs for processing of Al alloys: FEM study. Proc. Indian Natl. Sci. Acad. **79**(4), 829–836 (2013)
8. Sahai, Ankit, Sharma, Rahul S., HansRaj, K.: Evolution of strain in multi-pass hybrid equal channel angular pressing using 3D element analysis. Mater. Sci. Forum **762**, 283–288 (2013)
9. Sharma, R.S.: Shape Optimization of Forming Dies. LAP Lambert Academic Publishing (2016). ISBN—13: 978-3-659-92966-3
10. Raab, G.J., Valiev, R.Z., Low, T.C., Zhu, Y.: Continuous processing of ultrafine grained Al by ECAP-Conform. Mater. Sci. Eng. A **382**, 30–34 (2004)

Chapter 60
The Effect of Normal Load and Sliding Frequency on the Reciprocating Friction Behavior of Nanocrystalline CuO-Based Alumina Ceramics

Partha Haldar, Tapas Kumar Bhattacharya and Nipu Modak

Abstract This investigation reports the effect of normal load and sliding frequency on the tribological performance of nanocrystalline CuO-based alumina ceramics in relation with CuO addition. Tribological studies were conducted by reciprocating a silicon nitride ball on the prepared samples in dry condition in a linear reciprocating tribotester. Reciprocating friction tests were conducted at normal loads of 0.3, 0.5, 0.7, and 1.0 kgf and the frequencies of 15, 30, 45, and 60 Hz. Coefficient of friction is influenced by the normal load and sliding frequency levels. The friction coefficient increases with increasing sliding frequency, normal load, and nano-oxide addition. The coefficient of friction sharply increases at the level of sliding frequency from 30 to 45 Hz and normal load from 500 to 700 gmf. Since coefficient of friction gradually increases with increase in CuO weight percent in the alumina matrix, it can be inferred that these materials can be used as ceramic brake or clutch.

Keywords Alumina ceramics · Cuo nanocrystalline particle · Friction material · Wear · Dry reciprocating friction

60.1 Introduction

Research is continuing to find out tailor-made material required for each engineering applications. In recent years, use of alumina (Al_2O_3) ceramics has increased exponentially as components of bearings, aircraft brakes, and un-lubricated engines due to its excellent hardness and good wear resistance. In some of the applications, higher friction coefficient is advantageous, e.g., brake or clutch and in some cases the friction should be as minimum as possible, e.g., bearings. However, since alumina is a brittle material, the initiation and propagation of cracks limit its long term use as engineering components. Researchers have added one or several metals or

P. Haldar (✉) · T. K. Bhattacharya
Government College of Engineering & Ceramic Technology, Kolkata 700010, India
e-mail: partha.jumech@gmail.com

N. Modak
Mechanical Engineering Department, Jadavpur University, Kolkata 700032, India

M. S. Shunmugam and M. Kanthababu (eds.), *Advances in Micro and Nano Manufacturing and Surface Engineering*, Lecture Notes on Multidisciplinary Industrial Engineering,
https://doi.org/10.1007/978-981-32-9425-7_60

nonmetal materials into Al_2O_3 matrix to improve its mechanical and anti-wear properties. It has been reported that the wear resistance of alumina can be considerably improved by various types of secondary phases addition like zirconia [1], SiC [2], TiO_2 [3], etc. Haldar et al. [4] showed that addition of aluminum powder as a secondary phase improves mechanical property of a thermoset composite. Carter et al. studied the wear properties of commercial-grade alumina and 5, 10, 15, and 20 wt% zirconia-dispersed alumina at three different temperatures (at ambient temperature, 140 and 250 °C) with a pin on disk tribotester attached with a hot stage. The 5 wt% zirconia-dispersed alumina was found to have the minimum wear loss and they also reported that wear behavior of alumina was dependent on the relative humidity [5]. To understand the wear behavior of a material an important factor is the COF.

The objective of this work is to investigate the friction behavior of nanocrystalline CuO-based alumina ceramics reciprocating against a silicon nitride counterface. The effects of reciprocating frequency and normal load on the friction have been evaluated under different test conditions. This work helps in understanding the friction responses of CuO-based alumina ceramics under dry and reciprocating condition.

60.2 Experimental Work

60.2.1 Materials

High purity reactive alumina (Al_2O_3) was purchased from M/S Aloca. Chemical grade copper (II) nitrate trihydrate [$Cu(NO_3)_2.3H_2O$] and ethylene glycol (both 99.9% pure) were purchased from M/S Merck. These precursors were used as starting material without any further purification.

60.2.2 Synthesis of Nanocrystalline CuO Powder

The nanocrystalline CuO powder was synthesized by gel combustion technique. The nitrate precursor was dissolved in deionized water to make a homogeneous solution and ethylene glycol was added as a fuel in stoichiometric molar ratio. The solution was stirred at 85 °C on a hot plate until gel formation took place. The temperature was then increased to 175 °C and maintained until the gel underwent auto combustion and a fluffy black mass was produced. The as-burnt powder was ground in an agate mortar pestle and heat treated at in a muffle furnace in 600 °C for 2 h for proper crystallization.

60.2.3 Sample Preparation

Five sets of samples were prepared with addition of 0, 0.5, 1, 2, and 4 weight percent of nano-CuO to Al_2O_3 matrix and the samples are marked as ACuO-0, ACuO-0.5, ACuO-1, ACuO-2, and ACuO-4 to identify the samples containing alumina and respective weight percentage of CuO in it. To prepare the batches, the raw powders were weighed and mixed with required different weight percentages by making slurry with distilled water. Wet mixing (aqueous) was adopted for uniform mixing of the additives and to render constancy to the parameters. The mixed suspension was dried in a drier for 24 h followed by grinding of the dried powder in agate mortar pestle. 6% PVA (polyvinyl alcohol) was used as the binding agent. Conventional casting techniques are not practical because of the poor uniformity of dispersed particles. Therefore, the samples are produced by powder metallurgy method. The dried mixtures were cold-pressed in the form of cylindrical pellets (diameter ≈ 12.9 mm and thickness ≈ 3.8 mm) in a hydraulic press at a uniaxial pressure of 1000 kgf/cm^2. After 2 min pressure was released by operating the pressure releasing valve. All the green compacts were dried in air at 110 °C in a drier for 24 h to remove the binder from the samples. The green samples were then sintered at 1600 °C with a heating rate of 8 °C/min up to 1000 °C then 10 min soaking and 2 °C/min up to 1600 °C was maintained with a soaking time of 2 h at the maximum peak temperature. After the definite isothermal holding, the samples were slowly cooled down to room temperature in the furnace.

60.2.4 Test Procedure

Friction tester, TR-282, DUCUM, India, was used to conduct the reciprocating friction test of the specimens under observation to determine the friction behavior (dry condition) at different frequencies and normal loads. The test was conducted by selecting the test duration, normal load, and reciprocating frequency. A circular sample of 10 mm diameter and 3 mm thickness was prepared from the fabricated material as per the machine requirement. The flat surface of the sample comes in contact with the silicon nitride (Si_3N_4) ball as counterface. The surfaces of both the sample and the Si_3N_4 ball were cleaned with the soft tissue paper before the test. The sample and the ball were fixed in their respective positions of the test machine. The normal load to the ball was applied through a pivoted lever. The test was carried out by applying of normal loads(0.3, 0.5, 0.7, and 1.0 kgf) with a duration of 10 min at different frequencies 15, 30, 45, and 60 Hz, and the reciprocating stroke was fixed as 1 (one) mm. After the preset time was reached, the test was stopped using the timer mechanism provided with the testing machine. The friction force as well as the friction coefficient at the interface of the ball and specimen was recorded in the computer at each second. The ball is reciprocated on the sample involving friction in dry condition at different normal loads and frequencies to gather the information

Table 60.1 Process parameters and their levels

Control parameters	Units	Levels			
		I	II	III	IV
Sliding frequency	Hz	15	30	45	60
Equivalent sliding speed	m/s	0.03	0.06	0.09	0.12
Normal load	Kgf	0.3	0.5	0.7	1
Time	Min	10	10	10	10

of the material integrity level. The test parameters along with their different levels for this present work of study have been indicated in Table 60.1.

For all the samples, two sets of experimental scheme were adopted. In the first set, the normal load of 500 gmf and sliding time of 10 min were kept constant and the sliding frequency was varied as 15, 30, 45, and 60 Hz. In the second set, the sliding frequency of 30 Hz and sliding time of 10 min were kept constant and the normal load was varied as 300, 500, 700, and 1000 gmf.

60.3 Results and Discussions

The nanocrystalline CuO-based alumina ceramics densify more than 96% with apparent porosity less than 1%. COF is a system response and so it depends on number of parameters such as normal load, geometry, relative motion between the surfaces, reciprocating frequency, time as well as reciprocating distance, surface roughness of the reciprocating surfaces, type of material, system rigidity, temperature, stick-slip, relative humidity, and lubrication. Among these factors, present study has been focused on the friction behavior of CuO nanocrystalline reinforced alumina ceramics in dry reciprocating contacts against a silicon nitride ball with variation in normal load and sliding frequency only.

60.3.1 Effect of Reciprocating Frequency on Friction Coefficient

In reciprocating contacts, sliding frequency has an important role on friction of CuO nanocrystalline filled alumina ceramics. Figure 60.1a–e indicates the variation of friction coefficient with different sliding frequency levels at constant 500 gmf normal loads for all the samples where the sliding duration is 10 min.

The friction coefficient as obtained in all the graphs captured from the tribotester can be divided into two stages: wear in stage and stable stage [6]. In the wear in stage, contact occurs between the surface asperities of the sample with the ball. At this initial break-in period, the asperities deform, break or get ruptured. As a result, the COF is

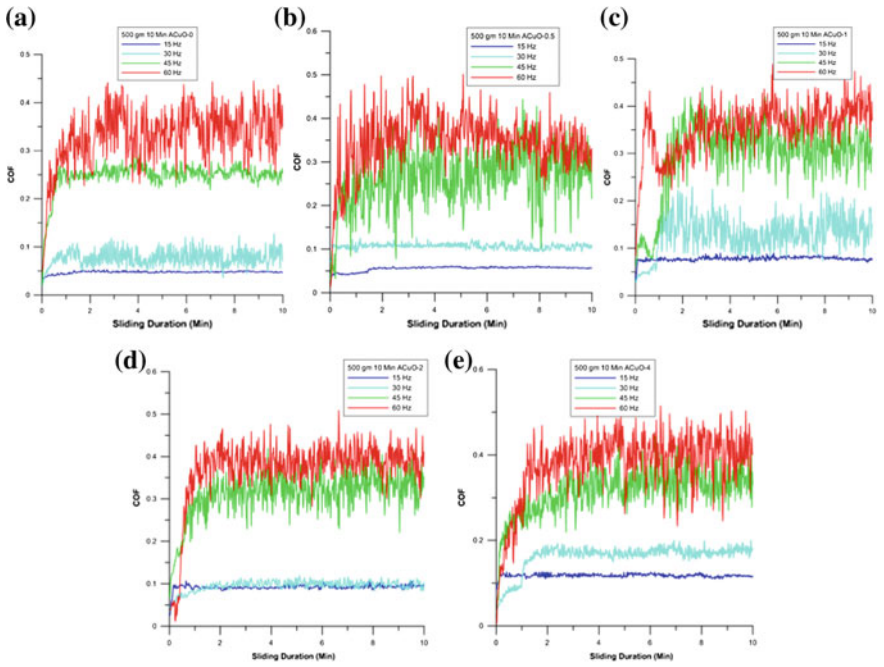

Fig. 60.1 Friction coefficient as a function of reciprocating frequency at 500 gm normal loads for **a** ACuO-0 **b** ACuO-0.5 **c** ACuO-1 **d** ACuO-2 **e** ACuO-4

unsteady at this stage. As the sliding continues, the worn track becomes flat and the coefficient of friction fixes at a steady level. This behavior can also be attributed to a polishing process during the wear test [7]. Moreover, the COF remained more or less stable with small fluctuations around an average value. Such fluctuations can be attributed to a non-uniform wear track or to a stick-slip mechanism [8]. The friction coefficients in the stable stage are listed in Table 60.2 as well as plotted in a graph as shown in Fig. 60.2.

In general, the COF increases with the increase in sliding velocity for any of the samples. Figure 60.2 indicates that the rate of increase in the value of COF as the sliding frequency increases from 30 to 45 Hz is more than any other consecutive intervals. With the increase in reciprocating frequency, the temperature rises at the

Table 60.2 COF of materials at different frequencies at constant normal load of 500 gm

Sliding frequency (Hz)	ACuO-0	ACuO-0.5	ACuO-1	ACuO-2	ACuO-4
15	0.048075	0.058086	0.079089	0.092889	0.117753
30	0.077682	0.106377	0.133391	0.145428	0.172533
45	0.253962	0.282067	0.315665	0.328496	0.335762
60	0.344184	0.355834	0.373471	0.39019	0.403312

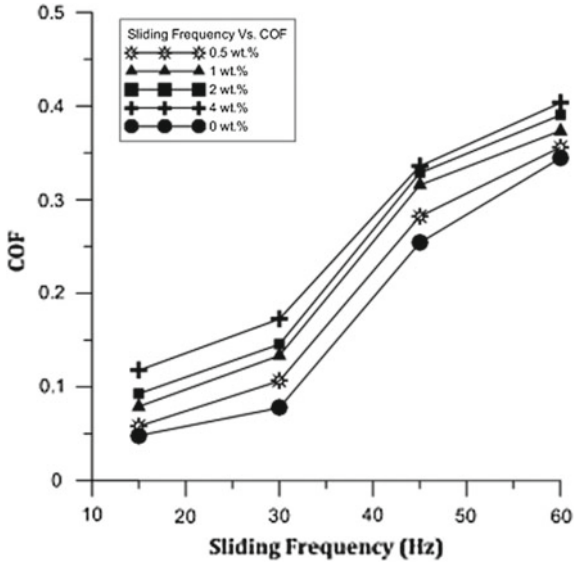

Fig. 60.2 Friction coefficient as a function of reciprocating frequency

contact zone due to the reduced cooling time per stroke of the silicon nitride ball. Heat generated at the contact surface may result increased adhesion with ball [9] leading to increase of friction coefficient. It is also observed that for any constant frequency, the lowest COF is obtained for ACuO-0 and as the weight percentage of CuO in alumina increases, the COF increases. Almost similar kind of observations is also reported by Pasaribu et al. for alumina-based ceramics [10].

60.3.2 Effect of Normal Load on Friction Coefficient

In this section, the variation of COF with different normal loads (0.3, 0.5, 0.7, and 1.0 kgf) at constant 30 Hz sliding frequency has been studied for all the five samples and shown in Fig. 60.3a–e, respectively.

Table 60.3 depicts the stable COF values obtained from the experimentation of the materials at different normal loads, at a constant sliding frequency. It is observed that with increase in normal load COF increases. Similar observation was reported for alumina-based ceramics by Wang et al. [6]. This may be due to formation of plastic deformation zone on the material surface due to larger value of normal load. Moreover, with increase in CuO in alumina, the COF also increases for all the cases. Figure 60.4 shows that the rate of increase in the value of COF as the normal load increases from 500 to 700 gmf is more than any other consecutive load intervals.

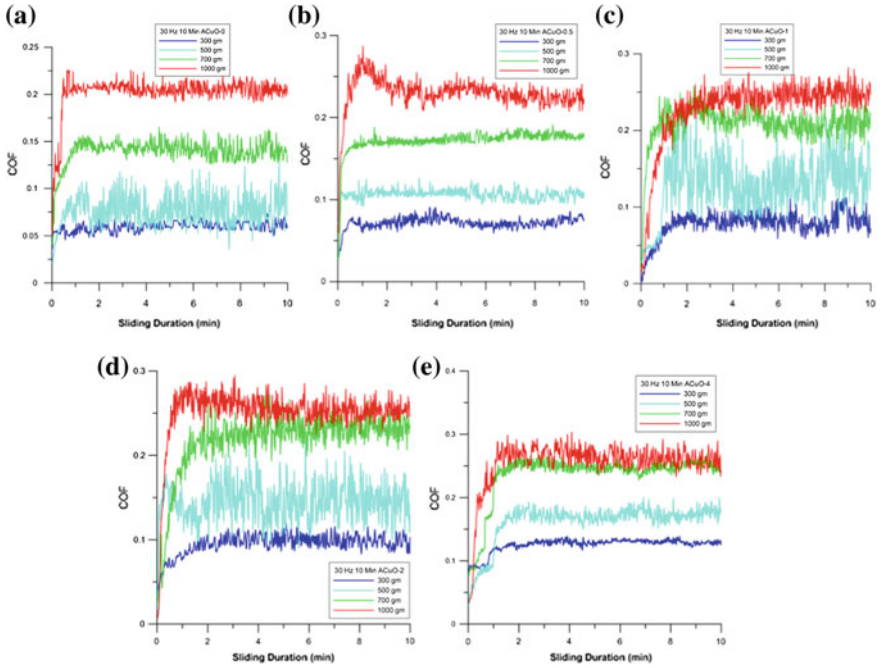

Fig. 60.3 Friction coefficient as a function of normal load at 30 Hz sliding frequency **a** ACuO-0 **b** ACuO-0.5 **c** ACuO-1 **d** ACuO-2 **e** ACuO-4

Table 60.3 COF of materials at different normal load at constant sliding frequency of 30 Hz

Normal load (gm)	ACuO-0	ACuO-0.5	ACuO-1	ACuO-2	ACuO-4
300	0.061038	0.072965	0.082544	0.09951	0.129988
500	0.077682	0.106377	0.133391	0.145428	0.172533
700	0.141231	0.176294	0.209632	0.231019	0.247942
1000	0.205162	0.227987	0.245924	0.253244	0.263298

60.4 Conclusions

The following inferences are drawn from the above study.

- The normal load and sliding frequency indeed have considerable effect on the friction behavior of nanocrystalline CuO-based alumina ceramics.
- For any of the materials under observation, with constant normal load of 500 gmf, with increase in sliding frequency the value of COF increases, this may be due to more adhesion of the reciprocating ball to the ceramic specimen.
- The rate of increment in COF from 30 Hz frequency to 45 Hz is more as compared to other consecutive frequency intervals.

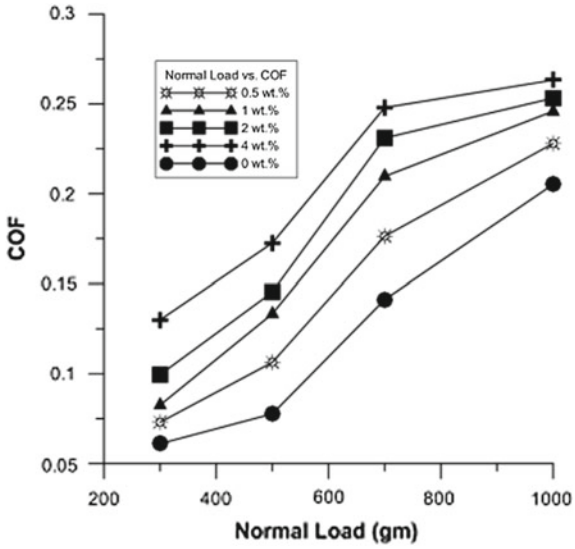

Fig. 60.4 Friction coefficient as a function of normal load

- As the CuO weight percent in alumina ceramics increases, the value of COF also increases for any constant sliding frequency level at 500 gmf normal load.
- For any of the materials under observation, with constant sliding frequency of 30 Hz, with increase in normal load the value of COF increases. This may be due to the formation of plastic deformation zone on the material surface due to larger value of normal load.
- The rate of increment in COF from 500 to 700 gmf normal load is more as compared to other consecutive load intervals.
- As the CuO weight percent in alumina ceramics increases, the value of COF also increases for any constant normal load at 30 Hz sliding frequency.

References

1. Elsen, S.R., Ramesh, T.: Analysis and optimization of dry sliding wear characteristics of zirconia reinforced alumina composites formed by conventional sintering using response surface method. Int. J. Refract. Met. Hard Mater. **58**, 92–103 (2016)
2. Rodríguez, J., et al.: Sliding wear of alumina/silicon carbide nanocomposites. J. Am. Ceram. Soc. **82**(8), 2252–2254 (2004)
3. Bagde, P., Sapate, S.G., Khatirkar, R.K., Vashishtha, N.: Friction and abrasive wear behaviour of Al_2O_3-13$TiO_2$and Al_2O_3-13TiO_2+ Ni Graphite coatings. Tribol. Int. **121**, 353–372 (2018)
4. Haldar, P., Modak, N., Sutradhar, G.: Comparative evaluation of mechanical properties of sisal-epoxy composites with and without addition of aluminium powder. Mater. Today Proc. **4**(2), 3397–3406 (2017)
5. Carter, G.A., van Riessen, A., Hart, R.D.: Wear of zirconia-dispersed alumina at ambient temperature, 140 °C and 250 °C. J. Eur. Ceram. Soc. **26**(16), 3547–3555 (2006)

6. Wang, J., et al.: Friction and wear behavior of microwave sintered Al_2O_3/TiC/GPLs ceramic sliding against bearing steel and their cutting performance in dry turning of hardened steel. Ceram. Int. **43**(17), 14827–14835 (2017)
7. Rodriguez-Suarez, T., et al.: Sliding wear behaviour of alumina/nickel nanocomposites processed by a conventional sintering route. J. Eur. Ceram. Soc. **31**(8), 1389–1395 (2011)
8. Parchovianský, M., et al.: Mechanical properties and sliding wear behaviour of Al_2O_3-SiC nanocomposites with 3–20 vol% SiC. J. Eur. Ceram. Soc. **37**(14), 4297–4306 (2017)
9. Yin, Z., et al.: Friction and wear behaviors of Al_2O_3/TiC micro-nano-composite ceramic sliding against metals and hard materials. Ceram. Int. **42**(1), 1982–1989 (2016)
10. Pasaribu, H.R., Sloetjes, J.W., Schipper, D.J.: Friction reduction by adding copper oxide into alumina and zirconia ceramics. Wear **255**(1–6), 699–707 (2003)

Chapter 61
Increase in Hardness and Wear Resistance of Ti-6Al-4V Surface by In Situ Laser Coating of Ti- and Al-Based Hard Ceramics

Dipanjan Dey, Kalinga Simant Bal, Imran Khan, Ishan Bangia, Anitesh Kumar Singh and Asimava Roy Choudhury

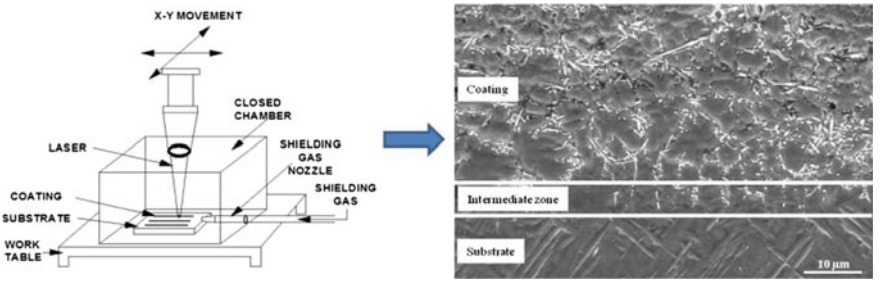

Abstract Ti-6Al-4V alloy finds wide application starting from aerospace to biomechanical industry due to its high strength-to-weight ratio and biological immunity, but it exhibits poor tribological properties. With the help of laser energy, a composite coating was developed on Ti-6Al-4V with preplaced powders as Al, TiO_2, and hexagonal BN. A self-propagating high-temperature synthesis (SHS) reaction occurred between the preplaced powders by laser triggering, which helped to generate coating on the substrate. Microstructure and elemental analysis of coating were studied through SEM, EDS, and XRD analysis and it was found that the coating consisted of Al_2O_3, TiB_2, and TiN. Hardness and wear resistance of the developed coating were improved significantly. Maximum hardness on coating was found to be more than six times higher than substrate hardness, and wear resistance was improved three times as compared to the substrate. The coefficient of friction of coating was comparable to substrate coefficient friction.

D. Dey (✉) · K. S. Bal · I. Khan · I. Bangia · A. K. Singh · A. Roy Choudhury
Department of Mechanical Engineering, Indian Institute of Technology Kharagpur, Kharagpur 721302, West Bengal, India
e-mail: dipanjan.29193@gmail.com

A. Roy Choudhury
e-mail: archie@mech.iitkgp.ac.in

M. S. Shunmugam and M. Kanthababu (eds.), *Advances in Micro and Nano Manufacturing and Surface Engineering*, Lecture Notes on Multidisciplinary Industrial Engineering,
https://doi.org/10.1007/978-981-32-9425-7_61

Keywords Ti-6Al-4V alloy · Laser cladding · SHS reaction · Hardness · Wear · Microstructural characterization

61.1 Introduction

Lasers can be used in various ways to enhance surface properties of the metallic substrates like cladding, remelting, phase transformation, etc. Among them, laser cladding has become popular in current years due to its unique features and excellent capabilities in various industries involved in high-value components repair, metallic coating, prototyping, and low volume manufacturing. The laser processing coating development technique utilizes laser technology, powder metallurgy, and rapid solidification to produce coating.

Laser cladding is used to make the coating of components like turbine blades, engine valves, aerospace components, etc. At present, titanium alloy is one of the promising material in manufacturing industry but it possesses low hardness and poor tribological property [1]. Self-propagating high-temperature synthesis (SHS) is a process that utilizes synthesis of ceramic composites via an exothermic reaction that is self-sustaining and energetically efficient [2, 3]. An SHS reaction is initiated at a minimum ignition temperature to manifest the heat of exothermic reaction. The exothermic reaction also volatilizes low boiling impurities which results in pure products. Due to high energy density, the laser beam can initiate SHS reactions producing novel material compositions [4–8]. Presence of exothermic reaction also avoids the need for expensive high powered laser equipment and facilities. So, coating consisting of high melting point powders can be coated with the help of the enthalpy released during SHS reaction triggered by laser energy. Surface properties were improved by developing metal matrix coating (MMC) on the substrate by SHS process with the help of laser [9]. In situ multi-component MMC coating was developed on titanium alloy by using boron carbide, hexagonal boron nitride, and titanium powder as a precursor powders [10]. Chatterjee et al. [11] developed coating of TiB_2, TiN, and Al_2O_3 by both in situ and ex situ process and then compared between the two processes with respect to homogeneous microstructure and hardness. It was found that in situ process showed better coating than ex situ process.

Previously, MMC coating of titanium boride, titanium nitride, and aluminum oxide had been developed on AISI low carbon steel using SHS reaction, and improvement in tribological properties was observed. But there have very few works on the development of MMC coating on titanium alloy with the help of SHS energy using laser beam. In this present study, an attempt has been made to enhance the tribological properties of Ti-6Al-4V alloy by developing composite MMC coating with the help of laser.

61.2 Experimental Detail

Ti-6Al-4V substrate of dimension 100 mm × 50 mm × 6 mm was grit blasted to (a) remove surface contaminations, (b) allow better adhesion between precursor powders and the substrate, and (b) create a favorable surface texture for coating. The precursor used in the present study was made by mixing micro-sized powder of aluminum (Al), titanium dioxide (TiO_2), boron nitride (BN), and titanium di-boride (TiB_2). Powders were mixed in the ratio of 2.15:4.79:3.99:1.38 according to their weight to achieve equal-molar ratio of each element in the developed coating. The average size of the precursor powder after mixing is around 45 μm. The self-propagating high-temperature synthesis (SHS) reaction likely to happen as below:

$$\mathrm{Al} + \mathrm{TiO_2} + \mathrm{BN} \rightarrow \mathrm{Al_2O_3} + \mathrm{TiB_2} + \mathrm{TiN} \tag{61.1}$$

Further, the precursor powder was mixed with Polyvinyl alcohol (4% aq.) to make precursor slurry to be applied to the surface of the grit-blasted Ti-6Al-4V substrate. To avoid formation of agglomeration, the mixture was stirred using a magnetic stirrer (Manufacturer: Spinot), and then sonicated in ultrasonic vibrator (Manufacturer: Toshcon, Model S11-1) for few minutes. The grit-blasted substrate surface was cleaned with acetone prior to the application of precursor slurry. A 100 μm thick coating of precursor powder slurry was applied on substrate surface using coater machine (Manufacturer: RK Control coater), and allowed to dry for few minutes on a hotplate.

Laser cladding was carried out on the preplaced substrate using Ytterbium fiber laser (IPG YLR-2000) having wavelength of 1.064 μm and maximum power 1750 W. Laser scanning was carried out at 1750 W and speed of 900 mm/min. To prevent atmospheric contamination during the laser scan, workpiece was kept inside perplex box flushed with argon gas. Focal spot diameter of 4 mm was used to carry out laser beam scanning. Photographic view of experimental set-up has been shown in Fig. 61.1.

The samples were cut by wire-EDM and polished using 1200#, 1500#, and 2500# SiC grit abrasive paper, followed by diamond polishing (1 μm). Then the polished samples were etched by Keller's reagent. Microscopic analysis was carried out using SEM, EDX, and XRD analytical techniques. Hardness test was carried out from the top of the coating toward substrate by Vickers microhardness testing machine with a load of 25 gf was applied for dwell time of 10 s. Wear test using ball-on-disk method was carried out on the laser cladded surface and substrate surface for comparison study. Tungsten carbide ball was used as the ball for the wear test. The sample was rotated at 300 rpm for 30 min, and a 2 kg load was applied. Wear rate of coating and substrate were calculated using the following equation:

$$\text{Wear rate} = \frac{dv}{2\pi r N T F} \quad \mathrm{mm^3/N\,m} \tag{61.2}$$

where dv is volume loss after wear test, r is radius of curvature of the wear track, N is rotational speed during wear test, T is duration of wear test, and F is applied load during wear test. Coefficient of friction was calculated from the relation of obtained frictional force and applied load.

61.3 Result and Discussion

61.3.1 Microstructural Analysis

Figure 61.2 shows the XRD analysis of laser clad surface. XRD analysis reveals that the composite coating formed after SHS reaction occurred between the precursor

Fig. 61.1 Photographic view of experimental setup

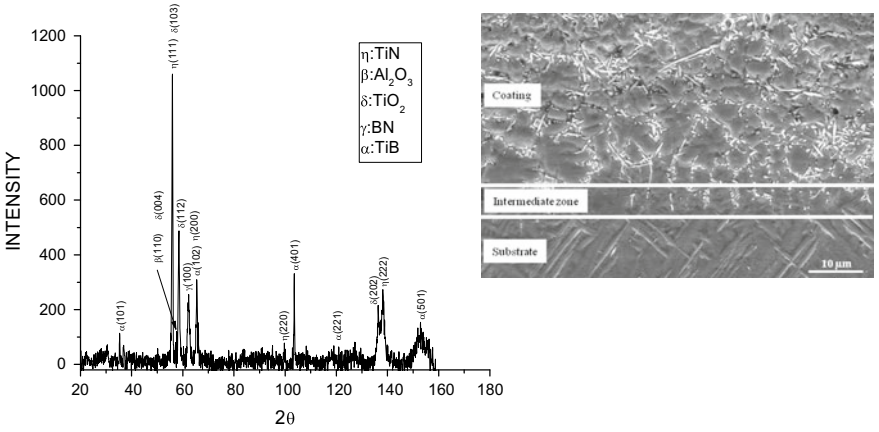

Fig. 61.2 X-ray diffraction (XRD) analysis of laser clad along with SEM image of coating

powders due to laser treatment. The composite coating consists of TiN, Al_2O_3, TiO_2, BN, and TiB_2.

SEM analysis of the microstructure of the coating is also shown in Fig. 61.2. It could be observed that there exist three different distinguishable regions. Bottom part consists of heat-affected substrate, followed by intermediate zone at the middle, and the top layer is coating portion. It has been shown in Fig. 61.2 that different types of shapes have been formed in the microstructure. Energy-dispersive X-ray spectroscopy (EDS) analysis on the coating and heat-affected substrate has been shown in Fig. 61.3. From the EDS report, it was observed that top layer and bottom layer of the coating were enriched with titanium, boron, and nitrogen, whereas aluminum and oxygen percentage were more at the middle. Hence, it might be possible that titanium boride and titanium nitride are formed in the top layer and bottom layer of the coating, while aluminum oxide might have precipitated at the middle of the coating. Solidification starts at the substrate coating interface because of heat loss by conduction through substrate. Hence solidification front moves from substrate toward top layer of the coating. As titanium boride and titanium nitride have higher melting point than aluminum oxide, titanium boride and titanium nitride solidify at the interface of substrate and coating. Simultaneously, a thin layer of titanium boride and titanium nitride is formed at the top of the coating due to rapid cooling through radiation and convection. The percentages of titanium boride and titanium nitride are higher at these zones also because of their higher melting point. Thus, the middle

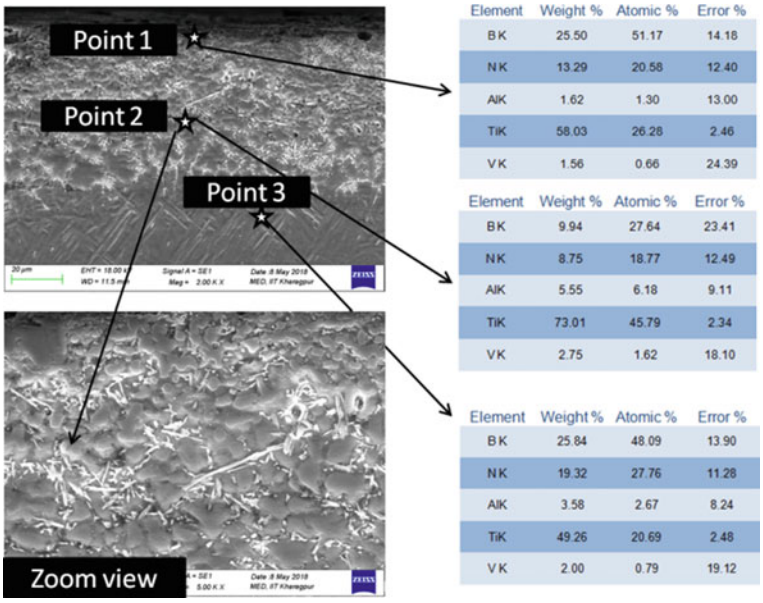

Fig. 61.3 Energy disperse X-ray spectroscopy analysis

portion of the coating that cools last because of lower melting point of aluminum is dense in aluminum oxide. Grains sizes are larger in the middle region of the coating compared to top and bottom layer of the coating as the middle portion solidifies at the end.

61.3.2 Hardness Analysis of the Coating

Microhardness at different regions in the coating has been shown in Fig. 61.4. It could be observed that microhardness of the coating was found to be six times higher than the substrate hardness. Maximum hardness of 1917 HV was achieved on the coating. From the XRD and EDS results, it has been reported that coating material consists of hard ceramic particles like titanium boride, titanium nitride, and aluminum oxide which lead to higher hardness value. It can be seen from Fig. 61.4 that microhardness decreases along the depth of the coating. Within first 40 μm from the top, coating has higher hardness value because of presence of the ceramic particles in the coating. After 40 μm, intermediate zone is present, where dilution of the substrate material has occurred. Hence, hardness was reduced due to presence of some portion of substrate material. However, after 65-μm thickness, there was no coating material, only heat-affected substrate material appeared, correspondingly hardness reduced to substrate hardness value.

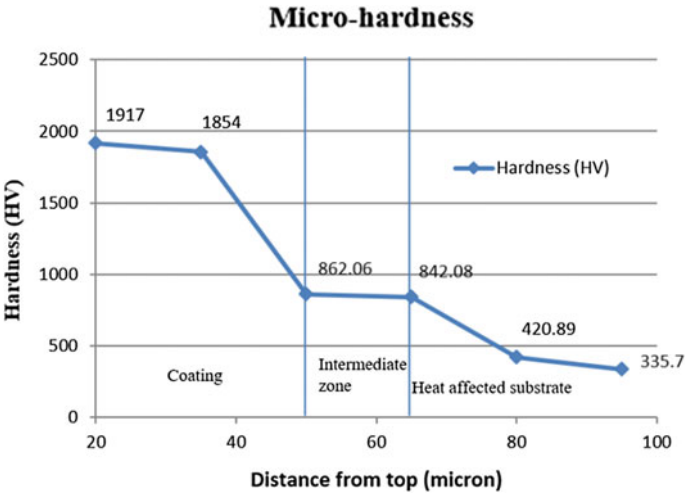

Fig. 61.4 Variation of microhardness at different regions

61.3.3 Wear Analysis

Wear test using ball-on-disk method was carried out on the substrate and coated sample. After the wear test, volume loss due to wear was determined using noncontact type surface profilometer. Cross-sectional profiles obtained from noncontact type profilometer have been shown in Fig. 61.5. It was observed that due to wear, volume loss of the substrate and coating were 7.31×10^{-4} mm^3/N m and 2.21×10^{-4} mm^3/N m, respectively; so volume loss (or wear rate) on coating was three times less as compared to the volume loss on the substrate. Average track width and depth of the worn coated sample are about 1.45 mm and 0.1 mm, respectively, whereas track width and depth of the worn substrate are 1.70 mm and 0.13 mm, respectively. Due to presence of hard ceramic material like aluminum oxide, titanium boride, titanium nitride, etc., coated sample proved to be more wear resistant than substrate material. Higher hardness leads to high wear resistance and it has been seen earlier that hardness on the coating is higher than the hardness on the substrate. SEM images of worn surface of the substrate and coated sample have been shown in Fig. 61.5.

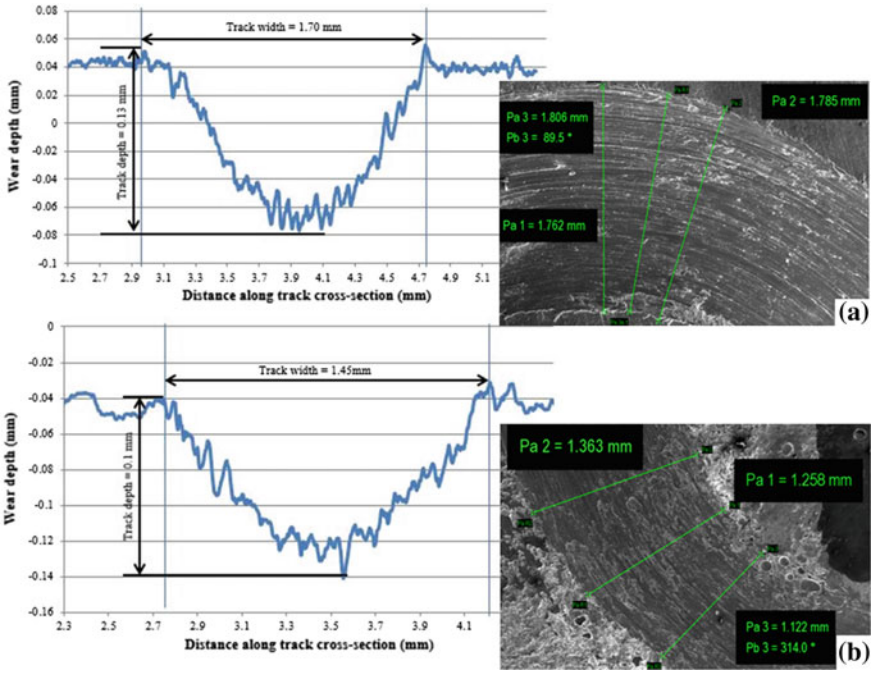

Fig. 61.5 Cross-sectional profile of wear track of **a** substrate, **b** coating. SEM images of wear track of **a** substrate, **b** coating

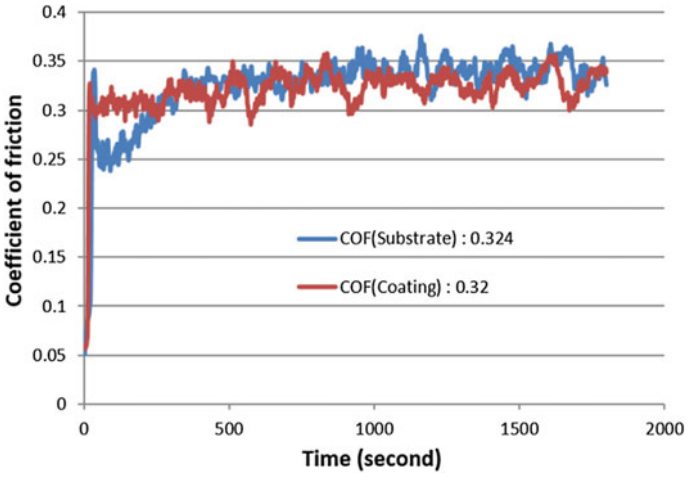

Fig. 61.6 Coefficient of friction of substrate and coating

61.3.4 Coefficient of Friction Analysis

Coefficient of friction was determined from the data obtained during wear test. Coefficient of friction was found to be marginally less for coated sample than that of substrate. Average coefficient of friction for coated sample is 0.320 while that of substrate is 0.324. At very high temperature and due to SHS reaction, most of the boron nitride was dissociated, and hence friction coefficient of the coating was not affected. From Fig. 61.6, it can be clearly seen that the friction coefficient was more or less constant during friction which indicates that stability of the coating for longer time.

61.4 Conclusions

After the investigation of the detailed study of the microstructure and mechanical properties of the coating, the following conclusions could be drawn:

1. Composite coating was successfully developed on the Ti-6Al-4V alloy substrate with the help of laser, triggered by self-propagating high-temperature synthesis reaction.
2. From SEM analysis, it was seen that different types of microstructures were formed in the coating depending on the cooling rate, melting temperature of the coating elements, etc.

3. XRD analysis and EDS analysis have reported that the developed coating consists of titanium boride, titanium nitride, aluminum oxide, titanium oxide, and boron nitride.
4. After the coating, hardness was enhanced by six times compared to Ti-6Al-4V alloy substrate. Hardness was found to decrease toward coating substrate interface.

References

1. Roy Choudhury, A., Ezz, T., Chatterjee, S., Li, L.: Microstructure and tribological behaviour of nano-structured metal matrix composite boride coatings synthesized by combined laser and sol–gel technology. Surf. Coat. Technol. **202**, 2817–2829 (2008). https://doi.org/10.1016/j.surfcoat.2007.10.013
2. Liu, C.T., Maziasz, P.J.: Microstructural control and mechanical properties of dual-phase TiAl alloys. Intermetallics **6**, 653–661 (1998). https://doi.org/10.1016/S0966-9795(98)00062-4
3. Chatterjee, S., Shariff, S.M., Padmanabham, G., Dutta Majumdar, J., Roy Choudhury, A.: Study on the effect of laser post-treatment on the properties of nanostructured Al_2O_3–TiB_2–TiN based coatings developed by combined SHS and laser surface alloying. Surf. Coat. Technol. **205**, 131–138 (2010). https://doi.org/10.1007/s00170-011-3739-y
4. Koechner, W.: Solid-State Laser Engineering. Springer, New York (1992)
5. Yong, Y., Lan, J., Li, X.: Study on bulk aluminum matrix nano-composite fabricated by ultrasonic dispersion of nano-sized SiC particles in molten aluminum alloy. Mater. Sci. Eng. A **380**, 378–383 (2004). https://doi.org/10.1016/j.msea.2004.03.073
6. Merzhanov, A.G.: History and recent developments in SHS. Ceram. Int. **21**, 371–379 (1995). https://doi.org/10.1016/0272-8842(95)96211-7
7. Borovinskaya, I.P.: Chemical classes of the SHS processes and materials. Pure Appl. Chem. **64**(7), 919–940 (1992). https://doi.org/10.1351/pac199264070919
8. Chatterjee, S., Shariff, S.M., Datta Majumdar, J., Roy Choudhury, A.: Development of nano-structured Al_2O_3-TiB_2-TiN coatings by combined SHS and laser surface alloying. Int. J. Adv. Manuf. Technol. **38**, 938–943 (2008). https://doi.org/10.1007/s00170-007-1143-4
9. Chatterjee, S., Ganesh, P., Palai, R., Wu, J.A., Kaul, R., Datta Majumdar, J., Roy Choudhury, A.: Effect of h-BN addition on the properties of nanostructured Al_2O_3–TiB_2–TiN based coatings developed by combined SHS and laser surface alloying. Surf. Coat. Technol. **204**, 1702–1709 (2010). https://doi.org/10.1007/s00170-011-3739-y
10. Haldar, B., Karmakar, S., Saha, P., Chattopadhyay, A.B.: In situ multi-component MMC coating developed on Ti-6Al-4V substrate. Surf. Eng. **30**, 256–262 (2014). https://doi.org/10.1179/1743294414Y.0000000252
11. Chatterjee, S., Dutta Majumdar, J., Singaiah, K., Shariff, S.M., Padmanabham, G., Roy Choudhury, A.: Performance evaluation of laser surface alloyed hard nanostructured Al_2O_3–TiB_2–TiN composite coatings with in-situ and ex-situ reinforcements. Surf. Coat. Technol. **205**, 3478–3484 (2011). https://doi.org/10.1016/j.surfcoat.2010.12.015

Chapter 62
Effect of Sigma Phase on Dry Sliding Wear Resistance and Surface Roughness of ASTM A890 Grade 6A Duplex Stainless Steels

P. Nithin Raj, Anandu P. Sivan, V. Riyas, K. Sekar and M. A. Joseph

Abstract ASTM A890 grade 6A super duplex stainless steel (SDSS) is a very popular duplex steel grade. The highly alloyed steel shows precipitation of various intermediate phases at different temperature ranges and among them, sigma is the most deleterious phase. The hard sigma phase accounts for a marked increase in wear resistance. There are, however, very few studies reported on the effect of sigma phase on the roughness of the worn surface. In this work, the material was heated to three different temperatures—850, 1000, and 1100 °C—soaked for 1 hour and later quenched in water. The sigma formation was observed to be the maximum at 850 °C while no trace of sigma could be spotted at 1100 °C. The wear volume was found to be the least for specimen quenched from 850 °C and highest for the sample quenched from 1100 °C. Roughness of the specimen was found to increase in accordance with the sigma content. The sample quenched from 850 °C was noted to have the highest surface roughness.

Keywords Super duplex stainless steel · Wear · Sigma phase · ASTM A890 6A

62.1 Introduction

Duplex stainless steels are composed of dual-phase microstructure with an approximately 50:50 volume fraction of body-centered ferrite and face-centered austenite. The presence of both these phases imparts the desired mechanical properties of DSS making it the most widely favored material in the oil and gas sectors, chemical industries, transportation, paper and pulp industries, marine industries, nuclear power plantsm etc. [1].

P. Nithin Raj (✉) · A. P. Sivan · V. Riyas · K. Sekar · M. A. Joseph
Mechanical Engineering Department, National Institute of Technology Calicut, Calicut 673601, Kerala, India
e-mail: nithinpanoli@gmail.com

M. S. Shunmugam and M. Kanthababu (eds.), *Advances in Micro and Nano Manufacturing and Surface Engineering*, Lecture Notes on Multidisciplinary Industrial Engineering,
https://doi.org/10.1007/978-981-32-9425-7_62

Dual-phase microstructure of SDSS offers better impact toughness, improved ductility, hardness, excellent corrosion resistance, and better weldability, making them a viable alternative for conventional ferritic and austenitic stainless steels [2].

When heated to higher temperature, DSS undergoes some solid-state transformations, resulting in the formation of various intermetallic phases. The formation of different phases depends on the amount of Cr, Mo, and W additions. Among these intermetallic phases, sigma phase plays a crucial role in the properties of the material. Sigma phase is very hard and brittle in nature. Sigma precipitation occurs between 700 and 1060 °C at high-energy nucleation sites, i.e., ferrite and ferrite–austenite boundaries. After nucleation, sigma propagates to the ferrite phase, since diffusion rate in ferrite is 100 times faster than austenite [3]. However, the toughness and corrosion resistance of SDSSs will get drastically reduced as the precipitation rate of sigma increases [4].

The wear-resistant behavior of different specimens treated at different heat treatment temperatures were studied in the past. Chowdhury et al. [5] measured the coefficient of friction and wear rate of stainless steels under the varying loads and sliding velocities and observed an increase in wear rate with load and sliding velocities. Many authors have investigated the effect of sigma phase on mechanical properties of SDSSs. However, very less information is available on the effect of sigma-phase precipitation on the roughness of wear surface of DSS. del Abra-Arzola et al. [6] have concluded that hardness imparted by the sigma phase provides improvement in wear resistance under dry sliding conditions after heat treating it for 5 min. Fargas et al. [7] verified that the hardness induced by sigma phase reduces the plowing wear mechanism thus confers a lower fatigue wear. Hardness imparted by sigma particles also proved to reduce subsurface plastic deformation.

The present work aims at confirming and quantifying the precipitation of sigma phase in SDSS at four different heat-treatment conditions. The effect of sigma on dry sliding wear characteristics and further material removal have also been recorded. The surface roughness of the specimen has been obtained using 3D profilometer and its dependence on the sigma precipitation has been noted.

62.2 Experimental Procedure

Super DSS ASTM A890 grade 6A was chosen as the material for study. The material was cast using an induction furnace and argon oxygen decarburization (AOD) technique into a test block. The test block was then subjected to homogenization heat treatment by soaking at 1160 °C for 8 h. Three sample blocks of 20 mm diameter and 120 mm length were made from the test block. The samples were heated to three different temperatures—850, 1000, and 1100 °C—with each specimen soaking for 1 hour followed by water quenching.

To analyze the sigma-phase formation in each condition, the microstructures of these samples were captured. Heat-treated samples were well polished with emery papers of grade 230, 400, 600, 1000, and 1500. A mirror-finished surface was

obtained by polishing using a velvet cloth coated with diamond paste. Electrolytic etching technique was used to obtain the microstructure. Samples were etched in 40% NaOH solution at a direct voltage of 5 V for 10 s. The microstructures were examined using metallurgical optical microscope—Olympus BX51. Hardness value is a direct indication of the sigma phase present, as the presence of this phase significantly increases the hardness of DSSs. The Vickers hardness of all the three samples was measured with 10 kgf load and dwell time of 10 s.

The dry sliding wear of the heat-treated conditions were analyzed and compared by pin-on-disk testing method (Fig. 62.2). For the wear test, the cylindrical pins were made from the heat-treated samples with 8 mm diameter and 30 mm length. Each of the specimens was polished to a surface roughness value lower than Ra = 0.6 μm, according to ASTM G-99 standard. The dry sliding wear test was conducted on pin-on-disk tribometer (MAGNON). The disk used was made of stainless steel with a hardness value of 780 HV. The constant linear speed of 4 m/s was set for the test and the sliding distance was varied as 1200, 1600, and 2000 m. Three different load conditions were also taken for doing the experimentation—40, 50, and 60 N.

All the specimens were cleansed using acetone before and after the test and weighed by an electronic weighing machine having a resolution of ±0.1 mg. In the weight-loss method, wear volume can be calculated using the formula: wear volume = (weight loss/density of the material) in mm^3; for super DSS, the density is 7.86 g/cc.

62.3 Results and Discussion

The Chemical composition of SDSS block was analyzed after homogenization heat treatment, using atomic emission spectroscopy. The results shown in Table 62.1 showed that every element is within the limits specified by ASTM standards. The material of this composition was subjected to heat treatment processes.

Three sample cylinders cut from the test block were heated to 850, 1000, and 1100 °C and soaked for 1 hour followed by water quenching. Sieurin et al. have found that the sigma-phase precipitation takes place at temperatures between 600 and 1000 °C [8]. The maximum precipitation was observed at 850 °C [7, 9]. 1050 °C is the maximum temperature up to which the sigma precipitation was reported in grade 6A SDSSs [8]. Hence the low sigma region temperature, 1000 °C was taken as the second temperature. Beyond 1050 °C, no sigma precipitation was noticed and hence 1100 °C was taken as the third condition. The minimum soaking temperature according to ASTM standard was taken as the third temperature, for a clean dual-phase structure. The microstructure of DSS samples after three heat treatments were analyzed. The microstructures of the heat-treated samples in Fig. 62.3 show the effect of temperature on precipitation of sigma phase. When electrolytically etched with NaOH, sigma phase appeared as red regions in the microstructure, white or gray is the austenite phase, and black color corresponds to the ferrite phase.

Table 62.1 Chemical composition of SDSS casting

Element	C	Si	Mn	P	S	Cr	Mo	N	Ni	W	Cu
Percentage	0.02	0.54	0.80	0.020	0.001	24.78	3.71	0.23	7.90	0.66	0.82

Fig. 62.1 Microstructure of grade 6A quenched from **a** 850 °C, **b** 1000 °C, **c** 1100 °C

Figure 62.1 clearly shows that the sample quenched from 850 °C has the maximum sigma-phase precipitation. As the temperature increases from 850 °C, precipitation rate of sigma phase decreases and at 1000 °C, very low percentage of sigma phase could be observed. The very small reddish precipitations that can be observed in the microstructure of the specimen soaked at 1000 °C followed by water quenching accords to the sigma phase. The specimen soaked at and quenched from 1100 °C has a clear dual-phase microstructure and no sigma phase. Figure 62.2 shows the percentage of each major phase present in the microstructure of heat-treated specimens, determined by manual point counting method ASTM A800/800M.

The specimen quenched from 1100 °C has almost equal amounts of austenite and ferrite. The results clearly show that the increase in sigma is due to the conversion of ferrite to sigma. The conversion is the maximum at 850 °C [9], for which it was selected as the first temperature for the experiment.

Hardness value is a clear indication of the variation of sigma phase in DSSs. Since sigma phase is hard and brittle in nature, the increase in sigma phase causes high hardness. Table 62.2 shows variation of hardness values at different heat-treatment

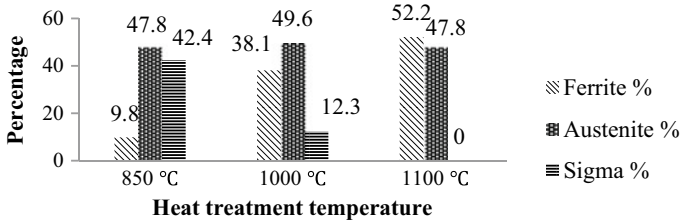

Fig. 62.2 Phase percentage variation with heat-treatment temperature

Table 62.2 Heat-treatment conditions and corresponding hardness value

Temperature (°C)	Vickers hardness (HV)
850	380
1050	245
1100	235

conditions. The hard surface results in a good range of increase in wear resistance of a material.

From the results, it is observed that the wear volume is highly depended on sigma-phase precipitation. Thus, the specimen quenched from 850 °C was observed to have the lowest wear volume and the specimen quenched from 1100 °C had the highest wear volume. In other words, the sigma phase play a crucial role in wear resistance of SDSS. 850 °C heat-treated sample exhibited the highest wear resistance due to the abundance of hard and highly brittle sigma phase. Another common trend noted from the graph (Fig. 62.3) is that, irrespective of the heat-treatment conditions, wear volume increases with sliding distance and load.

After the wear test, the worn surface morphology of all the pins was studied and also the roughness values were measured using 3D optical profilometer (Make: Alicona, Infinite focus-G5); images of the surface were converted to 2D and are shown in Fig. 62.6.

Surface image of the specimen quenched from 850 °C that exhibited abrasion wear marks as shown in Fig. 62.4a–c wear marks or grooves in direction of rotation

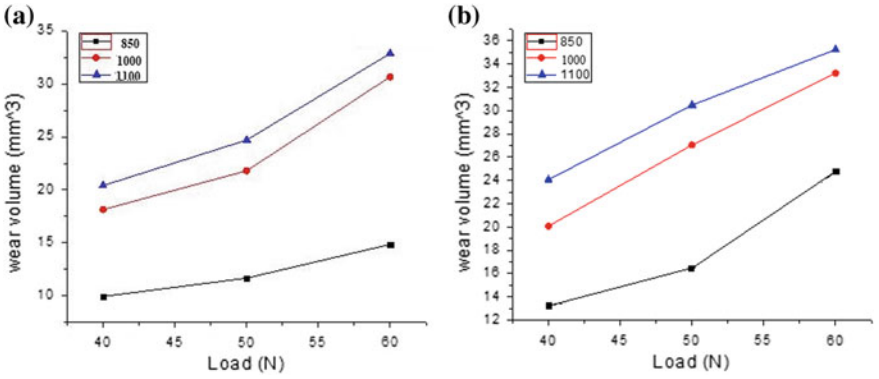

Fig. 62.3 Wear volume against load, **a** at sliding distance 1600 m and **b** at sliding distance 1200 m

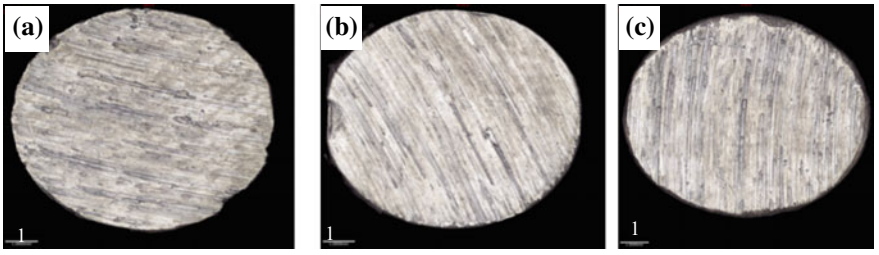

Fig. 62.4 Images obtained from 3D profilometer of **a** Specimen quenched from 850 °C. **b** Specimen quenched from 1000 °C. **c** Specimen quenched from 1100 °C

only. By comparison of three wear surfaces, Fig. 62.4a clearly exhibits the roughest surface of all three conditions. In Fig. 62.6b, the grooves or wear marks are deeper.

From the 3D profiles, the surface roughness values (S_a) of wear surface were calculated by the profilometer and were plotted against the applied load. The images obtained from 3D profilometer give a comprehensive view of the pin surface.

The surface roughness of grade 6A varies with different phase formations as shown in Fig. 62.5. Sigma, as obvious, is a brittle phase which is also observed to be the phase having the maximum roughness in DSSs. During dry sliding wear test, the specimen quenched from 850 °C and having a maximum sigma phase was found to exhibit the highest roughness albeit showing the lowest wear volume. The pin heat-treated at 1100 °C showed the lowest wear resistance with no sigma content but was spotted to have the lowest roughness values among the specimens studied.

The wear surface morphology was analyzed by Scanning Electron Microscopy. It has been seen observed that a rise in sliding distance causes plastic deformation leading to the formation of grooves along the sliding direction as shown in figures c and d. The sample with maximum amount of sigma phase, i.e., the sample quenched from 850 °C has shown the highest amount of cleavage mechanism and material removal. The α dual-phase sample quenched from 1100 °C has shown a surface material removal mechanism of abration. Cracks parallel to the sliding direction were also observed on the surface of the sample as shown in Fig. 62.6c, d. In Fig. 62.6c, the SEM image shows the initial formation and development of cracks.

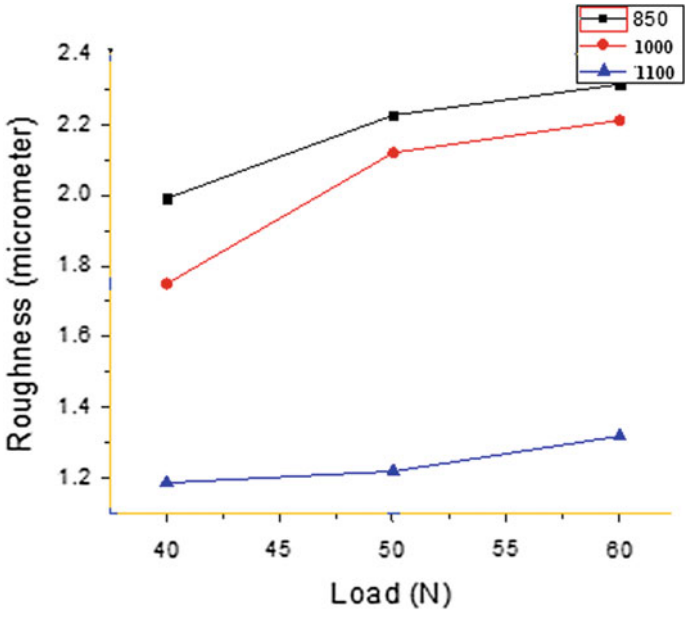

Fig. 62.5 Roughness of heat-treated specimen at three various loads

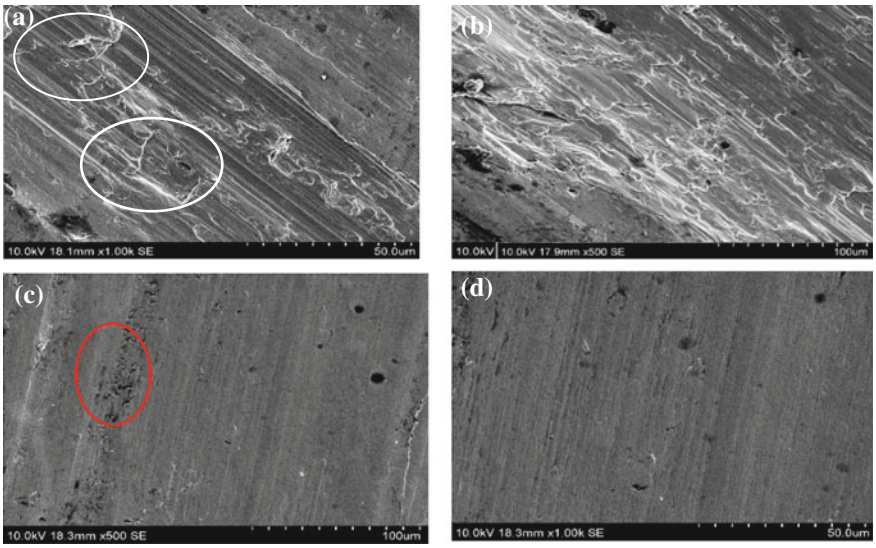

Fig. 62.6 SEM images of wear samples heat-treated at **a** and **b** 850 °C, **c** and **d** 1100 °C

62.4 Conclusions

In the present work, the effect of sigma-phase precipitation on wear behavior and surface roughness of super duplex grade ASTM A890 6A were studied and arrived at the following conclusions:

- The specimen quenched from 850 °C showed the highest amount of sigma-phase precipitation, i.e., more than 40% in the microstructure. Hence, it exhibited the highest hardness among all specimens. The specimen heat-treated at 1100 °C was found to have the lowest hardness due to the absence of sigma phase.
- Wear resistance also followed the same trend as hardness. The specimen quenched from 850 °C exhibited the highest wear resistance among all heat-treatment conditions. The wear volume of the sample quenched from 1100 °C is nearly double that of the specimen quenched from 850 °C at all the test conditions. The specimen heat-treated at 1000 °C showed intermediate hardness and wear resistance.
- The surface roughness was the lowest for austenite–ferrite dual-phase sample heat-treated at 1100 °C. The highest wear resistant specimen, quenched from 850 °C showed the highest surface roughness. The surface roughness values of specimen heat-treated at 1000 °C were found to be intermediate to the other two conditions. Nevertheless, the wear volume reduces, surface roughness highly augments with increase in the amount of sigma phase.

Acknowledgements The authors wish to acknowledge Mr. B. Raha (GM, R&D, Peekay Steels (P) Ltd. Calicut) and the management and staff of Peekay Steel Castings (P) Ltd. for the support they extended toward the completion of this project.
Authors would like to sincerely thank the Department of Science and Technology (DST), Govt. of India and Centre for Precision Measurements and Nanomechanical Testing, Department of Mechanical Engineering, National Institute of Technology Calicut, for providing me the facility purchased under the scheme "Fund for Improvement of Science and Technology" (FIST—No. SR/FST/ETI-388/2015) during the period of my project work.

References

1. Charles, J., Chemelle, P.: The history and developments, nowadays DSS properties and duplex market future trends. In: Proceedings of 8th World Duplex Stainless Steel Conference, Beaune, France (2010)
2. Paulraj, P., Garg, R.: Effect of intermetallics on corrosion behaviour and mechanical properties of duplex stainless steels and super duplex stainless steels. Adv. Sci. Technol. Res. J. **9**(27), 87–105 (2015). https://doi.org/10.12913/22998624/59090
3. Wang, Y.Q., Han, J., Wu, H.C., Yang, B.: Effect of sigma phase precipitation on the mechanical and wear properties of Z3CN20 cast duplex stainless steels. J. Nucl. Eng. Design **259**, 1–7 (2013). https://doi.org/10.1016/j.nucengdes.2013.02.037
4. Fargas, G., Mestra, A., Mateo, A.: Effect of sigma phase on the wear behavior of super duplex steels. J. Wear **303**(1), 584–590 (2013). https://doi.org/10.1016/j.wear.2013.04.010
5. Chowdhury, M.A., Nuruzzaman, D.M., Roy, B.K., Islam, A., Hossain, Z., Hasan, M.R.: Experimental investigation of friction coefficient and wear rate of stainless steel 202 sliding against smooth and rough stainless steel 304 counter-faces. Frict. Wear **1**(3), 34–41 (2013)
6. del Abra-Arzola, J.L., García-Rentería, M.A., Cruz-Hernández, V.L., García-Guerra, J., Curiel-López, F.F.: Study of the effect of sigma phase precipitation on the sliding wear and corrosion behaviour of DSS AISI 2205. Wear **400–401**, 43–51 (2018). https://doi.org/10.1016/j.wear.2017.12.019
7. Fargas, G., Mestra, A., Anglada, M., Mateo, A.: Effect of thermal treatments on the wear behaviour of DSSs. In: IOP Conference Series: Materials Science and Engineering, vol. 5, no. 1, p. 01. IOP Publishing (2009). https://doi.org/10.1088/1757-899x/5/1/012009
8. Sieurin, H., Sandström, R.: Sigma phase precipitation in duplex stainless steel 2205. Mater. Sci. Eng. A **444**, 271–276 (2007)
9. Martins, M., Casteletti, L.C.: Heat treatment influence on ASTM A890 Gr 6A super duplex stainless steel microstructure. Mater. Charact. **55**(3), 225–233 (2005). https://doi.org/10.1016/j.matchar.2005.05.008

Chapter 63
Investigation on the Structural and Wear Characteristics of Mg AZ91/Fly Ash Surface Composites Fabricated by Friction Stir Processing

Hemendra Patle, B. Ratna Sunil and Ravikumar Dumpala

Abstract Friction stir processing (FSP) is being used since many years for the fabrication of surface metal matrix composites. Several research studies have been done in the development of surface metal matrix composite through FSP. During FSP, hard ceramic particles are mixed within the soft matrix material through the stirring action of the friction stirring processing tool. In the present study, the surface composite was developed by friction stir processing on the surface of AZ91 magnesium alloy. Fly ash particles were used as secondary phase particles to fabricate surface composite. The fabricated surface metal matrix composite was characterized by using optical microscopy. Microstructural observation of the composite material shows significant grain refinement in stir zone compared to the base metal (AZ91 Mg). Material properties like hardness and wear resistance were studied. The results have confirmed that the hardness and wear resistance were improved for the composite material than the received material.

Keywords FSP · AZ91 Mg alloy · Fly ash · Surface composite · Microhardness · Wear · Coefficient of friction

63.1 Introduction

Metal matrix composite (MMCs) are the class of engineering materials which fulfill the requirements of advanced structures in aerospace, automobile, and marine applications [1–3]. Several methods have been developed for the development of metal matrix composites such as stir casting, powder metallurgy, spray deposition, squeeze casting, vapor deposition and diffusion bonding, but these methods develop

H. Patle (✉) · R. Dumpala
Department of Mechanical Engineering, Visvesvaraya National Institute of Technology (VNIT), Nagpur 440010, Maharashtra, India
e-mail: hemendrapatle876@gmail.com

B. Ratna Sunil
Department of Mechanical Engineering, Bapatla Engineering College, Bapatla 522101, India

M. S. Shunmugam and M. Kanthababu (eds.), *Advances in Micro and Nano Manufacturing and Surface Engineering*, Lecture Notes on Multidisciplinary Industrial Engineering,
https://doi.org/10.1007/978-981-32-9425-7_63

bulk MMCs. Surface metal matrix composites are the class of engineering materials which contain different surface characteristics other than the inner-core material. Surface MMCs contain hard ceramic secondary-phase particles in the surface while the core material is unaffected. Hence, the surface exhibits higher hardness, strength, and wear resistance without comprising the toughness of the material [4]. The high-energy laser beam, plasma spraying, centrifugal casting, and electron beam irradiation are such kind of techniques which are used to develop the MMCs [5–9]. However, all these techniques require melting of materials at a higher temperature which generates the detrimental phase due to the interfacial reaction in-between the matrix material and reinforcement particles which reduces the mechanical properties of the materials. Such problems can be avoided if the process is carried out in the solid phase only. Friction stir processing (FSP) provides such advantage to perform processing in the material solid state only. It modifies the microstructure of the surface of the material by producing dynamic recrystallization. Secondary phase particles are embedded on the surface of the materials through FSP and thus the process of surface MMCs fabrication is completed. Dynamic recrystallization further produces a fine-grained structure which alters the material properties which is another advantage of FSP. Mishra et al. [10] first developed Al5083/SiC surface composite using FSP. Later on, several researchers have developed FSP-based surface composite using aluminum, magnesium, copper, steel, and their alloys as matrix materials and different varieties of reinforcement particles such as Al_2O_3, SiC, TiC, B_4C, TiO_2, SiO_2, etc. [11–13]. Magnesium and magnesium-based alloys are the popular choices to construct lightweight structures for automobile and aerospace sector, etc. Magnesium has very low density (1.74 g/cm^3) and also contains excellent capability of shock and vibration absorption. Magnesium and its Al–Zn based alloys such as AZ31, AZ61, and AZ91 are suitable choices for constructing light metals based surface composites.

In this investigation, FSP was used for developing AZ91 Mg alloy based surface composites using fly ash as a secondary-phase particle. The microstructure of fabricated surface composite was investigated as well as hardness distribution within the stir zone and wear characteristics were also investigated.

63.2 Experimental Details

The sheets of AZ91 Mg alloy were used as the base material was obtained from exclusive magnesium, Hyderabad, India. Plates of size 100 × 50 × 7 mm^3 were used to perform the FSP experiments. Chemical composition of the base metal is given in Table 63.1.

Fly ash powder was obtained from Vijayawada Thermal Power Station (VTPS), Vijayawada, India. The obtained fly ash particles were washed with deionized water, dried and filtered using different sieves up to 53 μm. Figure 63.1 represents the used fly ash powder.

Table 63.1 Nominal composition of AZ91 Mg alloy (wt%)

Al	Zn	Mn	Si	Fe	Ni	Mg
8.7%	0.7%	0.2%	0.03%	0.0012%	0.002%	Bal.

Fig. 63.1 Fly ash powder

FSP was performed in an automated universal milling machine (Bharat Fritz Werner Ltd., India). The plate was fixed on a milling machine work bed. The plate was grooved in the center with a size of 2 × 1 mm^2. The groove was filled with fly ash powder. Two tools were used for the composite fabrication purpose. The tool was made of H13 tool steel and was hardened up to 55 HRC. A pinless tool of 15 mm shoulder diameter was used to close the groove so that particles do not get scattered during the FSP process. FSP was performed with the help of square taper pin tool. The tool was made of 15 mm shoulder diameter along with a tool pin of square tapered shape (4.25–2 mm taper along 3 mm pin height). Figure 63.2 represents the tool used for conducting the FSP experiments. The tool was allowed to penetrate the metal surface in such a way that the tool shoulder touched the work plate surface. The tool plunge depth was set to 0.1 mm so that the total penetration depth for the tool becomes 3.1 mm. Once the rotating FSP tool was penetrated into the metal plate, a preset feed rate was provided to the tool for further travel

Fig. 63.2 Photograph of the FSP tool

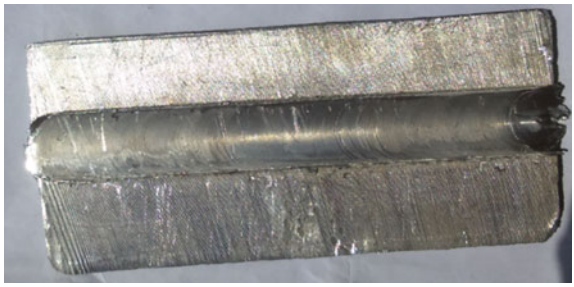

Fig. 63.3 Fabricated AZ91/fly ash surface composite plate

using automatic feed mechanism attached in the milling machine. Trial experiments were conducted to get defect-free processed zone. The defect-free process zone was obtained at tool rotational speed of 1400 rpm and 25 mm/min tool travel speed. Figure 63.3 represents the fabricated AZ91/fly ash surface composite plate. After the fabrication of surface composite, specimens were cut near the processed zone using wire-cut electric discharge machine (EDM). Surface composite AZ91/fly ash samples were subjected to microstructure characterization. Cross sections of the processed samples were polished by different grade emery paper followed by disk polishing using diamond paste (1–3 μm) and cleaned by ethanol. Then the samples were etched chemically using picric acid reagent (mixture of 5 g picric acid, 5 ml acetic acid, 100 ml ethanol, and 5 ml distilled water) and then cleaned and dried. Optical microscope (Leica, Germany) was used to conduct the microstructure observation on the cross section of the processed samples. Vickers microhardness tester (Omnitech, India) was used for microhardness measurement. Microhardness was taken across the processed zone, 3 mm from the top surface exactly to the middle area on the stir zone. 100 g load was applied for 10 s. XRD tests were conducted for the processed sample using (XRD, D8 Advance, Bruker, USA) CuKα radiation under scan range of 20°–80°.

To know the dry sliding wear behavior of fabricated surface composite, wear tests were performed on linear reciprocating tribometer (DUCOM TR-281). Type of contact was ball on plate (point contact), so that the ball moves in to and fro motion on the testing specimens. Tests were performed on the samples of the size of 20 * 20 * 5 mm^3. Samples were cut through the processed zone using Wire EDM. Ball material was AISI 52100 steel with 6 mm diameter. Wear tests were performed for both the base metal and composite specimens. Tests were conducted for 500 m sliding distance with a sliding velocity of 0.14 m/s with the applied load of 10 N. Tests were conducted at room temperature and 40–50% relative humidity. After the wear test, samples were cleaned with acetone and weight loss was measured using a balance with least count of 0.1 mg.

63.3 Results and Discussion

Figure 63.4 shows the microstructure of the base metal AZ91 Mg alloy and the microstructure of the fabricated AZ91/fly ash surface composite. The microstructure shows the significant grain refinement in the stir zone after the FSP processing. The microstructure of the FSP-processed zone illustrates that the size of the grains reduced after processing. Table 63.2 illustrates the average grain size of the BM AZ91 and SMMCs AZ91/fly ash. ImageJ software was used for the measurement of grain size. Table 63.2 results represent the remarkable grain refinement that takes place in the friction-stirred processed zone. Average grain size is reduced from 116 μm of the base metal AZ91 mg to 4.96 μm of SMMCs AZ91/fly ash. Morphology of grains clearly indicates that the dynamic recrystallization happened during the FSP process. Intense material flow, severe deformation, and high heat input generate dynamic recrystallization during the FSP process, which was described in the previous investigation [14]. Microstructure observations show that imperfections such as porosity, voids, and cracks are not present in the stir zone. Fly ash particles are distributed homogeneously within the stirred zone. Figure 63.5 shows the XRD patterns of the fly ash powder and fabricated surface composite AZ91/fly ash. SiO_2 (Quartz), Fe_2O_3 (Hematite), and $Al_6Si_2O_{13}$ (Mullite) phases were identified in fly ash powder. However, the amount of dispersed fly ash particles in the FSPed sample is very less as compared to the magnesium alloy. Hence, it was difficult to detect peaks corresponding to fly ash in the composite during XRD scanning.

Figure 63.6 illustrates the average hardness of the base metal Mg AZ91 and Mg AZ91/fly ash surface composite. The hardness of the surface composite increases up to 20% as compared to base metal AZ91 Mg alloy. According to Hall–Petch relation,

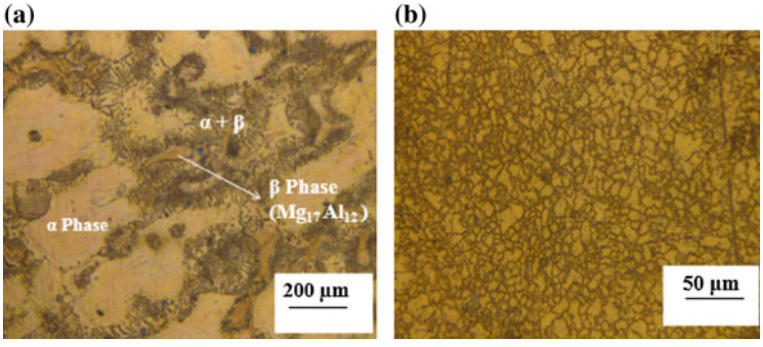

Fig. 63.4 Optical microscope image of the samples, **a** BM AZ91, **b** AZ91/fly ash

Table 63.2 Average grain size measured in both samples

Samples	BM AZ91 Mg alloy	SMMCs AZ91/fly ash
Grain size (μm)	116	4.96

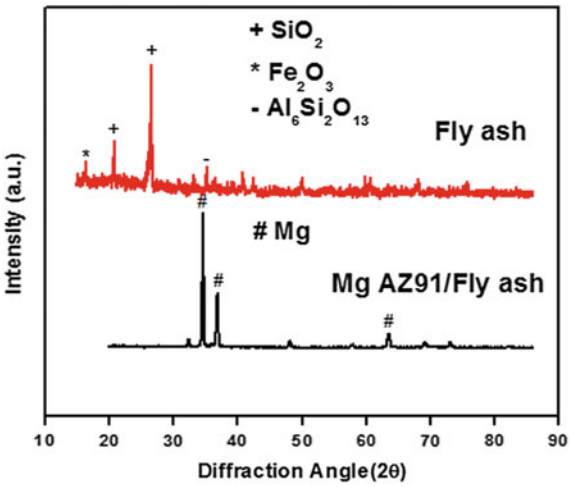

Fig. 63.5 XRD pattern of fly ash powder and Mg AZ91/fly ash surface composite

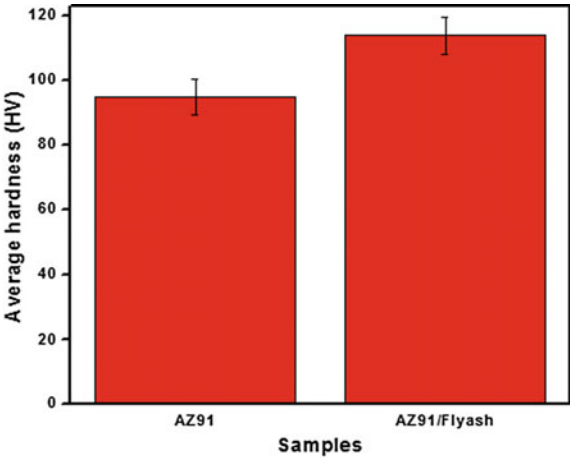

Fig. 63.6 Average microhardness of the samples

hardness increases due to the formation of fine-sized grains as a result of dynamic recrystallization produced by FSP. The presence of fly ash particles increased the hardness in the surface composite region up to 114 HV.

Dispersion of fly ash particles apply the pinning effects which prevent the grain growth and thus reduce the grain size and result in the enhancement of the hardness of the composite. Orowan strengthening mechanism is also responsible for the enhancement in the hardness. Figure 63.7 represents the coefficient of friction versus time duration graph for both specimens. Time duration is taken according to 500 m sliding distance. The coefficient of friction and weight loss of the base metal AZ91 and AZ91/fly ash surface composite are listed in Table 63.3. It was observed that the composite sample has less weight loss and coefficient of friction than the base metal.

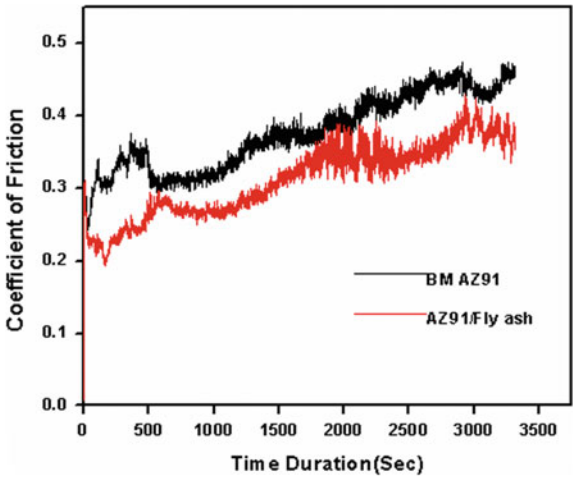

Fig. 63.7 Coefficient of friction obtained from wear tests

Table 63.3 Coefficient of friction and weight loss of both specimens

Specimens	Weight loss (mg)	Coefficient of friction
BM AZ91	10.6 ± 3	0.38 ± 0.2
AZ91/fly ash	5.5 ± 2	0.31 ± 0.06

FSP produced surface composite AZ91/fly ash shows significant weight reduction as almost half of the base metal AZ91. Presence of fly ash particles causes the strengthening of matrix material which resists the deformation of matrix material and also resists the penetration of slider ball on the surface of the matrix material. Higher hardness of the composite material can transform severe wear to mild wear as compared to the base metal. Fly ash particles act as load-bearing components to reduce the direct load and contact on the surface of the matrix material. High hardness and dispersion of fly ash particles enhance the wear resistance.

63.4 Conclusions

In the present study, the Mg AZ91/fly ash based surface composite was successfully produced by the FSP technique. The microstructure, hardness, and tribological characteristics of the produced Mg AZ91 based surface composite were investigated and compared with unprocessed Mg AZ91 alloy. The following conclusions were derived from this study:

- Mg AZ91/fly ash based surface composite was successfully developed using friction stir processing with a square taper pin tool.
- FSP of Mg AZ91 alloy resulted in significant modification in the microstructure and finer grain as well as enhanced hardness in the stir zone.

- Addition of fly ash particles through FSP and fabrication of surface metal matrix composite further refine the microstructure and enhanced the hardness up to 20%.
- Wear resistance of the fabricated surface composite was improved in comparison to that of the base metal. The friction coefficient and weight loss of Mg AZ91/fly ash based surface composite were less in comparison to the unreinforced AZ91 base metal. This is attributed to the enhanced hardness of the surface composite (Mg AZ91/fly ash).

Acknowledgements The authors like to thank DST (Department of Science & Technology, New Delhi, India, No. ECR/2016/000654) for providing financial support.

References

1. Sahraeinejad, S., Izadi, H., Haghshenas, M., Gerlich, A.P.: Fabrication of metal matrix composites by friction stir processing with different particles and processing parameters. Mater. Sci. Eng. A **626**, 505–513 (2015)
2. Kaczmar, J.W., Pietrzak, K., Woosinaski, W.: The production and application of metal matrix composite materials. J. Mater. Process. Technol. **106**, 58–67 (2000)
3. Kainer, K.U.: Metal Matrix Composites: Custom-Made Materials for Automotive and Aerospace Engineering. Wiley-VCHVerlag GmbH & Co., Weinheim (2006)
4. Singh, R.K., Gilbert, D.R., Fitz-Gerald, J., Lee, D.G.: Surface composite: novel method to fabricate adherent interfaces. Surf. Eng. **13**(5), 389–392 (1997)
5. Wang, X.H., Zhang, M., Du, B.S.: Fabrication of multiple ceramic particles reinforced iron matrix coating by laser cladding. Mater. Manuf. Process. **28**(5), 509–513 (2003)
6. Farayibi, P.K., Folkes, J.A., Clare, A.T.: Laser deposition of Ti-6Al-4V wire with WC powder for functionally graded components. Mater. Manuf. Process **28**(5), 514–518 (2013)
7. Ayers, J.D., Tucker, T.R.: Particulate-TiC-hardened steel surfaces by laser melt injection. Thin Solid Film **73**(1), 201–207 (1980)
8. Weisheit, A., Galan, G., Mordike, B.L.: Casting, semi-solid forming, and hot rolling. In: Hashmi, S. (ed.) Comprehensive Material Processing. Elsevier, USA (2014)
9. Riabkina-Fishman, M., Rabkin, E., Levin, P., Frage, N., Dariel, M.P.: Laser produced functionally graded tungsten carbide coatings on M2 high-speed tool steel. Mater. Sci. Eng. A **302**(1), 106–114 (2001)
10. Mishra, R.S., Mahoney, M.W., McFadden, S.X., Mara, N.A., Mukherjee, A.K.: High strain rate superplasticity in a friction stir processed 7075 Al alloy. Scripta Mater. **42**(2), 163–168 (1999)
11. Sunil, B.R., Reddy, G.P.K., Patle, H., Dumpala, R.: Magnesium based surface metal matrix composites by friction stir processing. J. Magnes. Alloys **4**, 52–61 (2016). https://doi.org/10.1016/j.jma.2016.02.001
12. Sharma, V., Prakash, U., Manojkumar, B.V.: Surface composites by friction stir processing: a review. J. Mater. Process. Technol. **224**, 117–134 (2015)
13. Sunil, B.R., Sampath, K.T.S., Chakkingal, U., Nandakumar, V., Doble, M., Prasad, V.D., Raghunath, M.: Friction stir processing of magnesium–nanohydroxyapatite composites with controlled in vitro degradation behavior. Mater. Sci. Eng. C **39**, 315–324 (2014)
14. Khayyamin, D., Mostafapour, A., Keshmiri, R.K.: The effect of process parameters on microstructural characteristics of AZ91/SiO_2 composite fabricated by FSP. Mater. Sci. Eng. A **559**, 217–221 (2013)

Chapter 64
Atmospheric Plasma Sprayed 25 wt.% WO_3-75wt.% SnO_2 Composite Coating: Investigations on Ethanol and Acetone Sensing Characteristics

Vibhav Ambardekar, P. P. Bandyopadhyay and S. B. Majumder

Abstract The present work explores ethanol and acetone sensing performance of atmospheric plasma sprayed 25 wt.% WO_3-75 wt.% SnO_2 coating deposited on alumina substrate. Sensing characterization of the coating was tested using a homemade static chamber in the presence of ethanol and acetone. Sensor response characteristics were also obtained by varying concentration of test vapour. Concentration dependent response transients were modeled using Langmuir-Hinshelwood isotherm to estimate characteristic time constant for ethanol and acetone sensing.

Keywords Atmospheric plasma spray · Composite coating · Gas sensor · Langmuir–Hinshelwood mechanism

64.1 Introduction

Atmospheric plasma spray (APS) is used to deposit thick coatings of metals, polymers and ceramics for various applications [1]. Mostly, APS used to deposit wear and corrosion resistant coatings [2, 3], thermal barrier coatings for various applications [4, 5]. The process offers faster rate of deposition which makes it suitable for mass production [6]. Recently, APS has been used to develop gas sensing elements using binary oxides such as WO_3 [7], ZnO [8], TiO_2 [9] and SnO_2 [10]. Composite coating of two binary oxides is reported to yield superior gas sensing performance [11]. However, limited attempts have so far been made to deposit composite coating using APS. In the present work, we have studied the gas sensing performance of plasma sprayed 25 wt.% WO_3-75 wt.% SnO_2 coating for ethanol and acetone sensing.

V. Ambardekar (✉) · P. P. Bandyopadhyay
Department of Mechanical Engineering, Indian Institute of Technology Kharagpur, Kharagpur 721302, India

S. B. Majumder
Materials Science Centre, Indian Institute of Technology Kharagpur, Kharagpur 721302, India

M. S. Shunmugam and M. Kanthababu (eds.), *Advances in Micro and Nano Manufacturing and Surface Engineering*, Lecture Notes on Multidisciplinary Industrial Engineering,
https://doi.org/10.1007/978-981-32-9425-7_64

64.2 Experimental

Commercially available tin oxide (SnO_2) and tungsten oxide (WO_3) powders were blended in suitable proportion to get 25 wt.% WO_3-75 wt.% SnO_2 composition. Alumina substrate was cleaned using acetone as a solvent before plasma spraying. The mixed powder was deposited on alumina substrate (19 mm × 9.5 mm × 0.65 mm) using a Sulzer Metco 9 MB plasma gun. Overheating of substrate was prevented using compressed air as a substrate cooling media. The process parameters for coating are tabulated in Table 64.1. As-sprayed coating was annealed at 600 °C for 60 min to improve the crystallinity and stabilize base resistance prior to gas sensing. To measure the resistance transients during gas sensing, two circular silver electrodes (approximate diameter ~2 mm) with a gap of 4 mm were painted on the surface of the annealed composite coating [10].

X-ray diffractometer (Empyrean, Panalytical, Netherlands) equipped with CuKα source (λ = 1.54 Å) was used to characterize the structure of the coating. The thickness was estimated from the cross sectional morphology of the coating using a field emission scanning electron microscope (Merlin, Zeiss, Germany). Sensing characteristics of ethanol and acetone vapour were measured using a static flow chamber. The details of the chamber and the sensing measurement are reported elsewhere [12]. Sensor response % (S %) was estimated from the measured resistance using the following expression [10, 13]:

$$S\,\% = \left[\left(R_a - R_{vap}\right)/R_a\right] \times 100 \tag{64.1}$$

where R_a and R_{vap} are the values of the equilibrium sensor resistance measured in air and vapour, respectively.

64.3 Results and Discussion

Figure 64.1a shows the X-ray diffractogram of an annealed composite coating. Diffraction peaks of WO_3 (monoclinic), SnO_2 (tetragonal) and Al_2O_3 (rhombohedral) substrate are indexed in Fig. 64.1a.

Figure 64.1b shows the surface morphology of the annealed coating. The coating consists of macropores (pore size > 50 nm) and mesopores (pore size in the range of 2–50 nm) as marked in Fig. 64.1b. The nature of porosity influences the gas sensing

Table 64.1 Process parameters used for composite coating

Spray distance (mm)	Current (A)	Voltage (V)	Plasma power (kW)	N_2 flow rate (slpm)	H_2 flow rate (slpm)	Feedstock flow rate (g/min)
100	350	~68	~24	50	0	~25

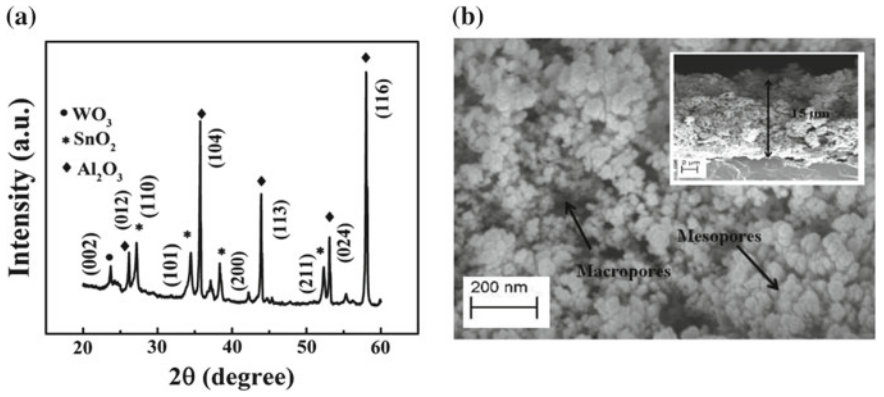

Fig. 64.1 **a** X-ray diffractogram of composite coating, **b** surface morphology of composite coating. Inset shows the cross-sectional morphology used to estimate the coating thickness

characteristics of composite coating. The inset of Fig. 64.1b shows the cross-sectional morphology of the composite coating. As shown in the inset, the coating is porous in nature with thickness estimated to be ~15 μm [10, 14].

Figure 64.2a shows the temperature dependent response % for ethanol and acetone sensing measured at 300 °C. For both these test vapours, highest response % was obtained at 300 °C. Figure 64.2b represents typical resistance transients obtained for 300 ppm ethanol and acetone measured at 300 °C, respectively. Sensor response time (τ_{res}) is defined as the time required to yield 90% drop in base resistance since the test gas is introduced in the chamber (marked by downward arrow in Fig. 64.2b). On the other hand, time required to yield 90% recovery in base resistance is termed

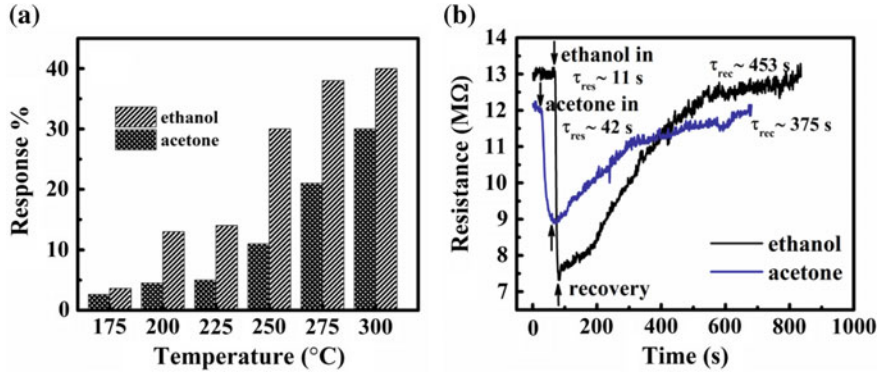

Fig. 64.2 **a** Temperature dependent response % of 300 ppm ethanol and acetone, **b** resistance transients of 300 ppm ethanol and acetone sensing measured at 300 °C. Response time (τ_{res}) and recovery time (τ_{rec}) values are marked in Fig. 64.2 (**b**)

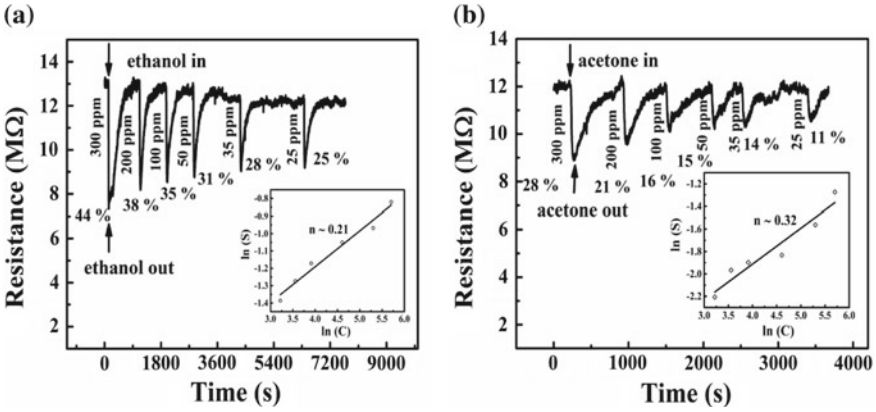

Fig. 64.3 The resistance transients of the different concentrations of the test vapour of **a** ethanol, **b** acetone measured at 300 °C. Inset shows the ln S versus ln C plot (symbols) and linear fit (solid line)

as recovery time (τ_{rec}) [12]. The estimated response and recovery time are marked in Fig. 64.2b. Response time for ethanol and acetone was 11 s and 42 s, respectively. On the other hand, recovery time for ethanol and acetone was estimated to be ~453 s and 375 s, respectively.

Figure 64.3 shows the resistance transients for (a) ethanol and (b) acetone sensing for which the concentration of test vapour was varied in the range of 25–300 ppm. The operating temperature was 300 °C for this measurement. In this measurement, sensor was subjected to test vapour at various concentrations. Measurements were conducted from 300 ppm down to 25 ppm. Sensor response and recovery was achieved at each concentration in order to get concentration dependent resistance transients for ethanol and acetone sensing, respectively. Inset shows the sensitivity of the sensor. The sensor response (S) follows the following relation with the test vapour concentration (C),

$$S = a \times C^{n} \tag{64.2}$$

where *a* is the sensitivity coefficient, and *n* is the sensitivity of the sensor. As shown in the inset of Fig. 64.3a, b, the slope of the linear fit of ln S versus ln C plot yield the sensitivity (n) for ethanol and acetone sensing. As marked in the inset of Fig. 64.3b, the composite coating has acetone sensitivity (~0.32) higher than ethanol sensing (~0.21) as marked in Fig. 64.3a.

Depending on the baseline recovery of the resistance transients, sensing mechanism is termed to be reversible or irreversible in nature. The mechanism of reversible and irreversible sensing has been reported elsewhere [15]. Gas sensing is said to be irreversible if baseline resistance in air recovers partially after removal of test gas. Reversible sensing is characterized by full recovery of baseline resistance. In the present work, reversible gas sensing characteristics were obtained during ethanol

and acetone sensing as shown in Fig. 64.3a, b, respectively. When the sensor is heated at high temperature, ambient oxygen species are chemically adsorbed by extracting electrons from metal oxide sensor. During gas sensing, test gas interacts with chemi-adsorbed oxygen to form oxidized products. The electrons released as a result of the interaction of test gas with chemi-adsorbed oxygen are returned to the conduction band. The reaction sequence is described as follows [13, 16]:

$$O_2(\text{ads}) + e^- \rightarrow O_2{}^-(\text{ads}) \tag{64.3}$$

$$O_2^-(\text{ads}) + e^- \rightarrow 2O^-(\text{ads}) \tag{64.4}$$

$$C_2H_5OH + 6O^- \rightarrow 3H_2O + 2CO_2 + 6e^- \tag{64.5}$$

$$CH_3COCH_3 + 8O^- \rightarrow 3CO_2 + 3H_2O + 8e^- \tag{64.6}$$

It is noted that the response % increases with increase in concentration. At low concentration, interaction of test vapour with chemically adsorbed oxygen (O^-) is less efficient which results into lower response %. On the other hand, at higher concentrations; there exists enough availability of test vapour species to interact with chemically adsorbed oxygen which results into higher response %. In short, enough availability of test vapour species owing to higher concentration, availability of O^- species owing to sufficient operating temperature are the key parameters for achieving useful sensing signal [16].

The time dependent sensor response for reversible sensing can be fitted non-linearly using the following relation [15]:

$$S(t) = S_{max}\left[1 - \exp(-t/\tau_{rev})\right] \tag{64.7}$$

The solid line in Figs. 64.4 and 64.5 represents the time dependent response % fitting for ethanol and acetone, respectively. Inset of Figs. 64.4e and 64.5e shows the variation of time constant with concentration for ethanol and acetone, respectively. Note that both ethanol and acetone sensing showed reversible behaviour. Atmospheric plasma spray process is suitable for mass production owing to its faster deposition rate [10]. For this advantage, it is possible to produce large number of gas sensors in a very short time. In the breath analysis application, such coating can be used to monitor alcohol content of drunken drivers. Since the blood alcohol content varies from person to person depending upon the dosage, change in electrical resistance would be different for different concentrations. As a result of reversible behaviour, coating is suitable for monitoring blood alcohol content. Considering

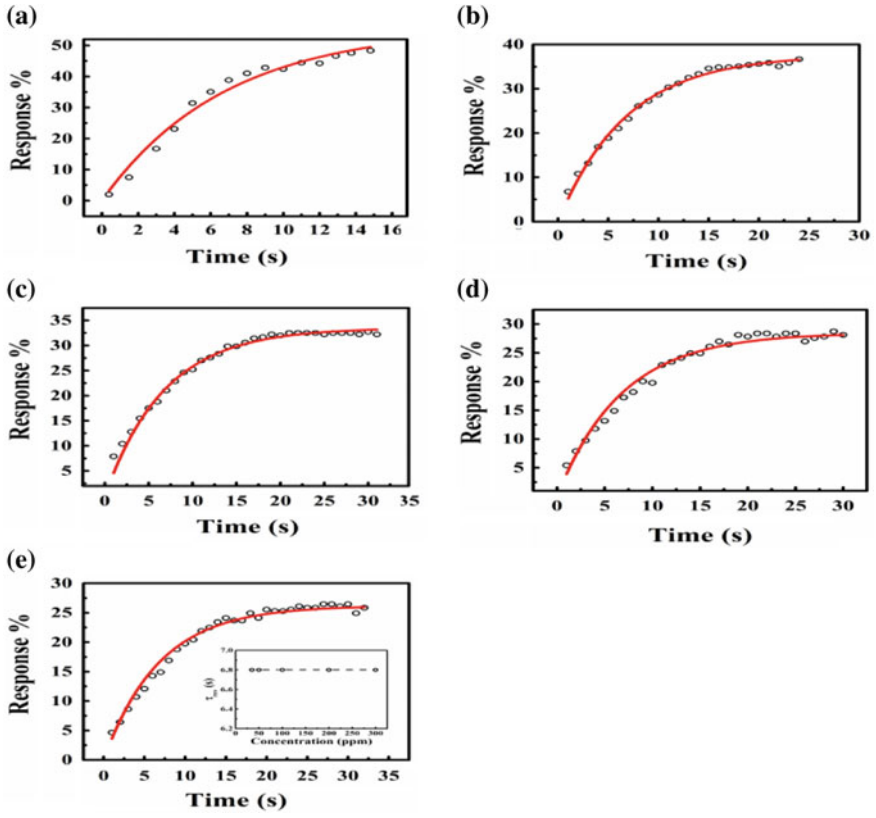

Fig. 64.4 Estimated time dependent response % (symbols) for **a** 300 ppm, **b** 200 ppm, **c** 100 ppm, **d** 50 ppm, **e** 35 ppm ethanol sensing. Solid lines are fitted using Eq. 64.7. The inset of this figure (**e**) shows the estimated variation of τ_{rev} with ethanol concentration

coating size, it is possible to encapsulate the coating with portable electronic circuit to develop a breath analyzer [13].

Figure 64.4 shows the estimated Time dependent response % fitting for (a) 300 ppm, (b) 200 ppm, (c) 100 ppm, (d) 50 ppm, (e) 35 ppm ethanol sensing. Similarly, Fig. 64.5 shows the estimated time dependent response % variation for (a) 300 ppm, (b) 200 ppm, (c) 100 ppm, (d) 50 ppm, (e) 35 ppm acetone sensing measured at 300 °C.

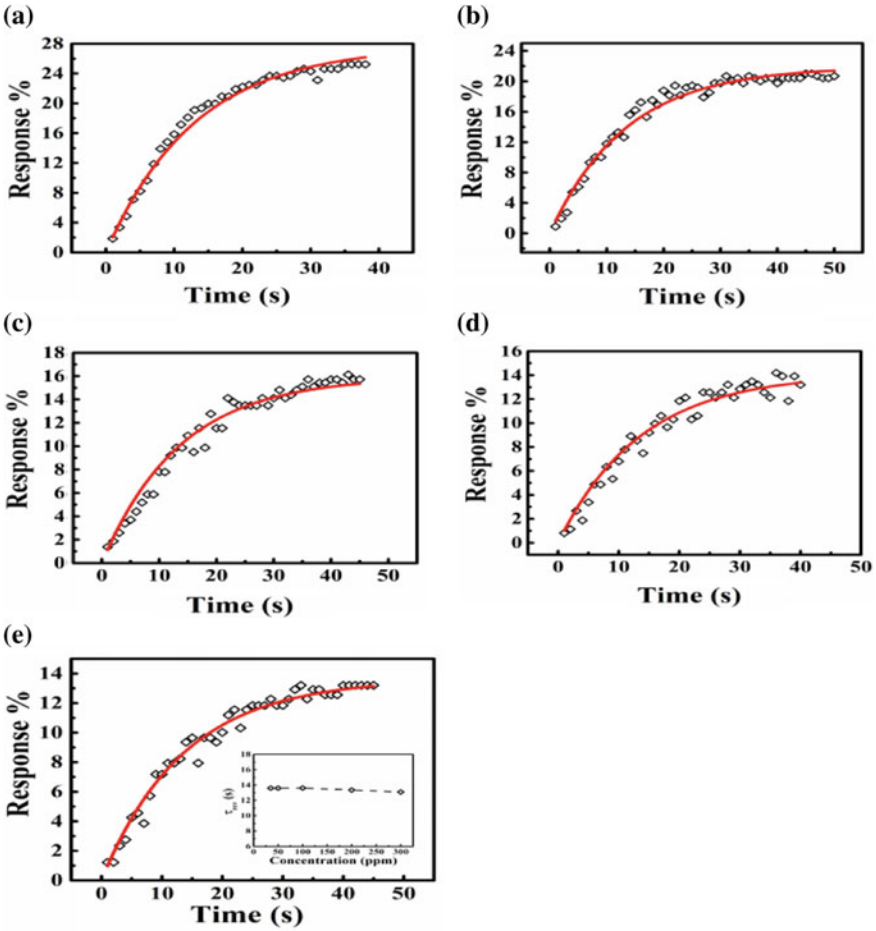

Fig. 64.5 Estimated time dependent response % (symbols) for **a** 300 ppm, **b** 200 ppm, **c** 100 ppm, **d** 50 ppm, **e** 35 ppm acetone sensing. Solid lines are fitted using Eq. 64.7. The inset of this figure (**e**) shows the estimated variation of τ_{rev} with ethanol concentration

64.4 Conclusions

In the present work, atmospheric plasma spray was used to deposit 25 wt.% WO_3-75 wt.% SnO_2 composite coating on alumina substrate for ethanol and acetone sensing application. The coating yield good sensing performance for ethanol and acetone sensing at 300 °C. Concentration dependent response characteristics were obtained at 300 °C for 25–300 ppm gas concentration. Time dependent response % was fitted using Langmuir-Hinshelwood mechanism and characteristic time constant was estimated for each gas concentration. Variation of characteristic time constant with

concentration exhibited reversible sensing mechanism. Ethanol sensor can be used to make breath analyzer suitable to monitor drink in driving.

Acknowledgements The above research work was partially supported by the research grant obtained from CSIR, Government of India; vide sanction Letter No. 03/(1371)/16/EMR-II, dated 10-05-2016 and DST, Government of India; vide sanction letter Nos. 5(1) 2017-NANO dated 28-03-2018 and DST/NM/NNETRA/2018(G)-IIT KGP dated 21-03-2018.

References

1. Bandyopadhyay, P.P.: Processing and Characterisation of Plasma Sprayed Ceramic Coatings on Steel Substrate. Ph.D. Dissertation, Indian Institute of Technology, Kharagpur (2000)
2. Jambagi, S.C., Kar, S., Brodard, P., Bandyopadhyay, P.P.: Characteristics of plasma sprayed coatings produced from carbon nanotube doped ceramic powder feedstock. Mater. Des. **112**, 392–401 (2016). https://doi.org/10.1016/j.matdes.2016.09.095
3. Hadad, M., Bandyopadhyay, P.P., Michler, J., Lesage, J.: Tribological behaviour of thermally sprayed Ti-Cr-Si coatings. Wear **267**, 1002–1008 (2009). https://doi.org/10.1016/j.wear.2009.01.013
4. Kar, S., Paul, S., Bandyopadhyay, P.P.: Processing and characterisation of plasma sprayed oxides: microstructure, phases and residual stress. Surf. Coat. Technol. **304**, 364–374 (2016). https://doi.org/10.1016/j.surfcoat.2016.07.043
5. Das, P., Paul, S., Bandyopadhyay, P.P.: Preparation of diamond reinforced metal powders as thermal spray feedstock using ball milling. Surf. Coat. Technol. **289**, 165–171 (2016). https://doi.org/10.1016/j.surfcoat.2015.12.022
6. Sampath, S.: Thermal spray applications in electronics and sensors: past, present, and future. J. Therm. Spray Technol. **19**, 921–949 (2010). https://doi.org/10.1007/s11666-010-9475-2
7. Zhang, C., Debliquy, M., Boudiba, A., et al.: Sensing properties of atmospheric plasma-sprayed WO_3 coating for sub-ppm NO_2 detection. Sens. Actuators B Chem. **144**, 280–288 (2010). https://doi.org/10.1016/j.snb.2009.11.006
8. Zhang, C., Debliquy, M., Liao, H.: Deposition and microstructure characterization of atmospheric plasma-sprayed ZnO coatings for NO_2 detection. Appl. Surf. Sci. **256**, 5905–5910 (2010). https://doi.org/10.1016/j.apsusc.2010.03.072
9. Gardon, M., Monereo, O., Dosta, S., et al.: New procedures for building-up the active layer of gas sensors on flexible polymers. Surf. Coat. Technol. **235**, 848–852 (2013). https://doi.org/10.1016/j.surfcoat.2013.09.011
10. Ambardekar, V., Bandyopadhyay, P.P., Majumder, S.B.: Atmospheric plasma sprayed SnO_2 coating for ethanol detection. J. Alloys Compd. **752**, 440–447 (2018). https://doi.org/10.1016/j.jallcom.2018.04.151
11. Ghosh, A., Schneller, T., Waser, R., Majumder, S.B.: Understanding on the selective carbon monoxide sensing characteristics of copper oxide-zinc oxide composite thin films. Sens. Actuators B Chem. **253**, 685–696 (2017). https://doi.org/10.1016/j.snb.2017.06.154
12. Ghosh, A., Maity, A., Banerjee, R., Majumder, S.B.: Volatile organic compound sensing using copper oxide thin films: addressing the cross sensitivity issue. J. Alloy. Compd. **692**, 108–118 (2017). https://doi.org/10.1016/j.jallcom.2016.09.001
13. Karmakar, M., Das, P., Pal, M., et al.: Acetone and ethanol sensing characteristics of magnesium zinc ferrite nano-particulate chemi-resistive sensor. J. Mater. Sci. **49**, 5766–5771 (2014). https://doi.org/10.1007/s10853-014-8302-4
14. Mukherjee, K., Majumder, S.B.: Analyses of response and recovery kinetics of zinc ferrite as hydrogen gas sensor. J. Appl. Phys. **106** (2009). https://doi.org/10.1063/1.3225996

15. Mukherjee, K., Gaur, A.P.S., Majumder, S.B.: Investigations on irreversible- and reversible-type gas sensing for ZnO and $Mg_{0.5}Zn_{0.5}Fe_2O_4$ chemi-resistive sensors. J. Phys. D Appl. Phys. **45**, 505306 (2012). https://doi.org/10.1088/0022-3727/45/50/505306
16. Barsan, N., Weimar, U.: Conduction model of metal oxide gas sensors. J. Electroceram. **7**, 143–167 (2001). https://doi.org/10.1023/A:1014405811371

Chapter 65
Microstructural and Size Accuracy Study of Electrochemical Machined Aluminium Alloy Features

R. K. Sahu, Vijay Kumar Pal and Pankaj Kumar

Abstract The present work focuses on the machining of aluminium 6061 alloy workpiece electrodes using Electro-Chemical Machining (ECM) by varying the control parameters like voltage, feed rate and machining time. Scanning electron microscopy study is carried out to examine the microstructure of the craters of definite morphology machined on the workpiece. Optimum parameter settings to maximize the length, width and depth of the obtained features were studied individually through a parametric experimental design layout of Taguchi. The results reveal that the optimal parameter settings are found to be different for each performance objective. As a result, the grey Taguchi method has been adopted to convert the three objectives into a single objective and by considering the performance objectives concurrently, the process parameters were optimized. The favourable parameters to maximize the responses are determined to be voltage—15 V, feed rate—0.3 mm/min and machining time—5 min. Further, the effect of process parameters on the microstructure and size accuracy of the Al alloy features is studied.

Keywords ECM · Craters · Microstructure · Size accuracy

R. K. Sahu (✉)
Department of Mechanical Engineering, National Institute of Technology Karnataka, Surathkal 575025, India
e-mail: ranjeet.nitrkl5@gmail.com

V. K. Pal
Department of Mechanical Engineering, Indian Institute of Technology Jammu, Jagti 181221, India

P. Kumar
Department of Mechanical Engineering, SRM Institute of Science and Technology, Kattankulathur 603203, India

M. S. Shunmugam and M. Kanthababu (eds.), *Advances in Micro and Nano Manufacturing and Surface Engineering*, Lecture Notes on Multidisciplinary Industrial Engineering,
https://doi.org/10.1007/978-981-32-9425-7_65

65.1 Introduction

Over the last few decades, advanced machining techniques are gaining remarkable market attention for the fabrication of precise and high-quality tiny and complex features. To achieve these characteristic features, conventional machining techniques are not appropriate because of their predominant tool wear, high initial cost of the setup, more power consumption and hard to meet the micron size of the tool electrode. So, it becomes imperative to search for an advanced machining technique that can meet the limitations of the conventional techniques. Electro-Chemical Machining (ECM) technique is one such technique which can overcome the above-mentioned issue and could produce accurate minute complex features like cooling holes in turbine blades, holes in printing nozzles, nuclear reactors and MEMS channels, and other promising fields [1]. These features can be accomplished in an efficient and cost-effective manner if the effect of ECM parameters such as voltage, feed rate, machining time, current density and conductivity of electrolyte on the microstructure and size accuracy of the features are properly studied through a structured methodology. The literature on the electrochemical machining of some engineering materials shows that ECM characteristic study of alloy steel using NaCl + H_2O_2 electrolyte solution was carried out to increase the ECM performance. The influence of parameters like voltage, IEG and concentration of electrolyte on the surface quality and microstructure of the machined surface was studied. The process parameters are optimized through particle swarm optimization-desirability function approach and the optimal conditions were found to be in proximity with the experimental results [2]. Thanigaivelan et al. [3] machined stainless steel by passing acidified sodium nitrate solution using ECM. The results reveal that the material removal rate was increased and the overcut was linear at higher concentration of sulfuric acid. Zhengyang et al. [4] conducted electrochemical machining on Ti 40 alloy by using electrolyte sodium chloride (NaCl) and potassium bromide (KBr). The tool wear rate was found to be negligible and the optimal values were observed to be voltage—30 V and frequency—1 kHz. Das et al. [5] machined steel with copper tool and KCl as electrolyte using the ECM process. The machining carried out by varying voltage, feed rate, IEG and concentration of electrolyte, and the parameters are optimized using weighted principal component analysis. The electrolyte concentration was found to be the main significant factor that influences the surface quality of the features. Chen et al. [6] conducted electrochemical machining of titanium alloy for blisk blades and studied the process parameters' influence on the surface quality of the workpiece. They observed the surface roughness of 0.192 μm at the optimal parameters of NaCl electrolyte concentration 13wt%, voltage 20 V, pulse frequency 0.4 kHz, duty cycle 0.3, temperature 23 °C and feed rate 0.5 mm/min. Li et al. [7] used a through-mask ECM technique for machining of Ti–6Al–4V sheets with 10% $NaNO_3$ electrolyte solution. They suggested that with suitably selected process parameters, machining precision and efficiency can be improved. The experimental results show that with voltage—35 V, pulse frequency—400 Hz and duty ratio—20%, high-quality holes with uniform size and good morphology were obtained in the 10% $NaNO_3$ solution.

Song et al. [8] produced the hydrophobic surface on an aluminium workpiece by single-step ECM method using NaCl + fluoroalkylsilane electrolyte solution. The texture of the surface was found to be rough on the Al workpiece with good anti-adhesion properties. Liu et al. [9] machined γ-TiAl workpiece via the ECM process using parameters such as voltage, feed rate, electrolyte pressure and temperature, and NaCl electrolyte. The optimum values were observed to be voltage—35 V, feed rate—2 mm/min, electrolyte pressure—0.8 MPa and temperature—35 °C.

The ECM machined features and their characteristics mainly depend on different process-related parameters. By properly adjusting the process parameters, quality can be considerably increased in a cost-effective way. From the detailed literature review, it was noticed that the process parameters' effect on the microstructure and size accuracy of Al alloy features produced using ECM is yet to be studied in detail. Therefore, in this study, geometrical features are machined on Al alloy electrode using ECM and the influence of process parameters on the microstructure and size accuracy of the features is studied through a structured grey Taguchi approach. In this study, the performance objectives of machined Al-6061 alloy features such as length, width and thickness are required to be minimized individually whereas the multiple performance characteristics, i.e. overall grey relational grade (GRG) should be maximized.

65.2 Experimental Details

Figure 65.1 shows the schematic diagram of the ECM experimental setup. It comprises a tool (cathode) and a workpiece (anode) separated by a small gap known as inter-electrode gap and is connected to the power supply (415 V, 3 phase DC, 50 Hz frequency). The setup also incorporates a machining cell, control panel and electrolyte circulation unit. In this work, three important process parameters like

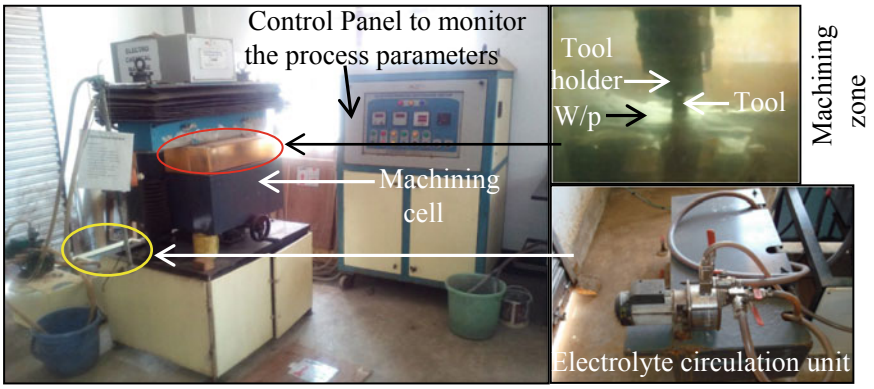

Fig. 65.1 Photographic view of the ECM setup

Table 65.1 Parameters and their levels

Parameter	Level			Unit
	1	2	3	
Voltage	5	10	15	V
Feed rate	0.1	0.2	0.3	mm/min
Machining time	5	7	9	min

voltage, feed rate and machining time are considered to study their influence on the length, width and depth of the features of Al alloy workpiece.

The factor levels are chosen based on the experience and allowable lowest and highest settings suggested by the machine manufacturer. Table 65.1 shows the process parameters at different levels. For full factorial design, 27 experiments will be required if three factors at three levels are used. But if Taguchi's experimental design is used, then the same results will be obtained by conducting less number of experiments. The experimental plan followed by the number of experiments to be carried out as per the plan is based on Taguchi's orthogonal array of design. Based on the experimental layout as shown in Sect. 65.4, the process parameters are arranged in Table 65.1. The workpiece Al-6061 alloy (50 mm × 50 mm × 3 mm) and tool—copper are held in their respective holders. The electrolyte from the electrolyte tank is pumped into the machining cell. The electrolyte is allowed to flow through the tool toward the workpiece. Finally, the material is removed from the workpiece by anodic dissolution. After machining, rectangular features are obtained, and are characterized and evaluated microscopically.

65.3 Methodology

In this study, signal-to-noise (S/N) ratio approach was adopted to optimize the control parameters for achieving better performance characteristics (responses) on the machining of Al alloy. The S/N ratio is used to determine the quality of responses deviating from the desired values. The S/N ratio usually depends on three categories of the performance characteristics for the analysis, i.e. smaller-the-better, larger-the-better and nominal-the-better. Since the objective of the present study is to decrease the length (L), width (W) and thickness (T), the smaller-the-better performance characteristic is taken for obtaining the optimal ECM parameters. The S/N ratio for smaller-the-better performance characteristic (in dB) can be expressed as [10]

$$\eta_{ij} = -10\log\left(\frac{1}{n}\sum_{k=1}^{n} y_{ijk}^2\right) \tag{65.1}$$

where n—number of repetitions and y_{ijk}—experimental value of the ith response in the jth experiment at the kth observation.

Let y_{ij}—performance value of attribute j of alternative i and the term Y_i can be expressed as

$$Y_i = (y_{i1}, y_{i2} \ldots, y_{ij}, \ldots, y_{in}) \tag{65.2}$$

Y_i can be normalized using one of Eqs. (65.3)–(65.5) [11].

$$Xij = (yij - aj)/(aj - bj); \quad i = 1, 2, \ldots, m; \quad j = 1, 2, \ldots, n \tag{65.3}$$

$$X_{ij} = \frac{a_j - y_{ij}}{a_j - b_j}; \quad i = 1, 2, \ldots, m; \quad j = 1, 2, \ldots, n \tag{65.4}$$

$$X_{ij} = 1 - \frac{\left|y_{ij} - c_j\right|}{\text{Max}\left\{a_j - c_{j,} c_j - b_j\right\}}; \quad i = 1, 2, \ldots .m; \quad j = 1, 2, \ldots n \tag{65.5}$$

where a_{ij} = Maximum $\{y_{ij}, i = 1, 2 \ldots m\}$; b_{jj} = Minimum $\{y_{ij}, i = 1, 2 \ldots m\}$; c_{ij} is the true value. Equations (65.3), (65.4) and (65.5) are applicable for larger-the-better, smaller-the-better and nominal-the-better performance characteristic, respectively. In the present study, Eq. (65.4) is used. The alternative performance i is considered for attribute j if grey relational value $X_{ij} = 1$. Thus, a reference sequence $X_0 = \{X_{0j}; X_{oj} = 1$ for $j = 1, 2 \ldots n\}$ is used for comparison of a sequence of alternatives i. The grey relation coefficient (γ) is calculated as [11]

$$\gamma\left(x_{oj}, X_{ij}\right) = \frac{\Delta_{min} + \xi \Delta_{max}}{\Delta_{ij} + \xi \Delta_{max}}; \quad i = 1, 2, \ldots, m; \quad j = 1, 2, \ldots n \tag{65.6}$$

$$\Delta_{ij} = \left|x_{0j} - X_{ij}\right|; \Delta_{max} = Max\left\{\Delta_{ij}, i = 1, 2, \ldots m; \quad j = 1, 2, \ldots n\right\}$$
$$\Delta_{min} = Min\left\{\Delta_{ij,} i = 1, 2, \ldots m; \quad j = 1, 2, \ldots n\right\}$$

ξ—distinguish coefficient (taken as 0.5 in this study), and this was chosen by assessment. The results in the grey relational analysis will vary with respect to the variation in distinguishing coefficients and will lead to the same optimal factors. Further, the grey relational grade (Γ) is determined as

$$\Gamma(x_0, X_i) = \sum_{j=1}^{n} W_j \gamma\left(x_{0j}, X_{ij}\right); \quad i = 1, 2, \ldots, m \tag{65.7}$$

W_j—weight of attribute j and typically depends on the proposed problem structure or chosen by assessment. $\sum_{j=1}^{n} W_j = 1$. The weights for length, width and depth are considered to be one-third.

65.4 Results and Discussion

The scanning electron microscope (SEM) images of features machined on each workpiece using the ECM process are shown in Fig. 65.2. The images have been taken at a certain position on each workpiece at a particular magnification (1000×). The corresponding features are obtained by machining each workpiece according to the experimental layout provided in Table 65.2. From the figure, it has been observed that the material has splashed uniformly throughout during the electrolysis. The grain boundaries do not seem to be much deformed as compared to Fig. 65.2c, h. This is attributed to the inefficient dislocation of atoms during the anodic dissolution of

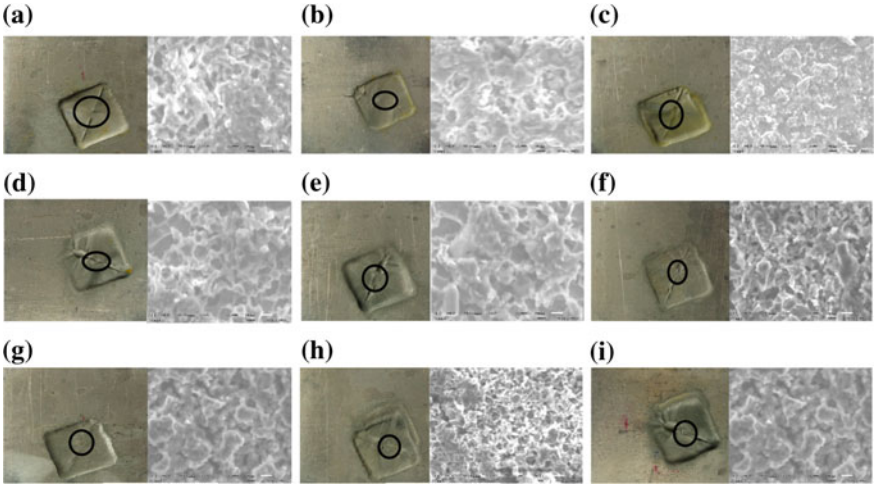

Fig. 65.2 SEM images of features machined on each workpiece using the ECM process

Table 65.2 Experimental layout with responses

Sl. No.	Voltage (V)	Feed (mm/min)	Machining time (min)	Size (mm)		
				Length	Width	Depth
1	5	0.1	5	19.5	19.7	0.394
2	5	0.2	7	19.8	21	0.376
3	5	0.3	9	21.5	19.5	0.562
4	10	0.1	7	20.5	19.8	0.508
5	10	0.2	9	20.8	20.1	0.839
6	10	0.3	5	19.9	19.2	0.285
7	15	0.1	9	21	19.4	0.657
8	15	0.2	5	19.1	20	0.399
9	15	0.3	7	19	18.7	0.911

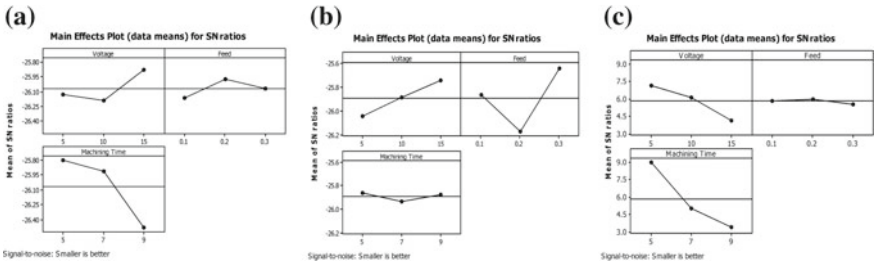

Fig. 65.3 Main effect plot for SN ratios, **a** length, **b** width and **c** depth

the workpiece. However, in Fig. 65.2c, h, it was evident that the atomic–molecular detachment is from the parent crystal lattices and coalesces with others in the array of coagulated form. This may be attributed to the high rate of electrolyte reaction occurring in the anodic portion of the pieces machined.

The process parameters affecting the responses like length, width and depth, and the optimization of these responses using grey Taguchi method have been investigated. The experimentally observed data (i.e. responses) based on the experimental layout are presented in Table 65.2. The responses as shown in Table 65.2 are optimized individually using the Taguchi method.

The optimum factor levels of three responses are obtained from the main effect plots (Fig. 65.3). The optimal parameter levels are observed to be different in the three responses. However, machining of Al-6061 alloy has to be carried out in such a fashion so that the optimized value of the three responses should arrive at the same time with a common setting of the factor level. To achieve the above, grey Taguchi method is used that converts the multi-objectives into a single objective and optimize the process parameters which could satisfy the performance objectives concurrently. In the current study, the inputs for the grey Taguchi are taken as length, width, and depth of the machined features. Since smaller-the-better performance characteristic is considered for the three responses, grey relation generation and coefficient are evaluated using Eqs. (65.4) and (65.6), respectively. The weights of the three responses are taken in equal proportions to determine the grey relation grade by using Eq. (65.7). Table 65.3 shows the results of the grey Taguchi method.

The main effect plot for grey relational grade (Fig. 65.4) shows the optimal parameter level as voltage (3) = 15 V, feed rate (3) = 0.3 mm/min and machining time (1) = 5 min. Therefore, from Fig. 65.4, it is observed that the parametric combination of voltage (3), feed rate (3) and machining time (1) results in maximization of responses of ECM processed Al-6061 alloy workpiece. The significant factors for affecting the multiple performance characteristics are shown in Table 65.4. It is inferred from the table that machining time has a significant effect on the responses followed by voltage and feed.

Table 65.3 Results of grey Taguchi method

Ex. No.	Grey relational coefficient			GRG
	Length	Width	Depth	
1	0.8	0.565	0.826	0.6699
2	0.64	0	0.855	0.5625
3	0	0.652	0.558	0.4782
4	0.4	0.522	0.644	0.5118
5	0.28	0.391	0.115	0.4015
6	0.64	0.783	1	0.7587
7	0.2	0.696	0.406	0.4818
8	0.96	0.435	0.818	0.7542
9	1	1	0	0.8111

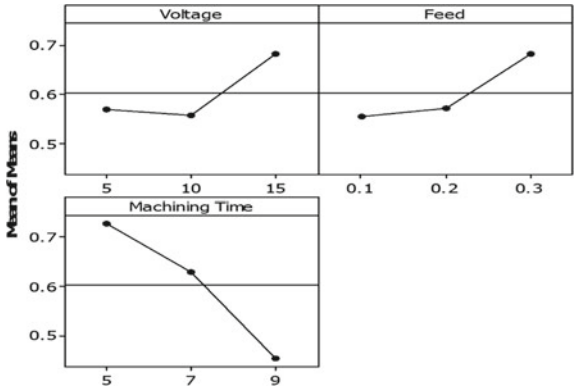

Fig. 65.4 Main effect plot for grey relational grade

Table 65.4 Significant factors for affecting the responses

Level	Voltage	Feed	Machining time
1	4.962	5.213	2.776
2	5.381	5.125	4.211
3	3.537	3.542	6.892
Delta	1.844	1.672	4.116
Rank	2	3	1

65.5 Conclusions

In this work, aluminium 6061 alloy workpiece electrodes were machined using Electro-Chemical Machining by varying the process parameters such as voltage, feed rate and machining time. The microstructure of the machined Al alloy features

of definite morphology was studied and the optimal size accuracy of the features was determined using the grey Taguchi method. The following conclusions are drawn.

1. The microstructure of the features were found to be different owing to the inefficient dislocation of atoms, atomic detachment from the parent lattices and coagulation.
2. Taguchi method fails to optimize length, width and depth due to the compounding effect and thus the grey Taguchi method had bee adopted to optimize the multi-responses.
3. The optimal parameters for maximization of the responses are found to be voltage—15 V, feed rate—0.3 mm/min and machining time—5 min.
4. The machining time has a significant effect on the microstructure and size accuracy followed by voltage and feed.

References

1. Karthick, K., Sahu, R.K., Pankaj, K.: Simulation study on performance characteristic of electrochemical micro machining process. In: IOP Conference Series: Materials Science and Engineering, vol. 402, pp. 012071/1–012071/9 (2018)
2. Ayyappan, S., Kumar, K.S.: Enhancing the performance of electrochemical machining of 20MnCr5 alloy steel and optimization of process parameters of PSO-DF optimizer. Int. J. Adv. Manuf. Technol. **82**, 2053–2064 (2016)
3. Thanigaivelan, R., Arunachalam, R.M., Karthikeyan, B., Longanathan, P.: Electro-chemical machining of stainless steel with acidified sodium nitrate electrolyte. Procedia CIRP **6**, 351–355 (2013)
4. Zhengyang, X., Jia, L., Dong, Z., Ningsong, Q., Xialong, W., Xuezhen, C.: Electrochemical machining of burnt-resistant Ti-40 alloy. Chin. J. Aeronaut. **28**, 1263–1272 (2015)
5. Das, M.K., Barman, T.K., Kumar, K., Sahoo, P.: Effect of process parameters on MRR and surface roughness in ECM of EN31 tool steel using WPCA. Int. J. Mater. Form. Mach. Process. **4**, 45–63 (2017)
6. Chen, X., Xu, Z., Zhu, D., Fang, Z., Zhu, D.: Experimental research on electrochemical machining of titanium alloy Ti60 for a blisk. Chin. J. Aeronaut. **29**, 274–282 (2016)
7. Li, H., Gao, C., Wang, G., Qu, N., Zhu, D.A.: Study of electrochemical machining of Ti-6Al-4V in $NaNO_3$ solution. Sci. Rep. **6**(35013), 1–11 (2016)
8. Song, J., Xu, W., Lu, Y.: One-step electrochemical machining of superhydrophobic surfaces on aluminum substrates. J. Mater. Sci. **47**, 162–168 (2012)
9. Liu, J., Zhu, D., Zhao, L., Xu, Z.: Experimental investigation on electrochemical machining of γ-TiAl intermetallic. Procedia CIRP **35**, 20–24 (2015)
10. Sahu, R.K., Mahapatra, S.S., Sood, A.K.: A study on dimensional accuracy of fused deposition modelling (FDM) processed parts using fuzzy logic. J. Manuf. Sci. Prod. **13**, 183–197 (2013)
11. Sood, A.K., Ohdar, R.K., Mahapatra, S.S.: Improving dimensional accuracy of fused deposition modeling processed part using grey Taguchi method. Mater. Des. **30**, 4243–4252 (2009)

Chapter 66
Establishing EDM as a Method for Inducing Hydrophobicity on SS 304 Surfaces

S. Jithin, Upendra V. Bhandarkar and Suhas S. Joshi

Abstract Different methods have been adopted by researchers to induce hydrophobicity on metallic surfaces which are inherently hydrophilic in nature. In this work, the authors are analysing the effect of different operating parameters, such as pulse on-time, discharge current and gap voltage, on the measured contact angle (MCA) obtained on stainless steel 304 after processing with EDM. It is also attempted to correlate different surface roughness parameters measured on the surfaces with MCA values. MCA values were obtained in the range 101.9° to 127.45° which shows the hydrophobic nature of SS 304 after EDM. MCA showed to increase with an increase in both pulse on-time and discharge current. MCA showed a maximum value at a gap voltage value of 50 V. Surface parameters such as S_{sk}, S_{mr1}, S_{mr2}, V_{vc}/V_{mc} and S_{al} showed good positive linear correlation with MCA. To the best of our knowledge, this work is the first one introducing EDM as a method for wetting property change in metals.

Keywords EDM · EDT · Contact angle · Hydrophobic · Surface roughness · SS 304

66.1 Introduction

Wetting of solid surfaces finds numerous applications in a number of diverse areas such as, bioimplants, aerospace, heat transfer, tribology, anti-ice formation, printing, froth floatation and lubrication. Wetting property of a surface is characterised by the angle between the line which represents the solid–liquid interface and the tangent to the liquid–fluid interface at the position where it meets the solid surface, which is

S. Jithin · U. V. Bhandarkar · S. S. Joshi (✉)
Department of Mechanical Engineering, Indian Institute of Technology Bombay, Mumbai 400076, India
e-mail: ssjoshi@iitb.ac.in

M. S. Shunmugam and M. Kanthababu (eds.), *Advances in Micro and Nano Manufacturing and Surface Engineering*, Lecture Notes on Multidisciplinary Industrial Engineering,
https://doi.org/10.1007/978-981-32-9425-7_66

known as the contact angle. When the liquid in concern is water, a contact angle value less than 90° means the surface is hydrophilic (pro-wetting) and a contact angle value higher than 90° means the surface is hydrophobic (anti-wetting). When the solid–liquid interface is perfectly planar, the contact angle is known as ideal or Young contact angle (YCA). However, actual solid surfaces have some inherent roughness and a mean line is taken to represent the solid–liquid interface. This contact angle measured is known as the apparent or measured contact angle (MCA). Wenzel has stated that the addition of roughness to a surface enhances its wetting properties. Thus, the provision of suitable micro-texture along with suitable surface chemistry reduces the free surface energy and thereby alters the wetting properties of a surface.

Most metal alloy surfaces are hydrophilic in their pure and un-textured form. The methods which have been adopted to induce hydrophobicity on metallic surfaces are laser surface texturing [1, 2], electrochemical machining [3, 4], surface coating [5] and plasma treatment [6]. Patel et al. [1] found out that surfaces with high areal density of micro-textures displayed higher values of MCA as compared to those displayed by surfaces with low areal density of micro-textures. They found out that the reduction in surface energy of the Ti6Al4V surface which leads to it becoming hydrophobic is due to an increase in the level of oxygen content on the surface in the form of an oxide layer formation. They also reported that high areal density of textures resulted in increased capillary action. In another work [2], these researchers also implanted micro-textures on SS 304, Ti6Al4V and some polymer surfaces to make them hydrophobic. Sun et al. [3] utilised electrochemical processing to induce superhydrophobicity on the zinc substrate surface with an MCA value of 165.3°. They also analysed the effect of the operating parameters such as, current, electrolyte type and concentration, on the surface morphology and wetting behaviour of the treated zinc substrates. They also reported that XRD of superhydrophobic surface showed the presence of ZnO, $Zn(OH)_2$ and $Zn5(OH)8Cl_2.H_2O$ in addition to Zn, which might have influenced the wetting behaviour of the Zn surface and lead to the superhydrophobicity. Song et al. [4] utilised electrochemical machining to generate copper substrate surfaces exhibiting superhydrophobic properties. Their process also boasts of being environment-friendly due to the usage of a neutral NaCl electrolyte. Panjwani et al. [5] utilised dip coating method to generate a thin film coating of Ultra-High-Molecular-Weight Polyethylene (UHMWPE) on Ti6Al4V alloy to induce hydrophobicity on its surface. The surfaces exhibited a water CA of $135.5 \pm 3.3°$ and they displayed allowable amounts of cytotoxicity in related tests. A PFPE overcoat improved self-lubrication and wear durability of the surface. Kyzioł et al. [6] performed Plasma Assisted Chemical Vapour Deposition (PA MW CD) on the titanium alloys such as, Ti6Al4V and γ-TiAl to improve mechanical and surface properties such as hardness, roughness, surface energy and contact angle toward improving the applicability of these alloys as bioimplants. γ-TiAl which was hydrophilic in nature, showed good hydrophobicity after plasma etching and SiCNH coating.

The advantages offered by electrical discharge machining (EDM) over other methods, which are currently in use for altering the wetting properties of metallic surfaces, are the possibility of generating surfaces with high roughness values which are devoid of any directional properties and the surface energy reduction on the surface, without requirement of any additional coating, due to the formation of compounds with carbon and oxygen atoms. To the best of our knowledge, our work will be the first on introducing the usage of EDM for wetting property alteration on metallic surfaces. Non-textured stainless steel 304 (SS 304) surface displays hydrophilic properties which enhance with an increase in the surface roughness [7]. Wetting properties of different stainless steel find importance in applications where metal–fluid contact occurs such as, energy generation, petrochemical and food storage [8]. In the present work, we study the change in the wetting properties of SS 304 surfaces subjected to the EDM process.

66.2 Materials and Methodology

66.2.1 Materials

Stainless steel 304 (SS 304) is selected as the work material on which the wetting properties need to be altered. SS 304 samples are precision milled to a dimension of 15 mm × 15 mm × 4 mm. Then they are polished using sandpaper of Grade 220 to obtain a flat and smooth surface. Copper rods of 10 mm diameter are selected as the tool electrode material. They are faced to obtain a smooth finish and the circular end is used in texturing of the samples. Paraffin oil is used as the dielectric. Four SS 304 samples (say, a, b, c and d) are fixed close together in the fixture to form a larger square of 30 mm × 30 mm dimension and the spark erosion process is performed with the central axis of the copper rod passing through the joint of these samples.

66.2.2 Electrical Discharge Machining Process

Experiments are conducted on Electronica Smart S50 CNC EDM. The operating parameters that varied during experimentation are pulse on-time, discharge current and gap voltage. These parameters are varied in the ranges of 10 µs–100 µs, 5 A–50 A and 10 V–100 V, respectively.

66.2.3 Contact Angle Measurement

GBX contact angle instrument, a telescope-goniometer, was used for contact angle measurements on the textured SS 304 samples. Sessile drop method, which is a frequently used method for contact angle measurement, is followed. It offers the advantages of requiring only smaller textured areas for measurement and smaller amounts of liquid for drop formation and additionally offers an approximate accuracy of ±2° [9]. The liquid used in the sessile drop method was deionized water and the drop size was kept constant at 1.8 μl.

66.2.4 Surface Roughness Measurement

Alicona Infinite Focus microscope, an optical profilometer, is used for the measurement of the surface roughness parameters. Measurements are done with a 10× magnification such that the field of view is of a similar area as compared to the drop size with nearly 1.5 mm diameter. A total of 25 different surface roughness parameters were measured on each of the electrical discharge textured surfaces. These parameters and their description are summarised in Table 66.1.

66.3 Results and Discussion

66.3.1 Contact Angle Analysis

Experiments are performed in EDM varying the parameters such as pulse on-time, discharge current and gap voltage to find the variation of the MCA with respect to these parameters. MCA values measured on different textured samples fall in the range 101.9°–127.45°. The effects of different parameters on MCA are discussed in the following sections.

Pulse on-time. The variation of MCA with pulse on-time is shown in Fig. 66.1a. It could be observed that the MCA shows an increase with the increase in pulse duration. The highest value of MCA is observed at a pulse on-time value of 75 μs. There is an increase in surface roughness with an increase in pulse duration in the EDM process. As per Wenzel, an increase in surface roughness leads to an increase in the wetting property of the surface. Thus an increased surface roughness could attribute to an increase in the contact angle.

Discharge current. The variation of MCA with discharge current is shown in Fig. 66.1b. It could be understood that MCA shows an increase with increase in the discharge current. Again, an increase in surface roughness with discharge current would have led to an increase in the contact angle.

Table 66.1 Surface roughness parameters

Sl. No.	Designation	Unit	Description
	Surface texture parameters		
1.	S_a	µm	Average height of selected area
2.	S_q	µm	Root-mean-square height of selected area
3.	S_p	µm	Maximum peak height of selected area
4.	S_v	µm	Maximum valley depth of selected area
5.	S_z	µm	Maximum height of selected area
6.	S_{10z}	µm	Ten-point height of selected area
7.	S_{sk}		Skewness of selected area
8.	S_{ku}		Kurtosis of selected area
9.	S_{dq}		Root-mean-square gradient
10.	S_{dr}	%	Developed interfacial area ratio
11.	FLT_t	µm	Flatness using least squares reference plane
	Bearing area parameters		
12.	S_k	µm	Core roughness depth, height of the core material
13.	S_{pk}	µm	Reduced peak height, mean height of the peaks above the core material
14.	S_{vk}	µm	Reduced valley height, mean depth of the valleys below the core material
15.	S_{mr1}	%	Peak material component, the fraction of the surface which consists of peaks above the core material
16.	S_{mr2}	%	Peak material component, the fraction of the surface which will carry the load
17.	V_{mp}	ml/m^2	Peak material volume of the topographic surface (ml/m^2)
18.	V_{mc}	ml/m^2	Core material volume of the topographic surface (ml/m^2)
19.	V_{vc}	ml/m^2	Core void volume of the surface (ml/m^2)
20.	V_{vv}	ml/m^2	Valley void volume of the surface (ml/m^2)
21.	V_{vc}/V_{mc}		Ratio of V_{vc} parameter to V_{mc} parameter
	Auto-correlation parameters		
22.	S_{al}	µm	Auto-correlation length
23.	S_{tr}		Texture aspect ratio
24.	S_{td}	°	Texture direction degree
25.	S_{tdi}		Texture direction index

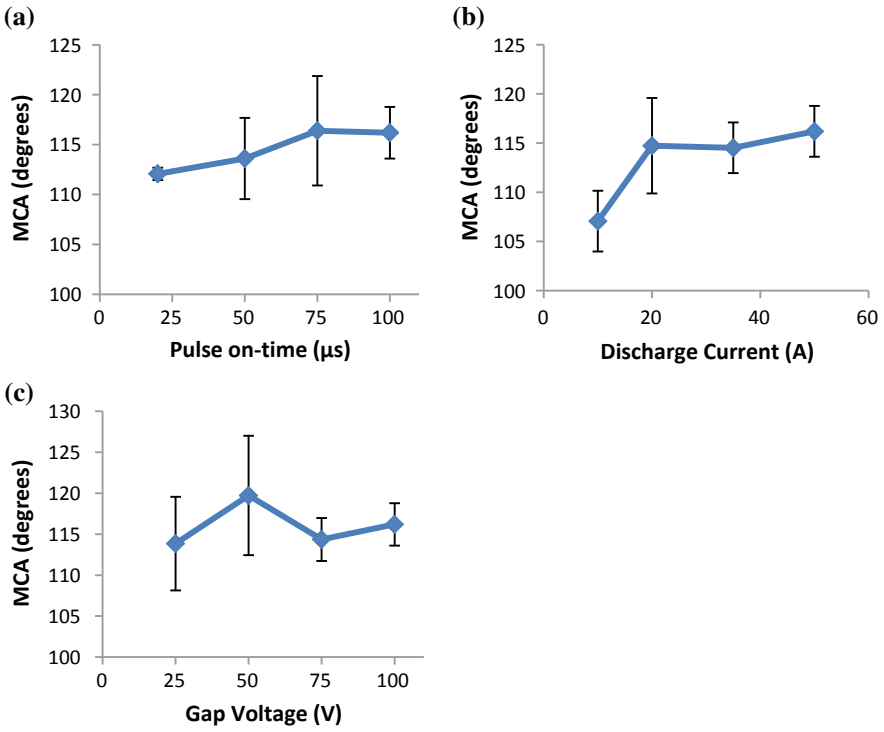

Fig. 66.1 Variation of MCA with, **a** pulse on-time, **b** discharge current, and **c** gap voltage

Gap voltage. The variation of MCA with gap voltage is shown in Fig. 66.1c. It could be observed that the highest value of MCA is obtained at a gap voltage of 50 V. This may be due to the suitable microstructure generation at the particular voltage value.

66.3.2 Correlation Between MCA and Surface Roughness Parameters

A correlation between MCA and surface roughness parameters of the EDMed surface is desired so as to know which parameter influences the hydrophobicity exhibited by the surface. Toward this, Pearson's correlation coefficient (r) between MCA values and corresponding surface roughness parameters measured is evaluated as follows [10]:

$$r = \frac{S_{xy}}{S_x S_y}. \tag{66.1}$$

where S_{xy} is the covariance and S_x and S_y are the standard deviation. Pearson's correlation coefficient gives the degree of linear relationship between the two variables. It can have a value between $+1$ and -1, where $+1$ represents full positive correlation, 0 represents no correlation and -1 represents full negative correlation. Pearson's correlation coefficient between MCA and different surface roughness parameters were evaluated and are given in Table 66.2.

It could be understood from Table 66.2 that good positive correlation with MCA is exhibited by surface parameters such as S_{sk}, S_{mr1}, S_{mr2}, V_{vc}/V_{mc} and S_{al} with r values greater than 0.35. The parameter which exhibited the highest correlation with MCA was S_{mr2} with an r value of 0.48. A good correlation with S_{sk} shows that the third-order roughness influences contact angle, the most. The correlation of the first-, second- and fourth-order roughness parameters such as S_a, S_q and S_{ku}, respectively, does not show good correlation with MCA. The variations of MCA with the parameters S_{sk}, S_{mr1}, S_{mr2}, V_{vc}/V_{mc} and S_{al} are shown in Fig. 66.2. It could be observed from these graphs that MCA increases with an increase in these parameters.

66.4 Conclusions

This work deals with introducing EDM as a method for inducing hydrophobicity on SS 304 surface. The following are the major conclusions:

1. This work introduces EDM as a feasible process to induce the wetting property change in metals from hydrophilic to hydrophobic.
2. Measured contact angle (MCA) shows a continuous increase with the parameters such as, pulse on-time and discharge current. With gap voltage, MCA shows a maximum value at a gap voltage value of 50 V.
3. Correlation between MCA and different surface roughness parameter is studied by evaluating Pearson's correlation coefficient (r). The surface parameters such as S_{sk}, S_{mr1}, S_{mr2}, V_{vc}/V_{mc} and S_{al} showed good positive linear correlation with MCA. Among these parameters, S_{mr2} showed the highest correlation with MCA with an r value of 0.48.

Table 66.2 Pearson's correlation coefficient between MCA and different roughness parameters

Parameter	S_a	S_q	S_p	S_v	S_z	S_{10z}	S_{sk}	S_{ku}	S_{dq}
r	0.08	0.05	0.02	−0.06	−0.01	−0.06	0.35	−0.16	−0.19
Parameter	S_{dr}	FLT_t	S_k	S_{pk}	S_{vk}	S_{mr1}	S_{mr2}	V_{mp}	V_{mc}
r	−0.18	−0.01	0.06	0.11	−0.20	0.38	0.48	0.10	0.08
Parameter	V_{vc}	V_{vv}	V_{vc}/V_{mc}	S_{al}	S_{tr}	S_{td}	S_{tdi}		
r	0.15	−0.17	0.37	0.36	−0.02	0.04	−0.09		

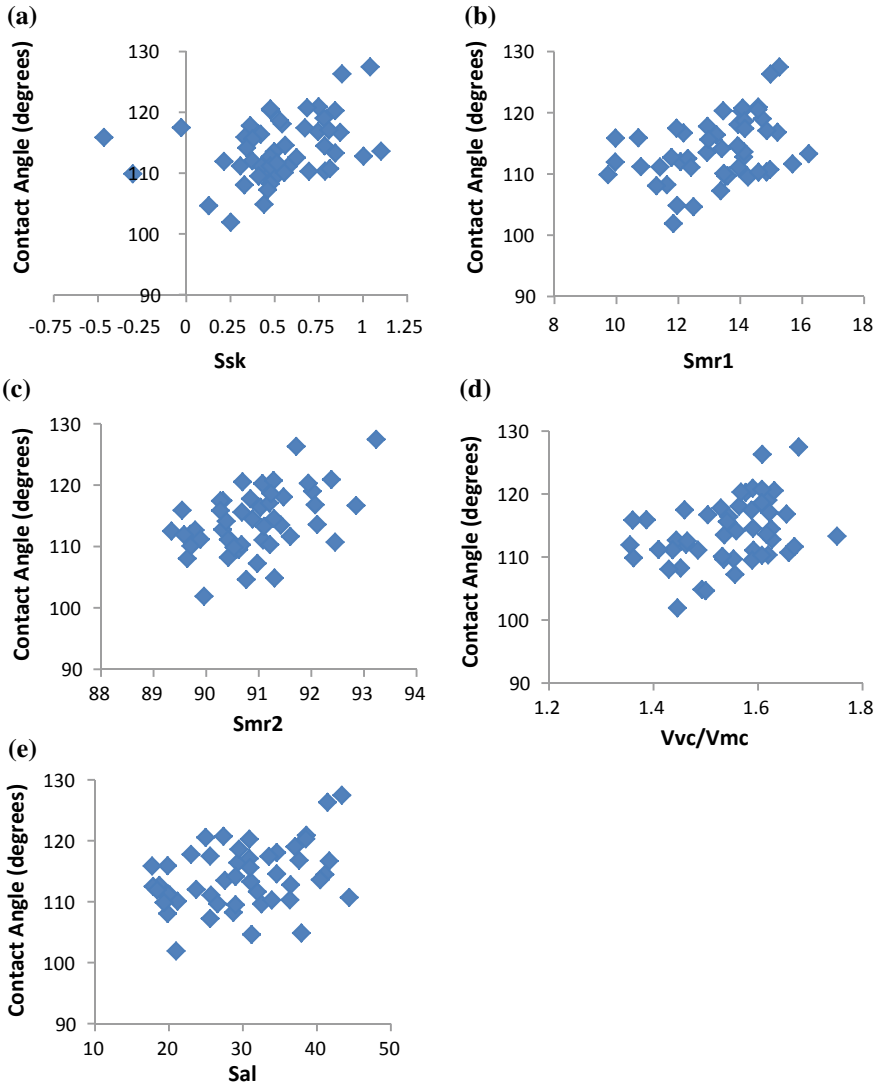

Fig. 66.2 MCA versus surface roughness parameters

References

1. Patel, D.S., Singh, A., Balani, K., Ramkumar, J.: Topographical effects of laser surface texturing on various time-dependent wetting regimes in Ti6Al4V. Surf. Coat. Technol. **349**, 816–829 (2018)
2. Singh, A., Patel, D.S., Ramkumar, J., Balani, K.: Single step laser surface texturing for enhancing contact angle and tribological properties. Int. J. Adv. Manuf. Technol. **100**, 1253 (2019)

3. Sun, J., Zhang, F., Song, J., Wang, L., Qu, Q., Lu, Y., Parkin, I.: Electrochemical fabrication of superhydrophobic Zn surfaces. Appl. Surf. Sci. **315**, 346–352 (2014)
4. Song, J., Xu, W., Lu, Y., Fan, X.: Rapid fabrication of superhydrophobic surfaces on copper substrates by electrochemical machining. Appl. Surf. Sci. **257**, 10910–10916 (2011)
5. Panjwani, B., Satyanarayana, N., Sinha, S.K.: Tribological characterization of a biocompatible thin film of UHMWPE on Ti6Al4V and the effects of PFPE as top lubricating layer. J. Mech. Behav. Biomed. Mater. **4**, 953–960 (2011)
6. Kyzioł, K., Kaczmarek, Ł., Brzezinka, G., Kyzioł, A.: Structure, characterization and cytotoxicity study on plasma surface modified Ti-6Al-4V and γ-TiAl alloys. Chem. Eng. J. **240**, 516–526 (2014)
7. Prajitno, D.H., Maulana, A., Syarif, D.G.: Effect of surface roughness on contact angle measurement of nanofluid on surface of stainless steel 304 by sessile drop method. J. Phys. Conf. Ser. **739**, 012029 (2016)
8. Kurtuldu, F., Altuncu, E.: Surface wettability properties of 304 stainless steel treated by atmospheric-pressure plasma system. In: 4th International Symposium on Innovative Technologies in Engineering and Science, pp. 1350–1357 (2016)
9. Yuan, Y., Lee, T.R.: Surface science techniques. In: Contact Angle and Wetting Properties. Springer, Berlin (2013)
10. Beins, B.C., McCarthy, M.A.: Research Methods and Statistics. Pearson Education Inc., New Jersey (2012)